

Gruppo Nazionale di Geofisica della Terra Solida

Atti del 40° Convegno Nazionale

27 - 29 GIUGNO 2022

TRIESTE - STAZIONE MARITTIMA

21° CONVEGNO NAZIONALE

Gruppo Nazionale di Geofisica della Terra Solida

40°
CONVEGNO NAZIONALE

27 - 29 GIUGNO 2022

TRIESTE - STAZIONE MARITTIMA

21° CONVEGNO NAZIONALE

GRUPPO NAZIONALE DI GEOFISICA DELLA TERRA SOLIDA

40° Convegno Nazionale

COMITATO TECNICO SCIENTIFICO

A seguito della Convenzione in atto tra Istituto Nazionale di Oceanografia e di Geofisica Sperimentale-OGS, Consiglio Nazionale delle Ricerche, Consorzio ReLUIS, Dipartimento della Protezione Civile, Istituto Nazionale di Geofisica e Vulcanologia e Sezione Italiana EAGE –SEG si è costituito il Comitato tecnico scientifico del Gruppo Nazionale di Geofisica della Terra Solida(GNGTS), così composto:

Presidente:
Alessandro REBEZ
Istituto Nazionale di Oceanografia
e di Geofisica Sperimentale - OGS
arebez@inogs.it

Componenti:
Daniela DI BUCCI
Presidenza del Consiglio dei Ministri,
Dipartimento della Protezione Civile
Daniela.DiBucci@protezionecivile.it

Claudio CHIARABBA
Istituto Nazionale di Geofisica
e Vulcanologia INGV
claudio.chiarabba@ingv.it

Paolo MESSINA
Consiglio Nazionale delle Ricerche CNR
paolo.messina@cnr.it

Paolo GASPERINI
Università degli Studi di Bologna
----mail------

Andrea TOGNARELLI
Università degli Studi di Pisa
----mail------

Angelo MASI
Consorzio della Rete dei Laboratori
Universitari di Ingegneria Sismica
ReLUIS, Università di Potenza
angelo.masi@unibas.it

Coordinatrice della Segreteria GNGTS:
Giulia MASSOLINO
Istituto Nazionale di Oceanografia
e di Geofisica Sperimentale - OGS
----mail------

Segreteria Organizzativa:
William TOSON, Muzio BOBBIO,
Alessandro ASTA, Luca PICOTTI
Istituto Nazionale di Oceanografia
e di Geofisica Sperimentale - OGS

Atti a cura di Alessandro Rebez e Giulia Massolino
con la collaborazione di Muzio Bobbio e William Toson

ISBN: 978-88-940442-9-4

Impaginazione:
Lugliоprint, Trieste

Care colleghe, cari colleghi,
inserire testo.

Nome Cognome

"...cerco qualcosa: un briciolo di conoscenza in questo nostro piccolo grande pianeta. E in me stesso..." L. C. 1989.

PREMIO DELL'ASSOCIAZIONE PER LA GEOFISICA "LICIO CERNOBORI" - 2022

L'Associazione per la Geofisica Licio Cernobori -AGLC, è nata il 30 ottobre del 2000 per ricordare Licio Cernobori, geofisico prematuramente scomparso nell'agosto 2000. Geologo, sismologo passato poi alla sismica crostale, Licio univa alla grande competenza scientifica, ad una serietà e correttezza morale rare, un carattere solare ed un'incredibile disponibilità verso colleghi, amici e studenti, descritta bene con le parole dell'amico e collega Alik Ismail Zadeh "He was happy working especially when working to help and encourage others".

La Sua passione per il lavoro ed il generoso impegno con cui ha contribuito a formare tanti giovani, non solo scientificamente, ha spinto un gruppo di amici e colleghi a creare qualcosa che potesse continuare idealmente nelle motivazioni che stavano alla base del pensiero di Licio.

L'Associazione ha come fine la promozione degli studi geofisici e soprattutto la formazione scientifica e la crescita dei più giovani.

Tale fine è stato perseguito in un primo tempo attraverso l'elargizione di un premio di studio presso l'Università di Trieste, aperto anche a laureandi/laureati in Geofisica Applicata di altre università o strutture scientifiche coinvolte in progetti comuni con l'Ateneo di Trieste (2001-2009).

Dal 2010, il suo decennale, l'AGLC ha iniziato la tradizione dei premi per i giovani relatori al Congresso annuale GNGTS. Dal 2012 il premio è stato suddiviso tre premi di 700,00 €, uno per ciascuno dei Temi del convegno: *Geodinamica, Caratterizzazione sismica del territorio e Geofisica applicata*.

Nel 2021, a poco più di vent'anni dalla scomparsa di Licio e dalla nascita dell'Associazione, ha avuto luogo un Workshop dei Giovani Ricercatori, in forma telematica, in cui i candidati hanno potuto presentare in anteprima il loro lavoro alla commissione ed ai colleghi. A rendere ancora più bello l'evento è stato il fatto che ricercatori che avevano in passato ricevuto il premio sono stati tra i convenors delle varie sessioni del workshop o inseriti nella commissione.

Quest'anno l'evento è stato ripetuto, sempre in modalità telematica, la settimana prima del convegno GNGTS (22-23 giugno 2022). Il II Workshop dei Giovani Ricercatori è stato quest'anno intitolato a Lorenzo Petronio, improvvisamente mancato ad aprile 2022, membro del Consiglio direttivo dell'AGLC, e da subito sostenitore dell'associazione e delle sue iniziative. Lorenzo era Dirigente Tecnologo dell'OGS, coordinatore del gruppo di geofisica a terra, e vice direttore della sezione GEO. Laureatosi in Scienze Geologiche presso l'Università di Trieste in Geofisica applicata, si era poi perfezionato con un Dottorato in Geofisica Applicata presso la Facoltà di Ingegneria. Lì la sua strada si era incrociata con quella di Licio, di 10 anni più vecchio

e che per Lorenzo era stato un riferimento. Lorenzo all'OGS ha portato tutta la sua curiosità ed entusiasmo, ma soprattutto la sua passion per la sismica in primo luogo. Il suo pallino era l'acquisizione, conscio che acquisire buoni dati è la condizione necessaria per qualsiasi successiva elaborazione ed interpretazione. E sono innumerevoli le applicazioni in cui ha portato la sua inventiva, caparbietà, e competenza. L'altra passione era la comunicazione, soprattutto ai giovani. Non mancava mai alle varie iniziative di OGS di divulgazione scientifica, e negli ultimi anni teneva le esercitazioni per un corso presso l'Università di Padova, i cui studenti ancora ricordano un insegnante preparato e dall'entusiasmo contagioso.

È stato quindi immediato, da parte dei rimanenti membri del CD, pensare di dedicare alla memoria del nostro caro amico il Workshop dei giovani ricercatori di quest'anno.

I lavori presentati erano 21, tutti di alta qualità, e ben presentati: la commissione ha discusso molto prima di scegliere i vincitori:

Davide Zaccagnino, per il lavoro: (D. Zaccagnino e C. Doglioni) *Tectonic setting and fault roughness vs. earthquake double couple*;

Teresa Tufaro, per il lavoro: (T. Tufaro, C. Amadio, M. Fasan, S. Noè, M. Santulin) *Proposta per una metodologia di valutazione del rischio sismico di una rete stradale nella Regione Friuli Venezia Giulia*;

Giacomo Roncoroni, per il lavoro: (G. Roncoroni, E. Forte, M. Pipan) *Deep Attributes: extraction of GPR statistical features with Deep Learning*.

I lavori sono poi stati ripresentati nel corso del successivo convegno GNGTS, e la premiazione è avvenuta nel corso dell'Assemblea del GNGTS, in quella che è ormai una bella consuetudine.

Per altre informazioni, per diventare socio, contribuire a continuare e migliorare le iniziative dell'Associazione per la Geofisica Licio Cernobori –AGLC, scrivete a HYPERLINK "mailto:-grossi@ogs.it," grossi@ogs.it, HYPERLINK "mailto:costa@units.it" costa@units.it, HYPERLINK "mailto:mromanelli@ogs.it" mromanelli@ogs.it, assoaglc@gmail.com.

Indice

Tema 1 - Geodinamica 1

Sessione 1.1 - Strutture sismogeniche, deformazione attività e sismicità associata in Italia. Nuove vedute e vecchi problemi 3

HOW TO ESTIMATE THE RELIABILITY OF MICRO-EARTHQUAKE FAULT PLANE SOLUTIONS?
G.M. Adinolfi, R. De Matteis, R. de Nardis, A. Zollo 5

INTEGRAZIONE E ANALISI DELLE STORIE SISMICHE DELLE LOCALITÀ ITALIANE
A. Antonucci, A. Rovida, V. D'Amico, D. Albarello 6

SEISMOGENIC FAULTS, LANDSLIDES AND TSUNAMIS IN THE IONIAN SEA: A CRITICAL ASSESSMENT
A. Argnani, A. Armigliato, F. Zaniboni, G. Gallotti, C. Angeli, M. Zanetti, S. Tinti 7

UNVEILING TRANS-RIDGE EN-ECHELON FAULT PATTERNS POSSIBLY RESPONSIBLE FOR THE 1857 BASILICATA EARTHQUAKE (Mw 7.1)
S. Bello, G. Lavecchia, C. Andrenacci, M. Ercoli, D. Cirillo, F. Carboni, M.R. Barchi, F. Brozzetti, ... 10

REVISIONE DELLA SISMICITÀ 'MINORE', UN CONTRIBUTO AL MIGLIORAMENTO DELLE STIME DI PERICOLOSITÀ
F. Bernardini, R. Camassi , C.H. Caracciolo, V. Castelli, E. Ercolani 12

WHAT WAS THE ROLE OF FAULTS IN THE EVOLUTION OF THE MONTEREALE BASIN (CENTRAL APENNINE)? CONSIDERATIONS AND NON-EXHAUSTIVE ANSWERS
E. Chiarini, G. Nirta, A. Sciortino, M. Spadi, M. Tallini 17

NEAR-SOURCE ATTENUATION AND SPATIAL VARIABILITY OF THE SPECTRAL DECAY PARAMETER KAPPA IN CENTRAL ITALY
R.R. Castro, L. Colavitti, C.A. Vidales-Basurto, F. Pacor, S. Sgobba, G. Lanzano 21

ACTIVE TECTONICS AND FAULT EVOLUTION IN THE WESTERN BALKANS
N. D'Agostino, A. Copley, J. Jackson, R. Koci, A. Hajrullai, L. Duni, N. Kuka 27

APPROCCIO NEOTETTONICO PER L'INDIVIDUAZIONE E DEFINIZIONE DELL'ATTIVITÀ E CAPACITÀ DELLA FAGLIA DI LEONESSA, APPENNINO CENTRALE
E. Falcucci, S. Gori, D. Maceroni, G. Dixit Dominus, F. Chiaretti, D. Cosentino, M. Moro, F. Doumaz, V. Materni, V. Sapia, G. Di Giulio, M.Vassallo, M.G. Di Giuseppe, R. Isaia, F. Tramparulo, M. Saroli, F. Galadini, V. Sepe 28

ASSESSING THE CAPABILITY OF THE PESCOPAGANO FAULT, PART OF THE ANTITHETIC FAULT OF THE 1980, MW 6.9 IRPINIA EARTHQUAKE (SOUTHERN ITALY)
L. Ferranti, F. Iezzi, A. Bacchiani, S. Buoninfante, F. Menna, M. Sposato, V. Di Fiore, D. Bellini, A. Citterio, R. Calabrò, C. Pasqua 30

3D-KERNEL BASED IMAGING OF AN IMPROVED ESTIMATION OF Q_c IN THE GARGANO PROMONTORY (SOUTHERN ITALY)
M. Filippucci, S. Lucente, E. Del Pezzo, S. de Lorenzo, G. Prosser, A. Tallarico 32

INFLUENCE OF FLUID MIGRATION AND FRACTURING IN THE CENTRAL ITALY SEISMIC SEQUENCE FROM SCATTERING ATTENUATION AND INTRINSIC ABSORPTION
S. Gabrielli, A. Akinci, F. Napolitano, E. Del Pezzo, L. De Siena 34

IL SISTEMA DI FAGLIE ATTIVE DEL GRAN SASSO ED IL CATASTROFICO TERREMOTO DEL 1349: UN'ATTRAZIONE FATALE
P. Galli, A. Galderisi, P. Messina, E. Peronace 38

A REGIONAL COLLECTION OF FAULT/SLIP DATA AND ASSOCIATED STRAIN PARAMETERS FOR THE INTRA-APENNINE EXTENSIONAL BELT OF CENTRAL ITALY
G. Lavecchia, S. Bello, C. Andrenacci, D. Cirillo, F. Ferrarini, R. de Nardis, G. Roberts, F. Brozzetti 41

DETECTION OF LOW FREQUENCY EARTHQUAKES AT MT. VESUVIUS
BY USING A FREQUENCY DOMAIN APPROACH
R. Manzo, D. Galluzzo, M. La Rocca, L. Nardone, R. Di Maio 44

EVOLUZIONE GEOMORFOLOGICA ED IMPLICAZIONI TETTONICHE TARDO
QUATERNARIE DELL'AREA DI CAMPO IMPERATORE (GRAN SASSO, ITALIA CENTRALE)
P. Messina, P. Galli, E. Peronace 48

VALUTAZIONE DEGLI EFFETTI DI AMPLIFICAZIONE SISMICA NELLE AREE
DEL COMUNE DI CANTIANO (PU) COLPITE DALLA SEQUENZA SISMICA DEL 1781
E. Paolucci, V. Castelli, G. Monachesi, M. Ariano, D. Albarello 50

HOLOCENE LARGE EARTHQUAKES RECORDED IN THE CALABRIA OFFSHORE SEDIMENTS
A. Polonia, E. Colizza, P. Galli, L. Gasperini, D. Insinga, R. Melis 52

INTERPRETAZIONE GEOLOGICA DELLA SEQUENZA SISMICA 2016–2017 DELL'ITALIA CENTRALE
A PARTIRE DA DATI DI SPOSTAMENTO AL SUOLO RILEVATI MEDIANTE GNSS E LIVELLAZIONE GEOMETRICA
R. Salvini, C. Vanneschi, C. Lanciano, R. Maseroli 56

A RESISTIVITY CRUSTAL PROFILE ACROSS THE SOURCE OF THE OCTOBER 30, 2016
Mw 6.5 NORCIA EARTHQUAKE (CENTRAL ITALY)
S. Tripaldi, M. De Girolamo, L. Improta, G. Romano, V. Sapia, A. Siniscalchi, I. Ventola, F. Villani 57

CONVERGENCE BETWEEN ADRIA AND EURASIA PLATES: INSIGHTS FROM GNSS
TIME SERIES IN NORTH-EEASTERN ITALY
L. Tunini, A. Magrin, D. Zuliani, G. Rossi 59

THE ROLE OF COULOMB STRESS TRANSFER IN THE EVOLUTION OF SEISMIC CYCLES:
INSIGHTS FROM THE CENTRAL APENNINE FAULT SYSTEM
G. Valentini, T. Volatili, P. Galli, E. Tondi 60

TECTONIC SETTING AND FAULT ROUGHNESS VS EARTHQUAKE DOUBLE COUPLE
D. Zaccagnino, C. Doglioni 64

SPATIAL AND TEMPORAL EVALUATION OF THE PARAMETERS
OF THE GUTENBERG-RICHTER LAW, CASE OF STUDY: ITALY
A. Figlioli, A. D'Alessandro, R. Martorana, A. Sulli, G. Vitale 66

THE SEA OF GALILEE (NORTHEAST ISRAEL), A PROMISING SITE FOR STUDYING
RELATIONSHIPS BETWEEN SEISMICITY AND FLUID-FLOW
L. Gasperini, M. Lazar, A. Polonia 71

PRELIMINARY ESTIMATION OF QB IN THE GARGANO PROMONTORY (SOUTHERN ITALY)
S. Lucente, T. Ninivaggi, S. de Lorenzo, E. Del Pezzo, M. Filippucci, A. Tallarico 73

A 41 ANNI DAL TERREMOTO DEL 1980: RESILIENZA E RICOSTRUZIONE NELL'ALTA VALLE DEL CALORE (AV)
M. Pizza, A.M. Michetti, M.F. Ferrario, A. Capone, R. Nappi, S. Porfido 75

PRESENT AND MEDIEVAL DESTRUCTIVE EARTHQUAKES IN DURRES (ALBANIA):
NEW INSIGHTS FROM INTEGRATED ARCHAEOLOGICAL AND GEOPHYSICAL STUDIES
D. Talone, S. Antonelli, F. Brozzetti, C. Casolino, C. Cirillo, E. Metalla, G. Lavecchia, R. de Nardis 80

Sessione 1.2 - Vulcani e campi geotermici 83

TOMOGRAFIA SISMICA DELL'AREA DEL CAMPO GEOTERMICO DI NESJAVELLIR (ISLANDA)
O. Amoroso, F. Napolitano, G.P. Hersir, T. Ágústsdóttir, V. Convertito, R. De Matteis, V. Hjörleifsdóttir,
S.H. Gunnarsdóttir, P. Capuano 85

LAND SURFACE TEMPERATURE (LST) DETECTED THROUGH LANDSAT 8 SATELLITE
MISSION AT CAMPI FLEGREI CALDERA (SOUTHERN ITALY)
A. Barone, E. Bellucci Sessa, S. Caliro, T. Caputo, R. Castaldo, G. Chiodini, S. Pepe, M. Silvestri,
D. Stroppiana, P. Tizzani 90

THE DYNAMIC EVOLUTION OF LARGE CALDERAS: CURRENT UNREST AT CAMPI FLEGREI, SOUTHERN ITALY
S. Carlino, C.R.J. Kilburn, S. Danesi, N.A. Pino 92

THE AEOLIAN ISLANDS: A POTENTIAL GEOTHERMAL ENGINE
C.G. Caruso, A. Gattuso, G. Lazzaro, M. Longo, M. Meschis, S. Scirè Scappuzzo, F. Italiano 94

STA/LTA AUTOMATIC CUT OF EXPLOSION QUAKES
A. Di Benedetto, A. Figlioli, A. D'Alessandro, G. Lo Bosco 95

REMOBILIZATION AND ERUPTION OF AN UPPER CRUSTAL CUMULATE MUSH:
THE SINGKUT CALDERA (NORTH SUMATRA, INDONESIA)
F. Forni, J.A. Oalmann, G. Fellin, S. Eisele, M. Phua, O. Bernard, M. Guillong, H. Rifai, C. Bouvet de Maisonneuv . 99

SLOW SLIP EVENTS AT MT. ETNA VOLCANO
M. Palano, F. Sparacino, P. Gambino, N. D'Agostino, S. Calcaterra 101

CHEMICAL ANOMALIES IN THE GAS PHASE RELEASED FROM THE SANTA VENERA AL POZZO
THERMAL SPRING (MT. ETNA, SICILY, ITALY): POSSIBLE INFLUENCE FROM LOCAL TECTONIC ACTIVITY
F. Sortino, S. Giammanco, P. Bonfanti, C. Bottari 103

3D- INFLATING SOURCE IMAGING AND STRESS/STRAIN FIELD ANALYSIS
AT CAMPI FLEGREI DURING THE MAJOR UNREST EPISODES
P. Tizzani, R. Castaldo, G. Solaro, S. Pepe, A. Pepe, V. De Novellis, A. Barone, A. Vitale, A. Tramelli 107

2021-2022 HUNGA TONGA-HUNGA HA'APAI ERUPTIONS STUDIED
FROM LITHOSPHERE, ATMOSPHERE AND IONOSPHERE
S. D'Arcangelo, A. Bonforte, A. De Santis, R. Maugeri, L. Perrone, M. Soldani, F. Brogi, M. Calcara,
S.A. Campuzano, G. Cianchini, A. Del Corpo, D. Di Mauro, A. Ippolito, S. Lepidi, D. Marchetti, C. Montagna,
A. Nardi, M. Orlando, A. Piscini, M. Regi, D. Sabbagh 108

RELATIVE EARTHQUAKE LOCATION AND PRELIMINARY SEISMOLOGICAL ANALYSES
ON LOW-ENERGY VOLCANIC SEISMICITY AT CAMPI FLEGREI
S. Danesi, N.A. Pino, S. Carlino, P. Ricciolino, D. Delle Donne, C. Martino 109

FIRST STEPS TOWARDS THE UPPER CRUSTAL STRUCTURE INVESTIGATION
IN THE AREA OF MEFITE D'ANSANTO (ITALY) BY USING TELESEISMIC EVENTS
G. Milano, A. Gervasi, S. Morabito, P. Cusano, P. Del Gaudio, D. Galluzzo, G. Gaudiosi, M. La Rocca,
L. Nardone, S. Petrosino, L. Zuccarello 112

MAGNETIC INVESTIGATION AT VULCANO ISLAND: PRELIMINARY RESULTS
FROM A MULTIDISCIPLINARY GEOPHYSICAL SURVEY
S. Scudero, S. Bongiovanni, A. D'Alessandro, A. Figlioli, R. Martorana, S. Speciale, A. Pisciotta, G. Vitale 115

FORECASTING SOIL CO2 FLUX AT MT. ETNA VOLCANO
S. Scudero, A. D'Alessandro 119

ANALYSIS OF EFFUSION RATE ON MT ETNA FLANK ERUPTIONS AND THEIR IMPACT
IN ASSESSING THE LAVA FLOW HAZARDS
F. Zuccarello, G. Bilotta, A. Cappello, G. Ganci 123

Sessione 1.3 - Modelli fisici per la Terra Solida e integrazione fra modellistica e dati di natura differenti 125

PERFORMANCE OF EMPIRICAL AND MODEL DERIVED ATMOSPHERE CORRECTIONS OF INSAR TIME SERIES
M. Bartola, C. Braitenberg, Y. Fialko 127

MAPPING THE 2021 LA PALMA ERUPTIVE SEQUENCE THROUGH MULTI-SPECTRAL
AND SAR IMAGES OF THE SENTINEL SATELLITES
C. Braitenberg, T. Pivetta, F. Stefan 130

LA SEQUENZA SISMICA DELLA TESSAGLIA (GRECIA CENTRALE) DEL MARZO 2021:
MODELLO GEODETICO DEDOTTO DA DATI SISMOLOGICI E INSAR
V. De Novellis, D. Reale, G.M. Adinolfi, V. Convertito, E. Sansosti 131

MANTLE DYNAMICS AND STRUCTURE FROM COUPLED GEODYNAMIC AND SEISMOLOGICAL MODELLING
M. Faccenda 137

COSEISMIC FOLDING DURING RAMP FAILURE AT THE FRONT OF THE SULAIMAN FOLD-AND-THRUST BELT
M.T. Javed, S. Barbot, F. Javed, C. Braitenberg, A. Ali 138

CALIBRAZIONE DEI COEFFICIENTI DI GARDNER SFRUTTANDO OSSERVAZIONI DEL CAMPO GRAVITAZIONALE:
IL CASO STUDIO DELLA PENISOLA ARABA E DELL'ALTOPIANO DELL'IRAN
G. Maurizio, M. Capponi, D. Sampietro, C. Braitenberg 144

A GEOLOGICAL REVIEW OF THE GARGANO PROMONTORY (SOUTHERN ITALY)
WITH SEISMIC AND GEODETIC DATA
S. Miccolis, M.M.C. Carafa, M. Filippucci, J.P. Merryman Boncori, A. Tallarico 148

LA SEQUENZA SISMICA DELLA TESSAGLIA (GRECIA CENTRALE) DEL MARZO 2021:
CARATTERIZZAZIONE DELLA STRUTTURA CROSTALE MEDIANTE TOMOGRAFIA SISMICA LOCALE
F. Napolitano, O. Amoroso, V. De Novellis, G.M. Adinolfi, V. Convertito, R. De Matteis, E. Sansosti, R. Caputo . . . 149

HOW DOES SEISMIC ATTENUATION CORRELATE TO RHEOLOGY
OF CRUSTAL ROCKS? RESULTS FROM NUMERICAL AND LAB EXPERIMENTS
M.A. Natale Castillo, M. Tesauro, M. Cacace, F.X. Thibault Passelegue, L. Pimienta, M. Violay 153

POST-RIFT THERMAL SUBSIDENCE: SHOULD WE ACCOUNT FOR THE LATERAL HEAT TRANSFER?
A NUMERICAL EXPERIMENT IN PALEO-BATHYMETRY RECONSTRUCTION
A. Pastorutti, M. Tesauro, C. Braitenberg, F. Colleoni, L. De Santis, M. Busetti 159

CRUSTAL STRUCTURES OF THE ZAGROS MOUNTAINS COLLISION BELT AND THE IRANIAN PLATEAU
FROM A COMBINATION OF ISOSTATIC, SEISMIC AND GRAVIMETRIC OBSERVATIONS
T. Pivetta, C. Braitenberg, A. Pastorutti, M. Tesauro 161

GEOPHYSICAL AND GEOLOGICAL INVESTIGATION IN THE AREA NE OF MENFI (SOUTH-WESTERN SICILY)
S. Bongiovanni, R. Martorana, A. D'Alessandro, C. Bignami, A. Canzoneri, A. Sulli 162

MULTIPHYSICS FINITE ELEMENT MODELLING OF SOLFATARA HYDROTHERMAL SYSTEM
R. Castaldo, A. Barone, G. Chiodini, G. Gola, G. Solaro, P. Tizzani 165

DESIGN AND REALIZATION OF A MEASUREMENT NODE FOR GRAVIMETRIC APPLICATIONS
J.J. Jiménez, A. Albano, V. Carbone, F. Lamonaca 167

ROLE OF CRUSTAL FLUIDS AND THERMO-MECHANICAL STRUCTURE FOR LOWER
CRUSTAL SEISMICITY: THE GARGANO PROMONTORY (SOUTHERN ITALY)
A. Lavecchia, M. Filippucci, A. Tallarico, G. Selvaggi, G. Cecere, S. Cloetingh 170

A MULTIPARAMETRIC AND MULTILAYER APPROACH TO STUDY THE PREPARATION PHASE
OF LARGE EARTHQUAKE OCCURRED IN JUNE 15 2019, M7.2 IN KERMADEC ISLANDS (NEW ZEALAND)
M. Orlando, A. De Santis, L. Perrone, M. Calcara, S.A. Campuzano, G. Cianchini, S. D'Arcangelo,
D. Di Mauro, D. Marchetti, A. Nardi, A. Piscini, D. Sabbagh, M. Soldani 171

A RECENT SEISMIC COUPLING ESTIMATION FOR THE AEGEAN - ANATOLIAN REGION
M. Palano, F. Sparacino, B.G. Galuzzi, M. Segou, C. Chiarabba 172

PARAMETRIC STUDY OF THE EFFECTS OF MICRO-CONTINENTS COLLISION
IN AN OCEANIC SUBDUCTION SYSTEM BY 2D NUMERICAL SIMULATIONS
A. Regorda, M. Roda, C. Thieulot 173

THE 1968 BELICE SEISMIC SEQUENCE (SOUTH ITALY): NEW RESULTS FROM DIGITIZED ANALOG DATA
S. Scolaro, B. Orecchio, J. Batlló, D. Stich, G. Neri, D. Presti, C. Totaro 174

THERMAL STRUCTURE OF THE UPPER MANTLE IN THE ZAGROS COLLISION ZONE AND SURROUNDINGS
M. Tesauro, A.Pastorutti, T. Pivetta, C. Braitenberg, I. Koulakov 176

APPLICATION OF GRAVITATIONAL GROUNDWATER FLOW SYSTEMS
TO IRPINIA AREA (SOUTHERN APENNINES, ITALY): PERSPECTIVES AND IMPLICATIONS
E. Vitagliano, N. D'Agostino 178

Tema 2 - Caratterizzazione sismica del territorio 181

Sessione 2.1 - Verso nuove modalità di stima della pericolosità da terremoti e maremoti: dati e procedure 183

PERICOLOSITÀ SISMICA PROBABILISTICA NELL'ISOLA DI ISCHIA: MODELLO CONCETTUALE E PRIMI RISULTATI
R. Azzaro, V. Convertito, S. D'Amico, H. Langer, B. Pace, L. Peruzza, G. Tusa, F. Visini 185

EARTHQUAKE SOURCE PARAMETERS ESTIMATED FROM DIRECT S-WAVES
AND CODA ENVELOPES ANALYSIS PERFORMED IN CENTRAL ITALY
D. Bindi, P. Morasca, D. Spallarossa, M. Picozzi, K. Mayeda, J. Roman-Nieves, J. Barno, W.R. Walter 191

APPLICATION OF THE EEPAS SEISMIC FORECASTING METHOD TO ITALY
E. Biondini, D. Rhoades, P. Gasperini 194

PROPOSAL OF ZONATIONS FOR THE REGIONALIZATION OF THE GROUND MOTION MODELS IN ITALY
G. Brunelli, G. Lanzano, L. Luzi, S. Sgobba 197

ANALYSIS OF RESIDUALS FROM A SET OF GROUND MOTION MODELS IN THE NEAR SOURCE
A. Chiecchio, R. Paolucci, M. Vanini 201

UN NUOVO APPROCCIO, 'TIME DEPENDENT', PER LA STIMA DELLA PERICOLOSITÀ SISMICA IN ITALIA
G. De Natale, P. Harabaglia, M. Vona, G. Martinelli, V. Marchitelli, C. Troise 205

PROBABILITY, CORRELATION, AND TRANSFER ENTROPY
BETWEEN WESTERN PACIFIC EARTHQUAKES AND NOAA ELECTRON BURSTS
C. Fidani, A. De Santis, L. Perrone 207

NESTOREV1.0: A MACHINE LEARNING-BASED MATLAB PACKAGE
FOR FORECASTING STRONG AFTERSHOCKS IN SEISMIC CLUSTERS
S. Gentili, P. Brondi, R. Di Giovambattista 211

ESTIMATING LOCAL EMPIRICAL SITE AMPLIFICATION MODEL FOR CITY OF LUCERNE IN SWITZERLAND
P. Janusz, V. Perron, C. Knellwolf, D. Fäh 212

HOMOGENIZATION OF MAGNITUDES OF THE ISC ONLINE BULLETIN
B. Lolli, D. Randazzo, G. Vannucci, P. Gasperini 217

LOCAL EARTHQUAKE CONDITIONAL PROBABILITY BASED ON LONG TERM CO_2 MEASUREMENTS
L. Pierotti, C. Fidani, G. Facca, F. Gherardi 218

THE RAPID ASSESSMENT OF SEISMIC MOMENT AND RADIATED ENERGY (RAMONES) SERVICE
D. Spallarossa, M. Picozzi, D. Scafidi, P. Morasca, D. Bindi, G. Tarchini 221

CARATTERIZZAZIONE DEL MOTO DEL SUOLO AD ISCHIA ATTRAVERSO SIMULAZIONE SINTETICHE
G. Tusa, V. Convertito, S. D'Amico, E. Giampiccolo, H. Langer, R. Azzaro 224

TEMPORAL VARIATIONS OF SEISMICITY FROM THE APPLICATION OF TSALLIS ENTROPY
E. Varini, R. Rotondi, G. Bressan 229

NESTOREV1.0 APPLICATION TO ITALIAN SEISMICITY
P. Brondi, S. Gentili, R. Di Giovambattista 230

KINEMATIC AND DEPTH CONTROL ON MAGNITUDE-FREQUENCY RELATIONS:
A CASE STUDY FROM SOUTHERN CALIFORNIA
A. Carducci, A. Petruccelli, Rita de Nardis, A. De Santis, G. Lavecchia 231

AN UPDATE OF THE CENTRAL ITALY ELECTROMAGNETIC NETWORK WITH RADON DETECTORS
C. Fidani, G. De Antoni, T. Milan, M. Siciliani, S. Tadioli 232

SIMULATIONS OF TSUNAMIS INDUCED BY SUBMARINE MASS FAILURES ON THE CALABRIAN IONIAN MARGIN
G. Gallotti, F. Zaniboni, A. Armigliato, S. Ceramicola, N. Markezic, C. Angeli, M. Zanetti 234

INTRODUCING INFERRED GEOMORPHOLOGICAL SEDIMENT THICKNESS
AS A NEW SITE PROXY TO PREDICT GROUND-SHAKING AMPLIFICATION
K. Loviknes, F. Cotton, G. Weatherill 235

ABOUT THE ROLE OF NW-TRENDING FAULT SYSTEMS IN THE MESSINA STRAITS AREA
G. Neri, P. Pino, D. Presti, S. Scolaro, S. D'Amico, C. Navarra, B. Orecchio, A. Torre 237

GEO-INQUIRE – A NEW OPPORTUNITY FOR EXPLOITING EUROPEAN GEOSCIENCE INFRASTRUCTURE
FOR CURIOSITY-DRIVEN RESEARCH THROUGH TEST SITES AND TRAINING
F. Cotton, A. Strollo, K. Fleming, G. Festa, S. Murphy, M. Majdański, Geo-INQUIRE Consortium 238

VARIABILITY OF SOURCE PARAMETERS IN CENTRAL-SOUTHERN EUROPE
M-H Yen, D. Bindi, R. Zaccarelli, A. Oth, B. Edwards, F. Cotton 239

Sessione 2.2 - Scienza e tecnica a supporto della prevenzione e della preparazione al terremoto 245

SEISMIC VULNERABILITY OF HISTORIC GLASS ENVELOPES: TOWARDS A STANDARDIZED EVALUATION
PROTOCOL FOR HARMONIZED PERFORMANCE CHECK
C. Bedon 247

MODELLO DI AMPLIFICAZIONE SISMICA PER LA SVIZZERA BASATO SU INDICATORI
DI CONDIZIONE DI SITO E SULLA RISPOSTA SISMICA LOCALE MISURATA ALLE STAZIONI SISMICHE
P. Bergamo, F. Panzera, C. Cauzzi, F. Glüer, V. Perron, D. Fäh 252

ASSESSMENT OF THE EFFECT OF SEISMIC SEQUENCES ON STEEL X-CBF FOR INDUSTRIAL BUILDINGS
L. Bomben, M. Fasan, C. Amadio 255

INVESTIGATION OF THE ROCK AVALANCHE DEPOSIT OF YANG JIA GOU
(SICHUAN-CHINA) THROUGH THE INTEGRATION OF PASSIVE SEISMIC TECHNIQUES
P. Capone, V. Del Gaudio, J. Wasowski, N. Venisti, H. Wei 261

MANAGING THE URBAN COMPLEXITY OF VERNACULAR APPENINE CENTERS: THE CASE STUDY OF SCARPERIA
V. Cardinali, M.T. Cristofaro, M. De Stefano, M. Ferrini, R. Nudo, B. Paoletti, M. Tanganelli 266

STIMA DEGLI EFFETTI DI SITO DA DATI DI VS IN EMILIA-ROMAGNA
G. Carloni, G. Ercolessi, L. Martelli 270

EFFICACIA DI STRATEGIE DI MITIGAZIONE SISMICA PER IL PATRIMONIO EDILIZIO ITALIANO IN MURATURA
P. Carpanese, V. Follador, M. Donà, F. da Porto 275

FRAGILITY CURVES FOR URM BUILDINGS TYPOLOGIES IN A HISTORICAL
CENTER OF CENTRAL ITALY: THE INFLUENCE OF SEISMIC INPUT
V. Cima, V. Tomei, E. Grande, M. Imbimbo 280

FIRST RESULTS OF AMBIENT NOISE DATA ANALYSIS
FROM THE ONGOING SEISMIC MICROZONATION OF THE APULIA REGION
V. Del Gaudio, J. Wasowski, C. Magrì 285

IRPINIA 1980-2020: OCCUPARSI DI RISCHIO SISMICO DURANTE UNA PANDEMIA
E. Ercolani, F. Brasini, V. Castelli, D. Modonesi, V. Pessina, R. Camassi 290

GROUND MOTION SIMULATIONS OF THE HISTORICAL FABRIANO (1741, Mw=6.17)
AND CAMERINO (1799, Mw=6.18) EARTHQUAKES (CENTRAL ITALY)
V. Gironelli, T. Volatili, L. Luzi, G. Brunelli, M. Zambrano, E. Tondi 294

SEISMIC LOSS ASSESSMENT FOR THE CITY OF AJDOVŠČINA (SLO)
L. Hofer, M.A. Zanini 297

SUI SIMULATORI DELLE CURVE HVSR
E. Lunedei, A. Tanzini, E. Paolucci, D. Albarello 301

SEISMO-STRATIGRAPHIC MODEL FOR THE MILAN (ITALY) METROPOLITAN AREA BY AMBIENT-VIBRATION
MONITORING AND IMPLICATIONS FOR SEISMIC SITE EFFECTS ESTIMATION
M. Massa, S. Lovati, R. Puglia, G. Brunelli, A. Lorenzetti, C. Mascandola, C. Felicetta, F. Pacor, L. Luzi 303

FRAGILITY ASSESSMENT OF GLASS COMPONENTS BY SINGLE-DEGREE OF FREEDOM APPROXIMATION
S. Mattei, C. Bedon 305

MACHINE LEARNING BASED HIGH RESOLUTION GROUND MOTION MAPS
F. Mori, M. Moscatelli 310

BB-SPEEDSET: AN OPEN-SOURCE DATASET OF NEAR-SOURCE BROADBAND EARTHQUAKE
GROUND MOTION FROM 3D PHYSICS-BASED NUMERICAL SIMULATIONS
R. Paolucci, C. Smerzini, M. Vanini 311

TOWARDS AN ALTERNATIVE APPROACH TO DEFINE THE DESIGN EARTHQUAKE SCENARIO AT A SITE
R. Paolucci, A. Chiecchio, M. Vanini 315

TESTING SITE AMPLIFICATION CURVES IN HYBRID BROADBAND GROUND-MOTION
SIMULATIONS OF M6.0, 24 AUGUST 2016 AMATRICE EARTHQUAKE, ITALY
M. Pischiutta, A. Akinci, C. Felicetta, F. Pacor, P. Morasca 319

SELECTION OF THE SEISMIC INPUT FOR SITE RESPONSE NUMERICAL SIMULATIONS
WITHIN THE SEISMIC MICROZONATION IN THE APULIAN REGION
A. Romeo, P. Pierri, D. Casarano, V. Del Gaudio 321

EMPIRICAL NONERGODIC GROUND SHAKING SCENARIOS FOR CENTRAL ITALY:
METHODOLOGY AND APPLICATIONS
S. Sgobba, F. Pacor, G. Lanzano 326

PHYSICS-BASED GROUND SHAKING SCENARIOS FOR EMPIRICAL FRAGILITY
STUDIES: THE CASE-STUDY OF THE 2009 L'AQUILA EARTHQUAKE
C. Smerzini, A. Rosti, R. Paolucci, A. Penna, M. Rota 329

FRAGILITY CURVES FOR REINFORCED CONCRETE FRAMES CHARACTERIZED BY DIFFERENT REGULARITY
G. Smiroldo, M. Fasan, C. Amadio 334

DALL'HVSR ALLA FUNZIONE DI RISPOSTA DI SITO:
POTENZIALITÀ E PROBLEMATICHE DEDOTTE DALLA MODELLAZIONE 1D
A. Tanzini, E. Paolucci, D. Albarello 342

PROPOSTA PER UNA METODOLOGIA DI VALUTAZIONE DEL RISCHIO SISMICO
DI UNA RETE STRADALE NELLA REGIONE FRIULI VENEZIA GIULIA
T. Tufaro, C. Amadio, M. Fasan, S. Noè, M. Santulin 345

MAPPE DI PERDITA REGIONALI PER LA MITIGAZIONE DEL RISCHIO SISMICO
M.A. Zanini, L. Hofer, F. Faleschini, C. Pellegrino 350

FIRST SEISMIC IMPACT ANALYSIS FOR PRE-ERUPTIVE EVENTS IN ISCHIA
G. Zuccaro, D. De Gregorio, F.L. Perelli 355

L'ANALISI DELLA CONDIZIONE LIMITE DELL'EMERGENZA A DIECI ANNI DALLA SUA ISTITUZIONE.
UN PRIMO STRUMENTO PER INDAGARNE GLI EFFETTI SULLA GOVERNANCE TERRITORIALE
M.S. Benigni, C. Fontana, M. Giuffrè, V. Tomassoni 360

STRUCTURAL MONITORING OF A HIGHWAY BRIDGE IN A HIGH-SEISMIC HAZARD URBAN AREA
A. D'Alessandro, S. Bongiovanni, A. Costanzo, A. Di Benedetto, A. Figlioli, S. Scudero, S. Speciale, G. Vitale 367

POSTHOLE BROADBAND SENSORS FOR THE UPGRADE OF THE SEISMIC NETWORK IN SICILY
WITHIN THE GRINT (ITALIAN RESEARCH INFRASTRUCTURE FOR GEOSCIENCES) PROJECT
A. D'Alessandro, S. Bongiovanni, P. Cosenza, A. Di Benedetto, A. Figlioli, S. Scudero, S. Speciale, G. Vitale 371

SEISMIC SITE AMPLIFICATION AT PERMANENT STATIONS IN NORTHEASTERN ITALY
P. Klin, G. Laurenzano, C. Barnaba, E. Priolo, S. Parolai 375

EARTHQUAKE MONITORING NETWORKS: A COMPARISON BETWEEN HIGH SEISMIC RISK COUNTRIES
S. Scudero, A. D'Alessandro 377

Tema 3 - Geofisica applicata 383

Sessione 3.1 - Geofisica per le Georisorse 385

R/V LAURA BASSI SOUTHERN OCEAN TRANSITS AS AN OPPORTUNITY TO COLLECT UNDERWAY DATA
IN ANTARCTIC WATER: ISOBATA PROJECT AND COLLABORATION AMONG PNRA PROJECTS
D. Accettella, A. Savini, M. Cuffaro, P. Divacco, F. Muccini, F. Coslovic, L. Facchin, R. Codiglia, D. Cotterle,
A. Cova, L. De Santis, L. Gasperini, V. Kovacevic, M. Santulin, R. Scipinotti, L. Ursella 387

INTEGRATED MULTI-GEOPHYSICAL AND GEOLOGICAL WORKFLOW
FOR GEOTHERMAL RESOURCE EXPLORATION AND CHARACTERIZATION
R. Bachrach, T. Cassola, L. Masnaghetti, G. Sosio 390

3D THERMAL MODELING CONSTRAINED BY CURIE ISOTHERM
Y. Kelemework, M. Fedi 392

UNDERGROUND HYDROGEN STORAGE IN ITALY
S. Mattera1, E. Barison1, F. Donda1, U. Tinivella1, B. Merson1, A. Réveillère2, C. Vincent3 394

A PILOT APPLICATION OF GUIDELINES FOR GEOPHYSICAL MONITORING
OF HYDROCARBON CULTIVATION: PRACTICAL ISSUES FROM THE CAVONE OIL FIELD
L. Zaccarelli, M. Anselmi, M. Vassallo, I. Munafò, L. Faenza, L. Sandri, A. Garcia, M. Polcari, G. Pezzo,
E. Serpelloni, L. Anderlini, M. Errico, I. Molinari, G. Zerbinato, A. Morelli 395

CHARACTERIZATION OF SEISMIC NOISE AMPLITUDE RECORDED BY A VERTICAL ARRAY INSTALLED
IN A DEEP BOREHOLE AT THE S. POTITO-COTIGNOLA GAS STORAGE FIELD (NORTHERN ITALY)
C. Rossi, F. Grigoli, P. Gasperini, S. Gandolfi, T. Gukov, C. Cocorullo, P. Macini 397

Sessione 3.2 - Geofisica per l'Ambiente 399

ON THE REVERBERATION EFFECT IN MULTI-CHANNEL ANALYSIS. SURFACE WAVES
POLARIZATION AS QUICK TOOL FOR SUBSOIL CHARACTERIZATION
I. Barone, J. Boaga, G.P. Deidda, G. Cassiani 401

MIOCENE MOUNDS AT THE ROSS SEA PALEO-CONTINENTAL SHELF:
EVIDENCE OF THE ONSET OF ANTARCTIC GLACIATIONS OR MUD VOLCANOES?
L. Barro Savonuzzi, G. Brancatelli, E. Forlin, L. De Santis, N. Wardell, R. Geletti, M. Busetti, A. Del Ben 402

DIAGNOSTIC MULTIDISCIPLINARY INVESTIGATIONS IN THE MOTHER CHURCH
AT MISTERBIANCO AT ETNA VOLCANO: A CASE-STUDY FROM THE 1669 ERUPTION
C. Bottari, P. Capizzi, R. Martorana, R. Azzaro, S. Branca, R. Civico, M. Fucile, E. Pecora 404

COOK GLACIER-OCEAN SYSTEM, SEA LEVEL AND ANTARCTIC
PAST STABILITY (COLLAPSE) PROJECT: PNRA CRUISE 2022 PRELIMINARY DATA
L. De Santis, F. Accaino, D. Accettella, J. Beagley, A. Bubbi, E. Colizza, F. Colleoni, F. Coslovich, D. Cotterle,
A. Cova, L. Facchin, A. Gallerani, L. Gasperini, D. Gei, R. Gerin, M. Giorgi, V. Kovacevic, P. Mansutti, E. Mauri,
S. Picotti, M. Petrini, E. Pochini, M. Santulin, R. Scipinotti, L. Ursella, A.C. Vallejo, F. Zgur, P. Zuppelli 410

QUALI PICCHI H/V SONO VERE RISONANZE NEL BACINO SEDIMENTARIO PADANO?
M. Di Donato, S. Castellaro 411

MULTISENSOR GEOPHYSICAL APPROACH FOR REBAR MONITORING
G. Fornasari, L. Capozzoli, G. De Martino, V. Giampaolo, E. Rizzo 416

LA STABILITÀ IN FREQUENZA DELLE RISONANZE NEI BACINI SEDIMENTARI
G. Lattanzi, S. Castellaro, M. Di Donato 418

QUATERNARY SLOPE INSTABILITY OFFSHORE SOUTHERN CALABRIA:
INSIGHTS ON POSSIBLE TRIGGERING MECHANISMS
N. Markezic, S. Ceramicola, L. Baradello, G. Brancatelli, D. Morelli, E. Colizza 423

PROSPEZIONI ELETTRO-MAGNETICHE NEL DOMINIO DELLA FREQUENZA
PER LA CARATTERIZZAZIONE DEL GHIACCIAIO DEL CALDERONE, GRAN SASSO D'ITALIA
M. Pavoni, A. Carrera, S. Urbini, F. De Blasi, J. Gabrieli, J. Boaga 427

ACTIVE AND PASSIVE SEISMIC AND ELECTRICAL METHODS FOR IMAGING
GAS UPWELLING FLOWS AT THE FIUMICINO COASTAL AREA (CENTRAL ITALY)
G. Penta de Peppo, G. De Donno, A. Bosman, E. Cardarelli, M. Cercato 430

OSSERVAZIONI CLIMATICHE E METEOROLOGICHE DAL RUMORE SISMICO
DEL SISMOMETRO IO.EVN (EVEREST - NEPAL)
F. Pettenati, M. Plasencia, G. Verza, D. Sandron 435

NOT ONLY CLEAN ICE INSIDE ALPINE GLACIERS:
A CASE STUDY ON THE SFORZELLINA GLACIER (CENTRAL ITALIAN ALPS)
I. Santin, E. Forte, M. Guglielmin 438

CHARACTERISATION OF ANTHROPOGENIC CAVITIES THROUGH INTEGRATED NON-INVASIVE
GEOPHYSICAL SURVEYS IN THE MEDIEVAL TOWN OF CAMPOROTONDO DI FIASTRONE, CENTRAL ITALY
A. Zaragoza, R. Teloni, M. Zambrano 442

HIGH RESOLUTION ELECTRICAL RESISTIVITY TOMOGRAPHY TO DETECT SUBSOIL
WATER SEEPAGE IN LANDSLIDES INVOLVING CLAY SLOPES
D. Barbero, A. Maroni, M. Naldi, S. Peyrot, E. Veronese 446

INTEGRATED ANALYSIS OF HVSR AND BOREHOLE DATA TO IMPROVE THE GEOLOGICAL MODEL
OF THE SUBSOIL OF PALERMO TOWN (SICILY, ITALY) IN THE ORETO RIVER AREA
A. Canzoneri, R. Martorana, M. Agate, P. Capizzi 452

SMALL-SCALE CHARACTERIZATION OF PLANT ROOT ARCHITECTURE
AND BIOMECHANICAL DYNAMICS VIA 4D ELECTRICAL RESISTIVITY TOMOGRAPHY
A. Carrera, J. Boaga, S. Sartori, W. Bertoldi 456

MULTIDISCIPLINARY STUDY OF NON-VOLCANIC DEGASSING VENT FIELD
IN THE SOLOPACA AREA (SOUTHERN APENNINES)
C. De Paola, S. Albanese, M. Ambrosino, S. Ciarcia, D. Cicchella, R. Di Maio, C. Fabozzi, P. Notaro,
F. Pagliara, E.P. Prinzi, R. Salone, S. Vitale 459

GPR AND ULTRASONIC TOMOGRAPHY APPLIED TO PRESTRESSED CABLES
FOR VERIFYING VIADUCT CONSERVATION STATE
D. Di Massa, P. Luiso, D. Fiore 463

A GEOELECTRICAL STUDY AT THE SALSE DI NIRANO MUD VOLCANIC FIELD
A. Falconieri, D. Patella, A. Piombo, G. Romano, A. Siniscalchi, A. Tallarico, M. Antonellini 467

THE SALSE DI NIRANO MUD VOLCANIC FIELD: NEW GEOPHYSICAL RESULTS
AND THEIR HYDROGEOLOGICAL IMPLICATIONS
A. Falconieri, D. Patella, A. Piombo, G. Romano, A. Siniscalchi, A. Tallarico 468

A MULTI-METHODOLOGICAL SURVEY FOR THE RECONSTRUCTION OF PILES'
GEOMETRY: THE CASE OF A VIADUCT IN CALENZANO (FI), CENTRAL ITALY
P. Luiso, M. Taddeo, D. Fiore 469

Sessione 3.3 - Metodi e Tecnologia Innovative 475

INDAGINE MAGNETOMETRICA DA DRONE
PER LA MAPPATURA DI UN DICCO INCASSATO IN ROCCE CARBONATICHE
F. Accomando, A. Bonfante, M. Buonanno, G. Florio, J. Natale, S. Vitale 477

A BAYESIAN APPROACH TO FULL-WAVEFORM INVERSION: PRELIMINARY RESULTS
S. Berti, M. Aleardi, E. Stucchi 478

GRAVITY AND GRAVITY GRADIENTS JOINT INVERSION IN SALT BASINS THROUGH AN INTEGRATED WORKFLOW
L. Bianco, M. Tavakoli, A. Vitale, M. Fedi 484

INVERSIONE CONGIUNTA DEI CAMPI DI GRAVITÀ E MAGNETICO: I PRIMI RISULTATI DEL PROGETTO XORN ED IL CASO STUDIO DEL COMPLESSO DI OKA (CANADA)
M. Capponi, D. Sampietro, G. Maurizio 485

DETERMINATION OF THE VS PROFILE IN A NOISY INDUSTRIAL SITE: FURTHER EVIDENCES ABOUT THE IMPORTANCE OF LOVE WAVES AND THE OPPORTUNITIES OF THE GROUP VELOCITY ANALYSIS
G. Dal Moro 489

MASW? OLTRE LA SOGGETTIVITÀ NELL'ANALISI DELLE ONDE DI SUPERFICIE: VELOCITÀ DI FASE E GRUPPO NELLA RI-ELABORAZIONE FVS DI UN VECCHIO E COMPLESSO DATASET MULTI-COMPONENTE
G. Dal Moro 494

UNA TECNICA PER LA SEPARAZIONE DELLE COMPONENTI REGIONALE E LOCALE DEI CAMPI DI POTENZIALE BASATA SULL'USO DI DERIVATE VERTICALI FRAZIONARIE
G. Florio, M. Fedi, F. Cella 499

PREDIZIONE DELLA FORMA D'ONDA DELLO SCUOTIMENTO IN PROFONDITÀ, A PARTIRE DA REGISTRAZIONI DI TERREMOTI IN SUPERFICIE: APPLICAZIONE A SITI ED EVENTI GIAPPONESI
M. Hallo, P. Bergamo, D. Fäh 500

INTRODUCTION TO INTERPOLATION UNCERTAINTY OF THE NATURAL NEIGHBORS METHOD (SIBSON)
M. Iurcev, M. Majostorovic, F. Pettenati 504

DEEP PRECONDITIONERS FOR SEISMIC INVERSE PROBLEMS WITH APPLICATION TO DEBLENDING
V. Lipari, P. Bestagini, M. Ravasi, S. Tubaro 507

FECS: UN NUOVO METODO PER IL FILTRAGGIO DEI CAMPI DI POTENZIALE
M. Maiolino, M. Fedi, G. Florio 510

DEEP ATTRIBUTES: EXTRACTION OF GPR STATISTICAL FEATURES WITH DEEP LEARNING
G. Roncoroni, E. Forte, M. Pipan 511

A SEMBLANCE BASED MICROSEISMIC EVENT DETECTOR FOR DAS DATA
J. Porras, F. Grigoli, E. Stucchi, K. Tuinstra, A. Tognarelli, F. Lanza, M. Aleardi, A. Mazzotti, S. Wiemer 515

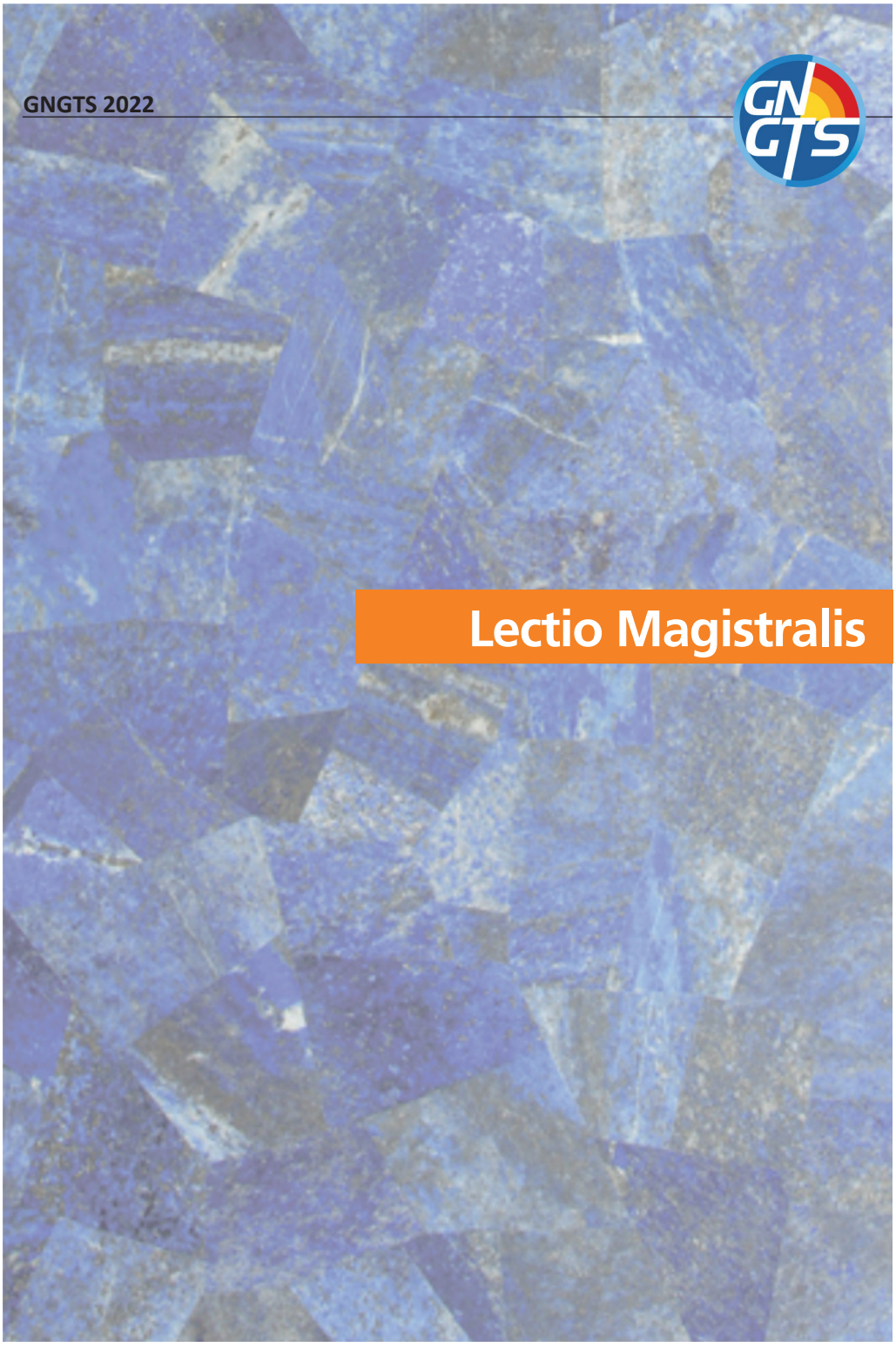
BAYESIAN APPROACH TO THE INVERSION OF MAGNETIC DATA FOR NEAR-SURFACE STUDIES. APPLICATION TO THE ARCHAEOLOGICAL SITE OF SAN PIETRO INFINE (SOUTHERN ITALY)
R. Salone, S. Tarantino, L. Spagnuolo, A. Frisetti, M. La Manna, A. Emolo, R. Di Maio 517

DIX INVERSION THROUGH MACHINE LEARNING
M. Tavoletti, F. Bleibinhaus, F. Grigoli, E. Stucchi 522

DEFINING THE BEST PROCESSING PROCEDURE FOR THE EVALUATION OF SEISMO-ELECTROMAGNETIC SIGNALS (SES) MEASURED DURING AN ACTIVE SEISMIC EXPERIMENT
I. Ventola, G. Romano, A. Siniscalchi, M. Balasco, S. Tripaldi 526

A STOCHASTIC ENSEMBLE BASED APPROACH FOR TIME-LAPSE ERT INVERSION
A. Vinciguerra, M. Aleardi, L. Meldgaard Madsen, T.S. Bording, A.V. Christiansen, E. Stucchi 528

UTILIZZO DI TECNICHE DI INTERFEROMETRIA TERRESTRE PER IL COLLAUDO DEL PONTE SAN GIORGIO DI GENOVA
S. Candela, C. Case, M. Cardamone, D. Fiore, F. Mittiga 532



Lectio Magistralis

SISMOLOGIA APPLICATA IN AREE DI FORTI TERREMOTI INTRA PLACCA: L'ESEMPIO DELLA VIA DELLA SETA

S. Parolai

Università degli Studi di Trieste - Dipartimento di Matematica e Geoscienze
via Weiss 4 Palazzina P - 34128 Trieste - email: stefano.parolai@units.it

Con il nome via della Seta vengono indicati una serie di percorsi che mettevano in comunicazione l'Europa con la Cina. Tutti questi percorsi attraversavano il territorio definito come Asia Centrale, oggi occupato principalmente da cinque paesi ovvero il Turkmenistan, l'Uzbekistan, il Tajikistan, il Kyrgyzstan e il Kazakhstan.

Durante il XIX secolo questo paesi furono al centro di una intensa attività militare e di spionaggio, che vide come protagonisti, in quello che Kipling definì "The Great Game", il Regno Unito e la Russia nella continua ricerca di un dominio od uno sbocco verso la ricca India. Gli avvenimenti di quel periodo, affascinanti da un punto di vista storico e che così tanto ci aiutano a capire gli avvenimenti attuali, sono stati narrati da Peter Hopkirk nel suo libro intitolato "The Great Game: On Secret Service in High Asia" (Hopkirk, 1990).

Mentre i due paesi belligeranti si affrontavano con un intricato gioco di spie, esploratori travestiti in territori sconosciuti, archeologi alla caccia di tesori di valore inestimabile sulle tracce della diffusione del buddismo, in questa area, con una delle più alte pericolosità sismiche al mondo, ebbero luogo forti terremoti intra-placca che hanno segnato lo sviluppo della sismologia.

Il primo terremoto sul quale ci soffermiamo è quello di Verny (nome dell'epoca dell'attuale Almaty, Kazakhstan), avvenuto nel giugno 1887 e di Magnitudo stimata 7.3 (Figura 1). Almaty all'epoca era un avamposto militare russo, fondato solo circa 30 anni prima (nel 1854), in un'area dominata dalle tribù nomadi. Non stupisce quindi che siano scarsissime le informazioni riguardanti eventi sismici precedenti. Tale terremoto, nonostante la forte Magnitudo e la breve distanza epicentrale stimata dalla città, fortunatamente, causò la perdita di solamente 300 vite (Nurmagambetov *et al.*, 1999).

Il terremoto segnò una svolta nella progettazione degli edifici in Almaty, che dapprima costruiti in pietra, vennero, sulla base delle indicazioni fornite da Zenkov (importante personalità locale) l'architetto comunale Gurde e il Prof. Mushketov, costruiti solamente in legno. Inoltre, nel 1900, sulla base dell'esperienza vissuta durante il terremoto di Verny fu proprio Zenkov a suggerire soluzioni che favorissero l'isolamento sismico degli edifici. Inoltre, vietò la costruzione con murature in pietra, mattoni e in argilla. La cattedrale di Almaty venne costruita con un sistema che venne definito "anti seismic basket" e resistette al terremoto successivo del 1911 di Kemin.

Questo terremoto, di magnitudo stimata 7.8-8, avvenne nel gennaio 2011 a circa 40 km dalla città di Verny. L'evento causò 390 decessi, diversi dei quali in una Verny che contava ancora circa lo stesso numero di abitanti del 1887 (Nurmagambetov *et al.*, 1999). Tuttavia a seguito di questo terremoto, e diversamente dall'evento del 1887, si osservarono grandi effetti di liquefazione e di cedimento del suolo (Figura 1). Le fratture generatesi, testimoniate anche da fotografie dell'epoca, misuravano alcuni metri di profondità ed un metro di larghezza. A seguito del terremoto venne organizzata una spedizione guidata da Bogdanovich che in quattro mesi di attività di campagna compì un rilievo di altissimo dettaglio degli effetti diretti ed indiretti del terremoto nella regione. Zenkov inoltre descrisse l'effetto delle coltri di materiali sedimentarie sciolte, che, in base alla sua esperienza, sembravano diminuire l'ampiezza dello scuotimento del suolo (probabilmente visto lo spessore delle coltri sedimentarie in Almaty, un effetto dell'attenuazione che prevale sulla amplificazione dovuta al contrasto di impedenza alle alte frequenze).

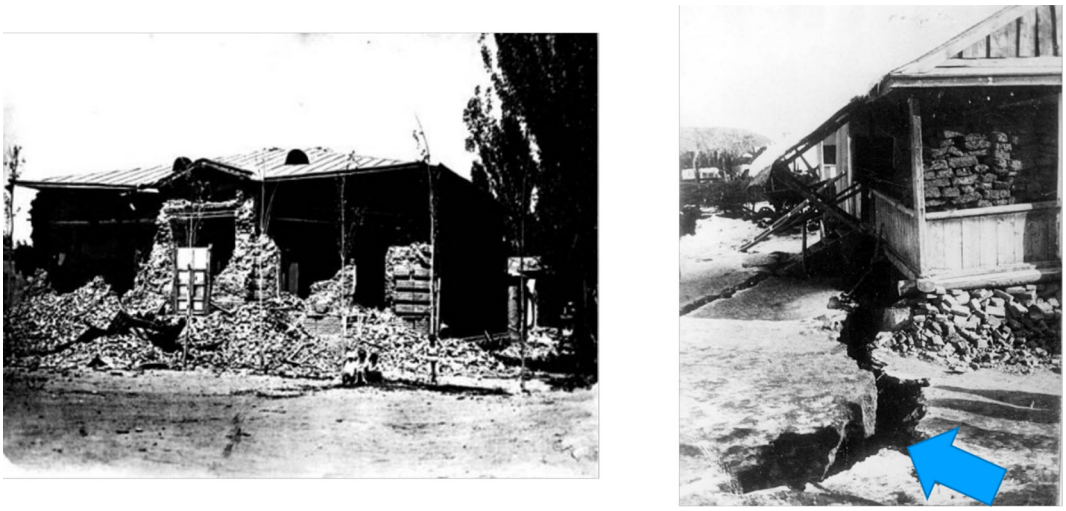


Fig. 1 - A sinistra) esempio di danno causato dal terremoto di Verny. A destra) danni e cedimenti del suolo causati dal terremoto di Kemin. (modificata da Nurmagambetov *et al.*, 1999).

Un terzo evento, il terremoto del 1948 di Ashgabat (Turkmenistan) di Magnitudo 7.3 (Sidorin, 2019) giocò un ruolo importante nello sviluppo della sismologia non solo della regione ma a livello mondiale. A seguito dello stesso, che causò un numero di morti stimati con grossa incertezza tra alcune centinaia sino a 120.000 (la cifra più attendibile è intorno ai 35.000 morti), venne sviluppata la rete sismometrica nell'ex Unione Sovietica ed iniziò una lunga ed importante tradizione in sismologia nell'ex Unione Sovietica e in particolare nei paesi centro asiatici. Non possiamo dimenticare, ad es., gli studi fondamentali per la sismologia di Kalturin e Rautian a Garm in Tajikistan.

La grande esperienza e le capacità sviluppate in Asia Centrale in ambito sismologico subirono un forte contraccolpo dopo la caduta del muro di Berlino. Nel frattempo le principali città dell'area erano cresciute a dismisura e la stessa Almaty non era più una piccola città di 30.000 abitanti ma un insediamento urbano di circa 1.500.000 persone.

Verso la fine della prima decade del XXI secolo, l'Helmholtz-Zentrum Potsdam Deutsches GeoForschungsZentrum GFZ, propose o fu coinvolto, in una serie di progetti scientifici che miravano alla stima della pericolosità e del rischio sismico, ed alla sua mitigazione, anche attraverso l'installazione di reti sismometriche, in Asia Centrale. Ne seguirono un vasto numero di attività di cui qua verrà fatto solo cenno di alcune ed in particolare a quelle legate alla stima degli effetti di sito nella città di Bishkek (capitale del Kyrgyzstan) e di Almaty (ex capitale del Kazakhstan).

A partire del 2008, ed in cooperazione con INGV e l'Istituto locale CAIAG, venne installata una rete sismometrica temporanea nell'area urbana di Bishkek. La rete, installata per diversi mesi, consentì la registrazione di molti eventi sismici locali e regionali (Parolai et al., 2010). I risultati misero anche in luce che utilizzando la Vs30 misurata dalla pendenza del rilievo topografico avrebbe portato a valutazioni non corrette dei fattori di amplificazione.

Le stazioni, inoltre, furono utilizzate per registrazioni di rumore sismico su stazione singola per il calcolo del rapporto H/V (e.g. Nakamura 1989). Utilizzando tecniche di K-means clustering (uno degli algoritmi di unsupervised learning) combinato a tecniche di cross-correlazione consentì, confrontando i rapporti spettrali H/V di rumore sismico e i rapporti spettrali standard di terremoti di incrementare la risoluzione spaziale della risposta di sito all'interno dell'area urbana (Ullah *et al.*, 2013)

Sempre al riguardo dello studio degli effetti di sito, ma anche per iniziare una serie di studi innovativi sull'interazione suolo-struttura, venne installato un array verticale con sensori accelerometrici sia in pozzo (il più profondo a 145 m di profondità) che in un edificio adiacente (Figura 2). I dati di tali installazione consentirono di studiare il fattore di qualità Q per la coltre sedimentaria del bacino, e di identificare fasi convertite profonde all'interfaccia tra i materiali sciolti ed il substrato roccioso, (Parolai *et al.*, 2013). Infine permisero di individuare, e stimarne l'energia, onde rilasciate dalla struttura a causa del suo scuotimento (Petrovic e Parolai, 2016).

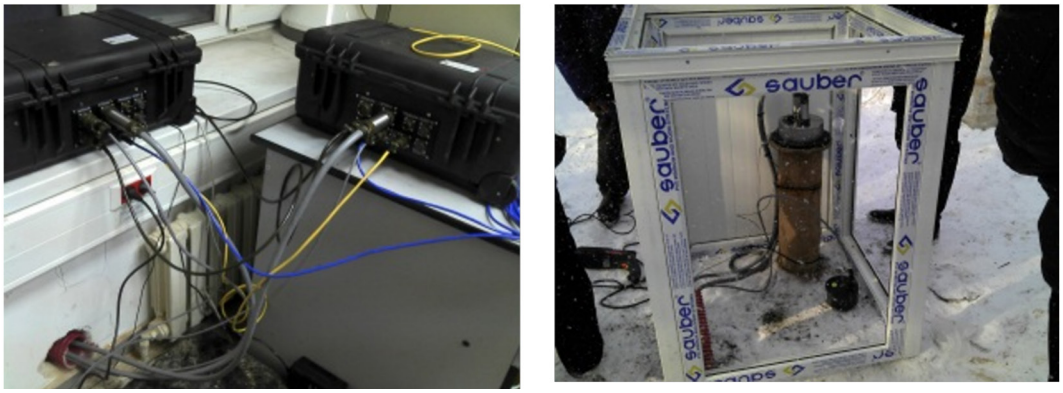


Fig. 2 - Installazione dell'array verticale a Bishkek (Kyrgyzstan).

In modo del tutto simile a quanto fatto per BIshkek, anche ad Almaty venne installata una rete sismometrica temporanea, così come vennero eseguite misure di rumore sismico su singola stazione. I dati registrati consentirono di stimare importanti effetti di amplificazione 2D e 3D nel bacino (Pilz *et al.*, 2018). Inoltre, le misure di rumore sismico furono utilizzate per l'applicazione di un approccio innovativo, che, a partire dai rapporti spettrali H/V di rumore sismico, ha consentito una ricostruzione ad alta risoluzione dei maggiori contrasti di impedenza, e delle faglie e discontinuità che li hanno generati (Parolai *et al.*, 2019).

Infine, i dati acquisiti sono stati preziosi per risolvere il quesito riguardante la maggiore generazione di fenomeni di liquefazione e di cedimenti del suolo da parte del terremoto di Kemin rispetto a quello di Verny (Alshembari *et al.*, 2019). Le simulazioni numeriche effettuate considerando i dati ottenute dagli esperimenti hanno evidenziato come l'occorrenza di liquefazione sia stata facilitata, all'epoca del terremoto di Verny, dalla presenza di uno strato superficiale di suolo congelato. Tale strato, impermeabile, non consentì la diffusione della pressione di poro che raggiunse, all'interfaccia tra lo strato congelato ed il terreno sottostante, i valori dello stress verticale.

Si vuole infine ricordare che tutte le attività sopra menzionate vennero svolte organizzando corsi, workshops e attività per facilitare il trasferimento della conoscenza, in stretta cooperazione con partners e utilizzatori locali.

Ringraziamenti. Un ringraziamento a tutti i compagni di avventura, e a chi mi ha fornito cortesemente del materiale per la presentazione, sperando di non aver dimenticato nessuno.
In ordine sparso: D. Bindi, A. Strollo, T. Boxberger, M. Pilz, S. Ullah, J. Zschau, S. Tyagunov, Massimiliano Pittore, Kevin Fleming, Marc Wieland, Joern Lauterjung, P. Augliera, E. D'alema, F. Maesano, R. Basili, R. Alshembari, N. Silacheva, S. Orunbaev, B. Moldobekov, D. Sandron, S. Usupaev, M. Picozzi, D. Di Giacomo, C. Milkereit.B. Petrovic, T. Abakanov., V. Poggi, C. Scaini, W. Frodella, V. Tofani

Tema 1

Geodinamica

Sessione 1.1

Strutture sismogeniche, deformazione attività e sismicità associata in Italia. Nuove vedute e vecchi problemi

Convenor: P. Galli e D'Agostino

HOW TO ESTIMATE THE RELIABILITY OF MICRO-EARTHQUAKE FAULT PLANE SOLUTIONS?

G.M. Adinolfi[1,3], R. De Matteis[1], R. de Nardis[2,3], A. Zollo[4]

[1] Dipartimento di Scienze e Tecnologie, Università degli Studi del Sannio, Benevento, Italy
[2] Dipartimento di Scienze Psicologiche, della Salute e del Territorio, Università di Chieti-Pescara "G. d'Annunzio", Chieti, Italy
[3] CRUST Centro inteRUniversitario per l'analisi SismoTettonica tridimensionale, Chieti, Italy
[4] Dipartimento di Fisica, Università di Napoli "Federico II", Complesso Universitario di Monte S.Angelo, Napoli, Italy

Earthquake focal mechanisms provide primary information on the kinematics of seismogenic faults and on the stress regime acting in a region. In the case of micro-seismicity monitoring, the source characterization is the most powerful tool for obtaining information on the fault structures, their stress level and for monitoring space-time evolution of seismicity due to natural or human-induced stresses. Despite the existence of several techniques operating in specific magnitude ranges, both in the time and frequency domain using different data as inputs (e.g., P polarities, S-wave polarization, S/P-amplitude ratios, etc.), the estimation of fault plane solutions can be a challenge when small magnitude earthquakes are analysed. The limited number of available data, the higher noise level or the weak knowledge of crustal structure at the wavelengths at which microearthquakes radiate severely affect the reliability of the focal mechanism solutions increasing their relative uncertainties.

In this work, we propose a useful methodology, as described in Adinolfi *et al.* (2022), to evaluate the reliability of earthquake focal mechanism as a function of magnitude, location, and kinematics of seismic source, using a Bayesian approach that jointly inverts the P/S long-period spectral-level ratios and the P polarities to infer the solution (De Matteis *et al.*; 2016). Additionally, from a theoretical point of view, we explore the capability of seismic networks, in terms of number and geographical location of stations, to constrain fault plane solutions of earthquakes taking into account the solution uncertainties. Hence, the proposed tool can be used with a double purpose: 1) to test the performance of local seismic networks to recover fault plane solutions and 2) to estimate the uncertainty of focal mechanism solutions when it is unavailable or not provided by other techniques.

We validate our methodology by computing synthetic data and testing the performance of the Irpinia Seismic Network, a local seismic network operating in the Campania–Lucania Apennines (Southern Italy) aimed to monitor the complex normal fault system activated during the M_s 6.9, 1980 earthquake. We prove the effectiveness of the proposed tool which can be easily customized for other case studies or network geometries.

References

Adinolfi, G. M., De Matteis, R., de Nardis, R., and Zollo, A.: *A functional tool to explore the reliability of micro-earthquake focal mechanism solutions for seismotectonic purposes,* Solid Earth, 13, 65–83, https://doi.org/10.5194/se-13-65-2022, 2022.

De Matteis, R., Convertito, V., and Zollo, A.: *BISTROP: Bayesian inversion of spectral-level ratios and P-wave polarities for focal mechanism determination,* Seismol. Res. Lett., 87, 944–954, https://doi.org/10.1785/0220150259, 2016.

INTEGRAZIONE E ANALISI DELLE STORIE SISMICHE DELLE LOCALITÀ ITALIANE

A. Antonucci[1], A. Rovida[1], V. D'Amico[2], D. Albarello[3]

[1] Istituto Nazionale di Geofisica e Vulcanologia, Milano, Italia
[2] Istituto Nazionale di Geofisica e Vulcanologia, Pisa, Italia
[3] Dipartimento di Scienze Fisiche, della Terra e dell'Ambiente, Università di Siena, Siena, Italia

La distribuzione spaziale degli effetti prodotti dai terremoti passati, espressi in termini di intensità macrosismica, costituisce lo strumento di base per la compilazione dei cataloghi sismici che, a loro volta, rappresentano un elemento chiave per le stime di pericolosità sismica. In Italia i dati di intensità di più di 3200 terremoti riferiti a 15343 località sono organizzati all'interno del Database Macrosismico Italiano – DBMI15 (Locati *et al.*, 2022) che rende disponibile la storia sismica di ciascuna località, ovvero la sequenza temporale di tutti gli effetti (valori di intensità) documentati dei terremoti passati.

Le ricostruzioni degli effetti provocati da uno o più terremoti possono tuttavia presentare dei vuoti informativi. Al fine di colmare questi vuoti, le intensità osservate in una località possono essere integrate grazie all'utilizzo di una relazione di attenuazione (Intensity Prediction Equation - IPE) che permette di calcolare l'intensità macrosismica in un dato sito in funzione della distanza dall'epicentro e della magnitudo/intensità epicentrale del terremoto (e.g., Pasolini et al., 2008). Un metodo alternativo per ridurre ed esprimere l'incertezza associata al valore di intensità stimato attraverso una IPE e per tenere conto del carattere discreto ed ordinale dell'intensità macrosismica è stato proposto da Antonucci *et al.* (2021). Questa metodologia utilizza un approccio probabilistico che permette di vincolare le stime fornite da una IPE sulla base dei valori di intensità osservati per un dato terremoto nelle località vicine (entro 20 km).

Al fine di individuare e valutare il numero degli effetti che, con una data probabilità, possono essersi persi in un dato sito, sono state integrate le storie sismiche di un insieme di località ed è stato confrontato il numero dei dati osservati e contenuti in DBMI15 sia con quelli calcolati utilizzando l'approccio probabilistico proposto da Antonucci *et al.* (2021), sia con quelli stimati a partire dal solo utilizzo di una IPE. Questa analisi mira a quantificare gli effetti che non sono stati osservati nel sito considerato ma che sono stati osservati nei siti vicini (entro 20 km) e gli effetti calcolati attraverso il solo utilizzo di una IPE, quando essi non sono stati documentati né nel sito considerato né nelle località limitrofe. I dati macrosismici osservati integrati con quelli calcolati possono essere utilizzati per definire la completezza delle informazioni disponibili in un sito, che a loro volta possono essere utilizzate per definire la completezza dei dati in un'area.

Bibliografia

Antonucci A., Rovida A., D'Amico V. and Albarello D.; 2021: *Integrating macroseismic intensity distributions with a probabilistic approach: an application in Italy*. Nat. Hazards Earth Syst. Sci., 21, 2299–2311, https://doi.org/10.5194/nhess-21-2299-2021.

Locati M., Camassi R., Rovida A., Ercolani E., Bernardini F., Castelli V., Caracciolo C.H., Tertulliani A., Rossi A., Azzaro R., D'Amico S. and Antonucci A.; 2022: *Database Macrosismico Italiano (DBMI15), versione 4.0*. Istituto Nazionale di Geofisica e Vulcanologia (INGV). https://doi.org/10.13127/DBMI/DBMI15.4.

Pasolini C., Albarello D., Gasperini P., D'Amico V. and Lolli B.; 2008: *The attenuation of seismic intensity in Italy, Part II: Modeling and validation*. B. Seismol. Soc. Am., 98, 692-708, http://dx.doi.org/10.1785/0120070021.

SEISMOGENIC FAULTS, LANDSLIDES AND TSUNAMIS IN THE IONIAN SEA: A CRITICAL ASSESSMENT

A. Argnani[1], A. Armigliato[2], F. Zaniboni[2], G. Gallotti[2], C. Angeli[2], M. Zanetti[2], S. Tinti[2]

[1] ISMAR-CNR, Bologna, Italy
[2] Istituto Nazionale di Geofisica e Vulcanologia, Pisa, Italia
[3] Department of Physics and Astronomy "A. Righi", University of Bologna, Italy

Rationale. The active tectonics of the Ionian region, and in particular of its western side, close to the coast of Sicily and facing the Mt. Etna volcano, have recently received a great deal of attention. In the last century this region has been characterized by a low-to-moderate seismicity, though in historical times it had been the site of the largest earthquakes witnessed in Italy, often accompanied by devastating tsunamis. Altogether the western Ionian and Calabrian regions can be considered as subject to a great geological hazard.

New data acquisition, particularly swath bathymetry and seismic profiles, both reflection and refraction, have contributed to clarify several tectonic aspects of this large and complex region; however, some issues remain elusive and discordant interpretations are often encountered in the abundant literature. Here we aim at addressing the historical record of earthquakes and tsunamis and at attempting to discuss the critical issues related to the potential tsunami sources (faults and landslides).

Of faults and landslides generating tsunamis. The seismological record of the great earthquakes that affected eastern Sicily and south Calabria is minimal: the most recent event is the December 1908 Messina earthquake, for which only limited instrumental records are available. Despite the broadly confined epicentral location in the offshore portion of the strait, and notwithstanding some seismological information (e.g., Pino *et al.,* 2009), the seismogenic fault has not yet been unambiguosly identified. Various faults have been proposed, often very different one from the other, and sometimes poorly constrained by data (e.g., Argnani, 2022). Irrespective of the proposed seismogenic fault, there is some convergence among the authors on the fact that coseismic slip alone is unlikely to be responsible for the observed tsunami (Piatanesi *et al.*, 1999; Tinti e*et al.*, 2008; Schambach *et al.*, 2020, 2021; Argnani, 2021). Some additional contribution is required either by landslides or by a secondary fault within a multiple rupture scheme (e.g., Gusman *et al.*, 2018). The critical analysis of the tsunamigenic sources proposed in the Messina Strait suggests that alternative hypotheses can still be explored.

For the older large tsunamigenic earthquakes (namely January 1693, December 1542 and February 1169; see the EMTC 2.0 by Maramai *et al.*, 2019) only chronicles are available, leaving even larger uncertainties. Partly because of this the 1542 and 1169 events have never received particular attention in the literature, and little is known on the sources of earthquakes and tsunamis. Instead, the potential sources of the 1693 earthquake and tsunami have been largely addressed.

Although the epicentral location of the 1693 earthquake is still debated, with some researchers that would locate it onshore (Sirovich and Pettenati 1999; Lavecchia *et al.*, 2007; Pirrotta and Barbano, 2020), it seems hard to escape the necessity of a seismogenic fault located offshore. A study conducted on a dense grid of seismic profiles along the Malta Escarpment has revealed the presence of an active extensional fault, about 40 km long, just off Augusta (Argnani and Bonazzi 2005; ME in Fig.1). Modelling indicates that this fault can originate the 1693 tsunami, roughly matching the observed regional distribution of maximum wave elevation (Argnani *et al.*, 2012). In the same study a large landslide that occurred at the fault scarp has also been modelled; its tsunamigenic contribution, however, remains limited, and cannot alone originate the tsunami waves observed along the coast of eastern Sicily. Therefore, the hypothesis that for the 1693 event a tsunamigenic earthquake originated offshore seems supported by modelling results, as well as by studies of inundation record

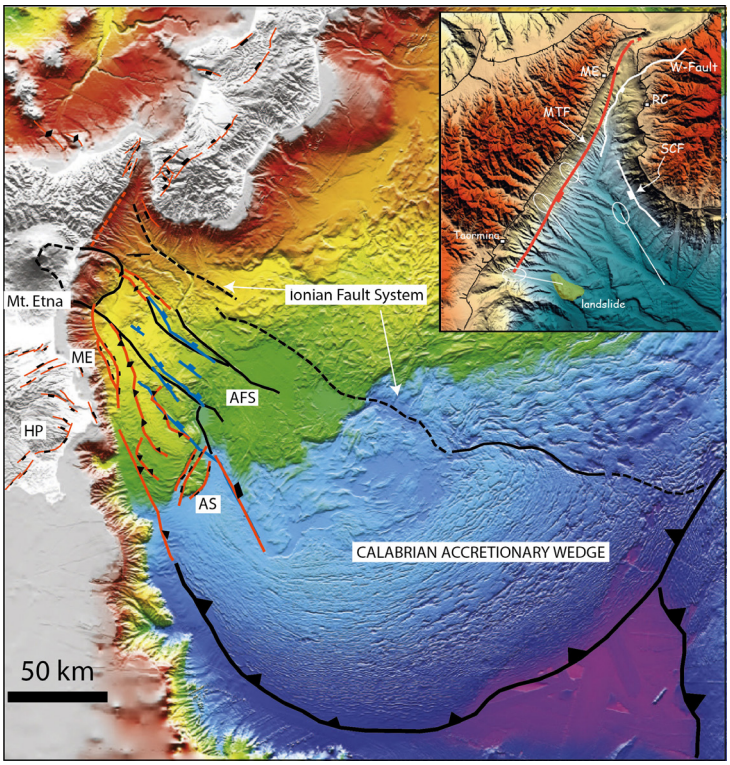


Fig. 1. - Simplified tectonic map of the western Ionian region, showing a compilation of the main structural features. Faults are from Argnani, 2014 (in red), from Gutscher *et al.*, 2017 (in black), and from Maesano *et al.*, 2020 (dark blue). Lines with rectangles: extensional faults; lines with triangles: thrusts and reverse faults, lines with diamonds: anticlines. The red dashed line in the Messina Strait represents a flexure. The North and South branches of the AFS are after Gutscher *et al.* (2017). The structures are superimposed on the morpho-bathymetry of Gutscher *et al.* (2017). HP Hyblean Plateau, ME Malta Escarpment, AS Alfeo Smt., AFS Alfeo Fault System. The map in the inset shows and enlargement of the Messina Strait with some of the recently proposed faults and landslides. MTF Messina-Taormina Fault (after Meschis *et al.*, 20), SCF South Calabria Fault (Argnani *et al.*, 2009). The W-Fault is after Barreca *et al.* (2021). ME and RC indicate the cities of Messina and Reggio Calabria, respectively. The greenish area is the landslides studied by Schambach *et al.* (2020), whereas the white ellipses with a direction line represent the landslides modelled by Favalli *et al.* (2009).

(Gerardi *et al.*, 2008). Different offshore faults and landslides have been proposed in the literature to account for the 1693 earthquake and tsunami. The tsunamigenic potential of some of these sources has been investigated.

References

Argnani A.; 2014: Comment on the article *"Propagation of a lithospheric tear fault (STEP) through the western boundary of the Calabrian accretionary wedge offshore eastern Sicily (Southern Italy)"* by Gallais *et al.*, 2013 Tectonophysics. Tectonophysics, 610, 195–199.

Argnani A., Brancolini G., Bonazzi C., Rovere M., Accaino F., Zgur F., Lodolo E.; 2009: *The results of the Taormina 2006 seismic survey: possible implications for active tectonics in the Messina Straits.* Tectonophysics, 476 (1–2), 159–169. https://doi.org/10.1016/j.tecto.2008.10.029.

Argnani A., Armigliato A., Pagnoni G., Zaniboni F., Tinti S. and Bonazzi C.; 2012: *Active tectonics along the submarine slope of South-Eastern Sicily and the source of the 11 January 1693 earthquake and tsunami.* Nat. Hazards Earth Syst. Sci., 12 (5), 1311–1319. https://doi.org/10.5194/nhess-12-1311-2012.

Argnani A.; 2021: Comment on *"New simulations and understanding of the 1908 Messina tsunami for a dual seismic and deep submarine mass failure source"* by L. Schambach, S.T. Grilli, D.R. Tappin, M.D. Gangemi, G. Barbaro [Marine Geology 421 (2020) 106093]. Mar. Geol., 442, 106634

Argnani A.; 2022: Comment on the paper by Barreca *et al.*: *"The Strait of Messina: Seismotectonics and the source of the 1908 earthquake"* (Earth-Science Reviews 218, 2021, 103685). Earth-Sci. Rev., 226, 103961.

Argnani A. and Bonazzi C.; 2005: *Malta escarpment fault zone offshore eastern Sicily: pliocene-quaternary tectonic evolution based on new multichannel seismic data.* Tectonics, 24. doi:10.1029/2004tc001656

Barreca, G., Gross, F., Scarfì, L., Aloisi, M., Monaco, C., Krastel, S.; 2021: *The Strait of Messina: seismotectonics and the source of the 1908 earthquake.* Earth-Sci. Rev., 103685. https://doi.org/10.1016/j.earscirev.2021.103685.

Favalli M., Boschi E., Mazzarini F. and Pareschi M.T.; 2009: *Seismic and landslide source of the 1908 Straits of Messina tsunami (Sicily, Italy).* Geophys. Res. Lett., 36. doi: 10.1029/2009/GL039135. L16304.

Gerardi P., Barbano M.S., De Martini P.M. and Pantosti D.; 2008: *"Discrimination of Tsunami Sources (Earthquake versus Landslide) on the Basis of Historical Data in Eastern Sicily and Southern Calabria".* Bull. Seism. Soc. Am., 98 (6), 2795–2805.

Gusman, A.R., Satake, K., Gunawan, E., Hamling, I., Power, W.; 2018: *Contribution from multiple fault ruptures to tsunami generation during the 2016 Kaikoura earthquake.* Pure Appl. Geophys. 175, 2557–2574. https://doi.org/10.1007/s00024-018-1949-z-.

Gutscher, M.-A., Kopp, H., Krastel, S., Bohrmann, G., Garlan, T., Zaragosi, S., *et al.*; 2017: *Active tectonics of the Calabrian subduction revealed by new multi-beam bathymetric data and high-resolution seismic profiles in the Ionian Sea (Central Mediterranean).* Earth Planet. Sci. Lett. 461, 61–72. doi:10.1016/j.epsl.2016.12.020

Lavecchia G., Ferrarini F., Nardis R., Visini F., Barbano M.S.; 2007: *Active thrusting as a possible seismogenic source in Sicily (Southern Italy): Some insights from integrated structural–kinematic and seismological data.* Tectonophysics 445, 145–167.

Maesano F. E., Tiberti M. M., and Basili R.; 2020: *Deformation and fault propagation at the lateral termination of a subduction zone: the Alfeo fault system in the Calabrian Arc, southern Italy.* Front. Earth Sci., 8, 107. doi:10.3389/feart.2020.00107

Maramai A., Graziani L. and Brizuela B.; 2019: *Euro-Mediterranean Tsunami Catalogue (EMTC), version 2.0.* Istituto Nazionale di Geofisica e Vulcanologia (INGV). https://doi.org/10.13127/tsunami/emtc.2.0

Meschis M., Roberts G.P., Mildon Z.K., Robertson J., Michetti A.M. and Walker, J.F.; 201: *Slip on a mapped normal fault for the 28th December 1908 Messina earthquake (Mw 7.1) in Italy.* Sci. Rep., 9 (1), 6481.

Piatanesi A., Tinti S., Bortolucci E.; 1999: *Finite-elements simulations of the 28 December 1908 Messina Straits (southern Italy) tsunami.* Phys. Chem. Earth, A 24 (2), 145–150.

Pino N.A., Piatanesi A., Valensise G. and Boschi E.; 2009: *The 28 December 1908 Messina Straits Earthquake (MW 7.1): a Great Earthquake throughout a Century of Seismology. Seismol.* Res. Lett., 80 (2), 243–259. https://doi.org/10.1785/gssrl.80.2.243.

Pirrotta C. and Barbano M.S.; 2020: *New Macroseismic and Morphotectonic Constraints to Infer a Fault Model for the 9 (Mw6.1) and 11 January (Mw7.3) 1693 Earthquakes (Southeastern Sicily).* Front. Earth Sci., 8:550851. doi: 10.3389/feart.2020.550851

Schambach L., Grilli S.T., Tappin D.R., Gangemi M.D. and Barbaro G., 2020: *New simulations and understanding of the 1908 Messina tsunami for a dual seismic and deep submarine mass failure source.* Mar. Geol., 421, 106093.

Schambach L., Grilli S.T., Tappin D.R., Gangemi M.D. and Barbaro G.; 2021: *Response to: Comment on "New simulations and understanding of the 1908 Messina tsunami for a dual seismic and deep submarine mass failure source"* by L. Schambach, S.T. Grilli, D.R. Tappin, M.D. Gangemi, G. Barbaro [Marine Geology 421 (2020) 106093]. Mar. Geol., 442 (2021) 106636

Sirovich L. and Pettenati F.; 1999: *Seismotectonic outline of South- Eastern Sicily: an evaluation of available options for the earthquake fault rupture scenario.* J. Seismol., 3, 213–233.

Tinti S., Armigliato A., Zaniboni F., Tonini R., Pagnoni G., Gallazzi G., Manucci A. and Pontrelli P., 2008. *Quale sorgente per il maremoto del 28 Dicembre 1908 nello Stretto di Messina? Terremoto, frana sottomarina o entrambe?* GNGTS, 27° Convegno Nazionale. Extended Abstract, 191–192.

UNVEILING TRANS-RIDGE EN-ECHELON FAULT PATTERNS POSSIBLY RESPONSIBLE FOR THE 1857 BASILICATA EARTHQUAKE (Mw 7.1)

S. Bello[1,2], G. Lavecchia[1,2], C. Andrenacci[1,2], M. Ercoli[2,3], D. Cirillo[1,2], F. Carboni[2,3], M.R. Barchi[2,3], F. Brozzetti[1,2]

[1] DiSPUTer, University G. d'Annunzio, via dei Vestini 31, Chieti 66100, Italy
[2] CRUST - Centro InteRUniversitario per l'analisi Sismotettonica Tridimensionale, Chieti, Italy
[3] Dipartimento di Fisica e Geologia, Università degli Studi di Perugia, Perugia, Italy

Identifying still unrecognized surface evidence of faults capable of releasing moderate-to-strong earthquakes is especially relevant for seismotectonic and seismic hazard purposes. This is the case of the Basilicata 1857 earthquake (Imax = XI MCS; Mw 7.2), which, in a time-lapse of ~3 minutes, released two distinct subevents generating devastation and victims (10.000 to 19.000 casualties) in a large area of the southern Apennines, between the Vallo di Diano and the Val d'Agri (Mallet, 1862; Branno *et al.*, 1983). There are many open questions regarding this earthquake, such as the causative fault (one or more seismogenic sources?), the possibility of a hidden source fault, and the lack of surface faulting events during the earthquake. Further questions regard the size and depth of the seismogenic fault segments, the dip-angle and dip direction (NE rather than SW) within the Val d'Agri (Benedetti et al., 1998; Burrato and Valensise 2008). Answering these open questions is crucial due to the study area's social and economic structure and heritage and the related seismic and anthropogenic hazards. Further, it should be especially considered that the Val d'Agri hosts a significant oil treatment center above the largest onshore hydrocarbons field in Europe.

Through an initial phase of satellite image interpretation, we have delineated an alignment of morphostructural elements, which we consider clues to guide a series of geological-structural field surveys. About 370 punctual structural data (fault plane and striation) were subsequently acquired over an area of ~900 km^2 and used to delineate a ~65 km-long SSW-dipping en-echelon fault system connecting the Auletta, Vallo di Diano, and Val d'Agri basins between the Caggiano and Montemurro villages. The fault system develops transversally across a portion of the Monti della Maddalena NNW-SSE striking ridge; therefore, it is referred to as Caggiano-Montemurro (CMF) trans-ridge fault. It is identified onsite as an alignment of rather continuous fresh scarps, bounding several narrow intramountain basins filled by late Quaternary clastic deposits.

Most commonly, active normal faults bound major Quaternary basinal depressions, thus geologists tend to limit the search for seismogenic faults in those contexts. However, the strong 1980 Irpinia earthquake (Mw 6.9) had already proven that faults capable of generating strong earthquakes can run for long distances in the highest portions of the massifs, generating small along-strike elongated intramountain basins (*i.e.*, a few tens or hundreds of meters) Pantosti and Valensise, 1990; Galli and Peronace, 2014; Bello *et al.*, 2021a). The similarities between the structural style of the fault-controlled small basins in the highest portion of the Monti della Maddalena massifs in the study area and the small basins along the Irpinia fault, can then be interpreted as similar evidence of recent fault activity. Furthermore, formal stress field inversion of fault/slip data surveyed along the CMF provides a N032-trending near-horizontal s3-axis, which is coaxial to that computed for the neighboring Irpinia area (Bello *et al.*, 2021a). These results highlight an evident deviation of the intra-Apennine tensional axis from a regional SW-NE trend to a WSW-ENE trend in the Campania-Lucania sector.

By applying commonly used along-strike segmentation criteria (see *e.g.*, Biasi and Wesnousky, 2016; Brozzetti *et al.*, 2019; Bello *et al.*, 2022), we subdivided the CMF into four levels of segmentation, all arranged in a right-lateral en-echelon pattern. In particular, we consider the CMF as a first-order master fault, subdivided into two ~30 km-long second-order "segments", seven ~10-15 km-long third order "sections" and fourteen ~5-7 km-long fourth order "sub-sections". The fault evidences disappear at surface when crossing the Val d'Agri basin. To constrain the fault structures in this key-area, we have operated a seismic

interpretation of two commercial reflection profiles, whose quality and interpretability were previously improved using pre-conditioning filters and seismic attribute analysis (*e.g.*, in Ercoli *et al.*, 2020; Barchi *et al.*, 2021).

Considering the continuity of the CMF, we hypothesize that the whole system may represent the master fault of the area and we speculate that the CMF, or a large portion of it, might be the fault responsible for the 1857 earthquake, during which, different sections could have released the two in-sequence events, in a time-lapse of ~3 minutes (Benedetti *et al.*, 1998; Burrato and Valensise 2008; DISS W.G., 2021). Assuming that the CMF can rupture entirely during any possible earthquake, even a complex one with several sub-events, and based on the empirical relationships for normal faults, we obtain that the CMF correlates to a maximum expected magnitude between 7 and 7.3, matching the estimated magnitude of the 1857 Basilicata earthquake. In the CMF, we find the simplest possible explanation, supported by literature data (Galli *et al.*, 2006; Zembo, 2010; Zembo *et al.*, 2009) and by the new constraints from this work. Our results can be used for guiding future high-resolution geophysical surveys (*e.g.*, GPR) and paleoseismological investigations, to give further insights.

References

Barchi, M. R., Carboni F., Michele M., Ercoli M., Giorgetti C., Porreca M., Azzaro S., Chiaraluce L.; 2021: *The influence of subsurface geology on the distribution of earthquakes during the 2016-–2017 Central Italy seismic sequence*. Tectonophysics 807, doi:10.1016/j.tecto.2021.228797.

Bello, S. de Nardis R., Scarpa R., Brozzetti F., Cirillo D., Ferrarini F., di Lieto B., Arrowsmith J R., Lavecchia G.; 2021: *Fault Pattern and Seismotectonic Style of the Campania – Lucania 1980 Earthquake (Mw 6.9, Southern Italy): New Multidisciplinary Constraints*. Frontiers in Earth Science 8, doi:10.3389/feart.2020.608063.

Bello, S. Andrenacci C., Cirillo D., Scott C. P., Brozzetti F., Arrowsmith J R., Lavecchia G.; 2022: *High-detail fault segmentation: Deep insight into the anatomy of the 1983 Borah Peak earthquake rupture zone (Mw 6.9, Idaho, USA)*. Lithosphere (1): 8100224. https://doi.org/10.2113/2022/8100224.

Benedetti, L., Tapponnier, P., King, G. C. P. & Piccardi, L. ; 1998: *Surface rupture of the 1857 Southern Italian earthquake?* Terra Nova 10, 206-210, doi:10.1046/j.1365-3121.1998.00189.x.

Biasi, G. P. & Wesnousky, S. G. ; 2016: *Steps and gaps in ground ruptures: Empirical bounds on rupture propagation*. Bulletin of the Seismological Society of America 106, 1110-1124, doi:10.1785/0120150175.

Branno, A., Esposito, E., Marturano, A., Porfido, S. & Rinaldis, V. ; 2021: ; 1983: *Studio, su base macrosismica, del terremoto della Basilicata del 16 dicembre 1857*. Boll. Soc. Natur. Napoli 92, 249-338

Brozzetti, F. Boncio P., Cirillo D., Ferrarini F., de Nardis R., Testa A., Liberi F., Lavecchia G.; 2019: *High-Resolution Field Mapping and Analysis of the August–October 2016 Coseismic Surface Faulting (Central Italy Earthquakes): Slip Distribution, Parameterization, and Comparison With Global Earthquakes*. Tectonics 38, 417-439, doi:10.1029/2018TC005305.

Burrato, P. and Valensise, G. ; 2008: *Rise and fall of a hypothesized seismic gap: Source complexity in the Mw 7.0 16 December 1857 Southern Italy earthquake*. Bulletin of the Seismological Society of America 98, 139-148, doi:10.1785/0120070094.

DISS Working Group; 2021: *Database of Individual Seismogenic Sources (DISS), Version 3.3.0: A compilation of potential sources for earthquakes larger than M 5.5 in Italy and surrounding areas*. Istituto Nazionale di Geofisica e Vulcanologia (INGV). https://doi.org/10.13127/diss3.3.0

Ercoli M., Forte E., Porreca M., Carbonell R., Pauselli C., Minelli G., Barchi M. R.; 2020: *Using seismic attributes in seismotectonic research: an application to the Norcia Mw = 6.5 earthquake (30 October 2016) in central Italy*. Solid Earth 11, 329-348, doi:10.5194/se-11-329-2020.

Galli P., Bosi V., Piscitelli S., Giocoli A. & Scionti V. ; 2006: *Late Holocene earthquakes in southern Apennine: Paleoseismology of the Caggiano fault*. International Journal of Earth Sciences 95, 855-870, doi:10.1007/s00531-005-0066-2.

Galli P. and Peronace E. ; 2014: *New paleoseismic data from the Irpinia Fault. A different seismogenic perspective for southern Apennines (Italy)*. Earth-Science Reviews 136, 175-201, doi:10.1016/j.earscirev.2014.05.013.

Mallet R. *Great Napolitan earthquake of 1857*. Vol. 1 1-544 (ING-SGA/Chapman and Hall, 1862).

Pantosti D. and Valensise G. ; 1990: *Faulting mechanism and complexity of the November 23, 1980, Campania-Lucania earthquake, inferred from surface observations*. Journal of Geophysical Research 95, doi:10.1029/jb095ib10p15319.

Zembo I.; 2010: *Stratigraphic architecture and quaternary evolution of the Val d'Agri intermontane basin (Southern Apennines, Italy)*. Sedimentary Geology 223, 206-234, doi:10.1016/j.sedgeo.2009.11.011.

Zembo I., Panzeri L., Galli A., Bersezio R., Martini M., Sibilia E.; 2009: *Quaternary evolution of the intermontane Val d'Agri Basin, Southern Apennines*. Quaternary Research 72, 431-442, doi:10.1016/j.yqres.2009.02.009.

REVISIONE DELLA SISMICITÀ 'MINORE', UN CONTRIBUTO AL MIGLIORAMENTO DELLE STIME DI PERICOLOSITÀ

F. Bernardini, R. Camassi , C.H. Caracciolo, V. Castelli, E. Ercolani

INGV- Istituto Nazionale di Geofisica e Vulcanologia, Sezione di Bologna

Premessa. La sismologia storica ha l'obiettivo di migliorare le conoscenze sulla sismicità del territorio nazionale, obiettivo essenziale per la caratterizzazione della sismicità e l'aggiornamento delle valutazioni di pericolosità e rischio. Questo obiettivo si consegue sia attraverso lo studio di terremoti forti, molti dei quali hanno margini di approfondimento rilevanti, che di terremoti di energia moderata e di tracce di eventi sconosciuti alla tradizione sismologica.

Dopo la pubblicazione del catalogo PFG [Postpischl, 1985], il primo catalogo parametrico pubblico di terremoti italiani, le ricerche sulla storia sismica del territorio nazionale hanno avuto un forte impulso soprattutto dalla prima metà degli anni '90 del secolo scorso con l'avvio di due iniziative, sostanzialmente complementari.

La prima è il progetto "CFTI" [Catalogo dei Forti Terremoti Italiani], sponsorizzato dall'ING/INGV, che aveva come obiettivo iniziale la revisione e l'approfondimento delle conoscenze su tutti i terremoti inclusi nel catalogo PFG con Io ≥VIII-IX MCS (346 terremoti) [Boschi *et al.*, 1995] ma che nelle versioni successive [Boschi *et al.*, 2000; Guidoboni *et al.*, 2007; 2019] ha progressivamente ampliato il proprio orizzonte anche a selezioni di terremoti con intensità minori ripresi da studi realizzati per progetti precedenti.

La seconda iniziativa è il progetto "Analisi Attraverso i Cataloghi" [Stucchi, 1993], promosso negli anni Novanta del Novecento dal GNDT/CNR a fini di valutazione della pericolosità sismica. Il primo obiettivo di questo progetto è stato la revisione speditiva di tutti i terremoti inclusi nel catalogo PFG con Io ≥VII-VIII senza un proprio studio di riferimento. Il lavoro è stato in seguito esteso anche a terremoti di energia minore (ma sempre al disopra della soglia del danno) per un totale di 621 studi che hanno contribuito alla compilazione del catalogo NT4.1 [Camassi e Stucchi, 1997]. Quest'ultimo lavoro si è basato principalmente sull'analisi e approfondimento delle informazioni fornite dalla principale compilazione sismologica italiana [Baratta, 1901] e da un'ampia griglia di compilazioni sismologiche descrittive [Perrey, 1848; Mercalli, 1883; Baratta, 1897; De Rossi, 1889, etc.] e sulla verifica delle fonti – bibliografiche, archivistiche, giornalistiche, epigrafiche – citate dalle compilazioni stesse. Lo schema di filiazione di Fig. 1 è relativo a un caso reale e mostra quanto complesso e allo stesso tempo promettente possa essere un percorso di indagine di questo tipo, il cui punto di partenza (e di forza) è quello di esplorare e utilizzare a fondo il ricco patrimonio di conoscenze reso disponibile dalla "tradizione sismologica", cioè dalle già citate compilazioni cronologico-descrittive di terremoti, prodotte in Italia e altri paesi europei dal XV secolo in poi. Questo approccio permette di ricostruire con un ottimo rapporto costi-benefici una immagine preliminare delle caratteristiche di ciascun evento studiato che rende disponibile una base di dati di pronto uso e al tempo stesso permette di orientare opportunamente le eventuali ricerche di approfondimento necessarie.

Il lavoro di revisione e aggiornamento. In un discreto numero di casi (263 eventi) il livello di verifica si è tuttavia sostanzialmente arrestato alle compilazioni sismologiche (nella finestra temporale 1000-1899) e - per gli studi realizzati nell'ambito di una estensione del progetto iniziale denominata "Analisi Attraverso i Bollettini" - alla rete di bollettini macrosismici prodotti tra il 1880-1980.

In seguito, grazie a ricerche svolte su aree ed eventi specifici (es. il terremoto umbro-marchigiano del 1997-1998) il numero di terremoti inclusi nelle successive versioni del catalogo parametrico nazionale CPTI sulla base di studi speditivi si è ridotto. Tuttavia, ancora

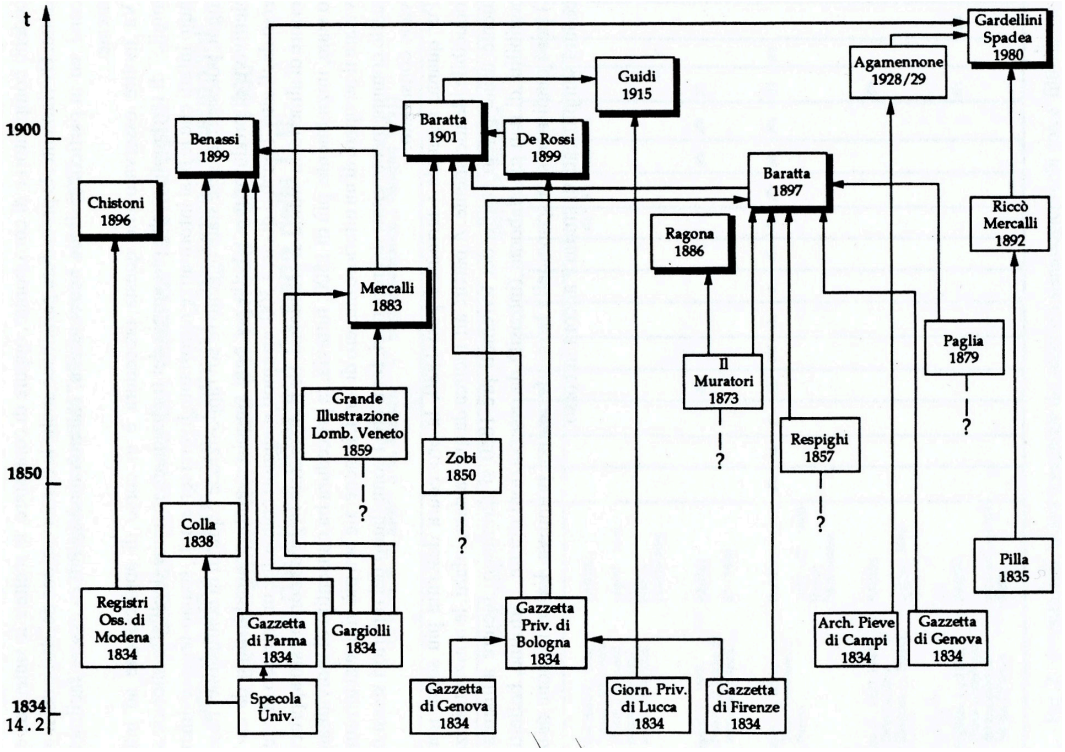


Fig. 1 - "Stemma" delle notizie relative al terremoto del 1834 [Stucchi, 1991].

nel 2017, non meno di 241 di questi studi preliminari relativi a eventi al di sopra della soglia di danno ma di energia moderata – restavano inediti in forma di cartelle manoscritte senza un supporto informatico che ne permettesse la fruizione mediante la piattaforma ASMI [Rovida *et al.*, 2017].

Nel 2017, nell'ambito dell'Allegato B2 della Convenzione DPC-INGV 2016-2017, sono state sistematicamente compilate schede digitali semplificate di tutti questi terremoti a partire dal materiale conservato nelle cartelle manoscritte. Le schede contraddistinte dalla sigla AMGNDT995 [Archivio Macrosismico GNDT, 1995] sono oggi disponibili sulla piattaforma ASMI.

Questa fase di lavoro ha reso evidente quanto datate e inadeguate fossero queste schede, per quanto riferite a terremoti di energia moderata. Si è ritenuto pertanto di avviare un lavoro di revisione e approfondimento di una selezione di questi terremoti.

I **241** studi preliminari sono stati analizzati a fondo, individuando tre livelli di priorità di revisione, avendo come riferimento la rilevanza dei singoli terremoti e soprattutto i potenziali margini di miglioramento delle conoscenze. Sono stati selezionati **72** terremoti, di cui è stata avviata la revisione secondo uno schema concordato con l'intero gruppo di lavoro.

I risultati. Nel corso del 2021 è stato completato lo studio per 24 di questi terremoti (Tab. 1), e di 6 di questi i risultati sono in corso di pubblicazione [Bernardini *et al.*, sottomesso]. Per gli altri terremoti lo studio è tuttora in corso.

Per ciascun terremoto lo studio è articolato secondo uno schema rigoroso, che prevede la descrizione del percorso di ricerca, la verifica dello studio preliminare, una ricerca ex novo – pur con i limiti imposti dalla situazione complessiva di questo momento storico - la revisione dell'intero periodo sismico – che qualche volta ha comportato la revisione di altri eventi prossimi nello spazio e nel tempo -, la verifica di possibili vittime, feriti ed effetti ambientali,

Tab. 1 - Terremoti attestati in CPTI15 da studi preliminari e rivisti nel corso del 2021; codice "ZZ"= falso; "ZD"=molto dubbio.

Year	Mo	Da	Ho	Mi	Epicentral Area	Mdp	Imax	Mdp_new	Imax_new
1311					Pinerolo	1	6	1	F [ZD]
1606	08	22			Bergamo	1	6-7	1	6-7
1621	08	09			Calabria	1	D	ZZ	-
1720	06	07			Tavoliere delle Puglie	7	6-7	9	5
1720	09	12			Calabria meridionale	2	6-7	1	HD
1762	07	23			Isola d'Ischia	1	6-7	1	5-6
1767	06	05	01	30	Valle Umbra	10	7-8	21	9
1767					Isola d'Ischia	1	D	ZZ	-
1836	06	12	02	30	Asolano	26	8	33	8-9
1864	03	15			Zocca	13	6-7	17	7
1882	08	16			Costa ascolana	13	7	13	6
1907	07	10	03		Pescocostanzo	1	4-5	1	5
1917	10	13	16	04	Val d'Agri	7	6	7	6
1921	08	28	10	45	Monti Sibillini	12	7	28	6-7
1923	06	28	15	12	Modenese	22	6	32	6
1925	03	15	17	15	Appennino tosco-em.	16	4-5	19	5
1928	04	21	13	56	Val d'Orcia	3	6-7	10	6-7
1940	01	31	11	Siena	30	6-7	38	6	
1949	10	08	03	08	Sicilia sud-orientale	32	7	40	6
1950	04	01			Livornese	15	7	37	7
1957	08	27	11	54	Appennino modenese	58	6	74	5-6
1959	03	24	10	24	Fiorentino	28	7	42	6-7
1963	08	09	06	05	Romagna	16	6	61	6-7
1971	10	04	16	43	Valnerina	43	6-7	94	7-8

la stima delle intensità per ogni scossa parametrizzabile e la disponibilità delle trascrizioni di tutte le fonti individuate.

In qualche caso, pertanto, la documentazione a supporto dello studio ha assunto dimensioni molto consistenti.

Il risultato complessivo è generalmente di un forte miglioramento delle informazioni disponibili, che consentirà di derivarne parametri epicentrali aggiornati e molto più solidi.

In due casi gli eventi in studio sono risultati falsi (9 agosto 1621 Calabria; 1767 Isola d'Ischia) e i due record dovranno essere rimossi dal catalogo; in un caso (1311 Pinerolo) il giudizio finale è "molto dubbio", ma non è stato possibile individuare la prova definitiva che ne imponga al momento una sua rimozione dal catalogo parametrico.

Nel corso della presente ricerca sono stati studiati anche 8 terremoti (Tab. 2) ancora presenti in CPTI15 come record originali PFG. Pur trattandosi di eventi minori, è ora possibile derivarne i parametri macrosismici.

Conclusioni. Dopo quasi 40 anni di ricerche sismologico storiche il bilancio è complessivamente positivo, anche se le condizioni di contesto sono mutate radicalmente. Per oltre un decennio le prospettive di sviluppo del settore sono state molto positive, il personale che ha dedicato la propria attività alla ricerca in questo settore era numericamente significativo e le competenze in gioco di buon livello.

Tab. 2 – Terremoti derivati dal catalogo PFG rivisti nel corso della presente ricerca.

Year	Mo	Da	Ho	Mi	Epicentral Area	Io	Mw	MdpN	Imax
1745	10	18			Cassinese	6	4,63	2	5-6
1841	10	06	03		Carnia	6	4,63	1	5
1906	06	04	23	20	Nicosia	6	5,15	1	5
1908	08	21	07	24	Cassinese	5-6	4,40	9	5
1918	02	08	18	49	Appennino forlivese	5-6	4,84	7	5-6
1949	12	06	03	46	Costa anconetana		4,38	3	4
1951	08	02	12	50	Appennino umbroreatino		4,44	48	5
1965	11	12	07	16	Marsica		4,39	12	4

Da oltre un decennio la situazione complessiva è mutata radicalmente, le energie umane e finanziarie si sono ridotte drasticamente ed è diventato sostanzialmente impossibile immaginare una progettazione di largo respiro. Tuttavia proprio di questo ci sarebbe bisogno, di progettazione di largo respiro e di un forte potenziamento del settore, reclutando personale giovane e motivato.

Se su diverse centinaia di terremoti, generalmente quelli più forti, il livello di approfondimento delle ricerche risulta elevato, tuttavia almeno il 60-70% dei circa 1500 terremoti significativi presenti in catalogo (indicativamente sopra la soglia del danno) sono ancora sostenuti da studi di carattere preliminare o speditivo, in molti casi decisamente obsoleti.

Per questo si è ritenuto di investire alcune energie nella revisione e nell'aggiornamento degli studi di questo tipo, considerando quanto importanti siano i terremoti di energia 'intermedia' nelle valutazioni di pericolosità sismica. Allo stesso tempo questo lavoro di revisione è stato finalizzato al reperimento e alla sistematizzazione di tutta la documentazione relativa, per consentire a chi in futuro vorrà ulteriormente approfondire lo studio di questi eventi di partire da una base informativa consolidata e facilmente accessibile.

Bibliografia

Archivio Macrosismico GNDT; 1995: *Studi preliminari di terremoti attraverso i repertori sismologici.* Archivio macrosismico del GNDT, Milano.

Baratta M.; 1897: *Materiali per un catalogo dei fenomeni sismi- ci avvenuti in Italia (1800-1872).* Memorie della Società Geografica Italiana, 7, 81-164.

Baratta M.; 1901: *I terremoti d'Italia; saggio di storia geografia e bibliografia sismica italiana.* Torino, 950 pp.

Bernardini F., Camassi R., Castelli V., Caracciolo C., Ercolani E.; 2022: *Materiali per un catalogo dei terremoti italiani. Sismicità minore del Novecento: alcuni casi tra gli anni 1949-1971.* Quaderni di Geofisica, sottomesso.

Boschi E., Ferrari G., Gasperini P., Guidoboni E., Smriglio G., Valensise G.; 1995: *Catalogo dei forti terremoti in Italia dal 461 a.C. al 1980,* ING-SGA, Bologna, 973 pp. , in Italian.

Boschi E., Guidoboni E., Ferrari G., Mariotti D., Valensise G., Gasperini P. (eds); 2000: *Catalogue of strong Italian earthquakes from 461 B.C. to 1997.* Ann. Geof. 43(4): 609–868.

Camassi R., Stucchi M.; 1997: *NT4.1: un catalogo parametrico di terremoti di area italiana al di sopra della soglia del danno,* Milano, 93 pp

De Rossi M.S., (ed); 1889: *Documenti raccolti dal defunto conte Antonio Malvasia per la storia dei terremoti ed eruzioni vulcaniche massime d'Italia*, Memorie della Pontificia Accademia dei Nuovi Lincei, 5, 169-289.

Guidoboni E., Ferrari G., Mariotti D., Comastri A., Tarabusi G., Valensise G.; 2007: *CFTI4Med, Catalogue of Strong Earthquakes in Italy (461 B.C.-1997) and Mediterranean Area (760 B.C.-1500).* INGV-SGA. http://storing.ingv.it/cfti4med/. Accessed 25 Feb 2022.

Guidoboni E., Ferrari G., Tarabusi G., Sgattoni G., Comastri A., Mariotti D., Ciuccarelli C., Bianchi M.G., Valensise G.; 2019: *CFTI5Med, the new release of the catalogue of strong earthquakes in Italy and in the Mediterranean area.* Sci Data 6(80):1–15. https://doi.org/10.1038/s41597-019-0091-9.

Mercalli G.; 1883: *Vulcani e fenomeni vulcanici in Italia,* Milano.

Perrey A.; 1848: *Mémoire sur les tremblements de terre de la peninsule italique, Mémoires couronnés et mémoires des savants étrangers,* 22, Académie Royale de Belgique, Bruxelles.

Postpischl D.; 1985: *Catalogo dei terremoti italiani dall'anno 1000 al 1980.* Progetto Finalizzato Geodinamica. Quaderni de La Ricerca Scientifica, n. 114, vol.2B

Rovida A., Locati M., Antonucci A., Camassi R. (a cura di); 2017: *Archivio Storico Macrosismico Italiano (ASMI)*. Istituto Nazionale di Geofisica e Vulcanologia (INGV). https://doi.org/10.13127/asmi

Stucchi M.; 1991: *Verso una razionalizzazione della base di dati macrosismici.* In: P. Albini P., Barbano M.S. (eds.), Atti del convegno del GNDT, Pisa 25-27 giugno 1990, 2, "Macrosismica", 1-23.

Stucchi M.; 1993: *Through catalogues and historical records: an introduction to the project "Review of Historical Seismicity in Europe"*, in Stucchi M. (ed.), Materials of the CEC project "Review of Historical Seismicity in Europe", 1, Milano, 3-14.

WHAT WAS THE ROLE OF FAULTS IN THE EVOLUTION OF THE MONTEREALE BASIN (CENTRAL APENNINE)? CONSIDERATIONS AND NON-EXHAUSTIVE ANSWERS

E. Chiarini[1], G. Nirta[1], A. Sciortino[2], M. Spadi[2], M. Tallini[2]

[1] Servizio Geologico d'Italia – ISPRA. Roma, Italy
[2] DICEAA - Università degli Studi dell'Aquila. Aquila, Italy

The Montereale basin is the northernmost of the intermontane basins along the Aterno River. It is located in the tectonically active axial sector of the central Apennine between the Western Fault Systems (WFS) and the eastern ones (EFS; Galadini and Galli 2000). In the last two decades, these fault systems were the source for several earthquakes with magnitude Mw ≥ 6.0. The basin is a structural depression located in a complex tectonic context, between the western limit of the E-W oriented Gran Sasso ridge and the SSW-NNE oriented Olevano-Antrodoco thrust system.

The basin is bordered to the NE by the Capitignano fault (CPF), while a second fault, the San Giovanni fault (SGF) is located in the center of the basin and seems to guide the formation of a sub-basin in the south-western sector (Fig. 1). The activity of the two faults has always aroused considerable interest because of their location between the active WFS and EFS, and for a long time represented an unsolved problem due to the lack of detailed studies on the quaternary stratigraphy of the basin. The SGF and CPF have been alternatively considered to be part of the Upper Aterno fault system in the WFS (Galadini and Galli 2000; Galadini *et al.*, 2000; Galadini and Messina, 2004), being part of the seismogenic source of the Laga Mt. fault in the EFS (Boncio *et al.*, 2004); or as a separate seismogenic source, capable of generating strong earthquakes (Lavecchia *et al.*, 2012).

Over the past decades, the basin and the surrounding areas have been studied during the national geological mapping program (sheet n. 348-Antrodoco; Chiarini *et al.*, 2014; Servizio Geologico d'Italia, 2022) and seismic microzonation studies (Tallini, 2017; Nocentini, 2018). Instead, the mapping of SGF and CPF has been carried out in detail in the in recent years (2021-2022) in the frame of the studies aimed at mapping the active and capable faults in the areas of the Montereale Basin that were affected by multiple seismic events since 24 August 2016 (Tallini *et al.*, 2021).

The analysis of the LiDAR digital terrain model allowed a more detailed mapping, in some cases substantially different from what has been published so far (Civico *et al.*, 2016). The features recognized on the digital topography were then verified on the ground and structural data were collected on the exposed fault scarps.

Thus, the fault traces were investigated by geophysical studies. A total of sixteen electrical resistivity tomographies (ERT), twelve across the CPF and four across the SGF, and two reflection seismic surveys across the CPF were performed. The results were integrated with the field data and the LiDAR analyses and allowed to choose the sites for three paleo-seismological trenches, one across the SGF and two across the CPF.

The trench across the San Giovanni fault (Fig. 1) is placed in the hangingwall of the faults detected in the paleoseismological trenches dug by Cinti *et al.* (2018). The trench exposed a sedimentary succession resting on the limestone substrate. The upper Pleistocene deposits, with an age <40,000 years, are faulted by splay faults of the main structure with decimetric offsets while the substrate is displaced by about 3 meters.

Two trenches were dug across the CPF, one at the base of the mountain front and one farther downstream (Fig. 1) to investigate a possible structure located within the Montereale basin. In the first case, the trench exposed faulted sediments, upper Pleistocene in age, while the arenaceous substrate shows a cumulative offset of about 2 m. In the second case, the upper Pleistocene sediments, that were investigated up to a depth of about 6 m, did not show clear faulting evidence.

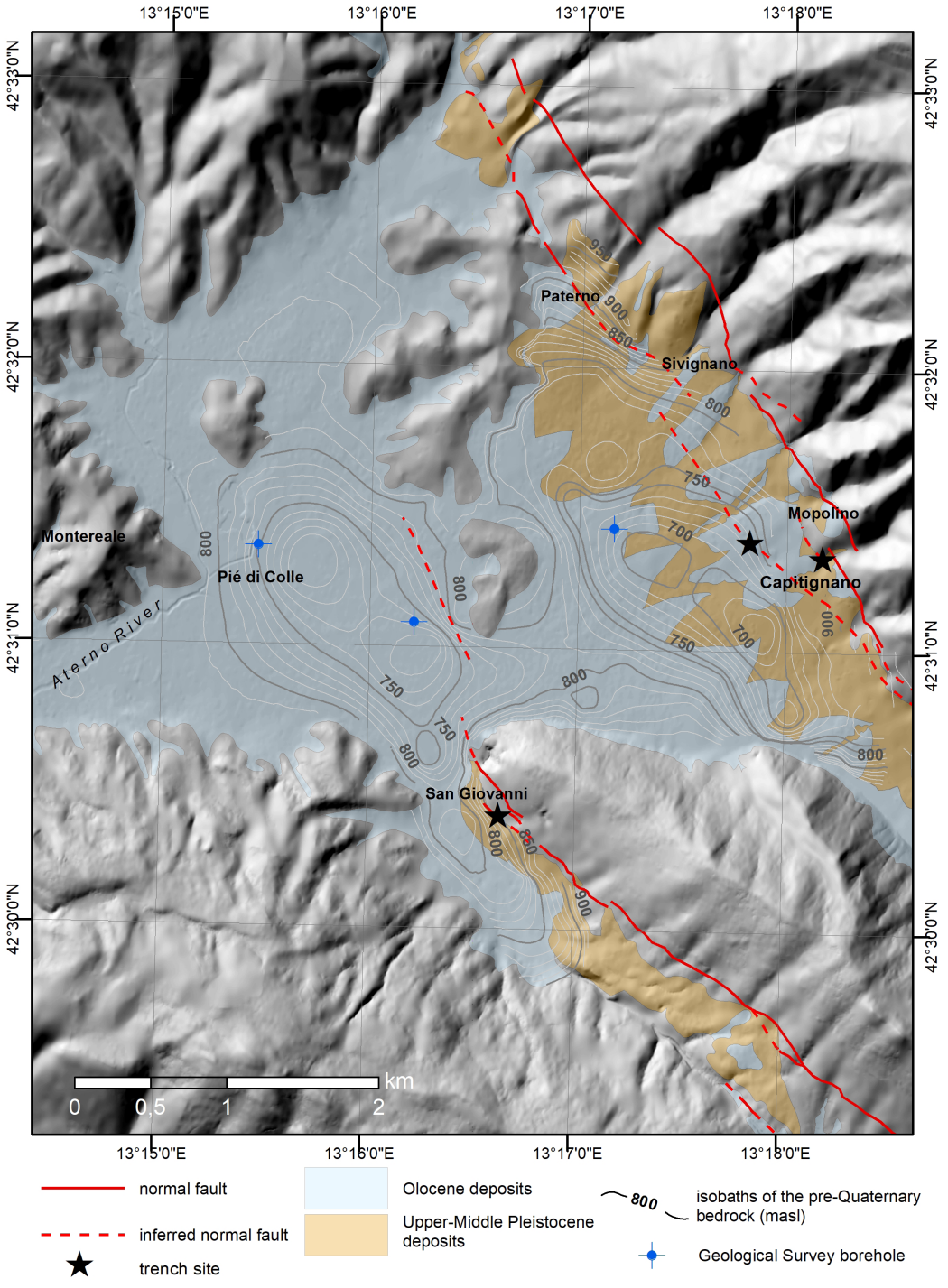


Fig. 1 - Geological sketch of the Quaternary infill of the Montereale intermontane basin. Isobaths of the pre-Quaternary substrate (masl) modified after Chiarini *et al.,* 2014.

Despite the Montereale basin is substantially undissected and therefore with scarce exposure of the Quaternary deposits, the reconstruction of the stratigraphic evolution was possible by integrating the field mapping with geophysical studies, core drillings, paleomagnetic analyzes and, ^{14}C and $^{39}Ar/^{40}Ar$ dating.

In the Montereale basin two different depocenters characterized by significantly different thickness of the Quaternary deposits can be recognized (Fig. 1), higher for the Capitignano depocenter, in the hangingwall of the CPF, and smaller in the depocenter of Piedicolle, at the northwestern tip of the SGF. Obtained data suggest that in the first phase of the sedimentary evolution of the basin, the fault-related subsidence exceeded the sedimentation rate, allowing the persistence of lacustrine sedimentation. Subsequently, between the early Pleistocene and middle Pleistocene, a slowdown in the activity of the CPF allowed the threshold between the two depocenters to be overcome and a drainage pattern similar to the current one to be established. Thus, the Montereale basin has followed the same evolutionary pattern recognized for other intermontane basins in the Central Apennines; it has been rather early captured by the Aterno hydrographic system, because of its position along the Apennine watershed and of the low tectonic subsidence (D'Agostino *et al.*, 2001). Geurts *et al.* (2020), argue that the integration of the intermontane basins in the hydrographic system of the Aterno network is part of the natural evolution of the hydrographic network rather than strictly related to the tectonic and climatic factors.

Between the late middle Pleistocene and the present, alternating aggradation and erosive episodes, suggest that the activity of the CPF was no longer able to compensate the sedimentary rates and therefore the evolution of the basin was essentially controlled by external factors (e.g. lowering of base level). However, the persistence of a modest tectonic activity is testified by the dislocation of the deposits of the upper Pleistocene along the CPF and SGF.

In addition to the clear societal impacts, this study aims to investigate a complex area where faults such as those studied, albeit of small extension, about 7 km that of San Giovanni and about 10 that of Capitignano, show clear evidence of having controlled the Quaternary sedimentation. Furthermore, the study of these "small" structures is important as it can provide information on the relationships and possible interactions with the "large" structures located in the most eastern (Laga and Gran Sasso) and western (Alto Aterno) fault systems.

References

Boncio P., Lavecchia G. and Pace B.; 2004: Defining a model of 3D seismogenic sources for Seismic Hazard Assessment applications: The case of central Apennines (Italy). Journal of Seismology, 8, 407-425

Chiarini E., La Posta E., Cifelli F., D'Ambrogi C., Eulilli V., Ferri F., Marino M., Mattei M. and Puzzilli L.M.; 2014: *A multidisciplinary approach to the study of the Montereale Basin (Central Apennines, Italy).* Rend. Fis. Acc. Lincei, **25** (2), 177-188.

Cinti F. R., Civico R., Blumetti A. M., Chiarini E., La Posta E., Pantosti D., Papasodaro F., Smedile A., De Martini P. M., Villani F., Pinzi S., Pucci S. and Brunori C. A.; 2018: *Evidence for surface faulting earthquakes on the Montereale fault system (Abruzzi Apennines, central Italy).* Tectonics, **37**. https://doi.org/ 10.1029/2017TC004780

Civico R., Blumetti A.M., Chiarini E., Cinti F.R., La Posta E., Papasodaro F., Sapia V., Baldo M., Lollino G. and Pantosti D.; 2016: *Traces of the active Capitignano and San Giovanni faults (Abruzzi Apennines, Italy).* Journal of Maps, 2016. http://dx.doi.org/10.1080/17445647.2016.1239229

D'Agostino N., Jackson J.A., Dramis F. and Funiciello R.; 2001: *Interactions between mantle upwelling, drainage evolution and active normal faulting: an example from the central Apennines (Italy).* Geophys. J. Int., **147**, 475-497.

Galadini F. and Galli P.; 2000: *Active tectonics in the central Apennines (Italy) - input data or seismic hazard assessment*. Natural Hazards, 22, 225-270

Galadini F., Messina P. and Sposato A.; 2000: *Tettonica quaternaria nell'Appennino centrale e caratterizzazione dell'attività di faglie nel Pleistocene superiore-Olocene.* In: Galadini F, Meletti C, Rebez A (ed) Le ricerche del GNDT nel campo della pericolosità sismica (1996-1999), CNR-GNDC, 157-169.

Galadini F. and Messina P.; 2004: *Early-Middle Pleistocene eastward migration of the Abruzzi Apennine (central Italy) extensional domain.* Journal of Geodynamics, **37**, 57-81.

Geurts A.H., Whittaker A. C. and Gawthorpe R. L.; 2020: *Transient landscape and stratigraphic responses to drainage integration in the actively extending central Italian Apennines.* Geomorphology, 353(2020) 107013. https://doi.org/10.1016/j.geomorph.2019.107013

Servizio Geologico d'Italia; 2022: *Carta Geologica d'Italia alla scala 1:50.000, F. 348 Antrodoco*. ISPRA, Roma. DOI: 10.15161/oar.it/75554

Lavecchia G., Ferrarini F., Brozzetti F., De Nardis R., Boncio P. and Chiaraluce L.; 2012: *From surface geology to aftershock analysis: Constraints on the geometry of the L'Aquila 2009 seismogenic fault system.* Ital. J. Geosc., **131**(3), 330-347.

Nocentini M.; 2017: *Studio di Microzonazione Sismica di Livello 3 nelle aree del territorio comunale di Capitignano (AQ).* Ordinanza Commissario Straordinario n.24 12/05/2017). www.sisma2016data.it/microzonazione/

Tallini M., Berti D., Chiarini E., D'Andrea V., Durante F., Ferri F., La Posta E., Macerola L., Nocentini M., Palucci D., Puzzilli L. M., Roma M. and Silvestri S.; 2017: *Macroarea Santa Lucia - Capitignano*. *Accordo CNR IGAG - DPC "Attività di supporto al Dipartimento della Protezione Civile nelle aree delle regioni Abruzzo, Lazio, Marche e Umbria interessate dagli eventi sismici a partire dal 24 agosto 2016" (Prot. CNR IGAG n°0001484 del 17/05/2017)*. Unpublished report, pp. 107.

Tallini M., Chiarini E., Nirta G., Spadi M., Sciortino A., Nocentini M., Di Marcantonio P., Ciampaglia A., Ferri F., Puzzilli L.M., Bellaveglia S., Bistocchi R., Sapia V., Materni V., Pischiutta M., Perini M., Fiera F. and Ranalli D.; 2021: *Ridefinizione delle Zone di Attenzione delle Faglie Attive e Capaci emerse dagli studi di microzonazione sismica effettuati nel territorio dei Centri abitati di Capitignano (Capoluogo e Frazione di Sivignano) e Montereale (Frazione di Paganica) in provincia de L'Aquila, interessati dagli eventi sismici verificatisi a far data dal 24 agosto 2016. Relazione della seconda fase. Accordo di collaborazione scientifica INGV-DICEAA (lotto 2)*. www.sisma2016data.it/faglie-attive-e-capaci/

NEAR-SOURCE ATTENUATION AND SPATIAL VARIABILITY OF THE SPECTRAL DECAY PARAMETER KAPPA IN CENTRAL ITALY

R.R. Castro[1], L. Colavitti[2], C.A. Vidales-Basurto[3], F. Pacor[2], S. Sgobba[2], G. Lanzano[2]

[1] Centro de Investigación Cientifica y de Educación Superior de Ensenada (CICESE), División Ciencias de la Tierra, Departamento de Sismología, Ensenada, Baja California, Mexico
[2] National Institute of Geophysics and Volcanology (INGV), Section of Seismology applied to Engineering, Milano, Italy
[3] Universidad Autónoma de Zacatecas, Unidad Académica de Ciencia y Tecnología de la Luz y la Materia (LUMAT), Zacatecas, Mexico

Introduction. The attenuation decay parameter (κ) is broadly used in many earthquake engineering applications, as for removing the path and site attenuation effects of ground motion prediction equations (Ktenidou *et al.*, 2014; Ktenidou *et al.*, 2015). The observed values of κ are usually the results of path effects, which are distance dependent, and attenuation near the source and the recording site.

As written in Anderson (1991) and Ktenidou *et al.* (2014), the distance dependence of κ is:

$$\kappa(r) = \kappa_0 + \kappa_s + \kappa_{avg}(r),$$

in which κ_0 is the near-site attenuation parameter, κ_s is the near-source attenuation parameter, and $\kappa_{avg}(r)$ is the average attenuation along the S-wave path.

In this work (more details are in Castro *et al.*, 2022a), we compare estimates of κ_s determined from two different techniques, and we also study the spatial variability of $\kappa_{avg}(r)$ using data from the dense array of Central Italy, which is characterized for being a seismically active region and tends to generate long sequence, as the case of Amatrice-Visso-Norcia sequence (Chiarabba *et al.*, 2018).

Data. Over the last 25 years, several earthquakes had occurred in this region, from the 1997-1998 Umbria-Marche sequence, to the 6 April 2009 M_w 6.1 L'Aquila mainshock, and the 2016-2017 M_w 6.5 Amatrice-Visso-Norcia sequence. For the scopes of this research, we analyzed both accelerograms and velocity records since 2008, which are used for phase picking and earthquake locations (Pacor *et al.*, 2016; Castro *et al.*, 2021). To analyze the spatial variability of κ, we used a dataset in which we considered events coming from different source areas based on the spatial clustering performed by Sgobba *et al.* (2021) for the Central Apennines region.

We selected events detected by at least three stations, and we set a threshold in which the ratio between the standard deviation of κ and the mean of κ was less than 50%. In this dataset, the selected events have magnitudes from M 3.2 to 6.3, focal depths between 6.1 and 17.1 km, and the hypocenter distances ranging between 7.1 and 168.8 km, for a total of 266 earthquakes, 353 stations, and 13,952 observations of κ (Fig. 1a).

We formed four groups of stations distributed by different quadrants, taking as axis of symmetry the average strike of the Apennine faults, which is approximately 150° along the NW-SE direction (Improta *et al.*, 2019; Vignaroli *et al.*, 2020) and follows the epicentral distribution of most of the selected earthquakes (Fig. 1b). The reason for this division of the $\kappa_{avg}(r)$ estimation in each quadrant is to analyze where there is any spatial variability of the spectral decay parameter.

METHOD. Estimates of kappa. We compute κ following the method proposed by Anderson and Hough (1984), in which the logarithm of the high-frequency S-wave spectral amplitude acceleration is least squared fitted and κ is computed from the slope of the linear fit. We used a semiautomatic technique to estimate κ from each record, which consists in precompute the slopes over 11 frequency bands, with variable length in the range between 8 and 38 Hz (Lanzano *et al.*, 2022), and then averaging these values to obtain the final estimate. The median value is

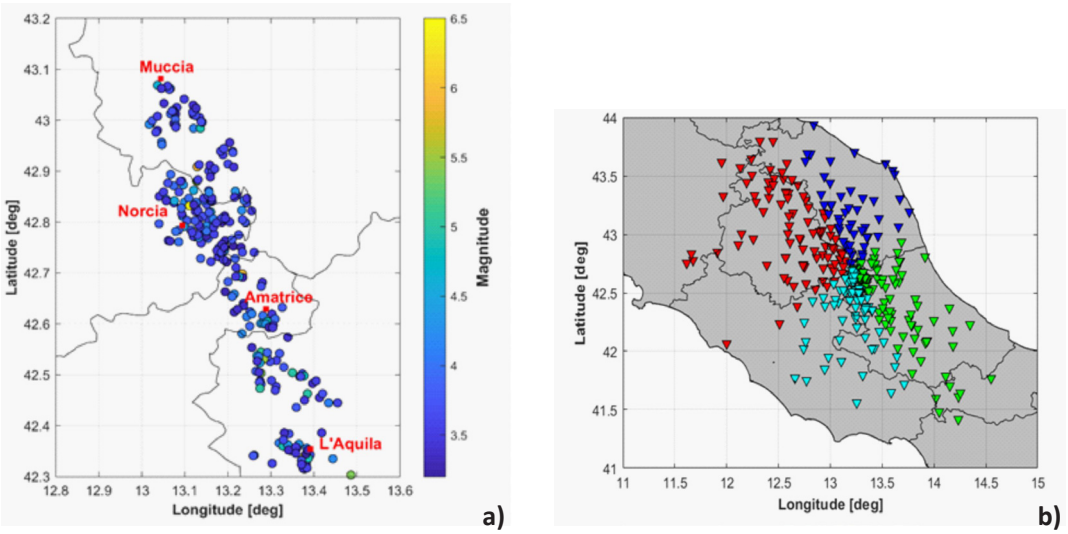


Fig. 1 - Distribution of epicenters a) and stations b) of the second data set analyzed. The dataset consists of 266 events, 353 stations and 13,952. The different colors on the epicenter indicate the magnitude of the earthquake, while map in b) the reverse triangles are stations in quadrant Q1, blue in Q2, green in Q3 and cyan in Q4.

discarded if the precomputed κ is available for less than half of the considered frequency range (e.g. 6 out of 11 values) and the associated standard deviation is larger than 0.015 s.

Nonparametric model. We defined $\kappa_{avg}(r)$ using a nonparametric approach as Anderson (1991), Anderson and Lei (1994), and Fernández *et al.* (2010), that characterizes the variation of the observed spectral decay parameter with distance. This technique looks for a function that describes the observed values of κ with hypocenter distance without assuming an *a priori* physical model for mathematical function.

The nonparametric method consists of finding a smooth function $\kappa_{avg}(r)$ assuming that κ varies slowly with distance. Using this technique, observed values of κ of earthquakes recorded at different hypocenter distances complement each other and allow definition of $\kappa_{avg}(r)$ at a wide distance range.

Independent Estimates of κ_s. κ_s can be also estimated by single earthquakes by assuming that:

$$\kappa(r) = \kappa_s + \kappa_{avg}(r),$$

For an individual earthquake, the observed values of κ versus distance r are linearly least squared fitted and κ_s would correspond to the value of κ at the origin. However, the least-square regression will tend to find the best fit to the mean values of the data and, because $\kappa_0 \geq 0$, κ_s will be overestimated. Thus, this estimate of κ_s must be corrected by subtracting the mean κ_0.

Results and discussions. Figure 2a shows the nonparametric function $\kappa_{avg}(r)$ and a sample of the observed κ values versus hypocenter distance from four different stations (AQU, AQV, ARRO and ARVD). As we can observe, the shape of $\kappa_{avg}(r)$ is the same for all sites, but it is scaled by the respective value of κ_0; for a given distance, κ shows great variability. These observations suggest that it should be a spatial variability of the attenuation between the different source-station paths, already observed in Castro *et al.* (2000) from the earthquakes

occurred during the 1997 Umbria-Marche sequence. Another possible reason for the scatter in the κ estimated is 3-D site effects that may generate complex site amplifications (e.g. Pitilakis, 2004; Bennington *et al.*, 2008).

Figure 2b compares the nonparametric function of the northwest quadrant (Q1), shown with plus symbols, follows the same rate of increase with distance as the other three regions up to 100 km and for greater distances shows greater attenuation than the other three quadrants. The southern quadrants (Q3 and Q4) have similar attenuation characteristics, whereas the northern region (Q2) shows less attenuation than the other zones.

In particular, the higher values of $\kappa_{avg}(r)$ are more evident in the southern sector, especially at the southwest quadrant (Q4 quadrant), which may be connected to a highly diffused fault

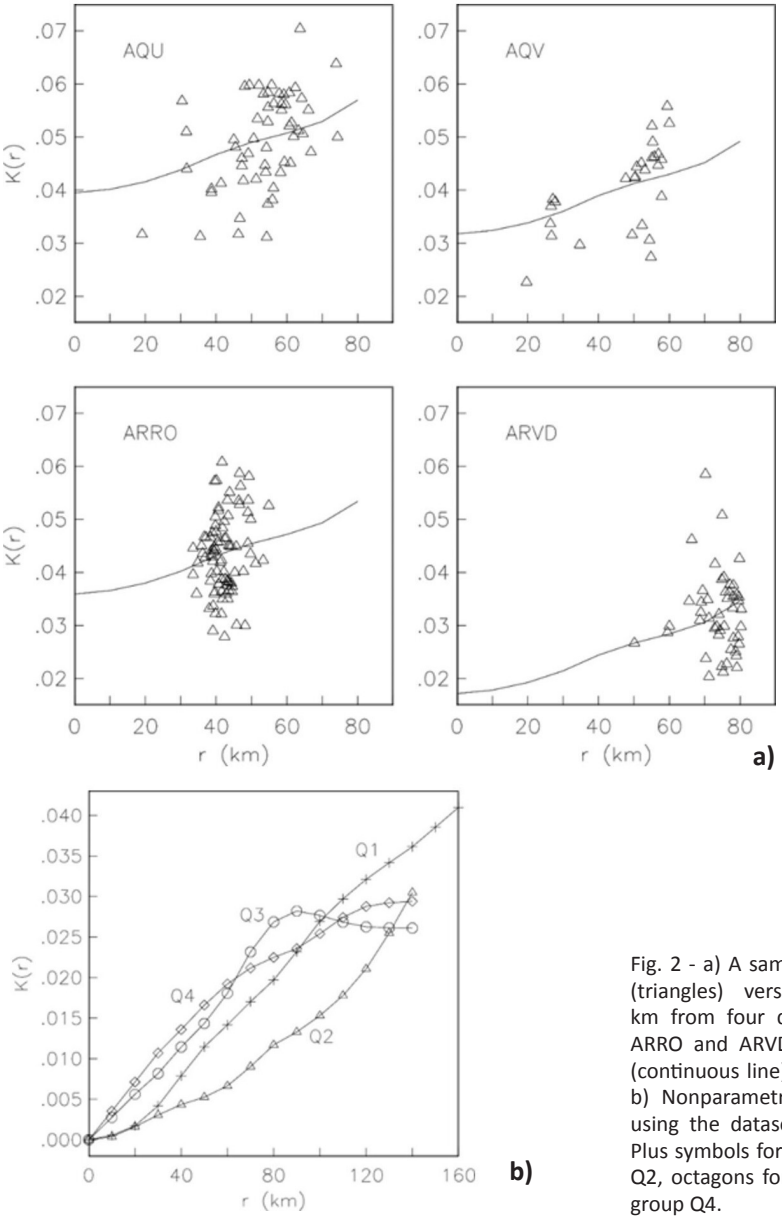


Fig. 2 - a) A sample of observed kappa values (triangles) versus hypocenter distance in km from four different stations (AQU, AQV, ARRO and ARVD) and the nonparametric fit (continuous line) obtained from the inversion. b) Nonparametric Kappa functions obtained using the dataset applied in the study area. Plus symbols for group Q1, triangles for group Q2, octagons for group Q3 and diamonds for group Q4.

segmentation (Chiarabba *et al.*, 2020; Akinci *et al.*, 2020), that led to both scattering and trapped waves, as also evinced by high-scattering anomalies focusing in the south and west zones (Gabrielli *et al.*, 2021). An increase of seismic attenuation is expected due to the large number of different tectonic features, which reflects in lower quality factor Q, which is typical of near-surface rocks. Moreover, according to Pastori *et al.* (2019), the area between Amatrice and Accumuli regions, can be considered as a heavily fractured zone in which fluids are preferentially channeled. On the other side, the eastern part of the Apennine chain is characterized by tectonic stability and less attenuation (Castro *et al.*, 1996; Malagnini *et al.*, 2002).

Figure 3a shows the distribution of the near-site attenuation parameter for reference rock stations identified according to Lanzano *et al.* (2020) using several proxies of the site response. We can observe that three sites in the north (APEC, ATPI, and CAFI) have high values of κ_0 that are close to the edge of basins where some sedimentation may be present. Figure 3b displays the distribution of non-reference sites and the values of κ_0 obtained for those stations. These outcomes with low values of κ_0 does not necessarily correlate with the $V_{s,30}$ of a given station, since κ_0 may include the effect of attenuation beyond the first 30 m from the surface, which are usually obtained using invasive methods that may alter the elastic properties of the rocks.

Conclusions and future perspectives. Our results shown that most of the high-frequency attenuation takes place near the site, because $\kappa_{avg}(r)$ contributes with only 20% of the spectral decay. The spatial variability of $\kappa_{avg}(r)$ suggest an anisotropic behavior of the high-frequency attenuation, probably related to different local geology, faulting activity and tectonic structures in the different directions with respect to the Apennine orientation (Castro *et al.*, 2022a). Moreover, we find that the higher values of $\kappa_{avg}(r)$ in the southern regions of Central Italy

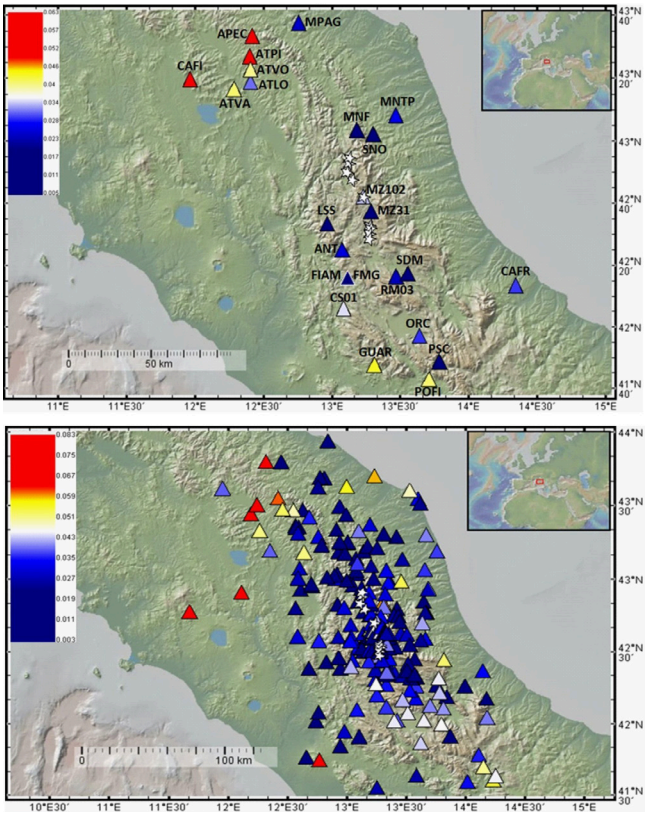


Fig. 3 - Spatial distribution of the near-site attenuation parameter κ_0 obtained for reference stations a) and non-reference stations. The stars are the location of earthquakes with magnitudes greater than 5 plotted for reference.

are likely related to a more active seismicity (Castro *et al.*, 2000; Tusa *et al.*, 2012) and to less attenuation in the more stable northeast region (Castro *et al.*, 1996; Malagnini *et al.*, 2002).

One of our goals in the future is to investigate the spectral decay parameter κ before and after the main events of Amatrice (M6.0) of 24 August 2016, and Norcia (M6.5) of 30 October 2016. Preliminary results (Castro *et al.*, 2022b) showed that for both two earthquake sequence, the temporal variation of κ parameter could be a good indicator to monitor the earthquake cycle.

Acknowledgements

We are very grateful to Daniele Spallarossa from the University of Genova for providing the data set used in this study. This research was supported by Istituto Nazionale di Geofisica e Vulcanologia (INGV) in the frame of the project Pianeta Dinamico (Working Earth) in the task concerning the Seismic attenuation and variability of seismic motion.

References

Akinci, A., Del Pezzo, E. and Malagnini, L.; 2020. *Intrinsic and scattering seismic wave attenuation in the central Apennines (Italy)*. Phys. Earth Planet. In., **303**, DOI: 10.1016/j.pepi.2020.106498.

Anderson, J. G.; 1991. *A preliminary descriptive model for the distance dependence of the spectral decay parameter in southern California*. Bull. Seismol. Soc. Am., **81**, 2186-2193. DOI: 10.1785/BSSA0810062186.

Anderson, J. G., and Hough, S.; 1984. *A model for the shape of the Fourier amplitude spectrum of acceleration at high frequencies*. Bull. Seism. Soc. Am., **74**, 1969-1984. DOI: 10.1785/BSSA0740051969.

Anderson, J. G., and Lei, Y.; 1994. *Nonparametric description of peak acceleration as a function of magnitude, distance, and site in Guerrero, Mexico*. Bull. Seismol. Soc. Am., **87**, 67-84. DOI:10.1785/BSSA0840041003.

Bennington, N., Thurber, C., and Roecker, S.; 2008. *Three-dimensional seismic attenuation structure around the SAFOD site, Parkfield, California*. Bull. Seismol. Soc. Am., **98**, 6, 2934-2947. DOI: 10.1785/0120080175.

Castro, R. R., Pacor, F., Sala, A., and Petrungaro, C.; 1996. *S wave attenuation and site effects in the region of Friuli, Italy*. J. Geophys. Res. 101, B10, 22, 3552-2,369. DOI: 10.1029/96JB02295.

Castro, R. R., Trojani, L., Monachesi, G., Mucciarelli, M., and Cattaneo, M.; 2000. *The spectral decay parameter in the region of Umbria-Marche, Italy*. J. Geophys. Res. 105, 23,811-23,823. DOI: 10.1029/96JB02295.

Castro, R. R., Pacor, F. and Spallarossa, D.; 2021. *Depth-dependent shear-wave attenuation in central Apennines, Italy*. Pure Appl. Geophys. 178, 2059-2075. DOI: 10.1007/s00024-021-02744-9.

Castro, R. R., Colavitti, L., Vidales-Basurto, C. A., Pacor, F., Sgobba, S., and Lanzano, G.; 2022a. *Near-Source Attenuation and Spatial Variability of the Spectral Decay Parameter Kappa in Central Italy*. Seismol. Res. Lett. XX, 1-12. DOI: 10.1785/0220210276.

Castro, R. R., Spallarossa, D., Lanzano, G., Colavitti, L., Pacor, F., Vidales-Basurto, C. A., and Sgobba, S.; 2022b. *Temporal Variation of the Spectral Decay Parameter Kappa in Central Italy*. Geophys. Res. Lett., *in prep*.

Chiarabba, C., De Gori, P., Cattaneo, M., Spallarossa, D., and Segou, M.; 2018. *Faults geometry and the role of fluids in the 2016-2017 central Italy seismic sequence*. Geophys. Res. Lett., **45**, 14, 6'963-6'971. DOI: 10.1029/2018GL077485.

Chiarabba, C., Buttinelli, M., Cattaneo, M., and De Gori, P.; 2020. *Large earthquakes driven by fluid overpressure: The Apennines normal faulting system case*. Tectonics, **39**, 4, e2019TC006014. DOI: 10.1029/2019TC006014.

Fernández, A. I., Castro, R. R., and Huerta, C. I.; 2010. *The spectral decay parameter kappa in northeastern Sonora, Mexico*. Bull. Seismol. Soc. Am., **100**, 196-206. DOI: 10.1785/0120090049.

Gabrielli, S., Akinci, A., Ventura, G., Napolitano, F., Del Pezzo, E., and De Siena, L.; 2021. *Changes in seismic attenuation due to fracturing and fluid migration during the 2016-2017 central Italy seismic sequence*. J. Earth Space Sci. Open Archive, **33**. DOI:10.1002/essoar.10507643.1.

Ktenidou, O.-J., Cotton, F., Abrahamson, N. A., and Anderson, J. G.; 2014. *Taxonomy of κ: A review of definitions and estimation approaches targeted to applications*. Seismol. Res. Lett. **85**, 1, 135-146. DOI: 10.1785/0220130027.

Ktenidou, O.-J., Abrahamson, N. A., Drouet, S., and Cotton, F.; 2015. *Understanding the physics of kappa (κ): Insights from a downhole array*. Geophys. J. Int., **203**, 1, 678–691. DOI: 10.1093/gji/ggv315.

Lanzano, G., Felicetta, C., Pacor, F., Spallarossa, D., and Traversa, P.; 2020. *Methodology to identify the reference rock sites in regions of medium-to-high seismicity: An application in central Italy*. Geophys. J. Int. **22**, 2053-2067. DOI: 10.1093/gji/ggaa261.

Lanzano, G., Felicetta, C., Pacor, F., Spallarossa, D., and Traversa, P.; 2022. *Generic-to-reference rocks scaling factors for the seismic ground motion in Italy*. Bull. Seismol. Soc. Am. DOI: 10.1785/0120210063.

Malagnini, L., Akinci, A., Herrmann, R. B., Pino, N. A., and Scognamiglio, L.; 2002. *Characteristics of the ground motion in northeastern Italy*. Bull. Seismol. Soc. Am. **92**, 6, 2186–2204.

Pacor, F., Spallarossa, D., Oth, A., Luzi, L., Puglia, R., Cantore, L., Mercuri, A., D'Amico, M., and Bindi, D.; 2016. *Spectral models for ground motion prediction in the L'Aquila region (central Italy): Evidence for stress-drop dependence on magnitude and depth*. Geophys. J. Int., **204**, 697-718. DOI: 10.1093/gji/ggv448.

Pastori, M., Baccheschi, P., and Margheriti, L.; 2019. *Shear wave splitting evidence and relations with stress field and major faults from the Amatrice-Visso-Norcia seismic sequence*. Tectonics, **38**, 3351-3372. DOI: 10.1029/2018TC005478.

Pitilakis, K.; 2004. *Site effects, in Recent Advances in Earthquake Geotechnical Engineering and Microzonation*. Springer, Dordrecht, 139-197.

Sgobba, S., Lanzano, G., and Pacor, F.; 2021. *Empirical nonergodic shaking scenarios based on spatial correlation models: An application to central Italy*. Earthq. Eng. Struct. Dynam., **50**, 1, 60-80. DOI: 10.1002/eqe.3362.

Tusa, G., Langer, H., Brancato, A., and Gresta, S.; 2012. *High-frequency spectral decay in P-wave acceleration spectra and source parameters of microearthquakes in southeastern Sicily, Italy*. Bull. Seismol. Soc. Am., **102**, 4, 1796-1809. DOI: 10.1785/0120110206.

Vignaroli, G., Mancini, M., Brilli, M., Bucci, F., Cardinali, M., Giustini, F., Voltaggio, M., Yu, T. L., and Shen, C. C.; 2020. *Spatial-temporal evolution of extensional faulting and fluid circulation in the Amatrice basin (central Apennines, Italy) during the Pleistocene*. Front. Earth Sci. **8**. DOI: 10.3389/feart.2020.00130.

ACTIVE TECTONICS AND FAULT EVOLUTION IN THE WESTERN BALKANS

N. D'Agostino[1], A. Copley[2], J. Jackson[2], R. Koci[3], A. Hajrullai[3], L. Duni[3], N. Kuka[3]

[1] Osservatorio Nazionale Terremoti, Istituto Nazionale Geofisica e Vulcanologia, Roma, Italy
[2] Bullard Laboratories, University of Cambridge, UK
[3] Department of Seismology, Institute of Geosciences, Energy, Water and Environment, Tirana, Albania

The western Balkans occupy a region influenced by two major active tectonic processes: the collision between the Adriatic Sea and the Dinarides in the west and the extension of the Aegean Sea and its surroundings as they move towards the Hellenic Trench. An understanding of the kinematics and dynamics of the western Balkans has significance for our understanding of continental tectonics in general. The region is rich in observational data, with many well-studied earthquakes, good geodetic coverage by GNSS, and abundant exposure of active faulting and its associated geomorphology, especially within the Mesozoic carbonates that cover much of the extensional areas. We first use such observations to establish the regional kinematic patterns, by which we mean a clarification of how active faulting achieves the motions observed in the deforming velocity field obtained from GNSS measurements. We then use observations from geomorphology and the evolution of drainage systems to establish how those kinematic and faulting patterns have changed and migrated during the Late Neogene-Quaternary. The kinematics, and its evolution, can then be used to infer characteristics of the dynamics, by which we mean the origin and effect of the forces that control the overall deformation. The principal influences are: (a) the distribution and evolution of gravitational potential energy (GPE) contrasts arising from crustal thickness variations and elevation, in particular the growth of topography by shortening in the Albanides-Hellenides mountain ranges and the high elevation of mainland Greece relative to the Mediterranean sea floor; (b) the ability of the boundaries of the region, along the Adriatic coast and in the Hellenic Trench, to support the forces arising from those GPE contrasts. The evolution in space and time indicates an interaction between the anisotropic strength fabric of the upper crust associated with faulting, and the more distributed and smoother patterns of flow that are likely to characterise the ductile deformation of the lower, aseismic part of the lithosphere --- both of which influence the deformation on the scale of 100—200~km.

APPROCCIO NEOTETTONICO PER L'INDIVIDUAZIONE E DEFINIZIONE DELL'ATTIVITÀ E CAPACITÀ DELLA FAGLIA DI LEONESSA, APPENNINO CENTRALE

E. Falcucci[1], S. Gori[1], D. Maceroni[1], G. Dixit Dominus[2], F. Chiaretti[3], D. Cosentino[2], M. Moro[1], F. Doumaz[1], V. Materni[1], V. Sapia[1], G. Di Giulio[1], M.Vassallo[1], M.G. Di Giuseppe[1], R. Isaia[1], F. Tramparulo[1], M. Saroli[1,4], F. Galadini[1], V. Sepe[1]

[1] Istituto Nazionale di Geofisica e Vulcanologia , Roma, Italia
[2] Università degli Studi Roma Tre, Roma, Italia
[3] Libero Professionista
[4] Università di Cassino e Lazio Meridionale - DiCeM – Cassino

Nell'ambito delle attività finalizzate alla ricostruzione delle aree interessate dalla sequenza sismica dell'Italia centrale del 2016-2017, l'accordo siglato tra il Commissario Straordinario del Governo – Presidenza del Consiglio dei Ministri, On. Avv. Giovanni Legnini, e l'Istituto Nazionale di Geofisica e Vulcanologia prevede una collaborazione per le attività di studio e di ricerca finalizzate alla ridefinizione della zonazione del territorio interessato da Faglie Attive e Capaci (FAC). Fra le faglie oggetto di approfondimento, è stato realizzato uno studio sull'attività e la capacità della faglia di Leonessa. L'attività e capacità di questa faglia è ancora oggetto di dibattito nella letteratura scientifica.

Lo studio ha previsto l'esecuzione di indagini geologiche, geomorfologiche, geognostiche e geofisiche lungo tutta la traccia della faglia. I risultati fin qui ottenuti hanno permesso di definire porzioni distinte di faglia in termini di attività e capacità. Il settore settentrionale della faglia, compreso fra la località di Fonte Filucca (situata poco a NO dell'abitato di Leonessa), a sud, e l'estremo settentrionale della faglia, non mostra evidenze di dislocazione verticale del substrato carbonatico, dislocazione verticale attesa, trattandosi di una faglia considerata distensiva e legata al regime sismotettonico in atto. La continuità geometrica e stratigrafico-strutturale fra le Formazioni del substrato pre-quaternario attraverso la faglia indica l'assenza di rigetti, almeno in questa settore, riferibile ad una faglia normale.

Nel settore meridionale della faglia, fra l'abitato di Piedelpoggio e l'estremo meridionale della struttura, le informazioni raccolte mostrano che questa interessa il substrato carbonatico, ma non sono state individuate evidenze di dislocazioni che coinvolgono i depositi quaternari. Peraltro, l'esposizione del piano di faglia sul substrato carbonatico avviene in modo discontinuo lungo i versanti, e solo in corrispondenza di incisioni trasversali alla traccia della faglia e di fenomeni gravitativi superficiali che, dunque, esumano per processi non tettonici (erosivi o legati a instabilità di versante) il piano di faglia alla base della scarpata.

Nel tratto compreso fra l'area di Fonte Filucca, a nord, e l'area dell'abitato di Piedelpoggio, a sud, ovvero nel settore centrale della faglia, dove sorge l'abitato di Leonessa, le indagini preliminari non hanno permesso di escludere che la faglia possa aver dislocato terreni quaternari, riferibili al Pleistocene Superiore-Olocene, per un tratto pari a circa 7 km di lunghezza. Le informazioni geofisiche acquisite hanno evidenziato "anomalie" potenzialmente associabili a dislocazioni nella porzione di faglia più prossima all'abitato di Leonessa. Tali anomalie possibilmente associate a dislocazioni tettoniche potrebbero aver interessato depositi quaternari i quali, secondo la letteratura disponibile, potrebbero essere più recenti di 40.000 anni, ovvero il limite cronologico inferiore entro il quale una faglia deve mostrare evidenze di attività per essere ritenuta capace, secondo le Linee Guida FAC (Commissione tecnica per la microzonazione sismica, 2015).

Quindi, tenendo in considerazione le incertezze e le osservazioni geofisiche preliminari, nell'ambito dell'ultima fase del progetto sono state effettuate ulteriori indagini di terreno in diversi settori della faglia, sempre per reperire nuovi dati circa l'attività tardo-quaternaria di questa e per valutare l'entità delle eventuali dislocazioni verticali tramite studi di dettaglio. In questo ambito, sono state analizzate le sequenze sedimentarie localizzate al letto e al

tetto della faglia ritenute da alcuni autori come dislocate dall'attività della struttura al fine di verificare che la dislocazione proposta fra i depositi al letto e al tetto della faglia sia riferibile a sequenze sedimentare crono-stratigraficamente correlabili. Infine, sono state pianificate lindagini "paleosismologiche", come previsto dalle Linee Guida FAC, per ottenere informazioni conclusive per la definizione dell'attività e capacità della faglia di Leonessa, nel suo tratto centrale, e la tracciatura delle eventuali Zone di Rispetto (ZR) e Zone di Suscettibilità (ZS) a cavallo della traccia.

Il presente lavoro evidenzia come solo un approccio metodologico di tipo neotettonico, che prevede il concetto di definizione di evoluzione tettonica quaternaria, risulta efficace per la valutazione dello stato di attività di una struttura tettonica e per la parametrizzazione del comportamento cinematico in chiave sismotettonica.

ASSESSING THE CAPABILITY OF THE PESCOPAGANO FAULT, PART OF THE ANTITHETIC FAULT OF THE 1980, Mw 6.9 IRPINIA EARTHQUAKE (SOUTHERN ITALY)

L. Ferranti[1], F. Iezzi[1], A. Bacchiani[1], S. Buoninfante[1], F. Menna[1], M. Sposato[1], V. Di Fiore[2], D. Bellini[3], A. Citterio[3], R. Calabrò[3], C. Pasqua[4]

[1] DiSTAR - Dipartimento di Scienze della Terra, dell'Ambiente e delle Risorse Università di Napoli "Federico II"
[2] CNR-ISPC - Istituto di Scienze del Patrimonio Culturale
[3] Edison SpA
[4] FrosioNext

The ~5 km long Pescopagano fault (PF) is part of the ~22 km long, NW-SE striking and SW-dipping Conza della Campania fault (CCF), which lies above the SW-dipping "antithetic fault" that failed 40 sec after and ~10 km NE of the mainshock rupture of the 1980 Mw 6.9 Campania-Basilicata earthquake (Bernard and Zollo, 1989; Pingue and De Natale, 1993; Pantosti and Valensise, 1990). According to seismicity data, the antithetic fault is considered a blind atructure (with possible reactivation of an inherited thrust fault), with un upper tip at 1.5-1.8 km depth (Amato and Selvaggi, 1993; Amoruso *et al.*, 2005). Alternatively, the 1980 antithetic fault was considered to have caused surface ruptures on some strands of the CCF, including the PF (Blumetti *et al.*, 2002; Bello *et al.*, 2020). The PF is comprised in the ITHACA Catalogue of the Active and Capable Faults (http://sgi2.isprambiente.it/ithacaweb/viewer/) and is assigned a mainly pre-historic (3-9 ka) activity, slip rate of 0.3 mm/yr and an association with the 1980 event. The latter scenario has major implications for the local seismic hazard and territorial management, but robust kinematic and paleoseismological constraints are lacking.

We report here the results emerging from a structural and paleoseismological study carried for the purpose of a major infrastructure planning and aimed at assessing the capability and, in case of positive answer, the magnitude of past surface ruptures.

The WNW-ESE striking, SSW-dipping PF cuts across Upper Cretaceous-Oligocene rocks of the Flysch Rosso formation, part of the Lagonegro basin succession, which forms one of the main litho-tectonic units of the Southern Apennines fold and thrust belt. The fault is divided in three strands. We studied in detail the central (Croce dello Staccato, CS) and eastern (Madonna di M. Mauro, MM) strands, of broadly similar length (~1 km). These two strands juxtapose massive to bedded marly calcilutites and fine-medium calciturbidites in the footwall (member FYRc of the Flysch Rosso Fm) against thinly bedded reddish-greenish claystones and cherty argillites in the hanging-wall (younger member FYRa). These relations indicate the PF is predominantly a normal fault. Borehole data suggest that the PF has a 60°-70° dip and a ~100 m max throw.

The fault scarp is rather degraded and only at one place along the eastern strand a limited (0.5 m high x 5 m wide) hanging-wall synthetic fault plane exposure is present. Altered tectogrooves with a ~90° pitch were observed on the 55° southward dipping fault plane, providing a N-S extension axis. The finding of a fresh ~8 cm high ribbon at its base, however, induced further investigations to prove or dismiss involvement of the fault during the 1980 or preceding earthquakes.

High-resolution seismic reflection profiles and seismic tomographies provided images down to ~20 m depth that revealed the existence of three seismic units in the Vp model. These units have locally sharp lateral contacts, suggesting the possible presence of faults.

Notwithstanding, three paleoseismological trenches co-linear with the seismic profiles documented that the fault scarp is sealed by several sedimentary units. The uppermost unit (U1) is composed by recent soil and colluvial deposits and was dated back to ~6 ka BP. Unit U2 includes laterally variable thickness of alluvial sands and gravels, which are often channelized in the upper part, and passes downward to alluvial to slope gravel wedges (U3). Units U2 and U3 rest with sharp erosive contacts on at least two generations of marshy clays (U4) developed at the expense of the FYR-a hanging-wall bedrock. Although radiometric age constraints are

so far available only for U1, we believe units U2 and U3 may span the transition from the last glacial to the deglacial conditions.

Based on trench observations, preliminary age assessment, and morpho-structural data, the PF did not cause surface ruptures since 6 ka BP and probably since the Latest Pleistocene. Structural data indicate that the PF lies in the back-limb of a steep N-verging Pliocene fold-thrust train, which about 2 km north of the PF, carries the Lagonegro rocks above Middle Pliocene clay and silt of the Ofanto basin along the E-W striking Ofanto thrust fault. Because the extension axis on the PF is sub-parallel to the Pliocene shortening axis, we regard the PF as a back-limb collapse structure developed during or after thrusting, suggesting that the PF may have an early Quaternary age at most. Structural reconstructions indicate that the fault merge with the Ofanto thrust ramp at ~2 km depth where it reaches the ~4 km depth of the base of the Lagonegro basinal rocks (Nicolai and Gambini, 2007) but not the 10-12 km nucleation depth of large earthquakes in the area.

References

Amato A. and Selvaggi G.; 1993: *Aftershock location and P-velocity structure in the epicentral region of the 1980 Irpinia earthquake*. Ann. Geofis., **36**, 3-15.

Amoruso A., Crescentini L. and Scarpa R.; 2005: *Faulting geometry for the complex 1980 Campania-Lucania earthquake from levelling data*. Geophys. J. Int., **162**, 156–168.

Bello S., de Nardis R., Scarpa R., Brozzetti F., Cirillo D., Ferrarini F., di Lieto B., Arrowsmith R.J. and Lavecchia G.; 2021: *Fault Pattern and Seismotectonic Style of the Campania – Lucania 1980 Earthquake (Mw 6.9, Southern Italy): New Multidisciplinary Constraints*. Front. Earth Sci. 8:608063.

Bernard P. and Zollo A.; 1989: *The Irpinia Italy 1980 earthquake: detailed analysis of a complex normal fault*. J. Geophys. Res., **94**, 1631-1648.

Blumetti A.M., Esposito E., Ferreli L., Michetti A.M., Porfido S., Serva L. and Vittori E.; 2002: *New data and the reinterpretation of the november 23, 1980, M 6.9, Irpinia-Lucania earthquake (Southern Apennine) coseismic surface effects*. Studi Geologici Camerti, **2**, 19–27.

Nicolai, C. and Gambini, R.; 2007: *Structural architecture of the Adria platform-and-basin system*, Boll. Soc. Geol. Ital., **7**, 21-37.

Pantosti D. and Valensise G.; 1990: *Faulting mechanism and complexity of the 23 November, 1980, Campania-Lucania earthquake inferred form surface observations*. J. Geophys. Res., **95**, B10, 15319-15341.

Pingue F. and De Natale G; 1993: *Fault mechanism of the 40 seconds subevent of the 1980 Irpinia (Southern Italy) earthquake from levelling data*. Geophys. Res. Lett., **20**, 911–914.

3D-KERNEL BASED IMAGING OF AN IMPROVED ESTIMATION OF Q_c IN THE GARGANO PROMONTORY (SOUTHERN ITALY)

M. Filippucci[1], S. Lucente[1], E. Del Pezzo[2,3], S. de Lorenzo[1], G. Prosser[4], A. Tallarico[1]

[1] Department of Earth and Geo-Environmental Science, University of Bari Aldo Moro (UniBa)
[2] National Institute of Geophysics and Volcanology (INGV), Osservatorio Vesuviano
[3] Instituto Andaluz de Geofisica, Universidad de Granada
[4] Department of Science, University of Basilicata (UniBas)

We investigated crustal seismic attenuation by the coda quality parameter *Qc* in the Gargano Promontory (Southern Italy), using a database composed of 191 small earthquakes ($1.0 \le M_L \le 2.8$) recorded by the local OTRIONS and the Italian INGV seismic networks, over three years of seismic monitoring. The database was recently released by Filippucci *et al.* (2021a). Following the single back-scattering theoretical assumption (Aki and Chouet, 1975), *Qc* was computed using different frequencies (in the range of 2-16 Hz) and different lapse times (from 10 to 40 s). Results in Fig. 1 indicate that the trend of *Qc* vs. frequency is like that observed in the same area with another dataset (Filippucci *et al.*, 2019), overlaps the trend obtained for the adjacent Apennine chain (de Lorenzo *et al.*, 2013) and other tectonic and volcanic regions in Italy (references in Fig. 1). The 3D mapping procedure was based on sensitivity kernels following the procedure described by Del Pezzo and Ibanez (2020). 3D images at different frequencies revealed that the Gargano Promontory is characterized by very low and homogeneous *Qc* at low frequencies, and by high and heterogeneous *Qc* at high frequencies (Filippucci *et al.*, 2021b). The lateral variations of *Qc* at 12 Hz follow the trend of the Moho in this region and are in good agreement with other geophysical observations.

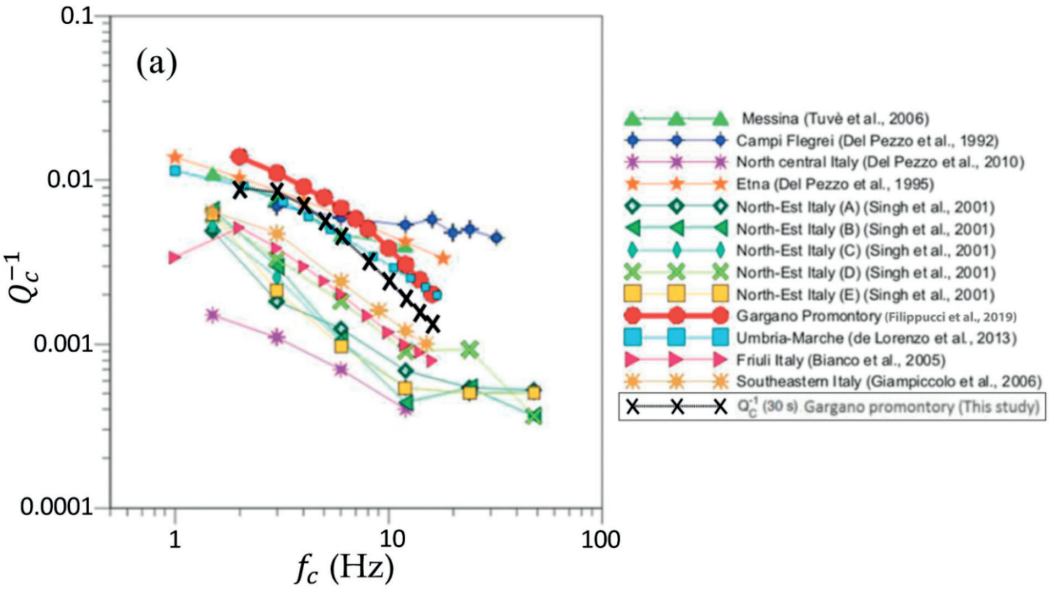


Fig. 1 - Comparison between the *Qc* estimates for each central frequency *fc* obtained in this work (t_L = 30 s) and the literature. (**a**) Literature referring to *Qc* studies from other areas of Italy (modified from Filippucci *et al.*, 2019). Letters from A to E refer to the subdivisions of Northeastern Italy by Singh *et al.* (2001).

Acknowledgements
This work was partially supported by Project PRIN n. 201743P29 FLUIDS (Detection and tracking of crustal fluid by multi-parametric methodologies and technologies).
E.D.P. was partially funded by the Spanish Mineco Project FEMALE, PID2019-106260GB-I00.
The computational work has been executed on the IT resources of the ReCaS-Bari data center, which have been

made available by two projects financed by the MIUR (Italian Ministry for Education, University and Re-search) in the "PON Ricerca e Competitività 2007–2013" Program: ReCaS (Azione I-Interventi di rafforzamento strutturale, PONa3_00052, Avviso 254/Ric) and PRISMA (Asse II-Sostegno all'innovazione, PON04a2_A).

References

Aki, K.; Chouet, B. Origin of Coda Waves: Source, Attenuation, and Scattering Effects. *J. Geophys. Res.* **1975**, *80*, 3322–3342.

Bianco, F.; Pezzo, E.D.; Malagnini, L.; Luccio, F.D.; Akinci, A. Separation of Depth-Dependent Intrinsic and Scattering Seismic Attenuation in the Northeastern Sector of the Italian Peninsula. *Geophys. J. Int.* **2005**, *161*, 130–142.

De Lorenzo, S.; Del Pezzo, E.; Bianco, F. Qc, Qβ, Qi and Qs Attenuation Parameters in the Umbria–Marche (Italy) Region. *Phys. Earth Planet. Inter.* **2013**, *218*, 19–30.

Del Pezzo, E.; Ibáñez, J.M. Seismic Coda-Waves Imaging Based on Sensitivity Kernels Calculated Using an Heuristic Approach. *Geosciences* **2020**, *10*, 304.

Filippucci, M.; Miccolis, S.; Castagnozzi, A.; Cecere, G.; de Lorenzo, S.; Donvito, G.; Falco, L.; Michele, M.; Nicotri, S.; Romeo, A.; et al. Seismicity of the Gargano Promontory (Southern Italy) after 7 Years of Local Seismic Network Operation: Data Release of Waveforms from 2013 to 2018. *Data Brief* **2021a**, *35*, 106783.

Filippucci, M.; Lucente, S.; Del Pezzo, E.; de Lorenzo, S.; Prosser, G.; Tallarico, A. 3D-Kernel Based Imaging of an Improved Estimation of (Q_c) in the Northern Apulia (Southern Italy). *Appl. Sci.* **2021b**, *11*, 7512. https://doi.org/10.3390/app11167512.

Filippucci, M.; Del Pezzo, E.; de Lorenzo, S.; Tallarico, A. 2D Kernel-Based Imaging of Coda-Q Space Variations in the Gargano Promontory (Southern Italy). *Phys. Earth Planet. Inter.* **2019**, *297*, 106313.

Giampiccolo, E., Tuvè, T., Gresta, S., & Patanè, D; S-waves attenuation and separation of scattering and intrinsic absorption of seismic energy in southeastern Sicily (Italy). *Geophys. J. Int.*, **2006**, *165*(1), 211-222.

Singh, S.; Herrmann, R.B. Regionalization of Crustal Coda Q in the Continental United States. *J. Geophys. Res. Solid Earth* **1983**, *88*, 527–538.

Tuvè, T.; Bianco, F.; Ibáñez, J.; Patanè, D.; Del Pezzo, E.; Bottari, A. Attenuation Study in the Straits of Messina Area (Southern Italy). *Tectonophysics* **2006**, *421*, 173–185.

INFLUENCE OF FLUID MIGRATION AND FRACTURING IN THE CENTRAL ITALY SEISMIC SEQUENCE FROM SCATTERING ATTENUATION AND INTRINSIC ABSORPTION

S. Gabrielli[1], A. Akinci[1], F. Napolitano[2], E. Del Pezzo[3,4], L. De Siena[5]

[1] Istituto Nazionale di Geofisica a Vulcanologia, Roma, Italy
[2] Università degli Studi di Salerno, Dipartimento di Fisica "E.R. Caianiello", Fisciano, Italy
[3] Istituto Nazionale di Geofisica e Vulcanologia, Osservatorio Vesuviano, Napoli, Italy
[4] Istituto Andaluz de Geofisica, Universidad de Granada, Granada, Spain
[5] Institute of Geosciences, Johannes Gutenberg University of Mainz, Germany

Quantifying seismic attenuation parameters in the crust, such as scattering and absorption, is fundamental in understanding the behavior of seismic events and, therefore, seismic hazard assessment.

Between August and October 2016, the Central Apennines (Italy) was struck by a cascading seismic sequence known as the Amatrice (Mw 6.0) - Visso (Mw 5.9) - Norcia (Mw 6.5) sequence, which has been considered connected to the fluid migration in the faults network, as suggested by previous studies (Miller *et al.*, 2004; Di Luccio *et al.,* 2010; Malagnini *et al.,* 2012; Chiodini *et al.,* 2004, 2020; Chiarabba *et al.*, 2020b).

Seismic attenuation imaging is a powerful tool to define the influence and abundance of fluids in a seismic sequence. Indeed, an increase in seismic attenuation can be associated with high fluid content and enhanced of permeability and fracturing.

Here, we present the separation of scattering and absorption contribution to the total attenuation of coda waves of the Central Italy seismic sequence, providing 2D images at different frequency bands of these quantities.

We used two datasets: the first one comprising ~3100 waveforms recorded before the sequence (March 2013-August 2016) and the second one comprising ~13900 waveforms (ML > 2.8) from the Amatrice-Visso-Norcia sequence.

The 2016-2017 sequence was further divided into three-time phases, each one related to a mainshock:

1) Amatrice sequence, including ~3600 waveforms recorded between 24/08/2016 and 25/10/2016
2) Visso sequence, including ~1600 waveforms recorded between 26/10/2016 and 29/10/2016
3) Norcia sequence, including ~8500 waveforms recorded between 30/10/2016 and 18/01/2017

The subdivision of the seismic sequence can highlight changes in attenuation in space and time, allowing us to interpret the possible patterns of fracture development and fluid migration in the seismogenic zone.

Methods. Scattering (Q_s) and absorption (Q_i) can be mapped in space using two seismic attributes:

1) Peak delay time, defined as the time difference between the S-wave arrival and the maximum amplitude of the event (Takahashi *et al.*, 2007);
2) Coda-waves attenuation (Q_c^{-1}), where coda waves are the wave trains following the S wave. When coda waves enter the diffusive regime (at late lapse times), coda attenuation can be considered equal to absorption (Qc ≈ Qi - Shapiro *et al.*, 2000)

Peak delay is associated with random inhomogeneities, measuring multiple forward scattering. One of the first applications of peak delay was in volcanic areas (Northeast Japan - Takahashi *et al.*, 2007). In tectonic zones, such as the Pyrenees (Calvet *et al.,* 2013) and the Vrancea region (Romania - Borleanu *et al.*, 2017), high peak delays detected fractured volumes. High peak delay values are also visible in the carbonate successions of the Pollino seismic gap (Southern Apennine - Napolitano *et al.*, 2020).

The amount of scattering accumulated along the seismic ray path is given by

$$\Delta log_{10} t(f) = log_{10} t_i^{PD}(f) - log_{10} t^{PD}(f) \quad (1)$$

Which is the difference between the measured peak delay time for the i-th waveform ($t_i^{PD}(f)$) and the theoretical peak delay obtained from:

$$log_{10} t^{PD}(f) = A(f) + B(f) \cdot log_{10} R_{Hypo} \quad (2)$$

with A(f) and B(f) as the coefficients of the resulting linear fit and R_{Hypo} is the hypocentral distance (between 20 and 100 km).

High scattering corresponds to positive values of $\Delta log_{10} t(f)$, representing heterogeneities (e.g., fractures and faults) in the crust, while low scattering-negative values characterize compact and rigid crust.

Qc measures the decay rate of the coda envelope with increasing lapse time from the origin time of the seismic event (Aki and Chouet, 1975). At first, to obtain Q_c^{-1} we linearize the equation of power spectral energy density (E(t,f)) as a function of the lapse time from the seismic event's origin time (t) (Aki and Chouet, 1975):

$$E(t,f) = S(f) t^{-\alpha} exp\left(\frac{-2\pi f t}{Q_c}\right)$$

where S(f) includes source and site terms and α is equal to 3/2, when propagation is constrained in a single layer in an anisotropic multiple scattering regime (Paasschens, 1997).

Then, to image Q_c^{-1} in 2D, we applied an inversion scheme using sensitivity kernel functions for the multiple-scattering regime (De Siena *et al.*, 2017; Del Pezzo *et al.*, 2018). The kernel functions are used to build the rows of the inversion matrix used in the inversion scheme. We then tested our resolution through a checkerboard test.

Results and Discussion. Peak delay results show a clear difference between the pre-sequence and sequence images, mainly at low frequencies (1.5 Hz – Fig. 1a), where we can define a spatial increase of scattering with time, attributed to structural discontinuities (faults and fractures) and lithology. High-scattering anomalies mapped by the peak delay delineate highly fractured carbonate formations (such as the Lazio-Abruzzi platform), while the Monti Sibillini thrust marks the strongest contrast in scattering.

Peak delay also shows a high scattering area corresponding to the Gran Sasso massif and L'Aquila zone, where an important seismic sequence (Mw 6.3) occurred in 2009.

In time and at low frequencies (1.5 Hz), the high-scattering is diffuse before the sequence, while between Amatrice and Norcia, the anomaly expands from the southern sector of the seismogenic zone to the fault network located in the W-SW of Norcia.

This change in time and space can be interpreted as micro-fracturing processes in the fault network during the seismic sequence.

While the structural elements appear pretty clearly in the scattering distribution, we cannot detect a similar pattern in the coda attenuation tomography (Fig. 1b). Absorption highlights a difference between the pre-sequence and the sequence, with high-absorption anomalies at low frequencies distributed around the Apennine Mountain chain. During the 2016-2017 sequence, the high absorption is then focused across the seismogenic zone.

Absorption mapping indicates a concentration of fluids along the seismogenic area during the 2016-2017 sequence. The time periods of Amatrice, Visso, and Norcia identify a progression related to a fluid migration from Amatrice. This spatial variation can be attributed to the deep migration of CO_2-bearing fluids across the fault network.

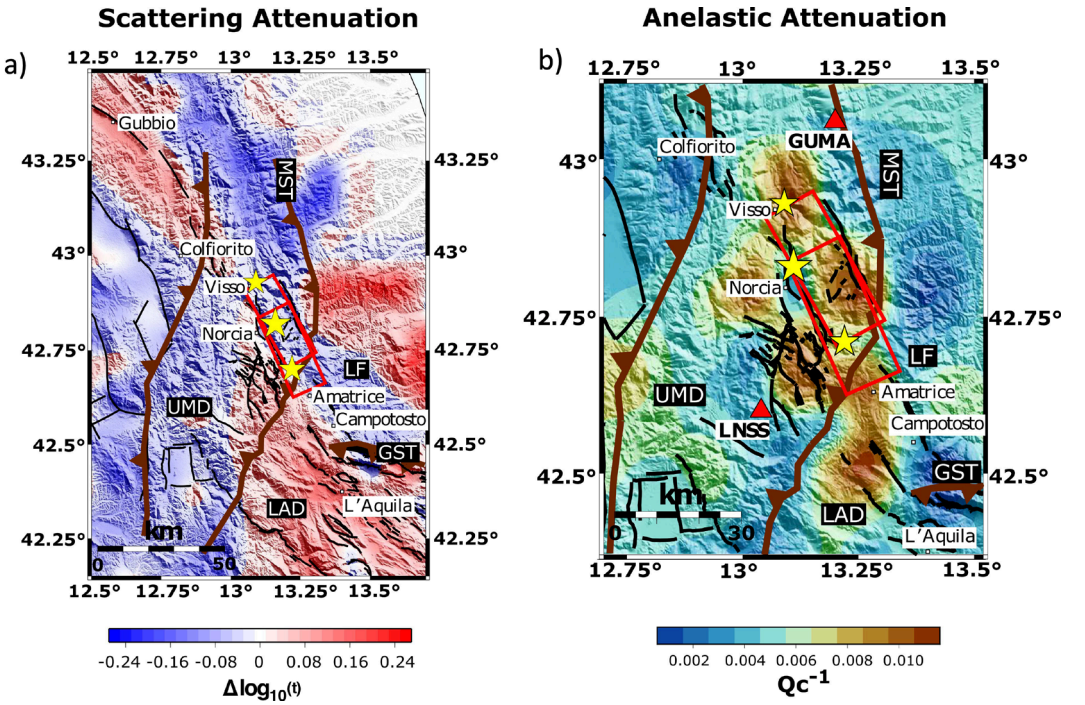


Fig. 1 - a) Spatial variation of Peak Delay at f_c = 1.5 Hz and b) Spatial variation of Q_c^{-1} at f_c = 1.5 Hz, both for the 2016-2017 seismic sequence. Red boxes are the fault plane activated during the AVN sequence and the black lines are the fault lines from the ITHACA catalog. Brown lines are the main thrust of the area (MST – Monti Sibillini Thrust; GST – Gran Sasso Thrust). The stars indicate the mainshocks of each 2016-2017 sequence. The main geological features are highlighted: LF - Laga Formation; UMD – Umbria-Marche Domain; LAD – Lazio-Abruzzi Domain.

To further look at this variation of Q_c^{-1} in time and space, we compared the averaged Q_c^{-1} between 2013 and 2017 at two seismic stations located in two different sections of the seismogenic zone: GUMA, in the north, and LNSS, in the south.

We observed a significant change in correspondence of the three mainshocks of Amatrice, Visso, and Norcia, with a different trend at the two stations. While at the station LNSS, southwest of Amatrice, the absorption decreases after the Amatrice earthquake, we noticed an increment at GUMA, northeast of the seismogenic zone and close to Visso, followed by a drop just after the Amatrice event and a rapid increase before Visso. At both stations, the absorption decreases after Norcia mainshock. These significant changes have a similar pattern to the temporal evolution of deep CO_2 degassing observed by Chiodini *et al.* (2020). The quick change in absorption between Visso and Norcia's mainshocks is also comparable with the Vp/Vs variation identified in the 4D velocity tomography of Chiarabba *et al.* (2020).

Overall, the results indicate a common characteristic of the Central Apennines seismic sequences: the deep migration of fluids rich in deep CO_2 along the seismogenic area. The seismic attenuation mechanisms mapped in this work allowed us to detect the area of extension of this migration both in time and space.

Acknowledgments
This work has been carried out in the framework of the project Pianeta Dinamico/2020-2021 supported by Ministero dell'Istruzione, dell'Università e della Ricerca (MIUR).

References

Aki, K., Chouet, B.; 1975. *Origin of coda waves: Source, attenuation, and scattering effects*. J. Geophys. Res. 80, 3322–3342. https://doi.org/10.1029/JB080i023p03322

Borleanu, F., De Siena, L., Thomas, C., Popa, M., Radulian, M.; 2017. *Seismic scattering and absorption mapping from intermediate-depth earthquakes reveals complex tectonic interactions acting in the Vrancea region and surroundings (Romania)*. Tectonophysics 706, 129–142.

Calvet, M., Sylvander, M., Margerin, L., Villaseñor, A.; 2013. *Spatial variations of seismic attenuation and heterogeneity in the Pyrenees: Coda Q and peak delay time analysis*. Tectonophysics 608, 428–439. https://doi.org/10.1016/j.tecto.2013.08.045

Chiarabba, C., Buttinelli, M., Cattaneo, M., De Gori, P.; 2020. *Large Earthquakes Driven by Fluid Overpressure: The Apennines Normal Faulting System Case*. Tectonics 39. https://doi.org/10.1029/2019TC006014

Chiodini, G., Cardellini, C., Amato, A., Boschi, E., Caliro, S., Frondini, F. and Ventura, G.; 2004. *Carbon dioxide Earth degassing and seismogenesis in central and southern Italy*. Geophys. Res. Lett., 31(7). https://doi.org/10.1029/2004GL019480

Chiodini, G., Cardellini, C., Di Luccio, F., Selva, J., Frondini, F., Caliro, S., ... & Ventura, G.; 2020. *Correlation between tectonic CO2 Earth degassing and seismicity is revealed by a 10-year record in the Apennines, Italy*. Science advances, 6(35).

De Siena, L., Amoruso, A., Pezzo, E. Del, Wakeford, Z., Castellano, M., Crescentini, L.; 2017. *Space-weighted seismic attenuation mapping of the aseismic source of Campi Flegrei 1983-1984 unrest*. Geophys. Res. Lett. 44, 1740–1748. https://doi.org/10.1002/2017GL072507

Del Pezzo, E., De La Torre, A., Bianco, F., Ibanez, J., Gabrielli, S., De Siena, L.; 2018. *Numerically calculated 3d space-weighting functions to image crustal volcanic structures using diffuse coda waves*. Geosci. 8. https://doi.org/10.3390/geosciences8050175

Di Luccio, F., Ventura, G., Di Giovambattista, R., Piscini, A., Cinti, F.R.; 2010. *Normal faults and thrusts reactivated by deep fluids: The 6 April 2009 Mw 6.3 L'Aquila earthquake, central Italy*. J. Geophys. Res. Solid Earth 115. https://doi.org/10.1029/2009JB007190.

Malagnini, L., Lucente, F.P., De Gori, P., Akinci, A., Munafo', I.; 2012. *Control of pore fluid pressure diffusion on fault failure mode: Insights from the 2009 L'Aquila seismic sequence*. J. Geophys. Res. Solid Earth 117. https://doi.org/10.1029/2011JB008911

Miller, S. A., Collettini, C., Chiaraluce, L., Cocco, M., Barchi, M., & Kaus, B. J.; 2004. *Aftershocks driven by a high-pressure CO 2 source at depth*. Nature, 427(6976), 724-727.

Napolitano, F., De Siena, L., Gervasi, A., Guerra, I., Scarpa, R., La Rocca, M.; 2020. *Scattering and absorption imaging of a highly fractured fluid-filled seismogenetic volume in a region of slow deformation.* Geosci. Front. 11, 989–998. https://doi.org/10.1016/j.gsf.2019.09.014

Paasschens, J.; 1997. *Solution of the time-dependent Boltzmann equation*. Phys. Rev. E 56, 1135–1141. https://doi.org/10.1103/PhysRevE.56.1135

Takahashi, T., Sato, H., Nishimura, T., & Obara, K.; 2007. *Strong inhomogeneity beneath Quaternary volcanoes revealed from the peak delay analysis of S-wave seismograms of microearthquakes in northeastern Japan*. Geophys. J. Int., 168(1), 90-99.

IL SISTEMA DI FAGLIE ATTIVE DEL GRAN SASSO ED IL CATASTROFICO TERREMOTO DEL 1349: UN'ATTRAZIONE FATALE

P. Galli[1,2], A. Galderisi[2], P. Messina[2], E. Peronace[2]

[1] Dipartimento della Protezione Civile, Rome, Italy
[2] Consiglio Nazionale delle Ricerche – Istituto di Geologia Ambientale e Geoingegneria (CNR-IGAG), Rome, Italy

Vent'anni dopo la pubblicazione dei risultati paleosismologici relativi ad alcuni segmenti del sistema di faglie normali del Gran Sasso (Giraudi e Frezzotti, 1995; Galli *et al.*, 2002), siamo tornati ad investigare l'attività successiva all'Ultimo Massimo Glaciale di altri tre segmenti degli otto principali che compongono il sistema, analizzandola in quattro diversi siti. Abbiamo condotto decine di profili topografici ad alta risoluzione attraverso le scarpate di faglia che interessano i versanti (Fig. 1), i conoidi alluvionali, i circhi glaciali, le morene ed il fondovalle di Campo Imperatore e delle aree limitrofe attraversate dai diversi segmenti e rami del sistema (Fig. 2). Grazie a numerose datazioni radiometriche su campioni raccolti negli scavi paleosismologici e in altri affioramenti chiave, integrandole con quelle effettuate nei precedenti lavori, siamo riusciti a definire un valore robusto dello slip-rate della faglia del Gran Sasso e ricostruito parte della sua storia sismica olocenica.



Fig. 1 - Veduta aerea obliqua verso sudest della scarpata di faglia Mandrucce-Vado di Corno, scolpita nella cataclasite del Calcare Massiccio. Il rigetto della superficie topografica è nell'ordine dei 20 m, ed è avvenuto presumibilmente dopo l'Ultimo Massimo Glaciale.

Le analisi paleosismologiche hanno permesso di riconoscere tre eventi di fagliazione consecutiva nel corso del tardo Olocene, separati da 3.3 e 2.2 ky, rispettivamente (Galli *et al.*, 2021). L'ultimo evento è databile nel XIII-XIV secolo d.C., un intervallo che coincide perfettamente con la sequenza sismica epocale del settembre 1349, una delle più catastrofiche sequenze italiane insieme a quelle del 1456 e del 1783.

La revisione e l'implementazione dei punti di intensità macrosismica di questa sequenza indicano l'esistenza di due distinte aree mesosismiche. Una, la più meridionale - ai confini tra l'Abruzzo, la Campania ed il Molise – è stata già associata per via paleosismologica alla rottura cosismica della faglia delle Aquae Iuliae (Galli e Naso, 2009), mentre la seconda - nell'Abruzzo



Fig. 2 - Contropendenze sul versante adriatico del Monte Brancastello lungo la scarpata di faglia nelle morene tardi glaciali. Sullo sfondo al centro il Corno Grande.

aquilano - si correla bene al sistema di faglie del Gran Sasso, distribuendosi ampiamente nel suo vasto blocco di tetto. Considerando la notevole lunghezza complessiva del sistema del Gran Sasso (45 km), abbiamo stimato una Mw≥7.0 in caso di rottura simultanea degli otto segmenti, un valore compatibile sia con la distruzione totale nel 1349 de L'Aquila (X grado MCS) e degli insediamenti limitrofi di *near-field*, che con i danni gravissimi a Sumona (VIII-IX MCS) ed agli edifici di grandi dimensioni ubicati anche a decine e decine di chilometri di distanza, a Roma, Viterbo, Orvieto e altrove (VII-VIII MCS) (Fig. 3).

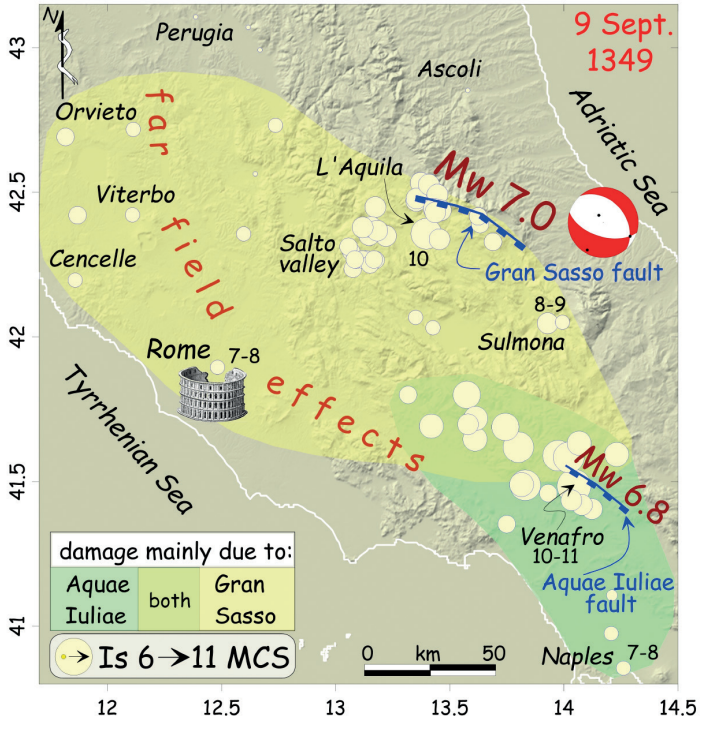


Fig. 3 - Distribuzione delle intensità macrosismiche relative alla sequenza del settembre 1349. Si ipotizza la rottura penecontemporanea della faglia delle Aquae Iuliae a sud e del Gran Sasso a nord come sorgenti della maggior parte degli effetti noti.

Sebbene sia caratterizzato da lunghi periodi di ricorrenza (i.e., 2.8 ±0.5 ky), i nostri risultati suggeriscono che il sistema di faglie del Gran Sasso possegga il più elevato potenziale sismogenico tra tutte le strutture attive appenniniche, con implicazioni notevoli in termini di rischio sismico associato, in considerazione sia dell'alto potere distruttivo nel near field (Galadini *et al.*, 2003) che della sua capacità di causare danni gravi a determinate tipologie di edifici posti anche ad un centinaio di chilometri di distanza.

Bibliografia citata

Galadini F., Galli P. & Moro M., 2003. *Paleoseismology of silent faults in the central Apennines (Italy): the Campo Imperatore fault (Gran Sasso Range fault system)*, Annals of Geophysics, 46, 793-814.

Galli P., Galadini F., Moro M., Giraudi C., 2002. *New paleoseismological data from the Gran Sasso d'Italia area (central Apennines),* Geophys. Res. Letters, 29(7) 10.1029/2001GL013292.

Galli P., Naso G., 2009. *Unmasking the 1349 earthquake source (southern Italy). Paleoseismological and archaeoseismological indications from the Aquae Iuliae fault*, J. Structural Geology, 31, 128-149.

Galli P., Galderisi A., Messina P., Peronace E., 2022. *The Gran Sasso fault system: Paleoseismological constraints on the catastrophic 1349 earthquake in Central Italy*, Tectonophysics, 822, 1-29, 10.1016/j.tecto.2021.229156.

Giraudi, C., Frezzotti, M., 1995. *Palaeoseismicity in the Gran Sasso massif (Abruzzo, Central Italy).* Quat. Int. 25, 81–93. https://doi.org/10.1016/1040-6182.

A REGIONAL COLLECTION OF FAULT/SLIP DATA AND ASSOCIATED STRAIN PARAMETERS FOR THE INTRA-APENNINE EXTENSIONAL BELT OF CENTRAL ITALY

G. Lavecchia[1,2], S. Bello[1,2], C. Andrenacci[1,2], D. Cirillo[1,2], F. Ferrarini[1,2], R. de Nardis[1,2], G. Roberts[3], F. Brozzetti[1,2]

[1] DiSPuTer - Dipartimento di Scienze Psicologiche, della Salute e del Territorio, Università G. d'Annunzio Chieti-Pescara, Chieti, Italy
[2] CRUST - Centro InteRUniversitario per l'analisi Sismotettonica Tridimensionale, Chieti, Italy
[3] Department of Earth and Planetary Sciences, Birkbeck, University of London

We present QUIN, a "QUaternary fault strain INdicators database", designed to integrate and unify published and new local-scale geological information and derive deformation and strain parameters for seismotectonic analysis (Lavecchia *et al.*, 2022). QUIN provides data on 3339 Fault Striation Pairs (FSPs; fault plane and slickenline), distributed within 455 survey sites exposed along the intra-Apennine Quaternary extensional faults of Central Italy (Fig. 1). The area covers an extent of ~550 km in an average NW-SE direction. QUIN gives information on FSP location, attitude and kinematics, and deformation axes (Fig. 2). Together with QUIN, we also provide an original shapefile of the Quaternary and, occasionally late Pliocene, faults hosting the FSP (Lavecchia *et al.*, 2021). Furthermore, we prepared a new compilation of simple graphical and numerical algorithms in MATLAB to perform kinematic analysis of fault-slip data (Andrenacci *et al.*, 2021).

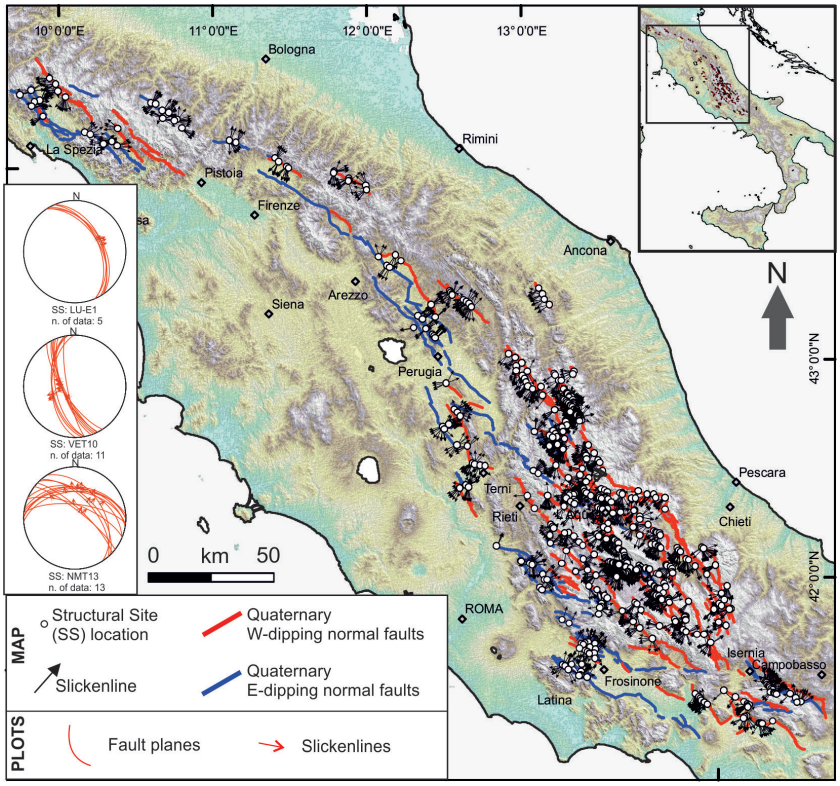


Fig. 1 - Structural Sites (SS) and slip vectors from the Fault/Striation Pairs (FSPs) data in the QUIN database (Lavecchia *et al.*, 2022); the SS are projected on a shaded relief map of northern-central Apennines of Italy along the trace of Quaternary normal faults hosting the SS; fault traces are derived from the Host Fault database (Lavecchia *et al.*, 2021). Stereoplots Lambert projection (lower hemisphere) at the map side represent examples of FSP data for three SS chosen across the Quaternary fault belt from north to south; key: LU-E1, VET10, NMT13 = SS short names as reported in the QUIN database.

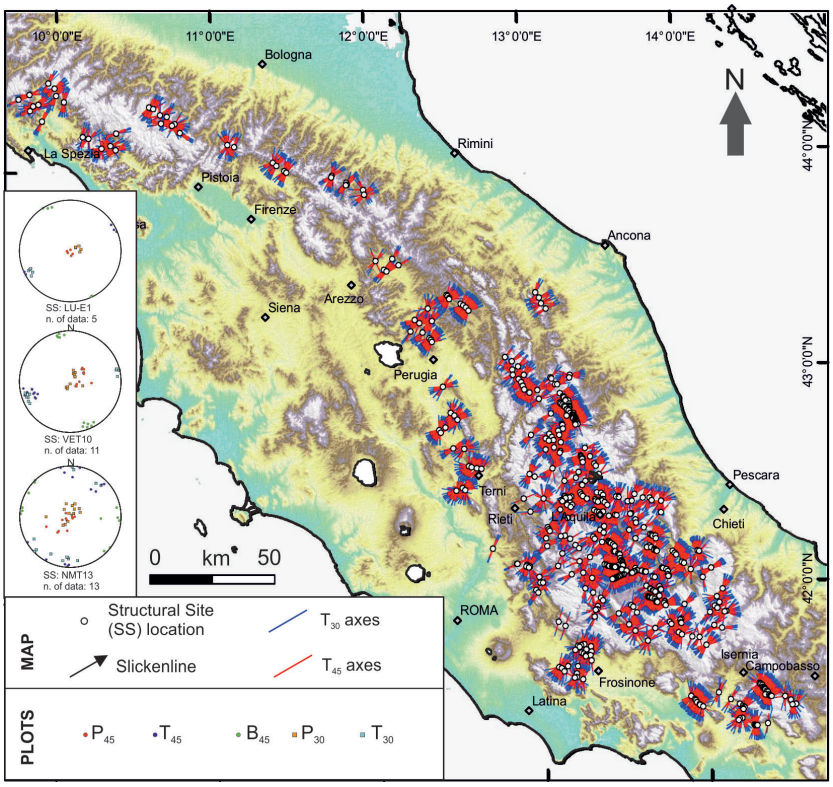


Fig. 2 - Tensional axes (T_{30}- and T_{45}) computed in the QUIN database (Lavecchia *et al.*, 2022) projected on a shaded relief map of northern-central Apennines of Italy. Stereoplots on the left of the figure represent the same SS as in Fig. 1 (also same location). Key: P_{45} and P_{30}= contractional axes, B_{45}= neutral axes; T_{45} and T_{30}= extensional axes.

To build a unified and comprehensive database, we followed the following sequential steps:

1) We recovered published FSP data (only data with both fault plane and slickenline attitudes) surveyed along the major intra-Apennine faults of Central Italy. Where the fault-slip attitudes were not tabulated in the original data source, we graphically derived them from their stereographic representation within the original paper.
2) We also extracted unpublished data from our field booklets and accompanying maps for FSP data surveyed in the last few decades. We projected the corresponding SS in map view on a GIS platform and identified information gaps.
3) We performed new field campaigns (from 2018 to 2021) to fill gaps in data and locally integrate the information.
4) With the previous steps, we recovered a total of 3339 FSP (2024 from literature and 1315 original), measured at 455 survey sites (SS). Each FSP corresponds to the raw data record of the QUIN fault/slip database.
5) We identified with a quality code the precision in reading the FSP attitudes from the original stereoplots.
6) We identified the spatial coordinates of each SS by georeferencing the location maps from the literature or our booklets. In some cases, tabulated Latitude and Longitude coordinates were available. The precision of the geographic location was also identified with a quality code.
7) Starting from the FSP data, we calculated the rake values (Aki and Richards format) and classified the FSP in kinematic classes corresponding to pitch ranges.

8) We calculated the principal deformation axes from the FSP data and/or from the plane attitude and rake.

The FSPs in the QUIN database refer to meso- and major-scale fault planes surveyed in Structural Sites (SS) located along or near to the Host Fault traces. We did not report fault planes without lineation data as they are unsuitable for kinematic analysis.

Making available a regional compilation of detailed fault traces and structural data is fundamental to constraining the geometry and kinematics of the intra-Apennine potentially seismogenic faults, also performing detailed studies on kinematic partitioning and rupture segmentation, both with classical methodologies and with new technologies.

Our data help to clarify and implement the contemporary geometric and kinematic deformation pattern of Central Italy that appears scattered and incomplete whenever exclusively derived from earthquake data. Each Structural Site with a sufficient and kinematically homogeneous fault population, represented as pseudo-focal mechanism, can be compared with seismological focal mechanisms, and used for formal stress field inversion. QUIN is useful to refine and locally extend the surface boundary of the Italian extensional seismogenic province, with relevance for hazard assessment evaluation, especially in areas that have not yet released earthquakes since historical times.

An extension of the database to southern peninsular Italy is underway within the frame of the MUSE-4D PRIN2017 project (Lavecchia PI).

References

Andrenacci C., Bello S., de Nardis R., Lavecchia G.; 2021: *Fault-Striation Pair Analysis (F-SPA) Tool.* Zenodo. https://doi.org/10.5281/zenodo.5910783.

Lavecchia G., Bello S., Andrenacci C., Cirillo D., Ferrarini F., Vicentini N., de Nardis R., Brozzetti F.; 2021: *Host Faults Database of central Italy.* Zenodo. https://doi.org/10.5281/zenodo.6412501.

Lavecchia G., Bello S., Andrenacci C., Cirillo D., Ferrarini F., Vicentini N., de Nardis R., G. Roberts, Brozzetti F.; 2022: *QUaternary fault strain INdicators database - QUIN 1.0 -first release from the Apennines of central Italy.* Scientific Data, accepted in May 2022.

DETECTION OF LOW FREQUENCY EARTHQUAKES AT MT. VESUVIUS BY USING A FREQUENCY DOMAIN APPROACH

R. Manzo[1,2], D. Galluzzo[2], M. La Rocca[3], L. Nardone[2], R. Di Maio[1]

[1] Dipartimento di Scienze della Terra, dell'Ambiente e delle Risorse, Università degli Studi di Napoli Federico II, Napoli, Italy
[2] Istituto Nazionale di Geofisica e Vulcanologia, Sez. di Napoli, Osservatorio Vesuviano, Italy
[3] Dipartimento di Biologia, Ecologia e Scienze della Terra, Università della Calabria, Rende, Italy

Introduction. The most common and recognised typologies of seismic events occurring in volcanic environments can be classified as: high frequency (*HF*) events, often identified as volcano-tectonic earthquakes (*VT*), earthquakes associated with explosive activity (explosion quakes), low frequency (*LF),* long period *LP* seismic events and volcanic tremor. The assessment of a volcano's eruptive potential, and the variation of its internal dynamics, can be provided through detection, identification and analysis of the different typologies of seismicity. In particular, the onset of low frequency events (*LF* or *LP*) or volcanic tremor is considered as a potential indicator of the awakening of volcanic activity related to in-depth magma movement or injection of fluids. Although high volcanic risk areas are monitored by modern high-sensitivity seismic instrumentation, the background noise compromises the detection and study of low-energy earthquakes. In this framework, a new multi-methodological analysis approach is provided to overcome this critical issue. In particular, in this note we present the results of the proposed approach applied to the densely urbanized area of Mt. Vesuvius, where low amplitude seismic signals due to local seismicity are recorded by a monitoring network equipped by broad band high sensitivity seismic stations. Our aim is to detect small low frequency events into the background noise by means of methodologies that operate in the frequency domain.

Methods. Nowadays, big data, not always manageable by seismologists' experience, requires new detection methodologies. To this end, the approach we propose focuses on the analysis of seismic signal spectral content using the following two techniques jointly:

- *Coherence analysis*: The coherence (K_{xy}) between two seismic signals (*x* and *y*) provides an indication of the similarity of their respective spectra in a specific frequency band:

$$K_{xy} = \frac{C_{xy}(f) * C^*_{xy}(f)}{P_x(f) * P_y(f)}$$

where $C_{xy}(f)$ is the cross-spectrum and $P_x(f) * P_y(f)$ is the eigenspectral product.
Coherence gives values between 0 and 1.

- *Spectral parameters analysis*: it takes into account the central frequency (Ω) and the form factor (δ) from the statistical moments of the seismic power spectrum. The first parameter represents the value around which most of the spectral energy is centered; the second one indicates the distribution of the spectral amplitudes around the central frequency.

Case study: Mt. Vesuvius. As it is well known, Mt. Vesuvius (southern Italy) represents one of the highest risk volcanoes in the world. In the last 40 years, it has been characterized by: volcano-tectonic events (*VT*, about 900 earthquakes per year in the last two years) of small magnitude ($M_D < 3$), sometimes occurring in low energy swarms and at depths between 0 and 2 km b.s.l.; several low-frequency events (*LF*) characterized by deeper hypocenters (La Rocca and Galluzzo, 2016). The two techniques described above were applied to the continuous seismic signals recorded from 2019 to 2020 by the monitoring seismic network installed at Mt.Vesuvius (Fig. 1). Taking into account some benchmark stations characterized by low

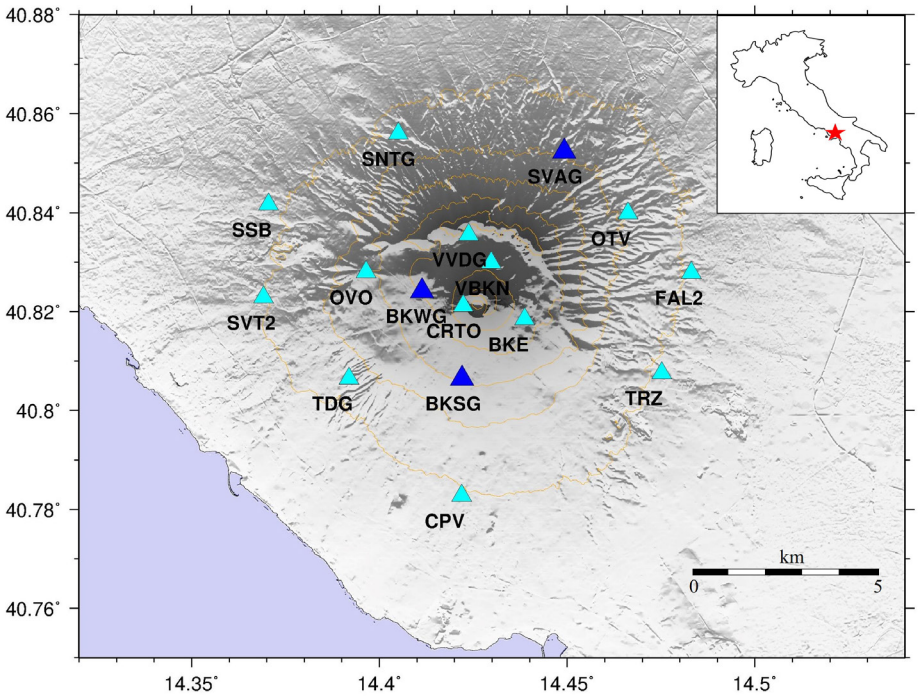


Fig. 1 - Mt. Vesuvius seismic network. The triangles indicate the seismic stations; the blue triangles show the stations used for the analyses presented in this work.

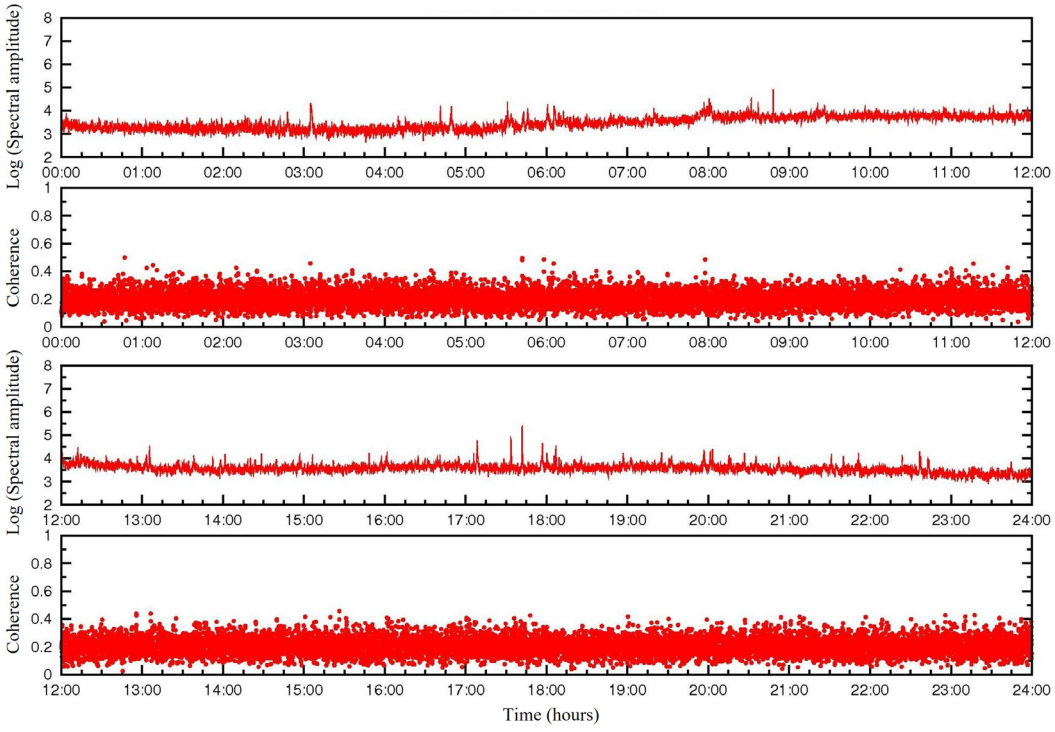


Fig. 2 - Coherence results obtained for the continuous signals recorded on December 01, 2019. The analysis is performed at 4 Hz.

background noise, *LF* seismic signals were idebtified as a result of joint coherence and spectral parameters analyses. The coherence was evaluated at a frequency equal to 4 Hz, which is the main frequency of *LF* signals (La Rocca and Galluzzo, 2016). All the analyses were performed on 30 s non-overlapping signal windows. In particular, all the time windows characterized by δ between 0.45 and 0.65, Ω between 3 and 6 Hz (Galluzzo *et al.*, 2020) and coherence ≥ 0.5 (Fig. 2) were selected. Fig. 3a shows an example of a low-frequency signal, initially masked by the high background noise and consequently filtered into the appropriate frequency band and

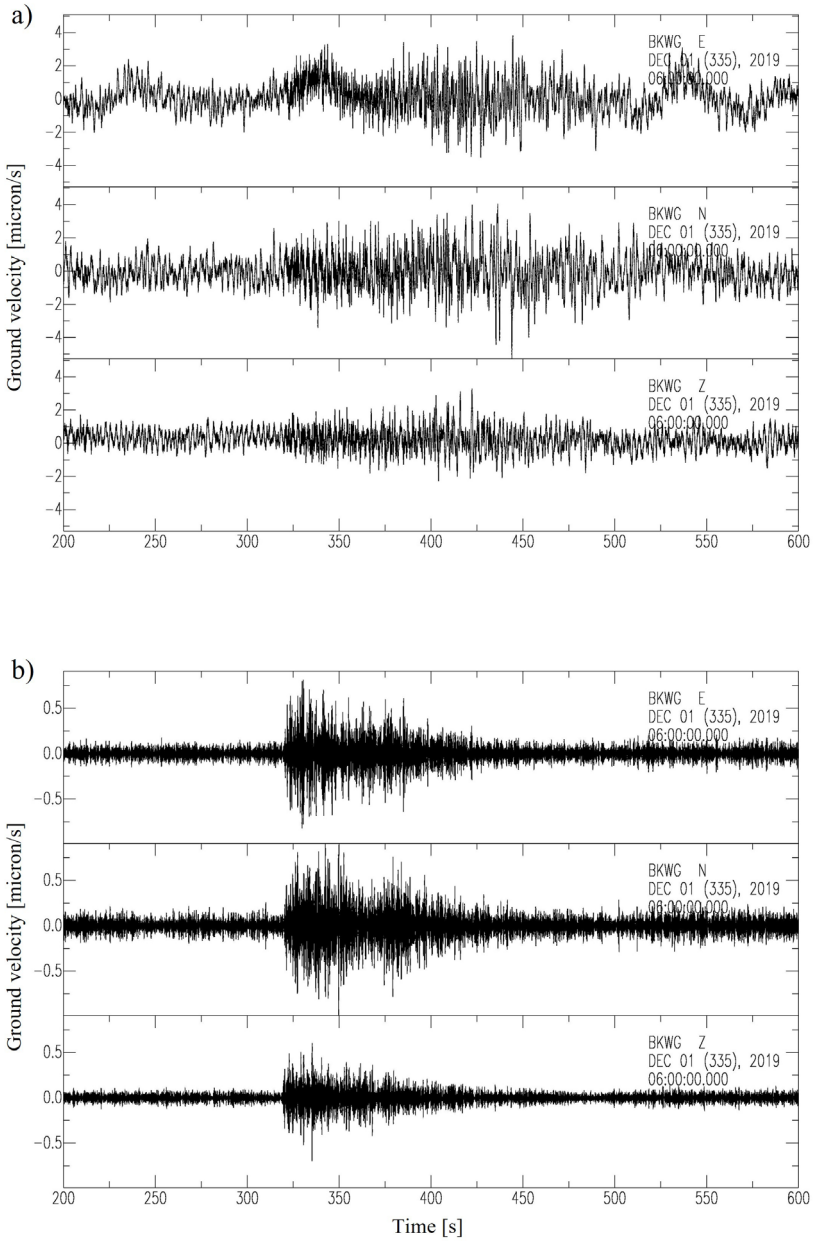


Fig. 3 - Low Frequency seismic event registered on December 01, 2019 at 06:05 am. a) Raw three-component signals recorded by the BKWG broad band station. b) Three-component signals filtered in the 3-6 Hz frequency band recorded by the BKWG broad band station.

identified by our approach (Fig. 3b). The size of these *LF* events is evaluated in terms of seismic moment (M_0) calculated according to Havskov and Ottemöller (2010):

$$M_0 = \frac{\Omega_0 4\pi\rho v^3}{R*Fs*G(\Delta, h)},$$

where Ω_0 is the spectral flat level, ρ is the medium density, *v is* the velocity of S wave at source, *R* is the average radiation pattern effect set to 0.6, *Fs* is the free surface operator equal to 2 and *G* is the geometrical spreading term as a function of epicentral distance Δ(m) and hypocentral depth *h*(m).

In this work, the detection procedure has identified about 30 low-frequency events, most of them not contained in the official catalogue, characterized by seismic moment M_0 in the range 10^{10} – 10^{13} Nm (10^6 – 10^7 Joule in terms of seismic energy).

Conclusions. Several neural network approaches are widely adopted to detect and classify the seismicity, especially in active volcanic areas where different types of seismic signals co-exist. In recent years, some methods based on spatial coherence of seismic signals recorded on active volcanoes have been proposed (Permana et al., 2022). The novelty of our methodology consists in combining two complementary techniques: the first one based on the spectral parameters analysis essentially applied to a single seismic station, and the second one based on the coherence analysis that highlights common features of the set of seismic stations used. Preliminary results obtained for Mt. Vesuvius are encouraging as the methodology has allowed to identify low-frequency events not catalogued by commonly used procedures.

References

Galluzzo, D., Nardone, L., La Rocca, M., Esposito, A.M., Manzo, R., Di Maio, R., 2020: *Statistical moments of power spectrum: a fast tool for the classification of seismic events recorded on volcanoes.* Advances in Geosciences, 52, 67-74.

Havskov, J. and Ottemöller, L., 2010: *Routine Data Processing in Earthquake Seismology*. Springer.

La Rocca, M. and Galluzzo, D., 2016: *Volcanic tremor at Mt. Vesuvius associated with low-frequency shear failures*. Earth and Planetary Science Letters, 442, 32-38.

Permana, T., Nishimura, T., Nakahara, T., Shapiro, N., 2022: *Classification of volcanic tremors and earthquakes based on seismic correlation: application at Sakurajima volcano, Japan.* Geophysical Journal International, 229, 1077-1097.

EVOLUZIONE GEOMORFOLOGICA ED IMPLICAZIONI TETTONICHE TARDO QUATERNARIE DELL'AREA DI CAMPO IMPERATORE (GRAN SASSO, ITALIA CENTRALE)

P. Messina[1], P. Galli[1,2], E. Peronace[1]

[1] Consiglio Nazionale delle Ricerche - Istituto di Geologia Ambientale e Geoingegneria, Rome, Italy
[2] Dipartimento della Protezione Civile, Rome, Italy

L'area oggetto di questo lavoro è centrata nella zona di Campo Imperatore, a sud del rilievo del Gran Sasso, a quote comprese tra 1500 e 2000 m s.l.m. Campo Imperatore è la più orientale ed elevata delle conche intermontane del settore centrale della catena appenninica. Tali conche, essendo principalmente di origine tettonica, hanno sempre destato un notevole interesse anche in termini di pericolosità sismica, in quanto la loro evoluzione geologica e geomorfologica è strettamente legata all'attività pleistocenica delle faglie bordiere che le hanno generate e che ne hanno guidato l'apertura nel tempo.

I rilievi geologici e geomorfologici sono stati condotti durante oltre un anno di attività di campagna in zone spesso difficili sia dal punto di vista logistico che climatico. Il lavoro di terreno è stato integrato da osservazioni ed interpretazioni di foto aeree alla scala 1:33.000 (IGM, 1954) o maggiore (RAF, 1944), immagini satellitari (Google Earth) e modelli digitali del terreno elaborati da carte topografiche a scala 1:5.000 e 1:10.000 della Regione Abruzzo. Ove le condizioni degli affioramenti e le tipologie dei depositi lo hanno permesso sono stati prelevati campioni di paleosuoli e carboni per datazioni al C14.

I rilievi, integrati dai numerosi dati acquisiti nelle campagne precedenti (Giraudi, 2003 e relativa bibliografia) hanno permesso di riconoscere il succedersi di numerosi episodi deposizionali ed erosivi, prevalentemente controllati dall'interazione tra l'attività delle diverse faglie che compongono il sistema di Campo Imperatore ed i fenomeni fluvio-glaciali avvenuti almeno dal Pleistocene Medio ad oggi (Giraudi, 2003 e relativa bibliografia; Kotarba *et al.*, 2001).

Il settore esterno ai limiti meridionali di Campo Imperatore, sino alle aree comunali di Castel del Monte, Santo Stefano di Sessanio e Assergi, è caratterizzato dalla presenza di un'importante superficie di spianamento areale sul substrato marino, già parzialmente segnalata in lavori precedenti ed attribuita genericamente al Pliocene Superiore (Galadini *et al.*, 2003 e relativa bibliografia). Questa superficie di spianamento areale è presente anche all'interno del bacino di Campo Imperatore, quasi esclusivamente tra la dorsale di Monte Bolza e la faglia delle



Fig. 1 - Paleosuperfice scolpita nei calcari mesozoici sulla quale, in sinistra idrografica della valle Cortina (al centro della foto), poggiano i diversi cicli di sedimenti quaternari. A destra della foto, la dorsale del Monte Bolza.

Cocchiarelle (Fig. 1). Sui bordi del bacino, lungo i versanti di faglia che hanno disarticolato e frammentato tale superficie, si sono successivamente deposti notevoli spessori (oltre 100 metri) di brecce carbonatiche, attribuite in molte aree dell'Abruzzo al Pleistocene inferiore, cui ha fatto seguito nei settori di tetto la messa in posto di depositi fluviali e fluvio-glaciali del Pleistocene medio e del Pleistocene Superiore - Olocene. Le fasi di deposizione sono state intervallate da fasi di erosione, principalmente di tipo lineare, dovute alle variazioni dei livelli di base sia locali che regionali, controllati sia da valli emissarie che da inghiottitoi carsici.

Nel bacino di Campo Imperatore, la successione sedimentaria quaternaria e le superfici di erosione sono state dislocate da una serie di faglie dirette, sintetiche e antitetiche dei segmenti principali costituenti il sistema di faglie del Gran Sasso, rappresentanti nel complesso la terminazione in superficie di una importante struttura sismogenica capace di generare terremoti di Mw≥7, ultimo dei quali quello del settembre 1349 (Galli *et al.*, 2021).

In questo lavoro, proprio grazie alla ricostruzione dell'evoluzione geologica quaternaria, è stato inoltre possibile ricostruire nel tempo l'attività di un'importante faglia antitetica (faglia delle Cocchiarelle, Fig. 2) che ha giocato un ruolo decisivo nell'evoluzione e nella distribuzione dei sedimenti nel settore a sud di monte Camicia.



Fig. 2 - Faglia delle Cocchiarelle nelle ruditi del Pleistocene Medio ad est di Colle Caciaro. Sullo sfondo, in basso, la parte terminale della valle Cortina, reincisa nei conglomerati del Pleistocene Superiore.

Bibliografia

Galadini F., Messina P., Giaccio B., Sposato A.; 2003. *Early uplift history of the Abruzzi Apennines (central Italy): available geomorphological constraints.* Quaternary International 101–102, pp. 125–135.

Galli P., Galderisi A., Messina P., Peronace E.; 2022. *The Gran Sasso fault system: Paleoseismological constraints on the catastrophic 1349 earthquake in Central Italy.* Tectonophysics, 822, pp. 1-29, 10.1016/j.tecto.2021.229156.

Giraudi, C.; 2003. *Middle Pleistocene to Holocene Apennine glaciations (Italy).* It. J. Quatern. Sci. 16, pp. 37–48.

Kotarba A., Hercman H., Dramis F.; 2001. *On the age of the Campo Imperatore glaciations, Gran Sasso Massif, Central Italy.* Geogr. Fis. Dinam. Quat., pp. 65-69.

VALUTAZIONE DEGLI EFFETTI DI AMPLIFICAZIONE SISMICA NELLE AREE DEL COMUNE DI CANTIANO (PU) COLPITE DALLA SEQUENZA SISMICA DEL 1781

E. Paolucci[1], V. Castelli[2], G. Monachesi[3], M. Ariano[1], D. Albarello[1]

[1] Dipartimento di Scienze Fisiche, della Terra e dell'Ambiente, Università degli Studi di Siena, Italia
[2] Istituto Nazionale di Geofisica e Vulcanologia, Bologna (Ancona), Italia
[3] Istituto Nazionale di Geofisica e Vulcanologia, ONT (Ancona), Italia

Il terremoto del 3 giugno 1781 (M_W 6.51±0.1; I_0=X MCS; Rovida *et al.*, 2022) è uno dei più forti dell'Appennino centro-settentrionale negli ultimi mille anni, il più forte che ha colpito la Regione Marche e il solo distruttivo nell'entroterra della provincia di Pesaro e Urbino. La base di dati macrosismici oggi disponibile su questo terremoto consiste di circa 850 documenti, di cui circa 700 di origine pubblica e prodotti tra il 3 giugno 1781 e il 1786. Il primo studio ad averli usati integralmente è Monachesi *et al.* (2019). Rispetto agli studi precedenti (Baratta, 1896; Monachesi e Vasapollo, 1986; Monachesi, 1987), questo studio permette un notevole miglioramento della ricostruzione della storia e dello scenario del terremoto, allargando notevolmente l'area danneggiata. Tutti i dati sono disponibili nel web server "AMeriGo" (Monachesi *et al.*, 2019), prodotto per conto del Servizio Regionale di Protezione Civile della Regione Marche come deposito dei dati sugli effetti dei più significativi terremoti dell'ultimo millennio nel territorio regionale. Seguendo questa ricostruzione, le intensità macrosismiche maggiori sono distribuite in una fascia lunga circa 30 km e larga circa 12 km, orientata in direzione NW-SE, con due addensamenti di effetti molto gravi a nord (Comuni di Piobbico, Apecchio, Sant'Angelo in Vado ed Urbania) e a sud (Comune di Cantiano), con un tratto intermedio (la parte sud-orientale del Comune di Cagli) caratterizzato da scenari di danno meno gravi.

Lo scopo di questo lavoro è quello di valutare se la concentrazione di elevati valori di intensità nel territorio di Cantiano vada messa in relazione con la prossimità ad una sorgente sismica (collegata con l'evolversi della sequenza, durata fino all'aprile del 1782) oppure ad eventuali fenomeni di amplificazione sismica dei terreni. Per esplorare quest'ultima ipotesi, è stata realizzata una campagna estensiva di misure sismiche di superficie presso le aree danneggiate, ovvero gli abitati storici di Cantiano e delle sue frazioni (Chiaserna, Ara Vecchia, Renaccio, Palcano e Borgo). In particolare, sono state realizzate 80 misure passive a stazione singola (analizzate con la tecnica HVSR; Nakamura, 1989) e 12 acquisizioni sismiche attive a stazione multipla (analizzate con la tecnica MASW; Foti *et al.*, 2011). L'analisi congiunta delle curve HVSR e delle curve di dispersione delle velocità delle onde di Rayleigh (Albarello *et al.*, 2011) ottenute da queste misure, ha permesso di ricostruire il profilo di velocità delle onde di taglio (Vs) rappresentativo delle varie località. Utilizzando questi risultati, l'entità degli eventuali effetti di amplificazione è stata infine stimata attraverso analisi di risposta sismica locale monodimensionali utilizzando un approccio lineare-equivalente (Kottke e Rathje, 2008).

Bibliografia

Albarello D., Cesi C., Eulilli V., Guerrini F., Lunedei E., Paolucci E., Pileggi D., Puzzilli L.M.; 2011: *The contribution of the ambient vibration prospecting in seismic microzoning: an example from the area damaged by the 26th April 2009 l'Aquila (Italy) earthquake*. Boll Geofis Teor Appl 52(3):513–538.

Baratta M.; 1896: *Sul terremoto di Cagli del 3 giugno 1781*. Memorie della Società Geografica Italiana, vol.5, pp. 363-383.

Foti S., Parolai S., Albarello D., Picozzi M.; 2011: *Application of surface wave methods for seismic site characterization*. Surv Geophys 32:777–825.

Kottke A.R. and Rathje E.M.; 2008: *Technical manual for Strata*. Report No.: 2008/10. Pacific Earthquake Engineering Research Center, University of California, Berkeley; release 0.8.0, available at https://github.com/arkottke/strata/releases, doi 10.5281/zenodo.3714128.

Monachesi G. e Vasapollo N.; 1986: *Terremoto di Cagli del 3 giugno 1781; un'analisi preliminare*. Atti della V convegno annuale del Gruppo Nazionale di Geofisica della Terra Solida, pp. 83-91.

Monachesi G.; 1987: *Revisione della sismicità di riferimento per i comuni di Cerreto d'Esi (AN), Esanatoglia (MC), Serra San Quirico (AN)*. Osservatorio Geofisico Sperimentale, Macerata, rapporto interno, 240 pp.

Monachesi G., Castelli V., Carluccio I., Locati M., Rovida A., Calamita C. e Camassi R.; 2019: *AM(eri)Go: alla scoperta degli effetti dei terremoti nelle Marche*. INGV&SPCRM, https://doi.org/10.13127/amerigo.1.

Nakamura Y.; 1989: *A method for dynamic characteristics estimation of subsurface using microtremor on the ground surface*. Q. Rep. Railw. Tech. Res. Inst., 30, 25–33.

Rovida A., Locati M., Camassi R., Lolli B., Gasperini P. e Antonucci A.; 2022: *Catalogo Parametrico dei Terremoti Italiani (CPTI15), versione 4.0*. Istituto Nazionale di Geofisica e Vulcanologia (INGV), https://emidius.mi.ingv.it/CPTI15-DBMI15/.

HOLOCENE LARGE EARTHQUAKES RECORDED IN THE CALABRIA OFFSHORE SEDIMENTS

A. Polonia[1], E. Colizza[2], P. Galli[3], L. Gasperini[1], D. Insinga[1], R. Melis[2]

[1] CNR-ISMAR, Via Gobetti 101, I-40129 Bologna, Italy
[2] Dip. di Matematica e Geoscienze, University of Trieste, Trieste, Italy
[3] Dipartimento Protezione Civile Nazionale, Rome, Italy

The Calabrian Arc (CA) is a subduction and rollback system related to the convergence between Africa and Eurasia plates, which produces uplifting coastal mountains, enhances discharge of sediments on the continental shelf and induces the frequent occurrence of earthquakes. It is populated by seismogenic structures capable of generating earthquakes exceeding Mw 6.7, as those occurred in 1638, 1783, 1905, and 1908.

Active deformation is observed onshore and in the submarine accretionary wedge, even though no thrust type earthquake has been reported to date. This occurrence has been interpreted as possibly related to a locked subduction thrust. Despite the very slow present-day plate convergence rate, in fact, subduction may be locally still active in the CA as suggested by GPS measurements of Calabrian motion relative to Apulia that show systematic residuals directed towards the Ionian Sea (D'Agostino *et al.*, 2008). This suggests active crustal compression and shortening taken up in the accretionary wedge, eventually accommodated by long-term slip on the subduction interface (Polonia *et al.*, 2011; Bortoluzzi *et al.*, 2017). Results of multi-scale structural analysis in the CA suggest that the crustal extensional faults onshore, the thrust faults within the accretionary wedge and the lithospheric faults segmenting the plate boundary (Polonia *et al.*, 2016) are seismogenic features that might be responsible for past historical earthquakes and likely source regions for future events (Galli *et al.*, 2007; Polonia *et al.*, 2012).

The seismicity of the Calabrian peninsula is one of the strongest of the Mediterranean region, both in terms of maximum magnitude and frequency (at least 25 M>6 earthquakes since 91 BCE between the Messina Strait and the Crati basin; Guidoboni *et al.*, 2019). Inland paleoseismic trenching permitted to discover some of the seismogenic sources responsible for the major earthquakes of Calabria, such as those occurred on 5 and 7 February, 1783 (Mw 7 and Mw 6.7, respectively), or the 9 June 1638 (Mw 6.7) (Galli and Bosi, 2002; 2003; Galli and Scionti, 2006). However, beyond sparse and uncertain reports from the 16th century, our knowledge of the regional seismicity starts with the onset of the 17th century, when several 5.5 ≤ Mw ≤ 6.8 events struck central and southern Calabria (Scionti *et al.*, 2006). Paleoseismological studies suggest that the 95% of the seismic moment release in the past millennium occurred between the disruptive earthquakes of March 1638 and those of 1905 and 1908. Considering that the average time-recurrence for characteristic earthquakes on each fault is much longer than the period of completeness of the Calabrian catalogue (Galli, 2020), the seismic catalogues missed most of the ancient twins of the major events which struck Calabria.

To reconstruct fault dynamics, it is essential to unravel past seismicity including the analysis of sedimentary events at sea, where high-energy sediment flows due to past earthquakes may have left their signature in the deep-sea environment. In this work, we analyze sediment samples collected in separate and disconnected sedimentary basins offshore Calabria to reconstruct resedimentation processes during the Holocene, and try to integrate inland and submarine information for a better assessment of tectonic activity and seismogenesis.

This approach was already tested offshore eastern Sicily where major historical earthquakes triggered the deposition of decimetric thick STs (Polonia *et al.*, 2013; 2017; 2022). Seismic shaking in the CA, in fact, is often associated with submarine slope failures, tsunamis and deposition of seismo-turbidites, which represent more than 90% of total sedimentation in the deep Mediterranean basins (Polonia *et al.*, 2017).

We analyse three sediment cores that were collected in confined depressions offshore Calabria at water depths ranging from 2050 to 2945 m (Fig.1). Their depositional sites lay in tectonically controlled basins in the inner accretionary wedge. The stratigraphic reconstruction is based on the identification of peculiar marker beds through the analyses of radiometric ages, XRF data, grain size and foraminifera associations. The sediment core shows a succession of turbidite beds, hemipelagic intervals and a tephra layer. The total thickness of pelagic layers implies that resedimentation processes represent 88% of total sedimentation.

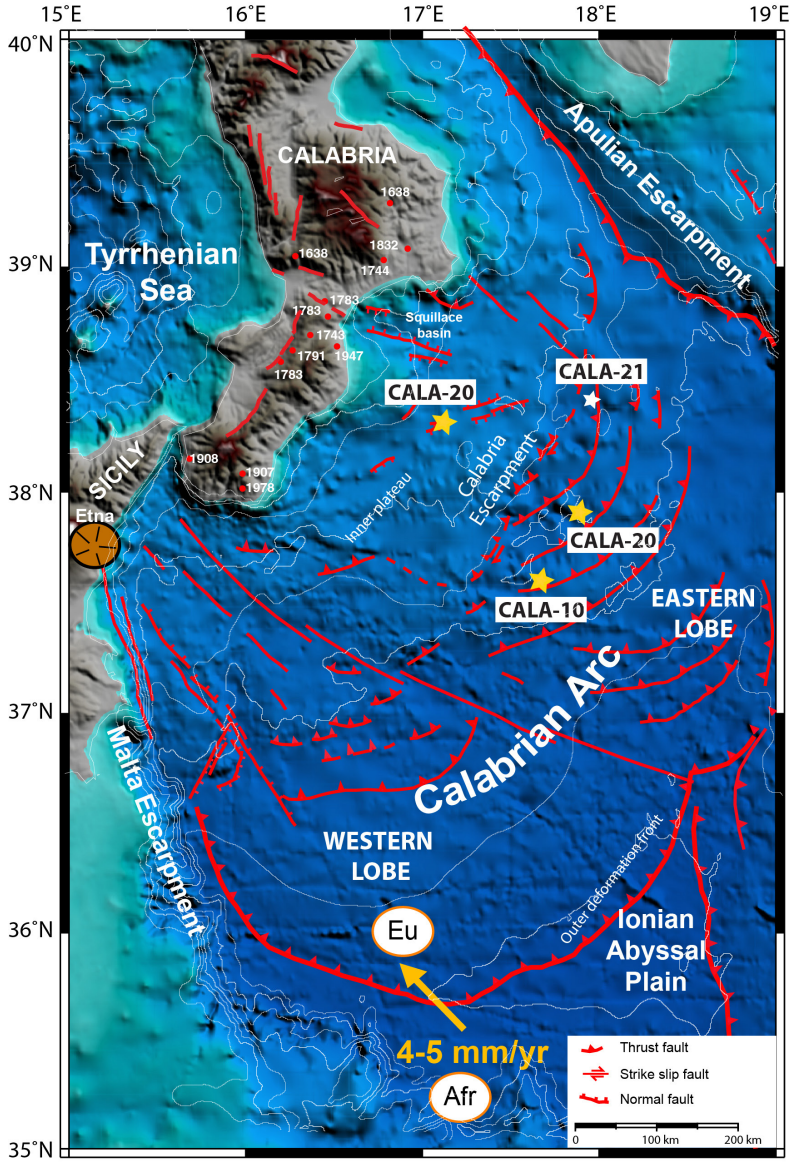


Fig. 1 - Geodynamic setting of the study area and structural map of the Calabrian Arc subduction system in the Ionian Sea as derived from the interpretation of available seismic data (Polonia *et al.*, 2011) integrated with multibeam bathymetry data. Yellow arrow indicates Europe (Eu) and Africa (Afr) slip vector in the Africa reference frame. Note the presence of seismogenic faults segmenting the margin both across and along strike (red lines). Green circles indicate sediment cores analyzed in this study while the white star represents core CALA 21 described in Polonia *et al.* 2015. Epicenters of historical earthquakes (Rovida *et al.*, 2022) are indicated by red circles.

Turbidite beds are marked by sharp peaks in grain size and magnetic susceptibility and are characterized by varying geochemical composition and foraminifera association including benthic species displaced from diverse bathymetric environments. We identified a total of 20 turbidite beds (T1-T20) deposited during the last 10 kyrs whose thickness vary between few centimetres to 1.5 m. They are generally normally graded. Some of them present multiple textural pulses (sand pulses in the lower part of the turbidite) without hemipelagic sediment in between.

The deposition time window of the thickest turbidite T5 is in good correlation with both the CE 365 Crete earthquake and tsunami and/or the twin of the 1783 event that occurred shortly before 374 CE (Galli and Bosi, 2002).

Four turbidite beds were emplaced during the last millennia. T1 and T2 deposition time windows suggest a link with two seismic sequences happened in CE 1783 and CE 1638, respectively. The ages of turbidites T3 and T4 are very similar suggesting two events very close in time. They match the age, within the errors intimately related to radiometric dating, of the paleoearthquakes recognized along the Lakes fault dated in the 7th century CE (Galli *et al.*, 2007) and the 951 CE earthquake sourced by the Rossano fault (Galli *et al.*, 2010).

The emplacement time of older turbidites (T6-T20) is less constrained relative to the most recent events. However, T8 is compatible with an ancient twin of the 1783 earthquake sourced by the Cittanova fault around 2.9 ka (Galli and Peronace, 2015), while T10 matches the occurrence of the event recorded by the Cirò Marina fault around 3.5 ka (Galli and Piscitelli, 2014). T17, matches another paleo-earthquake generated by the Cittanova fault around 6.2 ka (Galli and Peronace, 2015). T20, likely deposited between 9960-9600 BP and matches the event sourced always by the Cittanova fault around 10 ka (Galli and Peronace, 2015).

Within the uncertainties intimately related to the submarine paleoseismological method, the average recurrence time of re-sedimented deposits offshore Calabria is about 500 years but it is not constant in time showing periods of enhanced activity separated by more quiescent intervals. The same trend was found in other regions of the CA where the average recurrence of seismo turbidites is about 500 years but it varies between 100 and 700 years (Polonia *et al.*, 2015).

If we compare the age of seismo-turbidites with trench studies onland it is clear that the number of turbidites is larger in the submarine environment. All sedimentary events deposited during historical times can be correlated with earthquakes onland. However when we go back in time, not all the turbidites are correlated with known events onland. This suggests that fault activity onland needs to be reconstructed in more detail and/or that some of the turbidites are related to the activity of submarine faults, including the subduction thrust. Seismo-turbidites that do not correlate with earthquakes onshore and for which we can suggest a link with subduction activity are major events that can be correlated in different disconnected basins and have large repeat time in the order of ~1 ka.

Our results suggest that paleseismology onshore integrated with studies turbidite paleoseismology in confined submarine basins provides a more continuous and complete record of seismically triggered sedimentary events. Site selection plays a fundamental role and further work on gravity cores collected in proximal basins directly fed by single canyon systems and distal basins disconnected by canyons is fundamental to acquire more information on the link between seismo-turbidite generation, sediment source and causative faults.

References

Bortoluzzi, G. *et al.*; 2017. *Styles and rates of deformation in the frontal accretionary wedge of the Calabrian Arc (Ionian Sea): controls exerted by the structure of the lower African plate.* Ital. J. Geosci. **136,** 347–364.

D'Agostino, N., Avallone, A., Cheloni, D., D'Anastasio, E., Mantenuto, S., Selvaggi, G.; 2008. *Active tectonics of the Adriatic region from GPS and earthquake slip vectors.* J. Geophys. Res. 113, B12413. doi:10.1029/2008JB005860.

Galli P., Bosi V.; 2002. *Paleoseismology along the Cittanova fault. Implications for seismotectonics and earthquake recurrence in Calabria (southern Italy)*, J. of Geophys. Res., 107, B3, 10.1029/2001JB000234.

Galli P., Bosi V.; 2003. *Catastrophic 1638 earthquakes in Calabria (southern Italy): New insight from paleoseismological investigation,* J. of Geophys. Res., 108, B1 10.1029/2002JB01713.

Galli P., Peronace E.; 2015. *Low slip rates and multi-millennial return times for Mw 7 earthquake faults in southern Calabria (Italy),* Geophysical Research Letters, 13, 5258-5265.

Galli P., Piscitelli S.; 2014. *Surface breaks along the coastal plain of Cirò (Ionian Calabria, southern Italy). Geophysical and paleoseismological insights.* Natural Hazards, 71, 291-313.

Galli P., Scionti V.; 2006. *Two unknown M>6 historical earthquakes revealed by paleoseismological and archival researches in eastern Calabria (Southern Italy).* Seismotectonic implication, Terra Nova, 18(1), 44-49, 10.1111/j.1365-3121.2005.00658.x.

Galli P., Scionti V., Spina V.; 2007. *New paleoseismic data from the Lakes and Serre faults (Calabria, southern Italy). Seismotectonic implication*, Boll. Soc. Geol. It., 126, 347-364

Galli P., Spina V., Ilardo I., Naso G.; 2010. *Evidence of active tectonics in southern Italy: the Rossano Fault (Calabria),* in: Guarnieri P. (ed.) Recent Progress on Earthquake Geology, Nova Scientific Publisher Inc., New York, 49-78.

Guidoboni E., Ferrari G., Tarabusi G., Sgattoni G., Comastri A., Mariotti D., Ciuccarelli C., Bianchi M.G., Valensise G.; 2019. *CFTI5Med, the new release of the catalogue of strong earthquakes in Italy and in the Mediterranean area,* Scientific Data 6, Article number: 80 (2019). doi: https://doi.org/10.1038/s41597-019-0091-9.

Polonia, A., Torelli, L., Mussoni, P., Gasperini, L., Artoni, A., Klaeschen, D.; 2011. *The Calabrian Arc subduction complex in the Ionian Sea: Regional architecture, active deformation, and seismic hazard.* Tectonics 30, TC5018. doi:10.1029/2010TC002821.

Polonia, A., Torelli, L., Gasperini, L., Mussoni, P.; 2012. *Active faults and historical earthquakes in the Messina Straits area (Ionian Sea).* Nat. Hazards Earth Syst. Sci. 12, 2311-2328. doi:10.5194/nhess-12-2311-2012.

Polonia, A. et al.; 2013. *Turbidite paleoseismology in the Calabrian Arc subduction complex (Ionian Sea).* Geochem. Geophys. Geosyst. 14, 112–140.

Polonia, A. *et al.*; 2015. *Is repetitive slumping during sapropel S1 related to paleo-earthquakes?* Mar. Geol. 361, 41–52.

Polonia, A. *et al.*; 2016 *The Ionian and Alfeo-Etna fault zones: New segments of an evolving plate boundary in the central Mediterranean Sea?* Tectonophysics 675, 69-90.

Polonia, A. *et al.*; 2017. *A depositional model for seismo-turbidites in confined basins based on Ionian Sea deposits.* Mar. Geol. 384, 177–198.

Polonia A. *et al.*; 2021. *Deciphering co-seismic sedimentary processes in the Mediterranean Sea using elemental, organic carbon and isotopic data*. Geochemistry, Geophysics, Geosystems 22.

Polonia *et al.*; 2022. *Recognizing megatsunamis in Mediterranean deep sea sediments based on the massive deposits of the 365 CE Crete event.* Scientific Reports, 12 (1), 1-20. https://www.nature.com/articles/s41598-022-09058-3.

Rovida A., Locati M., Camassi R., Lolli, B., Gasperini P., Antonucci A.; 2022. *Catalogo Parametrico dei Terremoti Italiani (CPTI15)*, versione 4.0. Istituto Nazionale di Geofisica e Vulcanologia (INGV). https://doi.org/10.13127/CPTI/CPTI15.4

Scionti, V., Galli, P. and Chiodo, G.; 2006. *The Calabrian seismicity during the Viceroyalty of Naples: sources silence or silent sources? The case of the strong 1744 earthquake*, Boll. Geof. Teor. e Appl., 47, 53-72.

INTERPRETAZIONE GEOLOGICA DELLA SEQUENZA SISMICA 2016–2017 DELL'ITALIA CENTRALE A PARTIRE DA DATI DI SPOSTAMENTO AL SUOLO RILEVATI MEDIANTE GNSS E LIVELLAZIONE GEOMETRICA

R. Salvini[1], C. Vanneschi[2], C. Lanciano[1], R. Maseroli[3]

[1] Dipartimento di Scienze Fisiche, della Terra e dell'Ambiente e Centro di Geotecnologie CGT, Università di Siena; San Giovanni Valdarno (Arezzo, Italia)
[2] Regione Toscana, Sistema Informativo e Pianificazione del Territorio; Firenze (Italia)
[3] Istituto Geografico Militare; Firenze (Italia)

Tra agosto 2016 e gennaio 2017, una sequenza sismica molto energica ha indotto notevoli spostamenti al suolo sia di tipo orizzontale che verticale nell'Appennino centrale italiano. A seguito di tale evento, l'Istituto Geografico Militare (IGM), titolare e gestore delle reti geodetiche italiane, ha eseguito diversi rilievi topografici nell'area sismica al fine di aggiornare le coordinate dei vertici appartenenti alla rete geodetica IGM95. Le misurazioni sono iniziate nelle zone dove si sono verificate le deformazioni più significative, ovvero: Amatrice e Accumoli, in provincia di Rieti, e l'area tra Norcia e Castelluccio, in provincia di Perugia, fino a Visso (provincia di Macerata). I lavori di campagna si sono concentrati sulla misurazione aggiornata dei punti della rete IGM95, tramite GNSS, e delle linee di livellazione geometrica ad alta precisione. I rilievi si sono protratti fino al raggiungimento di zone ritenute oggettivamente stabili. La grande quantità di dati a disposizione è stata utilizzata in questo lavoro per una nuova interpretazione geologica della sequenza sismica. I dati, nel loro insieme, confermano molte delle precedenti ipotesi basate su dati derivati da tecniche analoghe ma anche differenti (es. interferometria SAR) pubblicate negli anni dalla comunità scientifica. Nel territorio analizzato, il confronto multitemporale tra le misure effettuate ha permesso un'accurata determinazione sia delle componenti planimetriche che di quelle altimetriche dello spostamento provocato dagli eventi sismici. I risultati confermano come la sismicità sia stata indotta dall'attività di un noto sistema di faglie normali. Tuttavia, i dati indicano anche la possibile influenza di un sovrascorrimento a carattere regionale che ha condizionato la propagazione degli eventi nell'area. Le mappe dello spostamento ottenute sono coerenti con altri lavori a carattere geodetico già pubblicati e con una propagazione della rottura guidata dalla struttura geotettonica documentata.

È possibile fare riferimento al seguente articolo Open Access per maggiori dettagli:

Salvini R., Vanneschi C., Lanciano C., Maseroli R. (2022): *Ground Displacements Estimation through GNSS and Geometric Leveling: A Geological Interpretation of the 2016–2017 Seismic Sequence in Central Italy*. Geosciences 2022, 12, 167. https://doi.org/10.3390/geosciences12040167.

A RESISTIVITY CRUSTAL PROFILE ACROSS THE SOURCE OF THE OCTOBER 30, 2016 Mw 6.5 NORCIA EARTHQUAKE (CENTRAL ITALY)

S. Tripaldi[1], M. De Girolamo[2], L. Improta[3], G. Romano[1], V. Sapia[3], A. Siniscalchi[1], I. Ventola[1], F. Villani[3]

[1] Dipartimento di Scienze della Terra e Geoambientali, Università degli Studi di Bari Aldo Moro, Bari, Italy
[2] CNR - Istituto di Metodologie per l'Analisi Ambientale, Potenza, Italy
[3] Istituto Nazionale di Geofisica e Vulcanologia, Roma, Italy

The Apennine seismic belt of Italy is an extensional province affected by multi-fault normal-faulting earthquakes or sequences (Chiarabba *et al.*, 2005). The geometrical complexity of the active normal fault systems dissecting the Apennines belt, characterized by a poly-phased tectonic evolution, may control multi-fault ruptures during a single seismic event or sequences spanning a period of days.

The 2016-2017 Amatrice-Visso-Norcia (AVN) normal-faulting sequence culminated with the Mw6.5 Norcia mainshock, represents a well-documented case of in-cascade reactivation of multiple fault segments. The geometry of the normal faults ruptured during the Norcia mainshock, the role of inherited thrust faults (i.e., Mt. Sibillini thrust) and of crustal fluids on the rupture process are still debated and contrasting finite-fault source models are present in literature (Walters *et al.*, 2018; Scognamiglio et al., 2018; Cheloni *et al.*, 2019).

Here we present first results from a magnetotelluric (MT) investigation performed along an approximately 20 km profile that extends from the Norcia basin to the Mt. Sibillini thrust across the Castelluccio basin. Thanks to the extreme sensitivity of the MT method to the physical and chemical rock properties and their interactions with fluids, we aim at reconstructing a reliable resistivity section across the zone of maximum co-seismic deformation of the Norcia earthquake to improve understanding of the rock properties in the crustal volume containing the slipped faults.

To this aim, geophysical outcomes from a 3-D geoelectrical survey (Sapia *et al.*, 2021), time domain electromagnetic soundings (Villani *et al.*, 2019) and aftershocks locations (Improta *et al.*, 2019) are integrated with the MT survey.

The data consists of 10 broadband MT soundings and 5 audiomagnetotelluric (AMT) soundings. The interdistance between each measurement sites varies from ~4000 to ~500 m, with a denser site spacing located in the Castelluccio basin and the Mt. Vettore fault system area. The complex MT impedance tensor Z estimates ranges from 10^{-4} s to 100 s. The dimensionality and directionality analysis of the geoelectrical structures has been investigated following the approach of the phase tensor analysis introduced by Caldwell *et al.*, 2005. In the longer period range, the strike direction of regional structures is almost consistent with the N25°W direction. The 2-D resistivity model, obtained using the nonlinear conjugate 2-D inversion algorithm of Rodi and Mackie (2001) must be considered preliminary. A series of tests are ongoing to assess reliability, geometries and depths of the imaged resistivity features that will be compared with the published interpretations of commercial reflection profiles (Porreca *et al.*, 2018; Buttinelli *et al.*, 2021). However, the recovered model unravels a remarkable drop of resistivity values just below the Castelluccio basin down to a depth of 6 km and delineates a low-resistivity crustal wedge bordered by the main of clusters of early aftershocks of the Mw6.0 Amatrice and Mw 6.5 Norcia mainshocks.

References

Buttinelli M., Petracchini L., Maesano F. E., D'Ambrogi C., Scrocca D., Marino M., Capotorti F., Bigi S., Cavinato G.P., Mariucci M.T., Montone P. and Di Bucci D.; 2021: *The impact of structural complexity, fault segmentation, and reactivation on seismotectonics: Constraints from the upper crust of the 2016–2017 Central Italy seismic sequence area*. Tectonophysics, 810, 228861.

Caldwell T. G., Bibby H. M. and Brown, C.; 2004: *The magnetotelluric phase tensor*. Geophysical Journal International, 158(2), 457-469.

Cheloni D., Falcucci E. and Gori S.; 2019: *Half-graben rupture geometry of the 30 October 2016 MW 6.6 Mt. Vettore-Mt. Bove earthquake, central Italy*. J. Geophys. Res.-Solid Earth, 124, 4091–4118. https://doi.org/10.1029/2018JB015851

Chiarabba C., Jovane L. and Di Stefano R.; 2005: *A new view of Italian seismicity using 20 years of instrumental recordings*. Tectonophysics, 395 (3–4), https://doi.org/10.1016/j.tecto.2004.09.013.

Improta L., Latorre D., Margheriti L., Nardi A., Marchetti A., Lombardi A.M., Castello B., Villani F., Ciaccio M. G., Mele F. M., Moretti M. and The Bollettino Sismico Italiano Working Group; 2019: *Multi-segment rupture of the 2016 Amatrice-Visso-Norcia seismic sequence (central Italy) constrained by the first high-quality catalog of Early Aftershocks*. Scientific Reports, 9(1), 1-13.

Porreca M., Minelli G., Ercoli M., Brobia A., Mancinelli P., Cruciani F., Giorgetti C., Carboni F., Mirabella F., Cavinato G., Cannata A., Pauselli C. and Barchi M. R.; 2018: *Seismic reflection profiles and subsurface geology of the area interested by the 2016–2017 earthquake sequence (Central Italy)*. Tectonics, 37(4), 1116-1137.

Rodi W. and Mackie R. L.; 2001: *Nonlinear conjugate gradients algorithm for 2-D magnetotelluric inversion*. Geophysics, 66(1), 174-187.

Sapia V., Villani F., Fischanger F., Lupi M., Baccheschi P., Pantosti D., Pucci S., Civico R., Sciarra A., Smedile A., Romano V., De Martini P. M., Murgia F., Materni V., Giannattasio F., Pizzimenti L., Ricci T., Brunori C. A., Coco I. and Improta L.; 2021: *3-D deep electrical resistivity tomography of the major basin related to the 2016 Mw 6.5 central Italy earthquake fault*. Tectonics, 40(4), e2020TC006628.

Scognamiglio L., Tinti E., Casarotti E., Pucci S., Villani F., Cocco M., Magnoni F. and Michelini A., Dreger D.; 2018: *Complex fault geometry and rupture dynamics of the MW 6.5, 30 October 2016, Central Italy earthquake*. J. Geophys. Res. 123, 2943–2964, https://doi.org/10.1002/2018JB015603.

Villani F., Sapia V., Baccheschi P., Civico R., Di Giulio G., Vassallo M. Marchetti and Pantosti, D.; 2019: *Geometry and structure of a fault-bounded extensional basin by integrating geophysical surveys and seismic anisotropy across the 30 October 2016 Mw 6.5 earthquake fault (central Italy): The Pian Grande di Castelluccio basin*. Tectonics, 38(1), 26-48.

Walters R. J., Gregory L.C., Wedmore L.N.J., Craig T.J., McCaffrey K., Wilkinson M., Chen J., Li Z., Elliott J.R., Goodall H., Iezzi F., Livio F., Michetti A.M., Roberts G., Vittori E.; 2018: *Dual Control of fault intersections on stop-start rupture in the 2016 Central Italy Seismic sequence*. Earth Planet. Sci. Lett., 500, 1–14, https://doi.org/10.1016/j.epsl.2018.07.0430012-821X.

CONVERGENCE BETWEEN ADRIA AND EURASIA PLATES: INSIGHTS FROM GNSS TIME SERIES IN NORTH-EEASTERN ITALY

L. Tunini, A. Magrin, D. Zuliani, G. Rossi

National Institute of Oceanography and Applied Geophysics (OGS) - Italy

It is widely known that deformation and seismicity characterize the North-Eastern Italy, and in particular the Friuli Venezia Giulia region, expressions of the interplay between Adria and Eurasia plates. The Friuli Venezia Giulia Deformation Network (FReDNet, http://frednet.crs.ogs.it/DOI/) is a permanent GNSS network established since 2002 by the Centro Ricerche Sismologiche of the National Institute of Oceanography and Applied Geophysics - OGS, in order to monitor the crustal deformation in this region, and to provide a valid contribution to the "Sistema di Monitoraggio terrestre dell'Italia Nord Orientale (SMINO)" of NE-Italy (Bragato *et al.*, 2021). FReDNet currently counts 19 permanent GNSS stations, which continuously provide real-time data and daily and hourly files in the standard *RINEX* format, accessible through a public ftp repository.

In order to place the regional deformation in a broader tectonic context, we processed the data coming not only from FReDNet but also from other geodetic networks covering northern Italy and surrounding areas (including some sites in Slovenia and Austria), available in the time interval 2002-2021. We used the GAMIT-GLOBK software package ver10.71 (Herring *et al.*, 2018) to be capable of processing multi-satellite data and to calculate the position and velocity for each station.

In this work, the processing strategies and data analyses of the GNSS time-series of NE-Italy stations are shown, as well as the outcoming deformation field. The preliminary results confirm the decrease in the velocity module from the Friuli plain toward the Alps, suggesting a possible deformation accrual in the latter.

This research was supported by OGS and CINECA under HPC-TRES program award number 2020-11. We acknowledge the CINECA award under the ISCRA initiative, for the availability of high performance computing resources and support (IscraC IsC83_GPSIT-2).

References

Bragato, P. L., Comelli, P., Sara., A., Zuliani, D., Moratto, L., Poggi, V., Rossi, G., Scaini, C., Sugan, M., and Barnaba C., et al. 2021. *The OGS - Northeastern Italy seismic and deformation network: Current status and outlook*, Seismol. Res. Lett. 92, no. 3, 1704–1716, doi: https://doi.org/10.1785/0220200372.

Herring, T.A. and King, R., Floyd, M.A. and McClusky, S. C. 2018. *GAMIT Reference Manual: GPS Analysis at MIT, Release 10.7*. Department of Earth. Tech. rep., Massachusetts Institute of Technology, Cambridge, Mass. URL: <http://geoweb.mit.edu/gg/Intro_GG.pdf>.

THE ROLE OF COULOMB STRESS TRANSFER IN THE EVOLUTION OF SEISMIC CYCLES: INSIGHTS FROM THE CENTRAL APENNINE FAULT SYSTEM

G. Valentini[1,2]., T. Volatili[1], P. Galli[3,4], E. Tondi[1,2]

[1] School of Science and Technology - Geology Division, University of Camerino, Italy
[2] National Institute of Geophysics and Volcanology, Rome, Italy
[3] Dipartimento Protezione Civile, Rome, Italy
[4] Consiglio Nazionale delle Ricerche, Istituto di Geologia Ambientale e Geoingegneria, Rome, Italy

The Central Apennine Fault System (CAFS in Cello *et al.*, 1997) is composed of several active normal to oblique faults that caused several destructive earthquakes during the last millennium. According to available seismic catalogues (CPTI15 - Rovida *et al.*, 2022; ISIDe working group, 2007) 18 seismic events with 5.8 ≤ Mw ≤ 7.0 in central Italy (since 1279A.D.) can be associated with CAFS-related structures. Seismicity appears to be concentrated in 3 distinct time-windows: in the 12th-13th and 17th-18th centuries and from the 1970s to 2017. The most recent seismic events struck the axial zone of the central Apennine fold-and-thrust belt between 1979 (Valnerina sequence) and 2016-2017 (Amatrice-Visso-Norcia sequence) also involving the northern area of the CAFS and its southern border (1997 Colfiorito-Sellano and 2009 L'Aquila sequences, respectively) causing severe damages and several casualties, leading to awaken interest in the study of the seismic behavior of these seismogenic structures.

In this study we reconstructed the CAFS seismic cycle (Tondi and cello, 2003) considering the 3 time-windows of seismicity over the last millennium and investigated the role of Coulomb stress transfer in promoting or inhibiting ruptures of neighboring faults. We conducted specific analyzes to understand how the permanent static stress change can affect either the individual seismic phases and the entire seismic cycle. Furthermore, considering the importance of fault geometry in influencing the result, we analyzed the effect of three-dimensional elliptical fault geometries in modelling static Coulomb stress transfer.

In order to reduce critical simplifications during the workflow, we tested a new detailed and multidisciplinary approach. We first selected 5 earthquakes from the ISIDe (Italian Seismological Instrumental and Parametric Data-Base) catalogue with Mw≥5.8 and 13 historical earthquakes from the CPTI15 (Catalogo Parametrico dei Terremoti Italiani) catalogue with Mw≥6 (Fig.1). Different magnitude thresholds between historical and instrumentals datasets were adopted to overcome the likely overestimation of the estimated magnitude for historical events (Vannucci *et al.*, 2021 and references therein). A causative fault has been associated to each studied earthquake after a detailed scrutiny of fault-related data present in literature (i.e., paleoseismological, structural, macroseismic). Secondly, the most reliable fault traces, with solid field-based constrains from literature (Tondi, 2000; Galderisi and Galli, 2020; Tondi *et al.*, 2020; Galli *et al.*, 2022 and references therein), have been elaborated in a Geographic Information System, GIS (Fig.1). The fault dataset was compiled with the following fields: i) fault name, ii) dip angle, iii) rake (using the Aki and Richards (1980) conventions), iv) dip direction, and v) length.

We estimated the seismic moment released by historical earthquakes and compared seismic energy released during the main time-windows of seismicity that clustered in the CAFS area together with the coseismic and cumulative displacements computed by these faults to better constrain the spatiotemporal evolution of the CAFS seismic cycle.

To analyze how faults interacted we propose a novel approach to model seismogenic sources for coulomb stress transfer calculation purposes.

This approach adopts as a cornerstone the hypothesis that the most reliable approximation of 2D-fault geometry is an ellipse (Barnett *et al.*, 1987; Walsh and Watterson,1987; Gupta and Scholz, 2000), this concept is strictly related to the variation in displacement that ranges from a maximum at the center of the fault to zero at the elliptical tip-line loop. Furthermore, faults are frequently modelled as planar geometries in coulomb calculations but as demonstrated by

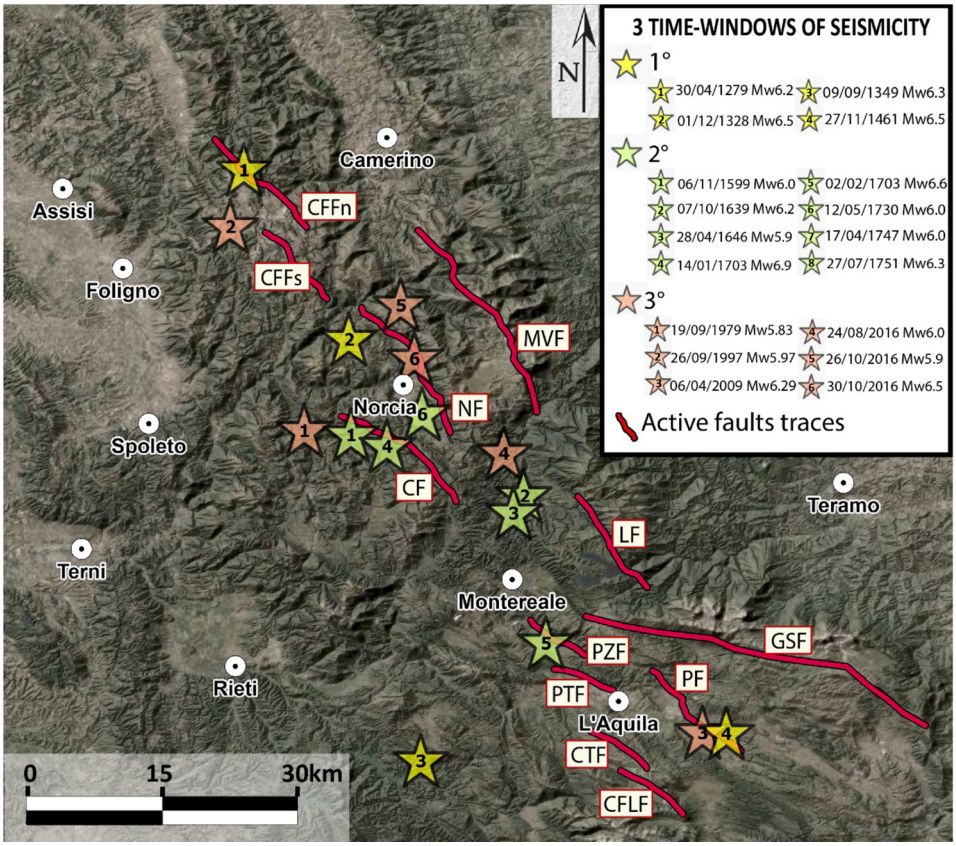


Fig. 1 - Map of the 18 seismic events with 5.8 ≤ Mw ≥ 7.0 in the CAFS area since 1279A.D. labelled according to the chronological order within each time-window of seismicity. Main active fault traces are also shown (CFFn – Colfiorito Fault nord; CFFs - Colfiorito Fault south; MVF – Monte Vettore Fault; NF – Norcia Fault; CF – Cascia Fault; LF – Laga Fault; GSF – Gran Sasso Fault; PZF – Pizzoli Fault; PF – Paganica Fault; PTF – Pettino Fault; CTF – Cerasitto Fault; CFLF – Campo Felice Fault) (Tondi, 2000; Galderisi and Galli, 2020; Tondi *et al.*, 2020; Galli *et al.*, 2022 and references therein).

Mildon *et al.* (2016), Coulomb stress transfer is highly sensitive to strike-variable geometries of the receiver faults. Since a realistic CAFS base model is of paramount importance in reducing calculation errors, we adopted a new strike-variable and ellipse-shaped three-dimensional model as input file for the Coulomb stress transfer simulations. To do so, we used "3-D Faults" (Mildon *et al.*, 2016) and "Coulomb 3.4" (Lin and Stein, 2004; Toda *et al.*, 2005) MATLAB codes. To test the efficiency and the effective influence of this new model in terms of coulomb stress transfer results, we performed calculations on both planar-rectangular faults and strike-variable and elliptic faults. We used the same receiver and source faults but two different geometric model to find and quantify differences.

We performed coulomb stress transfer simulations on each seismic event within each seismic sequence taking into account to respect the real rupture conditions (e.g., partial or entire rupture, slip distribution) of the earthquake.

Results confirmed that the cumulative seismic energy released during the last 1000 years was similar in the 3 main time-windows separated by ca. 350 years of time gap as hypothesized by Tondi and Cello (2003). Furthermore, the results obtained in the CAFS central area validate the thesis proposed by Galderisi and Galli (2020) regarding the mutual and alternating Coulomb stress transfer between Norcia Fault and Monte Vettore Fault.

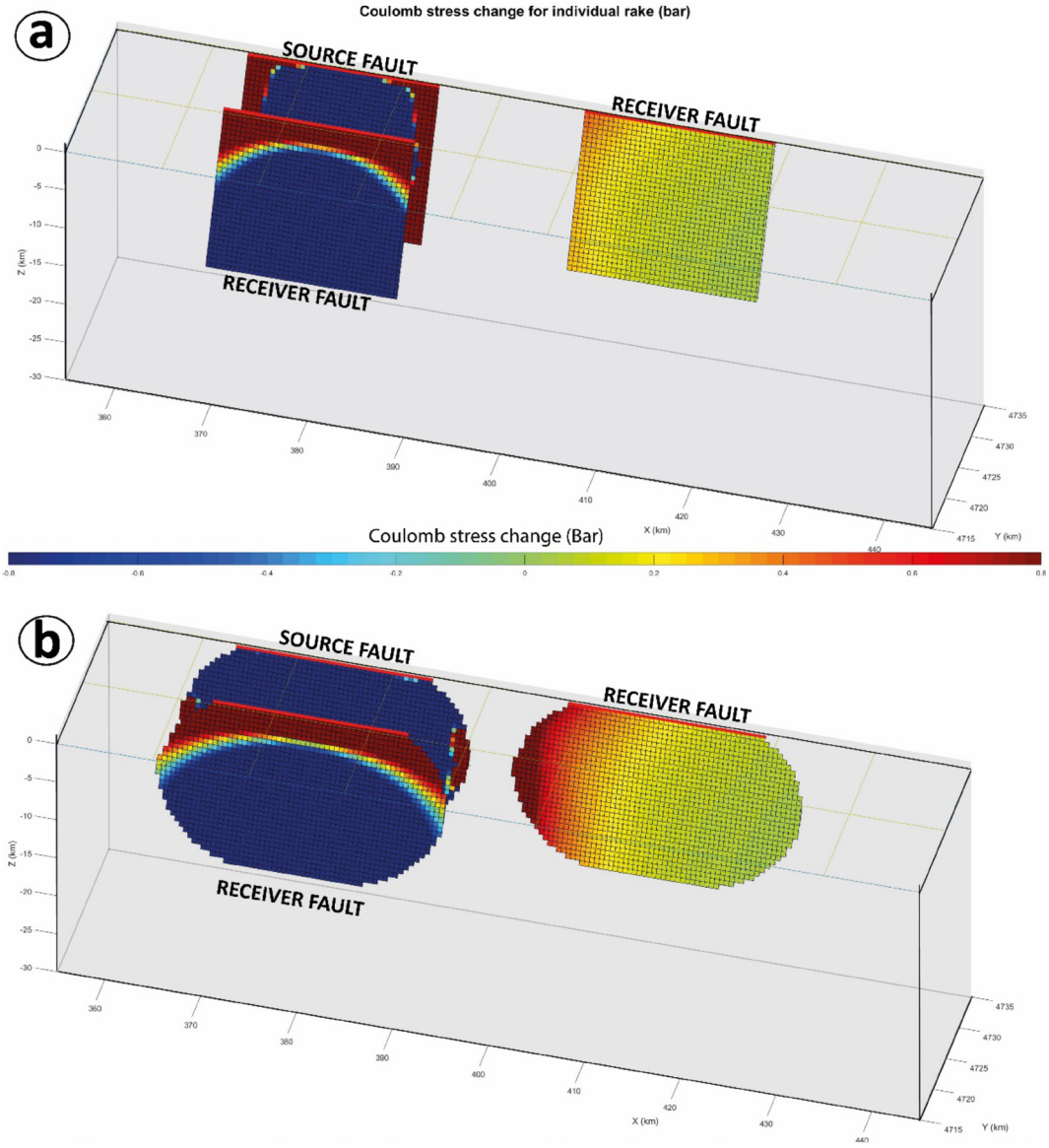


Fig. 2 - Example of Coulomb stress transfer calculated on pilot a) rectangular faults and b) elliptic faults. Two receiver faults are placed along strike and parallel respect to the source fault to show the Coulomb stress change in both directions. Red lines are the surface traces of the faults. Colours refer to the amount of Coulomb stress change expressed in Bar. Note the stressed (red) tip of the elliptic receiver fault along strike and the stress shadow on the parallel one.

The adoption of strike-variable and elliptic faults in static Coulomb stress transfer modelling revealed significant differences in terms of the amount of transferred stress and stress patterns on the receiver faults compared to the classical planar and rectangular faults. In particular, the effect of ellipticity in increasing lateral extension of the fault surfaces at about half of their maximum depth considerably reduces the distance between neighboring faults (Fig.2a and Fig.2b), increasing the degree of interaction and consequently the amount of static Coulomb stress transferred to the tips of the receiving faults located along strike of the source faults (Fig.2). We also found differences in the stress pattern generated on laterally sub-parallel

faults that experience a larger decrease in stress. We found a good agreement between the spatiotemporal evolution of CAFS earthquake sequence and the Coulomb static stress transfer between neighboring faults. Faults falling into the stress shadows were inhibited, avoiding their reactivation after a strong earthquake generated by the adjoining source fault, on the contrary, fault segments subjected to increased stress ruptured in shorter times than their characteristic return time.

The efficiency of this novel approach to the analysis of the seismic cycle and the influence of Coulomb static stress transfer have been successfully tested on historical seismic activity, giving insights on its possible future applicability in estimating active fault rupture susceptibility, integrating additional multidisciplinary data from research branches studying other factors which influence fault activity (e.g. circulation of fluids, regional stress, GNSS data, etc.). Important implications of this new methodology are desirable in the context of the seismic hazard assessment for the implementation of advanced and integrated strategies on seismic risk reduction and disaster management.

References

Aki K. and Richards P.G.; 1980: *Quantitative Seismology Theory and Methods* (Vol. 1). W. H. Freeman and Company, San Francisco.

Barnett J. A., Mortimer J., Rippon J. H., Walsh J. J. and Watterson J.; 1987: *Displacement geometry in the volume containing a single normal fault.* AAPG Bulletin, 71(8), 925-937.

Cello G., Mazzoli S., Tondi E. and Turco E.; 1997: *Active tectonics in the central Apennines and possible implications for seismic hazard analysis in peninsular Italy.* Tectonophysics, 272(1), 43-68.

Cello G., Tondi E., Micarelli L. and Mattioni L.; 2003: *Active tectonics and earthquake sources in the epicentral area of the 1857 Basilicata earthquake (southern Italy).* Journal of Geodynamics, 36(1-2), 37-50.

Galderisi A. and Galli P.; 2020: *Coulomb stress transfer between parallel faults. The case of Norcia and Mt Vettore normal faults (Italy, 2016 Mw 6.6 earthquake)*. Results in Geophysical Sciences, 1, 100003.

Galli P., Galderisi A., Messina P. and Peronace E.; 2022: *The Gran Sasso fault system: Paleoseismological constraints on the catastrophic 1349 earthquake in Central Italy.* Tectonophysics, 822, 229156.

Gupta A. and Scholz C. H.; 2000: *A model of normal fault interaction based on observations and theory.* Journal of Structural Geology, 22(7), 865-879.

Lin J. and Stein R. S.; 2004: *Stress triggering in thrust and subduction earthquakes and stress interaction between the southern San Andreas and nearby thrust and strike-slip faults.* Journal of Geophysical Research: Solid Earth, 109(B2).

Mele F., Castello B., Marcocci C., Moro R., Marchetti A. and Riposati D.; 2007: *ISIDe, Italian Seismological Instrumental and parametric Data-basE.* GNGTS 2007.

Mildon Z. K., Toda S., Faure Walker J. P. and Roberts G. P.; 2016: *Evaluating models of Coulomb stress transfer: Is variable fault geometry important?.* Geophysical Research Letters, 43(24), 12-407.

Rovida A., Locati M., Camassi R., Lolli B., Gasperini P. and Antonucci A.; 2022: *Italian Parametric Earthquake Catalogue CPTI15*, version 4.0.

Toda S., Stein R. S., Richards-Dinger K. and Bozkurt S. B.; 2005: *Forecasting the evolution of seismicity in southern California: Animations built on earthquake stress transfer.* Journal of Geophysical Research: Solid Earth, 110(B5).

Tondi E.; 2000: *Geological analysis and seismic hazard in the central Apennines (Italy).* Journal of Geodynamics, 29(3-5), 517-533.

Tondi E. and Cello G.; 2003: *Spatiotemporal evolution of the Central Apennines fault system (Italy).* Journal of Geodynamics, 36(1-2), 113-128.

Tondi E., Jablonská D., Volatili T., Michele M., Mazzoli S. and Pierantoni P. P.; 2020: *The Campotosto linkage fault zone between the 2009 and 2016 seismic sequences of central Italy: Implications for seismic hazard analysis.* GSA Bulletin, 133(7-8), 1679-1694.

Vannucci G., Lolli B. and Gasperini P.; 2021: *Inhomogeneity of macroseismic intensities in Italy and consequences for macroseismic magnitude estimation.* Seismological Society of America, 92(4), 2234-2244.

Walsh J. J. and Watterson J.; 1987: *Distributions of cumulative displacement and seismic slip on a single normal fault surface.* Journal of Structural Geology, 9(8), 1039-1046.

TECTONIC SETTING AND FAULT ROUGHNESS VS EARTHQUAKE DOUBLE COUPLE

D. Zaccagnino[1], C. Doglioni[1,2]

[1] Sapienza University, Earth Sciences Department, Rome, Italy
[2] Istituto Nazionale di Geofisica e Vulcanologia (INGV), Rome, Italy

The occurrence of earthquakes is the mirror of the stress patterns inside the brittle lithosphere. The statistical properties of seismicity are known to be affected by several factors such as the presence of fluids and the rheological features of rocks (Amitrano, 2012), with cross-scale effects on faulting and geologic structures (e.g., Schorlemmer et al., 2005; Diederichs *et al.*, 2019). We show that the tectonic setting directly impacts on the moment tensors of earthquakes. By analysing global and regional focal mechanisms of shallow seismicity (Dziewonski *et al.*, 1981), we find that thrust events are characterized by higher double-couple contribution with respect to normal and strike-slip fault earthquakes (Fig. 1). Different trends are also observed as a function of magnitude, i.e., reverse fault seismicity is featured by linearly increasing double-couple percentages as magnitude raises, while this phenomenon is not observed in normal and mixed events; on the contrary, the double-couple percentage of transcurrent fault sliding appears to be negatively correlated with their own sizes at large magnitudes. Our results are also coherent with the broadly studied stress dependence of the scaling exponent b-value of the Gutenberg-Richter law, which turns out to be anticorrelated to the double-couple contribution. Our work suggests that the structural and tectonic control of seismicity may seep out of the complexity of the seismogenic source marking the roughness of faults and the width of the dislocation zones, coherently with previous research (e.g., Frohlich, 1994; Julian *et al.*, 1998; Zaccagnino *et al.*, 2022); the sharper and concentrated the slip along a single fault as along thrust faults, the higher the double couple (Fig. 2). In this regard, we warn its potential effect in introducing a significant source of bias in magnitude estimation with dramatic impact for seismic forecasting.

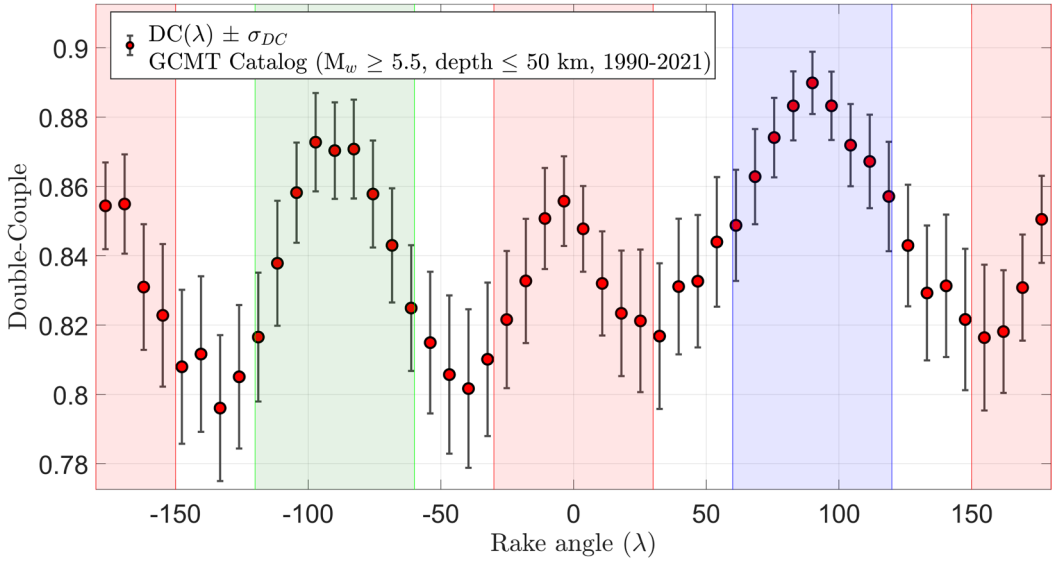


Fig. 1 - Trends of double-couple component of the seismic moment tensors in the GCMT catalogue. Seismicity is classified into normal (green), strike-slip (red), thrust (blue) and unknown according to the Aki-Richards definition (Aki and Richards, 2002).

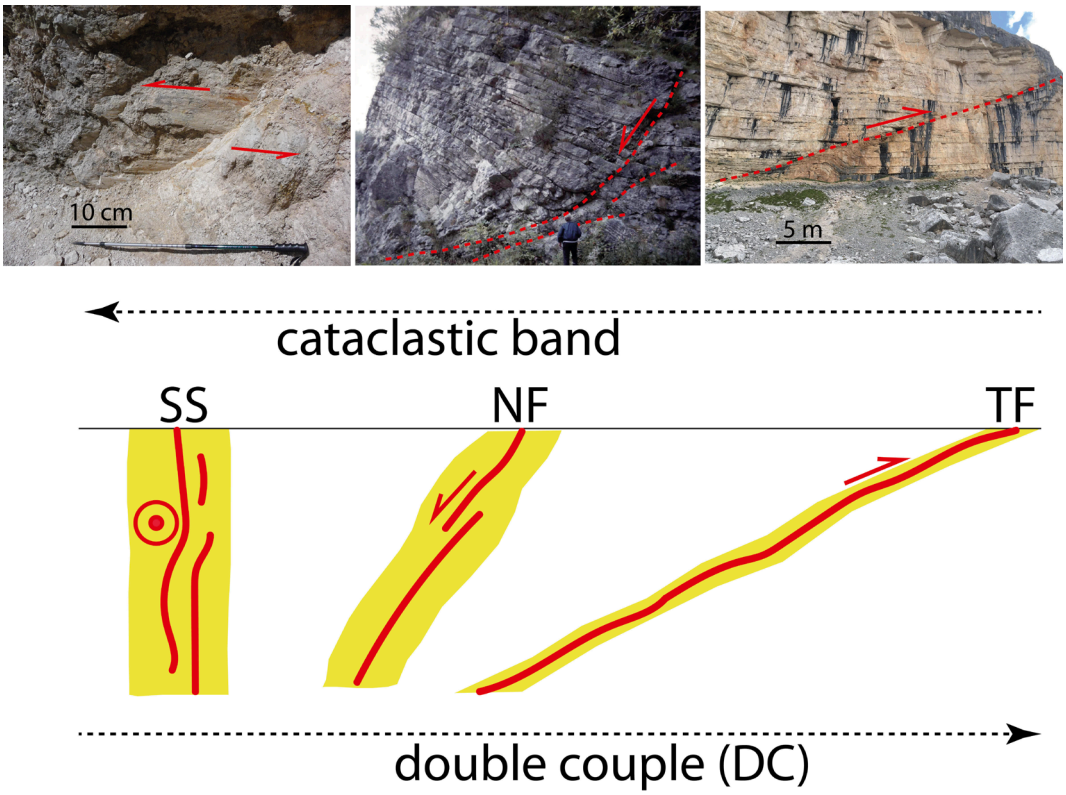


Fig. 2 - The width of the cataclastic band and the sharpness of faults tend to decrease moving from strike-slip (SS), normal faults (NF) to thrust faults (TF). Above, three examples from the Mesozoic carbonate rocks of the Dolomites (northern Italy). Thrusts are generally associated to sharper, continuous faults with respect to normal and strike-slip faults, characterized by multiple and anastomosed faults. This structural variation could explain why the coseismic slip along thrust faults shows higher double couple.

References

Aki K. and Richards P. G.; 2002: *Quantitative seismology*.

Amitrano D.; 2012: *Variability in the power-law distributions of rupture events. The European Physical Journal Special Topics*, **205**(1), 199-215.

Diederichs A., Nissen E. K., Lajoie L. J., Langridge R. M., Malireddi S. R., Clark K. J., ... and Tagliasacchi A.; 2019: *Unusual kinematics of the Papatea fault (2016 Kaikōura earthquake) suggest anelastic rupture*. Science advances, **5**(10), eaax5703.

Dziewonski A. M., T.-A. Chou and J. H. Woodhouse; 1981: *Determination of earthquake source parameters from waveform data for studies of global and regional seismicity*, J. Geophys. Res., **86**, 2825-2852, doi:10.1029/JB086iB04p02825.

Frohlich C.; 1994: *Earthquakes with non—double-couple mechanisms*. Science, **264**(5160), 804-809.

Julian B. R., Miller A. D. and Foulger G. R.; 1998: *Non-double-couple earthquakes 1. Theory*. Reviews of Geophysics, **36**(4), 525-549.

Schorlemmer D., Wiemer S. and Wyss M.; 2005: *Variations in earthquake-size distribution across different stress regimes*. Nature, **437** (7058), 539-542.

Zaccagnino D., Telesca L. and Doglioni C.; 2022: *Scaling properties of seismicity and faulting*. Earth and Planetary Science Letters, **584**, 117511.

SPATIAL AND TEMPORAL EVALUATION OF THE PARAMETERS OF THE GUTENBERG-RICHTER LAW, CASE OF STUDY: ITALY

A. Figlioli[1], A. D'Alessandro[2], R. Martorana[1], A. Sulli[1], G. Vitale[2]

[1] Università degli studi di Palermo, Dipartimento di Scienze della Terra e del Mare, Palermo, Italia
[2] Istituto nazionale di Geofisica e Vulcanologia, Osservatorio Nazionale dei terremoti, Roma, Italia

Introduction. In this work, calculation techniques are used to estimate the variation of the *b* value and the completeness magnitude both spatially and temporally. The computation of the completeness magnitude is closely related to the *b* value. If we underestimate the Mc, we could underestimate the *b* value. The parameters Mc, a value and *b* value are related through the Gutenberg-Richter law (Gutenberg and Richter, 1944). The completeness magnitude, known as the limiting magnitude threshold, is theoretically defined as the lowest magnitude at which 100% of earthquakes occur in a space-time volumes are detected (Mignan *et al.,* 2012). The estimating of *b* value is important for the scientific community (Gulia *et al.,* 2018; Gulia and Wiemer, 2019; Su and Han, 2021; Taroni, 2021). Studies of the *b* value increased in the recent years. It is thought that the *b* value has many significant interpretative ways out, among these there is the opportunity of using it as a precursor of possible seismic sequences (Lombardi, 2021). Other application of *b* value is to research the place of magma storage (Murru *et al.,* 2007) or the association of focal mechanism. Finally, the *a* value, is the parameter that indicates the number of events in the catalogue, thus describing the overall seismicity of the region.

In this scenario, we decided to use the earthquake catalogue, downloaded from the official earthquake website of Istituto Nazionale di Geofisica e Vulcanologia (http://terremoti.ingv.it/). In particular, we selected the period from 1^{est} January 1985 to 28 February 2022. This choice was prompted by the need to have a very large catalogue available, to be able to analyse as many periods as possible and areas of seismotectonic interest. Thanks to the use of the ZMAP software (Wiemer, 2001) that runs in a Matlab environment, we were able to extract the first maps relating to the Mc, *b* value and a value parameters. Especially, our goal is to test as many calculation techniques as possible in order to make reasonable comparisons and define which technique best describes the catalogue. There are many calculation techniques for the completeness magnitude, the most used are the following: MAXC (Maximum Curvature), MBS (Mc by B-value Stability), GFT(Goodness of Fit Test), EMR(Entire Magnitude Range). These techniques are based on calculation differently. In recent years, further techniques have developed that could make computing evolve in a much more sophisticated way (Taroni, 2021).

Data Analysis. In the first approach, we select the MAXC, the maximum curvature technique (Wiemer and Wyss, 2000). This technique consists of evaluate the maximum curvature by computing the maximum value of first derivative of the frequency-magnitude curve. This method is fast and uncomplicated, it is very performing to a small catalogue and give a stable completeness magnitude. When using this technique in the MATLAB environment, it is possible to change the input parameters to obtain as much as possible a good estimate of the completeness magnitude. To estimate the cumulative curve the input parameters are:

- Mc correction: it is a parameter that is taken into consideration to improve the estimate of the completeness magnitude. Using this MAXC technique, we tend to correct the value by bringing the estimate from the right side of the curve so that all values are representative of after this curve.
- Magnitude bin width: this parameter normally is never changed, by default it is 0.1
- Min of event: it allows to select the minimum number of earthquakes that we want to represent in the curve.

- B-value fit: it allows to correct the fit of the line that passes through the cumulative curve.

Figure 1 summarizes some aspects of all the Italian seismicity from 1985 to 2022. In the distribution of magnitude values vs time (fig. 1a) it is possible to notice the densities of distribution of black dots higher in some precise years, these representing important seismic swarms and earthquakes.

Fig. 1 b represents the variation of the *b*-value in relation to time. We note that there are important variations and above all the achievement of important values in specific moments and years.

The maximum curvature estimated for the whole INGV catalogue, period 1985-2022 is showed in fig 1 c. The completeness magnitude was found to be 2.7, with a correction factor of 1.5. The b-value is 1.1 +/- 0.01 and a-value is 7.434. Analogously, fig. 1 d represents the maximum curvature estimated only for the period from 1985 to 2005, before the upgrade of the Italian Seismic Network. For these data the completeness magnitude is 2.8 with a correction factor of 0.4. The b-value is 1.21 +/- 0.01 and the a-value is 7.484.

Finally, fig.1 e represents the maximum curvature estimated only for the period from 2005 to 2022. In this case the completeness magnitude is 2.0 with a correction factor of 0.8. The b-value is 0.97 +/- 0.00 and a-value is 6.658.

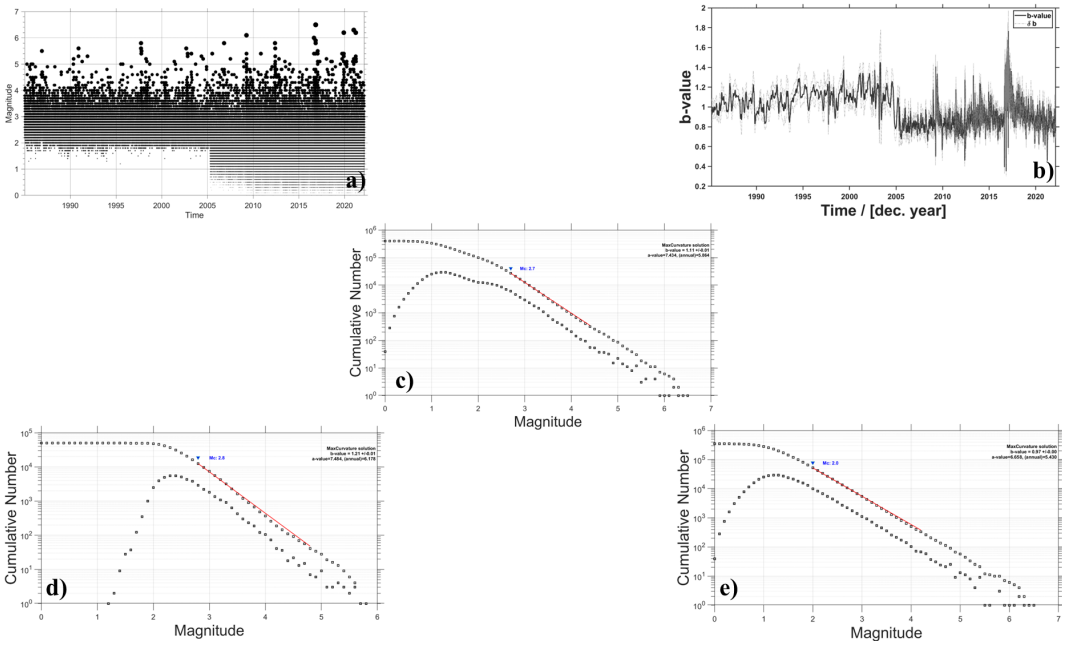


Fig. 1 - Some graphics about seismic catalogue of INGV. a)Time series 1985-2022 b)b-value variation relative time c) curve cumulative for 1985-2022 d)curve cumulative for 1985-2005 e)curve cumulative for 2005-2022.

Among the various possibilities of ZMAP, there is that of calculating the spatial variation of the fundamental parameters of the Gutenberg-Richter formula.

In fact, it was decided to create various maps to estimate the magnitude of completeness, b-value and the standard deviation of b.

For the creation of these maps, attention has fallen on recent seismicity, i.e. from 2015 onwards, including the seismic crisis in central Italy (2016-2018) and also the central southern crisis, including the 2017 Ischia earthquake and other events. Also in this case ZMAP gives the possibility to change the input parameters.

For maps the parameters are:

- Number of events > Mc node: this parameter allows to define how many events you would like to include in a grid node.
- Mc correction: is related to the cumulative curve
- Events with constant radius: this parameter allows you to select events with a constant radius of inclusion
- Grid size: parameter that allows you to have a large grid or a little grid and to obtain a more or less dense distribution of the parameters

Figure 2 presents the Italian seismic distribution in the period from 1st January 2015 to 28 February 2022. The various points change in size based on the magnitude and in colour based on the depth of the events (fig. 2a). The variation of the completeness magnitude is shown in fig. 2b: this map as well as the maps shown in Figure 3 have been created by providing the input parameters such as: minimum number of events greater than the mc at node 100, the grid size of 20 km , the Mc correction 0.9, constant radius of 60 km. Always using the MAXC as an analysis technique for the estimation of the magnitude of completeness. As regards the variation of the completeness magnitude, in figure 2 b, it could be said that in some areas there is a Mc equal to 1.6-1.8 very low values, certainly because there will be a density relative to the national seismic network. There are other areas that have higher values of Mc (yellow zones) which are probably areas where the national network is less dense.

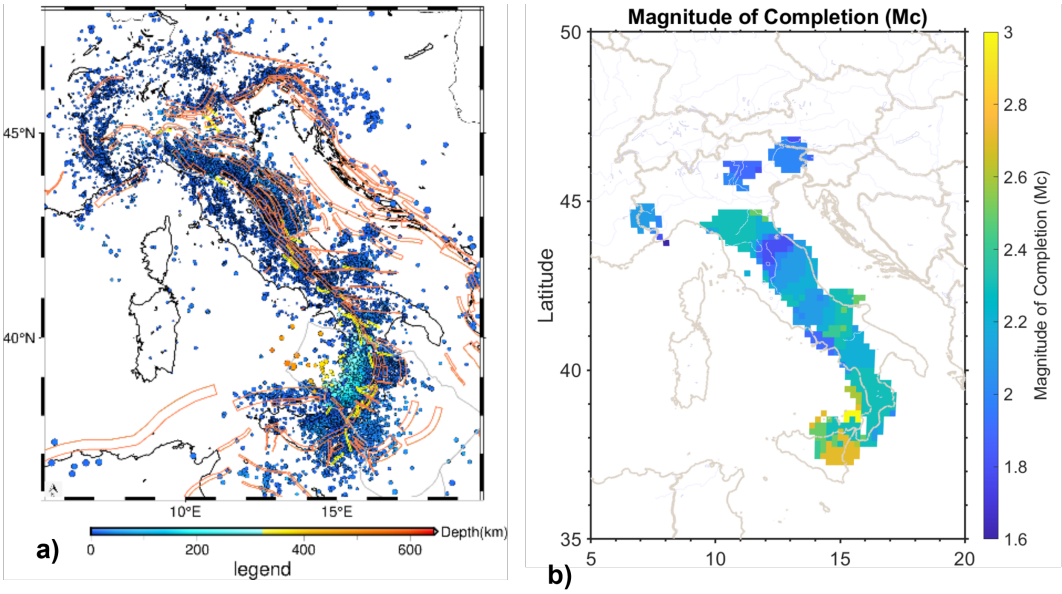


Fig. 2 - a) Seismic distribution from 2015 to today. b) Mc varation about 2015 to today.

To estimate the b-value, we can see how it varies from area to area. It is noted that some areas such as the central Apennines has a value of b about 1.2-1.4, the Calabrian arc has a value of about 0.9-0.7, eastern Sicily is presented with values 0.9-1.4, a part of the Tyrrhenian Sea has values about 1.0. For b-values greater than 1.0 there will be a predominantly relaxing dynamics, for values less than 1.0 there will be a compressive dynamic for values around 1.0 there will be a strike-slip dynamics (Petrucelli *et al.,* 2019).

Discussion. In this first approach towards the calculation of the completeness magnitude, it was decided to consider all the Italian seismicity, thus considering the whole seismic catalogue

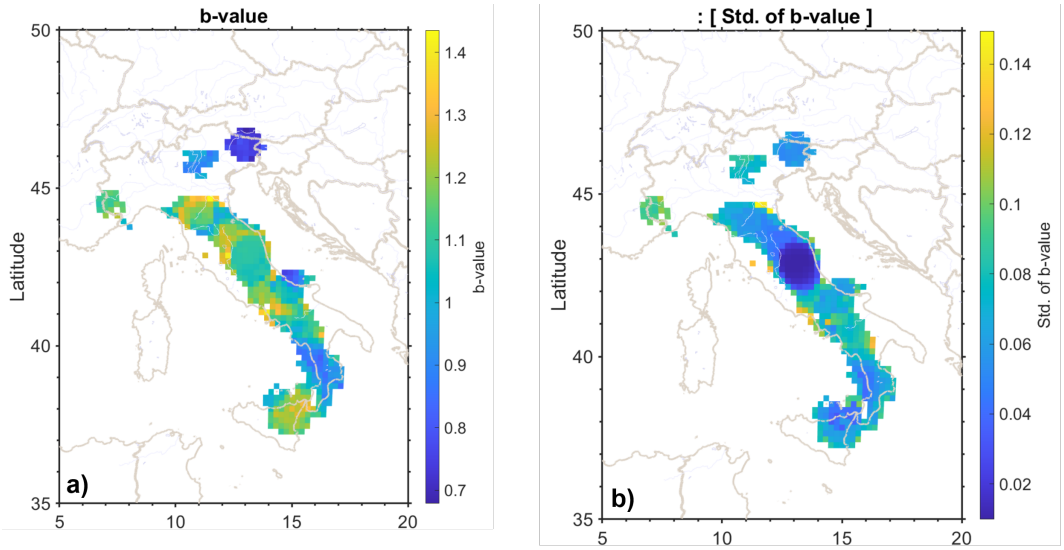


Fig. 3 - a) estimation of b-value varation from 2015 to today b) estimation of standar deviation for b-value stimation.

from 1985 to the present day. This choice was made to understand how the parameters of the mc vary after the upgrade of the national seismic network in 2005.

In fact, a difference in magnitude of completeness was obtained between the catalogue before 2005 and the one after. Before 2005 we have a Mc of 2.8, while after 2005 we have 2.0. The b-value before 2005 is 1.21 while after 2005 it is 0.97.

These differences can lead to attention in several respects. The first thing is is the decrease of the Mc after 2005, which however could be caused by the updating of the national network. The change in the b-value before 2005 and after 2005 may be due to a change in the tectonic activity of some areas. The variation of b-value is very significant in fact if we calculate a b-values greater than 1.0 there will be a predominantly relaxing dynamics, for values less than 1.0 there will be a compressive dynamic for values around 1.0 there will be a strike-slip dynamics (Petruccelli *et al.*, 2019). If we note the values obtained in this first approach and associate with the geodynamicists of Italy, the parameters are in line with the seismic and tectonic activity of the areas that greatest interest.

Among the purposes there is that of going to calculate the differences between the maps before 2005 and those after 2005, in order to understand if there are actually significant differences in estimated b-values. The variation in tectonics could be deduced from these calculations and clearly also from a bibliographic study. Another aspect that we would like to bring forward is to use other analyses already mentioned in the introduction in order to carry out and highlight the relative pros and cons in the use of a specific technique, up to the point of experimenting with the latest technique developed by Taroni et al., 2021.

Having made a choice that is to be able to use the entire national catalogue, the estimates of the magnitude of completeness and of the b-value can have various applications such as those in volcanic areas to understand if the variation of the b-value can be influenced by material in ascent and therefore by heat or also be influenced by mini cracks always due to material rising. Another important aspect for the purposes of this type of study is to better analyse a given seismic sequence where all the geophysical and geodynamic aspects are known and calculate the b-value, in order to understand if in future this variation of the b-value can be used as a possible precursor of a seismic sequence and an earthquake. Therefore, analysing the pre, during and post event would be an additional element to enrich the research of the calculation of b.

Reference

B. Gutenberg, C. F. Richter; *Frequency of earthquakes in California.* Bulletin of the Seismological Society of America 1944;; 34 (4): 185–188. doi: https://doi.org/10.1785/BSSA0340040185.

Gulia, L., Rinaldi, A.P., Tormann, T., Vannucci, G., Enescu, B., Wiemer, S., 2018. *The Effect of a Mainshock on the Size Distribution of the Aftershocks*. Geophys. Res. Lett. 45, 13,277-13,287. https://doi.org/10.1029/2018GL080619.

Gulia, L., Wiemer, S., 2019. *Real-time discrimination of earthquake foreshocks and aftershocks*. Nature 574, 193–199. https://doi.org/10.1038/s41586-019-1606-4.

Lombardi, A.M., 2021. *A Normalized Distance Test for Co-Determining the Completeness Magnitude and b-Value of Earthquake Catalogs*. J. Geophys. Res. Solid Earth 126, 1–14. https://doi.org/10.1029/2020JB021242.

Mignan, A., Woessner, J., 2012. *Understanding Seismicity Catalogs and their Problems: Estimating the magnitude of completeness for earthquake catalogs*. Community Online Resour. Stat. Seism. Anal. 1–45. https://doi.org/10.5078/corssa-00180805.

Murru, M., Console, R., Falcone, G., Montuori, C., Sgroi, T., 2007. *Spatial mapping of the b value at Mount Etna, Italy, using earthquake data recorded from 1999 to 2005*. J. Geophys. Res. Solid Earth 112, 1–15. https://doi.org/10.1029/2006JB004791.

Petruccelli, A., Schorlemmer, D., Tormann, T., Rinaldi, A.P., Wiemer, S., Gasperini, P., Vannucci, G., 2019. *The influence of faulting style on the size-distribution of global earthquakes.* Earth Planet. Sci. Lett. 527, 115791. https://doi.org/10.1016/j.epsl.2019.115791.

Su, Y., Han, P., 2021. in Yunnan Province , China 1–18.

Taroni, M., 2021. *Back to the future: Old methods for new estimation and test of the Gutenberg-Richter b-value for catalogues with variable completeness*. Geophys. J. Int. 224, 337–339. https://doi.org/10.1093/gji/ggaa464.

Wiemer, S., 2001. *A software package to analyze seismicity: ZMAP*. Seismol. Res. Lett. 72, 373–382. https://doi.org/10.1785/gssrl.72.3.373.

Wiemer, S., Wyss, M., 2000. *Minimum magnitude of completeness in earthquake catalogs: Examples from Alaska, the Western United States, and Japan*. Bull. Seismol. Soc. Am. 90, 859–869. https://doi.org/10.1785/0119990114.

THE SEA OF GALILEE (NORTHEAST ISRAEL), A PROMISING SITE FOR STUDYING RELATIONSHIPS BETWEEN SEISMICITY AND FLUID-FLOW

L. Gasperini[1], M. Lazar[2], A. Polonia[1]

[1] Istituto di Scienze Marine, CNR, Bologna
[2] University of Haifa, Israel

The Sea of Galilee (SoG) in northeast Israel (Fig. 1) is a freshwater lake located within a morphological depression along the Dead Sea Fault (DSF) system, in a tectonically complex area (Ben-Avraham et al., 1996). In fact, it lays where the N-S main fault system intersects a secondary pattern of NW-SE oriented faults which cause transtensive shear and strain partition along an area wider relative to the Dead Sea Fault principal displacement zone. A multiscale geophysical-geochemical survey led to the compilation of a new tectonic map of the Sea of Galilee region, at the boundary between the Africa/Sinai and Arabian plates, showing that the present-day most evident deformations occur along NNW-SSE oriented transtensional faults, forming a left-lateral bifurcation of Dead Sea Fault system and a rhomb-shaped depression called the *Capharnaum Trough* (Gasperini *et al.*, 2020). Low-magnitude (Ml=3-4) epicenters during recent seismic sequences are aligned along this feature, whose activity is highlighted by geophysical and geochemical observations (Haddad *et al.*, 2020).

High-resolution seismic reflection data indicate the widespread occurrence of gas-bearing sediments at the lake subseafloor (Lazar *et al.*, 2019), as well as fluid and gas escapes in correspondence of the main tectonic features (Gasperini *et al.,* 2020).

Large magnitude destructive earthquakes have struck the SoG region throughout historical times, as reported by modern paleoseismological and archeoseismological studies (e.g., Galli, 1999; Wechsler *et al.*, 2018).

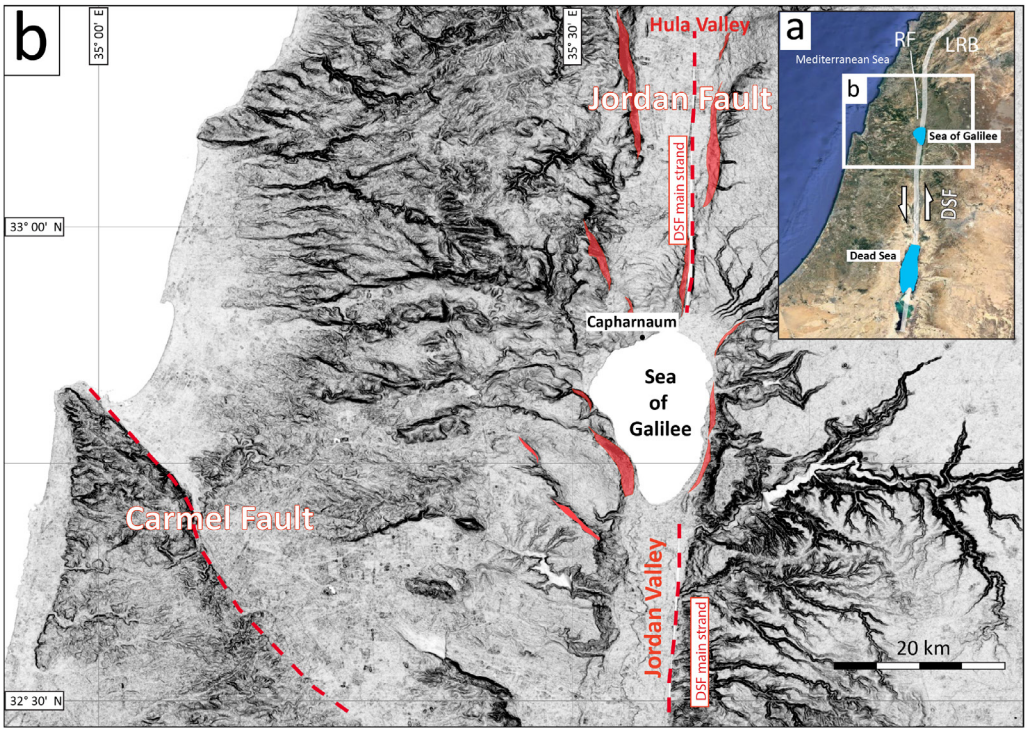


Fig. 1 - The Sea of Galilee along the Dead Sea Faults System. a) Satellite photo from Google Earth; b) morphotectonic map.

The estimated recurrence interval of Mw=6 earthquakes, in the order of 10^2 years, decreases to 10^3 years for Mw~7 earthquakes (Galli, 1999; Begin *et al.*, 2005). Historical earthquake catalogues report strong damage during the years 303, 363, 551, 749, 1202, 1759, and 1837 AD. The earthquake of January 18th, 749 was a large-magnitude event, with extensive damage centered around the northern part of the Jordan valley. This caused the destruction of Tiberias and Beit-She'an, and surface ruptures on the western shore of the SoG (Marco *et al.*, 2003). The earthquake of May 20, 1202 is probably the strongest affecting this region in historical times (Ambraseys and Melville, 1988). The earthquake of January 1st, 1837 also caused severe damage in Tiberias and Safed, again along the western shore of the SoG. During this event, seiching of the lake was reported, and largest macroseismic intensities were observed W of the SoG (Ambraseys, 1997).

The region is characterized by natural springs with ground waters in a wide range of temperatures and chemical compositions escaping from tectonic structures. Geochemical analyses show outgassing of mantle-derived fluids suggesting deep connections to the mantle at a regional scale.

At several thermal springs and wells, the emerging waters are gas-rich, and dissolved volatiles contain a mantle-derived component (e.g., Torfstein *et al.*, 2013, Inguaggiato *et al.*, 2016); it has been observed that this component progressively decreases from N to S along the DSF system (Torfstein *et al.*, 2013).

All these occurrences, and the relatively easy accessibility due to a shallow-water environment not requiring complex equipment's and technologies, make the Sea of Galilee an interesting site to study relationships between the seismic cycle and the presence/circulation of fluids in the substratum, and to design seafloor observatory experiments to study this interplay during seismic and interseismic phases.

References

Ambraseys, N.N., and Melville, C.P. (1988). *An analysis of the eastern Mediterranean earthquake of 20 May 1202,* in Lee, W. K. H., Meyers, H., and Shimazaki, K., eds., Historical Seismograms and Earthquakes of the World: San Diego, California, Academic Press, p. 181-200.

Ambraseys, N.N. (1997). *The earthquake of 1 January 1837 in southern Lebanon and northern Israel.* Annali di Geofisica, 4, 923-935.

Ben-Avraham, Z., Ten-Brink, U., Bell, R., Reznikov, M. (1996). *Gravity field over the Sea of Galilee: evidence for a composite basin along a transform fault.* J. Geophys. Res., 101: 533–544.

Galli, P. (1999). *Active tectonics along the Wadi Araba-Jordan Valley transform fault.* J Geophys Res 104:2777–2796. https://doi.org/10.1029/1998JB900013.

Gasperini *et al.*, (2020). *Neotectonics of the Sea of Galilee (northeast israel): implication for geodynamics and seismicity along the Dead Sea fault system.* Scientific Reports, 10, 1-17.

Haddad *et al.* (2020). *Tectonics of the Dead Sea fault driving the July 2018 seismic swarm in the Sea of Galilee (Lake Kinneret), Israel.* Journal of Geophysical Research: Solid Earth, 125, e2019JB018963.

Inguaggiato, C., Censi, P., D'Alessandro, W. and Zuddas, P. (2016). *Geochemical characterisation of gases along the dead sea rift: Evidences of mantle-co2 degassing.* Journal of Volcanology and Geothermal Research, 320: 50-57.

Lazar *et al.*, (2019). *Constraints on gas release from shallow lake sediments - a case study from the Sea of Galilee.* Geo-Marine Letters, DOI: 10.1007/s00367-019-00588-w.

Marco, S., Agnon, A., Ellenblum, R., Eidelman, A., Basson, U. and Boas, A. (1997). *817-year-old walls offset sinistrally 2.1 m by the Dead Sea Transform,* Israel: Journal of Geodynamics, v. 24, no. 1-4, p. 11-20.

Marco, S., Hartal, M., Hazan, N., Lev, L. and Stein, M. (2003). *Archaeology, history, and geology of the A.D.749 earthquake,* Dead Sea transform: Geology, v. 31, no. 8, p. 665-668.

Marco, S., Rockwell, T., Heimann, A., Frieslander, U. and Agnon, A. (2005). *Late Holocene activity of the Dead Sea Transform revealed in 3D palaeoseismic trenches on the Jordan Gorge segment:* Earth and Planetary Science Letters, v. 234, no. 1-2, p. 189-205.

Torfstein, A., Hammerschmidt, K., Friedrichsen, H., Starinsky, A., Garfunkel, Z. and Kolodny, Y. (2013). *Helium isotopes in Dead Sea Transform waters*. Chemical Geology, 352: 188-201.

Wechsler, N., Marco, S., Klaus-G. Hinzen, K-G., and Hinojosa-Prieto, H. (2018). *Historical earthquakes around the Sea of Galilee. In: Hippos-Sussita of the Decapolis, the first twelve seasons of excavations 2000-2011*, Vol. II, ed. M. Eisenberg, Publisher: The Zinman Institute of Archaeology,16-23.

PRELIMINARY ESTIMATION OF Q_β IN THE GARGANO PROMONTORY (SOUTHERN ITALY)

S. Lucente[1], T. Ninivaggi[1], S. de Lorenzo[1], E. Del Pezzo[2], M. Filippucci[1], A. Tallarico[1]

[1] Department of Earth and Geo-Environmental Science, University of Bari Aldo Moro (UniBa)
[2] National Institute of Geophysics and Volcanology (INGV), Osservatorio Vesuviano

We have examined 190 small earthquakes with magnitude ranging from 1.0 to 2.8 Ml, occurred in the Gargano Promontory (Apulia region, Italy) and recorded by OTRIONS local seismic network and by the INGV national seismic network, to estimate the quality factor of S waves (Q_β) for the Gargano area. Q_β has been estimated using the coda normalization method proposed by Aki (1980):

$$\left\langle ln\left[\frac{rA_\beta(r,f)}{A_c(r,f,t_L)}\right]\right\rangle\Big|_{r\pm\Delta r} = a - \frac{\pi f r}{Q_\beta(f)V_\beta} \quad (1)$$

where $A_\beta(r,f)$ the S wave amplitude spectrum recorded at a distance r from the earthquake and at a given frequency f, $A_c(r,f,t_L)$ the amplitude spectrum of the coda waves, sampled around the time elapsed from the origin time t_L, a is a constant, V_β is the S wave velocity. Spectral ratios in eq. (1) were computed taking t_L=30 s, considering different frequency bands in the range [3,12] Hz and applying a 15% cosine taper window to minimize aliasing effect.

The plot of the first member of eq. (1) versus distance is shown for all the considered frequencies in Fig. 1. The slope of the regression line allows the inference of Q_β. In Table 1 the estimation of Q_β and its error is reported.

Tab. 1 - Preliminary estimations of Q_β parameter at different frequencies in the Gargano area computed using V_β = 3.86 km/s.

Frequency	Q_β preliminary estimation
3 Hz	118.64 ± 22
4 Hz	130.95 ± 24
5 Hz	166.64 ± 29
6 Hz	182.14 ± 32
8 Hz	319.48 ± 52
10 Hz	420.39 ± 75
12 Hz	556.82 ± 100

The estimation of Q_β will allow us to separate the intrinsic and scattering attenuation in the Gargano area using the formulation proposed by Wennerberg (1993) and using the estimates of Q-coda recently obtained by Filippucci *et al.* (2021).

These Q_β results were compared with those obtained by De Lorenzo *et al*. (2013) for the Umbria-Marche region. Results at all frequencies indicate that Q_β estimated for the Gargano Promontory is higher than that estimated for central Italy. This difference can be ascribed to a different rheological behavior of the lithosphere in these two distinct geodynamic frameworks.

References

Aki K.; 1980: *Attenuation of shear-waves in the lithosphere for frequencies from 0.05 to 25 Hz*. Phys. Earth Planet. Inter. 21, pp. 50-60.

De Lorenzo S., Del Pezzo E. and Bianco F.; 2013: *Q_c, Q_β, Q_i and Q_s attenuation parameters in the Umbria-Marche (Italy) region*. Physics of the Earth and Planetary Interiors, 218, pp. 19-30.

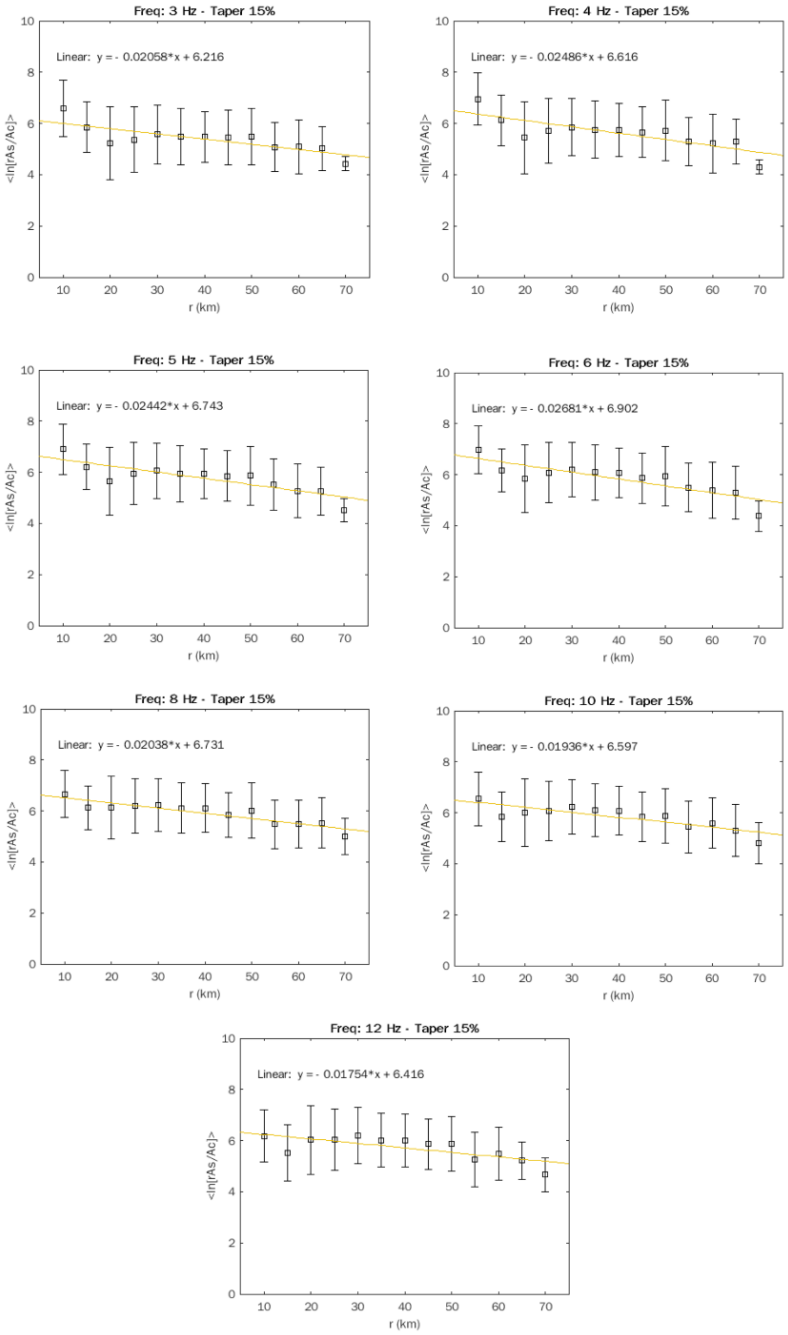


Fig. 1 - Natural logarithms of the ratios rA_β/A_c, at different frequencies, computed versus distance and averaged over the distance range $[r-\Delta r; r+\Delta r]$ with Δr = 2.5 km. The yellow line represents the linear regression whose parameters are over-imposed.

Filippucci M., Lucente S., De Lorenzo S., Del Pezzo E., Prosser G. and Tallarico A.; 2021: *3D-Kernel based imaging of an improved estimation of Q_c in the Northern Apulia (Southern Italy)*. Appl. Sci. 2021, 11, 7512. https://doi.org/10.3390/app11167512.

Wennerberg L.; 1993: *Multiple scattering interpretations of coda-Q measurements*. Bull. Seismol. Soc. Am., 83, pp. 279-290.

A 41 ANNI DAL TERREMOTO DEL 1980: RESILIENZA E RICOSTRUZIONE NELL'ALTA VALLE DEL CALORE (AV)

M. Pizza[1], A.M. Michetti[1,3], M.F. Ferrario[1], A. Capone[2], R. Nappi[3], S. Porfido[3,4]

[1] Università dell'Insubria, Como, Italy
[2] Libero professionista, Montella (AV), Italy
[3] INGV-Osservatorio Vesuviano, Napoli, Italy
[4] CNR- ISA, Avellino, Italy

Introduzione. L'obiettivo del presente lavoro è l'analisi dettagliata degli effetti cosismici ambientali e della vulnerabilità dell'ambiente fisico di quattro Comuni della Provincia di Avellino (Bagnoli Irpino, Cassano Irpino, Castelfranci e Montella), colpiti dal terremoto del 1980, situati lungo le rive del Fiume Calore Irpino e posti a poche decine di chilometri dall'epicentro.

Lo studio è relativo al percorso di resilienza durato oltre quarant'anni, affrontato da queste comunità, per le quali è stato possibile recuperare una gran mole di dati utili alla caratterizzazione del territorio e al percorso affrontato per la ricostruzione (Pizza *et al.*, 2020; Pizza, 2021).

Il terremoto del 1980. Il 23 novembre 1980, un forte terremoto colpì la Campania e la Basilicata, con una intensità macrosismica Io=X MCS e magnitudo M_w 6.9, che rappresenta ancora oggi l'evento sismico a più elevata energia avvenuto in Italia negli ultimi cento anni (Postpischl *et al.*, 1985; Rovida *et al.*, 2022). Il terremoto fu risentito in tutta Italia, colpì 800 località, furono distrutte complessivamente 77.342 abitazioni (4%), 275.263 (15%) furono gravemente danneggiate e 479.973 (26%) furono lievemente danneggiate. Le vittime furono 2.914, i feriti 8.848 e gli sfollati circa 280.000 (C.N.VV.F., 1980).

Il terremoto del 1980 provocò anche numerosi effetti sull'ambiente naturale, sia primari sia secondari. Nell'area epicentrale furono riscontrati effetti primari di fagliazione superficiale (Westaway and Jackson, 1984; Pantosti and Valensise, 1990; Blumetti *et al.*, 2002; Porfido *et al.,* 2007; Serva *et al.*, 2007; Porfido *et al.,* 2022). Tra gli effetti secondari, i fenomeni gravitativi furono i più diffusi, vennero riconosciute oltre 200 frane sismoindotte, fratture nel suolo, 21 casi di liquefazione e numerose variazioni idrologiche relative alla portata delle sorgenti e dei fiumi (Porfido *et al.*, 2007; Serva *et al.*, 2007). L'intensità epicentrale, stimata con la scala ESI-2007 (Michetti *et al.*, 2007), è pari al X grado.

Effetti ambientali sismoindotti nell'Alta Valle del Calore. Nell'area dell'Alta Valle del Calore furono rilevati numerosi effetti cosismici sull'ambiente naturale (Fig. 1). Fratture nel terreno furono osservate lungo il lineamento tettonico Calaggio-Croci di Acerno, di cui una beante, con apertura di pochi cm e lunghezza di oltre 1 km (Capone *et al.*, 1984). Furono osservati fenomeni gravitativi sia di modesta entità, relativi soprattutto a crolli, sia a più larga scala, come gli scorrimenti rotazionali osservati nei pressi dell'abitato di Castelfranci (estensione tra i 10 e i 20 ettari). Inoltre, furono osservati alcuni fenomeni di liquefazioni presso la Piana del Laceno e variazioni idrologiche nelle sorgenti di Cassano Irpino e Caposele, dove fu osservato un forte aumento della portata, durato pochi mesi e non correlabile con le precipitazioni cadute in quel periodo; oltre all'intorbidamento delle acque, fenomeno temporaneo di breve durata (Celico, 1981; Cotecchia and Salvemini, 1981; Esposito *et al.*, 2001).

Alta Valle del Calore: livello di danneggiamento post-sisma. I comuni compresi nell'area di studio contano complessivamente 13.036 abitanti (01.01.2022), Castelfranci attualmente è classificato nella I categoria sismica, gli altri comuni nella II (al 31.03.2022).

Questi comuni, a seguito del terremoto del 1980, hanno subito un danneggiamento al patrimonio edilizio non molto elevato, valutato con un'intensità compresa tra il VII e l'VIII

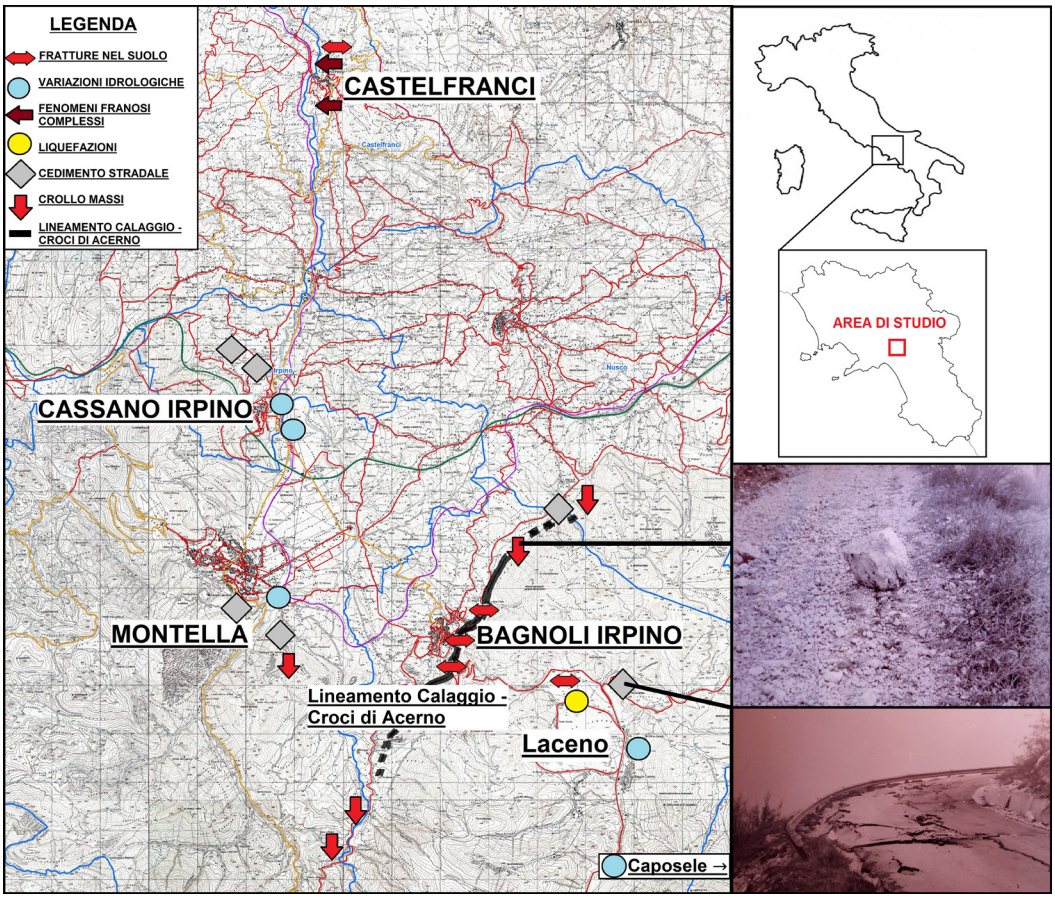


Fig. 1.

grado MCS, vale a dire un livello di danneggiamento molto diffuso, con pochi crolli totali o parziali.

Complessivamente, le unità edilizie dei quattro Comuni distrutte o danneggiate furono 4.755, le persone rimaste senzatetto furono 1.951 (11,9%), 16 le vittime (0,1%) e 320 feriti (2%) su un totale di 16.370 abitanti (Proietti, 1985-89).

Dalle analisi effettuate dopo il terremoto, risulta evidente che a Montella, il più vasto e popoloso dei comuni oggetto di studio, il livello di danneggiamento non sia stato uniforme. Infatti, la parte alta del paese subì un danneggiamento minore, da correlarsi al substrato costituito da litotipi calcarei, che a parità di tipologie edilizie, non determinarono condizioni di amplificazione del danno, mentre la parte inferiore dell'abitato subì un livello di danneggiamento più elevato, riconducibile a fenomeni di amplificazione sismica dovuta alla natura del substrato, costituito da materiali con caratteristiche geotecniche scadenti (Capone, 1991).

Il percorso di *resilienza e ricostruzione*. La resilienza è la capacità di raggiungere un adattamento positivo a fronte di eventi significativamente stressanti e traumatici (CARRI Report, 2013). Per questa specifica tematica è stata svolta un'indagine riguardante la *"ricostruzione"*, ovvero tutte le iniziative e tutti quei processi messi in atto per recuperare e far rinascere le comunità, così drammaticamente segnate dall'evento *"traumatico"* rappresentato dal terremoto del 1980.

Analizzare la fase dell'emergenza, indagare sulla gestione e sugli interventi eseguiti in questa fase è un tema di grande importanza, considerando che il terremoto del 1980 portò alla luce una profonda carenza nella gestione e nel coordinamento dei soccorsi.

Il terremoto avvenne alle 19:34 (ora locale), pertanto la notte tra il 23 e il 24 novembre e quelle successive vennero trascorse in sistemazioni temporanee di fortuna, generalmente all'aperto o in auto, anche per paura di nuovi crolli.

Per i comuni dell'area oggetto di studio è stato possibile tracciare un cronoprogramma degli interventi effettuati per far fronte alla prima fase di emergenza abitativa: entro la fine di Novembre 1980 vennero istallate le prime tende; in seguito, nel successivo mese di Dicembre 1980 giunsero le prime roulotte; nel mese di Giugno 1981 giunsero i primi container; infine, a un anno dal terremoto, vennero istallati i primi prefabbricati, al fine di garantire un ricovero più duraturo e confortevole alla popolazione (Fig. 2).

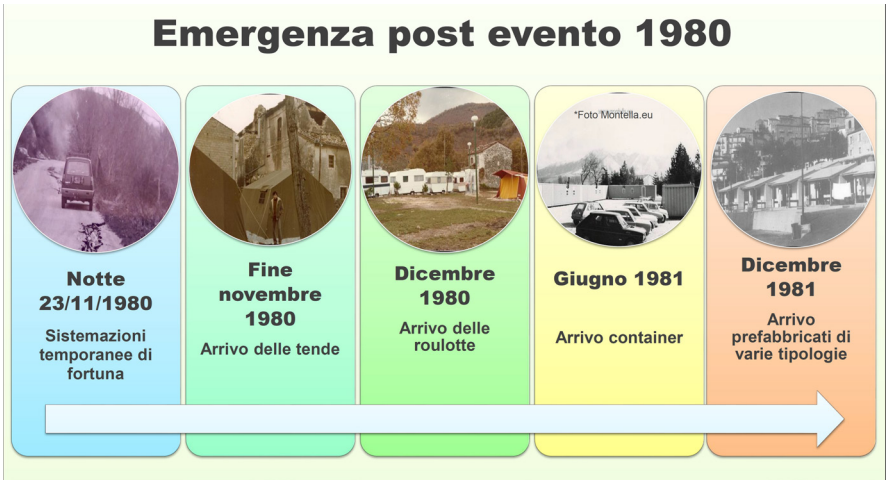


Fig. 2.

La presente ricerca ha avuto come obiettivo anche quello di mettere in evidenza le scelte fatte dagli Enti preposti, le tempistiche e la valutazione economica del processo di ricostruzione che, anche se approssimata per difetto, è necessaria per portare a termine quello che è stato un processo complesso e articolato, e che marginalmente continua a esserlo a oltre 40 anni di distanza dal terremoto (Fig. 3).

Le normative di riferimento per il processo di ricostruzione furono:

- L'ordinanza n. 80 del 6.1.1981, del C.S.G., che consentì i primi interventi ai fabbricati non gravemente danneggiati (entro £ 10.000.000).
- La Legge n. 219 del 14.5.1981, che fu il punto di riferimento dell'intera attività di ricostruzione e di sostegno delle zone colpite dal terremoto.

Particolare attenzione venne riservata alla pianificazione territoriale, infatti alcuni comuni (Cassano I. e Castelfranci) usufruirono delle microzonazioni sismiche preliminari, eseguite nell'ambito del PFG-CNR (AAVV, 1983).

Nei primi anni dopo il terremoto, i comuni si dotarono del Piano di Recupero (1981-84) che, eccetto per Montella, risultava essere il primo strumento urbanistico comunale. Contemporaneamente (1983-84) partirono i primi interventi di ricostruzione.

Verso la metà degli anni '80 (1984-88) i comuni si dotarono di un nuovo strumento urbanistico, il Piano Regolatore Generale, che per Castelfranci è ancora in vigore, per Bagnoli I. e Cassano I. rimase come riferimento per circa 30 anni, mentre a Montella il primo PRG venne sostituito da uno aggiornato nel 2001.

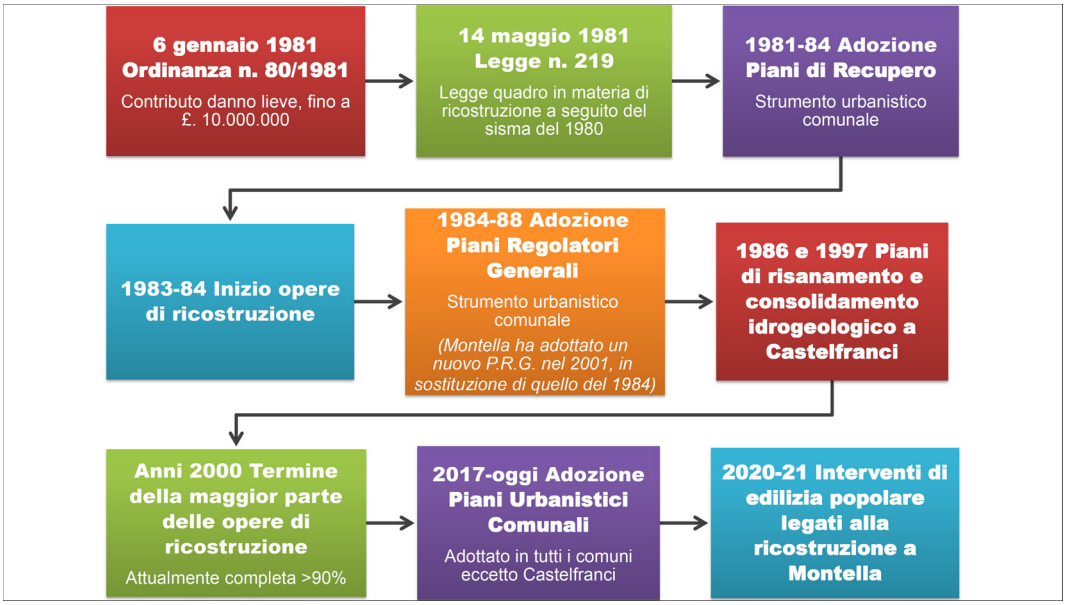


Fig. 3.

Considerata l'instabilità geologica del territorio su cui sorge l'abitato di Castelfranci, a rischio frane, si ritenne opportuno realizzare i Piani di risanamento (1986) e di consolidamento (1997) idrogeologico.

Nella seconda metà degli anni 2010 venne adottato il Piano Urbanistico Comunale, strumento di pianificazione attuale, adottato in via definitiva o preliminare a Montella, Bagnoli I. e Cassano I. (2017-2021), mentre nel 2021 è iniziato l'*iter* per l'approvazione a Castelfranci.

Negli anni 2000 terminò la maggior parte delle opere di ricostruzione nei paesi oggetto di studio. Allo stato attuale il processo di ricostruzione può dirsi completo per oltre il 90% e può dirsi pressoché completo per Bagnoli I., Cassano I. e Castelfranci. Nonostante i recenti interventi di edilizia popolare (2020-21), a Montella permangono poche opere ancora non terminate. Inoltre, sono ancora presenti dei prefabbricati, sebbene non più utilizzati e in fase di smantellamento.

Analizzando i costi della ricostruzione, l'importo stanziato nell'intera area terremotata corrisponde a circa 47,5 miliardi di Euro (Camera dei Deputati, 2009).

Secondo l'appositamente costituita Commissione Parlamentare d'inchiesta (1991), ultimo strumento in grado di discriminare le somme stanziate per ciascun paese, nei Quattro comuni analizzati, nel periodo 1981-87 sono stati stanziati complessivamente € 53.227.278. Questa cifra è da considerarsi assolutamente sottostimata, infatti, a titolo di esempio, per Castelfranci risultano stanziati €15.164.151 a fronte di una spesa reale per la ricostruzione pari a € 64.244.914 (Pizza, 2021).

Conclusioni. Ripercorrere il lungo cammino della *resilienza* e quindi della *ricostruzione* in questi quattro comuni, vuole offrire non solo uno spunto di riflessione ma vuole essere anche un suggerimento costruttivo per una migliore e, speriamo consapevole, programmazione del futuro dei centri storici abitati, in zona sismica, che tengano conto non solo degli scenari che prevedano effetti sul tessuto urbano, ma anche gli scenari che coinvolgano l'ambiente naturale, al fine di "*mitigare i pericoli, contenere gli effetti delle catastrofi quando si verificano e svolgere attività di recupero in modo da ridurre al minimo le interferenze sociali e mitigare gli effetti dei futuri terremoti*" (Bruneau *et al.*, 2003).

Riconoscimenti. All'AVUS 6.4.2009 un abbraccio ideale tra Irpinia e L'Aquila.

Bibliografia

AA.VV.; 1983: *Indagini di microzonazione sismica*. PFG, CNR pubbl. n.492.

Blumetti A.M, *et al.*; 2002: *New data and reinterpretation of November 23, 1980, M 6.9 Irpinia – Lucania earthquake (Southern Apennines) coseismic surface effects.* In Dramis F., Farabollini P., and Molin P. (eds), Studi Geol. Camerti, sp. issue, 19-27.

Bruneau M., *et al.*; 2003: *A framework to quantitatively assess and enhance the seismic resilience of communities*. Earthquake Spectra, 19, 733–752.

Camera dei Deputati XVI Legislatura, Dossier di documentazione; 2009: *I principali eventi sismici a partire dal 1968 - Normativa antisismica, finanziamenti, agevolazioni fiscali e contributive - Schede di lettura*. Docum. e ricerche, n.67 del 14/05/2009.

Capone A., *et al.*; 1984: *Piano di Recupero Comune di Bagnoli Irpino. Indagine geologico-tecnica in prospettiva sismica del territorio comunale*.

Capone A.; 1991: *Piano di Recupero Comune di Montella. Unificazione e ridefinizione dei piani di recupero precedentemente distinti in casali alti, bassi ed esterni*.

CARRI Report; 2013: *Definitions of community resilience: an analysis.* Community & Regional Resilience Institute, 1-14.

Celico P.; 1981: *Relazioni tra idrodinamica sotterranea e terremoti in Irpinia (Campania)*. Rend. SGI, 4; 103-108.

Commissione Parlamentare di inchiesta sulla attuazione degli interventi per la ricostruzione e lo sviluppo dei territori della Basilicata e della Campania colpiti dai terremoti del Novembre 1980 e Febbraio 1981; 1991: *Relazione conclusiva, con annesse appendici, della Commissione parlamentare d'inchiesta sull'attuazione degli interventi per la ricostruzione e lo sviluppo dei territori della Basilicata e della Campania colpiti dai terremoti del Novembre 1980 e Febbraio 1981.*

Coppola L., *et al.*; 1989: *Il gruppo di sorgenti di Cassano Irpino (Avellino - Italia meridionale): regime idrologico ed analisi strutturale del bacino di alimentazione*. Geol. Appl. e Idrogeologia, 24, 227-260.

C.N.VV.F.; 1980: *Annuario Statistico 1980 dell'attività svolta dal Corpo Nazionale dei Vigili del Fuoco.*

Cotecchia V. and Salvemini A.; 1981: *Correlazione tra eventi sismici e variazioni di portate alle sorgenti di Caposele e Cassano Irpino, con particolare riferimento al sisma del 23 novembre 1980*. Geol. Appl. e Idrogeologia, XVI, 167-192.

Esposito E., *et al.*; 2001: *Hydrological anomalies precursory of earthquakes in Southern Apennines (Italy)*. Natural Hazards and Earth System Sciences, 1, 137–144.

Guidoboni E., *et al.*; 2007: *CFTI4Med, Catalogue of Strong Earthquakes in Italy (461 B.C.-1997) and Mediterranean Area (760 B.C.-1500)*. INGV-SGA.

Michetti A.M., *et al.*; 2007: *Environmental Seismic Intensity Scale 2007 - ESI 2007*. Mem. Descr. Carta Geol. d'Italia, 74, 1-56.

Pantosti D. and Valensise G.; 1990: *Faulting mechanism and complexity of the 23 November 1980, Campania-Lucania earthquake, inferred from surface observations*. J. of Geophys. Res., 95, 15319-15341.

Pizza M., *et al.*; 2020: *Cassano Irpino: Esempio di ricostruzione dopo il terremoto del 1980*. Atti del 38° Convegno Nazionale GNGTS, 112-117.

Pizza M.; 2021: *La resilienza nell'Alta Valle del Calore (AV) 41 anni dopo il terremoto del 1980. L'esempio di Bagnoli Irpino, Cassano Irpino, Castelfranci e Montella*. Tesi in Scienze Ambientali, Univ. dell'Insubria. Relatore: Michetti A.M., Correlatore: Porfido S.

Porfido S., *et al.*; 2007: *Seismically induced ground effects of the 1805, 1930 and 1980 earthquakes in the Southern Apennines, Italy*. Boll. SGI, n. 126, 333-346.

Porfido S., *et al.*; 2022: *40 Years Later: New Perspectives on the 23 November 1980, Ms 6.9, Irpinia-Lucania Earthquake*. Geosciences. 12(4):173. https://doi.org/10.3390/geosciences12040173

Postpischl D., *et al.*; 1985: *The Irpinia earthquake of 23 november 1980*. In Atlas of Isoseismal Maps of Italian Earthquakes, CNR-PFG, n.114, 2A, 152-159.

Rovida A., *et al.*; 2022: *Catalogo Parametrico dei Terremoti Italiani (CPTI15), versione 4.0*. INGV.

Proietti G. (a cura di); 1985-89: *"Dopo la polvere". Rilevazione degli interventi di recupero post-sismico del patrimonio archeologico, architettonico ed artistico delle regioni Campania e Basilicata danneggiato dal terremoto del 23 novembre 1980 e del 14 febbraio 1981*. Min. per i Beni Culturali e Ambientali, Sopr. generale agli interventi post-sismici in Campania e Basilicata, 5 voll.

Serva L., *et al.*; 2007: *Environmental effects from five hystorical earthquakes in Southern Apennines (Italy) and macroseismic intensity assessment: Contribution to INQUA EEE Scale Project*. Quaternary Int., 173-174, 30-44.

Westaway R. and Jackson J. A.; 1984: *Surface faulting in the southern Italian Campania-Basilicata earthquake of 23 November 1980*. Nature, 312, 436-438.

PRESENT AND MEDIEVAL DESTRUCTIVE EARTHQUAKES IN DURRES (ALBANIA): NEW INSIGHTS FROM INTEGRATED ARCHAEOLOGICAL AND GEOPHYSICAL STUDIES

D. Talone[1,2], S. Antonelli[1], F. Brozzetti[1,2], C. Casolino[1], C. Cirillo[1,2], E. Metalla[3], G. Lavecchia[1,2], R. de Nardis[1,2]

[1] DiSPuTer, University of Chieti-Pescara "G. d'Annunzio", Chieti, Italy
[2] CRUST - Interuniversity Center for 3D Seismotectonics with Territorial Applications, Italy
[3] IAT – Albanian Institute of Archeology, Tiranë, Albania

Destructive earthquakes have recently struck the eastern coast of the Adriatic Sea, dramatically focusing attention on the high seismogenic potential of the Dinarides-Albanides thrust and fold belt. This orogenic system is characterized by seismogenic compression at crustal depths with earthquakes that rarely exceed M_W 7.0 and with a deformation rate between 2 to 4 mm/yr (Jouanne *et al.*, 2012, Métois *et al.*, 2015). The focal mechanisms show a pattern of P-axes perpendicular to the western thrusts. The historical and instrumental catalogs show that the peri-Adriatic belt experienced large and destructive earthquakes. Durres, one of the most important ports of Illyricum in the Mediterranean area, has been hit several times by earthquakes that caused significant human and economic losses. Notwithstanding the historical catalog is considered complete since 1200 AD for earthquakes of M>7.0 (Vittori *et al.*, 2021 and reference therein).

Recent archaeological investigations of the Roman amphitheater, located in the southern part of Durres town, highlight significant evidence of wall collapses in two well defined historical periods dated to the end of the XI and XIII centuries, respectively. The damages reported by the amphitheater, related to the XIII century, were commonly attributed to the well-documented 1270 earthquake (Guidoboni and Comastri, 2005; Vittori *et al.,* 2021), but what about the clear indications of collapses and reconstructions dated back to the XI century? The amphitheater stratigraphy documents the collapses of 1) the walls of some galleries, 2) the vault of Gallery VII onto the stairs and 3) the building with the artisanal function located at the limits of galleries VI and VII. This structure was reconstructed following the orientation of the previous one and increasing their size (Casolino, 2022).

Geological and geophysical investigations were carried out in July 2019, just before the 26 November 2019 Durres earthquake, to study eventually local amplification effects characterizing the amphitheater area and surroundings. A specific campaign of seismic noise measurements was performed inside and outside the amphitheater, and in other sites of Durres town. The HVSR results show amplification peaks at low frequencies (0.5 and 1 Hz) that rarely exceeds amplitude 2. It is worth noting that similar characteristics are observed both inside the amphitheater and far from it. Our results agree with the ones obtained by other investigators that carried out their measurements after the 2019 Durres earthquake (Mancini *et al.,* 2021). Therefore, all the available data confirm that local effects inside and in the surroundings of the amphitheater are negligible; consequently, all the observed collapses would be mainly attributed to a significant earthquake not far from the town. The available catalogs locate the 1270 earthquake in Durres, with an estimated epicentral intensity (Io) of IX-X MCS but, they do not report any information about earthquakes occurred along the Albanian coast at the end of the XI century.

To deep investigate on the possible occurrence of such an earthquake, we collected data from historical catalogs and specific papers available in the literature (Sulstarova and Kociaj, 1975; Antonopoulos, 1979; Molin and Guidoboni, 1989; Guidoboni and Comastri, 2005; Ambraseys, 2009; Grünthal *et al.*, 2012; Stucchi *et al.*, 2013; Rovida *et al.*, 2021) and we tried to reconstruct the Durres seismic history by integrating these information. We found that the Italian Archive of Historical Earthquake Data (CFTI5med) and the Parametric Catalogue of Italian Earthquakes CPTI15v.4 (Guidoboni *et al.*, 2018; Guidoboni *et al.*, 2019; Rovida *et al.*, 2020; Rovida *et al.*, 2022) report an earthquake occurred on 10 September

1087, along the Italian Adriatic coast of Puglia region. CFTI5med located this earthquake east of Barletta, with epicentral intensity Io = VIII MCS, Imax = IX while CPTI15v4 located it near Bari (Io VI-VII) on the base of a single source describing minor damage in the city (Protospatarius, 1844).

Integrating the historical information with archaeological and geophysical data for the Durres amphitheater, we advance the hypothesis that the 1087 earthquake was only felt on the Italian coast, but it had its epicenter in Albanian territory. This hypothesis can be supported by the observation of the recent earthquakes occurred along the Albanian coast and widely felt along all the Adriatic Italian coast i.e., the Durres 2019 earthquake (Mw 6.3), the Petrinja 2020 one (Mw 6.4), and the seismic event that occurred in Bosnia (22 April 2022, Mw 5.7).

Maps of the effects of these earthquakes (M_W >5.5) from the web questionnaires (Tosi et al., 2007) clearly show that the felt intensity in the Italian sites is up V MCS. In particular, many questionnaires after the 26 November 2019 (Mw 6.3, Io>VIII EMS-98), reported values of Is = V MCS mainly along the coast of the Puglia region. Can the 1087 earthquake be a Durres "lost" earthquake? The confirmation of this hypothesis could have important implication on seismic hazard evaluation.

References

Ambraseys, N., 2009. *Earthquakes in the Mediterranean and Middle East: A Multidisciplinary Study of Seismicity up to 1900.* Cambridge University Press, Cambridge. https://doi.org/10.1017/CBO9781139195430

Antonopoulos, J., 1979. *Catalogue of Tsunamis in the Eastern Mediterranean from Antiquity to Present Times.*

Casolino C., *L'età medievale (XI-XIII secolo)*, in Antonelli S., Metalla E., Moderato M., Sassi B. (eds), Dyrrachium IV. L'anfiteatro romano di Durrës (Albania). Scavi e ricerche (2004-2011), Bari in press.

Grünthal, G., Wahlström, R. *The European-Mediterranean Earthquake Catalogue (EMEC) for the last millennium*. J Seismol 16, 535–570 (2012). https://doi.org/10.1007/s10950-012-9302-

Guidoboni, E., Comastri, A., 2005. *Catalogue fo earthquakes and tsunamis in the Mediterranean area from the 11th to the 15th century*.

Guidoboni E., Ferrari G., Mariotti D., Comastri A., Tarabusi G., Sgattoni G., Valensise G. (2018) - *CFTI5Med, Catalogo dei Forti Terremoti in Italia (461 a.C.-1997) e nell'area Mediterranea (760 a.C.-1500)*. Istituto Nazionale di Geofisica e Vulcanologia (INGV). doi: https://doi.org/10.6092/ingv.it-cfti5

Guidoboni E., Ferrari G., Tarabusi G., Sgattoni G., Comastri A., Mariotti D., Ciuccarelli C., Bianchi M.G., Valensise G. (2019), *CFTI5Med, the new release of the catalogue of strong earthquakes in Italy and in the Mediterranean area*, Scientific Data 6, Article number: 80 (2019). doi: https://doi.org/10.1038/s41597-019-0091-9

Jouanne, F., Mugnier, J.L., Koci, R., Bushati, S., Matev, K., Kuka, N., Shinko, I., Kociu, S., Duni, L., 2012. *GPS constraints on current tectonics of Albania.* Tectonophysics 554–557, 50–62. https://doi.org/10.1016/j.tecto.2012.06.008

Mancini, M., 2020. *Site characterization in Durrës (Albania) from a seismic microzonation perspective.* BGTA Bollettino di Geofisica Teorica e Applicata. https://doi.org/10.4430/bgta0344

Métois, M., D'Agostino, N., Avallone, A., Chamot-Rooke, N., Rabaute, A., Duni, L., Kuka, N., Koci, R., Georgiev, I., 2015. *Insights on continental collisional processes from GPS data: Dynamics of the peri-Adriatic belts.* J. Geophys. Res. Solid Earth 120, 8701–8719. https://doi.org/10.1002/2015JB012023

Molin, D., Guidoboni, E., 1989. *I terremoti prima del Mille in Italia e nell'area mediterranea*.

Protospatarius L., Annales, ed. Pertz G. H., in *"Monumenta Germaniae Historica"*, SS., tomo 5, pp. 52-63, Hannover 1844

Rovida A., Antonucci A. (2021). *EPICA - European PreInstrumental Earthquake CAtalogue, version 1.1.* Istituto Nazionale di Geofisica e Vulcanologia (INGV). https://doi.org/10.13127/epica.1.1

Rovida A., Locati M., Camassi R., Lolli B., Gasperini P. (2020). *The Italian earthquake catalogue CPTI15.* Bulletin of Earthquake Engineering, 18(7), 2953-2984. https://doi.org/10.1007/s10518-020-00818-y

Rovida A., Locati M., Camassi R., Lolli, B., Gasperini P., Antonucci A., 2022. *Catalogo Parametrico dei Terremoti Italiani (CPTI15), versione 4.0.* Istituto Nazionale di Geofisica e Vulcanologia (INGV). https://doi.org/10.13127/CPTI/CPTI15.4

Stucchi, M., Rovida, A., Gomez Capera, A.A., Alexandre, P., Camelbeeck, T., Demircioglu, M.B., Gasperini, P., Kouskouna, V., Musson, R.M.W., Radulian, M., Sesetyan, K., Vilanova, S., Baumont, D., Bungum, H., Fäh, D., Lenhardt, W., Makropoulos, K., Martinez Solares, J.M., Scotti, O., Živčić, M., Albini, P., Batllo, J., Papaioannou, C., Tatevossian, R., Locati, M., Meletti, C., Viganò, D., Giardini, D., 2013. *The SHARE European Earthquake Catalogue (SHEEC) 1000–1899.* J Seismol 17, 523–544. https://doi.org/10.1007/s10950-012-9335-2

Sulstarova, E., Kociaj, S., 1975. *Katalogu i termeteve te shqiperise*.

Tosi, P., De Rubeis, V., Sbarra, P., and Sorrentino, D. (2007). *Hai Sentito Il Terremoto (HSIT)* https://doi.org/10.13127/HSIT

Vittori, E., Blumetti, A.M., Comerci, V., Di Manna, P., Piccardi, L., Gega, D., Hoxha, I., 2021. *Geological effects and tectonic environment of the 26 November 2019, M w 6.4 Durres earthquake (Albania)*. Geoph. J. Int. 225, 1174–1191. https://doi.org/10.1093/gji/ggaa582

Sessione 1.2

Vulcani e campi geotermici

Convenor: M. Palano e F. Forni

TOMOGRAFIA SISMICA DELL'AREA DEL CAMPO GEOTERMICO DI NESJAVELLIR (ISLANDA)

O. Amoroso[1], F. Napolitano[1], G.P. Hersir[2,6], T. Ágústsdóttir[2], V. Convertito[3], R. De Matteis[4], V. Hjörleifsdóttir[5], S.H. Gunnarsdóttir[2], P. Capuano[1]

[1] Dipartimento di Fisica "E.R.Caianiello" , Università degli Studi di Salerno, Fisciano (SA), Italy
[2] Iceland GeoSurvey (ÍSOR), Reykjavík, Iceland
[3] Istituto Nazionale di Geofisica e Vulcanologia, Osservatorio Vesuviano, Napoli, Italy
[4] Dipartimento di Scienze e Tecnologie, Università degli Studi del Sannio, Benevento, Italy
[5] Reykjavík Energy, Reykjavík, Iceland
[6] Precedentemente presso Iceland GeoSurvey

L'area geotermica di Hengill è il più grande campo geotermico ad alta temperatura presente in Islanda. Essa si trova nella regione sud-occidentale dell'isola, a circa 30 km ad est della città di Reykjavík, nella tripla giunzione formata dalla penisola di Reykjanes (RP), la zona vulcanica occidentale e la zona sismica sud islandese (Einarsson, 2008; Stefánsson *et al.*, 1993). L'area è caratterizzata dalla presenza di ialoclastite e basalto, formatisi durante eruzioni subglaciali e subaeree (Sæmundsson, 1992). A nord-est del vulcano Hengill si estende il sottocampo geotermico di Nesjavellir, localizzato su un'area fratturata lunga circa 40 km e larga 4 km in direzione NNE-SSW (Sæmundsson *et al.*, 2016). Le temperature del serbatoio variano tra 200 e 340 °C e l'energia viene utilizzata per la produzione di elettricità e per uso diretto della popolazione di Reykjavík. L'impianto, in attività dal 1990, consta di 30 pozzi di produzione, fornendo mediamente 120 MWe di energia elettrica e 300 MWt di capacità termica. Parte dell'acqua geotermica in eccesso viene reintrodotta nei pozzi di iniezione.

La sismicità dell'area di Nesjavellir viene registrata a partire dagli anni 70 ma dal 1990 la rete sismica è stata intensificata con l'installazione della rete South Iceland Lowland (SIL) gestita dal Icelandic Meteorological Office (IMO) (Stefánsson *et al.,* 1993; Jakobsdóttir, 2008). I dati mostrano che alla sismicità di background si accompagnano sciami frequenti di eventi connessi ad intrusioni di magma o migrazione di fluidi geotermici in roccia calda che creano fratture estese.

L'obiettivo del nostro lavoro è l'imaging 3D delle proprietà elastiche del campo geotermico di Nesjavellir mediante tomografia sismica a scala locale. Le immagini tomografiche in termini di velocità e del loro rapporto (V_p/V_s) sono poi analizzate insieme alla distribuzione della sismicità e confrontate con i valori di resistività e temperatura disponibili per l'area.

Dati. Come riportato sopra, la sismicità nell'area di Hengill è monitorata dalla rete SIL gestita da IMO. Nel 2016 Iceland GeoSurvey (ÍSOR) e ON Power (ON) hanno installato una rete sismica composta da 10 stazioni, per Reykjavík Energy nell'area di Hengill, migliorando la soglia di detezione dei terremoti della rete SIL preesistente. Nel 2018-2021, grazie ai progetti europei COntrol SEISmicity and Manage Induced earthQuakes (COSEISMIQ) e Science4CleanEnergy (S4CE), l'area è stata dotata di una fitta rete di stazioni. Ad oggi, un totale di 38 stazioni sismiche a tre componenti monitorano l'area di Hengill. Ai fini di questo studio, sono state utilizzate 14 stazioni permanenti e temporanee nelle vicinanze di Nesjavellir, appartenenti alle reti sopra menzionate (Figura 1).

Il set di dati disponibile consta di 6906 eventi sismici estratti dal catalogo di ÍSOR, di magnitudo locale -0.8≤ML≤3.8, registrati tra ottobre 2016 e giugno 2020 (Figura 1). Il numero di pick P ed S è rispettivamente pari a 31.320 e 25.624. Il rapporto V_p/V_s valutato tramite il diagramma di Wadati ha fornito un valore pari a 1.77±0.08, che risulta coerente con i valori presenti in letteratura per l'area di Hengill (Foulger 1995; Miller *et al.,* 1998; Tryggvason *et al.,* 2002; Jousset *et al.,* 2011).

Metodo. Al fine di ottenere un imaging sismico 3D dell'area di studio, abbiamo effettuato una tomografia sismica locale. Per prima cosa abbiamo selezionato gli eventi sulla base

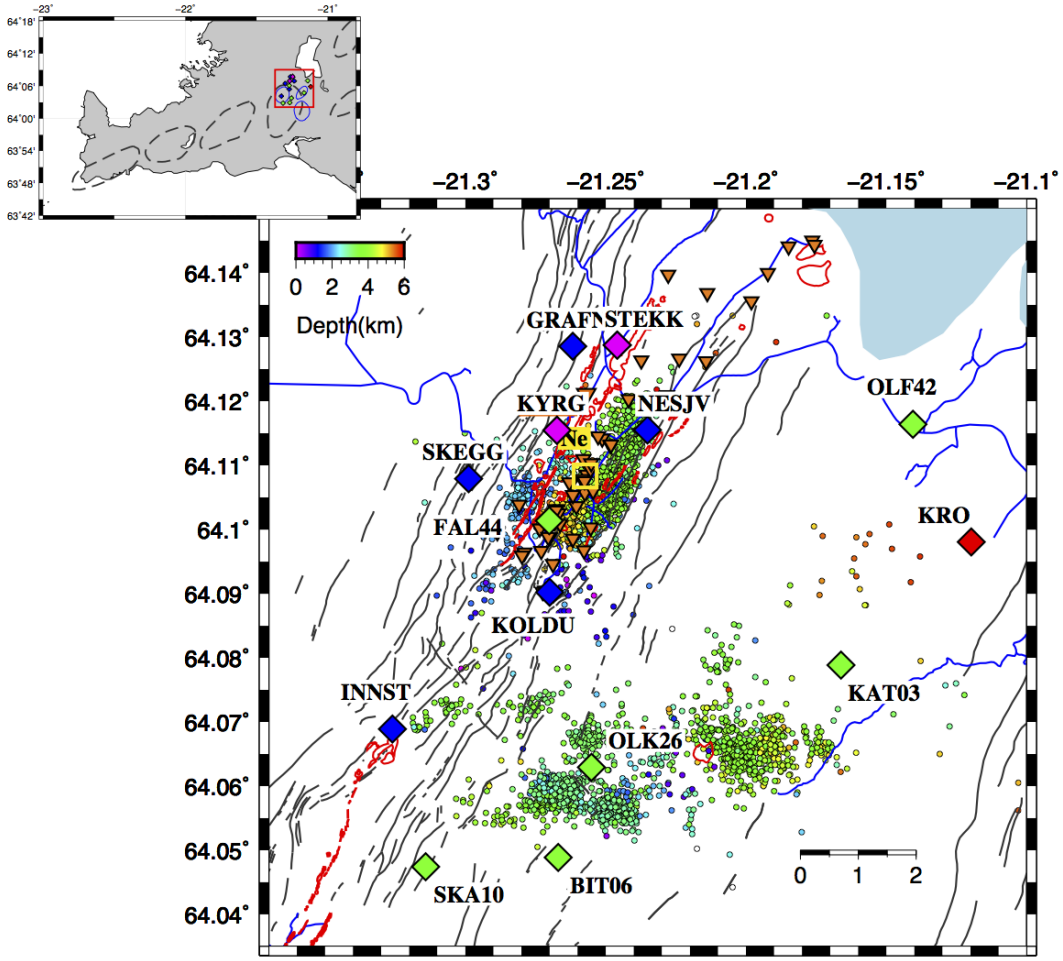


Fig. 1 - Stazioni sismiche ed eventi sismici. Mappa epicentrale degli eventi sismici estratti dal catalogo ÍSOR e rilocalizzati utilizzando il modello di velocità 3D ottenuto in questo studio mediante inversione tomografica. I rombi blu, verde, rosso e magenta rappresentano rispettivamente le stazioni sismiche della rete ÍSOR/ON, del progetto COSEISMIQ, della rete sismica SIL e del progetto S4CE dislocate nell'area di studio.

della qualità della ri-localizzazione preliminare. Gli eventi selezionati sono stati utilizzati per calcolare un modello di velocità 1D per le onde P mediante la procedura implementata nel codice VELEST (Kissling *et al.*, 1995). La rilocalizzazione di tutti gli eventi è stata effettuata con il software NonLinLoc (Lomax *et al.*, 2000), utilizzando il modello di velocità 1D per le onde P ottimizzato per l'area e rapporto V_p/V_S pari a 1.77 come stimato dal diagramma Wadati.

Abbiamo utilizzato una tecnica di inversione tomografica linearizzata per stimare sia i modelli 3D di velocità delle onde P che S che i parametri ipocentrali dei terremoti (La Torre *et al.*, 2004). I tempi di primo arrivo sono calcolati attraverso una soluzione alle differenze finite dell'equazione dell'iconale (Podvin e Lecomte, 1991) su una griglia fine di 100x100x100 m^3. I tempi di tragitto sono poi ricalcolati, al fine di ottenere una maggiore accuratezza, mediante integrazione numerica della lentezza lungo il raggio. La matrice tomografica è invertita mediante algoritmo LSQR di Paige e Saunders (1982). Il numero di iterazioni è stato fissato ad un massimo di 10 e la regolarizzazione dell'inversione è ottenuta attraverso il fattore di smorzamento, che è stato calibrato utilizzando l'approccio empirico della *L-curve*. La distribuzione spaziale delle stazioni e degli eventi ha permesso di indagare un volume di 12x10x13 km^3 (Figura 1). La

distribuzione della velocità in un mezzo continuo è descritta da una funzione di interpolazione trilineare basata su una griglia di nodi regolarmente distanziati. La spaziatura ottimale della griglia è stata scelta tenendo conto della dimensione del volume indagato, della geometria sorgente/stazione e corrisponde a 0.5x0.5x0.25 km^3. La funzione di *root mean square* (RMS), definita come la somma pesata del tempo quadratico di ritardo, viene analizzata *a-posteriori* e la convergenza viene raggiunta dopo 5 iterazioni con riduzione del valore di RMS pari a 80%. Infine, per determinare l'area ben risolta, abbiamo calcolato la Derivative Weight Sum (DWS) ed eseguito i checkerboard test.

Risultati. Il modello di velocità 1D per le onde P ottimizzato per l'area di Nesjavellir è rappresentato nella Tabella 1 e mostra un aumento complessivo di V_p da 3.32 km/s in superficie a 7.80 km/s a 10 km di profondità.

Tab. 1 - Modello di velocità V_p 1D ottenuto da VELEST.

Depth (km)	Velocity (km/s)
-0.70	3.32
0.00	3.33
1.00	4.43
2.00	4.89
3.00	5.95
4.00	6.13
5.00	6.63
6.00	7.41
7.00	7.56
10.00	7.80

Il modello di velocità 3D ottenuto mediante inversione tomografica è stato rappresentato attraverso sezioni orizzontali a diverse profondità e sezione trasversale (Figura 2). La migliore risoluzione si ottiene per profondità comprese tra 1 e 5 km. I valori di velocità di V_p e V_S variano rispettivamente da 3.2 a 6.7 km/s e da 2.3 a 3.6 km/s. Dalla superficie a 3 km di profondità, un'anomalia di basso V_p emerge inizialmente nel settore NW della mappa e si estende fino a 4 km di profondità. Il modello delle onde S (non mostrato in questo riassunto) presenta un'anomalia a bassa velocità da 1 km fino a 2,5 km di profondità solo nella parte settentrionale del modello.

Per profondità superiori a 3 km, viene rilevata la presenza di un'anomalia ad alta velocità dell'onda P, nel settore nord-ovest. Alle stesse profondità Vs non cambia in modo significativo. Le anomalie di velocità in V_p si riflettono nella complessità del modello V_p/V_S fino a 4 km. Per profondità maggiori di 4 km, l'area ben risolta ha un'estensione limitata, e il rapporto V_p/V_S raggiunge il valore più alto di 2.1 nella valle del Nesjavellir.

La sismicità è distribuita in due diversi gruppi (Figura 1): il primo a sud, tra le stazioni SKA10, OLK26, KAT03 e BIT06 e il secondo si trova nella valle del Nesjavellir a nord, tra le stazioni SKEGG, GRAFN, NESJV e KOLDU. Gli eventi appartenenti al primo gruppo fanno parte della sismicità che interessa una regione più ampia al di fuori dell'area di studio e non ben coperta dalle stazioni sismiche utilizzate in questo studio. Gli eventi sismici appartenenti al secondo gruppo sono localizzati nell'area di produzione di Nesjavellir e sono caratterizzati da un allineamento NNE-SSO in accordo con il sistema di faglie normali dell'area (Sæmundsson *et al.*, 2016; Helgadottir *et al.*, 2010).

La sismicità di Nesjavellir (secondo gruppo) presenta una peculiare distribuzione con la profondità. La sismicità superficiale, a 0.5-2.5 km di profondità, si trova nella parte sud-occidentale del campo geotermico di Nesjavellir. A est del campo, allineata con le faglie superficiali NNE-SSO, la sismicità è localizzata più in profondità a circa 3-6 km. La sismicità più superficiale è correlata spazialmente con un basso valore di V_p, basso valore di V_S e basso rapporto V_p/V_S. La sismicità che si verifica a profondità maggiori di circa 3 km sembra essere correlata con alti valori V_p e alti rapporti V_p/V_S (Figura 2).

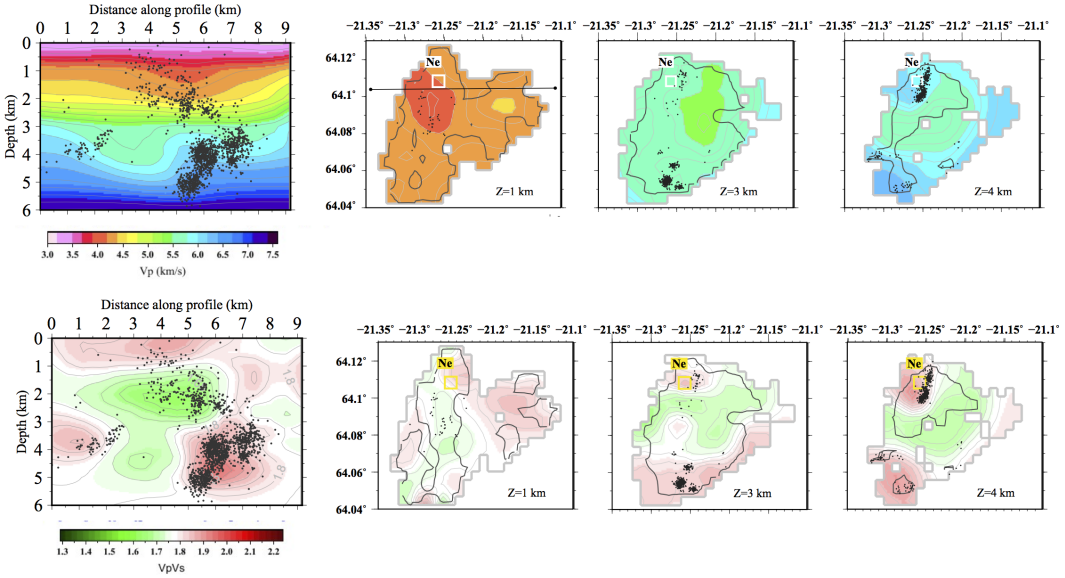


Fig. 2 - Immagini tomografiche in termini di V_p (in alto) e rapporto V_p/V_S (in basso). A sinistra sono rappresentate delle sezioni verticali, nei pannelli a destra i modelli sono rappresentati a profondità fissate. L'orientazione della sezione è riportata sul pannello che rappresenta V_p per profondità pari a 1km.

Ringraziamenti. Questo lavoro è stato sostenuto dal progetto S4CE ("Science for Clean Energy"), finanziato dal Programma Quadro R&I Horizon 2020 dell'Unione Europea, nell'ambito della convenzione di sovvenzione n. 764810 e dal progetto PRIN-2017 MATISSE, n. 20177EPPN2, finanziato dal Ministero dell'Istruzione e della Ricerca. Ringraziamo il progetto COSEISMIQ finanziato da Geothermica ERA-net (progetto n. 170167-4401) per i dati da sei delle loro stazioni e l'Icelandic Met Office (IMO) per i dati da una stazione. Ringraziamo ÍSOR e OR per i tempi di arrivo P ed S ottenuti mediante picking manuale.

Bibliografia

Einarsson P.; 2008: *Plate Boundaries, Rifts and Transforms in Iceland*. Jokull, 58, 35-58.

Foulger G. R.; 1995: *The Hengill geothermal area, Iceland: variation of temperature gradients deduced from the maximum depth of seismogenesis*. J. Volcanol. Geotherm. Res., 65(1-2), 119-133. doi: 10.1016/0377-0273(94)00088-X

Helgadóttir H. M., Snæbjörnsdóttir S. Ó., Níelsson S., Gunnarsdóttir S. H., Matthíasdóttir T., Harðarson B. S., Einarsson G. M. and Franzson H.; 2010: *Geology and Hydrothermal Alteration in the Reservoir of the Hellisheiði High Temperature System, SW-Iceland*, Proceedings World Geothermal Congress 2010 Bali, Indonesia, 25-9 April 2010.

Jakobsdóttir, S. S.; 2008: *Seismicity in Iceland: 1994-2007.* Jökull, *58*, 75-100.

Jousset P., Haberland C., Bauer K. and Arnason K.; 2011: *Hengill geothermal volcanic complex (Iceland) characterized by integrated geophysical observations.* Geothermics, 40(1), 1-24. doi: 10.1016/j.geothermics.2010.12.0081

Kissling E., Kradolfer U. and Maurer H.; 1995: *Program VELEST user's guide-Short Introduction.* Institute of Geophysics, ETH Zurich.

Lomax A., Virieux J., Volant P. and Berge-Thierry C.; 2000: *Probabilistic earthquake location in 3D and layered models*. In Advances in seismic event location (pp. 101-134). Springer, Dordrecht.

Miller A. D., Julian B. R. and Foulger G. R.; 1998: *Three-dimensional seismic structure and moment tensors of non-double-couple earthquakes at the Hengill–Grensdalur volcanic complex.* Geophys. J. Int., 133(2), 309-325, DOI 10.1046/j.1365-246X.1998.00492.x.

Paige C. C., and Saunders M. A.;1982: *LSQR: An algorithm for sparse linear equations and sparse least squares.* ACM Transactions on Mathematical Software (TOMS), 8(1), 43-71.

Podvin P. and Lecomte, I.; 1991: *Finite difference computation of traveltimes in very contrasted velocity models: a massively parallel approach and its associated tools.* Geophys. J. Int., 105(1), 271-284, DOI 10.1111/j.1365-246X.1991.tb03461.x.

Stefánsson R., Böðvarsson R., Slunga R., Einarsson P., Jakobsdóttir S., Bungum H., Gregersen S., Havskov J., Hjelme J. and Korhonen H.; 1993: *Earthquake prediction research in the South Iceland Seismic Zone and the SIL projec*t. Bull. Seismol. Soc. Am. 83(3), 696-716.

Sæmundsson K.; 1992: *Geology of the Thingvallavatn Area.* Oikos, 64(1/2), 40-68, DOI 10.2307/3545042.

Sæmundsson K., Sigurgeirsson M. Á., Hjartarson Á., Kaldal I., Kristinsson S. G. and Víkingsson S.; 2016: *Geological map of SW Iceland, 1:100 000 (2. edition).* Reykjavík: Iceland GeoSurvey.

Tryggvason A., Rögnvaldsson S. T. and Flóvenz, O. G.; 2002: *Three-dimensional imaging of the P-and S-wave velocity structure and earthquake locations beneath Southwest Iceland.* Geophys. J. Int., 151(3), 848-866, DOI 10.1046/j.1365-246X.2002.01812.x

LAND SURFACE TEMPERATURE (LST) DETECTED THROUGH LANDSAT 8 SATELLITE MISSION AT CAMPI FLEGREI CALDERA (SOUTHERN ITALY)

A. Barone[1], E. Bellucci Sessa[2], S. Caliro[2], T. Caputo[2], R. Castaldo[1], G. Chiodini[3], S. Pepe[1], M. Silvestri[4], D. Stroppiana[5], P. Tizzani[1]

[1] National Research Council (CNR), Institute for the Electromagnetic Sensing of the Environment (IREA), Naples, Italy
[2] National Institute of Geophysics and Volcanology (INGV), Osservatorio Vesuviano, Naples, Italy
[3] National Institute of Geophysics and Volcanology (INGV), Bologna, Italy
[4] National Institute of Geophysics and Volcanology (INGV), Osservatorio Nazionale Terremoti, Rome, Italy
[5] National Research Council (CNR), Institute for the Electromagnetic Sensing of the Environment (IREA), Milan, Italy

Nowadays, volcanoes and geothermal fields are increasingly monitored using remote sensing technologies, which are useful tools to investigate these systems with the retrieval of the space-temporal distribution of several parameters. In particular, the increasing availability of Earth Observation (EO) missions has allowed the study of the thermal features of these areas by providing estimates of the Land Surface Temperature (LST). This last parameter is turning out to be crucial for understanding endogenous phenomena as an indicator of the distribution of thermally anomalous zones at the ground surface (Caputo *et al.*, 2019; Silvestri *et al.*, 2020). Nevertheless, the different acquisition time, i.e, daytime and nighttime, and spatial and temporal resolution of the considered missions can affect the performed analysis and the detection of local thermal anomalies becomes challenging (Wang *et al.*, 2019; Sekertekin and Bonafoni, 2020).

In this framework, we show the preliminary results of a thermal study performed at Campi Flegrei caldera (CFc) by employing both daytime and nighttime imagery from Landsat 8 (L8) satellite mission and ground-based measurements related to 2013-2021 time interval. The CFc is a well-known volcanic area hosting processes of magmatic and hydrothermal natures, whose thermal anomalies may reflect both regional- and local-scale features in the space-time domain (Chiodini *et al.*, 2015; Caputo *et al.*, 2019; Castaldo *et al.*, 2021). In this framework, the thermal trends are derived from L8 thermal infrared (TIR) images that are characterized by a spatial resolution of 100 m (pixel size) and a frequency of acquisition of 16 days (Caputo *et al.*, 2019; Sekertekin and Bonafoni, 2020).

Firstly, we estimate the LST time series by considering approaches based on Radiative Transfer Equations (RTE); specifically, the daytime LST dataset is retrieved by using a surface emissivity determination method based on the Normalized Difference Vegetation Index (NDVI) (Jimenez-Munoz *et al.*, 2014), while the nighttime one is estimated through surface emissivity values provided by the Advanced Spaceborne Thermal Emission and Reflection Radiometer Global Emissivity Dataset (ASTER-GED) distributed by United States Geological Survey (USGS) web site (Silvestri *et al.*, 2019; Caputo *et al.*, 2019; Silvestri *et al.*, 2020; https://earthexplorer.usgs.gov). Both the datasets are resampled with a spatial resolution of 30 m and have variable frequency of observation of surface conditions since the L8 images with high cloud cover have been discarded from the data. We emphasize the thermal anomalies related to endogenous phenomena by processing the retrieved LST time-series following these steps: (i) removal of spatial and temporal outliers; (ii) correction for adiabatic gradient of the air with the altitude; (iii) detection and removal of the seasonal component. We show the datasets of estimated LST through mean temperature maps over the time interval 2014 - 2020 in Fig. 1. In particular, the daytime LST dataset (Fig. 1a) shows several thermal anomalous zones related to exogenous processes (e.g., anthropogenic structures, water, vegetation, …), whereas the nighttime LST distribution (Fig. 1b) clearly highlights a single positive thermal anomaly at Solfatara crater, suggesting the occurrence of geothermal endogenous phenomena. At Solfatara area, we also observe similar spatial and temporal distribution of LST anomalies in the daytime and nighttime datasets suggesting that the time step of LST time series could be enhanced by integrating both the datasets, at least for this specific area. Then, we consider the ground-based measurements collected by the Osservatorio Vesuviano, National Institute of Geophysics and Volcanology (OV

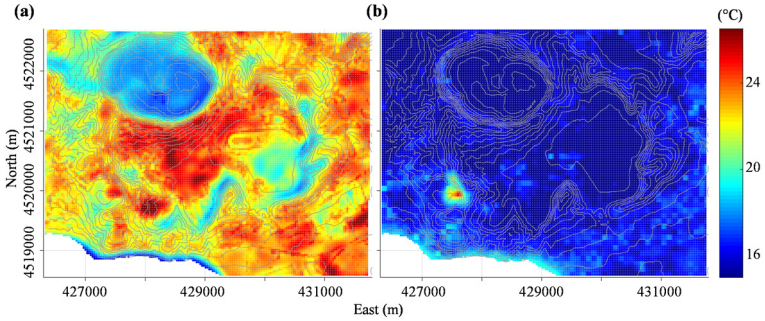


Fig. 1 - Temperature of the ground surface at Campi Flegrei caldera during 2014 - 2020. Mean temperature maps estimated through (a) daytime and (b) nighttime L8 LST datasets. Grey lines indicate the topography of the area.

- INGV, Italy, Naples). This dataset consists of 151 thermal measurements distributed within the 2004-2021 time-interval and acquired at a depth of 0.01 m below the ground surface. Unlike satellite images, this data is only related to the Solfatara crater and allows the characterization of its thermal anomaly, as well as the areas occupied by fumaroles. As for satellite-based estimation, we apply to the ground-based measurements corrections (i) and (iii). This dataset shows a mean thermal gradient representative of the entire area of about 0.3 °C/yr, with mean temperature values approaching 90 °C at the zones occupied by fumaroles.

Finally, we compare the evolution of the thermal anomalies at Solfatara crater provided by both the satellite and ground-based measurements, highlighting the role of the LST parameter in volcanic and geothermal frameworks. Indeed, the integrated use of the daytime and nighttime L8 LST datasets allows a better characterization of the thermal anomalies improving frequency of observation of thermal conditions of the surface. Although the medium spatial resolution of L8 thermal bands (100m) could be considered not appropriate to characterize fumaroles activities, we showed a good agreement between remote and ground-based thermal gradient. We remark the role of the thermal satellite data that can play for the spatial and temporal monitoring of the volcanic systems.

References

Caputo T., Bellucci Sessa E., Silvestri M., Buongiorno M.F., Musacchio M., Sansivero F. and Vilardo G.; 2019: *Surface Temperature Multiscale Monitoring by Thermal Infrared Satellite and Ground Images at Campi Flegrei Volcanic Area (Italy)*. Remote Sensing, 11, 9, 1007, DOI 10.3390/rs11091007.

Castaldo R., Tizzani P. and Solaro G.; 2021: *Inflating Source Imaging and Stress/Strain Field Analysis at Campi Flegrei Caldera: The 2009-2013 Unrest Episode*. Remote Sensing, 13, 12, 2298, 10.3390/rs13122298.

Chiodini G., Vandemeulebrouck J., Caliro S., D'Auria L., De Martino P., Mangiacapra A. and Petrillo Z.; 2015: *Evidence of thermal-driven processes triggering the 2005–2014 unrest at Campi Flegrei caldera*. Earth Planet. Sci. Lett., 414, 58-67, DOI 10.1016/j.epsl.2015.01.012.

Jimenez-Munoz J.C., Sobrino J.A., Skokovic D., Mattar C. and Cristobal J.; 2014: *Land surface temperature retrieval methods from Landsat-8 thermal infrared sensor data*. IEEE Geoscience and remote sensing letters, 11, 10, 1840-1843, DOI 10.1109/LGRS.2014.2312032.

Sekertekin A. and Bonafoni S.; 2020: *Land Surface Temperature Retrieval from Landsat 5, 7, and 8 over Rural Areas: Assessment of Different Retrieval Algorithms and Emissivity Models and Toolbox Implementation.* Remote Sensing, 12, 294, DOI 10.3390/rs12020294.

Silvestri M., Rabuffi F., Pisciotta A., Musacchio M., Diliberto I.S., Spinetti C., Lombardo V., Collini L. and Buongiorno M.F.; 2019: *Analysis of Thermal Anomalies in Volcanic Areas Using Multiscale and Multitemporal Monitoring: Vulcano Island Test Case*. Remote Sensing, 11, 2, 134, DOI 10.3390/rs11020134.

Silvestri M., Romaniello V., Hook S., Musacchio M., Teggi S. and Buongiorno M. F.; 2020: *First comparisons of surface temperature estimations between ECOSTRESS, ASTER and Landsat 8 over Italian volcanic and geothermal areas*. Remote Sensing, 12(1), 184., DOI 10.3390/rs12010184.

Wang K., Jiang Q., Yu D., Yang Q., Wang L., Han T. and Xu X.; 2019: *Detecting daytime and nighttime land surface temperature anomalies using thermal infrared remote sensing in Dandong geothermal prospect.* Int. J. Appl. Earth Obs. Geoinformation, 80, 196-205, DOI 10.1016/j.jag.2019.03.016.

THE DYNAMIC EVOLUTION OF LARGE CALDERAS: CURRENT UNREST AT CAMPI FLEGREI, SOUTHERN ITALY

S. Carlino[1], C. R.J. Kilburn[1,3], S. Danesi[2], N.A. Pino[1]

[1] INGV-Osservatorio Vesuviano, Naples, Italy
[2] INGV-Sezione di Bologna, Italy
[3] UCL Hazard Centre, Department of Earth Sciences, UCL, London, UK

Campi Flegrei is the largest active caldera in Europe. About 12-15 km across, it extends west from the suburbs of Naples to the Tyrrhenian Sea. About a third is partially submerged beneath the Bay of Pozzuoli; the remaining two-thirds are home to more than 360,000 people. The volcano has been restless since 1950. It last erupted in 1538 after an interval of about 3,000 years (Smith *et al.*, 2011). Previous intervals have been as short as decades or centuries (Smith *et al.*, 2011), so that a return to eruption after nearly 500 years is a realistic possibility. Caldera-wide ground movement has raised the coastal town of Pozzuoli, near the centre of greatest uplift, by more than 4 m and twice triggered evacuations of about 40,000 people (Barberi *et al.*, 1984). The current uplift began in 2005 with a previously unseen style of behaviour. The movement has been attributed to the ascent of magma (D'Auria *et al.*, 2015) or of magmatic gas (Chiodini *et al.*, 2021) to depths of about 3 km. Both interpretations assume a change in the external conditions feeding the volcano's magmatic system. We propose that the current uplift is instead being driven by internal changes in Campi Flegrei's crust as sections of faults are partially reopened. The re-opening favours new pathways to the surface for magmatic fluids, ranging from escaping gases to magma itself.

Campi Flegrei's current unrest began in 1950 and has developed in four episodes (Del Gaudio *et al.*, 2010; Kilburn *et al.*, 2017; Troise *et al.*, 2019). Measured at Pozzuoli, the first three episodes produced comparable amounts of uplift over similar durations: c. 74 cm in 1950-52, 159 cm in 1970-72, and 175 cm in 1982-84. The fourth episode has continued for nearly four decades, first with twenty years of subsidence that lowered Pozzuoli by 93 cm, and then by seventeen years of uplift that by the end of February 2022 had returned the surface to its 1984 position. The amounts and timescales of the first three episodes are consistent with the intrusion of magmatic sills (Woo & Kilburn, 2010); those of the fourth, and ongoing, episode are consistent with the permeable flow of a combination of magmatic gas and meteoric water (Kilburn *et al.*, 2017; Troise *et al.*, 2019).

We propose that the complete sequence describes the progressive stretching of the crust by repeated intrusions until its permeability had increased sufficiently for a major change in the flow of pore fluids. Our interpretation is supported by new data, which show that, by 2021, the regime of crustal deformation had changed from quasi-elastic (elastic with subordinate fracturing and faulting) to inelastic (dominated by fracturing and faulting). The change marks an evolution towards crustal rupture and has been observed at several volcanoes, including large calderas (Robertson and Kilburn, 2016; Kilburn, 2018). Rupture does not guarantee a magmatic eruption. However, it does favour an increase in the rate of escape of pressurized fluids that may trigger phreatic explosions. The presence of a new rupture also increases the possibility that any new magma reaching shallow depth will erupt, rather than intrude as had occurred between 1950 and 1984. As a result, it is unlikely that the volcano will replicate its behaviour during the past 70 years of unrest, so that new scenarios for emergency response must take account of its dynamical and structural evolution.

References

Barberi F., Corrado G., Innocenti F., Luongo. and G.; 1984: *Phlegraean Fields 1982-1984: brief chronicle of a volcano emergency in a densely populated area*. Bull. Volcanol., 4: 175-185.

Chiodini G., Caliro S., Avino R., Bini G., Giudicepietro F., De Cesare W., Ricciolino P., Aiuppa A.,

Cardellini C., Petrillo Z., Selva J., Siniscalchi A. and Tripaldi S.; 2021: Hydrothermal pressure-temperature control on CO_2 emissions and seismicity at Campi Flegrei (Italy). J. Volcanol. Geotherm. Res., 414, DOI 10.1016/j.jvolgeores.2021.107245.

D'Auria L., Pepe S., Castaldo R., Giudicepietro F., Macedonio G., Ricciolino P., Tizzani P., Casu F., Lanari R., Manzo M., Martini M., Sansosti E. and Zinno I.; 2015: *Magma injection beneath the urban area of Naples: a new mechanism for the 2012-2013 volcanic unrest at Campi Flegrei caldera*. Sci. Rep., 5, 1-11.

Del Gaudio C., Aquino I., Ricciardi GP., Ricco C. and Scandone R.; 2010: *Unrest episodes at Campi Flegrei: a reconstruction of vertical ground movements during 1905-2009*. J. Volcanol. Geotherm. Res., 195, 48-56.

Kilburn C.R.J.; 2018: Forecasting volcanic eruptions: beyond the failure forecast method. Front Earth Sci., 6, DOI 103389/feart.2018.00133.

Kilburn C.R.J., De Natale G.., Carlino S.; 2017: *Progressive approach to eruption at Campi Flegrei caldera in southern Italy*. Nature Com., 8, 1-8.

Robertson R.M., Kilburn C.R.J.; 2016: Deformation regime and long-term precursors to eruption at large calderas: Rabaul, Papua New Guinea. Earth Planet Sci Lett, 438: 86-94.

Smith V.C., Isaia R., Pearce N.J.G.; 2011: *Tephrostratigraphy and glass compositions of post-15 kyr Campi Flegrei eruptions: implications for eruption history and chronostratigraphic markers*. Quat. Sci. Rev., 30, 3638-3660.

Troise C., De Natale G., Schiavone R., Somma R., Moretti R.; 2019: *The Campi Flegrei caldera unrest: Discriminating magma intrusions from hydrothermal effects and implications for possible evolution*. Earth-Sci. Rev., 188, 108-122.

Woo J.Y.L., Kilburn C.R.J.; 2010: *Intrusion and deformation at Campi Flegrei, southern Italy: Sills, dikes, and regional extension*. J. Geophys. Res., 115, DOI 10.1029/2009JB006913.

THE AEOLIAN ISLANDS: A POTENTIAL GEOTHERMAL ENGINE

C.G. Caruso, A. Gattuso, G. Lazzaro, M. Longo, M. Meschis, S. Scirè Scappuzzo, F. Italiano
Istituto Nazionale di Geofisica e Vulcanologia, (INGV), Palermo, Italy

The Sicilian territory is characterized by a geothermal potential among the highest in Italy, with a variety of thermal manifestation spread over both onshore and offshore areas and including the volcanic islands where geothermal potential looks to be even higher. In spite of this manifest geothermal vocation, this resource has never been exploited for energy purposes. The areas with the largest availability of high-enthalpy fluids are the island of Pantelleria and the Aeolian arc. Here we focus the attention on the geochemical features of the submarine hydrothermal fluids vented over the Aeolian islands.

It is well known that the Aeolian Archipelago is located less than 40 km off the north-east coast of Sicily and includes seven subaerial volcanic edifices (Alicudi, Filicudi, Salina, Lipari, Vulcano, Panarea and Stromboli) and a number of submarine volcanoes (at least 5 main edifices: Eolo, Sisifo, Enarete, Alicudi and Filicudi North). The Aeolian arc represents the tectonically extending backarc basin associated with both the ongoing southeastwardly Ionian subduction process and the opening of Tyrrhenian Extensional Basin. It is one of the most active volcanic areas of the Mediterranean basin, affected by volcanic/hydrothermal activity. Structural trends and volcanic activity in the area are strongly controlled by the regional stress fields. Indeed, Quaternary NW-SE oriented crustal extension affecting the overriding plate of the Ionian subduction zone is seismically identified by historical damaging earthquakes, rupturing active normal faults, mostly NE-SW to N-S oriented such the likely tectonic link between Stromboli and Panarea Islands. Moreover, the shallow magma chambers, alongside the tectonic activity due to plate subduction and overriding plate crustal extension, deformation and cooling of erupted lavas results in convective circulation of dense, cold seawater through the cracked and fissured upper portions of the lithosphere; this circulation promotes the formation of venting sites that release hot hydrothermal fluids and dissolved elements. A widespread and intense submarine hydrothermal activity marked by long-lasting recharge and high-temperature/high-pressure characteristics, are clues for potentially exploitable geothermal energy sources. Indeed, the Aeolian arc is affected by numerous and distributed heat sources, generally represented by hot magmatic bodies at shallow depths (<10 km) in an extensional geodynamic setting. Vulcano, Panarea, Salina and Lipari exhibit some features that make them a potential site hosting exploitable submarine geothermal systems. All the observations done since late 90^s over the Aeolian islands, confirm that these areas are affected by hydrothermal fluid circulation; triggered by cold seawater entering into fractured rocks and getting superheated by magmatic bodies at crustal depths. The wide spread presence of submarine hydrothermal fluids, vented at temperatures in the range 40-150°C represents a challenge for a feature development of geothermal plants over the Aeolian arc. Clues of active venting of hydrothermal fluids have been further provided by the injection of magmatic-type volatiles into the sea water, as demonstrated by the anomalous ^{3}He content and the whole chemical composition of the gases. In this study we describe and discuss the geochemical features of the submarine hydrothermal fluids discharged over the Aeolian offshore. The results show how thermal energy of magmatic origin is still available over the archipelago providing significant perspectives for geothermal energy exploration.

Following the assumption that the submarine hydrothermal fluids may equilibrate inside a geothermal reservoir at some level beneath the seafloor, we propose the existence of reservoirs kept at boiling conditions by the thermal energy released by cooling magma batches located at shallow crustal levels. We constrained the chemical-physical conditions (pressure, temperature and redox) that buffer the chemical composition of the hydrothermal fluids as well as the processes (i.e. mixings, fractionations) governing their composition at the venting sites.

Preliminary geothermometric and geobarometric estimations indicate equilibrium temperatures in the range of 150-400°C besides H_2O pressures in the range of 70 bar and 250 bar.

STA/LTA AUTOMATIC CUT OF EXPLOSION QUAKES

A. Di Benedetto[1], A. Figlioli[2], A. D'Alessandro[3], G. Lo Bosco[1]

[1] Dipartimento di Matematica e Informatica, Università degli studi di Palermo, Palermo, Italy
[2] Dipartimento di Scienze della Terra e del Mare, Università degli studi di Palermo, Palermo, Italy
[3] Istituto Nazionale di Geofisica e Vulcanologia, Osservatorio Nazionale Terremoti, Rome, Italy

Introduction. The scientific community is committed to identifying and analysing seismic signals produced by volcanic activity, with the aim of characterizing possible precursors in order to using them as a pre-warning of activity. The most dangerous activity which has a greater impact on the population living in the inhabited centres adjacent to the volcano is paroxysm (Giudicedipietro *et al.*, 2020). In particular, one of the most dangerous volcano is Stromboli.

Stromboli volcano (926 m l.s.m.) belongs to the Aeolian archipelago in the Mediterranean Sea (Italy); it is geodinamically located between the subduction Ionian slab and the Tyrrhenian Sea. It is an open conduit, characterized by three summit craters (Fig. 1), with persistent strombolian activity, whose explosions occur every 15-20 minutes. Generally, its volcanic activity is classified into three classes: normal activity (precisely "explosion"), major explosion and paroxysm. To distinguish them, the variation of frequency and energy of activity has to be calculated (Calvari *et al.*, 2021). The permanent seismic network of INGV (Istituto Nazionale di Vulcanologia e Geofisica) is able to record seismic signals corresponding to the volcanic explosions, which are differentiated by: VLP (very long period), landslides, tornillos, Explosion Quakes (EQ). The main focus of this work is on this latter class, because clearly visible by the human eye along a seismic path. Their features are based on the variation in amplitude and frequency content, whose range is around 10-25 Hz. Another characteristic is that the EQ is preceded by VLP, and it is important in order to identify itself (Giudicepietro *et al.*, 2019). This feature allows describing the phenomena that occur in the plumbing system. In detail, the mechanism that activates the VLP and successively EQ, is a progressive degassing magma on the conduit. When the intensive increases, the conduit goes into resonance with the wall and produces a seismic wave. After the magma starts the migration and then arrives in the vent, the strombolian activity starts and in the raw signal, one can observe the EQ. The Stromboli systems are characterized by two reservoirs: a shallow conduit located by 3-4 km and a deep reservoir located by 11 km (Harris and Ripepe, 2007).

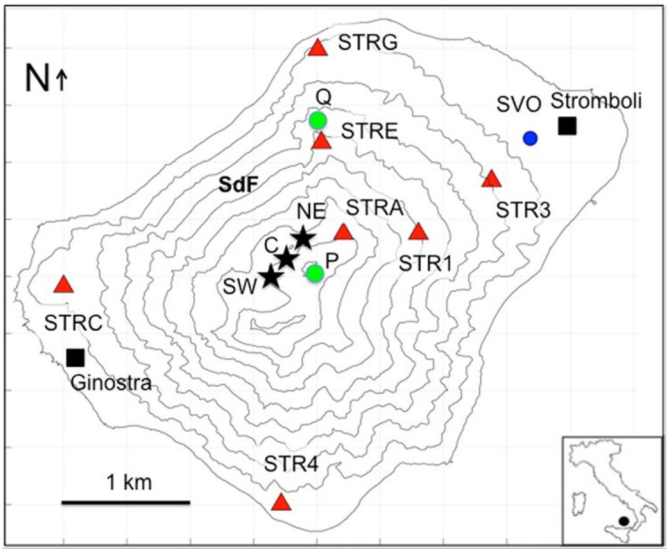


Fig. 1 - INGV seismic network on Stromboli.

STA/LTA automatic cut. The problem of detecting Seismo-volcanic events such as Explosion Quakes and their identification in the raw signal is a key problem when you need to collect data for future analysis in the seismo-volcanic field. With the continuous growth of data available over time, thanks to the expansion of the seismic networks, fulfilling this request by a human operator can result laborious and time-consuming. So, there is a need to use automatic methods for the extraction of the events. In Fenner *et. al.*, 2022, the authors try to solve this problem. In particular, they overcome the drawbacks of automatic collecting seismo-volcanic events in Stromboli volcano using a user-friendly approach called Adaptive-Window Volcanic Event Selection Analysis Module (AWESAM). AWESAM allows the generation of catalogues of seismo-volcanic events from recordings at a seismic station located in the proximity of a volcano. The catalogues contain information about the maximum amplitude, waveform, duration of the event and corresponding time of the seismo-volcanic events during a certain period. In the State-of-the-art there are many Volcano Seismic Recognition (VSR) systems that allow real-time monitoring and consistent catalogues. These VSR systems decrease their efficiency when used to recognize events from more than one station or related to different volcanoes. In Cortés *et. al.* (2021), the authors propose a Volcano-Independent VSR (VI.VSR) solution to generate labelled catalogues without the dependence on the volcanic context.

In this work, we have implemented a system to perform the automatic cut of the Explosion Quakes (EQ) from raw signals collected by Dario Delle Donne from Osservatorio Vesuviano (OV) INGV, using STA/LTA algorithm. In particular, the idea is to carry out a statistical study to find the combination of STA and LTA window sizes that automatically cut at best the EQs, with respect to the cuts made by an expert operator. The window sizes of STA / LTA where to search are stored in two lists of values, *sta_list* = {1,2,3,..,10} and *lta_list*= {10,20,30,..,100}. Note that both are of 10 elements.

Fig. 2a shows the case of three EQs, while Fig. 2b shows a detail on the last one. Fig. 2c reports the result of the STA/LTA algorithm on this EQ (bottom) and the trigger from STA/

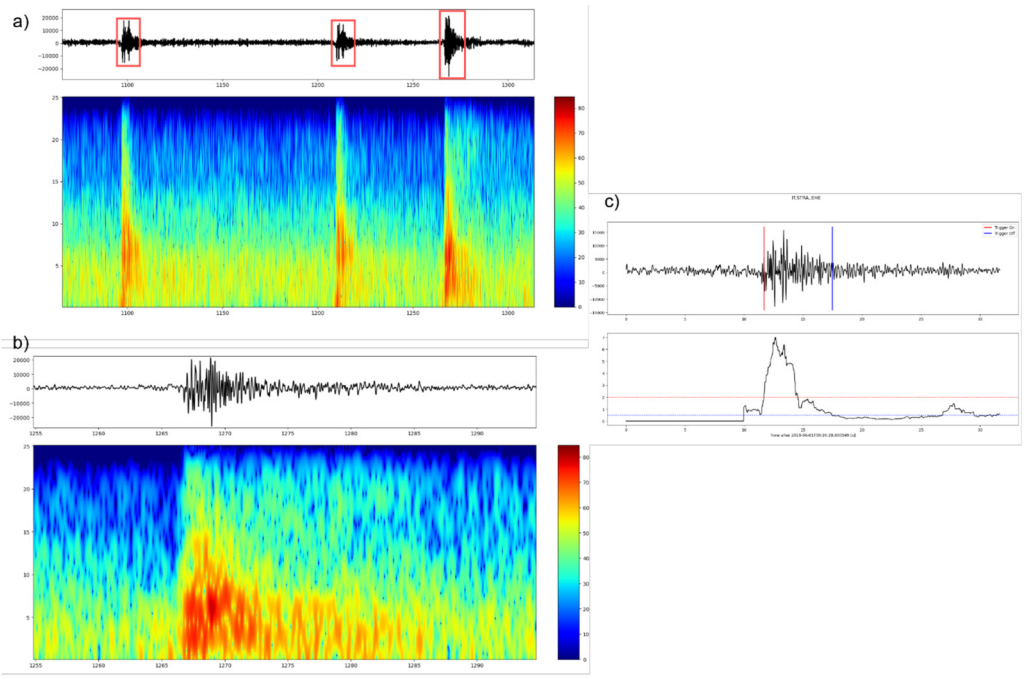


Fig. 2 - (a) Multiple EQs, (b) Zoom on third EQ, (C) STA/LTA performed on third EQ. Red Bar is Trigger On and Blue Bar is Trigger Off.

LTA (top): the red bar consists of Trigger on and the Blue bar on Trigger off. These results are obtained by fixing a couple of sizes for STA and LTA.

Note that the STA/LTA algorithm needs two input parameters to detect on and off triggers. In this work, we have considered these values as 4.0 and 1.0 respectively.

Starting from a set of signals cut by the operator, a comparison was made between the start and end times of the EQ events triggered by STA / LTA on the same signals. For each considered raw signal, STA / LTA outputs a list of triggers that are compared individually with the ones cut by the operator. For the comparison, the absolute deviation in terms of temporal distance is calculated. If the deviation is at most 10 (seconds), both for the start and for the end of the event, then the cut is considered to be correct. Regardless of this check, the triggers produced by STA / LTA are counted and indicated as *enq*.

Statistical measures and results. Two statistical measures were calculated to determine the effectiveness of the cut of the STA / LTA algorithm, i.e. the *quality index* (*qi*) and the *numerosity index* (*ni*). Let *m* be the mean of all the deviation computed between the correct (below 10 secs) STA/LTA cuts and the operator cuts, the *qi* is defined as

qi = 1-(m/10)

The *ni*, on the other hand, is defined to take into account the discrepancy among *enq* (the correct number of cuts by STA / LTA) and the number of cuts by the operator, indicated as *tnq*. In our data, the *tnq* is equal to 1506. The value of the *ni* is set in this way:

$$ni = \begin{cases} \frac{enq}{tnq} & if\ enq < tnq \\ \frac{tnq - mod(enq, tnq)}{tnq} & if\ tnq < enq < 2*tnq \\ 0 & otherwise \end{cases}$$

Finally, the product between the *qi* and the *ni*, named *qni*, is considered an overall measure to determine the effectiveness of the cut made by STA / LTA, and is defined as

*qni = qi * ni*

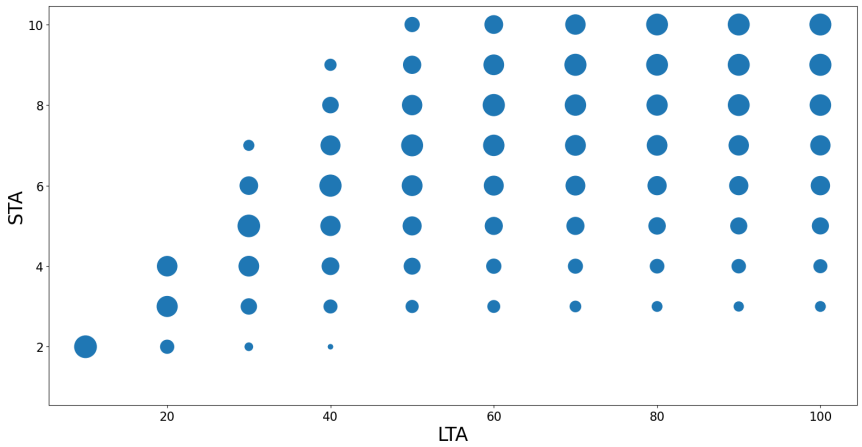


Fig. 3 - Results example for qni values.

Fig. 3, shows the *qni* values computed for 100 different couples of STA/LTA sizes, taken from *sta_list* and *lta_list*. i.e. the couples (1,10), (1,20), (1,30), …, (1,100), (2, 10), (2, 20), (2, 30), …, (2, 100), … (3,10), (3,20), (3,30), …, (3,100), … . The values of *qni* are represented by the radius of the blue circles, the abscissa of the circle indicates the LTA values while the ordinate the STA values. The larger the radius of the circles, the more reliable the combination of window sizes for automatic cutting. This result is an example of execution of the algorithm using a subset of the entire dataset, precisely, considering the raw data of 1 day: 27 raw signals of about 1 hour each with 153 EQ signals associated with.

Acknowledgements. The authors would like to thank Dario Delle Donne from INGV-OV, to give us the data from STRA Seismic Station.

References

Calvari S. Giudicepietro F., Di Traglia F., Bonaccorso A., Macedonio G. and Casagli, N.; 2021: *Variable Magnitude and Intensity of Strombolian Explosions: Focus on the Eruptive Processes for a First Classification Scheme for Stromboli Volcano (Italy)*. Remote Sensing, 13, 944, DOI 10.3390/rs13050944.

Cortés G., Carniel R. Lesage P., Mendoza M. and Della Lucia I.; 2021: *Practical Volcano-Independent Recognition of Seismic Events: VULCAN.ears Project.* Frontiers in Earth Sciences, 8, 702, DOI 10.3389/feart.2020.616676.

Fenner D., Rümpker G., Li W., Chakraborty M., Faber J., Köhler J., Stoecker H. and Srivastava N.; 2022: *Automated Seismo-Volcanic Event Detection Applied to Stromboli (Italy).* Frontiers in Earth Science, 10, DOI 10.3389/feart.2022.809037.

Giudicepietro F., Calvari S., Alparone S., Bianco F., Bonaccorso A., Bruno V., Caputo T., Cristaldi A., D'Auria L., Cesare W., Di Lieto B., Esposito A., Gambino S., Inguaggiato S., Macedonio G., Martini M., Mattia M., Orazi M., Paonita A. and Vita, F.; 2019: *Integration of Ground-Based Remote-Sensing and In Situ Multidisciplinary Monitoring Data to Analyze the Eruptive Activity of Stromboli Volcano in 2017-2018*. Remote Sensing, 11, 1813, DOI 10.3390/rs11151813.

Giudicepietro F., López C., Macedonio G. et al.; 2020: *Geophysical precursors of the July-August 2019 paroxysmal eruptive phase and their implications for Stromboli volcano (Italy) monitoring*. Sci. Rep. 10, 10296, DOI 10.1038/s41598-020-67220-1.

Harris, A. and Ripepe M.; 2007: *Synergy of multiple geophysical approaches to unravel explosive eruption conduit and source dynamics – A case study from Stromboli*. Chemie der Erde – Geochem., 67, 1-35, DOI 10.1016/j.chemer.2007.01.003.

REMOBILIZATION AND ERUPTION OF AN UPPER CRUSTAL CUMULATE MUSH: THE SINGKUT CALDERA (NORTH SUMATRA, INDONESIA)

F. Forni[1,2], J.A. Oalmann[2], G. Fellin[3], S. Eisele[2], M. Phua[2], O. Bernard[2], M. Guillong[3], H. Rifai[4], C. Bouvet de Maisonneuve[2]

[1] Department of Earth Sciences "Ardito Desio", University of Milan, Italy
[2] Asian School of the Environment/EOS, Nanyang Technological University, Singapore
[3] Institute of Geochemistry and Petrology, Department of Earth Sciences, ETH Zurich, Zurich, Switzerland
[4] Department of Physics, Faculty of Mathematics and Natural Sciences, Universitas Negeri Padang, Indonesia

Understanding the conditions and timescales of storage and remobilization of magma bodies in the upper crust is key to interpret the signals of potential reawakening of the volcanic activity at active volcanic systems.

In this study we provide the first volcanological and petrological characterization of the Singkut volcanic system located in northern Sumatra, ~35 km N of the Toba caldera and ~40 km SW of the major city of Medan.

Singkut is a ~9 km diameter caldera delimited by ~300 m-high rims where pre-caldera lavas are exposed. The inner part of the collapsed structure is occupied by three post-caldera volcanoes and currently hosts an active geothermal field. We utilize field observations and correlation with a distal marine tephra layer to map the extension and thickness of the tuff erupted during the caldera-forming eruption and use these data to estimate the erupted magma volume. We use major and trace element data of bulk-rock, matrix glasses and minerals to characterize the pre-eruptive conditions of pre- and post-caldera lavas and caldera-forming tuff and ^{14}C and U/Th-He zircon dating to determine the eruption ages. In addition, a combination of U/Th and U/Pb in-situ zircon dating and zircon trace element geochemistry provides insights into the mechanisms and timescales that led to the Singkut caldera-forming eruption and those that controlled the post-caldera activity.

Our data show that Singkut caldera formed ~50 ka during a large explosive eruption that deposited ~60 km^3 of pyroclastic material. The cataclysmic eruption was preceded by at least 200 ky of mostly effusive pre-caldera activity and followed by effusive and mildly explosive post-caldera activity, with the last eruption reported at 1881 AD. The lavas and pumices have

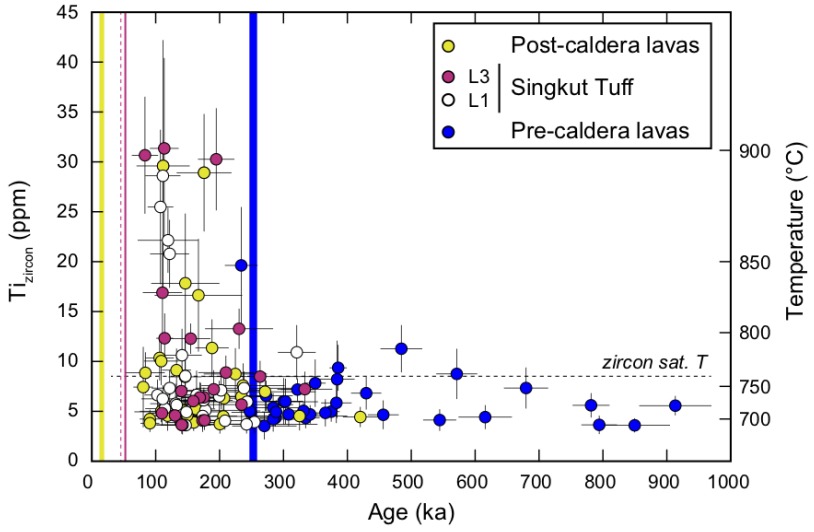


Fig. 1 - U/Pb and U/Th crystallization ages (ka) vs. Ti content (ppm) of zircons from the lavas and pyroclastics from the Singkut caldera. Crystallization temperatures estimated using Ti-in-zircon thermometry (Ferry and Watson, 2007). Vertical solid bars indicate eruption ages obtained via U/Th-He zircon dating including uncertainties while dashed bar indicate ^{14}C dates.

high crystallinity (24-62% crystals) and contain pl+amph+bt+opx+Fe-Ti ox+ap+zr±qtz. Notably, large and strongly resorbed quartz crystals are abundant in the pre-caldera lavas and scarce or absent in the caldera-forming tuff and post-caldera lavas. Bulk-rock composition of pumices and lavas varies from andesitic to dacitic, while the matrix glass in the pumices is rhyolitic. Trace element composition of glass (e.g., positive Eu anomalies) indicate resorption of feldspars. Crystallization ages of the youngest zircons in pre-caldera lavas overlap with eruption ages (~250 ka) while crystallization ages of the youngest zircons in the caldera-forming tuff and post-caldera lavas are significantly older (~100 ka) than the eruption ages (~50 and ~16 ka, respectively). Ti-in-zircon thermometry combined with zircon geochronology (Fig. 1) show that the Singkut magma body experienced a heating phase which started approximately upon eruption of the pre-caldera lavas and continued at least until the eruption of the post-caldera lavas. Such prolonged heating event determined progressive melting of the least refractory mineral phases (mostly quartz and feldspars) and hampered zircon crystallization for ~50 ky before the caldera-forming eruption and ~80 ky before the effusion of the post-caldera lavas. Heating was likely due to an increase of the recharge flux in the magma reservoir which reduced the crystallinity of the crystal mush and promoted remobilization and eruption of the Singkut magma body.

References

Ferry J. M. and Watson E. B.; 2007: *New thermodynamic models and revised calibrations for the Ti-in-zircon and Zr-in-rutile thermometers*. Contrib. to Mineral. Petrol. 154, 429-437.

SLOW SLIP EVENTS AT MT. ETNA VOLCANO

M. Palano[1], F. Sparacino[1], P. Gambino[2], N. D'Agostino[3], S. Calcaterra[2]

[1] Istituto Nazionale di Geofisica e Vulcanologia, Sezione di Catania, Osservatorio Etneo, Catania, Italy
[2] Italian Institute for Environmental Protection and Research (ISPRA), Rome, Italy
[3] Istituto Nazionale di Geofisica e Vulcanologia, Osservatorio Nazionale Terremoti, Rome, Italy

Mt. Etna is a basaltic Quaternary volcano located on the east coast of Sicily (South Italy) at the front of the Apennine-Maghrebian chain (Fig. 1). The volcano developed over the last 500 ka over metamorphic and sedimentary rocks on its western and northern slopes and over Quaternary plastic clays. The different geomechanical properties of these rocks coupled with the inhomogeneous long-term updoming of the volcano have produced a complex basement topography dominated by a 17 km-wide horseshoe-shaped depression beneath the eastern flank. Such a complex basement topography gently dips in SE direction and would lead to the large-scale seaward motion of the eastern flank of Mt. Etna as clearly documented since the early 1980s. At the surface, the unstable sector is defined by a 25 km-wide horseshoe-shaped region, which encompass the sedimentary depression and is bounded by the "NE Rift - Pernicana fault" and by the "South Rift - Mascalucia-Tremestieri - Aci Trezza fault system", respectively on its NE and SE half (Fig. 1).

We detected a set of slow slip events (SSE) occurred at Mt. Etna volcano during the 2006-2016 period by analysing the GNSS observations collected by the continuous networks:

- Etn@net, managed by the "Osservatorio Etneo" department of "Istituto Nazionale di Geofisica e Vulcanologia" and established since November 2000 (blue dots in Fig. 1).

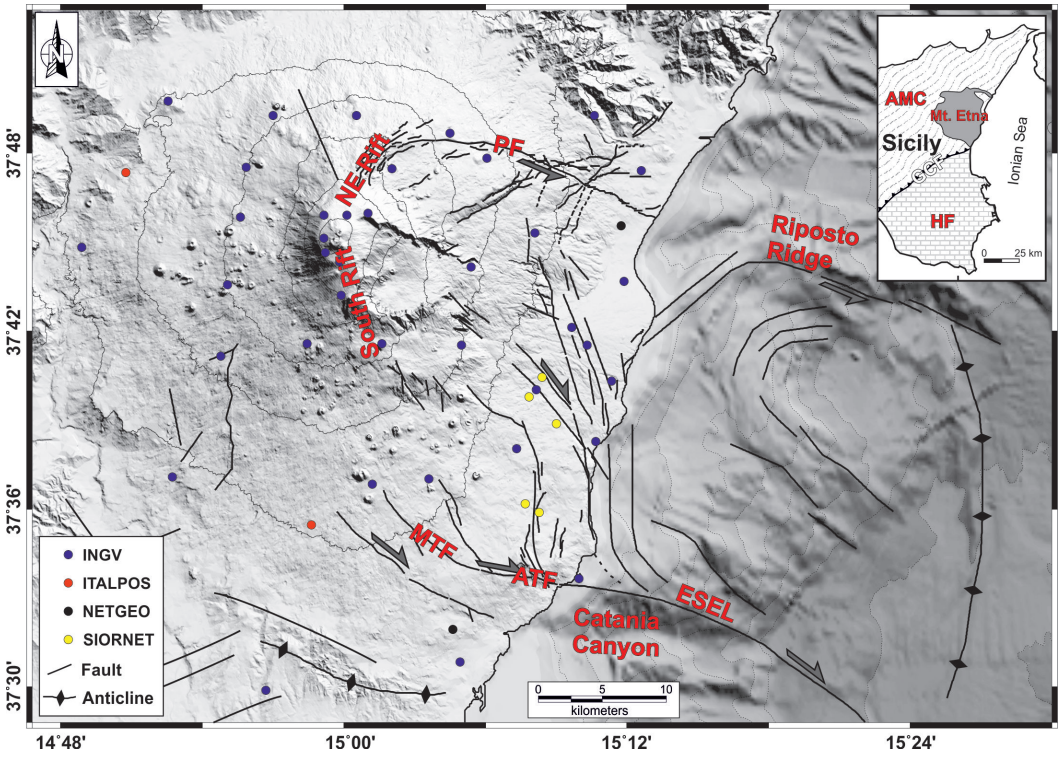


Fig. 1 - Simplified tectonic map of Mt. Etna and its eastern off-shore. Bathymetry is from www.emodnet-bathymetry.eu. cGNSS stations covering Mt. Etna volcano are reported as colored points. Abbreviations are as follows: PF, Pernicana fault; MTF, Mascalucia-Tremestieri fault; ATF, Aci Trezza fault; ESEL, ESE lineament. Inset: sketch map of eastern Sicily; AMC, Apennine-Maghrebian chain; HF, Hyblean Foreland; GCF, Gela-Catania Foredeep.

- SiOrNet, managed by the Geodetic Group of the Geological Survey of Italy-ISPRA and consists of 5 cGNSS stations installed along the SE slope of Mt. Etna (yellow dots in Fig. 1).
- Italpos, managed by Hexagon Geosystems (https://hxgnsmartnet.com/it-it) and developed to support commercial applications, such as mapping and cadastral purposes Only 2 stations are installed on the volcano edifice (red dots in Fig. 1).
- NetGEO, a network developed by Geotop (http://www.netgeo.it) since early 2012 to support commercial applications. Monuments consist on pillars or steel masts, anchored to buildings. Only 2 stations are installed on the volcano edifice (black dots in Fig. 1).

All collected data were processed using the GAMIT/GLOBK software and referred to a local reference frame in order to isolate the Mt. Etna volcanic deformation from the background tectonic pattern. By inspecting the resulting time-series of some selected GNSS stations we detected 11 SSEs with duration grossly ranging from 2 to 67 days. For each recognized SSE, we determine the amount of displacements by averaging site position in the 3 days preceding and following the event. Observed surface deformation for most of the detected slow slip events, concentrates on the south-eastern edge of the unstable flank while the slow slip events involving the north-eastern edge are less frequent. Such a pattern highlights the existence of two distinct families of events, involving two contiguous sectors of the unstable flank, which occasionally slip together in large slow slip events.

The displacement fields were used to constrain isotropic half-space elastic inversion models. To determine the spatial distribution of slip for each SSE, we adopted planar source (divided in 15 by 15 squared patches) with a fixed dip of 10°. Achieved results highlight that, for SSEs occurring more frequently, the slip distribution concentrates with values up to 6 cm on the southeastern sector of the planar source, ~10 km off-shore. Regarding the SSEs involving the north-eastern edge of the unstable flank, the slip distribution on the modelled surface concentrates ~12 km off-shore beneath the Riposto Ridge where a ~16-km-long tectonic lineament with a N102° attitude would represent the off-shore prolongation of the most active splay of the Pernicana fault.

Finally, equivalent seismic moments of slow slip events occurred in the last ten years (corresponding to magnitudes in the range 5.4-5.9) are larger than those associated to seismic events observed in the last 200 years, suggesting that most of the deformation affecting the eastern flank occurs aseismically.

CHEMICAL ANOMALIES IN THE GAS PHASE RELEASED FROM THE SANTA VENERA AL POZZO THERMAL SPRING (MT. ETNA, SICILY, ITALY): POSSIBLE INFLUENCE FROM LOCAL TECTONIC ACTIVITY

F. Sortino[1], S. Giammanco[2], P. Bonfanti[2], C. Bottari[2]

[1] Istituto Nazionale di Geofisica e Vulcanologia, sez. Palermo
[2] Istituto Nazionale di Geofisica e Vulcanologia, Osservatorio Etneo, Catania

Introduction. Among the many thermal manifestations that occur in Sicily (Carapezza *et al.*, 1977; Grassa *et al.*, 2006), that of Santa Venera al Pozzo (hereinafter referred to as SVP) is the only one, in mainland Sicily, that occurs in a volcanic area, namely that of Mt. Etna. In this area, the outcropping volcanic rocks are typically basalts, which constitute the majority of the rocks (Branca *et al.*, 2011). Furthermore, this site is located in an area marked by the crossing of some of the most important and seismically active tectonic faults of southern Italy (Bottari *et al.*, 2020). The name of SVP refers to the site (likely the Greek Akis, later Roman *Acium)*, located on the lower eastern slope of Mt. Etna volcano, next to the harbor of Capo Mulini and to the town of Acireale, in the province of Catania.

Near-continuous monitoring both of gas emissions (CO_2, CH_4 and H_2S) and of water temperature at Santa Venera al Pozzo thermal springs (SE foot of Mt. Etna volcano, Sicily, Italy) was conducted from December 2017 to April 2019, using a novel and cheaper Chromatography Monitoring System (CMS) coupled with a water temperature sensor.

Methods. *Free gases monitoring.* The CMS method used in this study is an automatic chromatographic system designed and built to allow a micro-gas-chromatograph (mod. Agilent490) to analyze natural gases, in our case free gas collected from the well headspace at the top of a water well. The micro-gas-chromatograph (μ-GC) used is set with a user-specified sampling frequency controlled by the instrument management software and it is a system made up of individual modules, each provided with an injector, a detector (Micro-TCD) and a chromatographic column that can be changed according to which gas species has to be determined. For the analysis of natural gases, two modules are normally used: one allows detecting He, Ne, O_2, N_2, CH_4, CO with a molecular sieve column (MS5A), whereas the other allows detection of air, CO_2, H_2S, SO_2, CH_4 and some light hydrocarbons with a Poraplot Q column (PPQ).

The μ-GC is powered with 12V batteries recharged by electric power. The instrument is controlled through the Galaxie software program installed on the embedded computer. This allows the remote control and maintenance of the system via internet connection, using Remote Desktop Protocol software. Computers, μ-GC, routers, batteries and bottle-carrier have been assembled inside a hermetic suitcase. The CMS needs an automatic sampling system that is activated simultaneously with the start of the analytical procedure. Sampling is controlled by the μ-GC, which activates an external pump, just before the start of the analysis, to suck the gas directly from the gas source. Our system is designed in order to act as a complete field laboratory and our data have accuracy similar to that of a laboratory gas-chromatograph, thus better than 2%. Furthermore, repeated calibration of the system during a one-year period using standards showed an instrumental drift close to 2% for all measured parameters.

For the purposes of our work, we set the CMS near the main thermal spring at SVP, pumping the gas out of a 30m-deep small well that was drilled in the 1980s.

Water temperature monitoring. In order to monitor the temporal changes of water temperature in the same borehole where gas measurements were carried out, we installed a temperature sensor with built-in data-logger (Gemini Dataloggers, mod. Tinytag Plus2) into water, close to the top of the borehole (about 2 m below water surface), whose total depth

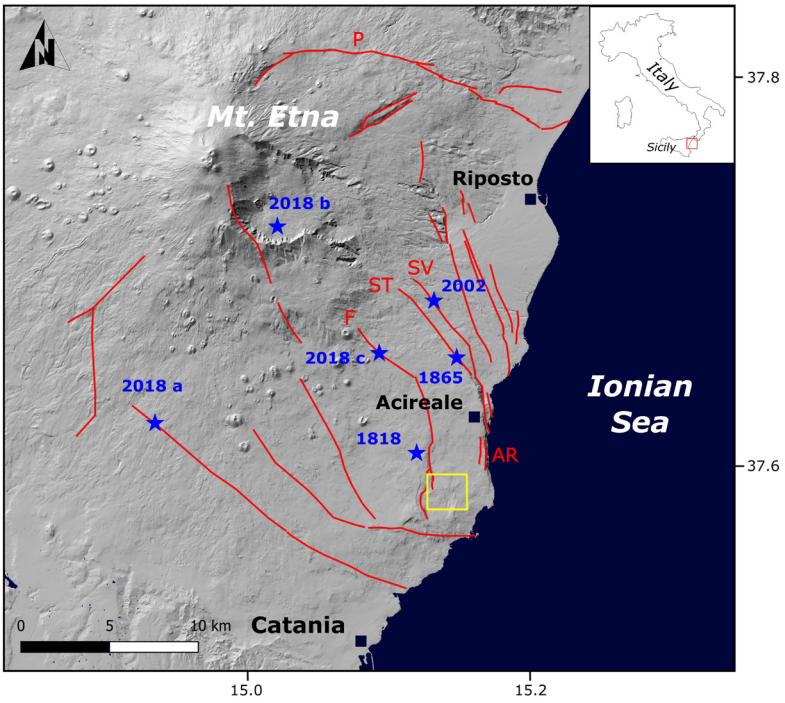


Fig. 1.

is about 40 m. The temperature monitoring started at the same time as the gas monitoring. The acquisition interval of the temperature sensor was set at 15 minutes and the data were stored into the data-logger to be then downloaded every month by connecting the sensor to a laptop computer.

Results and discussion. The results showed methane as predominant gas and temporal changes in gas concentrations that were in part due to daily fluctuations, which caused small amplitude variations, and in part due to non-environmental causes. These latter were correlated with the occurrence of strong earthquakes and slow tectonic events related to magmatic intrusions, but not with input of magmatic gases into the thermal aquifer, given the non-magmatic origin of all monitored gases. Methane spikes were observed during many volcano-tectonic events and call for a deep source of this gas. H_2S was detected only during the

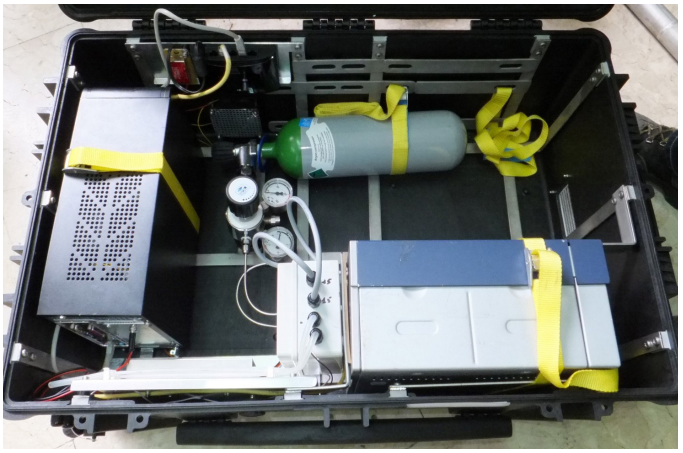


Fig. 2.

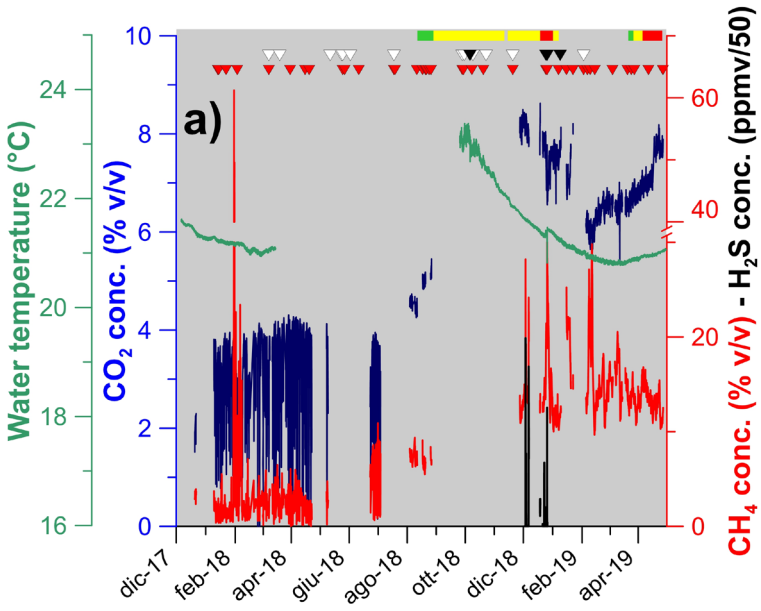


Fig. 3.

strongest local tectonic events, including a Mw 4.9 earthquake, suggesting that this gas has a common origin as CH_4 (i.e., mixing between microbial and thermogenic gas), but it is released only when tectonic stress is applied for sufficiently long periods as to cause H_2S oversaturation in the hydrothermal aquifer. Water temperature decreases were also observed immediately after the two strongest earthquakes in the area, which helped us produce a comprehensive model to explain the observed geochemical variations.

We model the geothermal system feeding the SVP thermal springs as a reservoir of fluids almost saturated in reduced gases (CH_4 and H_2S) and very sensitive to tectonic stresses acting on it. When tectonic forces change the aquifer permeability, the geothermal reservoir becomes saturated in deep gases (CH_4 and H_2S) and therefore it acts as a pressure valve that releases those gases depending on the rate and intensity of crustal stress acting on it. In this case, the relative proportions between CH_4 and H_2S depend on the stress rate and its influence on the different solubility of the two gases in water. Volcanic activity seemingly did not play a direct role in changing the chemical composition of SVP gases, although it likely induced tectonic movements at the scale of the volcano that in turn influenced the chemistry of emitted gases.

Methane is clearly derived from mixing between a thermogenic component and one originated from bacterial reduction of marine sulfates, as shown by its carbon isotopes analysis, thus ruling out any magmatic source of this gas. Slow stress accumulation could be the cause of long-term increases in CH_4 and maybe of CO_2 concentrations in the free gas phase, but not of H_2S because of its fast dissolution/oxidation in the thermal reservoir. Conversely, more impulsive stress changes, possibly associated either with strong earthquakes or with accelerated spreading of Mt. Etna flanks, could induce fast release both of CH_4 and of H_2S, thus revealing the common deep origin of the two gases. Carbon dioxide seems not to be affected in a similar significant way by such type of stress, thus highlighting its different, and shallower, origin. In any case, CH_4 is a proxy for the deep gas component and H_2S is an indicator of very strong and fast stress change, thus being a potential precursor of impending strong release of seismic energy (at least at the SVP site). Actually, anomalous H_2S gas pulses were seemingly correlated with shallow earthquakes that occurred along faults of the southern and southeastern flank of Mt. Etna, which affect in some ways the SVP site (Firetto Carlino *et al.*, 2019), whereas no correlation was found with the earthquakes magnitude.

Short-lived water temperature decreases during the strongest earthquakes of 2018-2019 excluded coseismal impulsive input of hot or cold water into the aquifer, but rather suggested temporary lowering of the water table level or accumulation of cold gas at the top portion of the monitored water well, replacing thermal water and hence decreasing the measured temperature.

We think that the data collected during the present investigation represent a base point for a predictive model of seismic and slow tectonic events based on high-frequency monitoring of geothermal fluid emissions.

References

Bottari C., Giammanco S., Cavallaro D., Sortino F., Scudero S., Amari S., Bonfanti P., Daolio M. and Groppelli G.; 2020: *How to reveal unknown hidden faults and historical earthquake damage applying multidisciplinary methods in archaeological sites: The case of mid- third century CE Mt. Etna earthquake (Eastern Sicily, Italy)*. Tectonophysics 790, 13. DOI 10.1016/j.tecto.2020.228544.

Branca S., Coltelli M., Groppelli G. and Lentini F.; 2011: *Geological map of Etna volcano, 1:50,000 scale*. Ital. J. Geosci., 130, DOI 10.3301/IJG.2011.15.

Carapezza M., Cusimano G., Liguori V., Alaimo R., Dongarrà G. and Hauser S.; 1977: *Nota introduttiva alle sorgenti termali dell'isola di Sicilia*. Boll. Soc. Geol. Ital., 96, 813-836.

Firetto Carlino M., Cavallaro D., Coltelli M., Cocchi L., Zgur F. and Patanè D.; 2019: *Time and space scattered volcanism of Mt. Etna driven by strike-slip tectonics*. Sci. Rep. DOI 10.1038/s41598-019-48550-1

Grassa F., Capasso G., Favara R. and Inguaggiato S.; 2006: Chemical and isotopic composition of waters and dissolved gases in some thermal springs of Sicily and adjacent Volcanic Islands, Italy. Pure Appl. Geophys. 163, 781-807, DOI 10.1007/s00024-006-0043-0.

3D- INFLATING SOURCE IMAGING AND STRESS/STRAIN FIELD ANALYSIS AT CAMPI FLEGREI DURING THE MAJOR UNREST EPISODES

P. Tizzani[1], R. Castaldo[1], G. Solaro[1], S. Pepe[1], A. Pepe[1], V. De Novellis[1,2], A. Barone[1], A. Vitale[1], A. Tramelli[2]

[1] National Research Council of Italy (CNR), Istituto per il Rilevamento Elettromagnetico dell'Ambiente, Napoli, Italy
[2] INGV sede di Napoli Osservatorio Vesuviano, Napoli, Italy

The Campi Flegrei (CF) volcanic area is a collapsed caldera with a well-documented and long history of ground inflation and deflation (bradyseismic activity). In the last 15 ka, ground deformations at long (resurgence) and short timescales have affected the inner caldera region (Cinque *et al.*, 1985, Di vito *et al.*, 1999). The high precision leveling networks integrated with a global positioning system (GPS) monitoring network and satellite data, have detected the unrest episodes that affects the formations of the Neapolitan Yellow Tuff (NYT) caldera. The major uplifts of 1.7 and 1.8 m were estimated at Pozzuoli harbor in 1970-1971 and 1982-1984, respectively (Battaglia *et al.*, 2006; De Natale *et al.*, 2006). After two decades of prevailing subsidence the CF area experienced a continuous slow uplift (with velocity increments in 2000-2001, 2005-2006 and 2012-2013 alternating with stationary deformation) (DelGaudio *et al.*, 2010; Bottiglieri *et al.*, 2010; De Martino *et al.*, 2014). The detected ground deformation pattern relevant to recent uplifts was almost radially symmetric with decreasing deformation velocity values moving from the Pozzuoli harbor towards the borders of the NYT caldera (Iuliano *et al.*, 2015; Trasatti *et al.*, 2015). In this study we analyze the last relevant uplift phenomenon at CF caldera in terms of temporal and spatial variations in the stress/strain field due to the effect of an inflating source. We start by performing a 3D stationary finite element (FE) modeling of integration of SAR multisensors satellite data and GPS mean velocities dataset to retrieve the geometry and location of the deformation source. In addition, we verify the reliability of model results by calculating the total horizontal derivative (THD) of the modeled vertical velocity component; the findings emphasize that the THD maxima overlap with the projection of source boundaries at the surface. After this, we generate a 3D time-dependent FE model, comparing the spatial and temporal distribution of the shear stress and volumetric strain with the seismic swarms beneath the caldera. The achieved results highlight that a low values of shear stress are observed corresponding with the shallow hydrothermal system where low-magnitude earthquakes occur, whereas high values of shear stress are found at depths where high-magnitude earthquakes nucleate. Finally, the volumetric strain analysis highlights that the seismicity occurs mainly at the border between compression and dilatation modeled regions, and some seismic events occur within compression regions (Castaldo *et al.*, 2015).

References

Battaglia M., Troise C., Obrizzo F., Pingue F. and De Natale G.; 2006: *Evidence for fluid migration as the source of deformation at Campi Flegrei caldera (Italy)*. Geophys. Res. Lett., 33, 01307.

Bottiglieri M., Falanga M., Tammaro U., De Martino P., Obrizzo F., Godano C. and Pingue F.; 2010: *Characterization of GPS time series at the Neapolitan volcanic area by statistical analysis*. J. Geophys. Res., 115, B10416.

Castaldo R., Tizzani P. and Solaro, G.; 2021: *Inflating Source Imaging and Stress/Strain Field Analysis at Campi Flegrei Caldera: The 2009–2013 Unrest Episode*. Remote Sens., 13, 2298, DOI 10.3390/rs13122298.

Cinque A., Rolandi G.T. and Zamparelli, V.; 1985: *L'estensione dei depositi marini olocenici nei Campi Flegrei in relazione alla vulcano-tettonica*. Boll. Soc. Geol. Ital., 104, 327-348.

De Martino P., Tammaro U. and Obrizzo F.; 2014: *GPS time series at Campi Flegrei caldera (2000-2013)*. Ann. Geoph., 57, S0213.

De Natale G., Troise C., Pingue F., Mastrolorenzo G., Pappalardo L., Battaglia M. and Boschi E.; 2006: *The Campi Flegrei caldera: Unrest mechanisms and hazard*. Geol. Soc. Lond. Spec. Publ., 269, 25-45.

Del Gaudio C., Aquino I., Ricciardi G.P., Ricco C. and Scandone R.; 2010: *Unrest episodes at Campi Flegrei: A reconstruction of vertical ground movements during 1905-2009*. J. Volc. Geoth. Res., 195, 48-56.

Di Vito M., Isaia R., Orsi G., Southon J., de Vita S., D'Antonio M., Pappalardo L. and Piochi M.; 1999: *Volcanism and deformation since 12,000 years at the Campi Flegrei caldera (Italy)*. J. Volcanol. Geotherm. Res., 91, 221-246.

Iuliano S., Matano F., Caccavale M. and Sacchi M.; 2015: *Annual rates of ground deformation (1993–2010) at Campi Flegrei, Italy, revealed by Persistent Scatterer Pair (PSP)-SAR interferometry*. Int. J. Remote. Sens., 36, 6160-6191.

Trasatti E., Polcari M., Bonafede M. and Stramondo S.; 2015: *Geodetic contraints to the source mechanism of the 2011–2013 unrest at Campi Flegrei (Italy) caldera*. Geoph. Res. Lett. 42, 3847-3854.

2021-2022 HUNGA TONGA-HUNGA HA'APAI ERUPTIONS STUDIED FROM LITHOSPHERE, ATMOSPHERE AND IONOSPHERE

S. D'Arcangelo[1,2], A. Bonforte[1], A. De Santis[1], R. Maugeri[1], L. Perrone[1], M. Soldani[1], F. Brogi[1], M. Calcara[1], S.A. Campuzano[3], G. Cianchini[1], A. Del Corpo[1], D. Di Mauro[1], A. Ippolito[1], S. Lepidi[1], D. Marchetti[4], C. Montagna[1], A. Nardi[1], M. Orlando[1], A. Piscini[1], M. Regi[1], D. Sabbagh[1]

[1] Istituto Nazionale di Geofisica e Vulcanologia (INGV), Rome, Italy
[2] Complutense University (UCM), Madrid, Spain
[3] Instituto de Geociencias IGEO, Madrid, Spain
[4] Jilin University, Changchun, China

On 15 January 2022 we assisted to the main explosion of the last eruption of Hunga Tonga-Hunga Ha'apai volcano. The volcanic event produced a great impact with a plume that reached the stratosphere and the destruction of most parts of the island due to the enormous energy released, estimated around 50 Megatons of TNT. The Lithosphere-Atmosphere-Ionosphere Coupling (LAIC) model helps us to understand how a single event can produce effects in different geolayers of the Earth. Based on this model, we studied the volcanic explosion taken into account the pre- and post-effects induced by pressure and acoustic-gravity waves. For what concerns the lithosphere, we realized a seismological analysis of the volcanic region, in the subduction zone, convergent plate boundary between the Pacific and Indo-Australian plate, using the USGS catalogue and taking into account their estimated magnitude of 5.8 from the seismic waves produced by the volcanic explosion. Then, passing to the atmospheric data, we applied the CAPRI (Climatological Analysis for Seismic Precursors Identification) algorithm to the ECMWF (European Centre for Medium-range Weather Forecasts) Reanalysis v5 (ERA5) of physical variables related to thermal radiative interaction of atmosphere with surface: skin temperature, air temperature, outgoing longwave radiation, cloud cover, relative humidity, ozone and surface pressure. This method allowed us to individuate anomalies in the time series and see their distribution with respect to the volcano position. In the end, for ionospheric analysis we proceeded to search for possible variations in the magnetic field inside the Dobrovolsky area concerned to the equivalent magnitude inherent to all energy released. The magnetic data was retrieved from the Swarm constellation satellites (Alpha, Bravo, Charlie), and from China Seismo-Electromagnetic Satellite (CSES-01). For this last, we investigated a Langmuir Probes (LAP) for plasma measurements. For Swarm magnetic and electron density data, we downloaded Level 1b data, freely available in the ESA Swarm FTP and HTTP Server.

RELATIVE EARTHQUAKE LOCATION AND PRELIMINARY SEISMOLOGICAL ANALYSES ON LOW-ENERGY VOLCANIC SEISMICITY AT CAMPI FLEGREI

S. Danesi[1], N.A. Pino[2], S. Carlino[2], P. Ricciolino[2], D. Delle Donne[2], C. Martino[2]

[1] INGV Sezione di Bologna, Italy
[2] INGV Osservatorio Vesuviano, Napoli, Italy

Introduction. The analysis of the distribution and occurrence of seismic activity in a volcanic environment can provide useful constraints for the study of the evolution of active magmatic and hydrothermal processes.

The present work intends to contribute to the comprehension of the Campi Flegrei caldera (CFc; Naples, Italy) unrest, through (i) the relative relocation of the diffuse seismicity recorded during the 1982-84 unrest and of the seismicity that occurred after 2005, when a new and ongoing unrest started again (ii) the seismological re-analysis of a few significant recent events.

The CFc is one of the most monitored volcanic area in the world, with a multi-parametric network of observing stations operating in the area (Bianco *et al.*, 2022). The key structure of Campi Flegrei caldera is composed by a 1-3 km depth high temperature hydrothermal system with an almost impermeable zone and its base. The temperature gradients measured in the deep borehole, down to a depth of about 3km, are > 150°C/km; a zone of pressurized gas and intrusion of sills at 3-4 km; a long-term magma reservoir at 7-9 km of depth that is persistently supplying CO_2 to the surface (*e.g.*, fumaroles at Solfatara-Pisciarelli) (Zollo *et al.*, 2008; Carlino *et al.*, 2012). An uncertainty still exists in assessing how any of the mentioned components of the magmatic system have contributed to the sequence of unrest starting from 1950.

Tramelli *et al.* (2021) used the Osservatorio Vesuviano (OV) catalogue of absolute seismic locations to infer statistical correlations between the seismic time series and independent geochemical/geophysical observations for the main phases of unrest at CF, in the time span between 2000 and 2020. They remarked a correlation between the cumulative number of events, the observed ground vertical deformation, and the increment of the CO/CO_2 ratio in the hydrothermal system.

It has been proved that fluid pressurization and heating at the CFc hydrothermal system level is the main forcing of the seismicity at 0.5-1 km depth (Chiodini *et al.*, 2021). The discussion on the interaction mechanisms between the rising of fluids from deeper volumes and the seismicity below the hydrothermal system (2-8 km depth) is still open (Buono *et al.*, 2022; Calò and Tramelli, 2018).

In this work we use the arrival times of seismic events from the OV database to perform a double-difference relative relocation of earthquakes for the main episodes of unrest in the 1982-84 years and after 2005. The resulting distribution of events suggests constraints to the preferential directions of rising fluids or, vice versa, structural barriers that can be interpreted jointly in the light of previous works and available tomographic models (De Siena *et al.*, 2017; Calò and Tramelli, 2018, and references therein).

Moreover, we present some preliminary results for the recent seismic events of magnitude Md≥3, and provide an estimate of some significant seismological parameters to add information about the seismic sources and the local surface deformation processes.

Methods and Results. We analyze P-wave and S-wave arrival times from the OV database for the two time frames 1982-1984 and 2005-2022 to perform a relative double-difference location with the HypoDD algorithm (Waldhauser and Ellsworth, 2000; Waldhauser, 2001).

After the pre-processing, 8142 and 5037 linked events were selected in the years 1982-84 and 2005-2022, respectively. For both datasets, we defined a loose inversion scheme and used a 12-layer, one-dimensional velocity model derived from the P-wave velocity structure for the CFc proposed by Vanorio et al. (2005), with Vp/Vs ratio fixed at 1.8. After the hypoDD

relocation, we obtained relative location for 3062 and 2603 events, respectively for the two time spans.

The seismicity distribution of the 1980s is widely scattered throughout the entire volume of the caldera and the average depth of events is placed around 2km, below the hydrothermal system, with a significant percentage of events located 3-4 km deep. The seismicity of the last decades is more concentrated around the volume of Solfatara, with mean depth around 1.3 km. The relative relocation shows some near-vertical fracturing alignments under the Solfatara that bend deep toward east (Bagnoli), suggesting that some of the preferred paths of rising fluids across the hydrothermal system could have an origin at a depth of about 2-4 km (De Siena *et al.*, 2017), where events of more significant magnitude are located (Md>2). Unlike what was observed in the 1980's, recent seismicity is almost completely absent west of the Solfatara and in particular below 1 km depth, suggesting the presence of an impermeable structural barrier, mainly oriented in the EW direction (in accord with Buono *et al.*, 2022, and Calò and Tramelli, 2018).

Since 2005, the OV catalog reports 4 events of magnitude Md>3 located in the CF area, two of them occurring in March 2022 (Table 1). We focused our attention on these events aiming at the quantitative estimation of some seismological parameters derived from waveform and spectral analysis.

Tab. 1 - Ipocentral parameters extracted from the Osservatorio Vesuviano (Istituto Nazionale di Geofisica e Vulcanologia) catalog for the events under study.

Origin Time (UTC)	Lat (°)	Long (°)	Depth (km)	Md
2019/12/06 00:17:23	40.8302	14.1493	2.3	3.1
2020/04/26 02:59:02	40.8292	14.1500	2.6	3.3
2022/03/16 14:14:34	40.8272	14.1402	2.7	3.5
2022/03/29 17:45:32	40.8293	14.1507	2.5	3.6

We determined the focal mechanism solutions with the FPFIT package from the P-wave first motion polarities (Reasenberg and Oppenheimer, 1985). For each event, we used the first motion polarities at seismic stations in a distance of 20 km from the epicenter. The 90% confidence intervals for the mechanism strike, dip, and rake are determined by finding how much each parameter may change without exceeding a critical misfit level between observed and predicted polarities. We used the resulting fault plane solutions to calculate the predicted surface vertical displacement and we compared it with the observed static displacement measured at close seismic stations following the method proposed by Zhu (2003). The permanent vertical displacement at each station is extracted from the zero-frequency seismic signal. It is worth noting that for low-energy events, such as those under attention, the measurement of the static displacement from seismic waveforms is exceptional and very valuable, as it is capable of detecting subsidence/uplift of the order of hundreds or even tens of micron, thus proving to be complementary to GPS data, which hardly can achieve sub-millimeter accuracy.

Moreover, in the near field significant co-seismic rotations can affect the horizontal components of the acceleration in seismic records. For the events under study, we deduced the tilt amplitude from the observed acceleration jumps at near-earthquake stations. The results show a good agreement with the measurements recorded at tiltmeter stations of the CF network and therefore can be useful for the definition of the near-field ground deformation and rotation arising from local earthquakes.

Finally, assuming the observed displacement spectrum formulation according to Boatwright (1980), we deduced the source parameters (corner frequency, source radius, seismic moment)

of the 4 earthquakes from the inversion of the displacement source spectra in the frequency range 0.5–15.0 Hz, to infer an estimate of the radiated seismic energy.

We believe that the seismological analysis of low-energy events in a volcanic environment can therefore be considered a valid support in the active monitoring of the unrest phases, together with observative monitoring systems.

References

Bianco F., Caliro S., Martino P. D., Orazi M., Ricco C., Vilardo G., et al.; 2022: *Campi Flegrei, A Restless Caldera in a Densely Populated Area*. Active Volcanoes World, 219-237. DOI 10.1007/978-3-642-37060-1_8.

Boatwright J.; 1980: *A spectral theory for circular seismic sources; simple estimates of source dimension, dynamic stress drop, and radiated seismic energy*. Bull. Seism. Soc. Am., 70, 1.

Buono G., Paonita A., Pappalardo L., Caliro S., Tramelli A., and Chiodini G.; 2022: *New insights into the recent magma dynamics under Campi Flegrei caldera (Italy) from petrological and geochemical evidence*. J. Geophys. Res. Solid Earth, 127, e2021JB023773, DOI 10.1029/2021JB023773

Calò M. and Tramelli A; 2018: *Anatomy of the Campi Flegrei caldera using Enhanced Seismic Tomography Models*. Sci. Rep., 8, 16254, DOI 10.1038/s41598-018-34456-x.

Carlino, S., Somma, R., Troise, C. and De Natale, G.; 2012: *The geothermal exploration of Campanian volcanoes: Historical review and future development*. Renew. Sust. Energ. Rev., 16(1), 1004-1030.

Chiodini G., Caliro S., Avino R., Bini G., Giudicepietro F., Cesare W. D., Ricciolino P., Aiuppa A., Cardellini C., Petrillo Z., Selva J., Siniscalchi A. and Tripaldi S.; 2021: *Hydrothermal pressure-temperature control on CO2 emissions and seismicity at Campi Flegrei (Italy)*. J. Volcanol. Geoth. Res., 107245, DOI 10.1016/j.jvolgeores.2021.107245.

De Siena L., Chiodini G., Vilardo G., Pezzo E. D., Castellano M., Colombelli S., et al.; 2017: *Source and dynamics of a volcanic caldera unrest: Campi Flegrei*, 1983-84. Sci. Rep. 7, 8099, DOI 10.1038/s41598-017-08192-7.

Reasenberg P. and Oppenheimer O.; 1985: *FPFIT, FPPLOT and FPPAGE; Fortran computer programs for calculating and displaying earthquake fault-plane solutions*, Open-File Report 85-739, DOI 10.3133/ofr85739

Tramelli A., Godano C., Ricciolino P., Giudicepietro F., Caliro S., Orazi M., De Martino P. and Chiodini G.; 2021: *Statistics of seismicity to investigate the Campi Flegrei caldera unrest*. Sci. Rep. 11, DOI 10.1038/s41598-021-86506-6.

Vanorio T., Virieux J., Capuano P., and Russo G.; 2005: *Three-dimensional seismic tomography from P wave and S wave microearthquake travel times and rock physics characterization of the Campi Flegrei Caldera*. J. Geophys. Res. Solid Earth 1978 2012 110. doi:10.1029/2004jb003102.

Waldhauser F. and Ellsworth W.L.; 2000: *A double-difference earthquake location algorithm: Method and application to the northern Hayward fault*. Bull. Seism. Soc. Am., 90, 1353-1368.

Waldhauser F.; 2001: *HypoDD: A computer program to compute double-difference earthquake locations*. USGS Open File Rep., 01-113.

Zhu, L.; 2003: *Recovering permanent displacements from seismic records of the June 9, 1994 Bolivia deep earthquake*. Geophys. Res. Lett. 30, 14, DOI 10.1029/2003gl017302.

Zollo A., Maercklin N., Vassallo M., Dello Iacono D., Virieux J. and Gasparini P.; 2008: *Seismic reflections reveal a massive melt layer feeding Campi Flegrei caldera*. Geophys. Res. Lett., 35, L12306, DOI 10.1029/ 2008GL034242.

FIRST STEPS TOWARDS THE UPPER CRUSTAL STRUCTURE INVESTIGATION IN THE AREA OF MEFITE D'ANSANTO (ITALY) BY USING TELESEISMIC EVENTS

G. Milano[1], A. Gervasi[2], S. Morabito[1], P. Cusano[1], P. Del Gaudio[2], D. Galluzzo[1], G. Gaudiosi[1], M. La Rocca[3], L. Nardone[1], S. Petrosino[1], L. Zuccarello[4]

[1] INGV- Sezione di Napoli 'Osservatorio Vesuviano', Naples, Italy
[2] INGV- Osservatorio Nazionale Terremoti, Rende (CS), Italy
[3] University of Calabria, Rende (CS), Italy
[4] INGV- Sezione di Pisa, Pisa, Italy

Further. "The role of FlUids in the pReparaTory pHase of EaRthquakes in Southern Apennines", is an INGV Department Strategic Project devoted to defining the role of fluids in earthquake genesis (https://progetti.ingv.it/it/progetti-dipartimentali/terremoti/further). One of the target areas of the multidisciplinary study is Mefite d'Ansanto, which is the largest area of non-volcanic low temperature CO_2 emission field on the Earth (Fig. 1). In particular, the Work Package 1.4 is dedicated to the application of methodologies in time and frequency domains, aimed to intercept eventual variations in fluid behavior before or in correspondence of local and regional earthquakes, using recordings from the INGV National Seismic Network and local networks. For this purpose, temporary acquisition surveys have been locally deployed (Cusano *et al.*, 2021).

In order to define how large and deep the area of diffuse CO_2 degassing is, we investigate the upper crustal structure utilizing teleseismic events. As well known in literature, among the techniques applied to investigate the crustal structure of an area, the analysis of teleseismic events provides information about the depth and dip of the principal crustal discontinuities. The methods are based on the identification of P-to-P and S-to-P converted phases generated by the interaction of an incident P or S wave with velocity discontinuities beneath the

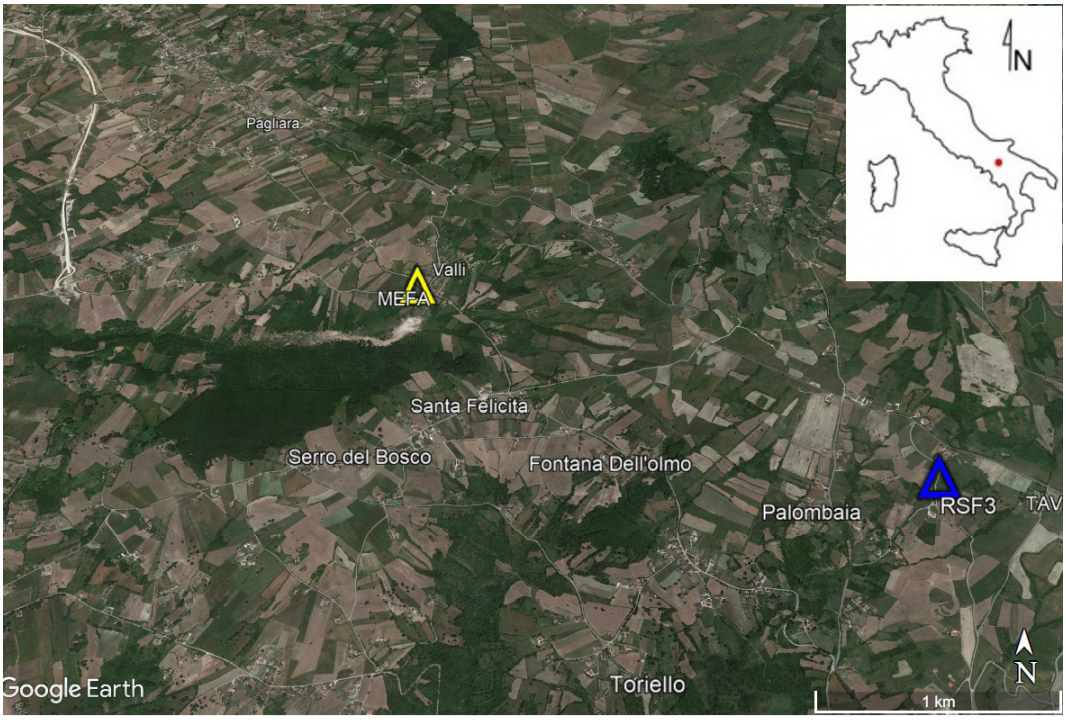


Fig. 1 - Map showing the Mefite d'Ansanto area (up-left) and the location of MEFA (yellow triangle) and RSF3 (blue triangle) stations (Map retrieved from GoogleEarthPro in 2022). In the up-right corner the Mefite position on the Italian territory is reported.

receiving station. Several techniques have been developed in order to isolate the effects of the local structure beneath the observation point from others (e.g. source function and path effects) and to translate this information into models for the crust. Some methods involve the modelling of the crustal structure beneath the observation point using synthetic seismograms for P and SV waves. These techniques imply the comparison between synthetics and observed data to obtain the best fit and can be applied to deep or intermediate earthquakes, since the incident time function of such events can be often modelled as a single unidirectional pulse. If data of deep or intermediate events are not available, before applying synthetic seismograms calculation, the observed data must be equalized to compensate for different source time functions. A method to equalize the data is the receiver functions technique. This technique, first proposed by Langston (1979), allows, removing source and path-effects, to identify converted and reverberated phases in the crust generated by the interaction of a teleseismic P wave with a discontinuity surface in the crust. Precise information on the deep crustal and upper mantle structure beneath a single three-component broadband seismograph can be obtained basing on the assumption that the vertical component of a teleseismic event contains undesired source and path effects and is not significantly contaminated by the near receiver structure.

Here we show a preliminary data analyses performed on teleseismic events recorded at MEFA station, a stand-alone seismic station equipped with a Guralp CMG40T 60s broadband sensor installed close to the Mefite emission vent on November 20, 2020, and at permanent seismic stations of the National and Irpinia Seismic Networks, located within 30 km away from Mefite vent and equipped with broadband sensors (Fig. 1).

As a first step we considered the telesismic events with M > 6.5 recorded at MEFA and RSF3 station. The latter is part of the Irpina Network and it is located about 3.6 km from MEFA (Figure 1). After visual inspection of the seismograms in the time domain, those showing strongly impulsive onset were selected. Considering that the seismic stations are equipped with broadband sensors having different frequency response, the signals of each station have been deconvolved for their own frequency response to perform a first equalization of the data. Figure 2 shows an example of telesismic event recorded at MEFA and RSF3 stations. Although this event is not characterized by strongly impulsive onset, the similarity between the components is very evident.

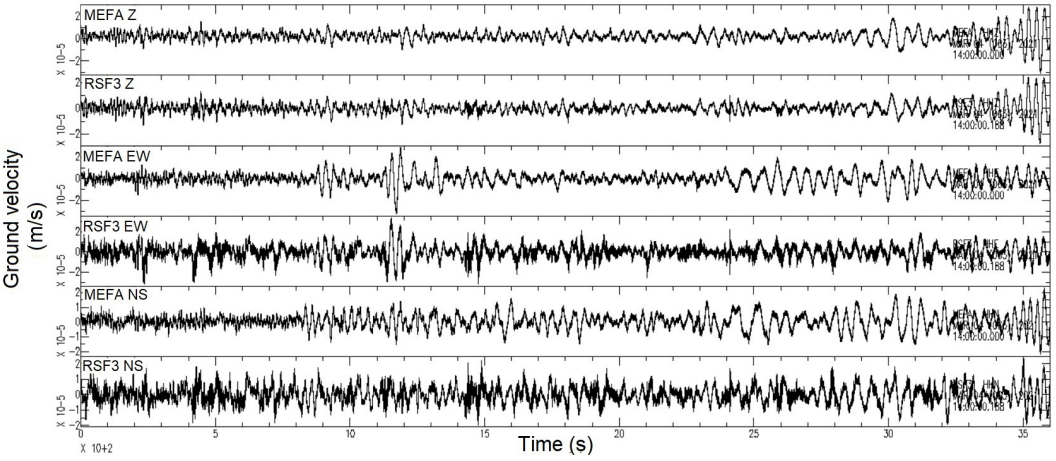


Fig. 2 - Example of teleseismic event recorder at MEFA and RSF3 stations. The seismograms are related to the event occurred in North Island, New Zealand: origin time 2020/03/04 13:27, hypocenter coordinates -37.0270° N, 179.4200° E, h=14 km b.s.l., Mw = 7.3. The seismograms are equalized taking into account that the sensors have different frequency response. The station name and the component are indicated for each trace.

Since P-to-S converted phases are generally more evident in the radial and tangential components of a record, the horizontal components of each selected event have been rotated versus back-azimuth. After applying a zero-phaseshift 5 Hz low-pass-filter to exclude undesired high frequency noise and to better evidence the direct P-wave, a first analysis of the seismograms in the time domain has been performed to identify, if any, P-to-S converted phases (Milano *et al.*, 2001) before applying the receiver functions technique.

The first results show a likelihood between the seismograms of MEFA and RSF3 while some discrepancies can be observed from the comparison between MEFA and the stations more than 5 km away from the latter. These results, even if preliminary, bode well for obtaining information on the identification of any discontinuities in the first 10 km of the crust.

References

Cusano P., Del Gaudio P., Galluzzo D., Gaudiosi G., Gervasi A., La Rocca M., Martino C., Milano G., Nardone L., Petrosino S., Torello V., Zuccarello L., Di Luccio F.; 2021: *Analysis of background seismicity recorded at Mefite d'Ansato CO2 emission field in the framework of FURTHER project: first results.* EGU General Assembly 2021, https://doi.org/10.5194/egusphere-egu21-10625

Langston C.A.; 1979: *Structure under Mount Rainier, Washington, inferred from teleseismic body waves.* J. Geoph. Res. V. 84, pp 4749-4762.

Milano G., Bianco F., Vilardo G.; 2001: *Evidences of P-S conversions beneath the Vesuvius volcanic area (South Italy) from teleseismic data.* Volcanology and Seismology, 2001 Volume 5, 73-80.

MAGNETIC INVESTIGATION AT VULCANO ISLAND: PRELIMINARY RESULTS FROM A MULTIDISCIPLINARY GEOPHYSICAL SURVEY

S. Scudero[1], S. Bongiovanni[2], A. D'Alessandro[1], A. Figlioli[2], R. Martorana[2], S. Speciale[1], A. Pisciotta[3], G. Vitale[1]

[1] Istituto Nazionale di Geofisica e Vulcanologia, Osservatorio Nazionale Terremoti, Rome, Italy
[2] Università di Palermo, Dipartimento di Scienze della Terra e del Mare, Palermo, Italy
[3] Istituto Nazionale di Geofisica e Vulcanologia, Sezione di Palermo, Palermo, Italy

Introduction. From the end of June 2021, changes in the monitored parameters (temperature, gas emission, seismicity, ground deformation) clearly indicate the beginning of a phase of unrest at Vulcano Island (Aeolian Islands, Italy). The anomalies consist in high temperatures of the fumaroles, increase of gas emissions from fumaroles and soils (both CO_2 and SO_2), ground deformation, and increased seismicity (Inguaggiato *et al.*, 2022). In the last decades, this volcano experienced frequent crises: 1978-1980, 1988-1991, 1996, 2004-2007, 2009-2010 (Inguaggiato *et al.*, 2022), while the last eruption occurred in 1888-1890. For its activity, Vulcano represents the source of many potentially interconnected hazards which determine a potentially high risk. (Hazard Selva *et al.*, 2020).

The Vulcano island has been widely investigated to understand its volcanic evolution (Gioncada *et al.*, 1998; Gioncada *et al.*, 2003; De Astis; 2013; Nicotra *et al.*, 2018), the dynamics affecting the plumbing and the hydrothermal systems (Alparone *et al.*, 2010; Cannata *et al.*, 2012; Alparone *et al.*, 2019), and the structure of the of the active "La Fossa" cone (Revil *et al.*, 2008; Barde-Cabusson *et al.*, 2009; Revil *et al.*, 2010). Many studies reveal a complex evolution in which the regional tectonic may play a major role. The occurrence volcanism in the southern Tyrrhenian is generally linked to large scale geodynamic processes, but, the volcanism in the southern sector of Aeolian Islands, where Volcano is located, would be also controlled by a regional-scale, lithospheric NNW-SSE trending right-lateral strike-slip fault system. Even though several evidence suggest its occurrence (Mazzuoli *et al.*, 1995; Ventura *et al.*, 1999, Mattia *et al.*, 2008; Barreca *et al.*, 2014; Cintorrino *et al.*, 2019), the field expression of this system is poorly constrained.

Bruno and Castiello (2009) revealed some faults affecting the SW base of the active cone by means of high-resolution seismic investigations. To better understand these features and

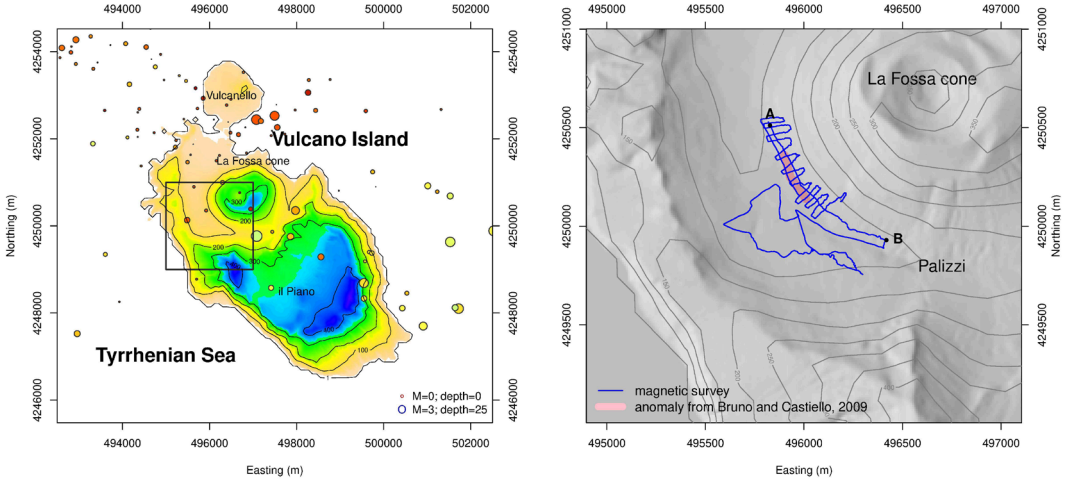


Fig. 1 - Left: relief map of Vulcano Island and the seismicity recorded in the period from January 2020 to April 2022 (Barberi *et al.*, 2020). Right: detail of the study area in the lower southwestern flank of La Fossa cone. The letters A and B indicate the tips of the section shown in Fig. 3.

provide a possible link to the larger scale tectonic framework, a campaign of multi-technique geophysical surveys has been carried out in April 2022. It involved electrical resistivity measurements, thermography, gravimetric and magnetic surveys; this paper presents the preliminary results of the magnetic survey (Fig. 1). In fact, magnetometry has been widely used to detect faults, or geological discontinuity in general, in volcanic contexts and at various scales (Bottari *et al.*, 2018, Napoli *et al.*, 2020).

Data and method. The magnetic survey was performed with the device G-858G produced by Geometrics Inc. The magnetometer was set in gradiometric configuration with the two sensors 2.0 m apart. The magnetometer is equipped with a GPS that provide the position and the time for each magnetic measure, taken every 0.5 s. The survey consists of more than 14,000 measurements taken along different tracks of total length equal to 6.6 km; the average spacing between two consecutive measures is about 0.5 m.

The data processing consists in the spikes removal and in a running average over 40 samples acting as a low-pass filter. The filter attenuates, the shorter wavelength component related to the shallower anomalies, enhancing the components with larger wavelength.

The investigated area extends at the southwestern base of the cone named “La Fossa” which is the active crater located within the caldera of Vulcano Island. In particular, the survey was focused in the area where the seismic investigation by Bruno and Castiello (2009) shows a velocity anomaly interpreted as a possible fault zone. In this area we performed back-and-forward profiles. Data, reduced with respect the International Geomagnetic Reference Field (IGRF), have been interpolated by kriging on a 5x5 m grid.

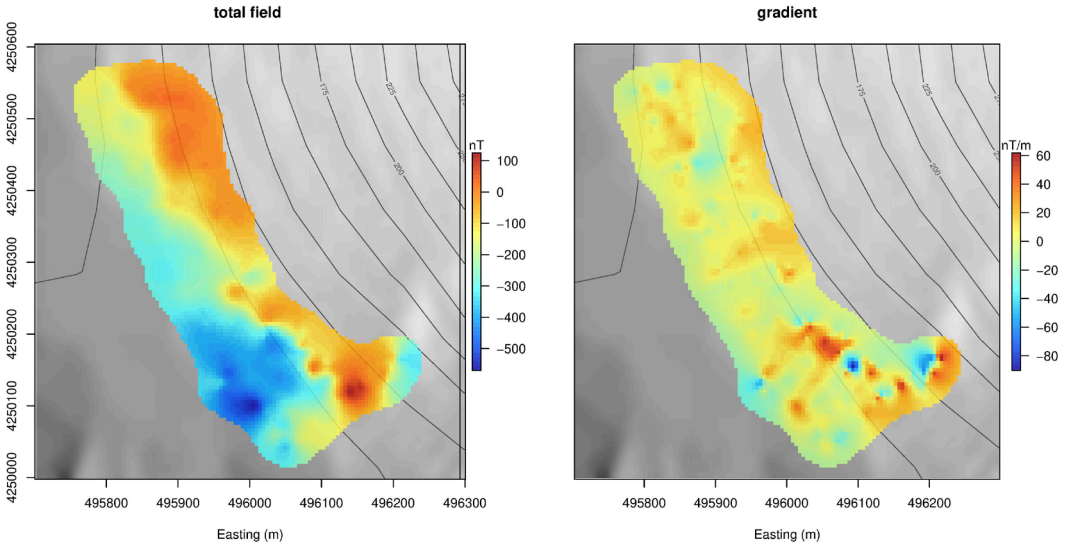


Fig. 2 - Maps of the total magnetic anomaly field (left) and of the vertical gradient (right). Elevation lines are 25 m spaced.

Results. The total-field magnetic anomaly map and the vertical gradient map are presented in Fig. 2. The total field is generally characterized by negative values. This is in agreement with the observations from other magnetic surveys (airborne, shipborne or ground-based) carried out at Vulcano Island (Supper *et al.*, 2004; De Ritis *et al.*, 2005; Okuma *et al.*, 2006; Blanco-Montenegro *et al.*, 2007; Napoli and Currenti, 2016). Those extend over the whole island but are at lower resolution. The total magnetic field shows an almost regular increase in the values moving upslope towards the cone (i.e. SW-NE direction). This can be interpreted with the

gradual thinning of the loose deposit at the foot of the slope, which completely disappears moving upwards (see elevation lines in the background). Moving southwards, the negative values reach the minimum roughly in correspondence of the anomaly suggested by Bruno and Castiello (2009) (Fig. 1). This trend is clearly recognizable in the section shown in Fig. 3 (see Fig.1 for the location) which extends even more southeastwards with respect the area displayed in Fig. 2. More to the south, the value of the total magnetic field increases and becomes positive. Again, this is in agreement with the other magnetic investigations previously mentioned.

The map of the vertical gradient (Fig. 2) shows several small-scale peaks (either negative and positive), with wavelengths in the order of some tens of meters. They are especially concentrated in the southernmost part of the surveyed area and recognizable also in the section (Fig. 3). They appear as bipolar anomalies, with adjacent positive and negative peaks and could be the result of some near-surface features.

The results coming from the other geophysical technique will represent the base for the modelling of the magnetic data. Moreover, the integration of all the available information will provide a robust interpretation of this key area of Vulcano Island.

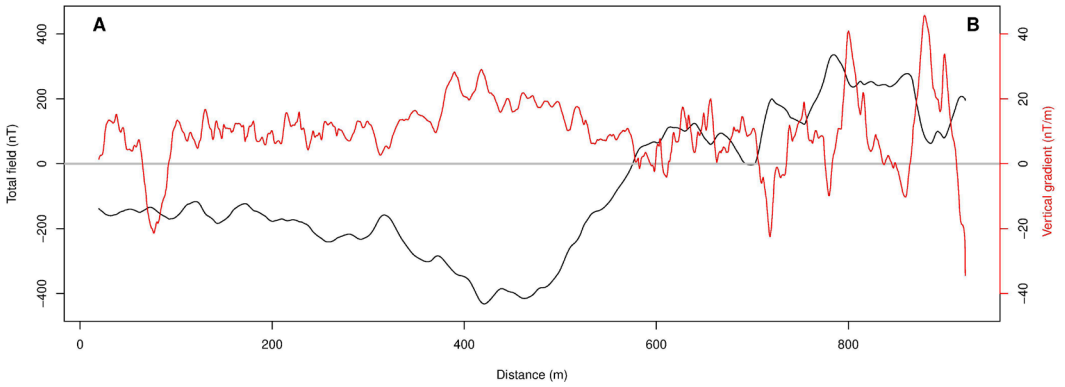


Fig. 3 - Filtered magnetic profile (40 samples running average) showing both the total field and the vertical gradient. See Fig. 1 for the location.

Acknowledgements. The authors thank Vincenzo Sapia (Istituto Nazionale di Geofisica e Vulcanologia, Sezione Roma2) who provided the magnetometer and supported the field activities.

References

Alparone S., Bonforte A., Gambino S., Guglielmino F., Obrizzo F. and Velardita R.; 2019: *Dynamics of Vulcano Island (Tyrrhenian Sea, Italy) investigated by long-term (40 years) geophysical data*. Earth-Sci. Rev., 190, 521-535.

Alparone S., Cannata A., Gambino S., Gresta S., Milluzzo, V. and Montalto P.; 2010: *Time-space variation of volcano-seismic events at La Fossa (Vulcano, Aeolian Islands, Italy): new insights into seismic sources in a hydrothermal system.* Bull. Volcanol., 72(7), 803-816.

Barberi F., Gandino A., Gioncada A., La Torre P., Sbrana A. and Zenucchini C.; 1994: *The deep structure of the Eolian arc (Filicudi-Panarea-Vulcano sector) in light of gravity, magnetic and volcanological data*. J. Volcanol. Geotherm. Res., 61(3-4), 189-206.

Barreca G., Bruno V., Cultrera F., Mattia M., Monaco C. and Scarfi, L.; 2014: *New insights in the geodynamics of the Lipari–Vulcano area (Aeolian Archipelago, southern Italy) from geological, geodetic and seismological data*. Journal Geodyn., 82, 150-167.

Barde-Cabusson S., Finizola A., Revil A., Ricci T., Piscitelli S., Rizzo E., Angeletti B., Balasco M., Bennati L., Byrdina S., Carzaniga N., Crespy A., Di Gangi F., Morin J., Perrone A., Rossi M., Roulleau E., Suski B. and Villeneuve N.; 2009: *New geological insights and structural control on fluid circulation in La Fossa cone (Vulcano, Aeolian Islands, Italy)*. J. Volcanol. Geotherm. Res., 185(3), 231-245.

Blanco-Montenegro I., de Ritis R. and Chiappini M.; 2007: *Imaging and modelling the subsurface structure of volcanic calderaswith high-resolution aeromagnetic data at Vulcano (Aeolian Islands, Italy).* Bull. Volcanol., 69, 643-659, DOI 10.1007/ s00445-006-0100-7.

Bottari, C., Martorana R., Scusero S., Capizzi P., Cavallaro D., Pisciotta A., D'Alessandro A., Coltelli M and Lodato L.; 2018: *Coseismic damage at an archaeological site in Sicily, Italy: evidence of roman age earthquake surface faulting*. Surv. Geophys., 39, 1263-1284.

Bruno P. P. G. and Castiello A.; 2009: *High-resolution onshore seismic imaging of complex volcanic structures: An example from Vulcano Island, Italy*. J. Geophys. Res., 114, B12303, DOI 10.1029/2008JB005998.

Cannata A., Diliberto I. S., Alparone S., Gambino S., Gresta S., Liotta M., Madonia P., Milluzzo V., Aliotta M. and Montalto P.; 2012: *Multiparametric approach in investigating volcano-hydrothermal systems: the case study of Vulcano (Aeolian Islands, Italy)*. Pure Appl. Geophys., 169(1), 167-182, DOI 10.1007/s00024-011-0297-z.

Cintorrino A. A., Palano M. and Viccaro M.; 2019: *Magmatic and tectonic sources at Vulcano (Aeolian Islands, Southern Italy): A geodetic model based on two decades of GPS observations*. J. Volcanol. Geotherm. Res., 388, DOI 10.1016/j.jvolgeores.2019.10

De Astis G., Lucchi F., Dellino P., La Volpe L., Tranne C. A., Frezzotti M. L., and Peccerillo A.; 2013: *Geology, volcanic history and petrology of Vulcano (central Aeolian archipelago)*. Geol. Soc., London, Memoirs, 37(1), 281-349.

De Ritis R., Blanco-Montenegro I., Ventura G. and Chiappini M.; 2005: *Aeromagnetic data provide new insights on the tectonics and volcanism of Vulcano island and offshore areas (southern Tyrrhenian Sea, Italy)*. Geophys. Res. Lett., 32 (L15305), DOI 10.1029/2005GL023465.

Gioncada A., Clocchiatti R., Sbrana A., Bottazzi P., Massare D. and Ottolini L.; 1998: *A study of melt inclusions at Vulcano (Aeolian Islands, Italy): insights on the primitive magmas and on the volcanic feeding system*. Bull. Volcanol., 60(4), 286-306.

Gioncada A., Mazzuoli R., Bisson M. and Pareschi, M. T.; 2003: *Petrology of volcanic products younger than 42 ka on the Lipari–Vulcano complex (Aeolian Islands, Italy): an example of volcanism controlled by tectonics*. J. Volcanol. Geotherm. Res., 122(3-4), 191-220.

Inguaggiato S., Vita F., Diliberto I. S., Mazot A., Calderone L., Mastrolia A. and Corrao M.; 2022: *The Extensive Parameters as a Tool to Monitoring the Volcanic Activity: The Case Study of Vulcano Island (Italy)*. Remote Sensing, 14(5), 1283.

Mattia M., Palano M., Bruno V., Cannavo F., Bonaccorso A. and Gresta S.; 2008: *Tectonic features of the Lipari–Vulcano complex (Aeolian archipelago, Italy) from 10 years (1996-2006) of GPS data*. Terra Nova, 20(5), 370-377.

Mazzuoli R., Tortorici L. and Ventura, G.; 1995: *Oblique rifting in Salina, Lipari and Vulcano islands (Aeolian islands, southern Italy).* Terra Nova, 7(4), 444-452.

Napoli R. and Currenti G.; 2016: *Reconstructing the Vulcano Island evolution from 3D modeling of magnetic signatures*. J. Volcanol. Geotherm. Res., 320, 40-49.

Napoli R., Currenti G. and Sicali A.; 2021: *Magnetic signatures of subsurface faults on the northern upper flank of Mt Etna (Italy).* Ann. Geophys., 64(1), PE108-PE108.

Nicotra E., Giuffrida M., Viccaro M., Donato P., D'Oriano C., Paonita A. and De Rosa R.; 2018: *Timescales of pre-eruptive magmatic processes at Vulcano (Aeolian Islands, Italy) during the last 1000 years*. Lithos, 316, 347-365.

Okuma S., Nakatsuka T., Supper R. and Komazawa M; 2006: *High-resolution aeromagnetic anomaly map of the Vulcano-Lipari volcanic complex, Aeolian Islands, Italy*. Bull. Geol. Surv. Japan, 57, 177-190.

Revil A., Johnson T. C. and Finizola A.; 2010: *Three-dimensional resistivity tomography of Vulcan's forge, Vulcano Island, southern Italy*. Geophys. Res. Lett., 37(15), L15308, DOI 10.1029/2010GL043983.

Revil A., Finizola A., Piscitelli S., Rizzo E., Ricci T., Crespy A., Angeletti B., Balasco M., Barde-Cabusson S., Bennati L., Boleve A., Byrdina S., Carzaniga N., Di Gangi F., Morin Julie, Perrone A., Rossi M., Roulleau E. and Suski B.; 2008: *Inner structure of La Fossa di Vulcano (Vulcano Island, southern Tyrrhenian Sea, Italy) revealed by high-resolution electric resistivity tomography coupled with self-potential, temperature, and CO2 diffuse degassing measurements*. J. Geophys. Res: Solid Earth, 113(B7), B07207, DOI 10.1029/2007JB005394..

Selva J., Bonadonna C., Branca S., De Astis G., Gambino S., Paonita A., Pistolesi M., Ricci T., Sulpizio R., Tibaldi A. and Ricciardi A.; 2020: *Multiple hazards and paths to eruptions: a review of the volcanic system of Vulcano (Aeolian Islands, Italy)*. Earth-Sci. Rev., 207, 103186.

Supper R., De Ritis R., Motschka K. and Chiappini M.; 2004: *Aeromagnetic anomaly images of Vulcano and southern Lipari Islands (Aeolian archipelago, Italy).* Ann. Geophys., 47(6).

Ventura G., Vilardo G., Milano G. and Pino N. A.; 1999: *Relationships among crustal structure, volcanism and strike–slip tectonics in the Lipari–Vulcano volcanic complex (Aeolian Islands, Southern Tyrrhenian Sea, Italy).* Phys. Earth Planet. Inter., 116(1-4), 31-52.

FORECASTING SOIL CO2 FLUX AT MT. ETNA VOLCANO

S. Scudero, A. D'Alessandro

Istituto Nazionale di Geofisica e Vulcanologia, Osservatorio Nazionale Terremoti, Rome, Italy

Introduction. Procedures for forecasting time series are various and the choice of the most suitable technique depends mainly on the type of data. In this contribution we deal with a very peculiar type of data. The monitoring of CO_2 flux may provide information about the magmatic processes and represent useful eruption predictors (Aiuppa *et al.*, 2007). For this reason, also the monitoring of diffuse soil CO_2 has become very important in recent years. At Mt. Etna Volcano (Sicily, Italy) a network of 14 sites records hourly measures of soil CO_2 (Gurrieri *et al.*, 2008; Liuzzo *et al.*, 2013); the data coming from all the sites, after a processing, are summarized to provide a unique, combined signal which is used as one of the indicators of the state of activity of the surveillance of the volcano. The procedure leading to the unique CO_2 signal consists in four steps: i) reduction from hourly to daily time series; ii) filtering of the periodic components at frequency > 7 day^{-1} after FFT analysis; iii) multiple linear regression and FFT filtering the atmospheric influences (between 300 and 400 day^{-1}); iv) normalization of each CO_2 flux series in the range 0-1 as preparatory step to obtain a unified signal of CO_2 flux from all the monitoring stations. Such procedure was, proposed by Liuzzo *et al.*, (2013), then further developed and validated during several eruptive episodes (Cannata *et al.,* 2015; Gurrieri *et al.*, 2021; Paonita *et al.*, 2021; Scudero *et al.*, 2022). In this paper we tested the short-term performance forecast of this unified CO_2 signal.

Method. Aiming at forecasting this unified signal we should keep in mind how it was previously processed and filtered. It can be considered as a univariate time series, and differently from the methods for multivariate series which are based on correlation, the univariate forecast relies on time-dependence.

A time series can be considered as the combination of an auto-correlated part related to the measure of the physical phenomenon, and stochastic/random part. It can be decomposed as the sum of a mean value and an error which cannot be explained by the mean. The former has been estimated by means of a moving window; in particular, we adopted a linearly weighted moving average in which the weight of each value within the window decreases in arithmetical progression moving away from the value to predict. The latter value, considering that data have been already filtered to remove the seasonal components, can be well approximated by a withe noise (WN). WN is characterized by equal intensity across all allowable frequencies; it has been simulated with an ARIMA(*p,d,q*) model in which all the three components (i.e. the autoregressive order *p*, the order of integration *d*, and the moving average order *q*) are equal to zero. The standard deviation of the WN over a given window width provide the stochastic component of the signal.

The appropriate values for the width of the windows (either for the mean and for the stochastic component) have been chosen after performing some tests. In particular, we performed some forecast simulations on portions of known signals and compared the density estimates of each time series before and after the forecasts. The comparison has been performed by means of a bootstrap hypothesis test of equality of the pairs of density estimations. The selected windows' widths, which minimize the differences between the densities, result proportional to the chosen steps of the forecast, namely 1, 5 and 10 days (Tab. 1). As the error estimation, the root mean square error (RMSE) and the determination coefficient (R^2) have been calculated. RMSE is the normalised mean of the squared difference between the observations and the predicted values and R^2 has been calculated with respect to the identity line. Moreover, we tested whether the regression lines between forecasted values and observation are significantly different from the identity line, since to obtain exactly the

identity line, the estimated regression coefficients, slope and intercept, must equal to 1 and 0, respectively. For this purpose, the t-statistic is used to check the null hypothesis that slopes of the linear models are equal to 1 and intercept are equal to 0. The probability values of the test are reported in Tab. 1.

Tab. 1 - Values of width of windows for the average component (*m*) and for the stochastic components (*n*) used for the estimates of the forecasts for the single time series and for the global signal. All the indicators described in the text are also reported.

			Time series				Combined global signal			
	m	***n***	**RMSE**	**R_2**	***pval*$_{slo}$**	***pval*$_{int}$**	**RMSE**	**R_2**	***pval*$_{slo}$**	***pval*$_{int}$**
1-day	2	1.2	0.072	0.831	0.022	0.008	0.143	0.615	0.052	0.107
5-days	6	1.2	0.077	0.806	0.046	0.104	0.206	0.105	8.1e-16	3.4e-15
10-days	11	1.2	0.082	0.786	0.371	0.793	0.171	0.424	3.7e-11	1.5e-8

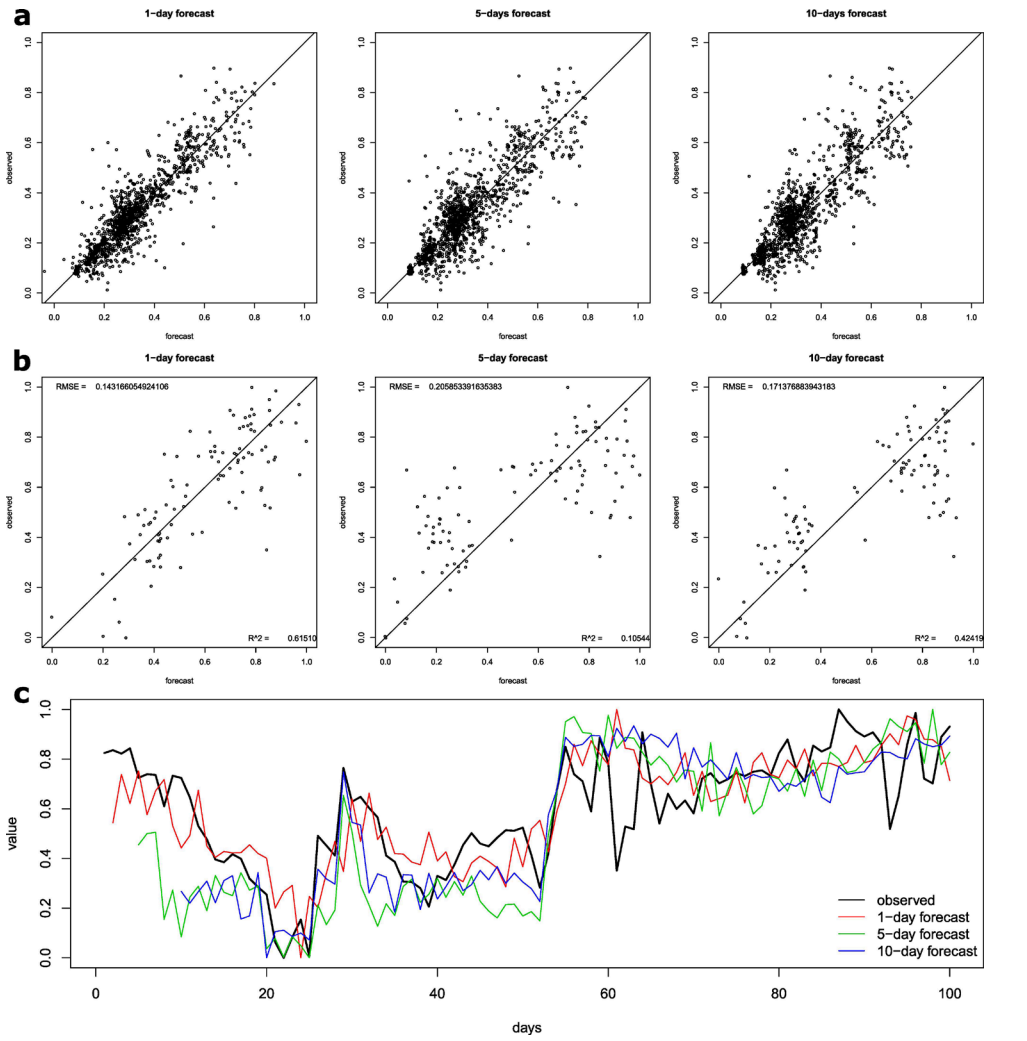


Fig. 1 - a) Forecast at 1-, 5-, and 10-step plotted against observed measurements for 100 predictions at the 14 series. b) Forecast of the global CO2 signal (calculated after Liuzzo *et al.*, 2013) at 1-, 5-, and 10-step plotted against observations for 100 predictions. c) Portion of the global signal and forecasts at 1-, 5-, and 10-step.

Results. The results of 100 rolling forecasts calculated simultaneously for the 14 series at 1-, 5-, and 10-step are reported in Fig.1a in comparison with the corresponding observations. The values of RMSE increase at increasing the step of the forecast while R^2 values decreases, indicating a progressive decreasing reliability of the forecast. However, the values of the t-test performed on the slope and intercept indicate a likely significant ($0.05 < p\text{-value} < 0.1$) difference from the identity for the 1- and 5- day forecast.

We are mainly interested to understand the capability to predict the global CO_2 signal for the whole network. The forecast from the single series have been combined following the procedure of Liuzzo *et al.*, (2013) and compared with the observation processed likewise (Fig. 1b). While the RMSE and R^2 values are respectively higher and lower, if compared with the single time series forecast, the t-test on the indicates that the adopted procedure is able to provide sufficiently accurate 1-day forecasts. However, the longer the span, the less reliable become forecasts, even though the first-order features of the signal are well approximated (Fig. 1c).

The analysis of the residuals is useful to check whether the predictions have adequately captured the information in the data. A good forecasting method will yield residuals with zero mean and normally distributed. The normal Q-Q residuals plots of the forecast of the single time series indicate a clear departure from the normality which is variously marked depending among the various series (Fig. 2). The observed departure from normality is similar for the three forecasts and could suggest that some information is left over when it should be accounted for in the prediction. Conversely, the normal Q-Q residuals plots of the combined signal shows a good fit of the normality assumption, especially for the 1-step forecast, while slight departures from the normality in the tails is observed for 5- and 10-step forecasts (Fig. 2, bottom row).

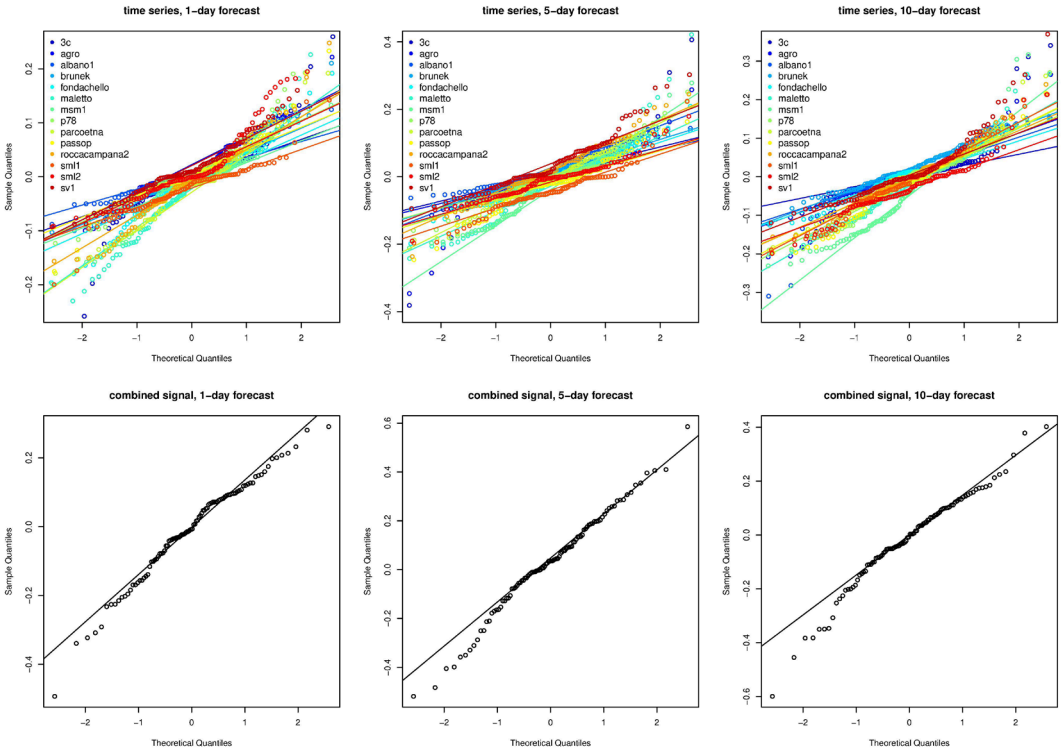


Fig. 2 - Top row: normal Q-Q plot of the residuals time series at 1-, 5-, and 10-steps for each of the 14 time series. Bottom row: normal Q-Q plot of the residuals time series at 1-, 5-, and 10-steps for the resulting combined signal.

We suggest that the most of the uncertainty on the single time series is canceled out when those are combined together and the forecast get reliable also for longer steps (Fig. 1c). This is a further evidence of the assumption at the base of the procedure to combine the time series into a unique signal as proposed by Liuzzo et al., (2013) and of it robustness in providing an estimate of global values for the whole CO_2 monitoring network.

Acknowledgements. The authors thank Marco Liuzzo, Sergio Gurrieri, and Giovanni Giuffrida (Istituto Nazionale di Geofisica e Vulcanologia) who provided the data.

References

Aiuppa, A., Moretti, R., Federico, C., Giudice, G., Gurrieri, S., Liuzzo, M., Ppale, P., Shinohara, H. and Valenza, M.; 2007: *Forecasting Etna eruptions by real-time observation of volcanic gas composition*. Geology, 35(12), 1115-1118.

Cannata, A., Spedalieri, G., Behncke, B., Cannavò, F., Di Grazia, G., Gambino, S., Gresta, S., Gurrieri, S., Liuzzo, M. and Palano, M.; 2015: *Pressurization and depressurization phases inside the plumbing system of Mount Etna volcano: Evidence from a multiparametric approach*. J. Geophys. Res.: Solid Earth, 120(9), 5965-5982.

Gurrieri, S., Liuzzo, M. and Giudice, G.; 2008: *Continuous monitoring of soil CO2 flux on Mt. Etna: The 2004–2005 eruption and the role of regional tectonics and volcano tectonics*. J. Geophys. Res:. Research: Solid Earth, 113(B9).

Gurrieri, S., Liuzzo, M., Giuffrida, G. and Boudoire, G.; 2021: *The first observations of CO2 and CO2/SO2 degassing variations recorded at Mt. Etna during the 2018 eruptions followed by three strong earthquakes*. It. J. Geosci. 140(1), 95-106.

Liuzzo, M., Gurrieri, S., Giudice, G., and Giuffrida, G.; 2013. *Ten years of soil CO2 continuous monitoring on Mt. Etna: Exploring the relationship between processes of soil degassing and volcanic activity*. Geochem. Geophys. Geosystems, 14(8), 2886-2899.

Paonita, A., Liuzzo, M., Salerno, G., Federico, C., Bonfanti, P., Caracausi, A., Giuffrida, G., La Spina, A., Caltabiano, T., Gurrieri, S. and Giudice, G.; 2021: *Intense overpressurization at basaltic open-conduit volcanoes as inferred by geochemical signals: The case of the Mt. Etna December 2018 eruption*. Sci. Adv. 7(36), eabg6297.

Scudero, S., D'Alessandro, A., Giuffrida, G., Gurrieri, S. and Liuzzo, M.; 2022: *Wavelet-based filtering and prediction of soil CO2 flux: Example from Etna volcano (Italy)*. J. Volc. Geotherm. Res. 421, 107421.

ANALYSIS OF EFFUSION RATE ON MT ETNA FLANK ERUPTIONS AND THEIR IMPACT IN ASSESSING THE LAVA FLOW HAZARDS

F. Zuccarello, G. Bilotta, A. Cappello, G. Ganci
Istituto Nazionale Di Geofisica E Vulcanologia, Catania, Italy

The rate at which lava is discharged plays a key role in controlling the distance covered by lava flows from eruptive vents among other physical factors (e.g., melt compositions, water content, lava viscosity, heat loss, topography of the terrain), and it constitutes a critical parameter for the physical-mathematical modelling of lava flows. Generally, lava effusion rate changes over time, but both for assessing long-term hazards and for real-time monitoring during on-going eruptions, the effusion rate has been assumed to be constant or to have a bell-shaped time-dependent behavior. Here, we investigated available time averaged discharge rates (TADRs) derived from field measurements and satellite thermal imagery for recent eruptions at Mt. Etna volcano (Italy), in order to define a possible generalized effusion rate trend to be used for simulating lava flow paths. Only flank eruptions were selected for this study, which represent the major source of hazard for the densely populated areas around the volcano. TADRs temporal series were normalized to obtain homogeneous curves in duration and sampling times, reducing redundancies and improving data consistency. Our data indicate a fast waxing phase where effusion rate peaks occur between the 0.5 and 29% of the total eruption time, then followed by a progressive decrease in the waning phase. Three characteristic curves have been built by calculating the 25^{th}, 50^{th} and 75^{th} percentiles associated to the occurrence of effusion rate peaks and to the slope variations of descending curves in the waning phase. Finally, these characteristic curves have been used to run numerical tests by means of the physics-based GPUFLOW model. Our tests showed how the different characteristic effusion rate curves can impact single vent scenarios, as well as on short- and long-term hazard maps. Statistics on the final emplacements revealed variations up to 40%, confirming the key role of the effusion rate in controlling the development of lava flow fields.

Sessione 1.3

Modelli fisici per la Terra Solida e integrazione fra modellistica e dati di natura differenti

Convenor: A.M. Marotta, C. Braitenberg e B. Orecchio

PERFORMANCE OF EMPIRICAL AND MODEL DERIVED ATMOSPHERE CORRECTIONS OF INSAR TIME SERIES

M. Bartola[1], C. Braitenberg[1], Y. Fialko[2]

[1] Department of Mathematics and Geoscience, University of Trieste, Trieste, Italy
[2] Institute of Geophysics and Planetary Physics, UC San Diego, San Diego, California

The reliability of differential interferometry SAR time series depends on the robustness in the calculated Line of sight (LOS) ground velocity. Orbital errors and atmospheric noise are more limiting for small-amplitude and low-rate signals, compared to large-amplitude rapid displacements caused by e.g. earthquakes or volcanic unrest. Orbital errors are reduced given precise orbital information while atmospheric noise is still a considerable challenge. Methods used to mitigate the atmospheric noise can be divided into those using SAR data, and external datasets. Each method has its own strengths and weaknesses (Li *et al.*, 2022), but none of them can remove entirely the atmospheric contribution that can consist of two parts: the stratified atmosphere and the turbulent mixing.

In this study we use two different methods, the Common Scene Stacking (CSS) (Tymofyeyeva and Fialko, 2015) and the Global Atmospheric Correction Online Service (GACOS) (Yu *et al.*, 2017; Yu *et al.*, 2018a; Yu *et al.*, 2018b). The CSS is an iterative method for the estimation of the atmospheric contribution based on the fact that interferograms sharing a common scene contain the same delay contributions. GACOS is model based and integrates the HRES-ECMWF and the GPS to generate high resolution maps of phase delays due to atmospheric moisture.

We used these methods on a rugged area straddling the Friuli Venezia Giulia and Veneto regions. In the area of interest, different weather conditions over the year are present, karstic channels characterize the underground in which, in combination with strong flood events, the water is over- pressurized and triggers surface deformation, and furthermore there are active seismic faults.

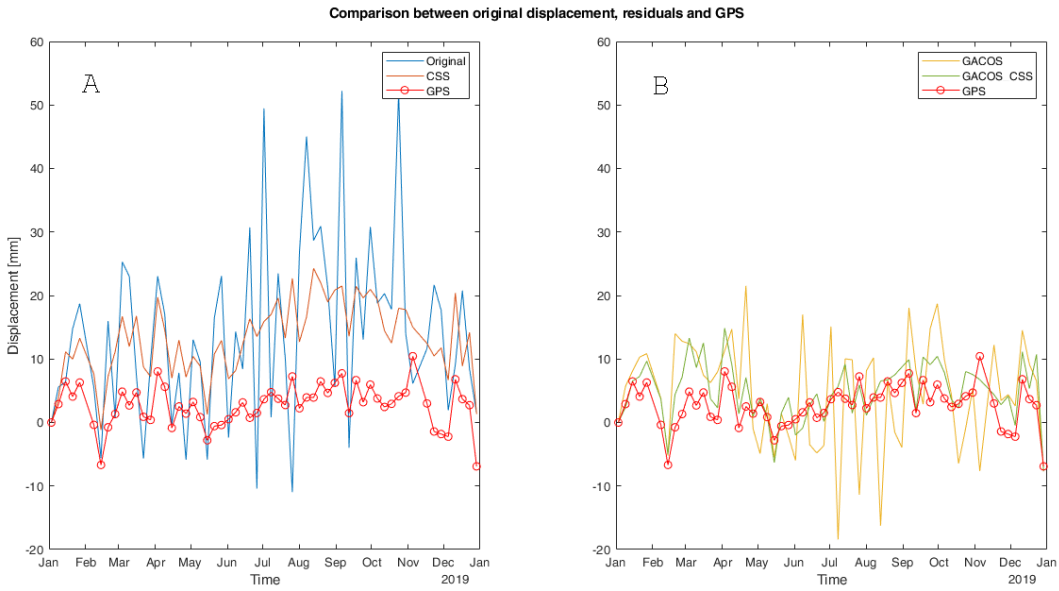


Fig. 1 - Comparison between the original displacement time series, the atmospheric corrections and GPS. The GPS line is the time series of the GPS CANV with a moving average filter of 5 days. The GPS data refer to the Nevada Geodetic Laboratory. A): Original time series, CSS correction residuals and GPS; B): GACOS correction residual, CSS correction residuals after the application of GACOS.

The SAR acquisitions are from the Sentinel 1 mission, spanning the year 2019, and processed with GMTSAR (Sandwell *et al.*, 2011; Sandwell *et al.*, 2016) using the Small BAseline Subset (SBAS) (Berardino *et al.*, 2002) algorithm. We applied the two methods of atmospheric corrections separately to estimate the effectiveness of both. We also use them in combination because of their different ability to remove atmospheric noise.

To assess the performance of the methods, separately and in combination, we referenced all the interferograms to one GPS station and we corrected the time series of all the scatters,

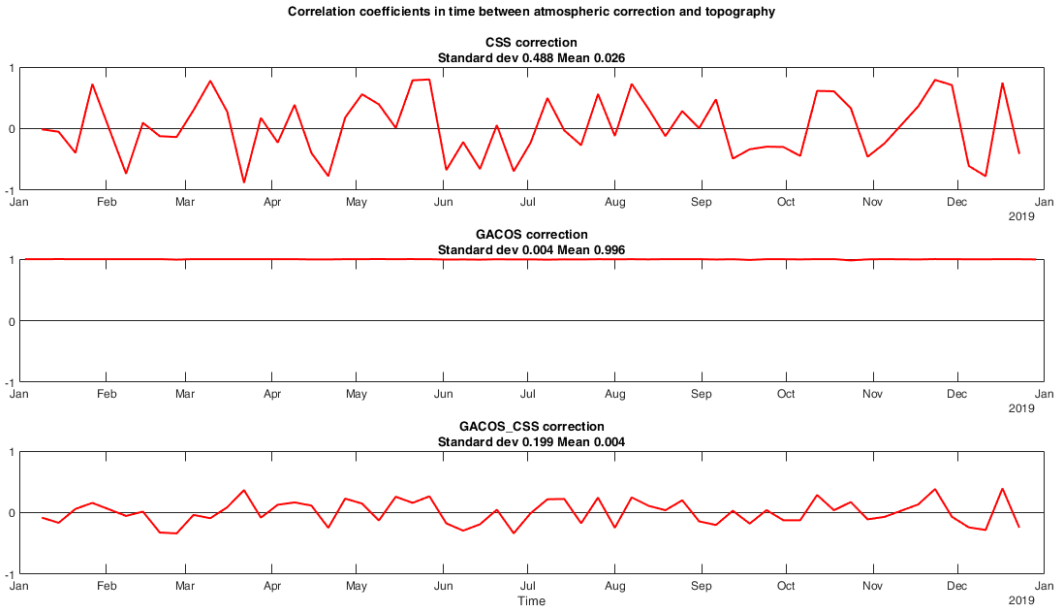


Fig. 2 - Correlation coefficients in time between atmospheric correction and topography. Top: CSS correction; Middle: GACOS correction; Bottom: CSS correction after the application of GACOS.

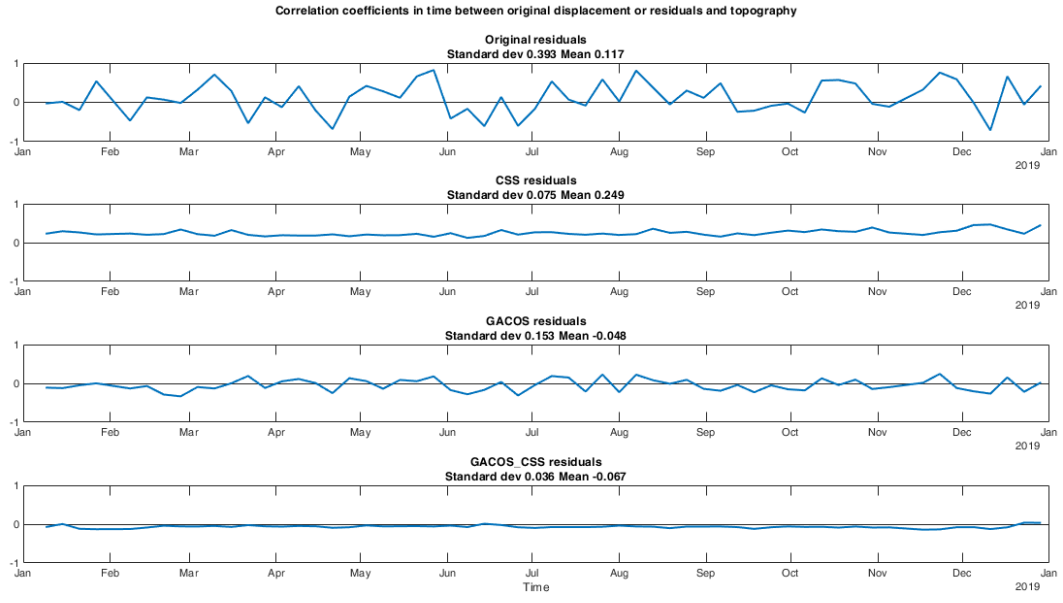


Fig. 3 - Correlation coefficients in time between original displacement time series or residuals and topography.

making it possible to compare the time series with other GPS in the area of interest (Fig. 1). The GPS time series are provided by the Nevada Geodetic Laboratory.

We analyzed the time series of displacement using the correlation coefficients between correction/residuals and topography on SAR points recovered in an area of 1 degree longitude by 0,5 degrees of latitude (Fig. 2 and 3).

We found that the CSS method is good at reducing scatter in the time series of displacement (Fig.1A) but in the residuals (Fig. 3) there is some remaining effect related to the topography contribution which manifests itself as a long-term deviation from the GPS.

GACOS corrects most of the topography contribution (Fig. 2) but it is less effective in the reduction of the short period (Fig. 1B and 3). Instead, the application of CSS after the correction of GACOS results in a curve that finds good correspondence with the GPS (Fig. 1B), having reduced both the high frequencies and the long-term deviation.

References

Berardino P., Fornaro G., Lanar, R., Sansosti E.; 2002: *A new algorithm for surface deformation monitoring based on small baseline differential SAR interferograms.* IEEE Transactions on geoscience and remote sensing, 40(11), 2375-2383.

Li Z., Duan M., Cao Y., Mu M., He X., Wei J.; 2022: *Mitigation of time-series InSAR turbulent atmospheric phase noise: A review*. Geodesy and Geodynamics.

Sandwell D., Mellors R., Tong X., Wei M., Wessel P.; 2011: *Open radar interferometry software for mapping surface deformation*, Eos Trans. AGU, 92(28), doi:10.1029/2011EO280002.

Sandwell D., Mellors R., Tong X., Xu X., Wei M., Wessel P.; 2016: *GMTSAR: An InSAR Processing System Based on Generic Mapping Tools.* UC San Diego: Scripps Institution of Oceanography

Tymofyeyeva E. and Fialko Y.; 2015: *Mitigation of atmospheric phase delays in InSAR data, with application to the eastern California shear zone.* Journal of Geophysical Research: Solid Earth, 120, 5952–5963. https://doi.org/10.1002/2015JB011886

Yu C., Li Z., Penna N. T., Crippa P.; 2018a: *Generic atmospheric correction model for Interferometric Synthetic Aperture Radar observations.* Journal of Geophysical Research: Solid Earth, 123(10), 9202-9222.

Yu C., Li Z., Penna N. T.; 2018b: *Interferometric synthetic aperture radar atmospheric correction using a GPS-based iterative tropospheric decomposition model.* Remote Sensing of Environment, 204, 109-121.

Yu C., Penna N. T., Li Z.; 2017: *Generation of real-time mode high-resolution water vapor fields from GPS observations.* Journal of Geophysical Research: Atmospheres, 122(3), 2008-2025.

MAPPING THE 2021 LA PALMA ERUPTIVE SEQUENCE THROUGH MULTI-SPECTRAL AND SAR IMAGES OF THE SENTINEL SATELLITES

C. Braitenberg, T. Pivetta, F. Stefan

Department of Mathematics and Geosciences, University of Trieste

The volcanic activity bears a hazard to a large portion of the population worldwide: it is estimated that about 8% of the world's population lives within 100 km from a volcano with at least one recent significant eruptive episode (Freire, 2019). Cohabiting with this hazard requires an extensive knowledge of the structure of the volcano, its historical and geological activity, and a monitoring system able to detect changes in deformation, increase in the seismicity and variation of physical and chemical parameters prior, during and after the event.

Mapping the past eruptions and their paths is a fundamental task to assess the risk and to plan possible counter-measures to limit the impact of future episodes. Satellite products, as those provided by the Sentinel missions, offer images with sufficient spatial and temporal resolution to fulfill this objective. Using satellite images in fact the user can rapidly estimate the areas involved by the volcanic activity during the eruption, even discriminating lava flows from the areas subjected to ashes fallout. In case of episodes lasting for weeks, a temporal evolution of the various paths followed by the lava is also obtainable.

In this contribution we present a study of the recent "La Palma" eruptive sequence, which lasted for 12 weeks (from 19th September to 13th December 2021) and that involved the central-western portion of the La Palma Island. We exploited both the multi-spectral observations of Sentinel-2 and the images of the SAR Sentinel-1, obtaining a collection of images of the whole eruptive sequence. The Sentinel-2 data was processed through Google Earth Engine (GEE), which allowed to mosaic the different scenes, to remove the effect of the clouds and to finally create false-color maps using various combinations of available bands. The SAR reflectance images were as well merged with GEE and were employed since the radar band is more penetrative and less sensitive to the ash clouds of the eruption.

The short-wavelength infrared (SWIR) bands of Sentinel-2, exploiting the sensitivity to the rock's temperature, was used to obtain a dynamic picture of the lava flows throughout the period of eruption.

The comparison of Sentinel-2 and the SAR images before and after the event allowed to:

1. precisely map the area that was covered by the fallen ashes
2. detect the vent from which the lava originated
3. identify a new portion of land emerging from the sea with area 400000 m^2 or 0.40 km^2
4. the volcanic hazard affected a total area of 12 km^2.

By the comparison with a map of the known volcanic eruptions, we found that the 2021 event is located between two older events occurred in 1470-1492 and 1949. The vent from which the lava flowed out, was formed during this eruption and it is located about 600 m west from the Cumbre Vieja, the axial ridge along which most of the magmatic manifestations occur.

References

Freire S., Florczyk A.J., Pesaresi M., Sliuzas R.; 2019: *An Improved Global Analysis of Population Distribution in Proximity to Active Volcanoes*, 1975–2015. ISPRS Int. J. Geo-Inf., *8*, **341**, https://doi.org/10.3390/ijgi8080341

LA SEQUENZA SISMICA DELLA TESSAGLIA (GRECIA CENTRALE) DEL MARZO 2021: MODELLO GEODETICO DEDOTTO DA DATI SISMOLOGICI E INSAR

V. De Novellis[1,2], D. Reale[1], G.M. Adinolfi[3], V. Convertito[2], E. Sansosti[1]

[1] Istituto per il Rilevamento Elettromagnetico dell'Ambiente, CNR, Napoli, Italia
[2] Istituto Nazionale di Geofisica e Vulcanologia, Osservatorio Vesuviano, Napoli, Italia
[3] Dipartimento di Scienze e Tecnologie, Università degli Studi del Sannio, Benevento, Italia

Introduzione. In questo lavoro proponiamo un modello geodetico per la sequenza sismica della Tessaglia (TSS), Grecia, del marzo 2021. Questa è stata la più grande sequenza sismica che ha interessato un dominio estensivo continentale in Grecia che è stato possibile monitorare con moderne tecniche geodetiche, grazie al breve tempo di rivista dei satelliti della costellazione Sentinel-1. Infatti, utilizzando un set di immagini di tale sensore mediante la tecnica InSAR, ulteriormente rafforzata dall'analisi dei dati sismici, si è potuto isolare il contributo degli eventi maggiori della sequenza e studiarne l'interazione. Inoltre, i dati sismologici e geologici disponibili indicano che il settore settentrionale della Tessaglia, proprio dove è stata registrata la sequenza sismica, rappresenta un gap sismico.

Dati sismologici. La sequenza è iniziata il 3 marzo 2021 (10:16:08 UTC) con un evento di magnitudo Mw 6.3, interessando un'area a circa 25 km a nord-ovest della città di Larissa (Figura 1a). Fortunatamente non ha provocato vittime, mentre solo 3 persone sono rimaste lievemente ferite a causa del crollo parziale di edifici con pareti portanti in muratura nel villaggio di Damasi, (Lekkas *et al.*, 2021). Le soluzioni ottenute da vari osservatori e istituti sismologici (AUTH, NOA, GCMT, USGS, OCA, INGV, GFZ) hanno mostrano che il primo evento è stato caratterizzato da un meccanismo di faglia normale (Figura 1a). Diverse repliche, in particolare quelle con M>5, si sono concentrate a sud-est durante le prime ore dopo il primo evento entro una distanza di 10 km. Nei giorni successivi, la TSS è stata caratterizzata da altri due eventi di magnitudo moderata: un Mw 6.0 il 4 marzo (18:38:19 UTC), localizzato a circa 12 km a nord-ovest e un Mw 5.6 il 12 marzo (12:57:50 UTC), localizzato 7 km più avanti verso NO. Eventi minori sono stati registrati anche fino a metà aprile, quando la sequenza è diminuita in frequenza e magnitudo (Figure 1a).

Al fine di vincolare la geometria e l'ubicazione delle principali strutture di faglia coinvolte durante la TSS, abbiamo considerato 1853 terremoti avvenuti nell'area dal 28 febbraio 2021 al 26 aprile 2021 con magnitudo compresa tra 0.2 e 6.3 (Figure 1b, c). I dati analizzati sono stati raccolti dall'Institute of Geodynamics of the National Observatory of Athens (NOA-IG) utilizzando le letture di fasi registrate a 116 stazioni sismiche.

La localizzazione degli epicentri (Figure 1c) suggerisce un allineamento di 40 km NO-SE, che è coerente con l'andamento regionale delle faglie rilevate in superficie mappate, sebbene i cluster di sismicità di 5-10 km di lunghezza rivelino strutture di faglie secondarie. Questo risultato è supportato dai grafici delle sezioni verticali, che mostra chiaramente piani con immersione NE, in accordo con le soluzioni di meccanismi focali (Figura 1d). Segnaliamo che la continuità di questi allineamenti sembra interrotta lateralmente. Come mostrato nelle sezioni 2 e 4, le posizioni dei terremoti sembrano mostrare piani di immersione NE e SO che replicano un insieme di faglie antitetico-sintetiche, tipiche delle aree di fagliazione normale attiva. Nell'area settentrionale, la localizzazione dei terremoti evidenzia un piano di faglia con immersione a sud (sezione 5). I nostri risultati mostrano una zona di faglia segmentata con strutture prevalentemente con andamento NE e geometrie complesse, tipiche dei normali sistemi di faglia come quelli attivati dai terremoti di Mw 6.1 de L'Aquila (2009) e del Centro Italia (2016-2017) (Castaldo *et al.*, 2018; Cheloni *et al.,* 2017; Lavecchia *et al.,* 2016).

Dati InSAR. La TSS è stata osservata dai passaggi di Sentinel-1 (S1) con un intervallo di ripetizione regolare di sei giorni lungo due orbite ascendenti (tracce 102 e 175) e due discendenti

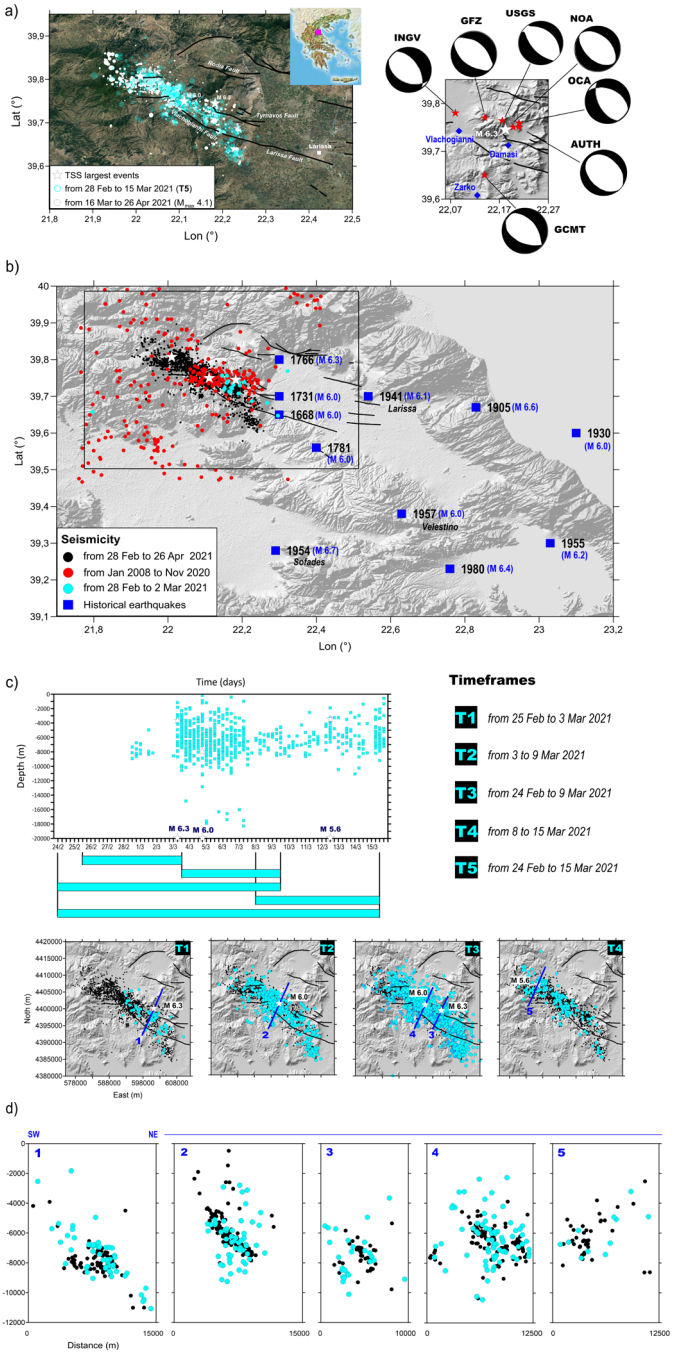


Fig. 1 - Area di studio e dati sismologici. (a; sinistra) Principali lineamenti tettonici rappresentati da linee nere ridisegnati da Caputo *et al.* (1993); epicentri degli eventi sismici accaduti dal 28 febbraio al 15 marzo 2021 e dal 16 marzo al 26 aprile 2021, rappresentati, rispettivamente, da cerchi azzurri e bianchi. (a; destra) area epicentrale dell'evento Mw 6.3 con meccanismi focali forniti da vari istituti europei; vengono mostrati anche i villaggi più danneggiati. (b) attività sismica registrata nell'area di Tyrnavos in epoca recente e in periodo storico; sono riportati anche i terremoti avvenuti nell'area della Tessaglia (dati riportati in Caputo, R. *et al.*, 2006). Evoluzione della sismicità. (c) Grafico della profondità rispetto al tempo della sismicità verificatasi tra il 28 febbraio e 15 marzo 2021; sono riportati anche gli intervalli temporali utilizzati per il modello (T). (d) Mappe e sezioni della sismicità ricollocata tracciate in base alla loro origine.

(tracce 7 e 80). Nel nostro lavoro consideriamo l'intervallo di tempo che va dal 24/02/2021 al 15/03/2021 e che comprende quattro acquisizioni per traccia (Figura 2). In particolare, sono disponibili acquisizioni quasi simultanee da orbite ascendenti e discendenti; infatti, la seconda immagine della traccia 102 è stata acquisita proprio tra i primi due maggiori terremoti (Mw 6.3 e 6.0); in questo modo è possibile separare i due contributi, sebbene siano avvenuti a sole 32 ore di distanza. Questo non accade per le altre tre orbite in cui gli interferogrammi tra la prima e la seconda acquisizione non contengono segnale e, quindi, non sono utili per l'analisi successiva.

Per facilitare la discussione, definiamo diversi "intervalli temporali" in base ai passaggi di Sentinel-1 e agli eventi che essi includono (Figure 1c, 2). In particolare, definiamo come T1 e T2 i due intervalli che coprono rispettivamente i singoli eventi Mw 6.3 e Mw 6.0.

Definiamo inoltre come T3 l'intervallo temporale che comprende sia il primo che il secondo evento principale; in questo caso abbiamo 7 interferogrammi: 4 interferogrammi "lunghi" (da fine febbraio all'8-9 marzo) e 3 interferogrammi "corti" (dal 2-3 all'8-9 marzo); chiaramente, quelli brevi non includono la traccia 102 poiché copre un solo evento. La Figura 2 mostra i quattro interferogrammi "lunghi" T3 accoppiati con gli stessi tempi di acquisizione.

Queste mappe mostrano tre evidenti lobi di deformazione lungo la direzione NNO-SSE situati nel bacino di Larissa; a sud sono evidenti i due lobi maggiori, associati al Mw 6.3, in particolare sui dati discendenti; questo *pattern* di spostamento raggiunge un valore massimo di ~-38 cm in linea di vista (LOS) su dati ascendenti (valori LOS negativi rappresentano allontanamento dal satellite). A NO di questo *pattern* si osserva un lobo più piccolo relativo al Mw 6.0. Notiamo anche che il *pattern* ascendente di T3 è abbastanza coerente con la sovrapposizione di T1 e T2 una volta presi in considerazione i diversi angoli di vista. I corrispondenti interferogrammi discendenti presentano caratteristiche simili, considerando l'effetto delle linee di viste opposte e di possibili componenti orizzontali. Inoltre, definiamo come T4 l'intervallo che copre solo l'evento Mw 5.6, che viene ripreso singolarmente da tutte e quattro le tracce. I corrispondenti interferogrammi mostrano un *pattern* di spostamento LOS negativo che si estende prevalentemente lungo la direzione EO, con un minimo di ~-10 cm, coerentemente con l'energia inferiore di questo evento rispetto ai precedenti.

Infine, introduciamo il T5 come l'intervallo temporale complessivo, cioè quello che include tutti e tre gli eventi principali. Si noti che più interferogrammi all'interno di un unico intervallo di tempo (Figura 2) comprendono sostanzialmente lo stesso segnale di spostamento poiché le quattro tracce considerate sono spostate nel tempo di non più di un giorno e non vi è alcuna attività significativa tra la fine di febbraio e l'inizio della sequenza.

Risultati. Il nostro modello mostra che l'attività sismica ha interessato porzioni distinte di un sistema di faglie precedentemente sconosciuto composto da tre piani di faglie (F1a, F1b e F2) che immergono a NE per i terremoti Mw 6.3 e 6.0, e da una piccola faglia (F3) che immerge a SE per il terremoto di Mw 5.6 (Figura 3). Tuttavia, l'attivazione di una parte delle faglie già note di Tyrnavos e Larissa durante le scosse di assestamento non può essere completamente esclusa. Per i primi due eventi, la componente di deformazione verticale evidenzia forti fenomeni di subsidenza che superano i ~40 cm. Inoltre, la componente orizzontale (EO) mostra un movimento significativo verso ovest (~20 cm): quest'ultimo movimento può essere messo in relazione con il movimento della faglia F1a, che presenta una leggera componente di scorrimento laterale sinistro.

Si osservano ampie e profonde crepe nel terreno generate dal Mw 6.3 in prossimità dei letti dei fiumi insieme al materiale liquefatto espulso; altre crepe erano parallele alla faglia di Vlachogianni. Alcuni rapporti tecnici mostrano allineamenti superficiali sparsi solo nella regione di Zarko (Lekkas *et al.*, 2021), che difficilmente possono essere associati a faglie. Tuttavia, la distribuzione della dislocazione dedotta dall'inversione dei dati InSAR mostra che

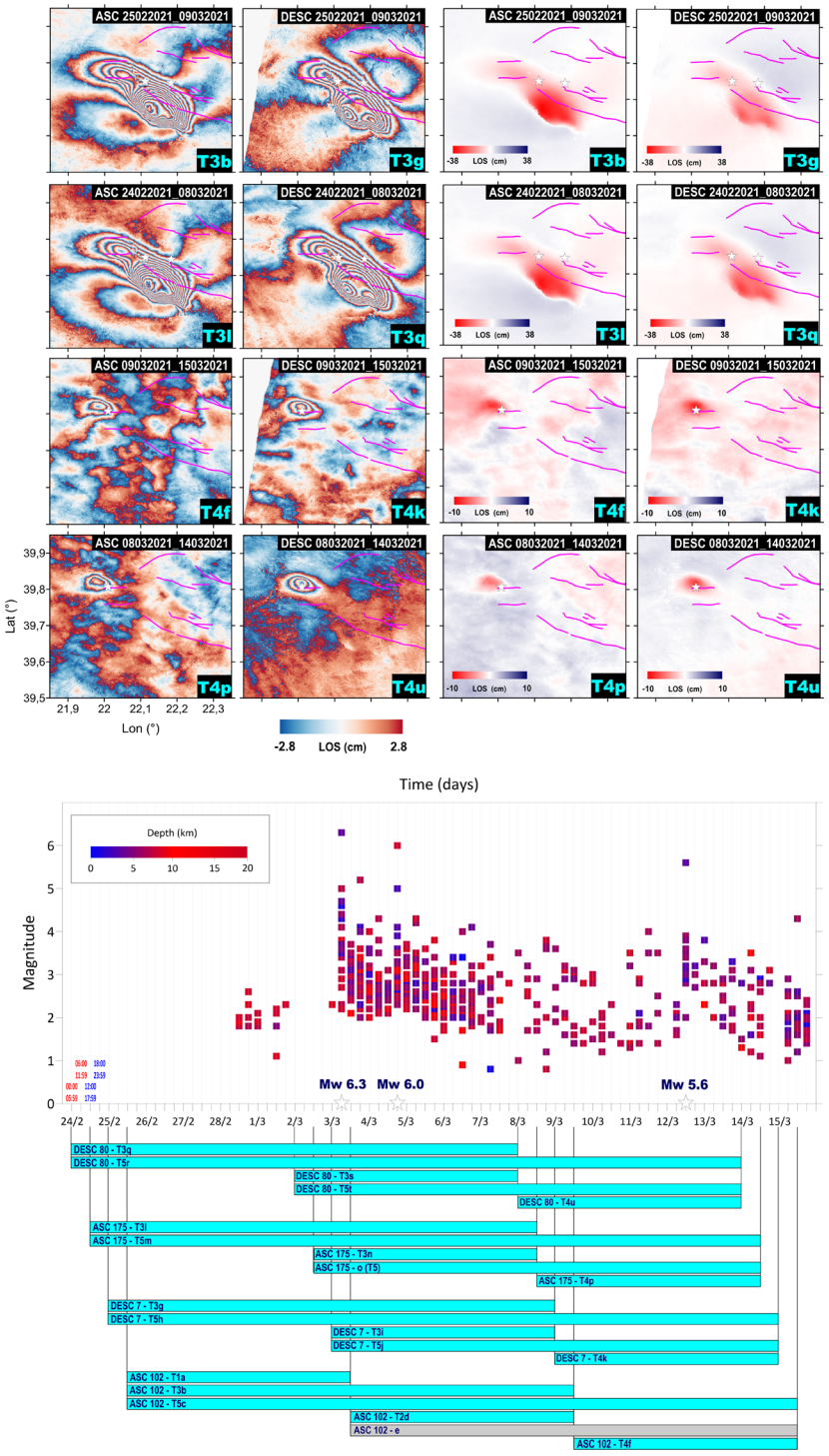
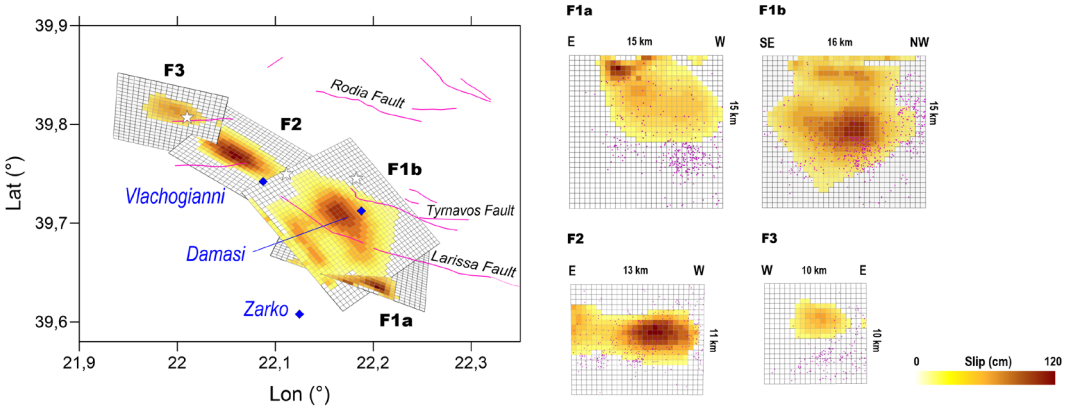


Fig. 2 - Interferogrammi InSAR Sentinel-1 utilizzati in questo studio con gli spostamenti misurati in linea di vista satellitare (LOS); i lineamenti tettonici e gli epicentri dei tre eventi maggiori sono indicati rispettivamente con linee magenta e stelle bianche. Nel grafico sottostante si riportano magnitudo vs intervallo di tempo per tutta l'attività sismica in relazione alle coppie interferometriche utilizzate per il modello. Le barre indicano i "timeframe" (T) presentati in Figura 1.



Fault	F1a	F1b	F2	F3
$slip_{max}$ (cm)	115.0	98.0	107.0	57.0
strike (°)	292.0	326.3	306.1	100.1
dip (°)	55.0	33.0	35.0	53.6
rake (°)	-112.6	-86.5	-81.4	-86.9
$depth_{top}$ (m)	1200.0	750.0	2500.0	400.0
C_{Lon} (°)	22.1921	22.1164	22.0620	21.9944
C_{Lat} (°)	39.6347	39.6713	39.7631	39.8269

Fig. 3 - Risultati dell'inversione analitica. Le quattro sorgenti (F1a, F1b, F2 e F3) e i relativi parametri ottenuti dalle soluzioni lineari invertendo per T3 + T4. I lineamenti di faglia e l'epicentro dei tre eventi maggiori sono rappresentati rispettivamente da linee magenta e da stelle bianche. I puntini viola rappresentano tutti gli eventi che si verificano sui piani di faglia.

i valori più alti sono confinati nell'area sud-est (nei pressi dei villaggi di Vlachogianni, Damasi, Zarko) e questo potrebbe spiegare la distribuzione dei danni osservati (Figure 1a, 3).

I risultati di un'analisi di stress di Coulomb indicano che la sequenza sismica si è sviluppata in una sorta di effetto domino. Per quanto riguarda l'evoluzione temporale della sequenza, l'innesco ritardato del terremoto di Mw 6.0 può essere spiegato dalla distribuzione degli eventi avvenuti in precedenza; in effetti, quella distribuzione avvolge le patch della faglia che si romperanno (Figura 3), una caratteristica descritta da Das et al. (1983) come manovra di accerchiamento. Ciò suggerisce che la nucleazione del terremoto si è verificata secondo un modello a cascata innescato dalla sua sequenza di *foreshocks*.

Per quanto riguarda il terremoto di Mw 5.6, i risultati mostrano che l'effetto più rilevante, in termini di contributo di stress statico, è dovuto all'evento di Mw 6.0. Ad ogni modo, il ritardo nell'innesco (circa 8 giorni dagli eventi Mw 6.3 e Mw 6.0) suggerisce che si sono verificati altri meccanismi oltre alla variazione di stress statico e triggering dinamico. È il caso, ad esempio, della diffusione della pressione del fluido di poro osservata in altre sequenze sismiche (Gavrilenko, 2005; Tung e Musterlark, 2018; Convertito *et al.*, 2020). Infatti, un aumento della pressione di poro può ridurre lo sforzo normale favorendone la rottura. Inoltre, i fluidi possono anche contribuire a diminuire l'attrito sul piano di faglia (Scholz, 2002). L'analisi di diffusività 1D eseguita indica che quasi tutta la sequenza, e in particolare il verificarsi di Mw 6.0 e 5.6, sono infatti compatibili con un meccanismo di diffusione della pressione di poro che è stata probabilmente innescata dal pattern di deformazione prodotto dagli eventi precedenti.

In quest'area sia la mancanza di registrazioni dei grandi terremoti storici, così come della mappatura di faglie passate, rendono difficile una stima del rischio sismico. Pertanto, l'identificazione di *blind faults* può contribuire in modo significativo a migliorare l'analisi della pericolosità sismica, in particolare per quelle con angolo di inclinazione moderato. In questo contesto, i prodotti InSAR si sono rivelati uno strumento estremamente utile per aiutare a

limitare le caratteristiche dei piani di faglia. Considerando la possibile presenza di una struttura di rottura multi-faglia e la complessità del inquadramento tettonico dell'area studiata, riteniamo che lo studio del meccanismo sismogenetico della blind fault meriti ulteriori approfondimenti attraverso dati aggiuntivi.

Riconoscimenti. Questo studio è stato finanziato da Pianeta Dinamico – Progetto Working Earth INGV-MUR. I dati di Sentinel-1 sono stati forniti attraverso il Programma Copernicus dell'Unione Europea. Tutti i set di dati generati durante e/o analizzati durante lo studio in corso sono disponibili nel repository Zenodo (10.5281/zenodo.5016812).

Bibliografia

Caputo, R. and Pavlides, S. (1993) *Late Cainozoic geodynamic evolution of Thessaly and surroundings (central-northern Greece)*. Tectonophys, 223, 339–362.

Caputo, R.; Helly, B.; Pavlides, S.; Papadopoulos, G. (2006) *Archaeo- and palaeoseismological investigationsin Northern Thessaly (Greece): Insights for the seismic potential of the region.* Nat. Haz., 39, 195–212

Castaldo, R., de Nardis, R., De Novellis, V., Ferrarini, F., Lanari, R., Lavecchia, G., *et al.* (2018) *Coseismic stress and strain field changes investigation through 3-D Finite Element modeling of DInSAR and GPS measurements and geological/seismological data: The L'Aquila (Italy) 2009 earthquake case study.* Journal of Geophysical Research: Solid Earth, 123, 4193– 4222. https://doi.org/10.1002/2017JB014453.

Cheloni, D., *et al.* (2017) *Geodetic model of the 2016 Central Italy earthquake sequence inferred from InSAR and GPS data*, Geophys. Res. Lett., 44, 6778– 6787, doi:10.1002/2017GL073580.

Convertito V, De Matteis R, Improta L and Pino NA (2020). *Fluid-Triggered Aftershocks in an Anisotropic Hydraulic Conductivity Geological Complex: The Case of the 2016 Amatrice Sequence, Italy.* Front. Earth Sci. 8:541323. doi: 10.3389/feart.2020.541323.

Das, S. and Kostrov, B. V. (1983) *Breaking of a single asperity: Rupture process and seismic radiation.* J. Geophys. Res. 88, 4277–4288.

Gavrilenko, P. (2005) *Hydromechanical coupling in response to earthquakes: on the possible consequences for aftershocks.* Geophys. J. Int. 161, 113–129. doi: 10.1111/j.1365-246X.2005.02538.x

Lavecchia, G., *et al.* (2016) *Ground deformation and source geometry of the 24 August 2016 Amatrice earthquake (Central Italy) investigated through analytical and numerical modeling of DInSAR measurements and structural-geological data*, Geophys. Res. Lett., 43, 12,389– 12,398, doi:10.1002/2016GL071723.

Lekkas, E.; Agorastos, K.; Mavroulis, S.; Kranis, C.; Skourtsos, E.; Carydis, P.; Gogou, M.; Katsetsiadou, K.-N.; Papadopoulos, G. (2021) *The early March 2021 Thessaly earthquake sequence.* Newsl. Environ. Disaster Cris. Manag. Strateg. 195.

Scholz, C. H. (2002) *The Mechanics of Earthquakes and Faulting*, 2nd Edn, Cambridge: Cambridge University Press.

Tung, S., and Masterlark, T. (2018) *Delayed poroelastic triggering of the 2016 October Visso earthquake by the August Amatrice earthquake, Italy.* Geophys. Res. Lett. 45, 2221–2229. doi: 10.1002/2017GL076453.

MANTLE DYNAMICS AND STRUCTURE FROM COUPLED GEODYNAMIC AND SEISMOLOGICAL MODELLING

M. Faccenda

Dipartimento di Geoscienze, Università degli Studi di Padova, Padova, Italy

The present-day mantle structure is mainly determined by means of seismological methods. The interpretation of seismological data (e.g., isotropic and anisotropic velocity anomalies) is however non-unique, as different processes occurring simultaneously can be invoked to explain the observations. A further complication arises when regional tomographic seismic models ignore seismic anisotropy, which generates apparent seismic anomalies due to non-uniform sampling of anisotropic areas. The presence of these apparent anomalies is quite problematic, as they strongly bias our understanding of the Earth's internal structure.

In order to decrease the uncertainties related to the interpretation of seismological observations, geodynamic modelling can be exploited to reproduce the micro and macro scale dynamics and structure of different tectonic settings, yielding a valuable first-order approximation of the rock isotropic and anisotropic elastic properties. The model output can be subsequently tested against observations by performing seismological synthetics (e.g., SKS splitting, travel-time tomography, receiver functions, azimuthal and radial anisotropy). When the misfit between the modelled and measured seismic parameters is low, the geodynamic model likely provides a good approximation of the recent dynamics and present-day structure of the tectonic setting. Such a model can then be used to give a more robust and physically-based interpretation of the observables and/or to further improve seismological models by providing a-priori information for subsequent (adjoint) inversions and/or to test new seismic inversion methods.

During the seminar I will show some applications of the methodology and present the new open source software ECOMAN, designed to Explore the COnsequences of Mechanical Anisotropy in the maNtle by means of coupled of geodynamic and seismological simulations.

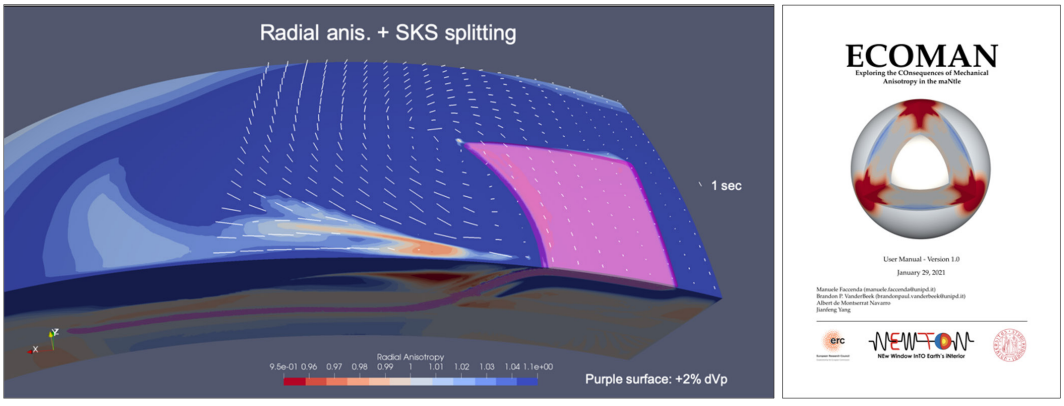


Fig. 1 - Left: geodynamic model of oceanic plate subduction and related seismic properties in spherical coordinates. The model is symmetric with respect to the vertical plane displayed in front. The plate (highlighted by the purple surface indicating +2% isotropic dVp anomaly) rolls back toward the right and finally stagnates into the mantle transition zone. The color scale indicates radial anisotropy, while the white bars at the surface display synthetic SKS splitting data. Right: cover of the ECOMAN software User Manual.

COSEISMIC FOLDING DURING RAMP FAILURE AT THE FRONT OF THE SULAIMAN FOLD-AND-THRUST BELT

M.T. Javed [1], S. Barbot [2], F. Javed [3], C. Braitenberg[1], A. Ali [4]

[1] Department of Mathematics and Geosciences, University of Trieste, Italy
[2] Department of Earth Sciences, University of Southern California, USA
[3] Centre for Earthquake Studies, National Centre for Physics, Pakistan
[4] Department of Earth Sciences, Quaid-i-Azam University, Islamabad, Pakistan

Abstract. The Sulaiman Fold Thrust (SFT) in Central Pakistan formed during the India-Eurasia collision in the late Cenozoic. However, the mechanics of shortening of the brittle crust at time scales of seismic cycles is still poorly understood. Here, we use spaceborne radar interferometry to analyze the deformation associated with the 2015 moment magnitude (Mw) 5.7 Dajal earthquake at the eastern boundary of the SFT. We use kinematic inversions to determine the distribution of slip on the frontal ramp and of flexural slip along active axial surfaces for the forward verging two end-member models: a double fault-bend fold system and a fault-propagation fold. In both models, a decollement branches into a shallow ramp at approximately 7 km depth with coseismic folding in the hanging wall. The Dajal earthquake ruptured the base of the foreland-vergent Boundary Thrust buried under sediment from the Indus River floodplain, representing fault-bending or fault-propagation folding near Sakhi-Sarwar fault-bend 30 km east of its surface exposure.

Introduction. The kinematics of crustal deformation at fold-and-thrust belts is complicated by the interaction between faulting and folding (Poblet and Lisle, 2011). Complex fault geometry causes shortening in the hanging wall that is accommodated by flexural slip, a type of plastic deformation that results from slip on multiple bedding planes in sedimentary strata (Sathiakumar *et al.*, 2020). Thrust-and-fold belts can also be found at the margin of collision zones and in other transpressive settings (Lai *et al.*, 2006). The role of folding on the long-term build-up of topography is well explained in various tectonic environments (Mahanjane and Franke, 2014). However, the mechanical coupling between folding and faulting during seismic cycles is still poorly understood. Some observations and modeling (Sathiakumar *et al.*, 2020) indicate that co-seismic folding is possible, but how this deformation occurs in the crust is still poorly resolved.

The western margin of the India-Eurasia collision belt, which accommodates 29 mm/yr of relative plate motion, provides an ideal setting to study the mechanics of an active fold-and-thrust belt (Reynolds *et al.*, 2015). The shear component is accommodated along the transform boundary of the Chaman Fault (CF) system but shortening is taken up by the transpressive Kirthar Fold Thrust (KFT) and the Sulaiman Fold Thrust (SFT). The historical earthquakes and fault plane solutions in the SFT belt are shown in Fig. 1a. The region is dominated by thrust events and a few strike-slip earthquakes (Ambraseys and Bilham, 2003, Pezzo *et al.*, 2014). Although the Central and Western SFT are characterized by well-developed fault-bend folding structures, the eastern SFT zone is under-developed (Jadoon *et al.*, 2019), experiencing only moderate-size NE-SW and E-W thrust earthquakes, with a deficit of large (Mw>6.0) earthquakes along the BT in the last several decades. Large cities with population of more than 3 million are located approximately 10 to 50 km from the BT.

On October 23, 2015, an Mw 5.7 earthquake occurred near Dajal, 55 km SSW of Dera Ghazi Khan, one of the most populated cities of Punjab province, Pakistan. The earthquake occurred at the eastern boundary of the SFT, providing an opportunity to study the interaction of coseismic slip and folding within an active fold-and-thrust belt. The 2015 Mw 5.7 Dajal, Pakistan earthquake occurred in a remote location, outside of any ground-based geodetic observatory. Fortunately, the deformation was captured by the spaceborne synthetic aperture radar Sentinel-1A. To document the surface deformation induced by the earthquake, we

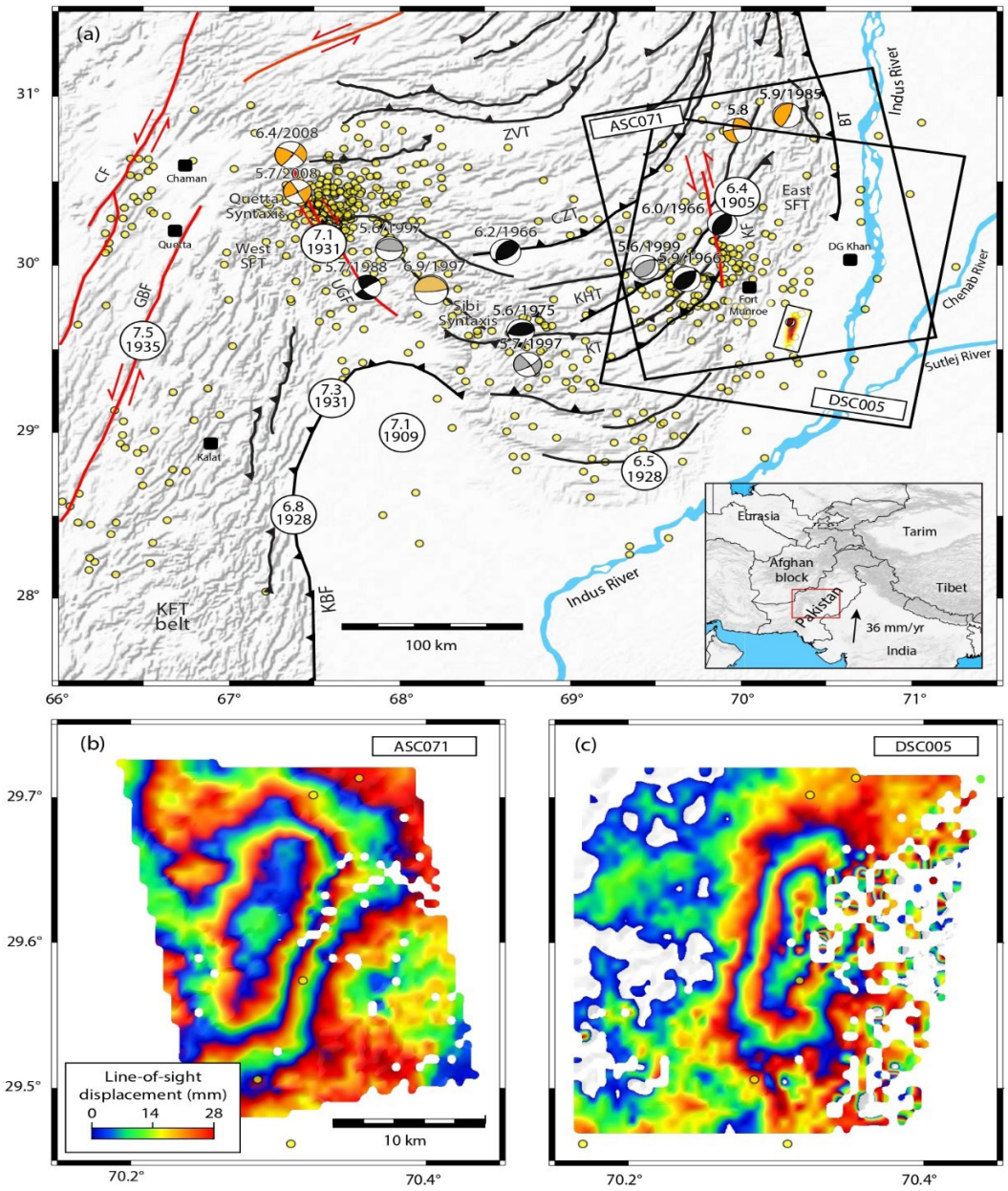


Fig. 1 - Tectonic settings and historical earthquake with M>3.5 on Sulaiman Fold Thrust (SFT) belt. (a) Faults are taken from (Pezzo *et al.*, 2014). The dark red moment tensor is the 2015 Dajal earthquake epicenter, shown above the slip distribution. Black boxes are showing the ascending (T071) and descending (T005) tracks of Sentinel-1A. The inset shows the geographical location of the SFT belt and the relative motion (36 mm/yr) between the Indian subcontinent and the Afghan block (Ul-Hadi *et al.*, 2013). b) and c) Ascending and descending interferograms of the 2015 Mw 5.7 Dajal earthquake, respectively.

generate the Sentinel-1A ascending (ASC071) and descending (DSC005) interferograms (Fig. 1b, c), allowing us to constrain two directions of motion. The LOS displacement is ~45 and ~50 mm due to thrust-dominated slip over a blind fault. The Dajal earthquake ruptured the base of the foreland-vergent Boundary Thrust buried under sediment from the Indus River

floodplain, representing the fault bending of the SFT belt 30 km east of its surface exposure. These observations document the seismic potential of blind ramps and axial surfaces in fold-and-thrust belts and the control on final rupture size by fault bends and surrounding folds.

Methodology. For radar image formation and post-processing, we use GMT5SAR (Sandwell *et al.*, 2011). The ascending and descending interferograms show line-of-sight displacements of approximately 45 and 50 mm, respectively. In a preliminary step, we estimate the simplified source parameters assuming coseismic rupture on a single fault plane, ignoring potential folding in the hanging wall. We constrain the dip, strike, depth, width, length, rake, and slip based on data from both interferograms using a Monte Carlo method for a rectangular patch of uniform slip (Bagnardi and Hooper, 2018). We determine the parameter uncertainties based on the semi-variograms of the interferograms. The seismic moment M_o = 3.94× 10^{17} Nm, assuming a shear modulus of 32 GPa, is calculated using the mean value of the probability distribution

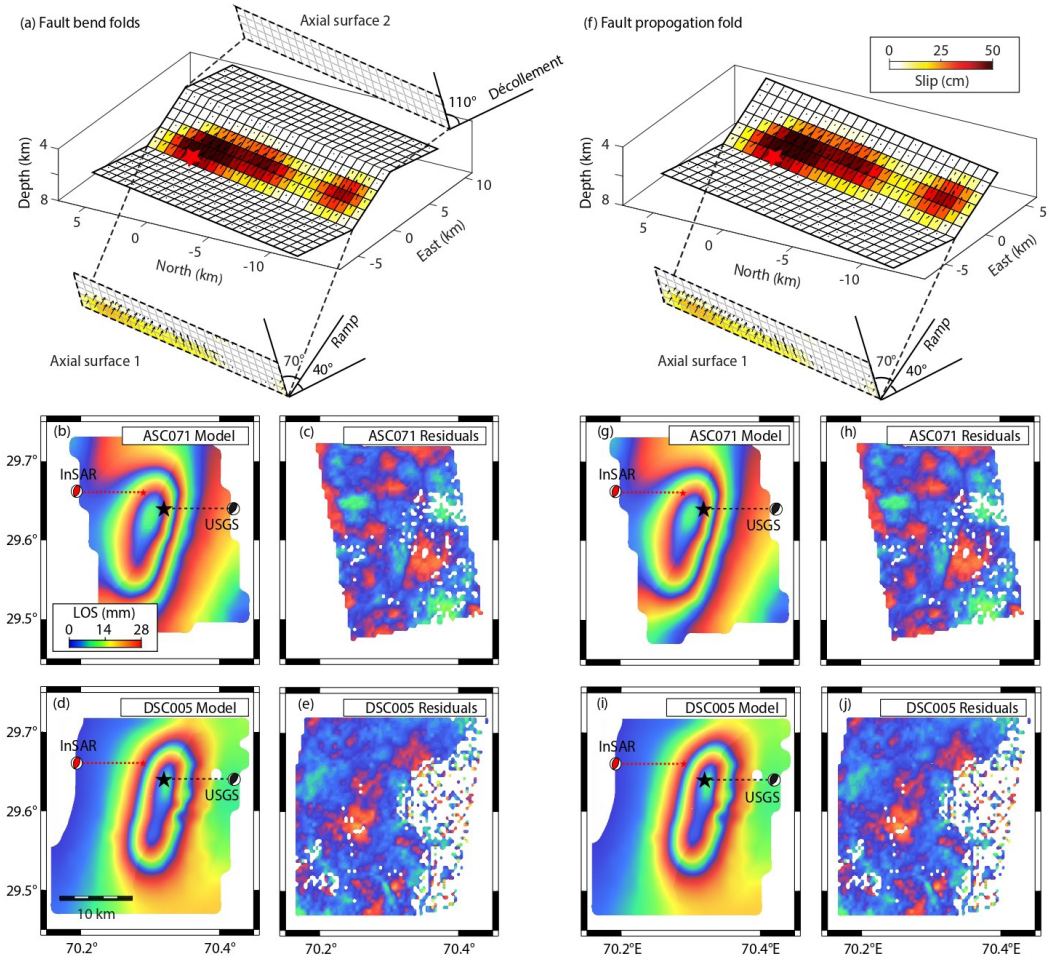


Fig. 2 - Finite kinematic models of the Mw5.7 Dajal earthquake on two-end member fault and fold geometry. a) Co-seismic slip distribution on the decollement-ramp-decollement system and associated flexural slip on two axial surfaces. b) Predicted line-of-sight (LOS) displacement for the ascending interferogram. c) Residuals with InSAR data. d) Predicted LOS displacement for the descending interferogram and e) associated residuals. f) Distribution of slip on the decollement-ramp system and associated flexural slip on the axial surface. g) Predicted LOS displacement for the ascending interferogram and h) corresponding residuals. i) LIS model for the descending interferogram and j) residuals.

of the source model parameters, corresponding to Mw 5.7. The centroid depth of 6.7 km is similar to past events in the Eastern SFT region (Reynolds *et al.*, 2015). This simple model indicates that the rupture took place on a 40˚ dipping thrust fault located east of the exposed SFT, buried deep below the Miocene or younger sediment of the Indus River floodplain. We use this result to construct a three-dimensional model of coseismic deformation compatible with the regional tectonic setting.

Based on the fold-and-thrust tectonic environment, we investigate two relevant end-member of fault-bend geometries of crustal deformation that involve fault slip at the base of the thrust sheet and folding in the overlying sedimentary strata. Using structural models compatible with long-term deformation, we seek to determine the distribution of fault slip and flexural slip that took place during the InSAR observation period. We model surface deformation due to slip on the ramp and the decollement using analytic solutions (Okada, 1985). In simple models of folding, flexural slip accommodates the advection of thrusted sediments through the active axial surface as they start or stop climbing the ramp. This localized plastic deformation can be represented by dislocation theory, whereby the nucleus of strain is defined by the normal direction of the axial surface and the direction of long-term motion (Sathiakumar *et al.*, 2020). The direction of long-term motion along the axial surfaces is the difference between the long-term velocity vectors for slip on the ramp and slip on the decollement (Daout *et al.*, 2016).

Discussions. We first consider the case of the double fault-bend fold system (Fig. 3a). We determine the distribution of slip on the ramp and on the two decollements, and of flexural slip over the two axial surfaces through a non-negative least-squares inversion where motion is aligned with the direction of long-term motion (e.g., Barbot *et al.*, 2013). We discretize the model into square patches of 800 m length allowing non-zero along-strike and down-dip slip. Our preferred model explains the observations well, with residuals less than 3.2 mm (Fig. 3e). The coseismic rupture is much elongated, almost entirely confined to the ramp, with along strike rupture propagation from north to south, parallel to the BT. Virtually no slip takes place on the shallower or deeper decollements (Fig. 3a). The model produces up to 15 cm of flexural slip along the deeper axial surface (axial surface 1), concentrated near the nucleation area to the north. There is virtually no flexural slip on the shallow axial surface (axial surface 2). For second case, we consider the case of the fault-propagation fold end-member (Fig. 3f), which we model as a ramp-decollement system with a single active axial surface that follows the hinge of the fault bend. We resolve the spatial distribution of fault slip and flexural slip using the same approach as above. The model reproduces the observations well, with residuals around 3.3 mm (Fig. 3h, j). The coseismic slip is entirely contained on the frontal ramp, with the maximum slip of 50 cm found at 6.5 km depth (Fig. 3f). The inversion reveals around 24 cm of flexural slip extending laterally following the pattern of coseismic slip (Fig. 3f).

The two-models perform almost equally well in terms of data reduction, but coseismic slip seems entirely confined to the ramp. As only the ramp and the lower axial surface exhibit much deformation, Occam's razor and the principle of parsimony suggest that the fault-propagation fold model, with much fewer degrees of freedom, is more meritorious. The amount of flexural slip in the fault-propagation fold model represents 70% of the expected value for coseismic folding. The remaining fraction may occur later in the postseismic period, when folding may also propagate up-dip of the axial surface through the entire sedimentary stack. The 2015 Mw 5.7 Dajal earthquake likely represents the rupture of the frontal section of the BT at the easternmost boundary of the SFT. The rupture can be understood as the seismic activity of the blind ramp of a fault-propagation fold.

We suggest that the Dajal earthquake occurred on the underlying ramp of an even less developed anticlinal structure formed by fault-propagation fold buried under the Miocene and

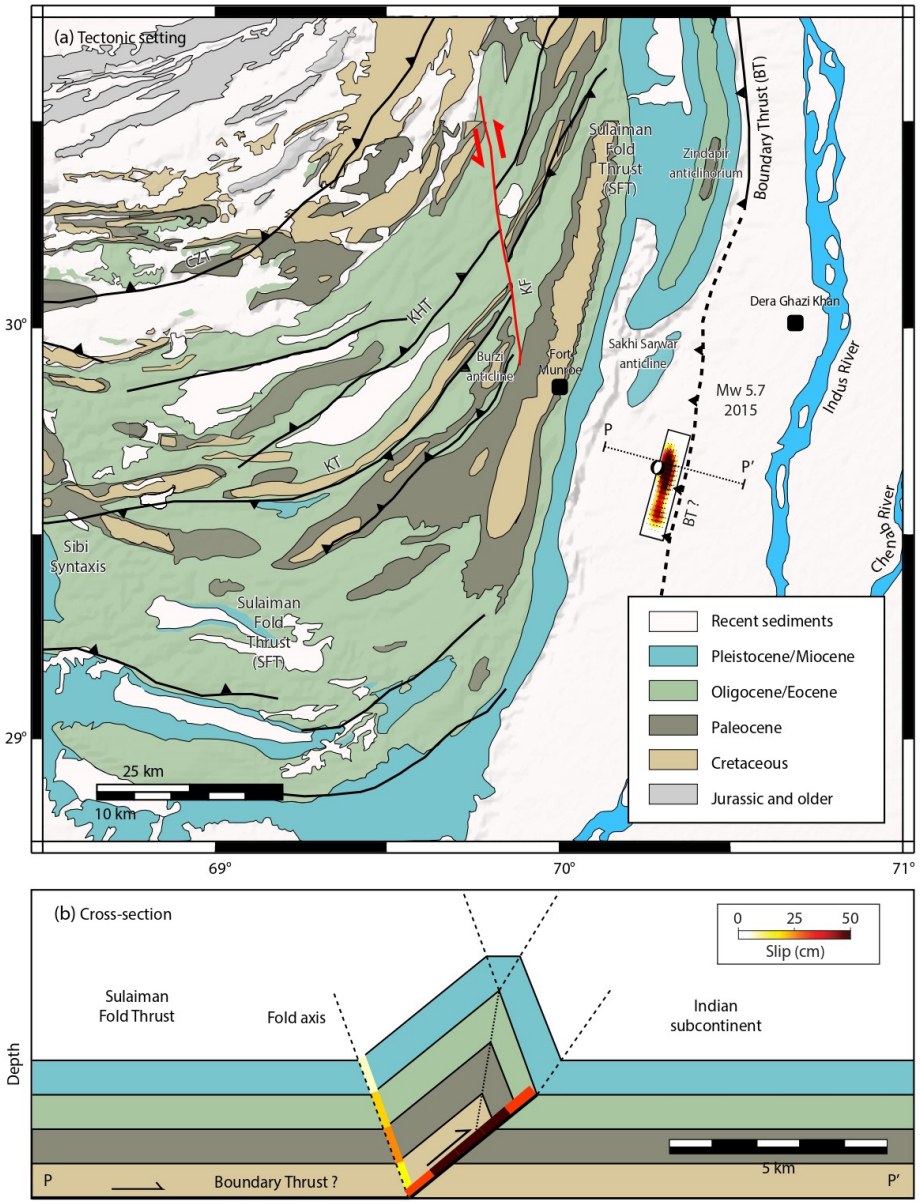


Fig. 3 - Blind frontal ramp of the Eastern Sulaiman Fold Thrust (SFT). a) Extension of the Boundary Thrust south of the Zindapir anticlinorium and the Sakhi Sarwar anticline. The ramp is buried under recent sediments from the Indus River ood plain, 30km east of the Eastern SFT. The dashed line with chevron is the proposed extension of the Boundary Thrust (BT). b) Cross-section across the Dajal earthquake epicentral area with a fault-propagation fold extending from the southern extension of the BT buried under Miocene or younger sediments.

younger sediments of the Indus River floodplain (Fig. 4). Our interpretation is substantiated by nearby seismic reflection profiles (Saif-Ur-Rehman et al., 2019) that suggest the presence of a shallow dipping decollement at a depth of 7 to 9 km. The basal decollement and forward-vergent blind ramp may constitute the eastern termination of the SFT, extending the BT farther south. The prolongation of the BT is compatible with the overall strike and longitude of the Dajal earthquake ramp. The buried BT may thrust the same sequence of Cretaceous-to-recent

sediments that is ubiquitous elsewhere in the SFT. If shortening continues, the anticlinal fold will eventually be exposed, as at the Sakhi Sarwar anticline farther north. It is possible that other thrusts may be found to the west, forming an imbricate structure that can host other earthquakes.

Conclusions

- The 2015 Mw 5.7 Dajal, Pakistan earthquake represents the seismic rupture of a frontal blind ramp of the SFT, presumably as the seismic expression of a fault-propagation fold.
- The earthquake illuminates the possible extension of the BT 30 km south of the Zindapir anticlinorium where it breaks the surface, corresponding to the propagation of the SFT some 30 km east into the Miocene and younger sediments of the Indus River floodplain.
- Despite this short period of observation, flexural slip is tantamount to 70% of the expected value for coseismic folding, indicating strong mechanical coupling and synchronicity between faulting and folding at the time scales of the seismic cycle.

Bibliography

Ambraseys, N., and Bilham, R. (2003). Earthquakes and associated deformation in northern Baluchistan 1892-2001. *Bulletin of the Seismological Society of America*, *93*(4), 1573-1605.

Bagnardi, M., and Hooper, A. (2018). Inversion of surface deformation data for rapid estimates of source parameters and uncertainties: A Bayesian approach. *Geochemistry, Geophysics, Geosystems*, *19*(7), 2194-2211.

Barbot, S., Agram, P., and De Michele, M. (2013). Change of apparent segmentation of the San Andreas fault around Parkfield from space geodetic observations across multiple periods. *Journal of Geophysical Research: Solid Earth*, *118*(12), 6311-6327.

Daout, S., Barbot, S., Peltzer, G., Doin, M. P., Liu, Z., and Jolivet, R. (2016). Constraining the kinematics of metropolitan Los Angeles faults with a slip-partitioning model. *Geophysical Research Letters*, *43*(21), 11-192.

Lai, K. Y., Chen, Y. G., Hung, J. H., Suppe, J., Yue, L. F., and Chen, Y. W. (2006). Surface deformation related to kink-folding above an active fault: Evidence from geomorphic features and co-seismic slips. *Quaternary International*, *147*(1), 44-54.

Mahanjane, E. S., and Franke, D. (2014). The Rovuma Delta deep-water fold-and-thrust belt, offshore Mozambique. *Tectonophysics*, *614*, 91-99.

Okada, Y. (1985). Surface deformation due to shear and tensile faults in a half-space. *Bulletin of the seismological society of America*, *75*(4), 1135-1154.

Pezzo, G., Merryman Boncori, J. P., Atzori, S., Antonioli, A., and Salvi, S. (2014). Deformation of the western Indian Plate boundary: insights from differential and multi-aperture InSAR data inversion for the 2008 Baluchistan (Western Pakistan) seismic sequence. *Geophysical Journal International*, *198*(1), 25-39.

Poblet, J., and Lisle, R. J. (2011). Kinematic evolution and structural styles of fold-and-thrust belts. *Geological Society, London, Special Publications*, *349*(1), 1-24.

Reynolds, K., Copley, A., and Hussain, E. (2015). Evolution and dynamics of a fold-thrust belt: the Sulaiman Range of Pakistan. *Geophysical Journal International*, *201*(2), 683-710.

Saif-Ur-Rehman, K. J., Ding, L., Jadoon, I. A., Baral, U., Qasim, M., and Idrees, M. (2019). Interpretation of the Eastern Sulaiman fold-and-thrust belt, Pakistan: A passive roof duplex. *Journal of Structural Geology*, *126*, 231-244.

Sandwell, D., Mellors, R., Tong, X., Wei, M., and Wessel, P. (2011). Gmtsar: An insar processing system based on generic mapping tools.

Sathiakumar, S., Barbot, S., and Hubbard, J. (2020). Earthquake cycles in fault-bend folds. *Journal of Geophysical Research: Solid Earth*, *125*(8), e2019JB018557.

CALIBRAZIONE DEI COEFFICIENTI DI GARDNER SFRUTTANDO OSSERVAZIONI DEL CAMPO GRAVITAZIONALE: IL CASO STUDIO DELLA PENISOLA ARABA E DELL'ALTOPIANO DELL'IRAN

G. Maurizio[1,2], M. Capponi[2], D. Sampietro[2], C. Braitenberg[1]

[1] Dept. of Mathematics and Geoscience, Trieste University, Trieste, Italy
[2] Geomatics Research & Development srl, Lomazzo, Italy

Introduzione. La stima di un modello 3D di densità crostali di partenza, da usare come riferimento per analisi gravimetriche, è un problema complesso, che viene tipicamente risolto convertendo variazioni di velocità di propagazione delle onde sismiche (disponibili grazie a studi di tomografia sismica) in variazioni di densità. Questa conversione dipende da diversi fattori come, ad esempio, la distribuzione di temperatura e la composizione della litosfera nell'area di studio. Essendo questi fattori tipicamente incogniti, in letteratura sono presenti diversi studi che propongono relazioni empiriche, basate su dati medi, per legare la distribuzione di densità e le variazioni di velocità sismica (e.g. Barton, 1986 oppure Fairhead, 2016). Una delle formule più usate è l'equazione di Gardner (Gardner *et al.,* 1974), utilizzata specialmente nella geofisica di esplorazione per la sua semplicità e rapidità nell'applicazione. In essa le velocità sono legate alle densità attraverso la seguente relazione:

$$\rho = \alpha V_p^{\beta} \tag{1}$$

dove α e β sono due costanti definite empiricamente. Nel loro lavoro, Gardner *et al.* (1974) propongono come valori di α e β rispettivamente 1.74 e 0.25 (supponendo V_p in km/s) sulla base di un elevato numero di campioni di laboratorio e osservazioni di diverse tipologie di rocce. Il risultato che ne deriva è una buona approssimazione media, sulla quale però restano molte incertezze dovute alle variazioni locali di tipologia e stato delle rocce considerate. Per migliorare quest'approssimazione, diversi autori (ad esempio Nwozor *et al.,* 2017) propongono una "localizzazione" dei coefficienti di Gardner basati su campioni specifici dell'area investigata.

L'obiettivo di questo lavoro è quello di testare, su un caso reale, la possibilità di ottimizzare localmente i parametri di Gardner, attraverso lo sfruttamento di osservazioni del campo gravitazionale, con il fine di realizzare, a partire da valori di velocità sismiche, un modello di densità tridimensionale vincolato e affidabile da sfruttare per ulteriori analisi (e.g. inversioni del campo gravitazionale/magnetico).

Il caso studio dell'Iran e della Penisola Araba. Per valutare la possibilità di ottimizzare localmente i parametri di Gardner attraverso l'uso del campo di gravità, abbiamo studiato un primo caso reale, nell'area che comprende la Penisola Araba e l'Altopiano dell'Iran. La prima operazione eseguita è stata la creazione di un volume di velocità, sul quale poter poi applicare l'algoritmo di correzione proposto. Il cubo di velocità considerato si estende da 10°N a 41°N in latitudine e da 36°E a 64°E in longitudine, fino a una profondità di 105 km. La risoluzione spaziale è di 0.25° (circa 27 km) in planimetria e varia tra 1 e 7 km nella direzione verticale. Il modello è stato realizzato unendo i valori di propagazione delle onde sismiche di taglio Vs, disponibili dal lavoro di Kaviani et. al. (2020) con la tomografia globale proposta da Simmons *et. al.* (2015). L'unione dei due modelli è stata effettuata attraverso una procedura di collocazione ai minimi quadrati (si veda e.g. Moritz (1978)). In particolare, la funzione di covarianza del segnale è stata modellata tramite una combinazione lineare di funzioni di Bessel del primo tipo (Sampietro *et al.* (2017), mentre per l'errore d'osservazione è stato considerato un rumore incorrelato con deviazione standard di 0.1 km/s per le velocità derivate da Kaviani e di 0.4 km/s per il modello di Simmons. È stata scelta questa tecnica in modo da poter ottenere insieme al volume di velocità, anche una stima dei relativi errori. Valori di velocità sismica a partire

dal modello globale di Simmons sono stati utilizzati come osservazioni nell'interpolazione esclusivamente per "riempire" eventuali aree estese (ovvero con un raggio maggiore della lunghezza di correlazione) dove il modello di Kaviani presentava assenze di dati. Il risultato è un cubo 3D omogeneo nell'area di interesse con le relative incertezze (Fig. 1).

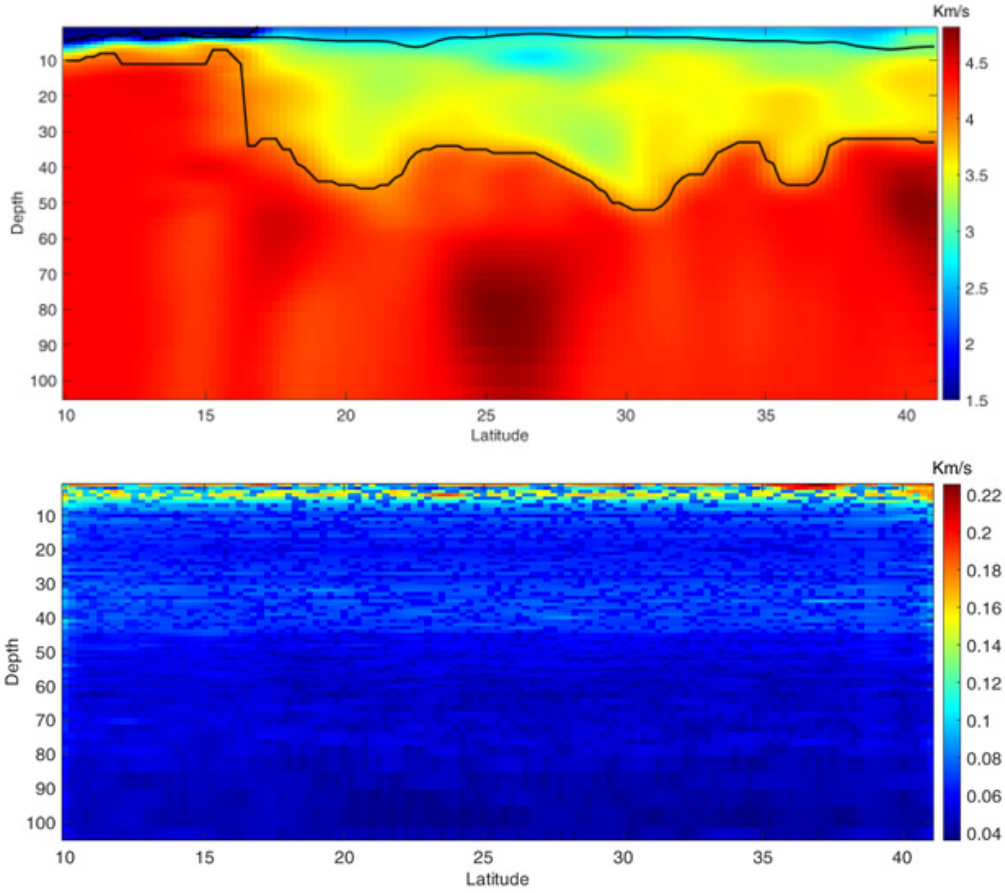


Fig. 1 - Sopra, esempio di sezione verticale di velocità del cubo finale realizzato integrando i valori di *Vs* di Kaviani *et al.*, 2020, con quelli di Simmons *et al.*, 2015. Le linee nere rappresentano gli orizzonti geologici considerati: batimetria, basamento e Moho. Sotto, la stima dell'errore di predizione.

Una volta stimato il cubo di velocità sismiche il modello è stato diviso in quattro parti: acqua, sedimenti, crosta e mantello. In particolare, la profondità della Moho è stata ottenuta utilizzando il gradiente verticale di velocità secondo quanto presentato in Tadiello e Braitenberg (2021). La stima della distribuzione di densità nel mantello è stata ottenuta utilizzando il software Perple_X supponendo una composizione chimica del mantello standard espressa secondo il sistema NCFMAS (Na_2O – CaO – FeO – MgO – Al_2O_3 – SiO_2) presa dal lavoro di Tunini *et al.* (2015), che riprende i valori di Griffin (2009), mentre quella dell'acqua è stata semplicemente fissata a 1020 kg/m^3. Densità di sedimenti e crosta sono state modellizzate tramite l'equazione di Gardner.

In questa analisi preliminare le due coppie di parametri per l'equazione di Gardner (una coppia per i sedimenti ed una per la crosta) sono stati stimate contemporaneamente utilizzando il metodo dei Minimi Quadrati linearizzato e opportunamente regolarizzato con il metodo delle pseudo-osservazioni (Sansò, 1996).

I risultati ottenuti, utilizzando come osservazioni i disturbi di gravità, sintetizzati sul livello del mare a partire dal modello XGM2019e (Zingerle *et al.,* 2020) e ridotto per l'effetto della topografia, dell'acqua e delle variazioni di massa nel mantello, mostrano come la semplice metodologia proposta vada a migliorare notevolmente il modello di distribuzione di densità rispetto a quello calcolato utilizzando i coefficienti standard proposti da Gardner. Le differenze fra i disturbi di gravità osservati e quelli calcolati vengono infatti sensibilmente ridotte, con valori di deviazione standard che passano da circa 180 mGal utilizzando i parametri standard proposti da Gardner et al., a circa 88 mGal utilizzando i parametri approssimati ($\hat{\alpha}$ = 1.744 g s/cm^3 km e $\hat{\beta}$ = 0.244 per i sedimenti, $\hat{\alpha}$ = 1.769 g s/cm^3 km e $\hat{\beta}$ = 0.302 per la crosta cristallina). Nella figura queste differenze sono bene evidenziate, con valori di δg che variano tra il modello standard ed il modello ottimizzato anche di oltre 200 mGal (Fig. 2).

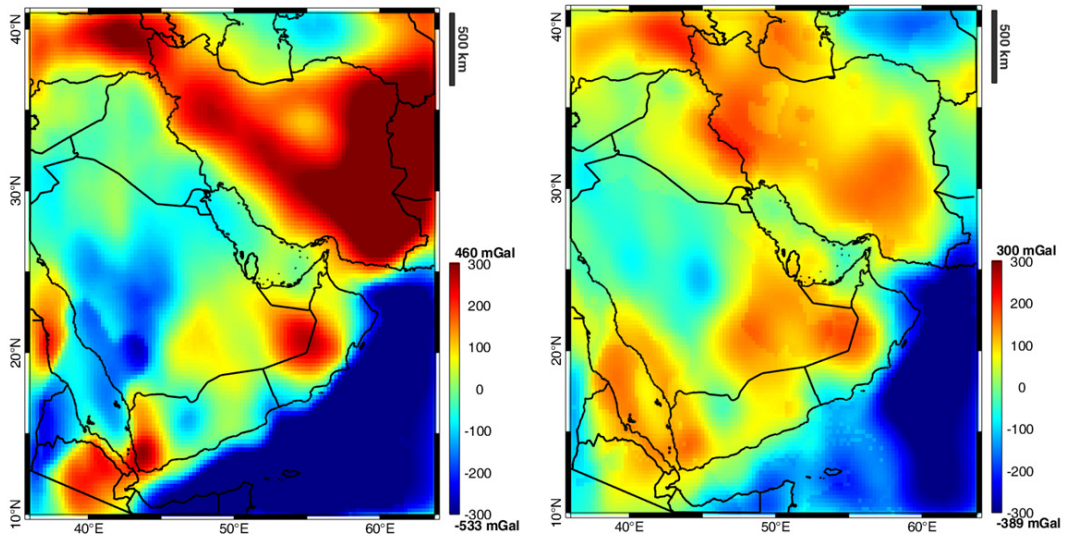


Fig. 2 - Mappe dell'anomalia di Bouguer per la zona analizzata. A sinistra i valori di δg risultante da un modello standard di Gardner, A destra la mappa risultante dall'utilizzo dei parametri stimati.

Conclusioni e Sviluppi Futuri. L'obiettivo del lavoro è stato quello di iniziare a testare la possibilità di utilizzare il campo di gravità per calibrare localmente i coefficienti di Gardner utilizzati nella conversione tra velocità e densità, permettendo quindi di realizzare un modello di densità più affidabile. I primi test effettuati, nel caso studio della Penisola Araba e Altopiano dell'Iran, hanno permesso di dimostrare come sia possibile, anche con metodi speditivi, di migliorare notevolmente il modello di distribuzione di densità derivati dalla tomografia sismica. Questi risultati preliminari sono un buon punto di partenza per procedere in futuro con l'ottimizzazione della stima dei coefficienti α e β mediante l'impiego di metodi Monte-Carlo, migliorando la modellizzazione di crosta e mantello (e.g. andando a valutare differenti composizioni chimiche), e introducendo all'interno dell'algoritmo una più dettagliata osservazione della geologia e geodinamica della zona, come ad esempio l'introduzione di un layer di crosta continentale profonda o l'utilizzo di diversi parametri di Gardner per diversi bacini sedimentari.

Bibliografia

Barton P. J.; 1986: *The relationship between seismic velocity and density in the continental crust—a useful constraint?.* Geophysical Journal International, 87(1), 195-208.

Connolly J. A. D.; 2005: *Computation of phase equilibria by linear programming: A tool for geodynamic modeling and its application to subduction zone decarbonation*, Earth Planet. Sc. Lett., 236, 524–541, https://doi.org/10.1016/j.epsl.2005.04.033, 2005.

Fairhead J. D.; 2016: *Advances in gravity and magnetic processing and interpretation*. EAGE Publications.

Gardner G. H. F., Gardner L. W. and Gregory A. R.; 1974: *Formation velocity and density—The diagnostic basics for stratigraphic traps*. Geophysics, 39(6), 770-780.

Griffin W.L., O'Reilly S.Y., Afonso J.C. and Begg G.; 2009: *The composition and evolution of lithospheric mantle: a re-evaluation and its tectonic implications*, J. Petrol., 50, 1185–1204.

Kaviani A., Paul A., Moradi A., Mai P. M., Pilia S., Boschi L., Rümpker G., Lu Y., Tang Z. and Sandvol E.; 2020: *Crustal and uppermost mantle shear wave velocity structure beneath the Middle East from surface wave tomography.* Geophysical Journal International, 221(2), 1349-1365.

Moritz H.; 1978: *Least-squares collocation.* Reviews of geophysics, 16(3), 421-430.

Nwozor K. K., Onuorah L. O., Onyekuru S. O. and Egbuachor C. J.; 2017: *Calibration of Gardner coefficient for density-velocity relationships of tertiary sediments in Niger Delta Basin*. Journal of Petroleum Exploration and Production Technology, 7(3), 627-635.

Sampietro D., Capponi M., Mansi A. H., Gatti A., Marchetti P. and Sansò F.; 2017: *Space-Wise approach for airborne gravity data modelling*. Journal of geodesy, 91(5), 535-545.

Sansò F.; 1996: *Elementi di teoria della probabilità*. Cittàstudi.

Simmons N. A., Myers S. C., Johannesson G., Matzel E. and Grand S. P.; 2015: *Evidence for long-lived subduction of an ancient tectonic plate beneath the southern Indian Ocean.* Geophys. Res. Lett., 42, 9270-9278, doi:10.1002/2015GL066237.

Tadiello D. and Braitenberg C.; 2021: *Gravity modeling of the Alpine lithosphere affected by magmatism based on seismic tomography*. Solid Earth, 12(2), 539-561.

Tunini L., Jiménez-Munt I., Fernandez M., Vergés J. and Villasenor A.; 2014: *Lithospheric mantle heterogeneities beneath the Zagros Mountains and the Iranian Plateau: a petrological-geophysical study*. Geophysical Journal International, 200(1), 596-614.

Wackernagel H.; 2003: *Multivariate geostatistics: an introuction with applications*. Springer Science & Business Media.

Zingerle P., Pail R., Gruber T. and Oikonomidou, X.; 2020: *The combined global gravity field model XGM2019e*. Journal of Geodesy, 94(7), 1-12.

A GEOLOGICAL REVIEW OF THE GARGANO PROMONTORY (SOUTHERN ITALY) WITH SEISMIC AND GEODETIC DATA

S. Miccolis[1], M.M.C. Carafa[2], M. Filippucci[1], J.P. Merryman Boncori[3], A. Tallarico[1]

[1] Dipartimento di Scienze della Terra e Geoambientali, Università degli Studi di Bari Aldo Moro, Bari, Italia
[2] Sezione di Sismologia e Tettonofisica, Istituto Nazionale di Geofisica e Vulcanologia, L'Aquila, Italia
[3] DTU Space Institute, Technical University of Denmark, DK-2800 Kongens Lyngby, Denmark

Understanding the active tectonic processes is fundamental for mitigating the seismic risk, though the actual limit of applied methodologies. Among the Italian areas still requiring further investigations, the Gargano Promontory (hereafter GP), in Southern Italy, represents a peculiar case. It has been recognized that the GP belongs to the Adriatic plate and that it consists of a carbonate-dolomitic succession with localized internal deformations. It is also known that strong earthquakes struck this area. Recent seismicity characterized by a constant low energy activity confirms the active deformation of the area, but its association with the active faults remains scarcely investigated and still debated. For this reason, we have investigated the GP seismicity through different approaches to increase the seismotectonic understanding of this area.

Relying on OTRIONS local seismic network (Tallarico, 2013), installed by the University of Bari Aldo Moro in cooperation with the National Institute of Geophysics and Volcanology), all the recorded events since 2013 were re-analyzed, providing a new seismic database of 635 microearthquakes used to retrieve focal mechanisms and the actual stress field of the GP (Miccolis *et al.*, 2021). Then, thanks to a collaboration with the Technical University of Denmark, we included in this study the Persistent Scatterers InSAR analysis (Ferretti *et al.*, 2001) to explore possible deformation patterns and observe the area's tectonic signal.

According to the results, a 40 km thick seismogenic layer has been identified with maximum earthquake frequency between 14 and 37 km deep, with prevalent compressive and transpressive kinematics. Moreover, a deep surface trending SW-NE and dipping towards NNW was observed and considered the most likely responsible for the observed seismicity. The integrated use of geodetic survey highlights a general uplift along the whole area, with low to very low rates, and large subsiding sector S of the GP most likely due to the excessive water extraction. However, it was impossible to detect a tectonic signal, which was hidden by a short-term and anthropic signal, and to observe localized displacements along specific structures. These observations confirm the large amount of bulk deformation observed with the GPS, E to the Apennines chain.

References

Ferretti, A., Prati, C., Rocca, F., 2001. *Permanent scatterers in SAR interferometry*. IEEE Trans. Geosci. Remote Sens. 39, 8–20. https://doi.org/10.1109/36.898661

Miccolis, S., Filippucci, M., de Lorenzo, S., Frepoli, A., Pierri, P., Tallarico, A., 2021. *Seismogenic Structure Orientation and Stress Field of the Gargano Promontory (Southern Italy) From Microseismicity Analysis*. Front. Earth Sci. 9, 589332. https://doi.org/10.3389/feart.2021.589332

Tallarico, A., 2013. OTRIONS Project. URL http://www.otrions. uniba.it/

LA SEQUENZA SISMICA DELLA TESSAGLIA (GRECIA CENTRALE) DEL MARZO 2021: CARATTERIZZAZIONE DELLA STRUTTURA CROSTALE MEDIANTE TOMOGRAFIA SISMICA LOCALE

F. Napolitano[1], O. Amoroso[1], V. De Novellis[2,4], G.M. Adinolfi[3], V. Convertito[4], R. De Matteis[3], E. Sansosti[2], R. Caputo[5]

[1] Dipartimento di Fisica "E.R. Caianiello", Università degli Studi di Salerno, Fisciano, Italia
[2] Istituto di Rilevamento Elettromagnetico dell'Ambiente, Consiglio Nazionale delle Ricerche, Napoli, Italia
[3] Dipartimento di Scienze e Tecnologie, Università del Sannio, Benevento, Italia
[4] Istituto Nazionale di Geofisica e Vulcanologia, Osservatorio Vesuviano, Napoli, Italia
[5] Dipartimento di Fisica e Scienze della Terra, Università degli Studi di Ferrara, Ferrara, Italia

Introduzione. Il 3 marzo 2021 alle ore 10:16 UTC nell'area del Nord Tessaglia nella Grecia Centrale a 25 km ONO circa dalla città di Larissa (Fig. 1a), un evento di magnitudo momento M_W 6.3 ha dato inizio ad una sequenza sismica terminata intorno alla metà di aprile dello stesso anno (De Novellis *et al.*, 2021). Oltre al *mainshock*, nei giorni successivi si sono verificati altri cinque eventi di magnitudo momento superiore a 5.0, fortunatamente senza causare decessi o danni seri a cose e persone. Considerando l'intensa sismicità storica e strumentale della Grecia centrale, questa zona della Tessaglia è catalogata come un'area caratterizzata da una sismicità meno frequente rispetto al contesto sismotettonico in cui è localizzata (Caputo, 1995).

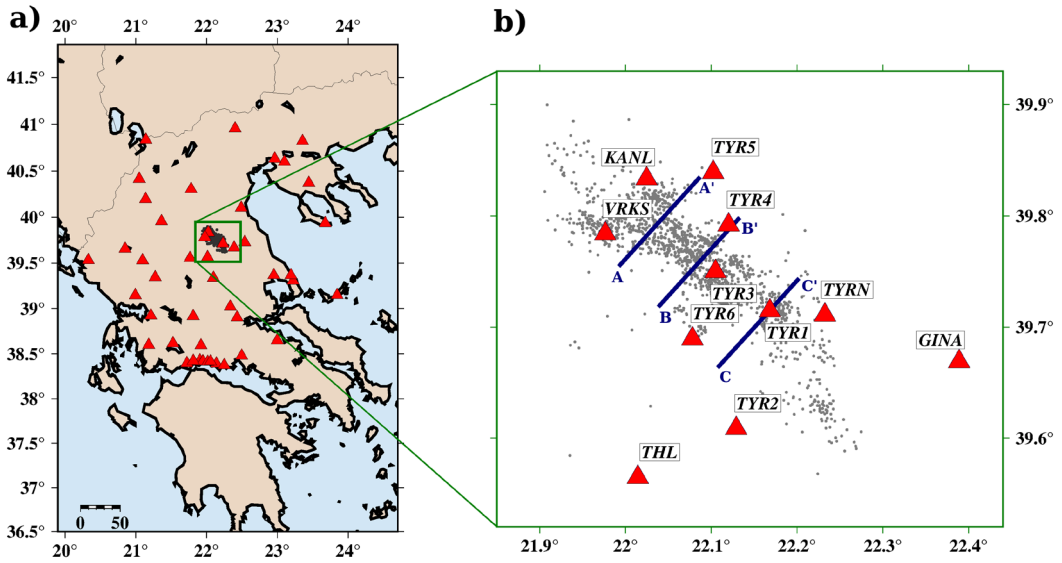


Fig. 1 - a) copertura della rete sismica (triangoli rossi) nell'area della Grecia centrale e sequenza sismica della Tessaglia del marzo 2021 e relativo zoom dell'area di studio (b). I triangoli rossi identificano le stazioni sismiche. I pallini grigi identificano gli eventi sismici rilocalizzati nel modello 3D. I profili AA', BB', CC', indicano le tracce delle sezioni verticali selezionate per mostrare i risultati tomografici.

L'obiettivo del presente lavoro è quello di caratterizzare le proprietà elastiche del volume crostale interessato dalla sequenza sismica e la possibile identificazione delle faglie su cui sono avvenuti i terremoti. Per raggiungere questo obiettivo, abbiamo realizzato una tomografia sismica 3D e la rilocalizzazione dei terremoti della sequenza. Abbiamo innanzitutto effettuato una selezione sul *dataset* iniziale di terremoti disponibili per l'area, sulla base del numero di fasi P ed S alle stazioni installate nell'area epicentrale. Gli eventi selezionati sono stati usati per determinare un modello di velocità 1D specifico per l'area, che è stato utilizzato come modello di partenza per l'inversione tomografica. Le immagini tomografiche in termini di V_p e V_p/V_S e

le localizzazioni dei terremoti ottenute con il nuovo modello, sono state confrontate con le faglie degli eventi principali della sequenza ottenute da De Novellis *et al.* (2021) dall'analisi dei dati InSar. Il confronto tra analisi indipendenti ha permesso di ottenere nuove informazioni più dettagliate circa le strutture tettoniche coinvolte nella sequenza sismica della Tessaglia e potrebbe essere il punto di partenza per una nuova valutazione della pericolosità sismica dell'area.

Dati. Abbiamo usufruito di un catalogo iniziale di 1853 eventi sismici avvenuti tra il 28 febbraio ed il 26 aprile 2021 (M_W 0.2-6.3), localizzati da De Novellis *et al.* (2021) utilizzando un modello di velocità 1D disponibile per l'area (Papadimitriou *et al.*, 2010), e i primi arrivi delle onde P ed S registrati a 116 stazioni (Figura 1a).

Per ottenere un'immagine tomografica accurata del volume crostale interessato dalla sequenza di terremoti, abbiamo selezionato i tempi di primo arrivo P ed S letti ad un massimo di 11 stazioni installate nell'area epicentrale (Fig. 1b). Sebbene la selezione di un'area più contenuta abbia favorito la scelta di una spaziatura tra i nodi dell'inversione tomografica più fitta, permettendo la produzione di immagini tomografiche di dettaglio, di contro il dataset iniziale si riduce a circa 1500 eventi per un totale di 7859 fasi P e 7767 fasi S. È da notare che nella nostra analisi non possiamo considerare i terremoti dei primi tre giorni della crisi sismica. Infatti, a causa della mancanza delle stazioni temporanee, non raggiungiamo un numero sufficiente di primi arrivi P ed S per una localizzazione affidabile degli ipocentri. Di conseguenza, anche gli eventi più forti della sequenza (M_W>5), avvenuti in questi giorni, non saranno considerati nell'analisi.

Metodologia. Per avere un modello tomografico 3D affidabile è necessario disporre di un modello 1D specifico per l'area in esame. Per questa ragione, il primo passaggio è stato la determinazione di un modello di velocità 1D specifico per l'area della sequenza oggetto di studio utilizzando il *software* VELEST (Kissling *et al.*, 1994) considerando un sottoinsieme di 596 eventi estrapolati dal *dataset* iniziale sulla base della qualità del dato e, utilizzando V_p/V_S =1.78 (De Novellis et al., 2021). Tale modello di velocità è stato successivamente utilizzato come modello di partenza per l'inversione tomografica.

L'approccio tomografico utilizzato è di tipo linearizzato e si basa sull'inversione congiunta dei tempi di arrivo delle onde P ed S per la stima del modello di velocità e i parametri ipocentrali dei terremoti (Latorre *et al.*, 2004). Il programma è stato già utilizzato con successo in diverse aree tettoniche, vulcaniche e geotermiche (per esempio Vanorio *et al.*, 2005; Amoroso *et al.*, 2018; Napolitano *et al.*, 2021) e in uno studio per il tracciamento dei fluidi in aree *off-shore* (De Landro *et al.*, 2020). Dopo una fase preliminare in cui sono stati testati e selezionati i migliori parametri che controllano l'inversione, abbiamo ottenuto le immagini tomografiche in termini di V_p, V_S e V_p/V_S. In particolare, i valori di V_p/V_S sono stati ottenuti dal rapporto ad ogni nodo tra i due modelli per le onde P ed S. La velocità, calcolata ai nodi della griglia di inversione spaziati di 4 km nel piano orizzontale ed 1 km in quello verticale, è poi stata rappresentata utilizzando una funzione di interpolazione trilineare su una griglia di passo 0.5 km nelle 3 direzioni. Abbiamo infine effettuato i *checkerboard test* per valutare la risoluzione delle immagini tomografiche.

Risultati e conclusioni. I risultati dell'inversione tomografica, vale a dire modello di velocità 3D per le onde P (da 4.6 a 6.9 km/s), il rapporto V_p/V_S (da 1.5 a 2.1) e le nuove localizzazioni dei terremoti sono mostrate nelle tre sezioni verticali AA', BB' e CC' (Fig. 2). Le sezioni, orientate SW-NE (segmenti blu in Fig. 1b), includono gli ipocentri (pallini grigio scuro in Fig. 2) a ±1000 m rispetto alla posizione della sezione. La parte risolta è racchiusa all'interno della linea grigio scura, ottenuta dai *checkerboard test*. Dalla tomografia si evidenzia un marcato salto di velocità,

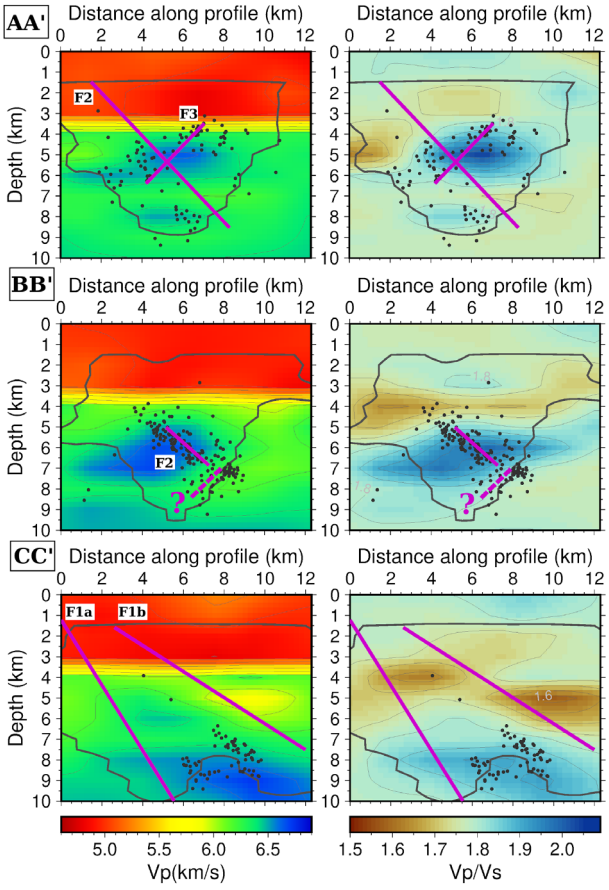


Fig. 2 - Sezioni verticali (AA', BB', CC') disposte in direzione SW-NE (vedi Fig. 1 per orientamento delle sezioni) dei modelli *Vp* e *Vp*/*Vs*. Sulle sezioni, lunghe 12 km e profonde 10 km, sono rappresentati gli ipocentri dei terremoti localizzati nel modello 3D. Le strutture F1a, F1b, F2 ed F3 sono quelle proposte da De Novellis *et al.* (2021). La struttura tratteggiata in viola rappresenta un possibile piano antitetico più profondo non identificato da De Novellis *et al.* (2021). La parte risolta ed interpretabile del modello è racchiusa dalla linea continua e chiusa grigia.

tra 3 e 4 km di profondità, per le onde P che passano da valori di 4.7 km/s a valori dell'ordine di 6.3 km/s. Considerando il più ampio contesto geologico e tettonico dell'area, è ragionevole ritenere che tale contrasto si verifichi in corrispondenza di un'importante zona di taglio a basso angolo che rappresenta lo scollamento basale durante la messa in posto dell'unità di tetto pelagonica, costituita prevalentemente da rocce metamorfiche, sui carbonati di piattaforma di pertinenza dell'unità di Gavrovo. Attualmente, questi ultimi affiorano ampiamente nella finestra tettonica del Monte Olimpo a circa 25 km di distanza dall'area investigata. I modelli di velocità delle onde P evidenziano inoltre un'anomalia di alto V_p (fino a 6.8 km/s) localizzata a 4-6 km di profondità nel settore NW del volume interessato dalla sequenza (Fig.2, sez. AA'), che si approfondisce fino a 8-10 km all'estremità SE (Fig.2, sez. CC'). L'alto V_p produce anomalie di alto V_p/V_S negli stessi volumi.

La distribuzione dei terremoti rilocalizzati nel modello 3D evidenziano una forte complessità delle strutture sismogeniche. Una prima chiara evidenza è la mancanza di terremoti al di sopra di 4 km di profondità, laddove avviene il brusco aumento di velocità delle onde P (sezioni AA', BB', CC' pannelli a sinistra). Gli ipocentri, infatti, sono quasi tutti localizzati in un volume allungato in direzione NW-SE e, similmente alle anomalie di V_p e V_p/V_S, si approfondiscono progressivamente passando da valori intorno a 4-6 km a NW (Fig 2, AA') fino a 8-10 km a SE (Fig. 2, CC'). All'estremità NW del volume sismogenico (Fig. 2, AA') la tomografia evidenzia un'estesa anomalia di alto V_p e alto V_p/V_S dove la sismicità potrebbe essere collegata all'interferenza di due strutture antitetiche similmente a quanto proposto da De Novellis *et al.* (2021; confronta le faglie F2 ed F3 riportate in sezione).

Nella zona centrale (Fig. 2, BB') la tomografia e l'allineamento degli ipocentri evidenziano tra i 4 ed i 7 km di profondità un piano di faglia con inclinazione di 40-50° verso NE, che trova corrispondenza col piano F2 ottenuto dall'analisi DInSAR di De Novellis *et al.* (2021). Nella stessa sezione, i nostri risultati indicano la presenza di un'ulteriore zona di debolezza crostale compresa tra i 7 ed i 10 km di profondità (Fig. 2, BB', linea tratteggiata viola) e con direzione di immersione opposta (SW). Infine, nel settore sudorientale dell'area di indagine (Fig. 2, CC') nuovamente in corrispondenza di una forte anomalia di alto V_p (circa 6.8 km/s) ed alto V_p/V_S (circa 1.9), gli ipocentri degli eventi rilocalizzati nel modello 3D indicano la presenza di due zone di taglio sintetiche caratterizzate da immersione NE e angoli di inclinazione intermedi (35-55°). Tenendo conto della geometria semplificata (planare) e delle incertezze sull'angolo di inclinazione (±10°), le strutture da noi evidenziate potrebbero corrispondere ai piani F1a ed F1b di De Novellis et al. (2021).

In sintesi, l'applicazione della tomografia sismica locale ha permesso di caratterizzare il volume crostale e le strutture sismogeniche coinvolte nella sequenza della Tessaglia del marzo 2021 con un notevole dettaglio, evidenziando l'assenza di ipocentri a profondità inferiori ai 4 km, e la concentrazione di eventi a profondità crescenti da NW (4-6 km) a SE (8-10 km).

I risultati ottenuti confermano la complessità sismotettonica dell'area le cui strutture di taglio si trovano probabilmente in una fase iniziale di sviluppo dovuto alla progressiva crescita verso ovest del Graben di Tyrnavos (Caputo, 1993) per accomodare lo stiramento crostale in atto nella regione egea. L'integrazione delle informazioni sismologiche con quelle geologiche e geodetiche disponibili in letteratura ha favorito un'analisi multidisciplinare permettendo così di dare un contributo alle conoscenze attuali di questo settore relativamente silente della Grecia Centrale dove era stato previsto un *gap* sismico (Caputo, 1995).

Riconoscimenti. Il lavoro è stato sostenuto dal progetto Horizon-2020 CORE, n. 101021746, finanziato dall'Unione Europea, dal progetto PRIN-2017 MATISSE, n. 20177EPPN2, finanziato dal Ministero dell'Istruzione e della Ricerca, e Pianeta Dinamico, Working Earth INGV-MUR project.

Bibliografia

Amoroso O., Festa G., Bruno P. P., D'Auria L., De Landro G., Di Fiore V., ... and Zollo A. (2018). *Integrated tomographic methods for seismic imaging and monitoring of volcanic caldera structures and geothermal areas.* Appl. Geophys., 156, 16-30. doi: 10.1016/j.jappgeo.2017.11.012.

Caputo R.; 1993: Morphotectonics and kinematics along the Tyrnavos Fault, northern Larissa Plain, mainland Greece. *Zeits. Geomorph. N.F.,* Suppl.-Bd. **94**, 167-185.

Caputo R.; 1995: Inference of a seismic gap from geological data: Thessaly (Central Greece) as a case study. *Ann. Geophys., 38(1)*. doi: 10.4401/ag-4127.

De Landro G, Amoroso O, Russo G, Zollo A.; 2020: 4D Travel-Time Tomography as a Tool for Tracking Fluid-Driven Medium Changes in Offshore Oil–Gas Exploitation Areas. Energies, 13(22):5878. doi: 10.3390/en13225878.

De Novellis V., Reale D., Adinolfi G. M., Sansosti E., and Convertito V.; 2021: *Geodetic Model of the March 2021 Thessaly Seismic Sequence Inferred from Seismological and InSAR Data.* Remote Sens., 13(17), 3410, doi: 10.3390/rs13173410.

Kissling E., Ellsworth W. L., Eberhart-Phillips D., and Kradolfer, U.; 1994: *Initial reference models in local earthquake tomography.* J. Geophys. Res. Solid Earth, 99(B10), 19635-19646. doi: 10.1029/93JB03138.

Latorre D., Virieux J., Monfret T., Monteiller V., Vanorio T., Got J. L., and Lyon-Caen H.; 2004: *A new seismic tomography of Aigion area (Gulf of Corinth, Greece) from the 1991 data set.* Geophys. J. Int., 159(3), 1013-1031. doi: 10.1111/j.1365-246X.2004.02412.x.

Napolitano F., Amoroso O., La Rocca M., Gervasi A., Gabrielli S. and Capuano P.; 2021: *Crustal Structure of the Seismogenic Volume of the 2010–2014 Pollino (Italy) Seismic Sequence From 3D P- and S-Wave Tomographic Images.* Front. Earth Sci. 9:735340. doi: 10.3389/feart.2021.735340.

Papadimitriou P., Kaviris G., Karakonstantis A., and Makropoulos K.; 2010: *The Cornet seismological network: 10 years of operation, recorded seismicity and significant applications.* Ann. Geol. Pays Hell., 45, 193-208.

Vanorio T., Virieux J., Capuano P., and Russo G. (2005). *Three-dimensional seismic tomography from P wave and S wave microearthquake travel times and rock physics characterization of the Campi Flegrei Caldera.* J. Geophys. Res. Solid Earth, 110(B3).

HOW DOES SEISMIC ATTENUATION CORRELATE TO RHEOLOGY OF CRUSTAL ROCKS? RESULTS FROM NUMERICAL AND LAB EXPERIMENTS

M.A. Natale Castillo[1], M. Tesauro[1,2], M. Cacace[3], F.X. Thibault Passelegue[4], L. Pimienta[5], M. Violay[4]

[1] University of Trieste, Department of Mathematics and Geosciences, Trieste, Italy
[2] Department of Earth Sciences, Utrecht University, Utrecht, Netherlands
[3] German Research Centre for Geosciences (GFZ) Potsdam, Germany
[4] Ecole Polytechnique Fédérale de Lausanne, Lausanne, Switzerland
[5] Université de Pau et des Pays de l'Adour, Pau, France

Introduction. The crust is characterized by strong thermo-physical heterogeneities, due to lateral and depth variations in the rock structure and composition. Exploration and exploitation of natural resources require a proper understanding of the mechanical rock properties composing this layer, which is in direct contact with the atmosphere and surface waters and thus control the presence and distribution of available natural resources (e.g., water, oil, gas). The rock properties are described by their strength variations within a specific geodynamic context (Burov, 2011). The depth of the transition from the brittle to ductile deformation (BDT) commonly refers to a pressure and temperature range, where rocks deform by an interplay of cracking and crystal plasticity, marking the progressive change in crustal rheology with increasing depth. This transition occurs at a variable depth, depending on the rock's structure, composition, hydrous conditions, and amount and type (compression or extension) of tectonic stress (e.g., Burov, 2011).

The mechanical behaviour of rocks, and in particular their transition from a brittle to a ductile deformation, has been extensively investigated through a vast amount of rheological experiments (e.g., Burgmann and Dresen, 2008), numerical models (e.g., Burov, 2011), and seismicity studies (e.g., Maggi *et al.,* 2000). In this respect, the analyses of seismic wave propagation in high-enthalpy geothermal regions, in presence of (partial) melting can improve our knowledge on physical rocks behaviour and provide an alternative assessment of the BDT. Indeed, viscous rocks deformation, depending on the rock structure, composition, and fluid content, as well as on the in-situ T-P conditions, can be analysed through the study of seismic attenuation, defined as the dissipation of seismic energy as it propagates through the rock medium. Seismic attenuation is usually described in terms of a "quality factor" Q, given by the inverse of the fractional loss of energy per wave cycle. Therefore, the estimation of the seismic quality factor (Q) can be used to quantify the energy loss of seismic waves, which provides an indirect measure of the anelastic behaviour of the Earth's materials. The Q-factor can be mathematically described by an Arrehenius-type equation, in a similar fashion to the viscous rocks deformation. Despite previous studies have discussed the existence of a correlation between seismic attenuation and the onset of viscous deformation in rocks, the sensitivity of this quantitative relationship to background tectono-thermal conditions and varying rock's physical properties have been not yet properly investigated. Some recent studies (e.g., Farina *et al.*, 2019) computed seismic wave properties relying on the Burgers mechanical model. This model, which is able to capture both transient and steady-state (secondary) creep in a consistent way, is described by a combination in series of a Zener and Maxwell model, being characterized by two (short- and long-term) viscosities (Karato, 2008).

In this study, we follow the numerical approach proposed by Farina *et al.* (2019) to compute the seismic quality factors for shear waves (Q_s) for different crustal rocks, under varying temperature and strain rate conditions. We further compare the obtained Q_s depth variations with variations in shear viscosities and computed ductile strength profiles. To this purpose, we chose two sialic rocks (granite and quartzite), under hydrated and anhydrous conditions and three mafic rocks (diabase, OPX and CPX), under anhydrous conditions only. In addition, we compute strength envelopes for all crustal rocks, temperature, and strain rate conditions. The comparison of the obtained results enables us to quantify the sensitivity of the seismic

attenuation and strength distribution on the input parameters and therefore to describe in a quantitative manner the correlation between computed Q_s reduction (i.e. seismic attenuation increase) and depth, as induced by the resolved ductile deformation. In addition, we have performed triaxial lab experiments, while monitoring ultrasonic P-waves, on a sample of Carrara marble, at ambient temperature and 180 MPa confining pressure, in order to constrain the energy loss variation at the BDT.

Method. As in previous studies (e.g., Farina *et al.*, 2019), we estimate Q_s through the frequency dependent shear modulus of the rock, according to the Burgers mechanical model. The shear viscosity (h_s), needed to calculate the shear modulus, is obtained by modelling viscous flow of the rocks, according to a power-law creep (Goetze and Evans, 1979), computed for seven different rock rheologies. We compute the differential stress using two different geotherms and three fixed values of strain rate (10^{-13} s^{-1}, 10^{-15} s^{-1}, and $10^{-17}s^{-1}$, respectively), consistent with global estimates, based on horizontal geodetic velocities (Kreemer *et al.*, 2014). The η_s is then computed as an effective viscosity, considering the relationship between the deviatoric stress and strain rate invariants.

The two geotherms (named '*warm*' and '*cold*' geotherm, respectively), used to compute h_s, reflect the possible thermal conditions of an old tectonically stable (intracratonic) and young, recently (re)activated area and are obtained with a resolution of 1 km up to a depth of 40 km, following the iterative method of Hasterock and Chapman (2011). We use surface heat flow (*SHF*) values of 50 mWm^{-2} and 80 mWm^{-2}, which can be considered as representative of the two end-member tectonic conditions. We assume a linear decrease in the concentration of the radiogenic heat from the surface to the bottom of the crust (e.g., Hasterock and Chapman, 2011), defining two ranges of values (from 2.1 to 0.1 mWm^{-3} and from 3.0 to 0.2 mWm^{-3}, respectively). The thermal conductivity is assumed to linearly increase with depth and we define a range between 1.5 and 3.5 $Wm^{-1}K^{-1}$, considering that sialic rocks have on average a thermal conductivity lower than ultramafic rocks (e.g., Goes *et al.*, 2020). The calculated geotherm presents a decrease in thermal gradients with depth, reflecting the decrease in the concentration of radiogenic heat input.

According to Farina *et al.* (2019), we use the Burgers mechanical model augmented with the Gassmann model to describe the effects of seismic wave's amplitude loss in wet and dry crustal rock rheologies, respectively. Since the viscoelastic modulus (and the viscoelastic compliance) of the system is a complex number, it can be demonstrated that the attenuation expressed as Q^{-1}, is equal to the ratio between the imaginary and real component of the modulus, named the "loss modulus" and "storage modulus", respectively. The ratio between the real and imaginary part of the squared shear complex velocities gives the shear seismic quality factor. Finally, we compute the yield strength envelopes (YSEs) by using the Byerlee's law (Byerlee, 1978) to approximate brittle conditions, while power-law dislocation creep (Goetze and Evams, 1979), describing ductile deformation, is estimated for all tested rheologies.

Results. An example of the yield strength envelopes among the seven selected rheologies, together with computed depth variations of h_s, Q_s, and Q_s reduction is displayed in Figs. 1 and 2 respectively. The Q_s reduction has been computed as the percentage of the complementary of the ratio between the Q_s value, obtained at each depth, and the maximum value of Q_s at the surface. Furthermore, we compute the mean of Q_s and h_s, between values obtained at the BDT depth for each strength envelope.

Among the tested rheologies of the sialic rocks, the dry granite is the stiffest, being characterized by the greatest BDT depth (up to a maximum of 19 km, Fig. 1A) and highest values of yield strength at the BDT (up to a maximum of 1000 MPa, Fig. 1A). The other sialic rheologies show similar strength profiles and BDT depths, due to their similar response,

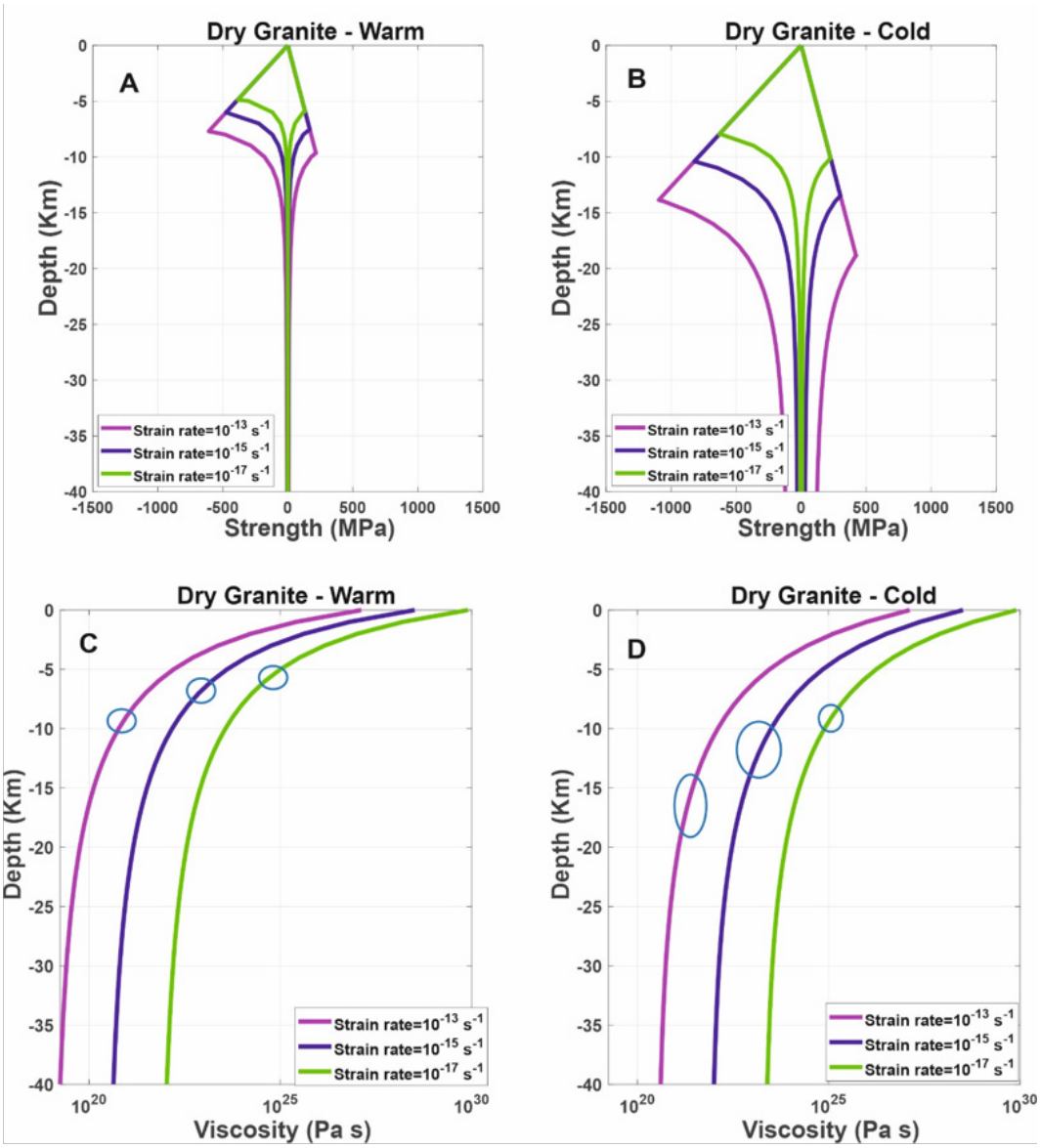


Fig. 1 - Results of the numerical tests on dry granite rheology: (A-B) strength (MPa) and (C-D) viscosity (Pa s) variation with depth, using three different values of strain rate and the (A and C) *'warm'* and (B and D) *'cold'* geotherm as input parameters. Light blue ellipses show the range of the BDT depth. See main text for further explanations.

expressed in term of strength variations, to the input temperatures and strain rate. We can further notice that the ranges of the depth to the BDT tend to increase for the '*cold*' geotherm and highest strain rate values (Fig. 1B), while the BDT temperature is more sensitive to the input strain rate and varies within a relatively narrow range.

Despite the differences in the strength envelopes, related to the change of the input parameters, we found that the mean values of the effective viscosity at the depth of the BDT remains almost constant for the same strain rate value. An increase by two orders of magnitude in strain rate results in approximately the same amount of decrease in the mean viscosity at the BDT (Figs. 1C-D). At the same depth, the mean value in the reduction of Q_s

shows a direct proportionality with the imposed strain rate values, while it seems to be less affected by changes in the other input parameters (Figs. 2C-D). Therefore, reduction in Q_s at the BDT is characterized by a specific order of magnitude for each strain rate value (10^{-12}, 10^{-10}, and 10^{-8} % for strain rate equal to 10^{-17}, 10^{-15}, and 10^{-13} s^{-1}, respectively).

As expected, below the BDT the yield strength reduces to negligible values (< 10 MPa) faster for hydrated rheology and when the '*warm*' geotherm and lowest strain rate value are used (Figs. 2A). In a similar fashion, also the viscosity values and reduction in Q_s at the base of the crust vary by some orders of magnitudes, depending on the input parameters.

On the other hand, mafic rheologies deform prevalently in brittle conditions and their

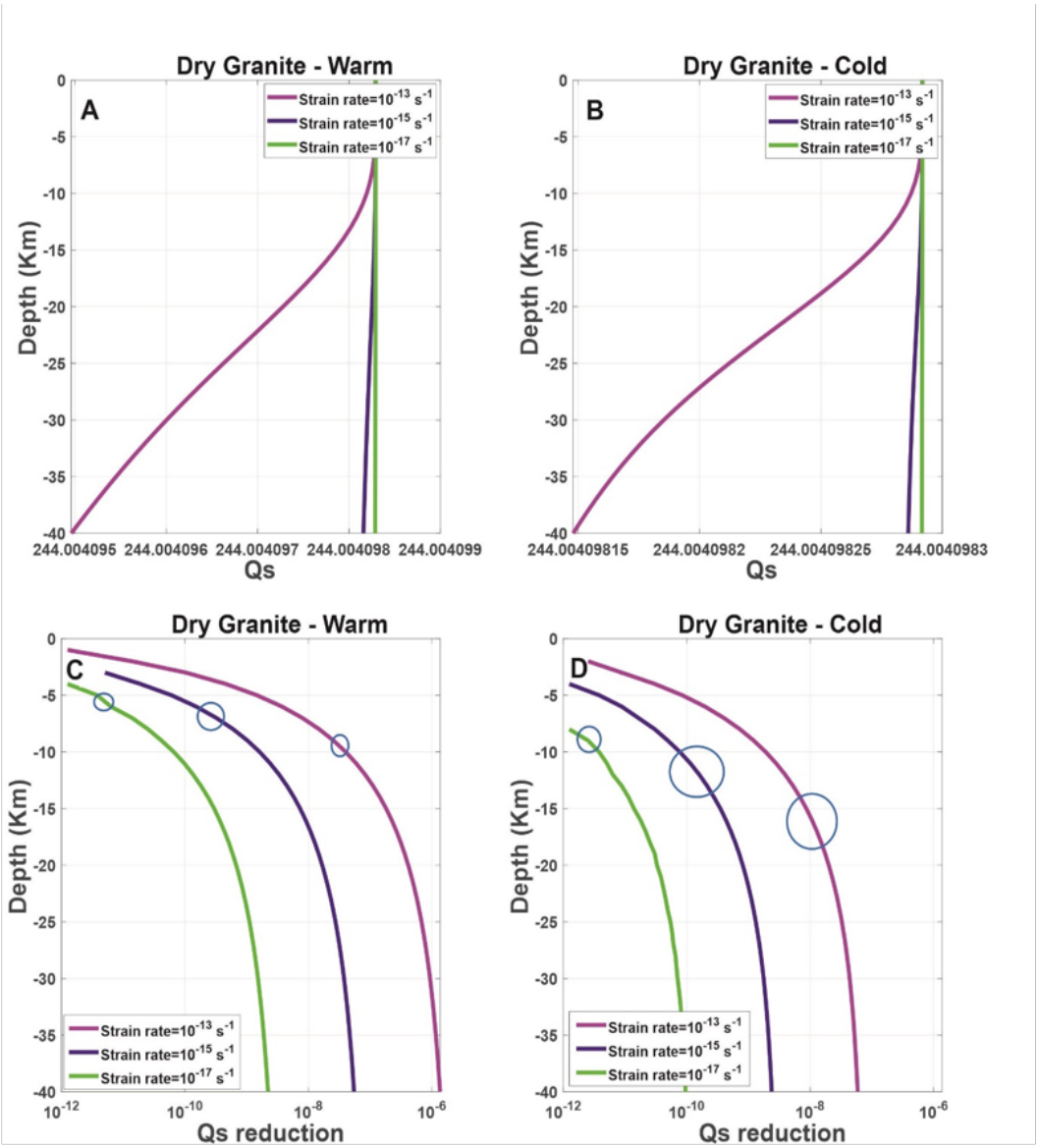


Fig. 2 - Results of the numerical tests on dry granite rheology: (A-B) Q_s and (C-D) Q_s reduction (%) variation with depth, using three different values of strain rate and the (A and C) *'warm'* and (B and D) *'cold'* geotherm as input parameters. Light blue ellipses show the range of the BDT depth. See main text for further explanations.

strength envelopes are characterized by maxima of the order of 1000 MPa associated to deeper BDT depths (usually > 10 km). In addition, when we consider the '*cold*' geotherm, a strain rate value of 10^{-15} s^{-1} or greater, and we assume extensional stress conditions, the selected mafic rocks deform only in brittle conditions. We could further observe that the depths to the BDT, when occur, and the intercepting temperatures span a range greater than those obtained for sialic rocks. In the same way, the mean viscosity values at the BDT are approximately one order of magnitude greater than those associated to the sialic rheologies. However, we demonstrated that, variations in Q_s, at the BDT depth are less affected by the input rheology and geotherm than variations in the rock's viscosity. The implication is that,

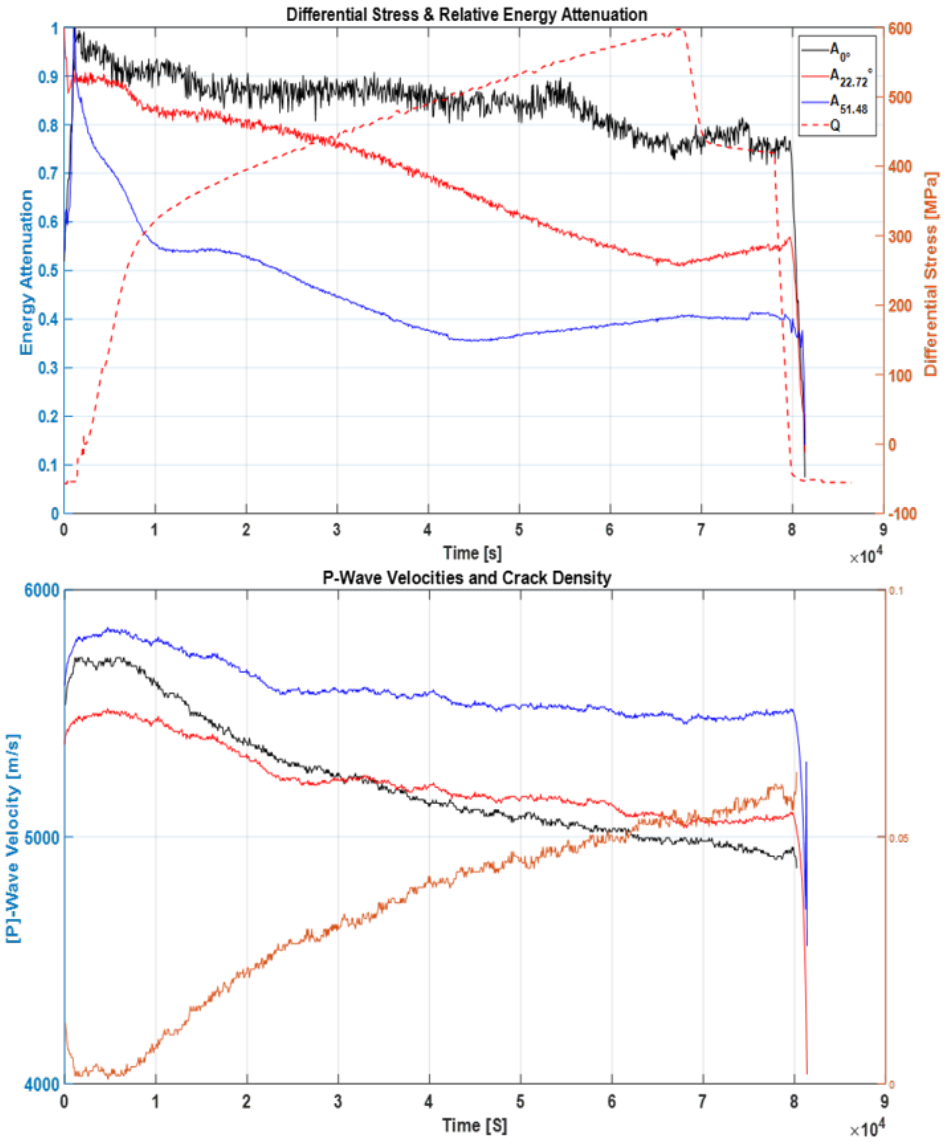


Fig. 3 - Mechanical and acoustic results from triaxial experiment on Carrara Marble deformed up to 180 MPa confining pressure. (A) Dashed line shows the differential stress derived from the mechanical experiment. Continuous lines represent energy of attenuation obtained from acoustic measurements in three angles, 0° (black), 22.72° (red), and 51.48° (blue). Brown line represents crack density variation throughout the experiment.

by knowing the average strain rate of an area, variations in Q_s can provide a useful attribute to identify the domain within the crust, where the deformation transitions from a brittle dominated to a more ductile deformation mode. In addition, this extrapolation is subjected to less uncertainties than other proxies in terms of variations of *P-T* conditions and flow law parameters.

The results of the lab experiments show that the BDT transition is characterized by the increase of crack-density with a progressive rate reduction. At the same time, both the seismic velocity and energy significantly decrease during the first phase of deformation (brittle regime) and tend towards an asymptotic value, when the sample approaches the ductile deformation (Fig. 3). We interpret the absence of an increase of energy loss at the BDT, as due to the persistent effect of the microfracturation. The last one usually accompanies the deformation mechanisms that occur at the BDT (e.g., pressure solution, twinning), masking the expected increase of attenuation at the beginning of the ductile conditions. This is a matter that still needs to be investigated. To this purpose, we should also consider that in the field fracturing causes an increase in the bulk rock permeability, favoring the influx of fluids, and precipitation of minerals (e.g., phyllosilicate), having a much weaker rheology than the rock matrix (e.g., Collettini *et al.*, 2019). Therefore, the *BDT* should rather identify a broader zone of finite thickness, in which both frictional and viscous deformation mechanisms are active, rather than a specific depth level.

References

Bürgmann R., Dresen G., 2008. *Rheology of the Lower Crust and Upper Mantle: Evidence from Rock Mechanics, Geodesy, and Field Observations*. Annu. Rev. Earth Planet. Sci. 36, 531–567.

Burov, E.B., 2011. *Rheology and strength of the lithosphere*. Mar. Pet. Geol. 28, 1402-1443.

Byerlee J., 1978. *Friction of Rocks.* In: Byerlee J.D., Wyss M. (eds) Rock Friction and Earthquake Prediction. Contributions to Current Research in Geophysics (CCRG) 6. Birkhäuser, Basel.

Collettini C., *et al.*, 2019. *Beyond Byerlee friction, weak faults and implications for slip behavior.* Earth Planet. Sci. Lett., 519, 245–263.

Farina, B., *et al.*, 2019. *Seismic properties in conductive and convective hot and super-hot geothermal systems.* Geothermics 82, 16-33.

Goes, S. *et al.*, 2020. *Continental lithospheric temperatures: A review.* Phys. Earth Planet. Int. 306, 106509.

Goetze, C., B. Evans, 1979. *Stress and temperature in the bending lithosphere as constrained by experimental rock mechanics*. Geophys. J. R. Astron. Soc. 59, 463–478.

Hasterok, D., Chapman, D.., 2011. *Heat production and geotherms for the continental lithosphere*. Earth Planet. Sci. Lett. 307, 59-70.

Karato, S. 2008. *Deformation of Earth Materials: An Introduction to the Rheology of Solid Earth.* Cambridge: Cambridge University Press.

Kreemer, *et al.*, 2014. *A geodetic plate motion and global strain rate model.* Geochem. Geophys. Geosyst., 15, 3849–3889.

Maggi, A., *et al.*, 2000. *A re-assessment of focal depth distributions in southern Iran, the Tien Shan and northern India: do earthquakes occur in the continental mantle?* Geophys. J. Int 143, 629-661.

POST-RIFT THERMAL SUBSIDENCE: SHOULD WE ACCOUNT FOR THE LATERAL HEAT TRANSFER? A NUMERICAL EXPERIMENT IN PALEO-BATHYMETRY RECONSTRUCTION

A. Pastorutti[1], M. Tesauro[1,2], C. Braitenberg[1], F. Colleoni[3], L. De Santis[3], M. Busetti[3]

[1] Dept. of Mathematics and Geoscience, Trieste University, Trieste, Italy
[2] University of Utrecht, Utrecht, Netherlands
[3] National Institute of Oceanography and Applied Geophysics - OGS, Sgonico, Italy

Assessing how past topographies and bathymetries evolved provides a critical constrain in paleo-climatic reconstruction. The available direct observations of the geologic record of elevation changes, e.g. from deep-drilling campaigns, are hindered by erosion, sedimentation, and the superposition of tectonic processes - including the lithospheric response to loads (sedimentary infills, water, and ice), the ongoing tectonic movements, dynamic topography, and thermal subsidence. Through data collection and/or modelling of vertical movements due to these concurrent phenomena, the changes in bathymetry and topography can be reconstructed through time - each of the involved terms is accounted for cumulatively. This procedure, implemented through iterative de-compacting and removal of overlying sediments layers, is referred to as "backtracking".

Among these terms, thermal subsidence describes the vertical contraction of the lithosphere due to post-rift cooling. The model of McKenzie (1978) provides a simple and effective analytical description of the subsidence, under the assumptions that rifting is instantaneous and heat transfer occurs only through vertical conduction. It has been shown that a range of finite extension durations can be modelled as instantaneous - the smaller the stretching factor, the longer the extensional phase that can be modelled as instantaneous, with acceptable omission respect to a time-evolving rift model. The 1-D conduction hypothesis, however, is likely to introduce non-negligible discrepancies: first, significant horizontal temperature gradients can be expected to develop in the directions normal to the extensional axis, resulting in deviations from vertical conduction; second, subsidence results in mass movement and consequent heat transfer, due to solid advection.

Therefore, we set up a 2-D thermophysical model of the lithosphere undergoing cooling, through conduction and advection, thickening and deformation. This allowed us to assess the amount of omitted subsidence, due to the 1-D conduction approximation, and its sensitivity to different parameter combinations (e.g. crust-mantle density, thermal diffusion and expansion parameters, stretching factor). In addition, it enabled defining a tentative criterion to deem the 1-D analytical model acceptable (under a range of conditions), in a similar way as it is done for the extension duration.

We implement this, using the open source Underworld2 modelling code (Mansour *et al.*, 2020), which relies on the Lagrangian integration point finite element approach (Moresi *et al.*, 2003) and provides a Python API to construct, run, and visualize the output of geodynamic models.

Our ultimate aim is to integrate the subsidence output of our numerical model in the comprehensive backtracking procedure of the open source software PALEOSTRIP (Colleoni *et al.*, 2021), replacing the 1-D thermal subsidence term and assessing the effect of including lateral heat transfer on the overall result.

Since thermophysical modelling comes at the cost of increased computational effort, we also propose an alternative approach to integrate 2-D thermal subsidence in PALEOSTRIP, based on an empirical fit on a set of numerical experiments. The benchmark data we rely on consists in the ANTOSTRAT data atlas (Brancolini *et al.*, 1995), using the depth of the mid-Miocene unconformity as the target of the backtracking procedure. In this region, located at the northwestern end of the West Antarctic Rift System, extension occurred in two main

episodes: a regional thinning associated with the breakup of New Zealand and Australia from Antarctica in the Cretaceous, and more focused extensional episodes during the Cenozoic, with the locus of extension moving progressively from east to the west.

References:

Brancolini, G., Busetti, M., Marchetti, A., De Santis, L., Zanolla, C., Cooper, A. K., 1995. *Seismic stratigraphic atlas of the Ross Sea, Antarctica*. In: Geology and seismic stratigraphy of the Antarctic margin, Antarctic Research series, edited by: Cooper, A. K., Barker, P., and Brancolini, G., vol. 68, 271–286. doi: 10.1029/AR068.

Colleoni, F., De Santis, L., Pochini, E., Forlin, E., Geletti, R., Brancatelli, G., Tesauro, M., Busetti, M., Braitenberg, C., 2021. *PALEOSTRIPv1.0 – a user-friendly 3D backtracking software to reconstruct paleo-bathymetries.* Geoscientific Model Development, 14(8), 5285–5305. doi:10.5194/gmd-14-5285-2021.

Mansour, J., Giordani, J., Moresi, L., Beucher, R., Kaluza, O., Velic, M., Farrington, R., Quenette, S., Beall, A., 2020. *Underworld2: Python Geodynamics Modelling for Desktop, HPC and Cloud*. Journal of Open Source Software, 5(47), 1797, doi:10.21105/joss.01797.

McKenzie, D. (1978). *Some remarks on the development of sedimentary basins*. Earth and Planetary Science Letters, 40(1), 25–32. doi:10.1016/0012-821X(78)90071-7.

Moresi, L., Dufour, F., Mühlhaus, H.-B. (2003). *A Lagrangian integration point finite element method for large deformation modeling of viscoelastic geomaterials*. Journal of Computational Physics, 184(2), 476–497. doi:10.1016/S0021-9991(02)00031-1.

CRUSTAL STRUCTURES OF THE ZAGROS MOUNTAINS COLLISION BELT AND THE IRANIAN PLATEAU FROM A COMBINATION OF ISOSTATIC, SEISMIC AND GRAVIMETRIC OBSERVATIONS

T. Pivetta, C. Braitenberg, A. Pastorutti, M. Tesauro

Dipartimento di Matematica e Geoscienze, Università di Trieste, Italia.

The Zagros Mountains belt is the result of the collision between the Arabian and Eurasian plates, after the consumption of the Neotethys ocean during the subduction process. The Zagros orogen is composed by a series of parallel thrusts NE-SW trending which extends for about 2000 km (Tunini *et al.*, 2014). The collision process has led to a complex crustal configuration with the juxtaposition of different terranes, from old metamorphic crustal rocks, to sedimentary and ophiolitic rocks typical of the marine and oceanic environment. Furthermore, the subduction process caused also the emplacement in the Iranian Plateau of a widespread tertiary volcanic and magmatic complex, the Urumieh Dokhtar Magmatic Arc.

Understanding the actual crustal configuration by estimating the Moho depths, the presence of eventual sub-surface magmatic bodies and underplating is a prerequisite for a consistent geological interpretation of the surface structures and topographic evolution in time.

In this study we take advantage of the recent satellite global gravity data in combination with topography, crustal velocity profiles (Gvirtzmann *et al.*, 2016) and seismic tomography (Kaviani *et al.*, 2020) to constrain the present crustal structure and the isostatic state of the area. In particular, we isolated the crustal root effect from the Bouguer anomalies by employing a statistical analysis (Pivetta e Braitenberg, 2020) between gravity and topographic loads. The crustal root effect is then inverted in terms of crustal undulation and an optimal density contrast at the Moho level is estimated by fitting the sparse seismic observations.

The Bouguer signals unrelated to Moho undulations, reflect density variations mostly depending on the surface geologic structures. The crustal model, defined by the Moho thickness and density contrasts, is discussed in terms of a final isostatic equilibrium in response to internal and topographic loading. This information is relevant for understanding the topography evolution.

Acknowledgements. Funding for this research was provided by MIUR (Italian Ministry of University and Research) PRIN funds –PRIN2017 project entitled “Intraplate deformation, magmatism and topographic evolution of a diffuse collisional belt: Insights into the geodynamics of the Arabia-Eurasia collisional zones”.

References

Gvirtzman Z., Faccenna C., and Becker, T. W.; 2016: *Isostasy, flexure, and dynamic topography*. Tectonophysics, **683**, 255–271, https://doi.org/10.1016/j.tecto.2016.05.041.

Kaviani, A., Paul A., Moradi A., Mai P. M., Pilia S., Boschi L., Rümpker G., Lu Y., Tang Z. and Sandvol, E.; 2020: *Crustal and uppermost mantle shear wave velocity structure beneath the Middle East from surface wave tomography*. Geophys. J. Int., **221**, 1349–1365, https://doi.org/10.1093/gji/ggaa075.

Pivetta T. and Braitenberg C.; 2020: *Sensitivity of gravity and topography regressions to earth and planetary structures*. Tectonophysics, **774**, 228299, https://doi.org/10.1016/j.tecto.2019.228299.

Tunini L., Jiménez-Munt I., Fernandez M., Vergés J., and Villaseñor A., 2014: *Lithospheric mantle heterogeneities beneath the Zagros Mountains and the Iranian Plateau: a petrological-geophysical study*. Geophys. J. Int., 200, 596–614, https://doi.org/10.1093/gji/ggu418.

GEOPHYSICAL AND GEOLOGICAL INVESTIGATION IN THE AREA NE OF MENFI (SOUTH-WESTERN SICILY)

S. Bongiovanni[1], R. Martorana[1], A. D'Alessandro[2], C. Bignami[2], A. Canzoneri[1], A. Sulli[1]

[1] Università di Palermo, Dipartimento di Scienze della Terra e del Mare, Palermo, Italy
[2] Istituto Nazionale di Geofisica e Vulcanologia, Osservatorio Nazionale Terremoti, Rome, Italy

Introduction. Following the seismic events that occurred from January to June 1968 in the Belice Valley, numerous geological studies have been conducted by various authors in south-western Sicily. Before these seismic events, which partially or totally destroyed some inhabited centers, the area was regarded as aseismic.

Within this area we identified numerous morphostructural features consisting of open fractures, which compose a single main feature with WSW-ENE trend. Two other features, orthogonal to these, have NNW-SSE trend. They are visible on Google Earth frames from 2014 to 2017 and they were subsequently filled by human activities. In 2019 July a seismic swarm has again affected the area and following this event a reopening of the fractures occurred.

The aim of this study is to understand the role of seismicity in the transformation of the territory, which may have created trenches and/or fractures of both tectonic and landslide nature.

The study area. The study area is located in southwestern Sicily, precisely NE and 5 km away from Menfi (Fig. 1).

The territory is characterized by a hilly landscape. The topographic features are closely linked to the combination of endogenous (tectonics, lithology) and exogenous (climate, vegetation) factors which allow to identify two sectors characterized by different evolution (Fig. 1):

a) the sector to the south of the main morphostructural feature, where the "Bertolino" quarry is located, characterized by Pleistocene silty-sandy clays. The slope is constantly evolving due to the erosive action of rainwater and the accumulation of erosion products;
b) the sector including the area of the morphostructural features, characterized by soils with a lithoid consistency (marly limestone, calcarenites). In this area, the erosive action is less incisive.

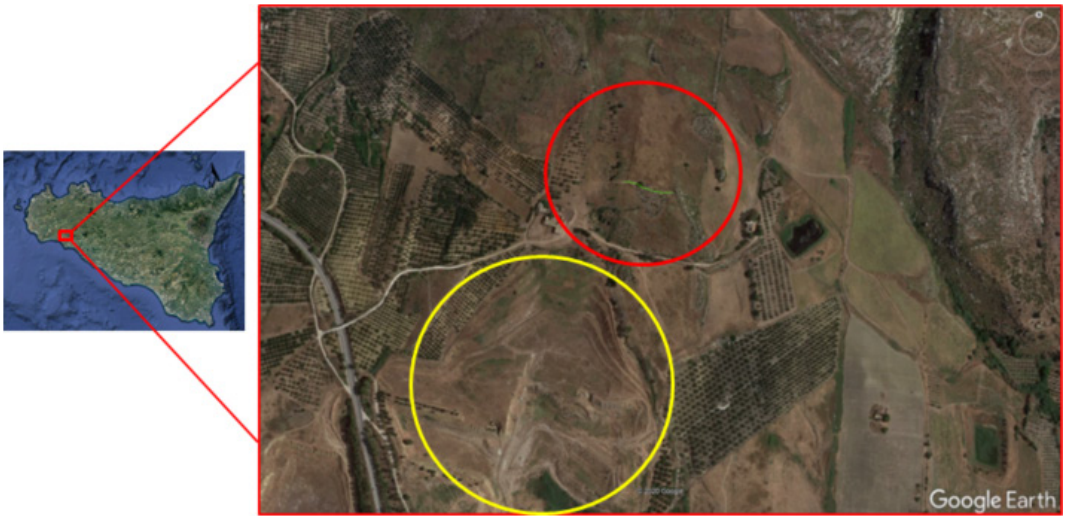


Fig. 1 - Location of the study area. Yellow circle: area where the "Bertolino" quarry is located; red circle: area in which the morphostructural features are present; green lines: main morphostructural features.

Materials and methods. The characterization of the morphostructural features was carried out with a multidisciplinary approach, by using the following techniques: geophysical investigations such as Multichannel Analysis of Surface Waves (MASW) surveys and microtremor recordings, particle size and morphological analysis of soil samples, morphological analysis by observation in situ and through Google Earth, and analysis of the displacement of the earth's surface using satellite interferometry technique (INSAR).

45 microtremor measurements (Fig. 2a) were carried out using Tromino® and these were analyzed with the HVSR technique (Nakamura, 1989; Bonnefoy-Claudet et al., 2006) and processed with the "GRILLA" software. A MASW acquisition (Fig. 2a) was also considered. This survey, consisting of a spreading with 12 geophones, intergeophonic distance of 2.5 m and offset of 5m, was processed using the winMASW® software.

In order to observe the displacements of the earth's surface and the ground deformation, the SBAS (Small Baseline Subset) interferometric technique was used (Ferretti *et al.*, 2007; Pepe and Sansoti, 2005). 91 satellite images, captured by the Sentinel 1-A satellite (both of the ascending and descending orbits) in the time interval from 9/10/2016 to 9/10/2019, were processed using ENVI 5.4 and SARscape 5.4.1 software.

Particle size analysis was performed on 22 soil samples, according to the protocols (Boggero *et al.*, 2011) (Fig. 2b). Approximately 100 grains were isolated from each sample and observed under a light microscope for morphoscopic analysis (Powers, 1952).

The morphological analysis was carried out through preliminary observation of images extrapolated from the historical imagery of Google Earth. Only images from 2014 were taken into consideration because the previous images have a poor resolution. Subsequently, the observation was made in situ at different periods of the year and the dimensions of the open fractures were measured.



Fig. 2 - a) Location of microtremor measurements., red line: MASW location; green lines: main morphostructural features; b) location of soil sampling.

Data interpretation and discussion. In the study area evidence suggests that the reopening of the fractures is connected to the seismic events that occurred in July 2019.

The Google Earth morphological analysis shows that until the end of 2018, the fracture is not open. From the in situ investigations, following the seismic swarm of July 2019, instead it becomes open again (in Fig. 3a an example of one of the fractures). We therefore hypothesized that the reopening of the fracture is a seismic-induced ground movement. The size and depth of these fractures supporting this hypothesis, considering that they remain almost the same from August 2019 to January 2020. In fact, in this period, strong rain events occurred but they did not cause significant changes. Therefore, the infiltration of rainwater was not charged as the cause. Sand samples were taken along the main fracture and have been analyzed in the

laboratory. Furthermore, the morphoscopic analyses evidenced quartz grains of clear marine origin and therefore cannot be current continental deposits.

These sands, in addition to being aligned along the fracture and limited in circular shapes, are found in correspondence of depressed areas with respect to the surrounding morphology. Based on these data, we hypothesize that these sands come from the subsoil. The uprising of these sands could be a signal of a seismic-induced structure and could be due to the fluidification of the soil linked to the seismic shaking and / or to the uprising of sandy material due to density difference caused by compression.

From the seismostratigraphic section, obtained from the MASW and HVSR inversions and joint-interpretation, an abrupt slope break of layers is noted (Fig. 3b). Two contributing causes have been hypothesized for this slope variation:

1: An inherited morphology and therefore a paleo-structure that produces unconformity between the first layer and the underlying one;
2: The presence of a discontinuity in the subsoil that is not visible on the surface.

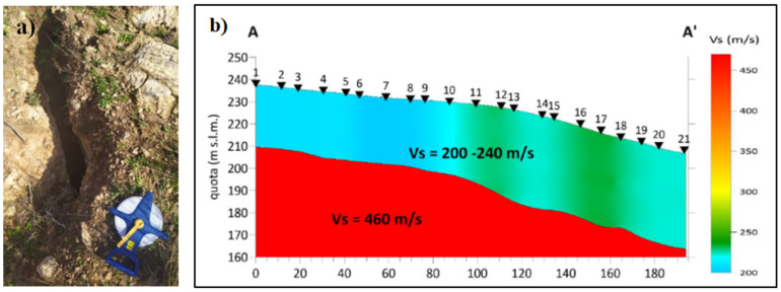


Fig. 3 - a) Example of one of the fractures; b) Seismostratigraphic section.

The multi-temporal interferometric analysis show excessive displacement velocities. These results were not considered reliable as, with the values obtained, there should be much larger fractures than those observed in situ. The unreliability of the products is due to a limitation of the interferometric technique, or the difficulty of operating in a predominantly natural area.

Conclusion. This multidisciplinary study suggests that the genesis of open fractures in the study area is directly or indirectly related to the seismic activity. Each single technique used highlighted elements that, in order to be proven, had to be compared with all the results.

Evidence of gravitational phenomena, absent in the official Italian hydrogeological database (P.A.I.), were observed, which should be considered in assessing the hazard of the area. Furthermore, the different seismic responses of the area upstream and downstream of the main morphostructural feature should be taken into consideration for any engineering works to be carried out within the area.

References

Boggero A., Zaupa S. and Guarneri I.; 2011: *Protocollo di campionamento ed analisi granulometrica di sedimenti lacustri.* Progetto LIFE+ 2008 ENV/IT/000413 INHABIT. Report CNR-ISE 2011, 14 pp.

Bonnefoy-Claudet S., Cotton F. and Bard P-Y.; 2006: *The nature of noise wavefield and its applications for site effects studies. A literature review*. Earth-Science reviews, vol. 79., pp. 205-227.

Ferretti A., Monti-Guarneri A., Prati C. and Rocca F.; 2007: *InSAR Principles: Guidelines for SAR Intrferometry Processing and Interpretation.* ESA Publications, TM-19. ISBN: 92-9092-233-8.

Nakamura Y.; 1989: *A method for dynamic characteristics estimation of subsurface usig microtremor on the ground surface.* Quaterly report Railway Tech. Res. Inst., Vol. 30, n.1, ISSN: 0033-9008.

Pepe A. and Sansoti E.; 2005: *On the generation of ERS/ENVISAT DInSAR time-series via the SBAS technique.* Iee Geoscience and remote sensing letters, vol.2, n.3, pp. 265-269.

Powers M. C.; 1953: *A new roundness scale for sedimentary particles*. Journal of Sedimentary Petrology, Vol. 23, n. 2., pp. 117-119.

MULTIPHYSICS FINITE ELEMENT MODELLING OF SOLFATARA HYDROTHERMAL SYSTEM

R. Castaldo[1], A. Barone[1], G. Chiodini[2], G. Gola[3], G. Solaro[1], P. Tizzani[1]

[1] National Research Council (CNR), Institute for the Electromagnetic Sensing of the Environment (IREA), Naples, Italy
[2] National Institute of Geophysics and Volcanology (INGV), Bologna, Italy
[3] National Research Council (CNR), Institute for Geosciences and Earth Resources (IGG), Pisa, Italy

In volcanic environments, fluids play a key role in controlling and governing the evolution of magmatic processes and eruptions. The high permeable volcanic rocks are readily infiltrated by meteoric water that may encounter fluids rising up from deep magma feeding systems, thus developing shallow hydrothermal systems. The reliable imaging of fluid storages and the accurate tracking of their movements within the crust are therefore critical in evaluating the nature and likelihood of future natural/man-induced earthquake or volcanic activity and their relative hazard monitoring and assessment.

In Campi Flegrei caldera, the Solfatara crater was formed at ~4.2 ka during the third epoch of caldera activity. It is a 0.5×0.6 km sub-rectangular depression, whose geometry is controlled by N40-50W and N50E trending fault systems. Nowadays, this crater is characterized by intense diffuse degassing and fumarolic emissions; specifically, a series of small uplift episodes and seismic swarms mainly occurred at Solfatara from 1984 to 2006, during the subsidence of whole caldera. These earthquakes are likely to be associated with a buried cavity filled with a water-vapour mixture at poor gas-volume fractions. In this scenario, we built up a 2D model by using the geological and geophysical data and fluid reservoir parameters (Fig. 1).

This information is used within a multiphysics Finite Element Model that allows for a description of time-dependent mixed conductive/convective thermal model. The model time evolution starts 4.2 ka: we first perform the preliminary stationary conductive thermal model

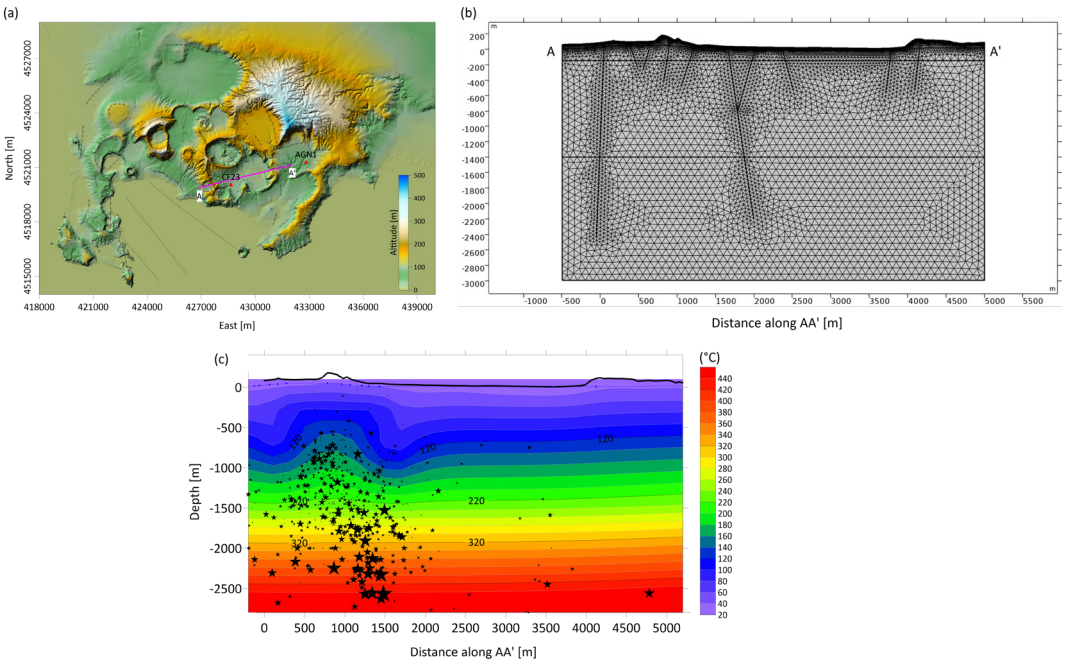


Fig. 1 - (a) DEM of Campi Flegrei caldera with the location of AA' model trace. (b) Geometry and triangular mesh of the FE model. The segments represent the domains limits and the considered fractures. (c) Conductive/convective thermal model results after 4.2 ka. The natural seismicity occurred between 2005 and 2020 is superimposed.

of the upper crust; then, we simulate in the time dependent study, by exploiting the Darcy law for the monophasic fluid circulation, the activation of a convective cell below the Solfatara crater, where a high number of earthquakes occurs.

The final goal of this study is the modelling of the inferred fluid circulation and the stress variations inside the crater, and the comparison with the recorded seismicity. These activities have been carried out in the framework of the FLUIDs PRIN project, which aims at the characterization and modeling of fluids migration at different scales (https://www.prinfluids.it/).

DESIGN AND REALIZATION OF A MEASUREMENT NODE FOR GRAVIMETRIC APPLICATIONS

J.J. Jiménez[1,3], A. Albano[2], V. Carbone[2], F. Lamonaca[1]

[1] Università della Calabria, Dipartimento di Ingegneria Informatica, Modellistica, Elettronica e Sistemistica
[2] Università della Calabria, Dipartimento di Fisica
[3] Universidad San Francisco de Quito, Instituto de Micro y Nanoelectrónica

Abstract. This paper focuses on the design and realization of a gravitational measurement node in Cosenza, southern Italy. This zone is of great interest from a geological point of view, as it is situated on the Calabrian arc, a zone known for its high seismic and volcanic activity. Tidal variations are utilized by researchers since comparing present and past records which can help detect seismic or volcanic anomalies which could lead to the timely detection of a possible natural disaster. This measurement node monitors tidal variations via gravitational alterations utilizing a LaCoste e Romberg Model G-1089 gravimeter. To further complete the gravitational node, measurements of correlated parameters of the gravitational force are also monitored. These parameters are surface inclination, barometric pressure, and temperature. This paper starts by discussing the importance of tidal variation monitoring in the region. A description of the technical features of the diverse hardware elements is followed by an explanation of the onsite implementation of the gravitational node. Finally, the acquired data is confronted with theorical values confirming the effectiveness of the proposed measurement node.

Introduction. Southern Italy, in particular Calabria, is an area of geophysical interest due to its high seismic and volcanic activity. With several active volcanoes from the Calabrian arc such as Etna, Stromboli Vulcano and Paranea in vicinity of highly populated areas, unexpected natural disasters could bring a lot of human and material loss. Furthermore, underground volcanoes such as Marsili, a submerged volcano located near the coast of Calabria, could induce a tsunami in case of an eruptive event, or in case of a collapse of the volcanic structure. One way to be prepared for a natural disaster is tidal analysis. Constant comparison of records of the amplitudes and phases of the tidal signals with models of the gravitational records are useful to timely detect volcanic and seismic actions (Albano, 2013). For this reason, monitoring of tidal variations via gravitational nodes are important, and this research focuses on creating a gravitational station in the area. In 2011 a clinogravimetric station started operating at Università della Calabria. However, due to the lack of proper maintenance the station stopped acquiring data in 2016. After obtaining positive results from an initial assessment of the equipment in November 2011, the station was completely reactivated by the end of March 2022. In this paper it is proposed a measurement node for gravimetric applications designed to guaranty a multiparametric acquisition of the tidal signals and of the magnitude influencing their acquisition.

Design of the Measurement Node. The gravitational station implemented is in charge of monitoring several parameters that have effects on the gravitational accelerations, according to models presented in (Albano, 2015). The parameters of interest for this station are: gravitational acceleration, inclination on the N-S and E-W axis, temperature and barometric pressure.

For the gravitational acceleration, the gravimeter G-1089 from LaCoste & Romberg was utilized. It has an operating range of 7000 mGal, with a resolution of 0.005 mGal and an accuracy of 0.04 mGal and contains three analog outputs (LaCoste, n/d). Two of them to measure the central and lateral levels and one for the feedback channel that gives information about the gravitational acceleration. For its correct operation, the gravimeter must maintain an internal temperature of 55.85 °C ± 0.04 °C. A polyurethane box was placed outside of the device to



Fig. 1 - Scheme of Connection of the Gravitational Node.

isolate it from external temperature variations, and it is additionally connected to a battery to maintain the device in operation and at the right temperature in the case of a power failure.

For the inclination, the tiltmeter Model 714 from Applied Geomechanics was utilized. It is capable of measurements with an angular range of ±8000.0 µrad, a resolution of 0.1 µrad and a linearity of 2% within the full span. Dual signals are used to measure the inclination in each of the two axes. Additionally, it measures the ambient temperature and its power supply (Applied, n/d).

As an acquisition system, the Agilent 34970A data acquisition and switching unit was utilized for this measurement node. With 6.5 digits of resolutions (22 bits) and a 0.004% accuracy for measuring DC voltage and the ability to monitor up to 120 channels with expansion cards, it proves to be adequate for this project (Agilent, n/d). After initial testing with more than 500 measurements of 8 different analog channels, the reading delay is 7.99 ms with σ = 2.06 ms for consecutive channels within the same scanning list and 140.0 ms with σ = 49.4 ms when changing from a scanning list to another one.

All this equipment was then calibrated on site according to manufacturers guidance to ensure the correct operation. The measurement node is located on Cube 41 B at Universitá della Calabria in Arcavacata di Rende, Cosenza. An underground / basement location was chosen to avoid noise from natural vibrations of the building that occur at higher floors and to avoid the disturbance of bystanders. Lastly, atmospheric information is supplemented from a metrological station located in the same university at Cube 41 C (within 20 m from the measurement node) via internet for the processing of the obtained data. Figure 1 shows the connection scheme of the diverse systems, while figure 2 shows images of the onsite implementation.

On the software side of the measurement node, custom software was developed in LabView that is in charge of: sampling the 8 signals with a sampling period of 5s, convert time



Fig. 2 - On-site Implementation of Gravitational Node.

and data into Universal Time Coordinates (UTC), communicate with the switching unit via SCPI directives, scaling the magnitudes and storing the measurements.

Experimental Results. After the onsite implementation and calibration of the equipment, gravitational variations were started to be detected due to tidal variations. Processing of the data, such as removing outliers and applying a 3rd degree polynomial approximation with a 512-point window. Figure 3 shows the experimental results obtained in the period between the 10th of April 2022 to the 21st of April 2022. The data plotted in red represent the theoretical gravitational acceleration while the data plotted in green represent the acquired data.

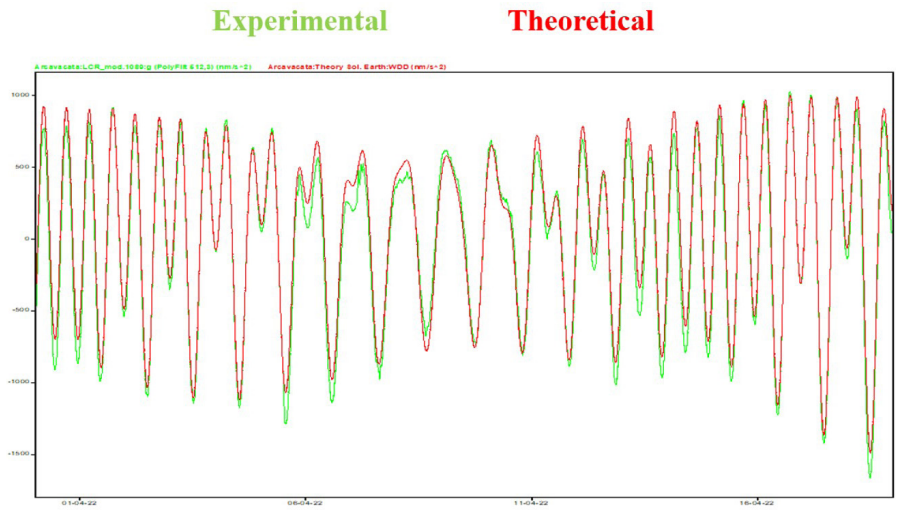


Fig. 3 - Theoretical vs Experimental Gravitational Force due to Tidal Variations.

Conclusions. The main objective of this research was to design and implement a measurement node for gravitational applications in Arcavacata di Rende, a small city in the north of Calabria. The preliminary obtained results proved to follow the theoretical tidal variations in the month of April 2022, which allows us to conclude that the gravitational node is working properly, and that the data obtained by it can be utilized in upcoming research projects.

In particular, we plan to apply data analysis techniques designed for nonlinear and non-stationary phenomena, as for example wavelets and the Empirical Mode Decomposition, to tidal time series, in order to investigate the properties of the deviation between empirical acquisition and theoretical models. This will allow us to investigate the physical properties of perturbation to the usual tides.

References

Agilent: *Agilent Technologies. Agilent 34970A Data Acquisition and Switching Unit Manual.* <https://www.avionteq.com/document/34901A-specification-sheet.pdf.>

Albano A., Corrado G.; 2013: *Five years of continuous gravity observations in the Neapolitan volcanic area*. Bollettino di Geofisica Teorica ed Applicata, 54, 1-21, DOI 10.4430/bgta0065.

Albano A., Corrado G., Gervasi A. and Guerra I.; 2015: *Continuous gravity and tilt observations in an active geodynamic area of southern Italy: the Calabrian Arc system.* Bollettino di Geofisica Teorica ed Applicata, 56, 1-18, DOI 10.4430/bgta0133

Applied Geomechanics: *700-Series Platform and Surface Mount Tiltmeters. User Manual.* <http://docs.eao.hawaii.edu/JCMT/elec/inclinometer/002/700Series_B88_1016F.pdf >

LaCoste and Romberg: *A New Generation Dynamic Gravity Meter Manual.* <http://www.lacosteromberg.com/pdf/airSea.pdf.>

ROLE OF CRUSTAL FLUIDS AND THERMO-MECHANICAL STRUCTURE FOR LOWER CRUSTAL SEISMICITY: THE GARGANO PROMONTORY (SOUTHERN ITALY)

A. Lavecchia[1,2], M. Filippucci[1], A. Tallarico[1], G. Selvaggi[2], G. Cecere[2], S. Cloetingh[3]

[1] Dipartimento di Scienze della Terra e Geoambientali, Università di Bari - Aldo Moro, Bari, Italy
[2] Istituto Nazionale di Geofisica e Vulcanologia, Centro Nazionale Terremoti, Rome, Italy
[3] Department of Earth Sciences, Utrecht University, Utrecht, The Netherlands

Several regions around the globe are characterized by a seismically active lower crust, at depths where lithological and thermal conditions suggest stress release by ductile flow. The Gargano Promontory (GP, southern Italy) is an example where a recently installed seismic network has recorded an intense seismic activity at depths between 20 and 30 km, i.e. in the lower crust. The GP is located in proximity of the Gargano-Dubrovnik lineament, a seismogenic zone separating the central and southern Adriatic basins. These two basins constitute sites of sediments accumulation since Tertiary times. Another important basin in the region is represented by the Apennine foredeep, that includes the Candelaro area. We analyze the possible mechanisms controlling the distribution of seismicity in the GP to identify the factors that make the lower crust seismically active. To this aim, we construct a thermo-rheological model of a layered continental crust, calibrated on the basis of geometrical, lithological and thermal constraints. The model takes into account a multiphase crustal lithology, the presence of fluids in the crystalline basement, lateral variations of the geotherm and the stress field. The numerical simulations show that the presence of fluids is a key factor controlling the cluster of seismicity in the lower crust. Moreover, the presence of water in the upper crystalline basement and sedimentary cover provides a plausible explanation for upper crustal seismicity in a zone of very high heat flow SW of the GP. The distribution of the seismicity is probably affected by the composition of the crystalline basement, with mafic bodies injected into the crust during the Paleocene magmatic phase that affected the Mediterranean region. In addition, the presence of deep, undetected structures may represent regions of fluid accumulation, therefore leading to clustering of the earthquakes. Based on our findings, we hypothesize that the presence of hydrous diapiric upwelling(s) in the upper mantle can feed a deep fluid circulation system, inducing lower crustal seismicity.

A MULTIPARAMETRIC AND MULTILAYER APPROACH TO STUDY THE PREPARATION PHASE OF LARGE EARTHQUAKE OCCURRED IN JUNE 15 2019, M7.2 IN KERMADEC ISLANDS (NEW ZEALAND)

M. Orlando[1], A. De Santis[1], L. Perrone[1], M. Calcara[1], S.A. Campuzano[2], G. Cianchini[1], S. D'Arcangelo[1,3], D. Di Mauro[1], D. Marchetti[4], A. Nardi[1], A. Piscini[1], D. Sabbagh[1], M. Soldani[1]

[1] Istituto Nazionale di Geofisica e Vulcanologia (INGV), Rome, Italy
[2] Instituto de Geociencias IGEO, Madrid, Spain
[3] Complutense University, Madrid, Spain
[4] Jilin University, Changchun, China

On June 15, 2019 a large M7.2 earthquake occurred in the Kermadec Islands (New Zealand) as the result of shallow reverse faulting movement within the Tonga-Kermadec subduction zone.

This work deals with a multiparametric and multilayer approach to study the earthquake related processes that occurred before the nucleation of the same seismic event.

We focused our analyses on seismic data by earthquake catalogues, atmospheric data by climatological archives and ionospheric data from ground to space, mainly from satellite, in order to disclose the possible Lithosphere-Atmosphere-Ionosphere Coupling (LAIC) effects.

In particular, for the ionospheric investigations, we analyze and compare the Global Navigation Satellite System (GNSS) receivers network and in-situ observations from space thanks to both Swarm constellation (ESA) and the China Seismo-Electromagnetic Satellite - CSES-01 (CNSA - ASI) dedicated to search for possible ionospheric disturbances before medium-large earthquakes.

This multiparametric analysis demonstrates an acceleration of geosystemic perturbations during a coupling between the Lithosphere-Atmosphere-Ionosphere (LAIC) before the large Kermandec 2019 seismic event, and finds that it is fundamental to understand better the LAIC in the occasion of complex phenomena such as earthquakes.

A RECENT SEISMIC COUPLING ESTIMATION FOR THE AEGEAN - ANATOLIAN REGION

M. Palano[1], F. Sparacino[1], B.G. Galuzzi[2], M. Segou[3], C. Chiarabba[4]

[1] Istituto Nazionale di Geofisica e Vulcanologia, Osservatorio Etneo - Sezione di Catania, Catania, Italy
[2] Department of Biotechnology and Biosciences, University of Milan-Bicocca, Milan, Italy
[3] British Geological Survey, The Lyell Center, Research Avenue South, EH14 4AP, Edinburgh, UK
[4] Istituto Nazionale di Geofisica e Vulcanologia, Osservatorio Nazionale Terremoti, Roma, Italy

We provide a novel estimation of the seismic coupling for the Aegean-Anatolian region by taking advantage of extensive seismic and geodetic datasets. Our approach estimates moment-rates and seismic coupling on 2° x 2° square cells with a 75% overlap and does not require an a priori zonation.

To compute input parameters for the coupling estimation, such as the maximum expected magnitude, the seismogenic thickness and the coefficients of the frequency-magnitude distribution relation, we compiled a set of historical and instrumental catalogs from existing seismicity records as well as an extensive combination of recent GNSS velocities integrated with recent literature solutions. Finally, the seismic coupling estimation enables characterizing the crustal deformation modality (seismic versus aseismic), as well as identifying potential seismic cycle gaps over the entire region, thereby providing additional constraints on modern seismic hazard estimates. In particular, seismic coupling is low (<35%) or intermediate (35% - 70%) in most of the study area, while the Karliova triple junction, a N-S-oriented belt along the boundary between western and central Anatolia, and the southeastern Peloponnese are fully coupled, suggesting a full seismic release of the measured deformation budget. Intermediate values of seismic coupling are observed for the eastern and central segments of the Northern and Eastern Anatolian Fault zones, where however the time period since the last large magnitude earthquakes clearly raises the possibility of impending earthquakes. Intermediate values of seismic coupling are also observed for part of the Hellenic volcanic arc, the Kefalonia Transform Fault and the Corinth gulf active faults. Here, considering the available historical records, these intermediate coupling values indicate either significant aseismic deformation or catalog incompleteness. A broad seismic gap is evidenced along the Hellenic subduction zone, because of the reduced coupling and the absence of ~M8 earthquakes in the last 700 years, at least. We conclude that in most of the central Aegean Sea aseismic deformation prevails, as suggested by the small value of coupling and the modest seismic release over the last millennium.

PARAMETRIC STUDY OF THE EFFECTS OF MICRO-CONTINENTS COLLISION IN AN OCEANIC SUBDUCTION SYSTEM BY 2D NUMERICAL SIMULATIONS

A. Regorda[1], M. Roda[1], C. Thieulot[2]

[1] Dipartimento di Scienze della Terra 'A. Desio', Universita degli Studi di Milano, Milano, Italy
[2] Department of Earth Sciences, Utrecht University, Utrecht, the Netherlands

Heterogeneities of the oceanic crust are very diffuse and considered to represent remnants of extinct arcs, abandoned spreading ridges, detached and submerged continental fragments, anomalous volcanic piles, and uplifted oceanic crust (Stein and Ben-Avraham, 2007; Vogt and Gerya, 2014). Here, we simulated the collision of micro-continents characterized by different sizes in an oceanic subduction with a continental overriding plate, to verify their effects on the thermo-mechanical evolution of the subduction systems.

Our results show that the subduction of a micro-continent has an impact on the thermal state of the subduction complex, the larger the micro-continent, the higher the temperature increase in the slab. From the mechanical point of view, larger micro-continents cause higher forces at the trench during the collision, with a consequent retreat of the trench toward the overriding plate. Consequently, for larger micro-continents the upper plate records higher compressive strain. In addition, if the micro-continent is larger than 100 km there is a jump of the subduction to the back of the micro-continent with the development of a new subduction zone. Lastly, a strain partition can be observed in the subducted micro-continent, from portions highly deformed to portions where the accumulated strain is almost zero.

References

M. Stein and Z. Ben-Avraham. Mechanisms of continental crust growth. 2007.

K. Vogt and T. V. Gerya. From oceanic plateaus to allochthonous terranes: Numerical modelling. Gondwana Research, 25(2):494–508, 2014. ISSN 1342-937X. doi:10.1016/j.gr.2012.11.002.1

THE 1968 BELICE SEISMIC SEQUENCE (SOUTH ITALY): NEW RESULTS FROM DIGITIZED ANALOG DATA

S. Scolaro[1], B. Orecchio[1], J. Batlló[2], D. Stich[3,4], G. Neri[1], D. Presti[1], C. Totaro[1]

[1] Department of Mathematics, Computer Sciences, Physics, and Earth Sciences, University of Messina, Messina, Italy
[2] Institut Cartogràfic i Geològic de Catalunya, Barcelona, Spain
[3] Departamento de Física Teórica y del Cosmos, Universidad de Granada, Granada, Spain
[4] Instituto Andaluz de Geofísica, Universidad de Granada, Granada, Spain

The 1968 Belice seismic sequence represents the strongest seismic activity recorded in historical times in western Sicily, along a segment of the Nubia-Eurasia convergent margin previously considered as seismically quiescent (see, e.g., Michetti *et al.*, 1995). The sequence lasted from about January to June 1968 and the primitive seismic network operating at the time in Sicily recorded more than 350 earthquakes (Valle, 1969). Seismic activity mainly occurred in the month of January when, according to the Parametric Catalogue of Italian Earthquakes (CPTI15; Rovida *et al.*, 2020), six shocks with magnitude greater than 5 struck the Belice Valley. We present the first estimates of moment tensor solutions and probabilistic nonlinear hypocenter locations for the most energetic earthquakes occurred during the January-June 1968 Belice sequence (Orecchio *et al.*, 2021). Poorly constrained and often controversial focal mechanism solutions and hypocenter locations available from the literature have led to uncertainties on the possible geometry and kinematics of the seismogenic source of the sequence, also having primary effects on the regional seismotectonic modeling and seismic hazard evaluations. In particular, the two most shared models proposed in the literature indicate thrusting on an about WSW–ENE striking plane or right-lateral transpression on a NNW–SSE-striking plane (Mckenzie, 1972; Gasparini *et al.*, 1985; Anderson and Jackson, 1987). Aiming to solve this ambiguity, we focused on the starting and most energetic phase of the sequence and we computed the moment tensor solutions for three of the strongest earthquakes by using digitized original seismograms and a time-domain waveform inversion algorithm properly implemented for analog seismic data (Stich *et al.*, 2005). We collected and selected the original seismograms recorded by long-period seismographs available from the digital archives of the SISMOS project (Michelini *et al.*, 2005). Each seismogram was digitized manually by using the software GIMP (GNU Image Manipulation Program), then it was interpolated and corrected for geometrical distortions and first arrivals were accurately verified. Moreover, we collected the arrival times from original bulletins and catalogs to analyze, by means of a Bayesian hypocenter location method, the spatial distribution of most energetic earthquakes.

Our results indicate that the 1968 Belice sequence was characterized by a mainly thrust faulting activity occurring on about E-to-NE trending structures, thus solving the dualism between models previously proposed in the literature. The main features of the causative source of the 1968 Belice seismic sequence in Sicily revealed by our analyses, well agree both with the geodynamic framework governed by the Nubia-Eurasia NNW-trending convergence and with the geological reconstructions of the regional thrust front in the western Sicily area (Monaco *et al.*, 1996; Lavecchia *et al.*, 2007). The time-domain moment tensor inversion also furnished the first direct estimate of moment magnitude for the analyzed events of the sequence, clearly showing the overall overestimation of the previous assessments coming from macroseismic data and/or conversion of instrumental estimates of Ms and mb. The results of this study, furnishing an improved knowledge of the most relevant seismic activity of western Sicily, have important consequences on local and regional seismotectonic modeling and seismic hazard evaluations of the study area.

References

Anderson H. and JacksonJ.; 1987: *Active tectonics of the Adriatic region*. Geophys. J. Roy. Astron. Soc.,**91**, 937–983.

Gasparini C., Iannaccone G., and Scarpa R.; 1985: *Fault-plane solutions and seismicity of the Italian peninsula*. Tectonophysics,**117**, nos. 1/2, 59–78.

Lavecchia, G., Ferrarini F., De Nardis R., Visini F., and Barbano M. S.; 2007: *Active thrusting as a possible seismogenic source in Sicily (southern Italy): Some insights from integrated structural–kinematic and seismological data*. Tectonophysics,**445**, 145–167, doi: 10.1016/j.tecto.2007.07.007.

McKenzie, D.; 1972: *Active tectonics of the Mediterranean region.* Geophys. J. Roy. Astron. Soc.,**30**, 109–185.

Michelini A., De SimoniB., AmatoA., and Boschi E.;2005: *Collecting, digitizing, and distributing historical seismological data*. Eos Trans. AGU 86, no. **28**, 261, doi: 10.1029/2005EO280002.

Michetti A. M., Brunamonte F., and Serva L.; 1995: *Paleoseismological evidence in the epicentral area of the January 1968 eartqhakes, Belice, southwestern Sicily*.In: L. Serva andD.B. Slemmons, Perspectives in Paleoseismology, Vol. 6, A.E.G. Special Publication, 127–139.

Monaco C., Mazzoli S., and Tortorici L.; 1996: *Active thrust tectonics in western Sicily (southern Italy): The 1968 Belice earthquake sequence*.Terra Nova,**8**, 372–381.

Orecchio B., Scolaro S., Batlló J., Neri G., Presti D., Stich D., and Totaro C.; 2021:*New Results for the 1968 Belice, South Italy, Seismic Sequence: Solving the Long-Lasting Ambiguity on Causative Source*.Seismol. Res. Lett.,**92** (4): 2364-2381, doi: 10.1785/0220200277.

Rovida A., Locati M., Camassi R., Lolli B., and Gasperini P.; 2020: *The Italian earthquake catalogue CPTI15*. Bull. Earthq. Eng.,**18**, no. 7, 2953–2984, doi: 10.1007/s10518-020-00818-y.

Stich D., BatllóJ., MaciàR., Teves-CostaP., and Morales J.; 2005: *Moment tensor inversion with single-component historical seismograms: The 1909 Benavente (Portugal) and Lambesc (France) earthquakes.*Geophys. J. Int.,**162**, no. 3, 850–858.

Valle P. E.; 1969: *Tentativo di controllo del periodo sismico siciliano iniziato il 14 Gennaio 1968*. Ann. Geophys.,**22**, 57–84(in Italian).

THERMAL STRUCTURE OF THE UPPER MANTLE IN THE ZAGROS COLLISION ZONE AND SURROUNDINGS

M. Tesauro[1,2], A.Pastorutti[1], T. Pivetta[1], C. Braitenberg[1], I. Koulakov[3,4]

[1] Trieste University, Italy
[2] University of Utrecht, Utrecht, Netherlands
[3] Trofimuk Institute of Petroleum Geology and Geophysics, SB RAS, Prospekt Koptyuga, Novosibirsk, Russia
[4] Novosibirsk State University, Novosibirsk, Russia

Late Mesozoic convergence between the Arabian plate and Eurasia generated subduction of the Neo-Tethys ocean beneath Central Iran, and the onset of the closure of the oceanic domain occurred in Late Cretaceous. The final closure of the Neo-Tethys ocean (~12 Ma) formed the Zagros collision zone composed of different parallel tectonic features extending from southwest to northeast, from the Turkish-Iranian border in the NW, to the Makran area in the SE (where oceanic subduction is still active): the Zagros Fold and Thrust Belt (ZFTB), the Sanandaj–Sirjan Metamorphic Zone (SSZ), and the Urumieh-Dokhtar Magmatic Assemblage (UDMA) (Mouthereau *et al.*, 2011). The ZFTB is the young and seismically active zone of the Zagros Mountains and is separated from the SSZ by the Main Zagros Thrust (MZT), which is considered to be the suture zone between the Arabian lower plate external zones to the SW and the Eurasian upper plate internal zones to the NE.

The SSZ consists mainly of Precambrian metamorphic rocks and igneous rocks, whose formation is related to the subduction of the Neo-Tethyan slab. The UDMA hosts abundant Tertiary magmatism, dominantly of arc or island-arc type. Central Iran, the UDMA and SSZ can together be considered to represent the upper plate domain during most of the recent convergence history leading to the Zagros orogeny (e.g. Agard *et al.*, 2011). The changes in arc magmatism during Eocene time, with a major shift from the SSZ to the UDMA, and with extensive magmatism affecting much of Iran have been attributed to a change in the slab dynamics: from a change in the slab dip angle to lateral slab tearing/break-off to slab folding at the mantle transition zone (e.g. Agard *et al.*, 2011). Currently, the convergence is accommodated across the Iranian Plateau and the surrounding mountain ranges, at a rate of 10–20 mm/yr, resulting in different styles of deformation in this active collision/subduction zone (e.g. Khorrami *et al.*, 2019).

Several models, based on the interpretation of seismic tomography and receiver function data, revealed high velocities beneath the Zagros in the upper mantle down to depths exceeding 200 km, implying a relatively thick lithospheric mantle (e.g. Priestley and McKenzie, 2006). However, some studies, based on the lack of deep seismicity in the Zagros and absence/reduction of high-velocity anomalies below 200 km depth, support the hypothesis of the slab break-off and delamination of the lower part of the Arabian lithosphere. In contrast, other studies reveal the slab continuity up to the depth of the transition zone (e.g., Wortel and Spakman, 2000; Koulakov *et al.*, 2011). Furthermore, according to some authors, thick high-velocity lithosphere of the Arabian Plate is extended beneath UDMA and southeastern Central Iran (e.g., Motaghi *et al.*, 2017; Mahmoodabadi *et al.*, 2020), while based on some others, thin lithosphere characterizes the UDMA (Mohammadi *et al.*, 2013**)** and the SSZ (e.g. Manaman *et al.,* 2011).

Therefore, up to now, a consensus has not been reached on the maximum depth and neither on the lateral extension of the subducting Arabian lithosphere. Other uncertainties are related to the dip and nature of the slab. In order to address these controversial issues, we analyze global and regional seismic tomography models and convert their absolute velocities in temperature, assuming the composition of a Phanerozoic mantle, taken from studies on xenolith samples. Indeed, the conversion in temperatures allows us to better identify the shapes of the upper mantle features. To this purpose, we use Perple_X (Conolly, 2005) that computes physical properties for a given mineralogical model, expressed by the main mantle

oxides. In addition, we compare the results obtained with the seismicity distribution (https://www.usgs.gov/programs/earthquake-hazards/national-earthquake-information-center-neic), as well as the depth of the Curie point (Li et al., 2019), and the effective elastic thickness obtained from isostatic analyses, in order to improve our understanding of the geodynamic setting of the area.

References

Agard, P., *et al.*, 2011. *Zagros orogeny: A subduction-dominated process*. Geological Magazine, 148(5–6), 692–725. https://doi.org/10.1017/S001675681100046X

Conolly, 2005. *Computation of phase equilibria by linear programming: A tool for geodynamic modeling and its application to subduction zone decarbonation*. Earth and Planetary Science Letters, 236, 524-541.

Khorrami *et al.*, 2019. *An up-to-date crustal deformation map of Iran using integrated campaign-mode and permanent GPS velocities*. Geophys. J. Int., 217, 832–843.

Koulakov, 2011. *High-frequency P and S velocity anomalies in the upper mantle beneath Asia from inversion of worldwide traveltime data*. Journal of Geophysical Research, 116, B04301, doi:10.1029/2010JB007938.

Li et al., 2019. *A global reference model of Curie-point depths based on EMAG2*. Scientific Reports, |7:45129 | DOI: 10.1038/srep45129.

Mahmoodabadi, M., *et al.*, 2020. *Shear wave velocity structure of the upper-mantle beneath the northern Zagros collision zone revealed by nonlinear teleseismic tomography and Bayesian Monte-Carlo joint inversion of surface wave dispersion and teleseismic P-wave coda*. Physics of the Earth and Planetary Interiors, 300, 106444. https://doi.org/10.1016/j.pepi.202

Manaman, N.S. and Shomali, H., 2010. *Upper mantle S-velocity structure and Moho depth variations across Zagros belt, Arabian–Eurasian plate boundary*. Physics of the Earth and Planetary Interiors, 180, 92–103

Mohammadi, N., *et al.*, 2013. *New constraints on lithospheric thickness of the Iranian plateau using converted waves*. Journal of Seismology 17:883–895 DOI 10.1007/s10950-013-9359-2.

Motaghi, K., *et al.*, 2017. *Underplating along the northern portion of the Zagros suture zone, Iran*. Geophys. J. Int., 210, 375–389.

Mouthereau, F., 2011. *Timing of uplift in the Zagros belt/Iranian plateau and accommodation of late Cenozoic Arabia-Eurasia convergence.* Geological Magazine, 148(5–6), 726–738. https://doi.org/10.1017/S0016756811000306

Priestley, K. and McKenzie, D. 2006. *The thermal structure of the lithosphere from shear wave velocities*. Earth and Planetary Science Letters, 244, 285–301.

Wortel, M.J.R. and Spakman, W., 2000. *Subduction and slab detachment in the Mediterranean-Carpathian region*. Science, 290, 1910–17.

APPLICATION OF GRAVITATIONAL GROUNDWATER FLOW SYSTEMS TO IRPINIA AREA (SOUTHERN APENNINES, ITALY): PERSPECTIVES AND IMPLICATIONS

E. Vitagliano, N. D'Agostino

Istituto Nazionale di Geofisica e Vulcanologia, Rome, Italy

In recent decades, gravity-driven groundwater flow models have been applied to a variety of scientific disciplines, such as hydrogeology, geotechnics, geothermal exploration, or environmental protection, and has provided successful results in terms of understanding the processes involved and predicting their effects. Herein, this geologic agent (Tóth, 1999) was applied to the southern Apennines to study the effect of groundwater circulation on various observational data (seismicity, geodesy) along the Irpinia Fault Zone (IFZ). The relationship between hydrologically-driven strain and temporal variation in seismicity has been recently addressed along fault segments activated during the 1980 M_S 6.9 Irpinia earthquake (D'Agostino *et al.*, 2018). The integration of continuous Global Positioning System (CGPS) data with hydro-meteorological and seismicity information has shown that low-magnitude events ($-0.1 \leq ML \leq 3.9$) along the IFZ are correlated with seasonal and multiannual hydrological signals. In addition, the extensional strain transient measured at several CGPS stations is characterised by seasonal oscillations and inter-annual trends in phase with hydrological recharge of karst aquifers. These correlations suggest the occurrence of horizontal seasonal dilation in late spring/early summer, strongly controlled by groundwater dynamics.

The points described suggest the emergence of key questions, such as: what path can meteoric water trace from inflow to outflow and what depth can it reach during the infiltration/migration process? How does it interact with the different layers (aquifer, aquitard, aquiclude) over time? What is the role of normal fault planes and thrust sheets as barriers or conduits for fluid circulation? How can pressure increment due to the hydrodynamic process interacting with the pressure regime of the rocks resulting in hydraulic leaking and fluid losses?

In this work, a multi-disciplinary approach to investigate the proposed issues is presented. First, regional groundwater flux (i.e., flow nets and intensities) and fluid-potential field were evaluated by applying the most frequently used equation, which combines Darcy's law with the equation of continuity and describes saturated flow under steady state and transient conditions (Hubbert, 1940; Lusczynsky, 1961; Tóth, 1978). Within the flow domain, the distributions of hydraulic head and flow were calculated by solving Laplace's equation under appropriate boundary conditions. According to Tóth's theory (Toth, 2009), flow patterns are calculated with respect to boundary conditions and head configuration. Moreover, final results depend on three main basin features: water-table relief, basin depth and macro-scale heterogeneity due to variations in rock permeability. Within the study, the variations of the water table were formulated based on the topography of the study area and reconstructed by testing various functions (e.g., sine wave, moving average, polynomial function), while the regional groundwater gradient was assumed from available wells and previous or analogue hydrogeological studies. The head formulation was treated in terms of both elevation/depth and pressures. In particular, the latter annotation allowed dynamic water pressure increments to be calculated and then compared to vertical pressure profiles available from exploration wells. These wells also allowed the definition of key petrophysical parameters (i.e., permeability, porosity, density, temperature) useful for identifying the physical properties of aquifers, aquitards and aquiclude, in relation to the site. The geometry of the flow domain was reconstructed using geological and structural studies available in the literature (e.g. Improta *et al.*, 2003; Nicolai and Gambini, 2007), plus reports prepared by Oil Companies that operated in the area during 1978-2002.

Although the study is still in progress, the work aims to present the multidisciplinary approach used, with particular emphasis on the role of pressure data in the treatment of fluid

circulation problems. In addition, the preliminary results obtained for a generalised vertical section examining regional karst aquifers show the strong control of basin compartmentalisation on fluid outflows (i.e., water, hydrocarbons, CO2).

Finally, the coupling of groundwater flow and heat transport in a heterogeneous anisotropic domain will be the next implication of the current study. Indeed, if the basin is characterized by more permeable lithology and the topography by high reliefs (e.g. Smith *et al.*, 1983), the near-surface thermal regimes can be highly influenced by active groundwater flow systems. As done in the central Apennines, where gravitational potential energy dissipation and geothermal heating have been calculated (e.g. Chiodini *et al.*, 2013), heat redistribution will be addressed by considering both conduction- and advection-dominated thermal regimes.

References

Chiodini G., Cardellini C., Caliro S., Chiarabba C., Frondini F.; 2013: *Advective heat transport associated with regional Earth degassing in central Apennine (Italy).* Earth Planet. Sci. Lett., **373**, 65–74, DOI 10.1016/j.epsl.2013.04.009

D'Agostino N., Silverii F., Amoroso O., Convertito V., Fiorillo F., Ventafridda G. and Zollo A.; 2018*: Crustal deformation and seismicity modulated by groundwater recharge of karst aquifers*. Geophysical Research Letters, **45**, 12253–12262, DOI 10.1029/2018GL079794

Hubbert M.K.; 1940: *The theory of groundwater motion.* J. Geol., **48**(8), 785-944.

Improta L., Bonagura M.T. Capuano P. and Iannaccone G.; 2003: *An integrated geophysical investigation of the upper crust in the epicentral area of the 1980 Ms=6.9 Irpinia earthquake (Southern Italy).* Tectonophysics, **361**, 139-169, DOI 10.1016/S0040-1951(02)00588-7

Lusczynski N.J.; 1961: *Head and flow of ground water of variable density.* J. Geophys. Res., **66**(12), 4247-4256.

Nicolai C., and Gambini R. ;2007: *Structural architecture of the Adria platform-and-basin system.* Ital. J. Geosci., Spec. Issue, **7**, 21-37.

Smith L. and Chapman D.S.; 1983: *On the thermal effects of groundwater flow 1: regional scale systems.* J. Geophys. Res., **88**, 593–608. DOI 10.1029/JB088iB01p00593

Tóth J.; 1978: *Gravity-induced cross-formational flow of formation fluids, Red Earth Region, Alberta, Canada: analysis, patterns and evolution.* Water Resources Research, 14(5):805–843, DOI 10.1029/WR014i005p00805

Tóth J.; 1999: *Groundwater as a geologic agent: an overview of the causes, processes, and manifestations.* Hydrogeology Journal, **7**(1), 1–14, DOI 10.1007/s100400050176

Tóth J.; 2009: *Gravitational systems of groundwater flow. Theory, Evaluation, Utilization*. Ed. Cambridge University Press, New York, 297 pp.

Tema 2

Caratterizzazione sismica del territorio

Sessione 2.1

Verso nuove modalità di stima della pericolosità da terremoti e maremoti: dati e procedure

Convenor: D. Di Bucci, D. Albarello e B. Pace

PERICOLOSITÀ SISMICA PROBABILISTICA NELL'ISOLA DI ISCHIA: MODELLO CONCETTUALE E PRIMI RISULTATI

R. Azzaro[1], V. Convertito[2], S. D'Amico[1], H. Langer[1], B. Pace[3], L. Peruzza[4], G. Tusa[1], F. Visini[5]

[1] Istituto Nazionale di Geofisica e Vulcanologia, Osservatorio Etneo, Catania (INGV-OE), Italy
[2] Istituto Nazionale di Geofisica e Vulcanologia, Osservatorio Vesuviano, Napoli (INGV-OV), Italy
[3] Università G. D'Annunzio Chieti-Pescara, Dipartimento di Ingegneria e Geologia, Italy
[4] Istituto Nazionale di Oceanografia e di Geofisica Sperimentale OGS, Trieste (OGS-TS), Italy
[5] Istituto Nazionale di Geofisica e Vulcanologia, Sezione di Pisa (INGV-PI), Italy

Introduzione. Le problematiche di pericolosità sismica nelle aree vulcaniche in cui accadono terremoti rilevanti includono aspetti non affrontati nelle analisi condotte a scala nazionale per l'aggiornamento della Mappa di Pericolosità Sismica. In seguito al terremoto di M_w 3.9, che ha danneggiato pesantemente Casamicciola e dintorni a Ischia nell'agosto 2017, sono state avviate ricerche finalizzate al miglioramento delle conoscenze in vari ambiti, e prodotti numerosi studi che hanno migliorato dati di base e modelli interpretativi.

Questo lavoro presenta i risultati preliminari di un progetto di ricerca svolto nell'ambito del Centro di Pericolosità Vulcanica dell'INGV, finalizzato alla valutazione della pericolosità sismica dovuta ai terremoti vulcano-tettonici dell'isola di Ischia.

Approccio metodologico e dati di input. Il calcolo di pericolosità sismica è stato eseguito seguendo la concettualizzazione metodologica tradizionale che prevede sorgenti a sismicità uniformemente distribuita e stazionaria nel tempo, implementata nel codice di calcolo OpenQuake (Pagani *et al.*, 2014). Quest'approccio è comunemente applicato in ambito internazionale ed è lo stesso utilizzato per l'aggiornamento della mappa nazionale MPS19 prodotta dal Centro di Pericolosità Sismica dell'INGV (Meletti *et al.*, 2021).

Di particolare dettaglio e specificità sono invece i dati di input utilizzati per definire le sorgenti, che sono: a) la geometria della faglia responsabile del terremoto di Casamicciola del 2017 (e dei suoi predecessori); b) il catalogo dei terremoti vulcano-tettonici per l'isola di Ischia, usati per calcolare i tassi di sismicità.

Riguardo il primo punto, sono stati considerati due modelli di faglia alternativi sviluppati da De Novellis *et al.* (2018) e da Calderoni *et al.* (2019), ritenuti entrambi rappresentativi della sorgente sismica del terremoto del 21 agosto 2017 (M_w 3.9). Il recente studio di Carlino *et al.* (2021), inoltre, dimostra che i terremoti storici distruttivi di Ischia (per es. 1881 e 1883) hanno avuto origine dalla stessa struttura sismogenetica dell'evento del 2017. I parametri utilizzati per definire la geometria tridimensionale della faglia sono riportati in Tab. 1: le due faglie differiscono per estensione ma soprattutto per la diversa immersione (opposta), che rimane ancora un punto dibattuto all'interno della comunità scientifica.

Il catalogo della sismicità di Ischia è quello di Selva *et al.* (2021), che copre un ampio intervallo temporale dall'VIII sec. A.C. al 2019, e integra dati strumentali recenti (dal 1991) con dati storico-macrosismici, oggetto di revisione e ri-parametrizzazione. Complessivamente

Tab. 1 - Parametri geometrico-cinematici dei due modelli di faglia proposti come responsabili del terremoto di Casamicciola del 2017.

	De Novellis *et al.* (2018)	**Calderoni *et al.* (2019)**
Cinematica faglia	Normale	Normale
Strike/dip/rake (°)	86/70/-80	206/50/-102
Lunghezza lungo lo strike	2000 m	3000 m
Lunghezza lungo l'immersione	1000 m	1458.1 m
Profondità minima	0 m	0 m
Profondità massima	800 m	957.6 m

sono disponibili 57 terremoti, a fronte dei 12 presenti nel catalogo parametrico italiano CPTI15 (Rovida et al., 2016) utilizzato in Meletti *et al.* (2021); di questi, 16 eventi sono caratterizzati da una intensità epicentrale I_0 al di sopra della soglia di danno (I_0 > V-VI MCS).

Modello. Il modello probabilistico di pericolosità sismica qui implementato tiene conto delle incertezze epistemiche che caratterizzano i dati di input mediante un approccio ad albero logico, basato sui seguenti nodi (Fig. 1):

1) modello di faglia;
2) tasso annuale di sismicità per sorgenti individuali su faglia;
3) ripartizione dei tassi di sismicità sui nodi della griglia della sismicità diffusa;
4) modelli di attenuazione del moto del suolo.

Vi è poi l'effetto della topografia, che viene gestita mediante la realizzazione di due alberi di calcolo indipendenti, per poterne valutare appieno l'impatto sui risultati.

Nodo 1. Il primo nodo dell'albero logico include l'incertezza legata alla geometria del modello di faglia. Sono stati considerati entrambi i modelli consolidati in letteratura, ossia quelli di De Novellis *et al.* (2018) e Calderoni *et al.* (2019) i cui parametri sono richiamati in Tab. 1.

Nodo 2. Il secondo nodo considera l'incertezza sul tasso annuale di terremoti (lambda, l ($M_w \geq m$) riferito ad una certa magnitudo m, nel nostro caso maggiore o uguale a 1). I tassi di sismicità attesi per l'isola di Ischia sono stati calcolati facendo riferimento ai risultati di Selva *et al.* (2021), che calcolano una distribuzione magnitudo-frequenza dei terremoti assumendo un modello cosiddetto *Tapered Gutenberg-Richter* con *b* = 1.11, l ($M_w \geq 1$) = 5.54 e *Corner magnitude* = 6.

Selva *et al.* (2021) riconoscono che la sismicità di Ischia, per intervalli temporali più brevi rispetto alla intera durata del catalogo, non è stazionaria, distinguendo almeno due periodi nei quali le occorrenze dei terremoti mostrano caratteristiche diverse: tra il 1750 e il 1884 vi è un rilascio di terremoti con $M_w \geq 3.6$ ad un tasso circa sette volte maggiore che nel periodo tra il 1885 e il 2019. Per tale motivo, abbiamo ritenuto importante distinguere due parametrizzazioni della distribuzione magnitudo-frequenza, caratteristici delle due fasi di relativo alto e basso tasso di sismicità, e una terza parametrizzazione rappresentativa dell'intero intervallo temporale. I tre modelli inseriti come rami dell'albero logico, differiscono quindi per il budget complessivo di momento sismico rilasciato, mediante tre valori di lamba: l ($M_w \geq 1$) = 7.35 yr^{-1} per il periodo a elevata sismicità, l = 4.42 yr^{-1} per il periodo a bassa sismicità, e l = 5.54 yr^{-1} nel periodo di completezza del catalogo.

Nodo 3. Il terzo nodo serve per modellare l'incertezza legata alla ripartizione dei tassi di sismicità di background, ossia non riconducibili alla faglia modellata, sui nodi di una griglia. I tassi di sismicità sono ripartiti tra i punti della griglia secondo due opzioni: a) il tasso per ciascuna magnitudo viene ripartito uniformemente tra i punti della griglia; b) il tasso per ciascuna magnitudo viene ripartito proporzionalmente alla densità di sismicità caratteristica dei punti della griglia, come calcolato in Selva *et al.* (2021), applicando un raggio di *smoothing* di 1.5 km.

Come primo step, seguendo le metodologie proposte in letteratura per la ripartizione dei tassi, (e.g., Woessner *et al.*, 2015) per il modello di sismicità a faglie e *background* del modello di pericolosità sismica europeo, abbiamo adottato un approccio che attribuisce la sismicità al di sopra di una certa magnitudo alle faglie, e la sismicità al di sotto della stessa al modello a griglia. Per Ischia, la soglia di magnitudo è M_w 3.6, ed è stata scelta sulla base della forma della *Tapered Gutenberg-Richter* di Selva *et al.* (2021). Al modello sorgente con sismicità diffusa sono attribuiti i tassi di sismicità da M_w 1 a M_w 3.5, alla faglia sono attribuiti i tassi di sismicità per M_w >3.5. Per quest'ultima, in particolare, poiché il calcolo della pericolosità necessita di

un numero finito di coppie magnitudo-tasso è necessario il valore di magnitudo più elevato da considerare. Dato che la formulazione di tipo *Tapered Gutenberg-Richter* non prevede una magnitudo massima, abbiamo fissato quest'ultima come quel valore di magnitudo cui corrisponde un tasso annuale maggiore o uguale di $1x10^{-6}$ yr^{-1}. Tale valore di magnitudo è sostanzialmente stabile al variare del lambda utilizzato, ed è pari a M_w 6.1, M_w 6.1 e M_w 6.2, rispettivamente per i valori di lambda di 4.42 yr^{-1}, 5.54 yr^{-1} e 7.35 yr^{-1}.

Per la sismicità diffusa abbiamo adottato un modello a griglia con passo di 0.005° in latitudine e longitudine, posta a un chilometro di profondità. Questa profondità corrisponde alla profondità media dei terremoti localizzati strumentalmente. Non essendo possibile valutare le orientazioni preferenziali e lo spessore sismogenetico dei futuri terremoti associabili alla sismicità diffusa, abbiamo adottato lo schema e i valori proposti in Visini *et al.* (2021). Per riprodurre orientazioni uniformemente distribuite in uno spazio tridimensionale, lo *strike* può assumere valori di 0°, 90°, 180° e 270°, il *dip* di 30°, 60° e 90° e il *rake* di -90°, 0° e 90°. Lo spessore sismogenetico è compreso tra 0 e 4 km.

Nodo 4. Il quarto nodo tiene conto dell'incertezza sui modelli di attenuazione del moto del suolo (GMPE). A questo scopo sono stati utilizzati gli unici modelli esistenti per aree vulcaniche italiane, ovvero quelli proposti da Lanzano e Luzi (2020) e Tusa *et al.* (2020).

La configurazione finale dell'albero logico è rappresentata in Fig. 1. I pesi dei rami sono stati assegnati sulla base delle capacità di ciascun ramo nel riprodurre le osservazioni macrosismiche in un periodo di completezza.

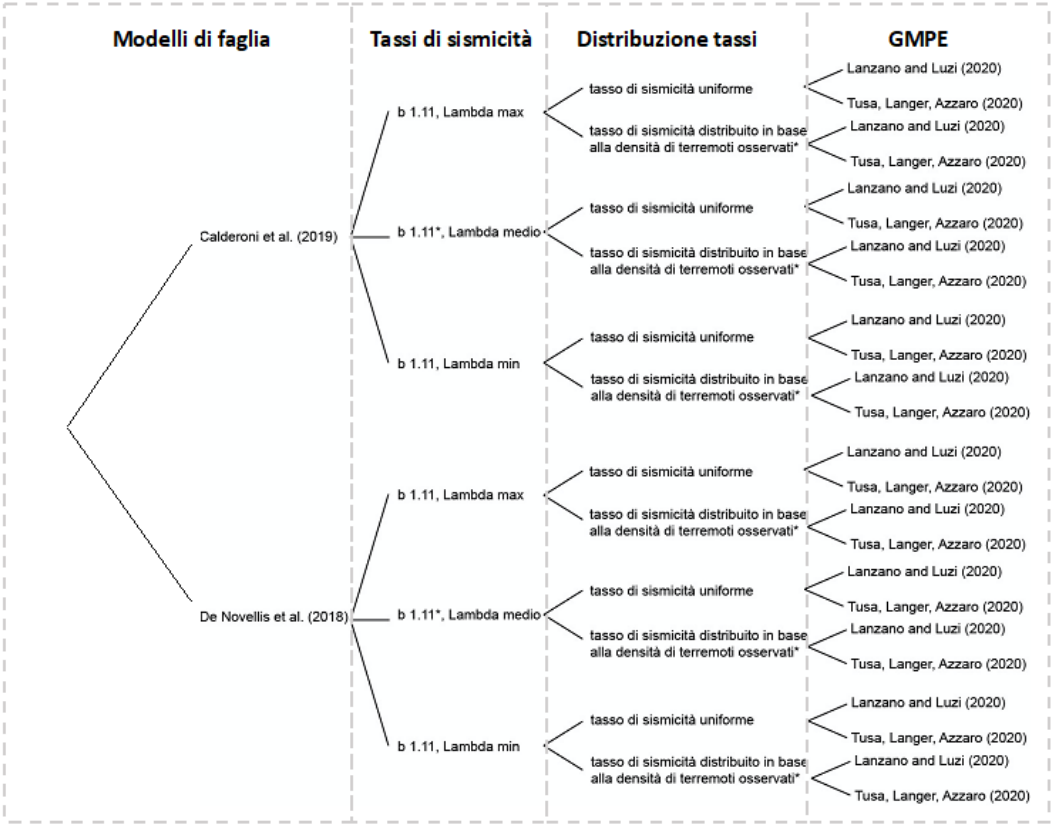


Fig. 1 - Configurazione dell'albero logico utilizzato per tener conto delle incertezze sui parametri di input per il calcolo della pericolosità sismica per Ischia.

Effetto della Topografia. Infine si considera l'effetto della topografia nel calcolo della distanza sito-sorgente, seguendo l'approccio di Peruzza *et al.* (2017). In un'area piccola come quella in esame e con forti differenze altimetriche, considerata l'estrema superficialità delle sorgenti e la forte attenuazione del moto del suolo, si ottengono stime più dettagliate e realistiche. A tal fine, è stato utilizzato un DEM con una risoluzione di 20 m.

Mappe di pericolosità sismica. I calcoli sono stati effettuati utilizzando la piattaforma di OPENQUAKE (Pagani *et al.*, 2014) per 4 periodi di ritorno (rispettivamente pari a 95, 285, 475, e 2475 anni), con percentuali di superamento del 10% e del 2%; il parametro del moto del suolo rappresentato è l'accelerazione orizzontale di picco PGA riferita a suoli di tipo "A"; i calcoli si riferiscono alle due opzioni, indicate rispettivamente "con topografia" e "senza topografia".

La Fig. 2 riporta, a titolo di esempio, la mappa riferita al 10% di probabilità di superamento nel tempo di esposizione di 50 anni. Si nota che la pericolosità non è uniforme su tutta l'isola, ma decresce piuttosto rapidamente: i valori più alti di PGA sono infatti concentrati nel versante nord dell'isola, dove sono localizzati i terremoti storici più forti ed il recente evento del 2017.

Si vede inoltre che la topografia ha un effetto decisamente non trascurabile sia nei valori massimi stimati che nella loro distribuzione areale. In particolare, le mappe "senza topografia" mostrano valori di PGA più elevati su un'estensione maggiore; questo deriva chiaramente dalla minor distanza sito-sorgente in quanto la quota di riferimento è posta a 0 m/slm.

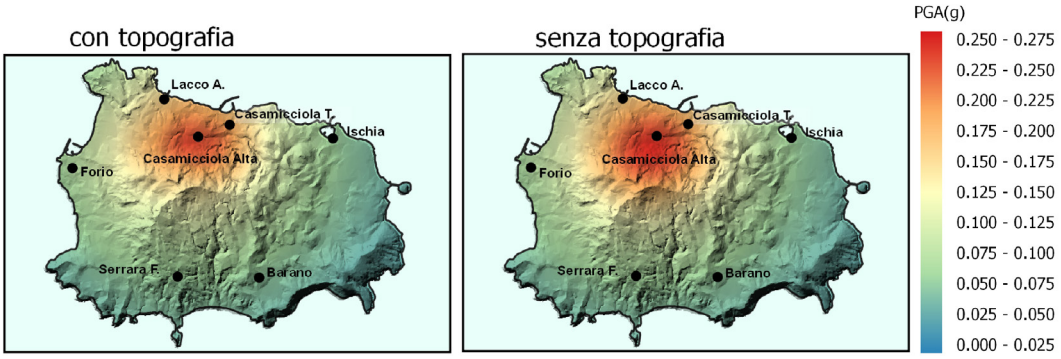


Fig. 2 - Mappe di PGA per suolo A con probabilità di superamento del 10% in 50 anni, corrispondente ad un periodo di ritorno di 475 anni.

Per confronto, la mappa di pericolosità sismica nazionale MPS04 (Stucchi *et al.*, 2011) in Fig. 3, riferimento ancora attuale per la classificazione e la normativa per le costruzioni, "copre" Ischia con appena 3 nodi della griglia. Inoltre, i valori di PGA con probabilità di superamento del 10% in 50 anni sono sensibilmente inferiori, compresi in un intervallo da 0.125 a 0.175g. Da notare che i valori riportati nella nuova mappa MPS19 (Meletti *et al.*, 2021) vanno da 0.075 a 0.100g, risultando quindi ancora inferiori.

Conclusioni. I risultati di questo primo studio di pericolosità sismica dell'isola di Ischia, ottenuto utilizzando dati e modelli specifici, confermano la necessità di procedere nelle aree vulcaniche con approcci *ad-hoc*.

Le analisi effettuate dimostrano in particolare che:

- i valori di pericolosità ottenuti mediante la modellazione delle sole sorgenti locali sono più elevati rispetto a quanto riportato nelle mappe nazionali MPS04 e MPS19.
- il modello di pericolosità a scala locale è caratterizzato da un notevole dettaglio areale, utile per una migliore pianificazione territoriale;

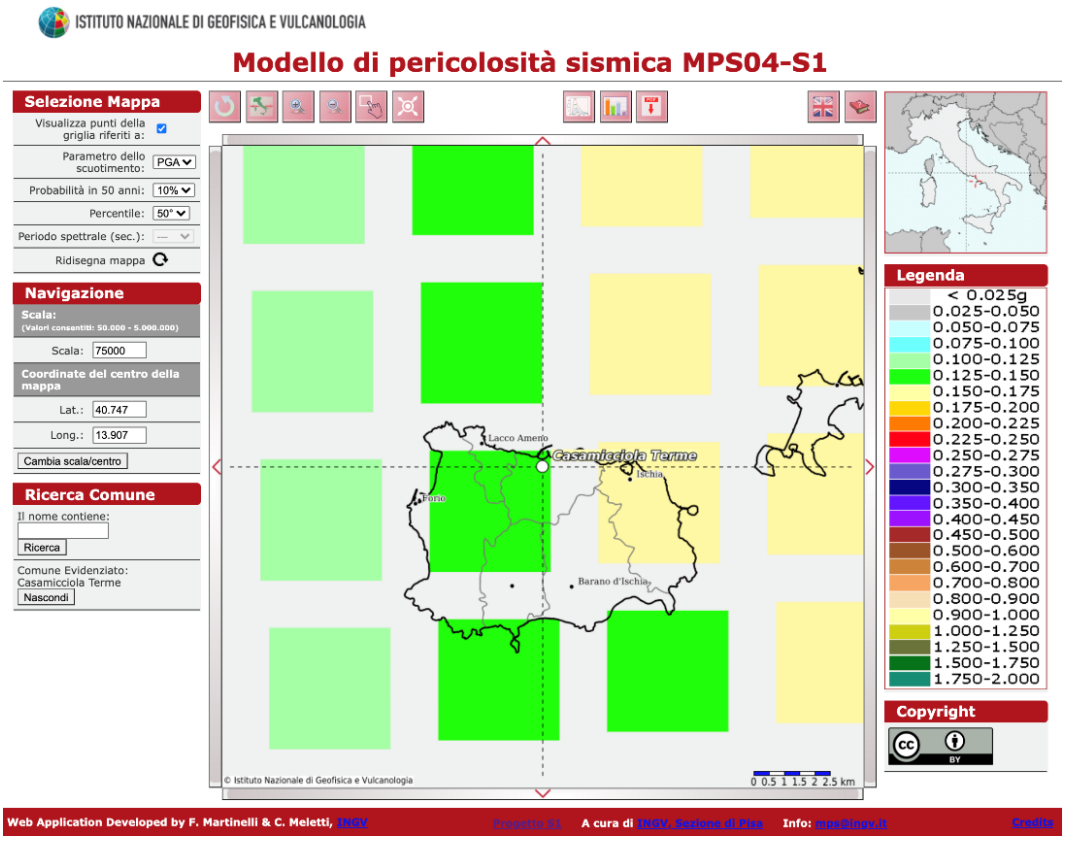


Fig. 3 - Mappa di PGA per suolo A con probabilità di superamento del 10% in 50 anni (periodo di ritorno di 475 anni) secondo il modello di pericolosità MPS04 (dati da http://esse1-gis.mi.ingv.it/).

- l'area a pericolosità più elevata corrisponde al settore nord dell'isola, dove sono localizzati, sia dai dati macrosismici che da quelli strumentali, i terremoti più forti;
- date le piccole distanze sito-sorgente, è necessario tener conto degli effetti topografici (quota).

Infine, il contributo degli effetti di sito è rilevante e richiederebbe di essere considerato. I valori di amplificazione ottenuti dagli studi di Microzonazione Sismica di terzo livello (http://www.commissarioricostruzioneischia.it/Esiti-Microzonazione.html) sono disponibili solo per poche località in un'area ristretta dell'isola; questo non ha consentito di modificare la mappa di pericolosità nella sua interezza.

Si auspica che il modello di dettaglio qui proposto per Ischia, ulteriormente implementato, possa essere considerato in futuri aggiornamenti della mappa di pericolosità sismica nazionale, così come già avvenuto per l'area etnea in MPS19 (Meletti *et al.*, 2021; Visini *et al.*, 2021).

Riconoscimenti. Lo studio presentato ha beneficiato del contributo finanziario della Presidenza del Consiglio dei Ministri - Dipartimento della Protezione Civile; rimane degli autori la responsabilità dei contenuti, che pertanto non riflettono necessariamente la posizione e le politiche ufficiali del Dipartimento.

Bibliografia

Calderoni G., Di Giovambattista R., Pezzo G., Albano M., Atzori S., Tolomei C., *et al.*; 2019: *Seismic and geodetic evidences of a hydrothermal source in the Md 4.0, 2017, Ischia earthquake (Italy)*. J. Geophys. Res. Solid Earth 124, 5014–5029. doi: 10.1029/2018jb016431.

Carlino S., Pino N.A., Tramelli A. *et al.,* 2021; *A common source for the destructive earthquakes in the volcanic island of Ischia (Southern Italy): insights from historical and recent seismicity*. Nat Hazards, 108, 177–201 (2021). https://doi.org/10.1007/s11069-021-04675-z.

De Novellis, V., Carlino, S., Castaldo, R., Tramelli, A., De Luca, C., Pino, N. A., *et al.*; 2018: *The 21st August 2017 Ischia (Italy) earthquake source model inferred from seismological, GPS and DInSAR measurements*. Geophys. Res. Lett. 45, 2193–2202. doi: 10.1002/2017gl076336.

Lanzano G., Luzi L.; 2020: *A ground motion model for volcanic areas in Italy*. Bull. Earthq. Eng., 18, 57–76, doi: 10.1007/s10518-019-00735-9.

Meletti C., Marzocchi W., D'Amico V., Lanzano G., Luzi L., Martinelli F., Pace B., Rovida A., Taroni M., Visini F., the MPS19 Working Group; 2021: *The new Italian seismic hazard model (MPS19)*. Ann. Geophys., 64, 1, doi:10.4401/ag-8579.

Pagani M., Monelli D., Weatherill G., Danciu L., Crowley H., Silva V., Henshaw P., Butler L., Nastasi M., Panzeri L., Simionato M., Viganò D.; 2014: *OpenQuake Engine: an open hazard (and risk) software for the Global Earthquake Model*. Seism. Res. Lett. 85, 692-702.

Peruzza, L., R. Azzaro, R. Gee, S. D'Amico, H. Langer, G. Lombardo, B. Pace, M. Pagani, F. Panzera, M. Ordaz, M. L. Suarez, G. Tusa; 2017: *When probabilistic seismic hazard climbs volcanoes: the Mt. Etna case, Italy – Part 2: Computational implementation and first results.* Nat. Hazards Earth Syst. Sci., 17, 1999–2015, https://doi.org/10.5194/nhess-17-1999-2017.

Rovida, A., Locati, M., Camassi, R., Lolli, B., Gasperini, P.; 2016: *Catalogo Parametrico dei Terremoti Italiani (CPTI15)*. Napoli: Istituto Nazionale di Geofisica e Vulcanologia, doi: 10.6092/INGV.IT-CPTI15.

Selva, J. *et al.;* 2021: *The Seismicity of Ischia Island, Italy: An Integrated Earthquake Catalogue From 8th Century BC to 2019 and Its Statistical Properties*. Frontiers, 9, 629736. https://doi.org/10.3389/feart.2021.629736.

Stucchi, M., Meletti, C., Montaldo, V., Crowley, H., Calvi, G.M., Boschi E.; 2011: *Seismic hazard assessment (2003-2009) for the Italian building code*. Bull. Seismol. Soc. Am., 101, 1885-1911.

Tusa, G., Langer, H., Azzaro, R.; 2020: *Localizing ground motion models in volcanic terranes: Shallow events at Mt. Etna, Italy, revisited*. Bull. Seismol. Soc. Am., DOI: 10.1785/0120190325.

Visini F., Pace B. *et al.*; 2021: *Earthquake rupture forecasts for the MPS19 seismic hazard model of Italy*. Ann. Geophys., 64, 2, SE220, doi:10.4401/ag-8608.

Woessner J., Danciu, L., Giardini, D., Crowley, H., Cotton, F., *et al.*; 2015: T*he 2013 European Seismic Hazard Model: key components and results.* Bull. Earthq. Engin., 13, 3553-3596, doi:10.1007/s10518-015-9795-1.

EARTHQUAKE SOURCE PARAMETERS ESTIMATED FROM DIRECT S-WAVES AND CODA ENVELOPES ANALYSIS PERFORMED IN CENTRAL ITALY

D. Bindi[1], P. Morasca[2], D. Spallarossa[3], M. Picozzi[4], K. Mayeda[5], J. Roman-Nieves[5], J. Barno[6], W.R. Walter[6]

[1] GFZ, Potsdam, Germany
[2] INGV, Milan, Italy
[3] UNIGE, Genoa, Italy
[4] University of Naples Federico II, Italy
[5] AFTAC, Patrick AFB, FL, USA
[6] LLNL, Livermore, CA, USA

The assessment of source parameters over a wide magnitude range is a fundamental issue in understanding the relationships between small and large events. However, effects of seismic wave propagation in attenuating media and limitations in the monitoring configuration, hamper our ability to discriminate between physical contributions to the observed source variability from uncertainties of the methods and data used to estimate the values. Moreover, since the impact of anelastic attenuation increases with increasing source-to-site distance and, along with near-surface attenuation effects, filters more severely high frequencies, the estimation of high-frequency source parameters is particularly challenging for small events (Abercrombie, 1995). Several studies investigated the limitations introduced by attenuation effects and by the limited available bandwidth on the estimation of source parameter for small earthquakes (e.g., Kwiatek and Ben-Zion, 2016; Abercrombie *et al.,* 2017). Recently, Bindi *et al.* (2020) investigated the reliability of the source parameters estimated in central Italy for magnitudes in the range from 1.5 to 6.5, using synthetic spectra generated for the same source-station geometry of an actual data set. The large redundancy in the earthquake and station sampling allowed for retrieving reliable source parameter down to magnitude about 1.8, with the near-surface attenuation parameter k_0 being the most impacting parameter for the determination of the corner frequency of small events.

Various approaches have been proposed throughout the years to estimate source parameters, such as empirical Green's function analysis based on direct waves to remove path and site effects (Prieto *et al.*, 2004; Ide *et al.*, 2003; Abercrombie, 2015) or coda waves (Mayeda and Walter, 1996; Mayeda *et al.*, 2003, 2007, Walter *et al.*, 2017), and data-driven spectral amplitude decomposition approaches (e.g., Andrews, 1986; Edwards *et al.*, 2008; Malagnini *et al.*, 2011; Oth *et al.*, 2011; Trugman and Shearer, 2017). Several investigations (e.g., Eken *et al.*, 2004; Gök *et al.*, 2016; Morasca *et al.*, 2005; Yoo and Mayeda, 2013; Holt *et al.*, 2021; Shelly *et al.*, 2022) demonstrated the ability of methods based on coda envelope measurements to obtain stable source measurements over a large frequency range thanks to the stable properties of coda waves (e.g., Aki, 1969; Aki and Chouet, 1975; Mayeda and Malagnini, 2010). The low sensitivity to source and path heterogeneity of coda waves, in fact, allows the assumption of simple 1D models to adequately describe a region using local to regional events recorded from as few as one station (Mayeda *et al.*, 2003).

The Central Italy region is ideal for comparing the outcomes of different approaches as it is characterized by high-quality data including recent well-recorded seismic sequences such as L'Aquila (2009) and Amatrice-Norcia-Visso (2016-2017). Morasca *et al.* (2022) applied the coda method by Mayeda *et al.* (2003) using the Coda Calibration Tool (CCT), a freely available Java-based code (https://github.com/LLNL/coda-calibration-tool) to obtain a regional calibration for Central Italy for estimating stable source parameters. For validating the source parameters through a comparison of the results achieved when different techniques are applied to different portions of the seismogram, the authors also performed a spectral amplitude decomposition (GIT, Generalized Inversion Technique) and investigated the strengths and limitations of the two methodologies. A data set including ~5000 earthquakes and more than 600 stations was considered for running the GIT analysis, while the authors used a small subset of 39 events spanning 3.5<Mw<6.3 and 14 well-distributed broadband stations for calibrating the model for

coda analysis. The robustness of the coda calibration procedure was tested by progressively reducing the number of calibration events and stations and applying each new calibration to the validation dataset. Even in the case of a reduction of 75% of the number of events and stations with respect to the best case, Mw and corner frequency estimates remained substantially stable. This confirmed the ability of the coda approach to obtain stable source parameters even with few calibration events and stations. The comparison between CCT and GIT results in terms of source spectral shape demonstrated their similarity over a large frequency range (0.4-25-Hz is the common range covered by both calibration approaches). Coda-derived spectra are within the 5th and 95th percentile of GIT apparent source spectra in all cases, and in general overlap the median GIT-derived spectra. The CCT and GIT calibrated models and parameters have been applied to the holdout dataset composed of 247 events (~1.7 < Mw < ~ 5.0) recorded in the same region. This comparison had a dual function: first, to validate the results of the coda calibration approach and second, to confirm that the CCT can be used in near real-time analysis to create catalogs characterized by homogeneous and reliable estimates of source parameters for small and large events using a common method. In term of source scaling, both GIT and CCT source parameters provided indication of increasing apparent stress with increasing magnitude, in particular below magnitude 5, with apparent stress varying in the range from ~0.01 to ~1 MPa.

Beside the source term, the CCT and GIT calibrations provide estimates of relative site amplification effects. In order to compare the site terms for stations used in both calibration procedures, the single station results were normalized to the respective network average (i.e., the evaluated amplifications were relative to the network average considering the set of stations used by each approach). The relative, weak-motion site terms obtained from for 14 stations analyzed with CCT and GIT approaches showed an overall good agreement for common pass bands, as expected by the dominance of *S*-waves in the scattered field (Aki, 1992; Zeng, 1993). The only striking amplification difference is observed below 2-Hz at one of the stations installed on unconsolidated sediments. Although several studies investigating the consistency of the S-wave and coda-wave site amplifications found a similarity of the results within a factor between 1.5 and 2 (Kato *et al.*, 1995; Bonilla *et al.*, 1997), a few larger discrepancies were observed either for stations installed over deep sediments (Margheriti *et al.*, 1994) or when recordings at epicentral distances smaller than the focal depth were analyzed (Su *et al.*, 1996).

In our talk, a summary of the analysis and results obtained by Bindi *et al.* (2020) and Morasca *et al.* (2022) is presented.

References

Abercrombie, R.E., (1995). *Earthquake source scaling relationship from 1 to 5 ML using seismograms recorded at 2.5 km depth*, J. Geophys. Res., 100, 24 015–24 036.

Abercrombie, R.E., (2015). *Investigating uncertainties in empirical Green's function analysis of earthquake source parameters*, J. Geophys. Res., 120, 4263–4277.

Abercrombie, R.E., S. Bannister, J. Ristau, and D. Doser (2017). V*ariability of earthquake stress drop in a subduction setting, the Hikurangi Margin, New Zealand*, Geophys. J. Int. 208, 306–320.

Aki, K., (1969). *Analysis of the seismic coda of local earthquakes as scattered waves*, J. Geophys. Res., 74, 615–631.

Aki, K., and B. Chouet (1975). *Origin of coda waves: source, attenuation and scattering effects*, J. Geophys. Res. 80, 3322-3342.

Aki, K. (1992). *Scattering conversions P to S versus S to P*, Bull. Seism. Soc. Am. 82, 1969-1972.

Andrews, D.J. (1986). *Objective determination of source parameters and similarity of earthquakes of different size,* in Earthquake Source Mechanics, S. Das, J. Boatwright, and C. H. Scholz (Editors), American Geophysical Union, Washington, pp. 259–267.

Bindi, D., D. Spallarossa, M. Picozzi, and P. Morasca (2020). *Reliability of source parameters for small events in central Italy: insights from spectral decomposition analysis applied to both synthetic and real data*, Bull. Seismol. Soc. Am. 110, 3139–3157, doi: 10.1785/0120200126.

Bonilla, L.F., J. H. Steidl, G. T. Lindley, A. G. Tumarkin, and R.J. Archuleta (1997). *Site amplification in the San Fernando Valley, California: Variability of site-effect estimation using the S-wave, coda, and HIV methods*, Bull. Seismol. Soc. Am 87, 710-730.

Edwards, B., A. Rietbrock, J. J. Bommer, and B. Baptie (2008). *The acquisition of source, path, and site effects from microearthquake recordings using Q tomography: Application to the United Kingdom*, Bull. Seismol. Soc. Am. 98, 1915–1935, doi: 10.1785/0120070127.

Eken, T., K. Mayeda, A. Hofstetter, R. Gök, G. Orgulu, and N. Turkelli (2004). *An application of the coda methodology for moment-rate spectra using broadband stations in Turkey*, Geophys. Res. Lett., 31, L11609, doi:10.1029/2004GL019627.

Gök, R., A. Kaviani, E.M., Matzel, M.E. Pasyanos, K. Mayeda, G. Yetirmishli, I. El-Hussain, A. Al-Amri, F. Al-Jeri, T. Godaladze, D. Kalafat, E.A. Sandvol, and W.R. Walter (2016). *Moment magnitudes of local/regional events from 1D coda calibrations in the broader Middle East region*, Bull. Seism. Soc. Am., 106, 10.1785/0120160045.

Holt, J., K. M. Whidden, K. D. Koper, K. L. Pankow, K. Mayeda, J. C. Pechmann, B. Edwards, R. Gök, and W. R. Walter (2021). *Toward Robust and Routine Determination of Mw for Small Earthquakes: Application to the 2020 Mw 5.7 Magna, Utah, Seismic Sequence*. Seismological Research Letters 92 (2A): 725–740. doi: https://doi.org/10.1785/0220200320.

Ide, S., G. C. Beroza, S. G. Prejean, and W. L. Ellsworth (2003), *Apparent break in earthquake scaling due to path and site effects on deep borehole recordings*, J. Geophys. Res., 108(B5), 2271, doi:10.1029/2001JB001617.

Kato, K., K. Aki, and M. Takemura (1995). *Site amplification from coda waves: validation and application to S-wave site response*, Bull. Seism. Soc. Am. 85, 467-477

Kwiatek, G., and Y. Ben-Zion (2016). *Theoretical limits on detection and analysis of small earthquakes*, J. Geophys. Res. 121, doi:10.1002/2016JB012908.

Malagnini, L., A. Akinci, K. Mayeda, I. Munafo, R.B. Herrmann, and A. Mercuri (2011). *Characterization of earthquake-induced ground motion from the L'Aquila seismic sequence of 2009*, Italy, Geophys. J. Int., 184, 325-337.

Margheriti, L., L. Wennerberg, and J. Boatwright (1994). *A comparison of coda and S-wave spectral ratios estimates of site response in the southern San Francisco bay area*, Bull, Seism. Soc. Am. 84, 1815-1830.

Mayeda, K. and Walter, W.R., (1996). *Moment, energy, stress drop, and source spectra of western United States earthquakes from regional coda envelopes*, J. Geophys. Res., 101, 11 195–11 208.

Mayeda, K., L. Malagnini, and W.R. Walter (2007). *A new spectral ratio method using narrow band coda envelopes: Evidence for non-self-similarity in the Hector Mine sequence*, Geophys. Res. Lett., doi:10.1029/2007GL030041.

Mayeda, K., A. Hofstetter, J. L. O'Boyle, and W. R. Walter (2003). *Stable and transportable regional magnitudes based on coda-derived moment rate spectra*, Bull. Seismol. Soc. Am., 93, 224–239.

Mayeda, K., and L. Malagnini (2010). *Source radiation invariant property of local and near-regional shear-wave coda: Application to source scaling for the Mw 5.9 Wells, Nevada sequence*, Geophys. Res. Lett. 37, L07306, doi:10.1029/2009GL042148.

Morasca, P., Mayeda K., Malagnini, L. and W.R. Walter (2005). *Coda Derived Source Spectra, Moment Magnitudes, and Energy-Moment Scaling in the Western Alps*. Geoph. J. Int. 160 (1), 263-275.

Morasca, P., D. Bindi, K. Mayeda, J. Roman-Nieves, J. Barno, W. R. Walter, and D. Spallarossa (2022). *Stable Source Spectra from Coda Envelopes and Direct S-Waves: Two Perspectives for the Determination of Source Parameters in Central Italy*, Geophysical Journal International, under review.

Oth, A., D. Bindi, S. Parolai, and D. Di Giacomo (2011). *Spectral Analysis of K-NET and KiK-net Data in Japan, Part II: On Attenuation Characteristics, Source Spectra, and Site Response of Borehole and Surface Stations*, Bull. Seismol. Soc. Am., 101 (2): 667–687, https://doi.org/10.1785/0120100135

Prejean, S. and Ellsworth, W., (2001). *Observations of earthquake source parameters at 2 km depth in the Long Valley caldera, eastern California*, Bull. seism. Soc. Am., 91, 165–177.

Prieto, G. A., P. M. Shearer, F. L. Vernon, and D. Kilb (2004). *Earthquake source scaling and self-similarity estimation from stacking P and S spectra*, J. Geophys. Res., 109, B08310, doi:10.1029/2004JB003084.

Shelly, D. R., K. Mayeda, J. Barno, K. M. Whidden, M. P. Moschetti, A. L. Llenos, J. L. Rubinstein, W. L. Yeck, P. S. Earle, R. Gök, and W.R. Walter (2022). *A Big Problem for Small Earthquakes: Benchmarking Routine Magnitudes and Conversion Relationships with Coda Envelope-Derived Mw in Southern Kansas and Northern Oklahoma*, Bull. Seismol. Soc. Am. 112(1) , 210-225, doi: 10.1785/0120210115.

Su, F., J. G. Anderson, J. N. Brune, and Y. Zeng (1996). *A comparison of direct S-wave and coda wave site amplification determined from aftershocks of Little Skull Mountain earthquake*, Bull. Seism. Soc. Am. 86, 1006-1018.

Trugman, D. T., and P. M. Shearer (2017). *Application of an improved spectral decomposition method to examine earthquake source scaling in Southern California*. Journal of Geophysical Research: Solid Earth, 122 (4), 2890–2910, doi: 10.1002/2017JB013971.

Walter, W.R., Yoo, S.-H., Mayeda, K. and Gök, R., (2017). *Earthquake stress via event ratio levels: application to the 2011 and 2016 Oklahoma seismic sequences*, Geophys. Res. Lett., 44, 3147–3155.

Yoo, S.-H., and K. Mayeda (2013). *Validation of Non-Self-Similar Source Scaling Using Ground Motions from the 2008 Wells, Nevada, Earthquake Sequence*, Bull. Seismol. Soc. Am., 103, 2520-2533, doi:10.1785/0120120327.

Zeng, Y. (1993). *Theory of scattered P- and S-wave energy in a random isotropic scattering medium*, Bull. Seism. Soc. Am. 83, 1264-1276.

APPLICATION OF THE EEPAS SEISMIC FORECASTING METHOD TO ITALY

E. Biondini[1], D. Rhoades[2], P. Gasperini[1,3]

[1] Dipartimento di Fisica e Astronomia, Università di Bologna, Italy
[2] GNS Science, New Zealand
[3] Istituto Nazionale di Geofisica e Vulcanologia, Sezione di Bologna, Italy

Abstract. The EEPAS (Every Earthquake a Precursor According to Scale) forecasting model is a space–time point-process model based on the precursory scale increase (Ψ) phenomenon and associated predictive scaling relations (Rhoades and Evison, 2004). It has been previously applied to New Zealand, California and Japan earthquakes with target magnitude thresholds varying from about 5 to 7. In all previous application, computations were made by the computer code implemented in Fortran language by the model authors. In this work we applied it to Italy using a suite of computing codes completely rewritten in Matlab and Python. We first compared the two software codes to ensure the convergence and adequate coincidence between the estimated model parameters for a simple region capable of being analyzed by both software codes, then using the rewritten codes we optimized the parameters for a different and more complex polygon of analysis for a retrospective forecasting experiment of Italian earthquakes from 1990 to 2019 with Mw³5.0 and compare its forecasting skill with other forecasting models.

Brief introduction on the EEPAS model. EEPAS (Every Earthquake as a Seismic Precursor According to Scale) is a seismic forecasting method based on the statistical analysis of seismicity (Rhoades and Evison 2004). Its basic assumption is that magnitudes and rates of minor seismicity increase before a strong shock. The hypothesis on the base of the EEPAS model is that each earthquake is considered as an individual precursor according to their appropriate magnitude scale, rather than as a possible member of a Ψ. The model defines the rate density of earthquakes occurrence $\lambda(t, m, x, y)$ for any time (t), magnitude (m) and location (x,y), where m exceeds a threshold magnitude M_T and (x,y) is a point in a region of surveillance, $\mathbb{R}$. Each earthquake (t_i, m_i, x_i, y_i) with t_i greater than a starting time, t_0, and m_i greater than a minimum magnitude M_C, contributes to a transient increment $\lambda_i(t, m, x, y)$ of the future rate density in its vicinity, given by the multiplication of the probability density function of time (1), magnitude (2) and location(3).

$$f_{1i}(t) = \frac{H(t-t_i)}{(t-t_i)\ln(10)\sigma_T\sqrt{2\pi}}\exp\left[-\frac{1}{2}\left(\frac{\log(t-t_i)-a_T-b_T m_i}{\sigma_T}\right)^2\right] \quad (1)$$

$$g_{1i}(m) = \frac{1}{\sigma_M\sqrt{2\pi}}\exp\left[-\frac{1}{2}\left(\frac{m-a_M-b_M m_i}{\sigma_M}\right)^2\right] \quad (2)$$

$$h_{1i}(x,y) = \frac{1}{2\pi\sigma_A^2 10^{b_A m_i}}\exp\left[-\frac{(x-x_i)^2+(y-y_i)^2}{2\sigma_A^2 10^{b_A m_i}}\right] \quad (3)$$

Where a_M, b_M, σ_M, a_T, b_T, σ_T, b_A, σ_A are free parameters of the model. The details of the EEPAS method are described in a number of papers (e. g. Evison and Rhoades 2005; Rhoades, 2011; Rhoades and Evison 2004; Rhoades, 2007).

Application to Italy. We applied the EEPAS model to Italy using data from the HORUS - HOmogenized instRUmental Seismic catalog (http://horus.bo.ingv.it) from 1960 to 2021

(Lolli *et al.*, 2020). As a surveillance region $\mathbb{R}$ we consider a regular tessellation of the Italian territory made by squares with side $L = 30\sqrt{2}km$ from 7°E to 19°E in longitude and from 36°N to 47°N in latitude. Because the completeness of the seismic catalogue is poor in offshore areas, according to Gasperini et al. (2021), we consider in our analysis only the squares within which at least one earthquake with Mw≥4.0 occurred inland from 1600 to 2021 according to the CPTI15 catalog excluding then all cells that are completely on marine areas. The cells that make up the surveillance region $\mathbb{R}$ are 177 (Fig. 1). We chose as target shocks threshold $m_T = 5.0$ because in Italy such earthquakes potentially cause damage to buildings and threat the health and the life of inhabitants. This choice is also consistent with most of the applications of EEPAS model to other regions of the World (Evison and Rhoades 2005, Rhoades 2011; Rhoades and Evison 2004; Rhoades 2007).We also chose the time interval from 1990 to 2021 for fitting and retrospective forecasting evaluation of the EEPAS model as the accuracy and completeness of the Italian catalog improved significantly since 1990 (Gasperini *et al.*, 2013).

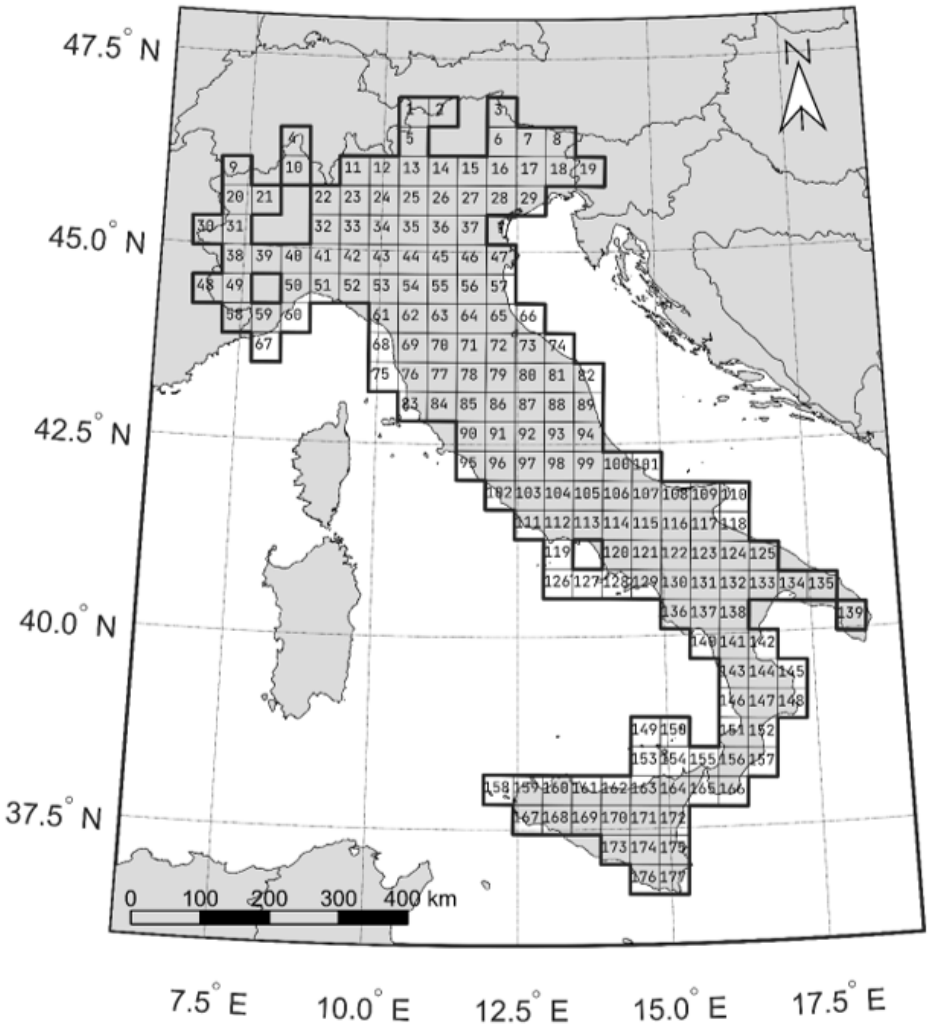


Fig. 1 - Tessellation of the Italian territory region used for the fitting of parameters and for the retrospective experiment. The thick black line delimits the analysis region R. The cells that compose are only those within which at least one earthquake with M≥4.0 from 1600 to 2021 have occured according to CPTI15 catalogue (Rovida *et al.*, 2020) and have $30\sqrt{2}$km of side.

Determination of model parameters. The high number of free parameters to be determined (in principle about 20), considering the parameters of the background model, the aftershock model, and the adjustment factor due to the missing contribution of earthquakes below the minimum completeness magnitude m_c the maximization of the log-likelihood function is very time consuming and subject to numerical instability. However, according to Rhoades and Evison (2004), simultaneous optimization of all parameters is not necessary because some of them, such as the b-value of the Gutenberg and Richter (1944) relation and other parameters can be, in fact, separately fitted or even be simply assigned based on previous works in the same area. For parameters that need to be fitted, the likelihood optimization was carried out using the downhill simplex method (Nelder and Mead, 1965), which is the same optimization method used by the authors for the application of EEPAS to New Zealand (Rhoades and Evison, 2004).

Forecasting skills evaluation and comparison with other forecasting models. We compared the obtained optimal log-likelihood and other statistic as the number of expected earthquake in the time period 1990-2021 obtained with the optimal fitted parameters, the information gain per earthquake (IGPE), AIC, ΔAIC and the information Gain obtained by the EEPAS model with to ones obtained by other rate-based model like Space Uniform Poisson model (SUP), Space Varying Poisson model (SVP), Past to Proximity Earthquake (PPE) and Epidemic Type Aftershock Sequence (ETAS) applied for Italy territory region using the same dataset and the same analysis grid (Table 1).

Tab. 1 - Comparison of skills statistics obtained by each model involved.

	SUP	SVP	PPE	EEPAS	ETAS-SUP	ETAS-SVP
Expected earthquakes	54.1/54	54.5/54	54/54	42.7/54	52.0/54	54.1/54
log-likelihood	-1030.8	-915.1	-1009.5	-983.1	-681.6	-672.8
IGPE	0	2.14	0.39	0.88	6.47	6.63
AIC	2063.7	1832.13	2027.05	1992.12	1379.25	1361.61
ΔAIC	0	2.14	0.34	0.66	6.34	6.50
G	1	8.53	1.48	2.42	643.63	757.84

References

Evison, F., & Rhoades, D. (2005). Multiple - mainshock events and long - term seismogenesis in Italy and New Zealand. *New Zealand Journal of Geology & Geophysics*, *48*, 523–536. https://doi.org/0028-8306/05/4803-0523.

Gasperini, P., Lolli, B., & Vannucci, G. (2013). Empirical calibration of local magnitude data sets versus moment magnitude in Italy. *Bulletin of the Seismological Society of America*, *103*(4), 2227–2246. https://doi.org/10.1785/0120120356.

Lolli, B., Randazzo, D., Vannucci, G., & Gasperini, P. (2020). The homogenized instrumental seismic catalog (HORUS) of Italy from 1960 to present. *Seismological Research Letters*, *91*(6), 3208–3222. https://doi.org/10.1785/0220200148.

Nelder, J. A., & Mead, R. (1965). A Simplex Method for Function Minimization. *The Computer Journal*, *7*(4), 308–313. https://doi.org/10.1093/comjnl/7.4.308.

Rhoades, D. A. (2007). *Application of the EEPAS Model to Forecasting Earthquakes of Moderate Magnitude in Southern California*. *78*(1), 110–115.

Rhoades, D. A. (2011). Application of a long-range forecasting model to earthquakes in the Japan mainland testing region. *Earth, Planets and Space*, *63*(3), 197–206. https://doi.org/10.5047/eps.2010.08.002.

Rhoades, D. A., & Evison, F. F. (2004). Long-range earthquake forecasting with every earthquake a precursor according to scale. *Pure and Applied Geophysics*, *161*(1), 47–72. https://doi.org/10.1007/s00024-003-2434-9.

Rovida, A., Locati, M., Camassi, R., & Lolli, B. (2020). The Italian earthquake catalogue CPTI15. In *Bulletin of Earthquake Engineering* (Issue 0123456789). Springer Netherlands. https://doi.org/10.1007/s10518-020-00818-y.

PROPOSAL OF ZONATIONS FOR THE REGIONALIZATION OF THE GROUND MOTION MODELS IN ITALY

G. Brunelli, G. Lanzano, L. Luzi, S. Sgobba

Istituto Nazionale di Geofisica e Vulcanologia (INGV), Milano, Italy

Introduction. The aim of this work is to identify homogeneous areas (e.g. zonation) where ground motion observations are spatially clustered and biased with respect to the median predictions of a GMM calibrated at a national scale. This goal is reached by the decomposition of the residuals, i.e. the logarithmic difference between observations and the predictions of a GMM, and their spatial analysis. The reference GMM for Italy, adopted in this study, is the most recent model calibrated for active shallow crustal events by Lanzano *et al.* (2019a), hereinafter ITA18, and for the ordinates of the acceleration response spectra (5% damping) of the horizontal components.

The zonation may be adopted to apply regional adjustments to the reference GMM, thus accounting for local source and attenuation effects. This may serve to improve the model accuracy for PSHA purposes or site-specific hazard studies, as well as for empirical earthquake scenarios and ShakeMap (Worden *et al.*, 2018; Michelini *et al.*, 2020).

Data and methods. For the aim of the proposed study, we exploit the ITACAext dataset (Brunelli *et al.*, 2022), that includes recordings of earthquakes of magnitude equal to or greater than 3.0, that occurred during the period 1972-2020, in Italy and in the neighboring countries. Further details are reported in Brunelli *et al.* (2021). The final subset for the analyses consists of 37,098 records of 1,863 earthquakes, recorded by 1,922 recording stations. In order to interpret the results of the residual analysis, we homogenize the estimates of moment magnitude (Mw) of the events by converting Mw calculated with the TDMT method (Time Domain Moment Tensor; Dreger *et al.*, 2003) into Mw estimated with the RCMT method (Regional Centroid Moment Tensor, RCMT; Pondrelli *et al.*, 2002), because in ITA18, the explanatory variable for magnitude scaling is the RCMT-Mw. For this purpose, we adopt the relations by Brunelli *et al.* (2021), modifying the empirical equations, initially proposed by Gasperini et al. (2012-2013).

The core of the analysis is the residual computation, i.e. difference between the (natural) logarithm of the observed ground motion $\log(Y)_{obs}$ and the corresponding prediction $\log(Y)_{pred}$, from a reference GMM. R_{es} is computed using ITA18, assuming R_{rup} as distance metrics and the ground motion parameters are the ordinates of the acceleration response spectra (5% damping) in the interval of vibration periods 0.01-10s. According to the well-established Al Altik *et al.* (2010) approach, the residuals R_{es} are decomposed into repeatable terms referring to event (δB_e), station ($\delta S2S_s$) and event- and site- corrected residuals (δW_{es}), by using a mixed-effect regression (Stafford, 2014; Bates, 2015). Several authors (Bindi *et al.*, 2018a; Bindi and Kotha, 2020) show that δB_e is correlated with source characteristics not captured by the standard magnitude scaling in GMMs, such as stress drop. The δW_{es}, instead, represent the aleatory leftover part of the residuals and should include regional propagation features or effects that are not captured by the reference model, such as directivity effects (Colavitti *et al.,* 2022). In this study, we investigate the spatial trend of between-event residuals, δB_e, to study the characteristics of the seismic sources and the δWes to find the anisotropies of the anelastic attenuation.

Proposed zonations. *Source effects*. For the purpose of regionalizing the source contribution to the ground motion, we consider, as a starting point, the seismogenic zonation ZS16 (Meletti *et al.*, 2019), developed *ad-hoc* in the framework of the latest probabilistic seismic hazard (PSH) model for Italy (MPS19, Meletti *et al.,* 2021). The proposed zonation modifies the initial ZS16, on the basis of the spatial distribution of the δB_e at short period (the vibration period interval

of the acceleration response spectra atT=0.07-0.4s). Furthermore, we take into account the spatial distribution and the focal mechanisms of shallow crustal earthquakes since 1985 and the seismogenic faults of DISS. The proposal of zonation for source correction is finally shown in Figure 1.

The areas in which the GMM for active crustal earthquakes can be applied are 21, but those in which it is actually possible to estimate corrective factors are only 17, because of the scarcity of recorded data; in addition, the ITA18 model cannot be applied to areas in which seismicity is caused by volcanic activity (flagged with number 100). We find that the areas in which the average seismic motion of ITA18 is affected by a median $\delta B_e > 0.2$ (natural log units), are located in northern Italy, in the Alpine chain (Western and Northern Alps, zones 1 and 2) and, remarkably, in the south, i.e., in the Apulian Foreland (13) and in the Western Lobe of the Ionian fault (16). In the latter cases, the mean observed seismic motion is 1.52 and 1.66 times higher than the median GMM prediction for zone 13 and 16, respectively. On the contrary, the areas, where the predicted ground motion overestimates the observations are found in southern Italy, i.e. the Molise region (12), Northern Sicily (19) and the Eastern Lobe of the Ionian Fault (14); the observed decrease in amplitude of ground motion is about 30% in zone 19. In the other cases the deviation from the reference model is within +/- 20%.

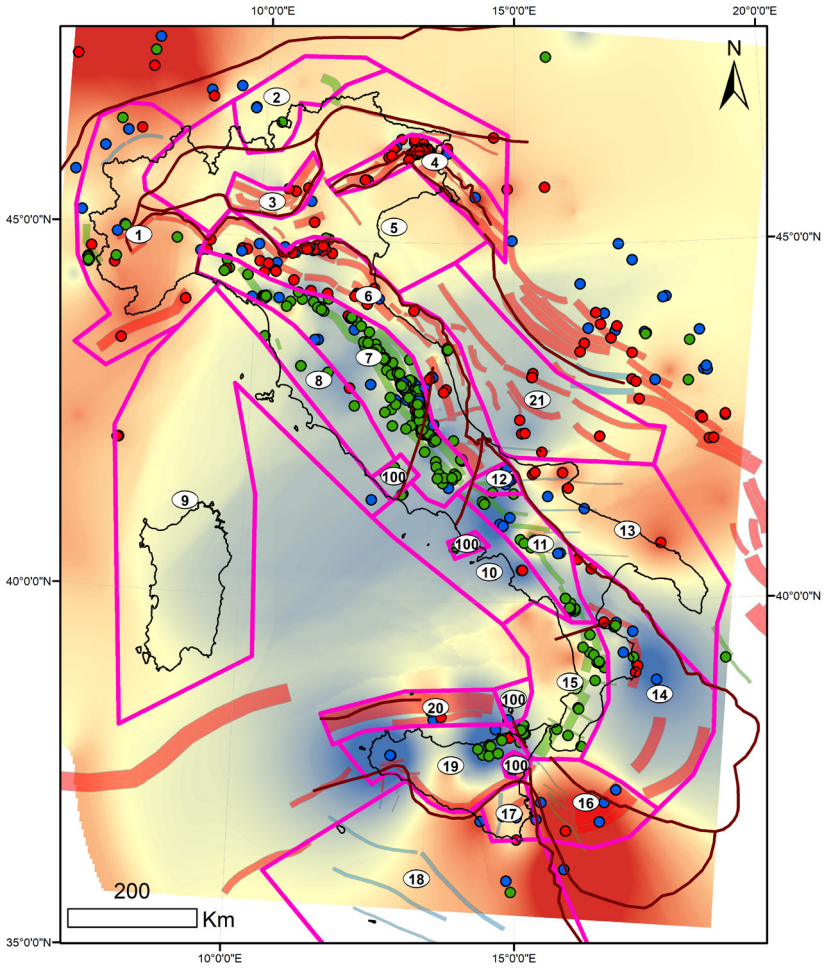


Fig. 1 - Zonation for regionalization of source effects (δB_e) into GMMs.

3.2 Propagation effects. In order to perform a zonation of ground motion attenuation, we assume that the event- and site- corrected residuals are totally justified by a regional deficit of anelastic attenuation, not explained by the model, named δc_3. The latter represents the correction of the anelastic attenuation coefficient c_3 of ITA18 that compensates the δW_{es} residuals record by record. For the purpose of studying the spatial variability of propagation effects, we assign δc_3 to the midpoint along the event-to-station path, as representative of the area affected by the wave propagation. Moreover, we consider only the recordings with source-to-site distances above 80km, because the effects of the anelastic attenuations become relevant for long event-station distances.

As a reference zonation for attenuation, we adopt the model developed by Basili *et al.* (2019) in the framework of TSUMAPS-NEAM project, aiming at developing the first probabilistic earthquake-induced tsunami hazard assessment (Seismic PTHA, S-PTHA) for the coasts of the northeast Atlantic ocean, the Mediterranean sea, and related seas (NEAM). The final proposal (Figure 2) to introduce local propagation effects into GMMs is a further simplification of TSUMAPS zonation, considering the short period δc_3 spatial trend. Some zones show significantly positive δc_3, such as North-western Alps (zone 1 in Figure 2) and Hyblean Plateau (zone 17). An increase in the attenuation is visible from the Adriatic coast (zones 8 and 11

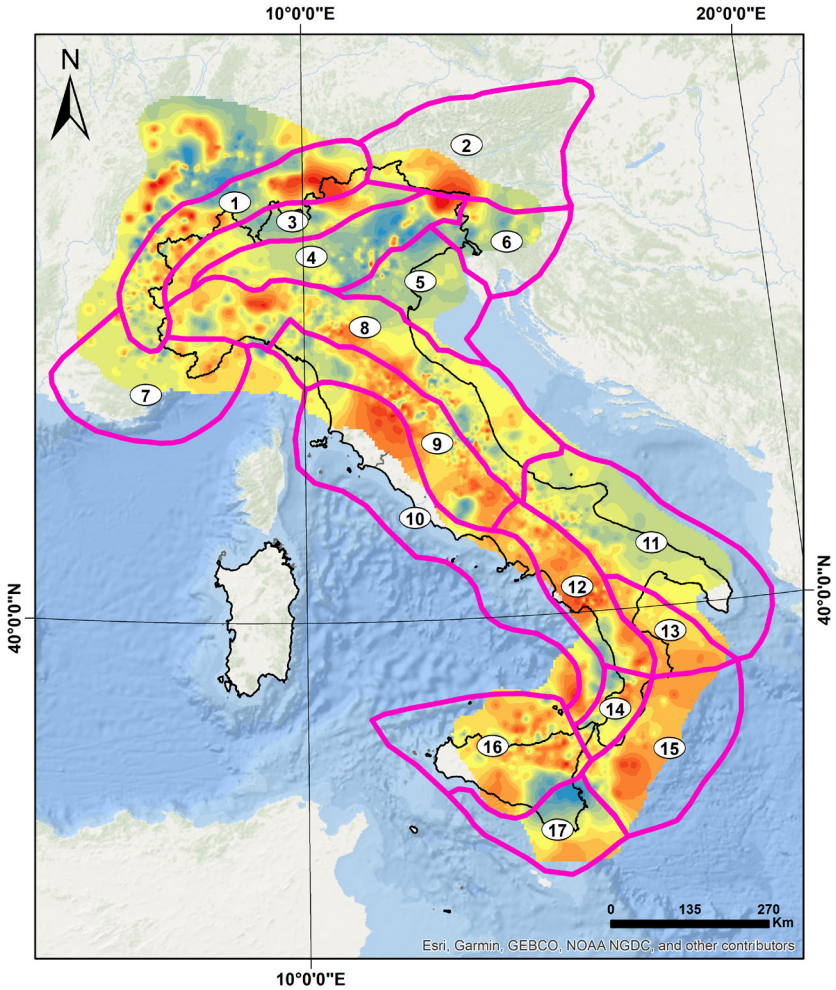


Fig. 2 - Zonation for regionalization of attenuation effects into GMMs.

characterized by positive δc_3), towards the Apennines (zones 9 and 12 with δc_3 close to zero) and the Tyrrhenian coast (zone 10 with negative value), as also observed by Kotha *et al.* (2020).

Acknowledgments. This research is supported by several projects, because of the many different theoretical and applicative implications: i) INGV Pianeta Dinamico (Dynamic Planet)-Working Earth project - Geosciences For The Understanding The Dynamics Of The Earth And The Consequent Natural Risks (CUP code D53J19000170001), funded by MUR (Italian Ministry of University and Research, fund aimed at the relaunch of investments of the central administrations of the State and the development of the country, law 145/2018) - Task S3 – 2021- Seismic attenuation and variability of seismic motion; ii) INGV-DPC agreement B1 2019–2021, with the aim of promoting research activities in the field of seismic hazard in Italy; iii) INGV-DPC agreement B2 2019–2021 (WP1-Task 5). We wish to thank our colleague Francesca Pacor for the scientific support and the fruitful discussions.

References

Al Atik, L., Abrahamson, N., Bommer, J.J., Scherbaum, F., Cotton, F., Kuehn N., 2010. *The variability of ground-motion prediction models and its components.* Seismol. Res. Lett. 81(5), 794-801.

Basili, R., Brizuela, B., Herrero, A., Iqbal, S., Lorito, S., Maesano, F.E., Murphy, S., Perfetti, P., Romano, F., Scala, A., Selva, J., Taroni, M., Thio, H.K., Tiberti, M.M., Tonini, R., Volpe, M., Glimsdal, S., Harbitz, C.B., Løvholt, F., Baptista, M.A., Carrilho, F., Matias, L.M., Omira, R., Babeyko, A., Hoechner, A., Gurbuz, M., Pekcan, O., Yalçıner, A., Canals, M., Lastras, G., Agalos, A., Papadopoulos, G., Triantafyllou, I., Benchekroun, S., Agrebi Jaouadi, H., Attafi, K., Ben Abdallah, S., Bouallegue, A., Hamdi, H., Oueslati, F., 2018. *NEAM Tsunami Hazard Model 2018 (NEAMTHM18): online data of the Probabilistic Tsunami Hazard Model for the NEAM Region from the TSUMAPS-NEAM project.* Istituto Nazionale di Geofisica e Vulcanologia (INGV). http://doi.org/10.5281/zenodo.3406625.

Bates, D., Mächler, M., Bolker, B., Walker S., 2015. *Fitting linear mixed-effects models using lme4.* J. Stat. Software 67(1), 1–48.

Bindi, D., Spallarossa, D., Picozzi, M., Scafidi, D., Cotton, F., 2018a. *Impact of Magnitude Selection on Aleatory Variability Associated with Ground-Motion Prediction Equations: Part I - Local, Energy, and Moment Magnitude Calibration and Stress-Drop Variability in Central Italy*. Bull. Seismol. Soc. Am. 108(3A), 1427-1442.

Bindi, D., Kotha, S.R., 2020. *Spectral decomposition of the Engineering Strong Motion (ESM) flat file: Regional attenuation, source scaling and Arias stress drop.* Bull. Earthq. Eng., 18(6), 2581-2606.

[dataset] Brunelli, G., Lanzano, G., D'Amico, M.C., Felicetta, C., Luzi, L., Mascandola, C., Pacor, F., Russo, E., Sgobba, S., 2022. V.3.2 ITACAext flatfile. doi:10.13127/itaca32/itacaext_flatfile.1.0.

Colavitti, L., Lanzano, G., Sgobba, S., Pacor, F., Gallovič, F., 2022. *Empirical Evidence of Directivity Patterns for Small-to-Moderate Earthquakes on Normal Faults: The Study Case of Central Italy.* J. Geophys. Res. Solid Earth (submitted).

Dreger, D.S., Lee, W.H.K., Kanamori, H., Jennings, P. C., Kisslinger, C., 2003. *Time-domain moment tensor INVerse codel (TDMT-INVC) release 1.1.* International Handbook of Earthquake and Engineering Seismology, Vol. B, 1627.

Kotha, S.R., Weatherill, G., Bindi, D., Cotton, F., 2020. *A regionally-adaptable ground-motion model for shallow crustal earthquakes in Europe.* Bull. Earthq. Eng. 18, 4091–4125.

Lanzano, G., Luzi, L., Pacor, F., Felicetta, C., Puglia, R., Sgobba, S., D'Amico, M., 2019a. *A revised ground motion prediction model for shallow crustal earthquakes in Italy.* Bull. Seismol. Soc. Am., 109(2), 525-54. https://doi.org/10.1785/0120180210.

Meletti, C., Visini, F., D'Amico, V., Pace, B., Rovida, A., 2019. *The seismicity model for Italy MA4, Internal report,* Seismic Hazard Centre NGV, Roma, 10 pp.

Meletti, C., Marzocchi, W., D'Amico, V., Lanzano, G., Luzi, L., Martinelli, F., Pace, B., Rovida, A., Taroni, M., Visini, F., 2021. *The new Italian seismic hazard model (MPS19).* Annals of Geophysics, 64(1).

Michelini, A., Faenza, L., Lanzano, G., Lauciani, V., Jozinović, D., Puglia, R., Luzi, L., 2020. *The new ShakeMap in Italy: Progress and advances in the last 10 yr.* Seismol. Res. Lett. 91(1), 317-333.

Pondrelli, S., Morelli, A., Ekström, G., Mazza, S., Boschi, E., Dziewonski, A.M., 2002. *European–Mediterranean regional centroid-moment tensors: 1997–2000.* Physics of the Earth and Planetary Interiors, 130(1-2), 71-101.

Stafford, P.J., 2014. *Crossed and nested mixed-effects approaches for enhanced model development and removal of the ergodic assumption in empirical ground-motion models.* Bull. Seismol. Soc. Am. 104(2), 702-719.

Worden C.B., Thompson E.M., Baker J.W., Bradley B.A., Luco N., Wald D.J., 2018. *Spatial and spectral interpolation of ground-motion intensity measure observations.* Bull. Seismol. Soc. Am. 108(2), 866–875. https://doi.org/10.1785/0120170201

ANALYSIS OF RESIDUALS FROM A SET OF GROUND MOTION MODELS IN THE NEAR SOURCE

A. Chiecchio, R. Paolucci, M. Vanini

Department of Civil and Environmental Engineering (DICA), Politecnico di Milano, Milano, Italy

Introduction. In a probabilistic framework, ground motion prediction models (GMMs) use datasets of recorded ground motion parameters at multiple stations from different earthquakes in various source regions to generate equations that are used to predict site-specific ground motions (Al-Atik *et al.*, 2010). Typically, these GMMs are based on observed records of past earthquakes, which describe the median and the standard deviation of the ground motion as a function of magnitude, distance, site, and other parameters (Villani and Abrahamson, 2015). During the last couple of decades, thanks to the advances made in terms of computing power and the development of newly published datasets, ground motion modelling had experienced a significant growth, with a range of predictor variables that are now used to describe the source, path, and site effect in detail. As a result, with an enormous number of GMMs being released in the recent years, some authors recommended criteria for the selection of models and suggested that these criteria could be used as a step to guide the publication of new ones (Douglas and Edwards, 2016). Furthermore, GMMs are a key pillar of a probabilistic seismic hazard analysis, and their true performance can be understood completely just when they are used in practice.

In order to provide an overview of the performance of several GMMs, this paper has tested a selection of models against a recently published dataset of near-source strong motion records: NESS2, which is the second version of the Near-Source Strong motion flat-file compiled by Sgobba *et al.* (2021) and available at http://ness.mi.ingv.it/ (Last access: 27/04/22). The analysis was made to consider the records in those conditions that have been demonstrated to dominate the hazard in the high seismically active regions of Italy, for the return period of upmost interest in seismic design (see Barani *et al.*, 2009), therefore testing the performance of GMMs in a range of magnitudes and distances typically poorly constrained by calibration datasets. For a detailed description of the method used and of related results, reference can be made to Paolucci *et al.,* 2022.

Data and analysis. The GMMs selected for the analysis are largely used ones, from the pioneering ground motion model of Ambraseys *et al.* (1996), to the models calibrated in the Italian context (e.g., Bindi *et al.*, 2011) and to the most recent GMM proposed by Kotha *et al.* (2020). Table 1 shows the GMMs selected, with their acronym, their distance metric (R metric) and their range of applicability (M-R). Note that wherever not specified, M is as a moment magnitude.

The NESS2 dataset consists of manually processed waveforms collected according to specific criteria, with a $M_w \geq 5.5$ and containing information about events, source parameters and high-quality metadata. The records of NESS2 used in this work were selected according to these conditions: (i) a Joyner and Boore source-to-site distance within 20km ($R_{jb} \leq 20$km), (ii) a moment magnitude ranging from 5.4 to 7.1, (iii) a soil class classified as EC8 class B (still soil conditions, CEN 2004). Fig. 1 shows the $(M_w – R)$ distribution of the NESS2 dataset and the ranges of the records used in this study, highlighted with the blue rectangle.

With the purpose of making a quantitative comparison between records and GM models, a residual analysis was performed at four selected periods of interest in seismic design: 0s (PGA), 0.5s, 1s and 2s. According to their definition by Strasser et al. (2008) and Al-Atik *et al.* (2010), total residuals were defined as the difference between the natural logarithm of records and the corresponding prediction from a specific GMM. In order to have a better understanding of the possible misfit of a given GMM with respect to records, residuals were then split into a

Tab. 1 - GMMs selected for this work. Rjb = Joyner and Boore distance, Repi = epicentral distance, Rhypo = hypocentral distance, Rrup = rupture distance.

GMMs	Acronym	R metric	Range of applicability	
			M	R (km)
Ambraseys et al. (1996)	AMB96	Rjb	Ms = 4 - 7.5	0 - 200
Sabetta and Pugliese (1996)	SP96	Rjb, Repi	4.6 - 6.8	0 - 100
Ambraseys and Douglas (2003)	AD03	Rjb	Ms = 5.8 - 7.8	0 - 15
Akkar and Bommer (2010)	AB10	Rjb	5 - 7.6	0 - 99
Bindi *et al.* (2011)	ITA10	Rjb	4.1 – 6.9	0 - 200
Akkar *et al.* (2014)	ASB14	Rjb, Rhypo, Repi	4.7 – 7.6	0 - 200
Campbell and Bozorgnia (2014)	CB14	Rrup	5.5 – 8.5	0 - 300
Boore *et al.* (2014)	BSSA14	Rjb	3 – 7.9	0 - 400
Chiou and Youngs (2014)	CY14	Rrup	3.5 – 8.0	0 - 300
Cauzzi *et al.* (2015)	CEA15	Rrup	4.5 – 7.9	0 - 150
Bindi *et al.* (2014)	ITA14	Rjb, Rhypo	4 – 7.6	0 - 300
Lanzano *et al.* (2019)	ITA18	Rjb, Rrup	3.5 - 8	0 - 200
Kotha *et al.* (2020)	K20	Rjb	3 – 7.4	0 - 545

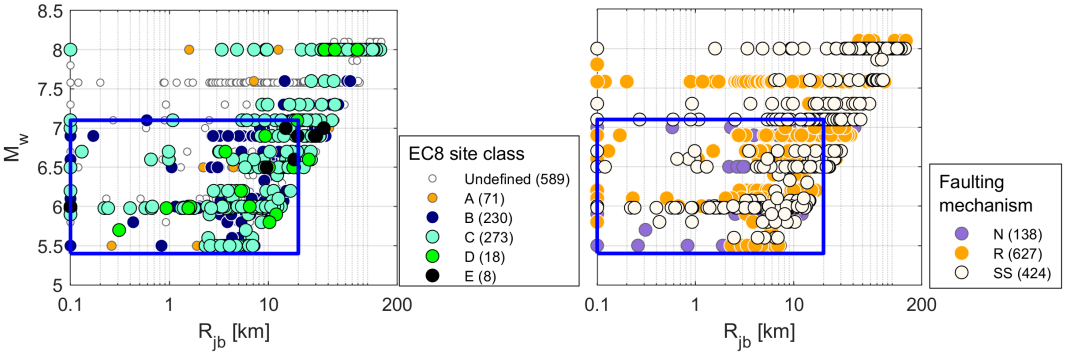


Fig. 1 - Magnitude and distance (M_w – R_{jb}) ranges of the records used in this study (blue rectangle), selected from the NESS2 dataset. (Left): distribution of NESS2 records with respect to their EC8 site class, (right): distribution of NESS2 records with respect to their faulting mechanism. (Adapted from Paolucci *et al.*, 2022).

between (dB_e) and a within component (dW_{es}). Between-event residuals (Eq. 1) represent the average shift of the observed ground motions of an individual earthquake *e* from the median predicted value μ_{es} obtained using a specific GMM (Chen and Faccioli, 2013). Note that, in Eq.1, y_{es} is the natural logarithm of the observation of earthquake *e* at station *s* and *NS* the total number of stations (recordings) available for earthquake (*e*). On the other hand, within-event residuals (Eq. 2) are defined as the misfit between an individual observation of earthquake *e* at station *s* (y_{es}) with respect to the event-corrected median estimate ($\mu_{es}+ \delta B_e$).

$$\delta B_e = \frac{1}{NS}\sum_{s=1}^{NS}\left(y_{es} - \mu_{es}\right) \quad (1)$$

$$\delta W_{es} = \left(y_{es} - \left(\mu_{es} + \delta B_e\right)\right) \quad (2)$$

Fig. *2* shows the mean between event residuals (mean δB_e) computed for the different GMMs under study; the values are shown separately for four periods (0s, 0.5s, 1s and 2s) and

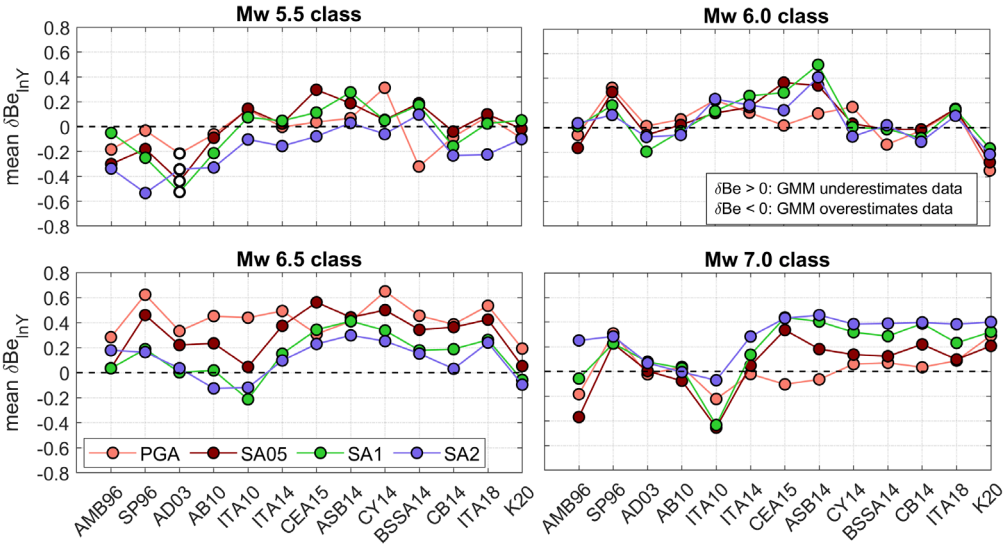


Fig. 2 - Mean between event residuals (δB_e) calculated for the selected set of GMMs. Results are shown for four magnitude classes separately: M_w 5.5 (M_w = 5.4÷5.6), M_w 6.0 (M_w = 5.9÷6.1), M_w 6.5 (M_w = 6.4÷6.6), M_w 7.0 class (M_w = 6.9÷7.1) and four different periods: 0s (light pink line), 0.5s (burgundy line), 1s (green line) and 2s (purple line). AD03 residuals for M_w 5.5 class are shown in white, because these magnitudes are out of the range of applicability of the model. Positive mean δB_e show an underprediction of observations, while negative values indicate an overprediction.

four magnitude classes M_w 5.5 (M_w = 5.4÷5.6), M_w 6.0 (M_w = 5.9÷6.1), M_w 6.5 (M_w = 6.4÷6.6), M_w 7.0 class (M_w = 6.9÷7.1). Note that the idea of this plot is not to give a ranking of the performance of GMMs, but to highlight any possible systematic misfit between GM models and observations of moderate-to-large magnitude earthquakes, in the near-source.

AD03 and AMB96 models show a great consistency with respect to observed records at almost all magnitudes. This tendency may be explained by the great number of records of the calibration datasets of the GMMs, within the magnitude and distance ranges considered in this analysis. The overall positive values of *δBe* at M_w 6.5 suggests a general tendency of GM models to underestimate data in this magnitude class.

Conclusions. This analysis provided a quantitative evaluation of the possible misfit of some of the most used and recent GMMs against observations in a M_w-*R* range dominating the hazard in the most seismically regions of Italy. By taking advantage of a newly published highly quality dataset such as NESS2, and by means of an extensive analysis of residuals and their components, our study provided some interesting insights into the predictive capability of models in such M_w-*R* ranges, showing the good agreement as well of some of the oldest models with respect to records.

We think that this kind of research may encourge the developing of new models constrained, as accurately as possible, in the near source of moderate to large magnitude earthquakes, typically poorly constrained by observations, taking possibly advantage of results from 3D physics-based numerical simulations, for the potential improvement of calibration datasets.

Acknowledgements and funding. This work has been partially supported by swissnuclear within the research activity "Development of advanced numerical approaches for earthquake ground motion prediction", in the framework of the Sigma2 project, and by the Department of Civil Protection within the ReLUIS project WP18 "Normative contributions related to seismic action". The authors are sincerely grateful to Sreeram Reddy Kotha, Ezio Faccioli and Chiara Smerzini for their useful comments.

References

Al Atik L., Abrahamson N.A., Bommer J.J., Scherbaum F., Cotton F, and Kuehn N.; 2010: *The variability of ground-motion prediction models and its components*. Seismological Research Letters, 81: 794-801. Doi:10.1785/gssrl.81.5.794.

Akkar S., Bommer J.J.; 2010: *Empirical equations for the prediction of PGA, PGV and spectral accelerations in Europe, the Mediterranean region and the Middle East*. Seismol Res Lett, 81:195–206. Doi:10.1785/gssrl.81.2.195.

Akkar S., Sandikkaya M.A., Bommer J.J.; 2014: *Empirical ground-motion models for point and extended-source crustal earthquake scenarios in Europe and the Middle East*. Bull Earthquake Eng, 12:359-387. Doi:10.1007/s10518-013-9461-4.

Ambraseys N.N., Simpson K.A. and Bommer J.J.; 1996: *Prediction of horizontal response spectra in Europe*. Earthquake Engineering and Structural Dynamics, 25: 371 – 400.

Ambraseys N.N. and Douglas J.; 2003: *Near-field horizontal and vertical earthquake ground motions*. Soil Dyn and Earthq Eng, 23:1–18. Doi:10.1016/S0267-7261(02)00153-7.

Barani S., Spallarossa D., Bazzurro P.; 2009: *Disaggregation of probabilistic ground-motion hazard in Italy.* Bulletin of the Seismological Society of America, 99: 2638-2661. Doi:10.1785/0120080348.

Bindi D., Pacor F., Luzi L., Puglia R., Massa M., Ameri G. and Paolucci R.; 2011: *Ground motion prediction equations derived from the Italian strong motion database*. Bull Seismol Soc Am, 9:1899–1920. Doi: 10.1007/s10518-011-9313-z.

Bindi D., Massa M., Luzi L., Ameri G., Pacor F., Puglia R., Augliera P.; 2014: *Pan – European ground-motion prediction equations for the average horizontal component of PGA, PGV, and 5% - damped PSA at spectral periods up to 3.0s using the RESORSE dataset*. Bull Earthq Eng, 12:391– 430. Doi: 10.1007/s10518-013-9525-5.

Boore D.M., Stewart J.P., Seyhan E., Atkinson G.M.; 2014: *NGA-West2 equations for predicting PGA, PGV, and 5% damped PSA for shallow crustal earthquakes*. Earthq Spectra, 30:1057–1085. Doi:10.1193/070113EQS184M.

Campbell K.W. and Bozorgnia Y.; 2014: *NGA-West2 ground motion model for the average horizontal components of PGA, PGV, and 5% damped linear acceleration response spectra*. Earthq Spectra, 30: 1087 – 1115. Doi: 10.1193/062913eqs175m.

Cauzzi C., Faccioli E., Vanini M. and Bianchini A.; 2015: *Updated predictive equations for broadband (0.01 – 10s) horizontal response spectra and peak ground motions, based on a global dataset of digital acceleration records*. Bull Earthq Eng, 13: 1587 – 1612. Doi:10.1007/s10518-014-9685-y.

Chen L., Faccioli E.; 2013: *Single-station standard deviation analysis of 2010–2012 strong-motion data from the Canterbury region, New Zealand*. Bull Earthquake Eng, 11,1617–1632. Doi: 10.1007/s10518-013-9454-3.

Chiou B.S.J., Youngs R.R.; 2014: *Update of the Chiou and Youngs NGA Model for the Average Horizontal Component of Peak Ground Motion and Response Spectra.* Earthq Spectra, 30:1117-1153. Doi:10.1193/072813EQS219M.

Comité Européen de Normalisation (CEN); 2004: *Eurocode 8: design of structures for earthquake resistance-Part 1: general rules, seismic actions and rules for buildings.* Comité Européen de Normalisation, Brussels.

Douglas J. and Edwards B.; 2016: *Recent and future developments in earthquake ground motion estimation*. Earth Sci Rev 160:203-219. Doi: 10.1016/j.earscirev.2016.07.005.

Kotha S.R., Weatherill G., Bindi D., Cotton F.; 2020: *A regionally adaptable ground-motion model for shallow crustal earthquakes in Europe*. Bulletin of Earthquake Engineering, 18: 4091 – 4125. Doi:10.1007/s10518-020-00869-1.

Lanzano G., Luzi L., Pacor F., Felicetta C., Puglia R., Sgobba S., D'Amico M.; 2019: *A revised ground-motion prediction model for shallow crustal earthquakes in Italy*. Bull Seismol Soc Am, 109:525–540. Doi: 10.1785/0120180210.

Paolucci R., Chiecchio A., Vanini M.; 2022: *The older the better? The strange case of empirical ground motion models in the near-source of moderate-to-large magnitude earthquakes*. Bull Earthquake Eng, 20:1325–1342. Doi:10.1007/s10518-021-01304-9.

Sabetta F. and Pugliese A.;1996: *Estimation of response spectra and simulation of nonstationary earthquake ground motions*. Bulletin of Seismological Society of America, 86: 337–352. Doi:10.1785/BSSA0860020337.

Sgobba S., Felicetta C., Lanzano G., Ramadan F., D'Amico M., Pacor F.; 2021: *NESS2.0: An Updated Version of the Worldwide Dataset for Calibrating and Adjusting Ground-Motion Models in Near Source*. Bulletin of the Seismological Society of America, 111: 2358–2378. Doi:10.1785/0120210080.

Strasser F.O., Bommer J.J. and Abrahamson N.A.; 2008: *Truncation of the distribution of ground-motion residuals*. J Seismol, 12:79-105. Doi:10.1007/s10950-007-9073-z.

Villani M., Abrahamson N.A.; 2015: *Repeatable Site and Path Effects on the Ground-Motion Sigma Based on Empirical Data from Southern California and Simulated Waveforms from the CyberShake Platform.* Bulletin of the Seismological Society of America, 105: 2681–2695. Doi: 10.1785/0120140359.

UN NUOVO APPROCCIO, 'TIME DEPENDENT', PER LA STIMA DELLA PERICOLOSITÀ SISMICA IN ITALIA

G. De Natale[1], P. Harabaglia[2], M. Vona[2], G. Martinelli[3], V. Marchitelli[4], C. Troise[1]

[1] Istituto Nazionale di Geofisica e Vulcanologia, Napoli, Italy
[2] Scuola di Ingegneria, Università Della Basilicata, Potenza, Italy
[3] Istituto Nazionale di Geofisica e Vulcanologia, Palermo, Italy
[4] Dipartimento Mobilità, Qualità Urbana, Lavori Pubblici, Ecologia e Ambiente, Regione Puglia, Bari, Italy

In questo lavoro, proponiamo un nuovo approccio, dipendente dal tempo, alla stima della pericolosità sismica in Italia. Tale approccio è basato su due osservazioni fondamentali:

1) I terremoti con magnitudo M≥6 tendono a raggrupparsi spazialmente (clustering);
2) Essi hanno luogo in aree in cui la sismicità di fondo è molto bassa o praticamente assente, ma contigue ad aree in cui il livello di sismicità è da lungo tempo più elevato della media (talvolta per decine di anni).

Tenendo conto di queste due osservazioni combinate, abbiamo sviluppato un metodo che permette di individuare, con un livello di probabilità del 75% in base a test retrospettivi sul catalogo, le aree in cui accadranno i terremoti con M≥6 nei successivi 20-30 anni. Il metodo sviluppato, a causa della notevole ampiezza delle aree individuate e delle finestre temporali, non è adatto per la previsione dei singoli terremoti, ma può avere un ruolo di primo piano nella pianificazione urbana delle aree ad alto rischio sismico. In pratica, poiché il metodo identifica un sottoinsieme enormemente ridotto, rispetto alle aree ad alto rischio sismico nell'intero territorio nazionale, di aree a maggiore probabilità di forti terremoti nell'immediato futuro, può essere molto utile, nell'ottica di una pianificazione ottimale tesa alla mitigazione del rischio sismico, per decidere le priorità nelle azioni di mitigazione del rischio. In ogni caso, se anche in alcune di tali aree non avverranno forti terremoti in tempi brevi, le azioni di mitigazione

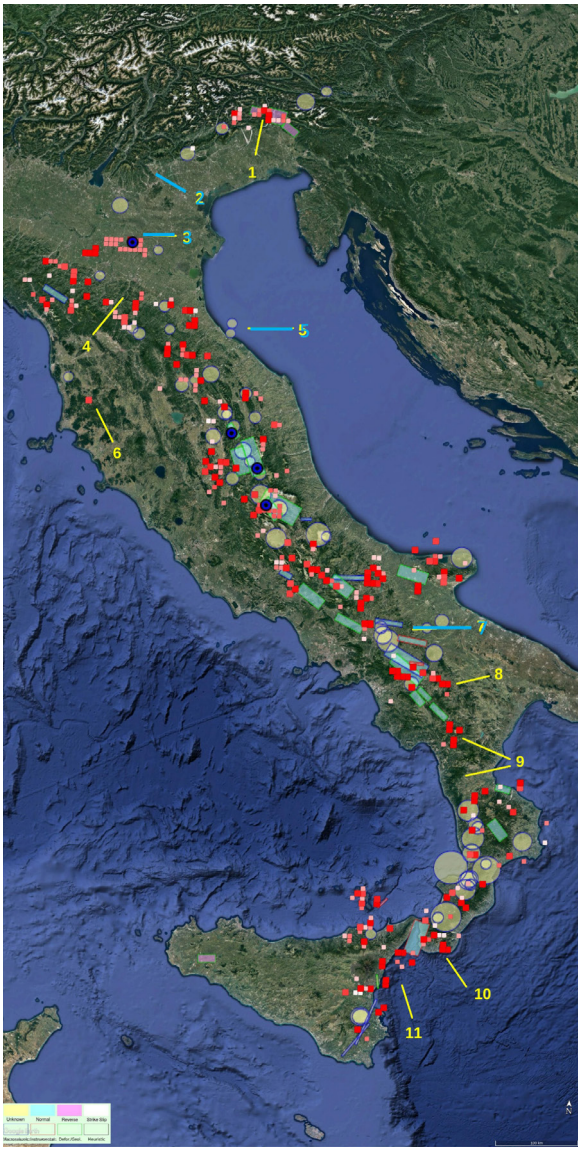


Fig. 1 - Nodi in prossimità dei quali vi è una maggiore probabilità di accadimento di eventi di M>6. La scala di colore va dal bianco al rosso ed è rappresentativa dell'indice di latenza. I nodi con indice di latenza superiore a 0.7, quelli quindi ad alto rischio di rottura, sono rappresentati da quadratini di maggiori dimensioni. Le aree con alta probabilità di terremoti con M≥6 sono indicate con numero e indice gialli; quelle con bassa probabilità con numero ed indice azzurro.

del rischio attraverso la pianificazione territoriale, i cui risultati persistono anche su orizzonti temporali molto lunghi, saranno comunque di alto valore e certamente tutt'altro che inutili in aree caratterizzate comunque da alto rischio sismico.

In fig.1 è mostrata l'attuale situazione della pericolosità sismica in Italia evidenziata con il nuovo metodo statistico.

Si nota che alcune aree notoriamente ad alta sismicità (con indici in giallo) sono caratterizzate da alta pericolosità sismica, mentre altre (con indici in azzurro) sono attualmente caratterizzate da bassa pericolosità. Nel complesso, si nota bene che, tra tutte le aree ad alta sismicità in Italia, quelle caratterizzate attualmente da alta pericolosità sismica nell'immediato futuro rappresentano un sottoinsieme relativamente piccolo, e sono quelle in cui bisognerebbe dare la più alta priorità agli interventi di mitigazione del rischio.

In generale, i risultati del metodo, puramente statistico, sono anche fondamentalmente in accordo con modelli fisici di trasferimento di sforzo tra sistemi di faglie contigui.

PROBABILITY, CORRELATION, AND TRANSFER ENTROPY BETWEEN WESTERN PACIFIC EARTHQUAKES AND NOAA ELECTRON BURSTS

C. Fidani[1,2], A. De Santis[1], L. Perrone[1]

[1] Istituto Nazionale di Geofisica e Vulcanologia, Roma, Italy
[2] Central Italy Electromagnetic Network, Fermo, Italy

A correlation between strong earthquakes (EQs) and high energy electron bursts (EBs) has been recently presented in several publications. The peak of correlation appeared when considering shallow EQs with hypocentre depth of less than 200 km, located in a large portion of the Earth's crust in the Western Pacific, with a minimum magnitude of 6. It evidenced that the 30-100 keV electron detections by the NOAA-15 satellite anticipate by1.5-3.5 h the EQ events. Using this result for EQ forecasting requires unambiguously definition of EBs to verify a precursor phenomenology (Wyss, 1997), which was obtained only considering EBs with L-shell in a restricted interval (Fidani, 2021; see also Figure 1). Here, a contribution is presented which links the analytical transfer entropy, TE (Schreiber, 2000; Bossomaier *et al.*, 2009) for digital variables to conditional probabilities and correlations. This approach refers to the information theory (e.g. Jaynes, 1957; Cover and Thomas, 2005), and has been recently utilized in the lithosphere to ionosphere system (Fidani, 2022). Thus, mutual information and transfer entropy have been evaluated in the context of precipitating EBs from the inner Van Allen belt, which preceded strong EQs.

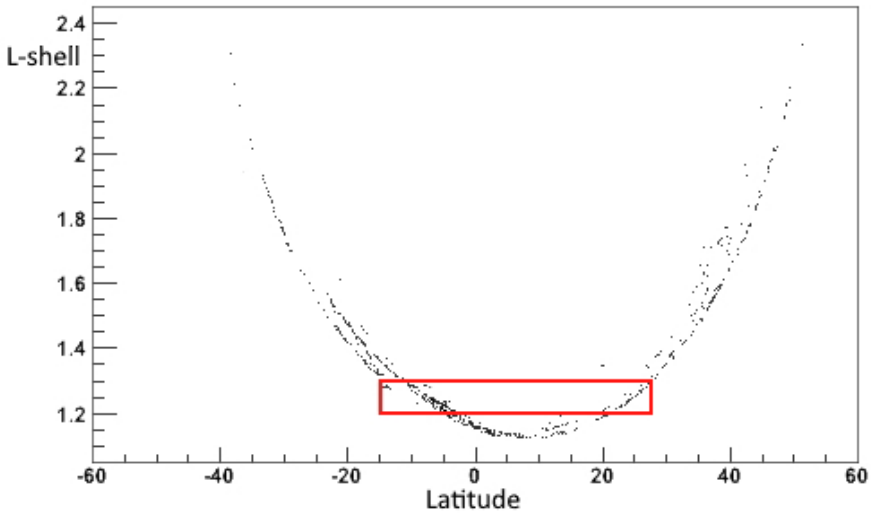


Fig. 1. L-shell intervals relative only to EBs which were considered to unequivocally discriminate the EBs to use for a possible forecasting experiment as proposed in Fidani, 2020 and 2021.

Considering EQ and EB as two sets of digital events, in the case of dependency between events each one contains information on the other. To quantify the amount of information that the EB event has on EQ, the mutual information (Cover & Thomas, 2005) is:

$$I(EQ;EB) = \Sigma\Sigma_{\{0,1\}} P(x,y) \log_2 \{P(x,y)/[P(x)P(y)]\}, \quad (1)$$

where P(x), and P(y) are defined as frequencies of EQ and EB, respectively, while P(x,y) is the joint probability. The logarithm base is 2 as digital events are considered. Making more explicit the mutual information:

$$I(EQ;EB) = \Sigma\Sigma_{\{0,1\}} P(x,y) [\log_2 P(x,y) - \log_2 P(x) - \log_2 P(y)]$$

$$= \Sigma\Sigma_{\{0,1\}} P(x,y) \log_2 P(x,y) - \Sigma_{x=\{0,1\}} \log_2 [P(x)] \Sigma_{y=\{0,1\}} P(x,y) - \Sigma_{y=\{0,1\}} \log_2 [P(y)] \Sigma_{x=\{0,1\}} P(x,y),$$

and being $\Sigma_x P(x,y) = P(y)$

$$I(EQ;EB) = \Sigma\Sigma_{\{0,1\}} P(x,y) \log_2 P(x,y) - \Sigma_{\{0,1\}} P(x) \log_2 P(x) - \Sigma_{\{0,1\}} P(y) \log_2 P(y)$$

$$= H(EQ) + H(EB) - H(EQ,EB), \quad (2)$$

that is the difference between the sum of EQ and EB entropies and the joint case: it is 0 when EQs and EBs are independent events, while it is > 0 when the events share some information, being $H(EQ,EB) < H(EQ) + H(EB)$. Relation (2) is symmetric resulting in that $I(EQ;EB) = I(EB;EQ)$. Being so, the mutual information is not able to detect the direction of the information flux between the events.

An asymmetric measure, named time-delayed mutual information (Jin *et al.*, 2006), can be obtained if an investigator is interested to elucidate when events present themselves in time domain by introducing a time-lag parameter Δt between events EQ and EB in (1). It describes the shared information between EQs and EBs at different times, introducing a consequentiality between two sets of events in a statistical way:

$$I(EQ;EB+\Delta t) = \Sigma\Sigma_{\{0,1\}} P(x,y+\Delta t) \log_2 \{P(x,y+\Delta t)/[P(x)P(y)]\}, \quad (3)$$

being $P(y+\Delta t) = P(y)$. Time-delayed mutual information works also when non-linear links characterize interactions between two event time series. However, shared history and common external driving effects between two processes seem to escape from identification by means of mutual information (Bossomaier *et al.*, 2009). Thus, the idea is to use the dynamic of events considering transition probabilities $P(x+1|x)$, where +1 is referred to the next time step, and the entropy rate $h(E) = H(E+1) - H(E) = - H(E+1|E)$. Then, in analogy with relation (2) and using the joint probability properties

$$H(EQ+1|EQ) + H(EB|EQ) - H(EQ+1,EB|EQ) =$$

$$= - \Sigma\Sigma_{\{0,1\}} P(x+1,x) \log_2 P(x+1|x) - \Sigma\Sigma_{\{0,1\}} P(y,x) \log_2 P(y|x) + \Sigma\Sigma\Sigma_{\{0,1\}} P(x+1,y,x) \log_2 P(x+1,y|x)$$

$$= \Sigma\Sigma\Sigma_{\{0,1\}} [- P(x+1,x,y) \log_2 P(x+1|x) - P(y,x,x+1) \log_2 P(y|x) + P(x+1,y,x) \log_2 P(x+1,y|x)]$$

$$= \Sigma\Sigma\Sigma_{\{0,1\}} P(x+1,y,x) [\log_2 P(x+1,y|x) - \log_2 P(x+1|x) - \log_2 P(y|x)]$$

$$= \Sigma\Sigma\Sigma_{\{0,1\}} P(x+1,y,x) \log_2 \{P(x+1,y|x)/[P(x+1|x) P(y|x)]\}, \quad (4)$$

which is the information difference between dependent and independent transitions indicated by $P(x+1,y|x)$ and $P(x+1|x) P(y|x)$, respectively. It is the conditional mutual information $I(EQ+1;EB|EQ)$ and is called transfer entropy $TE_{EB->EQ}$. Finally, being

$$P(EQ \cap EQ+1 \cap EB+\Delta t) = P(EQ \cap EQ+1|EB+\Delta t)P(EB+\Delta t), \quad (5)$$

where $P(EB+\Delta t) = P(EB)$, the transfer entropy can be obtained starting from conditional probabilities.

This prospective looks like handy when considering the correlation results between strong

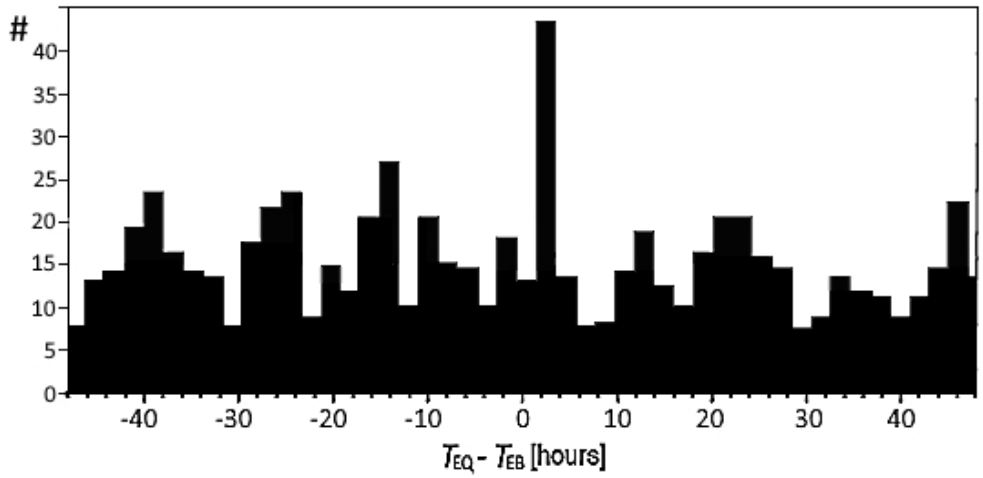


Fig. 2 - The correlation event histogram between EQs and EBs with a Δt range of -48 to 48 hours, in intervals of 2 hours, which are shifted by 1.5 hours with respect to the origin.

EQs and NOAA EBs. In fact, starting from Matthews correlations (Matthews, 1975), it can be shown that the conditional probabilities can be defined between EQs and EBs (Fidani, 2018). Moreover, correlation histograms calculated in past publications (Fidani, 2015), $\Sigma_{\{EQ;EB\}}$(EQ x EB) (see Fig. 2), were put in relation with the Matthews correlation coefficients corr(EQ,EB) (Fidani, 2020). Being so, the next relations need to be evaluated retrieving the relations (4) and (5):

$$P(EQ \cap EQ{+}1 \,|\, EB{+}\Delta t) = \tag{6}$$

$$= P(EQ \cap EQ{+}1) + corr(EQ \cap EQ{+}1, EB{+}\Delta t)\ \{[1 - P(EQ \cap EQ{+}1)]\ P(EQ \cap EQ{+}1)\ [1/P(MA) - 1]\}^{\wedge}½,$$

$$P(EQ{+}1 \,|\, EB{+}\Delta t) = P(EQ{+}1) + corr(EQ{+}1, EB{+}\Delta t)\ \{[1 - P(EQ)]\ P(EQ)\ [1/P(MA) - 1]\}^{\wedge}½, \tag{7}$$

$$P(EQ{+}1 \,|\, EQ) = P(EQ{+}1) + corr(EQ{+}1, EQ)\ [1 - P(EQ)], \tag{8}$$

$$P(EB{+}\Delta t \,|\, EQ) = P(EB{+}\Delta t) + corr(EB{+}\Delta t, EQ)\ \{[1 - P(EB)]\ P(EB)\ [1/P(EQ) - 1]\}^{\wedge}½, \tag{9}$$

where P(EQ+1) = P(EQ), and corr(EB+Δt,EQ) = − corr(EQ,EB+Δt).

The number of EQs that occurred during the 6953 pairs of hours were considered, which is N_{EQ} = 57, and P(EQ) = 0.0082 EQs for each pair of hours. A N_{EB} = 1892 EBs was considered in the same time interval, so that P(EB) = 0.27. Finally, a $N_{EQ \cap EQ+1}$ = 6 resulted in the same time interval, so that P(EQ∩EQ+1) = 0.000863 for each pair of hours. Then, calculating quantities (6-8) and summing in (4) for the couples of digital events, the transfer entropy is retrieved and shown in Figure 3, where mall negative terms of TE were set to 0 as by definition. A second peak, which does not appear in the correlation histogram of Figure 2, appears in the transfer entropy at a negative time delay Δt = 58.5 - 56.5 h. It represents a real novelty that arises from this analysis (Fidani, 2022). It means that EB shares a maximum amount of information with past EQs occurring around 2 days and 9.5 h before EBs. Given the significant reduction in the EQ auto-correlation due to the Cluster 2000 algorithm application (Reasenberg, 1985), the second peak in the present case is not very significant. Nevertheless, this is an example of how linear and non-linear contributions could be separated, making a distinction between correlation and auto-correlation in the particular case of binary events, respectively.

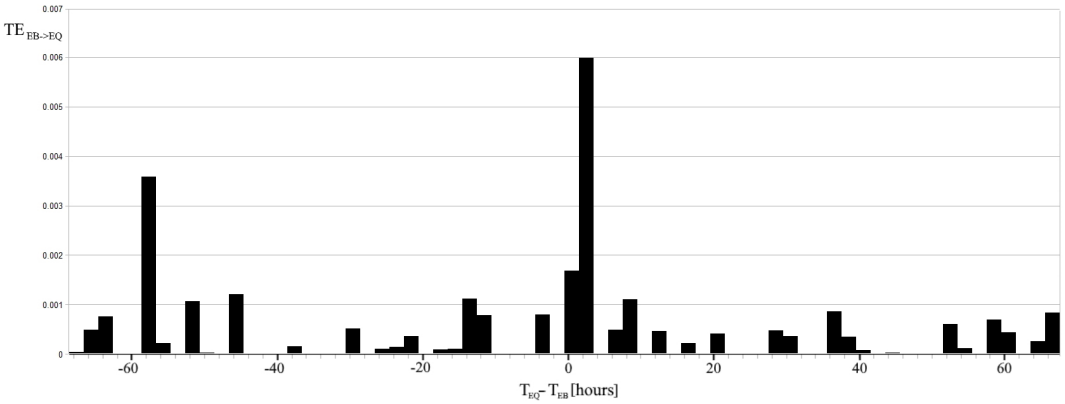


Fig. 3 - TE between EQs in the lithosphere and EBs in the ionosphere with respect to the time delay Δt, here extended in the range from -68.5 to 67.5 hours. The time bin is 2 hours.

References

Bossomaier, T.; Barnett, L.; Harré, M.; Lizier, J.T.; 2009: *An Introduction to Transfer Entropy: Information Flow in Complex Systems*. Biomed. Tech., **54**, 323–328.

Cover, T.M.; Thomas, J.A.; 2005: *Elements of Information Theory*, John Wiley & Sons: Hoboken, NJ, USA.

Fidani, C.; 2015: *Particle precipitation prior to large earthquakes of both the Sumatra and Philippine Regions: A statistical analysis*, J. Asian Earth Sci., **114**, 384-392.

Fidani, C.; 2018: *Improving Earthquake Forecasting by Correlations Between Strong Earthquakes and NOAA Electron Bursts*, TAO, **29**(2), 117-130.

Fidani, C.; 2020: *Probability, Causality and False Alarms using Correlations Between Strong Earthquakes and NOAA High Energy Electron Bursts*. Ann. Geophys., **63**(5), PA543.

Fidani, C.; 2021: *West Pacific earthquake forecasting by NOAA electron bursts with independent L-shells and ground based magnetic correlations.* Frontiers in Earth Science, **9**, 673105.

Fidani, C.; 2022: *Transfer Entropy of West Pacific Earthquakes to Inner Van Allen Belt Electron Bursts*. Entropy 2022, **24**, 359.

Jaynes, E. T.; 1957: *Information Theory and Statistical Mechanics*. Phys. Rev. **106** (4), 620.

Jin, S.-H.; Kwon, Y.-J.; Jeong, J.-S.; Kwon, S.-W.; Shin, D.-H.; 2006: *Differences in brain information transmission between gifted and normal children during scientific hypothesis generation*. Brain Cogn., **62**, 191–197.

Matthews, B. W.; 1975: *Comparison of the predicted and observed secondary structure of T4 phage lysozyme*. Biochimica et Biophysica Acta (BBA) - Protein Structure. **405** (2), 442–451.

Reasenberg, P.; 1985: *Second-order moment of central California seismicity, 1969–1982*. Journal of Geophysical Research, **90**(B7), 5479–5495

Schreiber, T.; 2000: *Measuring Information Transfer*. Phys. Rev. Lett., **85**, 461–464.

Wyss, M.; 1997: *Second Round of Evaluations of Proposed Earthquake Precursors*. Pageoph., **149**, 3–16.

NESTOREV1.0: A MACHINE LEARNING-BASED MATLAB PACKAGE FOR FORECASTING STRONG AFTERSHOCKS IN SEISMIC CLUSTERS

S. Gentili[1], P. Brondi[1], R. Di Giovambattista[2]

[1] National Institute of Oceanography and Applied Geophysics - OGS, Udine, Italy
[2] Istituto Nazionale di Geofisica e Vulcanologia, Roma, Italy

NESTORE (Next STrOng Related Earthquake) is an algorithm for probabilistic forecasting of clusters in which a strong mainshock is followed by at least one aftershock of similar magnitude (greater than or equal to that of the mainshock minus one).

Some previous versions of the algorithm have been successfully applied to California and Italian seismicity (Gentili and Di Giovambattista 2017, 2020, 2022). The algorithm analyzes selected seismicity features at increasing time intervals after mainshock occurrence, through a multiparameter pattern recognition approach based on decision trees. In particular, the analyzed features are related to the number of earthquakes, their energy, and spatiotemporal distribution, and are used to provide forecasting of the probability of strong subsequent events for the current seismic cluster. The main problems in this type of application are essentially two. The first is the number of available examples (clusters) which are generally on the order of tens, due to the limited time in which earthquake catalogs have high quality (maximum 50 years). In machine learning applications hundreds or thousands of examples are generally needed. The second is class imbalance, because a strong following earthquake is recorded only in a low percentage of the observed clusters. During these last years, the algorithm has been improved to increase its generalization capability despite the small number of clusters available in seismological databases and the presence of some outliers. A renewal of the old version of the software, both in terms of algorithm and usability, has been developed within the project "Analysis of seismic sequences for strong aftershock forecasting" funded by a grant of the Ministry of Foreign Affairs and International Cooperation in the framework of the scientific and technological collaboration between Italy and Japan.

The current version of the software, NESTOREv1.0, is now mature enough to be distributed to the scientific community to be applied and tested in new areas. The software, which will be available on GitHub in the coming months, has a GUI (Graphical User Interface) or can be launched directly from the MATLAB command line. In this presentation, we will show the structure of the software and some examples of software outputs.

In a related poster (Brondi *et al.*, 2022) we will show an example of the application of the new version of the algorithm to Italian seismicity.

Acknowledgements. Funded by a grant from the Italian Ministry of Foreign Affairs and International Cooperation.

References

Gentili S. and Di Giovambattista R.; 2017: *Pattern recognition approach to the subsequent event of damaging earthquakes in Italy.* Physics of the Earth and Planetary Interiors, **266**, pp. 1-17.

Gentili S. and Di Giovambattista R.; 2020: *Forecasting strong aftershocks in earthquake clusters from northeastern Italy and western Slovenia.* Physics of the Earth and Planetary Interiors, **303**, 106483.

Gentili, S. and Di Giovambattista, R.; 2022: *Forecasting strong subsequent earthquakes in California clusters by machine learning*, Physics of the Earth and Planetary Interiors, accepted.

Brondi, P., Gentili, S. and Di Giovambattista, R.; 2022: *NESTOREv1.0 application to Italian seismicity* Submitted to GNGTS 2022.

ESTIMATING LOCAL EMPIRICAL SITE AMPLIFICATION MODEL FOR CITY OF LUCERNE IN SWITZERLAND

P. Janusz[1], V. Perron[1], C. Knellwolf[2], D. Fäh[1]

[1] Swiss Seismological Service, ETH Zürich, Zürich, Switzerland
[2] Verkehr und Infrastruktur, Abteilung Naturgefahren, Kanton Luzern, Kriens, Switzerland

Introduction. Site response evaluation is a crucial component of seismic hazard and risk estimation, especially in densely populated urban environments that are particularly exposed. Recordings of weak earthquakes can be used to obtain empirical ground amplification using among others the standard spectral ratio (SSR - Borcherdt, 1970) or Generalized Inversion Techniques (GIT - Andrews, 1986). However, in cities located in areas of low to moderate seismicity, it may take several years to record a sufficient number of high-quality events due to strong background noise. In addition, because of the high cost of deploying dense long-term seismic monitoring networks and the lack of free-space areas in the city, the empirical methods based on earthquake observations do not allow to map site response with high spatial resolution. On the other hand, seismic ambient noise can be measured relatively cheap and fast even in the urban environment. However, as many authors show (e.g. Bonilla *et al.*, 1997; Field *et al.*, 1990; Perron *et al.*, 2018a), we are not able to estimate the correct amplitude of amplification function with methods based only on ambient noise such as noise-based spectral ratio (SSRn - Kagami *et al.*, 1982) or horizontal-to-vertical spectral ratio (HVSR - Nakamura, 1989; Nogoshi and Igarashi, 1971). Hence, we applied the hybrid SSR approach (SSRh - Perron *et al.*, 2018) that combines ambient vibration data and earthquake ground motion observation. Our study area is Lucerne in Central Switzerland which is a densely populated town located in a soft sedimentary basin. The seismicity in the area is low-to-moderate, however, there is historical evidence of several strong earthquakes with damage in the past (i.e. Mw 5.9 in 1601). In our project (Janusz *et al.*, 2022), we tested and tried to optimize the SSRh method and developed an amplification model in a broad frequency band for the area. This study is part of the URBASIS-EU project in the framework of the Horizon 2020 ITN.

Data. A small temporary seismic monitoring network consisting of 10 velocimeters (3-component short-period seismometers Lennartz 5 seconds LE-3D 5-s with Centaur digitizers) was installed respectively in 2019 and 2020 for a few months to record weak local and teleseismic earthquakes. In total, the network was operating for about 1 year. In addition, three accelerometers of the Swiss Strong Motion Network (SSMNet - Hobiger *et al.*, 2021; Michel *et al.*, 2014) located in the city center were used as supplementary. In June 2020 and April 2021, we carried out two ambient vibration measurement campaigns with the same setup (LE-3D 5-s – Centaur), we recorded noise for at least 1-2 hours at 100 points. Moreover, about 200 hundred single-station recordings performed in the past were added to our dataset (e.g. Poggi *et al.*, 2012).

Methodology. The SSRh method combines two methods earthquake-based (SSR) and noise-based spectral ratios (SSRn). In the first step (Fig. 1), a small seismic monitoring network consisting of a minimum of two stations where one is located on the rock and one in the basin has to be installed. Then, ambient vibration data has to be recorded simultaneously with earthquake monitoring stations allowing calculating SSRn between each site and basin-situated station. Finally, we correct the noise-based spectral ratio using the rock-relative SSR.

To obtain SSR functions, we processed 44 local and teleseismic earthquakes recorded between November 2019 and April 2021. We considered signals from the P-wave until the coda wave arrival (Perron *et al.*, 2018b) with a signal-to-noise ratio (SNR) higher than three. Then, the geometrical mean was calculated from several realizations and smoothed using the

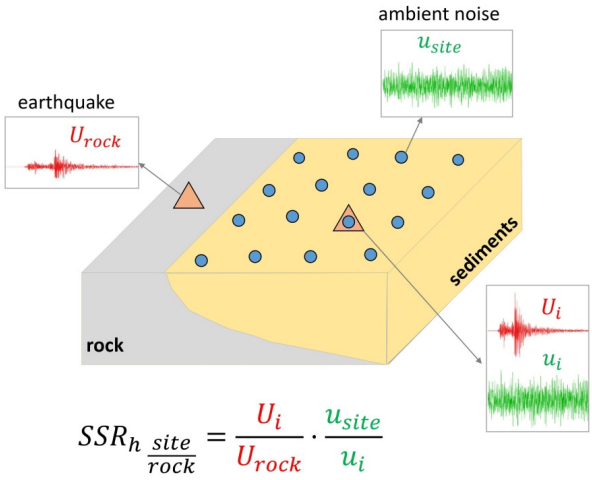


Fig. 1 - Graph showing the principle of the SSR_h method. Triangles indicate stations of the seismic monitoring network while circles are ambient vibration measurements. Capital *U* shows recorded earthquake ground motion and small *u* - ambient vibration data.

Konno and Ohmachi (1998) algorithm with a b-value of 40. To derive the SSRn, we divided ambient vibration recordings into shorter windows and calculate the geometrical mean of the spectral ratios for all windows, and smoothed with Konno and Ohmachi (1998) algorithm with a b-value of 40.

Because we installed more than one seismic monitoring station inside the basin, we obtained several SSRh functions for each point:

$$SSRh_{\frac{site}{rock}} = \frac{U_{basin}}{U_{rock}} \cdot \frac{u_{site}}{u_{basin}}$$

where *U* is Fourier amplitude spectra of earthquake ground motion and *u* of ambient noise. For each site, we calculated the weighted geometrical mean of all realizations with weight (*w*) being the squared inverse of the difference of f_0 values between the site (f_0^s) and basin station (f_0^b):

$$w = \frac{1}{(f_0^b - f_0^s)^2}$$

The final amplification functions are referenced to the local rock station, however, by multiplying them by the empirical spectral modelling (ESM) amplification function (Edwards *et al.*, 2013) for that local rock station, we can obtain amplification with respect to a Swiss reference rock profile (Poggi *et al.*, 2011). The ESM amplification functions are calculated routinely for all stations of the Swiss network. The final standard deviation is a joint geometric standard deviation of SSRn and SSR, and ESM amplification functions:

$$std(SSRh) = exp(\sqrt{log(std(SSR))^2 + log(std(SSRn))^2 + log(std(ESM))^2}$$

Moreover, we mapped the fundamental resonance frequency f_0 for the area using all available ambient vibration recordings. We used the RayDec analysis (Hobiger et al., 2009) to retrieve the ellipticity of the Rayleigh wave and picked manually f_0 values.

Summary of the results. In Fig. 2, we show the comparison between earthquake-based SSR functions and the hybrid SSRh method for stations of the temporary seismic monitoring network.

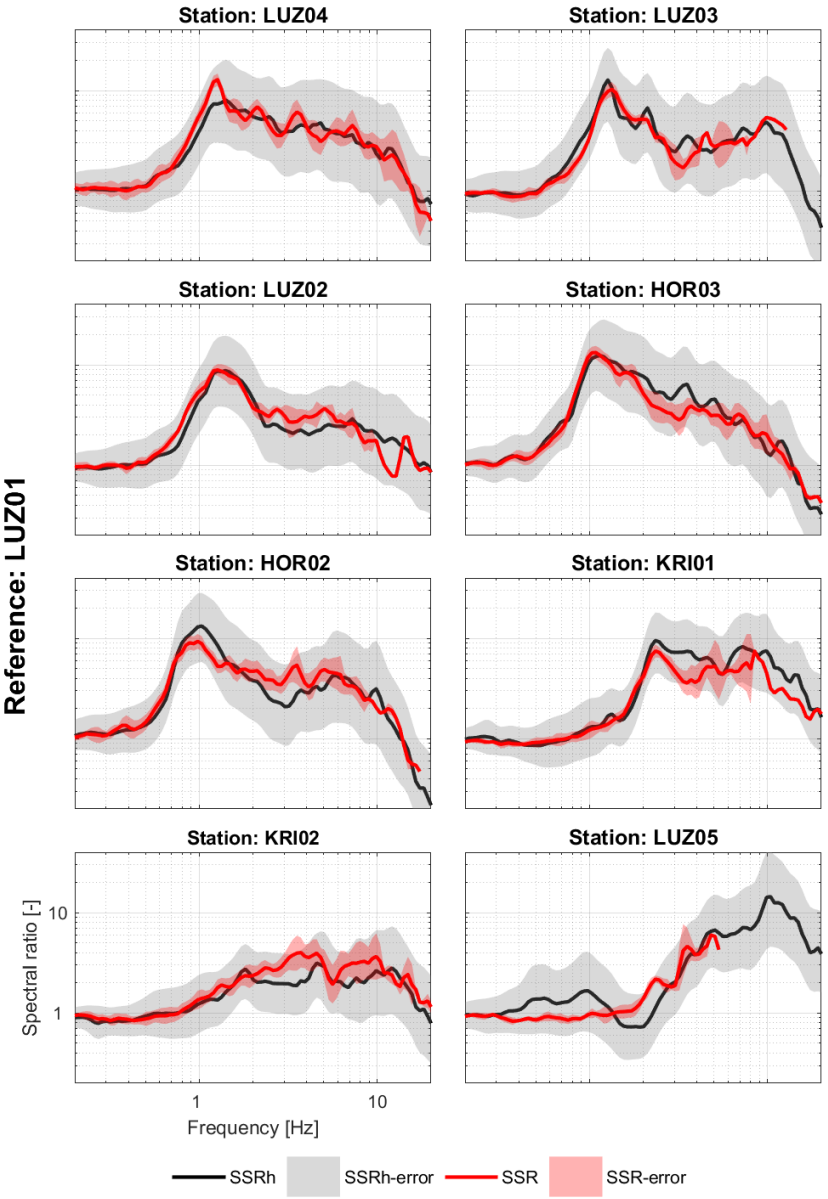


Fig. 2 - Comparison of the relative amplification function using the SSR and SSRh methods for all stations of the temporary seismic monitoring network.

The results are comparable, indicating that the SSRh method allows estimating amplification factors that are in good agreement with well-established methods based on earthquake ground-motion data. Even though the standard deviation for the noise-based spectral ratio is significantly higher than for SSR because of the variable nature of the ambient noise wavefield, the mean values can be used to derive a reliable local amplification model. The SSRh method is at the same time relatively cheaper than techniques based only on the earthquake ground motion data and allows for higher spatial resolution. Hence, we decided to evaluate the site response for the points where only ambient vibration recordings are available. The final local amplification model (Fig. 3) is referenced to Swiss reference bedrock conditions (Poggi *et al.*,

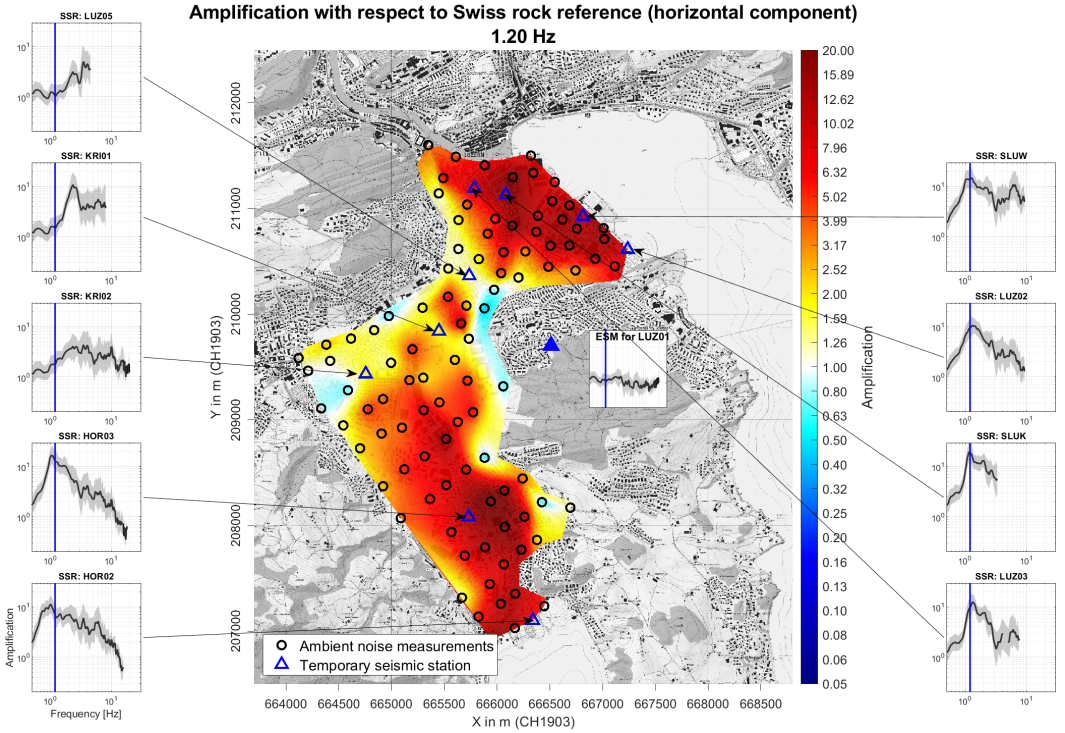


Fig. 3 - Local empirical amplification model with respect to Swiss rock reference (Poggi *et al.*, 2011) estimated using the SSRh method for 1.2 Hz. Blue triangles represent stations of the seismic monitoring network where earthquake recordings are available, black circles are ambient noise measurements. Base maps source: Federal Office of Topography (map.geo.admin.ch).

2011). The final model is consistent with some site response proxies such as the fundamental resonance frequency and geological data i.e. thickness of unconsolidated deposits derived from the gravity measurements. In the deep areas of the basin, the calculated amplification factors exceed 10 at the fundamental frequency (between 0.8 and 1.5 Hz) and remain high for the long frequency band. Even in the shallower parts characterized by sediments thickness less than 50 m, high amplification is expected. We can conclude that local seismic hazard is increased significantly in the Lucerne area.

Moreover, in our study, we test the influence of the location of the stations on the results. Because we deployed more than one temporary station in the basin, we can calculate several realizations of the SSRh function. Based on the test performed on the temporary network, we observe the correlation between the goodness of the fit between earthquake- and noise-based spectral ratios and the similarity of the site condition between the tested station pair. In other words, if two stations have similar site response and are located on similar site conditions demonstrated by similar f_0 values, the noise-based spectral ratio provides a good estimate of the SSR amplification function. In case stations have much different site response, we can still estimate the relative amplification; however, the fit becomes worse, especially at the fundamental frequency. Another influencing factor that was studied was the effect of variability of ambient vibration wavefield. Depending on the time of the day when ambient vibration was measured, the resulting SSRh functions show some differences, however, a mean value over a longer period (e.g. 24 hours) provides a stable result. We recommend that the method is tested using a small temporary network before applying the technique to the whole basin in order to investigate the impact of described factors.

References

Andrews, D. J. (1986). Objective Determination of Source Parameters and Similarity of Earthquakes of Different Size. In *Earthquake Source Mechanics* (Das, S., Boatwright, J., Scholz, C. H., Vol. 37, pp. 259–267). American Geophysical Union (AGU). https://doi.org/10.1029/GM037p0259

Bonilla, L. F., Steidl, J. H., Lindley, G. T., Tumarkin, A. G., and Archuleta, R. J. (1997). Site amplification in the San Fernando Valley, California: Variability of site-effect estimation using the S-wave, coda, and H/V methods. *Bulletin of the Seismological Society of America*, *87*(3), 710–730.

Borcherdt, R. D. (1970). Effects of local geology on ground motion near San Francisco Bay. *Bulletin of the Seismological Society of America*, *60*(1), 29–61.

Edwards, B., Michel, C., Poggi, V., and Fäh, D. (2013). Determination of Site Amplification from Regional Seismicity: Application to the Swiss National Seismic Networks. *Seismological Research Letters*, *84*, 611–621. https://doi.org/10.1785/0220120176

Field, E. H., Hough, S., and Jacob, K. H. (1990). Using microtremors to assess potential earthquake site response: A case study in Flushing Meadows, New York City. *Bulletin - Seismological Society of America*, *80*, 1456–1480. https://doi.org/10.1785/BSSA08006A1456

Hobiger, M., Bard, P.-Y., Cornou, C., and Le Bihan, N. (2009). Single station determination of Rayleigh wave ellipticity by using the random decrement technique (RayDec). *Geophysical Research Letters*, *36*, L14303. https://doi.org/10.1029/2009GL038863

Hobiger, M., Bergamo, P., Imperatori, W., Panzera, F., Marrios Lontsi, A., Perron, V., Michel, C., Burjánek, J., and Fäh, D. (2021). Site Characterization of Swiss Strong-Motion Stations: The Benefit of Advanced Processing Algorithms. *Bulletin of the Seismological Society of America*, *111*(4), 1713–1739. https://doi.org/10.1785/0120200316

Janusz, P., Perron, V., Knellwolf, C., and Fäh, D. (2022). Combining earthquake ground-motion and ambient vibration recordings to evaluate local high-resolution amplification model – insight from the Lucerne area, Switzerland. *Frontiers in Earth Science Geohazards and Georisks 10:885724. (Accepted)*. doi: 10.3389/feart.2022.885724

Kagami, H., Duke, C. M., Liang, G. C., and Ohta, Y. (1982). Observation of 1- to 5-second microtremors and their application to earthquake engineering. Part II. Evaluation of site effect upon seismic wave amplification due to extremely deep soil deposits. *Bulletin of the Seismological Society of America*, *72*(3), 987–998. https://doi.org/10.1785/BSSA0720030987

Konno, K., and Ohmachi, T. (1998). Ground-motion characteristics estimated from spectral ratio between horizontal and vertical components of microtremor. *Bulletin of the Seismological Society of America*, *88*(1), 228–241.

Michel, C., Edwards, B., Poggi, V., Bfurjánek, J., Roten, D., Cauzzi, C., and Fäh, D. (2014). Assessment of Site Effects in Alpine Regions through Systematic Site Characterization of Seismic Stations Assessment of Site Effects in Alpine Regions through Systematic Site Characterization of Seismic Stations. *Bulletin of the Seismological Society of America*, *104*(6), 2809–2826. https://doi.org/10.1785/0120140097

Nakamura, Y. (1989). A method for dynamic characteristics estimation of subsurface using microtremor on the ground surface. *Railway Technical Research Institute, Quarterly Reports*, *30*(1), 25–33.

Nogoshi, M., and Igarashi, T. (1971). On the Amplitude Characteristics of Microtremor (Part 2). *Zisin (Journal of the Seismological Society of Japan. 2nd Ser.)*, *24*(1), 26–40. https://doi.org/10.4294/zisin1948.24.1_26

Perron, V., Gélis, C., Froment, B., Hollender, F., Bard, P.-Y., Cultrera, G., and Cushing, E. M. (2018a). Can broad-band earthquake site responses be predicted by the ambient noise spectral ratio? Insight from observations at two sedimentary basins. *Geophysical Journal International*, *215*(2), 1442–1454. https://doi.org/10.1093/gji/ggy355

Perron, V., Laurendeau, A., Hollender, F., Bard, P.-Y., Gélis, C., Traversa, P., and Drouet, S. (2018b). Selecting time windows of seismic phases and noise for engineering seismology applications: A versatile methodology and algorithm. *Bulletin of Earthquake Engineering*, *16*(6), 2211–2225. https://doi.org/10.1007/s10518-017-0131-9

Poggi, V., Edwards, B., and Fäh, D. (2011). Derivation of a Reference Shear-Wave Velocity Model from Empirical Site Amplification Derivation of a Reference Shear-Wave Velocity Model from Empirical Site Amplification. *Bulletin of the Seismological Society of America*, *101*(1), 258–274. https://doi.org/10.1785/0120100060

Poggi, V., Fäh, D., Burjanek, J., and Giardini, D. (2012). The use of Rayleigh-wave ellipticity for site-specific hazard assessment and microzonation: Application to the city of Lucerne, Switzerland. *Geophysical Journal International*, *188*(3), 1154–1172. https://doi.org/10.1111/j.1365-246X.2011.05305.x

HOMOGENIZATION OF MAGNITUDES OF THE ISC ONLINE BULLETIN

B. Lolli[1], D. Randazzo[1], G. Vannucci[1], P. Gasperini[2,1]

[1] Istituto Nazionale di Geofisica e Vulcanologia, Sezione di Bologna, Italy
[2] Dipartimento di Fisica e Astronomia, Università di Bologna, Italy

We implemented an automatic procedure to download the hypocentral data of the online bulletin of the International Seismological Centre (ISC) so that to produce in near real-time a catalog of the Euromediterranean instrumental seismicity to be used for forecasting experiments and other statistical analyses. For the interval covered by the reviewed bulletin, we adopt the ISC locations and convert Ms and mb magnitudes computed by ISC to Mw using empirical relations and merge the so obtained proxies with real Mw provided by global and Euromediterranean moment tensor catalogs. For the most recent time intervals for which the revised bulletin is not available, we adopt the preferred (prime) location provided by the bulletin and convert to Mw the Ms and mb provided by some agencies and merge them with real Mw taken from online moment tensor catalogs. For magnitude conversions we use curvilinear relations defined in previous literature and the Chi-Square regression method that takes into account the uncertainties of both the dependent and independent variables.

LOCAL EARTHQUAKE CONDITIONAL PROBABILITY BASED ON LONG TERM CO_2 MEASUREMENTS

L. Pierotti[1], C. Fidani[2], G. Facca[1], F. Gherardi[1]

[1] Istituto di Geoscienze e Georisorse CNR, Pisa, Italy
[2] Central Italy Electromagnetic Network, Fermo, Italy

A network of automatic stations equipped with sensors for the continuous monitoring of geochemical parameters (Geochemistry Network of Tuscany, GNT) has been designed and realized at IGG-CNR-Pisa in keeping with the recommendations of the International Association for Seismology and Physics of Earth's Interior (IASPEI; Wyss, 1991; Wyss and Booth, 1997). The GNT is a part of a seismic prevention/prediction program, the Regional Government of Tuscany, Italy. It is operating since late 2002, and currently consists of six continuous automatic stations installed in the areas of highest seismic risk of Tuscany: Garfagnana, Lunigiana, Mugello, Upper Tiber Valley and Mt. Amiata. The main objective of the network is to study possible geochemical precursors to seismic activity (Cioni *et al.*, 2007). Specifically, temperature, pH, and electrical conductivity are measured using high precision portable instrumentation, while CO_2 is calibrated with standards of known concentration. The elaboration of long-term time series allowed for an accurate definition of the geochemical background, and for the recognition of a number of geochemical anomalies in concomitance with the most energetic seismic events occurred during the monitoring period (Pierotti *et al.*, 2015).

In the Garfagnana region, the Gallicano thermo-mineral spring is currently monitored with sensors for the simultaneous measurement of temperature (T), pH, electrical conductivity (EC), redox potential (ORP) and dissolved content of CO_2. The measurement of CO_2 dissolved concentration is done with an extraction cell specifically designed and realized in the IGG-CNR-Pisa laboratories (Cioni *et al.*, 2007). The station operates with flowing water (about 5 liters per minute), and a frequency acquisition of 1 s for all the parameters. Average, median and variance of the data are calculated over a period of 5 min and recorded with an in-situ data logger. Here, a first study of the possible correlation between regional seismic events and CO_2 anomalies is investigated between the beginning of April 2017 and the beginning of March 2021. Moreover, the correlations can be used to estimate the conditional probabilities of seismic events, so opening the possibility of an earthquake forecasting experiment using geochemical monitoring.

Earthquake data were downloaded from ISIDe Working Group, ''Italian Seismological Instrumental and parametric database'', http://iside.rm.ingv.it) to obtain a subset of ''significant events'' with magnitudes greater or equal to 1.0. The seismic dataset was declustered using zmap of MatLab, so to reduce the number of events to 339, see Figure 1. Earthquake locations were then compared with the Gallicano Station location, to consider only those seismic events which satisfy the relation between magnitude and distance equal to three Dobrovolsky radius:

$$D = 3\ 10^{0.43M} \quad (1)$$

The remaining set was digitized considering the presence of a seismic event if the distance of seismic event epicentres from the Gallicano Station position $D_{Gallicano} \leq D$ as "1" and the absence as "0", for each day. The resulting time series was characterized by 1435 days, where 47 "1" indicated the main shocks occurred at an interaction distance from Gallicano.

The CO_2 signal has been decomposed using the Census I method (Makridakis et al., 1998). According to Census technique, a time series (Xt) can be thought of as consisting of four different components: (1) seasonal (St), (2) trend (Tt), (3) cyclical (Ct), and (4) irregular (It) component. The difference between a cyclical and a seasonal component is that the latter occurs at regular (seasonal) intervals, while cyclical factors have usually a longer duration that varies from cycle to cycle. In the Census I method, the trend and cyclical components are combined into a single trend-

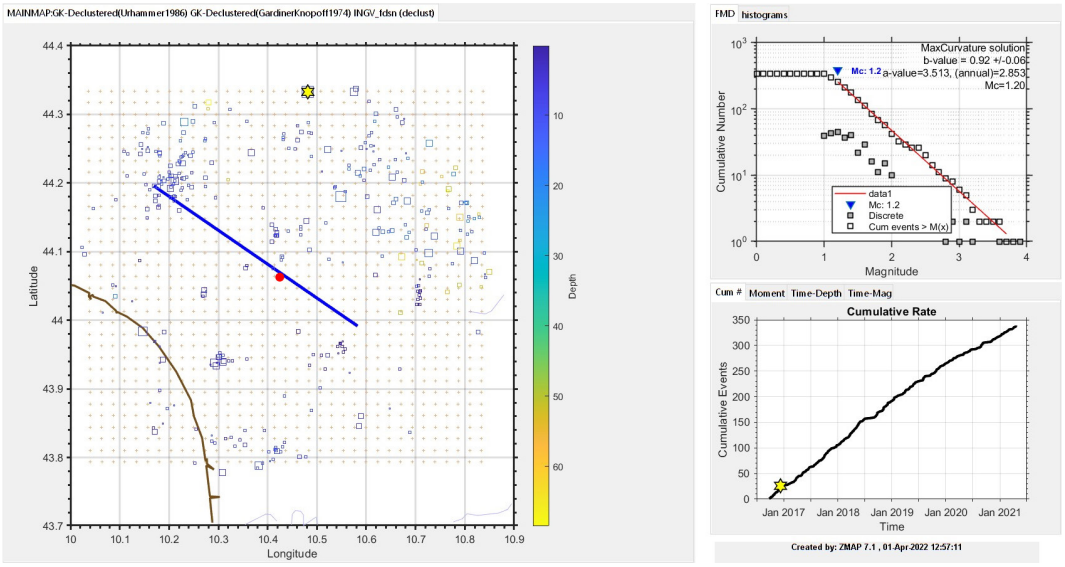


Fig. 1 - Declustered earthquake dataset displayed by z-map after that two declustering methods were used one after the other, completeness magnitude 1.2. The brown line is the Thyrrenian coastline; the blue line is the main local fault, and the red point along it marks the position of the Gallicano station. Dimensions and colours of square symbols indicate earthquakes magnitude and depths, respectively. The yellow star marks the most energetic seismic event occurred in the studied period. Statistical elaborations are provided in the two right boxes.

cycle component (TCt). The seasonal component also includes earth tides, that can affect the release of deep gas from the rocks (Sugisaki, 1981). In order to separate the irregular component from the original data series, all these components have been combined with the additive model (Xt = St + TCt + It). The additive model is applied because the seasonal fluctuations of the recorded geochemical signal are steady, and not dependent on the overall level of the series (Makridakis et al., 1998). The decomposition is performed following a step-by-step procedure: (i) determination of the duration of one season. In this study we consider a reference frame of 12 months, by exploring the effects (always negligible in our case study) of different setup with seasons of 6 and 3 months; (ii) computation of the centred moving average of the series, with a window width of one season; (iii) computation of the seasonal component (St) by subtracting the moving average from the original dataset; (iv) computation of the so-called ''seasonally adjusted series'' by removing the seasonal component from original series; (v) individuation of the trend/cycle component (TCt), by smoothing the seasonally adjusted series; (vi) calculation of the irregular component by subtracting the seasonal and trend/cycle components from the original data series. The irregular component of the CO_2 time series from Gallicano, retrieved during the same earthquake time interval is shown in Figure 2 left. Figure 2 right reports the histogram distribution of the irregular component and its fit. The histogram was fitted by a special function that defined a threshold over which CO_2 recordings had a 90% of probability to be not due by chance. It occurred when the modulus of the irregular component was above 0.0432. A set of 49 CO_2 anomalies were selected from the irregular component and indicated by "1" in the series of daily anomalies.

Starting from digital time series, the Pearson correlation (known as the Matthews correlation for the digital case) between regional seismic events and the Gallicano CO_2 anomalies was calculated (Fig. 3). Starting from Matthews correlations (Matthews, 1975), it was shown that the conditional probabilities can be defined between two sets of digital events (Fidani, 2018). Moreover, correlation histograms calculated in past publications (Fidani, 2015), were put in relation with the Matthews correlation coefficients (Fidani, 2020). Being so, indicating by EQ the earthquake event, by EC the CO_2 anomaly event, and by R = corr(EQ,EC) the Matthews

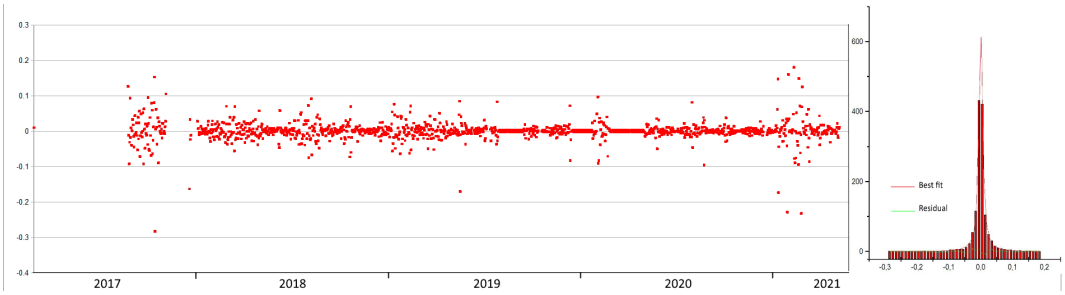


Fig. 2 - Time variation of the irregular component of CO_2 at Gallicano (values corrected by detrending the seasonal component). On the right, the histogram distribution is shown along with its best fit and residual curves.

correlation coefficient, the conditional probability of an EQ event given the observation of an EC event can be written

$$P(EQ|EC+\Delta t) = P(EQ) + corr(EQ,EC+\Delta t)\ \{[1 - P(EQ)]\ P(EQ)\ [1/P(EC) - 1]\}^{1/2}, \quad (2)$$

where $P(EQ) = N_{EQ}/N_d$, $P(EC) = N_{EC}/N_d$, and Δt is the time delay in days between the two events. Thus, $P(EQ) = 0.033$ and $P(EC) = 0.034$. Calculating (2), $P(EQ|EC+\Delta t) = 0.033 + 0.952\ R(\Delta t)$ If we start considering an average probability to observe an earthquake every 30 days, the observation of a CO_2 anomaly at Gallicano Station increase the earthquake probability to 0.131, with a probability gain near to 4, for earthquakes that at least satisfy the relation (1).

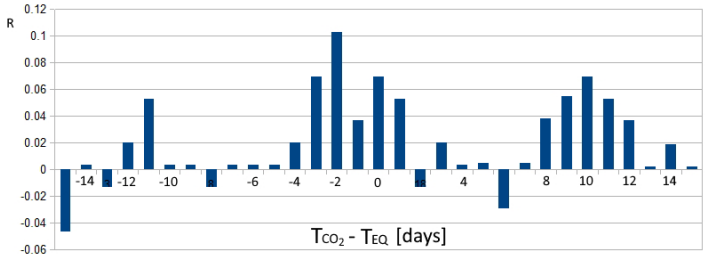


Fig. 3 - Matthew's correlation coefficients in the range Δt from -15 to +15 days, note that a pronounced peak occurs at -2 days, which means that CO_2 anomalies prevalently anticipate seismic activity of 2 days.

References

Cioni, R., Guidi, M., Pierotti, L., Scozzari, A.; 2007: *An automatic monitoring network installed in Tuscany (Italy) for studying possible geochemical precursory phenomena*. Nat. Hazards Earth Syst. Sci. **7**, 405–416.

Fidani, C.; 2018: *Improving Earthquake Forecasting by Correlations Between Strong Earthquakes and NOAA Electron Bursts*, TAO, **29**(2), 117-130.

Fidani, C.; 2020: *Probability, Causality and False Alarms using Correlations Between Strong Earthquakes and NOAA High Energy Electron Bursts*. Ann. Geophys., **63**(5), PA543.

Fidani, C.; 2021: *West Pacific earthquake forecasting by NOAA electron bursts with independent L-shells and ground based magnetic correlations.* Frontiers in Earth Science, **9**, 673105.

Makridakis, S., Wheelwright, S.C., Hyndman, R.J.; 1998: *Forecasting Methods and Applications*, third ed. John Wiley and Sons, New York, p. 642.

Matthews, B. W.; 1975: *Comparison of the predicted and observed secondary structure of T4 phage lysozyme*. Biochimica et Biophysica Acta (BBA) - Protein Structure. **405** (2), 442–451.

Pierotti, L., Botti, F., D'Intinosante, V., Facca, G., & Gherardi, F.; 2015: *Anomalous CO_2 content in the Gallicano thermo-mineral spring (Serchio Valley, Italy) before the 21 June 2013, Alpi Apuane earthquake (M= 5.2)*. Physics and Chemistry of the Earth, Parts A/B/C, **85**, 131-140.

Sugisaki, R.; 1981: *Deep-seated gas emission induced by the earth tide: a basic observation for geochemical earthquake prediction*. Science **212**, 1264–1266.

Wyss, M., 1991. Evaluation of Proposed Earthquake Precursors. In: Wyss M. (Ed.), Published by AGU in Cooperation with IASPEI. Special Publication, 94pp.

Wyss, M., Booth, D.C., 1997. *The IASPEI procedure for the evaluation of earthquake precursors*. Geophys. J. Int. **131**, 423–428.

THE RAPID ASSESSMENT OF SEISMIC MOMENT AND RADIATED ENERGY (RAMONES) SERVICE

D. Spallarossa[1,2], M. Picozzi[3], D. Scafidi[1], P. Morasca[2], D. Bindi[4], G. Tarchini[1]

[1] UNIGE, Genoa, Italy
[2] INGV, Milan, Italy
[3] University of Naples Federico II, Italy
[4] GFZ, Potsdam, Germany

Aim of this contribution is to introduce RAMONES (Rapid Assessment of MOmeNt and Energy Service), a service for disseminating through a web interface, the estimates of seismic moment (M_0) and radiated energy (E_R) for earthquakes occurring in central Italy with local magnitudes above 1.7 (Spallarossa *et al.*, 2021). The concept of RAMONES is to estimate M_0 and E_R directly from features extracted directly from recordings, namely the S-wave peak displacement (PD_S) and the integral of the squared velocity ($IV2_S$) evaluated over the S-wave window at local distances (Bindi *et al.*, 2020). In particular, RAMONES (http://www.distav.unige.it/rsni/ramones.php) implements a fully-automatic procedure based on the following actions: (1) locations and magnitudes of earthquakes occurring within the target region are retrieved from the National Institute for Geophysics and Volcanology (INGV) bulletin; (2) hypocentral information are used to extract segments from continuous data streams archived in the ORFEUS-EIDA, the Incorporated Research Institutions for Seismology (IRIS), and the DPC repositories; a cut-off corresponding to hypocentral distances shorter than 150 km is applied to the waveform (and relevant station metadata) download; (3) an automatic procedure (Scafidi *et al.*, 2016) is applied to detect the P and S onsets, and to estimate the local magnitude; different features are extracted from the recordings, including the peak displacement (PD_S) and the integral of the squared velocity ($IV2_S$) over the S-wave window, the peak ground velocity (PGV), and peak ground acceleration (PGA); (4) the seismic moment (M_0) and radiated energy (E_R) are estimated using empirical attenuation models as described in this contribution. Additional parameters, such as apparent stress (σ_a ; Wyss and Brune, 1968) and the moment magnitude (Mw) are computed and disseminated as well; (5) the results are stored in a PostgresSQL database and disseminated through a web interface.

A data set composed of 6515 earthquakes recorded in central Italy between 2008 and 2018 was used to calibrate the attenuation models relating M_o to PD_S and E_R to $IV2_S$, including station corrections. The calibration values for M_0 and E_R were extracted from the source spectra obtained by performing a decomposition of the Fourier amplitude spectra into source, propagation and site contributions, applying the so-called generalized inversion technique. To test the capabilities of RAMONES, we validate the attenuation models by performing residual analysis over about 60 earthquakes occurring in 2019 that were used for the spectral decomposition analysis but not considered in the calibration phase.

A web portal allows the users to interact with the database. The main page of RAMONES (Fig. 1) includes:

1) A map of the monitored region showing the epicenters of earthquakes processed by RAMONES since January 2020. Using the “change selection” option, the geographical extension, the depth and magnitude ranges, and the time span of interest can be configured by the user. In its actual configuration, RAMONES analyzes earthquakes with magnitudes above ML 1.7 occurring in central Italy.
2) Selecting “seismic station,” RAMONES shows a table reporting the main information of the stations stored in the database and actually used by the service (more than 1500 considering both the whole Italian territory and adding selected stations from seismic networks operating in neighboring countries). In particular, the table includes the following: station information (code, network, channels, latitude, longitude, elevation, and location) including links; link to metadata (dataless); link to an automatically

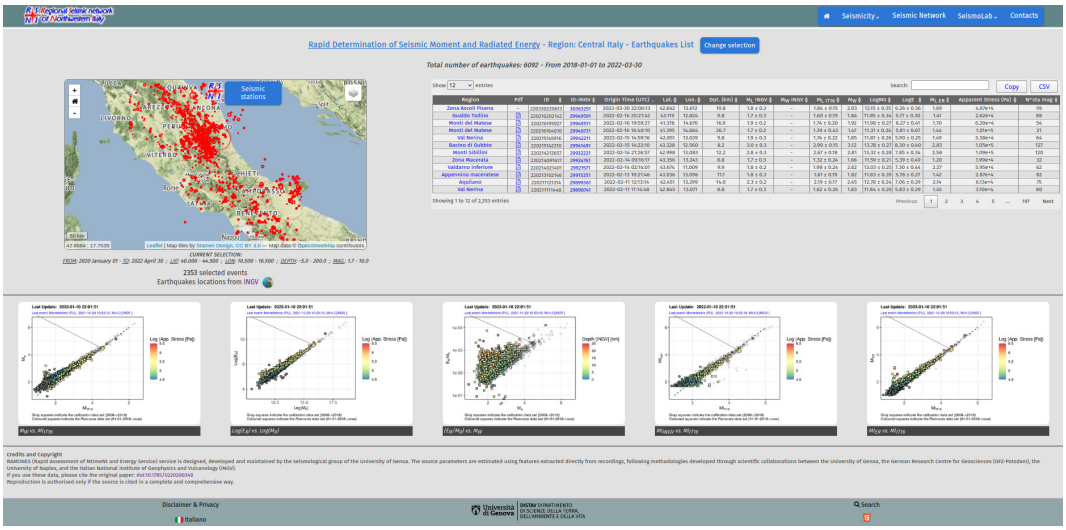


Fig. 1 - Screenshot of the RAMONES webpage (http://www.distav.unige.it/rsni/ramones-ci-lista.php).

generated summary document (Portable Document file Format) showing a map with the station location and horizontal-to-vertical (H/V) spectral ratios for both the S-wave phase window and noise window computed by the service; tools for searching, sorting, and exporting the station table are also available.

3) A table reporting the main information of the earthquakes stored in the RAMONES database and the associated source parameters. In particular, the table includes the following: the earthquake location (origin time, latitude, longitude, and depth) provided by the INGV bulletin and a link (ID-INGV) to the INGV event-specific webpage; the base-10 logarithm of the estimated seismic moment $\log M_0$ and radiated energy $\log E_R$. The empirical attenuation models used to compute these parameters are described in Spallarossa et al. (2021); several magnitude estimates are listed, along with the apparent stress σ_a (Wyss and Brune, 1968);
4) the first three columns provide additional links to the event-specific page (region), to a static image showing a few selected recordings (waves), and to an automatically generated summary document (PDF). Through the region-link in the first column, an event-specific page for the selected event is opened. This page provides a map with the location of the stations used by RAMONES for processing and the earthquake location; a summary of the source parameters of the selected events; a table listing various information extracted from each recording, including station metadata at the channel level; event metadata; PGA and PGV peak-parameters; hypocentral distance; source parameters and station local magnitude. Finally, it is also possible to download the information contained in the event-specific page into a PDF document;
5) the RAMONES homepage displays also five different figures which are automatically updated to summarize the scaling relationships among different source parameters

The distribution of the source parameters and their relevant scaling relationships are automatically computed and disseminated in the form of maps, parametric tables, figures, and reports available through the RAMONES web interface. In its current configuration, RAMONES updates are scheduled on a daily basis. Since January 2020, a testing operational phase has been running, and RAMONES has analyzed about 2500 earthquakes by April 2022 in the target region. The high potential of RAMONES is in its ability to provide timely information on the

temporal evolution of static and dynamic source parameters. This could be particularly useful during a seismic sequence, for a change in the source dynamics provides information on the mechanics of earthquake ruptures. Therefore, for rapid response applications, the RAMONES computations can be switched to a modality triggered by alerting messages such as those issued by the EMSC. Other lines of development for RAMONES regard data accessibility and the extension of the monitored region. Regarding the modalities to retrieve data from RAMONES, future effort will be dedicated to making operative representational state transfer (RESTful) webservices, preserving as much as possible the compatibility with FDSN standards for event, station, and data-select queries.

References

Bindi, D., D. Spallarossa, M. Picozzi, and P. Morasca (2020). *Reliability of source parameters for small events in Central Italy: Insights from spectral decomposition analysis applied to both synthetic and real data*, Bull. Seismol. Soc. Am. 110, 1–19, doi: 10.1785/0120200126.

Scafidi, D., D. Spallarossa, C. Turino, G. Ferretti, and A. Viganò (2016). *Automatic P- and S-wave local earthquake tomography: Testing performance of the automatic phase-picker engine RSNI-Picker,* Bull. Seismol. Soc. Am. 106, no. 2, 526–536, doi: 10.1785/0120150084.

Spallarossa, D., M. Picozzi, D. Scafidi, P. Morasca, C. Turino and D. Bindi (2021). *RAMONES, the Rapid Assessment of MOmeNt and Energy Service in Central Italy: Concepts, capabilities and future perspectives,* Seismological Research Letters, doi:10.1785/0220200348.

Wyss, M., and J. N. Brune (1968). *Seismic moment, stress, and source dimensions for earthquakes in the California–Nevada region,* J. Geophys. Res. 73, 4681-4694.

CARATTERIZZAZIONE DEL MOTO DEL SUOLO AD ISCHIA ATTRAVERSO SIMULAZIONE SINTETICHE

G. Tusa[1], V. Convertito[2], S. D'Amico[1], E. Giampiccolo[1], H. Langer[1], R. Azzaro[1]

[1] Istituto Nazionale di Geofisica e Vulcanologia, Osservatorio Etneo, Catania (INGV-OE), Italy
[2] Istituto Nazionale di Geofisica e Vulcanologia, Osservatorio Vesuviano, Napoli (INGV-OV), Italy

Introduzione. Il lavoro presentato nel presente contributo è stato svolto nell'ambito delle attività previste dal Task 13 (Valutazione della pericolosità sismica indotta da eventi locali ad Ischia) della Convenzione B2 DPC-INGV 2012-2021, il cui obiettivo principale era la stima della pericolosità sismica legata a terremoti vulcano-tettonici originati ad Ischia.

Come noto, uno degli elementi fondamentali per il calcolo della pericolosità sismica è la stima del moto del suolo – caratterizzato da parametri di interesse ingegneristico quali PGA, PGV, PSA, etc. – tramite equazioni predittive (Ground Motion Prediction Equation, GMPE o Ground Motion Model, GMM), la cui affidabilità dipende dalla quantità e dalla qualità dei dati a disposizione e, in particolare, dall'intervallo di magnitudo e di distanze sorgente-sito disponibili per la loro calibrazione. I parametri del moto del suolo, insieme alle loro distribuzioni, consentono di calcolare le probabilità di superamento di valori di riferimento utilizzati nel calcolo della pericolosità sismica. Ad Ischia le caratteristiche dell'attenuazione dello scuotimento con la distanza sono quelle tipiche dei terremoti superficiali in aree vulcaniche, mediamente più elevate rispetto ai contesti tettonici. Per questo motivo la valutazione dello scuotimento sismico rappresenta ancora oggi un aspetto critico, poiché l'uso di leggi di attenuazione prodotte per ambiti puramente tettonici comporta una forte e sistematica sottostima dello scuotimento atteso. Sfortunatamente, ad Ischia, poiché il numero di eventi per i quali si hanno a disposizione registrazioni strumentali è molto ridotto, la calibrazione di un adeguato modello di attenuazione del moto del suolo rappresenta un problema rilevante ai fini della stima della pericolosità sismica. Per superare questo problema è possibile integrare i pochi dati registrati con dati generati da simulazioni numeriche in modo da rendere il dataset di calibrazione il più completo possibile. Ai fini della generazione dei sismogrammi sintetici, che in questo lavoro sono stati calcolati attraverso l'approccio stocastico implementato nell'algoritmo EXSIM (Boore, 2005, 2009; Motazedian e Atkinson, 2005) per modello di faglia finita, è necessario disporre di un certo numero di parametri di input che tengano conto del modello crostale e quindi delle proprietà attenuative del mezzo di propagazione, della geologia di superficie, della geometria della sorgente e dei parametri che la caratterizzano (meccanismo focale, momento sismico, stress-drop, distribuzione dello slip, velocità di rottura, etc.).

In questo studio, il punto di partenza ha visto l'utilizzo dei terremoti di piccola magnitudo, registrati strumentalmente ad Ischia, attraverso i quali è stato possibile calcolare le leggi di scala e il parametro di attenuazione anelastica Q, da utilizzare per simulare il moto del suolo prodotto da eventi di magnitudo maggiore, come quello che ha interessato Ischia il 21 agosto 2017, oggetto delle nostre simulazioni stocastiche.

Stima dei parametri di sorgente dei dati strumentali attraverso inversione spettrale. Sono state applicate due diverse tecniche di inversione, che hanno visto l'utilizzo degli spettri in spostamento, per ricavare i parametri di sorgente (il momento sismico, M_0, dal livello spettrale a bassa frequenza e il raggio della sorgente, R, dalla frequenza d'angolo f_c) e Q utilizzando i dati strumentali di 6 eventi (Tab. 1), tra i quali l'evento del 21 agosto. La differenza tra le due tecniche risiede nel processo di inversione finalizzato a ridurre la correlazione tra i parametri da invertire. La prima prevede l'inversione spettrale attraverso l'algoritmo Simplex e una procedura multi-step (Convertito *et al.*, 2016); la seconda, è una procedura two-step basata su algoritmo grid search. I risultati dei due approcci sono del tutto sovrapponibili.

Tab. 1 - Elenco dei terremoti analizzati.

Tempo origine GMT	Lat (°)	Lon (°)	Prof. (km)	Magnitudo (Md)
2017-08-21 18:57	40.7385	13.8967	1.24	4.1
2017-08-23 03:04	40.7323	13.8947	0.57	2.1
2018-05-01 15:14	40.7315	13.9067	0.92	1.8
2018-08-08 08:02	40.7362	13.9002	1.58	2.5
2018-12-06 15:19	40.7378	13.8927	1.12	1.0
2019-01-06 05:45	40.7297	13.8807	0.00	1.2

I valori medi dei parametri di sorgente ottenuti dagli spettri P ed S dell'evento del 27 agosto 2017, normalizzati rispetto alla media tra tutte le stazioni (in media 8 per ogni fase analizzata) per ridurre eventuali effetti di sito, sono riportati in Tab. 2. M_0 è stato calcolato secondo Keilis-Borok (1959) considerando: velocità delle onde sismiche V_P 3 km/s e V_S 1.7 km/s; un mezzo con densità ρ di 2700 kg/m^3 e modulo di rigidità μ di 7.80 GPa. I valori di stress-drop statico ($\Delta\sigma$) e di R sono stati calcolati utilizzando il modello di Madariaga (1976) sia per la fase P che per la S; la magnitudo momento M_W è stata calcolata a partire dal momento sismico utilizzando la relazione di Hanks and Kanamori (1979).

Tab. 2 - Parametri della sorgente sismica del terremoto del 21/08/2017.

M_0 (N m)	Fc (Hz)	Mw	R (m)	Δ (MPa)	Spost. medio (cm)
1.80E+15	0.41	3.99	1272	0.40	4.35
± 1.59E+15	±0.22	±0.26	±311	±0.29	±3.33

Dall'analisi degli eventi sismici riportati in Tab. 1, è stato possibile calcolare le leggi di scala mostrate in Fig. 1. I parametri della sorgente sismica corrispondono ai valori medi calcolati tra tutte le stazioni sia per la fase P che per la S.

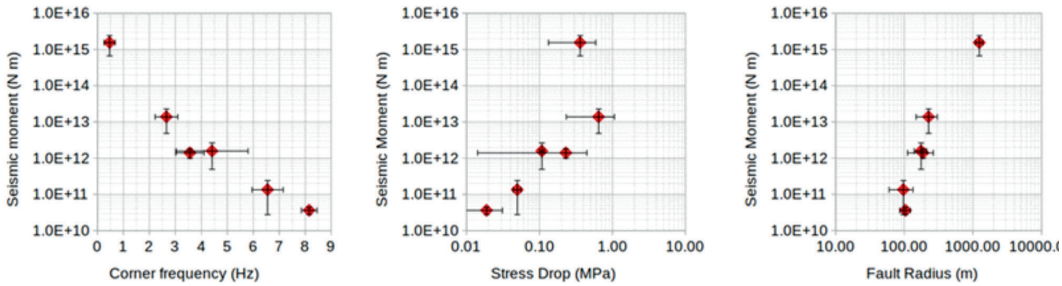


Fig. 1 - Relazione tra momento sismico e corner frequency, stress-drop statico e raggio della sorgente per i terremoti in Tab. 2. I punti rossi rappresentano la media dei valori calcolati alle varie stazioni; le barre di errore rappresentano la deviazione standard.

L'inversione congiunta dei parametri spettrali e di Q_P e Q_S, ha visto l'applicazione iniziale di un modello con Q indipendente dalla frequenza, che ha fornito i valori Q_P = 129 e Q_S = 130 per le stazioni con distanze ipocentrali minori di 50 km. Per le stazioni poste a maggiore distanza si ottiene invece Q_P = 225 e Q_S = 353. In un secondo step, sono stati fissati i parametri spettrali (Ω_0 e f_c) ed è stato imposto un coefficiente di variazione di Q con la frequenza pari a 0.6, come riportato in letteratura per i Campi Flegrei (Del Pezzo e Bianco, 2013). I valori ottenuti, confrontabili con quelli noti in letteratura, sono riportati in Tab. 3.

Tab. 3 - Valori di Q_p e Q_s dipendenti dalla frequenza ottenuti dall'inversione spettrale.

Stazioni	$Q_P=Q_{0P}f^n$	$Q_S=Q_{0S}f^n$
<50 km	$42f^{0.6}$	$51f^{0.6}$
<50 km	$53f^{0.6}$	$82f^{0.6}$

Simulazioni stocastiche per scenari di scuotimento. Come già asserito, quando non si dispone di un numero sufficiente di dati strumentali relativi agli eventi di maggiore interesse ai fini della pericolosità sismica, è possibile ricorrere alle simulazioni numeriche per la generazione delle storie sismiche e quindi ottenere lo scuotimento atteso su una griglia di punti o a siti predefiniti.

L'evento sismico di interesse per il presente studio è il terremoto del 21 agosto 2017 (M_w 4.1) per il quale si dispone di una sola registrazione strumentale sull'isola, ossia quella acquisita dalla stazione *strong motion* installata a Casamicciola (IOCA).

Uno degli algoritmi maggiormente usati in ambito sismologico è EXSIM, che utilizza un approccio stocastico con un modello di faglia finita (Boore, 2005, 2009; Motazedian e Atkinson, 2005) per simulare lo scuotimento relativo alle onde S, che sono spesso la parte del moto del suolo più importante nella stima della pericolosità sismica. EXSIM tiene conto della sorgente estesa dividendo il piano di faglia in piccole celle che vengono considerate come sorgenti puntiformi: la rottura inizia all'ipocentro o punto di nucleazione e si propaga attivando le varie celle che compongono l'area di rottura. Il moto del suolo totale simulato per ogni ricevitore si ottiene sommando il contributo di ciascuna cella dell'area di rottura, calcolato con l'approccio stocastico utilizzando il modello di sorgente puntiforme, con un adeguato tempo di ritardo rispetto alla nucleazione (Boore, 2005). Attraverso EXSIM, gli effetti della propagazione dalla sorgente al ricevitore sono modellati prendendo in considerazione gli effetti di durata sul moto del suolo, l'attenuazione anelastica e quella geometrica (Boore, 2009). Inoltre, la risposta sismica locale può essere modellata specificando le modifiche che il segnale in arrivo alla base di un deposito (crustal amplification) subisce nell'attraversare lo stesso e giungere in superficie (site amplification o funzione di trasferimento).

Per la definizione del modello crostale da adottare ai fini del calcolo della funzione di trasferimento, abbiamo preso in considerazione il modello proposto da Nardone *et al.* (2020) per l'isola d'Ischia, grazie al quale è stato possibile definire la profondità delle maggiori discontinuità. Quindi, supponendo i vari strati orizzontali ed indefinitamente estesi, e tenendo conto delle caratteristiche del suolo di superficie al di sotto della stazione IOCA (dal database ITACA, Luzi *et al.*, 2019; http://itaca.mi.ingv.it/ItacaNet_30/#/home), abbiamo calcolato la funzione di trasferimento.

Le sorgenti sismiche considerate per la generazione dei sismogrammi sintetici relativi all'evento del 21 agosto 2017 sono quelle modellate negli studi di De Novellis *et al.* (2018) e Calderoni *et al.* (2019), da ora in avanti indicate con gli acronimi DEN e CAL, rispettivamente. Entrambi i modelli prevedono un meccanismo di tipo dip-slip diretto, ma le direzioni di immersione sono opposte (verso N la sorgente CAL e verso S la sorgente DEN) così come diversa è la distribuzione dello slip sulla faglia, in entrambi i casi discretizzata attraverso celle aventi una lunghezza di 200 m ed una larghezza di 208.3 m e 200 m, rispettivamente per CAL e DEN.

Per ognuna delle geometrie di faglia considerate, sono stati simulati i valori di PGA e di PGV, entrambi misurati sulla componente orizzontale, al sito IOCA e ai 24 siti per i quali è riportata l'intensità macrosismica definita attraverso i rilievi diretti del gruppo QUEST (Azzaro *et al.*, 2017). In particolare, i valori simulati di PGA e PGV sono stati convertiti in intensità attraverso specifiche relazioni di conversione (Faenza e Michelini, 2010; Gomez-Capera *et al.*, 2020) e quindi confrontati con quelli del rilievo macrosismico. I valori di PGA e PGV sono stati anche confrontati con le relazioni di attenuazione del moto del suolo valide per le aree vulcaniche

proposte da Lanzano e Luzi (2020) e Tusa *et al.* (2020), quest'ultima calibrata per gli eventi superficiali all'Etna.

Lo scopo delle simulazioni è stato quello di investigare l'effetto dei parametri di input sull'entità del moto del suolo atteso. In particolare, sono stati analizzati: lo stress-drop, la velocità di rottura, f_{max} (che controlla il decadimento spettrale ad alta frequenza), lo spreading geometrico e la distribuzione dello slip, considerando anche modelli di slip uniforme e slip random. I risultati hanno mostrato che l'effetto più rilevante è dovuto, oltre che alla sorgente considerata, alla variazione di Δσ e ad f_{max} (Figg. 2 e 3). Il primo controlla i valori dei parametri strong-motion producendo una variazione dei valori assoluti, mentre la f_{max} controlla anche l'attenuazione con la distanza.

Dal confronto dei dati simulati con i valori predittivi dalle GMM di Lanzano e Luzi (2020) e Tusa *et al.* (2020), emerge che il valore di Δσ ottimale dovrebbe essere un valore intermedio tra circa 0.1 e 1.0 bar, poiché i dati tendono per lo più a distribuirsi lungo la curva corrispondente a ±1σ e non lungo la curva media. Per un valore di $\Delta\sigma$=0.5 bar ed una f_{max}=15 Hz i dati simulati riproducono in maniera più soddisfacente sia il dato osservato a IOCA che l'andamento previsto dai GMM. Notiamo che nell'interpretare i risultati ottenuti attraverso le simulazioni numeriche, ed in particolare il confronto con le intensità macrosismiche e le discrepanze tra i valori osservati e simulati, si deve tenere conto dei molteplici fattori che ne determinano la

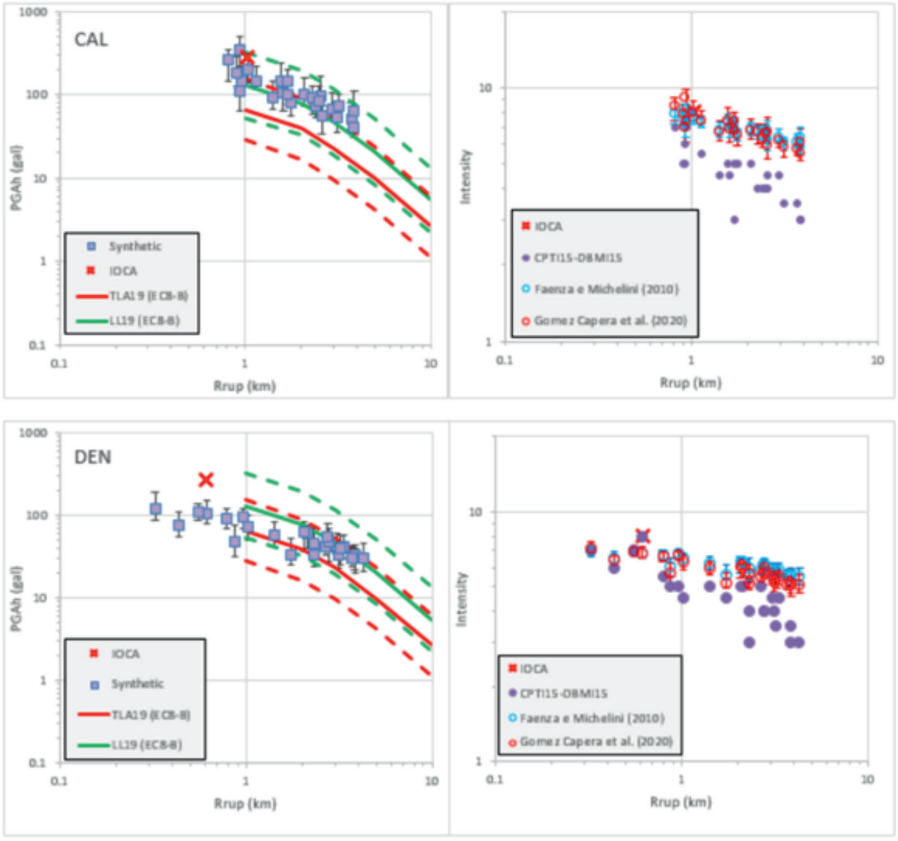


Fig. 2 - Confronto della distribuzione dei dati simulati in funzione della distanza dalla faglia ottenuti considerando le sorgenti di Calderoni *et al.* (2019) (CAL) e De Novellis *et al.* (2018) (DEN), usando i seguenti parametri di input: M_w *3.9, Δσ 0.5 bar,* f_{max} *15 Hz, Vr=0.5Vs.* A sinistra si riportano i valori di PGA confrontati con quelli predetti da Lanzano e Luzi (2020) e Tusa *et al.* (2020), per suoli di tipo B. La ics rossa indica i valori registrati alla stazione IOCA. A destra sono riportati i valori di intensità osservati con quelli simulati (la ics indica il dato macrosismico per Casamicciola).

variabilità e del ruolo giocato dalla geometria di faglia, dalla distribuzione dello slip e degli effetti legati alla geologia di superficie.

Le simulazioni numeriche eseguite hanno esplorato un ampio spazio di parametri e possono essere utilizzate sia per la definizione di GMM da dati sintetici - come fatto ad esempio per i Campi Flegrei da Convertito e Zollo (2011) per sorgenti che possono essere modellate come puntiformi - sia per il calcolo di scenari di scuotimento deterministici. L'uso di approcci ibridi probabilistico-deterministici (p.es., Convertito *et al.*, 2006) nelle analisi di pericolosità sismica riesce a sopperire alla mancanza di GMM specifici per l'area di interesse, come nel caso di Ischia; le stime della probabilità di superamento di valori del moto del suolo possono infatti essere sostituite dalle distribuzioni dei valori simulati.

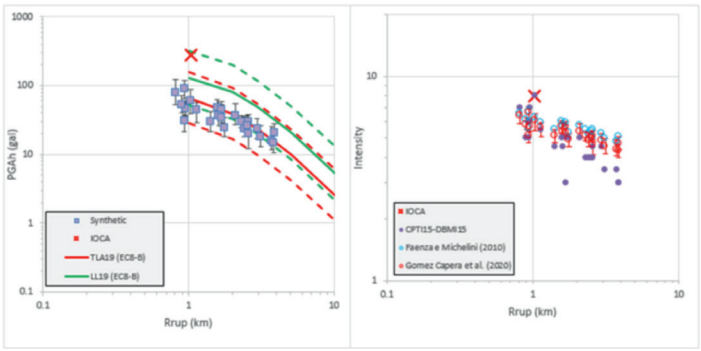


Fig. 3 - Dati simulati in funzione della distanza dalla faglia ottenuti per la sorgente di Calderoni *et al.* (2019) usando gli stessi parametri di input di Fig. 2 ma per $\Delta\sigma$=*0.1 bar.*

Ringraziamenti. Lo studio ha beneficiato del contributo finanziario della Presidenza del Consiglio dei Ministri - Dipartimento della Protezione Civile; rimane degli autori la responsabilità dei contenuti, che pertanto non riflettono necessariamente la posizione e le politiche ufficiali del Dipartimento.

Bibliografia

Boore D.M.; 2005: SMSIM-Fortran programs for simulating ground motions from earthquakes: version 2.3—A revision of OFR 96-80- A. U.S. Geol. Surv. Open-File Report 00 509, revised 15 August 2005, pp. 55. Available from the online publications link on http://www.daveboore.com/

Boore D.M.; 2009: *Comparing stochastic point-source and finite-source ground-motion simulations: SMSIM and EXSIM.* Bull. Seismol. Soc. Am., **99**, 3202-3216.

Calderoni G., Di Giovambattista R., Pezzo G. *et al.*; 2019: *Seismic and geodetic evidences of a hydrothermal source in the M_d 4.0, 2017, Ischia earthquake (Italy)*. J. Geophys. Res.: Solid Earth, **124**, 5014-5029.

Convertito V., A. Emolo A. and Zollo A.; 2006: *Seismic hazard assessment for a characteristic earthquake scenario: an integrated probabilistic - deterministic method*. Bull. Seism. Soc. Am., **96**, 377-391, DOI 10.1785/0120050024.

Convertito V., Zollo A.; 2011: *Assessment of pre-crisis and syn-crisis seismic hazard at Campi Flegrei and Mt. Vesuvius volcanoes*, Campania, southern Italy. Bull. Volcanol., **73**, 767-783, DOI 10.1007/s00445-011-045-2.

Convertito V., Pino N. A. and Di Luccio F.; 2016: *Investigating source directivity of moderate earthquakes by multiple approach: the 2013 Matese (southern Italy) MW = 5 event*. Geophys. J. Int., **207**, 1513–1528. https://doi.org/10.1093/gji/ggw360.

De Novellis V., Carlino S., Castaldo R., *et al.*; 2018: *The 21 August 2017 Ischia (Italy) earthquake source model inferred from seismological, GPS, and DInSAR measurements*. Geophys. Res. Lett., **45**. DOI 10.1002/2017GL076336.

Faenza L. and Michelini A.; 2010: *Regression analysis of MCS intensity and ground motion parameters in Italy and its application in ShakeMap*. Geophys. J. Int., **180**, 1138-1152.

Gomez-Capera A., D'Amico M., Lanzano G. *et al.*; 2020: *Relationships between ground motion parameters and macroseismic intensity for Italy*. Bull. Earth. Eng., **18**, 5143–5164.

Keilis-Borok V.I.; 1959: *On estimation of the displacement in an earthquake source dimension*. Ann. Geofis., **12**, 205-214.

Hanks T.C., Kanamori H.; 1979: *A moment magnitude scale*. J. Geophys. Res., **84**, 2348-50.

Lanzano G. and Luzi L.; 2020: *A ground motion model for volcanic areas in Italy*. Bull. Earth. Eng., **18**, 57–76.

Motazedian, D. and Atkinson, G.M.; 2005: *Stochastic finite-fault modeling based on a dynamic corner frequency*. Bull. Seism. Soc. Am., **95**, 995–1010.

Tusa G., Langer H., Azzaro R.; 2020: *Localizing ground-motion models in volcanic terranes: shallow events at Mt. Etna, Italy, revisited*. Bull. Seism. Soc. Am., DOI 10.1785/0120190325.

TEMPORAL VARIATIONS OF SEISMICITY FROM THE APPLICATION OF TSALLIS ENTROPY

E. Varini[1], R. Rotondi[1], G. Bressan[2]

[1] CNR, Institute for Applied Mathematics and Information Technologies "Enrico Magenes", Milano, Italy
[2] OGS, Seismological Research Center, Udine, Italy

The concept has recently taken hold that Earth's crust behaves as a complex, non-linear dynamic system characterized by long-range correlations (Bowman *et al.*, 2008, and references therein). In statistical seismology these features make some of the classical methods of analysis unsuitable. The Boltzmann-Gibbs (BG) entropy is appropriate to study systems where the elements interact locally in space and time while, if the interactions are long-range, new entropies that generalize some of the properties of BG entropy are more suitable. In this respect, Tsallis (1988) introduced a non-additive entropy that has proved useful for applications in many fields, from physics to chemistry, medicine, informatics, linguistics, economics, seismology.

We derive the probability distribution of the magnitude by maximizing a non-extensive generalization of the Boltzmann-Gibbs entropy given by the Tsallis entropy (Rotondi *et al.*, 2022). The shape parameter q of this distribution is called the entropic index and is found to characterize the subadditive ($q>1$) and superadditive ($q<1$) regimes.

Two active seismogenic areas in central Italy are analyzed, the former including the L'Aquila sequence occurred in 2009 and the latter the Amatrice-Norcia sequence occurred in 2016. Parameter estimation is performed by following the Bayesian approach in order to exploit prior knowledge on the phenomenon, e.g. that provided by Vallianatos *et al.* (2016).

To analyse in detail the variations of the q index and the entropy, we estimate these for time windows of a fixed number of events that shift at each new event. Both the q index and the Tsallis entropy show significant and lasting decreases before the first strong earthquake in the sequences, and sudden increases after them. This indicates that these quantities can be considered as indicators of the level of concentration of energy, and hence of the activation state of the systems. Further studies on different cases and seismotectonic settings are needed to test and consolidate the results.

References

Bowman D.D., Ouillon G., Sammis C.G., Sornette A. and Sornette D.; 1998: *An observational test of the critical earthquake concept*, J. Geophys. Res., **103**, 24359-24372.

Rotondi R., Bressan G. and Varini E.; 2022: *Analysis of temporal variations of seismicity through non-extensive statistical physics*, Geophys. J. Int., **230**, 1318-1337.

Tsallis C.; 1988: *Possible generalization of Boltzmann-Gibbs mechanics*. J. Stat. Phys., **52**, 479-487.

Vallianatos F., Papadakis G. and Michas G.; 2016: *Generalized statistical mechanics approaches to earthquakes and tectonics*, Proc. R. Soc. A, **472**, 20160497.

NESTOREV1.0 APPLICATION TO ITALIAN SEISMICITY

P. Brondi[1], S. Gentili[1], R. Di Giovambattista[2]

[1] CRS, National Institute of Oceanography and Applied Geophysics (OGS), Udine, Italy
[2] National Institute of Geophysics and Volcanology (INGV), Rome, Italy

Abstract. The Italian territory is one of the most seismically active areas in Europe, where large earthquakes are often followed by strong aftershocks. These intense subsequent events can lead to the collapse of already weakened buildings and to further loss of lives. Thus, their forecasting would be important in terms of seismic risk reduction and civil protection. Recently, the machine learning-based algorithm NESTORE (Next STrOng Related Earthquake) [Gentili and Di Giovambattista 2017, 2020, 2022] was proposed to forecast clusters in which the mainshock is followed by an aftershock of similar magnitude. Specifically, if the mainshock-aftershock magnitude difference is less than or equal to 1 the clusters are identified as type A, otherwise as type B. After the occurrence of a strong mainshock of magnitude M_m, the NESTORE most recent version of the software, called NESTOREv1.0 (Gentili *et al.*, 2022), computes nine parameters (features) related to the evolution of the number of events with $M>M_m-2$ and their spatial-magnitude distribution over time in the first hours after the mainshock. The values of these features are used to train nine independent decision trees in order to predict the A-type clusters as long as the strong following earthquake occurs at least 6 hours after the mainshock. NESTOREv1.0 is composed of three modules that respectively (1) identify clusters from a seismic catalog, (2) find appropriate thresholds for features to distinguish cluster types on a training dataset, and (3) use the result of the previous module to provide the probability of being type A for an independent test set. In our analysis, we considered for the Italian territory the seismicity recorded in the last 40 years by the ISIDE and OGS catalogs, the latter of which benefits from the dense OGS network in Northeast Italy. We selected clusters with local mainshock magnitude greater than 3.7 in Northeast Italy and greater than 4 in the remaining territory. We obtained 32 clusters for northeastern Italy and 45 for the rest of the national area, which is dominated by the central Apennines seismicity. Analysing the training results on the two catalogues, the NE area appears quite different from most of the national one, showing a smaller productivity both in terms of number of events and energy of the earthquakes. For this reason, two separate trainings of NESTORE are necessary for future correct forecasting, in good agreement with previous results on earlier versions on NESTORE (Gentili and Di Giovambattista, 2017, 2020). We detected another anomalous area in a smaller region between north-western Tuscany and the south-western part of Emilia-Romagna, with a seismicity characterized by bursts of earthquakes of short duration with anomalous productivity. Since the available training set for that region is almost exclusively populated by type B clusters, no separate training is possible, and we excluded the area from our analysis. By using ISIDE catalogue, we trained NESTOREv1.0 on the time-span 1980-2009 (corresponding to 22 clusters) and tested the forecasting capability on the clusters occurring between 2010 and 2021 (14 cases). The software test provides a correct forecasting for 86% of the cases, showing encouraging results for the application of NESTOREv1.0 in Italy.

Acknowledgements. Funded by a grant from the Italian Ministry of Foreign Affairs and International Cooperation

References

Gentili S. and Di Giovambattista R.; 2017: *Pattern recognition approach to the subsequent event of damaging earthquakes in Italy.* Physics of the Earth and Planetary Interiors, **266**, pp. 1-17.

Gentili S. and Di Giovambattista R.; 2020: *Forecasting strong aftershocks in earthquake clusters from northeastern Italy and western Slovenia*. Physics of the Earth and Planetary Interiors, **303**, 106483.

Gentili, S. and Di Giovambattista, R.; 2022: *Forecasting strong subsequent earthquakes in California clusters by machine learning*, Physics of the Earth and Planetary Interiors, accepted.

Gentili, S., Brondi, P. and Di Giovambattista, R.; 2022: *NESTOREv1.0: a machine learning-based Matlab package for forecasting strong aftershocks in seismic clusters* Submitted to GNGTS 2022.

KINEMATIC AND DEPTH CONTROL ON MAGNITUDE-FREQUENCY RELATIONS: A CASE STUDY FROM SOUTHERN CALIFORNIA

A. Carducci[1,2], A. Petruccelli[3], Rita de Nardis[1,2], A. De Santis[4], G. Lavecchia[1,2]

[1] Department of Psychological, Territory and Health Sciences, University of Chieti-Pescara, Italy
[2] CRUST-Interuniversity Center for 3D Seismotectonics with territorial applications
[3] Former Swiss Seismological Service, ETH Zurich, now at Leithà Srl - Unipol Group
[4] INGV-Istituto Nazionale di Geofisica e Vulcanologia, Roma, Italy

Abstract. We analyze the relationship between the frequency-magnitude parameter (e.g., *b*-value from the Gutenberg-Richter law) and fault kinematics in Southern California (SC), introducing a new faulting style parameter, referred to as A_λ. The value of this parameter strictly depends on stress ratio ϕ as a function of rakes λ, expressed by the equations:

$$A_\lambda = \{\phi_N(\lambda)\,,\ \lambda_N \in \left[-\frac{5}{6}\pi; -\frac{\pi}{6}\right] 1 + \phi_{SS}(\lambda)\,,\quad \lambda_{SS} \in [-\pi; -\frac{5}{6}\pi) \cup (-\frac{\pi}{6}; \frac{\pi}{6}] \cup \left(\frac{5}{6}\pi; \pi\right) 2 + \phi_R(\lambda)\,,\ \lambda_R \in [\frac{\pi}{6}; \frac{5}{6}\pi]$$

A_λ gives the advantage of associating kinematics and stress ratios to focal mechanisms without applying a formal inversion procedure. A_λ ranges can be distinguished as follows: $0 \le A_\lambda < 3$ for normal faults; $1 \le A_\lambda < 2$ for strike-slip faults; $2 \le A_\lambda < 3$ for reverse faults.

In this work, we first compile a high-resolution focal mechanism catalog (time range: 1981 - 2019, magnitude range: 0 - 7.3) by combining the coordinates of Southern California Seismic Network earthquakes by Hauksson *et al.* (2012) with the focal mechanisms dataset compiled by Yang *et al.* (2012). Subsequently, applying the A_λ parameter, we kinematically classify the resulting ~56700 focal mechanisms and calculate the Magnitude of Completeness Mc distributions for well-distinguished kinematic classes. The dataset displays sufficient spatial resolution to allow *b*-value computations along depth for the defined classes.

Finally, the linear relation $b(A_\lambda) = b_\lambda - k_\lambda A_\lambda$, analog to the one proposed by Wu *et al*. (2018) for the Taiwan area, is explored at different depth ranges within these distributions, respecting known rheological passages within the SC crust. We suggest that this equation is well suited to express the dependencies between b-value, kinematics, and depths.

References

Hauksson, E., Yang, W., Shearer, P.M., 2012: *Waveform Relocated Earthquake Catalog for Southern California (1981 to June 2011)*. Bull. Seismol. Soc. Am. **102**, 2239–2244. https://doi.org/10.1785/0120120010.

Wu, Y.-M., Chen, S.K., Huang, T.-C., Huang, H.-H., Chao, W.-A., Koulakov, I., 2018: *Relationship Between Earthquake b -Values and Crustal Stresses in a Young Orogenic Belt*. Geophys. Res. Lett. **45**, 1832–1837. https://doi.org/10.1002/2017GL076694.

Yang, W., Hauksson, E., Shearer, P.M., 2012: *Refined earthquake focal mechanism catalog for southern California (1981 - 2010)*, Supplementary. Bull. Seism. Soc. Am. **10**, 2011–2012.

AN UPDATE OF THE CENTRAL ITALY ELECTROMAGNETIC NETWORK WITH RADON DETECTORS

C. Fidani[1,2,3], G. De Antoni[2], T. Milan[2], M. Siciliani[3], S. Tadioli[3]

[1] Central Italy Electromagnetic Network, Fermo, Italy
[2] Osservatorio Geofisico di Novara, Novara, Italy
[3] Osservatorio Sismico "A. Bina", Perugia, Italy

The Central Italy Electromagnetic Network (CIEN) has measured various electric and magnetic phenomena on different frequency bands in association with Italian seismic activity (Fidani, 2011, 2015, 2017, 2020). To complete the descriptions of these phenomena and propose a physical model, capable of quantitatively describing these measurements, the monitoring of the network was extended to one of the hypothesized sources in the atmosphere, namely Radon gas decay (Pulinets *et al.*, 2015). The updating of CIEN with detectors for this radioactive gas, able to ionize the atmosphere, and therefore producing electric charges, began in 2020. Since then, CIEN has utilized a project of the Novara Geophysical Observatory, at http://www.osservatorionovara.it/.

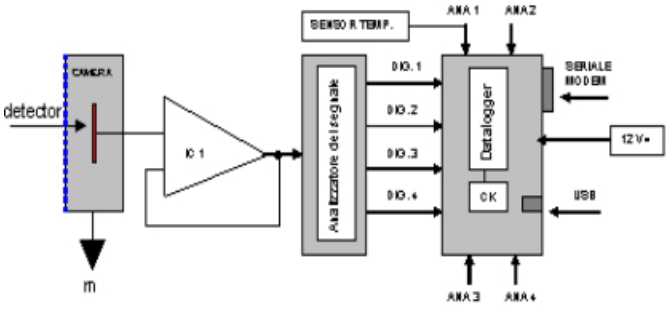


Fig. 1 - The block diagram of the detectors proposed by the Novara Geophysical Observatory team. The surprising aspect of both the camera and the signal analyser is that they are powered at low voltage.

The instrument is enclosed in a metal box divided into two sections (Fig. 1). The first measures 5x2x2.5 cm collection chamber. One of the walls is perforated to allow the Radon, carried by the air to enter. The second section measuring 5x8x2.5 cm is the housing of the electronic circuit. The collection chamber is basically a condenser in air. The walls themselves constitute one of the armatures and this is at mass potential. There is second armor (detector) and it is a small copper plate measuring 2x1 cm positioned at centre. This plate is at a potential of -6 Volts versus mass. The circuit is powered by a dual voltage of ± 12 Volts that comes reduced to ± 8 Volts to prevent voltage drops on the long power cable, which can on average be 10 meters and longer, disturbing the functioning of the circuit. When a 222Rn atom decays inside the chamber it emits a high α particle energy (about 5.6 MeV) which, along its path in the air, produces a trail of ions (about 25000 pairs / cm) capable of perturbing the surrounding electric field. Such a disturbance results in a very weak variation of the detector potential, estimated to be about 0.4 mV.

After the start, in 2017, of the experimental phase, a verification of the instrument functioning was carried out utilizing Torbernite samples and afterword quantitative comparisons were made to professional instruments. Moreover, the Novara Observatory has undertaken the monitoring at various sites around Novara and in Central Italy. Towards the end of 2019 one of the detectors was made available to CIEN and in the first months of 2020 it was installed at the Fermo station. A year later, CIEN built 4 other instruments, following the directives of the Novara observatory, and therein installed 3 of these in the municipality of Gubbio; see the installation setting of the historical centre of Gubbio in Fig. 2, and the fourth was installed in Perugia at the Bina Seismic Observatory.



Fig. 2 - Photos of the Radon Station settings in the historical centre of Gubbio; the Radon detector is on the right, which is inserted inside the tube shown in the centre; the tube is closed and is almost completely buried in the ground.

The counting rates of stations were determined using different solutions, by either serial ports which measure the port state changes or data loggers. For the station in the historical centre of Gubbio, the Lascar EL-USB-5 event, counts and State Data Logger with USB was used, (https://www.lascarelectronics.com/easylog-el-usb-5). This data logger can record up to 32,510 events, state changes and count events. Fast logging rates allow event capturing at speeds of up to four times per second and state changes at speeds of up to two times per second. Whereas event counting can operate at speeds of up to 100 times per second. Radon measurements were accompanied by measurements of temperature, pressure and humidity of the environments where they were the counting rates were taken. An example of a recording of Radon counting decay is shown in Fig. 3 for the station in the historic centre of Gubbio. These data are combined with the environmental data captured by the internal sensors of a PCE-FWS 20 weather station. Also, seismic events of greater intensity that occurred in the surroundings of the station have been stored in the database and plotted in Fig. 3.

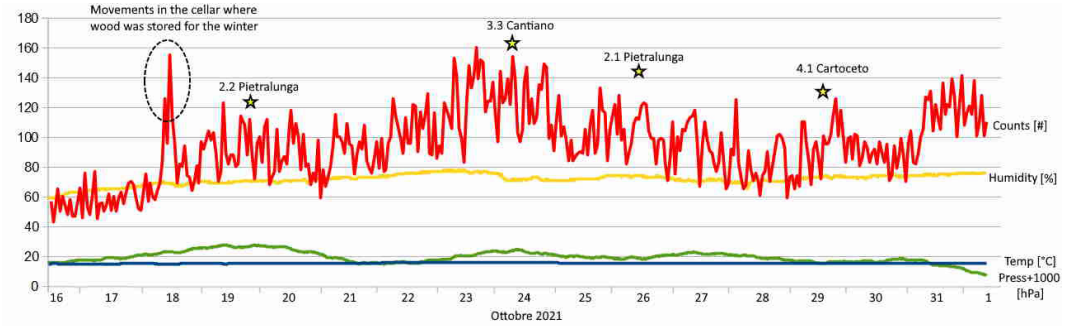


Fig. 3 - The counting rate of the Radon decay in Gubbio historical centre over a two-week period is shown in red; the relative humidity is indicated in yellow; while the overall pressure is shown in green; the local temperature is indicated in blue; the times of seismic event are indicated by yellow stars, whereas the unexpected event of anthropic influence is indicated by a broken line circle.

References

Fidani, C.; 2011: *The Central Italy electromagnetic network and the 2009 L'Aquila earthquake: observed electric activity*. Geosci. J., **1** (1), 3–25.

Fidani, C., and Martinelli, G.; 2015: *A possible explanation for electric perturbations recorded by the Italian CIEN stations before the 2012 Emilia earthquakes*. Boll. Geofis. Teor. Appl., **56**, 211–226.

Fidani, C., and Marcelli, D.; 2017: *Ten Years of the Central Italy Electromagnetic Network (CIEN) Continuous Monitoring*. Open Journal of Earthquake Research, **6**, 73–88.

Fidani, C., Orsini, M., Iezzi, G., Vicentini, N. and Stoppa, F.; 2020: *Electric and Magnetic Recordings by Chieti CIEN Station During the Intense 2016-2017 Seismic Swarms in Central Italy*. Front. Earth Sci., **8**, 536332.

Pulinets, S. A., Ouzounov, D. P., Karelin, A. V. and Davidenko, D. V.; 2015: *Physical bases of the generation of short-term earthquake precursors: a complex model of ionization-induced geophysical processes in the lithosphere atmosphere-ionosphere-magnetosphere system*. Geomagn. Aeron., **55**(4), 521–538.

SIMULATIONS OF TSUNAMIS INDUCED BY SUBMARINE MASS FAILURES ON THE CALABRIAN IONIAN MARGIN

G. Gallotti[1], F. Zaniboni[1], A. Armigliato[1], S. Ceramicola[2], N. Markezic[2], C. Angeli[1], M. Zanetti[1]

[1] Department of Physics and Astronomy "Augusto Righi" (DIFA), University of Bologna, Bologna, Italy
[2] National Institute of Oceanography and Applied Geophysics (OGS), Sgonico, Italy

The Calabrian Ionian margin is particularly prone to submarine mass movements, as testified by scars, canyons, deposits at the toe of the escarpment, and relatively high slope angles in the order of 3-8°. In this study, we present numerical investigations of submarine mass failures and of the ensuing tsunamis in one of the largest areas exposing several pieces of evidence of past mass failures. The approximately 100 km^2 Assi region reveals numerous slide deposits, suggesting sliding volumes ranging between 6 Mm^3 and 500 Mm^3. Numerical simulations of a selection of these slides characterized by distinct features (sliding volumes, detachment depths, and rheology) are performed. As the slides move along the seabed, the impulse given to the water column is estimated and the generation of the waves is reckoned. Eventually, tsunami propagation and inundation are simulated in the near field. We adopt a well-established set of numerical models developed by the Tsunami Research Team of Bologna University. Results prove the strong correlation between the slide characteristics and the generated waves. Local studies of this kind are essential in the investigation of tsunamis generated by submarine failures, whose hazard assessment in the Mediterranean region is still highly debated.

INTRODUCING INFERRED GEOMORPHOLOGICAL SEDIMENT THICKNESS AS A NEW SITE PROXY TO PREDICT GROUND-SHAKING AMPLIFICATION

K. Loviknes[1,2], F. Cotton[1,2], G. Weatherill[1]

[1] GFZ German Research Centre for Geosciences, Potsdam, Germany
[2] Institute for Geosciences, University of Potsdam, Potsdam, Germany

Local geological features can have a strong impact on earthquake ground shaking. Sites with mainly loose sediments have been observed to amplify the recorded ground motion. In many, non-site-specific, applications where seismic hazard and risk assessments must be computed on large regions, this site amplification is commonly characterized using the average shear-wave velocity of the upper 30 meters of the soil column (V_{S30}). For a single site the velocity profile and V_{S30} can be measured directly, for larger areas and regions, however, the V_{S30} must be inferred from other parameters. A much-used method to calculate V_{S30} is the model by Wald and Allen (2007) based on topographic slope from digital elevation models (DEMs). However, inferring V_{S30} based on topographic slope has several limitations, especially for basins and particular geological conditions (Lemoine *et al.,* 2012). Furthermore, the measured V_{S30} values should not be used interchangeably with inferred V_{S30} values without properly accounting for the additional uncertainty related to the V_{S30} calculations (Lemoine *et al.,* 2012, Weatherill *et al.,* 2020).

In this study we propose a geomorphological model for inferred sediment depth by Pelletier *et al.* (2016), as an alternative site proxy to predict ground motion site-amplification on a regional or global scale. The Pelletier *et al.* (2016) model uses DEM and geological maps to distinguish between landforms, lowlands, uplands, hillslopes and valley bottoms. The thickness of sediments, soil and intact regolith is then inferred for each landform using several global and regional values including geological maps, water table depth and climate data. The final model provides a global map of inferred regolith, soil and sediment thickness up to 50 meters. In this study we focus on the average soil and sediment thickness, from hereon called geomorphological sedimentary thickness, as shown in Fig. 1 for Europe.

To test whether the model can be used to predict ground-motion site amplification, we compare the geomorphological sedimentary thickness to inferred V_{S30}, topographic slope and empirical site amplification as shown in Fig. 2 for frequency f = 1.062 Hz. The empirical site

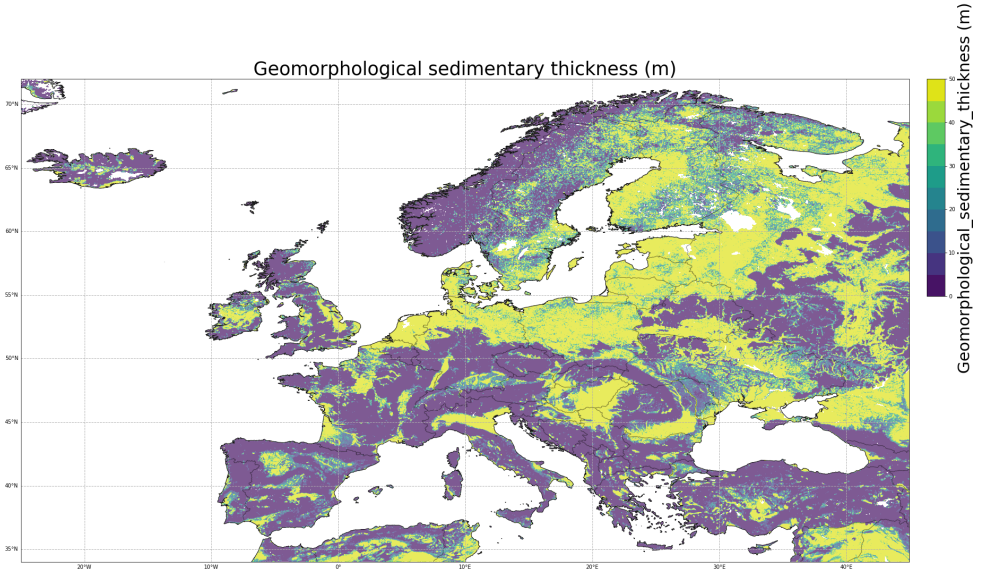


Fig. 1 - The inferred geomorphological sedimentary thickness for Europe from the Pelletier *et al.* (2016) model.

amplification is derived from the European Engineering Strong-Motion (ESM) dataset (Luzi *et al.*, 2020) as the site-to-site residuals ($\delta S2S_s$) derived from a simple GMM following the method of Kotha *et al.* (2018, 2020) and Weatherill *et al.* (2020). For each proxy we derive a simple site amplification model based on linear regression (black lines in Fig. 2) and evaluate the performance of each model. The results show that the geomorphological sedimentary thickness performs better than or equally well as the inferred V_{S30} and topographic slope. We therefore argue that the inferred geomorphological sedimentary thickness from the Pelletier *et al.,* 2016 model is a promising new alternative to traditional inferred proxies for predicting site amplification on a regional or global level and capture the epistemic uncertainty associated to the prediction of site amplification for large scale seismic hazard or risk studies.

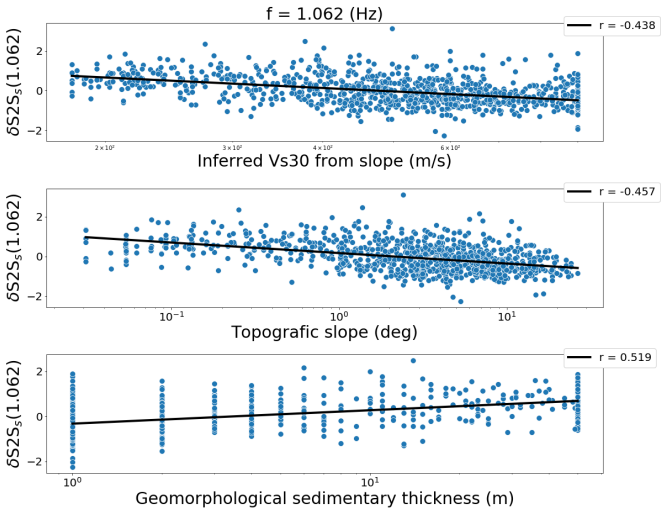


Fig. 2 - The linear regression (black lines) and correlation coefficient *r* between the empirical site amplification $\delta S2S_s$ for frequency *f* = 1.062 Hz and the inferred V_{S30} (top) and topographic slope (middle) and the geomorphological sedimentary thickness (bottom) at stations from the European Engineering Strong-Motion (ESM) dataset.

Acknowledgments. The authors are grateful to Jean Braun for valuable discussion and explanation on regolith. This research is funded by the European Commission, ITN-Marie Sklodowska-Curie New Challenges for Urban Engineering Seismology URBASIS-EU project, under Grant Agreement 813137.

References

Kotha, S.R., Cotton, F., and Bindi, D. (2018). *A new approach to site classification: mixed-effects ground motion prediction equation with spectral clustering of site amplification functions.* Soil Dynamics and Earthquake Engineering, 110, 318-329. https://doi.org/10.1016/j.soildyn.2018.01.051.

Kotha, S.R., Weatherill, G., Bindi, D. and Cotton, F. (2020). *A regionally-adaptable ground-motion model for shallow crustal earthquakes in Europe*. Bull Earthquake Eng 18, 4091–4125 https://doi.org/10.1007/s10518-020-00869-1.

Lemoine, A., Douglas, J., and Cotton, F. (2012). *Testing the Applicability of Correlations between Topographic Slope and VS_{30} for Europe.* Bulletin of the Seismological Society of America; 102 (6): 2585–2599. doi: https://doi.org/10.1785/0120110240.

Luzi L., Lanzano G., Felicetta C., D'Amico M. C., Russo E., Sgobba S., Pacor, F., and ORFEUS Working Group 5 (2020). *Engineering Strong Motion Database (ESM) (Version 2.0)*. Istituto Nazionale di Geofisica e Vulcanologia (INGV). https://doi.org/10.13127/ESM.2.

Pelletier, J.D., Broxton, P.D., Hazenberg, P., Zeng, X., Troch, P. A., Niu, G.-Y., Williams, Z., Brunke, M. A., and Gochis, D. (2016), *A gridded global data set of soil, immobile regolith, and sedimentary deposit thicknesses for regional and global land surface modeling*, J. Adv. Model. Earth Syst., 8, 41– 65, doi:10.1002/2015MS000526.

Weatherill G., Kotha S. R., and Cotton F. (2020). *Re-thinking site amplification in regional seismic risk assessment.* Earthquake Spectra., 36:274-297. doi:10.1177/8755293019899956.

Wald, D. J., Allen, T. I. (2007). *Topographic Slope as a Proxy for Seismic Site Conditions and Amplification*. Bulletin of the Seismological Society of America, 97 (5): 1379–1395. doi: https://doi.org/10.1785/0120060267.

ABOUT THE ROLE OF NW-TRENDING FAULT SYSTEMS IN THE MESSINA STRAITS AREA

G. Neri[1], P. Pino[1], D. Presti[1], S. Scolaro[1], S. D'Amico[2], C. Navarra[1], B. Orecchio[1], A. Torre[1]

[1] Department of Mathematics, Computer Sciences, Physics, and Earth Sciences, University of Messina, Messina, Italy
[2] Department of Geosciences, University of Malta, Msida, Malta

Re-examining the HVSR data published in a previous paper (Scolaro *et al.*, 2018) we focus on a clear change of peak frequency occurring across a NW-SE segment located in the historical centre of the town of Messina. This change can reasonably be imputed to lateral heterogeneity of the sedimentary cover passing from southwest to northeast across the segment and, possibly, to an increase of the thickness of the sediment pile corresponding to a decrease of the HVSR peak frequency. These data may suggest the existence of a fault in correspondence of the segment.

Neri *et al.* (2021) have shown that seismicity in the overall Straits area is often characterized by transtensional focal mechanisms with a right-lateral component. The same authors proposed a possible geodynamic interpretation of seismological evidences, according to which (i) southeastward rollback of the residual Ionian subducting slab, although very slow at present day, is a main source of extension in the Messina Straits area and (ii) southward decrease of trench retreat velocity when approaching the southern edge of the subducting slab produces a right-lateral component of faulting on NW-SE trending faults.

Also, we remark here that one of the strongest earthquakes occurred in the Messina Straits after the 1908 one, the magnitude 4.9 earthquake of January 1975 offshore Reggio Calabria, was characterized by a dextral strike-slip mechanism, with several features similar to mechanisms of recent seismicity obtained by Neri *et al.* (2021).

In the present work, we discuss a series of new analyses based on application of different geophysical and geological methodologies, with the aim of evaluating the real role of NW-trending fault systems in the Messina Straits, from the geodynamic point of view and with particular reference to seismogenesis in this high seismic risk area.

References

Neri G., Orecchio B., Presti D., Scolaro S., and Totaro, C.; 2021: *Recent Seismicity in the Area of the Major, 1908 Messina Straits Earthquake, South Italy*. Frontiers in Earth Science, **9**, 566, doi: 10.3389/feart.2021.667501.

Scolaro S., Pino P., D'Amico S., Orecchio B., Presti D., Torre A., Totaro C., Farrugia D. and Neri G.; 2018: *Ambient noise measurements for preliminary microzoning studies in the city of Messina, Sicily*. Annals of Geophysics, **61**(2), doi: 10.441/ag-7711.

GEO-INQUIRE – A NEW OPPORTUNITY FOR EXPLOITING EUROPEAN GEOSCIENCE INFRASTRUCTURE FOR CURIOSITY-DRIVEN RESEARCH THROUGH TEST SITES AND TRAINING

F. Cotton[1], A. Strollo[1], K. Fleming[1], G. Festa[2], S. Murphy[3], M. Majdański[4], Geo-INQUIRE Consortium

[1] GFZ - German Research Centre for Geosciences, Germany
[2] UniNA - University of Naples Federico II, Department of Physics, Italy
[3] IFREMER - French Research Institute for Exploitation of the Sea, France
[4] IGF-PAS - Institute of Geophysics Polish Academy of Sciences, Poland

The Geo-INQUIRE (Geosphere INfrastructure for QUestions into Integrated REsearch) project, supported by the Horizon Europe Programme, is setting out to strengthen collaboration between geoscience infrastructures in Europe for the provision of access to selected key data, products, and services. Such access will have the aim of making better known the resources available to researchers to engage in curiosity-driven studies into dynamic processes within the geosphere, allowing them to be monitored and modelled at new levels of spatial and temporal detail and precision. Included in such activities are efforts to overcome cross-domain barriers, especially the land-sea-atmosphere environments, and the exploitation of innovative data management techniques, modelling and simulations methods, developments in AI and big data, and the extension of existing data infrastructures to disseminate these resources to the wider scientific community. Geo-INQUIRE, starting in October 2022 and with a duration of 4 years, is calling upon the expertise of a partnership of 51 partners made up of major European research institutes, universities, national geological surveys, and consortia from within the ERIC (European Research Infrastructure Consortium).

Two critical and potentially high value-added activities within Geo-INQUIRE are the theme of this poster. The first involves the provision of Transnational Access (TA, both virtual and on-site) at six test beds located around Europe: the Bedretto Laboratory, Switzerland; the Ella-Link Geolab, Portugal; the Liguria-Nice-Monaco submarine fibre infrastructure, Italy/France; the Irpina Near-Fault Observatory and the Eastern Sicily facility, Italy; and the Corinth Rift Laboratory, Greece. The second series of activities concern the holding of training workshops (directed to researchers at all stages of their careers) dealing with the most effective use of the services and data provided by the Geo-INQUIRE partnership.

The test beds provide state-of-the-art research facilities covering the Earth's surface, subsurface, and marine environments over a range of spatial scales (small-scale laboratories to wide-spread field stations). They will facilitate the investigation of fundamental processes associated with geohazards and georesources, such as the preparatory phases of earthquakes, the movements of fluids within the Earth's interior, the interactions between ocean, the seabed, and the underlying Earth crust, and the impact of geothermal exploitation. Provision will be made for researchers to undertake their own experiments at these sites, with the resulting observations and results contributing to the already existing products, all in turn being made available via the project's strict adherence to FAIR principles. The first TA call is expected in summer 2023. The training activities in turn will aim at cross-disciplinary interoperability, with a number of online and onsite workshops and two summer schools dealing with existing big data sets and developments in data science relevant to the geosciences, high performance computing, and developing a cross-disciplinary and cross-domain multi-disciplinary awareness of the product and services available being hosted by the project. Two hackathon events will be organized in Cracow (Poland) and Bologna (Italy), where it is planned to focus on big data analysis and related software development. The first summer school will be organized in Catania (Italy) with a focus on cross-disciplinary data, including Solid Earth and Marine Sciences, related to the geohazards associated with Mount Etna.

Ultimately, Geo-INQUIRE, with its efforts to enhance the dissemination of a substantial product and service portfolio under continuous improvement, will enable the next generation of scientists to carry out leading-edge research addressing societal challenges from a multidisciplinary perspective, making intelligent use of these resources.

VARIABILITY OF SOURCE PARAMETERS IN CENTRAL-SOUTHERN EUROPE

M-H Yen[1,2], D. Bindi[1], R. Zaccarelli[1], A. Oth[3], B. Edwards[4], F. Cotton[1,2]

[1] GFZ-German Research Centre for Geosciences, Germany
[2] University of Potsdam, Germany
[3] European Center for Geodynamics and Seismology, Luxembourg
[4] University of Liverpool, England

Abstract. Source parameter, stress drop, is a key parameter estimating strong ground motion, as it controls the level of peak ground acceleration (Hanks and Johnson, 1976). A non-parametric spectral decomposition of the Fourier amplitude spectra (FAS) is applied to isolate source, site and path contributions, solving regional attenuation models for two spatial domains across the Alps. The source spectra isolated from the other site contributions are fitted to a standard omega square model (Brune model) to determine the seismic moment and the corner frequency. These values are in turn used to compute the stress drop considering a circular rupture model with uniform stress drop. Finally, we discuss the variability of stress drop with earthquake size from southern to northern Europe and their dependencies on the origin of earthquakes (induced and tectonic).

Introduction. The knowledge of source parameters is a crucial topic for the seismic hazard assessment, from ground-motion prediction equations to physics-based simulations. Stress drop is a key parameter in the estimation of strong ground motion, as it controls the level of peak ground acceleration (Hanks and Johnson, 1976). It determines the position of the corner frequency and the height of the high-frequency plateau in the Fourier amplitude spectrum of acceleration. Several studies of source parameters for different regions have been investigated such as Japan (Oth *et al.*, 2017), southern California (Baltay *et al.*, 2017, Trugman and Shearer, 2017), central Italy (Bindi *et al.*, 2019), and global datasets (Baltay *et al.*, 2019). However, modeling assumptions make the results difficult to compare between different studies, even in the same target regions.

In this study, we estimate source parameters of events in central-southern Europe from the stable part (mainly Switzerland and Germany) to the active part (mainly central and northern Italy) of the continent. A non-parametric spectral decomposition approach is applied on the Fourier amplitude spectra (FAS) of events in the region to determine the source spectra, site contributions and attenuation propagation effects, considering two regional attenuation models. To remove the trade-off between source and site terms, we constrain a-priori the site amplification at one reference station contributing to both attenuation domains. The obtained source spectra are fitted to a standard ω^2-model to evaluate the seismic moment and the corner frequency, which in turn are used to compute the stress drop. Finally, we discuss the variability of stress drop with earthquake size, regions, and source origins.

Data and Processing. The recordings from 1990 to 2020 in the regions were downloaded and processed by means of *stream2segment* (Zaccarelli *et al.*, 2019) using as event catalog the International Seismological Center, ISC. The database hosts about 52 million segments in total from 178,000 earthquakes recorded by 4,771 stations belonging to 118 either temporary or permanent networks. Due to potential noises and outliers in the datasets from the automatic downloaded and processed by the software, the quality control (signal-to-noise ratio and outlier detection) are applied. Finally, we select 4,380 earthquakes with a magnitude larger than 2.5 in central-southern Europe recorded by 996 stations (Fig. 1). We match the location and origin times of selected earthquakes with the EMEC catalog to identify induced events for the further discussion of the scaling relationship of source origins. The FAS are computed by the vector sum of two horizontal components, which is independent of the sensor orientation. The considered frequency band is from 0.3 to 25 Hz.

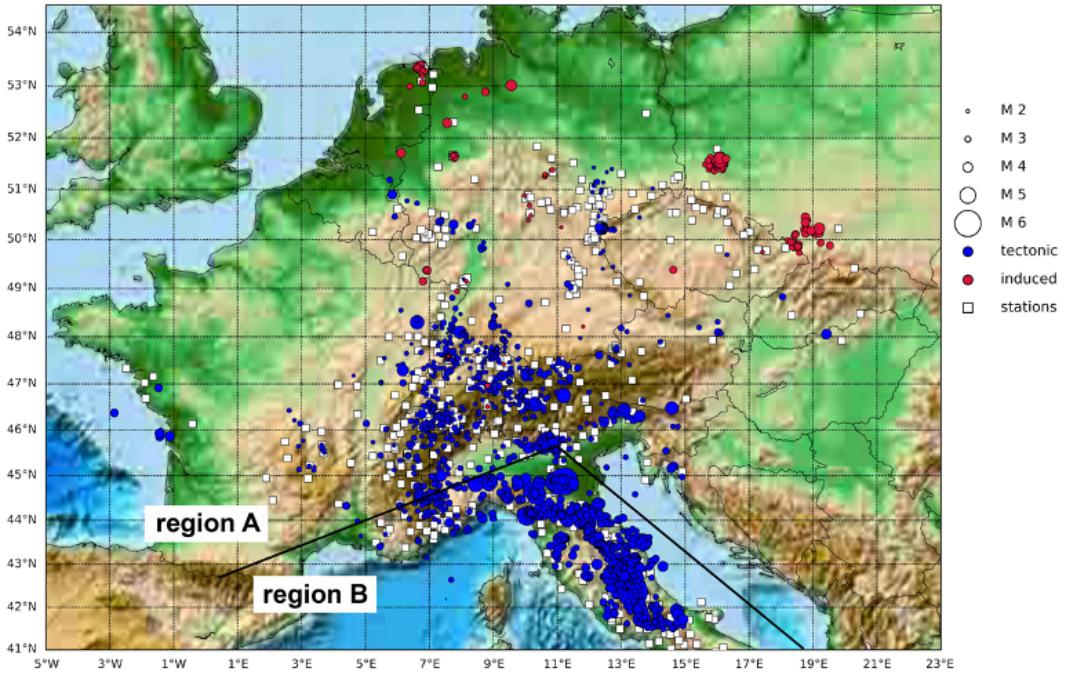


Fig. 1 - Map with earthquake (circle sizes depending on the earthquake magnitudes) and station locations used in this study. Circles in blue represent tectonic events and in red represent induced events.

An automatic algorithm is employed, which consists of removing the instrumental response and applying a Butterworth band-pass filter with high-pass magnitude dependent corner frequency: 0.08 Hz for magnitude above 6 to 0.3 for magnitudes between 3 and 6; and to 0.5 Hz for events smaller or equal to 3. A low pass corner frequency is fixed to 90% of the Nyquist frequency. The signal window is defined as the interval between the 2.5% and 97.5% percentile of the cumulative squared acceleration computed from the estimated P-wave arrival. We additionally applied signal-to-noise ratio (SNR) constraints and outlier detection to drop segments with the potential multiple-event signal and high-noise segments. Records with SNR smaller than 20 over the frequency range from 0.5 to 20 Hz are not further processed. The outlier detection is a modified Z-score method applied to the median absolute deviation of residuals. The residuals are with respect to predictions from Ground Motion Prediction Equations (GMPEs) considering the PGV and PGA for Europe and Middle East (Bindi et al., 2014) to detect the presence of outliers. The threshold is according to Iglewicz and Hoaglin (1993) that suggested the Z-score for the presence of outliers was greater than 3.5 or lower than -3.5.

Method. We perform a spectral decomposition approach to characterize the FAS into source, propagation and site contributions. The generalized inversion technique (GIT) (Castro et al., 1990) is a well-known method to derive frequency-dependent attenuation characteristics as well as source and site contributions. The FAS of ground motion can be written by the following system of linear equations:

$$log_{10}U_{ij}\left(f, r_{ij}\right) = log_{10}S_i(f) + log_{10}A\left(f, r_{ij}\right) + log_{10}Z_j(f) \quad (1)$$

We split the decomposition approach into two steps: first, we determine the attenuation models introducing a two domains regionalization. The regional attenuation models are

simultaneously determined by discretizing the distance range into a given number of intervals and determining the frequency-dependent attenuation value for each distance bin. The equation can be written as equation (2), where k=1.2 indicates the regional attenuation models.

$$log_{10}U_{ij}\left(f, r_{ij}\right) = log_{10}A^{k}\left(f, r_{ij}\right) + log_{10}R_{ij}(f) \quad (2)$$

A subsequent inversion allows separating source and site effects from the residual spectral amplitudes after correcting the regional attenuation functions:

$$log_{10}R_{ij}(f) = log_{10}S_{i}(f) + log_{10}Z_{j}(f) \quad (3)$$

Here, to constrain site amplifications of all stations to one reference condition, the reference site condition is set for the station CH.LLS, which is the reference site in the network CH managed by Swiss seismological service (SED). The reference site amplification is set to $e^{-\pi k_0 f}$ with k_0 = 0.007s (Pilz *et al.*, 2019).

After solving the constrained linear system of equations, the obtained source spectra are fit with the ω²-model (Brune, 1970, 1971) to estimate the corner frequency f_C and seismic moment M_0 (respectively moment magnitude M_W) by the following source model, consisting of a standard ω²-model multiplied by an exponential factor, κ_{source}, applied to frequencies above f_k:

$$S(f) = (2\pi f)^2 \frac{R^{\theta\varnothing}F}{4\pi\rho {V_S}^3 R_0} M^{\cdot}(f) e^{-\pi\kappa_{source}(f-f_k)}, with \quad M^{\cdot}(f) = \frac{M_0}{1+\left(\frac{f}{f_C}\right)^2} \quad , \quad (4)$$

where $S(f)$ represents the acceleration source spectrum at the reference distance R_0 = 10 km. $M^{\cdot}(f)$ denotes the moment-rate spectrum, $R^{\theta\varnothing}$ is the average radiation pattern of S-waves set to 0.55 (Boore and Boatwright, 1984), F=2 is the free surface factor, ρ=2.7 g/cm³ is the density and V_S = 3.3 km/s is the shear-wave velocity near the source.

Stress drop $\Delta\sigma$ was computed with the obtained corner frequency and seismic moment by the following equation (Eshelby, 1957):

$$\Delta\sigma = \frac{7M_o}{16r^3}, \quad (5)$$

where the rupture radius is given by

$$r = \frac{2.34V_S}{2\pi f_C} \quad (6)$$

Results

We derived spectral models for source, path, and site amplifications for southwestern Europe by analyzing events from the stable to the active part of the continent. Attenuation models have been derived for two different regions, which are the stable part (mainly Switzerland and Germany) and the active part of Europe (mainly central and northern Italy) (Fig. 2 (a) and (b)). The attenuation in region A (northern Europe) of each frequency almost decay the same as 1/R function up to 60 km. At large distances, it attenuates faster than a 1/R curve at frequencies larger than 10 Hz. The attenuation functions in region B (southern Europe) decay similarly for the entire frequency range at distances up to 50 km. At distances larger than 50 km, the attenuation functions at high frequencies attenuate faster. Southern Europe shows a stronger attenuation than northern Europe, especially at high frequencies. The attenuation-corrected spectra are decomposed into site and source contributions shown

in Fig. 2 (c) and (d). The relative amplification varies by a factor of around 10. We determine the seismic moment and the corner frequency by fitting an ω^2-model to the obtained source spectrum.

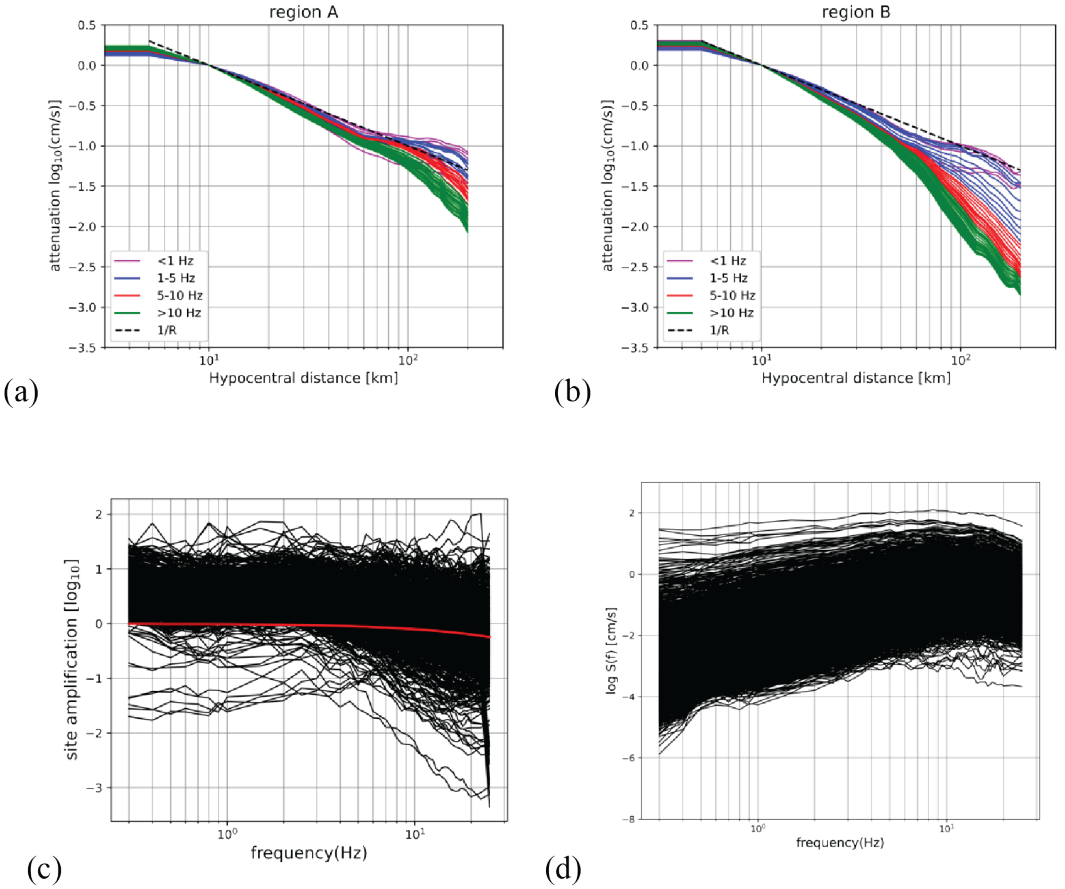


Fig. 2 - Regional attenuation models against hypocentral distance for frequencies from 0.3 to 25 Hz for (a) region A and (b) region B. (c) Site amplifications obtained by the spectral decomposition relevant to the reference site, CH.LLS (red curve). (d) Source spectra retrieved through the spectral decomposition approach.

We determine the seismic moment and the corner frequency by fitting the corrected source spectra with an ω^2-model. Finally, we evaluate the resulting stress drops for different source origins (induced and tectonic earthquakes) under the same assumptions (Fig. 3). Resulting stress drops show a clear scaling relationship with moment magnitudes, with stress drop increasing with earthquake magnitude for the tectonic events. The distributions of stress drop for two source origins are in the different ranges, which are in the range of 0.01-1 MPa for induced events and 0.1-100 MPa for the tectonic events. The scaling relationships of stress drops for two source origins confirm that the stress drop of the induced events are not following a scale with earthquake magnitude.

Acknowledgement. This study was supported by the European Union's H2020-MSCA-ITN-2018 program under grant agreement No 813137, project URBASIS.

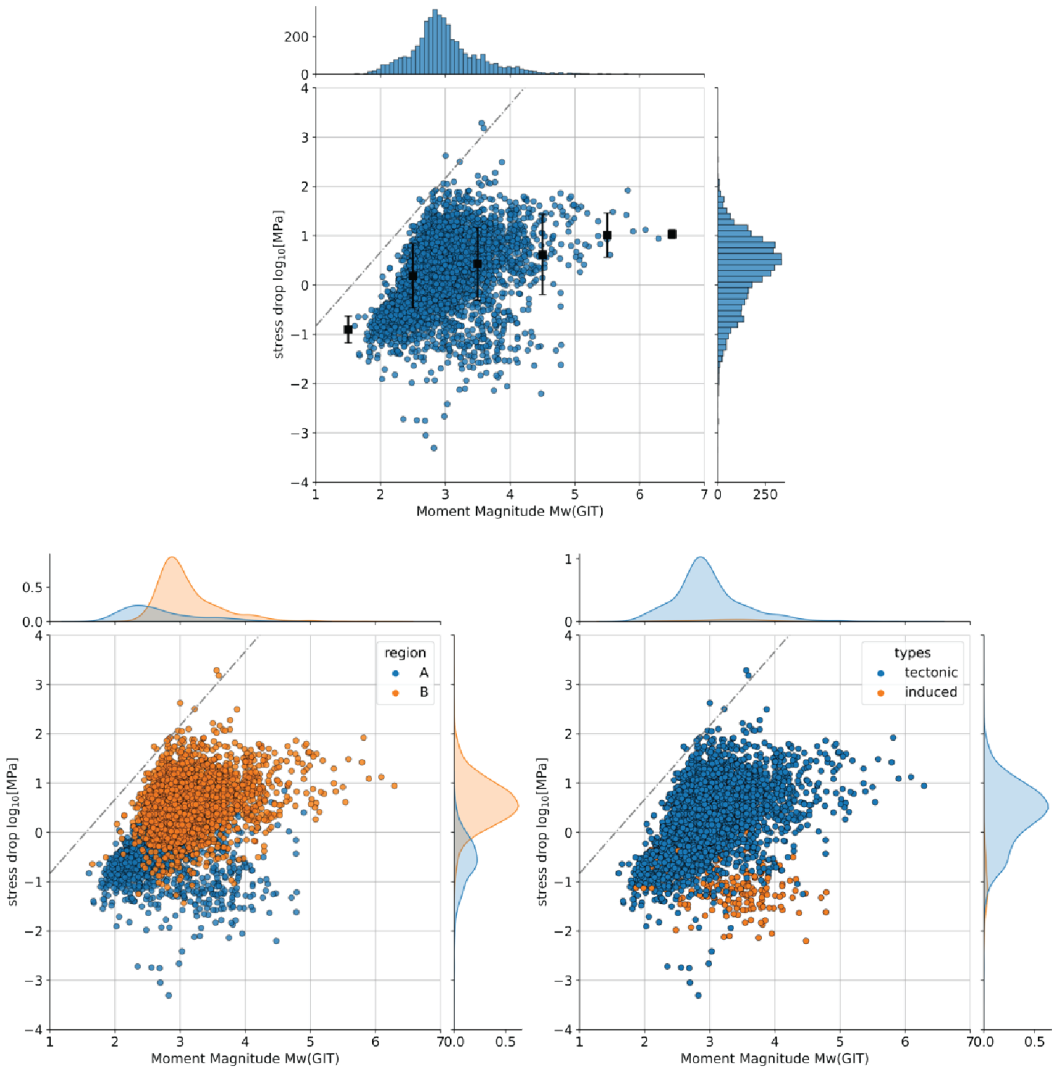


Fig. 3 – Stress drops scaling with fitting moment magnitudes and the distribution of the stress drops for two regions and source origins.

References

Baltay, A. S., T. C. Hanks, and N. A. Abrahamson, 2017, *Uncertainty, Variability, and Earthquake Physics in Ground-Motion Prediction Equations,* Bulletin of the Seismological Society of America, 107, no. 4, 1754–1772, doi: 10.1785/0120160164.

Baltay, A. S., T. C. Hanks, and N. A. Abrahamson, 2019, *Earthquake Stress Drop and Arias Intensity*, Journal of Geophysical Research: Solid Earth, 124, no. 4, 3838–3852, doi: https://doi.org/10.1029/2018JB016753.

Bindi, D., and S. R. Kotha, 2020, *Spectral decomposition of the Engineering Strong Motion (ESM) flat file: regional attenuation, source scaling and Arias stress drop*, Bull Earthquake Eng, 18, no. 6, 2581–2606, doi: 10.1007/s10518-020-00796-1.

Bindi, D., M. Massa, L. Luzi, G. Ameri, F. Pacor, R. Puglia, and P. Augliera, 2014, *Pan-European ground-motion prediction equations for the average horizontal component of PGA, PGV, and 5 %-damped PSA at spectral periods up to 3.0 s using the RESORCE dataset*, Bull Earthquake Eng, 12, no. 1, 391–430, doi: 10.1007/s10518-013-9525-5.

Boore, D. M., and J. Boatwright, 1984, *Average body-wave radiation coefficients*, Bulletin of the Seismological Society of America, 74, no. 5, 1615–1621, doi: 10.1785/BSSA0740051615.

Brune, J. N., 1970, *Tectonic stress and the spectra of seismic shear waves from earthquakes*, Journal of Geophysical Research (1896-1977), 75, no. 26, 4997–5009, doi: 10.1029/JB075i026p04997.

Brune, J. N., 1971, *Seismic sources, fault plane studies and tectonics*, Eos, Transactions American Geophysical Union, 52, no. 5, IUGG 178-IUGG 187, doi: 10.1029/EO052i005pIU178.

Castro, R. R., J. G. Anderson, and S. K. Singh, 1990, *Site response, attenuation and source spectra of S waves along the Guerrero, Mexico, subduction zone*, Bulletin of the Seismological Society of America, 80, no. 6A, 1481–1503, doi: 10.1785/BSSA08006A1481.

Eshelby, J. D., and R. E. Peierls, 1957, *The determination of the elastic field of an ellipsoidal inclusion, and related problems, Proceedings of the Royal Society of London.* Series A. Mathematical and Physical Sciences, 241, no. 1226, 376–396, doi: 10.1098/rspa.1957.0133.

Hanks, T. C., and W. Thatcher, 1972, *A graphical representation of seismic source parameters*, Journal of Geophysical Research (1896-1977), 77, no. 23, 4393–4405, doi: 10.1029/JB077i023p04393.

Iglewicz, B. and Hoaglin, D.C., 1993. H*ow to detect and handle outliers* (Vol. 16). Asq Press.

Oth, A., H. Miyake, and D. Bindi, 2017, *On the relation of earthquake stress drop and ground motion variability,* Journal of Geophysical Research: Solid Earth, 122, no. 7, 5474–5492, doi: 10.1002/2017JB014026.

Pilz, M., F. Cotton, R. Zaccarelli, and D. Bindi, 2019, *Capturing Regional Variations of Hard-Rock Attenuation in Europe,* Bulletin of the Seismological Society of America, 109, no. 4, 1401–1418, doi: 10.1785/0120190023.

Trugman, D. T., and P. M. Shearer, 2017, *Application of an improved spectral decomposition method to examine earthquake source scaling in Southern California*, Journal of Geophysical Research: Solid Earth, 122, no. 4, 2890–2910, doi: https://doi.org/10.1002/2017JB013971.

Zaccarelli, R., D. Bindi, A. Strollo, J. Quinteros, and F. Cotton, 2019, *Stream2segment: An Open-Source Tool for Downloading, Processing, and Visualizing Massive Event-Based Seismic Waveform Datasets*, Seismological Research Letters, 90, no. 5, 2028–2038, doi: 10.1785/0220180314.

Sessione 2.2

Scienza e tecnica a supporto della prevenzione e della preparazione al terremoto

Convenor: M. Dolce, F. Pacor e M. Polese

SEISMIC VULNERABILITY OF HISTORIC GLASS ENVELOPES: TOWARDS A STANDARDIZED EVALUATION PROTOCOL FOR HARMONIZED PERFORMANCE CHECK

C. Bedon

University of Trieste, Department of Engineering and Architecture, Trieste, Italy

Design of glass element under seismic loads. Glass components are of common use in modern architecture and even design concepts. Dedicated calculation methods can be adopted to ensure appropriate performances and safety levels in the framework of well-known Limit State concept for ordinary buildings.

More specifically, technical guidelines and documents of relatively recent elaboration are nowadays conceived to support structural designers in the realization of load-bearing glass elements with primary or secondary or even non-structural role in buildings, under the effects of various ordinary or accidental design actions (Bedon *et al.,* 2019). Among others, the CNR-DT 210/2013 technical document provides specifications for the seismic analysis and verification of building elements made of structural glass. In this context, the analysis against stress peaks and deformations should be carried out at the component level. Design detailing against seismic action depends on multiple structural and building parameters, as also schematized in Fig. 1. In doing so, the use of double (or more) laminated glass elements is privileged due to the additional plastic and dissipation role of bonding interlayers, hence resulting in improved post-failure mechanical performance and enhanced safety levels for customers.

Table 3.9. Classification of structural glass elements according to conditions of use. By definition non-structural construction products fall under class 0.

Type	Class for pre-glass-failure assessment*	Class for post-glass failure assessment
Vertical elements** with continuous edge restraint	1	1/NA***
Vertical elements** with fixing points	2/1	1/NA***
Horizontal roofs**	2	2/1
Railings with danger of fall	2	2/1
Reinforcement fins	2	2/1
Floors, load-bearing beams	2	2
Pillars	3 (specific analyses with Level II or Level III methods)	2 (with pre-failure actions)

Notes:
(*) Within the same category, the choice of the most or least restrictive class of assessment depends on the importance of the work, the degree of danger arising in the event of failure of the glass, and whether safety countermeasures can be immediately implemented in order to reduce the consequences of failure (e.g. propping, protection measures, fences, etc.).
(**) An element is considered vertical if the angle of its plane from the vertical is less than 15°. An element which does not fall under this definition is considered horizontal.
(***) NA stands for "No Assessment". When failure of the glass produces negligible risks in terms of damage or human life, post-failure assessment may be omitted.

Table 4.7. Performance levels required against seismic actions.

Name	Description
ND – No damage	It is assumed that the system is free of any damage that requires the glass panes to be replaced for the functionality of the building. Specifically, façade and roof elements must maintain their requirements of impermeability to wind and to rain.
SD – Slight damage	It is assumed that the system may suffer loss of functionality of some elements, the rapid replacement of which does not involve particular technical details, with the building remaining usable overall. There is no risk for users connected with partial failures.
HD – Heavy damage	The system suffers heavy damage, with a high degree of loss of functionality, with high costs in terms of re-establishing functionality, but without risks of falls of material which could potentially lead to high risk situations.
F – Failure	The system suffers severe damage and exhibits extended evidence of failure. Any falling material would cause risks comparable to those caused by other elements such as cornices and external cladding.

Table 4.8. Performance levels for the "glass" system

Level	Importance class			
LS	I	II	III	IV
SLO	-	-	ND_{45}	ND_{60}
SLD	SD_{35}	SD_{50}	SD_{75}	SD_{100}
SLV	HD_{333}	HD_{475}	HD_{713}	HD_{950}
SLC	-	-	F_{1463}	F_{1950}

Fig. 1 - Summary of relevant structural and seismic parameters for glass design (CNR-DT 210/2013).

In such a kind of design assumptions, a special consideration must be spent for existing (and even historic) glass components, which have been realized without specific consideration for minimum performance capacity against loading conditions of typical interest for buildings. Technical standard documents elaborated for load-bearing glass components are relatively recent. Often, moreover, technical drawings or documents and notes are not available for these glass systems, and hence a vulnerability analysis of the state-of-art situation can result in rather complex assumptions.

In this paper, a case-study glass envelope is taken into account and investigated towards the assessment of actual mechanical properties and load-bearing capacities for seismic (and multi-hazard) retrofit purposes. The attention is focused on the performance demand evaluation based on a possible harmonized framework and protocol resulting from the application of actual technical regulations for structural glass design and from the additional integration of in-field Operational Modal Analysis (OMA) experimental techniques for the Finite Element (FE), state-of-art numerical analysis.

Reference performance demand and indicators. According to CNR-DT 210/2013, the interaction between a given glass structure and the whole building must always be considered, together with the local behaviour of the glass elements.

The defined performance levels can be reached using design choices and construction measures that involve 1) the use of suitable glass types and sizes; 2) the use of intrinsically ductile systems or connecting systems with a ductile behaviour; 3) the use of connecting systems which guarantee the glass elements a) rigid rotation/translation inside the load-bearing structural system, b) suitable limitation of the stress level, towards the reference material strength.

The SLV (Limit state for the safeguard of human life) must make sure that the system capacity is not lower than the demand. The performance demand is defined in terms of forces and displacements, therefore there are two types of verifications:

1) resistance calculations, where it must be verified that the glass can support accelerations induced by the seismic event, and
2) displacement compatibility assessment, where it must be ensured that the interaction between the glass element and the rest of the building is compatible with the presence of glass. In general, this interaction is considered to be satisfactory if, at the SLV, the construction vibration does not lead to contact with the glass element and, therefore, that there are no hammering phenomena. It must also be guaranteed that the glass and/or the connection can compensate the movements of the remaining part of the load-bearing structure during the pre- and/or post-breakage phases. Displacements of the building and in particular inter-storey drift caused by seismic actions are the essential parameters for the design of glass panes, under SLV conditions as well as for the Damage Limit State (SLD). In general, these derive from the structural analysis of the building for the various limit states and performance levels required. The glass structure designer must consult these data in order to size the joints and connection systems of the glass elements with respect to the characteristics of the rest of the structure.

Analysis of a case-study system. The structural system object of study consists of a steel-glass envelope built in 1961, as a composition of glass panes and a grid of steel mullions and arched transoms (Fig. 2(a)). The facade belongs to the so-called Information and Documentation Centre (CID) museum, which is located in Torviscosa (Udine), see Fig. 2(b) and (Santi et al. 2022). The particular aspect of this system is presented by its shape (circle facade concept) and by its size (approximately 7 m of diameter), compared to the thickness and load-bearing capacity of single components (Fig. 2(c)). Glass elements are in fact shaped to follow the overall arched path and are characterized by simple monolithic (and relatively small) total thickness, compared to the covered surface. Moreover, steel members are reduced to a minimum (Fig. 2(d)), to preserve the transparency of the facade.

The present study took a major advantage from in-field experimental investigations carried out in Spring 2022 to achieve some important geometrical and mechanical characteristics of the envelope (Fig. 2(e)). From a geometrical relief and OMA vibration investigation,

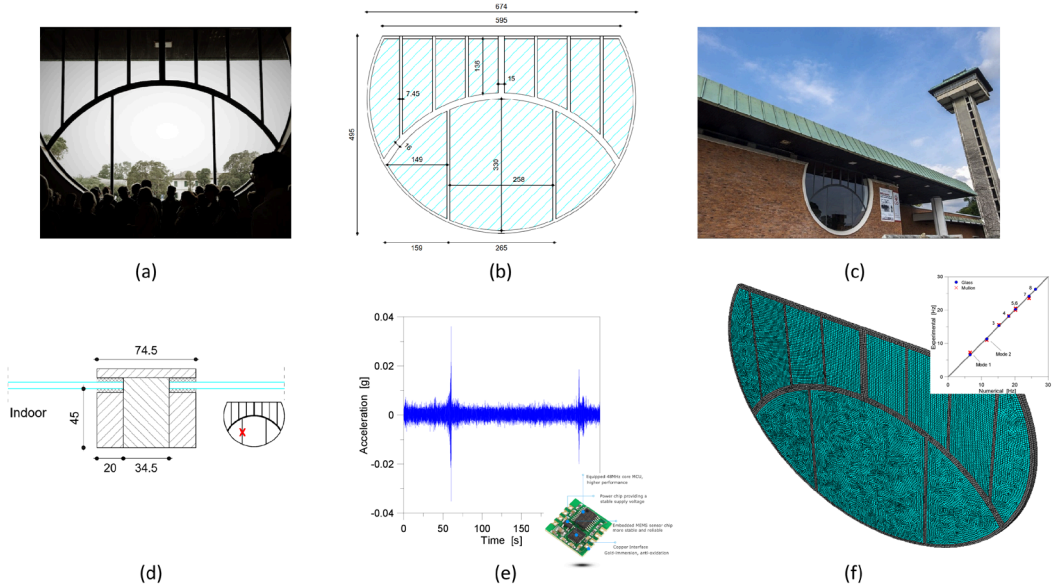


Fig. 2 - Examined glass envelope: (a)-(b) context view in the CID museum; (c) front view, with dimensions in cm; (d) detail of frame-to-glass connection (dimensions in mm); (e) in-field OMA investigation (Spring 2022); (f) Finite Element numerical model (ABAQUS).

in particular, the study resulted in up to 25 m^2 of covered surface and around 2350 kg for the facade components (of which around 310 kg of glass). The experimental analysis and interpretation of OMA results with the support of a validated structural FE numerical model (ABAQUS/Standard) also confirmed that monolithic glass panels have 5 mm of total thickness only (Fig. 2(f)), which is not in line with current requests as in CNR-DT 210/2013. This finding was confirmed by fundamental vibration frequencies of the system as in Fig. 2(f), with $f_1 \approx 6.5$ Hz for the envelope as a whole.

In terms of seismic analysis, according to CNR-DT 210/2013 recommendations, the primary construction falls in fact in a Class of use III (i.e., relevant buildings with possible overcrowding), with $V_N \geq 50$ years. Most importantly, the design tensile strength of glass under seismic action should be calculated as:

$$f_{g;d} = \frac{k_{mod} k_{ed} k_{sf} \lambda_{gA} \lambda_{gl} f_{g;k}}{R_M \gamma_M} \quad (1)$$

with $f_{g;k}$= 45 MPa; k_{mod} depending on the loading time (1 for instantaneous loads, 0.78 for transient seismic loads); R_M= 1 for second-class annealed glass; g_M= 2.5 for annealed glass. When the resistance check is carried out at a distance d from glass edges which is at least equal (or higher) than 5s = 25 mm (with s= 5 mm the thickness of glass), it is assumed that k_{ed}= 1 and l_{gl}= 1. Further, k_{sf}= 1 for float glass. Finally, l_{gA} is comprised between 0.75 and 1, to account for the area of glass under maximum stress and the statistically higher probability of the presence of defects in glass. Worth to note that for d < 5s, Eq. (1) suggests that $k_{ed} \rightarrow$ 0.7 (for annealed glass); $\lambda_{GA} \rightarrow$ 0.75; λ_{gl} < 1 (depending on size of glass and load pattern), thus reducing even down to ≈-50% the reference strength value for seismic verification.

Overall, the reference value for the resistance check to take into account for the present study should be assumed equal to ≈14 MPa (d > 5s) and ≈10 MPa (d < 5s). Further, the limit out-of-plane deflection for SLD (monolithic glass with linear supports at the edges) was derived equal to $u_{lim,out} = L/60 \approx$ 40 mm (with L= 2.58 m the minimum size of central glass panel).

Regarding the in-plane displacement capacity (inter-story drift accommodation), finally, this was set in $u_{lim,in}$ = 0.005*H*= 45 mm (with *H*= 9 m the total height of storey / building).

Results of local seismic analysis. The seismic performance of the glass envelope was numerically investigated by means of monotonic, linear application of an in-plane lateral force at the top of the envelope frame (*F*), as well as of an equivalent uniformly distributed pressure (Q). This is in line with CNR-DT 210/2013 provisions, where local verification is allowed for secondary glass elements belonging to primary buildings.

Overall, the attention was focused on the analysis of stress evolution and peaks in glass components, as well as on the deformation trends under seismic action. In Fig. 3, major trends of seismic response can be noticed. Figs. 3(a) and (b), in particular, represent the principal stress in glass and the out-of-plane glass deflection under the imposed in-plane seismic loads *F*. It can be seen, as also proposed in Figs. 3(d) and (e), the critical role of glass edges, which are subjected to major stress peaks. According to performance indicators as in Section 3, the present envelope would be able to accommodate a maximum in-plane displacement up to ≈0.0001*H*, thus rather small compared to current requirements. As far as the local seismic analysis is carried out in terms of out-of-plane equivalent pressure *Q*, see Fig. 3(c), maximum stress peaks are still achieved at the edges of central glass panel. The uniform pressure the system could resist is in this case in the order of ≈0.2 kN/m^2. The out-of-plane displacement for *Q*= 1kN/m^2 was measured in around a maximum of ≈20 mm, which is still far away from the reference limit value.

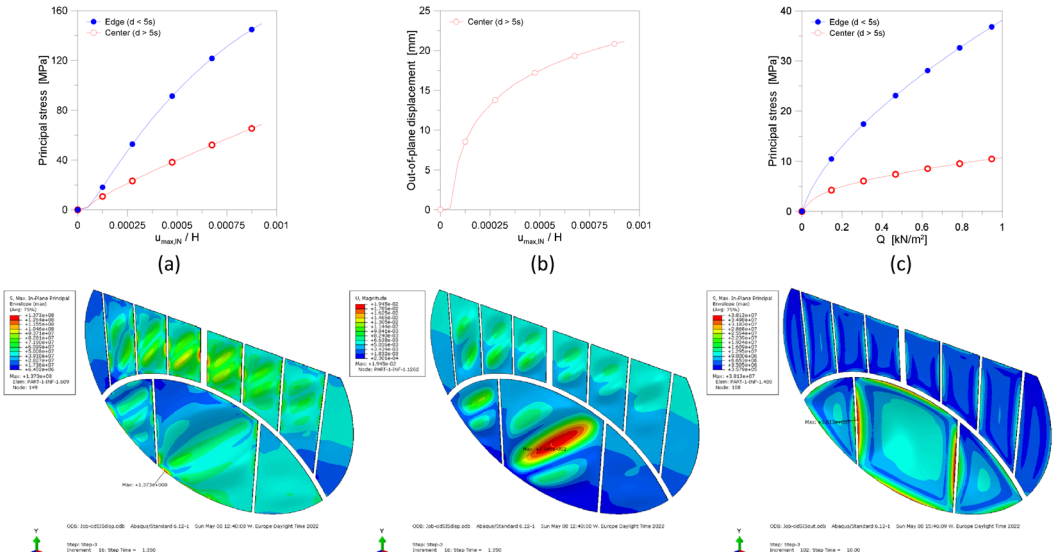


Fig. 3 - Seismic performance assessment based on local analysis (as from CNR-DT 210/2013): (a)-(b) maximum principal stress and out-of-plane deflection under in-plane seismic load, with (d)-(e) example of corresponding contour plot (legend values in Pa and m), and (c) principal stress under out-of-plane seismic load, with (f) corresponding distribution (ABAQUS).

Conclusions and future developments. The present results show that the region of edges is particularly critical for glass panels, both when exposed to in-plane or out-of-plane design actions. For the examined case-study system, a major issue was represented by the use of relatively thin glass components (monolithic elements with 5 mm in thickness) which were not specifically conceived to provide any kind of load-bearing capacity or seismic resistance and displacement accommodation. In this sense, a strong limitation affecting the possible

performance of glass components was represented by steel-to-glass connection detail as in Fig. 2(d), which resulted in a rather stiff connection not able to facilitate any kind of local displacement, or even to prevent localized stress peaks in glass components.

Overall, the study proved that existing / historic glass envelopes are highly vulnerable to seismic actions and – even in the form of secondary building components – should be somehow preserved against large displacement or stress demands from the primary buildings. In such a kind of consideration, the use of in-field OMA techniques to integrate the lack of technical specifications and drawings for the selected glass envelope (built up in 1961) provided great effort in the structural analysis of the state-of-art conditions and actual mechanical capacity of the façade. On one side, the investigation confirmed that existing glass envelopes and components are critical elements for safety of building customers, since not able to respond to actual design performance demands. At the same time, the investigation suggested that there is urgent need of harmonized methodological procedures and standardized evaluation framework that could be used for the vulnerability and risk analysis of historic heritage and for (when possible) retrofit proposals for existing glass components. As far as a general procedure inclusive of guideline rules and recommendations in support of the vulnerability analysis of existing / historic glass envelopes is currently missing (for in-field non-destructive assessment and numerical analysis), future studies will be spent for the proposition of damage indexes or methodologies in support of designers.

Acknowledgements. Dr. Maria Vittoria Santi (University of Udine) is gratefully acknowledged for technical support during the in-field experimental investigations. The Municipality of Torviscosa (UD) is also acknowledged for facilitating the experimental measurements.

References

Bedon C., Amadio C. and Noé S.; 2019: *Safety Issues in the Seismic Design of Secondary Frameless Glass Structures*. Safety, 5(4), 80.

CNR-DT 210/2013. *Istruzioni per la progettazione, l'esecuzione ed il controllo di costruzioni con elementi strutturali di vetro*. CNR, Roma, Italy.

Santi M.V., Lazzara M. and Frangipane A.; 2022: *Il Centro Informazione e Documentazione di Torviscosa, da architettura aziendale a spazio culturale, 1961 - 2021*. Proceedings of Colloqui.AT.e 2022 - Convegno Artec, 7-10 settembre, Genova, Italy.

MODELLO DI AMPLIFICAZIONE SISMICA PER LA SVIZZERA BASATO SU INDICATORI DI CONDIZIONE DI SITO E SULLA RISPOSTA SISMICA LOCALE MISURATA ALLE STAZIONI SISMICHE

P. Bergamo[1], F. Panzera[1], C. Cauzzi[1], F. Glüer[1], V. Perron[1,2], D. Fäh[1]

[1] Servizio Sismico Svizzero (SED) presso Politecnico federale di Zurigo (ETH), Zurigo, Svizzera
[2] Attualmente presso French Alternative Energies and Atomic Energy Commission (CEA), Cadarache, Francia

Mappare la risposta sismica locale è uno degli elementi fondamentali per gli studi di rischio sismico. Modelli accurati di amplificazione a scala locale sono generalmente redatti nell'ambito di studi di microzonazione (ad es. Lachet *et al.*, 1996, Michel *et al.,* 2017, Hailemikael *et al.*, 2020; Panzera *et al.*, 2022). D'altro canto, per i modelli di amplificazione ad ampia scala (ad es., scala nazionale) l'approccio seguito è generalmente piú approssimato, e può consistere nella mappatura di indicatori di risposta di sito (ad es. Vs30) usando parametri topografici e/o geologici quali basi per l'estrapolazione (Yong *et al.*, 2012, Vilanova *et al.,* 2018, Li *et al.*, 2022). Tuttavia, recentemente, lavori quali Weatherhill *et al.* (2020) e Falcone *et al.* (2021) hanno dimostrato la possibilità di rappresentare direttamente la risposta sismica locale su larga scala. Seguendo tali esempi, abbiamo preparato un insieme di mappe che predicono l'amplificazione di sito per l'intero territorio svizzero; queste carte sono parte integrante del progetto *"Earthquake Risk Model Switzerland"* (http://www.seismo.ethz.ch/en/research-and-teaching/ongoing-projects/#pr_00056.xml), volto a preparare un modello completo di rischio sismico per la Svizzera, comissionato dagli Uffici federali dell'ambiente e della protezione della popolazione e realizzato dal Servizio Sismologico Svizzero.

Il modello di risposta sismica locale si compone di carte che predicono l'amplificazione di sito per i seguenti parametri di scuotimento: *peak-ground velocity* (*PGV*), *pseudo-spectral acceleration* (*PSA*) ai periodi *T* = 1.0s, 0.6s e 0.3s. Per la loro realizzazione, abbiamo redatto un database di funzioni di amplificazione, ricavate mediante la tecnica *"empirical spectral modelling"* (Edwards *et al.*, 2013), per ~270 stazioni sismiche delle reti permanenti e

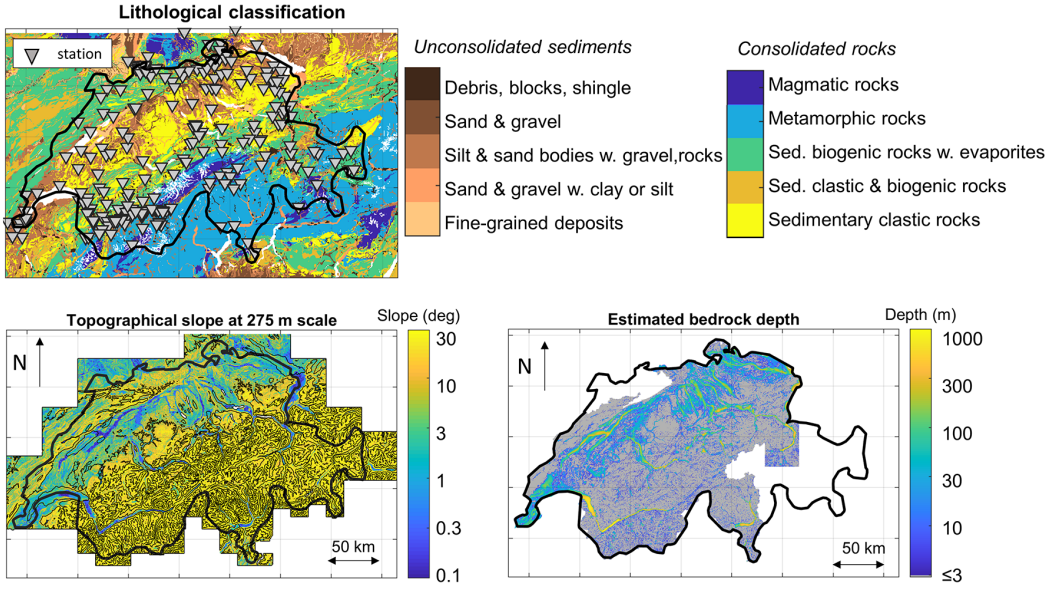


Fig. 1 – Indicatori di condizione di sito impiegati per il modello di amplificazione. In alto: mappa di classificazione litologica semplificata e posizione delle 270 stazioni sismiche per le quali viene calcolata la funzione di amplificazione locale. In basso a sinistra: pendenza topografica alla scala spaziale di 275 m. In basso a destra: mappa della profondità del bedrock secondo il modello geologico redatto da Swisstopo (2019).

temporanee svizzere (Fig., 1, riquadro superiore). Questi dati di amplificazione di sito sono stati poi incrociati con parametri geologici e topografici che possiedono un alto grado di correlazione con la risposta sismica locale (Bergamo et al., 2021; vedi esempi in Fig. 1, riquadri in basso). Infine, le mappe di amplificazione sono state ottenute implementando un metodo geostatistico di *"regression kriging"* (Hengl *et al.*, 2007), il quale permette di integrare direttamente i valori di amplificazione registrati ai siti instrumentati, cosi' da perfezionare localmente la predizione della risposta di sito. Le carte di amplificazione sono corredate da una stima dei relativi termini di incertezza (Edwards e Fäh, 2013), ovvero la *"site-to-site variability"* (φ_{S2S}) e la *"single-site, within-event variability"* (φ_{SS}; Fig. 2). Siccome il progetto *"Earthquake Risk Model Switzerland project"* prevede due moduli di stima del rischio, uno basato sull'accelerazione spettrale e uno sull'intensità macrosismica, le mappe di amplificazione per *PGV* e *PSA* ai periodi T = 1.0, 0.3s sono state anche convertite in carte di aggravamento dell'intensità macrosimsica (ΔI) ricorrendo alle relazioni di Faenza e Michelini (2010, 2011).

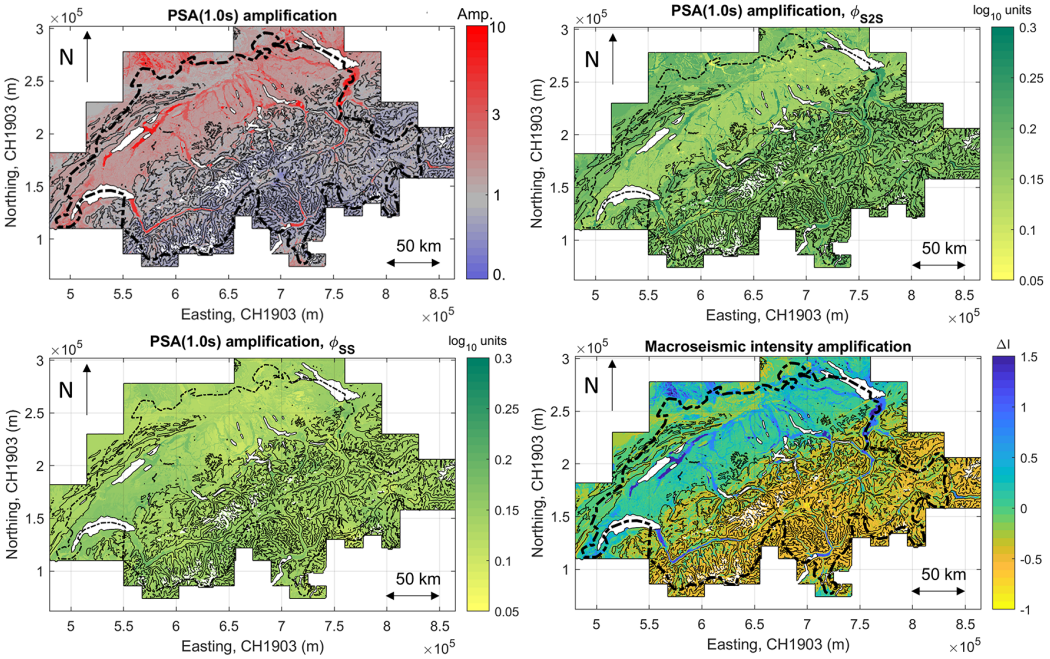


Fig. 2 – Esempio di mappe dal modello di amplificazione. In alto a sinistra: mappa di amplificazione per *PSA*(1.0s), relativa al profilo di velocità di riferimento svizzero (Vs30 = 1100 m/s, Poggi *et al.*, 2011). In alto a destra e in basso a sinistra: mappe della site-to-site variability (φ_{S2S}) e single-site, within-event variability (φ_{SS}) per l'amplificazione a *PSA*(1.0s). In basso a destra: mappa di amplificazione di intensità macrosismica, relativa al suolo di riferimento per il modello macrosismico di Fäh *et al.* (2011; Vs30 ≈ 450 – 700 m/s).

Le mappe di amplificazione sono in corso di validazione attraverso il confronto con osservazioni di intesità macrosismica da terremoti storici (Fäh *et al.*, 2011), con modelli di amplificazione locale che coprono specifiche aree urbane (Michel *et al.*, 2017, Panzera *et al.*, 2021, 2022, Janusz *et al.*, 2022, Perron *et al.*, 2022), e infine con misure di risposta di sito raccolte da stazioni non incluse nel dataset di calibrazione.

Riconoscimenti. Il presente lavoro é stato realizzato nell'ambito del progetto "ERM-CH Swiss Earthquake Risk Model" (finanziato dall' Ufficio federale dell'ambiente, dall'Ufficio federale della protezione della popolazione e da ETH Zurich).

Bibliografia

Bergamo P., Hammer C. and Fäh. D.; 2021: *Correspondence between site amplification and topographical, geological parameters: collation of data from Swiss and Japanese stations and neural networks-based prediction of local response*. BSSA, 112(2): 1008-1030, DOI 10.1785/0120210225.

Edwards B., Michel C., Poggi V. and Fäh D.; 2013: *Determination of site amplification from regional seismicity: Application to the Swiss National Seismic Networks*. Seismol. Res. Lett. 84(4) 611–621.

Edwards B. and Fäh, D.; 2013: *A stochastic ground-motion model for Switzerland*. BSSA, 103(1), 78–98.

Fäh D., Giardini D., Kästli P, et al.; 2011: *ECOS-09 earthquake catalogue of Switzerland release 2011*. Report and database. Sed/Ecos/R/001/20110417.

Faenza L., and Michelini A.; 2010: *Regression analysis of MCS intensity and ground motion parameters in Italy and its application in ShakeMap*. Geophys. J. Int. 180(3), 1138–1152.

Faenza L., and Michelini A.; 2010: *Regression analysis of MCS intensity and ground motion spectral accelerations (SAs) in Italy*. Geophys. J. Int. 186(3), 1415-1430.

Falcone G., Acunzo G., Mendicelli A., Mori F., Naso G., Peronace E., Porchia A., Romagnoli G., Tarquini E. and Moscatelli M.; 2021: *Seismic amplification maps of Italy based on site-specific microzonation dataset and one-dimensional numerical approach*. Engineering Geology, 289 (2021), 106170.

Hailemikael S., Amoroso S. and Gaudiosi, I.; 2020: *Guest editorial: seismic microzonation of Central Italy following the 2016–2017 seismic sequence*. Bull Earthquake Eng 18, 5415–5422 (2020).

Hengl T., Heuvelink G., and Rossiter D. G.; 2007: *About regression-kriging: From equations to case studies*. Computers & Geosciences, 33(10), 1301-1315.

Janusz P., Perron V., Knellwolf C., Imperatori W., Bonilla L. F., and Fäh D; 2021: *Combining recordings of earthquake ground-motion and ambient vibration analysis to estimate site response variability in the city of Lucerne, Switzerland*. EGU General Assembly 2021, online, 19–30 Apr 2021, EGU21-4380, https://doi.org/10.5194/egusphere-egu21-4380, 2021.

Michel C., Fäh D., Edwards B., and Cauzzi C.; 2017: *Site amplification at the city scale in Basel (Switzerland) from geophysical site characterization and spectral modelling of recorded earthquakes*. Physics and Chemistry of the Earth Parts A/B/C 98:27-40.

Lachet C., Hatzfeld D., Bard P.-Y., Thoodulidis N., Papaioannou C., and Savvaidis A. ;2016*: Site effects and microzonation in the city of Thessaloniki (Greece) comparison of different approaches*. BSSA 86 (6): 1692–1703.

Li M., Rathje E M., Cox B. R., and Yust M.; 2022: *Texas-specific VS30 map incorporating geology and VS30 observations*. Earthquake Spectra, 38(1):521-542.

Panzera F., Bergamo P., and Fäh D.; 2021*: Canonical Correlation Analysis Based on Site-Response Proxies to Predict Site-Specific Amplification Functions in Switzerland*. BSSA, 111 (4): 1905–1920.

Panzera F., Alber J., Imperatori W., Bergamo P. and Fäh, D; 2022: *Reconstructing a 3D model from geophysical data for local amplification modeling: The study case of the upper Rhone valley, Switzerland.* Soil Dynamics and Earthquake Engineering, 155, 107163.

Perron V., Bergamo P., and Fäh D.; 2022: *Site amplification at high spatial resolution from combined ambient noise and earthquake recordings in Sion, Switzerland*. Seismological Research Letters, accepted for publication.

Poggi V., Edwards B. and Fäh D.; 2011: *Derivation of a reference shear-wave velocity model from empirical site amplification*. Bull. Seismol. Soc. Am. 101(1) 258–274.

Swisstopo, Ufficio federale di Topografia; 2019: Modello di spessore dei sediment sciolti, https://www.swisstopo.admin.ch/it/geodata/geology/models/unconsolidated-deposits.html.

Vilanova S. P., Narciso J., Carvalho J. P., Quinta-Ferreira M., Pinto C. C., Moura R., Borges J. and Nemser E. S.; 2018: *Developing a Geologically Based Vs30 Site-Condition Model for Portugal: Methodology and Assessment of the Performance of Proxies*. Bull. Seismol. Soc. Am., 108(1) 322-337.

Weatherill G., Kotha S. R. and Cotton F.; 2020: *Re-thinking site amplification in regional seismic risk assessment*. Earthquake Spectra 36(S1) 274-297.

ASSESSMENT OF THE EFFECT OF SEISMIC SEQUENCES ON STEEL X-CBF FOR INDUSTRIAL BUILDINGS

L. Bomben, M. Fasan, C. Amadio

University of Trieste, Department of Engineering and Architecture, Trieste, Italy

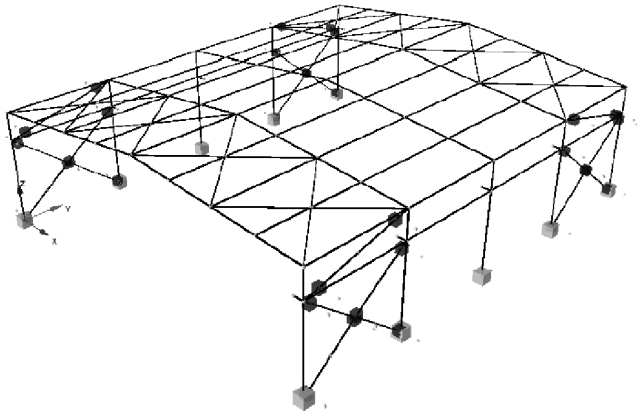
Background. It is known that earthquakes are not in general isolated events, but they can be followed by several after-shocks, that can have a comparable intensity to the main-shock. In fact, Ruiz Garcia in (Ruiz Garcia, 2014) underlined that, although the main-shock is always the event with the maximum magnitude, in a specific site an after-shock can have a higher PGA. This fact can lead to a progressive accumulation of damage, if the time span between the events is not enough to repair the structure. Current technical codes (British Standards Institution *et al.*, 2005; Ministero delle infrastrutture e dei trasporti, 2018) do not take into account the effect of the seismic sequences, thus the structures are designed only to withstand a single event.

Several past studies have already investigated on the effect of the seismic sequences on steel structures (Amadio *et al.*, 2003; Fragiacomo *et al.*, 2004; Hatzigeorgiou, 2010; Rinaldin *et al.*, 2020, 2017; Ruiz Garcia and Negrete-Manriquez, 2011), by evaluating both single-degree-of-freedom (SDOF) and multi-degree-of-freedom (MDOF) systems. Both moment resisting frames (MRF) and concentrically braced frames (CBF) have been analyzed, proving the great influence of the sequences to these structural types. Other studies, like in (Iervolino *et al.*, 2014; Lolli and Gasperini, 2003), are focused on the influence of the seismic sequences on the seismic hazard evaluation.

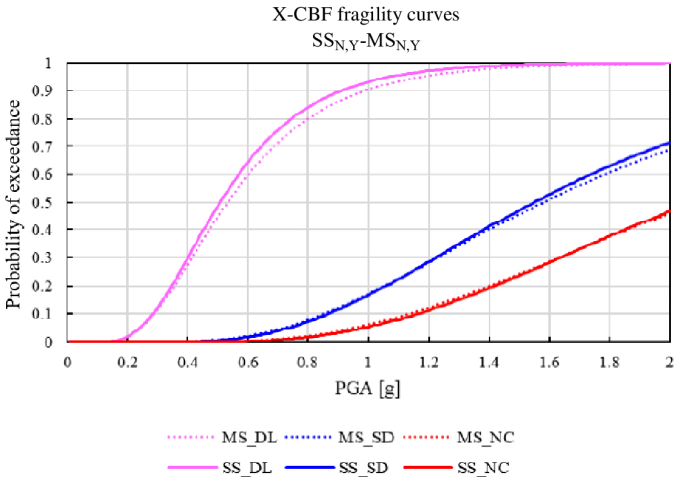
The present work concerns about the study of the effects of the seismic sequences on the design of mono-storey industrial buildings with X–concentrically braced frames (X-CBFs). First, a typical mono-story industrial building is analyzed (Section 2), subjected to natural seismic sequences. Then, the study focuses on the behavior of X – concentrically braced frames (Section 3), by considering both natural and artificial repeated ground shakings. A proper enlargement of the elastic response spectra is finally proposed, representative of the sequences effects and applicable on medium-high seismicity areas. This operation wants to give a first preliminary estimate of the increase of the seismic risk only on the seismic vulnerability side of this kind of structures.

Preliminary case study. The industrial steel building with X-CBFs designed by Scozzese *et al.* (ReLUIS *et al.*, 2018; Scozzese *et al.*, 2017), according to (Ministero delle infrastrutture e dei trasporti, 2008) and located in L'Aquila (Italy), has been analyzed as preliminary case study (Figure 1.a). The structure has been modeled with Seismostruct (Seismosoft, 2020), that considers a fiber approach to model the inelastic behavior of the elements, according to a force-based finite element formulation. The Menegotto-Pinto model (Menegotto and Pinto, 1973) has been chosen to represent the uniaxial stress-strain relationship of steel. With the aim to validate the model, a series of pushover analysis on the whole structure have been carried out and calculation of the braces buckling strength has been done (according to the relationships given in (British Standards Institution *et al.*, 2005)). The results have shown a great correspondence with the ones given in (ReLUIS *et al.*, 2018).

The system has been subjected to nonlinear dynamic analysis, through the application of both seismic sequences and the main shock (single events with maximum PGA). A series of relevant sequences of Italy and Japan has been selected. The events constituting the sequences have been obtained through the Engineering Strong Motion Database (INGV), for the Italian events, and Strong-motion seismograph networks (K-NET, KiK-net) for the Japanese ones. The sequences have been composed with MATLAB letting 30 seconds of rest between subsequent events, in order to completely stop the structure. In total, 40 seismic sequences have been



a)



b)

Fig. 1 - a) Structural scheme of the industrial building casa study; b) Fragility curve for X-CBF of the industrial building with PGA as IM: case with North-South seismic component (N) applied in longitudinal direction (Y), for both main-shocks (MS) and seismic sequences (SS) and for the three limit states (DL: limitate damage; SD: severe damage; NC: near collapse).

considered and compared with the 40 main events.

Then, fragility curves have been built, with the aim to evaluate the seismic vulnerability. As known, a fragility curve defines the probability of exceeding a certain level of damage (a limit state) with a parameter that indicates the seismic intensity (IM-Intensity Measure). In this work the "Cloud Analysis" method (Han *et al.*, 2015; Hosseinpour and Abdelnaby, 2017; Jalayer *et al.*, 2015; Porter, 2021) has been used, by considering PGA or Sa as IM, and the drift as "Engineering Demand Parameter" (EDP). Drift limit values given in (Applied Technology Council *et al.*, 1997) are considered, according to damage (DL), severe damage (SD) and near collapse (NC) limit states.

Globally, 160 nonlinear dynamic analyses have been performed, considering the two different combinations of seismic action directions. Fragility curves have been built by distinguishing the response of the moment resisting portal frames from the X-CBFs one.

The final results have shown that fragility curves due to seismic sequences are generally on the left compared to those of the single main events, therefore indicating a damage accumulation due to the succession of events. However, the increase of the probability of exceedance is quite limited and around a maximum value of 6% for the near-collapse limit

state, and lower for the other limit states. In particular, it is observed how the effect of the sequences is more relevant for the X-CBFs than the portal frames, for whom the effects are even lower. For example, a comparison between sequences and single events is given in Figure 1.b.

Finally, in order to have a more indicative estimate on the behaviour of X-CBF, it has been concluded that the following aspects are important:

- The relevant influence of the seismic weight, considering a larger number of portal frames stabilized by the X-CBF;
- The importance of the number of seismic events characterized by after-shocks with comparable intensity of the main-shock.

Analysis on the X-CBF. The study has then be focused on the evaluation of the single X-CBF. In particular, the "BC0" model experimentally tested by Wakabayashi in (Wakabayashi *et al.*, 2010) has been considered (the geometrical characteristics of the connecting plates have been taken from (Faggiano *et al.*, 2018)). The numerical model has been implemented with the Seismostruct code (Seismosoft, 2020).

First, the model has been properly calibrated on the basis of the experimental results. Then, two masses of 70 tons have been applied on the top of the columns. These masses correspond to the ones applied to an X-CBFs belonging to the same structure assessed in Section 2, but with 13 moment resisting portal frames instead of 5.

In addition to the calibrated model (with H100x50x4x6 brace), two more solutions have been investigated by varying the brace profile. In total, the three following profiles have been considered:

- RHS 120x40x4 ($\overline{\lambda}$ = 1,47)
- H100x50x4x6 ($\overline{\lambda}$ = 2,12)
- R50x20 ($\overline{\lambda}$ = 4.21)

Initially, 30 natural seismic sequences have been considered. The results of the analysis show a high increase of the ductility demand for those natural sequences which have after-shocks with a comparable intensity to the main-shock ones. For this reason, artificial sequences have also be taken into account, in addition to the natural ones, with the aim to estimate the maximum possible effects of seismic sequences and to be on the safety side. For artificial sequences, two different linear combinations have been formulated, by repeating three times a single scaled event:

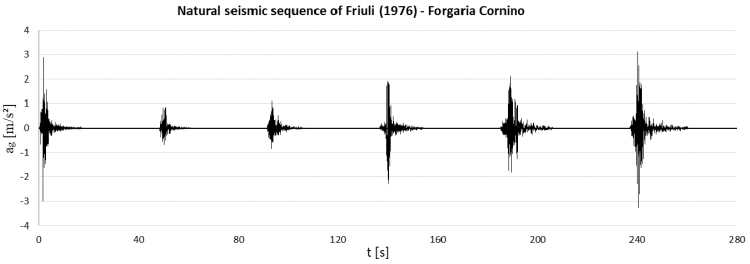
- combination 1 (30 sequences): single event x1 – x0.9 – x0.9
- combination 2 (30 sequences): single event x1 – x0.9 – x1

The effects of natural and artificial sequences have been evaluated, by comparing the displacement requests, obtainable with the main-shock and with the entire seismic sequences. For example, shear-displacement cycles for the natural sequence of Friuli – Forgaria Cornino and his main shock are given in Figure 2, where it is clearly observable the increment of the maximum displacement demand.

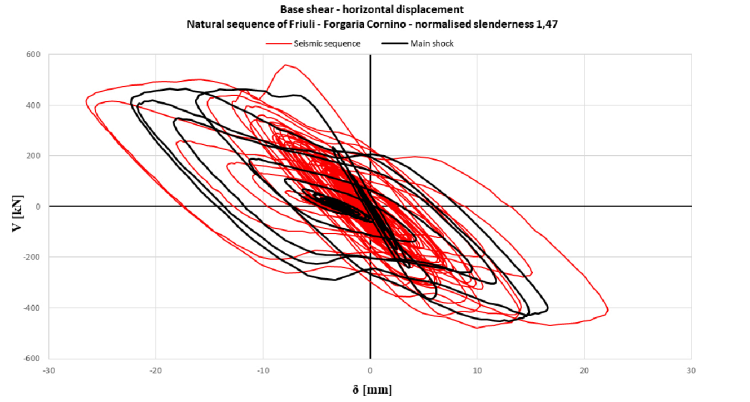
In order to give an overall mean assessment of the phenomenon, three different average indicators are evaluated. Different analysis group have been distinguished according to the sequence typology (natural or artificial) and the normalized slenderness (1.47, 2.12 or 4.21). The indicators are the following:

- $M1_{\delta} = \dfrac{\sum_{i}^{n°seq_j} \delta_{seq,max,i} / \delta_{main,max,i}}{n°seq_j}$ (1)

in which:



a)



b)

Fig. 2 - a) Natural sequence of Friuli-Forgaria Cornino; the 6th signal is considered as the main shock; b) Comparison between dynamic cycles from seismic sequence and main shock for the case of Friuli-Forgaria Cornino.

$\delta_{max,i}$: absolute value of the maximum displacement for a seismic sequence (seq) or the corresponding main shock (main);
n°seq$_j$: total number of sequences in a certain j-th group.

- $$M2_{\delta} = \frac{\sum_{i}^{n°seq_j} \max\left(\frac{\delta_{seq,max,+,i}}{\delta_{main,max,+,i}}; \frac{\delta_{seq,min,-,i}}{\delta_{main,min,-,i}}\right)}{n°seq_j} \quad (2)$$

in which:
$\delta_{max,+,i}$: maximum positive displacement for a seismic sequence (seq) or the corresponding main shock (main);
$\delta_{min,-,i}$: minimum negative displacement for a seismic sequence (seq) or the corresponding main shock (main).

- $$M3_{\delta} = \frac{\sum_{i}^{n°seq_j} \Delta_{\delta,seq,i} / \Delta_{\delta,main,i}}{n°seq_j} \quad (3)$$

in which: Δ_{δ}: = $\delta_{max,+} - \delta_{min,-}$ (4)

$M1_{\delta}$, by considering the maximum absolute value of displacements, leads to the lower indicator. It is higher than 1 only on the inelastic phase, so providing an indication on the increase of ductility demand due to the seismic sequences. On the contrary $M2_{\delta}$, by considering the maximum ratio between maximum positive and minimum negative displacements, leads to the higher indicator. $M3_{\delta}$, by estimating the maximum displacements excursion, leads to a medium value.

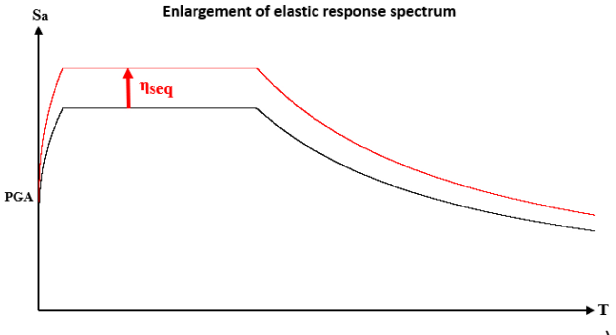
In general, the indicators increase as the normalized slenderness increase for the artificial sequences, however the trend is less clear for the natural sequences. With the aim to give an overall mean value, average values are calculated by mediating the values obtained for each different normalized slenderness (Table 1). In the Table 1, in order to underline what has been previously asserted, the indicators for a selection of 10 natural sequences, with after-shocks with comparable intensity to the main-shock ones, have also been reported.

Tab. 1 - Values of ductility indicators averaged on the different normalized slenderness.

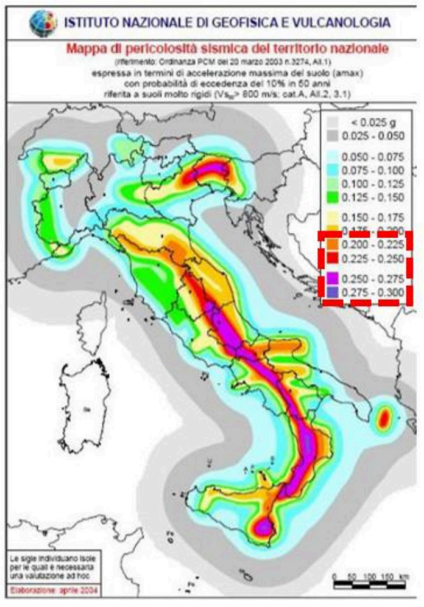
Increase ductility demand			
Seismic Sequences typology	**$M1_\delta$**	**$M2_\delta$**	**$M3_\delta$**
Natural – Totality (1)	2.44%	10.52%	4.44%
Natural – Selection (2)	6.16%	23.23%	10.57%
Artificial (3)	23.26%	41.73%	23.99%
Overall weighted averages (1,3)	16.32%	31.33%	17.47%

Generally, the effect of the seismic sequences can be significantly variable on the basis of the sequences and the indicators considered. It has to be underlined that with this approach the seismic hazard is considered the same as the one of the single main-event; only the seismic vulnerability has considered to be increased.

Conclusions. In this work the effect of the seismic sequences has been studied on steel X-CBFs for one floor industrial buildings. First, a whole industrial building has been evaluated. Then, the study has been focused on a single XCBFs, calibrated on experimental cyclical test. Three different average indicators have been formulated. The final average values give an estimate of the increase of ductility demand, by passing from single main events to repeated ground shakings. It shows a great variability depending on the sequence typology and the indicator considered. By assuming $M1_\delta$ and $M3_\delta$ as the most significative parameters, increments of 16.3% and 17.5% respectively have been calculated.



a)



b)

Fig. 3 - a) Enlargement of elastic response spectrum through the scale factor η_{seq} = 1.2; b) Seismic hazard map of the italian national territory; areas subjected to the enlargement of the elastic response spectrum are those characterized by PGA ≥ 0.2 g.

Since a major ductility request corresponds to an equivalent lower availability in terms of behaviour factor, an appropriate enlargement of the elastic response spectrum is proposed according to a conservative preliminary estimate of the scale factor η_{seq} = 1.2 (Figure 3.a). This coefficient can be then applied in medium-high seismic zone (PGA≥0.2 g - Figure 3b), where these events are more frequent. The proposed value can be applied only for dissipative or not dissipative X-CBF one floor industrial systems.

Funding. The research was financed by DPC-ReLUIS project 2019-2021 (WP12), Italy.

References

Amadio, C., Fragiacomo, M., Rajgelj, S., 2003. T*he effects of repeated earthquake ground motions on the non-linear response of SDOF systems.* Earthquake engineering & structural dynamics. 32, 291–308.

Applied Technology Council, United States, Federal Emergency Management Agency, Building Seismic Safety Council (U.S.), 1997. NEHRP guidelines for the seismic rehabilitation of buildings. Federal Emergency Management Agency, Washington, D.C.

British Standards Institution, European Committee for Standardization, British Standards Institution, Standards Policy and Strategy Committee, 2005. Eurocode 8, design of structures for earthquake resistance. British Standards Institution, London.

Engineering Strong Motion Database (INGV) [WWW Document], n.d.

Faggiano, B., Formisano, A., Vaiano, G., Mazzolani, F.M., 2018. *Numerical Study on Concentric Braced X Frames under Monotonic and Cyclic Loads*. KEM 763, 633–641.

Fragiacomo, M., Amadio, C., Macorini, L., 2004. *Seismic response of steel frames under repeated earthquake ground motions.* Engineering Structures Engineering Structures 26, 2021–2035.

Han, R., Li, Y., van de Lindt, J., 2015. *Impact of aftershocks and uncertainties on the seismic evaluation of non-ductile reinforced concrete frame buildings*. Engineering structures. 100, 149–163.

Hatzigeorgiou, G.D., 2010. *Ductility demand spectra for multiple near- and far-fault earthquakes.* SDEE Soil Dynamics and Earthquake Engineering 30, 170–183.

Hosseinpour, F., Abdelnaby, A.E., 2017. *Fragility curves for RC frames under multiple earthquakes.* SDEE Soil Dynamics and Earthquake Engineering 98, 222–234.

Iervolino, I., Giorgio, M., Polidoro, B., 2014. *Sequence-based probabilistic seismic hazard analysis*. Bulletin of the Seismological Society of America 104, 1006–1012.

Jalayer, F., Risi, R., Manfredi, G., 2015. *Bayesian Cloud Analysis: efficient structural fragility assessment using linear regression*. BULLETIN OF EARTHQUAKE ENGINEERING 13, 1183–1203.

Lolli, B., Gasperini, P., 2003. *Aftershocks hazard in Italy Part I: Estimation of time-magnitude distribution model parameters and computation of probabilities of occurrence.* Kluwer Academic Publishers.

Menegotto, M., Pinto, P.E., 1973. *Method of analysis for cyclically loaded R.C. plane frames including changes in geometry and non-elastic behaviour of elements under combined normal force and bending*. IABSE.

Ministero delle infrastrutture e dei trasporti, 2018. *Norme tecniche per le costruzioni 2018: Decreto 17 gennaio 2018 "Aggiornamento delle Norme tecniche per le costruzioni"* (G.U. 20 febbraio 2018, n. 42. s.o.).

Ministero delle infrastrutture e dei trasporti, 2008. *Nuove norme tecniche per le costruzioni: D.M. infrastrutture 14 gennaio 2008* pubblicato su S.O. n. 30 alla G.U. 4 febbraio 2008, n. 29 : circolare 02 febbraio 2009 n617/C.S.LL. PP. pubblicata su S.O. n. 27 alla G.U. 26 gebbraio 2009, n. 47. Dei, Roma.

Porter, K., 2021. *A Beginners Guide to Fragility, Vulnerability, and Risk* 1–29.

ReLUIS, Iervolino, I., Eucentre, 2018. *The implicit risk of code-conforming structures in italy: a joint Reluis-Eucentre project.* Doppiavoce, Napoli.

Rinaldin, G., Amadio, C., Fragiacomo, M., 2017. *Effects of seismic sequences on structures with hysteretic or damped dissipative behaviour.* Soil dynamics and earthquake engineering. 97, 205–215.

Rinaldin, G., Fasan, M., Sancin, L., Amadio, C., 2020. *On the behaviour of steel CBF for industrial buildings subjected to seismic sequences.* ISTRUC Structures 28, 2175–2187.

Ruiz Garcia, J., 2014. *Discussion on "Effects of multiple earthquakes on inelastic structural response."* Eng. Struct. Engineering Structures 58, 110–111.

Ruiz Garcia, J., Negrete-Manriquez, J.C., 2011. *Evaluation of drift demands in existing steel frames under as-recorded far-field and near-fault mainshockaftershock seismic sequences*. Engineering structures. 33, 621–634.

Scozzese, F., Terracciano, G., Zona, A., Della Corte, G., Dall'Asta, A., Landolfo, R., 2017. *Rintc Project: Nonlinear dynamic analyses of italian code-conforming steel single-storey buildings for collapse risk assessment.* https://doi.org/10.7712/120117.5513.17301

Seismosoft, 2020. SeismoStruct.

Strong-motion seismograph networks (K-NET, KiK-net) [WWW Document], n.d.

Wakabayashi, M., Matsui, C., Minami, K., Mitani, I., 2010. *Inelastic Behavior of Full-Scale Steel Frames with and without Bracings.* Disaster Prevention Research Institute, Kyoto University.

INVESTIGATION OF THE ROCK AVALANCHE DEPOSIT OF YANG JIA GOU (SICHUAN-CHINA) THROUGH THE INTEGRATION OF PASSIVE SEISMIC TECHNIQUES

P. Capone[1], V. Del Gaudio[1], J. Wasowski[2], N. Venisti[1], H. Wei[3]

[1] Dipartimento di Scienze della Terra e Geoambientali, Università degli Studi di Bari "Aldo Moro"- Bari, Italy
[2] Consiglio Nazionale delle Ricerche - Istituto di Ricerca per la Protezione Idrogeologica - Bari, Italy
[3] State Key Laboratory of Geo-Hazard Prevention and Geo-Environment Protection, Chengdu University of Technology, P.R. China

Introduction. One of the over 200,000 landslides triggered in the mountainous region of Longmen Shan (Sichuan – China) by the Mw 7.9 Wenchuan earthquake of May 12 2008 (cf. Xu *et al.,* 2014) was a large rock avalanche that dammed a stream in a gully named Yang Jia Gou. We investigated structure and physical properties of the rock avalanche deposit as a contribution to define the stability conditions of the landslide dam (e.g., Li *et al.*, 2021), whose partial failures have already caused dangerous downstream flooding. For this purpose, we used single-station recordings of ambient noise, acquired along two profiles passing across the rock avalanche deposit (Fig. 1), analyzed using the traditional HVNR method (Nakamura 1989) and a recently proposed technique, named HVIP (Del Gaudio, 2017).

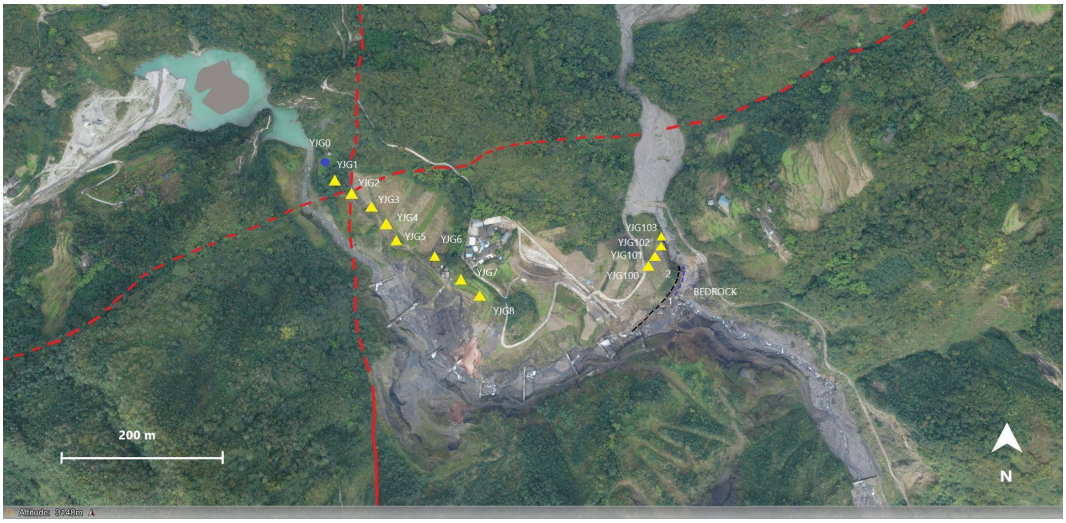


Fig. 1 - Google Earth image of the breached landslide dam in the gully named Yang Jia Gou with the positions of the ambient noise measurement stations. The blue point represents the reference station (YJG0) and the yellow triangles are measurement stations (YJG1-YJG8; YJG100-YJG103). Red lines are two faults reported from Wasowski *et al.* (2021): the continuous and dashed lines represent, respectively, the observed and inferred faults. The black dashed line, in the eastern part of the dam, represents the contact between the 2008 co-seismic rock avalanche deposit and the older (pre-historic) rock avalanche; the blue line indicates the contact between the base of the prehistoric rock avalanche and the slate bedrock (the continuous line is observed, the dashed line is presumed). Bedrock dips to the west at an angle of about 20°.

Both techniques are based on the calculation of curves of the H/V ratios between horizontal and vertical components of the ground motion as function of frequency. In presence of strong velocity contrast between a surface soft deposit and a stiffer substratum, these curves can present one or more peaks at site resonance frequencies which are related to peaks of Rayleigh wave ellipticity depending on the vertical layering of seismic wave velocity under the measurement station. These passive seismic techniques are cheaper and quicker than other seismic techniques and are particularly suitable for data acquisition on topographically complex sites. A limitation is the interpretative ambiguity because of the large number of unknowns to consider which requires the introduction of additional constraints in the parameterization to

reduce the variability of the fitting models. In the work of Del Gaudio *et al.* (2021), we used in combination electrical resistivity tomography (ERT), to extract from resistivity profiles, the thickness of the most superficial layer. The velocity vertical profiles resulted from the inversion of ellipticity curves at each ambient noise measurement station of a profile are synthesized in a Vs cross section (Fig. 2a).

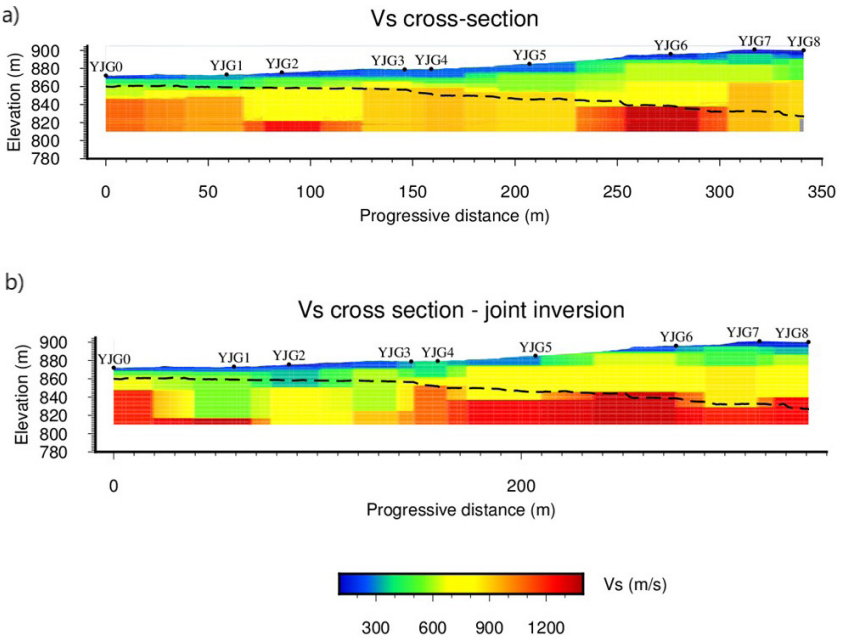


Fig. 2 - a) Cross section which synthesizes velocity ground profiles resulted from the inversion of the ellipticity curves. The dashed line represents the streambed profile (from Del Gaudio *et al.*, 2021); b) New cross section obtained from the joint inversion of the Rayleigh wave ellipticity curves and localized group velocity dispersion curves.

During the noise data acquisition, following the recommendations proposed for the HVIP technique (Del Gaudio, 2017), a fix "reference station" was kept in continuous recording. Thus, in this work, we exploit the availability of simultaneous and synchronized noise recordings to test the possibility of reducing the ambiguity of data interpretation by integrating the modelling procedure with the outcome of another passive seismic technique based on the cross-correlation analysis of noise recordings (Bensen *et al.,* 2007). This method can provide additional constraints for the subsoil velocity modelling from the calculation of dispersion curves of Rayleigh wave group velocities along the path between different couples of stations.

Method. The method HVIP (Del Gaudio 2017), introduced to obtain more stable amplitude values of H/V than HVNR, consists of an instantaneous polarization analysis of ambient noise recording. The innovation of the method consists in calculating the mean H/V values only on the samples with Rayleigh wave polarization. The H/V ratio is calculated instant by instant, in the time domain, on temporal series filtered on narrow frequency bands, by means of an analytic transform. Extracting only wave packets with a clear Rayleigh wave polarization reduces the H/V variability deriving from changes of composition of the wavefield, whose components (P, S, Rayleigh and Love waves) differently contributes to the horizontal and vertical amplitude of ground motion.

The cross-correlation method, applied to two simultaneous noise recording, in the hypothesis of a diffuse wave field, provides information about properties of the medium

between the two stations, exploiting the surface waves dispersive property. In practice, this method highlights the coherent portion of the signal acquired in the stations by multiplying the two temporal series shifted by different time intervals. The resulted function shows a maximum at the time shift corresponding to travel time of a wave group from one station to the other and provide an estimate of the Green function between the couple of stations (e.g., Derode *et al.,* 2003; Snieder 2004; Wapenaar 2004). In order to extract information on Rayleigh waves, the method is applied to the vertical component. The dispersion curves of group velocity are obtained from a FTAN analysis (Frequency-Time Analysis: Levshin et al. 1972), by picking points corresponding to the arrival time of wave energy maxima at different frequencies; this allows the determination of the velocity with which the energy of different frequency wavetrains propagates from one station to the other.

One problem of the cross-correlation method is the possible presence of a dominant noise source misaligned with respect to the station couple, which can cause the calculation of an overestimated apparent velocity. For this reason, in the implementation of this technique, we tested the application of a direction correction based on the results of the HVIP analysis. Indeed, this technique identifies all the time windows in which Rayleigh waves are dominant in the noise wavefield and provides the azimuth of their propagation direction. Thus, for the calculation of cross correlation, only these time intervals were considered and the times ΔT_g of the samples of the cross-correlation function were modified to take into account the effect of difference between the direction of wave propagation and that of the alignment of the couple of stations, according to the equation

$$\Delta T_g^* = \frac{\Delta T_g}{\cos\left(\alpha_L - \alpha_R\right)}\ , \tag{1}$$

where α_L is the azimuth of the line joining the two stations and α_R is the azimuth of the Rayleigh wave propagation direction.

The Rayleigh wave dispersion curves, obtained by cross-correlating the recording of the two station are a mean representation of the medium velocity between the two stations. To obtain more precise information about the medium around each station, we reconstructed more localized dispersion curves by subtracting, for each frequency, the arrival times at the two stations located before and after that of interest and dividing by their distance to calculate the localized group velocities. Rayleigh wave ellipticity curves, obtained by the HVIP method, and Rayleigh wave dispersion curves, obtained by the cross-correlation method, were then assumed as combined targets for a joint inversion. We use DINVER (Wathelet 2005), to search, for each station, 1D subsoil models consistent with both types of experimental data relative to the area around that station.

Results and discussion. Figure 2b shows a cross section derived synthetizing the 1D subsoil models, calculated for all the stations, so to construct a 2D velocity model. The introduction of other constraints resulted in a better resolution in depth with respect to the previous cross section (Fig. 2a). It is possible to distinguish the presence of a surface layer with Vs velocities lower than 800 m/s and a higher velocity material (Vs > 1000 m/s), which likely corresponds to the local slaty bedrock (Wasowski *et al.,* 2021). The depth of the bedrock between stations YJG4 and YJG8 coincides with the present level of the Yangjia gully streambed. This is probably related to the stiffness of the substratum, which is harder to erode by the stream respect to the landslide dam material. However, in the upstream part of the profile, in particular between stations YJG1 and YJG3, the higher velocity layer is located below the streambed. According to the analysis of remotely sensed data and field observations (Wasowski *et al.,* 2021), this

part of the section is crossed by two faults (Fig. 1). The deepening of the higher velocity layer, in the upstream part of the profile, can have two possible explanations. It can represent the downward displacement of the bedrock because of the faulting or it can reflect the lowering of velocity, in the section traversed by faults, due to the fracturing.

Further downstream the gully, the layer with velocity < 800 m/s corresponds to the deposit of the rock avalanche triggered in 2008. This is supported by the direct field evidence (Fig. 1) and the ground profile resulted from the inversion of other ambient noise data acquired in the south-eastern part of the study area (Fig. 3). In the ground profile, we observe the material with velocity < 800 m/s until the depth of 30 m; significantly, in that area the elevation difference between the top surface of the 2008 rock avalanche deposit and the streambed amounts to 30 m. The materials with velocities around 800 m/s are compatible with the older rock avalanche deposit, whose outcrops were locally recognized in the field (Fig. 1). At greater depths, we observe velocities higher than 1000 m/s, which can be associated to the slaty bedrock (Fig. 3). The reliability of the ground profiles decreases with depth, as the constraints provided by data for the model parameterization weaken, nevertheless, the modelling results provide a rough indication of the depth to bedrock under the gully streambed.

Conclusions. The integration of two passive seismic techniques proved useful in reducing interpretative uncertainties of subsoil velocity modelling of the Yang Jia Gou landslide dam

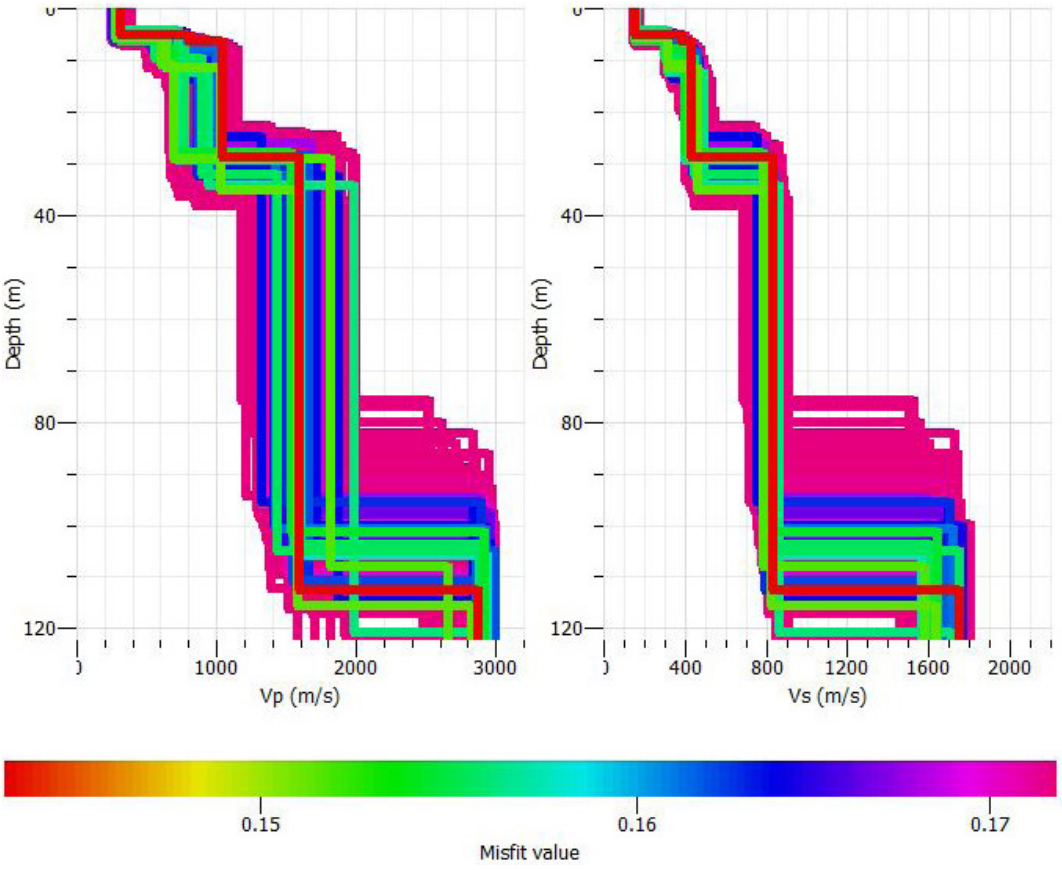


Fig. 3 - Vp (on the left) and Vs (on the right) logs obtained from the analysis of noise recordings acquired at measurement station YJG100. One can distinguish the upper layers with Vs < 800 m/s overlying a layer with Vs of about 800 m/s followed at greater depths by the material with velocity higher than 1000 m/s.

made of rock avalanche deposits. This resulted in a better resolution of the dam structure and thickness, and in a better definition of the bedrock depth. The bedrock is located below the gully streambed in the northwestern part of the landslide dam, while it nearly coincides with the gully streambed in the central and southeastern parts.

Acknowledgements. Maury McSaveney from GNS Sciences (New Zealand) provided valuable insight into the Yang Jia Gou geology and rock avalanche features of the geological interpretation of the survey results. Figures were prepared by using the Generic Mapping Tools (GMT) software package (Wessel *et al.,* 2019).

References

Bensen G.D., Ritzwoller M.H., Barmin M.P., Levshin A.L., Lin F., Moschetti M.P., Shapiro N.M. and Yang Y.; 2007: *Processing seismic ambient noise data to obtain reliable brod-band surface wave dispersion measurements*. Geophys. J. Int., 169, 1239– 1260.

Bonnefoy-Claudet S., Cotton F. and Bard P.Y.; 2006: *The nature of noise wavefield and its applications for site effects studies: a literature review*. Earth Sci. Rev., 79, 205–227.

Del Gaudio V.; 2017: *Instantaneous polarization analysis of ambient noise recordings in site response investigations*. Geophys. J. Int., 210, 443–464, doi: 10.1093/gji/ggx175.

Del Gaudio V., Wasowski J., Hu W., Capone P., Venisti N. and Li Y.; 2021: *Ambient noise and ERT data provide insights into the structure of co-seismic rock avalanche deposits in Sichuan (China)*. Bull. Eng. Geol. Env., 80, 1-18, doi: 10.1007/s10064-021-02346-8.

Derode A., Larose E., Campillo M. and Fink M.; 2003: *How to estimate the Green's function of a heterogeneous medium between two passive sensors? Application to acoustic waves*. Applied Physics Letters, 83, 3054–3056, doi: 10.1063/1.1617373.

Herrmann R.B.; 2013: *Computer programs in seismology: An evolving tool for instruction and research*. Seism. Res. Lettr., 84, 1081-1088, doi:10.1785/0220110096.

Levshin A.L., Pisarenko V.F. and Pogrebinsky G.A.; 1972: *On a frequency-time analysis of oscillations*. Ann. Geophys., 28, 211-218.

Li Y., Hu W., Wasowski J., Zheng Y. and McSaveney M.; 2021: *Engineering geology. Rapid episodic erosion of a cohesionless landslide dam: insights from loss to scour of Yangjia Gully check dams and from fume experiments*. Engineering geology, 280, 105971, doi: 10.1016/j.enggeo.2020.105971.

Nakamura Y.; 1989: *A method for dynamic characteristics estimation of subsurface using microtremor on the ground surface*. Q Rep Railw Tech Res Inst, 30, 25–33.

Snieder R.; 2004: *Extracting the Green's function from the correlation of coda waves: A derivation based on stationary phase*. Phys. Rev. E. 69, 046610.

Wapenaar K.; 2004: *Retrieving the elastodynamic Green's function of an arbitrary inhomogeneous medium by cross correlation*. Phys. Rev. Lett., 93, 254301.

Wasowski J., McSaveney M., Pisano L., Hu W. and Del Gaudio V.; 2021: *Recurrent rock avalanches progressively dismantle a mountain ridge in Beichuan County, Sichuan, most recently in the 2008 Wenchuan earthquake*. Geomorphology, 373, doi: 10. 1016/j.geomorph.2020.107492.

Wathelet M.; 2005: *Array recordings of ambient vibrations: surface-wave inversion*. PhD thesis, Université de Liège, Belgium.

Xu C., Yao X. and Dai F.; 2014: *Three (nearly) complete inventories of landslides triggered by the May 12, 2008 Wenchuan Mw 7.9 earthquake of China and their spatial distribution statistical analysis*. Landslides , 11, 441–461, doi: 10.1007/ s10346-460013-0404-6.

MANAGING THE URBAN COMPLEXITY OF VERNACULAR APPENINE CENTERS: THE CASE STUDY OF SCARPERIA

V. Cardinali, M.T. Cristofaro, M. De Stefano, M. Ferrini, R. Nudo, B. Paoletti, M. Tanganelli
Department of Architecture, University of Florence, Florence, Italy

The vernacular centers of the Apennine deserve special attention from administrators, stakeholders and the scientific community. The preservation of these minor clusters deals with significant seismicity of the areas threatening both cultural transmissions and people's life. Besides the main historical cities, Italy has grown through the development of minor centers controlling the surrounding territories (Sandoli *et al.,* 2022). The latter were realized through bearing wall structures realized in aggregate. Nowadays these buildings have undergone several alterations and interventions modifying their structural behaviors and performances. Hence, their seismic vulnerability assessment needs to be defined. At the urban scale, the investigations are targeted to determine damage scenarios for different seismic intensities. The available methodologies can be divided within empirical, analytical and hybrid approaches. Aiming to assess historical centers and urban masonry aggregates a relevant issue is given by the knowledge path. The significative dimensions of the investigated centers make the data acquisition more difficult starting from the survey activities as several properties interact in the definition of the structural units. The execution of scrupulous cognitive phases becomes unsustainable for costs and time-consuming issues. Hence, simplifications able to express the expected behavior of the buildings are required. Due to this, empirical and hybrid approaches are the preferred approaches, as analytical studies become too demanding to be pursued at the urban scale. In this paper, a methodological framework is presented (Fig. 1). The method has been applied to the historical city center of Scarperia, in Tuscany (IT) (Fig. 2-a). Scarperia is located in the Mugello area, which represents one of the most active seismic zones of the Tuscany region, along the Apennines. The city center was built *ex-novo* during the Medieval period by the Florentine Republic according to a regular scheme. The research includes a cognitive acquisition developed through an interdisciplinary approach targeted at identifying architectural and structural features of masonry building aggregates. To this aim, a multiscale approach has been conceived (Cardinali *et al.,* 2021).



Fig. 1 - Flow-chart of the multiscale vulnerability approach.

The methodology considers the management of the different information through two informative systems, GIS and BIM, selected according to the details of the evaluation. Initially, the structural units were investigated by external visual inspections, collecting the data in a GIS platform. The seismic vulnerability of the different units was evaluated through the Giovinazzi and Lagomarsino modifiers (2004) based on the EMS-98 scale (Grunthal 1998). The latter allows the identification of a vulnerability index based on the structural features of each structure (Fig. 2-b). Later, in-depth cognitive studies have been executed through a suitable approach for the geometrical survey. The cadastral plans of each house were collected and combined according to a laser scanner survey executed from the outside (Fig. 2-c). This new information allowed the adoption of a different empirical methodology, i.e., the GNDT second level assessment. To use this method further information are required, e.g., the resistant area along the two directions and other internal features. In addition, the GNDT sheet has been used adopting the aggregate rows implemented by Formisano *et al.* (2011). The latter introduces 5 new scores to account on the effects of adjacent buildings within masonry aggregates, as the initial GNDT method was conceived for single structures. The comparisons within the two empirical methodologies in terms of vulnerability indexes and damage scenarios highlights the significance of deepen cognitive studies at the aggregate level (Cardinali *et al.,* 2020). Specifically, the EMS-98 modifiers lead to more conservative results, highlighting a lower variability. On the other hand, the Formisano GNDT second level approach points out major differences, remarkable thanks to the deepen cognitive studies. In Fig. 2-d the Vulnerability curves adopting the second empirical approach are presented. The curves plot the Damage levels - DLi, with i=1,…,5 – (ordinate) according to different PGA values (abscissa). Namely, the DLs represent the performance point after which a Damage State occurs (DS). The DS are defined in accordance to EMS-98 scale (Grünthal, 1998): *DS0* – no damage, *DS1* – slight, *DS2* – moderate, *DS3* – heavy, *DS4* – very heavy, and *DS5* – collapse. The mean curve accounts the mean Vulnerability index coming from the different structural units of the center; in addition, the mean curve accounting on the standard deviation of the sample together with the min/max curves coming from the urban center are plotted. For a seismic action with 475 years return period, the mean expected damage for the historical center is divided with a 29% of probability to reach DL3, the 13% for DL4 and 25 % for DL2. In Fig. 2-f the damage scenarios for 475 years return period action are shown. The new available contents also provided the usage of BIM platforms to collect the architectural and spatial information of the urban clusters (Fig. 2-e). Additional studies have been targeted at the execution of analytical evaluations on case studies representative of the urban stock. To this aim, out-of-plane mechanisms have been studied considering different uncertainties and possible variabilities within the facades of the aggregates (Nale *et al.,* 2021). In addition, four case studies representative of the houses of the center of Scarperia have been investigated through equivalent frame modeling and nonlinear static analysis. The outcomes of the different phases have been discussed in terms of fragility curves (Fig. 2-g). Fragility curves define the probability of occurrence of a certain damage level as a function of the intensity measure of the ground motion (Matio and Tsionis, 2015). The latter have been defined according to different methodologies. The probability of the empirical ones was obtained by the damage distributions from the Vulnerability curves. The analytical ones have been derived by computing the threshold values and the relative dispersions (according to the Response Surface Method; Pinto *et al.,* 2004). The comparisons within local and global analysis showed the intrinsic relationships within the two types of seismic response of masonry structures, where the two behaviours express complementary possibilities. The comparisons within the empirical curves and the ones coming from the nonlinear static analysis show relevant variabilities, both referring to the thresholds of the different DLs as to the dispersion's computation (Chieffo and Formisano 2019). Further analytical studies are certainly encouraged in order to in-depth investigate the variabilities of the curves based on

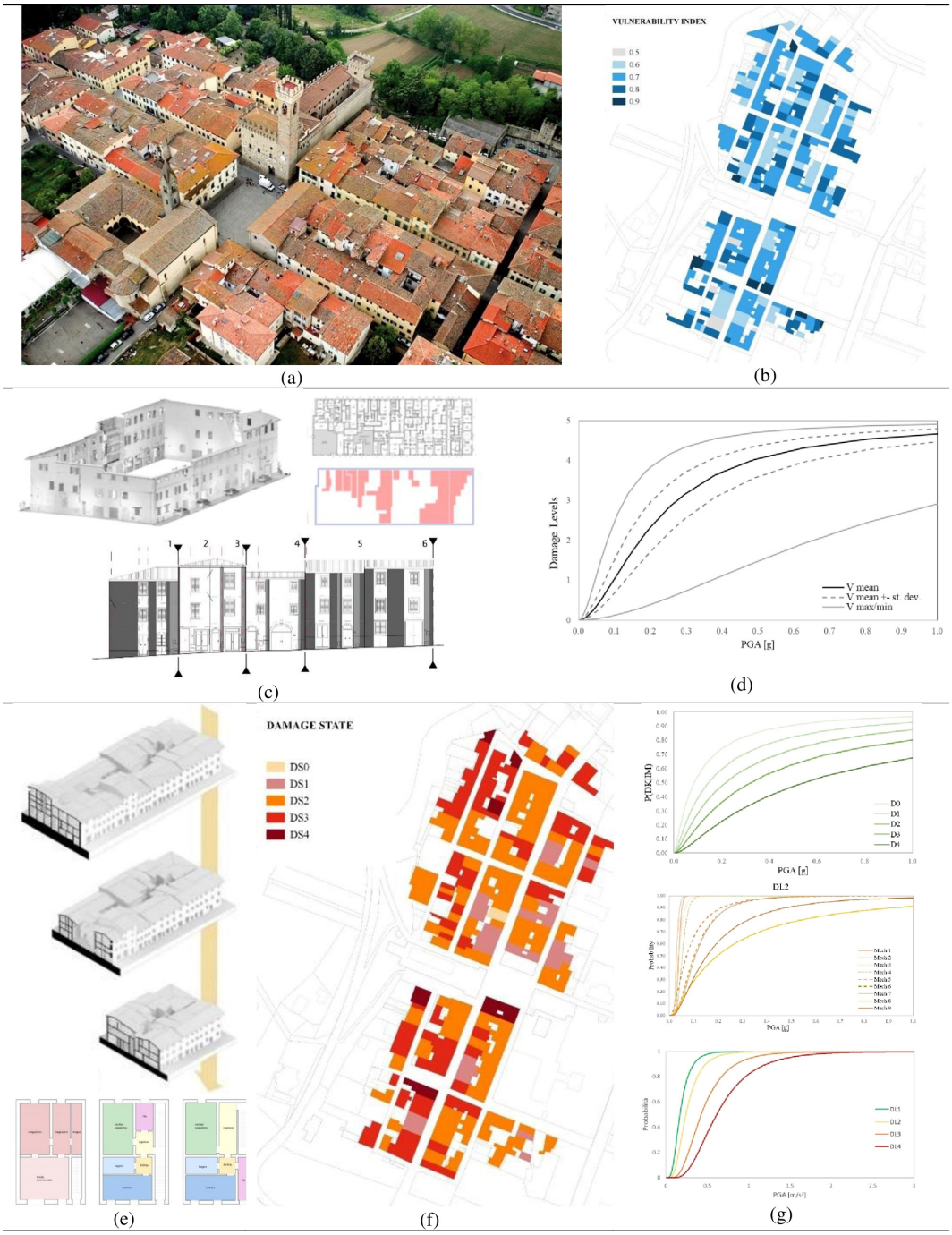


Fig. 2 - a) view of the city center of Scarperia; b) index-based vulnerability assessment of the structural units of the center; c) cognitive procedure: laser scanner survey and cadastral reconstruction of the aggregates; d) vulnerability curves of the historical center of the city; e) BIM implementation and analysis of representative units; f) damage scenarios for 475 years return period; g) different sets of fragility curves; from the top: empirical curves obtained from the damage distribution; analytical fragility curves derived from different out-of-plane actions; analytical fragility curves derived from nonlinear static analysis.

aleatory and epistemic uncertainties considered in the research. The procedure has shown the significance of the cognitive procedures towards the seismic vulnerability assessment of historical centers. The different outcomes of the work point out a discrete vulnerability requiring specific attentions. The research is still ongoing, and it is targeted at the calibration of the empirical methodologies by an implementation of the analytical outcomes into hybrid strategies. These studies will allow to forecast the risk-related economic direct and indirect losses, permitting to investigate the impact of strengthening solutions at the urban scale. In addition, these evaluations are at the basis of the emergency management and the evacuation planning useful in the post-event governance. In addition, the administration of historical center encourages to consider different risk sources into multi-hazard perspectives for a comprehensive urban management (Arrighi *et al.,* 2022).

Acknowledgements. This research belongs to the Protocol signed between the Municipality of San Piero e Scarperia and Department of Architecture of the University of Florence for the seismic vulnerability assessment of the historical centre of Scarperia.

References

Arrighi C., Tanganelli M., Cristofaro M.T., Cardinali V., Marra A., Castelli F., De Stefano M.; 2022: *Multi-risk assessment in a historical city*. Nat. Hazards.

Cardinali V., Cristofaro M.T., Ferrini M., Nudo R., Paoletti B., Tanganelli M.; 2020: *An interdisciplinary approach for the seismic vulnerability assessment of historical centres in masonry building aggregates: application to the city of Scarperia, Italy.* Int. Arch. Photogramm. Remote Sens. Spatial Inf. Sci., XLIV-M-1-2020, 667–674, https://doi.org/10.5194/isprs-archives-XLIV-M-1-2020-667-2020.

Cardinali V., Cristofaro M.T., Ferrini M., Nudo R., Paoletti B., Tanganelli M.; 2021: *A multiscale approach for the seismic vulnerability assessment of historical centres in masonry building aggregates: cognitive approach and interdisciplinary perspectives.* Int J Arch Herit. https://doi.org/10.1080/15583058.2021.1992536.

Chieffo N., Formisano; 2019: *Comparative Seismic Assessment Methods for Masonry Building Aggregates: A Case Study.* Frontiers in Built Environment, 5(), 123–. doi:10.3389/fbuil.2019.00123.

Formisano A., Florio G., Landolfo R., Mazzolani F.M.; 2011: *Un metodo per la valutazione su larga scala della vulnerabilità sismica degli aggregati storici.* XV Convegno ANDIS - L'Ingegneria Sismica in Italia.

Giovinazzi S., Lagomarsino, S.; 2004: *A macroseismic model for the vulnerability assessment of buildings.* 13th World Conference on Earthquake Engineering, Vancouver, Canada.

Grunthal, G.; 1998: *European Macroseismic Scale.* Chaiers du Centre Européen de Géodynamique et de Séismologie, vol. 15 Luxembourg.

Maio R., Tsionis G.; 2015: *Seismic fragility curves for the European building stock: review and evaluation of analytical fragility curves.* EUR 27635 EN. European Laboratory for Structural Assessment, Institute for the Protection and Security of the Citizen, Joint Research Centre of the European Commission, Ispra (Italy).

Nale M., Minghini F., Chiozzi A., Tralli A.; 2021: *Fragility functions for local failure mechanisms in unreinforced masonry buildings: a typological study in Ferrara, Italy.* Bull Earthquake Eng 19, 6049–6079 https://doi.org/10.1007/s10518-021-01199-6.

Pinto P. E., Giannini R., Franchin P.; 2004: *Seismic reliability analysis of structures.* Pavia: IUSS Press.

Sandoli A., Calderoni B., Lignola G.P., Prota A.; 2022: *Seismic vulnerability assessment of minor Italian urban centres: development of urban fragility curves.* Bull Earthquake Eng. https://doi.org/10.1007/s10518-022-01385-0.

STIMA DEGLI EFFETTI DI SITO DA DATI DI Vs IN EMILIA-ROMAGNA

G. Carloni[1], G. Ercolessi[2], L. Martelli[3]

[1] Università di Bologna - Dip. Scienze Biologiche, Geologiche e Ambientali, Italy
[2] Unione dei Comuni della Bassa Romagna, Italy
[3] Regione Emilia-Romagna - Geologia, suoli e sismica, Italy

Introduzione. La Vs, ovvero la velocità di propagazione nel terreno delle onde di taglio S, è un parametro fondamentale per la conoscenza e mitigazione del rischio sismico. Il profilo di Vs o il suo valore medio equivalente, Vs_{eq}, della porzione di sottosuolo soprastante il *bedrock* sismico sono dati necessari per la valutazione dello scuotimento sismico in superficie, analisi richiesta sia per la microzonazione sismica (Gruppo di lavoro MS, 2008) sia per determinare l'azione sismica di progetto (EN 1998-1, 2004; NTC, 2018).

La riclassificazione sismica del territorio nazionale (OPCM 3274/2003) e l'aggiornamento delle norme tecniche per le costruzioni, che richiedono la caratterizzazione geotecnica e geofisica del sottosuolo almeno fino alla profondità di 30 m e la stima dell'azione sismica per ogni progetto, nonché l'obbligatorietà, in Emilia-Romagna, dell'analisi della pericolosità sismica locale per la pianificazione urbanistica (DAL 112/2007) e i contributi nazionali previsti dall'art. 11 L 77/2009 per studi di microzonazione sismica (MS) hanno comportato un grande incremento di indagini geotecniche e geofisiche, e quindi di misure di Vs.

Dopo più di 10 anni di applicazione delle moderne norme tecniche (NTC, 2008) e grazie ai numerosi studi di MS e interventi di riparazione e ricostruzione nell'aree colpite da terremoti (S. Sofia 2003, Monghidoro 2003, Appennino reggiano-parmense 2008, pianura emiliana 2012) la quantità di dati di Vs nel territorio regionale era tale da tentare un'analisi e stima degli effetti di sito a scala regionale, secondo l'approccio semplificato delle NTC (2018) o le procedure speditive di MS di livello 2 (DAL 112/2007; Gruppo di lavoro MS, 2008).

Disponendo già di buone conoscenze litostratigrafiche su tutto il territorio, nel 2018 l'ex Servizio Geologico della Regione ha iniziato ad archiviare le misure di Vs in una banca dati GIS ed ha tentato prime valutazioni a scala regionale degli effetti di sito (Naso *et al.*, 2019; Faravelli *et al.*, 2021). Tutto ciò con l'intento di fornire all'Amministrazione documenti aggiornati sull'effettiva distribuzione della pericolosità sismica.

Ad oggi la MS è in via di completamento e si dispone di indagini geofisiche in quasi tutti i Comuni della regione. Si è quindi deciso di completare l'archiviazione dei dati e aggiornare le cartografie regionali di Vs e di pericolosità sismica al sito.

Purtroppo, la distribuzione dei dati non è omogenea ma risente della localizzazione delle indagini, molto più numerose nelle aree di interesse urbanistico (centri abitati e aree di espansione) e meno frequenti nelle aree rurali.

Analisi dei dati. I dati derivano dalle indagini già disponibili nella banca dati geognostici regionale e dai numerosi studi di MS condotti a scala comunale, che comprendono anche le indagini per le ricostruzioni post sisma.

Le informazioni della Vs richieste per la MS e la progettazione sono i valori dal bedrock sismico alla superficie (profilo di Vs), nel caso di analisi dettagliate della risposta sismica, o il valore di Vs_{eq}, nel caso di stime speditive (EN 1998-1, 2004; NTC, 2018; DAL 112/2007; Gruppo di lavoro MS, 2008); il parametro Vs_{eq} è definito dall'espressione:

$$Vs_{eq} = \frac{H}{\sum_{i=1}^{n} \frac{h_i}{Vs_i}}$$

dove H è la profondità del bedrock sismico, n è il numero degli strati, h_i è lo spessore dell'i-esimo strato e Vs_i è la velocità delle onde di taglio nell'i-esimo strato

Nelle aree geologicamente stabili in cui il solo effetto locale atteso è l'amplificazione, per determinare lo scuotimento al sito tramite procedure speditive è generalmente ritenuto sufficiente il valore di Vs_{30}, ovvero il valore medio equivalente nei primi 30 m di sottosuolo (EN 1998-1, 2004; NTC, 2018), ottenuto ponendo H=30 m nella precedente espressione e considerando le proprietà degli strati fino a tale profondità (Fig. 1A).

Per la MS di livello 2, nei casi in cui l'aumento di Vs con la profondità non sia graduale ma sia presente, ad una profondità di almeno 3 m, una discontinuità tale che $Vs_2/Vs_1>2$, dove Vs_1 è il valore di Vs sopra la discontinuità e Vs_2 è il valore di Vs sotto la discontinuità, è richiesta la stima di Vs_{eq} della porzione superiore a più bassa velocità; tale valore è generalmente indicato come Vs_H, dove H è lo spessore per il quale è stato calcolato il valore medio equivalente di Vs (Fig. 1B).

Sono stati così analizzati tutti i documenti delle prove di misura di Vs, che consistono soprattutto in prove dirette puntuali tipo down-hole (DH), cross-hole (CH), penetrometrie statiche con cono sismico (SCPT) e dilatometrie con punta sismica (SDMT), prove lineari indirette attive tipo MASW o passive tipo ReMi e bidimensionali tipo ESAC.

Nei Comuni in cui tali prove non erano disponibili, profili di Vs e valori di Vs_{eq} sono stati derivati da misure di rumore ambientale a stazione singola (HVSR), utilizzando la relazione:

$$Vs = \frac{F}{4H}$$

dove F è la frequenza di risonanza e H è la profondità del contrasto di impedenza responsabile degli effetti osservati (conoscendo H è quindi possibile ottenere il valore medio di Vs nell'intervallo di terreno di spessore H, spesso corrispondente alla copertura soprastante il substrato).

Le prove analizzate sono state quindi codificate in base al valore di Vs_{30} e Vs_H e secondo la classificazione delle categorie di sottosuolo della normativa tecnica (NTC, 2018).

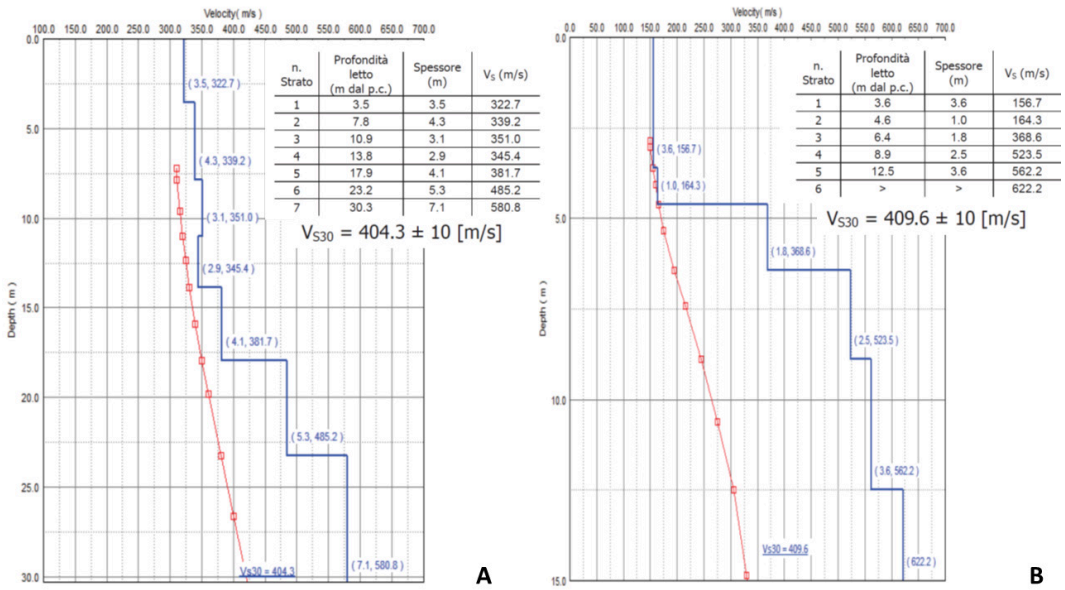


Fig. 1 - A) esempio di profilo di Vs per cui è stata stimata la Vs_{30}, si noti l'aumento piuttosto graduale di Vs con la profondità; B) esempio di profilo di Vs per il quale è ritenuta necessaria la stima di Vs_H; si noti la discontinuità a -4,6 m e il significativo e repentino aumento di velocità (Vs_H =158,3 m/s; Vs_{30}=409,6 m/s).

Purtroppo, non tutte le misure disponibili sono risultate utilizzabili; sono state infatti scartate le prove che fornivano Vs poco attendibili (es. valori molto diversi rispetto a quelli di prove limitrofe in contesti litostratigrafici omogenei).

In sintesi, le prove archiviate utili sono: 320 DH, 39 CH, 770 SCPT, 8 SDMT, 5319 MASW, 2525 ReMi, 507 ESAC e 2325 HVSR. Sono state archiviate anche le prove non sufficientemente profonde per definire una classe di sottosuolo (139) ma che forniscono comunque indicazioni sulla Vs nei primi metri di sottosuolo.

Le Vs in Emilia-Romagna. In figura 2 è mostrata la distribuzione delle misure di Vs in Emilia-Romagna, rappresentate per classi di Vs secondo gli abachi regionali per la MS di livello 2 (DAL 112/2007).

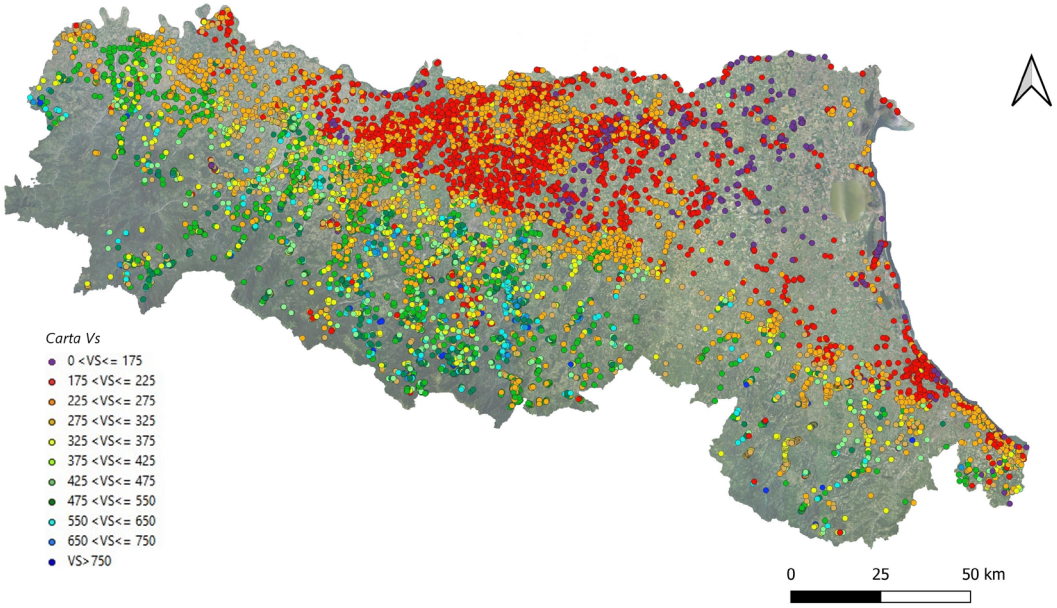


Fig. 2 - Misure di Vs in Emilia-Romagna.

Le velocità più elevate (Vs_{30}>750 m/s), tipiche di terreni rigidi, sono poche e presenti esclusivamente nel settore appenninico. La scarsa quantità di misure in terreni rigidi risente della distribuzione delle prove; queste sono localizzate soprattutto in aree d'interesse urbanistico (centri abitati e aree di espansione) che, nell'Appennino emiliano-romagnolo, raramente sono in zone rocciose ma si concentrano nei fondivalle e sui versanti meno acclivi, ovvero su terreni detritici recenti, poco o per niente consolidati. Di conseguenza, gran parte dei siti hanno valori di Vs_{30} compresi tra 325 e 750 m/s e valori di Vs_H minori di 350 m/s.

Nei fondivalle e sui versanti Vs è generalmente minore di 350 m/s nelle coperture detritiche, non elevata nei primi 5÷10 m del substrato per poi aumentare rapidamente con la profondità. Valori di Vs non elevati (Vs<500 m/s) nella parte alta del substrato spesso corrispondono a zone di alterazione. In questi contesti è importante quindi calcolare anche Vs_H dove H è lo spessore dell'intervallo soprastante il substrato roccioso non alterato. Lo spessore H è generalmente inferiore ai 50 m.

Nella fascia pedeappenninica, dove si concentrano i terreni grossolani di conoide fluviale, spesso Vs_{30} è maggiore di 300 m/s e non di rado il tetto delle ghiaie sepolte dà origine ad un importante contrasto di Vs. In questo contesto è infatti frequente che i terreni ghiaiosi abbiano Vs maggiore di 400 m/s mentre i terreni fini soprastanti hanno spesso Vs minore di 200÷250

m/s (Fig. 1B). Anche in tali casi è importante calcolare il valore di Vs_H dove H è lo spessore dei terreni fini soprastanti le ghiaie.

Infine, in pianura Vs è quasi sempre minore di 250 m/s. Le velocità più basse si misurano soprattutto dove maggiore è lo spessore dei sedimenti alluvionali, soprattutto nel settore orientale.

La carta degli effetti locali attesi in Emilia-Romagna. Una delle possibili applicazioni di questa banca dati è la stima a scala regionale degli effetti locali, importante supporto per definire strategie di riduzione del rischio sismico.

L'elaborazione più immediata è la classificazione del territorio nelle categorie di suoli A-E (EN 1998-1, 2004; NTC, 2018).

Ad ogni punto di misura di Vs può essere poi associato un coefficiente di amplificazione S in base alla categoria di suolo (v. Tab. 3.2.IV delle NTC, 2018). Ciò permette di calcolare il valore di accelerazione atteso al sito, a_{max}, con la relazione:

$$a_{max} = S \times a_g = (S_S \times S_T) \times a_g$$

dove a_g è l'accelerazione di picco su suolo rigido e pianeggiante (classe di sottosuolo A), S_S è il coefficiente di amplificazione stratigrafica e S_T quello di amplificazione topografica.

In figura 3 è mostrata la mappa di a_{max} stimata nei siti di misura di Vs.

Il valore di a_g è derivato dal modello di pericolosità MPS04 (Meletti et al., 2006); S_S considerato è quello massimo indicato nella Tab. 3.2.IV delle NTC (2018) mentre S_T è stato assunto pari a 1 poiché quasi tutti i siti di misura di Vs sono in zone non suscettibili di amplificazione topografica.

Studi di MS e analisi di risposta sismica locale hanno però dimostrato che la valutazione degli effetti locali può essere significativamente diversa da quella stimata con le classi di sottosuolo A-E. Ad esempio, alcuni siti di fondovalle e pedemontani classificabili come B mostrano localmente amplificazioni maggiori, dell'ordine di quelle delle classi C, D ed E, mentre siti classificabili come D in zone con bedrock sismico a profondità maggiori di 300 m (delta del Po

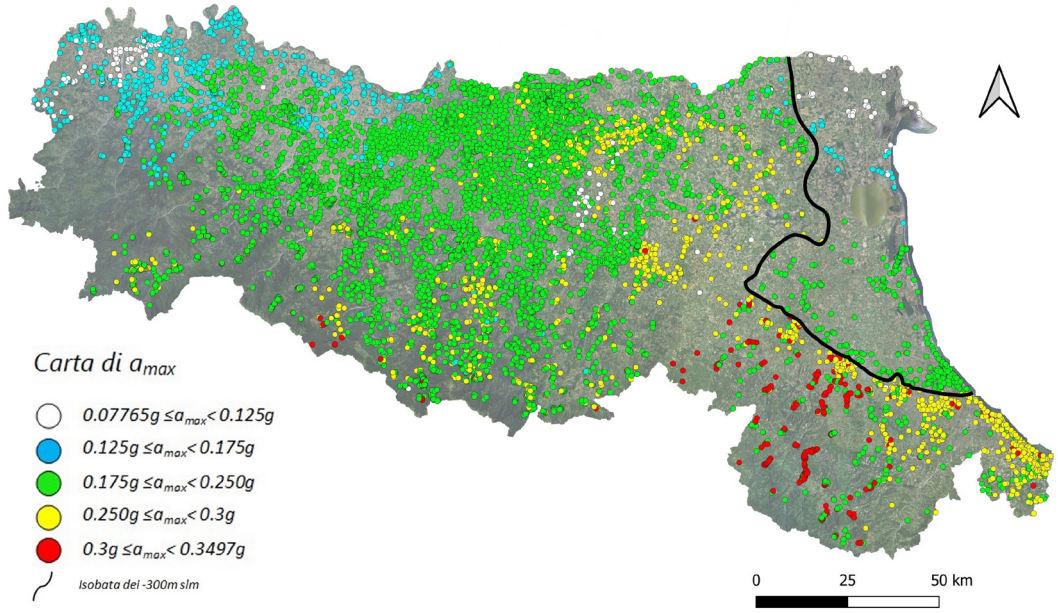


Fig. 3 - mappa di a_{max} stimata nei siti di misura di *Vs* (ζ=5%; T_R=475 anni); il settore ad ovest della linea nera è caratterizzato da profondità del bedrock sismico maggiore di 300 m.

e costa a nord di Rimini), mostrano sempre amplificazioni molto minori, dell'ordine di quelle attese per la classe B. Per questo motivo, per il calcolo di a_{max} nei siti con bedrock sismico a profondità maggiore di 300 m (Mascandola *et al.*, 2019; Martelli, 2021) è stato considerato un coefficiente di amplificazione tipo classe B.

Un possibile sviluppo è quindi una valutazione più realistica dello scuotimento atteso in superficie, ad esempio applicando i criteri di MS di livello 2 degli indirizzi regionali (Tento *et al.*, 2014; DGR 476/2021 e DGR 564/2021), che permettono una stima speditiva, tramite abachi, sia dei fattori di amplificazione, per vari intervalli di periodi T, sia dello scuotimento in superficie (in cm/s^2) per $0{,}1s \leq T \leq 0{,}5s$ (H_{SM} di Naso *et al.*, 2019).

Bibliografia

DAL 112/2007: Delibera Assemblea Legislativa Regione Emilia-Romagna n. 112 del 2/5/2007: *Approvazione dell'atto di indirizzo e coordinamento tecnico ai sensi dell'art.16 comma 1, della L.R. 20/2000 per "Indirizzi per gli studi di microzonazione sismica in Emilia-Romagna per la pianificazione territoriale e urbanistica".* BURERT n. 64 del 17/05/2007.

DGR 476/2021: Delibera Giunta Regione Emilia-Romagna n. 476 del 12/4/2021: *Aggiornamento dell'«Atto di coordinamento tecnico sugli studi di microzonazione sismica per la pianificazione territoriale e urbanistica (artt. 22 e 49, LR 24/2017)» di cui alla deliberazione della Giunta Regionale 29 aprile 2019, n. 630*. BURERT n. 111 del 20/04/2021 – Parte seconda n. 93.

DGR 564/2021: Delibera Giunta Regione Emilia-Romagna n. 564 del 26/4/2021: *Integrazione della propria deliberazione n. 476 del 12 aprile 2021 mediante approvazione dell'allegato A, «Atto di coordinamento tecnico sugli studi di microzonazione sismica per la pianificazione territoriale e urbanistica (artt. 22 e 49, L.R. n. 24/2017)».* BURERT n. 137 del 12/05/2021 – Parte seconda n. 113.

EN 1998-1; 2004: *Eurocode 8: design of structures for earthquake resistance - Part 1*: *general rules, seismic actions and rules for buildings*. CEN European Committee for Standardization, Bruxelles, Belgium, 229 pp.

Faravelli M., Bozzoni F., Zuccolo E., Di Meo A., Quaroni D., Polli D., Rodriguez-Plata R., Martelli L., Borzi B. and Lai C. G.; 2021: *Mesozonazione del rischio sismico: la piattaforma WebGIS di EUCENTRE per la Regione Emilia-Romagna*. Progettazione Sismica – Vol. 13, N.3, 3-23 DOI 10.7414/PS.13.1.3-https://doi.org/10.7414/PS.13.1.3

Gruppo di lavoro MS; 2008: *Indirizzi e criteri per la microzonazione sismica*. Conferenza delle Regioni e P. A. – Dip. Protezione Civile.

Martelli L.; 2021: *Assessment of Seismic Bedrock in Deep Alluvial Plains. Case Studies from the Emilia-Romagna Plain*. Geosciences, 11, 297. https://doi.org/10.3390/geosciences11070297

Mascandola C., Massa M., Barani S., Albarello D., Lovati S., Martelli L. and Poggi V.; 2019: *Mapping the Seismic Bedrock in the Po-Plain (Italy) through ambient vibration* monitoring. Bull. Seism. Soc. Am., 109(1), 164-177. doi: 10.1785/0120180193

Meletti C., Montaldo V., Stucchi M. and Martinelli F.; 2006: *Database della pericolosità sismica MPS04*. Istituto Nazionale di Geofisica e Vulcanologia (INGV) DOI: 10.13127/SH/MPS04/DB

Naso G., Martelli L., Baglione M., Bramerini F., Castenetto S., D'Intinosante V. and Ercolessi G.; 2019: *Maps for land management: from geology to seismic hazard*. Boll. Geof. Teor, Appl., 60, 277-294, doi:10.4430/bgta0263

NTC; 2008: *Nuove Norme Tecniche per le Costruzioni*. Ministero Infrastrutture, Decreto 14/01/2008, G. U. Rep. Italiana 4/2/2008 n. 29, Suppl. Ord. n. 30.

NTC; 2018: *Aggiornamento delle "Norme Tecniche per le Costruzioni.* Ministero Infrastrutture e Trasporti, Decreto 17/01/2018. G. U. Rep. Italiana 20/2/2018, n. 42, Suppl. Ordin. n. 8.

Tento A., Martelli L. and Marcellini A.; 2014: *Abachi per la valutazione dei fattori di amplificazione per le indagini di microzonazione sismica di secondo livello in Emilia-Romagna*. Atti 33° convegno GNGTS, Bologna 25-27/11/2014, sess. 2.2, 289-294.

EFFICACIA DI STRATEGIE DI MITIGAZIONE SISMICA PER IL PATRIMONIO EDILIZIO ITALIANO IN MURATURA

P. Carpanese, V. Follador, M. Donà, F. da Porto

Dipartimento di Geoscienze, Università degli Studi di Padova, Italia

Introduzione. Negli ultimi decenni, l'Italia è stata colpita da eventi sismici che hanno causato migliaia di vittime e circa 180 miliardi di euro di perdite economiche (DPC 2018). Queste perdite non sono più sostenibili e risulta necessario perseguire politiche di mitigazione sismica su larga scala.

In questo contesto, il Dipartimento della Protezione Civile (DPC) sta lavorando in sinergia con la comunità scientifica per valutare le possibili strategie da adottare (Dolce et al. 2021, da Porto *et al.,* 2021). In particolare, il lavoro presentato in questo articolo fa parte di un progetto che coinvolge ReLUIS (Rete dei Laboratori Universitari di Ingegneria Sismica), il cui scopo è quello di sviluppare modelli di vulnerabilità su larga scala per edifici nello stato originario e dopo il consolidamento, per poi eseguire analisi costi-benefici in modo da individuare l'efficacia e la convenienza di diversi interventi di mitigazione sismica proposti.

Per fare ciò, è necessario innanzitutto valutare la variazione della vulnerabilità tra la configurazione *as-built* e il caso in cui siano stati eseguiti particolari interventi di retrofit, ad esempio tramite il confronto di curve di fragilità. In questo contributo, sono state ottenute curve di fragilità attraverso una procedura meccanica semplificata per edifici residenziali italiani con diversi tipi di intervento anti-sismico. Lo studio si concentra su edifici in muratura, divisi in macro-tipologie secondo l'epoca di costruzione (Pre-1919, 1919-1945, 1946-1960, 1961-1980) e il numero di piani (Low-Rise, ovvero 1 o 2 piani, oppure Mid-Rise, 3 piani o più).

I modelli di vulnerabilità sono stati poi implementati nella piattaforma IRMA (Italian Risk MAps) sviluppata dal Centro Europeo di Formazione e Ricerca in Ingegneria Sismica Eucentre (Borzi *et al.,* 2021), per produrre mappe di rischio sismico mitigate e non, e quindi evidenziare i benefici che gli interventi proposti possono portare in diverse zone del territorio italiano.

Interventi e curve di fragilità mitigata. Per sviluppare i modelli di fragilità mitigata, sono stati selezionati gli interventi di retrofit da implementare per ogni macro-tipologia di edificio considerata, sulla base di letteratura specifica e anche osservazioni dirette sul campo (Saretta *et al.,* 2021). Nello specifico, gli interventi sono stati raggruppati in tre categorie: a) interventi che aumentano la resistenza e la compattezza delle pareti; b) interventi che migliorano i collegamenti parete-parete e parete-orizzontamento; c) interventi che aumentano la rigidezza degli orizzontamenti.

Gli interventi di rinforzo delle pareti possono essere di vario tipo, sulla base della tipologia della muratura (da Porto *et al.,* 2018). Per quanto riguarda gli edifici storici, la struttura portante è solitamente composta da muratura in pietra (più o meno regolare) o in mattoni pieni. Negli edifici in muratura portante più recenti, invece, si usano solitamente mattoni pieni o semipieni. Nel caso di murature incoerenti, sono stati simulati interventi di iniezione di miscele consolidanti (Silva *et al.,* 2014a; 2014b), mentre per le murature composte da elementi più regolari, intonaci in cemento armato (Modena *et al.,* 2009) o FRCM-TRM (Fibre/Fabric Reinforced Cementitious Matrix/Mortar - Textile Reinforced Mortars) (CNR-DT 215/2018; Giaretton *et al.,* 2018). Tali interventi di rinforzo delle murature sono stati proposti in due step (MUR1, MUR2) nel caso di edifici storici (pre-1945), in cui il primo step considera l'applicazione di interventi leggeri, mentre il secondo step implica l'applicazione di più interventi. Nel caso di edifici moderni (1946-1980), date le tipologie di muratura più regolari, è stato assunto come sufficiente un unico intervento (MUR).

Per quanto riguarda gli interventi volti a migliorare le connessioni tra gli elementi strutturali di un edificio in muratura, la soluzione più efficace e diffusa è l'inserimento di tiranti (CAT)

o cerchiature (CERCH) (Modena *et al.,* 2009). Le cerchiature svolgono la stessa funzione dei tiranti, ma sono posizionate sulla faccia esterna delle pareti. In questo studio, l'intervento di cerchiatura è stato considerato come l'equivalente delle catene per gli edifici più recenti, poiché il risultato del posizionamento delle cerchiature è quello di contrastare i meccanismi fuori piano, come per i tiranti, senza la necessità durante l'intervento di svolgere operazioni all'interno dell'edificio.

Infine, gli interventi volti ad aumentare la rigidezza degli orizzontamenti (SOL) sono stati differenziati sulla base della tipologia di edificio, e presentano delle differenze significative se eseguiti su edifici storici o più recenti. Per i solai lignei degli edifici storici viene previsto un irrigidimento tramite la posa di tavolato in legno, singolo o doppio, in direzione ortogonale o a 45° sopra l'esistente (Valluzzi *et al.,* 2010), mentre per solai realizzati in laterocemento senza presenza di cappa collaborante ed eventualmente senza cordolo si è pensato ad un rinforzo tramite la sostituzione/aggiunta di una soletta armata e con l'inserimento di adeguati collegamenti alle pareti lungo tutto il perimetro.

Gli interventi precedentemente descritti sono stati studiati singolarmente (MUR1, MUR2, MUR, CAT, CERCH, SOL) o in maniera combinata (MUR1+CAT, MUR1+SOL, MUR2+CAT, MUR2+SOL, MUR+CERCH, MUR+SOL), e sono stati implementati su un database di 445 edifici, appartenenti alle 4 classi di età precedentemente definite.

La modellazione è stata effettuata tramite il software Vulnus vb 4.0, sviluppato presso l'Università di Padova. Vulnus analizza gli edifici in muratura portante sulla base di informazioni limitate, come la geometria, le proprietà dei materiali, i dettagli costruttivi e altre informazioni qualitative (Valluzzi, 2009). Nello specifico, Vulnus calcola tre indici: I1, associato alla resistenza in piano; I2, relativo all'accelerazione di innesco dei principali meccanismi fuori piano; e I3, un indice qualitativo. I tre indici, attraverso l'adozione della teoria dei *fuzzy sets*, sono utilizzati per elaborare tre curve di fragilità: una curva *White* di probabilità centrale, e due curve di probabilità estrema (*Upper-* e *Lower-Bounds*). Le tre curve, descritte da distribuzioni lognormali cumulative, rappresentano la probabilità di superare uno stato di danno moderato-grave, associato ad un DS2-3 con riferimento alla scala di danno EMS98 (Grünthal, 1998), in funzione della PGA.

Le curve, ottenute implementando ogni edificio del database nel software, sono state post-processate secondo la metodologia di Donà *et al.,* 2021, in modo tale da ottenere dei set di fragilità completi per ogni macro-tipologia, sia nella condizione *as-built*, che nelle varie opzioni di retrofit analizzate (Follador *et al.,* 2021).

Mappe di rischio sismico e beneficio atteso. Una volta definite le curve di fragilità per le strategie di intervento (Follador *et al.,* 2021), queste possono essere implementate nella piattaforma IRMA (Borzi *et al.,* 2021), la quale permette di elaborare dati di pericolosità sismica, vulnerabilità ed esposizione in Italia, al fine di produrre mappe di danno e di rischio sismico, sia a tempo condizionato (ovvero per uno specifico periodo di ritorno), sia a tempo incondizionato (per una finestra temporale di osservazione).

Nelle elaborazioni qui presentate, sono state effettuate valutazioni sulle perdite economiche dirette. In IRMA, il costo di ricostruzione è assunto pari a 1350 €/m^2, e ad ogni stato di danno è associata una percentuale di perdita rispetto al costo totale (2% per DS1, 10% per DS2, 30% per DS3, 60% per DS4 e 100% per DS5) (Di Ludovico et al. 2017a, b).

Inizialmente, è stato calcolato il beneficio atteso in una determinata finestra temporale. Il beneficio è definito come la differenza tra le perdite economiche per uno scenario in cui tutti gli edifici si trovano nella configurazione *as-built* e il caso in cui una strategia di intervento sia implementata in maniera estesa a livello nazionale. Essendo il beneficio profondamente influenzato dall'esposizione, i risultati sono proposti in termini di beneficio normalizzato, calcolato come il rapporto tra il beneficio in ogni comune e la superficie degli edifici che

gli appartengono (quindi, in rapporto all'esposizione totale). In Fig. 1 vengono riportate le mappe di beneficio normalizzato (in €/m^2), a livello provinciale, riferite all'epoca Pre-1919. Va notato come risultati simili possano essere raggiunti sia tramite interventi combinati, sia tramite interventi singoli maggiormente impattanti (per esempio, la mappa MUR1+CAT è molto simile a quella relativa a MUR2). Inoltre, in alcuni casi si vede come la combinazione di interventi più leggeri porti a dei benefici molto simili a quelli ottenuti con interventi più pesanti (per esempio, MUR1+SOL raggiunge già un buon livello di beneficio, lo stesso raggiunto dall'intervento più pesante MUR2+SOL). Queste considerazioni possono rivelarsi significative in fase di pianificazione di azioni di mitigazione a scala territoriale.

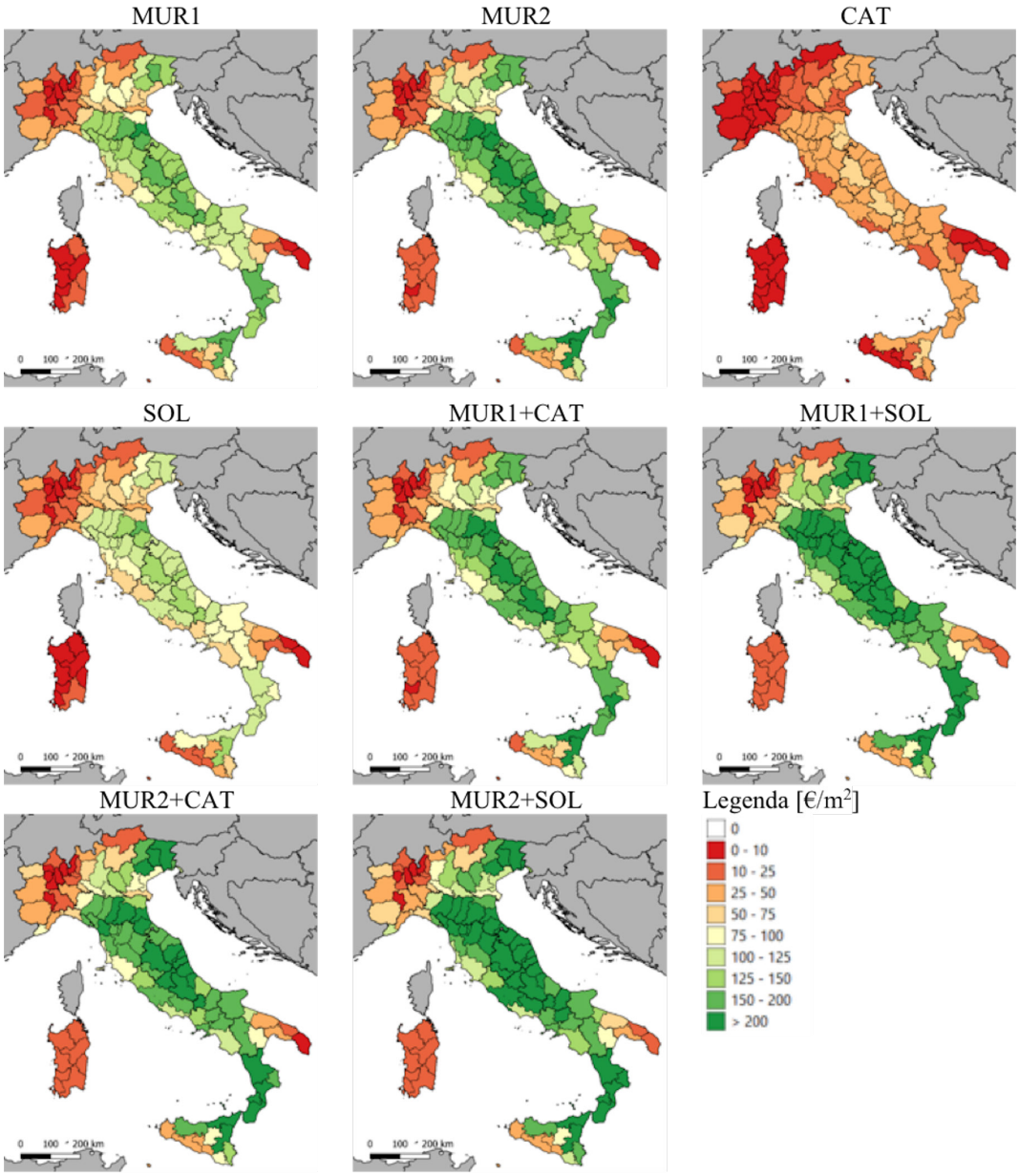


Fig. 1 - Mappe di beneficio normalizzato riferite agli interventi di retrofit considerati, per l'epoca Pre-1919.

Conclusioni. Le curve di fragilità elaborate permettono di produrre mappe di rischio sismico relative al patrimonio edilizio residenziale in muratura italiano, che mostrano la differenza in termini di perdite economiche tra la configurazione *as-built* e quella relativa all'applicazione sistematica di diversi interventi di retrofit.

Le mappe presentate in questo lavoro possono rappresentare strumenti essenziali per le autorità e gli enti gestori del rischio (come il Dipartimento della Protezione Civile), al fine di promuovere una mitigazione del rischio il più possibile mirata a livello nazionale.

Un possibile futuro sviluppo di questo lavoro è quello di svolgere analisi di rischio più dettagliate tenendo in considerazione, ad esempio, le perdite economiche indirette e le perdite di vite umane. Infine, stimando il costo di implementazione dei vari interventi considerati, si potranno svolgere delle analisi di costo-beneficio per avere indicazioni sulla convenienza economica degli interventi in varie zone d'Italia, informazione necessaria per operare una prioritizzazione degli stessi.

Riconoscimenti. Si ringrazia il Dipartimento della Protezione Civile Italiana, che ha finanziato questo studio nell'ambito del Progetto ReLUIS-DPC 2019-2021 - Work Package 4: MARS (MAps of Risk and Scenarios of seismic damage) - Task 6: Strategie preventive.

Bibliografia

Borzi B., Onida M., Faravelli M., Polli D., Pagano M., Quaroni D., Cantoni A., Speranza E. and Moroni C.; 2021: *IRMA platform for the calculation of damages and risks of Italian residential buildings.* Bull. Earthq. Eng, **19(8)**, 3185-3208. https://doi.org/10.1007/s10518-020-00924-x

CNR-DT - Consiglio Nazionale delle Ricerche; 215/2018: *Istruzioni per la progettazione, l'esecuzione ed il controllo di interventi di consolidamento statico mediante l'utilizzo di compositi fibrorinforzati a matrice inorganica.* Roma, 2019.

da Porto F., Valluzzi M.R., Munari M., Modena C., Arêde A., Costa A.; 2018: *Strengthening of stone and brick masonry buildings.* In: Costa A., Arêde A., Varum H. (eds.), Strengthening and retrofitting of existing structures, Series: Building Pathology and Rehabilitation, Vol. IX, Springer, 59-84; https://doi.org/10.1007/978-981-10-5858-5_3.

da Porto F., Donà M., Rosti A., Rota M., Lagomarsino S., Cattari S., Borzi B., Onida M., De Gregorio D., Perelli F. L., Del Gaudio C., Ricci P. and Speranza E.; 2021: *Comparative analysis of the fragility curves for Italian residential masonry and RC buildings.* Bull. Earthq. Eng, **19(8)**, 3209–3252, https://doi.org/10.1007/s10518-020-01009-5

Di Ludovico M., Prota A., Moroni C., Manfredi G. and Dolce M.; 2017a: *Reconstruction process of damaged residential buildings outside historical centres after the L'Aquila earthquake: part I—"light damage" reconstruction*. Bull Earthq Eng. https ://doi.org/10.1007/s1051 8-016-9877-8

Di Ludovico M., Prota A., Moroni C., Manfredi G. and Dolce M.; 2017b: *Reconstruction process of damaged residential buildings outside historical centres after the L'Aquila earthquake: part II—"heavy damage" reconstruction.* Bull Earthq Eng. https ://doi.org/10.1007/s1051 8-016-9979-3

Dolce M., Prota A., Borzi B., da Porto F., Lagomarsino S., Magenes G., Moroni C., Penna A., Polese M., Speranza E., Verderame G. M. and Zuccaro G.; 2021: *Seismic risk assessment of residential buildings in Italy*. Bull. Earthq. Eng, **19(8)**, 2999-3032. https://doi.org/10.1007/s10518-020-01009-5

Donà M., Carpanese P., Follador V., Sbrogiò L. and da Porto F.; 2021: *Mechanics-based fragility curves for Italian residential URM buildings.* Bull. Earthq. Eng, **19(8)**, 3099-3127. https://doi.org/10.1007/s10518-020-00928-7

DPC - Dipartimento della Protezione Civile Italiana; 2018: *National risk assessment - Overview of the potential major disasters in Italy: seismic, volcanic, tsunami, hydro-geological/hydraulic and extreme weather, droughts and forest fire risks*.

Follador V., Donà M., Carpanese P. and da Porto F.; 2021: *Fragility curves for Italian residential masonry buildings with retrofit interventions.* COMPDYN 2021, Athene, Greece, June 28-30, 2021, 3083–3097. https://doi.org/10.7712/120121.8698.18819

Giaretton, M., Dizhur, D., Garbin, E., Ingham, J. and da Porto, F.; 2018: *In-plane strengthening of clay brick and block masonry walls using textile-reinforced mortar*. J. Compos. Constr., **22(5)**. https:///doi.org/10.1061/%28ASCE%29CC.1943-5614.0000866

Grünthal G.; 1998: *European Macroseismic Scale*. Chaiers du Centre Européen de Géodynamique et de Séismologie, **15**, Luxembourg

Modena C., Casarin F., da Porto F., Garbin E., Mazzon N., Munari M., Panizza M. and Valluzzi M.R.; 2009: *Structural interventions on historical masonry buildings: review of Eurocode 8 provisions in the light of the Italian experience*. Cosenza E. (ed.) Eurocode 8 Perspectives from the Italian Standpoint, Doppiavoce, Napoli, Italy, 2009, pp. 225 – 236.

Saretta Y., Sbrogiò L., Valluzzi M.R.; 2021: *Seismic response of masonry buildings in historical centres struck by the 2016 Central Italy earthquake. Calibration of a vulnerability model for strengthened conditions*. Construction and Building Materials, 299:123911; doi: 10.1016/j.conbuildmat.2021.123911

Silva B., Dalla Benetta M., da Porto F. and Valluzzi M.R.; 2014a: *Compression and Sonic Tests to Assess Effectiveness of Grout Injection on Three-Leaf Stone Masonry Walls*. Int. J. Archit., **8**, 408-435. https://doi.org/10.1080/15583058.2013.826300

Silva B., Dalla Benetta M., da Porto F., Modena C.; 2014b: *Experimental assessment of in-plane behaviour of three-leaf stone masonry walls*. Construction & Building Materials, 53:149-161; doi: 10.1016/j.conbuildmat.2013.11.084

Valluzzi M.R., Garbin E., Dalla Benedetta M. and Modena C.; 2010: *In-plane strengthening of timber floors for the seismic improvement of masonry buildings*. World Conf. on Timber Engineering (WCTE), Curran Associates, Red Hook, NY, 2010.

Valluzzi M.R.; 2009: *Manuale d'uso del programma Vulnus_4.0*, programma originario di Bernardini A., Gori R., Modena C., versione Vb a cura di Valluzzi M.R., con contributi di Benincà G., Barbetta E., Munari M.

FRAGILITY CURVES FOR URM BUILDINGS TYPOLOGIES IN A HISTORICAL CENTER OF CENTRAL ITALY: THE INFLUENCE OF SEISMIC INPUT

V. Cima[1], V. Tomei[1], E. Grande[2], M. Imbimbo[1]

[1] Department of Civil and Mechanical Engineering, University of Cassino and Southern Lazio, Cassino, Italy
[2] Department of Engineering Science, University G. Marconi, Rome, Italy

Introduction. It is well known that unreinforced masonry building typologies (URM) of Italian historical centers are particularly vulnerable toward out-of-plane mechanisms (Sorrentino *et al.*, 2019), as even highlighted by recent seismic events of Central Italy (2016-2017). A first step toward prevention and mitigation actions, aimed to safeguard the building heritage of historical centers, is certainly represented by the prediction, at a large scale, of the potential damages that buildings may suffer after a seismic event of a certain intensity. The fragility curves can provide an adequate and useful tool for this purpose, as evidenced by numerous studies available in the current literature (Cima *et al.*, 2021a, 2021b, 2021c; Zucconi *et al.*, 2021).

The aim of this research is, then, to propose an approach for evaluating fragility curves of unreinforced masonry building typologies typical of a given geographical area with regard to the most probable out-of-plane mechanisms. The detection of these typologies is based on the data collected within the CARTIS project (DPC/ReLUIS 2019-2021) and reported in the CARTIS database (Zuccaro *et al.*, 2016). In the proposed procedure, both spectral-shapes derived by the Italian code and combinations of natural spectra, have been considered in order to analyze their influence on the fragility curves. The procedure is applied to the building typologies detected in the historical center of Sora in the province of Frosinone (Lazio Region), a medium size town of Central Italy assumed by the authors as a case study.

An approach for deriving typological fragility curves. Starting from the most common URM building typologies identified in the historical center of Sora within the CARTIS project (DPC/ReLUIS 2019-2021) and reported in the CARTIS database (Zuccaro *et al.*, 2016), the proposed approach leads to the derivation of typological fragility curves with regard to out-of-plane mechanisms for two different damage limit states DS_i: moderate damage and complete damage. The first limit state is representative of the activation of the mechanism while the second one is representative of the achievement of the Life-saving Limit State (Circolare 2019).



Fig. 1 - Maps of the historical center of Sora.

The approach foresees, for each of the identified typology, a preliminary analysis finalized to identify, on the basis of a qualitative approach, the most probable out-of-plane mechanism of each building (Saccucci *et al.*, 2019, 2021). In this context, the URM buildings of the historical center of Sora (Fig. 1) have been divided in two typologies, MUR 1 and MUR 2, which mainly differs in terms of age of construction and type of masonry, as reported in Tab.1.

Tab. 1 - Characteristics of the building typologies identified in the historical centers of Sora.

Building typology	**MUR 1**	**MUR 2**
Type of masonry	Irregular masonry with rough stones	Regular masonry with square stones
Age of Construction	<1860	1861-1945
Number of floors	2-4	2-4
Average floor height	2.5-3.49 m	2.5-3.49 m
Specific Use	Residential use, storage use	Residential use, commercial use, storage use
Slabs	Timber floors	Hollow core concrete
Roof	Gabled roof	Gabled roof and flat roof
Materials of the roof	Timber and reinforced concrete	Timber and reinforced concrete

On the basis of this preliminary analysis, the building typologies have been divided into categories, each one characterized by the same type of failure mechanism and the same number of floors. Subsequently, for each category, a virtual set of 3000 buildings has been generated through a Monte Carlo procedure, by varying the geometrical parameters that affect the out-of-plane behavior (wall thickness, story height, percentage of holes in the façade) and the masonry specific weight. In particular, the values of the geometrical characteristics have been generated by considering a lognormal distribution with the mean and the standard deviation derived from the collected data of the building typologies; the values of the masonry specific weight have been generated by considering a uniform distribution, assuming values that vary in the range suggested by the Italian code (Circolare 2019-Tab. C8.5.1).

Then, for each virtual building the proposed approach consists of the following steps:

- performing a non-linear kinematic analysis in order to evaluate the capacity curve of the considered mechanism under the following hypothesis: rigid block, no-tensile strength, limited compressive strength (Lagomarsino and Resemini, 2009) and absence of sliding between blocks;
- assessing, for each damage limit state DS_i, the corresponding damage thresholds, C_{DSi}, representative of the capacity of the mechanism;
- applying the Capacity Spectrum Method (Freeman, 1998) to define the maximum displacement demand for each damage level, D_{DSi};
- evaluating the Damage Indexes, DI_{DSi}, i.e. the ratio between the maximum displacement demand, D_{DSi}, and the damage threshold, C_{Dsi}, for each damage level.

The procedure ends with the derivation of the fragility curves for each identified category.

Regarding the damage thresholds, the first limit state is achieved when:

$$C_{DS1}=d_y \quad (1)$$

where d_y is the spectral displacement corresponding to the intersection between the capacity curve of the mechanism and a pseudo-elastic branch that describes the response of the structure until the activation of the mechanism (Circolare 2019). The second limit state is defined by the following damage threshold:

$$C_{DS2}=0.4\cdot d_0 \quad (2)$$

where d_0 is the spectral displacement corresponding to a spectral acceleration equal to zero.

In order to apply the Capacity Spectrum Method, the seismic input has been evaluated by considering the spectra obtained from spectrum-compatible accelerograms referring to 8 different return periods T_R. To this purpose, the software REXEL (Iervolino et al., 2010) has been employed.

For each damage limit state, DS_i, the fragility curve can be obtained as a function of a specific Intensity Measure IM, indicative of the intensity of the seismic input, through a conditional probability cumulative distribution function:

$$f_{DSi} = p\left(C_{DSi} \le D_{DSi|IM}\right) = p\left(DI_{DSi} \ge 1_{|IM}\right) \quad (3)$$

By considering the Peak Ground Acceleration, PGA, as IM, and assuming a log-normal distribution, fragility curves can be derived through the following equation (CNR-DT, 2014):

$$f_{DSi} = p\left(DI_{DSi} \ge 1_{|PGA}\right) = 1 - \Phi\left(\frac{\ln 1 - \mu_{\ln DI_{DSi|PGA}}}{\sigma_{\ln DI_{DSi|PGA}}}\right) = \Phi\left(\frac{\mu_{\ln DI_{DSi|PGA}}}{\sigma_{\ln DI_{DSi|PGA}}}\right) \quad (4)$$

where:

- $\Phi[\bullet]$ is the lognormal standard distribution function;
- $\mu_{lnDIiIPGA}$ is the mean value of the logarithm of the variable DI_{DSi} conditioned on the given value of PGA;
- $\sigma_{lnDIiIPGA}$ is the dispersion of the natural logarithm of the variable DI_{DSi} conditioned on the given value of PGA.

The conditional mean values of the variable DI_{DSi} have been defined for each value of the PGA through the following expression:

$$\mu_{\ln DI_{DSi|PGA}} = A_{DSi} + B_{DSi} \cdot \ln(PGA) \quad (5)$$

where A_{DSi} and B_{DSi} are coefficients obtained by a linear regression of the logarithm of the DI_{DSi} versus the logarithm of the PGA (Nielson and DesRoches, 2007).

On the other hand, the dispersion values have been evaluated through the following equation:

$$\sigma_{\ln ID_{DSi|PGA}} = \sqrt{\sigma_m{}^2 + \sigma_{rtr}{}^2} \quad (6)$$

where:

- σ_m represents the uncertainty of the model, estimated applying the equation:

$$\sigma_m = \sqrt{\frac{\left(\sum_i^{nPGA} \ln(DI_{50}) - (A_{DSi} + B_{DSi} \cdot \ln(PGA))\right)^2}{n-2}} \quad (7)$$

being n the number of the generated virtual buildings;

- σ_{rtr} represents the uncertainty due to the record-to-record variability, estimated as (Lagomarsino and Cattari, 2014):

$$\sigma_{rtr} = \frac{1}{2} \cdot \left| \ln\bar{D}I_{16} - \ln\bar{D}I_{84} \right| \quad (8)$$

In the last two equations, DI_{50}, DI_{16} and DI_{84} denote the variables representative of the damage state evaluated by considering the 50th, 84th and 16th percentile of the selected records, respectively.

Finally, to analyze the effect of the response spectra shapes on the fragility curves, these latter have been derived by using also the spectra proposed by the Italian code (NTC 2018). To this purpose the dispersion σ_{rtr} has been assumed equal to the one derived from the accelerograms selected with REXEL.

Results and discussion. Some of the results obtained by the proposed approach are herein reported in terms of fragility curves (Fig. 2) for the two structural typologies MUR1 and MUR2 defined in Table 1. In particular, they refer to the set of two-storey buildings, of MUR1 and MUR2, prone to the global overturning mechanism (Fig. 2a) and to the global overturning along openings (Fig. 2b). The fragility curves shown in red colour are evaluated by considering the spectral shapes derived by natural accelerograms (REXEL), while the ones in blue colour are evaluated by considering the smoothed spectra proposed by the Italian code (NTC 18).

In this context, it is important to highlight that in the first case the record-to-record variability has been taken into account by means of the dispersion σ_{rtr} directly evaluated on the natural records, while in the second case (smoothed spectra proposed by the Italian Code), the dispersion σ_{rtr} has been set equal to the ones evaluated on natural records. It means that the blue and red curves have the same value of the record-to-record variability, but different model dispersions and different values of $\mu_{lnDI|PGA}$. Despite this, the fragility curves appear similar to each other, and in particular those evaluated through the NTC18 spectra show to be more conservative. This suggests that, for the sake of simplicity, it is possible to obtain realistic

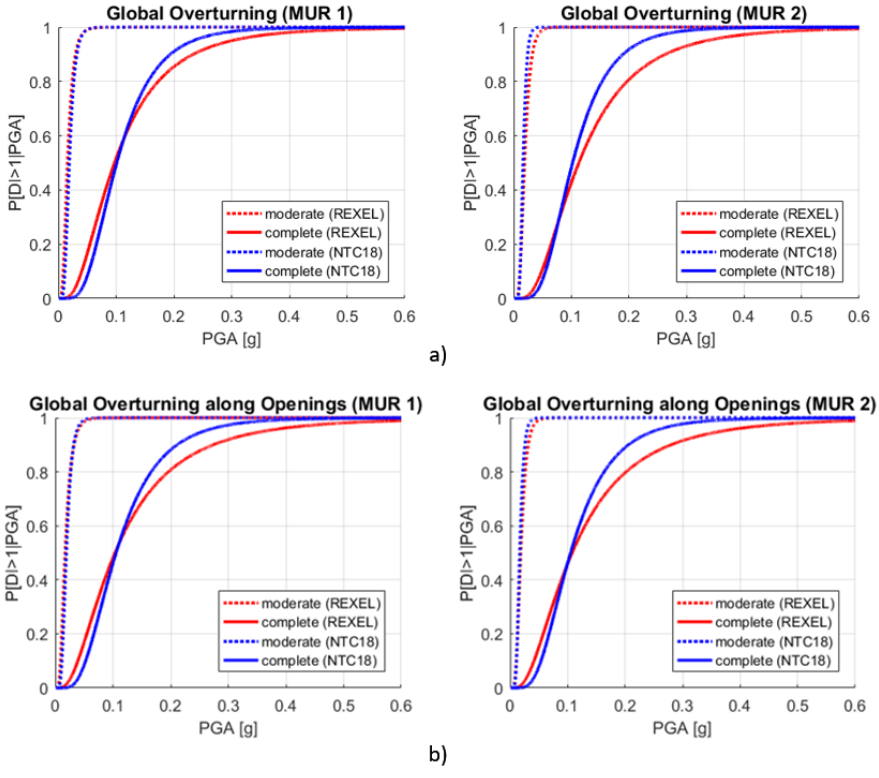


Fig. 2. Fragility curves for the set of two-storey buildings, be parto of the two structural typologies MUR 1 and MUR 2: a) global overturning mechanism; b) global overturning along openings.

results by employing the smoothed spectra derived by the Italian Code (NTC18), provided that a record-to-record variability is derived a priori on natural records.

In conclusion, the proposed approach constitutes a practical tool to carry out large-scale vulnerability assessments of existing buildings and, with this meaning, it could be useful as a decision-making tool in order to identify the most vulnerable area of a specific region and, thus, the priority of interventions. In this context, the presence of specific databases able to support the construction of reliable fragility curves are of particular importance. In this regard, the CARTIS project assumes a fundamental role, in that it pursues the objective of collecting the main characteristics of existing buildings, through the compilation of specific forms, and making them available to the scientific community.

Acknowledgments. The financial support by ReLUIS (Network of the Italian University Laboratories for Seismic Engineering – Italian Department of Civil Protection) is gratefully acknowledged.

References

Cima V., Tomei V., Grande E. and Imbimbo M.; 2021a: *Curve di fragilità per meccanismi di collasso fuori piano di tipologie edilizie in muratura rappresentative dell'edificato dei centri storici del basso Lazio*. GNGTS 2021, on line, in press.

Cima V., Tomei V., Grande E. and Imbimbo M.; 2021b: *Fragility curves at regional basis for unreinforced masonry buildings prone to out-of-plane mechanisms: the case of Central Italy*. Structures, 34, 4774–4787. https://doi.org/10.1016/j.istruc.2021.09.111.

Cima V., Tomei V., Grande E. and Imbimbo M.; 2021c: *Seismic vulnerability of Italian historical towns: the case of Borgo San Rocco*. In: "Proceedings of the 22nd Conference on the Rehabilitation and Reconstruction of Buildings". Advances in Science and Technology, 109, pp.1–7. https://doi.org/10.4028/www.scientific.net/AST.109.1

CNR-DT; 2014: *Istruzioni per la Valutazione Affidabilistica della Sicurezza Sismica di Edifici Esistenti CNR-DT 212/2013.* CNR – Commissione Di Studio per La Predisposizione e l'analisi Di Norme Tecniche Relative Alle Costruzioni.

Freeman S. A.; 1998: *The Capacity Spectrum Method as a Tool for Seismic Design*. In: "Proceedings of the 11th European conference on earthquake engineering", France: Paris, pp. 6-11.

Iervolino I., Galasso C. and Cosenza E.; 2010: *REXEL: Computer aided record selection for code-based seismic structural analysis*. Bulletin of Earthquake Engineering, 8, 339–362. https://doi.org/10.1007/s10518-009-9146-1.

Lagomarsino S., and S. Resemini, 2009, The assessment of damage limitation state in the seismic analysis of monumental buildings: Earthquake Spectra.

Lagomarsino, S. and S. Cattari; 2014: *Fragility Functions of Masonry Buildings*: In: Pitilakis, K., Crowley, H., Kaynia, A. (eds) SYNER-G: Typology Definition and Fragility Functions for Physical Elements at Seismic Risk. Geotechnical, Geological and Earthquake Engineering, 27. Springer, Dordrecht. https://doi.org/10.1007/978-94-007-7872-6_5.

Nielson B. G. and R. DesRoches; 2007: *Seismic fragility methodology for highway bridges using a component level approach.* Earthquake Engineering and Structural Dynamics, 36(6), 823-839.

Saccucci M., Cima V., Grande E., Imimbo M. and Pelliccio A.; 2019: *Valutazione della vulnerabilità sismica degli aggregati in muratura: il caso di Borgo San Rocco a Sora (Italia)*. In: "Proceedings of the XVIII ANIDIS Conference Seismic Engineering in Italy". Ascoli Piceno, pp. 152 – 162.

Saccucci M., Cima V., Grande E., Imimbo M. and Pelliccio A.; 2021: *The Knowledge Process in the Seismic Assessment of Masonry Building Aggregates – An Italian Case Study*. In: "International Conference on Critical Thinking in Sustainable Rehabilitation and Risk Management of the Built Environment", Springer, Cham, pp. 330–347.

Sorrentino L., Cattari S., da Porto F., Magenes G. and Penna A.; 2019: *Seismic behaviour of ordinary masonry buildings during the 2016 central Italy earthquakes*. Bulletin of Earthquake Engineering, 17, 5583–5607. https://doi.org/10.1007/s10518-018-0370-4.

NTC18; 2018: *Aggiornamento delle "Norme Tecniche per le Costruzioni"* (in Italian). Ministerial Decree 17 January 2018.

Circolare 2019; 2019: *Istruzioni per l'applicazione dell'«Aggiornamento delle "Norme tecniche per le costruzioni"» di cui al decreto ministeriale 17 gennaio 2018* (in Italian)**.**

Zuccaro G., Dolce M., De Gregorio D., Speranza E. and Moroni C.; 2016: *La Scheda Cartis Per La Caratterizzazione Tipologico- Strutturale Dei Comparti Urbani Costituiti Da Edifici Ordinari. Valutazione dell'esposizione in analisi di rischio sismico*. GNGTS 2015, Trieste, pp. 281-287.

Zucconi, M., Ferlito R. and Sorrentino L.; 2021: *Typological Damage Fragility Curves for Unreinforced Masonry Buildings affected by the 2009 L'Aquila*, *Italy Earthquake*. The Open Civil Engineering Journal, 15, 117–134. https://doi.org/10.2174/1874149502115010117.

FIRST RESULTS OF AMBIENT NOISE DATA ANALYSIS FROM THE ONGOING SEISMIC MICROZONATION OF THE APULIA REGION

V. Del Gaudio[1], J. Wasowski[2], C. Magrì

[1] Dipartimento di Scienze della Terra e Geoambientali, Università degli Studi di Bari "Aldo Moro"– Bari, Italy
[2] Consiglio Nazionale delle Ricerche – Istituto di Ricerca per la Protezione Idrogeologica - Bari, Italy

Introduction. Seismic Microzonation (SM) of Italy is ongoing according to standardised rules, with the financial support of the National Civil Protection Department and co-funded by the Regional Administrations. The main purpose is to provide the municipalities exposed to seismic risk with information needed to increase the safety level in the design of engineering structures and to optimise the urban planning provisions. One of the products expected from the SM investigations is a map of the site resonance frequencies, based on the results of acquisition and analysis of ambient noise data processed with the technique of the calculation of the horizontal-to-vertical spectral ratios (HVSR - Nakamura 1989). According to the national provisions, such a map is required at a first stage of the SM to provide information useful for earthquake resistance design and for the definition of the geological model to be used in the numerical analysis of local site response properties.

Apulia present rather heterogeneous conditions in terms of distances from seismogenic zones and with regard to local geological-geomorphological conditions. Major seismogenic structures within the Apulian territory are located in its northernmost area (Foggia Province - cf. Del Gaudio *et al.*, 2007). However, damaging effects can derive from earthquakes occurring in the southern Apennines or in Adriatic-Ionian areas facing the Apulia coasts, especially in presence of local conditions for site amplification.

There is a lack of rigorous observations on the effects of strong earthquakes in Apulia. Therefore, it is crucial to have the possibility of assessing the potential impact of future earthquakes based on a combination of detailed geological mapping, ambient noise analysis and numerical modelling. The present study reports the first outcomes derived from the implementation of systematic ambient noise analysis in Apulia within the SM investigations in progress.

Geological Context. The Apulian territory extends through a variety of geological domains with different litho-stratigraphic and structural characteristics. The north-western part of Apulia includes the Daunia Mountains, which are made of the frontal thrust sheets of the southern Apennine chain and are characterized by a diffuse presence of clay-rich flysch sequences. To the east of the Daunia Mountains there is the Tavoliere area, which represents a part of the Apenninic foredeep; this area includes few hundred meter thick alluvial plain deposits overlying a carbonate platform. Still further east, there is the Apulian carbonate platform, locally constituting the Apennine chain foreland. This area includes two major blocks separated by transverse fault systems: i) the Gargano plateau, to the north, more uplifted and affected by active fault systems, and ii) the Murgian plateau, topographically lower and less seismically active. Recent deposits of incoherent materials of different types locally cover both blocks.

Ambient noise measurements. Measurements of ambient noise were carried out in different municipalities at sites assumed to have different seismic responses and within the zones most relevant for the SM, e.g. in built up areas or near strategic infrastructures for the emergency management. At this stage, the measurements were acquired for 6 municipalities located on the Daunia Mountains, 6 in the Tavoliere plain and 3 in the Gargano area. Overall, 589 noise recordings at 345 sites have been acquired to date.

The ambient noise data have been acquired with different instruments and processed using different software. The guidelines given to professionals recommend the acquisition of

recordings at each site preferably in a couple of distinct but close locations, rather than at a single station. In this way, the check of the representativeness of the results for the area surrounding the measurement site is facilitated. Previous studies reported that, while the resonance frequencies resulting from different acquisitions are generally consistent, variations of environmental conditions can determine strong changes in the amplitude of the H/V spectral peaks, likely for changes in the composition of the noise wavefield (cf. Del Gaudio *et al.*, 2021). Furthermore, sometimes a poor ground/sensor coupling can lead to an underestimate of the amplitude of the resonance effects. Therefore, on the final map of site resonances, we suggest to report the mean value of frequency and amplitude of the H/V peaks obtained from the couple of measurements if they appear consistent. When the two measurements provide rather different amplitudes, we advocate the selection of the major peak for the most relevant resonance frequency.

H/V results and comparisons. The first H/V results pointed out some peculiarities in the pattern of resonance properties in the different macro-areas so far investigated.

Regarding the Daunia Mountains, there are rapid spatial variations in resonance in relation to the heterogeneities of mechanical properties of different flysch materials even within the same geological unit. However, in general, H/V ratios do not show high values and very clear peaks, likely for the lack of strong impedance contrasts between surface materials and the underlying units. Indeed, a competent rocky substratum is often found at considerable depths. Figure 1 shows an example from the Municipality of Volturara Appula (FG), where clear H/V peaks with amplitude ≈ 3-4 at frequencies of 3-4 Hz characterize sites within outcropping quartzarenites of the "Flysch Numidico" and on the pelitic facies of the "Flysch di San Bartolomeo". No evident peaks were observed at sites located on the arenaceous facies of the latter Flysch or on the chaotically deformed clay-rich "Flysch Rosso". Locally on slopes, the presence of significant resonance can be also related to the impedance contrast between landslide bodies and a stiffer substratum.

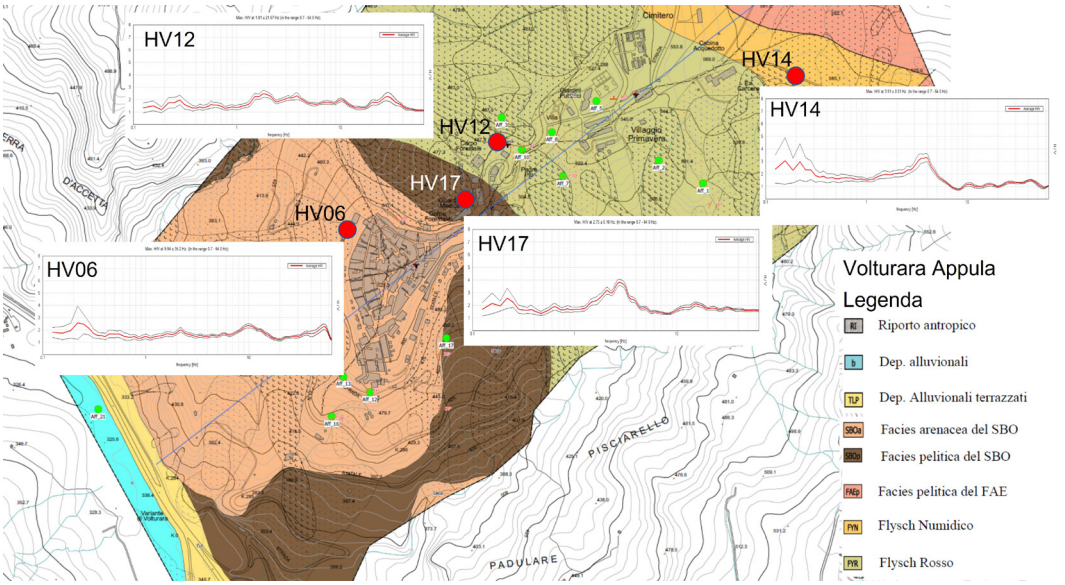


Fig. 1 - Geological map of the municipality of Volturara Appula involved in the SM studies. Red dots represent the locations of ambient noise measurement sites on the outcrops of: arenaceous (HV06) and pelitic (HV17) facies of the Flysch di San Bartolomeo, the "Flysch Rosso" (HV12), consisting of clays/clay-shales, and the quartzarenitic "Flysch Numidico" (HV14). The results of the HVSR analysis are shown as insets (data from Gruppo di Lavoro ASSET, 2022).

Differently, the area of the Tavoliere plain is characterized by a diffuse presence of pronounced low frequency resonances (< 1 Hz) related to the impedance contrast between the deepest foredeep deposits, consisting of Early Pleistocene clays ("Argille Subappennine"), and the underlying Cretaceous carbonate rocks of the Apulian platform. The resonance frequencies show regional variations: for instance at Foggia, in the central part of the plain they are observed at 0.2-0.4 Hz, whereas at Trinitapoli, few km away from the Adriatic coast, they are found at 0.6-0.7 Hz. This variation can correspond to a decrease of the depth of the calcareous substratum which, according to the borehole stratigraphy (Foggia_003: cf. Cavinato *et al.*, 2010) is at about 550 m under Foggia, whereas it could be approximately halved under Trinitapoli.

The above-mentioned resonance frequencies are considered as the fundamental site resonance frequencies (labelled as F0), but they fall outside the most relevant frequency range for the SM mapping (0.9 – 10 Hz). Thus, they can be of interest just for the definition of the geological model of the study area. However, there are also secondary resonances (labelled as F1/F2 for increasing frequencies), which appear in relation to the presence of layering within the foredeep deposits (e.g., between the "Argille Subappennine" and more recent alluvial deposits), or even, within both of these deposits. These additional resonances show a more irregular spatial distribution, as effect of local variations of the deposits' composition (e.g. for the presence of sandy or conglomeratic bodies). There is scarcity of direct information on the compositional variations of the deposits, because the available boreholes are generally shallow (in the order of 20 m). Thus, the resonance frequencies revealed by ambient noise analysis are valuable to distinguish areas with potentially different site response properties.

As an example, a diffuse "sampling" of the resonance frequencies at Foggia pointed out the presence of zones with the first secondary resonance frequency (F1) between 0.6 - 0.9 Hz, 5 -10 Hz, 10 – 20 Hz or over 20 Hz, and in some cases with the presence of peaks within more than one of these ranges (Fig. 2). Even where these resonances are scarcely significant

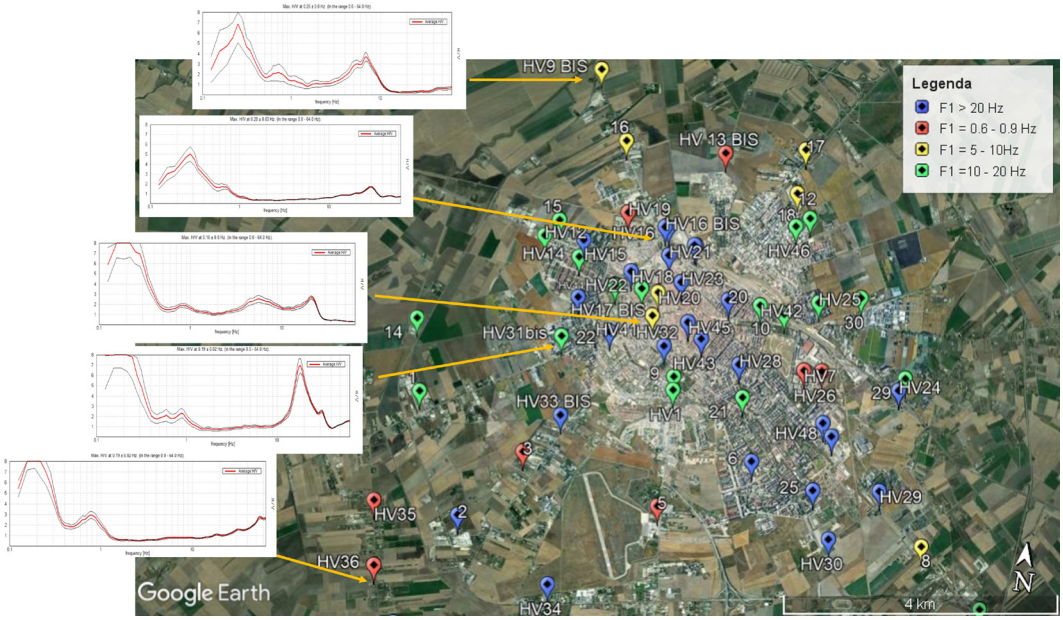


Fig. 2 - Examples of HVSR results obtained at Foggia by Cardillo, 2022. Sites differing by the range of the most clear secondary resonance frequency F1 are labelled with different colours. In some cases, few peaks can be recognised within different frequency bands, in relation to the resonances caused by laterally discontinuous layering observed within the foredeep deposit at different depths.

for ordinary building design, they provide additional details for the geological modelling that represents the basis for successive numerical simulations of the site response.

The sites investigated on the Gargano plateau are characterized by the presence of carbonate rocks whose age ranges from Cretaceous to Eocene. Although the outcropping units consist of stiff rocks, they are locally intensely fractured (e.g., along major faults) or covered by incoherent deposits derived from the dismantling of the same rocks. The thickness of such deposits can amount up to a few tens of meters. The variability of site conditions is reflected by the presence of alternance of sites with flat HVSR curves in the range 0.9-10 Hz and sites where pronounced peaks are observed in the same range. Figure 3 shows examples from the municipality of San Marco in Lamis, whose built up area is located in a valley filled with eluvial-colluvial materials. Such setting leads to strong resonance effects at frequencies variable from 4 to 8 Hz, with a frequency increase likely associated to the thinning of the deposit. The resonances found at frequencies higher than 10 Hz reflect the presence of thinner surficial layers of softer material (e.g., soils or anthropic backfill). Where carbonate rocks crop out, the HVSR values are lower and typically below the threshold of significance for the identification of site amplification effects (commonly considered at the level of H/V = 2); moderate peaks are locally observed at frequencies around 10 Hz or higher, possibly related to the presence of surface layers of weathered/fractured rock.

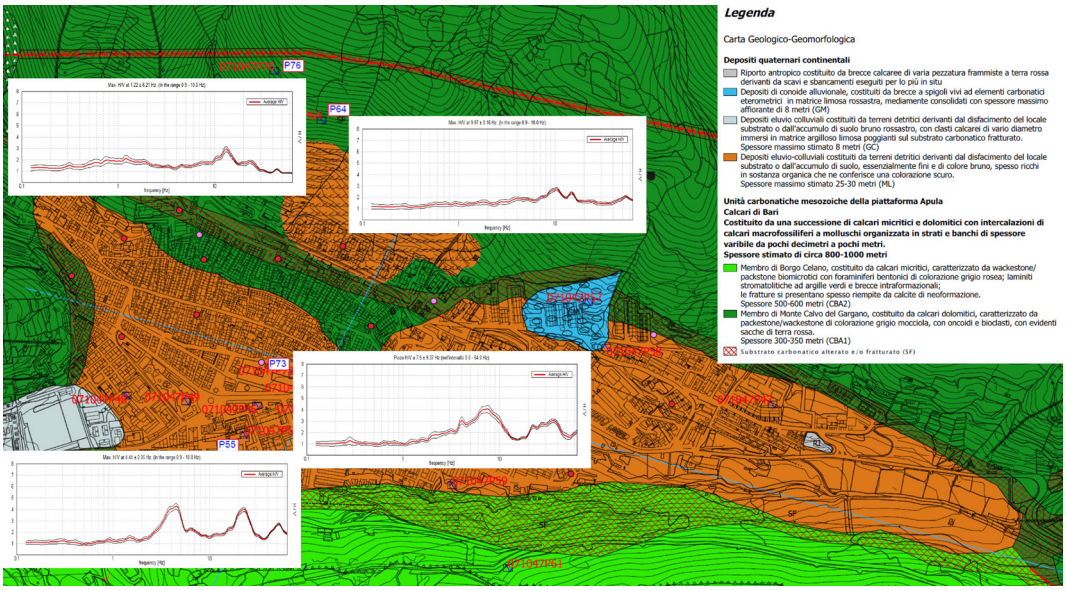


Fig. 3 - Geological map of the area investigated during the SM of San Marco in Lamis (FG) with few examples of the results of HVSR analysis of ambient noise data (after Pitullo, 2022).

Conclusion. The ongoing Seismic Microzonation of 84 Apulian municipalities offers the opportunity to acquire a large amount of valuable data for the assessments of local seismic hazard in a region where this kind of efforts have until now been almost neglected. In this context, ambient noise analysis based on the HVSR technique allowed us to recognise a variety of litho-stratigraphic conditions that can lead to seismic ground motion amplifications. At this regard, quite different situations are encountered in the main geological domains of the Apulia region: the investigated sites in the Daunia Mountains show generally moderate resonance phenomena with short distance variations related to the diffuse presence of heterogeneous flysch materials and the absence of a shallow stiff substratum; the sites in the Tavoliere plain present strong resonance peaks at very low (< 0.9 Hz) frequencies (irrelevant

for the SM purposes), related to the impedance contrast between the foredeep deposits and deep carbonate substratum; the Gargano area is locally characterized by strong resonance phenomena at frequencies affecting the seismic response of ordinary building, especially in the presence of few tens of meters thick incoherent deposits directly overlying a stiff carbonate substratum.

Acknowledgements. This study was conducted with the financial support of the National Department of Civil Protection and of the Civil Protection Office of the Apulian Regional Administration. We are grateful to Eng. Tiziana Bisantino for the support provided to our studies as responsible for the management of the SM activity for the Regional Civil Protection Office. This study reports a summary of the advances in knowledge on local seismic hazard gained by the authors during their activity of assistance in the acquisition and processing of data by a large number of professionals involved in the seismic microzonation of Apulia. We express our gratitude to all of them.

References

Gruppo di lavoro ASSET - Agenzia Strategica per lo Sviluppo Ecosostenibile del Territorio della Regione Puglia (M. Luisi, G. Vessia, D. Bruno, D. Milella, D. Attolico, N. Florio, L. Grosso, T. Scolamacchia and A. Valerio); 2022: *Microzonazione sismica di livello I - Relazione Illustrativa – Regione Puglia – Comune di Volturara Appula (FG)*, 142 pp.

Cardillo G.; 2022: *Microzonazione sismica di livello I - Relazione Illustrativa – Regione Puglia – Comune di Foggia*, 132 pp.

Cavinato G. P., Cavuoto G., Coltella M., Cosentino G., Paolucci E., Peronace E. and Simionato M.; 2010: *Studio di fattibilità per il monitoraggio e la messa in sicurezza delle aree urbane a rischio di stabilità statica e vulnerabilità strutturale del Comune e della Provincia di Foggia - CIPE 20/2004. Rapporto Tecnico Scientifico IGAG, 526 pp.*

Del Gaudio V., Pierri P., Frepoli A., Calcagnile G., Venisti N. and Cimini G.; 2007: A critical revision of the seismicity of Northern Apulia (Adriatic Microplate - Southern Italy) and implications for the identification of seismogenic structures. Tectonophysics, 436 (1/4), 9-35, doi:10.1016/j.tecto.2007.02.013.

Del Gaudio V., Wasowski J., Pierri P., Moretti A. and Ferrini G.; 2021: *Multi-temporal analysis of ambient noise polarization to characterize site response in the town of Amatrice, shattered by the 2016 central Italy earthquake*. Geophys. J. Int., 224, 739–759, doi: 10.1093/gji/ggaa335.

Nakamura Y.; 1989: *A method for dynamic characteristics estimation of subsurface using microtremor on the ground surface*. Q Rep Railw Tech Res Inst 30:25–33.

Pitullo G.; 2022: *Microzonazione sismica di livello I - Regione Puglia – Comune di San Marco in Lamis.*

IRPINIA 1980-2020: OCCUPARSI DI RISCHIO SISMICO DURANTE UNA PANDEMIA

E. Ercolani[1], F. Brasini[2], V. Castelli[1], D. Modonesi[2], V. Pessina[3], R. Camassi[1]

[1] INGV - Istituto Nazionale di Geofisica e Vulcanologia, Sezione di Bologna, Italy
[2] CUG - Con Un Gioco, Cooperativa sociale, Roma, Italy
[3] INGV- Istituto Nazionale di Geofisica e Vulcanologia, Sezione di Milano, Italy

Introduzione. Nell'anno scolastico 2020-2021 il progetto EDURISK (Camassi *et al.*, 2004; 2005) ha attivato un progetto educativo sul tema del rischio, coinvolgendo alcuni Istituti Comprensivi dell'Irpinia (Tabella 1) in una riflessione sul terremoto del 23 novembre 1980.

Questo evento, oltre ad essere, ad oggi, il più forte terremoto della storia italiana recente, ha coinvolto l'intera comunità nazionale, lasciando tracce profonde nel territorio e nelle menti e determinando cambiamenti importanti nella società, a partire dalla nascita del Servizio Nazionale della Protezione Civile, che ha rivoluzionato l'approccio al tema della riduzione dei rischi, con il coinvolgimento sempre più forte dei cittadini nelle strategie di riduzione dei rischi, sia individualmente che come associazioni di volontariato.

Il quarantennale del terremoto ha dato l'occasione per ripensare a temi molto importanti per le nostre comunità: cosa sappiamo sulla pericolosità sismica, dopo quarant'anni di studi geologici, sismologici e storici; quale consapevolezza del rischio hanno i nostri territori; se e come abbiamo ridotto la vulnerabilità delle nostre case, qual è oggi la nostra capacità di risposta a un evento del genere; quale è il ruolo dei cittadini.

Riflettere su un terremoto mentre la società si scopriva impreparata e vulnerabile di fronte a un rischio sanitario avrebbe potuto sembrare fuori luogo. Ma è proprio in momenti simili che le comunità possono toccare con mano quanto le scelte attive dei cittadini, i comportamenti individuali e il rispetto delle regole siano importanti per ridurre un rischio che coinvolge tutti.

Tab. 1 - Scuole coinvolte nel "Progetto Irpinia" (2020-2021).

Istituto comprensivo [IC] [Scuola primaria e secondaria]	Località	Insegnanti coinvolti	Classi scuola primaria	Classi scuola secondaria
IC "A. Manzi", Calitri	Calitri	4	2	2
	Conza della Campania	1	1	
	Sant'Andrea di Conza	1		1
IC Colle Sannita	Colle Sannita	3		2
	Circello	1		1
IC	Rionero in Vulture	6	4	2
IC "Tasso"	Bisaccia	3		3

Il "Progetto Irpinia". Il primo tema divenuto centrale nello sviluppo di progetti educativi per le scuole è stato quello dell'esigenza di trasformare tutte le attività in formato gestibile a distanza, esigenza divenuta tassativa solo a inizio autunno. Già dai primi mesi del 2020, tuttavia, lo staff EDURISK aveva ideato una serie di attività realizzabili sia autonomamente dalle scuole (con assistenza da remoto) sia in modalità digitale con la presenza in diretta di componenti dello staff EDURISK (Ercolani *et al.*, 2022).

Le enormi difficoltà che le scuole hanno dovuto affrontare nella seconda parte dell'anno scolastico 2019-2020, infatti, sono state motivo di mobilitazione per rendere disponibili proposte di attività che potessero aiutare insegnanti e studenti ad affrontare una situazione tanto complessa. Per questo, già nella primavera del 2020, a tutti gli Istituti che avevano manifestato interesse per il progetto è stata fornita una proposta di lavoro sul tema del rischio,

descritta più avanti, che diversi insegnanti hanno sperimentato come occasione di riflessione sul particolare momento che stavano vivendo.

Dopo numerosi contatti con la rete di scuole interessate, abbiamo concordato una soluzione digitale del progetto, basata su incontri preparatori con insegnanti e una serie di incontri laboratoriali con una selezione di classi.

La formazione degli insegnanti. La prima fase del progetto ha coinvolto gli insegnanti in un percorso di lavoro organizzato su tre incontri. Il primo è stato dedicato - attraverso giochi di ruolo - a riflettere su come il tema del rischio terremoto riguarda ciascuno di noi, come individui, come cittadini e come comunità. I temi della cittadinanza, della responsabilità e del rispetto delle regole sono diventati immediatamente centrali.

Nella seconda fase è stato approfondito il tema del rischio sismico, con attività e modelli ad hoc: individuazione del problema, elaborazione dei dubbi e delle diverse visioni relative al rischio e ai modi per affrontarlo (giochi di ruolo, attività di dibattito e confronto). Uno dei temi più sviluppati è stato quello della condivisione delle conoscenze sulla storia sismica del territorio, attraverso la condivisione di memorie prossime personali o familiari: un tema che sarebbe poi divenuto centrale anche nei laboratori svolti con le classi e che per questo è stato oggetto di progettazione con gli insegnanti nella terza fase della formazione.

Il passaggio finale è stato infatti quello della progettazione didattica collettiva di attività che sono poi state realizzate nelle classi.

I laboratori interattivi. Il lavoro nelle classi, svolto per forza di cose a distanza, comprendeva tre tipi di attività: un "gioco di discussione" destinato a chiarire il concetto di rischio, i diversi atteggiamenti individuali possibili nei confronti del rischio, le responsabilità che entrano in gioco, le incertezze che si possono provare ecc.; un "gioco di invenzione narrativa", consistente nello scrivere e illustrare una storia a partire da uno schema comune; e la raccolta di storie e testimonianze familiari sul terremoto del 1980 o su altri terremoti.

Il gioco del rischio. Il primo laboratorio mirava ad avviare una discussione sul tema del rischio a partire da un gioco di ruolo basato su situazioni realistiche, come quella di un gruppo di amici che, durante una escursione nel bosco, si trova improvvisamente bloccato da un incendio. I partecipanti sono stati invitati a considerare tre possibili soluzioni per superare il blocco, analizzando le possibili conseguenze di ciascuna di esse, le proprie sensazioni e le scelte che avrebbero fatto. La discussione scaturita da questa proposta è stata sempre molto interessante e si è spontaneamente focalizzata su temi delicati, come l'incertezza con cui ci si deve confrontare in situazioni reali e l'esigenza di essere coinvolti nelle decisioni che possono avere conseguenze, dirette o indirette, per tutti noi.

Il terremoto immaginario. Il secondo laboratorio consisteva nell'inventare, raccontare e illustrare una storia in quattro episodi, a partire da uno schema predeterminato che prevedeva il verificarsi di un forte terremoto nell'Appennino meridionale. Nella composizione delle storie, di pura invenzione, i ragazzi hanno dovuto immaginare come potrebbe essere l'esperienza reale di un terremoto e quali conseguenze potrebbe avere. La discussione seguita alla condivisione delle storie ha consentito poi di riflettere sui tanti modi in cui si può pensare ad un evento del genere, provando anche a immaginare come comunicare ad altri ciò che si è imparato da questa esperienza.

A caccia di storie. Il terzo laboratorio, preparato in classe insieme agli insegnanti e in seguito condotto individualmente dagli studenti, prevedeva la raccolta e discussione di memorie personali di eventi calamitosi (terremoti ma non solo) interrogando familiari o conoscenti e

restituendone i ricordi in forma di intervista classica o di racconto libero. Per gli studenti questa è stata una occasione preziosa per discutere in famiglia di una esperienza ormai lontana nel tempo, ma di cui quasi tutti i genitori e parenti hanno fatto esperienza. Anche questa è stata un'opportunità per riflettere e discutere su una caratteristica del territorio di cui i ragazzi non avevano avuto esperienza diretta.

Dalle memorie alle tracce materiali e culturali. Fina dall'inizio il progetto EDURISK ha avuto come tema centrale il lavoro sulla memoria. La conoscenza di ciò che è avvenuto in un territorio nel passato aiuta a conoscere meglio quel territorio, ad apprezzarne le fragilità, a osservarne le trasformazioni riconoscendole come conseguenze di scelte fatte dalle comunità. Tutto il lavoro di raccolta, condivisione e discussione di memorie aveva proprio l'obiettivo di guidare i partecipanti a conoscere meglio il territorio in cui vivono e a riconoscerne le caratteristiche meno appariscenti.



Fig. 1 - Romagnano, insediamento abbandonato dell'Irpinia.

Nel passato dell'Irpinia ci sono diversi terremoti distruttivi, che nel corso dei secoli hanno lasciato tracce profonde in questo territorio. Tracce materiali, in primo luogo, a volte riconoscibili solo da occhi esperti, a volte invece ben visibili, in forme anche spettacolari. Tra esse quelle più drammatiche, dal punto di vista visivo ed emotivo, sono gli insediamenti abbandonati (Fig.1) (Camassi, 2004; Azzaro *et al.*, 2006; 2008). Se ne trovano un po' dappertutto in Italia ma l'Irpinia è particolarmente ricca di testimonianze di questo tipo, in qualche caso valorizzate da ottimi interventi di riqualificazione.

Più difficili da individuare, ma molto suggestive, sono le tracce culturali: tradizioni locali, religiose o laiche, il culto dei santi protettori da terremoti, riti e tradizioni, tracce linguistiche, ecc. Un lavoro che è emerso spontaneamente dalle attività laboratoriali del progetto è stato proprio quello del censimento di queste tracce, materiali e culturali ma tutte molto preziose per promuovere iniziative di sensibilizzazione e comunicazione del rischio.

Conclusioni. Questo percorso di educazione al rischio, sviluppato durante una particolarissima situazione di emergenza mondiale, in occasione del quarantennale di un forte terremoto, ha reso evidente quanto sia importante per le comunità locali, raccogliere, conservare e condividere le esperienze fatte, le 'storie individuali' di chi ne fa parte, per comprendere quanto siano importanti le scelte fatte come individui e come comunità. Questo percorso di ricostruzione della memoria, di conoscenza del proprio territorio e della sua storia è un approccio con cui le persone possono coltivare il proprio senso di appartenenza, condividere le proprie emozioni e sentirsi più profondamente coinvolti nella riduzione del rischio.

Riconoscimenti. Il lavoro è stato possibile grazie alla disponibilità e alla passione di Dirigenti e Insegnanti degli Istituti Comprensivi IC "A. Manzi", Calitri di Calitri, Conza della Campania e Sant'Andrea di Conza; degli Istituti Comprensivi IC "Colle Sannita" di Colle Sannita e Circello; dell'Istituto Comprensivo IC "Rionero in Vulture" di Rionero in Vulture; dell'Istituto Comprensivo IC "Tasso" di Bisaccia

Questo lavoro è stato realizzato nell'ambito della Convenzione fra INGV e Dipartimento nazionale della Protezione Civile, Allegato A, tematica "M"; rimane degli autori la responsabilità dei contenuti, che pertanto non riflettono necessariamente la posizione e le politiche ufficiali del Dipartimento

Bibliografia

Azzaro, R., Camassi, R., Cascone, M., Peruzza, L., Amantia, A., Guglielmino, F., Mangiagli, S.; 2006: *Earthquakes and ghost towns in Sicily (Southern Italy): a journey through the places of memory. A proposal of virtual seismic itineraries as an educational tool*. First European Conference on Earthquake Engineering and Seismology, 3-8 september 2006, Geneve (Switzerland), Abstract Book, SS-3, p. 149.

Azzaro, R., Cascone, M., Camassi, R., Amantia, A., Gugliemino, F., Mangiagli , S. Peruzza, L.; 2008: *Earthquakes and ghost towns in Sicily. A journey through places of memory*. EDURISK-INGV, Catania, DVD.

Camassi, R.; 2004: *I paesi abbandonati*. Parametro. Rivista internazionale di architettura e urbanistica, 251, 50-55.

Camassi, R., Azzaro, R., Castelli, V., La Longa, F., Meletti, C., Pessina, V., Peruzza, L.; 2004: *The EDURISK project: a recent experience in earthquake education in Italy*. XXIX General Assembly of the European Seismological Commission, Potsdam (Germany) September 12-17 2004, abstract, 17.

Camassi, R., Azzaro, R., Castelli, V., La Longa, F., Pessina, V., Peruzza, L.; 2005: *"Knowledge and practice". Educational activities for reduction of earthquake impact: the EDURISK project*, 250th Anniversary of the 1755 Lisbon Earthquake, 100-101.

Ercolani E., Camassi R., Brasini F., Modonesi D., Castelli V., Pessina V.; 2022: *Comunicare ed educare al rischio, le strade possibili.* Sottomesso.

GROUND MOTION SIMULATIONS OF THE HISTORICAL FABRIANO (1741, Mw=6.17) AND CAMERINO (1799, Mw=6.18) EARTHQUAKES (CENTRAL ITALY)

V. Gironelli[1,2], T. Volatili[1], L. Luzi[3], G. Brunelli[1,3], M. Zambrano[1], E. Tondi[1,2]

[1] School of Science and Technology – Geology Division, University of Camerino, Italy
[2] National Institute of Geophysics and Volcanology, Rome, Italy
[3] National Institute of Geophysics and Volcanology, Milan, Italy

The determination of the ground-shaking induced by destructive earthquakes is becoming a crucial aspect in the analysis of the seismic hazard assessment. The increasing importance in addressing the ground motion is related to the evaluation of the seismic site response in case of earthquake occurrence to plan the appropriate emergency activities, especially in areas characterised by an intense seismic history, as the Italian territory.

Peninsular Italy has a long-term seismicity testified by one of the most complete and historically extensive seismic catalogues in the World. Specifically, the high seismic activity of central Italy is broadly documented by seismic records since historical times. Recent seismicity is testified by three destructive seismic sequences which struck central Apennines with moderate to significant mainshock magnitudes ($5.7 \leq Mw \leq 6.5$), the 1997 Colfiorito, the 2009 L'Aquila and the 2016-2017 Central Italy sequences.

Seismic hazard studies aimed at the ground motion assessment in earthquake scenarios are based on the seismological parameters reported in the instrumental seismic catalogues. Currently, there are powerful applications like the software package ShakeMap® developed by the U. S. Geological Survey Earthquake Hazards Program (Wald *et al.*, 2005) which, through an interpolation algorithm, exploits the instrumental data to rapidly assess the intensity of the ground shaking generated by the earthquake. However, the accuracy of these tools diminishes in estimating the ground motion for poorly constrained events like historical earthquakes due to the increasing number of uncertainties (i.e., absence of strong motion records, estimated magnitudes and epicenters location, unknown or debated seismogenic sources, etc.). Besides the disadvantages associated with the pre-instrumental seismicity, the uncertainty associated with the local site conditions imposed is the crucial aspect of this procedure.

In this study, we propose an alternative approach for generating ground motion simulations through a Geographical Information System (GIS) to ensure a more flexible customisation of the input parameters relatively designed for specific study cases.

A parameter to account for the local site amplifications, is the average shear wave velocity of the uppermost 30 m (Vs,30), (FEMA 273, 1997). In this work, we created a Vs,30 map of the Umbria and Marche regions, integrating data of the local near-surface from the Italian seismic microzonation dataset. A total of 4154 Vs profiles, from geophysical tests (i.e., Down-Hole, Cross-Hole, SAWS, MASW, REMI etc.), have been analysed to calculate the Vs,30.

The spatial distribution of Vs,30 was performed based on the 1:100.000 geological map of Italy (Amanti *et al.*, 2002). For the sake of simplification, we adopted a new classification grouping similar geological formations in terms of lithological characteristics. Along with the Vs,30 data, this hybrid raster map has been compiled assigning to each measurement the relative slope value, derived from a 30 m resolution DEM, taking advantage from the approach of Wald and Allen (2007). Finally, a statistical analysis was performed to evaluate any dependency among Vs,30, lithology, and topography.

The results show that the Vs,30 is primarily controlled by lithological aspects (Fig. 1). Consistently, the more competent limestone geologic formations are characterised by high Vs,30 median values (600-800 m/s), whereases marly/clayish rocks and quaternary deposits report low Vs,30 median values (300-500 m/s).

The workflow presented in this study was applied to examine the two largest historical events that affected the central Italy during the 18th century: the Fabriano (1741, Mw=6.17,

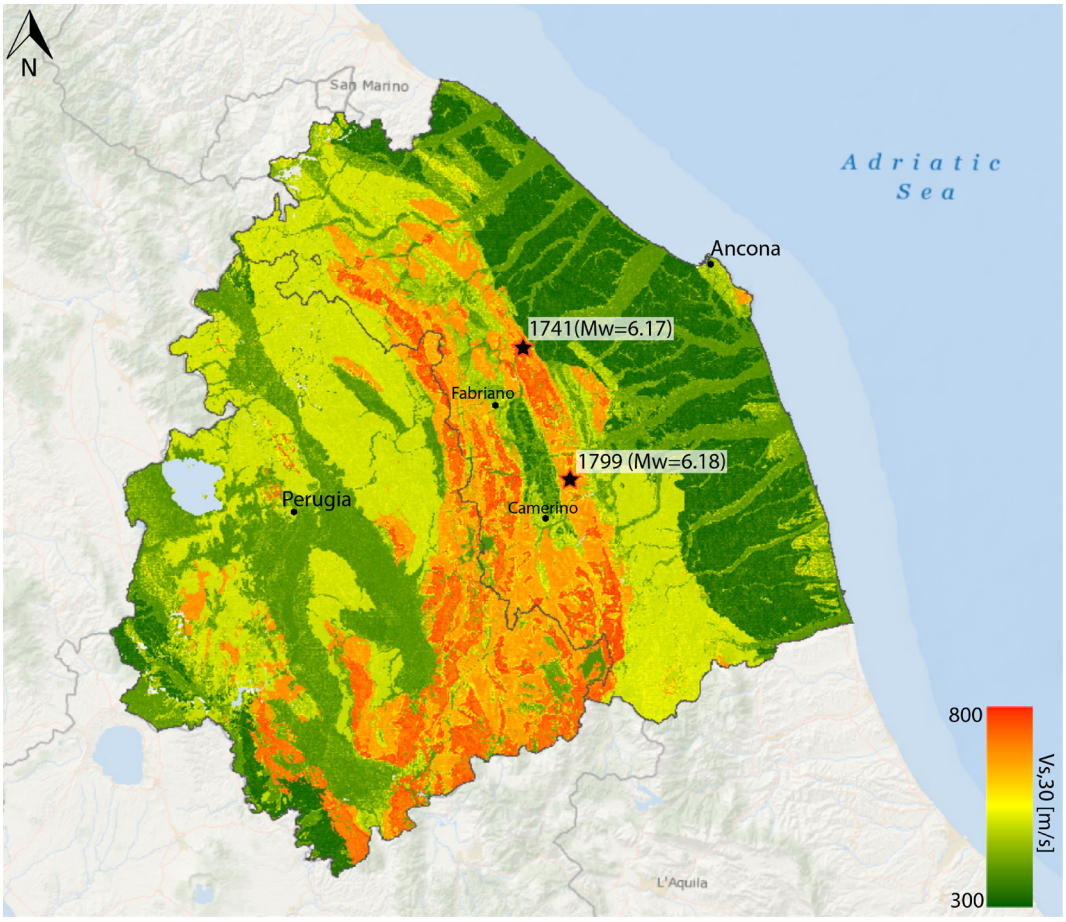


Fig. 1 - Map of shear-wave velocity (Vs,30) of the Umbria and Marche regions. The black stars show the estimated epicenter locations of the two studied historical earthquakes, Fabriano (1741, Mw=6.17) and Camerino (1799, Mw=6.18).

Imax IX MCS) and Camerino (1799, Mw=6.18, Imax IX-X MCS) earthquakes (DBMI15 v4.0, Locati *et al.*, 2022).

To reproduce the ground motion of the Fabriano and Camerino historical earthquakes, including site effects, we integrated in GIS the resulting Vs,30 base map with the Ground Motion Prediction Equation (GMPE, ITA18) proposed by Lanzano *et al.*, (2019). In this case study, given the absence of any earthquake-related surface fault rupture, we adopted the Joyner-Boore (1981; RJB) distance, which is the shortest distance from a site to the surface projection of the seismogenic structure. The seismogenic sources used in these simulations are ITIS048 "Fabriano" and ITIS049 "Camerino" from the DISS database (DISS Working Group, 2021).

The outcomes of this workflow are maps of ground motion parameters (GMPs), such as peak ground acceleration (PGA), peak ground velocity (PGV), and peak spectral acceleration (PSA).

Finally, the outcomes have been further investigated by converting the GMPs into macroseismic intensities using empirical relationships (Gomez *et al.*, 2020). A comparison of the synthetic intensity distribution with the observed macroseismic intensity (DBMI15 v4.0, Locati *et al.*, 2022) led to developing speculations about the characteristics of the still debated causative faults.

The presented workflow is highly adaptable to different localities and geological conditions. This contribution, improving the analysis of historical seismicity, can be advantageous to planning activities in the context of the seismic hazard assessment.

References

Amanti, M., Battaglini, L., Campo, V., Cipolloni, C., Congi, M.P., Conte, G., ... and Zonetti, C. (2008). *The Lithological map of Italy at 1: 100.000 scale: An example of re-use of an existing paper geological map.* In 33rd International Geological Conference, IEI02310L–6-14th August, Oslo (Norway).

Basili, R., Burrato, P., De Santis, G. M., Fracassi, U., Maesano, F.E., Tarabusi, G., ... and DISS Working Group. (2021). *Database of Individual Seismogenic Sources (DISS), Version 3.3. 0: A compilation of potential sources for earthquakes larger than M 5.5 in Italy and surrounding areas.*

FEMA 273. (1997). *NEHRP guidelines for the seismic rehabilitation of buildings: FEMA 273, Federal Emergency Management Agency.* Dev. by Appl. Technol. Counc.

Gomez-Capera, A. A., D'Amico, M., Lanzano, G., Locati, M., and Santulin, M. (2020). *Relationships between ground motion parameters and macroseismic intensity for Italy.* Bulletin of Earthquake Engineering, 18(11), 5143-5164.

Joyner, W.B., and Boore, D.M. (1981). *Peak horizontal acceleration and velocity from strong-motion records including records from the 1979 Imperial Valley, California, earthquake.* Bulletin of the seismological Society of America, 71(6), 2011-2038.

Lanzano, G., Luzi, L., Pacor, F., Felicetta, C., Puglia, R., Sgobba, S., and D'Amico, M. (2019). *A Revised Ground-Motion Prediction Model for Shallow Crustal Earthquakes in Italy.* Bulletin of the Seismological Society of America, 109(2), 525-540.

Locati, M., Camassi, R., Rovida, A., Ercolani, E., Bernardini, F., Castelli, V., … Antonucci, A. (2022). *Database Macrosismico Italiano (DBMI15), versione 4.0*.

Wald, D.J., Worden, B.C., Quitoriano, V., and Pankow, K.L. (2005). *ShakeMap manual: technical manual, user's guide, and software guide.*

Wald, D.J., and Allen, T.I. (2007). *Topographic slope as a proxy for seismic site conditions and amplification.* Bulletin of the Seismological Society of America, 97(5), 1379-1395.

SEISMIC LOSS ASSESSMENT FOR THE CITY OF AJDOVŠČINA (SLO)

L. Hofer, M.A. Zanini

Dipartimento di Ingegneria Civile, Edile e Ambientale, Università degli Studi di Padova, Padova, Italia

Introduction. Nowadays, seismic risk is matter of concern for public authorities and private entities since numerous fatalities and significant economic losses can be caused by a seismic event. This is mainly due to urbanization, growing population and the increase of Gross Domestic Product (GDP). These three factors imply a concentration of people and goods, thus increasing their exposure to natural hazards more than in the past. In addition, the vulnerability of many structures and infrastructures is still high, since retrofitting and re-building are time and money consuming processes (Zanini *et al.,* 2019; Hofer *et al.,* 2020). This study, developed within the framework of the INTERREG Project CROSSIT-SAFER (Project Interreg V-A Italy-Slovenia), aims to assess the susceptibility to earthquake-induced losses for the city of Ajdovščina (SLO). To this aim, an in-depth vulnerability and exposure assessment of the residential building stock of the city of Ajdovščina has been performed and then 864 seismic scenarios have been simulated. Results consist in a chart showing the expected losses as a function of magnitude and the epicentral distance from the city center. Furthermore, the effect of different uncertainty sources is considered in the development of such loss analysis chart for a proper risk management.

Residential buildings portfolio. The exposure of the city of Ajdovščina is modelled at building level. This means that the expected losses are computed for each single building and are aggregated only at the end of the computation stage to obtain the expected losses at municipality level. For each of the 5583 considered buildings, the information made available were the construction year, the construction material, the number of floors and the total built area. Starting from these data, the seismic vulnerability of the analyzed asset has been characterized by setting a building taxonomy consisting of 8 taxonomy class (*TCs*), and for each of them finding a suitable set of fragility curves related to 4 Damage States *DSs* (i.e. DS_1 – slight, DS_2 – moderate, DS_3 – extensive and DS_4 – collapse). Fig.1a shows the percentage of each building taxonomy class, together with the construction year (Fig.1b) and number of floors distributions (Fig.1c).

Masonry buildings represent the 35% of the building portfolio of Ajdovščina. They were constructed mostly between 1970 and 2000 and the 70% of them has less than 2 floors. As regards reinforced concrete structures, they were subdivided in two class depending on the number of storeys (1-2 storeys and 3+). They were considered seismically designed since most of them were built after 1964, year in which first building code explicitly addressing seismic action and design came into force in Slovenia (Babič *et al.,* 2021). Then, the 35% of the buildings of Ajdovščina is represented by old stone structures, built between 1600 and 1920. A small percentage (4%) is represented by wood structures, some old and others relatively new. Also, a small quantity of precast buildings (1%) is present in Ajdovščina, all built after 1970. Finally, remaining 20% of structures have been considered representative of other mixed structural types, i.e., combined stone-masonry and RC-masonry structures. For each *TC* a suitable set of fragility functions with PGA as reference intensity measure has been assumed between those proposed in literature: Tab. 2 lists all the adopted fragility curves parameters.

Shaking scenarios. Shake fields associated to each simulated seismic scenario, are computed assuming Peak Ground Acceleration (PGA) as reference intensity measure and adopting the Ground Motion Prediction Equation (GMPE) proposed by Bindi *et al.,* 2011. Losses are computed for each building as expected values of the reconstruction cost associated to each damage level, according to the procedure reported in HAZUS-MH, assuming a unitary

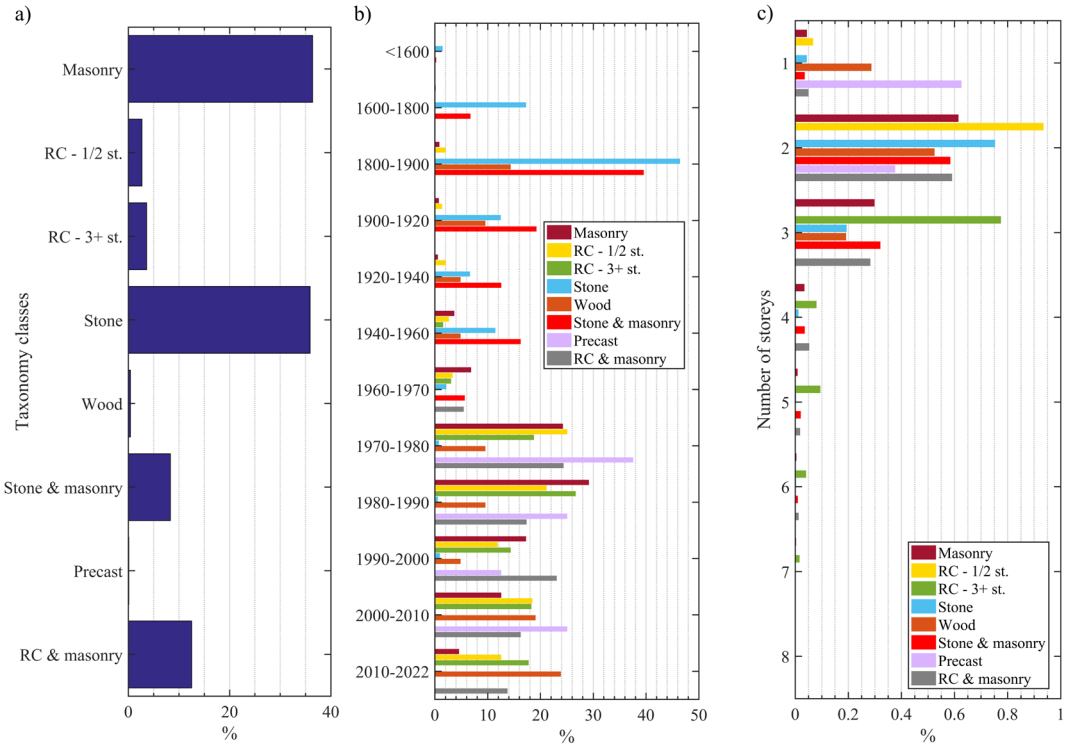


Fig. 1 - Exposure model for the Municipality of Ajdovščina: subdivision of buildings according to the adopted taxonomy (a), construction year (b) and number of storeys (c) distributions.

Tab. 1 - Fragility curves parameters.

	Taxonomy class	Reference	DS1		DS2		DS3		DS4	
			μ [g]	σ [g]	μ [g]	σ [g]	μ [g]	σ [g]	μ [g]	σ [g]
1	Masonry	Kostov *et al.* (2004)	0,16	0,15	0,23	0,22	0,26	0,24	0,45	0,42
2	RC, 1-2	Ahmad *et al.* (2010)	0,09	0,03	0,13	0,06	0,26	0,10	0,52	0,19
3	RC, 3+	Ahmad *et al.* (2010)	0,09	0,03	0,12	0,05	0,19	0,08	0,33	0,12
4	Stone	Ahmad *et al.*, 2010	0,09	0,06	0,11	0,07	0,15	0,07	0,18	0,07
5	Wood	HAZUS W1 - PC	0,22	0,16	0,36	0,25	0,63	0,45	0,95	0,67
6	Stone & masonry	Kostov *et al.*, 2004	0,18	0,12	0,23	0,15	0,30	0,19	0,32	0,20
7	Precast	HAZUS PC2L - HC	0,29	0,21	0,44	0,31	0,85	0,60	1,51	1,07
8	RC & masonry	Kostov *et al.*, 2004	0,16	0,15	0,26	0,24	0,41	0,38	0,56	0,52

replacement cost (URC) equal to 1200 €/m^2. Fig. 2 shows the position of all the simulated epicenters, located at 5, 10, 20, 30, 40 and 50 km far from the city center; all the four cardinal directions are tested for considering the uncertainty arising from the randomness of the epicenters location.

Furthermore, since the exact soil characteristics for each building is unknow, the two most likely soil categories are considered in the analysis, i.e. soil B and C types. Finally, three different level of repair cost ratio (RCR) are adopted in the analysis in order to consider the potential variability of losses (Dolce *et al.*, 2021). Regarding the magnitude M_w, a set of 6 values are considered, i.e. 5, 5.3, 5.5, 5.7, 6 and 6.5. Considering all the uncertainty sources (earthquake location, soil characteristics and RCR), for each of the 6×6 couples of distance R and magnitude

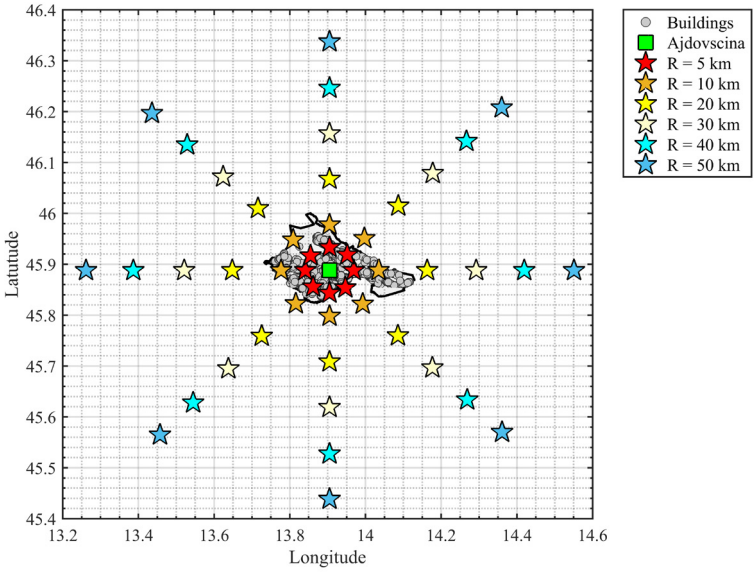


Fig. 2 - Building portfolio spatial distribution and location considered epicenters.

M_W, 48 combinations are tested. Thus, the mean, the standard deviation and the coefficient of variation (*CoV*) are computed for each *R* - M_W couple for properly characterized the expected value and the associated uncertainties.

Results. Fig. 3a shows the expected losses in % terms on the total exposed value (*TEV*, 3.9 billion €). Earthquakes with magnitude ranging between 6.3 and 6.5 and occurring between 5 and 8 km from the city center, are able to produce expected losses equal to the 60% of the

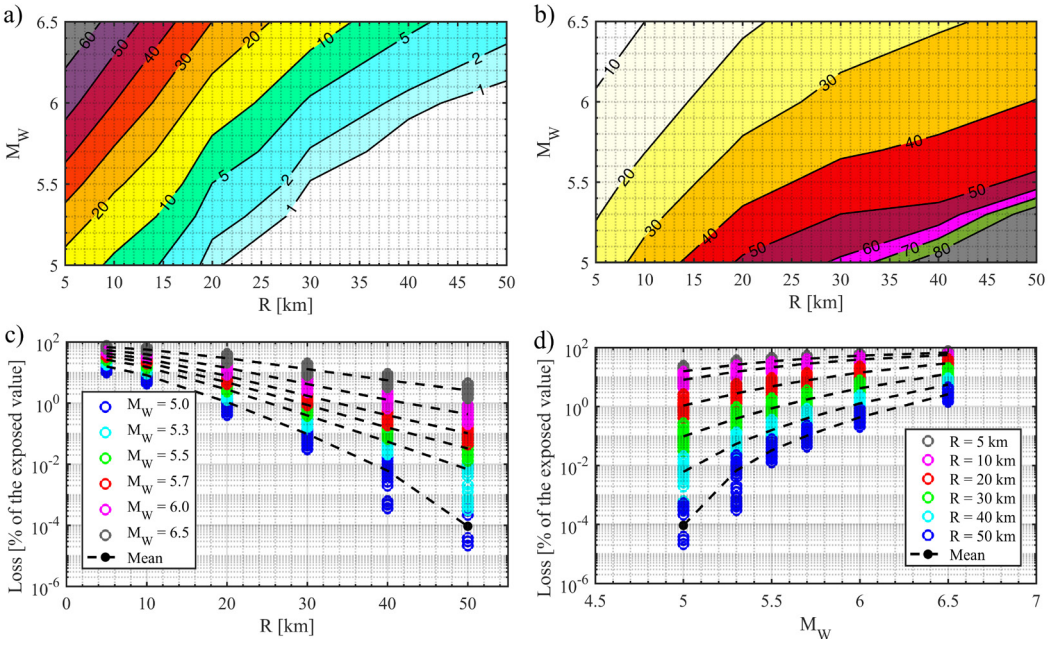


Fig. 3 - Expected losses in % terms on the total exposed value (a), coefficient of variation of the expected losses (b) expected losses as function of epicentral distance (c) and earthquake magnitude (d).

TEV. High magnitude earthquakes (M_W = 6÷6.5), occurring 50 km far from the city center, cause expected losses ranging between 1÷5% *TEV*. On the contrary, low magnitude earthquakes (M_W = 5÷5.5) cause expected losses ranging between 10÷30% of the *TEV* when occurring in the first 10 km from the city center, while are negligible when occurring starting from 30 km far from the city center. Fig. 3b shows the behavior of the coefficient of variation, highlighting how higher uncertainties are associated to smaller losses since the damage distribution is more uncertain for lower PGA, than respect to higher shaking values. Finally, Fig. 3c and Fig. 3d shoes the expected losses as a function of respectively the epicentral distance and the earthquake magnitude. These last plots can be particularly useful for authorities for assessing seismic risk, and for civil protection purposes for the emergency management.

Acknowledgements. This work was funded by the European Commission (project Interreg V-A Italy-Slovenia 2014-2020 CROSSIT SAFER) within the European Territorial Cooperation program "INTERREG". The project partners are also gratefully acknowledged.

References

Ahmad, N., Crowley, H., Pinho, R.: *Analytical fragility functions for reinforced concrete and masonry buildings aggregates of Euro-Mediterranean regions - UPAV methodology.* Syner-G Project, 2009/2012, Internal report, 2011.

Babič A., Dolšek M., Žižmond J., 2021, *Simulating Historical Earthquakes in Existing Cities for Fostering Design of Resilient and Sustainable Communities: The Ljubljana Case*, Sustainability 13.

Bindi D., Pacor F., Luzi L., Puglia R., Massa M., Ameri G., *et al.* 2011, *Ground motion prediction equations derived from the Italian strong motion database.* Bull Earthq Eng, 9(6):1899–920.

Dolce, M.; Prota, A.; Borzi, B.; da Porto, F.; Lagomarsino, S.; Magenes, G.; Moroni, C.; Penna, A.; Polese, M.; Sperenza, E.; *et al.* (2021). *Seismic risk assessment of residential buildings in Italy: Methodology overview and main results.* Bull. Earthq. Eng., 19, pages2999–3032.

HAZUS-MH MR4. (2003). *"Multi-hazard loss estimation methodology - Earthquake model."* Dept. of Homeland Security Emergency Preparedness and Response Directorate Federal Emergency Management Agency, Washington, DC.

Hofer L., Zanini M.A., Gardoni P., 2020, *Risk-based catastrophe bond design for a spatially distributed portfolio,* Structural Safety, 83: 101908.

Kostov, M., Vaseva, E., Kaneva, A., Koleva, N., Verbanov, G., Stefanov, D., Darvarova, E., Salakov, D., Simeonova, S., Cristoskov, L.: 2004: *Application to Sofia.* Report RISK-UE WP13.

Project Interreg V-A Italy-Slovenia 2014-2020 CROSSIT SAFER, https://www.ita-slo.eu/en/crossit-safer.

Zanini M.A., Hofer L., Pellegrino C., 2019, *A framework for assessing the seismic risk map of Italy and developing a sustainable risk reduction program.* International Journal of Disaster Risk Reduction, 33: 74-93.

SUI SIMULATORI DELLE CURVE HVSR

E. Lunedei, A. Tanzini, E. Paolucci, D. Albarello

Dipartimento di Scienze Fisiche, della Terra e dell'Ambiente, Università degli Studi di Siena, Italia

Le misure dei rapporti fra le componenti spettrali orizzontali e verticali del moto del suolo dovuto alle vibrazioni sismiche ambientali (rappresentate dalle note curve HVSR) giocano un ruolo centrale per la caratterizzazione della risposta sismica locale, in particolare negli studî di microzonazione sismica. Oltre che per la stima immediata delle frequenze di risonanza dei siti esaminati, queste misure vengono impiegate per vincolare il profilo di velocità delle onde di taglio nelle procedure d'inversione numerica dei dati geofisici, delle quali sono state sviluppate, negli ultimi decenni, varie versioni, che si differenziano nettamente fra loro, principalmente per i diversi metodi con cui è realizzata la modellazione diretta delle grandezze fisiche coinvolte, in particolare della curva HVSR stessa. Si va da approcci molto semplificati, basati sull'ipotesi che la curva HVSR rappresenti direttamente la funzione di trasferimento delle onde SH od il rapporto fra le funzioni di trasferimento delle onde P ed SH, a modelli via via più complessi, che associano la curva HVSR all'ellitticità delle onde di Rayleigh, alla combinazione di componenti multimodali di onde di Love e Rayleigh, fino a modelli di campo completo basati sull'ipotesi di sorgenti superficiali distribuite o d'un campo d'onda diffuso (la bibliografia raccoglie alcuni riferimenti a tali approcci).

Considerando anche la diversa entità del peso computazionale di tali modelli, un'ampia discussione è sorta in questi anni sul livello d'approssimazione con cui essi sono in grado di riprodurre la curva HVSR, discussione essenzialmente legata alla qualità delle ipotesi alla base di ciascun modello. Questo studio intende contribuire a questa discussione, spostando l'oggetto della comparazione dalle ipotesi ai risultati prodotti: si confrontano infatti le curve HVSR sintetiche generate da differenti modelli diretti applicati a 1600 profili sismostratigrafici simulati numericamente e rappresentativi delle situazioni tipiche dell'Appennino Meridionale. Le curve HVSR ottenute per tutti questi profili sono state messe a confronto per valutare l'effettiva eterogeneità dei risultati e quindi la sensibilità di questi ultimi alle diverse ipotesi soggiacenti a ciascun modello. N'è emerso un valore assai elevato della correlazione fra le curve prodotte dai diversi modelli per lo stesso profilo sismostratigrafico, con valori del coefficiente di correlazione di Pearson prossimi a 0,9. Questo suggerisce l'esistenza d'una qualche caratteristica comune ai vari modelli, che li rende quasi equivalenti per quanto concerne il risultato prodotto, indipendentemente dalla complessità delle specifiche ipotesi sulle quali la modellazione diretta del rapporto spettrale H/V giace. Questa evidenza, pur preliminare, suggerisce che inseguire una sempre maggiore complessità della modellazione diretta (che va, sovente, a scapito dell'efficienza della procedura d'inversione), pur conservando un interesse per la comprensione del fenomeno delle vibrazioni ambientali, potrebbe risultare di scarsa utilità pratica, vista la sostanziale omogeneità dei risultati prodotti dai diversi modelli. Se adeguatamente confermata, quest'osservazione deporrebbe a favore dell'uso di modelli semplificati per la simulazione della curva HVSR, i quali, pur basandosi su una descrizione meno accurata del reale campo d'onda delle vibrazioni ambientali, potrebbero contribuire alla realizzazione di procedure d'inversione più efficienti e meno soggette ad instabilità numeriche. L'abbreviazione dei tempi d'esecuzione potrebbe agevolare l'uso di procedure d'inversione maggiormente esplorative e quindi maggiormente capaci d'esprimere l'effettivo livello d'incertezza associato alle soluzioni trovate dall'algoritmo d'inversione medesimo. Rimane aperto l'interessante problema teorico di spiegare la ragione dell'omogeneità dei risultati a fronte della notevole eterogeneità delle ipotesi soggiacenti ai diversi modelli di simulazione diretta della curva HVSR.

Bibliografia

Arai H., Tokimatsu K.; 2000: *Effect of Rayleigh and Love waves on microtremor H/V spectra*, Proceedings of the 12th World Conferences on Earthquake Engineering (WCEE), Auckland, New Zealand, http://www.nicee.org/wcee/.

Bonnefoy-Claudet S., Köhler A., Cornou C., Wathelet M., Bard P.Y.; 2008: *Effects of Love waves on microtremor H/V ratio*, Bulletin of the Seismological Society of America, 98(1), 288–300, doi:10.1785/0120070063.

Herak M.; 2008: *ModelHVSR - A Matlab® tool to model horizontal-to-vertical spectral ratio of ambient noise*, Computers & Geosciences, 34(11), 1514–1526, doi:10.1016/j.cageo.2007.07.009.

Lontsi A.M., García-Jerez A., Molina-Villegas J.C., Sánchez-Sesma F.J., Molkenthin C., Ohrnberger M., Krüger F., Wang R., Fäh D.; 2019: *A generalized theory for full microtremor horizontal-to-vertical [H/V(z, f)] spectral ratio interpretation in offshore and onshore environments*, Geophys. J. Int., 218, 1276–1297, doi:10.1093/gji/ggz223.

Lunedei E., Malischewsky P.; 2014: *A review and some new issues on the theory of the H/V technique for ambient vibrations*, Theme Lecture nell'ambito della *Second European Conference on Earthquake Engineering and Seismology (2ECEES)*, Istanbul (Turkey), 24-29 August 2014, published on A. Ansal (editor) "Perspectives on European Earthquake Engineering and Seismology - Volume 2", Springer International Publishing ed. [ISBN: 978-3-319-16963-7 (printed) 978-3-319-16964-4 (electronic)], pp. 371-394, doi:10.1007/978-3-319-16964-4, free access on http://link.springer.com/book/10.1007%2F978-3-319-16964-4.

Lunedei E., Albarello D.; 2021: *Synthetic spectral structure of the seismic ambient vibrations generated by a distribution of superficial random sources with a finite extension*, Soil Dynamics and Earthquake Engineering, 151, 106949, doi:10.1016/j.soildyn.2021.106949.

Molnar S., Sirohey A., Assaf J., Bard P.-Y., Castellaro S., Cornou C., Cox B., Guillier B., Hassani B., Kawase H., Matsushima S., Sánchez Sesma F.J., Yong A.; 2022: A review of the microtremor horizontal-to-vertical spectral ratio (MHVSR) method, J. Seismol., doi:10.1007/s10950-021-10062-9.

Nakamura Y.; 2000: *Clear identification of fundamental idea of Nakamura's technique and its applications*, Proceedings of the 12th World Conference on Earthquake Engineering (WCEE), Auckland, New Zealand, http://www.nicee.org/wcee/.

Sánchez-Sesma F.J., Rodriguez M., Iturraran-Viveros U., Luzon F., Campillo M., Margerin L., García-Jerez A., Suarez M., Santoyo M.A., Rodriguez-Castellanos A.; 2011: A theory for microtremor H/V spectral ratio:application for a layered medium. Geophys. J. Int., 186, 221–225, doi:10.1111/j.1365-246X.2011.05064.x.

Tran Thanh Tuan, Scherbaum F., Malischewsky P.G.; 2011: *On the relationship of peaks and troughs of the ellipticity (H/V) of Rayleigh waves and the transmission response of single layer over half-space models*, Geophys. J. Int., 184, 793–800.

SEISMO-STRATIGRAPHIC MODEL FOR THE MILAN (ITALY) METROPOLITAN AREA BY AMBIENT-VIBRATION MONITORING AND IMPLICATIONS FOR SEISMIC SITE EFFECTS ESTIMATION

M. Massa, S. Lovati, R. Puglia, G. Brunelli, A. Lorenzetti, C. Mascandola, C. Felicetta, F. Pacor, L. Luzi
National Institute of Geophysics and Volcanology (INGV), via Alfonso Corti 12, 20133, Milano, Italy

A urban-scale seismo-stratigraphic model for the Milan (Italy) metropolitan area was developed based on a combination of seismic passive and active data supported by a dense grid of geological and stratigraphic information both from shallow and deep vertical wells (Massa *et al.*, 2022). The area, involving more than 3.0 milion people and a high density of industrial facilities, is located at the North Western limit of the Po Plain, a very large sedimentary basin located between the thrust belts of the Alps and the Apennines and characterized by a complex buried tectonic structures.

The studied area is characterized by a low rate of annual seismicity (http://terremoti.ingv.it). In particular, in the last 40 years no local earthquakes with magnitude > 4.5 have occurred. However, the area has often undergone ground motion over the long-period, namely in the case of distant earthquakes with higher magnitude, such as the 2012 Emilia, Mw 5.8, seismic sequence (Luzi *et al.*, 2013). Long-period ground motion amplification is a significant issue in the Po Plain, where resonance phenomena at low frequencies have been well-documented by many studies (e.g. Luzi *et al.*, 2013; Milana *et al.*, 2013; Massa and Augliera, 2013; Paolucci *et al.*, 2015; Mascandola *et al.*, 2017).

This work is an attempt to investigate the influence of the shallow to deep (down ~ 1.8 km) alluvial deposits for the Milan metropolitan area, where amplification effects in the frequency range 0.2 to 8 Hz are observed. Therefore, a detailed seismo-stratigraphic model obtained from the analysis of existing geological and stratigraphic data (e.g. Regione Lombardia, ENI-AGIP, 2002; GeoMol, 2015; Ispra 2016; ViDEPI project, 2009) and newly acquired geophysical data is proposed.

In particular, new 37 single-station and 4 ambient-vibration arrays measurements were acquired in the area using seismometers with owner period of 5s, together with 4 active multichannel analysis of surface waves (*MAWS)*. The passive microtremor arrays were performed with different geometrical configurations and a maximum aperture of about 600 m.

To estimate the resonant frequencies of the soft sediments, the horizontal to vertical spectral ratio technique (*HVSR*) was applied to the ambient-vibration recordings, while to determine the Rayleigh-wave dispersion curves from passive array, the data were analyzed using the conventional frequency-wavenumber (*f-k*), the modified spatial autocorrelation (*mSPAC*) and the extended spatial autocorrelation (*ESAC*) methods. The array data were used to determine the local V_S profiles via joint inversion of the Rayleigh-wave dispersion and ellipticity curves deduced from the *HVSR*.

The results from *HVSR* show three main bands of amplified frequencies, the first in the range 0.15-0.25 Hz, the second from 0.4 Hz to 0.65 Hz and the third from 2 Hz to 8 Hz. A decreasing trend of the main peaks is observed from the northern to the southern part of the city, allowing to hypothesize a gradual increase of depth of the relative regional chrono-stratigraphic unconformities.

The passive ambient noise array and *MASW* show a clear dispersion of the fundamental mode of the Rayleigh-wave in the range 0.4 Hz to 30 Hz, allowing to obtain detailed V_s profiles with depth down to about 1.8 km. The results obtained from ambient noise *HVSR* are compared to the HVSR curves considering 17 earthquakes with magnitude from 3.7 to 5.8 recorded by the IV.MILN station (http://terremoti.ingv.it/instruments/station/MILN) in the last 10 years.

The Vs profiles are finally validated through 1D numerical models performed assuming a linear elastic behavior of the soil using the SHAKE91 code (Idriss and Sun, 1993).

References

Idriss I.M., Sun J.I. (1993). *User's Manual for SHAKE91: A Computer Program for conducting Equivalent Linear Seismic Response Analyses of Horizontally Layered Soil Deposits*; Center for Geotechnical Modeling, Department of Civil and Environmental Engineering, University of California: Davis, CA, USA.

ISPRA, Servizio Geologico d'Italia, regione Lombardia (2016). *Carta Geologica d'italia alla scala 1:50.000, Foglio 118 Milano (con note illustrative).* A cura di Francani V., Piccin A., Credali M., Berra F., Battaglia D., Gattinoni P., Rigamonti I., Rosselli S.

GeoMol Team (2015). *GeoMol – Assessing subsurface potentials of the Alpine Foreland Basins for sustainable planning and use of natural resources* – Project Report, 188 pp. (Augsburg, LfU).

Luzi L., Pacor F., Ameri G., Puglia R., Burrato P., Massa M., Augliera P., Franceschina G., Lovati S., Castro R. (2013). *Overview on the strong motion data recorded during the May–June 2012 Emilia seismic sequence*, Seismol. Res. Lett. 84, no. 4, 629–644.

Mascandola C., Massa M., Barani S., Lovati S., Santulin M. (2017). *Long-Period Amplification in Deep Alluvial Basins and Consequences for Site-Specific Probabilistic Seismic-Hazard Analysis: An Example from the Po Plain (Northern Italy)*, Bull. Seismol. Soc. Am., 107(2), 770-786.

Massa M., Lovati S., Puglia R., Brunelli G., Lorenzetti A., Mascandola C., Felicetta C., Pacor F., Luzi L. (2022). *Seismo-stratigraphic model for the urban area of Milan (Italy) by ambient-vibration monitoring and implications for seismic site effects assessment*, Frontiers, under revision.

Massa M., Augliera P. (2013). *Teleseisms as estimator of experimental long period site amplifications: example in the Po Plain (Italy) from the 2011, Mw 9.0, Tohoku-Oki (Japan) earthquake*, Bull. Seism. Soc. Am., 103 (5): 2541-2556.

Milana G., Bordoni P., Cara F., Di Giulio G., Hailemikael S., Rovelli A. (2013). *One-dimensional velocity structure of the Po River plain (northern Italy) assessed by combining strong motion and ambient noise data*, Bull. Earthq. Eng. 12, no. 5, 2195–2209.

Paolucci E., Albarello D., D'Amico S., Lunedei E., Martelli L., Mucciarelli M., Pileggi D. (2015). *A large scale ambient vibration survey in the area damaged by May–June 2012 seismic sequence in Emilia Romagna, Italy,* Bull. Earthq. Eng., 13(11), 3187-3206.

Regione Lombardia, Eni Divisione Agip (2002). *Geologia degli acquiferi Padani della Regione Lombardia*, a cura di Cipriano Carcano e Andrea Piccin. S.EL.CA., Firenze (in Italian).

ViDEPI project (2009). *Visibilità dei dati afferenti all'attività di esplorazione petrolifera in Italia* Ministero dello sviluppo economico DGRME - Società Geologica Italiana, Assomineraria.

https://www.videpi.com

FRAGILITY ASSESSMENT OF GLASS COMPONENTS BY SINGLE-DEGREE OF FREEDOM APPROXIMATION

S. Mattei, C. Bedon

University of Trieste, Department of Engineering and Architecture, Trieste, Italy

Introduction. In the last decades, the design of structural elements is increasingly winking to systems characterized by unconventional materials, or rather to elements not commonly used for the construction practice of the country to which it refers. These materials, such as structural glass (Haldimann *et al.*, 2008), pultruded profiles, etc, are gradually making their way into the construction market, sometimes used in combination with other commonly used materials to offer better characteristics, such as fibre-reinforced concretes. Although glass has been used for hundreds of years in the construction of buildings, it has always played a secondary role, to which no load-bearing capacity is entrusted. Generally, glass elements are used in practical construction to bring light to the structures, improving their aesthetics and sustainability taking into account the low impact that has on the environment. Moreover, the consideration of the contribution of glass curtain walls in the structural dynamic response has been highly recommended due to its significant influence on the lateral resistance.

However, within the performance-based earthquake engineering framework the estimation of expected losses is an aspect that must not be overlooked, since the observed damage of this type of elements during a seismic event leads to a lowering of the performance level of the entire building (Karavasilis T.L. and Seo C.Y., 2011), such as in the case of masonry infill walls in RC buildings. An efficient method to quantitively address the seismic structural vulnerability is related to the generation of fragility curves designed ad hoc for the single system components in order to combine the dynamic response of structural and non-structural elements (Bianchi *et al.*, 2019). However, the derivation of these curves involves the use of methods which, although a reliable result is provided, require a large amount of uncertainties to be included and a very high computational burden (Zentner *et al.*, 2017).

Therefore, this work aims to provide an application of theoretical methodology that can simplify the seismic response evaluation of glass systems. In detail, the paper presents and discusses seismic fragility assessment of glass systems by using the equivalent Linear Single-Degree-of-Freedom (SDOF) and Non-Linear SDOF calibrated on pushover analyses obtained for FE models in ABAQUS/CAE. The structural response is also compared to that of the numerical non-linear dynamic analyses performed on a three-dimensional structural model.

Background on fragility assessment of glass systems. Fragility function, in a simplified sense, is described as the probability of exceeding a limit value of the damage state for a specific seismic intensity:

$$F_i(EDP_i) = \Phi\left(\frac{\ln\left(\frac{IM}{\theta}\right)}{\beta}\right) \quad (1)$$

Where the subscript i denotes the damage state threshold, EDP corresponds to the demand parameter, IM represents the intensity measure of the seismic event, Φ is the standard normal cumulative distribution function, θ and β are respectively the median and the logarithmic standard deviation of the data.

In recent years several authors developed glass curtain wall fragility curves at different relevant damage states which are divided in serviceability or ultimate limit states. According to Porter *et al.* (2008), fragility curves may be derived by various methods, based on analytical,

empirical, hybrid or expert judgment elicitation approaches. In particular, in order to assess the vulnerability of a glass façade, the empirically based approach has been the most used so far. In general, glass cracking or fall-out and gasket seal degradation are indicated as collapse references as a consequence of the observed experimental failures. The research work of O'Brien *et al.* (2012) embodies several experimental campaigns addressed by different authors (Behr, 1998; Behr A.R. and Belarbi A., 1996; Memari *et al.*, 2003; Memari *et al.*, 2011) with the aim of deriving fragility curves for 15 glazing system configurations, in which variable features include materials, panel sections and geometrical properties. Firstly, the seismic evaluation of glass systems response in terms of probability of damage, for each damage state considered, need to identify the inter-story drift ratios as EDP (engineering demand parameter) which was obtained from test results. Therefore, the Method A and Methods B were used to derive the dynamic fragility curves depending on the occurrence of the failure.

As can be easily deduced, the disadvantages of using the empirical approach relate to the availability of specific testing machines, significant time and high costs. Consequently, an analytical procedure was proposed by Nuzzo *et al.,* 2020 based on the same configurations in order to investigate the accuracy of the method by a comparison of results.

Further support is given by the application of numerical Cloud Method (Jalayer *et al.,* 2014) in Mattei S. and Bedon C. (2021) by considering structural and non-structural glass systems, with different geometries and boundaries. In this case, the extended and expertly developed numerical modelling in a Finite Element software is a required contribution.

Discussions of results. In order to determine the dynamic response of a structure it is necessary to carry out an analysis of the vibrations induced on it by external actions or by assigned initial boundary conditions. Vibration means a mechanical oscillation around an equilibrium point, and can be harmonic, periodic or random. Recalling also the D'Alembert's principle of dynamic equilibrium, a system is in equilibrium at each time instant if all the forces acting on the mass are considered (the elastic or inelastic resisting force f_S, the damping resisting force f_D and the arbitrary external force p(t)) including the fictitious inertia force f_I:

$$f_I + f_D + f_S = p(t) \tag{2}$$

Moreover, the system is assumed to have linear viscous damping, instead for the contribution of static force, both hypotheses of elastic and inelastic behaviour of the system are considered.

Thus, the two equations of motion governing the response of a single degree of freedom system are reported as function of displacement u, velocity $\dot{u}$ and acceleration $\ddot{u}$:

$$m\ddot{u} + b\dot{u} + ku = -m\ddot{u}_g(t) \tag{3}$$

Where m, b and k represent respectively the mass, the critical damping factor and the stiffness of the SDOF system. Finally, $\ddot{u}_g(t)$ denotes the seismic input applied to the overall system, i.e. the ground acceleration. On the other hand, for inelastic systems the Eq. 3 should be replaced by Eq. 4:

$$m\ddot{u} + b\dot{u} + f_S(u) = -m\ddot{u}_g(t) \tag{4}$$

Where $f_s(u)$ is the inelastic resisting force.

The closed-form solution of these equations does not exist because of the variability of the action and the non-linearity of the system. This type of problem can be solved numerically for each time step *i*, having each accelerogram as discretized with a constant Δt equals to 0.005 s.

In this study, the glass system considered has been the subject of in-depth analysis in a previous article (Mattei S. and Bedon C., 2021). In particular, the earlier analyses concerned FEM simulations by means the software Abaqus/CAE with the purpose of investigating its dynamic response and, through the application of Cloud analysis, of calculating specific component fragility curves. The main features of the non-structural glass component considered are summarized below: the glass panel is bounded to metal supports in aluminium (as shown in Fig. 1) on only two sides with adhesive joints; the materials are defined as perfectly elastic: $\sigma_{t,glass}$ = 45MPa and σ_{all} = 235Mpa and the connection is modelled with axial connectors in the normal and tangential direction of the wire-to-ground type. In addition, stress values are monitored at each step of analyses in order to make the results of the FE analysis and numerical analysis consistent.

In this work, a simplified method is presented, which provides an assessment of the response of the system under consideration and, thus, characterises it by means of fragility curves that can be used with a good approximation for the design of any glass panel by adapting the approach to specific cases, and then varying the oscillator parameters or also characterizing multi-degree of freedom systems through the respective equivalent SDOF. Then, in order to simplify and make even more immediate the derivation of fragility curves for glass building components, such systems can be converted into SDOF relying on the definition of Single-Degree of Freedom oscillator's parameters and backbone parameters by a static pushover analysis on a three-dimensional model (i.e., Fig.1(b)). The latter should be able to reproduce the three main magnitudes of the system in seismic vibration in order to schematize it adopting as the only degree of freedom the horizontal displacement in the plane of the panel.

Suppose that the mass is concentrated in a point and is subjected to the inertial force that is due to the application of an acceleration at the base, and in particular in correspondence of the bottom aluminium transom wedged to the substructure, the displacement is derived from the numerical resolution of the governing equations Eq. 2 and Eq. 3, through the Newmark Iterative Method.

Seismic signals applied to the approximate system are the same as those used in nonlinear dynamic analyses on the FE three-dimensional model. In Fig. 2 are reported the maximum in-plane horizontal relative displacements as response to each accelerogram relative to the

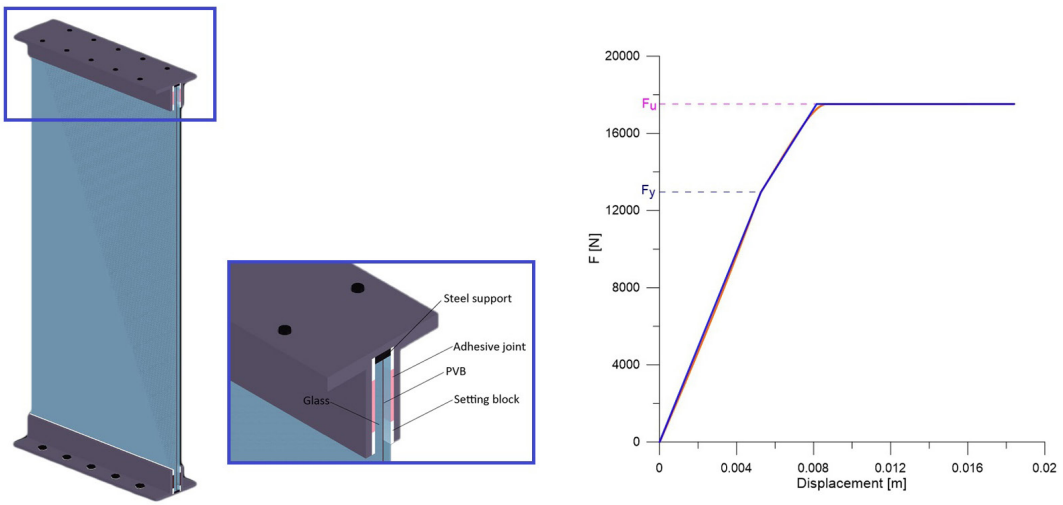


Fig. 1 - (a) Schematic representation of case-study and (b) backbone curve.

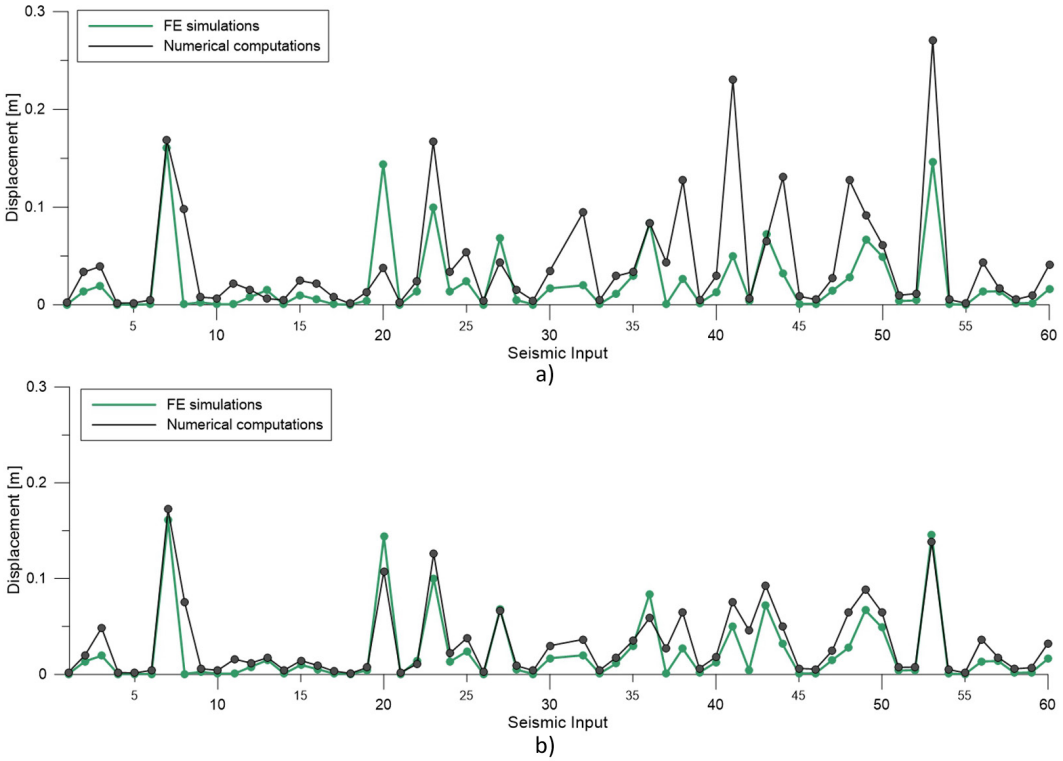


Fig. 2 - Maximum displacements by Finite Element simulations in Abaqus/CAE and numerical resolutions according to Newmark method considering an elastic (a) and inelastic (b) SDOF.

case of elastic (i.e., Fig.2(a)) and inelastic (i.e., Fig.2(b)) SDOF considering the typical damping of 5%. For this last parameter different percentages are chosen that cover the whole range of possible values.

Finally, in Fig. 3 are reported the IM-based fragility curves by software simulations and numerical calculations, differentiating the concept of operations depending on the assumption of elastic (i.e., Fig.3(a)) or inelastic (i.e., Fig.3(b)) SDOF by the use of Cloud Analysis. In this regard, the choice of the EDP-threshold against which the parameters defining the cumulative probability curve (mean θ, and random dispersion β) are calculated is rather complex. In the context of global regulatory framework and in the case of seismic design, no specific formulations are foreseen but reference is often made to guidelines (CNR-DT 210/2013). Generally, the in-plane horizontal relative displacement is considered as engineering demand parameter and according to Italian technical code (NTC-2018) the typical non-damage reference value of inter-story drift ratio is indirectly defined as the corresponding to 0.002h, that is 7 mm for h=3.5 m. The findings allowed to observe that, for example, taking as a reference a cumulative probability (F_i by Eq. 1) equal to 0.5, the corresponding values of PGA are underestimated by 23% and 20%, for v=0.05, respectively in the case of elastic linear and inelastic behaviour.

It is well known that the derivation of fragility curves is a time-consuming process, thus the aim of this work is to provide a simplified approach for the estimation of physical damage. Consequently, this study developed through an actual numerical application, a simplified method for the characterization of the seismic behaviour of a sub-structural glass facade wall given the current growth in the glass demand for construction field. In doing so, an interesting comparison was carried out between the seismic performance results by numerical analyses on a FE three-dimensional models and by the exposed method based on SDOF approximation.

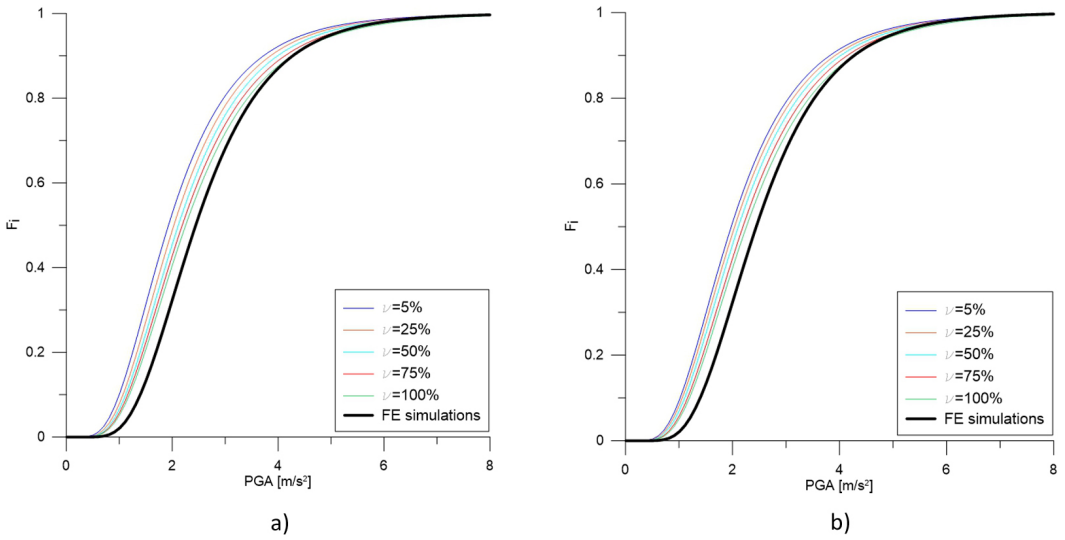


Fig. 3– IM-based fragility curves for (a) Linear SDOF and (b) Non-Linear SDOF.

It can be noted that the pushover-based inelastic single-degree of freedom system provides results very close to those achieved by non-linear dynamic analyses in ABAQUS/Standard, and thus can be used as a viable alternative in the context of preliminary investigations about seismic vulnerability but leading to more conservative probabilistic values. However, further studies on different glass panel configurations or taking into account the interaction with the primary structure are needed in order to assess the accuracy of the procedure.

References

Behr R.A. and Belarbi A.; 1996: *Seismic test methods for architectural glazing systems*. Earthq. Spectra, 12 (1).

Behr R.A.; 1998: *Seismic performance of architectural glass in mid-rise curtain wall*. J. Archit. Eng., 94-98.

Bianchi S., Ciurlanti J. and Pampanin S.; 2019: *Seismic vulnerability of non-structural components: from traditional solutions to innovative low-damage systems*. Proceedings SECED 2019 Conference.

CNR-DT 210/2013. *Istruzioni per la progettazione, l'esecuzione ed il controllo di costruzioni con elementi strutturali di vetro*.

Haldimann M., Luible A. and Overend M.; 2008: *Structural use of glass*. Zurich (CH): IABSE. ISBN 978-3-85748-119-2.

Jalayer F., De Risi R., Manfredi G.; 2014: *Bayesian Cloud Analysis: Efficient structural fragility assessment using linear regression*. Bull.Earthq.Eng., 13, 1183:1203.

Karavasilis T. L. and Seo C.Y.; 2011: *Seismic structural and non-structural performance evaluation of highly damped self-centering and conventional systems*. Eng. Struct., 33(8), 2248-2258.

Mattei S. and Bedon C.; 2021: *Analytical Fragility Curves for Seismic Design of Glass Systems Based on Cloud Analysis*. Symmetry, 13(8), 1541.

Memari A.M., Behr R.A., Kremer P.A.; 2003: *Seismic Behavior of Curtain Walls Containing Insulating Glass Units*. J. Archit. Eng., 9 (2), 70-85.

Memari A.M., O'Brien W.C., Kremer P.A. and Behr R.A.; 2011: *Architectural Glass Seismic Behavior Fragility Curve Development*. Report No. FEMA P-58/BD-3.9, 2011, 2.

NTC-2018. *Norme Tecniche per le Costruzioni, Ministero delle Infrastrutture e dei Trasporti, Decreto Ministeriale 17 gennaio 2018*.

Nuzzo I., Aiello C., Bonati A., Caterino N., Coppola O. and Occhiuzzi A.; 2020: *Fragility curves of glass facades via analytical simplified modelling*. 17th World Conference on Earthquake Engineering, 17WCEE, C003314.

O'Brien W.C., Memari A.M., Kremer P.A. and Behr R.A.; 2012: *Fragility Curves for Architectural Glass in Stick-Built Glazing Systems*. Earthq. Spectra, 2 (28), 639-665.

Porter K. A., Kennedy R., Bachman R.; 2007: *Creating Fragility Functions for Performance-Based Earthquake Engineering*. Earthq. Spectra, 23, 471-489.

Zentner I., Gündel M. and Bonfils N.; 2017: *Fragility analysis methods: Review of existing approaches and application.* Nucl. Eng. Des., 323, 245-258.

MACHINE LEARNING BASED HIGH RESOLUTION GROUND MOTION MAPS

F. Mori, M. Moscatelli
CNR IGAG

Abstract. Gli eventi sismici passati hanno dimostrato che i danni e il numero di vittime dipendono sia dal forte movimento del suolo (cioè dagli effetti della sorgente) che dagli effetti locali del sito. La variabilità della distribuzione del moto del suolo è causata dall'impostazione stratigrafica e/o topografica locale e dalle morfologie sepolte, che possono dare origine ad amplificazioni e risonanze rispetto al moto del suolo previsto nel sito di riferimento. Pertanto, le condizioni locali del sito possono influenzare il collasso completo o la perdita di funzionalità di strutture, infrastrutture e *lifelines*. Per questo motivo, la previsione in tempo quasi reale della variazione del moto del suolo su area vasta è una questione cruciale per supportare la gestione del sistema dell'emergenza. Per raggiungere questo obbiettivo è stato adottato un approccio di machine learning al fine di produrre mappe di scuotimento ad alta risoluzione considerando sia le condizioni stratigrafiche che morfologiche. Un set di circa 7.500 dati accelometrici dal nuovo flatfile ITACA e circa 46.000 dati geologici e geofisici del database della Microzonazione Sismica costituiscono il dataset utilizzato per l'allenamento ed il test del modello di regressione gaussiano. Il parametro di risposta sismica (di picco e spettrale) è stimato utilizzando dodici predittori con la possibilità di integrare in tempo quasi reale i dati delle stazioni all'interno del framework di allenamento e predizione della mappa di scuotimento con risoluzione di 50 metri.

BB-SPEEDSET: AN OPEN-SOURCE DATASET OF NEAR-SOURCE BROADBAND EARTHQUAKE GROUND MOTION FROM 3D PHYSICS-BASED NUMERICAL SIMULATIONS

R. Paolucci, C. Smerzini, M. Vanini

Department of Civil and Environmental Engineering, Politecnico di Milano, Milano, Italy

Introduction. Empirical Ground Motion Models (GMM) (Douglas and Edwards 2016) and ShakeMaps (Wald *et al.,* 2021) represent the reference tool of choice for seismic hazard and risk analyses, but, in spite of their considerable growth and ease of use within the performance-based earthquake engineering framework, they still have some drawbacks. First, the paucity of ground motion recordings in the proximity of the earthquake source still persists and prevents an accurate and robust prediction of the ground motion (and of its uncertainty) in the variety of source-to-site conditions which are typically found in the near-source region (Paolucci *et al.,* 2022). Second, empirical GMMs typically reproduce the spatial correlation of ground motion through simplified approaches based on the stochastic simulation of spatially correlated random fields under the hypotheses of ergodicity, isotropy and stationarity. Such assumptions are hardly found in near-source conditions and may not be suitable to reproduce scenario- and region-specific features of ground motion spatial correlation and cross-correlation (Chen and Baker 2019; Infantino *et al.,* 2021; Schiappapietra and Smerzini 2021).

As in most fields of science, when the experimental observations are limited, numerical modeling may be employed to fill in the gap and gain insight where information from nature is scarce. In this perspective, with the advancement of high-performance computing (HPC) resources, physics-based numerical simulations (PBS) have started to play a role in providing region- and site-specific predictions of seismic shaking and they can be employed, in addition to or in place of observations, to shed light on the physics of near-fault ground shaking and on its spatial variability (McCallen *et al.,* 2021). Based on the rigorous solution of the elastodynamics equation, PBS provides ground motion time histories reflecting the physics of the whole seismic wave propagation problem, from the fault rupture to the propagation path and local site response at shallow geology.

With a long-lasting expertise gained (i) in the development of the open-source spectral element code SPEED (Mazzieri *et al.,* 2013), (ii) in the advancement of techniques to enrich at high frequencies the PBS results (Paolucci et al. 2018), (iii) in the validation of PBS results against near-source ground motions recorded from different earthquakes in Italy and worldwide and in the application to several scenario case studies (e.g. Paolucci *et al.,* 2015; 2021a; Smerzini *et al.,* 2017, amongst others), the research group of Politecnico di Milano has constructed the BB-SPEEDset, an open-source dataset of near-source broadband accelerograms obtained from the source-to-site 3D numerical simulation of seismic wave propagation (Paolucci *et al.,* 2021b).

Overview of BB-SPEEDset. BB-SPEEDset has been constructed by assembling a large set of waveforms simulated by SPEED, in most cases validated against recordings of real earthquakes, and post-processed with an effective workflow apt to generate broadband accelerograms. The generation of broadband time histories starting from low-frequency SPEED results makes uses of a technique based on Artificial Neural Networks – ANN2BB (Paolucci *et al.,* 2018; 2021b), trained on strong motion records.

The dataset includes a total of 12058 three-component simulated waveforms from earthquake scenarios with moment magnitude (M_w) from 5.5 to 7.4 and Joyner-Boore distances (R_{jb}) up to 80 km, see Fig. 1. Strike-slip, normal and thrust events are included in the dataset. Most records refer to normal (50%) and strike-slip (41%) focal mechanisms, while only 9% is from thrust earthquakes. As regards the distribution of BB-SPEEDset with respect to site conditions,

parametrized in terms of the V_{S30}, about 40% of data corresponds to soil conditions with V_{S30}< 800 m/s, and about 60% to rock conditions, with dominance for hard rock sites with V_{S30} larger than 1000 m/s. Within the soil classes, the majority of waveforms is on stiff soil with V_{S30} > 400 m/s, but an appreciable number of data is on very soft sites with V_{S30} as low as 150 m/s.

In addition to the accelerograms, a flat-file provides, for each scenario and each selected receiver, a list of source metadata, post-processing metadata, receiver metadata, site response proxies, source-to-site distances and a broad spectrum of intensity measures (IM). The fields of the flat-file are consistent with the ones adopted in state-of-the-art near-source recorded flat-files, such as the NESS2 dataset (Sgobba *et al.,* 2021). In addition to standard peak IMs, such as Peak Ground Acceleration (PGA), Peak Ground Velocity (PGV), Peak Ground Displacement (PGD) and response spectral accelerations (SA), a variety of integral and frequency-related IMs is included, such as the Housner Intensity (HI), the Cumulative Absolute Velocity (CAV), the Arias Intensity (IA), the IA-based duration (e.g., time interval between 5% and 95% of the total IA, Ds595). Furthermore, in the flat-file compilation, special care was given to the characterization of pulse-like waveforms according to the algorithm proposed by Shahi and Baker (2014), which are of particular interest in earthquake engineering applications owing to their increased damage potential.

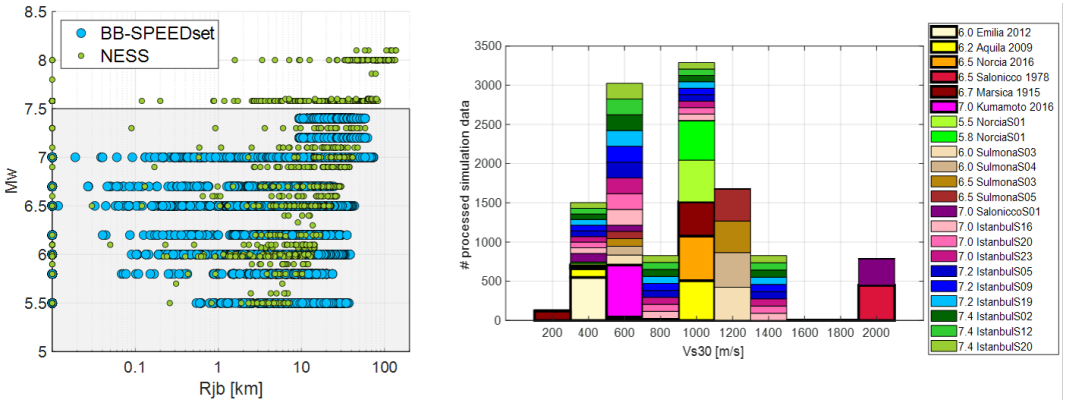


Fig. 1 – Overview of BB-SPEEDset: distribution of data with respect to M_w-R_{jb} (left) and Vs30 (right). In the M_w-R_{jb} plot, the NESS2 dataset is also shown for comparison. Adapted from Paolucci *et al.* (2021b).

A wide set of consistency checks were made to validate the BB-SPEEDset for its future engineering use, by comparing the statistical distributions of different IMs, their attenuation with distance, the features of directional and impulsive near-source accelerograms, with those obtained from recorded ground motions.

As an illustrative example, Fig. 2a shows the cumulative distribution function of selected IMs, namely, PGA and PGV (RotD50 component) as computed from the entire BB-SPEEDset flat-file, in comparison with those obtained from NESS dataset, for the same Mw-Rjb range of data. In Fig. 2b, the trend of the period of the impulsive waveform T_p (according to Shahi and Baker, 2014) as a function of PGD/PGV, for NESS (left), and BB-SPEEDset (right), is shown. Closed-form analytical relationships between T_p and PGD/PGV ratios are also shown in Fig. 2b for Ricker waveleft and double-impulse functions. The comparisons of Fig. 2 (along with other checks not shown here for brevity) point out that the IMs and ground motion features from BB-SPEEDset are consistent, on statistical basis, with those from near-source recorded dataset, as no systematic bias is found.

Finally, to appreciate the level of detail of information stored in BB-SPEEDset, Fig. 3 shows the results which can be extracted by the dataset for a specific earthquake, namely the 2009

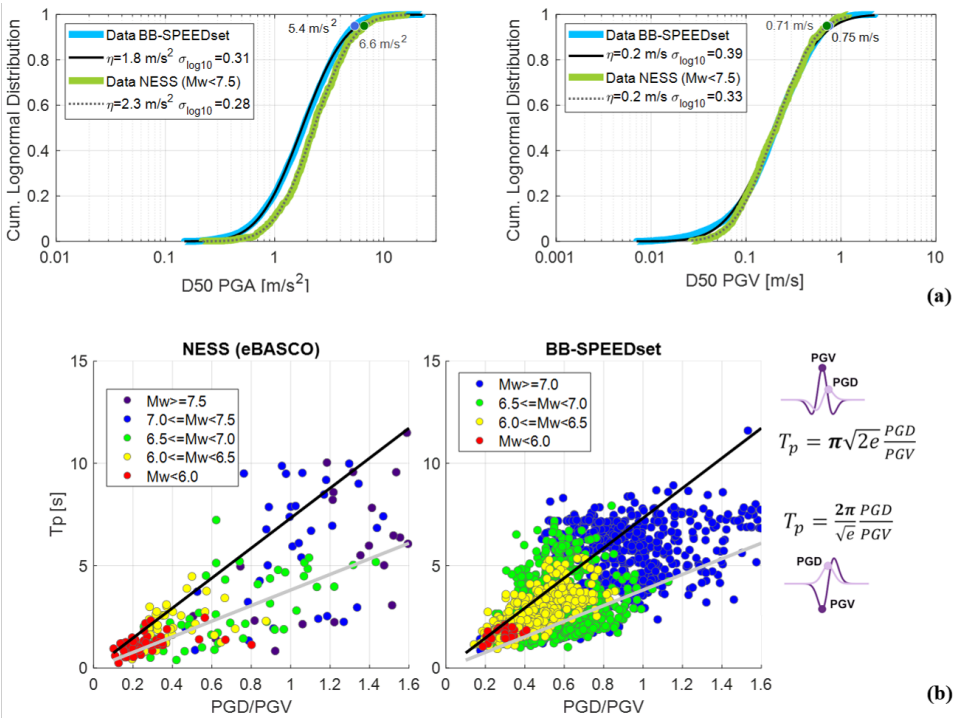


Fig. 2 - Consistency checks between BB-SPEEDset and NESS2 datasets: (a) cumulative distribution functions of RotD50 PGA and PGV from BB-SPEEDset (blue) and NESS (green); (b) pulse period (T_p) as a function of PGD/PGV for the NESS dataset (left) and the BB-SPEEDset dataset (right), together with analytical relationships for Ricker wavelet and double-impulse functions. Adapated from Paolucci *et al.* (2021b).

L'Aquila earthquake. The figure depicts the map of PGA, PGV and PGD, together with the broadband three-component (EW, NS and UD) acceleration, velocity and displacement time histories at selected receivers. Note that the simulated time histories have realistic features in terms of duration, amplitudes and frequency content, with displacement waveforms showing permanent displacements related to the co-seismic slip on the fault. Furthermore,

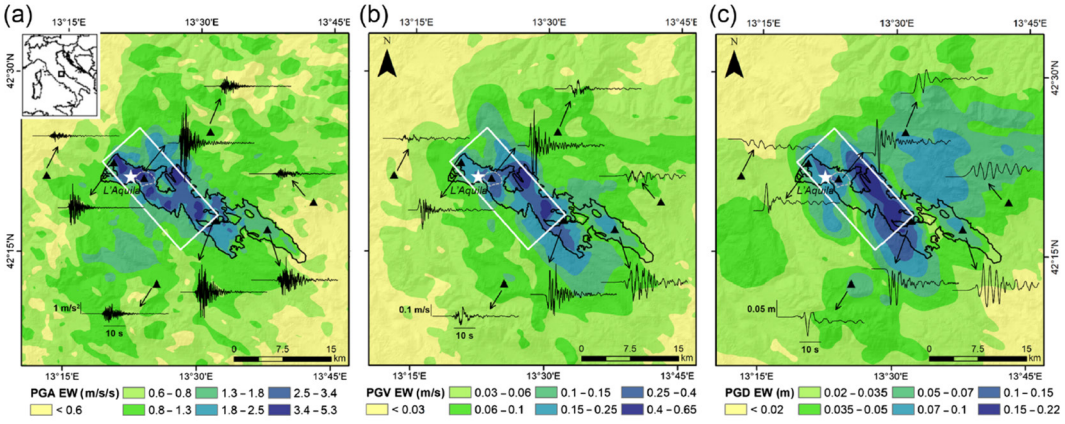


Fig. 3 – M_w 6.2 L'Aquila 2009: peak ground motion maps (left: PGA; center: PGV; right: PGD) and selected broadband waveforms (left: acceleration; center: velocity; right: displacement), EW component, from BB-SPEEDset. From Paolucci *et al.* (2021b).

the spatial correlation of both short- and long-period IMs is well captured, as also supported by independent studies (Infantino *et al.,* 2021).

Conclusions. In this contribution we have presented the BB-SPEEDset, a new validated dataset of near-source broadband earthquake ground motions from 3D PBS obtained with the spectral element computer code SPEED. This is expected to provide researchers and practitioners with a large set of accelerograms obtained from the simulation of real or scenario earthquakes, which, due to the realistic geological and seismotectonic characteristics adopted in their simulation, can be used in place of real accelerograms when these are scarcely available, such as in the near field of strong earthquakes (with impulsive features) or in complex geological configurations.

We envisage that the BB-SPEEDset, either in the present version, or in the following ones enriched by further simulated scenarios, will serve as the basis for several new achievements for an improved characterization and engineering usage of near-source earthquake ground motions, such as for the development of near-source non-ergodic GMMs, to provide region- and site- specific input motions for non-linear structural analyses of engineered systems, to construct region-specific models for spatial correlation of earthquake ground motion.

References

Chen Y, Baker J (2019) *Spatial correlations in CyberShake physics-based ground-motion simulations* Bull Seismol Soc Am 109:2447-2458.

Douglas J, Edwards B (2016) *Recent and future developments in earthquake ground motion estimation* Earth-Sci Rev 160:203-219.

Infantino M, Smerzini C, Lin J *et al.* (2021) *Spatial correlation of broadband ground motions from physics-based numerical simulations* Earthq Eng Struct Dyn 50:2575-2594.

Mazzieri, I, M. Stupazzini, R. Guidotti, and C. Smerzini (2013) *SPEED: SPectral Elements in Elastodynamics with Discontinuous Galerkin: a non-conforming approach for 3D multi-scale problems*, Int J Numer Meth Eng 95, no. 12, 991–1010.

McCallen, D.M., A. Petersson, A. Rodgers, A. Pitarka, M. Miah, F.M. Petrone, B. Sjogreen, N. Abrahamson, H. Tang (2021). *EQSIM-A multidisciplinary framework for fault-to-structure earthquake simulations on exascale computers part I: Computational models and workflow.* Earthq Spectra 37:707-735.

Paolucci, R., I. Mazzieri, and C. Smerzini (2015). *Anatomy of strong ground motion: near-source records and 3D physics-based numerical simulations of the Mw 6.0 May 29 2012 Po Plain earthquake*, Italy, Geophys. J. Int. 203, 2001–2020.

Paolucci, R., F. Gatti, M. Infantino, C. Smerzini, A. G. Özcebe, and M. Stupazzini (2018). *Broadband Ground Motions from 3D Physics-Based Numerical Simulations Using Artificial Neural Networks,* Bull. Seism. Soc. Am. 108, 1272-1286.

Paolucci, R., I. Mazzieri, G. Piunno, C. Smerzini, M. Vanini, A.G. Özcebe (2021a). *Earthquake ground motion modelling of induced seismicity in the Groningen gas field*, Earthquake Engineering and Structural Dynamics 50, 135–154, doi: 10.1002/eqe.3367.

Paolucci R, Smerzini C, Vanini M (2021b) *BB-SPEEDset: A Validated Dataset of Broadband Near-Source Earthquake Ground Motions from 3D Physics-Based Numerical Simulations* Bull Seismol Soc Am 111:2527-2545.

Paolucci R, Chiecchio A, Vanini M (2022) *The older the better? The strange case of empirical ground motion models in the near-source of moderate-to-large magnitude earthquakes* Bull Earthq Eng 20:1325-1342.

Schiappapietra E, Smerzini C (2021) *Spatial correlation of broadband earthquake ground motion in Norcia (Central Italy) from physics-based simulations* Bull Earth Eng 19:4693-4717.

Sgobba, S., C. Felicetta, G. Lanzano, F. Ramadan, M. D'Amico, and F. Pacor, (2021). *NESS2.0: an updated version of the worldwide dataset for calibrating and adjusting ground motion models in near-source*, Bull. Seism. Soc. Am, submitted.

Shahi, S.K., and J.W. Baker (2014). *An Efficient Algorithm to Identify Strong-Velocity Pulses in Multicomponent Ground Motions,* Bull. Seism. Soc. Am. 104, no. 5, 2456–2466. doi: 10.1785/0120130191.

Smerzini, C., K. Pitilakis, and Hashemi K. (2017). *Evaluation of earthquake ground motion and site effects in the Thessaloniki urban area by 3D finite-fault numerical simulations,* Bulletin of Earthquake Engineering 15, no. 3, 787–812.

Wald DJ, Worden CB, Thompson EM, Hearne M. (2021) *ShakeMap operations, policies, and procedures.* Earthquake Spectra, doi:10.1177/87552930211030298.

TOWARDS AN ALTERNATIVE APPROACH TO DEFINE THE DESIGN EARTHQUAKE SCENARIO AT A SITE

R. Paolucci, A. Chiecchio, M. Vanini

Department of Civil and Environmental Engineering, Politecnico di Milano, Milano, Italy

Introduction. The estimation of the characteristics of the ground shaking that occurs during damaging earthquakes is critical both for an efficient risk mitigation and for a correct design of seismic resistant structures (Douglas and Aochi, 2008). In this context, Probabilistic Seismic Hazard Analyses (PSHA) give an estimate of motion that structures and infrastructures need to withstand in terms of clear and communicable probabilities able to support and guide decision making in the mitigation process (Weatherill *et al.*, 2020). The primary advantage of a PSHA, over alternative representations of the earthquake threat, is the possibility of integrating over all possible earthquake occurrences and ground motions (McGuire, 1995). In this framework, the final output of such analyses is given in terms of a Uniform Hazard Spectrum (UHS), which represents the convolution of many different earthquake magnitude and distance (M_w - R) pairs for a fixed annual probability of exceedance. Nevertheless, as many practical applications require the knowledge of the earthquake scenario which is mostly contributing to the hazard at the site under study, in the last couple of decades it has become common practice to disaggregate the hazard into its scenario contributions: magnitude (M_w), source-to-site distance (R) and epsilon (ε). This latter quantity defines the number of standard deviations by which the logarithmic ground motion prediction deviates from the median value (Barani *et al.*, 2009).

Despite their extensive use, the disaggregation procedures developed in the last years suffer from a series of uncertainties which limit their practical application and often make results interpretation ambiguous. The selected (M_w - R) pairs depend on different choices, some of which may be of crucial importance. Besides the dependence on the structural periods, (M_w - R) analyses are developed for a specific branch of the logic tree used in the PSHA, so for a specific combination of ground motion models (GMMs), their values may be calculated from mean, modal or median contributions, evaluated with different procedures (e.g., different bin values). While modal values represent the most likely combination of (M_w - R) pair, mean values are simpler and easier to be understood, but their results may be sometimes poorly related to the physical, known, dominating sources at the site.

In order to shed light and, possibly, overcome these ambiguities, this work suggests an alternative approach to disaggregation that aims at defining a Best Matching Scenario Earthquake (BMSE), fitting the UHS at a specific site and for a return period of interest, at all structural periods, using one, or a combination, of GMMs predictions. In practice, for a given target spectrum, the method selects iteratively the (M_w - R - ε) triplet that minimizes, with an acceptable tolerance, the difference between the "predicted" spectral amplitudes and the "target" ones.

Method. An application of the method to a few sites of the Italian territory is illustrated herein, taking as reference (target spectra) the UHS calculated for the official Italian Seismic Hazard (SH) Map (Mappa di Pericolosità Sismica, MPS04 Working group, 2004). The GMM selected for the calculation of the prediction was the model of Ambraseys *et al.* (1996), that is one of the GMMs used in the framework of the MPS04 SH analysis. For these preliminary analyses we have used, for simplicity, a value of ε=0 (corresponding to the median spectrum prediction).

The difference (Eq. 1) between the logarithm of the AMB96 prediction (Sa_{GMM}) and the logarithm of the UHS target (Sa_{Target}), for a specific (M_w - R) pair, was therefore computed. The spectrum associated to the (M_w – R) scenario that minimized the maximum difference over all periods i (see Eq. 2) was considered as the Best Matching Scenario.

$$diff\left(M_w,\ \mathrm{R},\ T_i\right) = \log 10\left[\mathrm{Sa}_{\mathrm{GMM}}\left(M_w,\ \mathrm{R}, T_i\right)\right] - \log 10\left[\mathrm{Sa}_{\mathrm{Target}}\left(T_i\right)\right] \quad (1)$$

$$err = \min_{M_w,\,\mathrm{R}}\left[\max_i \left| diff\left(M_w,\ \mathrm{R},\ T_i\right)\right|\right] \quad (2)$$

Results. Fig. 1 shows the *(M_w – R)* scenarios computed using the BMSE for a return period of 475yr, for the three sites selected as reference: Milano, Bologna and L'Aquila. The sites are

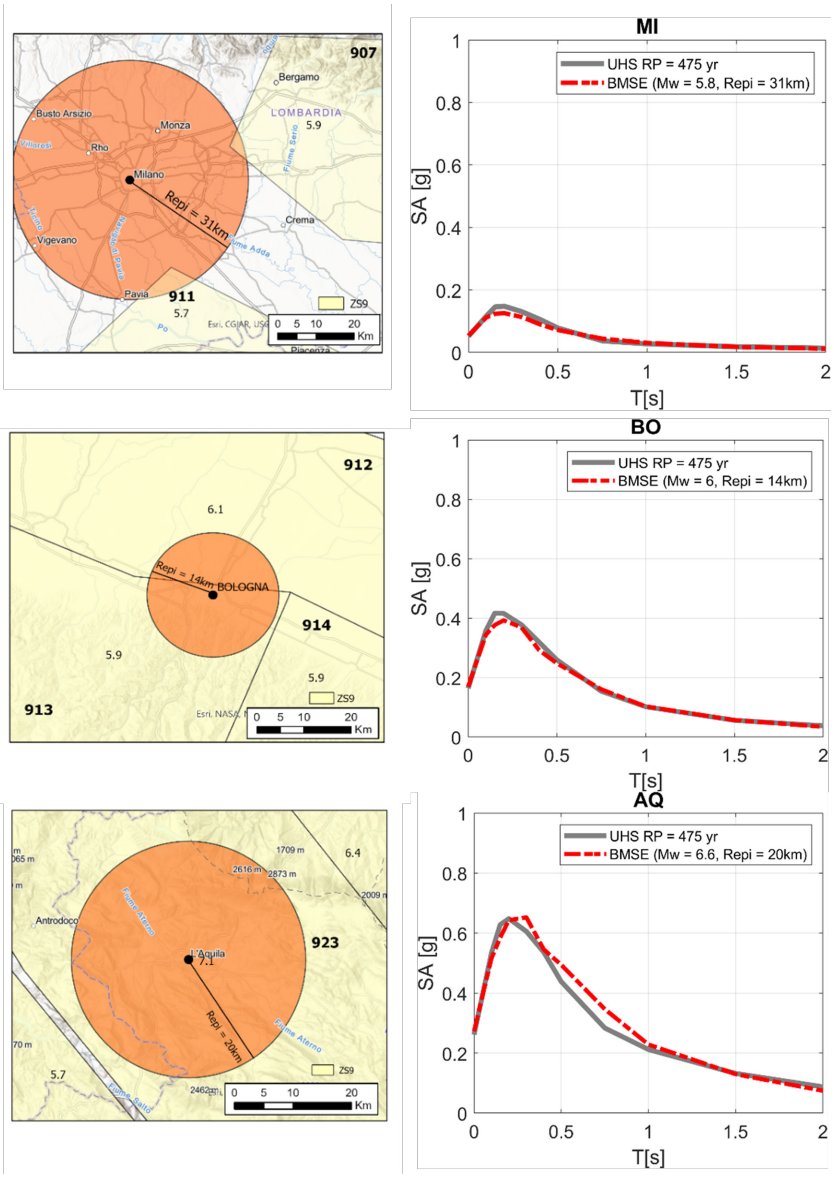


Fig. 1 - Best fitting earthquake scenarios, in terms of magnitude M_w and distance R_{epi}, for three sites of the Italian territory: Milano, Bologna and L'Aquila. The plots on the left show the position of the site with respect to the seismogenic sources of the ZS9 model used in the MPS04 SH analyses. The numbers are the maximum magnitudes associated to the seismogenic sources. The circles show the scenario epicentral distances R_{epi}. The plots on the right show the best fitting (M_w – R_{epi}) spectrum (red dashed lines) together with the corresponding UHS target (grey solid lines). All the results refer to a return period of 475 years and an ε value of 0.

shown on the left together with the nearest seismogenic sources of the ZS9 model used in the MPS04 SH analyses (Meletti *et al.*, 2008). The circles show the scenario epicentral distances R_{epi}. The best fitting spectra are shown on the right (in red dashed line) together with the corresponding target UHS spectra (grey solid line). As remarked, ε was considered equal to zero.

Results are in close agreement with the seismogenic framework of the analysis: the best matching scenario is an earthquake that is compatible with the sources that have been used to calculate the hazard. For Milano, for instance, the best fitting scenario is an earthquake that may be generated on source 907 or 911, at a distance of about 30 km, with a magnitude that is quite near the maximum magnitude that characterizes the seismogenic sources (shown on each plot).

Table 1 shows the calculated BMSE for the three reference sites compared with the probabilistic disaggregation results from Barani et al. 2009 study, for the same return period but different structural periods. The disaggregation performed by Barani et al. shows different scenarios for each site: a smaller magnitude local scenario, mostly contributing to the higher frequencies, and a higher magnitude distant scenario, dominating at longer periods. Note that, while the results from the BMSE are related to the median predictions of the GM model (ε=0), the results from Barani et al. have ε values considerably higher than 1, and this is the reason for the difference in the $(M_w – R)$ scenario values. The higher ε values are related to the coda of the distributions of the GM models having higher uncertainties.

The discrimination among different best matching scenarios for the same site is currently not possible, but further research is being under development.

Tab. 1 - Best Matching scenarios earthquakes calculated for the three reference sites, compared with the disaggregation results from Barani *et al.,*-- 2009, for the same sites and return period.

	BMSE				**Mean values from Barani *et al.* (2009)**		
Site	Mw	Repi [km]	ε	T (s)	$\hat{M}w$	$\hat{R}epi$ [km]	$\hat{\varepsilon}$
Milano	5.8	31	0	0.2 1	5.1 5.5	65 109	1.88 1.58
Bologna	6	14	0	0.2 1	5 5.4	9.6 18.6	1.11 1.4
L'Aquila	6.6	20	0	0.2 1	5.8 6.5	9.3 18.2	1.13 0.91

Conclusions. As a first conclusion, this work shows how the results obtained with the Best Matching Scenario Earthquake fitting procedure were found to be generally consistent with the seismotectonic framework of Italy: the calculated earthquake scenarios showed values of magnitude and distance in general agreement with the seismogenic sources used to calculate the hazard at most of the considered sites.

Although these results are just preliminary, they are indeed quite appealing in the sense of finding an alternative approach that may overcome the drawbacks of probabilistic disaggregation. As main advantages, the resulting scenarios: (i) are not related to a specific structural period, (ii) do not depend on the choice of the moment value of the statistical distribution of magnitudes and distances, (iii) can be obtained using the same GMMs of a PSHA, with the same weighting, (iv) can be of immediate and simple use even to non-expert users.

As future research, the authors are working on further site-specific validations, as well as on the possible identification of more than one 'best' scenario, which is of particular interest in areas where the hazard is dominated by different sources.

Acknowledgements and funding. This work has been supported by the Department of Civil Protection within the DPC-ReLUIS project WP18 "Normative contributions related to seismic action (CONpAS)", Task 5 "Definition of the design earthquake scenario". This work has also been supported by PON Ricerca e Innovazione (Next Generation EU) which funded the Ph.D. grant of the author A. Chiecchio.

References

Ambraseys N.N., Simpson K.A. and Bommer J.J.; 1996: *Prediction of horizontal response spectra in Europe*. Earthquake Engineering and Structural Dynamics, 25: 371 – 400.

Barani S., Spallarossa D., Bazzurro P.; 2009: *Disaggregation of probabilistic ground-motion hazard in Italy.* Bulletin of the Seismological Society of America, 99: 2638-2661. Doi:10.1785/0120080348.

Douglas J. and Aochi H.; 2008: *A Survey of Techniques for Predicting Earthquake Ground Motions for Engineering Purposes*. Surveys in Geophysics, 29: 187-220. Doi:10.1007/s10712-008-9046-y.

McGuire R.K.; 1995: *Probabilistic seismic hazard analysis and design earthquakes: Closing the loop*. Bulletin of the Seismological Society of America, 85: 1275-1284. Doi: 10.1785/BSSA0850051275.

Meletti C., Galadini F., Valensise G., Stucchi M., Basili R., Barba S., Vannucci G., Boschi E.; 2008: *A seismic source zone model for the seismic hazard assessment of the Italian territory*. Tectonophysics, 450: 85-108. Doi: 10.1016/j.tecto.2008.01.003.

MPS Working Group; 2004: *Redazione della Mappa di Pericolosità Sismica Prevista dall'Ordinanza PCM del 20 Marzo 2003 n.3274, All. 1, Rapporto Conclusivo per il Dipartimento della Protezione Civile*. Istituto Nazionale di Geofisica e Vulcanologia (INGV), Milano-Roma, Italy, Aprile 2004.

Pasolini C., Gasperini P., Albarello D., Lolli B. and D'Amico V.; 2008: *The Attenuation of Seismic Intensity in Italy, Part I: Theoretical and Empirical Backgrounds*. Bulletin of the Seismological Society of America, 98: 682-691. Doi: 10.1785/0120070020.

Sgobba S., Felicetta C., Lanzano G., Ramadan F., D'Amico M., Pacor F.; 2021: *NESS2.0: An Updated Version of the Worldwide Dataset for Calibrating and Adjusting Ground-Motion Models in Near Source*. Bulletin of the Seismological Society of America, 111: 2358–2378. Doi:10.1785/0120210080.

Weatherill G., Kotha S.R. and Cotton F.; 2020: *A regionally – adaptable "scaled – backbone" ground motion logic tree for shallow seismicity in Europe: application to the 2020 European seismic hazard model*. Bulletin of Earthquake Engineering, 18: 5087–5117. Doi: 10.1007/s10518-020-00899-9.

TESTING SITE AMPLIFICATION CURVES IN HYBRID BROADBAND GROUND-MOTION SIMULATIONS OF M6.0, 24 AUGUST 2016 AMATRICE EARTHQUAKE, ITALY

M. Pischiutta[1], A. Akinci[2], C. Felicetta[3], F. Pacor[3], P. Morasca[3]

[1] Istituto Nazionale di Geofisica e Vulcanologia, Sezione Roma2, Italy
[2] Istituto Nazionale di Geofisica e Vulcanologia, Sezione Roma1, Italy
[3] Istituto Nazionale di Geofisica e Vulcanologia, Sezione Milano, Italy

This research focuses on predicting and assessing earthquake impact due to future scenarios regarding the ground motion seismic hazard by accounting mainly for site effect in the Central Apennines. To this end, we produced synthetic broad-band seismograms by adopting a hybrid simulation technique for the Mw6.0 Amatrice earthquake, Central Italy, on 24 August 2016, accounting for site conditions by means of amplification curves, computed with different approaches. Simulations were validated by comparing with data recorded at 57 strong-motion stations, the majority installed in urban areas. This station sample was selected

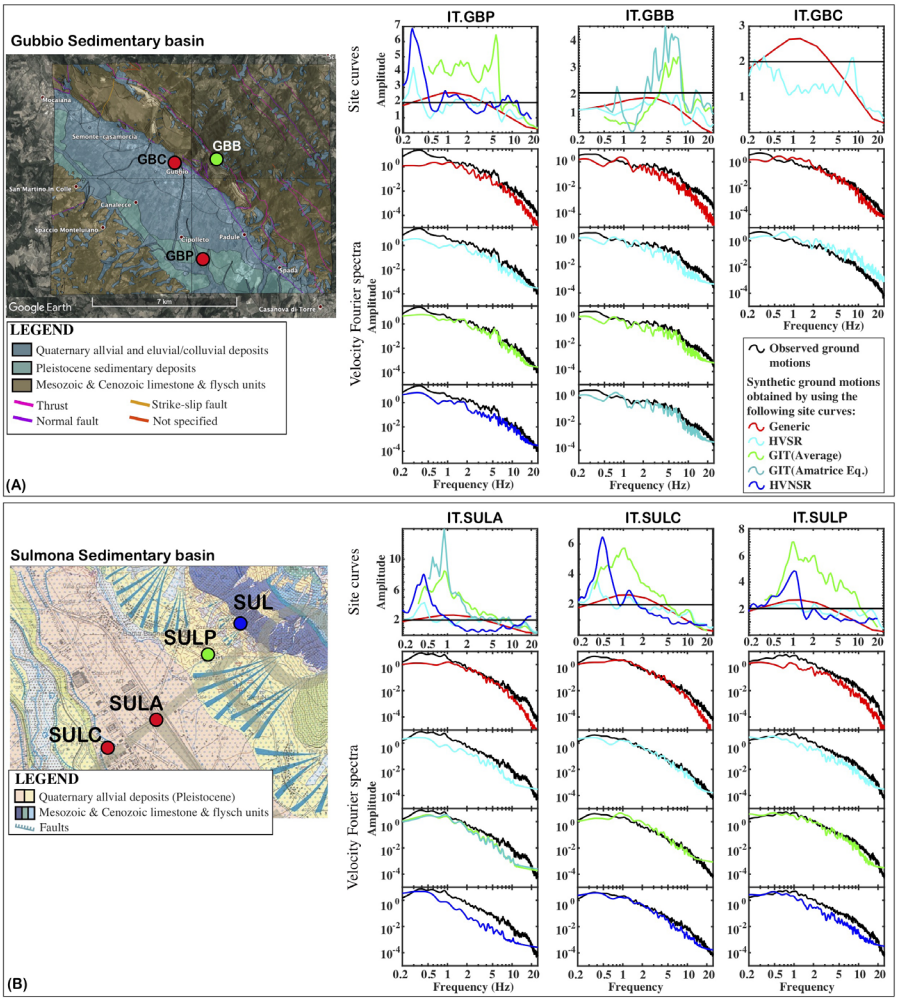


Fig. 1 - Simulation results and records of Amatrice earthquake at Gubbio (panel A) and Sulmona sedimentary basins (panel B). For each site we add: a rough geological map of the area (provided in the ITACA database); the applied generic and empirical site curves at each station (consistently with Fig. 2); Synthetic velocity Fourier spectra were obtained using the different site curves and recorded velocity Fourier spectra (geometric mean of the two horizontal components).

among stations recording the Amatrice earthquake within an epicentral distance of 150 km and potentially prone to experience site amplification effects because of lying in particular site conditions (sedimentary basins, topographic irregularities, fault zones). The evaluation of amplification curves best suited to describe local effects is of great importance because many towns and villages in central Italy are built in very different geomorphological conditions, from valleys and sedimentary basins to topographies.

In order to well reproduce observed ground motions, we accounted for the site amplification effect by testing various generic and empirical amplification curves such as Horizontal-to-Vertical Spectral Ratios (calculated from Fourier spectra using both earthquakes, HVSR, and ambient noise, HVNSR, recordings), and those derived from the Generalized Inversion Technique (GIT). The site amplifications emanated from GIT improve the match between observed and simulated data, especially in the case of stations installed in sedimentary basins, where the empirical amplification curve effectively reproduces spectral peaks (ex. Gubbio and Sulmona sedimentary basins, see Figures 1 and 2). On the contrary, the worst performances are for the spectral ratios between components, even compared to the generic site amplification, although the latter ignores the strong bedrock/soil seismic impedance contrasts.

At sites on topography, we did not observe any systematic behavior, the use of empirical curves ameliorating the fit only in a small percentage of cases.

This is a novel application considering that usually studies adopting stochastic modelling refer to bedrock conditions, or otherwise they use generic site amplification curves. Conversely, empiric site amplification curves that we implemented in our simulation, are able to account for site-specific frequency effects caused by local geological structure. Therefore, our results may provide a valuable framework for developing ground-motion models for earthquake seismic hazard assessment and risk mitigation, especially in urban areas located in the seismically active central Italy region.

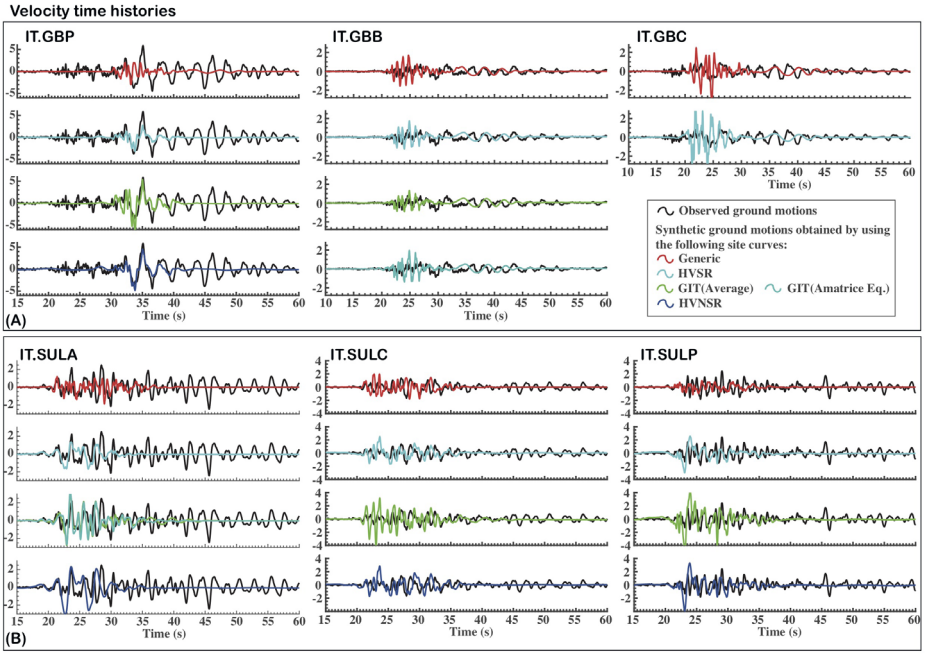


Fig. 2 - Velocity time series at Gubbio (panel A) and Sulmona (panel B) sites. In black, we plot recorded seismograms (arithmetic mean of the two horizontal components). Colored lines depict synthetic hybrid seismograms obtained from the HF and LF contributions (see section 2.3), obtained through the EXSIM code seismic source inversion by Tinti *et al.* (2016). They were obtained by using empirical site curves in the EXSIM code: GIT (green), HVSR (cyan), and HVNSR (blue).

SELECTION OF THE SEISMIC INPUT FOR SITE RESPONSE NUMERICAL SIMULATIONS WITHIN THE SEISMIC MICROZONATION IN THE APULIAN REGION

A. Romeo[1], P. Pierri[1], D. Casarano[2], V. Del Gaudio[1]

[1] Dipartimento di Scienze della Terra e Geoambientali, Università degli Studi di Bari "Aldo Moro", Bari, Italy
[2] Consiglio Nazionale delle Ricerche – Istituto di Ricerca per la Protezione Idrogeologica - Bari, Italy

Introduction. Seismic Microzonation (SM) studies are ongoing in the Apulian region, where seismic hazard depends on two types of active seismogenic structures: 1) autochthonous faults, mainly located in northern Apulia, capable of causing highly energetic earthquakes with rather long return times; 2) tectonic structures located in neighbouring regions, which can generate very strong earthquakes. This region presents a considerable heterogeneity of site conditions due to different geological-structural domains: orogenic belt (Daunia Mounts), foredeep (Tavoliere Plain) and foreland (Gargano, Murge). This geologic variability implies a heterogeneity of seismic scenarios potentially capable of affecting local seismic hazard.

The site response properties can be obtained by numerical simulations that require the selection of waveforms to be used as seismic inputs. Accelerometric databases collect real waveforms for a variety of seismic scenarios, however often not representative of the studied area; so we combined real and synthetic accelerograms.

In this paper we propose an approach to optimise the selection of the seismic inputs for seismic response numerical simulations. The results of the first tests of its application appear promising and the method will be implemented in the third level studies of SM planned for the Apulia region.

Method. The proposed approach for the selection of the accelerograms to be used in numerical simulations of site response consists in the following stages:

1) determination of spectral acceleration values (SA) having, on soils of category A, an exceedance probability of 10 % in 50 years, which correspond to the ordinates of the elastic design spectrum for safety verification at the Ultimate Limit State;
2) definition of the parameters (earthquake magnitude, distance and style of fault) of seismic scenarios contributing to 2/3 of the total basic seismic hazard expressed by PGA values having an exceedance probability of 10 % in 50 years;
3) extraction, from accelerometric databases, of real accelerograms as compatible as possible with the seismic scenarios defined at the stage 2);
4) selection, among the accelerograms found at stage 3), of the 4 accelerograms best fitting, in the period range 0.05-2 s, the SA values determined at the stage 1);
5) calculation of the differences between the median values of the SA values of the accelerograms selected at the stage 4) and the design spectrum obtained at the stage 1);
6) definition of a target spectrum in the range 0.05-2 s for the generation of simulated accelerograms, by subtracting the differences obtained at the stage 5) from the design spectrum obtained at the stage 1);
7) generation of 20 simulated accelerograms for each scenario defined at stage 2) and selection of the 3 accelerograms, relative to different scenarios, best fitting the target spectrum calculated at the stage 6).

The spectra to be determined at the stage 1) can be derived for any point of the Italian territory following the Italian Building Code (MIT, 2018 – hereinafter NTC18).

In the implementation of the proposed method, the seismic scenarios to be defined at the stage 2) are identified from a disaggregated analysis of the seismic hazard (Bazzurro and Cornell, 1999). The results of this type of analysis for PGA values having 10 % exceedance probability in 50 years are provided by INGV for a grid of points spaced by about 5 km, covering

the entire Italian territory (http://esse1-gis.mi.ingv.it). For each investigated zone where numerical simulation of site response are planned, the closest node of the grid is selected to obtain the parameters of the scenarios satisfying the criterion indicated for the stage 2). The results of the disaggregation analysis are reported as fractions of the contribution to hazard for combinations of linearly spaced intervals of magnitude (M) and distance (D), thus we select the smallest number of M/D interval combinations whose cumulative contribution to hazard exceed 2/3 of the total (Fig. 1). All the combinations within such intervals are considered representative of scenarios among which to search for accelerograms that could be used as seismic inputs of site response simulations.

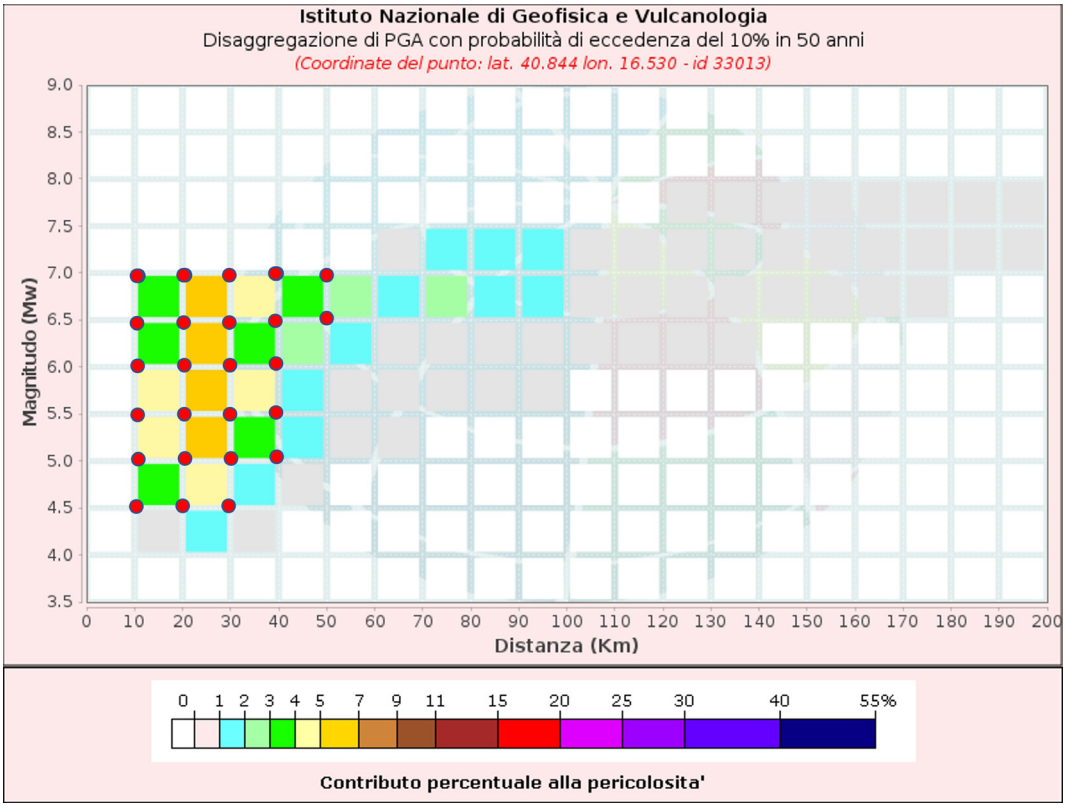


Fig. 1 - Example relative to Altamura, showing the selection of the scenario parameters for which accelerograms are considered in the following stage of the proposed procedure, in search of those accelerograms whose SA values match the local design spectrum. Red dots represent the M/D combinations taken into consideration in the search for accelerograms from the available databases.

Regarding the real records to be extracted at the stage 3) from existing databases, in our tests we have used the RexelWeb tool (Sgobba *et al.*, 2021) linked to the databases ITACA (Russo *et al.*, 2022) and ESM (Luzi *et al.*, 2020), which provide Italian and European accelerograms. In addition to RexelWeb, we have used also the international database CESMD (www.strongmotioncenter.org). These web resources allow to extract accelerograms recorded within a selected distance interval from the location of events with magnitude falling in a selected range and caused by a predefined type of fault. Thus, the results of the analysis carried out at the stage 2) are used to define the upper and lower bound of magnitude and distance to be used in the accelerogram selection.

The stages from 4 to 7 were carried out through a computer programme purposely written in FORTRAN, which incorporates a routine for the simulation of non-stationary stochastic ground motions, according to the method proposed by Sabetta *et al.* (2021), derived from the code provided by the authors. This programme, first examines the real accelerograms extracted from the available databases during the stage 3), finding the four whose SA values best fit those of the design spectrum at selected values of periods between 0.05 and 2 s. Then the target spectrum for the simulated accelerograms is calculated according to the criterion defined for the stage 6 and, for each M/D combination defined at the stage 2), 20 randomly varying accelerograms are generated. For each scenario, the procedure selects the accelerogram whose SA values best fit the target spectrum at the same periods used for the selection of the real accelerograms and, finally, the 3 scenarios providing the best fitting supply the chosen accelerograms.

Discussion. In this study we focused our attention on simulated and natural accelerograms. As a matter of fact, natural records are not always available (or not in a sufficient number) for predefined scenarios. Sometimes the range of the parameters (earthquake magnitude, distance and style of fault) of the scenarios to be represented by the selected seismic inputs need to be enlarged to find enough waveforms among which to select those best fitting the spectrum defined at stage 1), so simulated accelerograms may be the only way to obtain more appropriate records for the representation of relevant scenarios.

According to the Italian National Guidelines for the SM Studies (Gruppo di Lavoro MS, 2008) the minimum size of the accelerogram set used as seismic input should be 7 records, of which at least 4 should be real accelerograms; these records should be representative of the ground motion recorded on a stiff ground. The most recent update of the National Guidelines for the execution of SM studies (CTMS, 2020), specifies that, as final product, these studies should draw three maps reporting a subdivision of the investigated territory into "Microzones" characterised by different amplifications of spectral accelerations for 3 period ranges (0.1-0.5 s, 0.4-0.8 s, 0.7-1.1 s). Thus, the seismic input from which numerical simulations derive the estimate of such amplification should show a compatibility with the elastic design spectrum at the site of the simulation, at least in a range of periods from 0.1 to 1.1 s. However, in the stage 4) and 6) of the proposed procedure we have slightly enlarged this range to avoid the selection of accelerograms whose acceleration response spectrum deviates significantly from the design spectrum immediately outside the period range of interest.

The selection of real and simulated accelerograms best fitting the target spectra is based on finding the minimum misfit between the acceleration response spectra of the examined records and of the target spectrum, according to the formula proposed by Iervolino *et al.* (2010).

This formulation was directly used for the selection of the 4 real accelerograms best fitting the design spectrum. For the simulated seismograms, considering that they are generated according to a stochastic approach, the adopted procedure admits the possibility of scaling the generated accelerogram by a constant factor K calculated as that minimizing the misfit.

However, during the examination of all the accelerograms generated, only the 60 ones for which the factor K has the values closest to 1 are considered as candidates for the selection of those providing the minimum misfit. This expedient avoids taking into consideration accelerograms derived from scenarios that provide SA values too much far from the target spectrum.

The use, as target spectrum, of one modified with respect to the local design spectrum, according to the criterion defined for the stages 5) and 6), was motivated by the consideration that the median of the SA values for the real accelerograms selected could present a significant discordance at some period intervals. In view of obtaining a final set of 7 accelerograms for

which the median of the SA values be as close as possible to the local design spectrum, the modification of the target spectrum for the simulated accelerogram leads to a compensation for the discordance affecting the subset of the real accelerograms.

In the implementation of the proposed procedure some alternative options could be followed. The set of periods for which the misfit is calculated could be spaced by a linearly or logarithmically constant interval. Another possibility of alternative choices concerns the selection of accelerograms that can be representative of scenarios most contributing to hazard for each of the 3 relevant period intervals. It could be desirable that accelerograms representative of all these scenarios be included in the final set of 7 accelerograms. Therefore the programme allows to choose, for the real accelerograms, in addition to the accelerogram best fitting the entire design spectrum, other 3 accelerograms providing the best fitting in each of the mentioned period range. This criterion is then used also for the selection of the 3 simulated accelerograms.

Tests of applications of the procedure according to these alternative options are underway for sites located in the different geological domains of the Apulia region, in order to assess whether the different options may be preferable in the presence of different characteristics of the basic seismic hazard.

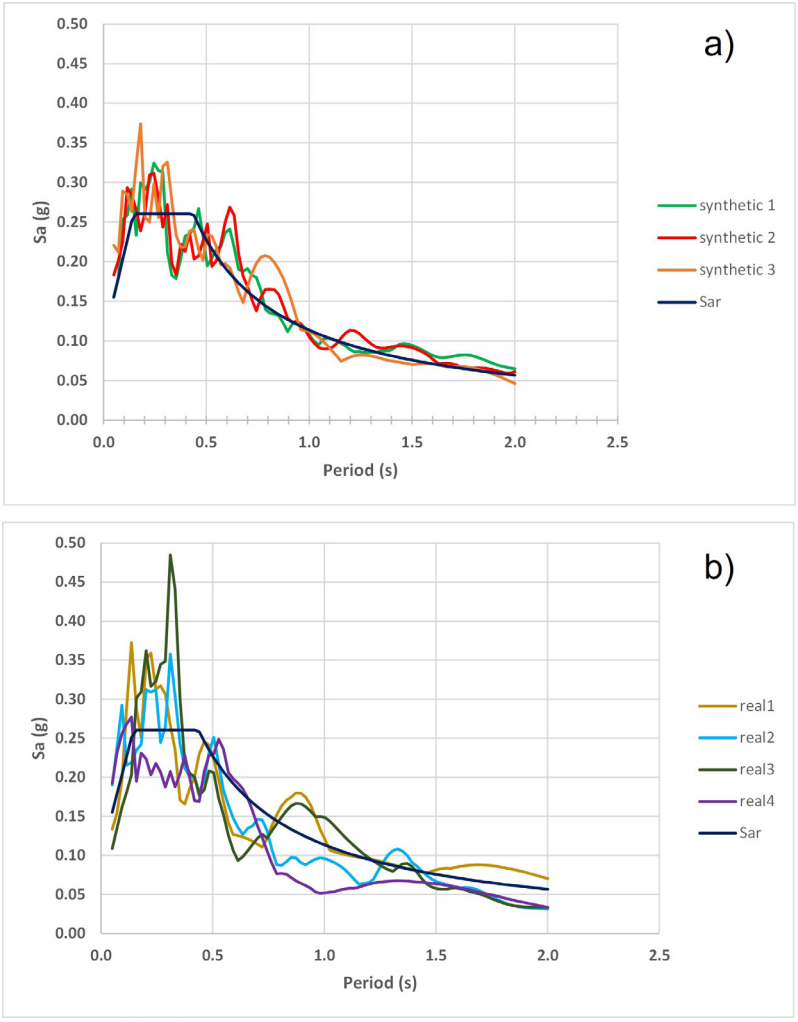


Fig. 2 - Spectral acceleration response (coloured curve) of the real (a) and simulated (b) accelerograms selected, through the proposed procedure, for the site response simulations at Altamura and comparison with the local design spectrum on soils of category A for the Ultimate State limit (black line).

First results show that the procedure allows to select a set of accelerograms combining the requirements of representing differentiated seismic scenarios and maintaining a good average agreement with the local design spectrum without introducing, to reach this agreement, accelerograms characterised by SA values strongly discarding both by excess and by defect from those of the design spectrum. As an example, Fig. 2 shows the set of accelerograms obtained for Altamura (BA) compared to the local design spectrum calculated according to the NTC18. Fig. 3 shows the median of the SA values for the selected set of accelerograms compared to the NTC18 spectrum.

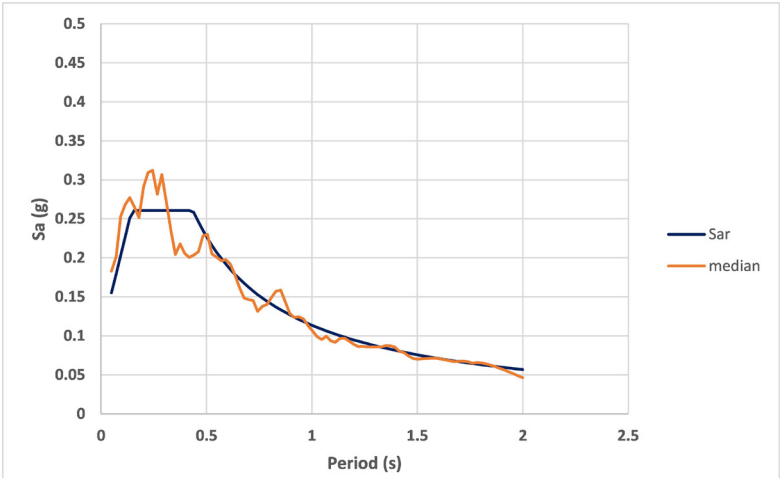


Fig. 3 - Comparison between the median of the spectral acceleration responses of the seven accelerograms selected as seismic inputs for site response simulation at Altamura, compared with the local design spectrum on soils of category A for the Ultimate State Limit.

Acknowledgements. This study was conducted within the programme of SM of the Apulia Region, financed by the National Department of Civil Protection and by Civil Protection Office of the Apulian Regional Administration. We are particularly grateful to Antonio Pugliese for having provided the original source code in FORTRAN of the programme NERO_LITE for the generation of the simulated seismograms.

References

Bazzurro P. and Cornell C.A.; 1999: *Disaggregation of seismic hazard.* Bull Seism. Soc. Amer. 89:501-520.

CTMS; 2020: *Microzonazione sismica - Standard di rappresentazione e archiviazione informatica - Versione 4.2*. Roma, 138 pp.

Gruppo di lavoro MS; 2008. *Indirizzi e Criteri per la Microzonazione Sismica*. Conferenza delle Regioni e delle Province autonome - Dipartimento della protezione civile, Roma, 3 vol. e DVD.

Iervolino I., Galasso C. and Cosenza E.; 2010: *Rexel: computer aided record selection for code-based seismic structural analysis*. Bull Earthq Eng 8:339-362.

Luzi L., Lanzano G., Felicetta C., D'Amico M. C., Russo E., Sgobba S., Pacor, F., and ORFEUS Working Group 5; 2020: *Engineering Strong Motion Database (ESM) (Version 2.0)*. Istituto Nazionale di Geofisica e Vulcanologia (INGV).

MIT; 2018: *Aggiornamento delle "Norme tecniche per le costruzioni".* Supplemento ordinario alla "Gazzetta Ufficiale n. 42 del 20 febbraio 2018 - S.O. n. 8.

Russo E., Felicetta C., D'Amico M., Sgobba S., Lanzano G., Mascandola C., Pacor F. and Luzi L.; 2022: *Italian Accelerometric Archive v3.2.* Istituto Nazionale di Geofisica e Vulcanologia, Dipartimento della Protezione Civile Nazionale, doi: 10.13127/itaca.3.2.

Sabetta F., Pugliese A., Fiorentino G., Lanzano G. and Luzi L.; 2021: *Simulation of non-stationary stochastic ground motions based on recent Italian earthquakes*. Bull. Earth. Eng. 19:3287-3315. https://doi.org/10.1007/s10518-021-01077-1.

Sgobba S., Felicetta C., Russo E., D'Amico M., Lanzano G., Pacor F., Luzi L., Baraschino R., Baltzopoulos G. and Iervolino I.; 2021: *The online graphical user interface of REXELweb for the selection of accelerograms from the Engineering Strong Motion database (ESM)*. 39° Conference of Gruppo Nazionale di Geofisica della Terra Solida (GNGTS), 22 - 24 July 2021, online.

EMPIRICAL NONERGODIC GROUND SHAKING SCENARIOS FOR CENTRAL ITALY: METHODOLOGY AND APPLICATIONS

S. Sgobba, F. Pacor, G. Lanzano

Istituto Nazionale di Geofisica e Vulcanologia (INGV), Sezione di Milano, Italy

Earthquake-induced shaking scenarios represent increasingly crucial elements for the description of seismic motion and its spatial variability, which are key-elements in understanding the processes of past events as well as for seismic risk purposes in engineering applications and civil protection strategies. Today, great resources are devoted to the generation of such scenarios mainly based on the adoption of physically-based 3D numerical simulations, performed with different techniques, which provide a physical representation of the finite fault rupture process, seismic wave propagation and attenuation. However, these methods, while providing more realistic fields of motion, often require complex modeling of the fault rupture and the crustal medium, apart from being computationally expensive. Empirical approaches to shaking scenarios generation have also emerged in recent years (e.g. USGS ShakeMap; Worden *et al.*, 2018), which are essentially based on the use of existing ground motion models (GMMs), providing the probability distribution of a given ground motion parameter as a function of basic explanatory variables, such as event magnitude, source-site distance, and soil conditions.

Although GMMs provide robust estimates of the median ground motion, they are affected by inherent limitations such as the insufficiency in dealing with the spatial correlation that causes isotropic and stationary description of ground motion, a poor link with the physical parameters and, mostly, the assumption of ergodicity. The latter means that the models are calibrated on a global scale, assuming that the variability at a single site from a specific source is identical to that derived from multiple sites over large regions (Anderson and Brune, 1999). This hypothesis causes a great uncertainty associated with the model's predictions, thus essentially neglecting those characteristics that imprint to seismic motion peculiar and systematic effects on a regional scale, such as source scaling and attenuation features. More accurate predictions can be obtained by relaxing the ergodic assumption in favor of non-ergodic approaches, in which the repeatable terms of variability due to source-, path- and –site effects are used to provide region-specific corrections of the median predictions, as well as to move part of the aleatory variability into epistemic uncertainty (e.g. Rodriguez-Marek *et al.,* 2013; Landwehr *et al.,* 2016, Kuehn *et al.,* 2019; Abrahamson *et al.,* 2019, Sgobba *et al.,* 2019, Lanzano *et al.,* 2021, Parker *et al.,* 2022, among others). An example of a fully nonergodic methodology for Central Italy is provided by Sgobba *et al.* (2021), which is the base of the approach presented here.

Methodology. Following the study by Sgobba *et al.* (2021), the estimates of an *ad-hoc* regional GMM calibrated at reference level (i.e. without site amplification) are adjusted for between-event and source region correction and combined with the maps of the source-to-site paths and site-response, being capable of generating nonergodic predictions of ground shaking on a regular grid (1.6x1.6 km).

The systematic and repeatable effects of ground motion, estimated via residual analysis, are identified in the following components (more details can be found in Sgobba *et al.*, 2021):

- A correction of the location-to-location terms (δL2L) defined as the average between-event term within the source region. The location terms are computed by means of a clustering approach in which the events are aggregated and averaged within polygonal areas identified on the basis of spatial-temporal criteria of clustering. δL2L reflect the average stress-drop within the source region;
- A map of the propagation effects based on the (non-stationary) spatial correlation of the path-to-path terms (δP2P), i.e. the systematic deviations of ground motion along each

source-to-site path. These are related to anomalies in crustal velocity, density or in the attenuation function.

- A map of the site effects based on the spatial correlation of the site-to-site residual terms (δS2S). These are calculated with respect to the average ground motion level at the reference sites, so they can be considered as a proxy of the amplification function of the site;

The method provides more accurate predictions with respect to standard GMM applied in Italy along with less total uncertainty (Sgobba *et al.*, 2021).

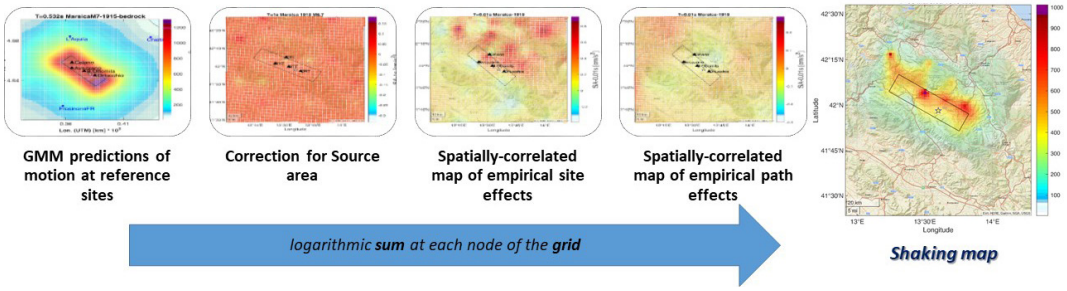


Fig. 1 - Sketch of Sgobba *et al.* (2021) method for the generating empirical shaking scenarios at the site.

Findings and developments. The approach has been applied to past events, as well as for predictive purposes of virtual events, leading to build a portfolio of scenarios for Central Italy that include the main events occurred in the area in the last years, such as L'Aquila Mw6.0 2009, Amatrice Mw6.1 2016, Norcia Mw6.5 2016 or historical events like Gubbio Mw 5.6 1984 and Fucino Mw6.7 1915 (example of map in Fig. 2).

The application of the method to the reconstruction of historical events in the pre-instrumental era is strategic, as it allows new insights to be gained into the study of such events thanks to the exploitation of the extensive sampling of records available in this region to date.

The obtained spatially-variable fields reproduce anisotropy and non-stationarity of the main ground motion patterns related to physical features not captured by ergodic GMMs, such as systematic effects linked to the seismic source and the crustal propagation that are documented in the literature for the selected events with reference to instrumental data or macroseismic observations.

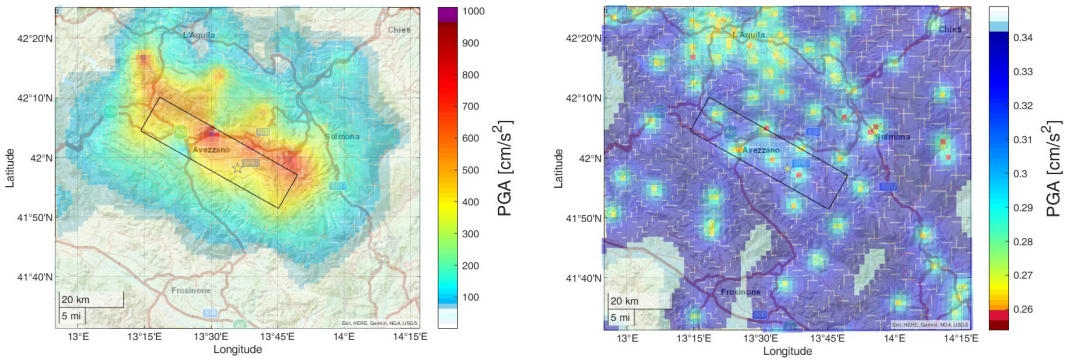


Fig. 2 - Example of shaking map of the historical earthquake Mw6.7 1915 Fucino (median field) (a) and variability map (b) for PGA. Star indicates the epicenter of the event, black triangles indicate the observing sites, the rectangle represents the fault rupture projection.

The method shows the ability to characterize the heterogeneity of the ground motion of earthquakes even considering the effects of finite fault and site response in complex conditions (2D and 3D).

For instance, our study finds that the empirical observations of path-specific residuals correlate well with expected propagation effects in Central Apennine region, which reflect the underlying geomorphological structure and the evidences on the rheology and tectonic stability of portion of earth crust (i.e., amplification of ground motion corresponds to lower attenuation). Local effects due to shallow geology or basin effects at long-periods are also captured by the site corrections and consequently by the final shaking maps.

The application potential of this promising methodology is mainly intended in the field of site-specific hazard and risk assessments with the aim to:

- assessing the shaking pattern of events in near real-time;
- post-processing past and historical earthquakes;
- designing an intermediate-level technique for scenarios simulation, useful until the results of numerical models are made available;
- preliminarily judge the reasonability of numerically simulated scenarios;
- reproducing scenarios of potential future events.

Ongoing developments include the adoption of an advanced approach for geospatial modeling of the empirical site functions at those sites that lack direct observations to get more accurate site maps, as well as the integration of the empirical effects of rupture directivity in the predictions.

The approach proposed here is very promising in densely sampled areas because the estimation of repeatable site, propagation and source terms is reliable. In areas where records are limited, the development of hybrid ground motion models, based on the integration of observed and simulated data, could be a viable alternative.

Acknowledgments. This study has also benefited from funding provided by the agreement B1, DPC-INGV 2019–2021 between INGV and the Italian Dipartimento della Protezione Civile (DPC).

References

Abrahamson, N. A., Kuehn, N., Walling, M., and Landwehr, N. (2019). *Probabilistic Seismic Hazard Analysis in California Using Nonergodic Ground-Motion Models.* Bull. Seismol. Soc. Am., 109(4), 1235-1249. https://doi.org/10.1785/0120190030.

Anderson, J. G., and Brune, J. N. (1999). *Probabilistic Seismic Hazard Analysis without the Ergodic Assumption.* Seismol. Res. Lett., 70(1), 19-28. https://doi.org/10.1785/gssrl.70.1.19.

Lanzano, G., Sgobba, S., Caramenti, L., Menafoglio, A. (2021). *Ground-Motion Model for Crustal Events in Italy by Applying the Multisource Geographically Weighted Regression (MS-GWR) Method*. Bulletin of the Seismological Society of America; 111 (6): 3297–3313. doi: https://doi.org/10.1785/0120210044

Landwehr, N., Kuehn, N. M., Scheffer, T., and Abrahamson, N., 2016. *A Non Ergodic Ground-Motion Model for California with Spatially Varying Coefficients*. Bull. Seism. Soc. Am. 106(6), 2574-2583. https://doi.org/10.1785/0120160118.

Kuehn, N. M., Abrahamson, N. A., and Walling, M. A., 2019. *Incorporating Nonergodic Path Effects into the NGA-West2 Ground-Motion Prediction Equations.* Bull. Seism. Soc. Am. 109(2), 575-585. https://doi.org/10.1785/0120180260.

Parker, G. A., Stewart, J. P., Boore, D. M., Atkinson, G. M., and Hassani, B. (2022). *NGA-subduction global ground motion models with regional adjustment factors.* Earthq. Spectra 38(1), doi:10.1177/87552930211034889.

Rodriguez-Marek, A., F. Cotton, N. A. Abrahamson, S. Akkar, L. Al Atik, B. Edwards, G. A. Montalva, and H. Dawood; 2013: *A model for single-station standard deviation using data from various tectonic regions*, Bull. Seismol. Soc. Am. 103, 3149–3163

Sgobba S., Lanzano G., Pacor F., Puglia R., D'Amico M., Felicetta C., Luzi L. (2019) *Spatial Correlation Model of Systematic Site and Path Effects for Ground-Motion Fields in Northern Italy.* Bulletin of the Seismological Society of America. Vol. 109, No. 4, pp. 1419–1434

Sgobba, S, Lanzano, G, Pacor, F. *Empirical nonergodic shaking scenarios based on spatial correlation models: An application to central Italy.* Earthquake Engng Struct Dyn. 2021; 50: 60– 80. https://doi.org/10.1002/eqe.3362

Worden, C. B., Thompson, E. M., Baker, J. W., Bradley, B. A., Luco, N., and Wald, D. J. (2018). *Spatial and Spectral Interpolation of Ground- Motion Intensity Measure Observations.* Bull. Seism. Soc. Am., 108 (2), 866-875. https://doi.org/10.1785/0120170201.

PHYSICS-BASED GROUND SHAKING SCENARIOS FOR EMPIRICAL FRAGILITY STUDIES: THE CASE-STUDY OF THE 2009 L'AQUILA EARTHQUAKE

C. Smerzini[1], A. Rosti[2], R. Paolucci[1], A. Penna[2], M. Rota[3]

[1] Department of Civil and Environmental Engineering, Politecnico di Milano, Milano, Italy
[2] Department of Civil Engineering and Architecture, University of Pavia, Pavia, Italy
[3] EUCENTRE Foundation, Pavia, Italy

Introduction. With the advancement of high-performance computing resources, three-dimensional physics-based numerical simulations (PBS) have started to play a role in providing realistic, region- and site-specific predictions of seismic shaking and they can be employed, in addition to or in place of empirical approaches for ground motion prediction. In the recent past, the issues related to seismological (i.e. in terms of ground motion waveforms and intensity measures) and engineering validation (i.e. in terms of engineering demand parameters) of PBS results have already found considerable attention (e.g., Taborda and Bielak 2013; Lee *et al.,* 2020; Paolucci *et al.*, 2021; Petrone *et al.*, 2021). However, in view of the seismic risk applications at urban scale (see e.g., Smerzini and Pitilakis 2018; Stupazzini *et al.*, 2021; Riaño *et al.,* 2021), it is also of paramount importance to verify whether a PBS scenario is suitable to characterize the distribution of ground motion intensity for the calibration of empirical fragility curves.

As a matter of fact, in standard approaches, the ground shaking scenario is given either by ShakeMaps (Wald *et al.,* 2021; Michelini *et al.,* 2020), in case a sufficient number of records is available, or by empirical Ground Motion Models (GMM), as it is often the case for historical earthquakes with no instrumental records. However, in all such cases, there is a large level of uncertainty when a ground motion level is associated to the specific site where an earthquake effect is observed. Besides, the estimated ground motion is typically available only through its peak values, with no information on other parameters related to the time history itself, such as duration and frequency content. Instead, the PBS ground motion scenario, upon validation, may provide a complete picture of the variability of the ground motion waveforms, supporting the derivation of empirical fragility curves with a wider set of intensity measures (IM).

The main aim of this work is to explore and validate the use of ground shaking scenarios generated by means of 3D PBS for empirical fragility studies. To this end, the case study of the Mw6.2 April 6, 2009 L'Aquila earthquake is considered because of the availability, on one side, of a comprehensive database of post-earthquake damage surveys (Dolce *et al.,* 2019; Rosti *et al.,* 2021a; 2021b), and, on the other, of a validated numerical model for PBS (Evangelista *et al.,* 2017).

Case study and methodology. In this work, the case-study of the 2009 L'Aquila earthquake is considered (see Fig. 1). The 3D spectral element model of the L'Aquila earthquake derives from a previous study (Evangelista *et al.,* 2017), which was focused on the calibration and the validation of the numerical model by the SPEED code (Mazzieri *et al.,* 2013) on the available recordings (see top right panel in Fig. 1). To overcome the frequency limit of the numerical model, the ANN2BB technique proposed by Paolucci *et al.* (2018) and further improved in Paolucci *et al.* (2021), is used to enrich the PBS signals at high frequency.

In order to derive empirical fragility curves, the up-to-date version of the L'Aquila damage database (Rosti *et al.,* 2018; 2020), now available in the Observed Damage Database - DaDo (Dolce *et al.,* 2019), is considered. For the objective of this study, which is to compare the effect of different approaches for the characterization of ground shaking in the empirical fragility analysis, we considered a subset of the damage dataset corresponding to the detailed study area depicted in Fig. 1. The considered dataset, hereafter referred to as detailed dataset, counts 7987 residential buildings, 4564 (57%) of which refer to masonry, whereas 3423 (43%)

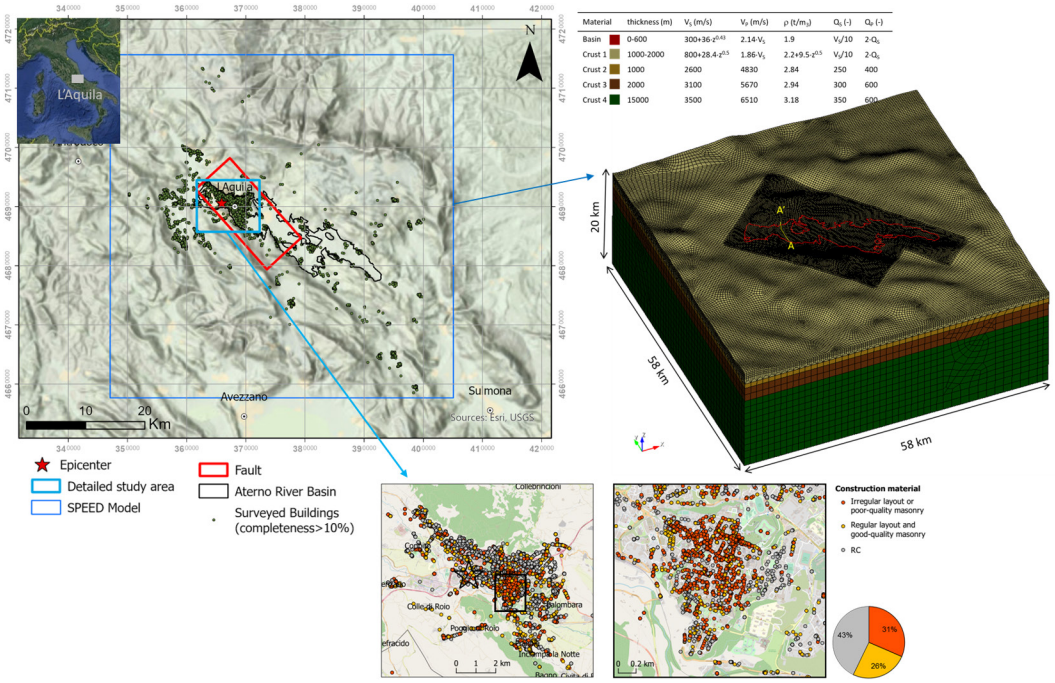


Fig. 1 - The case study of the Mw6.2 2009 L'Aquila earthquake: area under study (top left), 3D PBS model by SPEED (top right) and damage database in the detailed study area addressed in this work (bottom).

are RC buildings. The dataset adopts the typological building classification adopted in Rosti *et al.* (2021a,b).

Empirical fragility curves are derived by statistical processing of the damage database for several masonry and RC building typologies representative of the Italian building stock. Fragility curves are calibrated by characterizing the ground motion intensity at the buildings located within the L'Aquila municipality, i.e. the area severely affected by the earthquake, using the broadband shaking scenarios from the PBS. In line with existing literature studies, the cumulative lognormal distribution is adopted for describing the probability of reaching or exceeding a preselected damage level, as a function of the seismic intensity measure. The ground motion IMs selected for the fragility analysis is PGA, which is the reference ground motion intensity measure used in the Italian national platform for seismic risk assessment (Borzi *et al.,* 2021; Dolce *et al.,* 2021). Although not reported here for brevity, other IMs, such as PGV and SAavg (weighted average spectral acceleration in the range 0-1s) were considered for the derivation of the fragility curves. As a verification benchmark, fragility curves are derived, through the same statistical approach, using the latest version of the ShakeMap (v4) according to Michelini *et al.* (2020).

Results. Fig. 2a shows the comparison between the ground shaking scenario, in terms of Peak Ground Acceleration (PGA), obtained from PBS (left) and from the ShakeMap (right). The maximum horizontal component (Hmax) is shown to enable a consistent comparison between the two approaches, since ShakeMaps are released only for the Hmax component. Note that the PBS scenario is computed by spatially interpolating the PGA values computed directly from the broadband acceleration time histories obtained by the simulation approach combined with the ANN2BB procedure. It is found that PBS provides a realistic spatial distribution of PGA values, which reflects the physical features of the source rupture and of local site response, while the ShakeMap provides a smooth pattern with limited spatial variability.

Fig. 2b and 2c show the empirically-derived fragility curves for irregular mid/high-rise masonry and post-1981 RC building typologies as a function of PGA, the latter being estimated using both the PBS (solid lines) and the ShakeMap (dashed lines). The two sets of curves (PBS Vs ShakeMap) turn out to be consistent, without any systematic bias. PBS-derived fragility curves tend to be less conservative than ShakeMap-derived ones for masonry buildings (especially for the MH class), while a reverse trend is found for RC buildings.

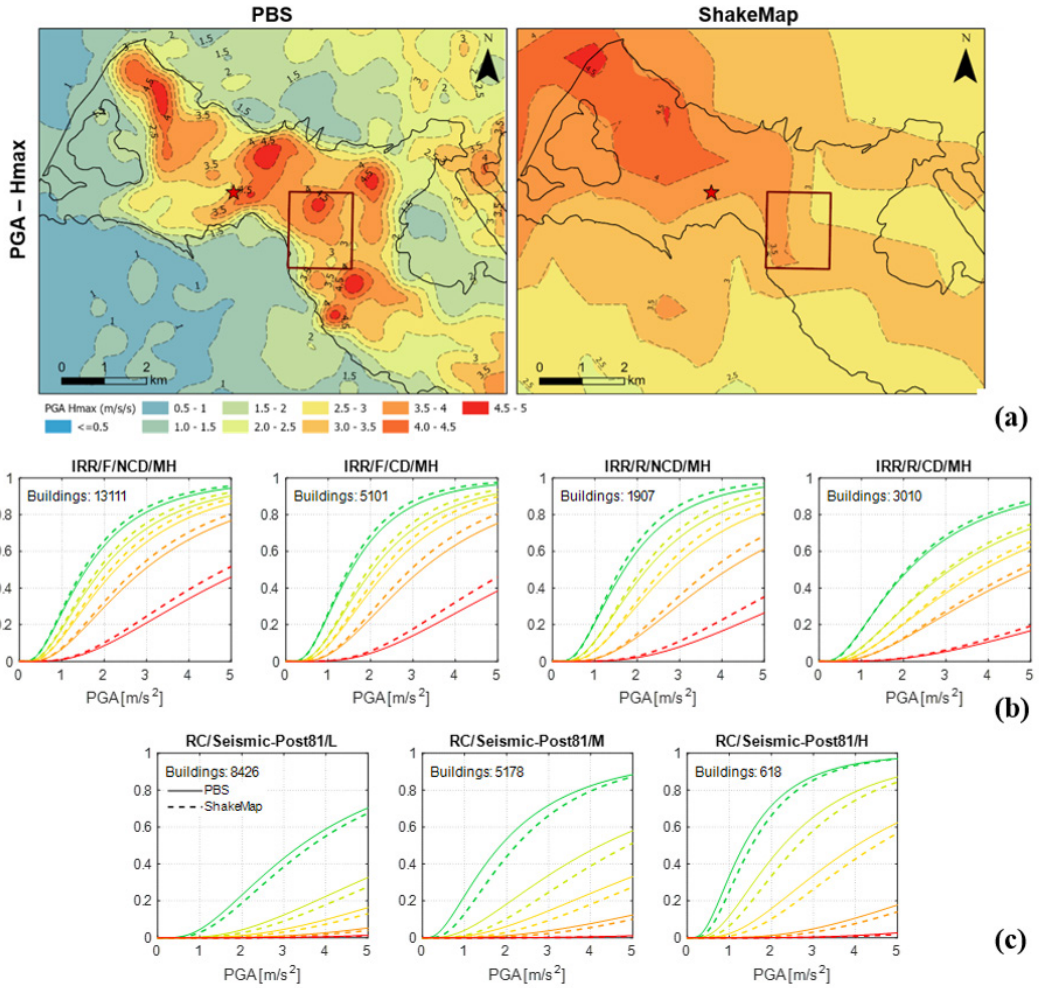


Fig. 2 - (a) Comparison between the map of PGA-Hmax in the detailed study area from PBS (left) and from the ShakeMap (right). (b) Fragility curves of irregular mid/high-rise masonry building typologies as a function of PGA estimated from PBS (solid lines) and ShakeMap (dashed lines). (c) As in (b) but for low, mid and high-rise seismically designed (post 1981) RC buildings.

Finally, the two sets of fragility models, from PBS and ShakeMap, are coupled with the corresponding ground shaking scenarios to check the consistency of the predicted damage levels and of their spatial distribution in the L'Aquila municipality area, with respect to the observed ones. In Fig. 3a, the spatial distribution of prescribed damage levels (i.e. DS1, DS3 and DS4) is shown, as obtained from PBS and ShakeMap. Results are displayed in terms of expected exceedance probabilities evaluated at the building level. In addition to this comparison at spatial scale, Fig. 3b illustrates the comparison between the observed and predicted global

damage distributions for masonry, RC and all buildings within the detailed study area mapped in panel (a) of the same figure. Results show that both approaches, PBS and ShakeMap, generally well reproduce the observed seismic damage in the detailed study area. Predictions are aligned with observations for all levels of damage from DS2 to DS5, indicating the general fitness of both procedures to reproduce observed seismic damage.

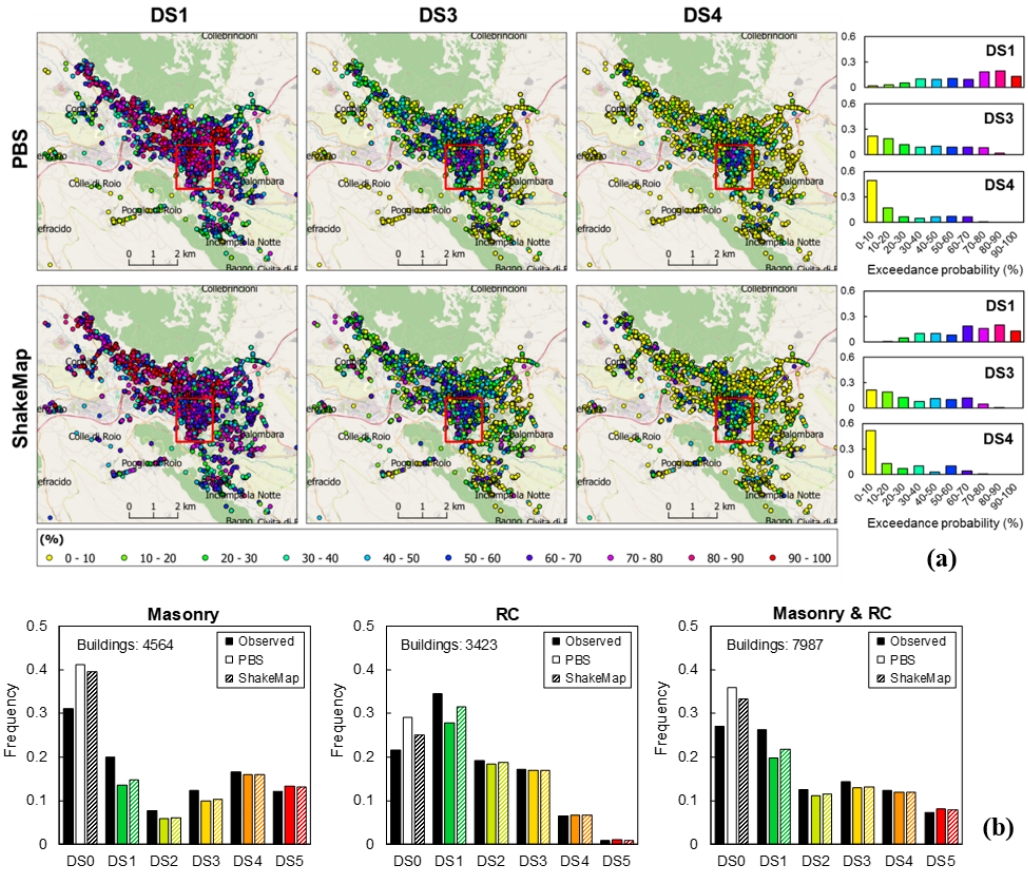


Fig. 3 - (a) Expected exceedance probabilities of preselected damage levels in the detailed study area. (b) Comparison between observed and predicted global damage distributions for masonry, RC and all buildings in the same area.

Conclusions. This work validates the use of ground shaking scenarios obtained by 3D PBS as a basis to constrain the intensity measures for empirical fragility analyses from past earthquakes, with application to the 2009 L'Aquila earthquake. Fragility curves are calibrated for several masonry and RC building typologies representative of the Italian building stock by characterizing the ground motion intensity at the buildings located within the L'Aquila municipality, using the broadband shaking scenarios from the PBS. The comparison of the fragility curves derived from PBS with those obtained from the ShakeMap available for the L'Aquila earthquake highlights that the PBS-based fragility analysis does not show any systematic bias with respect to standard approaches. The validation of the PBS approach is confirmed also by the comparison of damage predictions with the post-earthquake observations. This study points out the advantages of simulation-based seismic shaking scenarios for empirical fragility studies, particularly when strong-motion recordings are insufficient or not available, as for historical earthquakes.

References

Borzi B, Onida M, Faravelli M, Polli D, Pagano M, Quaroni D, Cantoni A, Speranza E, Moroni C (2021) *IRMA platform for the calculation of damages and risks of Italian residential buildings.* Bull Earthq Eng, 19: 3033-3055.

Dolce M, Speranza E, Giordano F, Borzi B, Bocchi F, Conte C, Di Meo A, Faravelli M, Pascale V (2019) *Observed damage database of past Italian earthquakes: the DaDO WebGIS.* Boll Geofs Teor Appl, 60(2): 141-164.

Dolce M, Prota A, Borzi B, da Porto F, Lagomarsino S, Magenes G, Moroni C, Penna A, Polese M, Speranza E, Verderame GM, Zuccaro G (2021) *Seismic risk assessment of residential buildings in Italy*. Bull Earthq Eng, 19: 2999-3032.

Evangelista L, Del Gaudio S, Smerzini C, D'Onofrio A, Festa G, Iervolino I, Landolfi L, Paolucci R, Santo A, Silvestri F (2017) *Physics-based seismic input for engineering applications: a case study in the Aterno River valley, Central Italy*, Bull Earthq Eng, 15(7): 2645–2671.

Lee RL, Bradley BA, Stafford PJ, Graves RW, Rodriguez-Marek A (2020) *Hybrid broadband ground motion simulation validation of small magnitude earthquakes in Canterbury, New Zealand.* Earthquake Spectra 36(2): 673-699.

Mazzieri I, Stupazzini M, Guidotti R, Smerzini C (2013) *SPEED: SPectral Elements in Elastodynamics with Discontinuous Galerkin: a non-conforming approach for 3D multi-scale problems*, Int J Numer Meth Eng 95, no. 12, 991–1010.

Michelini A, Faenza L, Lanzano G, Lauciani V, Jozinovic D, Puglia R, Luzi L (2020) *The New ShakeMap in Italy: Progress and Advances in the Last 10 Yr.* Seismol Research Letters, 91(1): 317-333.

Paolucci R, Gatti F, Infantino M, Smerzini C, Ozcebe AG, Stupazzini M (2018) *Broadband Ground Motions from 3D Physics-Based Numerical Simulations Using Artificial Neural Networks,* Bull. Seism. Soc. Am., 108(3A): 1272–1286.

Paolucci R, Smerzini C, Vanini M (2021) BB-SPEEDset: *A Validated Dataset of Broadband Near-Source Earthquake Ground Motions from 3D Physics-Based Numerical Simulations*, Bull. Seism. Soc. Am., 111(5): 2527-2545.

Petrone F, Abrahamson N, McCallen D, Miah M (2021) *Validation of (not-historical) large-event near-fault ground-motion simulations for use in civil engineering applications,* Earthquake Engng Struct Dyn. 50:116–134.

Riaño AC, Reyes JC, Yamín LE, Bielak J, Taborda R, Restrepo D (2021) *Integration of 3D large-scale earthquake simulations into the assessment of the seismic risk of Bogota, Colombia*, Earthquake Engng Struct Dyn.; 50(1): 155– 176, https://doi.org/10.1002/eqe.3373.

Rosti A., Rota M, Penna A (2018) *Damage classification and derivation of damage probability matrices from L'Aquila (2009) post-earthquake survey data*. Bull Earthquake Eng, 16: 3687–3720 https://doi.org/10.1007/s10518-018-0352-6.

Rosti A, Rota M, Penna A (2020) *Influence of seismic input characterisation on empirical damage probability matrices for the 2009 L'Aquila event.* Soil Dyn Earthq Eng, 128, https://doi.org/10.1016/j.soildyn.2019.105870.

Rosti A, Rota M, Penna A (2021a) *Empirical fragility curves for Italian URM buildings.* Bull Earthq Eng, 19: 3057-3076.

Rosti A, Del Gaudio C, Rota M, Ricci P, Di Ludovico M, Penna A, Verderame GM (2021b) *Empirical fragility curves for Italian residential RC buildings*. Bull Earthq Eng, 19: 3165-3183.

Smerzini C, Pitilakis K. (2018) *Seismic risk assessment at urban scale from 3D physics-based numerical modeling: the case of Thessaloniki,* Bull. Earthq Eng, 16(7): 2609-2631.

Stupazzini M, Infantino M, Allmann A, Paolucci R (2021) *Physics-based probabilistic seismic hazard and loss assessment in large urban areas: a simplified application to Istanbul.* Earthquake Engng Struct Dyn. 50: 99-115.

Taborda R, Bielak J (2013) *Ground-Motion Simulation and Validation of the 2008 Chino Hills, California, Earthquake.* Bulletin of the Seismological Society of America; 103 (1): 131–156.

Wald DJ, Worden CB, Thompson EM, Hearne M. (2021) *ShakeMap operations, policies, and procedures.* Earthquake Spectra, doi:10.1177/87552930211030298.

FRAGILITY CURVES FOR REINFORCED CONCRETE FRAMES CHARACTERIZED BY DIFFERENT REGULARITY

G. Smiroldo, M. Fasan, C. Amadio

University of Trieste, Department of Engineering and Architecture, Trieste, Italy

Introduction. In this work, a comparison between fragility curves developed for regular and non-regular reinforced frames is presented. The fragility curves are develop through the "Cloud Analysis" procedure, which evaluates the structural response via Non-Linear Time History Analysis (NLTHA). Three 3D reinforced concrete multi-story frames characterized by different regularity are analysed in this work.

Both maximum inter-story drift and maximum chord rotation demand capacity ratio are used as Engineering Demand Parameters, calculated by the Italian Code. To complete the develop of the fragility functions, scalar intensity measures are selected among the most referred in practice and literature, both structure independent and structure dependent.

This work shows the influence of regularity in the damage levels of the buildings and the uncertainties given by the selection criteria for EDP limits necessary for a correct representation of the Limit State.

Reference structures and non-linear time history analysis settings. The reference structures adopted are three multi-storey reinforced concrete frames built with different level of regularity. The first structure, called "Regular Frame" ("RF") is characterized by a square plan of 15m width, subdivided in three bays with 5m length each. A strength class C20/25 was adopted for concrete, while steel bars type B450C as defined by the Italian Building Code are used.

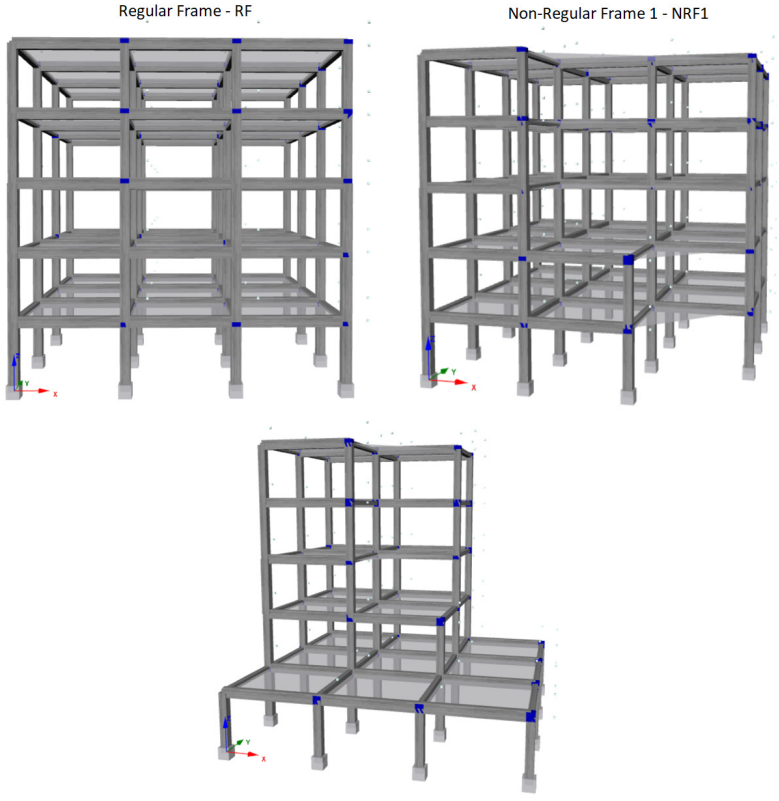


Fig. 1 - Frames.

Using a response spectrum analysis to obtain the maximum stress values, beams and columns are designed according to the Italian Building Code (NTC18) considering a low ductility class (Class B) and adopting a behaviour factor equal to 3.9. The weak beam/strong column capacity design criteria are applied and shear forces in members are evaluated from the flexural capacity of their critical regions preventing any shear weak failure. Floors are considered as rigid diaphragms and a fixed support is applied at the base nodes.

The Torsional Irregularity Ratio (TIR) (ASCE/SEI 7-16, 2014), which is the ratio of the maximum drift at building's edge to the average drift. To obtain a suitable in plant and in height non-regularity, building parts were removed, i.e. beam elements and column elements. Thus, two more buildings were derived, characterized by different levels of regularity, called "Non-Regular Frame 1" (NRF1) and "Non-regular Frame 2" (NRF2). The TIR of the structures are shown in Table 1 – TIR :

The three structures are shown in the *Fig 1 – Frames.*

Tab. 1 - TIR.

	RF	NRF1	NRF2
TIR	1.1	1.15	1.

The vibrational modes properties and mass participation ratios (MPR) of the designed structures are summarized in the following *Table 2 – Vibrational periods and masses*:

Tab. 2 - Vibrational periods and masses.

Regular Frame 'RF'				
Mode	**Period [s]**	**[Ux]**	**[Uy]**	**[Rz]**
1	0.956	0.00%	80.03%	0.00%
2	0.857	0.00%	0.00%	80.74%
3	0.745	82.17%	0.00%	0.00%
4	0.291	0.00%	11.70%	0.00%
5	0.263	0.02%	0.00%	11.47%
6	0.241	10.88%	0.00%	0.02%
Non-Regular Frame 1 NRF1				
Mode	**Period [s]**	**[Ux]**	**[Uy]**	**[Rz]**
1	0.986	0.01%	76.78%	1.13%
2	0.839	1.97%	1.08%	75.54%
3	0.730	78.70%	0.01%	1.40%
4	0.300	0.00%	12.85%	0.12%
5	0.266	0.08%	0.14%	13.23%
6	0.242	11.94%	0.00%	0.01%
Non-Regular Frame 2 'NRF2'				
Mode	**Period [s]**	**[Ux]**	**[Uy]**	**[Rz]**
1	1.014	0.33%	63.84%	5.16%
2	0.738	30.11%	1.88%	34.90%
3	0.658	40.84%	0.28%	15.41%
4	0.303	0.00%	16.41%	0.29%
5	0.236	6.89%	0.69%	6.95%
6	0.221	8.54%	0.38%	10.22%

Non-linear time history analysis (NLTHAs) are performed using the software Seismostruct (Seismosoft 2022). Both material and geometrical non-linearities are included. Material non-linearities are accounted for using a force-based inelastic frame element (infrmFB) that adopts a diffused plasticity model using fibre-section discretization. A total number of 5 integration sections with 150 discretized fibres is used for each beam element.

To simulate the rigid slab at each floor, "rigid diaphragm constraints" have been used. As described in the Seismostruct Manual, the simultaneous use of diffused plasticity model and rigid diaphragm constraint will generate very high fictitious axial internal forces in horizontal elements. To prevent this interaction, beams are released from the axial constraint through rigid links to which is given no axial stiffness and infinite stiffness in the other degrees of freedom, as described in Barbagallo *et al.*

A Rayleigh damping is used, for which it is necessary to define two vibrational periods and a target damping factor for each of the two chosen modes. The two periods are chosen in order to avoid over damping of higher model and elongated modes due to plastic deformations and consist in 1.5 times the first vibrational period and the period that leads to a cumulative mass participation ratio of 90%. The target damping factor is 3% (ASCE 2014). The Hilber - Hughes – Taylor integration scheme is used.

Seismic input and intensity measure selection. Fragility is usually evaluated through structural responses estimated via Non-Linear Time History Analysis (NLTHA). There are several procedures to develop fragility functions based on NLTHAs such as Incremental Dynamic Analysis (IDA) (Vamvatsikos and Cornell 2002), and Cloud Analysis (CA) (Luco and Cornell 2007; Jalayer *et al.,* 2015, 2017).

In this paper, the Cloud Analysis procedure is selected to develop fragility curves, considering a set of 62 unscaled ground-motion records, chosen from European Strong Motion Database. When adopting the cloud method for fragility evaluation a few points should be considered (Jalayer *et al.,* 2017):

- The records should cover a wide range for the selected IM;
- A significant number of records (about 20-30%) should lead to an exceedance of the selected EDP capacity for the selected performance level;
- Not more than 10% of records from the same event should be selected.

To compose the fragility curves, each record is represented by intensity measures combined in the horizontal components. D.M. Boore *et al.* assess it is not precautionary to use raw geometric mean for combining the horizontal components of the records. Thus, they proposed a new bi- dimensional parameter of the intensity measures of ground motion records, called RotDpp, which it is used in this work for each intensity measure.

Both structure independent and structure dependent scalar intensity measures are selected among the most referred in practice and literature: the structure independent ones (i.e. they do not depend on vibrational properties of the structure) are the Peak Ground Acceleration (PGA), Housner Intensity and the Cumulative Absolute Velocity (Reed and Kassawara, 1990). The latter is expressed in eq.(1):

$$CAV = \int \left| a_g(t) \right| dt \tag{1}$$

One of the most used IMs is the spectral acceleration at first mode $S_a(T_1)$. As the reference structure and NLTHAs are 3D, the IM should account for the main vibrational properties in both directions. Hence here spectral acceleration is evaluated at a mean period $T1m$ evaluated as the average of the values of the fundamental periods in each direction (FEMA 2018), expressed in eq.(2):

$$S_a(T_{1m}) = S_a\left(\frac{T_{1x} + T_{1y}}{2}\right) \tag{2}$$

Another IM used is the Pseudo Spectral Velocity (PSV), calculated as the SRSS combination of horizontal direction components, derived from the components of Spectral Displacement S_d, which is given by the ESM flat-file, multiplied for the frequency of the reference structure in both directions, as expressed in eq.(3) and eq.(4):

$$\omega = \frac{2\pi}{T} \tag{3}$$

$$PSV = S_d * \omega \tag{4}$$

One IM most referred in literature is the Housner Intensity, calculated as the integral of the response spectrum in terms of pseudo-velocity, in the interval between 1s and 2.5s, as expressed in eq.(5). This IM is correlated to the potential damage provided by the reference record, and it is structure independent:

$$Housner = \int_{0.1}^{2.5} PSV\left(T, \xi = 0.05\right) dt \tag{5}$$

The last IM used in this work is the Modified Acceleration Spectrum Intensity (MASI), calculated as the integral of the response spectrum in terms of pseudo-acceleration, derived by the spectral displacement multiplied for the square of the frequency of the reference structure, expressed by eq.(6) and eq.(7):

$$PS_a = S_d * \omega^2 \tag{6}$$

$$MASI = \int_{0.1}^{1} PS_a\left(T, \xi = 0.05\right) dt \tag{7}$$

Each IM is represented by the RotD100 parameter, that is the RotD at the 100th percentile.

Engineering Demand Parameters selection. Generally, structural damage as dynamic response is correlated with inter-storey drift ratio (IDR) occurring at each floor. To use a unique directionless value, the resultant inter-storey drift is calculated via SRSS combination of the IDR in the two orthogonal directions. Finally, the maximum inter-storey drift (MIDR) observed in the building is adopted as a single EDP to define the level damage reached in the structures.

In this work, a more sophisticated EDP is used and compared with the maximum IDR. It is the Chord-rotation Capacity- demand Ratio (CRC), calculated for each local axis of horizontal elements ends defined by the Italian Building Code (C.S.LL.PP 2018) at C8.7.2.1, as the following eq. (8):

$$\theta_u = \frac{1}{\gamma_{el}} 0.016 \bullet \left(0.3^{\nu}\right) \left[\frac{\max(0.01; \omega')}{\max(0.01; \omega)} f_c\right]^{0.225} \left(\frac{L_V}{h}\right)^{0.35} 25^{\left(\alpha \rho_{sx} \frac{f_{yw}}{f_c}\right)} \left(1.25^{100\rho_d}\right) \tag{8}$$

Finally, the maximum chord-rotation capacity demand ratio (MCRC) observed in the building is adopted as a single EDP.

Fragility curves development. Fragility curves allow engineers to estimate the probability of attainment of a definite damage state (e.g., Collapse Limit State) given a specified magnitude of an Engineering Demand Parameter, EDP (e.g., inter-storey drift ratio). As mentioned in the § 3, in this work fragility functions are developed via Cloud Analysis Procedure, using the regression line intercept *"b"* and slope *"a"* within the bi-logarithmic plane. The curves are presented in the form of cumulative distribution function by eq.(9) with respect to the IM.

$$P\left[EDP \geq EDP_{pl} \mid IM\right] = 1 - \Phi\left(\frac{\ln\left(EDP_0\right) - \ln\left(aIM^b\right)}{\sigma}\right) = \Phi\left(\frac{\ln(IM) - \ln(\lambda)}{\zeta}\right) \quad (9)$$

Where:

- aIM^b is the equation of the regression line of the reference correlation;
- σ is the standard deviation of the reference correlation;
- $\lambda = \frac{\ln(EDP_0) - \ln(a)}{b}$;
- $\zeta = \sigma/b$.

In order to generate fragility curves for MIDR and MCRC two performance level are considered, (NTC2018): Life Safety (LS) and Collapse Prevention (CP).

For MIDR the assumed capacity thresholds are identified by means of pushover analysis carried out for each structure. The thresholds are as follows:

- CP: evaluated as the MIDR at which the collapse chord rotation defined as per the Italian Building Code: (C.S.LL.PP 2018) is attained:
  - $EDP_{CP_{RF}} = 5\% \bullet h$
  - $EDP_{CP_{NRF1}} = 5\% \bullet h$
  - $EDP_{CP_{NRF2}} = 5\% \bullet h$

  With *"h"* the inter-storey height.

- LS: defined as $\frac{3}{4} edp_{CP}$:

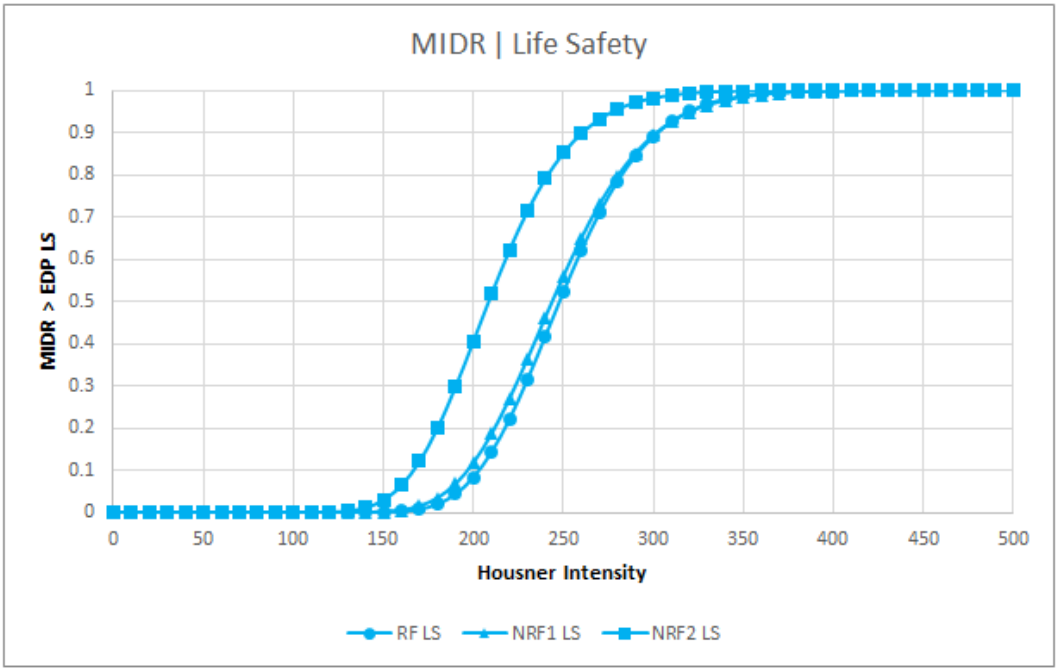
  - $EDP_{LS_{RF}} = 3.75\% \bullet h$
  - $EDP_{LS_{NRF1}} = 3.75\% \bullet h$
  - $EDP_{LS_{NRF2}} = 3.75\% \bullet h$

For MCRC the assumed capacity thresholds edp_{pl} are identified as follows:

- CP: defined as the chord-rotation demand and chord-rotation capacity ratio is equal to 1:
  - $EDP_{CP_{RF}} = 1$
  - $EDP_{CP_{NRF1}} = 1$
  - $EDP_{CP_{NRF2}} = 1$

- LS: defined as $\frac{3}{4} edp_{CP}$:

  - $EDP_{LS_{RF}} = 0.75$
  - $EDP_{LS_{NRF1}} = 0.75$
  - $EDP_{LS_{NRF2}} = 0.75$



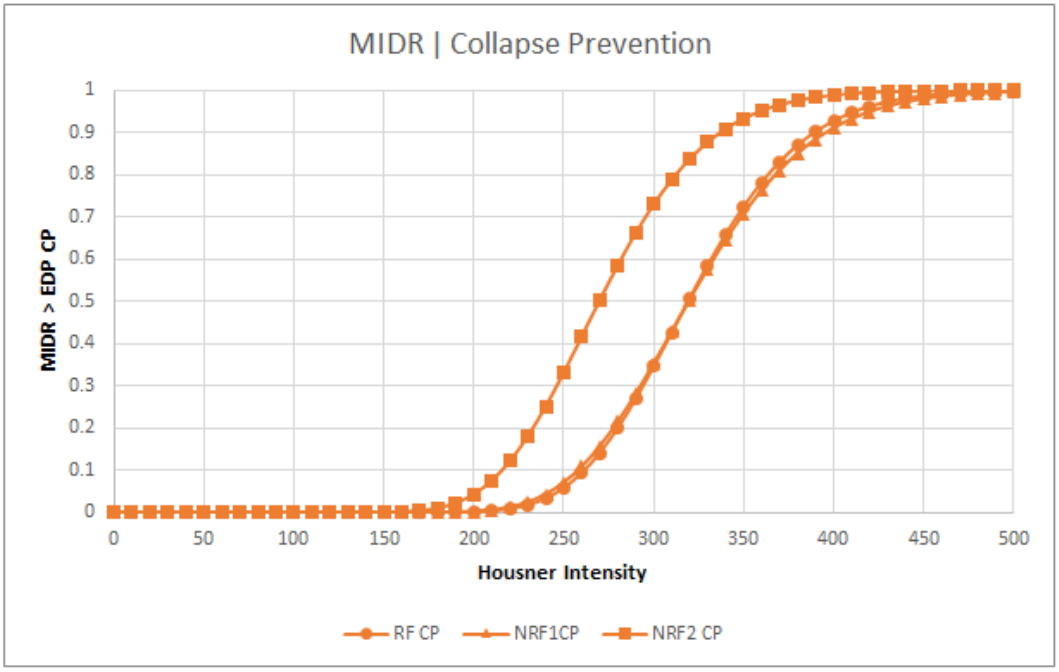


Fig. 2.

Results and conclusions. In this work, a comparison between buildings characterized by different in-plant and in-height regularity is analysed. It is also evaluated the influence of two different Engineering Demand Parameter in the development of fragility curves.

The best correlations between IM and EDP are characterized by lesser standard deviations, as shown in the *Table 3- Standard deviation*:

Tab. 3 - Standard deviations.

Correlations (MIDR - IM)	RF	NRF1	NRF2
ln(MIDR)-ln(RotD100_SaT1)	0.43	0.43	0.43
ln(MIDR)-ln(RotD100_pga)	0.50	0.48	0.47
ln(MIDR)-ln(RotD100_PSV)	0.43	0.43	0.43
ln(MIDR)-ln(RotD100_CAV)	0.48	0.47	0.47
ln(MIDR)-ln(RotD100_housner)	0.18	0.19	0.19
ln(MIDR)-ln(RotD100_MASI)	0.45	0.44	0.42
Correlations (MCRC - IM)	**RF**	**NRF1**	**NRF2**
ln(MCRC)-ln(RotD100_SaT1)	0.53	0.50	0.45
ln(MCRC)-ln(RotD100_pga)	0.61	0.57	0.50
ln(MCRC)-ln(RotD100_PSV)	0.53	0.50	0.45
ln(MCRC)-ln(RotD100_CAV)	0.58	0.55	0.51
ln(MCRC)-ln(RotD100_housner)	0.26	0.22	0.21
ln(MCRC)-ln(RotD100_MASI)	0.55	0.52	0.45

This table shows that the best correlation is between both EDP and the Housner Intensity, so it will be used as the reference for the fragility curves results.

The results show a clear dynamic response difference of the buildings varying the regularity: the RF structure suffers less displacements overall than the NRF2 structure, as shown in the *Fig 2 – MIDR Fragility Curves*. The highest deformability of the NRF2 structure derives from the higher non-regularity and torsional effects.

The threshold selection is a key factor for the right construction of the fragility curves. In this work, the MIDR thresholds are identified via pushover analysis of the buildings, although pushover analyses are not recommendable for studying buildings characterized by high levels of non-regularity, since the first vibration mode is not well defined. The implementation of the chord-rotation capacity as an Engineering Demand Parameter has the aim to implicitly consider the Collapse Prevention Limit State reached by every element of the reference structure avoiding the necessity to assess non-regular structure capacity by means of pushover analysis. Thus, the fragility curves constructed with the MCRC as EDP are more representative of the real behaviour of the buildings. These fragility curves confirm the high deformability of NRF2, but also an aggravation of the dynamic response of the structures, suggesting that the use of MCRC as EDP leads to a more cautionary reading than MIDR, as shown in *Fig 3 – MCRC Fragility curves*.

References

ASCE; 2014: *Seismic Evaluation and Retrofit of Existing Buildings.* American Society of Civil Engineers, Reston, VA.

Barbagallo F., Bosco M., Marino E. M., Rossi P.P., 2019: *On the fibre modelling of beams in RC framed buildings with rigid diaphragm*. Department of Civil Engineering and Architecture, University of Catania, Catania, Italy

Boore D. M, Watson-Lamprey J., Abrahamson N. A.; 2006: *Orientation-Independent Measures of Ground Motion*. Bulletin of the Seismological Society of America, Vol. 96

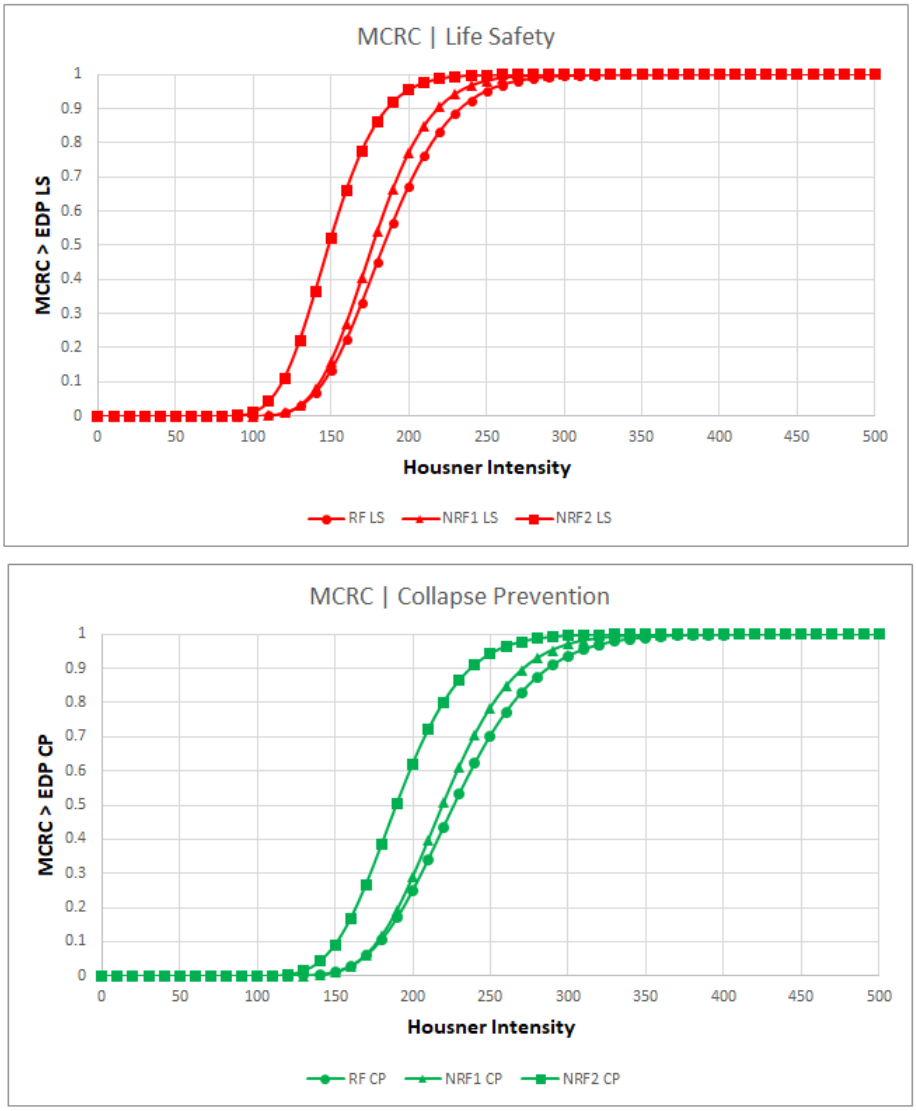


Fig. 3.

C.S.LL.PP; 2018: *Norme tecniche per le costruzioni*. Rome, Italy.

FEMA; 2018: *Seismic Performance Assessment of Buildings*. FEMA P-58-1. Washington, D.C, U.S.A.

Jalayer F., De Risi R., Manfredi G.; 2015: *Bayesian Cloud Analysis: Efficient structural fragility assessment using linear regression.* Bull.Earthq.Eng., 13, 1183:1203, doi: 10.1007/s10518-014-9692-z.

Jalayer F., Ebrahimian H., Miano A., et al; 2017: *Analytical fragility assessment using unscaled ground motion records.* Earthquake Engineering and Structural Dynamics 46:2639–2663. doi: 10.1002/eqe.2922

Luco N., Cornell C. A.; 2007*: Structure-specific scalar intensity measures for near-source and ordinary earthquake ground motions*. Earthquake Spectra 23:357–392. doi: 10.1193/1.2723158

Reed J. W., Kassawara R. P.; 1990: *A criterion for determining exceedance of the operating basis earthquake.* Nuclear Engineering and Design 123:387–396. doi: 10.1016/0029-5493(90)90259-Z

Seismosoft; 2022: *SeismoStruct 2022 – A computer program for static and dynamic nonlinear analysis of framed structures.*

Vamvatsikos D., Cornell C. A.; 2002: *Incremental dynamic analysis.* Department of Civil and Environmental Engineering, Stanford University, U.S.A.

DALL'HVSR ALLA FUNZIONE DI RISPOSTA DI SITO: POTENZIALITÀ E PROBLEMATICHE DEDOTTE DALLA MODELLAZIONE 1D

A. Tanzini, E. Paolucci, D. Albarello

Dipartimento di Scienze Fisiche, della Terra e dell'Ambiente, Università degli Studi di Siena, Italia

Introduzione. La valutazione della pericolosità sismica di sito è un elemento fondamentale per la pianificazione di azioni volte a ridurre efficacemente il rischio associato ad eventuali futuri terremoti. La pericolosità sismica è largamente influenzata da configurazioni sismo-stratigrafiche e morfologiche su piccola scala, responsabili di fenomeni di amplificazione del moto sismico dovuti alla presenza di forti contrasti di impedenza nel sottosuolo (fenomeni di risonanza sismica). La modellazione fisica è lo strumento principale per valutare questi effetti in mancanza di dati sui terremoti. In particolare, l'analisi della risposta sismica unidimensionale (1D) è lo strumento più comune per questa finalità e i codici numerici sono largamente utilizzati nell'attività professionale (es. STRATA (Kottke e Rathje, 2008)). Questi modelli richiedono essenzialmente la definizione della velocità dell'onda di taglio (Vs) e delle curve di decadimento riferite alla parte superficiale del sottosuolo (< 100 m di profondità). Nel caso di studi di microzonazione sismica (WSGM, 2008), per rilevare la presenza di eventuali fenomeni di risonanza sono necessarie procedure a basso costo, soprattutto in mancanza di informazioni dettagliate sulla configurazione sismo-stratigrafica nel territorio indagato. A questo scopo, i rapporti spettrali fra le componenti orizzontali e verticali (HVSR) delle vibrazioni ambientali (Bard, 1998) sono ampiamente utilizzati per dedurre direttamente i fenomeni di risonanza relativi alle onde S durante i terremoti. Recentemente, Zhu *et al.* (2020) hanno esaminato risultati empirici e fornito nuovi esiti a sostegno di questa possibile applicazione, utilizzando come riferimento le curve di risposta di sito ottenute da array in pozzo. In particolare, si sono concentrati sulla possibilità di utilizzare i massimi della curva HVSR per rilevare la frequenza F_d caratterizzata dal massimo effetto di amplificazione (di seguito A_d) e la più bassa frequenza F_0 caratterizzata da una certa amplificazione A0. Tuttavia, gli approcci empirici possono influenzare l'identificazione di questi parametri a causa delle procedure di analisi utilizzate per ottenere le curve (suddivisione del segnale in finestre, lisciamento, ecc..). Inoltre, questo bias può essere più significativo se entrambe le curve presentano picchi multipli. Lo scopo del presente lavoro è esplorare questa tematica seguendo un approccio 1D puramente teorico, ovvero confrontando i risultati dei modelli fisici rappresentativi della curva HVSR e della curva di risposta di sito.

Profili sismo-stratigrafici. I profili sismo-stratigrafici utilizzati per le simulazioni numeriche sono stati ottenuti considerando otto configurazioni litostratigrafiche rappresentative di diversi ambienti deposizionali e litologie. Ogni configurazione è caratterizzata da una successione di unità geologico-tecniche ciascuna parametrizzata in termini di spessore e Vs minimi e massimi: queste informazioni sono state ottenute considerando i dati geognostici e sismici ricavati da studi di microzonazione sismica eseguiti in diversi comuni dell'Appennino Meridionale. In particolare, randomizzando i parametri che definiscono queste configurazioni tramite il modello di Toro (1995), sono stati generati 1600 profili sismo-stratigrafici (200 per ogni configurazione).

Simulazioni numeriche. Le curve di risposta di sito relative ai 1600 profili sono state ottenute in termini di funzioni di trasferimento dell'accelerazione orizzontale (ATF) dalle simulazioni di risposta sismica 1D eseguite con il software STRATA utilizzando una procedura lineare equivalente. Le curve di decadimento e i valori di peso specifico sono stati dedotte da database italiani e da letteratura internazionale (es. Ciancimino *et al.*, 2019). Il moto di input da applicare alla base dei profili considerati è stato determinato considerando la carta italiana di pericolosità sismica (http://esse1-gis.mi.ingv.it/mps04_eng.jsp) con una probabilità del 10% di essere superata in 50 anni. In particolare, sono stati scelti sette accelerogrammi naturali che

soddisfano la spettro-compatibilità per l'area considerata: la loro magnitudo momento varia da 6.0 a 6.9 e le loro distanze epicentrali da 11 a 94 Km. Un gruppo di sette curve ATF è stato quindi ottenuto per ciascun profilo e la curva mediana è stata scelta come rappresentativa.

Le curve HVSR sono state simulate utilizzando due diversi modelli del campo d'onda completo delle vibrazioni ambientali: uno basato sull'approccio di campo diffuso (di seguito DFA; García-Jerez *et al.*, 2016) e l'altro basato sull'ipotesi di sorgenti distribuite in superficie (di seguito DSS; Lunedei e Albarello, 2016). Il modello DSS include gli effetti dello smorzamento, mentre il modello DFA è puramente elastico. Per entrambi gli approcci sono stati considerati dieci modi per le onde di superficie (Rayleigh e Love) e la curva HVSR è stata calcolata come:

$$HVSR = \sqrt{\frac{2P_H}{P_V}}, \quad (1)$$

dove P_H e P_V rappresentano rispettivamente gli spettri di potenza della componente orizzontale e verticale del campo d'onda delle vibrazioni ambientali.

Discussione e conclusioni. Come prima analisi, le curve HVSR ottenute dal modello DSS sono state confrontate con le corrispettive del modello DFA al fine di verificare l'esistenza di differenze significative tra i due approcci teorici. In particolare, calcolando i coefficienti di correlazione di Pearson, la loro distribuzione di valori, caratterizzata da una mediana e da una media pari rispettivamente a 0.95 e 0.92, mostra una elevata correlazione tra i due tipi di HVSR. Alla luce di questi risultati, il modello DSS è stato considerato come rappresentativo solamente per la sua capacità di modellare lo smorzamento dei materiali.

Dopo questa prima valutazione, i valori di F_0 e F_d insieme ai rispettivi valori di A_0 e A_d sono stati identificati dalle curve HVSR e ATF e i loro confronti sono mostrati in Fig. 1. La bontà delle correlazioni è stata stimata considerando il coefficiente di correlazione di Pearson. Inoltre, come proposto da Zhu *et al.* (2020), per quantificare quanto i confronti si discostano dalla linea 1:1, sono stati adottati dei benchmark contrassegnati dalle linee dove i rapporti F_{ATF}/F_{HVSR} (e A_{ATF}/A_{HVSR}) sono pari a 0.5, 0.8, 1.25 e 2. Le percentuali dei casi al di fuori di questi limiti e i valori del coefficiente di correlazione sono riepilogati nella Tab. 1.

Per quanto riguarda i confronti delle frequenze di picco (Fig. 1a, c), risulta evidente come la curva HVSR sia un proxy affidabile per i valori di F_0 e meno efficace per i valori di F_d. In particolare, le percentuali dei casi al di fuori degli intervalli $0.8 < F_{0_ATF}/F_{0_HVSR} < 1.25$ e $0.5 < F_{0_ATF}/F_{0_HVSR} < 2$ sono rispettivamente del 40% e del 10%: valori leggermente inferiori (31% e 8%) sono stati ottenuti da Zhu *et al.* (2020) confrontando curve empiriche. Per quanto riguarda il confronto dei valori di F_d, le percentuali dei casi al di fuori degli intervalli $0.8 < F_{d_ATF}/F_{d_HVSR} < 1.25$ e $0.5 < F_{d_ATF}/F_{d_HVSR} < 2$ sono maggiori di quelle rilevate dal lavoro preso come riferimento (40% e 16%): in questo caso, è possibile notare la presenza di un numero significativo di forti sottostime e sovrastime di F_{d_ATF} da parte della curva HVSR.

Tab. 1 - Valori delle percentuali dei casi al di fuori dei benchmark proposti per i valori di F_0, F_d, A_0 e A_d.

	F_0	F_d	A_0	A_d
Coefficiente di correlazione di Pearson	0.85	0.44	0.51	0.51
% dei casi dove $F(o A)_{ATF}/F (o A)_{HVSR} < 0.8$	40	33	7	4
% dei casi dove $F(o A)_{ATF}/F (o A)_{HVSR} > 1.25$	-	15	41	41
% dei casi dove $F(o A)_{ATF}/F (o A)_{HVSR}$ è fuori dall'intervallo [0.8-1.25]	40	49	48	45
% dei casi dove $F(o A)_{ATF}/F (o A)_{HVSR} < 0.5$	10	11	2	-
% dei casi dove $F(o A)_{ATF}/F (or A)_{HVSR} > 2$	-	13	1	1
% dei casi dove $F(o A)_{ATF}/F (o A)_{HVSR}$ è fuori dall'intervallo [0.5-2]	10	25	3	1

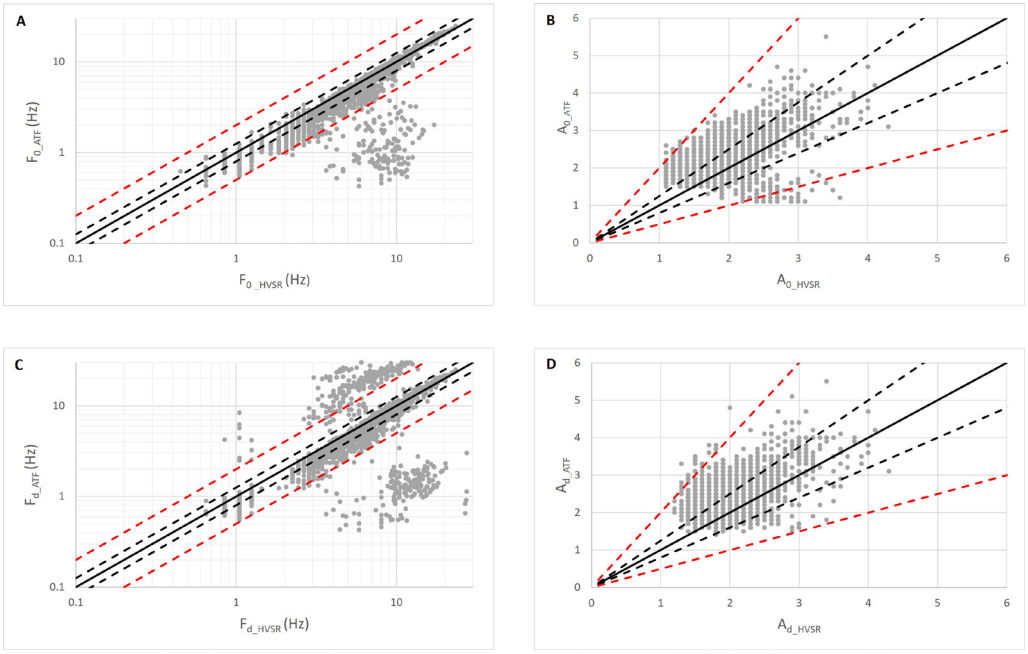


Fig. 1 - Correlazioni tra i valori di F_0, A_0, F_d e A_d appartenenti al confronto HVSR-ATF. La curva HVSR è rappresentata dal modello DSS. La linea nera continua rappresenta la linea 1:1, le linee tratteggiate nere e rosse delimitano gli intervalli di riferimento $0.8 < F_{ATF}/F_{HVSR} < 1.25$ (o $0.8 < A_{ATF}/A_{HVSR} < 1.25$) e $0.5 < F_{ATF}/F_{HVSR} < 2$ (o $0.5 < A_{ATF}/A_{HVSR} < 2$).

I confronti riferiti ai valori di A_0 e A_d (Fig. 1b, d) sono caratterizzati da un andamento molto simile attorno alla linea 1:1 con valori di correlazione identici (Tab. 1). È possibile notare che la maggior parte degli outliers sono inclusi nell'intervallo $1.25 < A_{ATF}/A_{HVSR} < 2$: ciò significa che la curva HVSR tende a sottostimare in maniera simile i valori di A_{0_ATF} e di A_{d_ATF}. Questa caratteristica è in accordo anche con quanto emerge dal confronto empirico relativo ai valori di A_0 (Haghshenas *et al*., 2008).

Bibliografia

Bard P.Y.; 1998: *Microtremor measurement: A tool for site effects estimation?* Second International Symposium on the Effects of the Surface Geology on Seismic Motion ESG98, Yokohama, Japan, 1-3 December 1998, 1251-1279.

Ciancimino A., Lanzo G., Alleanza G.A., Amoroso S., Bardotti R., Biondi G., Cascone E., Castelli F., Di Giulio A., D'Onofrio A., Foti S., Lentini V., Madiai C., Vessia G.; 2019: *Dynamic characterization of fine-grained soils in Central Italy by laboratory testing*. Bull Earthq Eng 18:5503-5531, https://doi.org/10.1007/s10518-019-00611-6.

García-Jerez A., Piña-Flores J., Sánchez-Sesma F.J., Luzón F., Perton M.; 2016: *A computer code for forward calculation and inversion of the H/V spectral ratio under the diffuse field assumption*. ComputGeosci 97, 67–78, https://doi.org/10.1016/j.cageo.2016.06.016.

Haghshenas E., Bard P.Y., Theodulidis N. and SESAME WP04 Team; 2008: *Empirical evaluation of microtremor H/V spectral ratio*. Bull. Earthq. Eng. 6, 75–108, DOI:10.1007/S10518-007-9058-X.

Kottke A.R. and Rathje E.M.; 2008: *Technical manual for Strata*. Report No.: 2008/10. Pacific Earthquake Engineering Research Center, University of California, Berkeley; release 0.8.0, available at https://github.com/arkottke/strata/releases, doi 10.5281/zenodo.3714128.

Lunedei E, Albarello D.; 2016: *Power spectral density function and spatial autocorrelation of the ambient vibration full-wavefield generated by a distribution of spatially correlated surface sources*. Geophys J Int; 204:1817–37, https://doi.org/ 10.1093/gji/ggv559.

Toro G.R.; 1995: *Probabilistic models of site velocity profiles for generic and site-specific ground-motion amplification studies*. Technical Report 779574, Brookhaven National Laboratory, Upton, New York.

WGSM (Working Group on Seismic Microzoning); 2008: *Indirizzi e criteri per la microzonazione sismica*. Conferenza delle Regioni e delle Province autonome – Dipartimento della Protezione Civile, Roma, 3 vol. e DVD. https://www.centromicrozonazionesismica.it/it/download/category/7-indirizzi-e-criteri-per-la-microzonazione-sismica.

Zhu C., Cotton F., Pilz M.; 2020: *Detecting Site Resonant Frequency Using HVSR: Fourier versus Response Spectrum and the First versus the Highest Peak Frequency*. Bull. Seismol. Soc. Am., 110(2): 427-440, doi: https://doi.org/10.1785/0120190186.

PROPOSTA PER UNA METODOLOGIA DI VALUTAZIONE DEL RISCHIO SISMICO DI UNA RETE STRADALE NELLA REGIONE FRIULI VENEZIA GIULIA

T. Tufaro[1], C. Amadio[1], M. Fasan[1], S. Noè[1], M. Santulin[2]

[1] Università degli studi di Trieste, (DIA) Trieste, Italia
[2] Istituto Nazionale di Oceanografia e Geofisica Sperimentale OGS Trieste, Italia

Introduzione. Le reti di trasporto stradale rivestono un ruolo fondamentale e strategico. In occasione di un terremoto, l'interruzione di uno o più archi stradali potrebbe impedire di portare i soccorsi alla popolazione colpita in aree ristrette del territorio servito, o più in generale, provocare un degrado dell'efficienza del sistema di comunicazioni che si appoggia sulla rete stradale stessa. Lo studio propone una metodologia per la realizzazione di mappe tematiche utili alla valutazione preliminare di possibili danni provocati da eventi sismici a una rete di trasporto stradale, con gli obiettivi di:

- programmare azioni di mitigazione del rischio sismico per le infrastrutture e strutture esistenti coinvolte;
- migliorare la programmazione e il coordinamento delle operazioni di gestione delle emergenze;
- fornire indicazioni per possibili viabilità alternative che consentano di mantenere il servizio accettabile nonostante l'interruzione di porzioni di percorribilità strategica e/o importante;

Tali mappe possono essere utilizzabili dagli enti presenti sul territorio, come ad esempio il *Dipartimento della Protezione Civile* e/o gli Enti Gestori (*Autostrade per l'Italia, Autovie Venete, Anas S.p. A e Friuli Venezia Giulia Strade S.p. A.).*

Stato dell'Arte. Fra le numerose metodologie sviluppate per l'analisi del rischio sismico di rete vanno ricordate: a) il Progetto autostradale FHWA-MCEER (Werner *et al.*, 2001); b) REDARSTM[STM] 2, c) HAZUS (HAZUS-MH, 2004); d) MAEViz (Elnashai *et al.*, 2008); e) (RISK-UE (2001–2004); Mouroux e Le Brun, 2006; Vacareanu *et al.*, 2004); f) SYNER-G project (2009-2011); g) INFRARISK e h) Retis-Risk (Sextos *et al.*, 2017). In Italia, nel triennio 2009 - 2012 il DPC ha finanziato *EUCENTRE* che si è proposto di definire delle procedure per la valutazione del rischio simico delle reti italiane.

Metodologia. La metodologia delineata è ispirata a *(*Sextos *et al., 2017)* modificandola: nella definizione dell'oggetto di valutazione del rischio, nelle modalità di valutazione della pericolosità sismica e della esposizione. La rete stradale considerata nello studio è rappresentata in (Fig. 1a). I dati di definizione della rete (individuata tramite nodi e archi stradali) sono stati tratti dal database EAGLE FVG. Tra i nodi contigui punti critici oggetto di possibile danno da sisma sono stati individuati nei ponti presenti lungo gli archi stradali (Fig.1a). I ponti, la cui posizione è individuata dalle coordinate geografiche sono classificati secondo le tipologie strutturali proposte da (Nielson, 2005).

Rete di collegamenti esposti al Rischio Sismico

Per la valutazione del livello di servizio della rete, o più in generale, per la valutazione del rischio sismico del sistema di rete di trasporto appoggiata sulla rete stessa, la metodologia proposta fa uso del concetto di "collegamento", definito, dall'insieme dei primi n_p percorsi più veloci, che permettono di collegare in maniera bidirezionale due nodi i e j della rete (Fig.1c). La ricerca dei possibili n_p percorsi più brevi da assegnare all'i-esimo collegamento è eseguita tramite il tool *Analysis Network in QGIS (3.10).*

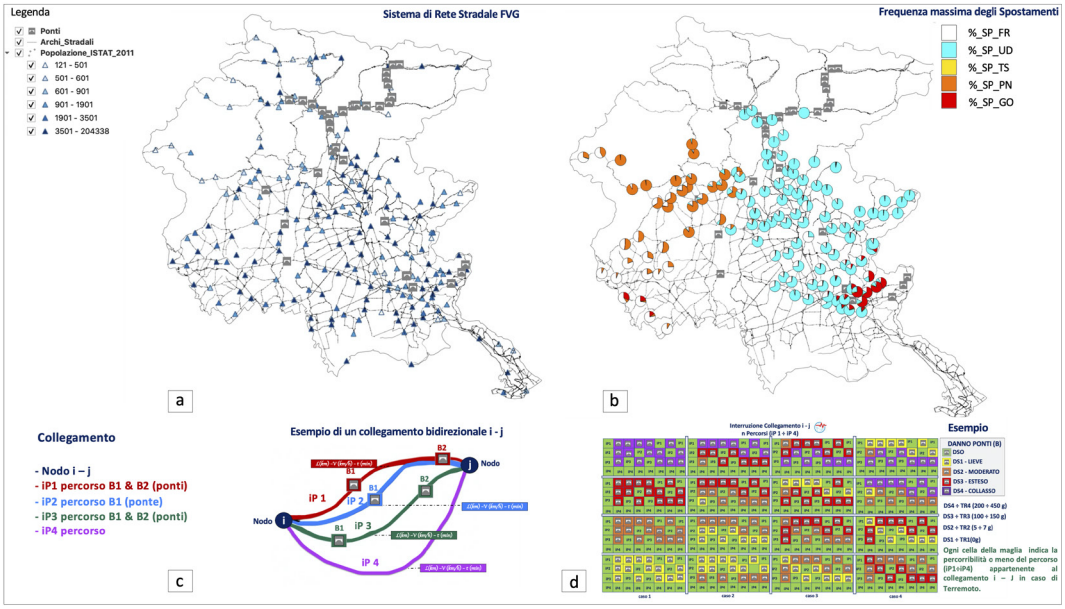


Fig. 1 - a) Sistema di Rete Stradale nella Regione FVG; b) Distribuzione della frequenza massima degli spostamenti effettuati dalla popolazione valutata tramite le matrici di pendolarismo (ISTAT 2011) su un campione di 129 comuni. %_SP_FR (in bianco) indica la frequenza massima degli spostamenti effettuati fuori regione, mentre: %_SP_TS (in ocra), %_ SP_UD (in ciano), %_SP_PN (in arancione) e %_SP_GO (in rosso) indicano quelle effettuate rispettivamente nelle province di: Trieste, Udine, Pordenone e Gorizia; c) Esempio di collegamento; d) Esempio delle interruzioni possibili da sisma per il collegamento in (Fig.1c).

Pericolosità sismica. L'analisi di Pericolosità sismica è possibile sia tramite l'approccio probabilistico *(PSHA)* e sia tramite l'approccio deterministico *(DSHA*). In un primo momento, la pericolosità sismica di sito è calcolata senza considerare alcuna correlazione spaziale tra i valori di PGA. É prevista l'adozione di una procedura di valutazione multi-sito. Per caratterizzare le sorgenti sismogenetiche, sia dal punto di vista geometrico che sismologico, che interessano la Regione FVG sono utilizzati il Catalogo Parametrico dei Terremoti Italiano (*CPTI15)* e il Database delle Sorgenti Sismogenetiche Individuali (*DISS 3.2.1*). In QGIS, sono state caricate 15 faglie e 171 terremoti (Fig. 2a), in formato vettoriale. Per ciascuna sorgente è stata definita l'area buffer di influenza. Le dimensioni dell'area corrispondono alla distanza dalla sorgente, corrispondente a uno scuotimento di 0.15g, calcolata attraverso l'utilizzo della relazione di attenuazione di (Bindi *et al.,* 2011), partendo dal valore di magnitudo massima associata ad ogni sorgente. A causa della sovrapposizione grafica è stato deciso di raggruppare le 15 aree buffer in 6 macroaree: Montello, Polcenigo M., Sequals, Gemona S., Medea e Idrija come mostrato in (Fig. 2b). Successivamente, sono stati definiti i corrispondenti sei sotto-cataloghi sismici (Fig. 2b). Quest'ultimi sono stati raggruppati, nell'approccio *(PSHA),* per il calcolo dei tassi di ricorrenza ottenuti della relazione di (Gutenberg e Richter, 1944), con b-value calcolato pari a 1.08 e standard deviation 0.18. Una volta definiti gli a- e b-values e le magnitudo minima e massima per ciascuna macroarea, è stato costruito il file di input per *(OQ),* prendendo in considerazione soltanto la variabilità epistemica delle GMMs utilizzate: (Bindi *et al.*,11, Bindi *et al.,* 14 e Cauzzi *et al.*, 15) (Fig. 2c). Con l'approccio *(DSHA*) per ogni macroarea sono stati calcolati gli scenari per i terremoti storici più significativi tratti da *(CPTI15)* con la *GMMs di* Cauzzi *et al.(2015)* in (Fig. 2d).

Danno sismico di percorso. Il danno sismico subito dall'ip - esimo percorso di un collegamento è espresso dal rapporto:

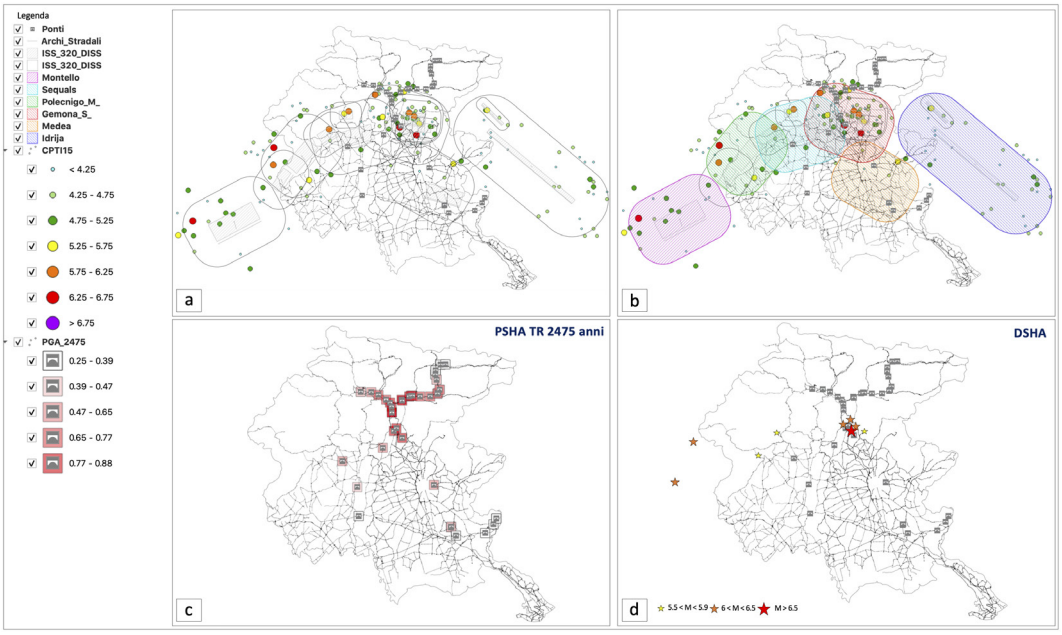


Fig. 2 - a) Distribuzione di 15 sorgenti sismogenetiche (*DISS 3.2.1*) e degli eventi sismici *(CPTI15)*; b) sei macroaree buffer*;* c) Distribuzione della PGA per un TR di 2475 anni (*PSHA*); d) Distribuzione dei terremoti più significativi *(CPTI15)* per l'approccio *(DSHA).*

$$Dpj = \frac{TRj}{TRj,max} \qquad (0 \ \ Dpj \ 1)$$

Dove TRj è il tempo di ripristino associato al ponte maggiormente danneggiato tra quelli eventualmente presenti lungo il percorso stesso, TRj, max è il massimo tempo di ripristino possibile fra tutti i ponti del percorso. La valutazione del tempo di ripristino associato al singolo ponte danneggiato da sisma è svolta utilizzando le curve di fragilità tipologiche di letteratura, per la valutazione del livello di danno strutturale (DS0 ¸ DS4), in (Fig. 3) funzione della PGA e associando al livello di danno strutturale un conseguente tempo di ripristino secondo la Tab 1.

Tab. 1 - Distribuzione del tempo di ripristino espresso in giorni, associato ad ogni livello di danno (TR0 ÷ TR4).

DANNO	DS0	DS1	DS2	DS3	DS4
TR (Giorni)	0	0	5÷7	120÷150	200÷450
	TR0	TR1	TR2	TR3	TR4

Il valore assegnato all'interno del campo di variazione corrispondente a ciascun livello di danno dipende dalla tipologia strutturale del ponte. Il valore Trj,max su citato corrisponde per ciascuna tipologia al valore corrispondente di livello di danno strutturale DS4. Ai percorsi lungo i quali non fossero presenti i ponti (come detto unici elementi sismicamente danneggiabili considerevoli) è sempre associato un valore Dpj nullo. In Fig. 3a è riportato come esempio il danno strutturale valutato per i valori di PGA ottenuti con l'approccio PSHA per un periodo di ritorno di 2475 anni, mentre in Fig. 3b) quello di ripristino. In Fig. 3c l'esempio della distribuzione di danno strutturale valutata per i terremoti storici più significativi ricadenti in ogni macroarea, tramite l'approccio di scenario (DSHA). I diagrammi, illustrano la % di danno strutturale valutata al 50 – esimo, all'84 - esimo e al 95 - esimo percentile dei valori di PGA calcolati per ogni scenario. Da un'analisi qualitativa risulta che le tre macroaree più influenti

per il sistema di rete investigato sono quelle di: Sequals, Gemona South e Medea. In Fig. 3d l'esempio per il terremoto di Gemona South del 1976 con M = 6.45. I digrammi, illustrano la % dei tipi di suolo e di danno strutturale associati ai ponti lungo gli archi stradali. Nello specifico, il 12 % dei ponti è su suolo di tipo A (EC8, in grigio) e presenta danno nullo (DS0), mentre l'88% risulta su suolo di tipo B (EC8, in rosa) e presenta un 75% di danno nullo (DS0), un 22% di danno lieve (DS1) e un 3% di danno moderato (DS2).

Danno sismico di collegamento. Il danno sismico associato all'i-esimo collegamento è calcolato secondo l'espressione:

$$DCic = \sum_{j}^{np} \left(\frac{DPjkj}{np}\right)$$

Con $kj = 1 - 0.8 * \frac{tvj - tv,min}{tvmax - tvmin}$

Dove:

- tvj indica il tempo di viaggio in condizioni normali dell'j-esimo percorso;
- tv, min = min (tvj);
- tv, max = max (tvj).

Ai fini delle valutazione del rischio sismico associabile al singolo collegamento, a ciascuno di essi è associato un indicatore di esposizione totale (Ec). L'indicatore si compone di due contributi: esposizione diretta (Edc) e esposizione indiretta (Eic). Per il calcolo di (Edc) sono considerate due quantità: il numero di persone che percorrono il collegamento in un intervallo temporale (EUtc) e il numero di infrastrutture presenti lungo i percorsi del collegamento

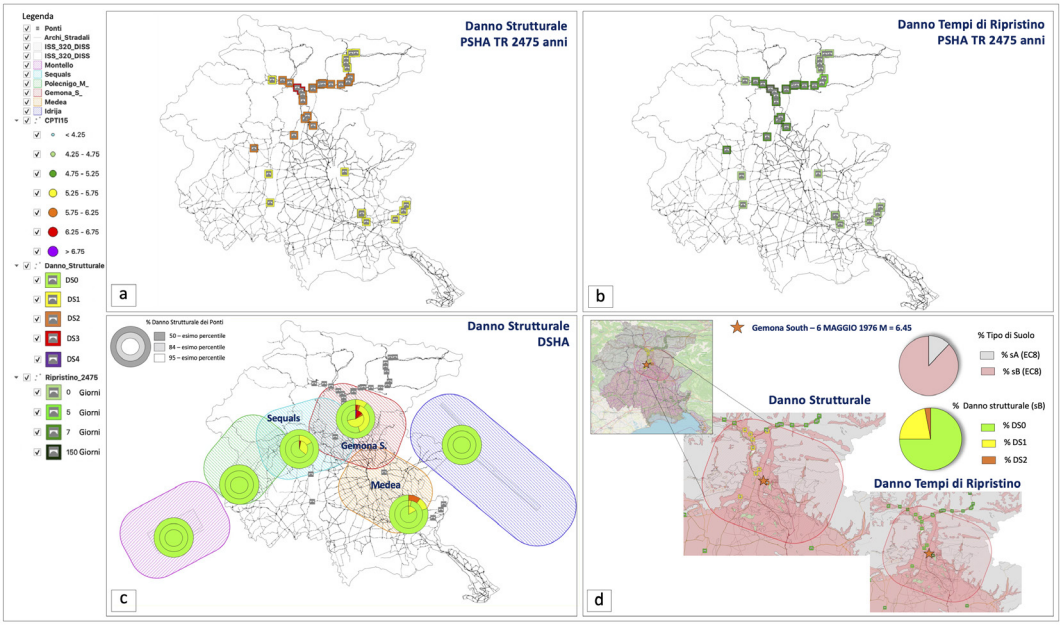


Fig. 3 - a) Scenario di danno strutturale, per un TR di 2475 anni (*PSHA).* DS0 - danno nullo, DS1 - danno lieve, DS2 - danno moderato, DS3 - danno esteso e DS4 - collasso; b) Scenario di ripristino, per lo scenario illustrato in (Fig. 3a); TR1 è stato attribuito al DS1 (pari a 0 giorni per tutte le tipologie di ponte, TR2 al DS2 (pari a 5 giorni per MSSS slab a 7 giorni per MSC concrete e MSSS concrete), TR3 al DS3 (pari a 100 giorni per la prima tipologia e 150 per le altre) infine TR4 al danno DS4 (pari a 200 giorni per la prima e 450 giorni per le altre); c) Scenari di danno strutturale, valutati con l'approccio *(DSHA);* d)Scenario di danno strutturale e di ripristino, valutato per il terremoto di Gemona South.

(Einfc). L' esposizione indiretta (Eic) è calcolata in riferimento alla domanda non assegnata per effetto della chiusura di un percorso e al valore massimo della stessa. Il valore di (Eic) sarà tanto maggiore quanto il numero di persone che non potranno percorrere il tratto a causa dell'interruzione da sisma. Tramite le matrici di pendolarismo come indicato in (Fig. 2b), è stimata la frequenza massima degli spostamenti associata a (Edc) e (Eic).

Conclusioni. La valutazione del rischio sismico del sistema di rete stradale si concentra particolarmente sulla fragilità dei singoli elementi strutturali (strutture da ponti) e sull'esposizione diretta degli utenti della strada. Nella gestione emergenza post disastro, l'efficienza della rete stradale è essenziale. Pertanto, la valutazione preventiva del rischio sui rami della rete stradale è fondamentale al fine di programmare l'adeguamento sismico dei collegamenti che sono strategici per un suo efficiente funzionamento.

Bibliografia

Bindi D., Pacor F., Luzi L., Puglia R., Massa M., Ameri G., Paolucci R.; 2011: *Ground motion prediction equations derived from the Italian strong motion database.* Bull Earthquake Eng, 9(6), 1899–1920. doi:10.1007/s10518-011-9313.

Bindi D., Massa M., Luzi L., Ameri G., Pacor F., Puglia R., Augliera P.; 2014: *Pan-European ground-motion prediction equations for the average horizontal component of PGA, PGV, and 5%-damped PSA at spectral periods up to 3.0 s using the RESORCE dataset*. Bulletin of Earthquake Engineering, 12(1):391430, 2014a. doi: 10.1007/s10518-013-9525-5.

Cauzzi C., Edwards B., Clinton D. Fäh, J., Wiemer S., Kästli P., Cua G., Giardini D.; 2015: *New predictive equations and site amplification estimates for the next-generation Swiss ShakeMaps.* Geophysical Journal International, 200:421438, 2015a. doi: 10.1093/gji/ggu404.

Dijkstra E. W.; 1959: *A note on two problem in connexion with graphs.* Numerische Mathematik, 1:269–271, 1959.

DISS Working Group; 2018: *Database of Individual Seismogenic Sources (DISS), Version 3.2.1: A compilation of potential sources for earthquakes larger than M 5.5 in Italy and surrounding areas.* http://diss.rm.ingv.it/diss/, Istituto Nazionale di Geofisica Vulcanologia, doi: 10.6092/INGV.IT-DISS3.2.1.

Eurocode 8 *(ENV 1998-1-1 : Design provisions for earthquake resistance of structures - Part 1-1: Generalrules - Seismic action and general requirements for structures.)*

Gutenberg B, Richter C. F.; 1944. *Frequency of earthquakes in California.* Bulletin of the Seismological Society of America, 34, 185–188.

HAZUS-MH; 2004: *Software Programme for Estimating Potential Losses from Disasters, Federal Emergency Man.* Agency, Washington DC.

Mouroux P., Brun B.L.; 2006: *Presentation of RISK-UE Project.* Bull Earthquake Eng 4, 323–339 (2006). https://doi.org/10.1007/s10518-006-9020-3.

Nielson B.G.; 2005: *Analytical Fragility Curves for Highway Bridges in Moderate Seismic Zones thesis.* QGIS 3.10 [Computer Software]. 2021 Retrieved from https://qgis.org/en/site/forusers/download.html.

RISK-UE; 2001–2004: *An advanced approach to earthquake risk scenarios, with applications to different European cities* Website http://www.risk-ue.net.

Rovida A., Locati M., Camassi R., Lolli B., Gasperini P., Antonucci A.; 2022): *Catalogo Parametrico dei Terremoti Italiani (CPTI15), versione 4.0.* Istituto Nazionale di Geofisica e Vulcanologia (INGV). https://doi.org/10.13127/CPTI/CPTI15.4.

Sextos A.G., Kilanitis I. and Kappos A.J.; 2017: *Seismic resilience assessment of the western Macedonia highway network in Greece.* In: 6th ECCOMAS Thematic Conference on Computational Methods in Structural Dynamics and Earthquake Engineering, Rhodes Island, 2017.

Sextos A.G., Kilanitis I. and Kyriakou K.; 2017: *Resilience of road networks to earthquakes.* In: 16th World Conference on Earthquake Engineering, Santiago, 2017.

SYNER-G project; 2009-2011: *Systemic Seismic Vulnerability and Risk Analysis for Buildings, Lifeline Networks and Infrastructures Safety Gain*, www.syner-g.eu.

Stergiou E., Kiremidjian A.S.; 2008: *Treatment of Uncertainties in Seismic-Risk Analysis of Transportation Systems,* University of California, Berkeley, U.S.

Vacareanu R., Lungu D., Aldea A., Arion C.; 2004: *RISK-UE Project: an advanced approach to earthquake risk scenarios with application to different European towns*, Assessing and Managing Earthquake Risk, Springer.

Werner S.D., Lavoie J.P., Eitzel C., Cho S., Huyck C., Ghosh S., Eguchi R.T., Taylor C.E., Moore J.E.; 2001: *REDARS 1: Demonstration Software for Seismic Risk Analysis of Highway Systems.* MCEER-03-SP01, Multidisciplinary Center for Earthquake Engineering Research, University at Buffalo, 17-34.

MAPPE DI PERDITA REGIONALI PER LA MITIGAZIONE DEL RISCHIO SISMICO

M.A. Zanini, L. Hofer, F. Faleschini, C. Pellegrino

Dipartimento di Ingegneria Civile, Edile e Ambientale, Università degli Studi di Padova, Padova, Italia

Introduzione. Nel contesto dell'analisi del rischio sismico alla scala territoriale, risulta fondamentale poter disporre di accurate stime delle potenziali perdite alle quali un territorio può essere esposto. I principali eventi sismici verificatisi in Italia negli ultimi decenni hanno infatti evidenziato come il patrimonio costruito italiano sia caratterizzato tutt'oggi da una elevata vulnerabilità strutturale, e come già in presenza di eventi di media intensità, relativamente frequenti nel contesto italiano, siano sufficienti a causare perdite non trascurabili, sia a livello economico che a livello di vite umane. Questo deriva essenzialmente da due fattori: il primo riguarda l'aumento dell'esposizione derivante dalla crescente urbanizzazione, mentre il secondo è legato all'elevata vulnerabilità di gran parte del patrimonio costruito italiano, che in molti casi si presenta datato e non conforme agli attuali standard di sicurezza previsti dalla normativa vigente. Ciononostante, il *retrofit* sismico si configura ancora come una pratica relativamente poco diffusa soprattutto per l'edificato privato, presentandosi come un investimento oneroso e di non immediato beneficio. Inoltre, la penetrazione di una copertura assicurativa a livello nazionale per il trasferimento del rischio sismico è ancora limitata sull'intero territorio nazionale (Zanini *et al.,* 2015 e Hofer *et al.,* 2015). Negli ultimi anni, la ricerca scientifica a livello nazionale, si è spinta verso lo sviluppo di mappe di rischio sismico, in grado di fornire agli enti governativi un quadro quantitativo della distribuzione spaziale dello stesso per una nazione (Zanini *et al.,* 2019 e Dolce *et al.,* 2021). A partire dal calcolo del rischio sismico per il territorio nazionale, sono state proposte delle strategie per l'implementazione su scala territoriale di un piano per il *retrofit* sismico degli edifici (Zanini *et al.,* 2019) ed anche delle soluzioni basate sull'utilizzo di CAT bond per il trasferimento del rischio al mercato finanziario (Hofer *et al.,* 2020). In questo contesto, il presente lavoro ha l'obiettivo di elaborare delle mappe di perdita condizionate a determinati valori di magnitudo utili per una sistematica stima previsionale delle potenziali perdite attese a seguito dell'occorrenza di un evento sismico. I risultati illustrati nel presente lavoro, si inseriscono nell'ambito dei prodotti del Progetto Europeo INTERREG CROSSIT-SAFER che coinvolge la Regione Veneto e la Regione Friuli-Venezia Giulia, assieme ad altri *partner* italiani ed esteri.

Metodologia e modelli adottati. Il patrimonio costruito residenziale italiano è rappresentato a scala comunale utilizzando i dati censuari dell'ISTAT2011 (Istituto Nazionale di Statistica, 2011). Il valore unitario del costo di ricostruzione viene assunto omogeneo nell'area di studio pari a 1200 €/m^2. In Fig. 1a viene riportato il modello di esposizione utilizzato per il calcolo delle perdite, calcolato come prodotto della superficie totale costruita in ogni comune, moltiplicata per il costo unitario di ricostruzione. Sulla base dei dati disponibili nel modello di esposizione, è stata definita una specifica tassonomia per la caratterizzazione della vulnerabilità sismica del patrimonio costruito residenziale. Nello specifico, sono state considerate 2 classi di edifici in muratura (pre-1919 e post 1919), 2 classi di edifici con struttura portante a telaio in calcestruzzo armato non progettati sismicamente (con numero di piani al massimo pari a 2, o superiore ai 3), 2 classi di edifici con struttura portante a telaio in calcestruzzo armato progettati per resistere alle azioni sismiche (con numero di piani al massimo pari a 2, o superiore ai 3), e 2 classi di edifici a struttura mista muratura-calcestruzzo armato non progettati sismicamente e resistenti alle azioni sismiche. Per ciascuna delle 8 tipologie strutturali è stato adottato un *set* di curve di fragilità (Tab. 1), in accordo a Zanini *et al.,* 2019. In Fig. 1b viene invece riportata la distribuzione delle otto categorie strutturali all'interno di ogni comune dell'area di studio. Si nota come gran parte dell'edificato residenziale sia costituito da strutture in muratura, in molti casi costruite negli anni '20. Per quanto riguarda la generazione degli scenari sismici,

gli epicentri considerati nelle simulazioni di scenario sismico sono collocati su di una griglia di calcolo di maglia quadrata di circa 7 km di lato, ricedenti all'interno delle Zone Sismogenetiche previste dal modello sismogenetico di Meletti et al. 2008 e in un intorno di 50 km dai confini delle due regioni (Veneto e Friuli Venezia Giulia) per le quali si sono andati a valutare le conseguenze a livello economico – in termini di costo di riparazione del danno sismico – stimate per ciascuno degli scenari simulati. I nodi della griglia di calcolo sono rappresentati in blu in Fig. 1a. Si assume che non possano avvenire terremoti al di fuori delle zone sismogenetiche e che gli eventi sismici con epicentri distanti più di 50 km dai confini di Veneto e Friuli-Venezia Giulia abbiano un contributo trascurabile al fine del calcolo delle perdite totali per i territori regionali analizzati. Per il calcolo delle perdite, vengono considerati 5 livelli di danneggiamento crescente (DS_0 - nessun danno, DS_1 - danno lieve, DS_2 - danno moderato, DS_3 - danno esteso, DS_4 - collasso), e per ciascuno di essi vengono utilizzati tre valori di percentuali di costo di riparazione (*RCR*) al fine di calcolare in valore medio e il valore inferiore e superiore delle perdite attese (Vettore *et al,.* 2020).

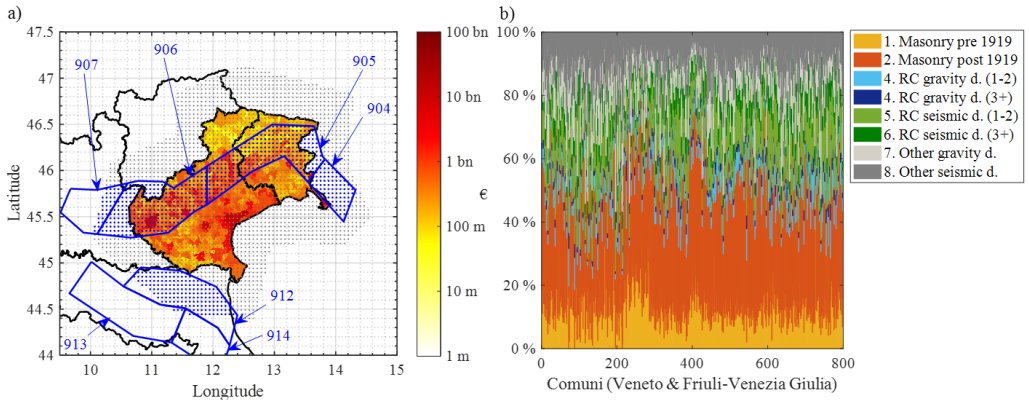


Fig. 1 - Modello di esposizione per le regioni Veneto e Friuli-Venezia Giulia, con griglia di calcolo (punti blu) e Zone Sismogenetiche coinvolte nel calcolo (a); distribuzione delle otto categorie strutturali all'interno di ogni comune dell'area di studio (b).

Tab. 1 - Parametri delle curve di fragilità.

#	Categoria strutturale	Riferimento	DS1		DS2		DS3		DS4	
			ϑ [g]	β	ϑ [g]	β	ϑ [g]	β	ϑ [g]	β
1	Masonry pre 1919	Kostov *et al.,* 2004	0.10	0.79	0.14	0.80	0.17	0.81	0.24	0.80
2	Masonry pre 1919	Kostov *et al.,* 2004	0.12	0.79	0.17	0.81	0.19	0.79	0.33	0.79
3	RC gravity d. (1-2)	Ahmad *et al.,* 2011	0.09	0.33	0.12	0.44	0.25	0.37	0.33	0.36
4	RC gravity d. (3+)	Ahmad *et al.,* 2011	0.08	0.32	0.11	0.43	0.17	0.40	0.22	0.38
5	RC seismic d. (1-2)	Ahmad *et al.,* 2011	0.09	0.33	0.12	0.44	0.24	0.37	0.48	0.36
6	RC seismic d. (3+)	Ahmad *et al.,* 2011	0.08	0.32	0.11	0.41	0.17	0.39	0.31	0.36
7	Other gravity d.	Kostov *et al.,* 2004	0.11	0.79	0.16	0.78	0.27	0.78	0.35	0.79
8	Other seismic d.	Kostov *et al.,* 2004	0.12	0.79	0.19	0.79	0.30	0.79	0.41	0.79

Per ogni scenario generato, la mappa di scuotimento viene calcolata in corrispondenza del centroide comunale attraverso la legge di attenuazione proposta da Bindi *et al.,* 2011, mentre la categoria di sottosuolo viene ricavata da Forte *et al.,* 2019. Per ogni epicentro della griglia vengono simulati otto livelli di magnitudo (4.5, 4.75, 5, 5.25, 5.5, 5.75, 6, 6.5). Secondo Barani *et al.,* 2009, solo nelle zone 905 e 906 può essere raggiunta la magnitudo di 6.5; tuttavia, per

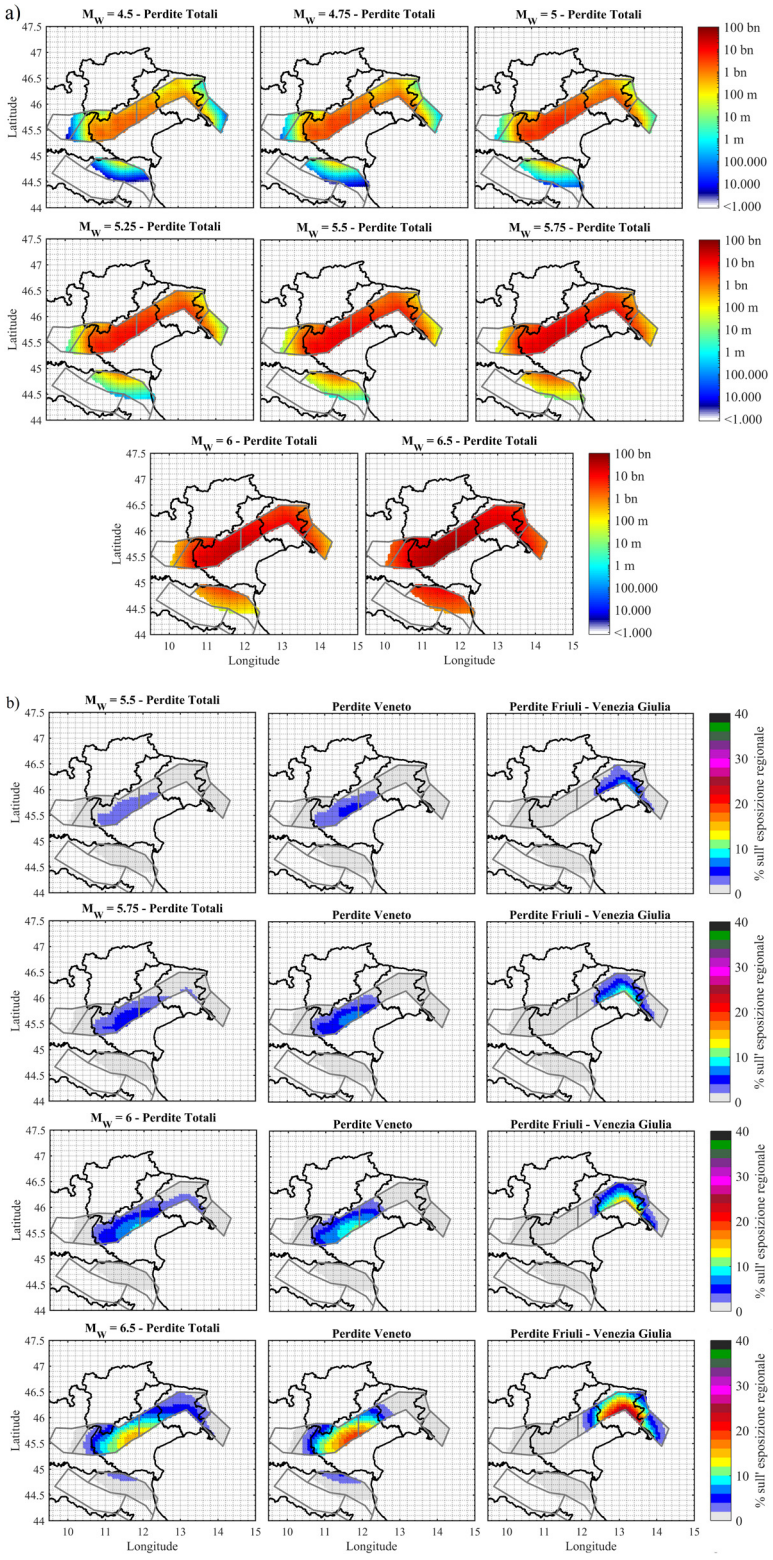


Fig. 2 - Perdite per diversi livelli di magnitudo e diversi epicentri in termini assoluti (a) e termini relativi (b).

ottenere delle mappe complete e confrontabili, essa viene simulata anche nelle altre zone sismogenetiche. Sono stati calcolati complessivamente un totale di 20'136 scenari, derivanti dalla combinazione di 8 differenti valori di magnitudo simulate in ciascuno degli 839 punti di calcolo, con l'utilizzo di 3 *set* di valori percentuali del costo di riparazione.

Risultati. I risultati delle analisi vengono riportati in Fig. 2. In particolare, ogni punto della Fig. 2a rappresenta la perdita provocata da un terremoto di data magnitudo, avente come epicentro il punto di analisi stesso. Pertanto, grazie a queste mappe, è possibile ricavare i danni diretti associati ad ogni potenziale terremoto che interessi l'area oggetto di studio. A partire da una magnitudo pari a 5, nelle aree a maggiore esposizione ubicate all'interno delle zone sismogenetiche si raggiungono perdite nell'ordine del miliardo di euro. In Fig. 2b, i risultati vengono forniti per le magnitudo maggiori anche in termini di perdita percentuale sul valore esposto totale, rispettivamente di 327 miliardi di € per le due regioni, suddivisi in 261 miliardi di € per il Veneto e 66 miliardi per il Friuli-Venezia Giulia.

Tali valori di perdita adimensionalizzati risultano particolarmente utili qualora ci si voglia riferire a valori differenti di costi di ricostruzione e valore dell'immobile. Infine, dalle mappe calcolate è possibile ricavare delle curve di perdita che esprimono le potenziali perdite attese in funzione della magnitudo di un determinato evento sismico che si verifichi in un certo luogo del territorio regionale. La Fig. 3 riporta tali curve per due possibili epicentri; il primo nei pressi di Vittorio Veneto (12.2669, 45.9341 - TV), il secondo nei pressi di Tramonti (12.7841 – 46.2952 - PN). Le curve di perdita così ottenute permettono di ricavare facilmente i valori stimati di perdite totali che si verificherebbero nei territori regionali di Veneto e Friuli-Venezia Giulia qualora soggetti ad eventi sismici localizzati nei nodi della griglia di calcolo. Si nota l'influenza decisiva dell'esposizione nel calcolo delle perdite attese, che, per un terremoto di M_W = 5 possono arrivare a 2.9 miliardi nel caso del primo epicentro, mentre si fermano a 500 milioni nel caso del secondo. In Fig. 3 si nota infine l'effetto dell'adozione di diversi set di RCR.

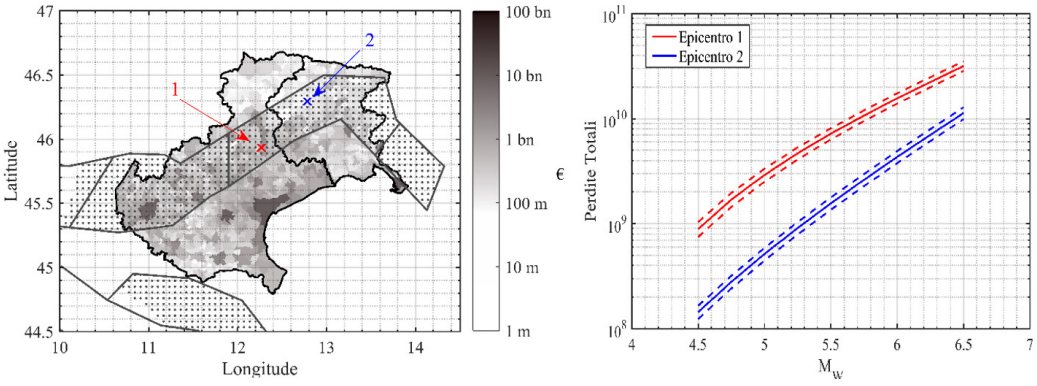


Fig. 3 - Curve di perdita per due possibili epicentri.

Ringraziamenti. I risultati illustrati nel presente lavoro sono stati finanziati dalla Commissione Europea tramite il progetto Interreg V-A Italy-Slovenia 2014-2020 CROSSIT SAFER, nell'ambito del Programma Europeo di Collaborazione Territoriale INTERREG.

Bibliografia

Ahmad, N., Crowley, H., Pinho, R.: *Analytical fragility functions for reinforced concrete and masonry buildings aggregates of Euro-Mediterranean regions - UPAV methodology.* Syner-G Project, 2009/2012, Internal report, 2011.

Barani S, Spallarossa D, Bazzurro P. *Disaggregation of probabilistic ground-motion hazard in Italy.* Bull Seismol Soc Am 2009;99(5):2638–61.

Bindi D, Pacor F, Luzi L, Puglia R, Massa M, Ameri G, *et al. Ground motion prediction equations derived from the Italian strong motion database.* Bull Earthq Eng 2011;9(6):1899–920.

Dolce M., Prota A., Borzi B., Da Porto F., Lagomarsino S., Magenes G., Moroni C., Penna A., Polese M., Speranza E., Verderame G.M., Zuccaro G., *Seismic risk assessment of residential buildings in Italy*, Bulletin of Earthquake Engineering, 19:2999–3032

Forte G., Chioccarelli E., Cito P., De Falco M., Santo A., Iervolino I. (2019) *Seismic soil classification of Italy based on surface geology and shear-wave velocity measurements.* Soil Dynamics and Earthquake Engineering, 122: 79-93.

Kostov, M., Vaseva, E., Kaneva, A., Koleva, N., Verbanov, G., Stefanov, D., Darvarova, E., Salakov, D., Simeonova, S., Cristoskov, L.: 2004: *Application to Sofia*. Report RISK-UE WP13.

Zanini, M.A., Hofer, L., Pellegrino, C. (2015). *Le polizze assicurative come strumento finanziario per il trasferimento del rischio sismico: stato dell'arte.* In: Atti del XVI Convegno ANIDIS. ISBN: 978-88-940985-6-3, L'Aquila, Italia, 13-17 settembre 2015

Hofer, L., Zanini, M.A., Pellegrino, C. (2015). *Pericolosità ed esposizione a livello mondiale: elementi primari da considerare per l'adozione di politiche di trasferimento del rischio all'industria assicurativa.* In: Atti del XVI Convegno ANIDIS. ISBN: 978-88-940985-6-3, L'Aquila, Italia, 13-17 settembre 2015

Hofer L., Zanini M. A., Gardoni Paolo (2020). *Risk-based catastrophe bond design for a spatially distributed portfolio.* STRUCTURAL SAFETY, vol. 83, 101908, ISSN: 0167-4730, doi: 10.1016/j.strusafe.2019.101908

Meletti C, Galadini F, Valensise G, Stucchi M, Basili R, Barba S, *et al. A seismic source zone model for the seismic hazard assessment of the Italian territory.* Tectonophysics 2008;450:85–108.

Vettore M., Donà M., Carpanese P., Follador V., Da Porto F., Valluzzi MR., (2020) *A Multilevel Procedure at Urban Scale to Assess the Vulnerability and the Exposure of Residential Masonry Buildings: The Case Study of Pordenone, Northeast Italy*, Heritage 3, 1433–1468.

Zanini M.A., Hofer L., Pellegrino C., 2019, *A framework for assessing the seismic risk map of Italy and developing a sustainable risk reduction program.* International Journal of Disaster Risk Reduction, 33: 74-93.

FIRST SEISMIC IMPACT ANALYSIS FOR PRE-ERUPTIVE EVENTS IN ISCHIA

G. Zuccaro[1,2], D. De Gregorio[1], F.L. Perelli[2]

[1] Department of Structures for Engineering and Architecture, University of Naples "Federico II"
[2] LUPT-PLINIVS Study Centre, University of Naples Federico II, Napoli, Italy

Introduction. Subject of this abstract is the development of first seismic impact analysis for pre-eruptive events in Ischia, based on exposure analysis conducted in the framework of agreements between the Department of Civil Protection and the PLINIVS Study Centre.

The assessment of seismic impact in Ischia has been conducted through scenario analysis, estimating the probabilistic distribution of damage induced by a single seismic event (reference scenario), as a convolution of the three random variables: hazard, exposure and vulnerability [1].

Hazard is the probability of occurrence of a single event, of a given severity, in the specific area and in a specific period. Exposure is the geographical distribution in quantitative and qualitative terms of the different elements at risk that characterize the area under consideration (buildings and occupants), whose conditions and/or functioning may be damaged, altered or destroyed due to the occurrence of the seismic event. Vulnerability is the sensitivity of an exposed element to the natural event. It can be evaluated as the probability that the exposed element will suffer a certain level of damage or change of state, with reference to an appropriate scale, because of a natural event of assigned intensity.

According to INGV-OV, as reference hazard has been chosen the last event that occurred having more energy, taken from the Parametric Catalogue of Italian Earthquakes CPTI15, version 2.0 [2].

The exposure assessments are conducted based on data collected, while the vulnerability curves adopted are those developed by the authors through empirical approach from the analysis of damage induced by earthquakes occurred on the Italian territory.

The damage on people and buildings has been assessed by the E.A.S.E. model, a procedure developed by the PLINIVS Study Centre in which the investigated area is discretized in a grid with cells of 250 m x 250 m and defines, for each cell, a hazard value and an exposure. The outcomes of the model are the probable number of lost and unsafe buildings, and the probable number of deaths, injured and homeless. In this work only the estimation of lost and unsafe buildings is presented.

The Hazard. The event of 21 August 2017 (Lat. 40.738; Long. 13.897) of magnitude 3.91 and depth 1.5 km, inferred from the Parametric Catalogue of Italian Earthquakes CPTI15, version 2.0, has been adopted as the reference hazard.

Immediately after the event, INGV developed and made available a shake-map that provides an immediate visualization of the shaking level of the affected area. The shake-map reports the peak values recorded by accelerometers and seismometers, mainly provided by the National Accelerometric Network (RAN) of the Civil Protection Department and by the National Seismic Network (RSN) of INGV, present in the area of the earthquake. Where no observed values are present, the software interpolates the data using ground motion attenuation laws, which are empirical laws for predicting shaking parameters as a function of distance, magnitude and ground conditions.

The confidence of a shaking map is a function of the density of recording stations contributing to the calculation. The case of the Ischia earthquake is particularly complex and difficult to make an accurate reproduction of the real shaking observed using the ShakeMap procedure because:

- there is only one usable datum on the Island of Ischia (IOCA seismic station, accelerometric sensor, located at the Casamicciola Observatory);

- the currently developed Shakemap procedure uses predictive ground motion laws that have not been implemented for volcanic areas;
- local ground motion amplification effects were observed at the IOCA station.

For the reasons stated above, the Shakemaps of the 21 August 2017 Ischia earthquake do not allow to accurately represent the shaking due to the earthquake on the island [3]. They are essentially derived from the application of the attenuation law alone [4, 5] and represent a compromise, leading to an underestimation of the shaking in the epicentral area, but to a more correct estimate of the shaking of the rest of the Island, in agreement with the available macroseismic surveys [6].

Having observed the low accuracy of the shakemap, it was considered to produce acceleration maps by interpolating the macroseismic intensity distribution maps in each cell 250m x250m [7] (represented in Fig. 1) and using as acceleration-intensity conversion law of Faenza and Michelini (2010).

The exposure. Exposure has been defined as the distribution of vulnerability of the ordinary buildings present in the investigated area. Based on typological characteristics, buildings are grouped by classes of behaviour towards seismic phenomena, called vulnerability classes. In the present work, four behavioural classes have been considered, indicated with the letters from A (worst behaviour) to D (best behaviour). The construction of the exposure model has made use of several data collection surveys through the compilation of typological forms:

- The CARTIS form, that provides information for sectors, for the 6 municipalities of Ischia [8] ;
- The CARTIS BUILDING for 2,000 buildings appropriately chosen within the areas identified in the CARTIS form referred to in the previous point;
- The PLINIVS form for 3,000 buildings (about 10% of the island's building aggregates).

The analysis of the buildings has been conducted through expeditious visual survey and compilation of the Level I form for the collection of parameters that influence the seismic and volcanic vulnerability of the buildings.

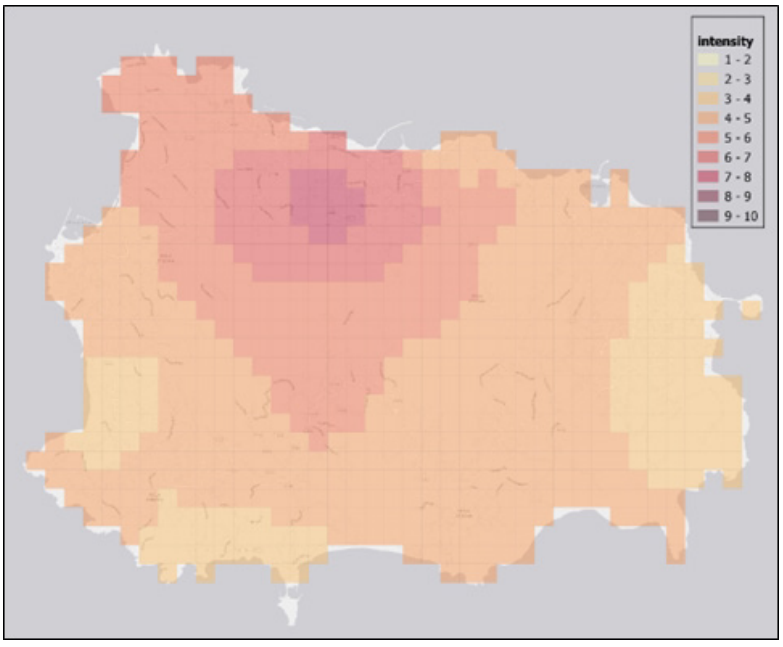


Fig. 1 - Map of seismic intensity of the seismic event of Ischia (21 August 2017).

Each building surveyed is assigned the seismic vulnerability class according to the European macro-seismic classification E.M.S. 98, in accordance with the 1st level "SAVE" methodology. This methodology [9, 10] provides for the assignment of a base score, depending on the type of vertical structure, which is subsequently improved through the application of modifier coefficients (based on typological, geometric and structural characteristics of the building). The influence of each parameter has been previously calibrated on the statistics of seismic damage detected following earthquakes in the past. The score which is reached defines the final speditive evaluation of the vulnerability class.

At the end, to assess the distribution of vulnerability classes for each minimum reference unit of the E.A.S.E. model a procedure based on statistical correlations between data from the 2011 ISTAT census and data collected in the field has been adopted [11]. ISTAT data on buildings refer to individual census sections, which may also contain several cells; therefore, a criterion for assigning census data to each cell was adopted according to the procedure proposed in Zuccaro 2021 [12]. The application of the procedure has produced the following distributions of vulnerability classes of the ordinary buildings reported in Fig 2.

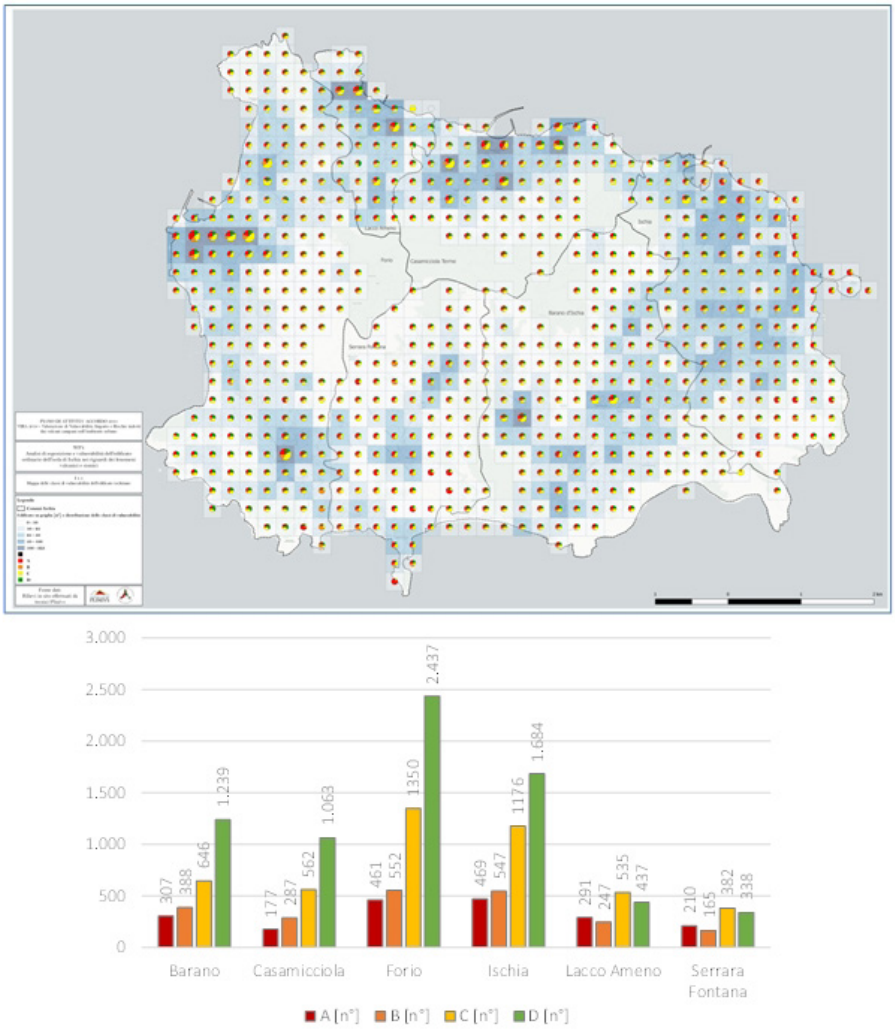


Fig. 2 - Buildings distribution (for cell in the map – for municipality in the histogram) on the vulnerability classes.

The vulnerability. The seismic vulnerability of ordinary buildings is represented, by classes, by the damage probability matrices which relate the seismic intensity and the discrete damage parameter Di (D0: no damage; D1: light damage; D2: moderate damage; D3: severe damage; D4: partial collapse; D5: total collapse). The DPMs used in the article have been built through a statistical analysis of damages observed following earthquakes occurred in Italy since 1980 (Zuccaro and De Gregorio, 2015 [13]).

Impact. To estimate the damage caused by the reference earthquake, the input data are combined. The model discretizes the area under consideration through a square-mesh grid of size 250x250m. To each cell are assigned:

- hazard data, in terms of macro-seismic intensity,
- exposure data, in terms of number of buildings for each structural vulnerability class,

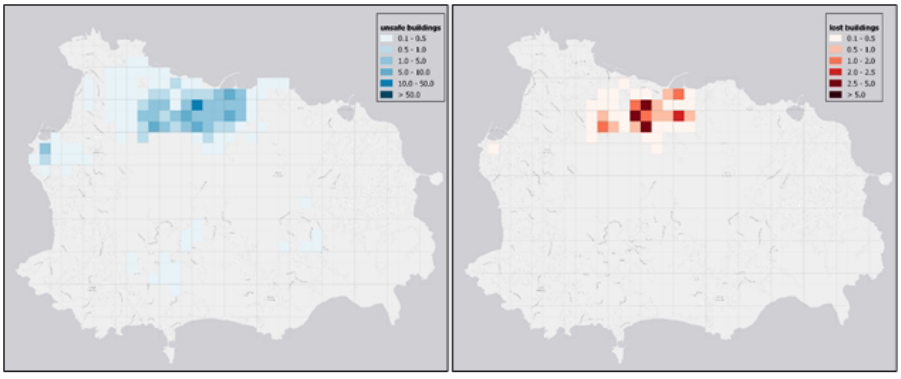
Combining these data with seismic vulnerability (percentiles 16, 50 and 84%), the model provides, cell by cell, the number of collapsed buildings (D4+D5), the number of not available buildings (0.6xD3 + D4 + D5).

With reference to the outcomes reported in Fig. 3, the municipalities with the greatest damage to buildings and occupants are Casamicciola and Lacco Ameno.

Validation. The elaborations are congruent with the damage observed following the reference seismic event [7], which caused severe damage in a rather circumscribed area.

A further validation has been done by estimating the damages to people and buildings through the IRMA (Italian Risk MAp) platform developed by Eucentre for the Department of Civil Protection (Borzi *et al.*, 2018 [14]), a tool that can produce impact scenario at municipality scale. Exposure and vulnerability used as input are consistent or at least comparable with those used for the National Risk Assessment. To compare the results, we proceeded to assess the damage induced by the reference event, having assumed the following factors:

- HAZARD: the same shake map adopted for the elaborations presented here was adopted;



MUNICIPALITY	E.A.S.E. Model		IRMA Platform	
	Collapsed Buildings	Uninhabitable buildings	Collapsed Buildings	Uninhabitable buildings
Serrara Fontana	0	1	0	1
Lacco Ameno	2	7	3	10
Ischia	0	0	0	0
Forio	0	1	0	1
Casamicciola	11	35	40	100
Barano di Ischia	0	1	0	1

Fig. 3 - Map of unsafe and lost buildings with E.A.S.E. model and comparison of the outcomes obtained by the E.A.S.E. model and the IRMA platform.

- VULNERABILITY: some specific vulnerability curves present in the platform were selected (Perelli et al. [15] for masonry and Rosti et al. [16] for reinforced concrete);
- EXPOSURE: building data provided by the 2011 ISTAT census.

Differently from the E.A.S.E. model, IRMA platform considers a single value of PGA on the entire municipality, corresponding to the PGA reported in the ShakeMap in correspondence of the centroid of the municipality. The scenarios calculated under these assumptions, through the IRMA platform, returned the results Fig. 3, which are comparable with the values estimated with the E.A.S.E. model.

The results show that the impacts achieved with the two models are orders of magnitude comparable. The biggest differences are found on the municipality of Casamicciola, which, being very large and having the centroid close to the epicenter, shows a clear overestimation of losses compared to the E.A.S.E. model.

References

1. Unesco, (1972). *Smithsonian Institution/SEAN, 1989. Global Volcanism Smithsonian Institution*, Prentice Hall, New Jersey, USA.
2. Rovida A., Locati M., Camassi R., Lolli, B., Gasperini P., 2019. *Catalogo Parametrico dei Terremoti Italiani (CPTI15), versione 2.0.* Istituto Nazionale di Geofisica e Vulcanologia (INGV). https://doi.org/10.13127/CPTI/CPTI15.2.
3. Michelini A., Luzi L., Lanzano G., Puglia R., Felicetta C., D'Amico M., Russo E., Pacor F., Faenza L., Lauciani V., Cultrera G., Milana G. (2107). *Il terremoto di Casamicciola del 21 agosto 2017: osservazioni sul moto del suolo.* Archivi Blog INGV 14 settembre 2017.
4. Faenza L. and Michelini A. (2011). *Regression analysis of MCS intensity and ground motion spectral accelerations (SAs) in Italy.* Geophysical Journal International 186 (3), 1415-1430.
5. Faenza L. and Michelini A. (2010). *Regression analysis of MCS intensity and ground motion parameters in Italy and its application in ShakeMap*. Geophys. J. Int. (2010) 180, 1138–1152 doi: 10.1111/j.1365-246X.2009.04467.x
6. QUEST (2017). *Rilievo macrosismico per il terremoto Isola di Ischia del 21 agosto 2017 – Aggiornamento al 25 agosto 2017 (ore 20)*, coordinamento del rilievo A. Tertulliani e R. Azzaro.
7. Azzaro R., Tertulliani A., Del Mese S., Graziani L., Maramai A., Martini G., Paolini S., Screpanti A., Verrubbi V., Arcoraci L. (2017). *Il terremoto di Casamicciola (IschIa) del 21 agosto 2017: effetti macrosismici e confronto con la sismicità storica dell'area.* 36° Convegno Nazionale GNGTS, Trieste, 14-16 novembre 2017, Sessione 1.1.
8. Zuccaro, G., Dolce, M., De Gregorio, G., Soeranza, E. (2015), *La scheda CARTIS per la caratterizzazione tipologico-strutturale dei comparti urbani costituiti da edifici ordinari. Valutazione dell'esposizione in analisi di rischio sismico* - Convegno Nazionale GNGTS.
9. Zuccaro, G. and Cacace, F. (2006). *Valutazione speditiva della Vulnerabilità per gli edifici strategici della Regione Campania,* Ingegneria Sismica. n° 2/2006.
10. Zuccaro, G. and Cacace, F. (2015). *Seismic vulnerability assessment based on typological characteristics. The first level procedure "SAVE".* Soil Dynamics and Earthquake Engineering (2015), pp. 262-269. DOI information: 10.1016/j.soildyn.2014.11.003.
11. Cacace, F., Zuccaro, G., De Gregorio, D., Perelli, F.L. (2018). *Building Inventory at National scale by evaluation of seismic vulnerability classes distribution based on Census data analysis: BINC procedure.* INTERNATIONAL JOURNAL OF DISASTER RISK REDUCTION, p. 384-393, ISSN: 2212-4209.
12. Zuccaro, G.; De Gregorio, D.; Leone, M.F.; Sessa, S.; Nardone, S.; Perelli, F.L. (2021) *CAESAR II Tool: Complementary Analyses for Emergency Planning Based on Seismic Risks Impact Evaluations*. Sustainability 2021, 13, 9838. https://doi.org/10.3390/su13179838.
13. Zuccaro, G. and De Gregorio, D. (2015). *Vulnerability of exposed elements*. In Italian: Vulnerabilità dei beni esposti. In: Urciuoli Gianfranco. (a cura di): Urciuoli Gianfranco, Gestione e mitigazione dei rischi naturali. p. 15-27, NAPOLI: Doppiavoce, ISBN: 978-88-89972-58-8.
14. Borzi, B.; Onida, M.; Faravelli; M., Polli, D.; Pagano, M.; Quaroni, D.; Cantoni, A.; Speranza, E.; Moroni, C. (2020); *IRMA platform for the calculation of damages and risks of Italian residential buildings,* Springer Nature B.V. 2020
15. Perelli, F.L.; De Gregorio, D.; Cacace, F.; Zuccaro, G.(2019) *Empirical vulnerability curves for Italian masonry buildings*. In Proceedings of the 7th International Conference on Computational Methods in Structural Dynamics and Earthquake Engineering (COMPDYN 2019), Crete Island, Greece, 25–27 May 2019; Volume 1, pp. 1745–1758. Available online: https://2019.compdyn.org (accessed on 22 August 2021).
16. Rosti, A., Del Gaudio, C, Di Ludovico, M., Magenes, G., Penna, A., (2019) *Use of empirical fragility curves for assessing seismic risk at the national scale* - Atti del XVIII Convegno ANIDIS L'ingegneria Sismica in Italia : Ascoli Piceno, 15-19 settembre 2019.

L'ANALISI DELLA CONDIZIONE LIMITE DELL'EMERGENZA A DIECI ANNI DALLA SUA ISTITUZIONE. UN PRIMO STRUMENTO PER INDAGARNE GLI EFFETTI SULLA GOVERNANCE TERRITORIALE

M.S. Benigni, C. Fontana, M. Giuffrè, V. Tomassoni

Consiglio Nazionale delle Ricerche (CNR)
Istituto di Geologia Ambientale e Geoingegneria (IGAG) - Roma Italy

Introduzione. Il contributo proposto è frutto di una ricerca in corso, nata negli ultimi mesi, in occasione dei dieci anni dall'emanazione delle prime ordinanze in attuazione del *Piano Nazionale per la prevenzione del rischio sismico* (articolo 11 della Legge 77/2009), che hanno previsto l'introduzione degli studi di Microzonazione Sismica (MS) e dell'analisi della Condizione Limite dell'Emergenza (CLE) per i comuni a maggiore pericolosità sismica ($ag \geq 0.125$ g).

Concentrandosi in particolar modo sulla CLE, è utile proporre nel primo decennale dalla sua introduzione, una riflessione in merito all'effettiva incidenza dell'analisi sul processo di mitigazione del rischio sismico e sul grado di assimilazione da parte delle realtà territoriali e locali di una cultura della prevenzione e della gestione del rischio.

È evidente che la valutazione delle ricadute di queste attività sul governo del territorio non può prescindere dal confronto con i territori stessi e quindi con gli attori che hanno gestito tutte le fasi amministrative ed esecutive del programma, a partire dai referenti regionali. Si ritiene infatti che tale confronto possa essere un'efficace modalità per individuare le effettive dinamiche che gli studi hanno innescato, sia da un punto di vista della pianificazione territoriale, sia da quello della conoscenza e consapevolezza raggiunte dalle comunità locali.

Con questo obiettivo è stato costruito un questionario, che in questa prima fase di lavoro è stato condiviso con tutti i referenti delle Regioni che hanno aderito al finanziamento del Piano Nazionale per la prevenzione del rischio sismico, con l'auspicio che possa coinvolgere in una fase successiva anche gli uffici comunali più aderenti alle dinamiche locali. L'intento è avvalorato dall'esplicita indicazione normativa presente nelle varie ordinanze circa la necessità che le Regioni determinino "le modalità di recepimento di tali analisi negli strumenti urbanistici e di pianificazione dell'emergenza vigenti" (comma 3, art.18 O.P.C.M. n. 4007/2012 e successive).

Allo stato attuale il lavoro si trova ancora ad uno stadio preliminare e poiché i risultati dell'indagine conoscitiva non sono ancora disponibili, il seguente documento deve essere letto da un lato come base di lavoro utile a fornire un quadro complessivo degli obiettivi e dei contenuti specifici del questionario, dall'altro come spunto per avviare una riflessione più ampia sulla necessità di ripensare la pianificazione territoriale e urbanistica nel nostro paese anche in funzione degli strumenti di mitigazione del rischio sismico.

Strumenti per la mitigazione del rischio sismico: criticità e potenziali sinergie con la pianificazione urbanistica e territoriale. La definizione di un sistema di politiche e strumenti per la mitigazione dei rischi naturali è stata oggetto, a partire dagli anni ottanta, di un'intensa sperimentazione tecnico-scientifica sul territorio nazionale.

Tuttavia il prevalere di logiche emergenziali, l'elevata frammentazione delle competenze e la settorialità degli strumenti a disposizione hanno limitato l'efficacia di tali processi, confinando il tema della riduzione dei rischi ad ambiti prevalentemente tecnici, con una limitata attenzione all'integrazione delle diverse conoscenze nei processi decisionali per il governo del territorio (Galderisi *et al.*, 2017). Lo stesso Piano di Protezione Civile, nato come strumento per affrontare e gestire in modo efficace un evento calamitoso, ma anche come riferimento per impostare azioni e interventi di tipo ordinario in rapporto al governo del territorio (Art. 3, Legge n. 225/1992), ha assunto negli anni un carattere meramente formale (Ioannilli, 2019).

Infatti la preparazione all'emergenza e la predisposizione del Piano di Protezione Civile non vengono considerate attività complesse ma piuttosto operative e tecniche, atti formali a fronte di dettami legislativi e normativi.

Negli ultimi dieci anni, con l'aggravarsi della frequenza e della severità degli eventi, in particolare sismici, che hanno colpito il nostro Paese, è stato emanato il *Piano Nazionale per la prevenzione del rischio sismico,* che sta finanziando un programma di indagini di MS, di analisi della CLE e di interventi strutturali sugli edifici, tramite ordinanze ministeriali. Tali fondi vengono affidati alle Regioni e gestiti in accordo con i comuni interessati. In particolare la CLE, introdotta dall'O.P.C.M. n. 4007/2012, si configura come uno strumento tecnico, di verifica dei Piani di Protezione Civile, che definisce un sistema minimo da mettere in sicurezza per mantenere la tenuta delle funzioni strategiche essenziali per la gestione dell'emergenza e delle loro relazioni, di connessione ed accessibilità a scala urbana.

In questo quadro, l'introduzione degli studi di MS e CLE gioca un ruolo rilevante nei confronti della pianificazione del territorio. Permette infatti, in linea generale, il potenziale passaggio da un approccio settoriale, impostato su logiche puntuali e operative, ad una visione di insieme maggiormente strutturata, fondata sul riconoscimento dei rapporti fisici e funzionali che intercorrono tra le grandezze strategiche ed il sistema urbano complessivo, se pure limitatamente alla funzione di gestione dell'emergenza (Ioannilli, 2013). Al contempo l'affiancamento degli studi di MS e CLE offre un livello di conoscenza di notevole rilevanza, fornendo uno strumento conoscitivo di base, al fine di stabilire gerarchie di pericolosità utili per la programmazione di interventi di riduzione del rischio sismico a varie scale, orientare la scelta di aree per nuovi insediamenti, definire gli interventi ammissibili in una determinata area, programmare le indagini e i livelli di approfondimento, stabilire orientamenti, modalità e priorità di intervento nelle aree urbanizzate (Baglione *et al.*, 2015).

Ad oggi, lo stato di attuazione degli studi di MS e CLE, finanziati finora nelle diverse ordinanze, ha raggiunto una copertura pari al 61% per la MS e al 56% per la CLE rispetto al totale dei comuni programmati (Figura 1).

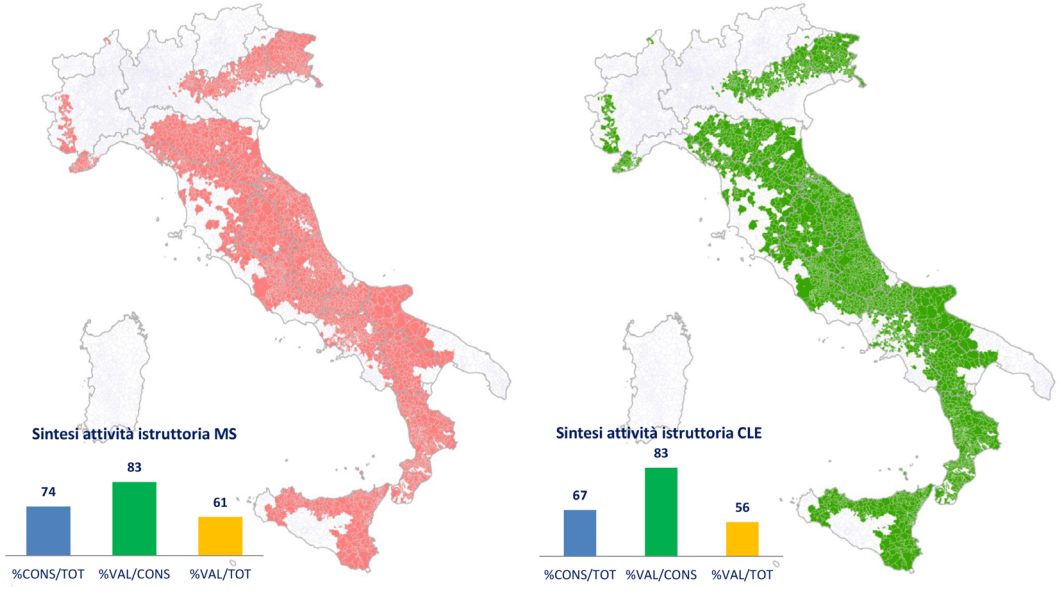


Fig. 1 - Sintesi aggiornata ad aprile 2022. In blu la percentuale degli studi consegnati su quelli previsti, in verde quella degli studi validati su quelli consegnati, in giallo quella degli studi validati sul totale di quelli previsti - fonte Commissione Tecnica per la Microzonazione Sismica, Dipartimento di Protezione Civile.

Il questionario: obiettivi, ideazione e costruzione. Per valutare le ripercussioni sul governo del territorio di tali studi, è stata programmata un'indagine conoscitiva, qui presentata in via preliminare, basata su un questionario specifico sottoposto ai 17 referenti regionali che hanno aderito al finanziamento del Piano Nazionale per la prevenzione del rischio sismico.

Nello specifico l'attività di indagine è orientata verso tre obiettivi principali:

1) Analizzare le procedure amministrative previste nelle Regioni, per valutare la definizione dei ruoli, le modalità di distribuzione delle risorse e di gestione con gli Enti locali e l'efficienza organizzativa;
2) Analizzare se e in che modo i contenuti delle analisi della CLE hanno supportato gli Enti nella verifica del sistema di gestione dell'emergenza;
3) Analizzare le ripercussioni degli studi effettuati sulle attività di pianificazione e gestione del territorio e sulla consapevolezza del rischio da parte delle comunità locali.

Il questionario è articolato secondo i tre obiettivi appena enunciati ed è impostato su una modalità di indagine *semi-strutturata* (prediligendo risposte di tipo booleano o compilabili attraverso la scelta in un menù predefinito, ma lasciando anche la possibilità di aggiungere commenti in campi specifici), in modo da guidare e facilitare la compilazione, ma anche ricevere informazioni aggiuntive che possano arricchire il quadro complessivo. L'indagine è stata inviata attraverso la segreteria della Commissione tecnica per il supporto e monitoraggio degli studi di MS e CLE sotto forma di modulo online. La Figura 2 riporta a titolo esemplificativo alcune delle domande per ogni sezione.

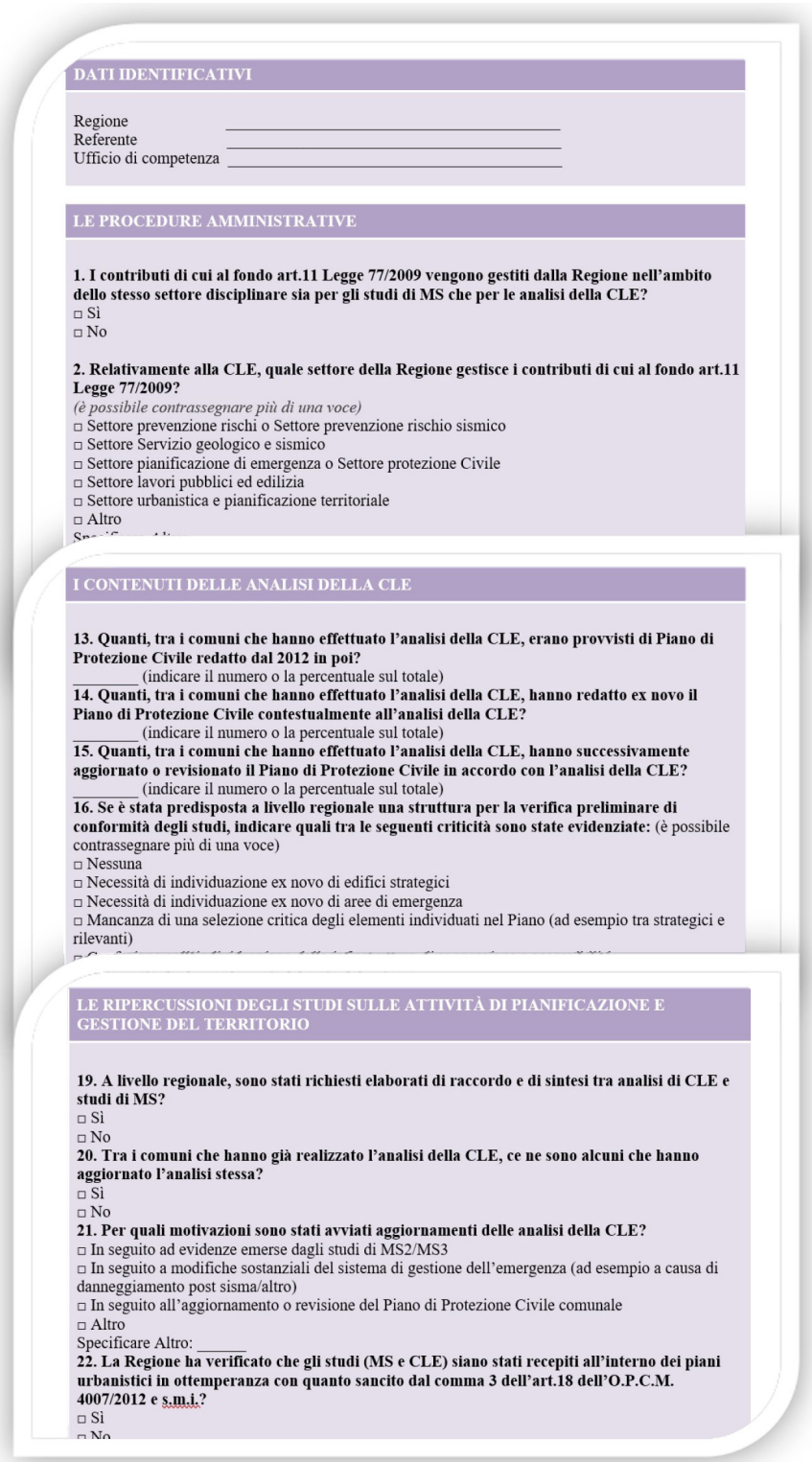
Le procedure amministrative. Indagare sulle procedure amministrative risulta cruciale ai fini della ricerca dal momento che l'iter dell'intero processo, dall'adesione al programma alla validazione degli studi, è articolato, lungo e non privo di imprevisti.

Un aspetto di carattere generale è quello dell'individuazione degli attori coinvolti nella gestione dei fondi, nella programmazione degli studi e nella verifica di conformità degli stessi, almeno nella fase preliminare. Il carattere di interdisciplinarietà di tale attività richiede la collaborazione di diversi settori tecnico-amministrativi: i contributi finanziari, in considerazione delle finalità dell'intervento, possono ad esempio essere gestiti dal settore che si occupa di prevenzione rischio sismico o dal settore geologico, ma anche dal settore relativo alla pianificazione di emergenza o all'edilizia e lavori pubblici. Data la complessità di tale gestione, è di notevole interesse l'osservazione di quali settori tecnico-amministrativi si siano posti come referenti rispetto alla gestione del programma, se abbiano agito autonomamente oppure abbiano collaborato con altri uffici e su quali aspetti.

Il tema degli affidamenti di incarico per la realizzazione degli studi rappresenta un panorama altrettanto articolato. Infatti questi possono essere gestiti a livello centrale direttamente dalla Regione, tramite bandi di gara pubblici, oppure a livello locale dalle amministrazioni comunali, che possono sia effettuare lo studio al proprio interno o affidarlo a professionisti esterni. In ogni caso, l'analisi della CLE richiede che gli Enti, oltre a fornire la documentazione di base, prendano parte ad una serie di decisioni che costituiscono il presupposto dell'analisi stessa. Per cui è fondamentale valutare quanto lo studio effettuato si confronti in modo diretto con le realtà locali, e in che modo sia stato articolato il coordinamento regionale durante l'intero iter procedurale.

Un altro aspetto rilevante ai fini dell'indagine è rappresentato dal livello di partecipazione dei comuni beneficiari dei contributi per MS e CLE alla procedura di redazione di tali studi sul loro territorio. Tale misura ci permette di monitorare non solo l'attenzione degli Enti Locali verso questi temi, ma anche l'efficacia delle attività di sensibilizzazione svolte dalle Regioni.

Infine, un'ulteriore questione riguarda il livello di cooperazione tra comuni limitrofi nello svolgere le attività di mitigazione del rischio. Questo aspetto appare rilevante per l'indagine perchè avvia una riflessione sulle modalità di associazione degli Enti locali e sull'esistenza o meno di una visione integrata del territorio.



DATI IDENTIFICATIVI

Regione _____
Referente _____
Ufficio di competenza _____

LE PROCEDURE AMMINISTRATIVE

1. I contributi di cui al fondo art.11 Legge 77/2009 vengono gestiti dalla Regione nell'ambito dello stesso settore disciplinare sia per gli studi di MS che per le analisi della CLE?
□ Sì
□ No

2. Relativamente alla CLE, quale settore della Regione gestisce i contributi di cui al fondo art.11 Legge 77/2009?
(è possibile contrassegnare più di una voce)
□ Settore prevenzione rischi o Settore prevenzione rischio sismico
□ Settore Servizio geologico e sismico
□ Settore pianificazione di emergenza o Settore protezione Civile
□ Settore lavori pubblici ed edilizia
□ Settore urbanistica e pianificazione territoriale
□ Altro

I CONTENUTI DELLE ANALISI DELLA CLE

13. Quanti, tra i comuni che hanno effettuato l'analisi della CLE, erano provvisti di Piano di Protezione Civile redatto dal 2012 in poi?
_____ (indicare il numero o la percentuale sul totale)
14. Quanti, tra i comuni che hanno effettuato l'analisi della CLE, hanno redatto ex novo il Piano di Protezione Civile contestualmente all'analisi della CLE?
_____ (indicare il numero o la percentuale sul totale)
15. Quanti, tra i comuni che hanno effettuato l'analisi della CLE, hanno successivamente aggiornato o revisionato il Piano di Protezione Civile in accordo con l'analisi della CLE?
_____ (indicare il numero o la percentuale sul totale)
16. Se è stata predisposta a livello regionale una struttura per la verifica preliminare di conformità degli studi, indicare quali tra le seguenti criticità sono state evidenziate: (è possibile contrassegnare più di una voce)
□ Nessuna
□ Necessità di individuazione ex novo di edifici strategici
□ Necessità di individuazione ex novo di aree di emergenza
□ Mancanza di una selezione critica degli elementi individuati nel Piano (ad esempio tra strategici e rilevanti)

LE RIPERCUSSIONI DEGLI STUDI SULLE ATTIVITÀ DI PIANIFICAZIONE E GESTIONE DEL TERRITORIO

19. A livello regionale, sono stati richiesti elaborati di raccordo e di sintesi tra analisi di CLE e studi di MS?
□ Sì
□ No
20. Tra i comuni che hanno già realizzato l'analisi della CLE, ce ne sono alcuni che hanno aggiornato l'analisi stessa?
□ Sì
□ No
21. Per quali motivazioni sono stati avviati aggiornamenti delle analisi della CLE?
□ In seguito ad evidenze emerse dagli studi di MS2/MS3
□ In seguito a modifiche sostanziali del sistema di gestione dell'emergenza (ad esempio a causa di danneggiamento post sisma/altro)
□ In seguito all'aggiornamento o revisione del Piano di Protezione Civile comunale
□ Altro
Specificare Altro: _____
22. La Regione ha verificato che gli studi (MS e CLE) siano stati recepiti all'interno dei piani urbanistici in ottemperanza con quanto sancito dal comma 3 dell'art.18 dell'O.P.C.M. 4007/2012 e s.m.i.?
□ Sì
□ No

Fig. 2 - Stralci a titolo esemplificativo delle tre sezioni in cui è articolato il questionario.

I contenuti delle analisi della Condizione Limite dell'Emergenza. Come noto, l'analisi della CLE è uno strumento per la verifica dell'esistenza e della consistenza di una parte del sistema di gestione dell'emergenza (edifici strategici, aree di emergenza e infrastrutture di connessione e accessibilità), già individuata nel Piano di Protezione Civile, costituendo quindi una verifica indiretta dello strumento di pianificazione stesso. Infatti solo in caso di inesistenza o inadeguatezza dei Piani si può procedere, in fase di analisi, all'individuazione ex novo degli elementi riconosciuti come strategici per la gestione dell'emergenza, attraverso un processo di condivisione e partecipazione tra soggetti istituzionali e altri soggetti coinvolti a livello territoriale (Bramerini *et al.*, 2014). Inoltre ove l'analisi della CLE portasse alla luce incongruenze e necessità di aggiornamento e revisione degli strumenti di Piano, possono essere valutate dall'Amministrazione, consapevole delle criticità dei propri territori, azioni conseguenti, quali nuove indicazioni di pianificazione, discipline d'uso e priorità di intervento, usufruendo anche di altri finanziamenti.

In tal senso, indagare come è stata effettuata l'analisi della CLE e su quali contenuti di base può essere utile per comprendere il livello di attenzione e approfondimento che l'amministrazione comunale adotta nell'ambito delle attività tecniche e di protezione civile di propria competenza.

Le ripercussioni degli studi sulle attività di pianificazione e gestione del territorio. Le conoscenze acquisite dalla redazione delle analisi della CLE consentono di spostare l'attenzione dalle singole aree e manufatti al sistema di relazioni e interconnessioni, e, se recepite negli strumenti di pianificazione in regime ordinario e in modo consapevole, possono avere ricadute rilevanti ai fini dell'attivazione di politiche di prevenzione per la salvaguardia di un territorio. L'individuazione degli elementi della CLE, compresi gli aggregati interferenti, oltre a definire le priorità di intervento per la messa in sicurezza del sistema di gestione dell'emergenza, può anche avere ricadute di più ampio raggio: laddove tali interventi coinvolgono parti storiche o ambiti urbani con maggiore afferenza della popolazione, essi possono produrre effetti anche sulla riqualificazione degli spazi urbani, la rivitalizzazione degli insediamenti, il recupero edilizio e dei beni culturali (Fazzio *et al.*, 2014). Tale apporto risulta ancora più rilevante quando le analisi vengono prodotte in accordo con gli studi di MS, dando un quadro chiaro di quali parti del sistema urbano siano potenzialmente a rischio. Di conseguenza è possibile ipotizzare ambiti mirati di intervento all'interno degli strumenti urbanistici per la mitigazione del rischio (la riduzione della vulnerabilità degli edifici, dell'esposizione, attraverso scelte di delocalizzazione delle funzioni).

Un ulteriore aspetto da prendere in considerazione nel valutare le implicazioni che gli studi possono avere sulle attività di pianificazione riguarda il livello di approfondimento e aggiornamento degli studi stessi. La sovrapposizione degli studi di MS di primo livello con le analisi di CLE permette di identificare se gli elementi nodali per la gestione dell'emergenza ricadono in zone critiche dal punto di vista della pericolosità sismica; gli studi di MS di secondo e terzo livello, invece, effettuati per definire con maggior dettaglio le criticità di alcune parti del territorio (ad esempio i perimetri delle aree instabili o l'idoneità delle aree adibite ad insediamenti temporanei post-sisma o ad aree di emergenza), possono modificare notevolmente le conoscenze che hanno determinato la scelta di un particolare assetto del sistema di gestione dell'emergenza.

Risulta dunque necessario che entrambi gli studi siano periodicamente aggiornati e che tali aggiornamenti siano recepiti negli strumenti di pianificazione e gestione del territorio (in ottemperanza con quanto sancito dal comma 3 dell'art.18 dell'O.P.C.M. 4007/2012 e successivi).

Sviluppi di tali studi, che possono rafforzare il loro rapporto con la pianificazione territoriale, riguardano il superamento della scala comunale verso una visione di livello intercomunale.

Ne costituiscono un esempio in tal senso i risultati ottenuti nell'ambito del Progetto "PON Governance e Capacità Istituzionale 2014-2020" coordinato dal Dipartimento di Protezione Civile: a partire dagli studi disponibili a scala comunale è stata perfezionata una metodologia di selezione degli elementi di interesse strategico (Carbone *et al.*, 2019), finalizzata a definire il sistema di gestione dell'emergenza funzionale a scala territoriale.

Tale visione più ampia appare maggiormente adeguata per la programmazione delle azioni di mitigazione del rischio e per la definizione delle priorità di intervento, consentendo valutazioni di operatività su sistemi di gestione dell'emergenza omogenei e confrontabili (Cassone *et al.*, 2016).

Un ultimo aspetto di indagine è quello che riguarda la consapevolezza acquisita dai territori interessati dal programma di finanziamenti in atto. Risulta di particolare rilievo verificare se la redazione degli studi abbia portato ad iniziative di diffusione dei risultati ottenuti, di comunicazione delle conoscenze raggiunte e di formazione alla gestione dei rischi tramite eventi, attività o corsi tecnico-professionali.

Prime conclusioni e prossimi passaggi. A dieci anni dall'emanazione delle prime ordinanze in attuazione del Piano Nazionale per la prevenzione del rischio sismico, una riflessione sull'effettiva incidenza dell'analisi della CLE sul processo di mitigazione del rischio sismico e sulle ricadute sugli strumenti di governo del territorio appare opportuna: ad una maggiore efficienza in termini di utilizzo delle risorse e di impegno dei finanziamenti per la produzione di studi ed indagini, potrebbe infatti non corrispondere un altrettanto efficace successivo utilizzo degli stessi risultati ottenuti.

È evidente che la valutazione di questi aspetti non può però esulare dal confronto con i territori stessi e quindi con gli attori che hanno gestito tutte le fasi amministrative ed esecutive del programma. Per avviare tale confronto, è stato ideato e costruito un questionario fondato su tre obiettivi principali: i) analisi delle procedure amministrative, ii) analisi dei contenuti della CLE, iii) analisi delle ripercussioni degli studi sulle attività di pianificazione e gestione del territorio. Il questionario è stato sottoposto in questa prima fase ai referenti regionali, quali primi destinatari delle risorse statali.

Poiché i risultati dell'indagine non sono ancora disponibili, il lavoro descritto nelle pagine precedenti ha l'obiettivo di presentare il questionario, che deve essere inteso quale strumento pensato per avviare un'indagine qualitativa preliminare degli effetti dell'analisi della CLE sulla governance territoriale, uno strumento utile per far emergere valutazioni non indagabili in modo diretto e che se ampliato in una fase successiva anche ai referenti comunali potrebbe permettere di raccogliere ed elaborare un campione decisamente vasto di informazioni e dati utili.

Il lavoro, che come ribadito si trova ad uno stadio preliminare, sarà sviluppato una volta ricevute le risposte al questionario, nelle seguenti fasi: a) elaborazione dei dati ricevuti e prime valutazioni sugli effetti dell'analisi della CLE sulla governance territoriale, b) analisi statistiche realizzate sui dati di MS e CLE raccolti nel DB a supporto del "Portale informativo e cartografico della Microzonazione Sismica e della Condizione Limite per l'Emergenza", c) approfondimento dei quesiti esposti nel questionario per un ampliamento del campione di indagine alla scala locale comunale.

Bibliografia

Baglione M., D'Intinosante V., P. Fabbroni V. (2015). *«La conoscenza del rischio sismico attraverso gli studi di microzonazione sismica della Regione Toscana: risultati, strumenti e metodologie proposte per la pianificazione territoriale»*. In: Atti del 34° Convegno Nazionale GNGTS, Trieste, 17-19 novembre 2015.

Bramerini F., Castenetto S., Conte C., Naso G. (2014). *«Analisi della Condizione Limite dell'Emergenza (CLE): considerazioni preliminari sui dati raccolti»*. In: Atti del 33° Convegno Nazionale GNGTS, Bologna, 25-27 novembre 2014.

Carbone G., Cianci E., Donolo R.M., Fazzio F., Gigliotti A., Tomassoni V. (2019). *«Linee Guida Individuazione Elementi Strutturali minimi del Contesto Territoriale (CLE di CT)»*. Report PON Governance and Institutional Capacity 2014-2020 - Rischio sismico e vulcanico.

Cassone F., Giuffrè M., Bramerini F., Naso G., Castenetto S., Ciaccasassi P. (2016). *«Dalla CLE comunale alla CLE per Contesto Territoriale»*. In: Atti del 35° Convegno Nazionale GNGTS, Lecce, 22-24 novembre 2016

Fazzio F., Parotto R., Giuffrè M. (2014). *«Ripensare la prevenzione urbanistica del sisma. Le condizioni limite per gli insediamenti»*. In: Urbanistica Informazioni n.257 – VIII giornata di studio INU. Una politica per le città italiane. Napoli 12 dicembre 2014

Galderisi A., Limongi G., Treccozzi E. (2017). *«Conoscenza e gestione dei rischi tra frammentazione e settorialità. Il caso Napoli»*. In: Atti della XX Conferenza Nazionale SIU. Roma: Planum Publisher.

Ioannilli M. (2013). *«Pianificazione dell'emergenza e prevenzione strutturale del rischio: il ruolo della CLE»*. In: Urbanistica Dossier. Roma: INU Edizioni, 31-34.

Ioannilli M. (2019). *«Sicurezza territoriale, governo del territorio, protezione civile»*. In: Il Piano di emergenza nell'uso e nella gestione del territorio. Milano: Franco Angeli Edizioni, 36-48.

STRUCTURAL MONITORING OF A HIGHWAY BRIDGE IN A HIGH-SEISMIC HAZARD URBAN AREA

A. D'Alessandro[1], S. Bongiovanni[2], A. Costanzo[1], A. Di Benedetto[3], A. Figlioli[2], S. Scudero[1], S. Speciale[1], G. Vitale[1]

[1] Istituto Nazionale di Geofisica e Vulcanologia, Osservatorio Nazionale Terremoti, Rome, Italy
[2] Università di Palermo, Dipartimento di Scienze della Terra e del Mare, Palermo, Italy
[3] Università di Palermo, Dipartimento di Matematica e Informatica Palermo, Italy

Introduction. The stress factors acting on the structures can be due to natural or anthropogenic factors: earthquakes atmospheric agents (wind, thermal cycles), vibration due traffic flow, applied loads. All these factors, may lower the resistance properties of the structure therefore the Structural Health Monitoring (SHM) represents a fundamental tool to integrate and support conservation strategies of infrastructures and to preserve their functions. The function which describes the behavior of a structure will be dependent on the structural parameters obtained with the building monitoring. Such parameters may change after an earthquake, or even after extreme phenomena, and the continuous SHM enable to verify if the general parameters of the building have changed as today widely accepted (Calvi *et al.*, 2006 for a complete review).

In the framework of RAFAEL (System for Risk Analysis and Forecast for Critical Infrastructures in the AppenninEs dorsaL Regions) project, the case study as critical infrastructure to monitor is a bridge in Catania (Sicily, Italy). This viaduct is called "San Paolo bridge (Fig. 1); the choice of this structure has several reasons: i) it is the longest viaduct in the highway surrounding the city of Catania and part of the E45 European motorway corridor; ii) the seismic hazard of Catania is among the highest in Italy (expected horizontal peak acceleration up to 0.25 g); iii) the viaduct was built about 35 years ago, when the seismic classification and building codes were different. In this paper, we present the preliminary results of the tests performed for the characterization of the structure and its foundation soil.



Fig. 1 - a: Google Earth view of S. Paolo bridge (the arrows indicated the segment under investigation) and plan view of sensors location for the experiments; b: lateral view (southern flank) of the structure; c: location of the posthole (50 m deep) seismometer and ground-level accelerometer.

Geophysical investigations and bridge experiments. The bridge has a total length of about 378 m and consists of 10 spans. The first and last span have a length of 33.55 m, the remaining have a length of 34 m except for the span between columns 6 and 7 which has a double length of 73 m. The bridge is supported by 9 columns and the monitored span is between the columns 4 and 5 (Fig. 1).

Geophysical investigations have been carried out in order to characterize the soil foundation below the bridge. These investigations would have also suggested the depth of the seismic bedrock, and therefore the depth of the perforation in which install a sensor with the objective to record the ground motion without being altered by the interaction with the bridge.

The seismic tomography was realized under the western half of the bridge (columns 1-6). The resulting 2D profile shows a difference in the thickness of the surface layer between the two ends of the investigated line. It also clearly highlights the foundations in correspondence of the pillars (Fig. 2a). This difference in thickness at the ends of the investigated line was also observed by two 1D profiles obtained from MASW (Fig. 2b, c). Finally, from the microtremor measurements it is possible to observe the presence of two frequency peaks: one of about 1.6 Hz and one of about 4.3 Hz (Fig. 2d).

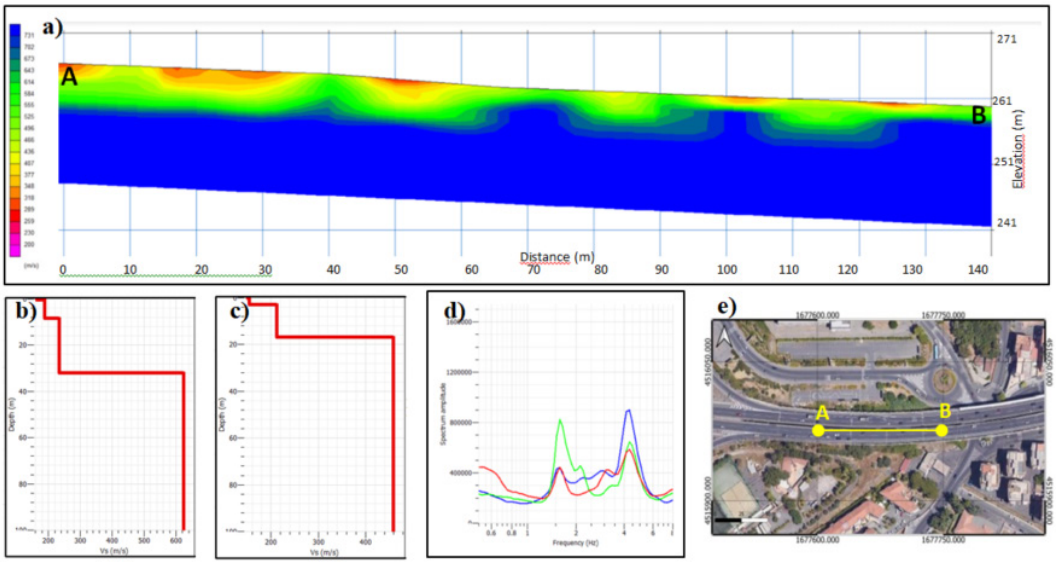


Fig. 2 - Results of geophysical surveys: seismic tomography (a), MASW (b and c), microtremor (d), and their location (e).

The results of the preliminary geophysical investigation suggested to drill the perforation at least 40 m deep. The perforation has been finally drilled down to 51 m and posthole 3-axial seismometer (model Nanometrics Trillium PH 120 s) has been placed its bottom (Fig. 1c) and set at 100 Hz sampling rate. A 3-axial accelerometer (Nanometrics Titan) has been placed at surface, next to the perforation top (Fig. 1c), at sample rate of 200 Hz. This couple of sensors, installed in January 2022, will be maintained installed for a long-term monitoring. In order to calibrate the velocimeter in the well, a velocimeter was installed at ground surface. Both sensors acquired a seismic event that occurred in January 2022. The difference between the surface and down-hole sensor is notable (Fig. 3). While the former is constantly affected by the noise of the morning traffic over the bridge (Fig. 3a), in the latter the waveforms of the event are clearly recognizable (Fig. 3b) even though a notable amount of noise is still present.

In order to characterize the vibrating modes of the bridge, a devoted experiment had been carried out in April 2022. It was a temporary experiment lasting some hours; because the

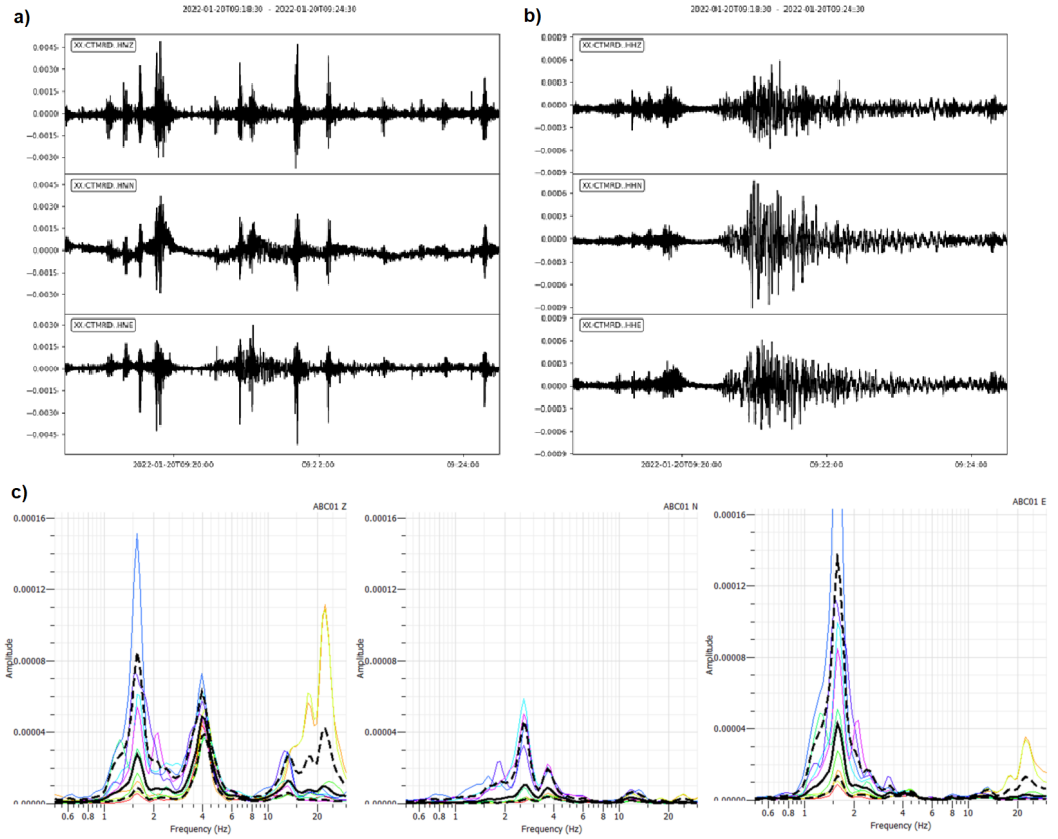


Fig. 3 - Comparison of the waveforms of a Mw 4.3 (20-01-2022 09:19:57) at 166 km recorded at S. Paolo bridge recorded with a Trillium PH 120 s located at ground surface (a) and recorded with an identical sensor placed at 51 m depth (b). Amplitude spectra for the three components of one of the velocimeters placed over the viaduct (c, see text for further information).

sensors were placed directly above the road, it was necessary to close the bridge to traffic. Overall, a set of 6 monitoring sites were placed in both edges of the road segment as reported in Fig. 1a. At each node were employed both a 3-axial velocimeters (Nanometrics Trillium Horizon 20s) and 3-axial accelerometers (Nanometric Titan). All the sensors were aligned in the same direction so that the two horizontal components coincide with the longitudinal and transversal directions of the bridge (Fig. 1a).

The tests consisted in the passage of a fully loaded vehicle at increasing velocity (20 km/h, 50 km/h and 80 km/h); the passage of a fully loaded vehicle, in an almost static way, over an obstacle of increasing thickness (2.5 cm, 5 cm, 9 cm) about 23 m from the column 4; the passage of a fully loaded vehicle at increasing velocity (20 km/h, 50 km/h, 60 km/h) braking at the centre of the span. As an example, we report the amplitude spectra of the signals triggered by the braking truck at 50 km/h speed over the monitored bridge segment (Fig. 3c). The spectra highlight differences between the components either in the frequencies and in the amplitudes which are ascribable to the mode of vibrations of the bridge.

Conclusions. The tests carried out at S. Paolo bridge are of extreme importance. In fact, with reference to road bridges of significant importance, dynamic load tests are mandatory in addition to static ones (NTC 2018). Dynamic monitoring consists in the processing of data detected by control instrumentation in response to dynamic disturbances present on the

structure to determine the natural frequencies and the corresponding shapes of the vibrating modes.

Monitoring of vibration frequencies serve as a useful reference for evaluating the degradation in stiffness or strength of the structure, and even for identifying possible damages in the structure, say, due to long-term overloading and impacts by heavy trucks or earthquake shakings (Yangh *et al.*, 2004).

The development of a dynamic monitoring system therefore requires a knowledge of the natural frequencies and the shapes of the vibration modes of the structure and it is possible to obtain it by taking advantage of the vibrations induced by wind and traffic (Magalhães *et al.*, 2008). Among the significant sources of environmental excitation there is also the earthquake that produces a transient stress, the spectrum of which varies from one event to another. The limits of applicability of this excitation are linked to the fact that an earthquake is a sporadic event and can be detected with permanent monitoring systems (Aceti and Bressan, 2014).

The recorded data will allow to determine the natural frequencies and of the relative forms of the modes of vibration for the evaluation the dynamic behavior of the structure and to calculate the response of the structure following any dynamic stress acting on known characteristics such as an earthquake or a dynamic load of exercise.

Acknowledgements. The authors thank Dr. Giuseppe Macaluso and all the other members of ANAS team for support in the activities.

References

Aceti M. and Bressan M. D.; 2014: *il valore delle prove dinamiche nel collaudo di infrastrutture civili.* Thesis in civil engineering, Università degli Studi di Milano.

Branca S., Coltelli M., Groppelli M. and Lentini F.; 2011. *Geological Map of Etna Volcano*. Ital. J. Geosci., 130, n.3.

Calvi G. M., Pinho R. and Crowley H.; 2006: *State-of-the-knowledge on the period elongation of RC buildings during strong ground shaking.* In Proceedings of the 1st European conference of earthquake engineering and seismology, Geneva, Switzerland, paper (Vol. 1535).

Cantero D., Hester, D., and Brownjohn, J.; 2017: *Evolution of bridge frequencies and modes of vibration during truck passage*. Eng. Struct., 152, 452-464, doi: 10.1016/j.engstruct.2017.09.039

D.M. 17/10/2018. *Norme Tecniche per le Costruzioni (NTC 2018)*. G.U. n.42 del 20/02/2018, suppl. ord. n. 8, cap. 9, p.299.

Magalhães F., Cunha A. and Caetano E.; 2008: *Dynamic monitoring of a long span arch bridge*. Eng. Struct., 30, 3034-3044.

Meletti C., Montaldo V., Stucchi M., and Martinelli F.; 2006: *Database della pericolosità sismica MPS04*. Istituto Nazionale di Geofisica e Vulcanologia (INGV). https://doi.org/10.13127/sh/mps04/db

Ren W., Zatar W. and Harik I.; 2004: *Ambient vibration-based seismic evaluation of a continuous girder bridge*. Eng. Struct., 26, 5, pp. 631-640, doi: 10.1016/j.engstruct.2003.12.010

Yang Y.B., Lin C.W. and Yau J.D.; 2004: *Extracting bridge frequencies from the dynamic response of a passing vehicle*. J. Sound Vib., 272, pp. 471-493, doi:10.1016/S0022-460X(03)00378-X.

POSTHOLE BROADBAND SENSORS FOR THE UPGRADE OF THE SEISMIC NETWORK IN SICILY WITHIN THE GRINT (ITALIAN RESEARCH INFRASTRUCTURE FOR GEOSCIENCES) PROJECT

A. D'Alessandro[1], S. Bongiovanni[2], P. Cosenza[3], A. Di Benedetto[1], A. Figlioli[2], S. Scudero[1], S. Speciale[1], G. Vitale[1]

[1] Istituto Nazionale di Geofisica e Vulcanologia, Osservatorio Nazionale Terremoti, Rome, Italy
[2] Università di Palermo, Dipartimento di Scienze della Terra e del Mare, Palermo, Italy
[3] Istituto Nazionale di Geofisica e Vulcanologia, Sezione di Palermo, Palermo, Italy

Introduction. GRINT Italian Research Infrastructure for Geosciences" is a project in the framework of the "Programma Operativo Nazionale" (PON) of the Italian Ministry for the University and Research. This plan envisages both the upgrade of monitoring systems in the already existing nodes, and the integration of new nodes. The main objective is to build a multiparametric network which integrates the main seismic network, with the monitoring of other geophysical signals, aimed at recognizing the phases of an earthquake: from the preparatory processes, to the trigger and arrest. Such upgrade will provide also the improvement of a series of seismological products: waveforms, seismological studies, bulletins for the seismic surveillance.

Sicily (Italy) is one among the target areas of the GRINT project. Here, the plan for the modernization started some years ago (D'Alessandro *et al.*, 2021) and the existing multi-parametric monitoring infrastructure will benefit of GRINT project. The activity is mainly of technological nature. It consists of the technical enhancement and upgrade of existing systems, an upgrade of seismic stations with installation of sensors covering the entire bandwidth of the seismic signal, both velocimeters and accelerometers. New nodes will be integrated in the existing network. The new seismic sensors are posthole broad-band velocimeters. They are installed in apposite perforations or wells that intercept the bedrock. Such solution reduces the level of seismic noise whose sources are almost always superficial (i.e. anthropogenic sources, wind, atmospheric pressure, vegetation) and makes as stable as possible parameters such as temperature, pressure and humidity. Together with sensors, power-supply systems, data loggers, real-time data transfer systems will be updated to optimize the performances, reduce the costs and the maintenance, and ensure the full operational services also during possible crisis. In addition, radon sensors will be installed in some seismic stations of the network.

In detail, this contribution introduces the experiences gained by the group Osservatorio Nazionale Terremoti (ONT, INGV) which operates in Sicily, and concerns the installation of post-hole broad-band sensors. This activity at such extended scale (35 sensors to be installed) can be considered as a pioneering one in Italy. We introduce the adopted procedures and the technical challenges faced for the optimal and effective deployment of the borehole sensors.

Post-hole sensors: installation and signal characterization. Sicily (Italy) is one among the target areas of the GRINT project. Here, the plan for the modernization started some years ago (D'Alessandro *et al.*, 2021) and the existing multi-parametric network will benefit of GRINT project. The installation of broadband posthole sensors thanks to GRINT project will allow the acquisition of high quality data directly usable for all the aims of the earthquake network.

The main reason for installing a seismometer in a well is to search for an environment in which the seismic-environmental noise is lower than the surface and consequently the signal-to-noise ratio (SNR) is maximized. The reduction of noise for well installations is strictly dependent on the frequency and is also variable on the different components. At frequencies of a few Hz, reductions of the order of 20 dB are observed already at a depth of a few tens of meters and reductions of up to 40 dB at a few hundred meters. For frequencies higher than 10

Hz, noise attenuations of even 40 dB are observed at depths of a few tens of meters (Greig *et al.,* 2014; Withers *et al.,* 1996; Hutt *et al.,* 2017)

Among the sensors used for installation in wells, the "borehole" and "posthole" seismometers are generally distinguished. While the former are designed for deep drilling (hundreds and thousands of meters) and are equipped with lateral anchoring systems to the well casing, the latter are designed for installation at the bottom of shallow drillings (<50 m), even without coating (Hayman, 2014).

The posthole sensor is the model Trillium Compact PH from Nanometrics. It is a compact (3.2 kg, 97x160 mm) sensor with bandwidth up to 120 s. When connected with Nanometrics Centaur digital recorder, a graphical interface allows to set the sensors and also to access the digital level integrated within the sensor. The installations have been carried out either in already existing wells and specifically drilled perforation. Of course, in both cases, some characteristics should be preliminarily evaluated. Devoted geophysical investigation (seismic tomography, MASW, ambient noise characterization) have been carried out to fully characterize the sites. Before the installation, the well is inspected by means of a borehole camera to verify the integrity of the casing and of the bottom (Fig. 1).



Fig. 1 - Installation operation at various sites. a: visual inspection by means of a borehole camera; b: the lowering of the sensor inside a drilled perforation; c: details of the pulley aligned on the top of a pre-existing well; d: final set-up of the earthquake monitoring site: note the posthole sensor placed at surface next to the well and the accelerometer for its later replacement; e: lab testing for the anchoring system.

The metered cable of the camera also helps to estimate the depth of the well and therefore to design the waterproof extension supply cable and the stainless steel retaining cable. Then, the well is filled some tenths of meters of sands to constitute a bed for the sensor. The sensor, along with its cable, is lowered within the hole by means of the retaining cable (diameter 3 mm). The two cables are tightened together with plastic ties at distance of about 1.5 m during the descent. The descent is controlled with a hand winch screwed into a portable wooden tripod and a pulley which is aligned to the top of the hole (Fig. 1). A digital dynamometer provides the indication of the load under the pulley, so that the operators are able to detect exactly the touchdown of the sensor and arrest its lowering. After a final camera check, another layer of sands is then released in the well to cover the sensor. Now the sensor can be connected to the data logger and powered to check the digital leveling system. By means of gentle maneuvers

on the retaining cable, together with a bit of luck, the sensor is leveled at its best. Anyway, the tilt tolerance of the downhole sensor is ±2.5°. In some cases, the conditions of a pre-existing wells may suggest to locate the posthole sensor along the casing, rather than the bottom. To face these situation, an electro-mechanical positioning system is under development. It is based on two curved metal plates mounted on an electrical powered jack, which also serves as base for the sensor (Fig. 1e). The system has been designed to be with the center of mass aligned with the upper anchoring, to ensure a levelling within the tolerance limits.

An identical post-hole sensor is then located at surface: it will serve as a reference for the orientation of the down-well sensor. This sensor will be later replaced (weeks to month) with an accelerometer, then, the site in its final configuration is integrated within the rest of the earthquake monitoring network The horizontal axes of sensors are normally oriented along the north and the east directions using a magnetic compass, but this operation is not possible for posthole installation. It is of fundamental importance to determine the orientation before to integrate its data within the network. There are many studies establishing the orientation of a borehole instrument using different methods, such as receiver functions, body-wave polarization studies, surface-wave polarization studies, ambient seismic noise, and seismic noise from ocean waves (see Lin *et al.*, 2022 for an overview). In the present study, we use an approach based on the cross-power spectra of the seismic noise between the two sensors. The cross-power spectra is determined between horizontal components of the surface reference sensor and the posthole sensor. The horizontal components of the posthole sensor are rotated by applying a rotation matrix. The rotation was exacted in steps of 1°; the cross power spectrum is then calculated at angular step in the whole range of available frequencies (120s - 50 Hz). For the purposes of estimating the correct horizontal orientation of the sensor in the well, only low frequencies (<1 Hz) are considered. Fig. 2 shows the average value of the cross power spectrum in the 120s - 1 Hz range, as a function of the rotation angle. The maximum value of the average cross power spectrum identifies the best estimate of the rotation angle. The closer the maximum value is to unity, the more robust is the estimate of the rotation angle. The estimations of the angular correction are quite reliable (Fig. 2) and in the case of FAVA site it has been further refined using the signal of a teleseism.

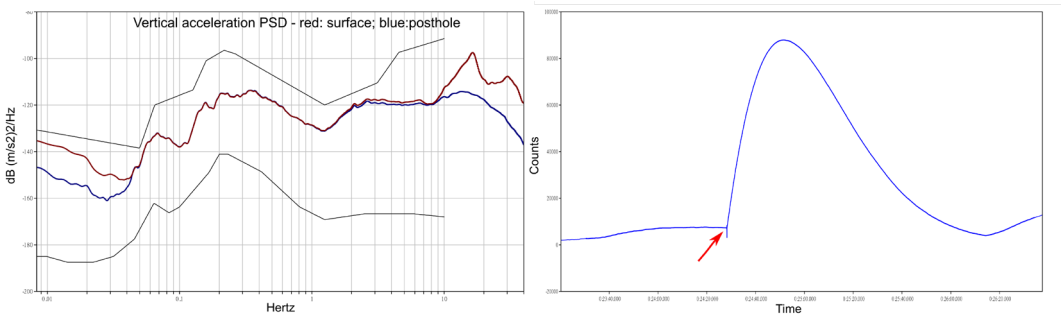


Fig. 2 - Estimation of the angular deviation of the pairs of horizontal components of the two sensors (i.e. surface and down-well). The vertical dashed lines correspond to the maximum values of the coherence and indicate the angular correction (21° for LIBRI and 349° for FAVA).

The analyses of the early signals show some anomalous waveforms which have been interpreted as the results of micro cracks consequent to the stabilization of the sandy bed which surrounds the sensor. The occurrence of such oscillations decreases with time and they disappear after some weeks. The reduction of the background noise has been evaluated comparing the power spectral densities of the surface and posthole sensors (Fig. 3). Below 3 s, and down to 120 s, the reduction of the power is more than 10 dB. This reduction at very

low frequencies is essentially linked to a better thermal stability of the sensor, therefore to a reduction of the instrumental self-noise. The power is reduced also above 2 Hz, and even more clearly above 10 Hz. At high frequencies, the noise reduction is essentially linked to the physical attenuation of the wavefield. In the band between 0.3 Hz and 2 Hz the power is almost identical.

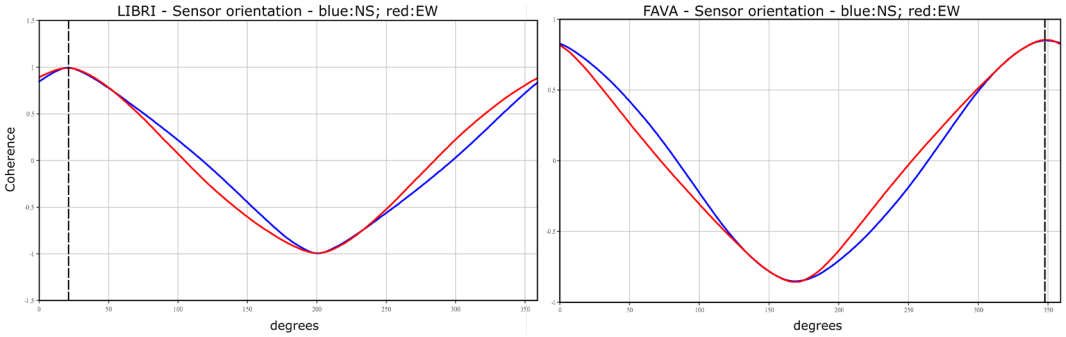


Fig. 3 - Left: a comparison between the acceleration power spectral densities (24 hours signal) for the vertical components at FAVA site (62.5 m deep); red line: surface sensor; blue line: posthole sensor. Right: a micro-crack (red arrow) triggers a low-frequency asymmetric oscillation at LIBRI site (27 m deep).

Conclusion. The upgrade of the earthquake monitoring network in Sicily thanks to the GRINT project represents a main advancement that makes the infrastructure more efficient, reliable, and sustainable for the next decade. In particular, the integration of the posthole seismometers will provide better quality data which will enhance a variety of high-quality seismological studies and will better support the Istituto Nazionale di Geofisica e Vulcanologia in the seismic surveillance of this region characterized by the highest seismic hazard of the whole Italy.

References.

D'Alessandro A., D'Anna R., Di Gangi F., Passafiume G., Scudero S., Speciale, S., Vitale G., Bignami Christian, Piersanti A., Cannelli V., Galli G., Mineo R., Alessandro G., Buonmestieri S., Rao S. and Stramondo S.; 2021: *Sullo sviluppo della rete multiparametrica in Sicilia.* Quaderni di Geofisica, 172, pp. 1-40.

Greig W., Spriggs N. and Bainbridge G.; 2014: *Comparison study between vault seismometers and posthole seismoter.* 2nd European Conference Of Earthquake Engineering And Seismology, Istanbul, 25-29 August 2014.

Hayman, M. B. ; 2014: *Downhole Seismometers*. Encyclopedia of Earthquake Engineering, pp .1-22.

Hutt C. R., Ringler A. T. and Gee L. S.; 2017: *Broadband Seismic Noise Attenuation versus Depth at the Albuquerque Seismological Laboratory.* Bull. Seismol. Soc. Am., 107(3), pp. 1402-1412.

Lin Y. Y., Chen D. Y., Kuo C. H., Lin C. J., Chen W. Y. and Wen Y. Y.; 2022: *Orientation Corrections of a Borehole Seismometer Network in Taiwan Using Teleseismic Earthquakes.* Seis. Res. Lett.

Withers M. M., Aster R. C., Young C. J. and Chael, E. P.; 1996: *High-frequency analysis of seismic background noise as a function of wind speed and shallow depth*. Bull. Seismol. Soc. Am., 86(5), pp. 1507-1515.

SEISMIC SITE AMPLIFICATION AT PERMANENT STATIONS IN NORTHEASTERN ITALY

P. Klin, G. Laurenzano, C. Barnaba, E. Priolo, S. Parolai

Istituto Nazionale di Oceanografia e di Geofisica Sperimentale - OGS, Trieste, Italy

The awareness of the seismic risk in northeastern Italy has fostered the deployment of an ever-growing number of permanent stations devoted to seismic monitoring and emergency management purposes (Bragato *et al.*, 2021). The evaluation of seismic site amplification at the seismological stations represents a prerequisite for the correct usage of the earthquake recordings in many applications ranging from the rapid quantification of the earthquake impact on the territory (e.g. Poggi *et al.*, 2021), to earthquake source characterization studies (e. g. Franceschina *et al.*, 2013). In the present study, we exploit the considerable number of earthquake recordings collected in northeastern Italy, from 1996 to 2017, to estimate the site response at the recording network stations in terms of the following quantities

1) frequency-dependent amplification function $A(f)$ with respect to a reference site and
2) median amplification factors for peak ground acceleration (PGA) and velocity (PGV) with respect to a well-established ground-motion prediction equation (GMPE).

The analysis is based on the recordings of 368 earthquakes in the magnitude range of M 3.2–5.8 collected by 67 stations in a distance range of 10–300 km. The stations are located in an area that spans the territories of Friuli-Venezia Giulia, Veneto and Trentino-Alto Adige/ Südtirol regions and the bordering parts of Lombardia and Emilia-Romagna.

We evaluate $A(f)$ in the frequency band 0.5–20 Hz through the decomposition of the S-wave amplitude spectra in terms of source, propagation, and site response. We solve the decomposition with a nonparametric, single step generalized inversion technique – GIT (Oth *et al.*, 2011). We select the station Forcella Aurine (FAU), in the central part of the map in Fig. 2, as the reference station for the GIT analysis, in virtue of the absence of peaks in the microtremor horizontal to vertical spectral ratio (HVSR). On the basis of the minimum (A_{min}), maximum (A_{max}) and average (A_{avg}) values of $A(f)$, we group the retrieved amplification functions into the following five categories of stations:

a. Neutral ($A_{min} > 0.5$ and $A_{max} < 2$),
b. Deamplifiying (non-neutral stations with $A_{avg} < 1.0$),
c. Narrowband amplification (stations with $A_{max} > 2$ and $A_{max} A_{min} > (A_{avg})^2$)
d. Broadband low amplification (non-neutral and non-narrowband stations with $1.0 < A_{avg} < 2.0$),
e. Broadband high amplification (non-narrowband stations with $A_{avg} > 2.0$)

The stations considered in the present work are mapped in Fig. 1 with the color of the group they result to belong. We can observe that only 11 out of 66 stations belong to the neutral category (i.e., amplification function with values bounded in the interval 0.5–2 and that we can assume flat and unitary with respect to station FAU). A minor percentage (7%) exhibits narrowband amplification, whereas most stations (44) belong to the categories of broadband amplification. 23 of these (34% of network stations) exhibit a mean amplification value larger than 2. The deamplification in a number of stations could be due to their installation on a medium that is stiffer than the one at the reference station and thus presents a relatively lower rock site amplification. We evaluate the amplification factor for PGA and PGV with respect to the GMPE ITA10 for Eurocode 8 site class A (Bindi et al., 2011) following the approach presented in Laurenzano *et al*. (2019) and find that only a limited fraction of stations presents an amplification factor near unity. Most stations exhibit either positive or negative bias, consistently with the amplification functions obtained with GIT.

We found good correlation between the amplification factors and the frequency-averaged amplification functions, which suggests the possibility of predicting time-domain peak ground-motion values from amplification functions estimated by generalized inversion.

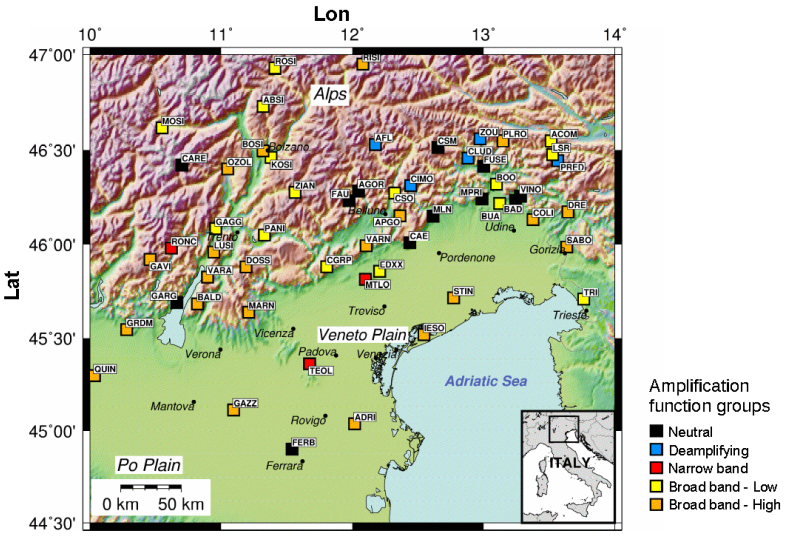


Fig. 1.

Due to the lack of shear-wave velocity profiles at most of the considered stations, we are unable to compare the observed site amplification with the site description in terms of the standard soil classes based average shear-wave velocity in the uppermost 30 m depth (Borcherdt, 1994). However, we perform a comparison of the site amplification with two qualitative site classifications, one based on geomorphology (Biolchi et al., 2011) and the other one based on the local geology. Our finding that neither geological nor geomorphologic classifications permit to predict the site amplification category with sufficient confidence, confirms the unreliability of rapid site-response identification approaches based on terrain classification.

The estimation of the amplification functions by means of the application of GIT on a database of past recordings, as illustrated in the present work (see Klin et al., 2021 for a more complete description), provides an advisable solution for the accurate interpretation of data from any regional network, in monitoring applications as well as in studies related to seismic hazard.

References

Bindi, D., F. Pacor, L. Luzi, R. Puglia, M. Massa, G. Ameri, and R. Paolucci; 2011: *Ground motion prediction equations derived from the Italian strong motion database*, Bull. Earthq. Eng. **9** no. 6, 1899–1920, doi: 10.1007/s10518-011-9313-z.

Biolchi, S., L. Zini, P. Leita, and P. Malisan; 2011: *Mapping the geomorphological scenarios of the Friuli Venezia Giulia region (NE Italy): a tool for the evaluation of the local seismic amplification.*, Il Quatenario **24**, 79–80.

Borcherdt, R. D.; 1994: *Estimates of Site-Dependent Response Spectra for Design (Methodology and Justification)*, Earthq. Spectra **10** no. 4, 617–653, doi: 10.1193/1.1585791.

Bragato, P. L. et al.; 2021: *The OGS–Northeastern Italy Seismic and Deformation Network: Current Status and Outlook*, Seismol. Res. Lett., doi: 10.1785/0220200372.

Franceschina, G., S. Gentili, and G. Bressan; 2013: *Source parameters scaling of the 2004 Kobarid (Western Slovenia) seismic sequence*, Phys. Earth Planet. Inter. **222**, 58–75, doi: 10.1016/j.pepi.2013.07.004.

Klin, P., G. Laurenzano, C. Barnaba, E. Priolo, and S. Parolai; 2021: *Site Amplification at Permanent Stations in Northeastern Italy*, Bull. Seismol. Soc. Am. **111** no. 4, 1885–1904, doi: 10.1785/0120200361.

Laurenzano, G., C. Barnaba, M. A. Romano, E. Priolo, M. Bertoni, P. L. Bragato, P. Comelli, I. Dreossi, and M. Garbin; 2019: *The Central Italy 2016–2017 seismic sequence: site response analysis based on seismological data in the Arquata del Tronto–Montegallo municipalities*, Bull. Earthq. Eng. **17** no. 10, 5449–5469, doi: 10.1007/s10518-018-0355-3.

Oth, A., D. Bindi, S. Parolai, and D. Di Giacomo; 2011: *Spectral Analysis of K-NET and KiK-net Data in Japan, Part II: On Attenuation Characteristics, Source Spectra, and Site Response of Borehole and Surface Stations*, Bull. Seismol. Soc. Am. **101** no. 2, 667–687, doi: 10.1785/0120100135.

Poggi, V., C. Scaini, L. Moratto, G. Peressi, P. Comelli, P. L. Bragato, and S. Parolai; 2021: *Rapid Damage Scenario Assessment for Earthquake Emergency Management*, Seismol. Res. Lett., doi: 10.1785/0220200245.

EARTHQUAKE MONITORING NETWORKS: A COMPARISON BETWEEN HIGH SEISMIC RISK COUNTRIES

S. Scudero, A. D'Alessandro

Istituto Nazionale di Geofisica e Vulcanologia, Osservatorio Nazionale Terremoti, Rome, Italy

Introduction. A country-scale earthquake monitoring network usually extends over areas in the range of 10^5 - 10^6 km^2 (D'Alessandro *et al.*, 2019) and, from its initial planning to its final configuration may be necessary several years to decades. Throughout this process, the final geometrical arrangement of the nodes could turn remarkably different from the initial, planned configuration. As a counterpart, in some cases, the long time span necessary to build up the networks turned into a benefit because of the concurrent technological improvements of sensors, transmission systems, etc. In all the cases, it is always opportune to verify periodically whether the distribution of nodes within a given network satisfies its final needs and objectives, also because the knowledge about the seismicity of a given area may evolve over time. In this work, we propose the application of the statistical approach proposed by Siino *et al.*, (2020) for the evaluation of the earthquake monitoring networks in three countries characterized by high seismic hazard, namely Italy, New Zealand, and Taiwan. This approach considers the spatial distribution of the nodes of the network together with the ancillary information related to the aims of the network itself (e.g. earthquakes' distribution, seismic hazard, population). Data are analysed by means of descriptive spatial statistics and point process methods following the approach proposed by Siino *et al.*, (2020) and also employed by Scudero and D'Alessandro (*submitted*) to get insights about the distribution of the earthquake networks with respect to the related data sets.

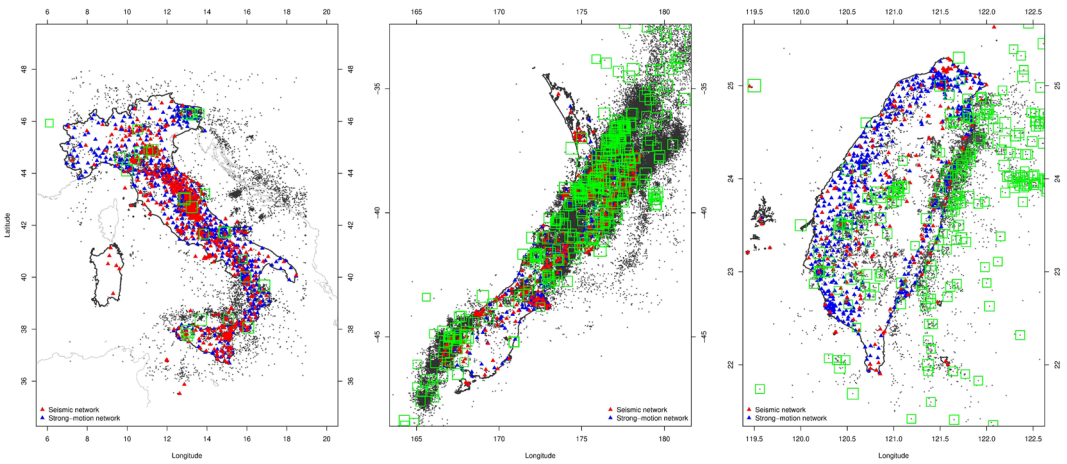


Fig. 1 - Maps of Italy, New Zealand, and Taiwan. The instrumental seismicity is represented with grey dots, while the M>5.5 earthquakes with green squares. The triangles indicate the seismic (in red) and strong motion (in blue) networks. Details about the data are provided also in Tab. 1.

Results. The data considered for this study are displayed in Fig. 1. Technical details about the earthquake monitoring networks can be retrieved for Italy (Dolce, 2009; Michelini *et al.*, 2016), New Zealand (Patterson *et al.*, 2007; Uma *et al.*, 2011), and Taiwan (Tsai and Lee, 2005; Hsiao *et al.*, 2009; Chang *et al.*, 2012; Shin *et al.*, 2013). A comparison between the networks and the earthquake catalogues is provided in Tab.1. In particular, concerning the earthquake monitoring networks, we distinguish the broad-band, or in general, the velocimetric sensors, from the strong-motion sensors (i.e. accelerometers). While the former

Tab. 1 - Comparison of characteristics of the earthquake monitoring networks of each country and details of the earthquake catalogues.

	Italy	New Zealand	Taiwan
Surface area (km^2)	300*10^3	268*10^3	36*10^3
N. seismic stations	604	562	278
Density seismic stations (n/km^2)	1.99*10^{-3}	2.10*10^{-3}	7.68*10^{-3}
N. strong-motion stations	647	363	716
Density strong-motion stations (n/km^2)	2.14*10^{-3}	1.35*10^{-3}	19.78*10^{-3}
N. instrumental earthquakes M>3	1172	101761	9235
N. earthquakes M>5	79	328	287
Average population density (people/km^2)	189	18	583

has mainly the objective of the seismic surveillance of the territory (i.e. earthquake locations) and the seismological studies, the latter network collects full records of strong earthquakes to understand the seismic activities under different geological conditions and it also serves as the basis for intensity assessment and to design the earthquake-resistant building codes.

Insights about the degree of coverage of a seismic network in term can be provided counting the number of events at increasing distance from each seismic station. The plots in Fig. 1 (upper row) display the cumulative curves, one for each seismic stations, for the three countries. The steeper the curves, the better the position of the considered seismic station with respect to the local seismicity (distance shorter than 100 km). In all the three cases, many stations are clustered and follow the same increasing trend; other seismic stations are more scattered. In this diagram it is possible to distinguish which stations are optimally placed (i.e. high number of earthquakes recorded at short distance) from the bad placed stations

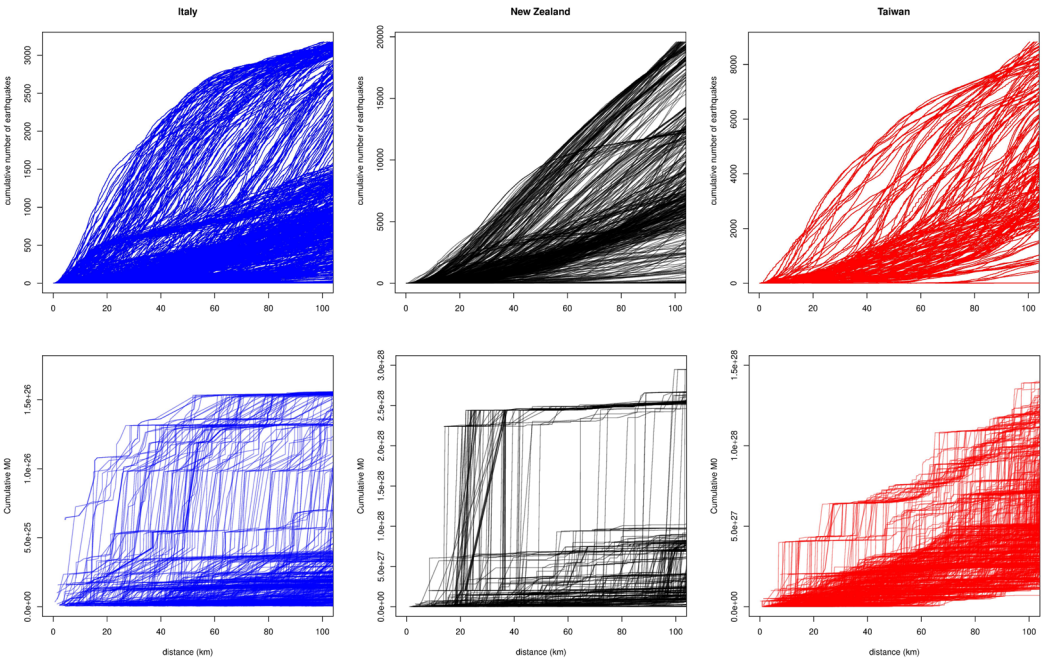


Fig. 2 - Top row: cumulative number of instrumental earthquakes located at increasing distance from each seismic station. Bottom row: cumulative seismic moment of events M>=5 (either measured or estimated for historical earthquakes) located at increasing distance from each strong motion station.

(i.e. few earthquakes recorded at long distance). Similarly, the cumulative seismic moment M_0 with increasing distance is computed around each node of the strong-motion networks (Fig. 2, bottom row). The seismic moment M_0 for historical earthquakes and instrumental earthquake with M_w>5 is calculated by converting the provided values of the moment magnitude by means of the relation proposed by Hanks and Kanamori (1979): $M^0 = 10^{(Mw+10.7)\pm1.5}$. In this diagram it is possible to distinguish which stations are optimally placed (i.e. high M_0 at short distance) from the bad placed stations (i.e. low M_0 at long distance) with respect to the largest events. For each country, some strong-motion stations follow the same trend, while others are scattered.

Of course, the number of earthquake and the released seismic moment are different between the various countries (Tab. 1), so that to compare the three networks we normalized the two series of plots considering the maximum values at a distance of 100 km (Fig. 3). In this way the plots indicate how the earthquake network of each country is optimized for its type and distribution of seismicity, with respect the other countries' networks. For the seismic network (Fig. 3, left), Italy seems to have a network which better fits the seismicity within the whole range of distance considered; conversely, the seismic stations in Taiwan appears to be generally worse placed. For the strong motion network, Italy and Taiwan record relatively higher values of M_0 at short distance (< 20 km); at larger distance the networks of Italy and New Zealand record the relatively higher M_0. A limitation to this comparison is represented by the different time span of the historical catalogues: the Italian one extends for more than 1,000 years, while the other are definitely shorter.

In the comparisons, it should be also taken into account that the density of both seismic stations and strong-motion stations is similar for Italy and New Zealand but it is greatly higher in Taiwan (Tab. 1). For instance, Italy and New Zealand count one seismic station every 500 km^2 while Taiwan counts one seismic station every 130 km^2. The same occur for the strong-motion stations (460, 740 and 50 km^2, the density for the three countries, respectively) and can be related also to the different population density of the countries (Siino *et al.*, 2020). The different density of the earthquake monitoring network can account for some of the differences highlighted by the plots in Fig. 3.

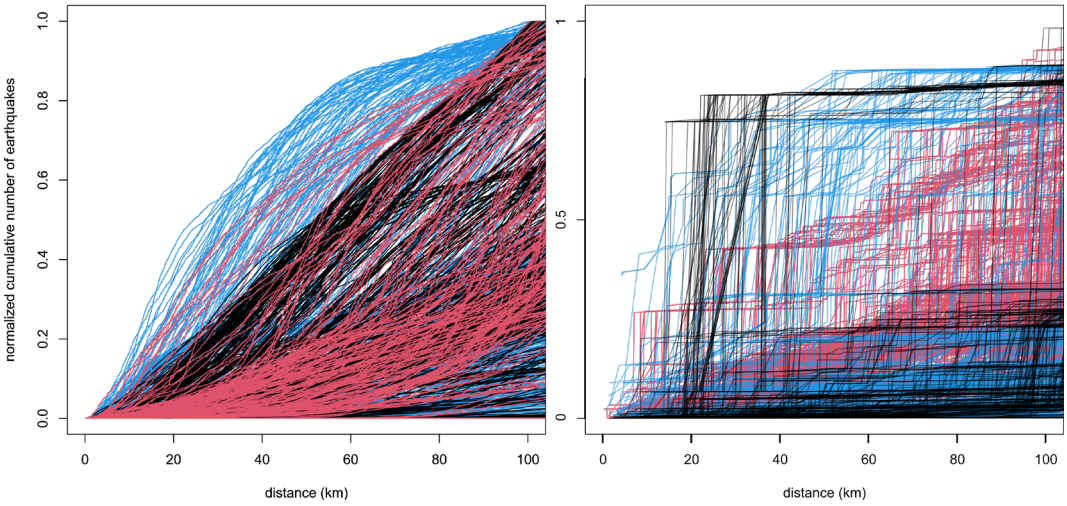


Fig. 3 - Cumulative number of instrumental earthquakes located at increasing distance from each seismic station, and cumulative seismic moment at increasing distance from each node of the strong-motion network. The curves have been normalized considering the maximum number of earthquakes and the maximum seismic moment recorded at a distance of 100 km Code color: Italy (blue lines), New Zealand (black lines), and Taiwan (red lines).

Conclusion. The assessments of the coverage of seismic and strong motion networks (and consequently their performance) are not only desirable but also of crucial importance to find areas where the networks need to be concentrated or, conversely, where the networks are redundant. the approach of Siino *et al.*, (2020), based on descriptive spatial statistics, could be a very informative tool to assess the degree of coverage of already developed networks as a function of the spatial distributions of other parameters (including complex and irregular distributions. It also can be exploited to compare different strategies in earthquake monitoring developed in different countries.

References

Chang, C. H., Yih-Min, W., Da-Yi, C., Shin, T. C., Tai-Lin, C. and Wen-Yen, C.; 2012: *An examination of telemetry delay in the Central Weather Bureau Seismic Network*. TAO: Terrestrial, Atmosph. Oceanic Sci., 23(3), 261.

D'Alessandro, A., Costanzo, A., Ladina, C., Buongiorno, F., Cattaneo, M., Falcone, S., La pIana, C., Marzorati, S., Scudero, S., Vitale, G., Stramondo, S. and & Doglioni, C.; 2019: *Urban seismic networks, structural health and cultural heritage monitoring: the national earthquakes observatory (INGV, Italy) experience*. Front. Built Env. 127.

Dolce M; 2009: Qui dpc, il monitoraggio sismico del dipartimento della protezione civile. Progettazione sismica: 95–98

Hanks, T. C. and Kanamori, H.; 1979: *A moment magnitude scale*. J Geophy. Res.: Solid Earth, 84(B5), 2348-2350.

Hsiao, N. C., Wu, Y. M., Shin, T. C., Zhao, L. and Teng, T. L.; 2009: Development of earthquake early warning system in Taiwan. Geophys. Res. Lett. 36(5).

Patterson, N., Gledhill, K. and Chadwick, M.; 2007: *New Zealand National Seismograph Network* Report for the Federation of Digital Seismograph Networks Meeting, 2007. In Perugia, Italy: 2007 FDSN Meeting.

Michelini, A. and coauthors; 2016: *The Italian National Seismic Network and the earthquake and tsunami monitoring and surveillance systems*. Adv. Geosci. 43, 31-38.

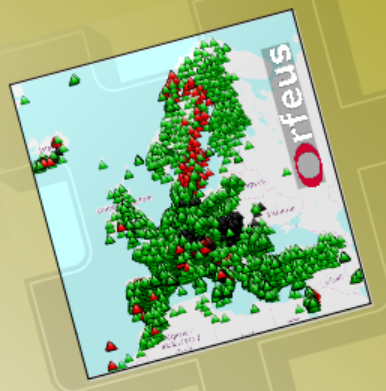
Shin, T. C., Chang, C. H., Pu, H. C., Hsiao-Wei, L., and Leu, P. L; 2013: *The geophysical database management system in Taiwan*. TAO: Terrestrial, Atmosph. Oceanic Sci. 24(1), 11.

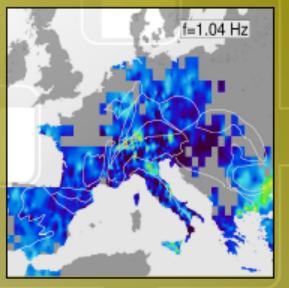
Siino, M., Scudero, S., Greco, L. and D'Alessandro, A.; 2020: *Spatial analysis for an evaluation of monitoring networks: examples from the Italian seismic and accelerometric networks*. J. Seism. 24(6), 1045-1061.

Scudero, S. and D'Alessandro, A.; Submitted*: Evaluation of the earthquake monitoring network in Taiwan*.

Tsai, Y. B. and Lee, C. P; 2005: *Strong motion instrumentation programs in Taiwan*. In Directions in strong motion instrumentation (pp. 255-278). Springer, Dordrecht.

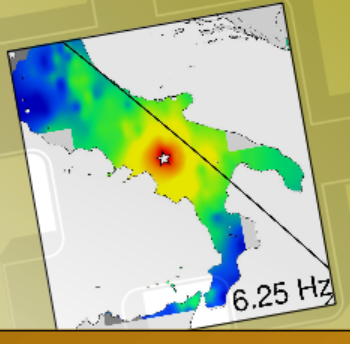
Uma, S. R., King, A., Cousins, J. and Gledhill, K.; 2011: *The GeoNet building instrumentation programme.* Bull. New Zealand Soc. Earthq. Eng. 44(1), 53-63.





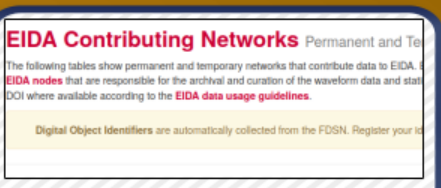
Empirical Shaking Scenarios in Europe

D. Bindi, R. Zaccarelli, H.N.T. Razafindrakoto, M-H Yen, F. Cotton
GFZ-Potsdam



About half a million spectra are processed to isolate source, propagation and site effects in Europe. Amplification maps and the attenuation results are used to synthesize shaking maps in the Fourier domain.

DATA



https://www.orfeus-eu.org/data/eida/

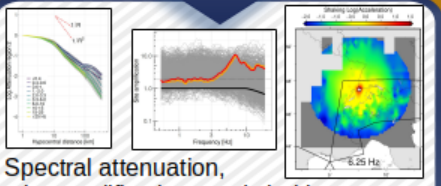
TOOLS



Download & Processing

GIT – Spectral decomposition

PRODUCTS



Spectral attenuation, site amplifications and shaking maps

Bibliografia

Alshembari, R., S. Parolai, T. Boxberger, D. Sandron, M. Pilz, and N. Sylacheva (2019). *Seasonality in Site Response: An Example from Two Historical Earthquakes in Kazakhstan*, Seismol. Res. Lett. 91, 415–426, doi: 10.1785/0220190114.

Hopkirk P.,The Great Game: On Secret Service in High Asia, 1990, John Murray/Kodansha International publs., UK, ISBN978-1-56836-022-5

Nakamura, Y. (1989). *A Method for Dynamic Characteristics Estimation of Subsurface Using Microtremor on the Ground Surface.* Vol 30. Quarterly Reports, Railway Technical Research Institute, 8–12.

Nurmagambetov, A., N. Mikhailova, and W. Iwan (1999). *Seismic hazard of the Central Asia region, in Seismic Hazard and Building Vulnerability in Post-Soviet Central Asian Republics*, S.A. King, V. I. Khalturinand, and B. E. Tucker (Editors), KluwerAcademic Publishers, Dordrecht, The Netherlands, 1–43.

Petrovic B, Parolai S (2016) *Joint deconvolution of building and downhole strong-motion recordings: evidence for the seismic wavefield being radiated back into the shallow geological layers.* Bull Seismol Soc Am 106:1720–173

Parolai S., Orunbaev,S, Bindi D.,* Strollo A., Usupaev S., Picozzi M., Di Giacomo D., Augliera P., D'Alema E., Milkereit. C., Moldobekov B., and J. Zschau, 2010, *Site Effect Assessment in Bishkek (Kyrgyzstan) using Earthquake and Noise Recording Data*, Bulletin of the Seismological Society of America, Vol. 100, No. 6, doi: 10.1785/0120100044

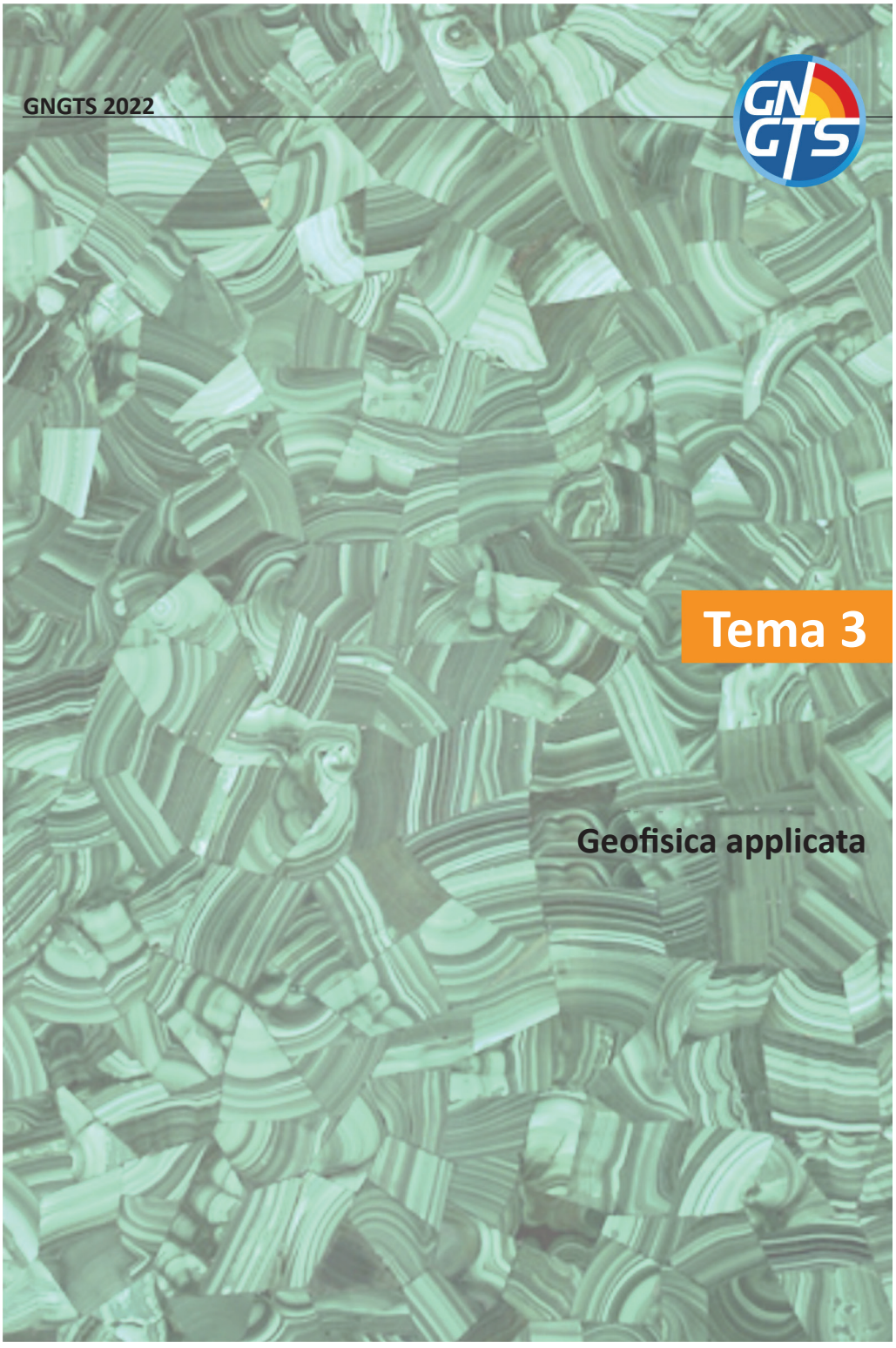
Parolai, S., D. Bindi, S. Ullah, S. Orunbaev, S. Usupaev, B. Moldobekov,and H. Echtler (2013). *The Bishkek vertical array (BIVA): Acquiring strong motion data in Kyrgyzstan and first results,* J. Seismol. 17, no. 2, 707–719.

Parolai S, Maesano FE, Basili R, Silacheva N, Boxberger T and Pilz M, (2019) *Fingerprint Identification Using Noise in the Horizontal-to-Vertical Spectral Ratio: Retrieving the Impedance Contrast Structure for the Almaty Basin (Kazakhstan).* Front. Earth Sci. 7:336. doi: 10.3389/feart.2019.00336

Pilz, M., Parolai S., Petrovic B., Silacheva N., Abakanov T., Orunbaev S. and, Moldobekov B.,2018m *Basin-edge generated Rayleigh waves in the Almaty basin and corresponding consequences for ground motion amplification,* Geophysical Journal International, Volume 213, Issue , Pages 301–316, https://doi.org/10.1093/gji/ggx555

Sidorin, A. Ya., 2019, *Effects and Lessons of the 1948 Ashgabat Earthquake*, ISSN 0747-9239, Seismic Instruments, Vol. 55, No. 3, pp. 271–282, ISSN 0747-9239, Allerton Press, Inc., Russian Text © A.Ya. Sidorin, 2018, published in Voprosy Inzhenernoi Seismologii, 2018, Vol. 45, No. 3, pp. 84–97.

Ullah, S., Bindi D., Pittore, M., Pilz, M., Orunbaev, S., Moldobekov, B., Parolai S. (2013), *Improving the spatial resolution of ground motion variability using earthquake and seismic noise data: the example of Bishkek (Kyrgyzstan)*, Bull Earthquake Eng (2013) 11:385–399, DOI 10.1007/s10518-012-9401-8



Tema 3

Geofisica applicata

Sessione 3.1

Geofisica per le Georisorse

Convenor: M. Giustiniani, P. Mazzucchelli e V. Lipari

R/V LAURA BASSI SOUTHERN OCEAN TRANSITS AS AN OPPORTUNITY TO COLLECT UNDERWAY DATA IN ANTARCTIC WATER: ISOBATA PROJECT AND COLLABORATION AMONG PNRA PROJECTS

D. Accettella[1], A. Savini[2], M. Cuffaro[3], P. Divacco[1], F. Muccini[4], F. Coslovic[1], L. Facchin[1], R. Codiglia[1], D. Cotterle[1], A. Cova[1], L. De Santis[1], L. Gasperini[5], V. Kovacevic[1], M. Santulin[1], R. Scipinotti[6], L. Ursella[1]

[1] National Institute of Oceanography and Applied Geophysics – OGS, Sgonico, Italy
[2] Università Milano Bicocca – UniMiB-DISAT, Milano, Italy
[3] National Research Council – CNR-IGAG, ROMA, Italy
[4] National Institute of Geophysics and Volcanology – INGV, ROMA, Italy
[5] National Research Council – CNR-ISMAR, Bologna, Italy
[6] ENEA-UTA, Bologna, Italy

ISOBatA, *Italian Southern Ocean Bathymetry for the exploitation of opportunistic seafloor dataset in the Antarctic water and surrounding areas*, is an Italian Project funded by the Italian National Research Antarctic Program (PNRA), supported by *Seabed2030* (Jakobsson *et al.,* 2017, Mayer *et al.,* 2018) and *IBCSO* - International Bathymetric chart of Southern Ocean (Arndt, JE *et al.,* 2013). The project focuses on efficiently exploiting bathymetric and geophysical datasets obtained from ship-based research surveys collected during transit times of the renewed Icebreaker R/V Laura Bassi. Emphasis is given to seafloor acoustic mapping data, ensuring the Italian greatest contribution to the mapping of Antarctic waters, magnetometer and ADCP data as well are taken into consideration.

In order to improve all efforts in mapping the gaps in the bathymetric coverage of the world's ocean, the project partners OGS, CNR-IGAG and University of Milano-Bicocca, in cooperation with the infrastructural support and logistic, designed and planned the R/V Laura Bassi data acquisition strategy along preferred corridors back and forth New Zealand and Mario Zucchelli Station (MZS). A case study area (i.e.: The Emerald Fracture Zone – EMZ – and

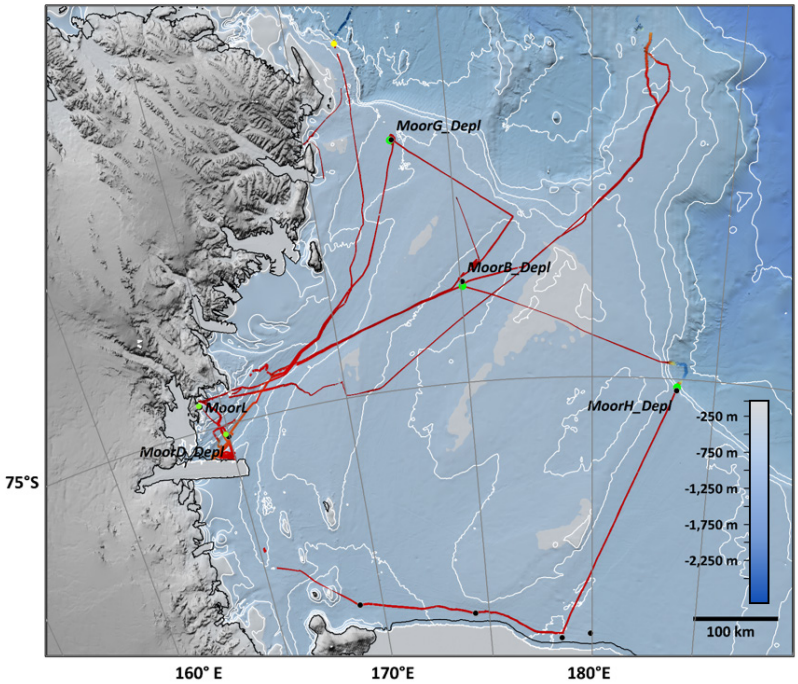


Fig. 1 - Ross Sea Map. Red areas: multibeam coverage acquired during 2021-2022 PNRA survey. Green dots: MORSEA mooring points. Purple rectangle: Mooring G area (Fig.2). Black dots MORSEA planned waypoints.

Macquarie Triple Junction – MTJ - in the SW Pacific Ocean), (Choi *et al.,* 2017, Lodolo *et al.,* 2013) was chosen to test the acquisition potential during transit time in remote areas, for the 3-years project period.

An expected output of the ISOBATA project is the compilation of a structured "Antarctic Data Storage Repository" that can be shared at international level, as the project aims at fulfilling SCAR, CONMAP, IHO and Seabed 2030 guidelines. Accordingly, we planned to develop best practices and dedicated workflows to implement QC in multi-beam data acquisition procedures during transit times, as well as in the processing, analysis and archiving of data and metadata.

The first oceanographic expedition (XXXVII PNRA Antarctic Expedition) took place last winter and made us aware of a variety of critical issues associated with collection of underway data in remote waters. The investigation went beyond the limits of the predefined plan, engaging in interesting interactions and collaborations with other oceanographic and geophysical projects (Fig.1, Fig.2). We are planning for the future to develop an underway data acquisition strategy that can investigate air-water-seafloor interactions.

Our work would like to open a discussion to address the need for standardization in data acquisition during transit times. Our experience has particularly highlighted that this should include provisions in accordance with the geomorphological/geographical nature of the working areas, as well as receiving important support from the maritime industry and perhaps additional stakeholders.

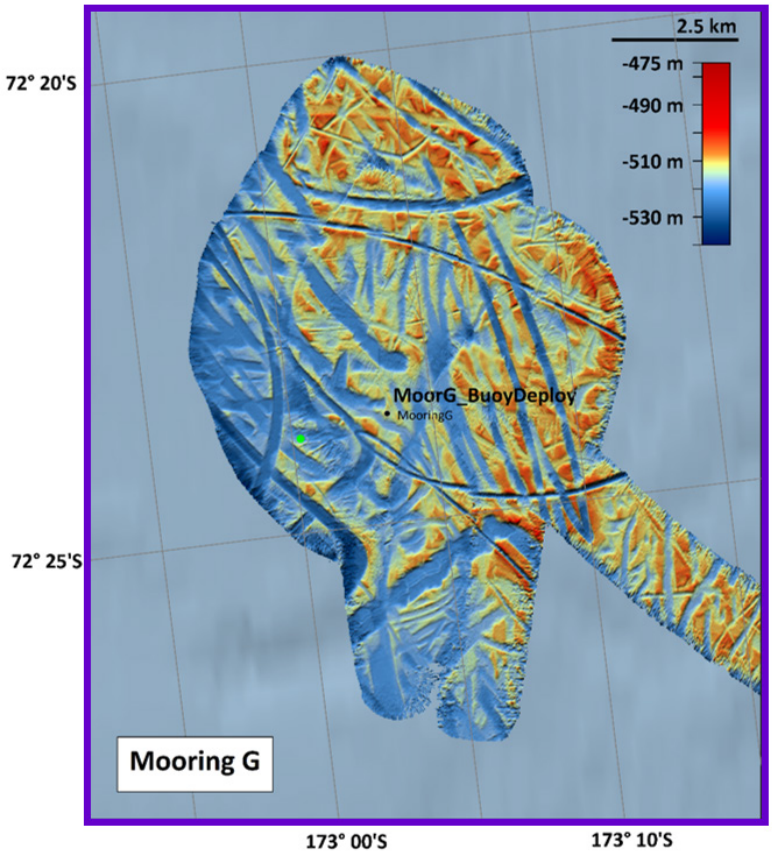


Fig. 2 - Opportunistic multibeam data acquired in Mooring G area. Bathymetry shows linear and curvilinear iceberg trajectory scours. Elliptical scours are due to interaction with tidal current (Newton *et al.,* 2016).

Acknowledgements. We sincerely thank the Captain F. Sedmak, all crew members, marine hydrographers, researchers, UTA-ENEA colleagues, doctors and travellers on board the Bassi XXXVII PNRA Antarctic Expedition who helped us during the project, enjoyed spare time and "lived" during the 111 days that the ISOBatA working group spent on board. Thanks to Pasquale Castagno (Univ. Partenope, Na) and Pierpaolo Falco (Univ. Politecnica Delle Marche) who supplied us with XBT and CTD data during the II° leg.

References

Arndt, J. E., Schenke, H.-W., Jakobsson, M., Nitsche, F. O., Buys, G., Goleby, B., M.Rebesco, F. Bohoyo, J.Hong, J. Black, R. Greku, G. Udintsev, F. Barrios, W. Reynoso-Peralta, M. Taisei, and R.Wigley; 2013: *The international bathymetric chart of the southern ocean (IBCSO) version 1.0 – a new bathymetric compilation covering circum-antarctic waters.* Geophys. Res. Lett., **40**, 1–7. DOI 10.1002/grl.50413

Choi H., Kim S. S., Dyment J., Granot R., Park S. H., and Hong J. K.; 2017: *The kinematic evolution of the Macquarie Plate: A case study for the fragmentation of oceanic lithosphere.* Earth and Planetary Science Letters, **478**, 132–142. DOI: 10.1016/j.epsl.2017.08.035

Jakobsson, M., Allen, G., Carbotte, S. M., Falconer, R., Ferrini, V., Marks, K., et al.; 2017: *The Nippon Foundation - GEBCO - Seabed 2030: Roadmap for Future Ocean Floor Mapping.* Available at: https://www.gebco.net/documents/seabed_2030_roadmap_v10_low.pdf 2017AGUFMOS14B..01J

Lodolo E., Coren F., and Ben-Avraham Z. (2013). *How do long-offset oceanic transforms adapt to plate motion changes? The example of the Western Pacific-Antarctic plate boundary.* Journal of Geophysical Research, **118**:1195–1202. DOI 10.1002/jgrb.50109

Mayer, L., Jakobsson, M., Allen, G., Dorschel, B., Falconer, R., Ferrini, V., et al.; 2018: *The nippon foundation—GEBCO seabed 2030 project: the quest to see the world's oceans completely mapped by 2030.* Geosciences, **8**:63. DOI: 10.3390/geosciences8020063

Newton, A. M. W., Huuse, Mads. & Brocklehurst, S. H., (2016*): Buried iceberg scours revealed reduced North Atlantic Current during stage 12 deglacial.* Nature Communication **7**, DOI: 10.1038/ncomms10927

INTEGRATED MULTI-GEOPHYSICAL AND GEOLOGICAL WORKFLOW FOR GEOTHERMAL RESOURCE EXPLORATION AND CHARACTERIZATION

R. Bachrach[1], T. Cassola[2], L. Masnaghetti[3], G. Sosio[4]

[1] Schlumberger, Denver, USA
[2] Schlumberger, The Hague, Netherlands
[3] Schlumberger, Milan, Italy
[4] Schlumberger, Paris, France

Identifying and confirming the resource is a crucial aspect for the success of a geothermal project. Reducing the uncertainties associated with the structural settings, the lithology and properties of the potential reservoirs, and the expected temperature of the geothermal fluid allow de-risking the subsequent activities, and increasing the chances of success of the first well drilled in a prospect, which is the costliest item in the project lifecycle.

Geophysics-centered, data-driven solutions are the keystone of this effort, aiming at integrating the information available prior to drilling to quantify the relevant properties of the subsurface and setting the stage for further geological, fluid and heat flow, and geomechanical modeling. These solutions can be delivered in a consolidated digital platform to perform the workflow in the most consistent fashion across different disciplines.

The analysis of the geothermal potential based on acquired geophysical data is the first step. Magnetotelluric and gravity data provide a cost-effective source of 3D data to delineate the structural lineaments and fault network, defining the geological framework at the basin scale or at smaller scales. Multi-physics measurements and interpretation allow to map the lateral changes in lithology, supported by rock-physics characterization of the reservoir properties.

Highly automated solutions utilizing advanced litho-petro-elastic engines are used for accurate modeling of subsurface properties and temperature in 3D (Fig. 1). Thermal properties

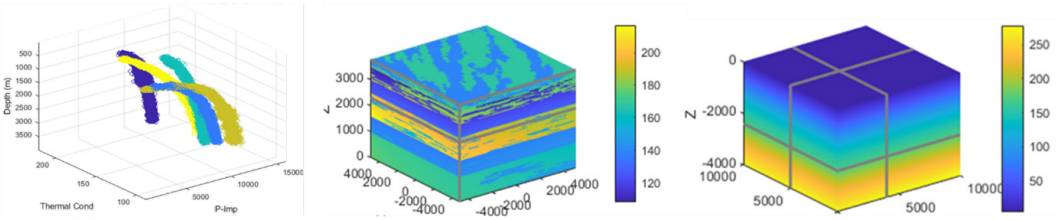


Fig. 1 - Utilization of advanced litho-petro-elastic models (left) to estimate thermal conductivity (center) and temperature distribution (right).

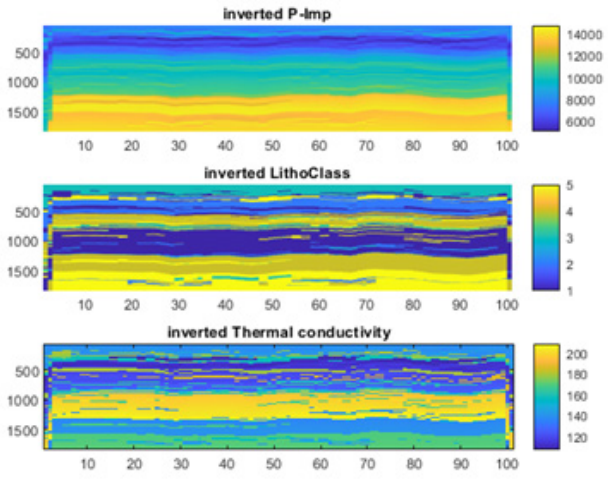


Fig. 2 - Inverse geothermal modeling used to derive impedance, lithology and thermal conductivity.

such as thermal conductivities can be derived from temperature measurements by means of inverse geothermal modeling, integrated with geophysical observations with data assimilation techniques, to identify potential geothermal "sweet spots" and deviations from the background model (Fig. 2).

Basin modelling techniques can be used to compute pre-drill distributions of pore pressure, temperature, porosity and permeability, thus de-risking the placement of the first well; overpressurized hydrocarbon accumulations such as shallow gas pocket can also be detected, further reducing the risks in the drilling operations (Fig. 3).

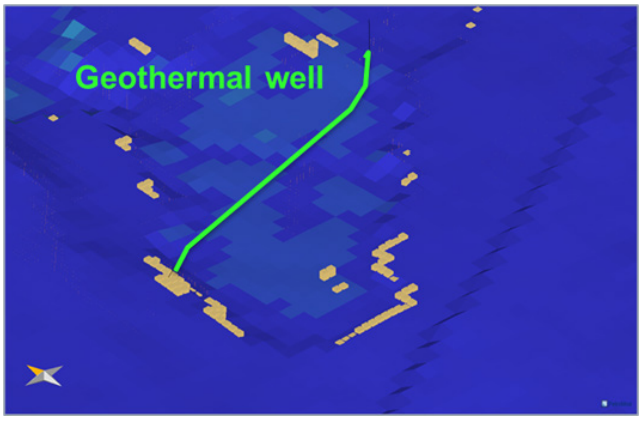


Fig. 3 - overpressured gas accumulations in the vicinity of a geothermal well (adapted from Omodeo Salè *et al.,* 2020).

Finally, natural fractures can be modeled in 3D based on different geological processes (tectonic paleo-stress, association to fault, fault damage zones, thermal cooling, mechanical effects) and from different sources of information, improving the success rates in localizing "sweet spots" for resource targeting.

The resulting model can be enriched with offset well data to further characterize the expected heat and fluid flow behavior, as well as the geomechanical stability of the target formations, of the fault network, and of the planned wellbores.

Case studies from different areas in Europe will be presented to provide examples of the application of these techniques.

References

Omodeo Sale, S., Eruteya, O.E., Cassola, T., Baniasad, A. and Moscariello, A; 2020: *A basin thermal modelling approach to mitigate geothermal energy exploration risks: The St. Gallen case study (eastern Switzerland).* Geothermics, 87, no. 101876, DOI: 10.1016/j.geothermics.2020.101876

3D THERMAL MODELING CONSTRAINED BY CURIE ISOTHERM

Y. Kelemework, M. Fedi

University of Naples Federico II, Department of Earth, Environment and Resources Sciences, Naples

The knowledge of subsurface temperature distribution is very important to identifying potential geothermal regions and understanding a variety of geologic processes, though it is one of the most poorly known geophysical parameters. To obtain information about temperature distribution in the crust and mantle, the surface observations (e.g., surface heat flux and near-surface temperature) could be extrapolated to the crust or lithosphere base using the heat conduction model (e.g., Cermak and Bodri, 1986; Lin *et al.*, 2014). Near-surface heat flow and temperature measurements, along with geochemical models, are often used to characterize the shallow thermal gradient of the crust (e.g., Artemieva, 2011). However, measurements of temperature and heat flow from boreholes are neither uniformly distributed nor consistently deep, and thus they are not enough in inferring deep thermal distributions. Thus, deriving an accurate thermal model of the deep crust is more challenging and requires the knowledge of crustal thickness and related thermal and physical parameters. Moreover, in young and active regions the temperature distribution could be significantly affected by near-surface processes and may completely hinder the deep geothermal gradient and heat flow. Thus, considering the surface heat flow in such regions to be representative of the deep thermal state may lead to wrong geotherm and thermal models (e.g., Della Vedova, 2001). We also need to know the boundary conditions at the top, bottom, and vertical boundaries. Although the surface and vertical boundaries can easily be assumed, the bottom boundary is usually unknown.

To partially alleviate the above-mentioned problems, geophysical and petrological models that do not require data from boreholes can be used to infer deep thermal structures and may help to derive deep thermal constraints and may complement near-surface data. These techniques include the Curie depth point, xenolith, and seismic data among others. The Curie depth point estimated from magnetic data has been commonly used to infer the deep thermal structure (e.g., Tanaka *et al.*, 1999; Bouligand *et al.*, 2009; Kelemework *et al.*, 2021). Curie temperature isotherm (580°C) is the temperature at which magnetic bodies lose their magnetization and become paramagnetic due to increasing temperature with depth. The Curie depth point varies as a function of both local geothermal gradient and lithological composition, and this introduces some uncertainties. Notwithstanding, Curie depth point derived from magnetic data using spectral analysis remains the most common technique to infer deep thermal structure. Furthermore, detailed results of the deep thermal distribution can be obtained by using Curie depth points as constraints by assigning them to the lower thermal boundary condition of a thermal model. Mather and Fullea (2019), for example, constrained the geotherm beneath the British Isles from Bayesian inversion of Curie depth.

In this study, we aimed at building a 3D thermal model constrained by Curie depth points. In addition, crustal structures modeled from seismic and potential field data are used to assign physical parameters (thermal conductivity, heat production). We present a case study from Southern Italy. We also attempt to compare the Curie depth-derived model with geothermal models derived from borehole temperature data wherever possible. 3D thermal models may help to better model more complex geological structures, especially for studying temperature distributions in the contact zones of distinct geologic and tectonic provinces, where significant lateral and vertical variations in the subsurface temperature distributions are expected.

Our preliminary 3D thermal model constrained by Curie depth points is shown in Figure 1. The computed temperature distributions of the crust seem to vary in relation to the volcano-tectonic history and the physical properties of the lithosphere. It is evident from the 3D thermal model that the southeastern Tyrrhenian Sea, including the Aeolian volcanic arcs, is characterized by high thermal gradients with a temperature of 580°C at about 8 - 10 km. This

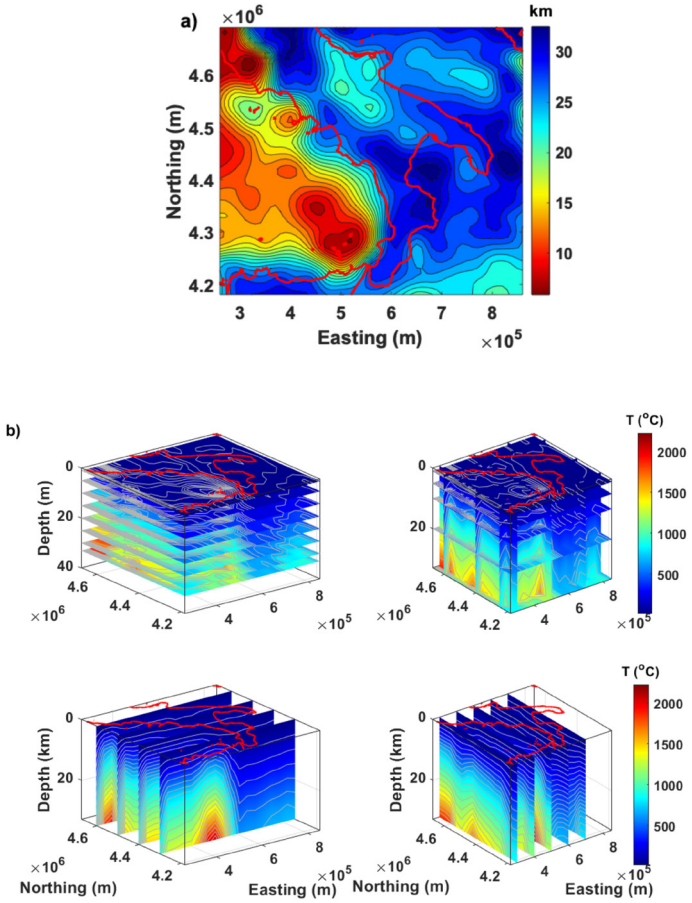


Fig. 1 - Curie depth points map (a) estimated using spectral methods (Kelemework *et al.*, 2021) and 3D thermal distribution model (b) constrained by the Curie points, beneath Southern Italy.

value is observed at about 34 km in the Calabrian arc and the Apennines thrust and fold belts with a sharp thermal gradient along the Tyrrhenian coastlines.

Acknowledgments. This project is funded by Eni.

References

A. Tanaka, Y. Okubo and O. Matsubayashi: *Curie point depth based on spectrum analysis of the magnetic anomaly data in East and Southeast Asia* // pp. 461–470.

B. Della Vedova, S. Bellani, G. Pellis and P. Squarci: *Deep temperatures and surface heat flow distribution*. In G.B. Vai and I.P. Martini (Eds.), Anatomy of an orogen: The Apennines and adjacent Mediterranean basins // pp. 65–76.

B. Mather, and J. Fullea: *Constraining the geotherm beneath the British Isles from Bayesian inversion of Curie depth: integrated modelling of magnetic*, geothermal, and seismic data // pp. 839-850.

C. Bouligand, J.M.G. Glen and R.J. Blakely: *Mapping Curie temperature depth in the western United States with a fractal model for crustal magnetization.*

C. Lin, F. Berntsson, Z. Zhang, P. Wang, J. Wu and T. Xu: *Seismically constrained thermo-rheological structure of the eastern Tibetan margin: implication for lithospheric delamination* // pp. 122–134.

I. Artemieva: *Lithosphere: an interdisciplinary approach.* Cambridge University Press // pp. 794.

V. Cermak, and L. Bodri: *Two-dimensional temperature modelling along five east European geotraverses* // pp. 133–163.

Y. Kelemework, M. Fedi, and M. Milano: *A review of spectral analysis of magnetic data for depth estimation* // pp. J33-J58.

UNDERGROUND HYDROGEN STORAGE IN ITALY

S. Mattera[1], E. Barison[1], F. Donda[1], U. Tinivella[1], B. Merson[1], A. Réveillère[2], C. Vincent[3]

[1] Istituto Nazionale di Oceanografia e Geofisica Sperimentale - OGS, Italy
[2] Geostock SAS Rueil-Malmaison, France
[3] British Geological Survey, UK

Hydrogen is largely recognised as one of the main alternatives to fossil fuels because it does not emit any carbon dioxide when used. It is therefore an important part of the solution to meet the 2050 climate neutrality goal of the European Green Deal.

Since hydrogen does not exist in nature in its pure state, it has to be separated from chemical compounds, by electrolysis from water or by chemical processes from hydrocarbons or other hydrogen carriers, through energy-consuming processes.

The overall efforts are moving toward the "green" hydrogen, produced from water by electrolysers powered by renewable energies, which do not produce carbon emissions but are subjected to intermittent, and seasonal and geographically constraints. For this reason and in the perspective of an increase in green H_2 production, underground hydrogen storage assumes a strategic importance.

There are cases of pure hydrogen underground storage in salt caverns in Europe (e.g. in Teeside, UK since 1972), but no examples of industrial pure hydrogen storage in depleted hydrocarbon fields or aquifers, which could allow a potential larger storage capacity compared to salt caverns.

The EU H2020 Hystories "Hydrogen Storage in European Subsurface" project aims at studying the potentialities of pure hydrogen underground storage in depleted hydrocarbon fields and aquifers in Europe, by identifying the suitable sites and providing subsurface technical and economic feasibility studies.

The know-how from the underground natural gas and CO_2 geological storage is a starting point to define guidelines for hydrogen storage, i.e. to set the geological characteristics of the caprock-reservoir system. Nevertheless, the specific characteristics of the H_2 molecule require an in-depth study, because of the high capacity of H_2 to create chemical bonds and to feed the microbial activity inside the reservoir, which could lead to an alteration of pure H_2 and/or to hydrogen-consuming processes (e.g. Heinemann *et al.*, 2021).

The National Institute of Oceanography and Applied Geophysics-OGS is the only Italian research partner involved in the Hystories project, as Third Party through CO_2GeoNet. In the frame of the project, OGS identified several sites potentially suitable for hydrogen storage in the Italian subsoil both on- and offshore, in aquifers and in depleted hydrocarbon fields, which will be briefly presented and discussed. We also performed a more detailed, site-specific study of an onshore site in north-eastern Italy, which consists in a petrophysical characterization of the potential hydrogen storage reservoir by using the available geophysical dataset and theoretical models.

Acknowledgments. This project has received funding from the Fuel Cells and Hydrogen 2 Joint Undertaking (now Clean Hydrogen Partnership) under Grant Agreement No 101007176. This Joint Undertaking receives support from the European Union's Horizon 2020 Research and Innovation Programme, Hydrogen Europe and Hydrogen Europe Research.

References

Heinemann N.; Alcalde J.; Miocic J. M.; Hangx S. J. T.; Kallmeyer J; Ostertag-Henning C; Hassanpouryouzband A. T.; Thaysen E. M.; Strobel G. J.; Schmidt-Hattenberger C.; Edlmann K.; Wilkinson M.; Bentham M.; Stuart Haszeldine R.; Carbonell R. and Rudloff A.; 2021: *Enabling large-scale hydrogen storage in porous media, the scientific challenges.* Energy Environ. Sci., **14**, 853-864. DOI 10.1039/d0ee03536j.

A PILOT APPLICATION OF GUIDELINES FOR GEOPHYSICAL MONITORING OF HYDROCARBON CULTIVATION: PRACTICAL ISSUES FROM THE CAVONE OIL FIELD

L. Zaccarelli[1], M. Anselmi[2], M. Vassallo[3], I. Munafò[3], L. Faenza[1], L. Sandri[1], A. Garcia[1], M. Polcari[2], G. Pezzo[2], E. Serpelloni[1], L. Anderlini[1], M. Errico[1], I. Molinari[1], G. Zerbinato[1], A. Morelli[1]

[1] Istituto Nazionale di Geofisica e Vulcanologia, sezione di Bologna, Bologna, Italy
[2] Istituto Nazionale di Geofisica e Vulcanologia, Osservatorio Nazionale Terremoti, Roma, Italy
[3] Istituto Nazionale di Geofisica e Vulcanologia, sezione Roma1, Roma, Italy

In this contribution we present the outcomes of two years of seismic, deformation, and pore pressure monitoring of the Cavone oil field in the Mirandola exploitation permit (Emilia Romagna, Northern Italy, Fig.1). This has been the first attempt of third-party monitoring following the governmental guidelines for hydrocarbon cultivation activities in Italy.

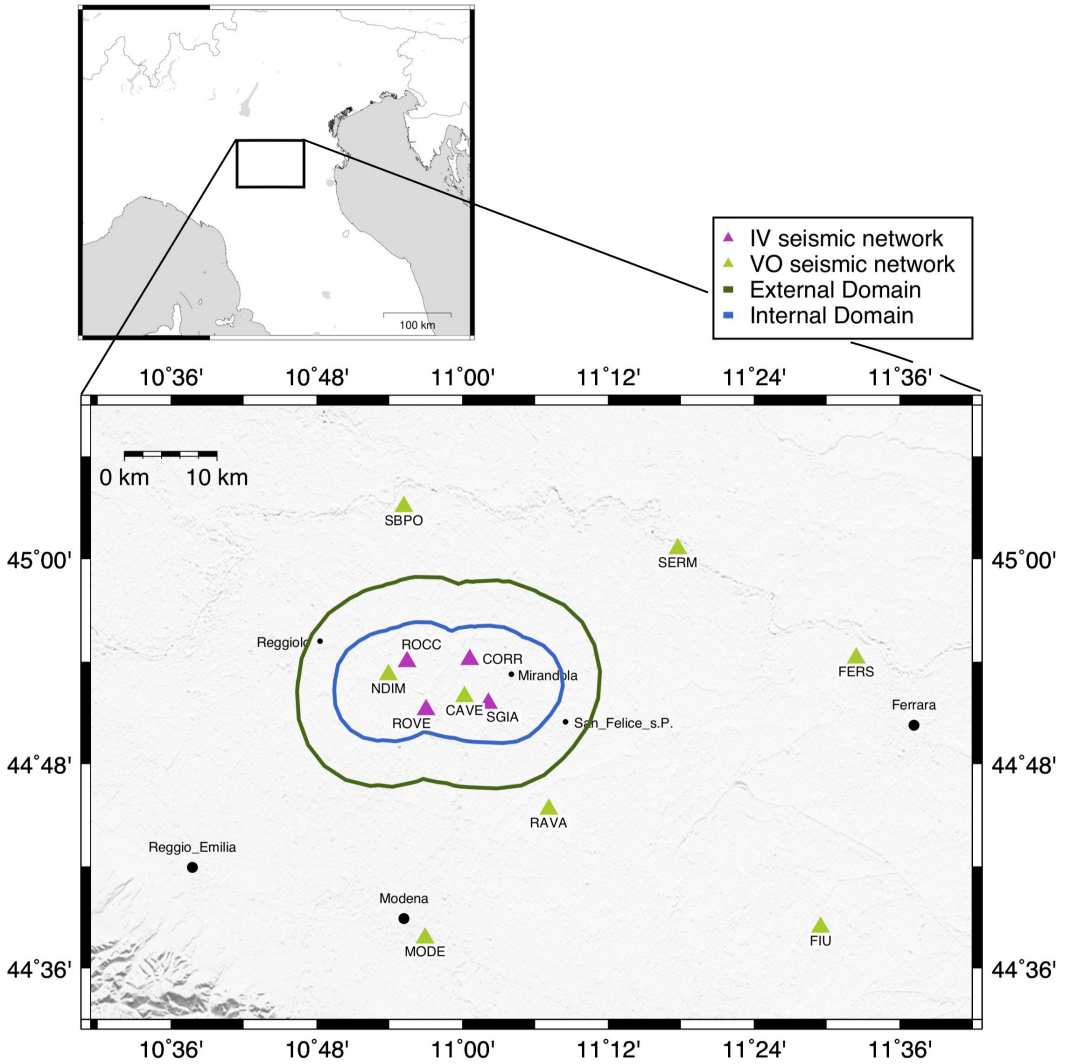


Fig. 1 - Map of the monitored area with the sketch of the two observation domains (Internal and External in blue and dark green respectively), and the location of the seismic stations pertaining to the local (VO, purple triangles) and national (IV, green triangles) seismic networks.
The inset on top shows the position of the region in northern Italy.

The Cavone oil field production water re-injection activity was speculated of possibly influencing the 2012 ML 5.8 Mirandola earthquake source. According to the Italian government guidelines, a monitoring center should analyze geophysical measurements related to seismicity, crustal deformation and pore pressure in quasi real-time. In case of significant earthquakes (i.e. events with magnitude and location included in critical ranges and observation domains, Fig.1) a traffic light system would be used to regulate exploitation and underground operations.

For a 2-year-long period of guidelines experimentation, we analyzed the different kinds of available data, and then we tested the existence of possible relations among their temporal trends. We could profit by the presence of the Italian seismic network (IV, Fig.1) in the area, therefore by integrating these data with those of the local seismic network (VO, Fig.1). Despite the short time window and the scarce quantity of data collected, we were able to perform all the required analyses and extract as much meaningful and statistically reliable information from the data.

Here we discuss the most important observations drawn from the monitoring results, and highlight the lessons learned by describing practical issues and limitations that we have encountered in carrying out the tasks as defined in the guidelines. Our main goal is to contribute to the discussion about how to better monitor the geophysical impact of this kind of anthropogenic activity.

The lack of an assessment of background seismicity in an unperturbed situation -due to long time extraction activities- makes it difficult to get a proper picture of natural background seismic activity, which would be instead an essential reference information for tectonically-active regions, such as Northern Italy. Nevertheless we could demonstrate the importance not only of a wider and more dense seismic network, but more than that of the borehole sensor deployment, in order to improve the microseismic detection capabilities in such a noisy environment as the Po plain.

CHARACTERIZATION OF SEISMIC NOISE AMPLITUDE RECORDED BY A VERTICAL ARRAY INSTALLED IN A DEEP BOREHOLE AT THE S. POTITO-COTIGNOLA GAS STORAGE FIELD (NORTHERN ITALY)

C. Rossi[1,2,3], F. Grigoli[4], P. Gasperini[2], S. Gandolfi[3], T. Gukov[5], C. Cocorullo[1,6], P. Macini[3]

[1] Seismix srl, Palermo, Italy
[2] Dipartimento di Fisica e Astronomia, Alma Mater Studiorum Università di Bologna, Italy
[3] Dipartimento di Ingegneria Civile, Chimica, Ambientale e dei Materiali, Alma Mater Studiorum Università di Bologna, Italy
[4] Dipartimento di Scienze della Terra, Università di Pisa, Italy
[5] Edison Stoccaggio S.p.A., Italy
[6] Solgeo srl, Bergamo, Italy

With the growing number of industry-related seismicity events and their effects, the monitoring and analysis of such events have become increasingly important. Seismic monitoring network in areas interested by underground fluids production activities has a fundamental role to characterize seismicity, to control the industrial operation and to assess the seismic hazard. Furthermore, a proper seismic network allows to detect even low magnitude events occurring in the area surrounding the industrial site. The capability to detect weak events can provide useful information about the reservoir condition, as well as the distribution and geometry of active faults and geo(mechanic) discontinuities even close to the industrial site.

After the natural M6 earthquake occurred in Emilia Romagna region (2012), the Italian Ministry for Economic Development (MiSE) published a reference document "Guidelines for monitoring seismicity, ground deformation and pore pressure in subsurface industrial activities" (Dialuce *et al.*, 2014). According to such document, the monitored area is divided into an inner survey domain, which consists of a volume around the reservoir, properly sized depending on the industrial activity type, and an extended survey domain surrounding the inner part. For the inner survey domain, seismic monitoring network should be able to locate and size seismic events starting from ML (local magnitude) ranging between 0 and 1 ($0 \leq ML \leq 1$). However, such low magnitude detection capability is affected by the level of anthropogenic noise at the site as well as by the sedimentary cover rocks type and thickness. As suggested in the above guidelines, the reduction of high level of noise and thus the improvement of sensitivity and capability of the seismic network, can be achieved by installing seismic stations at depth in boreholes. Furthermore, the analysis of amplitude noise reduction as function of depth can be useful to design a seismic network able to reduce the signal to noise ratio (SNR) and thus to detect and locate such low-magnitude events.

Here we analyse continuous seismic noise from January 2019 to December 2021 recorded at underground gas storage site of S. Potito-Cotignola in the Po Valley (Italy). We use a broadband (BB) seismic station at surface and a vertical array composed by 6-short period 3-components seismometers installed at depth ranging between 35 to 285 m in borehole at the same location of the BB sensor, installed at industrial site. We aim to characterize the seismic noise by computing power spectral density (PSD) and quantify the amplitude noise reduction in terms of dB as a function of depth for different frequencies. Furthermore, for each sensor-depth, we even compute the SNR selecting 3 seismic events with different magnitude and epicentral distance recorded.

We found that 1) the maximum difference between the deepest instrument and the one at the surface is about -33 dB at 5Hz, while for the most extreme frequencies of the investigated range the noise reduction ranging from -10 to -15; 2) the dependence of noise levels (in dB) with depth follows a logarithmic empirical law; 3) the lower magnitude event shows the maximum difference of SNR between the deepest sensor and the one at surface of about 20 dB, in agreement with the noise amplitude level reduction range.

References

Dialuce G., Chiarabba C., Di Bucci D., Doglioni C., Gasparini P., and Lanari R., Priolo E., Zollo A.; 2014: *Guidelines for monitoring seismicity, ground deformation and pore pressure in subsurface industrial activities*, Italian Ministry for the economic development (MiSE), 34 pp.

Sessione 3.2

Geofisica per l'Ambiente

Convenor: E. Forte, M. Cercato e C. Comina

ON THE REVERBERATION EFFECT IN MULTI-CHANNEL ANALYSIS. SURFACE WAVES POLARIZATION AS QUICK TOOL FOR SUBSOIL CHARACTERIZATION

I. Barone[1], J. Boaga[1], G.P. Deidda[2], G. Cassiani[1]

[1] Dipartimento di Geoscienze, Università degli Studi di Padova, Padova, Italy
[2] Dipartimento di Ingegneria civile, ambientale e architettura, Università degli Studi di Cagliari, Cagliari, Italy

It is known that resonance phenomena linked to buried impedance contrast can be adopted for subsoil characterization (Lunedei and Malischewsky 2015). Since the 70's resonance effects were observed and analyzed, both in case of telluric events and microtremors studies (Nogoshi and Igarashi 1970). From the multi-component analysis of horizontal and vertical components of soil motion, we can retrieve information about the presence of an impedance contrast, the depth and the rigidity of the layers involved (e.g. HVSR technique). These measurements have strong implications on seismic microzonation studies, since the presence of an impedance contrast may lead to strong amplifications in case of earthquake events (Bonnefoy-Claudet *et al.,* 2004), while the local resonance frequency of the subsoil has great importance for the a-seismic design. Surface waves polarization phenomena were also observed in case of strong impedance contrast in the investigated subsoil, leading to the osculation modes phenomenon (Malischewsky *et al.,* 2008, Hobiger *et al.,* 2009, Boaga *et al.,* 2013).

Nowadays, the standard approaches for the determination of the soil resonance frequency and of the shear-wave velocities are single-station noise multi-component recordings (HVSR technique) and multi-channel analysis of surface waves (MASW; Park *et al.,* 1999), the latter generally making use of single-component receivers. We here observe, in both synthetic and real datasets, a reverberation effect in controlled-source vertical receiver arrays, due to the presence of a buried impedance contrast. This reverberation is linked to the polarization of Rayleigh wave motion, and is clearly visible both in time domain (shot gathers before any processing) and in frequency domain (clear peak in the amplitude spectrum). We here show the strong dependency of the vertical reverberation frequency on the shear-wave velocity contrast, and on the shear-wave velocity, depth and Poisson's ratio of the top layer, and its relation to the site resonance frequency. In conclusion, when seismic reverberations are observed on vertical-component data, a very quick characterization of the first subsoil can be deducted, without the need of multi-component analysis, multi-component sources or long acquisition time.

References

Lunedei E. and Malischewsky P.; 2015: *A Review and Some New Issues on the Theory of the H/V Technique for Ambient Vibrations*. In A. Ansal (ed.), Perspectives on European Earthquake Engineering and Seismology. Geotechnical, Geological and Earthquake Engineering, **39**, doi:10.1007/978-3-319-16964-4_15.

Nogoshi M. and Igarashi T.; 1970: *On the propagation characteristics of microtremor*. Journal of the Seismological Society of Japan, **23**(4), pp. 264–280.

Park C. B., Miller R. D. and Xia J.; 1999: *Multichannel analysis of surface waves*. Geophysics, **64**, pp. 800–808, doi: 10.1190/1.1444590.

Boaga J., Cassiani G., Strobbia C. and Vignoli G.; 2013: *Mode misidentification in Rayleigh waves: ellipticity as a cause and a cure*. Geophysics, **78**(4), pp. 1–12, doi: 10.1190/GEO2012-0194.1.

Malischewsky P. G., Scherbaum F., Lomnitz C., Tran Thanh T., Wuttke F. and Shamir G.; 2008: *The domain of existence of prograde Rayleigh-wave particle motion for simple models*. Wave Motion, **45**(4), pp. 556–564, doi: 10 .1016/j. wavemoti.2007.11.004.

Bonnefoy-Claudet S., Koeler A., Cornou C., Wathelet M., and Bard P. Y.; 2008: *Effects of Love waves on microtremor H/V ratio.* Bulletin of Seismological Society of America, **98**, pp. 288–300.

Hobiger M., Le Bihan N., Cornou C. and Bard P. Y.; 2009: *Rayleigh wave ellipticity estimation from ambient seismic noise using single and multiple vector-sensor techniques*. Proceedings of 17th European Signal Processing Conference (EUSIPCO 2009).

MIOCENE MOUNDS AT THE ROSS SEA PALEO-CONTINENTAL SHELF: EVIDENCE OF THE ONSET OF ANTARCTIC GLACIATIONS OR MUD VOLCANOES?

L. Barro Savonuzzi[1], G. Brancatelli[2], E. Forlin[2], L. De Santis[2], N. Wardell[2], R. Geletti[2], M. Busetti[2], A. Del Ben[1]

[1] Dept. of Mathematics and Geoscience, Trieste University, Trieste, Italy
[2] National Institute of Oceanography and Applied Geophysics – OGS, Sgonico, Italy

Buried features, with the top lying between a few meters to 150 m below the seafloor, were identified, on high-resolution seismic reflections, in an area of about 257.5 km^2 in the southern Roosevelt Sub-basin, along the front of the Ross Ice Shelf (Antarctica), where the water depths is 700-900 m.

These features were interpreted as buried moraines deposited under marine conditions at water depth of several hundred meters, near the paleo-shelf edge and predating 25 Ma, thus placing the onset of the West Antarctic Ice Sheet (WAIS) growth and marine expansion in the late Oligocene (Sorlien *et al.,* 2007). Conversely Marschalek *et al.* (2021) suggest a much younger age for the WAIS based on the provenance of sediments at IODP site U1521, in the central-eastern Ross Sea.

Buried and modern, mound-shaped features with similar size and acoustic facies of those occurring in the Roosevelt Basin have been identified in the other sectors of the Ross Sea and interpreted as relict depositional/erosive structures formed by glacial advances and retreats (Perez *et al.*, 2021), but also as volcanic structures (Boehm *et al.*, 1993; Lawer e*et al.*, 2012), or mud volcanoes related to the occurrence of free gas and gas hydrates (Geletti and Busetti, 2011). Sedimentary mounds like those observed in the Ross Sea may have an accretion carbonate component, as observed in medium-low latitudes, also in cold regions (Wheeler *et al.*, 2005; Hovland, 2008; Somoza *et al.*, 2015), but they are strongly unlikely in an extreme polar environment which is thermodynamically unfavorable to calcifying organisms.

Unfortunately, although mounds are quite common in the Ross Sea, their origin is currently unknown, because they have never been directly sampled yet and their composition and age can only be inferred by their acoustic character.

This work presents new geophysical analyzes of the seismic reflection profiles across the buried Roosevelt Subbasin mounds to test previous hypotheses about their origin and formulate alternative explanation.

PSDM (Pre-Stack Depth Migration) of the seismic profiles allowed better definition of geometries and seismic velocities, mitigating pull-up effects. The processing steps allowed us to improve the signal-to-nose ratio, attenuate random noise and multiple reflections, improve temporal and spatial resolution, and define an accurate velocity field

The acoustic facies, velocity, size and shape of the buried features observed in the sediments filling the Roosevelt Subbasin are compared to those of the other Ross Sea mound provinces, by using published data (Geletti and Busetti, 2022, Bohem *et al.*, 1993) and by reprocessing the multichannel seismic profile BGR80-100 that intersects some circular-shaped, mounded features on the sea floor, along the continental slope and shelf near Cape Adare.

The seismic velocity of the mounds (~ 2800 m/s, Fig. 5), the chaotic internal facies and the strong amplitude reflector at their base are consistent with compacted, glacial material, which would support the hypothesis of Sorlien *et al.* (2007), who classify them as morainal structures.

However, the possibility that the structures do not have an elongated, but circular shape lead us to consider alternatives for the origin of the mounds.

The acoustic blanking observed beneath the mounds, interrupting the continuity of the reflectors may be indeed indicative of chimneys beneath the buried mounds within which upward migration of gas and fluids occurs along fractured and faulted sediments (e.g. Løseth *et al.*, 2009). This would explain the reflectors offset and upward bending (in depth migrated

seismic profiles). Therefore we suggest the hypothesis that the mounds of the Roosevelt Subbasin formed as mud volcanoes instead of glacial moraines.

The age of the Roosevelt Subbasin mounds is inferred by indirect correlation and comparison with the eastern Ross Sea seismic sequences, after Brancolini *et al.* (1995) and the recent work by Perez *et al.* (2021), that improved the chronostratigraphic framework (after the IODP Exp 374, McKay, De Santis, Kulhanek *et al.*, 2019; Perez *et al.,* 2021).

The sea bed where the mounds grew is an erosional surface truncating with low angle a package of sub-horizontal reflectors, however it doesn't show glacial valleys incisions or other peculiar features suggesting deep erosion from grounding ice streams. The base of the mounds is possibly a transgressive marine surface, a residual, coarse sedimentary lag, swept by bottom currents, similar to the present day sea bed in the outer continental shelf. This would justify the strong amplitude of the reflector lying at the base of the mounds. The occurrence of current typical moat-sediments drifts within the mounds and the aggradational geometry of the strata infilling the depressions among the mounds would indicate open marine sediment deposition during a period of relative high sea level, during and after the mound formation.

The two hypothesis to explain the origin of the buried mounds in the Roosevelt Subbasin risen by Sorlien et al. (2017) and by our work, have implications for quite a diverse WAIS scenario, and confirming one of them with future shallow drilling would be very important for ice sheet volume and thermal rheology modelling reconstructions. The seismic profiles reprocessed for this work are used to locate drill sites and define targets of the IODP Pre-998 proposal (McKay, De Santis *et al.*, 2020).

References

Bohem G., Brancolini G., Fais S., Snidarcig A., Vesnaver A.; 1993. BGTA vol. XXXV, 137-138.

Brancolini G., Busetti M., Marchetti A., De Santis L., Zanolla C., Cooper A.K., Cochrane G.R., Zayatz I., BelYaev V., Knyazev M., Vinnikovskaya O., Davey F.J., Hinz K.; 1995: *Descriptive text for the seismic stratigraphic atlas of the Ross Sea, Antarctica*. Geology and seismic stratigraphy of the Antarctic Margin, Antarctic Research Series, vol. 68, 271-286.

Hovland, M.; 2008. *Deep-water coral reefs: Unique biodiversity hot-spots*. Springer Science & Business Media.

Lawver L., Lee J., Kim Y., Davey F.; 2012. *Geosphere*, 8(3), 645-653. doi:10.1130/GES00766.1;

Løseth, H., Gading, M., and Wensaas, L.; 2009: *Hydrocarbon leakage interpreted on seismic data*. Marine and Petroleum Geology, 26(7), 1304-1319.

Geletti and Busetti 2011. J. Geophys. Res. Solid Earth, 116(B4)

McKay, R. M., De Santis, L., and Kulhanek, D. K.; 2019: *Ross Sea West Antarctic Ice Sheet History*. Proceedings of the International Ocean Discovery Program, 374.

Marschalek, J, Zurli, L, Talarico, F, Van de Flierdt, T, Vermeesch, P, Carter, A, Beny, F, Bout-Roumazeilles, V, Sangiorgi, F, Hemming, S, Perez, L, Colleoni, F, Prebble, J, Van Peer, T, Perotti, M, Shevenell, A, Browne, I, Kulhanek, D, Levy, R, Harwood, D, Sullivan, N, Meyers, S, Griffith, E, Hillenbrand, C-D, Gasson, E, Siegert, M, Keisling, B, Licht, K, Kuhn, G, Dodd, J, Boshuis, C, De Santis, L, McKay, R. *A large West Antarctic Ice Sheet explains early Neogene sea-level amplitude*. Nature 600, 450–455 (2021). https://doi.org/10.1038/s41586-021-04148-0

Pérez, L. F., Santis, L. D., McKay, R. M., Larter, R. D., Ash, J., Bart, P. J., Böhm G., Brancatelli G., Browne I., Colleoni F., Dodd J.P., Geletti R., Harwood D.M., Kuhn G., Laberg J.S., Leckie R.M., Levy R.H., Marschalek J., Mateo Z., Naish T.R., Sangiorgi F., Shevenell A.E., Sorlien C.C, van de Flierdt T., International Ocean Discovery Program Expedition 374 Scientists; 2021: *Early and middle Miocene ice sheet dynamics in the Ross Sea: Results from integrated core-log-seismic interpretation*. Bulletin, 134(1-2), 348-370. doi: https://doi.org/10.1130/B35814.1

Sorlien C. C., Luyendyk B. P., Decesari R. C., Wilson D. S., Bartek L. R.; 2007: *Oligocene development of the West Antarctic Ice Sheet recorded in eastern Ross Sea strata.* The Geological Society of America, V.35, 5, 467-470.

DIAGNOSTIC MULTIDISCIPLINARY INVESTIGATIONS IN THE MOTHER CHURCH AT MISTERBIANCO AT ETNA VOLCANO: A CASE-STUDY FROM THE 1669 ERUPTION

C. Bottari[1], P. Capizzi[2], R. Martorana[2], R. Azzaro[1], S. Branca[1], R. Civico[3], M. Fucile[4], E. Pecora[1]

[1] Istituto Nazionale di Geofisica e Vulcanologia, Sezione di Catania, Osservatorio Etneo, Catania, Italy
[2] Università degli Studi di Palermo, Dipartimento di Scienze della Terra e del Mare, Palermo, Italy
[3] Istituto Nazionale di Geofisica e Vulcanologia, Sezione di Roma1, Roma, Italy
[4] Topcon Positioning Italy, Ancona, Italy

Introduction. Misterbianco is a small and important town located on the southern slope of the Mt. Etna (Fig. 1). Its position at the periphery of the volcano, in front of the Simeto river valley and dominating the Catania plain, enabled the town to richness importance in the local territorial framework until the mid of the 17th century (Amico, 1757). From that time, the old town of Misterbianco (known as *Monasterium Album*) underwent two natural catastrophes that heavily conditioned the history of this part of Sicily: the 1669 Etna eruption and the 1693 earthquake. The eruption caused a lava field extending for 40 km^2 and a maximum flow length of 17 km that greatly impacted the territorial setting of the southern flank of Mt. Etna (Branca *et al.*, 2015). Lava buried villages and minor settlements, reached the city of Catania and finally entered into the sea. A large part of the architectural heritage was destroyed and the landscape after the eruption turned into a wasteland. After two decades, the 1693 earthquake produced large destruction in the whole south-eastern Sicily (Boschi and Guidoboni, 2001).

The few remnants surveying the 1669 eruption are not adequately exploited as well the Sanctuary of Monpilieri and the Chiesa Madre (Mother Church) of the old Misterbianco (Fig. 1a-b). The first one, located next to the 1669 main vent, was buried beneath a 15 m thick lava; whereas the second one was partially covered by lava flow and the bell tower of the church was the only still standing portion, hereinafter named *Campanarazzu* (Fig. 1c).

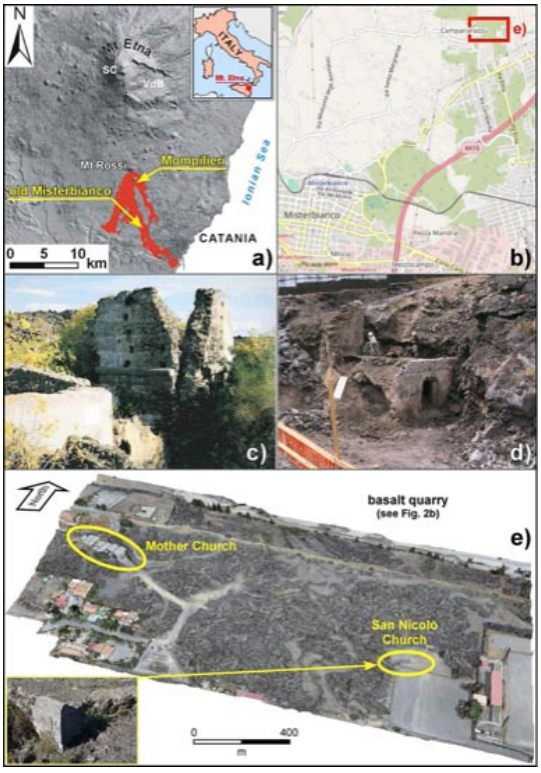


Fig. 1 - a) Map of the 1669 lava flow with the position of "buried" churches of Mompilieri and old Misterbianco; b) The old settlement (red box) is nowadays located few kilometers from the new Misterbianco; c) The bell tower of the Mother Church was the only structural element standing out from the lava field; d) The remains of the church during the excavation works; e) Orthophoto-mosaic overlapped on the digital surface model of the investigated site, showing the position of the Mother Church and the San Nicolò Church.

In this site, the excavations performed by the Soprintendenza of Catania allowed to unearth the remains of the Mother Church (Fig. 1d-e) while an accurate restoration plan reinforced the structure and recovered the remains of the chapels ornaments (Garozzo *et al.*, 2019).

A diagnostic multidisciplinary study focusing specifically on the Mother Church building is here presented aimed at i) defining the spatial relation of the church's structure with the 1669 lava field (Fig. 1e); ii) identifying possible hidden features inside the edifice; iii) reconstructing the historical evolution of the original building. To this end, we firstly made a drone survey to map in detail the investigated area; then, we used different diagnostic techniques such as ground penetrating radar (GPR) to uncover buried crypts below paved floor, infrared thermography (IRT) and terrestrial laser scanner (TLS) to detect previous structural modifications and deformation of architectural elements caused by the push and weight of the 1669 lava flow.

The 1669 Eruption. The 1669 eruption represents the largest flank eruption documented in historical times that caused the most damage to cultivated areas and settlements in the Etna region (Branca *et al.*, 2015). During this event, lasted four months from 11 March to 11 July, about 600 million m^3 of lava were erupted with an average effusive rate of 58±10 m^3/s, covering an area of 40 km^2 on the southern flank of the volcano (Fig. 2a). The development of a

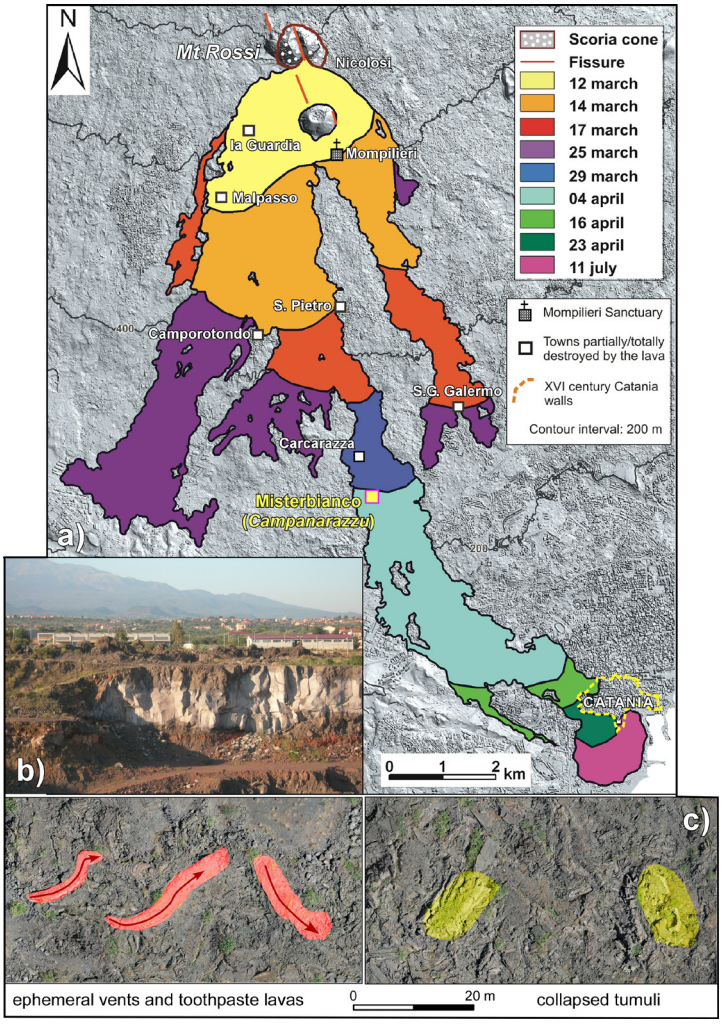


Fig. 2 - a) The 1669 lava flow field map and location of the main settlements run over by the lava; b) view of the basalt quarry 300 m north-east of the Mother Church; c) detail of the DSM showing the typical features of lava morphology in the investigated area.

complex lava tube network promoted lava field lengthening as far as the coastline, destroying villages and partially damaging the western part of Catania (Branca *et al.*, 2013). The 1669 event was accompanied by an intense seismic swarm.

Between 11 and 25 March the lava field covered 72% of the total area, and three branches of the lava field were developed; whereas at the end of March, the central branch reached the old site of Misterbianco.

In those months, the ephemeral vents led to the formation of new lava flows that developed in the Misterbianco territory, producing a gradual thickening of the lava field (Branca *et al.*, 2013). As a result, the thickness of the lava field reaches 21 m in a quarry located about 300 m northeast of the study area (Fig. 2b). Overall, the morphology of the lava field consists of toothpaste lavas, often appearing fractured and tilted with the presence of several ephemeral vents and small tumuli (Fig. 2c).

The Chiesa Madre: historical background. The oldest document mentioning the *Chiesa Madre* dates back to the 14th century; during time the structure was modified with the addition of new rooms, a central nave, new altars and chapels were added (Garozzo 2017-2018).

Today the building is characterised by a Latin cross plan with a nave 26 m long and 9 m wide along which there are eight altars (Fig. 3a). The presbytery has a rectangular-shaped room with a pseudo-apse: it also has an entrance door on the left, which was closed during the eruption with massive stones in order to prevent lava flowing into the church. A smaller door located to the right gives access to the gothic chapel. Along the southern wall of the nave there is the bell tower, which is the only original element standing out from the 1669 lava.

Multidisciplinary surveys. A diagnostic multidisciplinary survey was performed in the Mother Church site, including both the inner of the building and the environmental setting on a surface of ca. 10 ha.

For this study, we applied the following four different methods: i) aerial photogrammetry by drone to obtain a high-resolution mapping of the studied site within the 1669 lava flow; ii) ground-penetrating radar (GPR) to detect voids below the church floor related to buried structures (i.e. tombs, crypts etc.); iii) terrestrial laser scanner (TLS) to recognize fractures and deformations in structural and architectural elements; iv) infrared thermography (IRT) to identify modifications before the 1669 lava flow not reported in the historical documents.

Structure-from-Motion aerial photogrammetry. The aerial photographic survey of the Misterbianco site produced a high-resolution digital surface model (DSM) and an orthophotomosaic by using the Structure-from-Motion technique (SfM). We used a DJI Phantom 4 ProV 2.0 in order to acquire 540 aerial images with a constant flight altitude of about 50 m above ground level.

The photogrammetric acquisition was characterized by the following steps: i) identification of key points and image matching followed by scattered point cloud; ii) filtering of the scattered point cloud thus deleting incorrect geometry of those points characterized by significant coupling errors; iii) generation of the dense point cloud; iv) generation of the digital surface model (DSM) and of the orthophotomosaic (Fig. 1e).

Terrestrial Laser Scanner. The TLS survey of the Mother church was performed through the integrated use of laser scanning and photogrammetric technologies, in order to acquire geometric and spatial data of the historical heritage. For this purpose, we used a TOPCON GLS-2000S scanner, featuring a maximum distance of 130 m, with field angles of 360° (horizontal) and 270° (vertical). The survey was performed from outside to inside of the building with 11

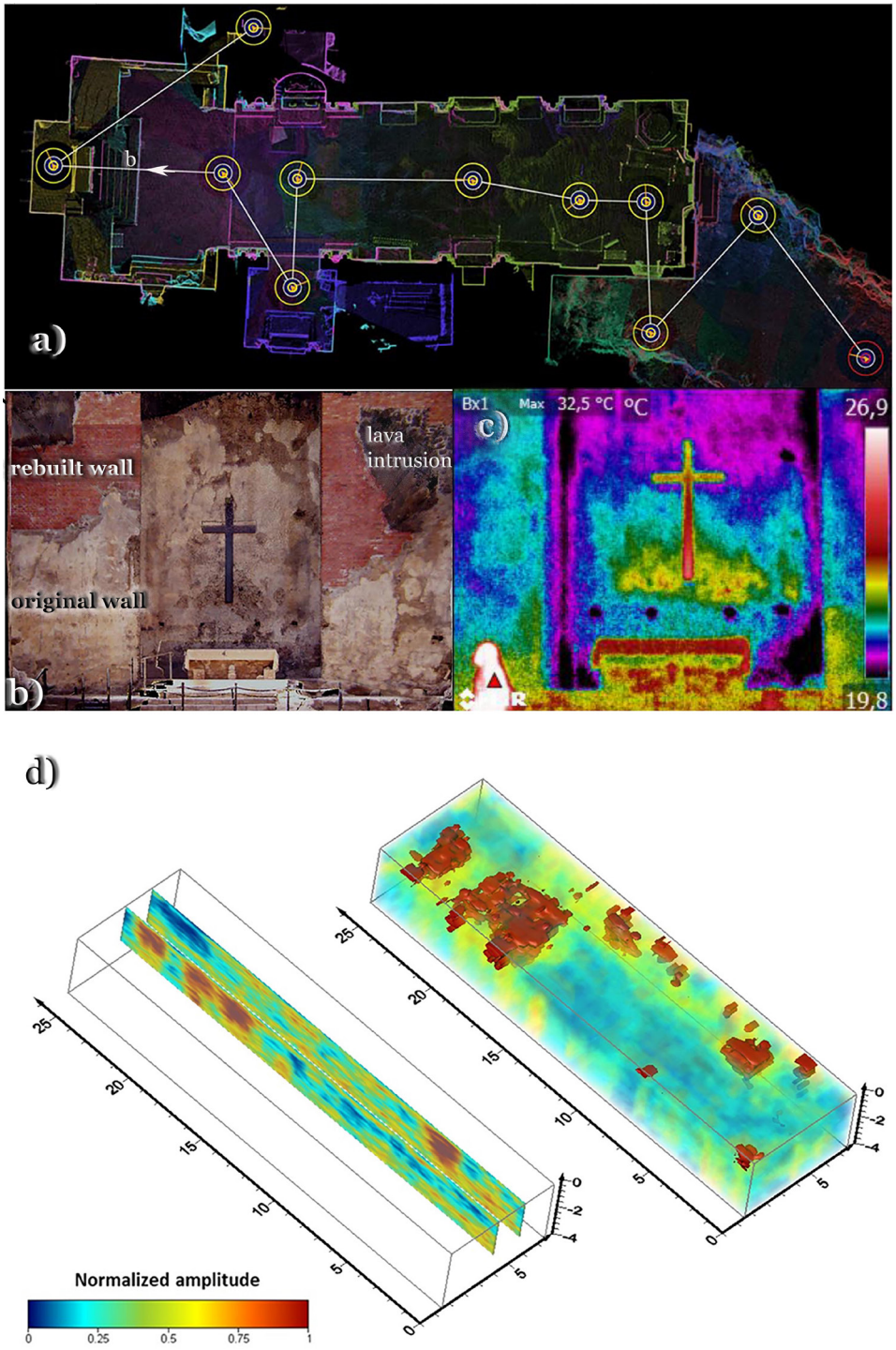


Fig. 3 - a) plan of the church, the circles indicate the TLS measurement points, the acquisition phase was performed in Traverse mode; b) point cloud of the altar area, it is still possible to observe the consistency of the original wall, the reconstructed portion (red bricks) and the lava intrusion; c) IRT image of the wall behind the altar area (presbytery); d) Three-dimensional GPR model (on the right) of the subsoil of the church showing the areas of major reflectivity; vertical sections of the model (on the left).

scans – 3 external and 8 internal-in a Traverse mode (Fig. 3a), aligned through survey prism in order to optimize the data acquisition of the whole building. This method allowed the strict placement of the external and the internal data of the building, avoiding cloud alignment operation in the post-processing phase.

Ground Penetrating Radar. The GPR survey inside the church was aimed at collecting data about the presence of unknown structures, chambers, and tombs under the floors of the church and the crypts. For this research, the GPR survey was performed using a RIS MF HI-MOD system (IDS GeoRadar s.r.l.), equipped with an array of multi-frequency of two antennas of 600 MHz and 200 MHz. The antennas have been selected according to the resolution and depth of investigation, therefore we used both antennas simultaneously, one with 600 MHz to get a good superficial resolution and another one with 200 MHz to get a suitable depth. The measurements were carried out along parallel profiles through the nave of the church; in all, 15 profiles have been acquired and spaced 0.5 m, the investigated area measuring 7.5x25.5 m. Data were collected using the reflection technique.

Data elaboration was performed with Reflex software. To get a 3D model of reflectivity of subsoil, we used a time-slice technique, which consists in the construction of horizontal sections at certain reflection times (time-slices) or depths (depth-slices). The first two meters of the 3D model were obtained using the data acquired with the 600 MHz antenna, while up to four meters deep, the data acquired with the 200 MHz antenna were considered.

Fig. 3d shows a view from the top of the reflectivity model superimposed on the plan. It can be noted that the locations of the high reflectivity anomalies often coincide with those of the tombstones, indicating the presence of numerous burials immediately below the paved floor of the church.

Infrared Thermography. The thermographic survey of the Mother Church was carried out by using a Flir T 530 thermal imaging camera. The measurement scale used is between -20 ° C and 120 ° C. The thermographic analysis was carried out on the wall surface as it appeared, in conditions of normal thermal operation. The investigated walls of the church are the southern one, located between the bell tower and the Crocifisso altar (Fig.3 a), and the western one corresponding to the presbytery (Fig.3a-c). In the Mother Church, the thermographic images captured the most common lithotypes used in the area (lime, mortar and volcanic rock). The thermographic signal detected a significant difference of the temperature among materials. For this reason, it was not only possible to analyze wall textures covered by the plaster, but also to discriminate among the different lithotypes used in the masonry. Furthermore, the images highlighted the presence of a probable wall structure under the plaster. This structure was identified due to the different thermal response between the filling and the surrounding masonry.

Conclusions. By analysing the lava field structure, it can be presumed that the church suffered two main phases of lava flow impact. The first one when the basal lava flow surrounded the northern and western part of the edifice with a lava front some dozens meters thick; inhabitants, aware of the risk, closed the southern door of the presbytery with stones. At a first moment, the northern and western walls were weakened by the lava thrust, and shortly after they collapsed.

The impact of the second phase is related to the evolution of the lava flow field that gradually covered the site (Fig. 2c). Lava gradually filled the church's nave destroying the wooden remains but preserving the paved floor, and cooked the lime of the altars.

Looking at the internal part of the church through the results of GPR, IRT and TLS surveys, it was possible to identify some modifications suffered by the edifice before its destruction.

The IRT technique allowed highlighting an anomaly in the presbytery wall due to the different thermal response between the filling and the surrounding masonry; no other anomalies were detected.

The GPR survey performed through the nave allowed recognising the crypts below the paved floor; some anomalies are clearly located in correspondence of the trapdoors visible along the nave, thus determining clearly positions and dimensions. At the same time the GPR reflections allowed verifying crypts' status: they seem to be intact and empty.

The TLS survey provided an accurate picture of the fractures and deformations inside the church: the most damaged portion is the altar area. Furthermore, other fractures are recognised in the lintel door of the bell tower and in some altars. However, it is not possible to identify the original cause of the damage since the use of bulldozers in the excavations worsened in some way the original setting of the site.

In conclusion, the survey confirms that lava did not damage the lower part of the church, whereas the walls reacted in a completely different way, firstly the lava weakened the northern and western walls and shortly after entered from the roof. The reconstruction interventions made by the restoration plan are consistent with our results.

References

Amico V.; 1757: *Dizionario topografico della Sicilia*, Tradotto dal latino ed annotato da Gioacchino Di Marzo, ristampa anastatica; Forni Ed., Palermo.

Boschi E. and Guidoboni E.; 2001: *Catania, terremoti e lave: dal mondo antico alla fine del Novecento*. INGV Roma, Bologna SGA.

Branca S., Azzaro R., De Beni E., Cheser D., and Duncan A.; 2015: *Impacts of the 1669 eruption and the 1693 earthquakes on the Etna Region (Eastern Sicily, Italy): An example of recovery and response of a small area to extreme events*. J. Volcanol. Geotherm. Res., **303**, 25-40.

Branca S., De Beni E., and Proietti C.; 2013: *The large and destructive 1669 AD eruption at Etna volcano: Reconstruction of the lava flow field evolution and effusion rate trend*. Bull. Vulcanol., **75**, 694.

Garozzo R.; 2017-2018: *La chiesa madre dell'antica Misterbianco in contrada Camapanazzu*, Tesi di Laurea, Università di Catania.

Garozzo R., Lo Turco M., Santagati, C.; 2019: *Modelli informativi e gestione della complessità per un progetto integrato di conoscenza*. Diségno**, 4**, 225-236.

COOK GLACIER-OCEAN SYSTEM, SEA LEVEL AND ANTARCTIC PAST STABILITY (COLLAPSE) PROJECT: PNRA CRUISE 2022 PRELIMINARY DATA

L. De Santis[1], F. Accaino[1], D. Accettella[1], J. Beagley[2], A. Bubbi[1], E. Colizza[3], F. Colleoni[1], F. Coslovich[1], D. Cotterle[1], A. Cova[1], L. Facchin[1], A. Gallerani[4], L. Gasperini[4], D. Gei[1], R. Gerin[1], M. Giorgi[1], V. Kovacevic[1], P. Mansutti[1], E. Mauri[1], S. Picotti[1], M. Petrini[1], E. Pochini[1], M. Santulin[1], R. Scipinotti[5], L. Ursella[1], A.C. Vallejo[6], F. Zgur[1], P. Zuppelli[1]

[1] National Institute of Oceanography and Applied Geophysics – OGS, Sgonico, Italy
[2] University of Otago, Dunedin, Nuova Zelanda
[3] Dept. of Mathematics and Geoscience, Trieste University, Trieste, Italy
[4] National Research Council –Marine Science Institute– CNR-ISMAR, Bologna, Italy
[5] ENEA-UTA, Bologna, Italy
[6] R&E Ocean Community Conservation Foundation, Oakville, ON, Canada

The Cook Glacier drains most of the Antarctic ice sheet covering the Wilkes Subglacial Basin (WSB), with an ice volume equivalent to a global sea rise of approximately 3-4 m. In this area of Antarctica, the base of the ice sheet is below sea level, and consequently it is vulnerable to variations in ocean temperature.

Long-term climate projections suggest that in this area of eastern Antarctica, hitherto considered colder and more stable, a rapid retreat of the ice sheet can be triggered in response to the intrusion of warm ocean waters (Circumpolar Deep Water, CDW). The disintegration of much of the ice shelf in front of the Cook in the 1970s and 1980s and the acceleration of the flow of ice in the eastern and inland areas of the WSB (2003-2007) could represent clues to the change in the balance of the system. However, neither the morphobathymetry of the continental shelf facing the Cook glacier, nor the present and past oceanography of the area is known. Therefore, it is not possible to know if there are or have been the conditions for the CDW to penetrate to the Cook grounding line. This information is essential for predicting the timing and modalities of the Cook glacier's reaction to ocean warming in the coming decades.

The COLLAPS (Cook glacier-Ocean system, sea LeveL and Antarctic Past Stability) project funded by the PNRA (National Research Program in Antarctica) aims to fill the lack of data and measurements in this area, about the current and past environment through a multidisciplinary geological, geophysical and oceanographic survey.

During the PNRA campaign of 2022, the COLLAPSE project mapped in detail with the geophysical instrumentation (Multibeam, subbottom Topas, multi-channel seismic and magnetometer) present on board the research ice breaker L. Bassi, two systems of canyons and embankments located at the mouth of the glacial valleys of the Cook and of Ninnis. Sediment cores were collected on each of them with the aim of obtaining information on the rate of accumulation, the origin of the sediments and the different processes active on the seabed today and in recent periods. It will therefore be possible, albeit indirectly, to reconstruct the dynamics of the different glaciers as a function of climatic variations and ocean circulation and estimate their respective contribution to global sea level rise.

During the COLLAPSE 2022 campaign, measurements of temperature, salinity, speed of currents and content of suspended biogenic material and on the seabed in the different areas of the embankment were also carried out. This information will be used to know the parameters that characterize the current environment, to be used as a reference guide to recognize similar characteristics in the geological record of the cores.

Acknowledgements.
We sincerely thank the Bassi's Commander Sedmak, the crew members, the logisticians, the technicians and the researchers on board the Bassi who did their utmost to carry out the various activities envisaged by the project, We thank Flippo Muccino (INGV) for making the magnetometer available and for acquiring magnetic data in the COLLAPSE project area, which were not initially foreseen. Thanks to Paul Watcher, German Space Agency (DLR) for providing the Sentinel-1D and Sentinel-3 sea ice satellite images in addition to the AMSR2 satellite data available in ship, thanks to Stefano Ferriani (ENEA). Thanks to IHS for licensing the Kingdom interpretation software. Thank Amy Leventer (Colgate Univ. NY, USA) and Mauro Celussi (OGS) for providing all the material for the water filtering. Thanks to Pasquale Castagno (univ Partenope, Na), Dongseob Shin (KOPRI) and Craig Stevens and Philip Sutton (NIWA, NZ) who supplied us with XBT and XCTD

QUALI PICCHI H/V SONO VERE RISONANZE NEL BACINO SEDIMENTARIO PADANO?

M. Di Donato, S. Castellaro

Dipartimento di Fisica e Astronomia – Alma Mater Studiorum Università di Bologna, Bologna, Italia

Delle curve H/V del microtremore è comunemente detto che la loro frequenza ricalca le frequenze di risonanza attese nel sito in termini di onde SH, mentre la loro ampiezza sarebbe una sottostima dei rapporti H/V in condizioni sismiche (SESAME, 2004; Molnar *et al.,* 2018).

Nei bacini a basso rapporto di aspetto (ossia molto larghi rispetto alla profondità, quindi assimilabili a condizioni 1D), l'ampiezza dei picchi H/V del microtremore è generalmente legata ad un minimo locale nella componente verticale del moto (Fig. 1A, B), legato ad una caratteristica dell'ellitticità dell'onda di Rayleigh che si verifica a frequenze prossime a quella di risonanza delle onde SH (Lermo and Chavez-Garcia 1994, Tuan *et al.,* 2011)

In altri casi, oltre a detto minimo sulla verticale, possono comparire dei picchi sulle componenti orizzontali (Fig. 1C, D) la cui presenza può essere associata a fenomeni di risonanza vera e propria delle onde SH, oppure ad altri fenomeni connessi alle onde di superficie (es. onde di Love).

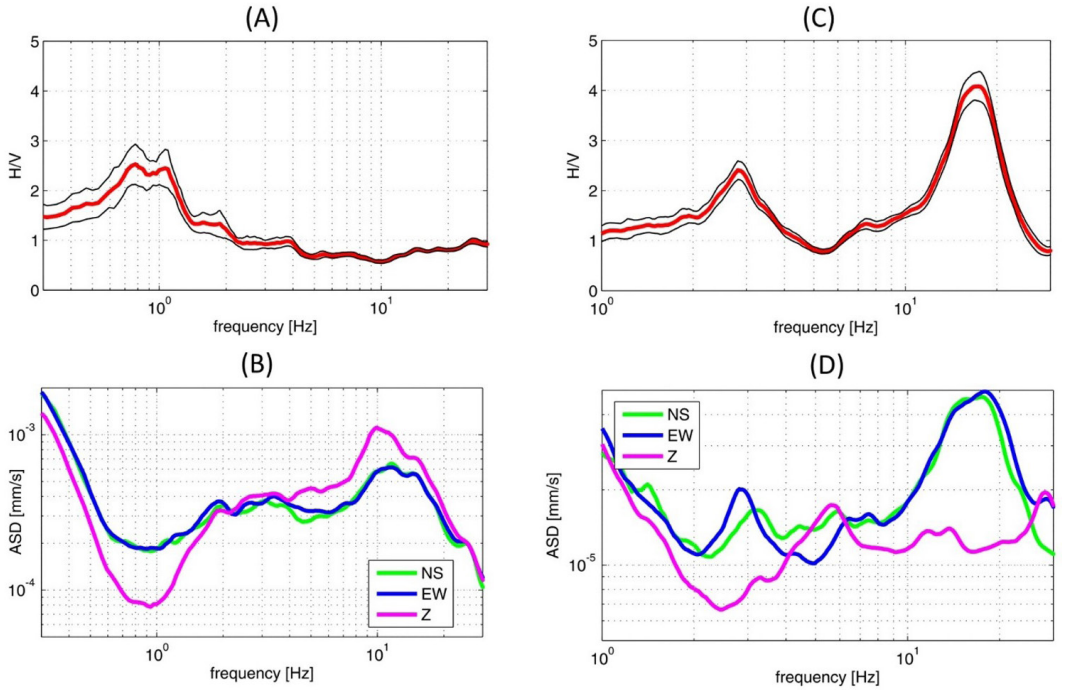


Fig. 1 – A), C) curve H/V del microtremore e B), D) spettri delle singole componenti del moto da cui sono derivate. Nel caso A), B) si osserva che il picco H/V è determinato da un minino locale della componente spettrale verticale. Nel caso C), D) i picchi H/V sono determinati principalmente da dei massimi locali nelle componenti spettrali orizzontali (Castellaro, 2016).

Più spesso nelle zone di pianura, dove dominano le risonanze così dette monodimensionali, i picchi H/V sono legati al solo minimo locale sulla componente verticale (caso A, B in Fig. 1). Nei bacini sedimentari montani a rapporti di aspetto alti, invece, dominano le risonanze in senso stretto, che appaiono come picchi nitidi sulle componenti orizzontali del moto (vd. anche presentazione di Lattanzi *et al.*, 2022, in questo convegno e Fig. 1C, D). In questi ambienti sono peraltro ben riconoscibili modi di vibrare distinti nelle direzioni principali orizzontali.

In questo lavoro ci concentriamo sulla Pianura Padana che è un bacino sedimentario a rapporto di aspetto molto basso. Stiamo costruendo un modello dinamico tridimensionale agli elementi finiti del bacino padano e il nostro obiettivo è di calibrare il modello sfruttando le frequenze di risonanza misurate localmente.

Per il bacino Padano sono comunemente riconosciute, tramite tecnica H/V, risonanze caratteristiche attorno a 0.8 Hz (Tarabusi and Caputo 2016, Mascandola *et al.*, 2019, Martelli 2021) e talvolta anche a frequenze minori. Al di là del caso della zona della dorsale Ferrarese, ove le frequenze di risonanza legate al bedrock a bassa profondità sono decisamente chiare, l'analisi da noi condotta di altre 22 stazioni sismiche dislocate nella pianura (Fig. 2) sembrerebbe mostrare che i picchi spettrali a frequenze minori di 0.6 Hz siano in realtà associati a perturbazioni atmosferiche o a forzanti di tipo marino, poiché non sono pressoché mai picchi stabili in frequenza. Compaiono, scompaiono, e traslano in una ampia gamma di frequenze e sono più abbondanti in inverno che in estate. Da una risonanza legata alla stratigrafia ci aspettiamo invece una forte stabilità in frequenza nel tempo (non invece una stabilità in ampiezza). Nel bacino padano ci sono con molta probabilità risonanze stratigrafiche anche a frequenze inferiori a 0.6 Hz ma la potenza delle forzanti sembra sovrastarle.

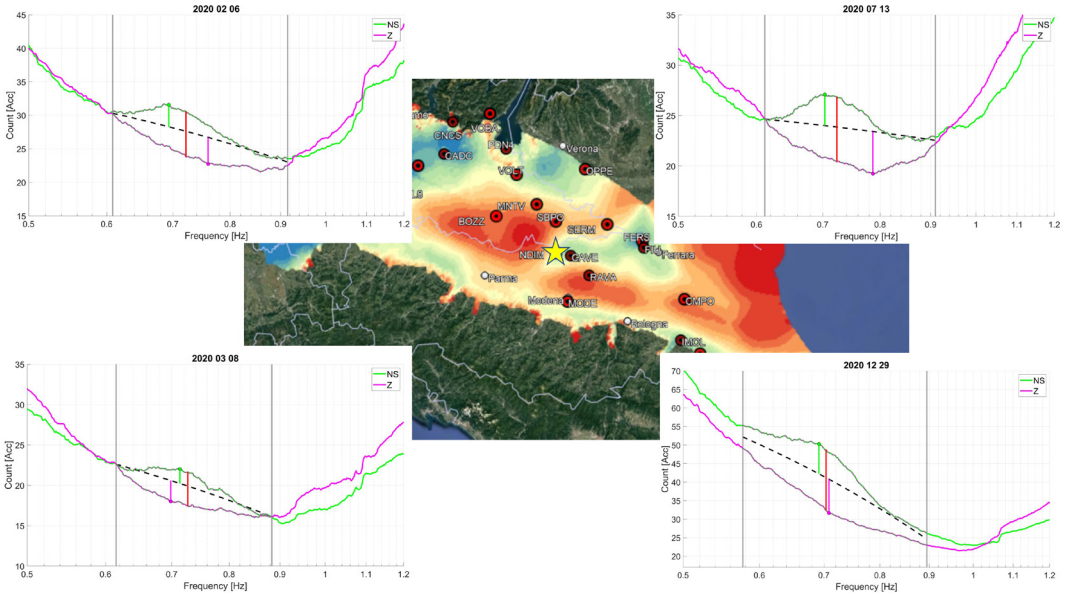


Fig. 2 – *Cerchi rossi nella mappa:* alcune delle stazioni sismiche permanenti analizzate nella Pianura Padana. *Stella gialla:* stazione sismica presso Novi di Modena (NDIM). *Vertici del pannello centrale*: spettri in ampiezza in accelerazione in diversi giorni dell'anno della stazione NDIM. La curva verde rappresenta la componente orizzontale (NS) e magenta la verticale (Z). Le barre di colore verde, magenta e rosso indicano il massimo della componente orizzontale rispetto al rumore di fondo (linea a tratteggio), il minimo della componente verticale rispetto alla stessa linea del rumore di fondo e l'ampiezza massima del rapporto H/V nell'intervallo di frequenza considerato (linee verticali).

Abbiamo pertanto selezionato alcune stazioni sismiche che presentassero caratteristiche di stabilità in frequenza nel tempo dei picchi nelle componenti spettrali orizzontali (risonanze longitudinali/trasversali in s.s.) e nei picchi delle curve H/V del microtremore sotto 1 Hz (Fig. 2). Per queste stazioni, abbiamo studiato cosa governa l'ampiezza delle curve H, V e H/V su base annuale. L'obiettivo è riconoscere, tra le altre cose, in quali condizioni di tremore ambientale risultano eccitate le risonanze in senso stretto (picchi sulle componenti orizzontali del moto) e studiare la variabilità nella stima delle risonanze attraverso i massimi sulle orizzontali, i minimi sulle verticali o i picchi H/V.

Presentiamo qui il caso della stazione Novi di Modena (NDIM), stazione di tipo accelerometrico, equipaggiata con strumento Kinemetrics Episensor e lo generalizzeremo nei prossimi mesi con i risultati di altre stazioni padane che stiamo già analizzando.

Come illustrato in Fig. 2, abbiamo scritto un algoritmo che identifica in automatico le forme ad ogiva che si instaurano negli spettri orizzontali e verticali del tremore sismico in corrispondenza delle frequenze di picco H/V. La distanza massima tra H e V (tratto rosso in Fig. 2) indica l'ampiezza del rapporto H/V calcolato nel modo convenzionale descritto per esempio in SESAME (2004).

Abbiamo considerato come livello medio del rumore di fondo il segmento che collega gli estremi delle ogive (tratteggi grigi n Fig. 2) e, rispetto a tale livello convenzionale medio del rumore di fondo, abbiamo calcolato l'ampiezza del picco orizzontale (tratto verde in Fig. 2) e l'ampiezza del minimo della componente verticale (tratto magenta in Fig. 2). Assumiamo questi valori come indicatori rispettivamente dell'ampiezza della risonanza in senso stretto (massimo delle componenti orizzontali) e delle caratteristiche legate alle onde di superficie di tipo Rayleigh (minimo sulla verticale).

In generale osserviamo che:

1. la frequenza calcolata mediamente attraverso il minimo della verticale è maggiore di quella calcolata attraverso il massimo delle componenti orizzontali (Fig. 3B)
2. la frequenza di picco dell'H/V è un valore intermedio tra le due (cfr. anche Tab. 1).

Tab. 1 - Tabella riassuntiva dei valori medi e relative deviazioni standard per la frequenza e l'ampiezza calcolati per la stazione sismica NDIM.

	Frequenza [Hz]		**Ampiezza [unità dell'accelerometro]**
Da minimo della verticale	I trimestre	0.733 ± 0.007	4.063 ± 2.147
	II trimestre	0.748 ± 0.008	
	III trimestre	0.752 ± 0.012	
	IV trimestre	0.731 ± 0.019	
Da massimo delle orizzontali	I trimestre	0.707 ± 0.014	3.228 ± 2.072
	II trimestre	0.698 ± 0.013	
	III trimestre	0.721 ± 0.017	
	IV trimestre	0.691 ± 0.008	
Da H/V	0.716 ± 0.027		1.319 ± 0.105

Pertanto, se i massimi locali sulle componenti spettrali verticali fossero le vere risonanze SH dei bacini, questi valori sarebbero leggermente sovrastimati in frequenza quando si identificano per via indiretta attraverso la tecnica H/V. Leggera sovrastima che, in ogni caso, a frequenze minori di 1 Hz significa differenze di diverse decine di metri in termini di profondità dei riflettori associati.

Notiamo anche che nei mesi estivi la frequenza tende ad essere maggiore che nei mesi invernali (Fig. 3B), e questo ricalca quanto discusso da Lattanzi *et al.* (2022) in questo stesso convegno. Le possibili ipotesi per questo aumento in frequenza sono descritte in dettaglio in quel lavoro (effetti termici sul bacino, effetti barometrici, deriva termica del clock che governa la frequenza di campionamento degli strumenti, sensibilità del picking dei valori di massimo e minimo spettrale al livello di rumore di fondo generale, effetto delle variazioni termiche sugli altri componenti elettronici dei circuiti force-balanced operanti presso le stazioni sismiche/accelerometriche impiegate), a cui rimandiamo. Nella figura 3A osserviamo anche che nei mesi estivi l'ampiezza sia del minimo spettrale verticale, sia del massimo spettrale orizzontale, decresce, rispetto al livello di rumore di fondo, verosimilmente come effetto di una minore

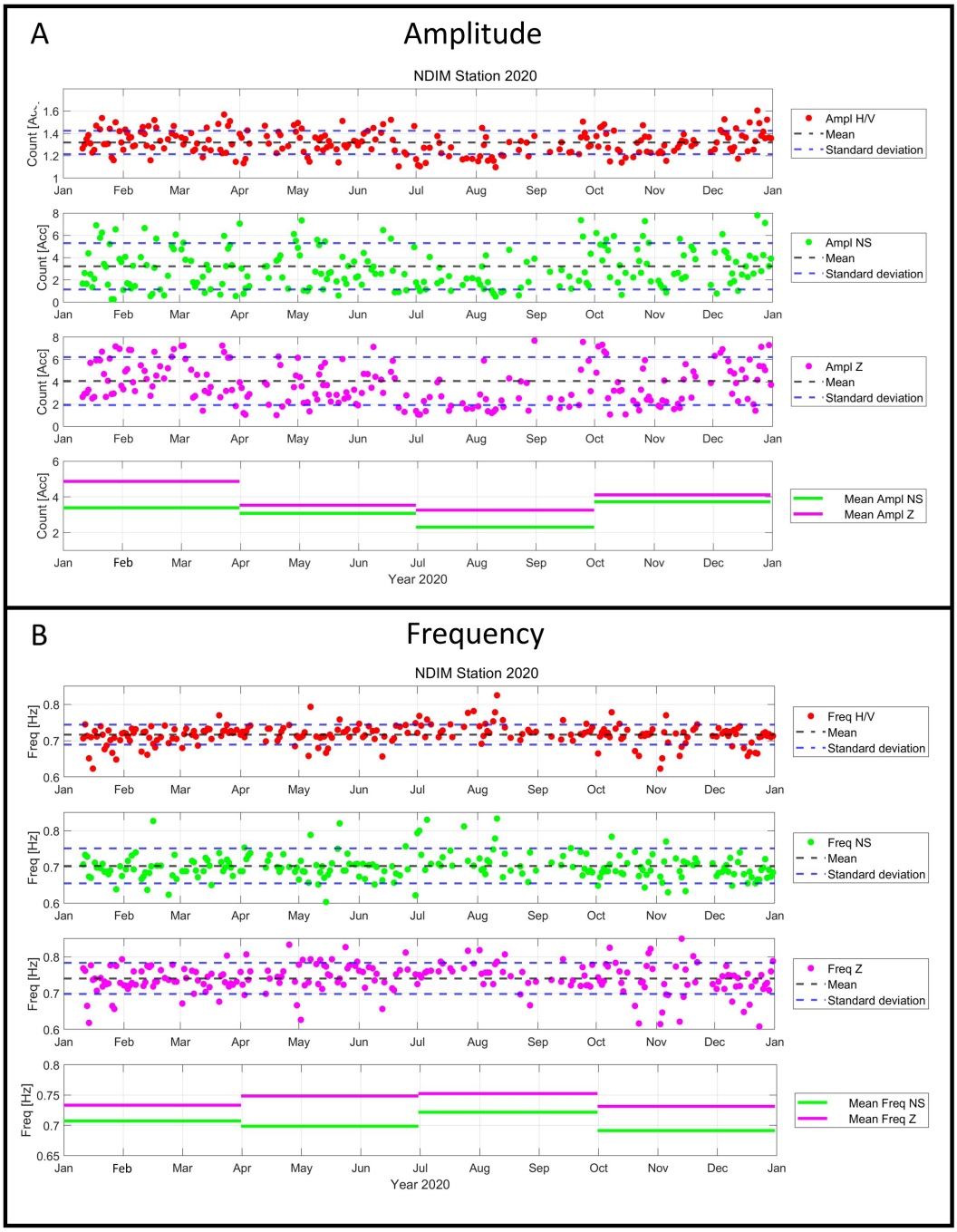


Fig. 3 – *A)* Distribuzione delle ampiezze di picco del rapporto H/V (rosso), del massimo locale sulla componente NS (verde) e del minimo locale della componente Z (magenta) nel 2020. Media e deviazione standard in nero e blu tratteggiato. Nel pannello inferiore valore medio trimestrale delle ampiezze delle rispettive componenti. *B)* Come A) ma in frequenza.

eccitazione generale della valle. La diminuzione delle due grandezze non è però dello stesso ordine di grandezza, poiché cala anche l'ampiezza del rapporto H/V associato.

È la componente verticale a decrescere in modo più marcato, il che suggerirebbe che sia l'ellitticità dell'onda di Rayleigh a risentire maggiormente del livello di eccitazione esterna, rispetto all'eccitazione per risonanza stratigrafica.

Riferiamo anche che le componenti EW del tremore sismico registrate dalle stazioni indicate in Fig. 2 appaiono difficilmente impiegabili per questo studio in quanto risultano mediamente molto più disturbate nell'intervallo di frequenze di interesse. Il motivo è da cercare probabilmente nella direttività delle forzanti che sono prevalentemente marine nel bacino padano, e quindi con direttività all'incirca EW.

Lo studio proseguirà nel tentativo di capire quale sia il livello di rumore di fondo massimo (inteso come forzante) che permette la visibilità o meno delle caratteristiche di risonanza locale del bacino padano e di stabilire quali dei picchi H/V, che sono comunemente misurati in superficie, siano effettivamente caratteri stabili a livello locale (e con quale risoluzione in frequenza) e quali siano invece prevalentemente legati alle forzanti di tipo meteorico e marino.

Bibliografia

Castellaro S.; 2016: *The complementarity of H/V and dispersion curves*, Geophysics 81 T323-T338.

Lachet C. & Bard P.Y.; 1994: *Numerical and theoretical investigations on the possibilities and limitations of Nakamuras technique*, J. Phys. Earth, 42, 377–397.

Martelli L.; 2021: *Assessment of Seismic Bedrock in Deep Alluvial Plains. Case Studies from the Emilia-Romagna Plain*. Geosciences, 11, 297. https://doi.org/ 10.3390/geosciences11070297.

Mascandola C., Massa M., Barani S., Albarello D., Lovati, S. Martelli, L.; Poggi V.; 2019: *Mapping the Seismic Bedrock in the Po-Plain (Italy) through ambient vibration monitoring*. Bull. Seism. Soc. Am. 109, 164–177.

Molnar S., Cassidy J.F., Castellaro S., Cornou C., Crow H., Hunter J.A., Matsushima S., Sánchez-Sesma F.J., Yong A.; 2018: *Application of Microtremor Horizontal-to-Vertical Spectral Ratio (MHVSR) Analysis for Site Characterization: State of the Art*, Surveys in geophysics 39 613 – 631.

SESAME Project,; 2004: *Guidelines for the Implementation of the H/V Spectral Ratio Technique on Ambient Vibrations. Measurements, Processing and Interpretation.* SESAME European Research Project WP12 - Deliverable D23-12.

Tarabusi G. & Caputo R.; 2016: *The use of HVSR measurements for investigating buried tectonic structures: The Mirandola anticline, northern Italy, as a case study.* Int. J. Earth Sci.106, 341–353.

Tuan T. T., Scherbaum F., Malischewsky P. G.; 2011: *On the relationship of peaks and troughs of the ellipticity (H/V) of Rayleigh waves and the transmission response of single layer over half-space models*. Geophys. J.Int., 184, 793–800.

MULTISENSOR GEOPHYSICAL APPROACH FOR REBAR MONITORING

G. Fornasari[1,2], L. Capozzoli[2], G. De Martino[2], V. Giampaolo[2], E. Rizzo[1,2]

[1] University of Ferrara, Dipartimento di Fisica e Scienze della Terra, Ferrara, Italy
[2] CNR – IMAA, Laboratorio Hydrogeosite, Marsico Nuovo, Italy

Introduction. This work describes a laboratory test on rebar corrosion monitoring by a multisensor geophysical methods: GPR and electrical methods. Rebar corrosion is one of the main causes of deterioration of engineering reinforced structure. This degradation reduces the service life and durability of the structures. Such degradation can result in the collapse of engineering structures. Non-destructive testing and evaluation of the rebar corrosion is a major issue for predicting the service life of reinforced concrete structures. The experiments were performed at Geophysical laboratory of University of Ferrara, where a concrete sample of about 500mm x 300mm with one steel rebar of 10 mm diameter and 40cm long was used. The experiment defined an accelerating rebar corrosion with direct current (DC) power supply along the rebar and a partial immersion of the sample in a 5% sodium chloride (NaCl) solution inducing the corrosion phenomena. The 2GHz GPR antenna by IDS and Self-Potential with unpolarized referenced electrode acquired by Keithley multivoltmeter at high impedance were used for rebar corrosion monitoring. The collected data were used for an integration observation to define the evolution of the phenomenon of corrosion on the reinforcement bar.

Methods. Laboratory sample was built with fast concrete based on special binders, quartz and synthetic additives and develops high mechanical strength in a very short time. The sample was built with one improved grip steel rebar of 10 mm diameter and a length of 350 mm (fig.1). The exposed length of the rebars is 2.5 cm per side. The concrete thickness was 30 mm in the upper part and 40 mm in the lower part. For each survey with the georadar 60 radargrams of 500 mm length are acquired; the trace increment set is 1.379mm and the sampling is 512. After each georadar survey, Self-Potential (SP) acquisition was carried out on the sample. The SP signals is based on the electrical and electrolytic continuity between rebar in concrete, reference electrode on the sample surface and a high-impedance voltmeter. The

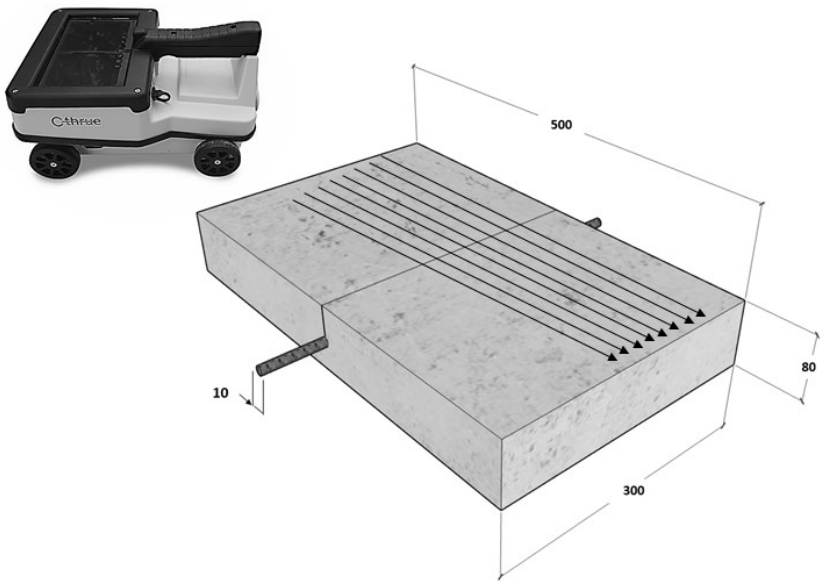


Fig. 1 - Laboratory sample and acquisition with the GPR C-TRUE antenna.

SP was acquired by a fixed cable to the rebar and an unpolarizable electrode as reference (Petiau electrode). The measurements were carried out by covering the entire surface of the sample according to a predetermined mesh of 54 points. The unpolarizable electrode was connected to the Keithley multivoltmeter at high impedance, while the positive pole was connected to the armature bar. At each movement of the electrode, the measurement of the spontaneous potential in (mV) and the contact resistance (Ohm) was carried out. Once the accelerated corrosion test was started, geophysical investigations were carried out every 24 h. The power supply was turned off after 15 days from the start of the test. At the end of the corrosion of the concrete sample, and disconnected the power supply, we performed 5 investigations to define a final state of the phenomenon. Finally, the sample was taken out of the water and NaCl solution and once it had completely dried. The acquired radargrams were elaborated by Reflex software and

Results and discussions. The acquired radargrams were elaborated with ReflexW (Sandmeier software) and the base elaboration was applied. Moreover, an envelope trace analysis was applied. The envelope data set of each radargrams was compared with the previous one and the trace corresponding to the steel rebar was studied on all radargrams. The envelope signal of the steel rebar shows an increase in the strength of signal as corrosion increases. A greater increase in the envelope signal was observed where we observed greater corrosion in the steel rebar inside the sample and near the edges of the concrete, where the bar had a large damage due to corrosion.

The acquired SP signals and the contact resistances were depicted as a map distribution. The contour maps defined a strong variation in the potential data highlighting the dangerous corrosion phenomena where the GPR depicted large envelope signals.

From the investigations conducted on the reinforced concrete sample using GPR and studying the envelope signal over time, we obtained a correlation with the spontaneous potential investigations in defining the areas where we had corrosion and the areas of the steel rebar most corroded.

Moreover, extrapolating laboratory results performed with a single rebar to a large structure with interconnected rebars thus remains challenging. Therefore, during the next experiments, special care must be taken regarding the design and preparation of the samples to obtain meaningful information for field application.

References

Ahmad Zaki, Megat Azmi Megat Johari, Wan Muhd Aminuddin Wan Hussin and Yessi Jusman (2018). International Journal of Corrosion Volume 2018, Article ID 5389829, 10 pages https://doi.org/10.1155/2018/5389829

Ramzi Adriman; Israr Bin M. Ibrahim; Syifaul Huzni; Syarizal Fonna; Ahmad Kamal Ariffin (2022). *Improving half-cell potential survey through computational inverse analysis for quantitative corrosion profiling.* Case Studies in Construction Materials, ISSN: 2214-5095, Vol: 16, Page: e00854

Romain Rodrigues, Stéphane Gaboreau, Julien Gance, Ioannis Ignatiadis, Stéphanie Betelu. *Reinforced concrete structures: A review of corrosion mechanisms and advances in electrical methods for corrosion monitoring.* Construction and Building Materials, Elsevier, 2020, pp.121240. f10.1016/j.conbuildmat.2020.121240ff. ffhal-02979786ff

LA STABILITÀ IN FREQUENZA DELLE RISONANZE NEI BACINI SEDIMENTARI

G. Lattanzi, S. Castellaro, M. Di Donato

Dipartimento di Fisica e Astronomia – Alma Mater Studiorum Università di Bologna, Bologna, Italia

Le frequenze di risonanza dei corpi sedimentari sono impiegate da diversi anni sia agli scopi di previsione della risposta sismica locale, sia – mediante inversione di diverso tipo – come strumenti di prospezione geofisica per stimare le profondità dei bedrock sismici.

È opinione comune che, affinché le frequenze di risonanza siano riconoscibili in condizioni di eccitazione ambientale, i bacini sedimentari debbano essere eccitati da rumore bianco o che l'andamento della forzante debba essere eliminato attraverso i rapporti spettrali H/V. Il microtremore ambientale, però, non è decisamente bianco (Peterson, 1993) e dividere le componenti orizzontali (H) per quelle verticali (V) non è concettualmente appropriato perché anche le componenti verticali portano in sé – pure se con minore ampiezza - le risonanze verticali. In realtà, nei bacini sedimentari profondi, le frequenze di risonanza emergono chiaramente anche osservando semplicemente gli spettri individuali del moto in condizioni di microtremore. Negli ultimi anni è stata dedicata particolare attenzione allo studio delle risonanze in questi bacini (valli alpine) poiché i rapporti tra le frequenze modali nelle diverse direzioni principali e le successioni di modi superiori sono legate alla forma del bacino (Sgattoni e Castellaro, 2020; Castellaro e Musinu, 2021) e possono essere impiegate come strumento di prospezione geofisica.

Sperimentalmente, il riconoscimento delle frequenze modali può essere effettuato usando i rapporti spettrali tra coperture e bedrock (Roten *et al.*, 2006), impiegando stazioni multiple sincronizzate (Ermert *et al.*, 2014), o anche stazioni singole (Sgattoni and Castellaro, 2020). L'uso di stazioni multiple permette di ricostruire anche le forme modali e quindi di associare le frequenze di risonanza a modi specifici di vibrare del bacino ma in realtà anche le registrazioni di stazioni asincrone hanno, per via indiretta, questa possibilità.

Un aspetto fondamentale dell'impiego delle frequenze di risonanza come strumento di prospezione sismostratigrafica è stabilire con quale precisione sia possibile determinare sperimentalmente le autofrequenze. In questo studio ci siamo pertanto concentrati sulla stabilità temporale delle frequenze di risonanza nei bacini alpini.

Abbiamo selezionato 4 stazioni sismiche poste entro grandi bacini alpini in Italia (GARG, valle dell'Adige), Francia (OGFO, valle del Isère) e Svizzera (SIOO, SEFS, valle del Rodano e del Reuss rispettivamente), tutti con rapporti di aspetto compresi tra 0.3 e 0.6. Tali stazioni sismiche, appartenenti a diverse reti, sono equipaggiate con accelerometri e distribuiscono dati in continuo accessibili mediante la piattaforma IRIS.edu.

Abbiamo analizzato i dati di microtremore di dette stazioni, ruotandoli dagli assi NS, EW standard di acquisizione, alle direzioni principali delle valli (longitudinale e trasversale) e sono emersi in tutti i casi in modo molto netto i modi longitudinali di vibrare (L_i), i modi trasversali (T_i) e in molti casi anche quelli verticali (V_i), le cui forme caratteristiche sono date in Figura 1. Per i principi base dell'identificazione modale sperimentale si rimanda a Sgattoni e Castellaro (2020) e Castellaro e Musinu (2021).

In queste stazioni abbiamo studiato l'andamento delle frequenze modali su 5 anni, processando i dati su finestre di 10 minuti per 30 minuti, 1 ora e 6 ore giornaliere, e studiando segmenti di registrazione che andassero da 30 min fino a 5 anni. In media per ciascun set di 5 anni abbiamo calcolato circa 275.000 valori di frequenza per ciascun modo di vibrare, su base di finestre spettrali di 10 minuti di durata. Abbiamo verificato che aumentare la dimensione delle finestre non porta ad una maggior chiarezza del risultato.

Abbiamo potuto osservare che la stabilità in frequenza dei modi di vibrare identificati è quasi sorprendente a qualsiasi scala temporale li si osservi (Figura 2). Che le risonanze siano proprietà intrinseche dei corpi sedimentari e, in quanto tali, stabili nel tempo è assolutamente

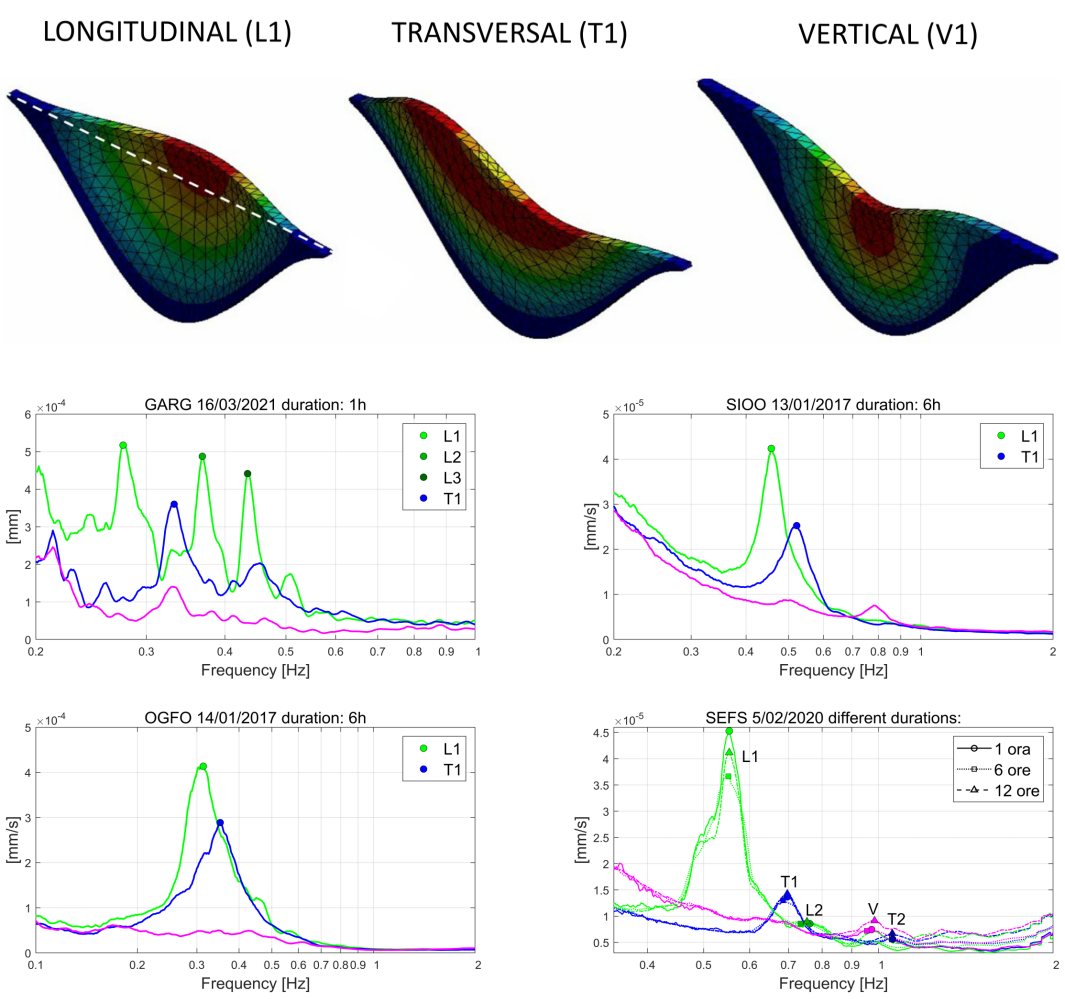


Fig. 1- in alto: rappresentazione delle forme modali di una sezione tipica trasversale di un bacino sedimentario fluviale: modo longitudinale (L1), trasversale (T1) e verticale (V1). In basso: spettri delle singole componenti del microtremore (verde, componente longitudinale: blu componente trasversale, magenta componente verticale) delle quattro stazioni sismiche oggetto di studio. Gli spettri sono mediati su finestre della durata riportata nel titolo o legenda di ciascun grafico.

chiaro dal punto di vista teorico, tuttavia è meno scontato che lo siano anche in condizione di eccitazione non libera ma forzata da forzanti decisamente non stazionarie quali il microtremore sismico. I modi di vibrare appaiono oltretutto nitidamente stabili in frequenza sia alla scala di poche ore, giornaliera, sia alla scala annuale e pluriennale. In Figura 2 riportiamo il caso della stazione GARG, monitorata per oltre un anno, e la stabilità in frequenza dei suoi primi 3 modi longitudinali e del primo trasversale.

In Tabella 1 riportiamo la frequenza media calcolata annuale e le percentuali di incertezza quando la stima viene effettuata su base di misure di 30 minuti, 1 ora, 6 ore, 12 ore, 1 settimana, 1 mese.

Questo è un risultato molto importante perché conforta sul fatto che in queste grandi valli alpine le caratteristiche proprie dinamiche della valle (i modi propri) dominano indipendentemente dalla forzante. La forzante ha invece un grande peso sull'ampiezza dei modi stessi ed anche sul loro smorzamento, come mostreremo in sede di presentazione.

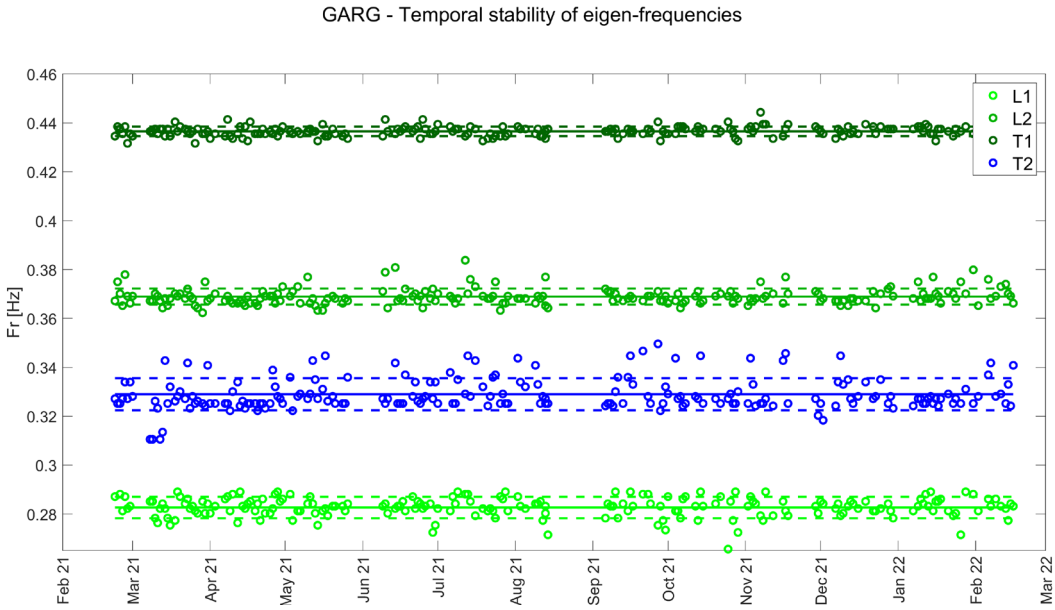


Fig. 2 - Frequenze modali longitudinali (L1, L2, L3) e trasversali (T1) registrate dalla stazione GARG, collocata all'interno della valle dell'Adige nel corso dell'anno 2021, su misure giornaliere di durata oraria. Sono inoltre indicati con linea continua il valore medio e con linea tratteggiata la deviazione standard calcolate. In questo caso i dati vengono da una stazione sismica predisposta allo scopo dagli autori.

Tab. 1 - Valore medio annuale delle autofrequenze riconosciute per la stazione SEFS e percentuali di incertezza associata quando la stima viene effettuata su base di misure di 30 minuti, 1 ora, 6 ore, 12 ore, 1 settimana e 1 mese.

	L1	L2	T1	T2	V1
Valore medio [Hz]	0.552	0.751	0.696	1.060	0.978
Incertezza su 30 min	5.5%	2.6%	4.1%	2.5%	3.3%
Incertezza su 1 h	3.4%	2.1%	2.0%	2.3%	3.3%
Incertezza su 6 h	0.6%	2.1%	1.6%	1.4%	2.7%
Incertezza su 12 h	0.6%	1.7%	0.6%	1.2%	2.4%
Incertezza su 1 sett.	0.1%	0.5%	0.5%	0.4%	0.6%
Incertezza su 1 mese	0.1%	0.2%	0.3%	0.2%	0.6%

Uno zoom sui dati (Figura 3) rivela però un'altra caratteristica: le frequenze di risonanza, particolarmente per i modi superiori, mostrano una fluttuazione annuale netta, aumentando d'estate e diminuendo di inverno, il che si tradurrebbe in:

a. un aumento della rigidezza estiva oppure
b. una diminuzione della massa estiva oppure
c. una diminuzione dello smorzamento nel caso estivo.

Sebbene l'ultima ipotesi sia anche plausibile (in estate l'ampiezza media del moto è minore per via della minor sollecitazione atmosferica e lo smorzamento è noto diminuire con l'ampiezza del moto), abbiamo pensato a diverse possibili cause per questa evidenza sperimentale:

1) ***Effetti termici*** sul bacino e/o sulle rocce circostanti, che includono il bacino. Riteniamo l'ipotesi poco probabile poiché l'effetto dell'irraggiamento solare cessa a pochi metri di profondità mentre questi bacini sono profondi centinaia di metri e perché l'aumento di temperatura generalmente nei corpi elastici comporta una diminuzione di rigidezza,

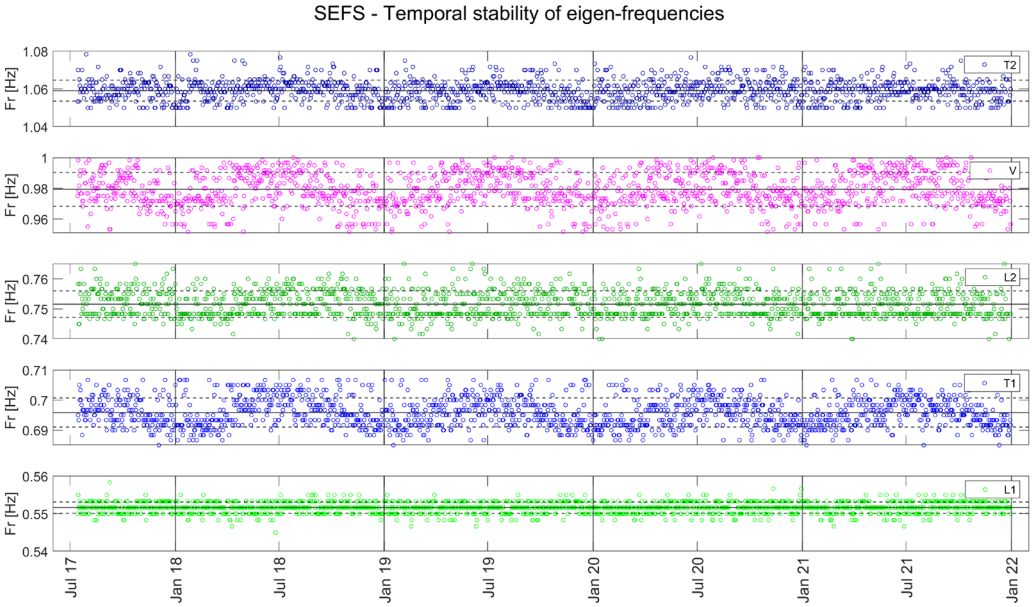


Fig. 3 - Frequenze modali longitudinali (L1, L2), trasversali (T1, T2) e verticali (V) relative alla stazione SEFS, equipaggiata con sensore accelerometrico forced-balance e collocata all'interno della valle del Reuss. Lo studio è stato effettato su misure giornaliere aventi durata di sei ore per l'intervallo di tempo compreso tra luglio 2017 e dicembre 2021. Sono inoltre indicati con linea continua il valore medio e con linea tratteggiata la deviazione standard calcolate per ogni frequenza modale riconosciuta.

e quindi di frequenza, mentre noi osserviamo un aumento di frequenza. Non è probabilmente nemmeno pensabile che la valle risponda alle fluttuazioni termiche con un ritardo (inerzia) di 6 mesi.

2) ***Effetti barometrici*** legati al fatto che tra estate e inverno la pressione atmosferica (quindi il carico sulla valle) cambia. Tradotte in variazione di massa sul bacino, le fluttuazioni barometriche (100 kPa minima estiva, 104 kPa massima invernale) equivalgono però ad un aumento/diminuzione di massa equivalente pari a poche decine di centimetri di spessore di terreno.
3) ***Deriva termica del clock che governa la frequenza di campionamento degli strumenti***. Poco plausibile in quanto i dati di campionamento sono corretti secondo il tempo assoluto fornito dal GPS.
4) ***Problemi di picking dei dati.*** I picchi di risonanza in inverno appaiono più netti perché l'eccitazione è maggiore. In questo caso la frequenza centrale del picco sarebbe campionata con maggior precisione mentre d'estate il picco spettrale è più basso e ampio e questo potrebbe portare ad una fluttuazione maggiore nei valori di frequenza di picco registrati in automatico. In questo caso però ci si aspetterebbe che il picking fosse poco preciso in modo casuale per eccesso e per difetto, in estate, cosa che non è. In estate la frequenza appare sistematicamente maggiore che in inverno.
5) ***Effetto delle variazioni termiche sugli altri componenti elettronici dei circuiti force-balanced*** (condensatori, costanti di tempo dei circuiti e così via).

Tale fluttuazione è apprezzabile anche su scala giornaliera, seppur meno accentuata, con un aumento relativo delle frequenze modali nelle ore diurne rispetto a quelle notturne.

Nel momento in cui scriviamo la ricerca è ancora aperta e stiamo studiando nel dettaglio i dati di altre stazioni e la questione elettronica connessa a questa tipologia di strumenti per tentare di dare risposta e a queste domande.

Nel frattempo, però, possiamo asserire che nelle grandi valli alpine le frequenze modali possono essere stabilite con fiducia anche con indagini molto semplici, a stazione singola ed estremamente brevi (pochi minuti) perché sono assolutamente stabili nel tempo, a meno di frazioni di percento ed in qualsiasi condizione meteo.

Sottolineiamo che tutto il nostro lavoro si è concentrato solo sulle autofrequenze maggiori di 0.2 Hz poiché sotto 0.2 Hz i fenomeni metereologici sono invece dominanti e si sovrapporrebbero a qualsiasi altra risonanza.

Bibliografia

Castellaro S. and Musinu G.; 2021: *Resonance vs. Shape of Sedimentary Basins*, Bull. Soc. Seism. Am., under review.

Ermert L. and Poggi V., Burjánek J., Fäh D.; 2014: *Fundamental and higher two-dimensional resonance modes of an Alpine valley*, Geophys. J. *Int* **198** 795–811.

Peterson J.; 1993: *Observations and modeling of seismic background noise.* USGS Open-File Report 93-322.

Roten D., and Fäh D., Cornou C., Giardini D.; 2006: *Two-dimensional resonances in Alpine valleys identified from ambient vibration wavefields,* Geophys. J. Int. **165** 889-905.

Sgattoni G. and Castellaro S.; 2020: *Detecting 1D and 2D ground resonances with a single-station approach*, Geophys. J. Int. **223**, 471-487.

QUATERNARY SLOPE INSTABILITY OFFSHORE SOUTHERN CALABRIA: INSIGHTS ON POSSIBLE TRIGGERING MECHANISMS

N. Markezic[1], S. Ceramicola[1], L. Baradello[1], G. Brancatelli[1], D. Morelli[2], E. Colizza[3]

[1] Istituto Nazionale di Oceanografia e di Geofisica Sperimentale – OGS, Trieste, Italy
[2] Università degli Studi di Genova – DISTAV, Genova, Italy
[3] Università degli Studi di Trieste – DISGAM, Trieste, Italy

Introduction. Submarine landslides are considered one of the most damaging geohazards to coastal population and infrastructures, and they frequently interest areas where submarine canyons incise continental margins. With the increased requirement of coastal geohazard assessment, seabed mapping and near seabed investigation become important prerequisite to reconstruct submarine failure and triggering mechanisms. The seabed morphology of the Ionian Margin of Calabria, a tectonically active margin, has been a matter of interest in the frame of the Italian projects MaGIC (Marine Geohazards along the Italian Coasts) and RITMARE (La Ricerca Italiana per il Mare). Numerous slide scars indicative of slope failures have been revealed by means of seabed mapping integrated with sub-bottom profile interpretation (Ceramicola *et al.,* 2014; Ceramicola *et al.,* 2014b; Morelli *et al.,* 2011). We here present an analysis of the possible triggering mechanism of slope failure that acted and influenced the stability of the seafloor, during the Quaternary evolution of the Assi slide in southern Calabria.

Geological setting. The Assi slide lies on the seabed of a forearc basin generated during the SE migration of the Calabrian arc since the Middle Miocene (Van Dijk, 1992; Roda *et al.,* 1964). The SE migration has slowed during the last 10 Ma (Mattei *et al.,* 2007) when a rapid uplift of onshore areas initiated (Westaway, 1993; Van Dijk 1992) steepening the slope offshore southern Calabria. This area is highly affected by canyon incisions remarkably close to the coastline, which are crucial in sediment transport from coastal areas into deep-water. In fact, the continental slope is eroded by several scarps that indicate recurrent and retrogressive slope failures. The Assi slide is located between the Siderno canyon system and the Assi canyon (Fig. 2).

Data. The geophysical datasets were acquired during three research campaigns: MESC (funded by the OGS and organized in collaboration with the University of Trieste, in 2005), MAGIC (funded by the Italian Civil Protection with the OGS, from 2005 to 2009) and GSGT15 (funded by MIUR in the framework of the project RITMARE, in 2015). Swath bathymetric data were acquired with Reason Seabat 8111 (100 kHz) and 8150 (12 kHz) for the creation of DTMs with a 10x10, 20x20 and 50x50 grid size. The sub-bottom profiler used is the Benthos Chirp II. Among these data, the ViDepi wells LUCIANA_001 e LUISA_001 were used to calibrate where possible the sub-bottom data.

Seabed mapping and acoustic facies mapping. Morphobathymetric data revealed numerous scarps on the continental slope in a depth range that goes from – 200 m to -950 m, as well as concave upwards and convex downwards morphological profiles indicating deposits and voids created by the failures. The slide scarps follow the slope dip orientation which is approximately 2°. The scarps located on the upper part of the continental slope are smaller but more arcuate, while those situated on the lower portion of the continental slope exhibit a larger lateral extension and height (Fig. 1).

Four acoustic facies were identified on the sub-bottom profiles: B, G, H and T (Fig. 1). The B echo-facies identifies a distinct bottom echo and an alternation of high-amplitude seismic reflectors and acoustic blanking levels in sub-bottom echoes. We infer these facies is related to hemipelagic or low-turbidite sedimentation with high-energetic processes. The G echo-facies

displays discontinuously bedded high-amplitude seismic reflectors with acoustic blanking zones suggesting fluid migration in the sediments. The H echo-facies shows a high-amplitude bottom echo with irregular hyperbolae with variable elevation of their vertex and no sub-bottom seismic reflectors. We suppose it is related to landslide deposits. The T echo-facies comprises a high-amplitude bottom echo followed by sub-parallel sub-bottom echoes that contain transparent lenticular bodies we infer relate to debris flow deposits.

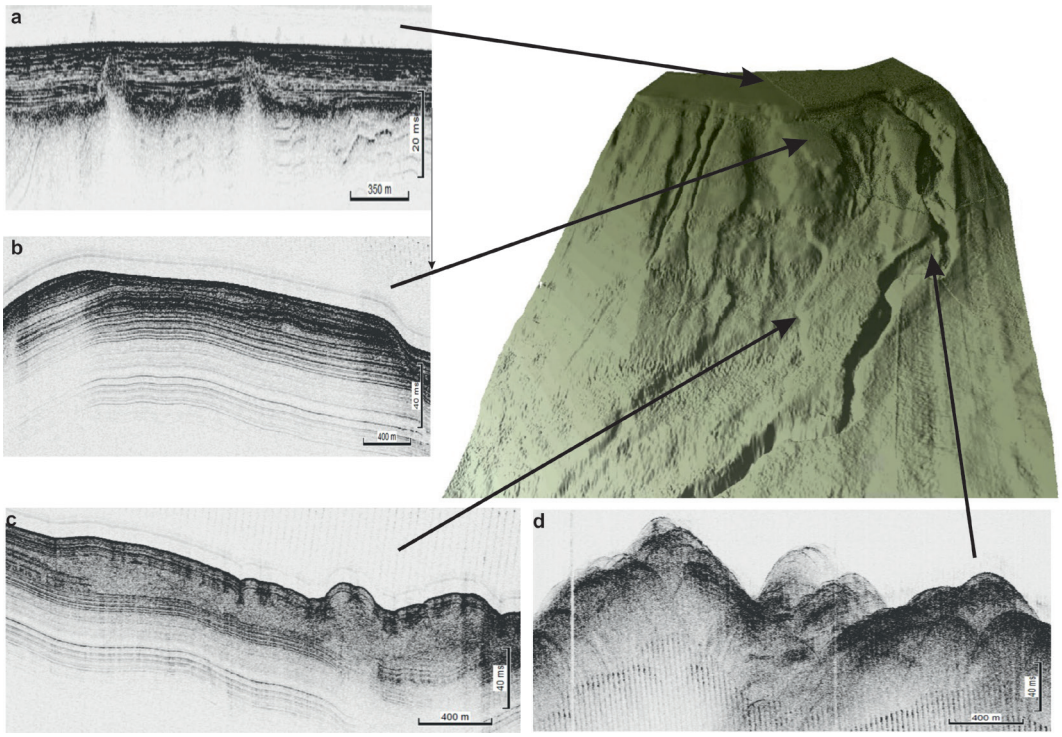


Fig. 1 - Four acoustic facies were identified on sub-bottom profiles. The G facies (a), B (b), T (c) and H (d) and their distribution along the study area.

Sub-bottom data allowed us to identify 4 relict pockmarks (on the continental shelf and slope), three main unconformities, polygonal faults, gas charged sediments and unstratified deposits. The unconformities mapped are low-angle and present on the continental shelf and slope. From the seabed down, the A1 unconformity is an erosive unconformity that correspond to the LGM episode and covers all the slide scarps. The U2 unconformity represents the glide plane for the inferred slope failures as a weak layer in the sedimentary column and extends from the headwall to the frontal ramp of the mapped slope failures (Fig. 2). The U3 unconformity is the basal glide plane of a failure that occurred before those interested by the U2 unconformity and mapped on the seabed, located on the lower part of the continental slope.

Triggers for slope failure. Excess pore-pressure has been suggested as a triggering mechanism of the multiple slope failure as a response to climatic cyclicity. It is known that upwards migrating fluids increase pore pressures within marine clays (Bunz *et al.,* 2005) which leads to a decrease in frictional resistance to sliding (Masson *et al.,* 2006). According to the Videpi wells present in the study area, clays are the lithology that occur along the margin. The overpressure that acts oppositely to the lithostatic pressure makes sediments extremely weak (Bunz *et al.,* 2005). Weak layers that correspond to the U2 and U3 unconformity, could also be

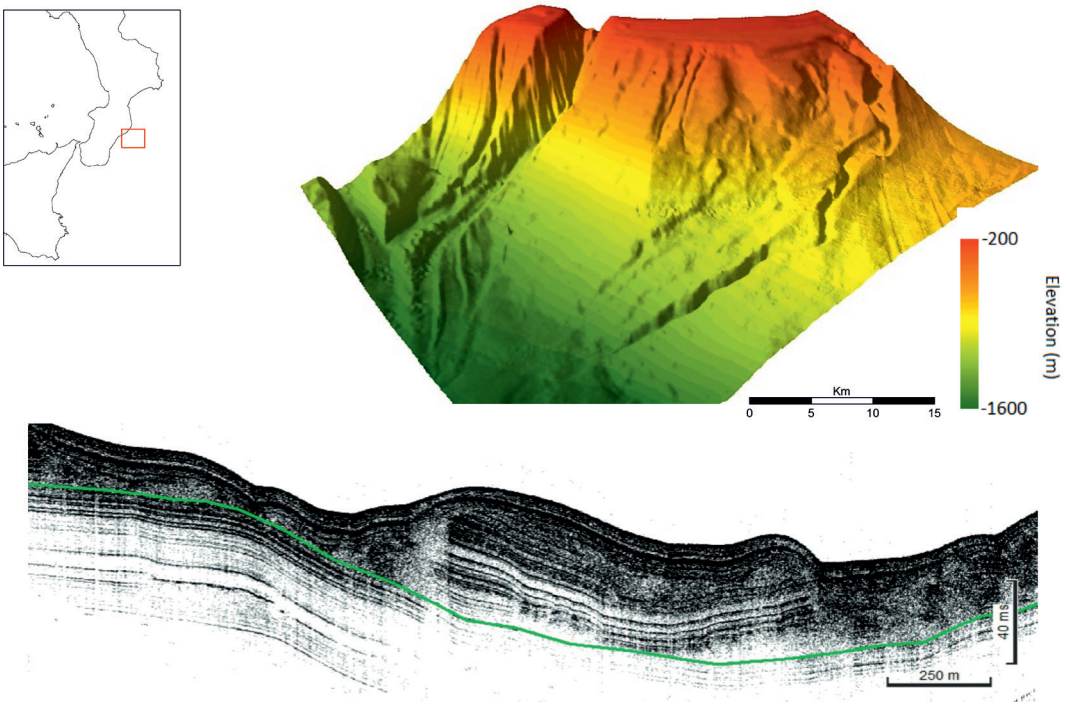


Fig. 2 – Location of the study area and the U2 unconformity which we infer may represent the glide plane for the mapped slope failures.

sediments deposited or reworked by bottom currents, which are also known sources of this type of layers (Rebesco, 2005) or a metastable fine-grained layer that liquified under cyclic loading (Barnes *et al.,* 1991). The presence of a weak layer is consistent with the deposition of an unit at a lower sea-level as during glacial periods, and the information provided by the wells present in the study area. Indirect evidence of migrating fluids are pockmarks and the presence of polygonal faults. Other factors that had an impact on the seafloor stability are the rapid uplift since Early Pliocene and the erosion which can lead to a local oversteepening of the slope (Morgenstern, 1967).

Conclusion. The integration of seabed mapping and acoustic facies represent a particularly useful tool in assessing geohazards and, in this case, determining the possible triggers of submarine landslides. The presence of gas in the sediments, combined with the identification of a weak layer constitute the main factors that controlled the occurrence of slope failures along the study area.

Acknowledgements. The authors acknowledge the Italian Civil Protection for funding the MAGIC project and MIUR (Italian Ministry of University and Research) for funding the RITMARE project and HIS Kingdom Suite for providing the educational grant. We are also grateful to colleagues Andrea Cova and Edy Forlin for the processing of multibeam data in the framework of the MAGIC project. Geophysical data have been acquired on board of the R/V Explora.

References

Barnes P.M.; Lewis K.B.; 1991: *Sheet slides and rotational failures on a convergent margin: the Kidnappers Slide, New Zealand.* Sedimentology, 38, 205-221.

Bunz S.; Mienert J.; Bryn P.; Berg K.; 2005: *Fluid flow impact on slope failure from 3D seismic data: a case study in the Storegga Slide.* Basin research, 17, 109-122.

Ceramicola S.; Tinti S.; Zaniboni F.; Praeg D.; Planinsek P.; Pagnoni G.; Forlin E.; 2014: *Reconstruction and tsunami modelling of a submarine landslide of the Ionian margin of Calabria (Mediterranean Sea).* Proceedings of World Landslide Forum 3, 2-6 June 2014, Beijing. Landslide Science for a Safer Geoenvironment, 3, Targeted Landslides, Ed. Springer.

Ceramicola S.; Forlin E.; Praeg D.; Cova A.; 2014: *Submarine Mass-Movements along the slopes of the active Ionian continental margins and their consequences for marine geohazards (Mediterranean Sea).* Advances in natural and technological hazards research, 37, 295-306.

Mangano G.; Ceramicola S.; Zecchin M.; Brancatelli G.; Critelli S., 2022: *Geohazard-Related Geomorphic features in the Crotone-Spartivento Basin (Southern Italy): an Expression of Calabrian Arc Kinematics.* OMC Med Energy Conference and Exhibition (Price for best Presentation).

Masson D.G.; Harbitz C.B.; Wynn R.B.; Pedersen G.; Lovholt F.; 2006: *Submarine landslides: processes, triggers, and hazard prediction.* Philos. Trans. R. Soc. A Math. Phys. Sci, 364.

Mattei M.; Cifelli F.; D'Agostino N; 2007: *The evolution of the Calabrian Arc: evidence from paleomagnetic and GPS observations.* Earth Planet Sci Lett, 263, 259-274.

Morelli D.;2011: *Geomorphic setting and geohazard-related features along the Ionian Calabrian margin between Capo Spartivento and Capo Rizzuto (Italy).* Mar Geophys Res, 32, 139-149.

Morgenstern N.; 1967: *Submarine slumping and the initiation of turbidity currents.* Turbidites and Deep-Water sedimentation: short course syllabus of pacific section, Soc Econ Paleontol Mineral, 1-38.

Rebesco M.; Camerlenghi A.; 2008: *Contourites.* Developments in sedimentology.

Roda C.;1964: *Distribuzione e facies dei sedimenti neogenici nel bacino Crotonese.* Geol. Rom, 3, 319-366.

Van Dijk J.; 1992: *Late Neogene forearc basin evolution in the Calabrian arc (Central Mediterranean): tectonic sequence stratigraphy and dynamic geohistory.* Geologica Ultraiectina, 92, 1-287.

Westaway R; 1993: *Quaternary uplift of Southern Italy.* J Geophys Res, 98, 21741-21772.

PROSPEZIONI ELETTRO-MAGNETICHE NEL DOMINIO DELLA FREQUENZA PER LA CARATTERIZZAZIONE DEL GHIACCIAIO DEL CALDERONE, GRAN SASSO D'ITALIA

M. Pavoni[1], A. Carrera[1], S. Urbini[2], F. De Blasi[3], J. Gabrieli[3], J. Boaga[1]

[1] Dipartimento di Geoscienze, Università degli Studi di Padova, Padova, Italy
[2] INGV, Dipartimento Ambiente, Roma, Italy
[3] Istituto Scienze Polari, CNR, Venezia, Italy

Il Ghiacciaio del Calderone (Fig. 1), situato in Abruzzo all'interno del massiccio del Gran Sasso, è l'unico ghiacciaio appenninico e il più meridionale d'Europa. Esso si sviluppa sul versante settentrionale del Corno Grande (Pietracamela, Teramo) ad una quota compresa tra i 2630-2830 metri s.l.m. L'aumento delle temperature medie annue degli ultimi decenni ha portato ad una veloce regressione del ghiacciaio (Pecci *et al.*, 2008), che ad oggi può essere considerato un rock covered glacier, essendo il rimanente nucleo massivo di ghiaccio ricoperto da uno spessore metrico di detrito di versante.



Fig. 1 - Foto del Ghiacciaio del Calderone circondato dalle tre cime del Corno Grande del Gran Sasso (Agosto del 2017).

Nell'ambito del progetto Ice Memory (ISP-CNR e Università Ca' Foscari Venezia), è stato scelto di carotare il Ghiacciaio del Calderone in modo tale da estrarre e conservare un campione di ghiaccio indisturbato e salvaguardarne così le importanti informazioni paleoclimatiche. Per definire il punto più idoneo dove effettuare l'operazione di carotaggio (Aprile 2022), cioè dove lo spessore di ghiaccio massivo è massimo, sono state eseguite delle misure geofisiche con metodi elettromagnetici (13 Marzo 2022). Oltre alle indagini GPR (Ground-Penetrating-Radar), impieganti nuove tipologie di antenne digitali (GSSI – 200 MHz), tecnica storicamente utilizzata con successo in glaciologia, è stato scelto di testare anche il metodo FDEM (Frequency Domain Electro-Magnetometry), che al contrario non viene tipicamente applicato in questi ambienti di studio. La necessità di indagare il sottosuolo dalla superficie fino a diverse decine di metri di profondità ha richiesto l'utilizzo di uno specifico strumento FDEM bi-statico in grado di garantire diverse distanze tra antenna emittente e ricevente (CMD-DUO, GF Instruments – Fig. 2). Lo strumento utilizza un'unica frequenza di 925 Hz ma consente di effettuare le misure con 3 differenti spaziature (10, 20 e 40 m) e 2 orientazioni delle antenne (orizzontale e verticale). In questo modo, per ogni punto di misura, si ottengono 6 differenti valori di conducibilità apparente, che consentono di caratterizzare verticalmente le proprietà elettriche del sottosuolo fino a 60 metri nominali di profondità.



Fig. 2 - Preparazione delle antenne trasmittente e ricevente durante le misure effettuate con lo strumento CMD-DUO (Marzo 2022).

Nella campagna di indagine del 13 Marzo 2022, sono state acquisite linee di misura comuni con il metodo GPR e FDEM, così da confrontare i risultati della prima tecnica, notoriamente affidabile in ambienti di ghiacciaio, con quelli ottenuti dal processing dei dati acquisiti con lo strumento FDEM. Quest'ultima operazione è stata eseguita utilizzando il software EMagPy (McLachlan *et al*., 2021). Il codice consente, una volta definite le caratteristiche delle antenne (frequenza, distanza e orientazione) e il profilo di conducibilità elettrica nel sottosuolo, di applicare il metodo Full Maxwell forward model, che descrive la propagazione dei campi elettromagnetici in un mezzo, e calcolare, con l'approssimazione di LIN (Low Induction Number), le diverse conducibilità apparenti che verrebbero teoricamente misurate dallo strumento. Applicando il processo di modellazione inversa è quindi possibile trovare, per ogni punto di misura, il profilo di conducibilità elettrica che meglio riproduce le misure acquisite sul campo.

Nel caso studio del Calderone sono stati acquisiti un centinaio di punti di misura per ogni linea di indagine e, dopo aver filtrato i data sets da misure anomale, è stato applicato il metodo di Gauss-Newton per ottimizzare il processo di inversione, valutando il parametro di regolarizzazione con l'analisi L-curve (Hansen *et al*, 2001). Per ogni linea di indagine i profili ottenuti sono stati interpolati tra loro, considerando anche la topografia irregolare, e plottati in pseudo-sezioni 2D di conducibilità elettrica. Bisogna però sottolineare che l'ambiente altamente resistivo impone serie limitazioni legate alla capacità risolutiva dello strumento (0.1 mS/m). I valori di conducibilità elettrica, sia apparenti che invertiti, non sono perciò attendibili in termini di valori assoluti. I risultati ottenuti in termini relativi consentono però di definire una struttura del sottosuolo del tutto simile a quella evidenziata dai radargrammi lungo i medesimi transetti. Nelle Fig. 3A-B vengono rappresentate rispettivamente la sezione di conducibilità e il radargramma per una linea di indagine longitudinale allo sviluppo del ghiacciaio. Il risultato della tecnica GPR mette bene in evidenza l'area con ghiaccio massivo (delimitato con il tratteggio bianco), dove l'assorbimento del segnale è praticamente nullo. Tale area combacia quasi perfettamente con il layer a minor conducibilità della sezione 3A (conducibilità < 10 mS/m), dimostrando la sensibilità della tecnica FDEM nel rilevare le aree con presenza di ghiaccio puro rispetto a quelle dove invece è probabilmente mescolato a importanti frazioni di deposito. Anche lo spessore e la profondità del layer di ghiaccio massivo, che raggiunge un massimo di circa 20 metri nel radargramma (freccia gialla in Fig. 3B), può essere stimato con buona approssimazione nella sezione di conducibilità FDEM. L'esito positivo delle misure FDEM è confermato anche dai risultati della seconda linea di investigazione, questa volta trasversale allo sviluppo del ghiacciaio. Anche in questo caso infatti è evidente che la sezione di conducibilità (Fig. 3C) ricalca quasi perfettamente la struttura del sottosuolo definito dal radargramma (Fig. 3D). Dal risultato dell'indagine FDEM possiamo quindi nuovamente stimare correttamente la presenza, la profondità e lo spessore del layer con ghiaccio più massivo.

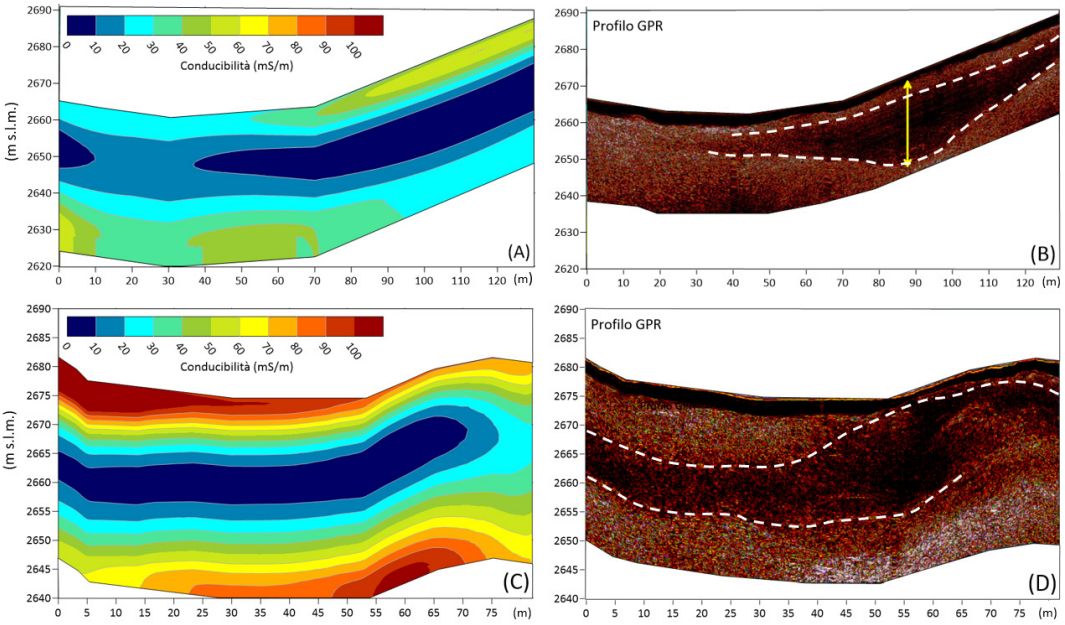


Fig. 3 - A) Sezione di conducibilità elettrica ottenuta dall'inversione dei dati FDEM acquisiti lungo una linea longitudinale allo sviluppo del ghiacciaio Calderone e il corrispettivo B) radargramma (freccia gialla rappresenta il massimo spessore di ghiaccio massivo rilevato). C) Sezione di conducibilità elettrica ottenuta per una linea di indagine trasversale al ghiacciaio e il corrispettivo D) radargramma. Da notare che nei radargrammi le linee tratteggiate bianche delimitano aree con assorbimento minimo del segnale e quindi con presenza di ghiaccio più massivo.

I risultati ottenuti sono importanti nell'ottica di applicare la tecnica FDEM in ambienti di rock glaciers. Tale metodo, con antenne bi-statiche a minor separazione, è già stato utilizzato con successo per mappare lo spessore dello strato attivo di queste forme periglaciali (Boaga *et al.*, 2019; Pavoni *et al.*, 2021). L'integrazione di misure acquisite con lo strumento CMD-DUO consentirebbe quindi di estendere l'investigazione più in profondità e mappare così anche la base dello strato di sottosuolo ghiacciato, definendo così il suo spessore. Questo tipo di caratterizzazione viene solitamente eseguita con misure di tomografia elettrica, molto più dispendiose da un punto di vista logistico, fisico e temporale, rendendo difficile la mappatura di vaste aree, che al contrario potranno essere realizzate più agevolmente e rapidamente utilizzando strumenti FDEM bi-statici.

Riconoscimenti. Gli autori ringraziano Massimo Pecci e Pinuccio d'Aquila per la collaborazione alle indagini. Si ringrazia inoltre il Corpo Nazionale dei Vigili del Fuoco per il supporto logistico.

Bibliografia

Boaga J., Phillips M., Noetzli J., Haberkorn A., Kenner, R. and Bast A; 2020: *A comparison of frequency domain electromagnetometry, electrical resistivity tomography and borehole temperatures to assess the presence of ice in a rock glacier.* Frontiers in Earth Science, 593.

Hansen P.; 1999: *The L-Curve and Its Use in the Numerical Treatment of Inverse Problems.* Computational Inverse Problems in Electrocardiology, 4, 119–142.

McLachlan P., Blanchy G. and Binley A.; 2021: *EMagPy: Open-source standalone software for processing, forward modeling and inversion of electromagnetic induction data*. Computers & Geosciences, 146, 104561.

Pavoni M., Sirch F. and Boaga J; 2021: *Electrical and Electromagnetic Geophysical Prospecting for the Monitoring of Rock Glaciers in the Dolomites, Northeast Italy*. Sensors, 21, 1294.

Pecci M., D'Agata C. and Smiraglia, C.; 2008: *Ghiacciaio del Calderone (Apennines, Italy): the mass balance of a shrinking Mediterranean glacier*. Geografia Fisica e Dinamica Quaternaria, 31(1), 55-62.

ACTIVE AND PASSIVE SEISMIC AND ELECTRICAL METHODS FOR IMAGING GAS UPWELLING FLOWS AT THE FIUMICINO COASTAL AREA (CENTRAL ITALY)

G. Penta de Peppo[1], G. De Donno[1], A. Bosman[2], E. Cardarelli[1], M. Cercato[1]

[1] "Sapienza" University of Rome - DICEA, Italy
[2] Istituto di Geologia Ambientale e Geoingegneria (IGAG), Consiglio Nazionale delle Ricerche s.c. DICEA, Italy

Introduction. The accurate location of gas upwelling flows is still an open problem for non-invasive imaging techniques. Gas blowouts may represent a serious threat to human health in urban areas or when planning future urbanization. Natural gases found in the shallow subsurface can have different causes, even if the most abundant are undoubtedly carbon dioxide (CO_2) and methane (CH_4). These gases are generally of deep origin and rise toward the surface through faults, cracks and voids but also due to anthropogenic causes, such as borehole drilling.

For these reasons, previous works have been focused on locating gas in the shallow subsurface (e.g. Carcione *et al.*, 2011), even if a codified procedure for the identification of these gases through non-invasive investigations has not been found. In such geological scenarios, where borehole drilling is not recommended, non-destructive geophysical surveys are the only cost-effective choice for imaging the gas pathways. Geoelectrical methods can be diagnostic for gas detection, as they can highlight the resistivity contrast between a water-saturated (conductive) and a gas-saturated (more resistive) medium. Seismic reflection methods can complement and validate the electrical models, by inferring the subsoil layering down to significant depths as well to locate the gas upwelling flows often visible on the seismic sections as blank zones of low-amplitude signal levels (e.g. Riedel *et al.*, 2002).

This work aims to combine high-resolution seismic and electrical methods to retrieve an accurate image of the gas upwelling flows in the coastal area of Fiumicino, 25 km western of Rome. To these aims, we performed active (multibeam bathymetry, high-resolution seismic sub-bottom profiler, electrical resistivity tomography) and passive (ambient noise recordings and self-potential) geophysical methods, to reduce the ambiguities often arising when geophysical techniques are applied standalone.

Study area, data acquisition and processing. The study area is located on the Tiber delta, made by Pleistocene-Holocene sediments. The near-surface layering consists of three main geological units separated by unconformity surfaces (Milli *et al.*, 2013), from the bottom to the top: i) Lower Pleistocene clay and silty clay, ii) Middle Pleistocene gravels and sandy gravels (PGS), iii) Upper Pleistocene to Holocene clay and peaty clay. The top of the PGS formation is the most permeable layer hosting a ground aquifer where gas rising from depth may accumulate. Conversely, the uppermost clays act as an impervious cap rock for PGS gravels allowing gas pressurization (Carapezza *et al.*, 2015).

Previous investigations included boreholes (see Sella *et al.*, 2013) and soil gas surveys (Bigi *et al.*, 2014). PGS unit was found in these boreholes between 42 and 52 m b.s.l., while the maximum gas concentrations CO_2 and CH_4 were found at the "Capo due Rami" site, on the right bank of the river (Fig. 1).

We carried out geoelectrical investigations along four different profiles (L1-L4), almost parallel to the Tyrrhenian coast. At the "Capo due Rami" site, we used also passive geophysical methods (self-potential and ambient noise recordings) to improve the diagnostic capability of the non-invasive surveys. A high-resolution (HR) seismic reflection (sub-bottom) profile was acquired along the Tiber river at the "Capo due Rami" site (Fiumara Grande branch), together with a multibeam investigation of the river bed.

The multibeam surveys were performed using the Teledyne Reson SeaBat 7125 echo-sounder (400 kHz) using the multibeam transducers in standard mode (look down) and rotating

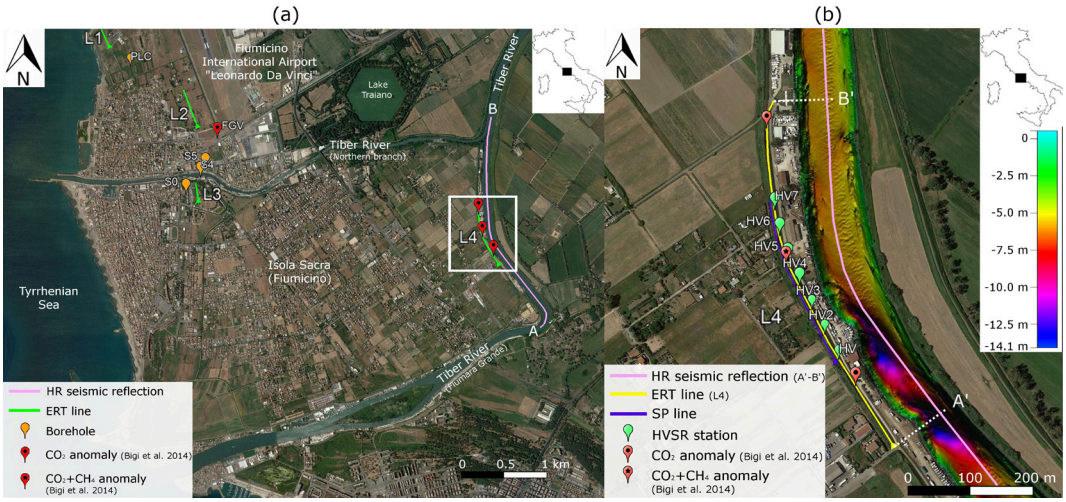


Fig. 1 - (a) Aerial plan of the surveyed areas and map of the geophysical investigations with available boreholes after Sella *et al.* (2014) and anomalous gas emission points after Bigi *et al.* (2014). FGV: Fiumicino Gas Vent. (b) Detail of the area within the white rectangle in Fig. 1a, with high-resolution multibeam bathymetry.

the head 30 ° to investigate the riverbanks up to hydrographic zero. The vessel positioning was supplied in real-time by an Applanix Position and Attitude System (POS/MV 320 V5) using RTK corrections received by a GPS master base-station belonging to the GNSS National Dynamic Network (http://www.igmi.org/rdn/) and processing kinematic (PPK) techniques for very highly accurate positioning of the navigation lines. Multibeam data were processed using Caris Hips & Sips 9.1 to generate a high-resolution Digital Elevation Model (DEM) with a 0.2 m cell size. The high-resolution (HR) seismic (sub-bottom) profiling was performed using a Benthos Chirp III source with a sweep between 2 and 7 kHz and a single-channel zero-offset configuration (Bosman and Orlando, 2017). GNSS positioning of the single-channel seismic was conducted in RTK mode with centimetric accuracy. Raw data were processed through Geo Suite All Works software, and we set a value of 1470 m/s for the time-depth conversion.

The electrical resistivity tomography (ERT) profiles were acquired using the IRIS Instruments Syscal Pro resistivimeter with 48 stainless steel electrodes spaced 5 or 10 m apart, depending on the external limitations. Multiple gradient array is employed for ERT acquisition, as it combines good signal strength in extreme conductive environments with good resolution and depth of investigation. The ERT apparent resistivity dataset was inverted using the VEMI algorithm (De Donno and Cardarelli, 2017), where the 2.5D forward solution is achieved using a finite element approach with quadrangular elements, while a Gauss-Newton iterative procedure is used for data inversion.

Self-potential (SP) data were acquired with an offset of 180 m to the first electrode of the L4 line, by a string of 10 non-polarizable electrodes ($Cu/CuSO_4$), spaced 5 m apart, rolled along the investigated profile by overlapping an electrode pair for each baseline. At each station, a small hole (~10 cm deep) was dug to improve the electrical contact between the electrode and the ground. The electrodes are connected to the Syscal Pro via the same equipment used for ERT survey. For each line, we performed from 5 to 10 repetitions every 2 minutes starting from 20 minutes after the electrode plug-in , to check the robustness and consistency of the measurements. SP data were filtered for outliers and inverted using the SP2DINV software (Ahmed *et al.*, 2013), achieving a current density model directly related to the underground sources.

For ambient noise recordings, we used a three-component Sara seismic sensor with a natural period of 5 s; the duration of the seismic noise records was set to 45 minutes

employing a sampling frequency of 100 Hz. Time alignment of samples and positioning were guaranteed by a GPS. We processed the ambient noise signals using the open-source software Geopsy (Wathelet *et al.*, 2020) to obtain the HVSR curves and the resonance frequency, and to extract the directivity information of the signals by plotting the spectral ratio as a function of both frequency and azimuth. Data processing was performed following the guidelines and recommendations of the SESAME project (Bard *et al.*, 2004).

Results. The HR seismic profile A-B, shown in Fig. 2a, highlights two main reflections, due to the river bed (blue line) and the unconformity surface between Pleistocene/Holocene clayey sediments and PGS gravels (green line), together with several blank zones, likely associated with gas accumulation. Conversely, there are no pieces of evidence of major faults in the shallow subsurface along the investigated line, as well as on the river bed (Fig.1b).

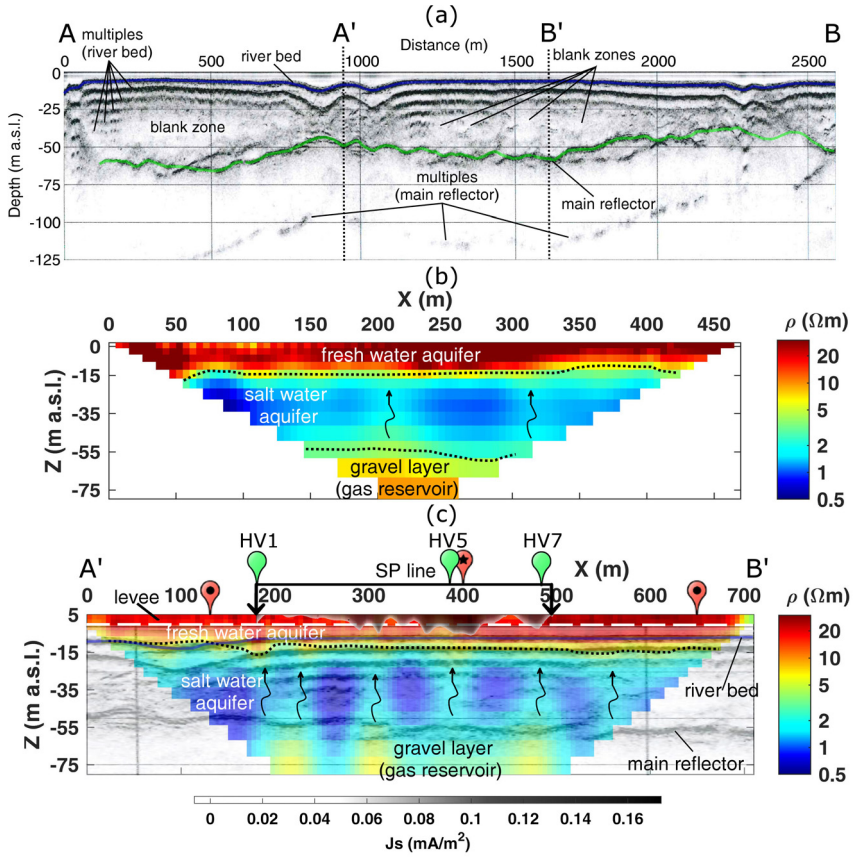


Fig. 2 - (a) HR seismic sub-bottom profile A-B. (b) Resistivity model for the L2 line. (c) Resistivity model for the L4 line, where HR seismic sub-bottom profile A'-B' and current density model are superposed. Gas upwelling flows are marked with black arrows.

The inverted model of the L2 line (Fig. 2b) gives information about the electrical properties of groundwater (salinity) and natural gases in the study area. We detect a moderately resistive layer (20-30 Ωm) down to 15 m b.s.l., while resistivity abruptly decreases to 0.5-1.5 Ωm between 15 and 55 m b.s.l., due to the presence of saline intrusion inland. Then, we observed a resistivity increase in the gravel PGS formation, which is known to host the gas reservoir. A slight increase in the resistivity of the middle layer (ρ >1.5 Ωm) can be likely attributed to the

presence of gas upwelling flows if compared with L1 and L3 model, where this effect is not visible.

In Figure 2c, we present the results achieved at the "Capo due Rami" site, where the presence of gas vents was well documented. The electrical layering, already seen on L2 (Fig. 2b) is confirmed also for the L4 line, with the location of the unconformity surface in agreement with the A'-B' seismic sub-bottom profile. We detect 6 anomalous zones (black arrows), likely due to gas upwelling flows, of which the most significant are located between 280-310, 380-410 and 460-480 m on the surface. This evidence is confirmed by the SP model that shows the maximum values of current density around the three main anomalies (Fig. 2c), and by previous measurements of gas concentration (Bigi et al., 2014).

The H/V spectra (Fig. 3) exhibit only moderate amplification effects, where the main peak is located at 1.8 Hz for HV1-HV3. Given the depth of the unconformity surface from the seismic reflection, we can estimate the shear wave velocity of the overlying sediments, under the hypothesis of a 1-D simple model, between 300 and 370 m/s (Bard *et al.*, 2004). For the last stations (HV5-7) a secondary peak at 4.5-5 Hz becomes prevalent and for HV5 a clear effect of directionality is visible. Although this effect was already observed in gas emission areas as well as in fault systems (e.g. Pischiutta *et al.*, 2013), the investigation of the structural causes of this effect is beyond the scope of this work.

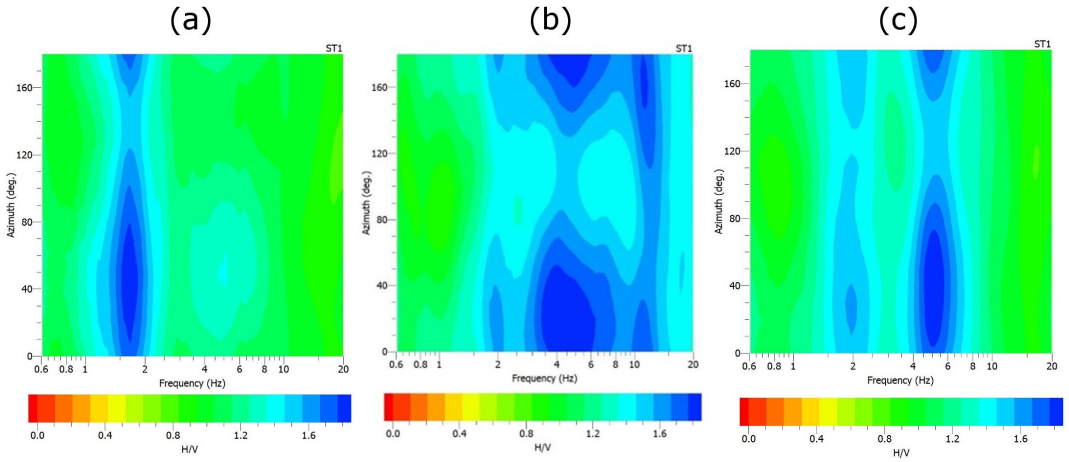


Fig. 3 - Directionality of ambient noise recording for HV1 (a), HV5 (b) and HV7 (c) stations (for the location of stations see Fig. 1b and 2c).

Conclusions. This work demonstrated the diagnostic potential of integrating active (HR sub-bottom seismic profiler, multibeam bathymetry and ERT) and passive (SP and HVSR) geophysical data for imaging natural gas emissions at the Fiumicino coastal area. The seismic sub-bottom profile in the Tiber River, together with the multibeam bathymetry, give a HR image of the shallow subsoil (DOI ~60 m), locating the unconformity surface between Pleistocene/Holocene clayey sediments and PGS gravels and highlighting several blank zones likely associated with the gas emissions.

Through the combination of ERT (DOI ~80 m) and SP (DOI ~20 m) methods on a selected site, we reconstructed a three-layer model, where local increases in resistivity in the middle clayey layer are related to upwelling gas flows from the underlying gravel layer (gas reservoir).

The analysis of ambient noise recordings allows a first approximation estimate of shear wave velocity (given the depth of the unconformity surface), while a clear directional effect is seen nearby the main anomaly due to the gas emissions.

Acknowledgments. This work was founded by “Sapienza” University of Rome, Grant no. 171/D/2016- Principal Investigators: Ettore Cardarelli (2016-18) and Giorgio De Donno (2019-22). The authors wish to thank Francesco Pugliese (“Sapienza” University of Rome) and MSc and BSc students Francesco Giaconi and Michele Tomassetti (“Sapienza” University of Rome) for their help during field acquisition.

References

Ahmed A. S., Jardani A., Revil A. and Dupont J. P.; 2013: *SP2DINV: A 2D forward and inverse code for streaming potential problems*. Computers & Geosciences, 59, 9-16.

Bard P., Duval A., Koehler A. and Rao S.; 2004: *Guidelines for the implementation of the h/v spectral ratio technique on ambient vibrations measurements, processing and interpretation.* SESAME European research project, December, 1–62.

Bigi S., Beaubien S.E., Ciotoli G., D’Ambrogi C., Doglioni C., Ferrante V., Lombardi S., Milli S., Orlando L., Ruggiero L., Tartarello M.C. and Sacco P.; 2014: *Mantle-derived CO2 migration along active faults within an extensional basin margin (Fiumicino, Rome, Italy)*. Tectonophysics, 637, 137-149.

Bosman A. and Orlando L.; 2017: *Bedforms on the lowermost reach of the Tiber River (Rome, Italy): Preliminary results from integrated geophysical surveys and samplings*. In: Atlas of Bedforms in the Western Mediterranean (pp. 95-98). Springer, Cham.

Carapezza M. L., Tarchini L., Granieri D., Martelli M., Gattuso A., Pagliuca N. and Sciarra A.; 2015: *Gas blowout from shallow boreholes near Fiumicino International Airport (Rome): Gas origin and hazard assessment.* Chemical geology, 407, 54-65.

Carcione J. M., Gei D., Picotti S. and Michelini A.; 2011: *Cross-hole electromagnetic and seismic modeling for CO2 detection and monitoring in a saline aquifer.* Journal of Petroleum Science and Engineering, pp.162-172.

De Donno G. and Cardarelli E.; 2017: *VEMI: a flexible interface for 3D tomographic inversion of time- and frequency-domain electrical data in EIDORS*. Near Surf. Geophys., 15, 43-58.

Milli S., D’Ambrogi C., Bellotti P., Calderoni G., Carboni M. G., Celant, A. and Ricci V.; 2013: *The transition from wave-dominated estuary to wave-dominated delta: the Late Quaternary stratigraphic architecture of Tiber River deltaic succession (Italy).* Sedimentary Geology, 284, 159-180.

Pischiutta M., Anselmi M., Cianfarra P., Rovelli A. and Salvini F.; 2013: *Directional site effects in a non-volcanic gas emission area (Mefite d’Ansanto, southern Italy): Evidence of a local transfer fault transversal to large NW–SE extensional faults?.* Physics and Chemistry of the Earth, Parts A/B/C, 63, 116-123.

Riedel M., Spence G. D., Chapman N. R. and Hyndman, R. D.; 2002: *Seismic investigations of a vent field associated with gas hydrates, offshore Vancouver Island.* Journal of Geophysical Research: Solid Earth, 107(B9), EPM-5.

Sella P., Billi A., Mazzini I., De Filippis L., Pizzino L., Sciarra A. and Quattrocchi F.; 2014: *A newly-emerged (August 2013) artificially-triggered fumarole near the Fiumicino airport, Rome, Italy.* Journal of Volcanology and Geothermal Research, 280, 53-66.

Wathelet M., Chatelain J.L., Cornou C., Di Giulio G., Guillier B., Ohrnberger M. and Savvaidis A.; 2020: *Geopsy: A User-Friendly Open-Source Tool Set for Ambient Vibration Processing.* Seismological Research Letters, 91(3), 1878-1889, doi:10.1785/0220190360.

OSSERVAZIONI CLIMATICHE E METEOROLOGICHE DAL RUMORE SISMICO DEL SISMOMETRO IO.EVN (EVEREST - NEPAL)

F. Pettenati[1], M. Plasencia[1], G. Verza[2], D. Sandron[1]

[1] Istituto di Oceanografia e di Geofisica Sperimentale, OGS, Trieste, Italy
[2] EvK2cnr, Bergamo, Italy

Introduzione. Le origini climatologiche e meteorologiche del rumore sismico rilevato da un sismometro non sono una novità. Un riassunto sulla natura del rumore sismico è esposto nell'articolo di Bonnefoy-Claudet *et al.* (2006). La banda di periodi sopra 1s è in gran parte dovuta a questi fenomeni. Perturbazioni a larga scala, come i monsoni, vengono rilevati su periodi T maggiori di 2s (fino oltre 10s); i cicloni sopra gli oceani da periodi T tra 0.3 e 3s, mentre fenomeni meteorologici a scala locale tra T 0.2 e 0.7s. Viengono qui presentate le analisi del rumore sismico di 8 anni di attività del sismometro broadband IO.EVN, installato presso il Laboratorio /Osservatorio Piramide (Everest - Nepal). Iniziando dall'analisi per il controllo qualità (McNamara and Buland, 2004), sono stati rilevati diversi fenomeni, grazie anche alla quasi assenza di rumore antropico, vista la collocazione della struttura in una valletta laterale della valle del Khumbu in Himalaya. L'analisi dei Probability Density Function (PDF) per le tre componenti, per un periodo continuo di dati dal 2016 al 2019, mostra la "moda" molto vicino alle curve standard di riferimento (Peterson 1993). Tuttavia, analizzando più in dettaglio la componente verticale, concentrandosi sull'intervallo 5 - 9 s, si può vedere che il suo livello di rumore è più alto, fino a 3db, rispetto alle componenti orizzontali.

Tifoni del Golfo del Bengala. L'evidenza di tifoni accaduti a oltre 500 km di distanza, sono molto evidenti sulle componenti di periodo T 3 e 5 s. La Fig. 1 mostra le serie temporali su quattro componenti, per i tifoni "Fani" (aprile-maggio 2019 - https://en.wikipedia.org/wiki/Cyclone_Fani)) e "Amphan" (maggio 2020 - https://en.wikipedia.org/wiki/Cyclone_Amphan) del Golfo del Bengala. In particolare, Fani (Fig. 1a) raggiunse la sua massima intensità (Very Sever Storm) il 3 maggio 2019 sulle coste dello stato di Odisha a 700 km da IO.EVN, mentre Amphan (Fig. 1b) tra il 17 e 18 maggio 2020 raggiunse lo status di Very Sever Storm entrando in terraferma a circa 500 km dalla stazione. Dalle figure si può vedere un incremento di oltre 20 dB del livello di rumore.

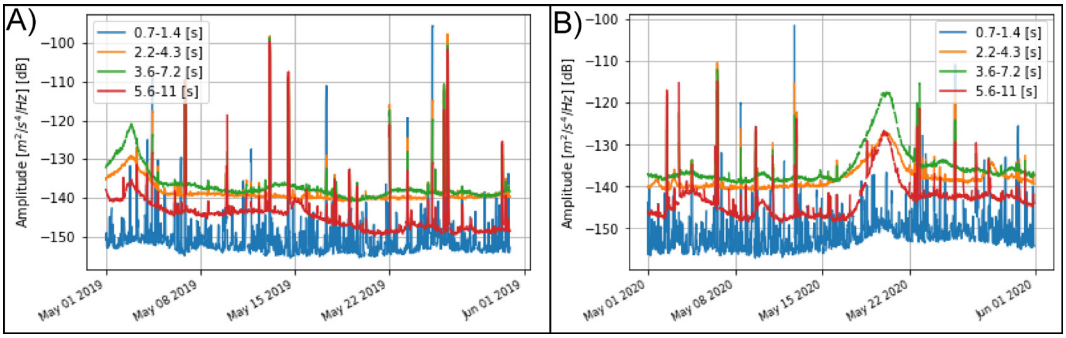


Fig. 1 - Serie temporali in quattro componenti di periodo T (rosso 1 s; arancio 3 s; verde 5 s; rosso 8 s): A) tifone Fani (26/04 - 05/05/2019); B) Amphan (16/05 – 21/05/2020). Le componenti che risentono l'influenza dei tifoni sono quelle con T > 1 s.

Relazioni stagionali. Il confronto del livello medio di rumore registrato a diverse stagioni è riportato in Fig. 2, per i dati del periodo 2016-2019. I dati sono stati divisi, per l'intero dataset, in tre stagioni differenti: "stagione fredda" da ottobre a febbraio (S1); "stagione di mezzo" da

maggio giugno (S2) e “stagione umida” da giugno a settembre (S3). L’effetto dei monsoni (T > 2s) è evidente per i rapporti S3 vs S1 e S3 vs S2, ma l’aumento del livello di rumorosità in dB, attorno a T = 10s, è molto limitato. Molto più marcate sono le ampiezze dei rapporti S3 vs S1 e S3 vs S2 tra T 0.04 a 0.4s in tutte le componenti e con un delta pari a 4 dB.

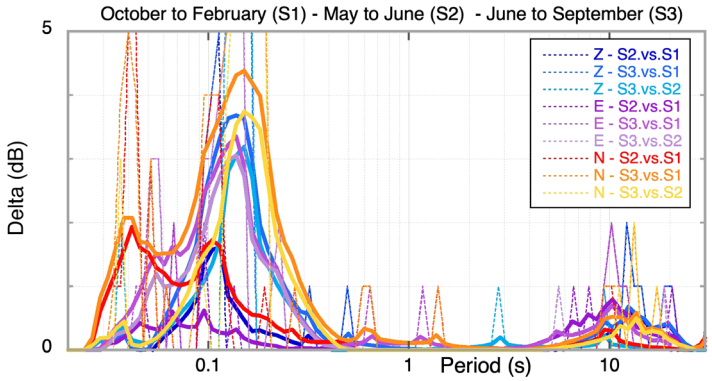


Fig. 2 - Rapporti di rumore sismico tra tre stagioni selezionate, con i dati del periodo 2016-2019: S1 ottobre- -febbraio; S2 maggio - giugno: S3 giugno – settembre.

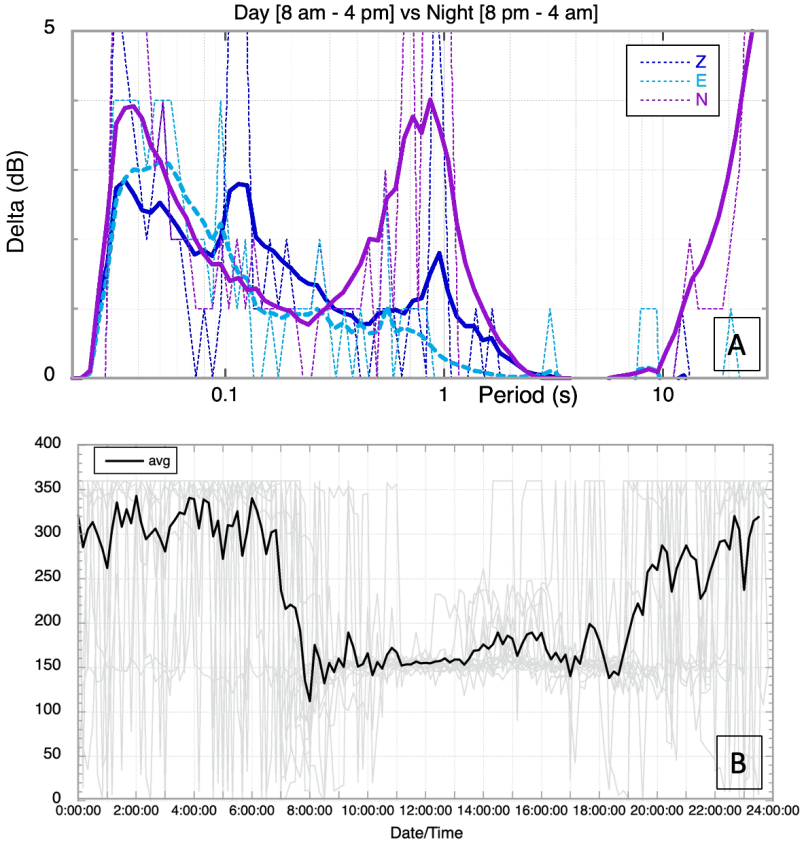


Fig. 3 - Analisi del rumore sismico, con i dati del periodo 2016-2019, A) per il rapporto dati ore diurne versus ore notturne; B) direzione del vento nella fascia oraria di 24 ore, con i dati della stazione meteo del Laboratorio/ Osservatorio Piramide (dati concessi da EvK2cnr).

Relazioni diurne-notturne. Un'analisi è stata effettuata anche per diverse fasce orarie del giorno (Fig. 3a), sempre per il periodo 2016-2019: una principalmente notturna (8 pm - 4 am) e una principalmente diurna (8 am - 4 pm). In questo caso si osserva un livello di rumore generalmente più elevato durante le ore diurne. La componente verticale Z mostra picchi di circa 3 dB di ampiezza tra 0.03 e 0.06 s e tra circa 0.12 e 0.2 s. Un terzo picco, inferiore a 2 dB, è centrato sul periodo di 1 s. La componente N mostra due picchi di 4 dB tra 0.03-0.04 e 0.7-0.1 s. Un ulteriore picco intorno a 20 s. La componente E mostra solo un ampio picco tra 0.03 e 0.1 s che tende a zero a periodi più alti.

Discussione. L'influenza sul rumore ambientale di cicloni tropicali (tifoni nell'emisfero orientale) è ben evidente anche a grandi distanze e rivelabili anche su periodi T > 3s. I tifoni comunque, sono molto energetici, classificati "Very Sever Storm" dall' IMD (Indian Meteorological Department). Le analisi dei dati meteorologici mostrano un aumento della velocità del vento tra le 08:00 e le 18:00, con direzione prevalente attorno i 150° e durante le ore notturne con direzione 300° (Fig 3b). L'aumento in dB nei rapporti tra stagione umida (S3) versus le altre stagioni, si colloca attorno a periodi tipici di eventi meteo locali (T 0.2 e 0,7s), su tutte le componenti. Il rapporto tra dati diurni e notturni, mostra una banda principale della componente N tra 0.2 - 1.5 s e per la Z due picchi, uno a 0.12 s e uno ad1 s. L'analisi sulle relazioni tra giorno e notte, soprattutto la componente N, conferma quindi l'influenza di un vento locale che si orienta lungo la valletta del sito orientata per 120° - 130°. Di giorno una termica che risale la valle e di notte un vento freddo che scende dal ghiacciaio limitrofo (ghiacciaio del Lobuche). Questo farebbe oscillare la terrazza dove è collocato lo shelter della stazione IO.EVN, su una parete orientata in direzione circa 30°. Le componenti interessate sono la Z e soprattutto la N (la terrazza si allunga parallelamente alla parete).

Rimangono due dubbi da risolvere, guardando le Fig.s 2-3: a) le bande sotto 0.1 s per le componenti N e Z, che nelle due figure sono in accordo; sono legate principalmente alla attività antropica, che potrebbe essere spiegata solo da macchinari nella Piramide che si attivano solo durante il giorno (per il momento non si hanno riscontri); b) l'aumento di 3 dB della componente Z per periodi tra 5 e 9 s nei PDF di McNamara and Buland (2004). Tale aumento però non è riscontrabile sulla componente Z delle due figure.

I periodi T < 0.1 s sono anche tipici del rumore sismico dei ghiacciai di fusione (Preiswerk e Walter 2018; Köhler et al. 2019) ma l'attività del ghiacciaio Lobuche che confina con la valle della Piramide, deve essere ancora verificata.

Riferimenti

Bonnefoy-Claudet, S., Cotton, F. & Bard, P.Y., 2006. The nature of seismic noise wavefield and its implications for site effects studies. A literature review, *Earth-Sci. Rev.*, **79**(3), 205-227, doi: 10.1016/j.earscirev. 2006.07.004.

Köhler, A., Maupin, V., Nuth, C., Van Pelt, W., 2019. Characterization of seasonal glacial seismicity from a single-station on-ice record at Holtedahlfonna, Svalbard, Annals of Glaciology **60**(79), 23-36, doi: 10.1017/aog.2019.15.

McNamara, D. and Buland R. P., 2004. Ambient noise levels in the Continental United States, *Bull. Seismol. Soc. Am.*, **94**(4):1517-1527, doi:10.1785/012003001.

Peterson J. R, 1993. Observation and modelling of seismic background noise, Open-File Report **93-322**, USGS, p. 42-A49, https://doi.org/10.3133/ofr93322.

Preiswerk L.E. and Walter F., 2018. High-Frequency (>2 Hz) Ambient Seismic Noise on High-Melt Glaciers: Green's Function Estimation and Source Characterization, J. Geoph. Res. Earth Surface, 123, 8, 1667-1681, https://doi.org/10.1029/2017JF004498.

NOT ONLY CLEAN ICE INSIDE ALPINE GLACIERS: A CASE STUDY ON THE SFORZELLINA GLACIER (CENTRAL ITALIAN ALPS)

I. Santin[1], E. Forte[1], M. Guglielmin[2]

[1] Department of Mathematics and Geosciences, University of Trieste, Trieste, Italy
[2] Department of Theoretical and Applied Sciences, Insubria University, Varese, Italy

Introduction. The Sforzellina Glacier is a small debris-covered glacier in the South-East sector of the Stelvio National Park. Its evolution has been monitoring since 1950 by analysing its front retreat and since 1990 by geophysical techniques (Guglielmin *et al.,* 1995) in order to evaluate the total ice mass of the glacier, and, consequently, the total stored water. The Sforzellina Glacier is in almost constant retreat and shrinking since the Little Ice Age (LIA), except a small advance around 1980 (Cannone *et al.,* 2008), as proved by the complex morainic system located on the glacier foreland and the progressive debris accumulation on the Glacier surface (Tarca and Guglielmin, 2022). Debris-covered glaciers are characterized by peculiar features, driven by processes that are largely absent from their clean-ice counterparts (Miles *et al.,* 2020). In fact, debris accumulated on the surface is only the most evident deposition zone, as the spatial distribution of debris inside and on the glacier, known as glacial debris cascade, is the result of the combination among debris sources, transport paths and deposition zone (Kirkbride, 2011). As debris is added on the accumulation area, it is progressively buried by snow or entrained in crevasses and follows englacial paths until the emergence in the ablation zone. On the contrary, debris supplied in the ablation zone tends to remain on the surface or emerging on the glacier surface along the flow lines. Glacier downward movements drive the transport of englacial debris across the ice thickness and affect the deposition of basal debris, in relation to the bedrock physical properties, such as roughness, morphology and thermal conditions. The properties and transport of debris and its direct effect on the surface insulation have been well studied and modelled by Reznichenko *et al.,* 2010, Anderson and Anderson, 2016, and Giese *et al.,* 2021, but geophysical techniques, especially Ground Penetrating Radar (GPR), can provide high resolution imaging and accurate spatial reconstruction of the debris distribution. As a matter of fact, GPR can not only provide a detailed imaging of the internal structure of glaciers, but also characterize different frozen materials. In this work, we aim at imaging the distribution of the debris inside the Sforzellina Glacier exploiting GPR data and highlighting strengths and limitations of such a technique.

Methods. A ground-coupled GPR survey was carried out in September 2021 on the Sforzellina Glacier, resulting in a 2 km-long dataset of GPR profiles, located both outside and inside the actual glacier boundary (Fig.1). A Malå Geoscience ProEx GPR system, equipped with 250 MHz shielded antennas, triggered by an electro-mechanical odometer, was used to perform the survey. Even with the good quality of the raw GPR data, processing was essential to increase the signal/noise ratio and to improve the imaging while maintaining the original data signature and preserving the amplitude contrasts further used for different glacial facies characterization. The processing flow includes drift removal (zero-time correction), bandpass filtering (corner frequencies are 20–80–350–650 MHz, with a typical not symmetrical trapezoidal shape to limit Gibbs phenomena), background removal, exponential amplitude recovery, topographic (static) correction, depth conversion and migration. For the last three steps, we considered a simplified velocity field with velocity values equal to 17 cm ns^{-1} for ice and to 13 cm ns^{-1} for the debris, on the basis of dedicated diffraction hyperbolas analyses and correlations with direct data on selected locations. Both migrated and not migrated data are essential for interpretation and facies definition. In particular, scattering is very helpful to discriminate between different glaciological units. GPR interpretation was supported by GPR attribute analysis, which allowed to better image

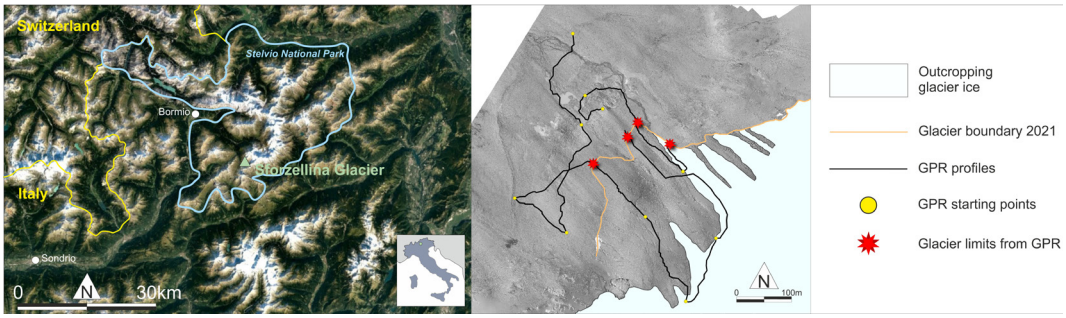


Fig. 1 - (A) Location map of the Sforzellina glacier inside the Stelvio National Park (B) Ortophoto of the glacier in black and white colour, with superimposed the GPR profiles (black lines) and their starting points (yellow dots).

and understand the boundaries and the geometries of the EM facies and horizons on GPR data. We focused on amplitude-, phase- and frequency-related attributes, integrating them during data interpretation.

Results and discussions. Spatial distribution of debris inside and on the Sforzellina Glacier encompasses all the different cases, being both supraglacial, englacial and subglacial. In GPR profiles, debris appears generally with a high amplitude scattered facies. The main issue for the identification of surficial debris on GPR data is the maximum optical resolution limit of a GPR antenna, which is roughly equal (at maximum) to a quarter of the dominant wavelength. So, for a 250 MHz central frequency antenna, the maximum attainable resolution corresponds to about 15 cm for a EM velocity of 10 cm ns^{-1}. Such velocity value resulted from the calibration of GPR data with direct measurements of debris thickness allowing to calculate a mean EM velocity. So, surficial debris cannot be imaged and properly identified if debris thickness is lower than at least 15 cm since it interferes with the direct ground wave. A high scattered zone imaged in GPR profiles can be associated to a mixture of ice and englacial debris, which causes scattering phenomena of the EM wave, as described in Forte *et al.,* 2021. In the Sforzellina Glacier, a high scattered facies is clearly imaged along profiles in the accumulation area, with a peculiar shape and extension (Fig. 2A). Similarities with the glacier discussed in Forte *et al.,* 2021, especially in terms of morphologies, relation with the ice-rock interface and response to the GPR attribute analysis, allowed to assess with a high level of confidence that also the high scattered zone inside the Sforzellina Glacier is related to englacial debris. In addition, englacial debris can be found in the shear zones, as expression of ice dynamics and englacial debris movements. As a matter of fact, in Fig. 2B-C we can easily note many high amplitude-reflections, crossing the entire ice thickness with a peculiar geometry due to the downward movement of the glacier, which encounters an obstacle in the bedrock undulating morphology. Usually this consideration is left on the background or even completely disregarded, but both bedrock depressions and highs highly affect ice thickness and dynamics and, as a consequence, the internal glaciological structures behaviour, as it is apparent in Fig. 2B. Shear zones take charge of debris from the base of the glacier and release it close to or on the surface. The glacier bottom can be defined as either ice-bedrock or ice-debris interface. This specification is needed because in some GPR profiles, below the ice, a peculiar EM facies has been noted. It is characterized by a very high amplitude and continuous reflection on top (white line in Fig. 2C), some local scattering and layering, and a low amplitude mainly continuous reflection at the base (red dotted line in Fig. 2C). This facies could be associated with a ground moraine with material deposited by moving ice and dropped by the glacier when it becomes too heavy to move. The aforementioned shear zones could take charge of the smallest debris materials and releasing them on the surface, while creating denser zones of debris cover on the surface.

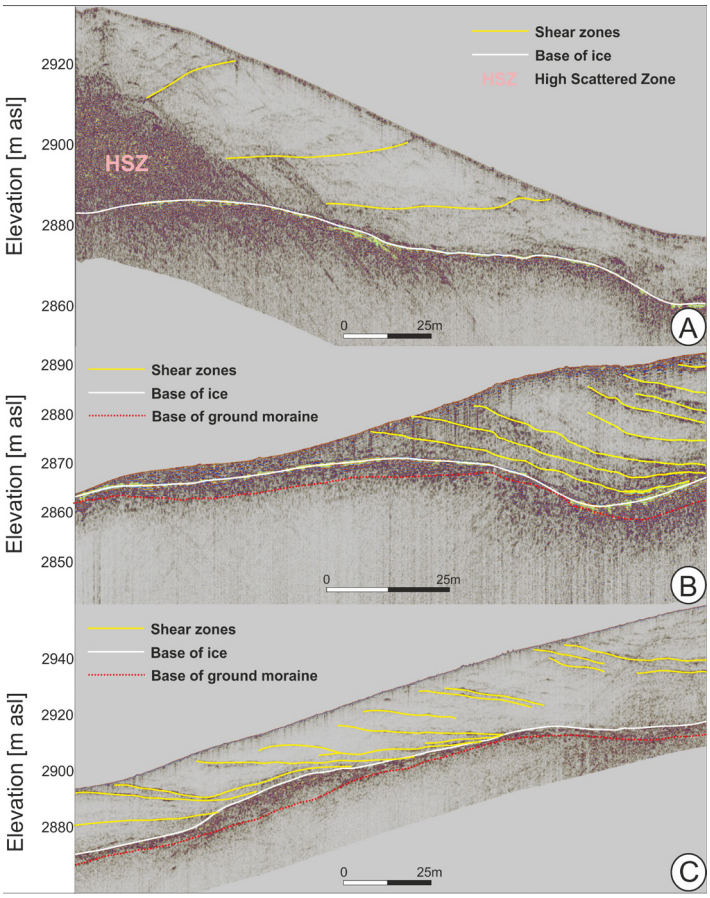


Fig. 2 - Three exemplary GPR profiles, showing the distribution of englacial and subglacial debris inside the Sforzellina Glacier. Coloured lines represent shear zones (yellow), base of the ice (white) and base of the ground moraine (red). HSZ stands for high scattered zone. Please note that A and B have the same horizontal scale, which is different from B.

The interpretation of GPR dataset and EM facies was integrated by GPR attribute analysis, whose potential in supporting the interpretation has been proved once again (Fig. 3). While the phase-related attributes allowed a more constrained interpretation of horizons identified in GPR profiles, highlighting the lateral continuity of horizons even with low signal/noise ratio, composite sweetness attribute allowed to better detect the boundaries between zones having different physical characteristics, often enhancing the signature of different reflection amplitudes (Fig. 3B). As far as different domains inside the glacier, as “clean” or “dirt” ice, they can be identified and discriminated exploiting frequency-related attributes, which highlight the different spectral contents in relation to the physical properties of materials as well as the facies geometries and boundaries (Fig. 3C).

Conclusion. With this work, we analysed the debris on and within the Sforzellina Glacier proving that GPR is reliable and effective tool to improve the reconstruction of the internal structure of the glacier. As a matter of fact, direct observations and measurements limited only to the surface or to shallow depths lead to a misunderstanding of the internal structure of the Sforzellina debris-covered glacier, as only surficial debris thickness can be detected. The main limitation of GPR is the resolution of low debris thickness zones, due to the frequency of the antenna system chosen to perform the survey. However, 250 MHz antennas seem to provide the best trade off between resolution and penetration depth, the first reaching 15-20 cm and the latter exceeding 50 m. Further studies are addressed to quantitative estimates of debris content and its grain size distribution.

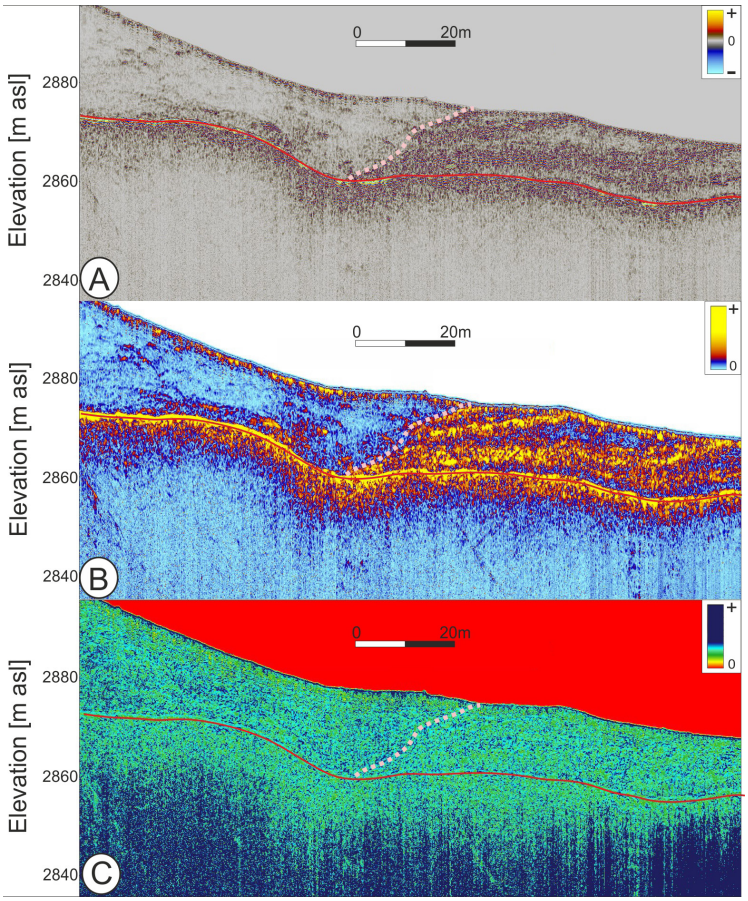


Fig. 3 - GPR attributes analysis: (A) Amplitude display of a GPR profile after processing, (B) Sweetness, (C) Dominant Frequency. Red solid line marks the base of the glacier, while the pink dotted line represent the contact between clean (on the left) and dirt (on the right) ice.

References

Anderson, L.S. and Anderson, R.S., 2016. *Modeling debris-covered glaciers: response to steady debris deposition.* The Cryosphere, 10, 1105–1124, doi:10.5194/tc-10-1105-2016.

Cannone, N., Diolaiuti, G., Guglielmin, M., Smiraglia, C., 2008. *Accelerating climate change impacts on alpine glacier forefield ecosystems in the European Alps.* Ecological Applications, 18, 3, 637-648.

Forte, E., Santin I., Ponti, S., Colucci, R.R., Gutgesell, P., Guglielmin, M., 2021. *New insights in glaciers characterization by differential diagnosis integrating GPR and remote sensing techniques: a case study for the Eastern Gran Zebrù glacier (Central Alps).* Remote Sensing of Environment, 267, 112715.

Guglielmin, M., Nardo, A., Smiraglia, C., 1995. *Lo spessore dei ghiacciai della Valfurva – Misurazioni tramite sondaggi elettrici verticali*. (in Italian).

Giese, A., Arcone, S., Hawley, R., Lewis, G., Wagnon, P., 2021. *Detecting supraglacial debris thickness with GPR under suboptimal conditions*. Journal of Glaciology, 67(266), 1108–1120. https://doi.org/10.1017/jog.2021.59.

Kirkbride, M. P., 2011. *Debris-Covered Glaciers.* in Encyclopedia of Snow, Ice and Glaciers (eds. Singh, V., Singh, P. & Haritashya, U.) 180–182 (Springer Netherlands, 2011). doi:10.1007/978-90-481-2642-2_622.

Miles, K.E., Hubbard, B., Irvine-Fynn, T.D.L., Miles, E.S., Quincey, D.J., Rowan, A.V., 2020. *Hydrology of debris-covered glaciers in High Mountain Asia.* Earth-Science Reviews, 207, 103212.

Reznichenko, N., Davies, T., Shulmeister, J., McSaveney, M., 2010. *Effects of debris on ice-surface melting rates: An experimental study*. Journal of Glaciology, 56(197), 384-394. doi:10.3189/002214310792447725.

Tarca, G. and Guglielmin, M., 2022. *Evolution of the sparse debris cover during the ablation season at two small Alpine glaciers (Gran Zebrù and Sforzellina, Ortles-Cevedale group).* Geomorphology, https://doi.org/10.1016/j.geomorph.2022.108268.

CHARACTERISATION OF ANTHROPOGENIC CAVITIES THROUGH INTEGRATED NON-INVASIVE GEOPHYSICAL SURVEYS IN THE MEDIEVAL TOWN OF CAMPOROTONDO DI FIASTRONE, CENTRAL ITALY

A. Zaragoza[1], R. Teloni[2], M. Zambrano[1]

[1] School of Science and Technology - Geology Division, University of Camerino, Italy
[2] GeoMORE s.r.l., spinoff of Geology Division, University of Camerino, Camerino, Italy

Introduction. The detection and characterisation of underground cavities and critical areas in urban cities has garnered significant interest from both engineering and historical perspectives. The increasing concern for underground structures is related to the proven correlation between the presence of cavities and the seismic amplification phenomena during strong earthquakes (Lancioni *et al.*, 2014). On the other hand, underground structures in urban areas can represent significant historical and cultural heritage to be preserved and promoted for tourism. However, securing and enhancing this patrimony can be particularly challenging (Argentieri *et al.*, 2018). In fact, direct detection of underground cavities is not often possible due to different issues like filling, blocked access, and refurbishing older urban pavements. In this regard, indirect identification of cavities through integrated geophysical methods may represent a valid solution. The Ground Penetrating Radar (GPR) is perhaps the most adapted tool for the detection of cavities in urban environments for its simple logistic and high resolution. However, this technique is sensible to the presence of underground services, tubes, and metallic meshes characteristic of the first meters of urban subsurface. Other method of popular use for the detection of cavities is the Electrical Resistivity Tomography (ERT). In the case of urban environments, flat electrodes are highly recommended since positioning classic vertical electrodes (drilling the pavement) is not always possible because of the historical and architectonic value of the urban pavements (Park *et al.*, 2017). In this work, we implement both techniques for the detection of known underground cavities with the intention of extrapolated its signature to other sites where cavities are presumably located. To do this, we have selected as study case the medieval village of Camporotondo di Fiastrone (MC), located in Central Italy. The town is characterised by a series of hypogenous structures in gravelled alluvial terraces, likely excavated for storage, cooling, and defensive purposes. Only some cavities are known and accessible, whereas the location of most of them remains unknown, representing a potential risk for the human activities. In this regard, buildings with nearby cavities were largely damaged by the 2016-17 seismic sequence in the central Apennines, Italy (Mw = 6.5, 30/10/2016) highlighting the seismic hazard connected to the presence of cavities. Through the methodology proposed in this work, we were able to detect and characterise the shallow cavities (depth < 6 m) present within the village of Camporotondo di Fiastrone, useful for the urban development planning of the post-seismic reconstruction phase.

Methods. In this study, in order to create a catalogue of the existing underground cavities, we have combined the generation of geological models (sections at large and detailed scale), review of historical data and witnesses' interview, visiting of accessible cavities, and geophysical surveys (forward modelling, electrical tomography, and ground penetrating radar survey). The geological models were carried out through the integration of geological map, seismic microzonation data and direct observations. All the wells coming from the microzonation were revised and the gravel base was determined, a very important marker when defining the geological context of the cavities. To document the distribution of cavities the first step was searching for historical ones (cavities that are in the memory of citizens and mentioned in historical sources). In general, the location and geometry of these features are partially known, and their remembrance is handed down from person to person. During this operational phase

we realized that many of the cavities had been made inaccessible, the cause was very often linked to past earthquakes (1997-2016).

The geophysical surveys consisting of non-invasive ERT and GPR data were combined with geological and stratigraphical analysis of underground sediments using well logs. For the GPR, two different antennas (200MHz, 400MHz) integrated to the SIR 4000 system (GSSI) were used. The GPR techniques was used to check and verify if the ERT surveys was capable into cavities detection. In the case of the electrical tomography (Wenner-Schlumberger array, 64m long, 32 electrodes, 2m electrode spacing), unexpensive flat-base electrodes in combination of an electroconductive gel (Vasconez-Maza *et al.*, 2020) were implemented to avoid pavement damages and, at the same time, reducing its electrical resistance. In addition to the previous information, the historical records and oral communications were combined into a GIS database and contrasted with historical maps of the village. Further analysis consisted in a comparison between the resulted map of the underground cavities and the distribution of buildings damaged by the 2016/17 seismic sequence of Central Italy. This method allowed us to detect a complex cavity network under the town centre (Fig. 1).



Fig. 1 - Map of historical cavities distribution, verified and no longer accessible in relation with the survey line and some detailed photo of the C1 cavity.

Results. For the interpretation phase, we combined both geophysical surveys and geological data from wells with cavities map (Fig. 2). The cavities were divided into historical, inaccessible, and verified. These hypogea were excavated between 3 to 6 meters depth with the main purpose of storing water and food.

In the case of the ERT, it was not possible to completely define the geometry of the cavities. In the ERT section, there is a highly resistivity area in coincidence of the cavity C3 location, whereas the cavity C1 is not so evident. However, the presence of these structures is related to an increment of the resistivity in the adjacent area hosting the cavities and a thinning of the low resistivity layers above (Fig. 2a). These results can be easily misinterpreted as a thinning of soil or weathered sediments.

In figure 2b we can observe the GPR survey, carried out whit a 200MHz antenna, 23m long and parallel to the ERT one. In the case of GPR, we found that the upper part first 2-3 meters is the underground services (water, electricity) may create significant disturbance. By

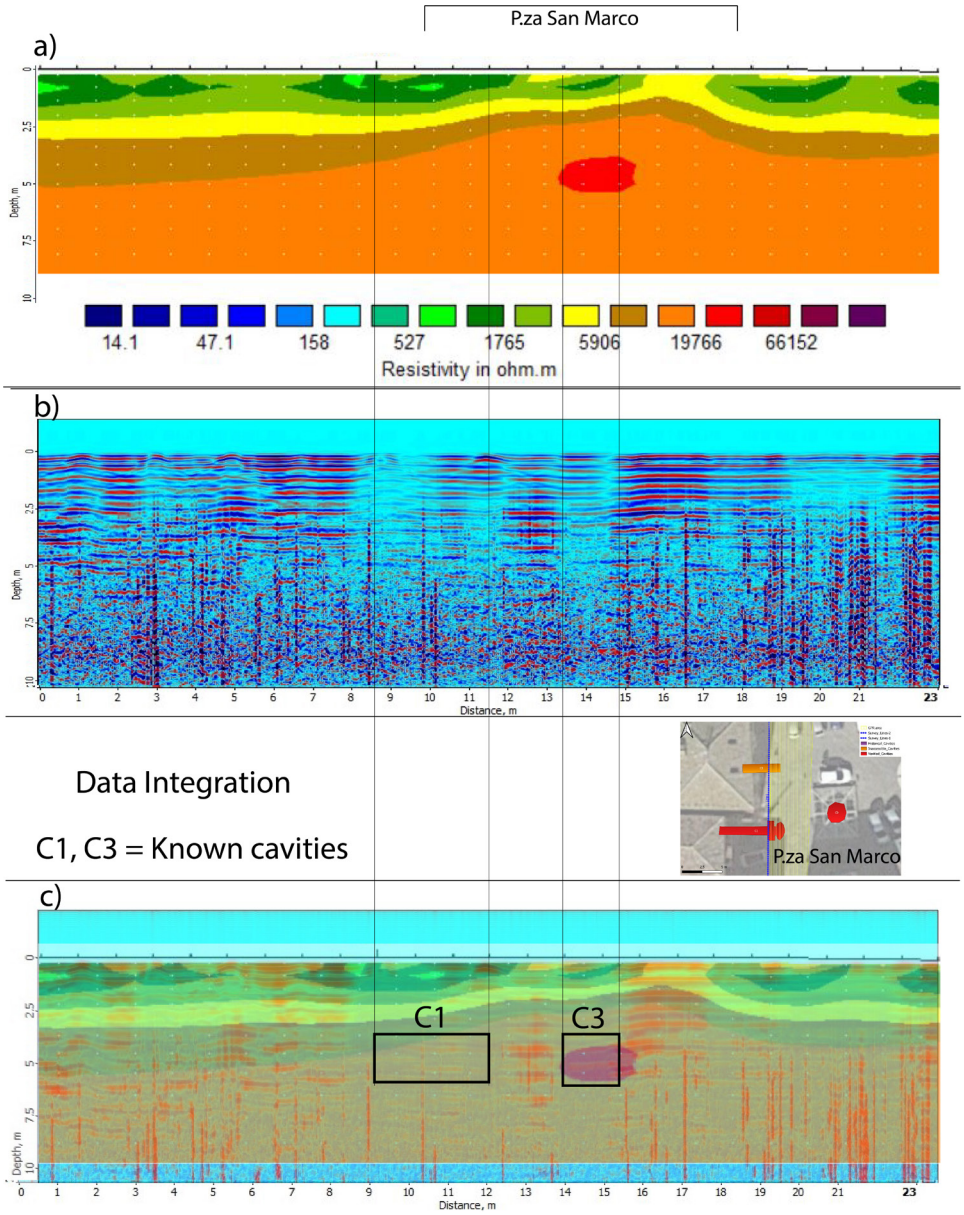


Fig. 2 - Data Integration, a) ERT Survey line 1, after the inversion and interpretation, b) GPR survey line (antenna 200MHz) parallel to the ERT-line 1, c) Superposition of the ERT and GPR surveys.

knowing the depth of the roof of some cavities, we estimated a dielectric constant of near 14, expected due to the moist sediments. At the expected depth, the cavities can be interpreted as a sharped lack of continuity of some reflectors. However, the shadow cause by the shallow anomalies may trick the interpretation without this previous knowledge.

In figure 2c we have overlaid the fig. 2a and 2b to compare and find the best possible location and geometry for the cavities' distribution during a blind interpretation. The comparison shows that the two cavities are excavated to the same depth (between 3m and 6m) and furthermore, the anomalies seem to correspond with the positions of the cavities found during the various inspections.

Discussion and conclusions. The significancy of this study is root in the combination of valuable information and methods: a) direct inspection and oral communication with residents were transcribed for the first time; b) geological data of the study area were modelled in order to have a 3D reconstruction of the hill where the village of Camporotondo di Fiastrone is located; c) multiple geophysical methods with innovative non-invasive technique were combined and tested to identify underground anomalies or heterogeneities. The obtained database could be of paramount importance for the urban planning to evaluate different hazard and risk scenarios, understanding the interaction between cavities and buildings. On the other hand, the detection of unknown cavities may help in preserving the cavities as patrimonial elements, favouring the touristic development of the area.

In conclusion:

1) From the investigations and considerations carried out, we can affirm that geophysics plays a vital role in the characterisation of the surface cavities present within the historic centre of Camporotondo di Fiastrone. Through a non-invasive methodology, ERT, we successfully detect both known cavities and potentially new ones.
2) Using a non-invasive non-destructive flat electrode combined with an electroconductive gel to improve the electrical contact, it was possible to overcome the problems and challenges of cavity investigations in an urban environment.
3) The cavities inside historic centres, such as the one in the present study, can represent a potential risk during seismic events. In the cavities, they also preserve a historical and cultural heritage to protect and enhance, it is therefore essential to create a database that contains all information and allows us to collect as much information as possible to understand their origin, history, and future development.
4) The presence of cavities is characterized by an increment of the resistivity in the area hosting the cavities and can be misinterpreted as a thinning of the soil/weathered levels. In the GPR section, the cavities are shown as a lack of continuity of the reflectors, but the noise and the shadow effect cause by shallower underground services makes no straightforward their interpretation.

This type of study was carried out to encourage and improve the knowledge of our historic centres for a possible safety and to enhance the artistic and cultural heritage for the urban redevelopment. The proposed approach can be easily used both in other countries and in different contexts.

References

Argentieri, A., Di Nezza, M., Di Filippo, M., Piro, M., Rotella, G., Cecchini, F., and Margottini, S. (2018). *Cavità di origine antropica e sicurezza degli edifici scolastici nella città di Roma: i casi di studio di via Asmara (Municipio II) e via Diana (Municipio V)*. Geologia dell'Ambiente.

Carey, A. M., Paige, G. B., Carr, B. J., and Dogan, M. (2017). *Forward modelling to investigate inversion artifacts resulting from time-lapse electrical resistivity tomography during rainfall simulations.* Journal of Applied Geophysics, 145, 39-49.

Del Prete, S. (2008). *Speleologia in Cavità Artificiali in Campania.* Geologi, 25, 16-23.

Lancioni, G., Bernetti, R., Quagliarini, E. and Tonti, L. (2014). *Effects of underground cavities on the frequency spectrum of seismic shear waves.* Advances in Civil Engineering, 2014.

Park, C. S., Jeong, J. H., Park, H. W., and Kim, K. (2017). *Experimental study on electrode method for electrical resistivity survey to detect cavities under road pavements.* Sustainability, 9(12), 2320.

Vásconez-Maza, M. D., Martínez-Pagán, P., Aktarakçi, H., García-Nieto, M. C., and Martínez-Segura, M. A. (2020). *Enhancing electrical contact with a commercial polymer for electrical resistivity tomography on archaeological sites: A case study*. Materials, 13(21), 5012.

HIGH RESOLUTION ELECTRICAL RESISTIVITY TOMOGRAPHY TO DETECT SUBSOIL WATER SEEPAGE IN LANDSLIDES INVOLVING CLAY SLOPES

D. Barbero[1], A. Maroni[2], M. Naldi[3], S. Peyrot[4], E. Veronese[5]

[1] Geological, Geotechnical and Geophysical Office of Dr. Diego Barbero, San Martino Alfieri (AT), Italy
[2] Geology Student, University of Turin, Italy
[3] Techgea s.r.l., Torino, Italy
[4] Geologist, Freelance professional, Torino, Italy
[5] Laboratorio Accreditato Analisi Ambientali Arcadia s.r.l, Tromello (PV), Italy

Introduction. The Electrical Resistivity Tomography (ERT) is a useful tool to define not only the shallow subsurface stratigraphy of complex geological area involved by landslides, but also to locate in clay soils underground water seepage.

In active landslides, the identification of layers of saturated clays in slopes forming the sliding surface, is of primary importance to optimize emergency actions first and then the final design of the slopes stabilization, with a relevant cost saving.

Previous researches about the combination of different geophysical surveys with geotechnical tests on subsoil characterization (see Barbero and Naldi, 2018a; Barbero and Naldi, 2018b; Barbero *et al.*, 2020) highlighted not only a better comprehension of the failure mechanisms of unstable slopes, but also a correct interpretation of environmental issues in support of environmental geology.

In this short note, we report on two case histories of geophysical investigation by means of hight resolution Electrical resistivity tomography surveys of landslide bodies located in the southern Piedmont (Asti Province) shaped in the same litotype (Lugagnano Clay).

Geological context. The investigated areas are located in the western side of the Asti Reliefs (elevation 130-320 m a.s.l.) in the central Piedmont hilly region (Fig. 1). The sedimentary

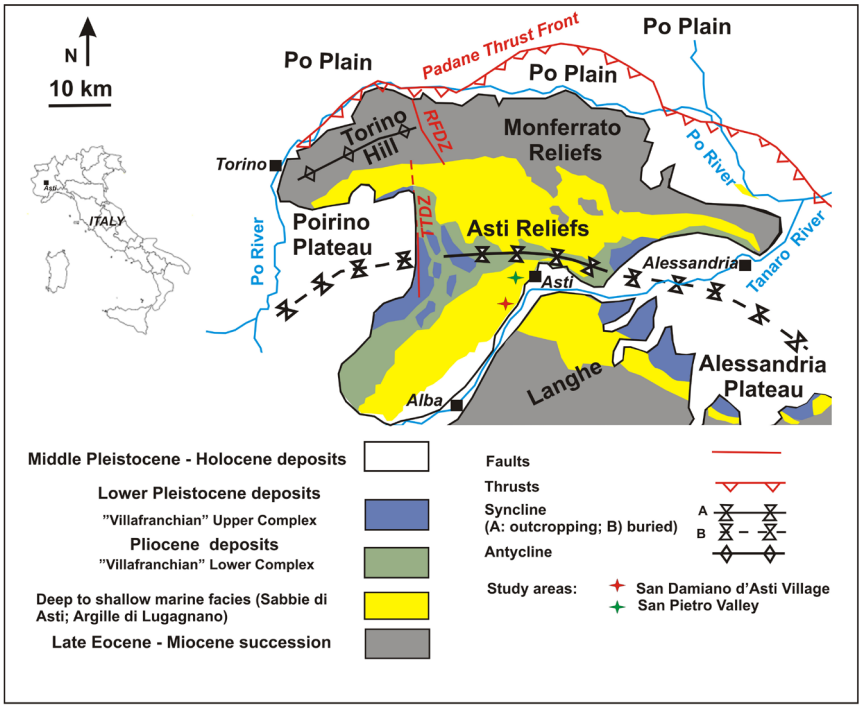


Fig. 1 - Schematic geological and structural map of southern Piedmont region (RFDZ: Rio Freddo Deformation Zone; TTDZ: Torrente Traversola Deformation Zone) (after Forno *et al.*, 2015).

succession is defined, in the lower bands of the hilly reliefs, by deep marine clay deposits (Lugagnano Clay) and littoral sandy deposits (Asti Sand) referred to the Pliocene (Zanclean). These sediments are usually covered by the "villafranchian succession" comprising deltaic deposits (Lower Complex) and fluvial deposits (Upper Complex), referred to the Piacenzian and Calabrian respectively, separated by an unconformity (Cascina Viarengo Surface) (Carraro Ed, 1996; Forno *et al.*, 2015). Above these sediments a widespread silty and subordinately gravelly fluvial cover of middle and upper Pleistocene occurs (Carraro and Valpreda, 1991).

The fluvial deposits appear as a terraced fluvial succession that develops at different heights at the top of the hill ridges in the Asti Reliefs frequently involved by surficial landslides (mudflows) (Barbero *et al.*, 2014a; Barbero *et al.*, 2014b).

The whole sedimentary sequence is deformed by the Asti Syncline consisting of a wide E-W regional scale fold developed in the central hilly area (Poirino Plateau, Asti Reliefs and Alessandria Plateau) (Fig. 1). Recent geological researches (Forno *et al.*, 2014; Gattiglio *et al.*, 2015), regarding the Plio-Pleistocene evolution of the western edge of the Asti Reliefs, emphasized the presence of a N-S deformation zone, named T. Traversola Deformation Zone (TTDZ). This structure corresponds to a scarp with, a rectilinear trend in map view, a height up to a hundred meters and a length of about 30 km, delimiting the Asti Reliefs from the Poirino Plateau.

Landslide in San Damiano d'Asti village case study. *Geological and morphological setting.* Detailed geological and morphological surveys have been carried out (Barbero *et al.*, 2015). The investigated side is located in the lower band of a hilly ridge gently sloping towards SSW (**A** in Fig. 2). The landslide involves a slope shaped in the marine succession formed by gray-blue

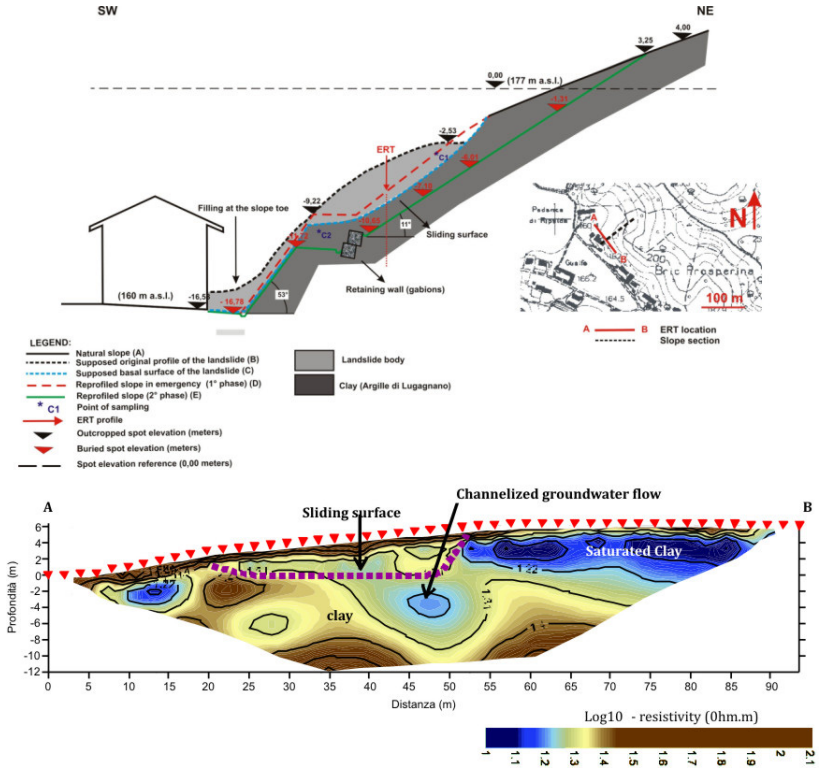


Fig. 2 - Landslide section profile and re-profiling design with ERT location (above), Geoelectrical tomography section (below).

clay massive deposits rich in microfossils (Lugagnano Clay), with horizontal-parallel bedding (strike of 230/20), locally outcropping. The paleontological content allows to refer these sediments to the Zanclean Stage and of the Pliocene Serie (Boni *et al.*, 1969). These sediments show numerous sub-vertical fractures with strike 300/90 and 340/90, some of which are characterized by water circulation.

The landslide body covering the substrate is made of silty-clay deposits with a strong brown color (7.5 YR) with grey mottles and pseudogleys. The landslide sedimentological features suggests that the phenomenon involved the soil developed on the clay substrate and its colluvial cover, that show similar features. The mechanism of the landslide is due to a main rotational slide, that involved the weathered clay substrate, followed by a liquefaction affecting the colluvial cover. It shows a maximum thick of 4 m. The supposed original topography of the landslide body and its basal surface are reported (**B** and **C** in Fig. 2, respectively). The trend of this basal surface is connected to the presence of a terrace, evidenced in the lateral sectors of the slope, not involved in the mass movement, and locally covered by the landslide. A first re-profiling of the side was made in emergency, in order to remove the unstable mass (**D** in Fig. 2) which does not reach the basal surface of the landslide (**C** in Fig. 2). The proposed re-profiled slope is also reported (**E** in Fig. 2), entirely developed in the substrate.

Electrical Resistivity Tomography (ERT). The purpose of electrical surveys is to determine the subsoil resistivity distribution, which is correlated to variations in mineral and fluid content, porosity and degree of water saturation in the rock. Electrical resistivity method is based on measuring the electrical potentials between one electrode pair while transmitting a direct current between another electrode pair (Reynolds, 1997). According to the landslide morphology, characterized by a stepped slope profile, only one traverse line was conducted approximately in the middle of the landslide, using a combination of Wenner and Schlumberger configuration (Fig. 2). Profile ERT, striking E-W, was performed across slope with 48 electrodes with a spacing of 2 m. Electrical data, including resistivity and induced polarization, were processed with the algorithm developed by Loke and Barker (1996).

The ERT image resistivity profile (Figure 3) shows a layered sequence of low resistivity (wet clay, with resistivity from 10 to 20 ohm.m) and medium resistivity soft sediments (silt and clay, with resistivity values up to 100-120 ohm.m). The colluvial cover (with high porosity) is very thin (less than 1 m of thickness) and shows values of 100-120 ohm.m. The landslide mass has a similar resistivity. The most interesting feature of the section is a globular anomaly of low-resistivity just below the inferred sliding surface. This anomaly is probably related to a channelized groundwater flow along a fractured zone. This groundwater circulation pattern is typical of this kind of sediments. The pore water pressure increases within this fractured zone during heavy rainfall. Consequently, the triggering of shallow movements of the overlying clay can be supported. The determination of size and depth extent of the groundwater channelized flow was, therefore, important to define the boundary conditions to quantify this effect using geotechnical modeling.

Unstable slope of a hilly ridge in San Pietro Valley, Asti City case study. *Geological and morphological setting*. The investigated area is located in a hilly ridge gently sloping towards N in the western side of Asti City along the San Pietro Valley (Fig.3). The slope is shaped in the transitional facies of marine succession, formed by silty-sand (Asti Sand) outcropping in the upper band of the hilly ridge and gray-blue clay (Lugagnano Clay) outcropped in the lower band of the slope (see geological map in Fig. 3). Along the lower band of the hilly ridge, shallow landslides occurred in the clay sediments, showing a horizontal-parallel bedding with localized sub-vertical fractures lacking of water seepages.

The reason of the geoelectrical survey was due to a high humidity on the walls of the house

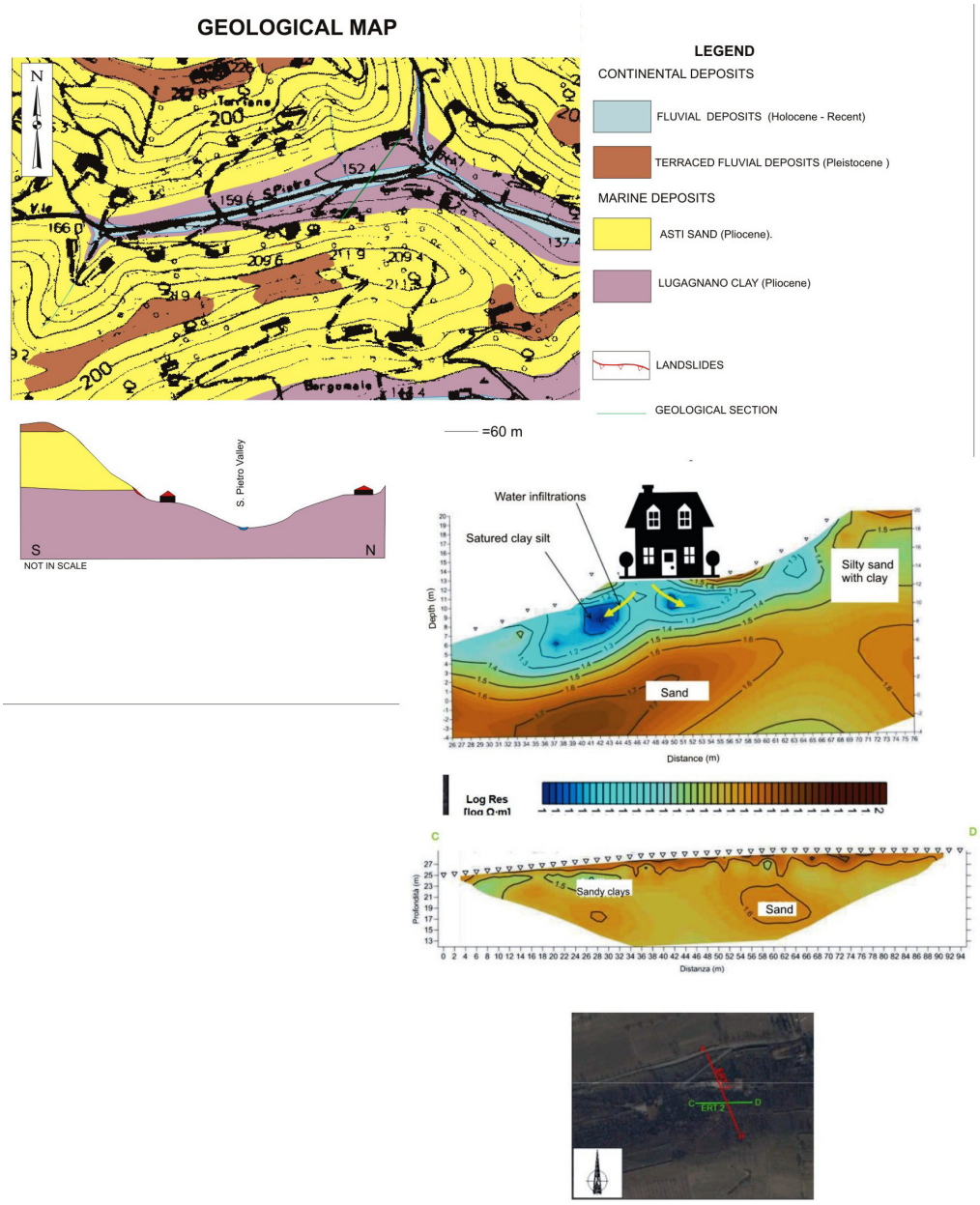


Fig. 3: Detailed geological maps of the area of San Pietro Valley (Asti city) (above); Geoelectrical tomography sections (below).

located along the hilly ridge. Previous geotechnical investigations by penetration tests and pits carried out around the house, revealed the presence of water below the floor of the house.

Electrical Resistivity Tomography (ERT). In order to understand the provenience of the humidity of the house, two ERT were performed. The ERT 1 section was made using 48 electrodes with a 3 m center distance; the stringing with a total length of 141 meters made it possible to reach a depth of investigation equal to 24 meters (in central position). The ERT 2 section has been created using 48 electrodes with 2 m center distance for a string length

of 94 meters, ensuring a depth of investigation of about 15 m. A mixed sequence Wenner Schlumberger 48 channels was adopted for the acquisition of electrical resistivity data for a total of 545 measurement quadripoles for each line.

The ERT1 section (Fig. 3) is the most interesting for the purposes of lithostratigraphic characterization. As illustrated in Figure 3, an electro-stratigraphic sequence is highlighted characterized by an alternation of sandy levels (with electrical resistivity values between 70 and 100 Ω×m, shades of ocher-brown color) and sandy levels with a clayey matrix (with values of electrical resistivity between 30 and 70 Ω×m, green-ocher color tone). The most interesting element from a geological point of view is represented by the strong anomaly conductive visible under the access road to the building. This anomaly (with resistivity lower than 10 Ω×m, blue color tone) is localized around the building. From the lithological point of view - given the strong homogeneity of the subsoil found both in the rest of section ERT1 and in section ERT2 - this anomaly corresponds with soils probably saturated with a predominantly loamy-clayey matrix.

Since there are no feeding areas from the overhanging slope, and since, on the other hand, a possible supply from the area of the building itself, it is believed that the presence of humidity both to be connected to the activity related to the building (gargoyles of the downspouts with direct discharge in the subsoil, direct discharges into the subsoil, rupture of water collection pipes, rupture of pipes of drinking water, etc.).

The ERT2 section highlights an extremely homogeneous lithostratigraphic situation without anomalies attributable to the presence of water; this supports the hypothesis that infiltration of water occurs in the area of the building.

Conclusions. This note shows as the combination of geophysical methods can lead to a better comprehension of the failure mechanisms of unstable slope. Both cases studied show the identification of channelized groundwater flow into clayey soils by means of geoelectric surveys (ERT) requires an accurate and careful interpretation of the geophysical data integrated with a detailed geological survey and/or geotechnical tests for the calibration of the results.

In details, in the first case study, the ERT survey has localized the saturated clay along which occurred the sliding. According to this information, a first remediation action (D in Fig. 2) was the re-profiling of the slope to remove the unstable mass upon the gliding surface (emergency action). Subsequently, the stabilization of the slope has included both drainage interventions (to control the water pressure), a more efficient re-profile of the ground surface (E in Fig. 2) and the positioning of retaining wall at the toe of the slope. In the second case history, the geoelectric survey showed that: i) the lithostratigraphic setting is rather homogeneous, characterized by a stratigraphic sequence with sandy levels alternating with sandy-clayey levels. There was no evidence of the presence of an aquifer or of localized occurrences of water seepage; ii) strong conductive anomalies were found around the building attributable to presence of fine matrix soils in conditions of high saturation. Such saturation seems to derive from superficial infiltrations located near the building.

References

Boni A., Boni, P. Braga G., Bruno G., Casnedi R., Corsi M., Gatto G.O., Gatto P., Mosna S., Motta E., Perotto G., Rampoldi R.; 1969: *Foglio 69 "Asti".* Carta Geologica d'Italia alla scala 1:100.000, II ed., Serv. Geol. It., Roma.

Barbero D., Boano P., Forno M.G.; 2014a: *Fenomeni di instabilità di versante in un tratto Astigiano della valle del Fiume Tanaro che interessano forme fluviali sospese.* In: Atti e contributi del convegno "L'alluvione del 5-6 Novembre 1994 in Piemonte: venti anni di attività nella previsione e prevenzione in ambito gelogico-idraulico", 28-29 ottobre 2014, Torino, Regione Piemonte, Ordine Reg. Geol. Piemonte, CNR-IRPI, GEAM (Eds), 123-128.

Barbero D., Doglione A., Forno M.G., Gattiglio M.; 2014b: *The importance of stratigraphic and structural aspects in the mitigations of landslides involving slopes near Aguggia (San Damiano d'Asti)*, In: Miscellanea INGV Abstract Volume AIQUA Congress 2015: "The Plio-Pleistocene continental record in Italy: highlight on stratigraphy and neotectonics", 24-26 Febbraio 2015, Torino, Monegato, G., Gianotti, F., Forno, M. G. (Eds), AIQUA, 11-12.

Barbero D., Forno M.G., Naldi M., Tissoni A.; 2015: *Electrical Resistivity Tomography in Support of Geological Surveys of Landslides Involving Clay Slopes in Asti Reliefs.* Proceeding of the 21th European Meeting of Environmental and Engineering Geophysics – Near Surface Geoscience Conference, Turin 6-10 September 2015. DOI: 10.3997/2214-4609.201413692

Barbero D., Naldi M.; 2018a: *Prospezione geofisica multi-parametrica per la caratterizzazione di un'area in frana.* Atti del 37° Convegno Nazionale del Gruppo Nazionale di Geofisica della Terra Solida, Bologna 19-21 Novembre 2018, Centro Stampa della Regione Emilia-Romagna, p.604-610.

Barbero D., Naldi M.;2018b: *Indagine geoelettrica a supporto della verifica del materiale di copertura di una discarica dismessa nel Piemonte sudoccidentale.* Atti del 37° Convegno Nazionale del Gruppo Nazionale di Geofisica della Terra Solida, . Bologna 19-21 Novembre 2018, Centro Stampa della Regione Emilia-Romagna, p.610-614.

Barbero D., Tissoni A., Maroni A., Peyrot S.; 2020: *Geotechnical study of a landslide reactivation in clay soils (Central Piedmont, NW Italy).* Journal of Geotechnical Engineering, 7(1). p.21-36 DOI: https://doi.org/10.37591/joge.v7i1.2917

Carraro F., Valpreda E., 1991: *The Middle-Upper Quaternary of the Asti Basin*. Il Quaternario It. Journ. Quatern. Sci, 4(1), 151-172.

Carraro F. (Ed.); 1996: *Revisione del Villafranchiano nell'area-tipo di Villafranca d'Asti.* Il Quaternario (It. Journ. Quatern. Sc.), 9 (1): 5–119.

Forno M.G., Gattiglio M., Comina C., Barbero D., Boano P., Doglione A; 2014: *La franosità lungo la zona di deformazione del T. Traversola.* GEAM: Atti e contributi del convegno "L'alluvione del 5-6 novembre 1994 in Piemonte. Venti anni di attività nella previsione e prevenzione in ambito geo-idraulico", Torino 28-29 Ottobre 2014, LI.PE, p.123-128.

Forno M.G., Gattiglio M., Comina C., Barbero D., Bertini A., Doglione A., Irace A., Gianotti F., Martinetto E., Mottura A., Sala B.; 2015: *Stratigraphic and tectonic notes on the Villafranca d'Asti succession in type-area and Castelnuovo Don Bosco sector (Asti reliefs, Piedmont).* Alpine and Mediterranean Quaternary, 28(1), 5-27

Loke M., H., Barker R.D.; 1996: *Practical techniques for 3D resistivity surveys and data inversion.* Geophysical prospecting, 44, 499-523.

Reynolds J.; 2011: *An Introduction to Applied and Environmental Geophysics.* John Wiley & Sons Inc; 2nd edition

INTEGRATED ANALYSIS OF HVSR AND BOREHOLE DATA TO IMPROVE THE GEOLOGICAL MODEL OF THE SUBSOIL OF PALERMO TOWN (SICILY, ITALY) IN THE ORETO RIVER AREA.

A. Canzoneri, R. Martorana, M. Agate, P. Capizzi
University of Palermo, Department of Earth and Marine Sciences (DISTEM), Italy

Introduction. In the present work the preliminary results are presented, related to the joint examination of boreholes and seismic data acquired in the area of the Palermo plain located near the bed of the Oreto River. This study was developed to define a more reliable model of the stratigraphic, geotechnical and geophysical features of the Palermo plain and to provide a more detailed definition of the depth of the bedrock and the thickness of the sedimentary cover.

Geomorphological and geological setting: the Palermo plain and the Oreto River. The Palermo plain displays a maximum extension of about 6 km and an altitude between 0 m and 150 m. s.l.m. This area is located between the Tyrrenian Sea and the Meso-Cenozoic carbonate reliefs that develop their structure mainly along a N-S alignment, in the western sector, and along a NW-SE trend in the eastern corner of the plain.

Meso-Cenozoic carbonate rocks and Cenozoic flyschoid deposits composing the mountains surrounding Palermo town have been intercepted and recognised by some boreholes at depths over a hundred meters beneath the Palermo plain. These older lithologies are up-covered by 1.5-0.8 Ma aged calcarenitic and sandy deposits. This stratigraphic setting is the results of the "Calabrian" marine transgression that affected the area starting from the Pleistocene. Quaternary marine sediments, forming a shallowing upward succession named as "Sintema di Marsala" (Agate *et al.*, 2017), deposited during this event. These rocks outcrop in a large area of the plain.

In particular these rocks are composed by conglomerates, sands, blue clays ("Ficarazzi clays"; Ruggieri *et al.*, 1975) and variously cemented sandy and bioconstructed deposits of the "Palermo Calcarenites".

Above these marine rocks, the coastal conglomerates and sands of "Sintema of Buonfornello-Campofelice" (middle Pleistocene) and of the "Sintema of Barcarello" (upper Pleistocene may also outcrop. These latter, consist of conglomerates and variously cemented sandstones and colluvial deposits of coastal environment (Cappadonia *et al.*, 2020).

The Holocene deposits along the coast and within the current hydrographic network complete the stratigraphic succession.

The main course of the Oreto River has a length of about 20 km. This develops approximately from the above describes zone of the change in orientation of the Palermo Mounts, up to its outflow located in the Gulf of Palermo. In the Palermo plain the riverpath is confined within a valley carved in the Oligo-Miocene deposits of the Numidian Flysch.

In the stretch of the river flowing in the urban area, represented in Fig. 1, the river course takes on a meandering trend with recessed shapes and several meters high banks consisting of Pleistocene deposits.

The final stretch of the watercourse, modified by the hydraulic structures realized in the early decades of the 1900, was originally characterized by a meandering morphology and anastomized in several free branch before its mouth (Agnesi, 2021).

The geological setting of the study area defines two different groundwaters reservoirs: one superficial linked to the calcarenitic rocks and a deeper one connected to the presence of fractured Meso-Cenozoic carbonates (Cusimano *et al.*, 2004).

The study area (Fig. 1) corresponds to the zone enclosed between the coastline at east and a western sector in which the town ring road intersects the river path. Northern and southern

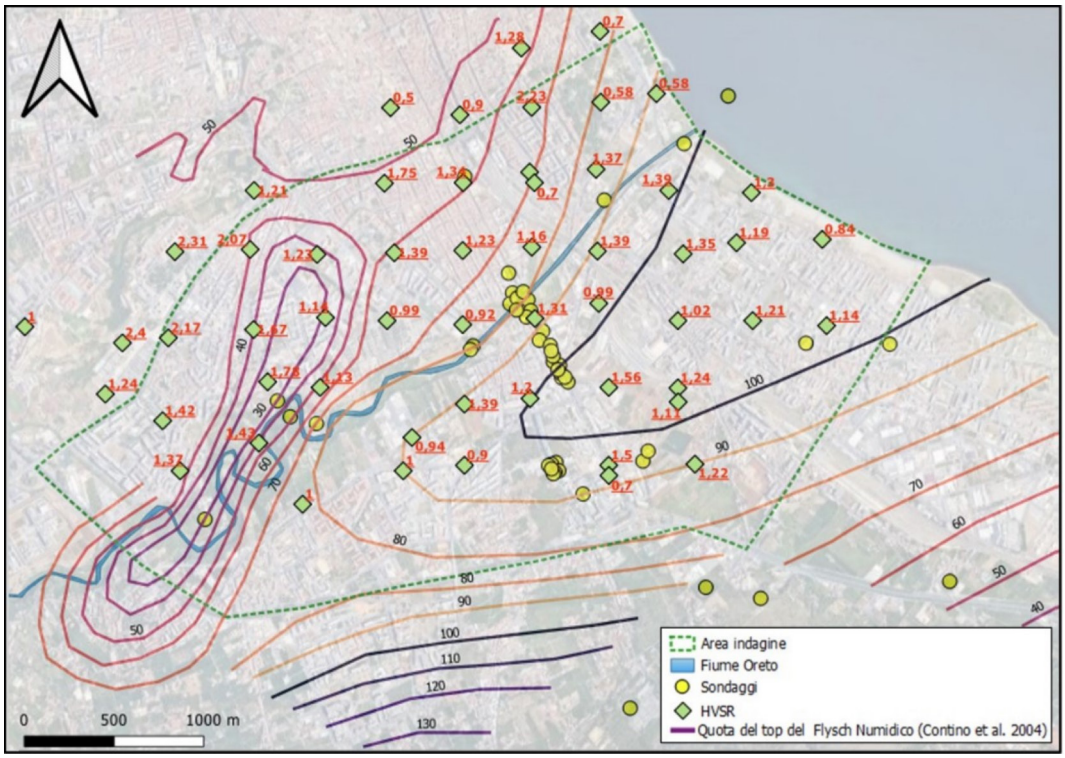


Fig. 1 - Map of the studied area (enclosed by the green dotted line) with the position of the stratigraphic boreholes (yellow dots) and of the seismic noise recordings (green squares) analyzed. Frequencies of the main peaks (numbers in red) are indicated for each noise recording. The iso-depth lines of the Numidian Flysch, defined by Contino *et al.,* 2006, are showed in color-scale.

limits of the area are represented by two of the main road axes of Palermo; respectively the northern axis of "Via Lincoln-Corso Tukory-Via Ernesto Basile" and the southern axis of Via Giafar.

Avalaible datasets and preliminary analysys. In the above-described area 54 recordings of environmental seismic noise were analyzed. These were carried out in 2016 for the preparation of the "General Town Plan - Palermo 2025 (PRG 2.0)". The position of microtremor measurements is represented in Fig. 1.

The recordings, each of 30 minutes, were analyzed according to the HVSR technique (Nakamura, 1989) and the signals, before being processed, were filtered, excluding from the analysis those time windows probably affected by transient anthropogenic noise.

The analysis of the HVSR curves (Fig. 2) allowed to recognize a general trend characterized by the presence of a main peak between about 0.8 Hz and 2.5 Hz and by other secondary peaks at higher frequencies, generally between 15 Hz and 35 Hz. Furthermore, a sharp velocity inversion, defined by the H/V ratio lower than 1, has been recognized for a frequency range between 2.5-3 Hz and 15-20 Hz.

Moreover, 50 lithological boreholes located in the studied area (Fig. 1) were taken into consideration. These data are stored in the CityGIS database (Giammarinaro and Maiorana, 2001) managed by the Department of Earth and Marine Sciences of the University of Palermo, that collects stratigraphic and geotechnical data.

A preliminary qualitative joint analysis of the boreholes and the microtremor data was realized. The analysis has been implemented by previous bibliographic information on the

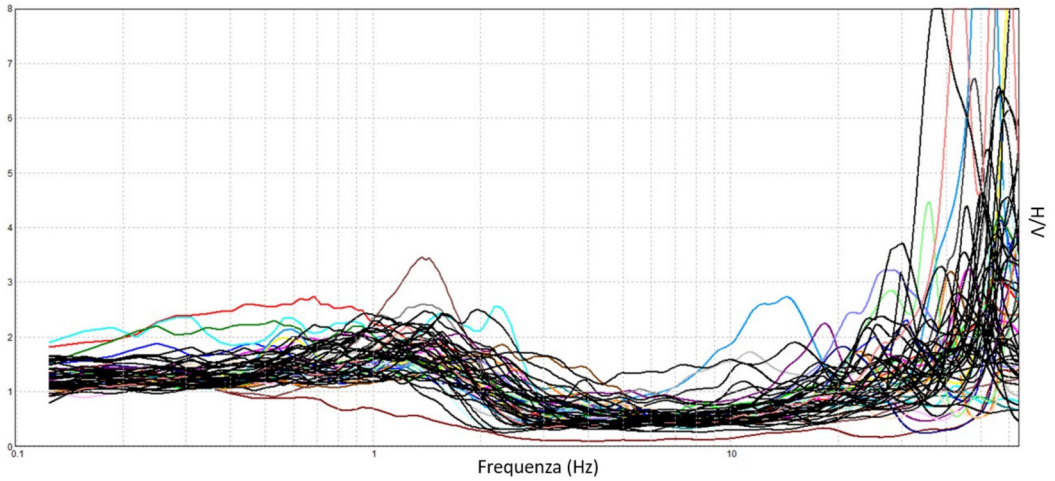


Fig. 2 - Overlapping of all considered HVSR curves.

Palermo Plain (Giammarinaro *et al.*, 2000; Canzoneri *et al.*, 2002; Martorana *et al.,* 2018; Cappadonia *et al.,* 2020; Agnesi, 2021).

This approach proved useful to correlate the available data with the bedrock depth maps defined basing on the stratigraphic data of the Oreto River. In particular Figure 1 shows the iso-depth contour lines of the top of the Numidian Flysch, as reported by Contino et al. (2000).

Basing on the analysis of the HVSR curves trend (Fig. 2), a geological-stratigraphic model has been developed for the studied area. According to this model, the low frequency main peaks (0,8 -2.5 Hz) are probably generated by the contact between the Pleistocene clays and the higher portions of the Numidian Flysch.

The blunt shape of the peaks also suggests that these are probably caused by the contact between the Oligo-Miocene Flysch deposits and the underlying Meso-Cenozoic carbonate basement.

The reversal of velocity, that is evident at higher frequencies in almost all the H/V curves, could be attributed to the contact between calcarenite deposits and the underlying Pleistocene clays.

For even higher frequencies, the further increase of the spectral ratio and the presence of other secondary peaks could be attributed to the boundary between alluvial, colluvial and coastal Holocene surface soils and the underlying more cemented portions of the “Sintema di Barcarello” and “Sintema Buonfornello-Campofelice”, as well as to the presence of the Calabrian calcarenites in this area, well recognizable along the outcrops that border the Oreto River.

The future aim of this work is to deepen and develop these preliminary results through a planning of detailed geophysical investigations, that will be realized in different profiles of the study area. In particular, we will focus on the mouth of the Oreto River and on sectors in which the river course seems to be controlled by tectonic structures.

This approach, in addition to increasing the geological knowledge on the subsoil in the Oreto river area, has a double value: on the one hand, to define with more accuracy the features of the area in terms of local seismic response and, on the other, to describe the sedimentary deposits overlying an impermeable bedrock, that could be sites of surface aquifers.

Bibliography

Agate M., Basilone L., Di Maggio C., Contino A., Pierini S. and Catalano, R.; 2017: *Quaternary marine and continental unconformity-bounded stratigraphic units of the NW Sicily coastal belt*. Journal of Maps, 13(2), pp. 425-437.

Agnesi V. (edited by); 2021*: La geomorfologia di Palermo*. Sapienza Università Editrice.

Canzoneri V., Giammarinaro M.S., Gugliuzza G. and Vallone P.; 2002: *Area urbana palermitana: analisi delle proprietà geotecniche dei terreni supportata da tecnologia GIS*. Opere Geotecniche in ambiente urbano, pp. 37-44.

Cappadonia C., Di Maggio C., Agate M. and Agnesi V.; 2020: *Geomorphology of the urban area of Palermo (Italy)*. Journal of Maps, 16(2), pp. 274-284.

Contino A., Giammarinaro M. S., Vallone P., Varsalona S. and Zuccarello, A.; 2006: *Analisi stratigrafico geotecnica del settore meridionale della città di Palermo finalizzata alla caratterizzazione di fattori di pericolosità sismica in esso presenti*. Boll. Soc. Geol. It., 125 (3), pp. 329-343

Cusimano G., De Maio M., Gatto L., Hauser S. and Pisciotta A.; 2004: *Application of SINTACS method to the aquifers of Piana di Palermo, Sicily, Italy*. Geofísica Internacional, 43(4), pp. 661-670.

Giammarinaro M.S., Canzoneri V., Spotorno R., Sulli A. and Catalano R.; 2000: *Historical Centre of Palermo: effects of the lithotechnical successions on the bulk contribution to seismic response*. Mem. Soc. Geol. It., vol. 55, pp. 439-447.

Giammarinaro M.S. and Maiorana S.; 2001: *Una applicazione GIS dedicata ai sistemi urbani*. Geologi di Sicilia, 3, pp. 21-25.

Martorana M., Agate M., Capizzi P., Cavera and D'Alessandro A.; 2016: *Seismo-stratigraphic model of La Bandita area in the Palermo Plain (Sicily, Italy) through HVSR inversion constrained by stratigraphic data*. Italian Journal of Geoscience, 137(1), pp. 73-86, https://doi.org/10.3301/IJG.2017.18.

Nakamura Y.; 1989: *A method for dynamic characteristics estimation of subsurface using microtremor on the ground surface*. Railway Technical Research Institute, Quarterly Reports, 30(1).

Ruggieri G. and Sprovieri R.; 1975: *Ricerche sul Siciliano di Palermo: le argille del fiume Oreto.* Boll. Soc. Geol. It., 94, pp. 1316-1622.

SMALL-SCALE CHARACTERIZATION OF PLANT ROOT ARCHITECTURE AND BIOMECHANICAL DYNAMICS VIA 4D ELECTRICAL RESISTIVITY TOMOGRAPHY

A. Carrera[1], J. Boaga[1], S. Sartori[2], W. Bertoldi[2]

[1] Dipartimento di Geoscienze, Università degli Studi di Padova, Padova, Italy
[2] Dipartimento di Ingegneria Civile Ambientale e Meccanica, Università degli Studi di Trento, Trento, Italy

In this work we introduce an application of time-lapse 3D micro-electrical tomography (ERT) to track the plant-soil interaction in the radical zone. The goal of the study focused on a non-invasive analysis of the roots apparatus of two characteristic species of riparian vegetation, a poplar (*Populus nigra)* and an alder (*Alnus incana)*, in order to understand the different soil-vegetation interactions and the botanical influence who can exercise on the river morphology. Generally, alders have a fasciculated root system with greater biomass and concentrate in the most superficial layers compared to poplars which instead develop vertical roots in search of the water table. Indeed, the root system, besides providing nutrients to the plant and ensuring anchorage, enhancing soil cohesion, increasing the research interest in the biomechanical action for riverbanks reinforcement (Bertoldi and Gurnell, 2020; Sartori, 2021).

For this reason, we tried to recreate a controlled environment where to examine the plants growth in terms of aerial and especially root biomass, taking advantages of the interesting perspectives provided by ERT (Boaga *et al.*, 2013; Vanella *et al.*, 2018; Ehosioke *et al.*, 2020; Mary *et al.*, 2020). Having to adapt quickly to environmental changes (e.g. river flooding, dry events), the riparian species show rather high growth rates, so that even in short time spans it is possible to study their development.

We designed, built and installed a 3D electrical tomography system for the monitoring of the two riparian species root zone, in an experimental apparatus located at the University of Trento, Italy (Fig. 1).



Fig. 1. - Instrument connections and 3D electrical tomography system configuration.

On two PVC bins, filled with different materials and housing three specimens of each of the two plants respectively, small holes were drilled in the bottom to simulate the presence of the water table and allow water from irrigation or rainfall to flow through and not completely saturate the bin.

The micro-ERT apparatus consists of 48 buried metal plugs, inserted on the bin sides in 4 vertical rows, plus other 24 mini-electrodes on the ground surface.

We adopted a time-lapse approach, conducting repeated ERT acquisitions over time in order to assess the evolution of the system's dynamics under changing moisture conditions: a first time-zero measure, six acquisitions every 1.5 hour after the irrigation and a last control measurement after 24 hours from the test beginning. As a basic starting point, we checked the experimental design and the acquisition sequence through synthetic modeling (Fig. 2), with a special focus on sensitivity and coverage.

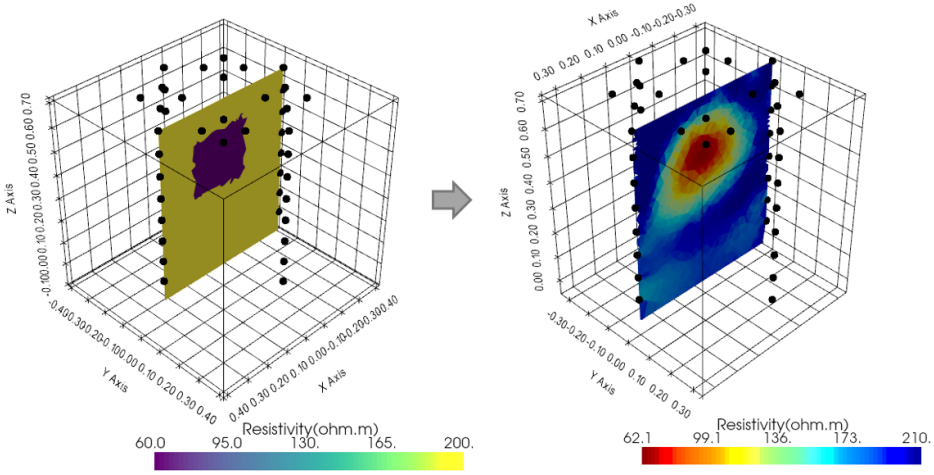


Fig. 2 - Synthetic modeling before the experiment.

Data were acquired using the MAE X612EM+ multichannel georesistivimeter, with dipole-dipole skip 0 acquisition sequence, including reciprocal measurements. Before each acquisition the contact resistance check was carefully performed, to ensure a good current injection and the reliability of the experiment.

Processing and time-lapse inversion of the datasets (Fig. 3) were conducted through ResIPy (Blanchy *et al.*, 2020).

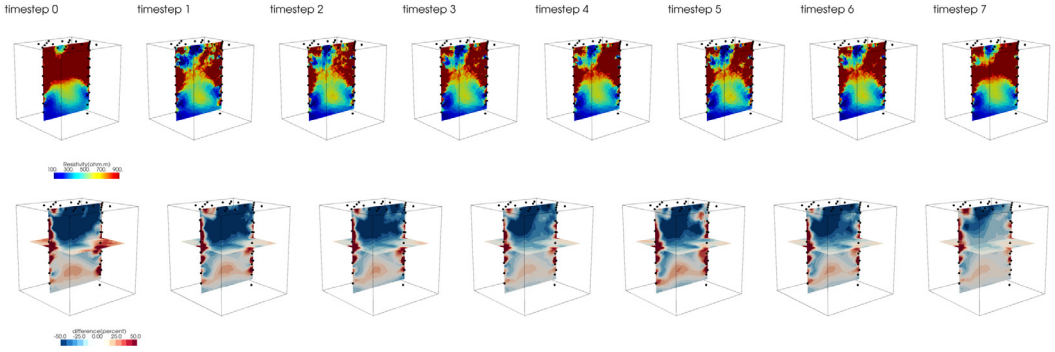


Fig. 3 - Resistivity and relative differences time-steps sections for the *Alnus incana*.

At the end of the experiment, the plants were uprooted to analyze and compare the roots vertical distribution of the two species. A good correspondence between the direct observations and those obtained by electrical tomography was observed.

Further tests could be carried out during the entire growth period of the plants, allowing the gradual development of the roots to be monitored. In addition, further refinement would ensure the use of this approach in the natural environment, where roots are particularly developed but difficult to access (Beff *et al.*, 2013).

Nevertheless the complexity of the investigated system, in term of interactions between soil moisture, mineralogy and pore water salinity on the electric response, the results demonstrate how the small scale 4D ERT is a promising approach able to non-invasively characterize the root zone, especially in terms of suction regions.

References

Beff, L., T. Günther, B. Vandoorne, V. Couvreur, and M. Javaux. 2013. *Three-dimensional monitoring of soil water content in a maize field using Electrical Resistivity Tomography.* Hydrol. Earth Syst. Sci. 17(2): 595–609. doi: 10.5194/hess-17-595-2013.

Bertoldi, W., and A.M. Gurnell. 2020. *Physical engineering of an island-braided river by two riparian tree species: Evidence from aerial images and airborne lidar.* River Res. Appl. 36(7): 1183–1201. doi: 10.1002/RRA.3657.

Blanchy, G., S. Saneiyan, J. Boyd, P. McLachlan, and A. Binley. 2020. *ResIPy, an intuitive open source software for complex geoelectrical inversion/modeling.* Comput. Geosci. 137: 104423. doi: 10.1016/j.cageo.2020.104423.

Boaga, J., M. Rossi, and G. Cassiani. 2013. *Monitoring Soil-plant Interactions in an Apple Orchard Using 3D Electrical Resistivity Tomography.* Procedia Environ. Sci. 19: 394–402. doi: 10.1016/j.proenv.2013.06.045.

Ehosioke, S., F. Nguyen, S. Rao, T. Kremer, R.E. Placencia-Gomez, *et al.* 2020. *Sensing the electrical properties of roots: A review.* Vadose Zo. J. 19(1). doi: 10.1002/VZJ2.20082.

Mary, B., L. Peruzzo, J. Boaga, N. Cenni, M. Schmutz, *et al.* 2020. *Time-lapse monitoring of root water uptake using electrical resistivity tomography and mise-à-la-masse: A vineyard infiltration experiment.* SOIL 6(1): 95–114. doi: 10.5194/SOIL-6-95-2020.

Vanella, D., G. Cassiani, L. Busato, J. Boaga, S. Barbagallo, *et al.* 2018. *Use of small scale electrical resistivity tomography to identify soil-root interactions during deficit irrigation.* J. Hydrol. 556: 310–324. doi: 10.1016/J.JHYDROL.2017.11.025.

MULTIDISCIPLINARY STUDY OF NON-VOLCANIC DEGASSING VENT FIELD IN THE SOLOPACA AREA (SOUTHERN APENNINES)

C. De Paola[1], S. Albanese[1], M. Ambrosino[2], S. Ciarcia[2], D. Cicchella[2], R. Di Maio[1], C. Fabozzi[2], P. Notaro[3], F. Pagliara[1], E.P. Prinzi[4], R. Salone[1], S. Vitale[1]

[1] Dipartimento di Scienze della Terra, dell'Ambiente e delle Risorse, Università di Napoli Federico II, Napoli, Italy
[2] Dipartimento di Scienze e Tecnologie, Università degli Studi del Sannio, Benevento, Italy
[3] EalCUBO (Environment, Earth, Engineering) Soc. Coop., Arcavacata, Cosenza, Italy
[4] Dipartimento per il Servizio Geologico d'Italia,ISPRA, Roma, Italy

Introduction. In the southern Apennines (Fig. 1a), evidence of non-volcanic degassing is widespread reported (Ascione *et al.*, 2018; Di Maio *et al.*, 2021 and references therein). Geochemical surveys indicate that the gases are mainly formed by CO_2 (Ascione *et al.*, 2018). In particular, degassing vents are focused along the SW margin of the Matese Mts (Fig. 1a). The main vents are located at north in Ciorlano, Pratella and Ailano areas (Ascione *et al.*, 2018; Di Maio *et al.*, 2021), and at south in the Telese-Solopaca sector (Fig. 1a). The CO_2 flux reaches high values in these areas, with the Ciorlano vent being one of the world's highest non-volcanic CO_2 fluxes (Ascione *et al.*, 2018). Geophysical investigations on these non-volcanic vents (De Paola *et al.*, 2019; Di Maio *et al.*, 2021) mark a close relation between degassing and tectonics, indicating that the fluids migrate upward along preferred pathways corresponding to damage and cataclastic zones of major faults. The SW margin of the Matese Mts is delimited by the Southern Matese Fault (SMF; Boncio *et al.*, 2022) system characterized by different segments with dominant normal kinematics that lowered the SW area (Alife and Telese plains; Fig. 1a).

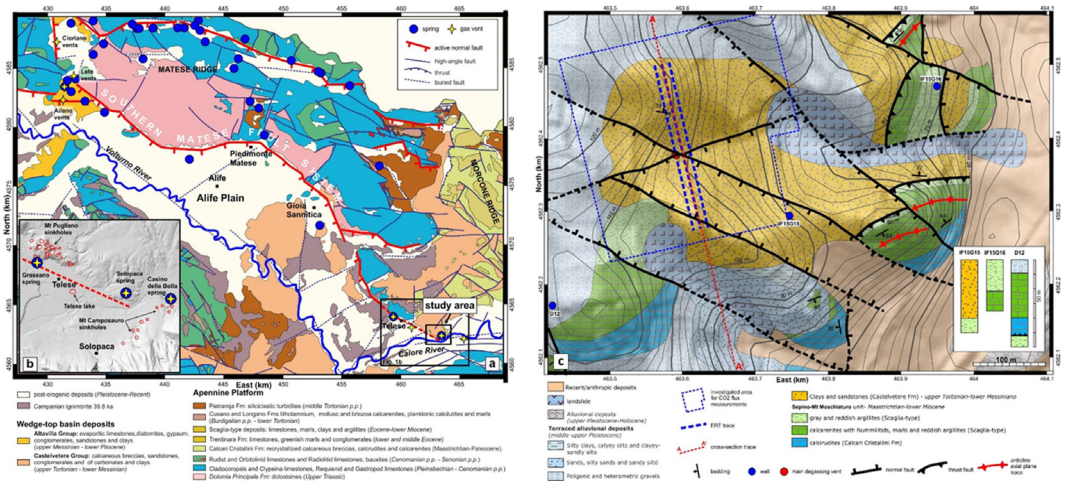


Fig. 1 - (a) Geological map of the southern Matese Mts (after Vitale and Ciarcia, 2018 modified). (b) DTM of the Telese-Solopaca area. (c) Geological map of the study area.

Historical seismicity occurs along the southern margin of Matese Mts, including the ancient earthquake that occurred in 346 CE (M 7.0) that Boncio *et al.* (2022) indicate as resulting from the reactivation of the entire SMF system. Despite the historical earthquake occurrences, instrumental seismic activity is presently negligible. The SMF system seems to continue southward, bounding the hills northward of Solopaca town (Boncio *et al.*, 2022); however, geological evidence is a few, and in general, the area is poorly studied. Hence, we analyzed the area northward of the Solopaca town where a CO_2 degassing vent field occurs, never studied before. We performed stratigraphic, structural, geophysical and geochemical investigations in order to reconstruct the tectonic architecture of the area and shed light on the possible southward prosecution of the SMF system.

Stratigraphical and structural survey. The study area is located along the Matese Mts and the Morcone ridge (Fig. 1b). Here, an Upper Cretaceous-lower Miocene margin to slope succession is exposed, corresponding to the Sepino-Mt Moschiaturo unit (Vitale and Ciarcia, 2018). We performed a geological survey of the area that allowed us to draw a geological map (Fig. 1c). The rocks exposed in the study area are formed at the base by margin calcirudites frequently recrystallized (Calcari Cristallini Fm), passing upward to slope Scaglia-type deposits, including calcarenites with Nummulitids, reddish argillites and clays, and finally to deep basin reddish and greyish clays and argillites. In the study area, the scaglia-type deposits are unconformably covered by sandstones and clays of the Castelvetere Fm. Finally, terraced Quaternary conglomerates, arenites and clays cover the whole succession. The area is characterized by the presence of a degassing spring, defined by aligned with the main centre forming a degassing pool of ca 50 cm in diameter. Generally, sulfur mineralizations are widespread around the gas emissions. Other minor gas vents are scattered in the area, marked by the absence of vegetation and circular halos. The entire succession is crosscut by normal faults. N-S and ENE-WSW normal faults are dislocated by NW-SE faults defined by dominant normal kinematics.

Geoelectrical survey. In the last decades, several stratigraphic and structural studies devoted to the understanding of the processes governing the fluids flow along active fault systems have proven the potentiality of the geophysical methods in reconstructing the architecture of geological contexts characterized by strong emissions of CO_2 (e.g. Byrdina *et al.*, 2009; Pettinelli *et al.*, 2010; Di Maio *et al.*, 2021). In particular, electrical resistivity tomography (ERT) is shown to be among the most appropriate methods for identifying the underground spatial distribution of CO_2, whose migration towards the surface in non-volcanic areas is essentially controlled by fractures, faults and/or structural highs of the carbonate reservoir (e.g. Rogie *et al.*, 2000). In order to obtain a very high-resolution resistivity distribution of the investigated underground volume, a non-conventional 3D ERT data acquisition technique was used, which proved to be very effective in geological contexts similar to the one under study (e.g. Di Maio *et al.*, 2021). The survey was realized in an area of size 20 m x 235 m by using 144 electrodes (Fig. 1c). The apparent resistivity dataset was collected by the IRIS Syscal Pro Switch multi-channel georesistivimeter (IRIS Instruments) using the pole-dipole electrode array, which allowed a measurement sequence consisting of 1414 current injections and 13368 measurement quadrupoles, resulting in an investigation depth of about 45 m.

The acquired data were inverted by the ERTLab64 software (Geostudi Astier Srl, Livorno, Italy, & Multi-Phase Technologies LLC, Nevada, USA), which is based on a smoothness-constrained least-squares approach that uses tetrahedral meshes to correctly account for surface topography (for details, the reader is referred to Morelli and LaBrecque, 1996 and references therein). The final 3D inversion model of the investigated volume was attained with a root mean square (RMS) error of less than 5%. As can be seen in Fig. 2, the resistivity values range from a few Wm to about 80 Wm, which, as inferred from the geological survey and the stratigraphic logs available in the neighbouring of the study area, are consistent with sedimentary formations consisting of calcirudites, calcarenites, argillites, clays and sandstones. In particular, the lowest resistivity values (blue zones in Fig. 2) are reasonably correlated to the occurrence of significant fluid circulation; whilst, the relatively high resistive zones (red areas in Fig. 2) are ascribable to the presence of a mixture of water and CO_2, the latter being responsible for the increase in the resistivity values. The net contrast between the resistive and conductive zones, which is observed approximately in the central portion of the investigated volume (black dashed line in Fig. 2), could be associated with the presence of NW-SE striking fault systems that would favour the uprising of CO_2 gas flow.

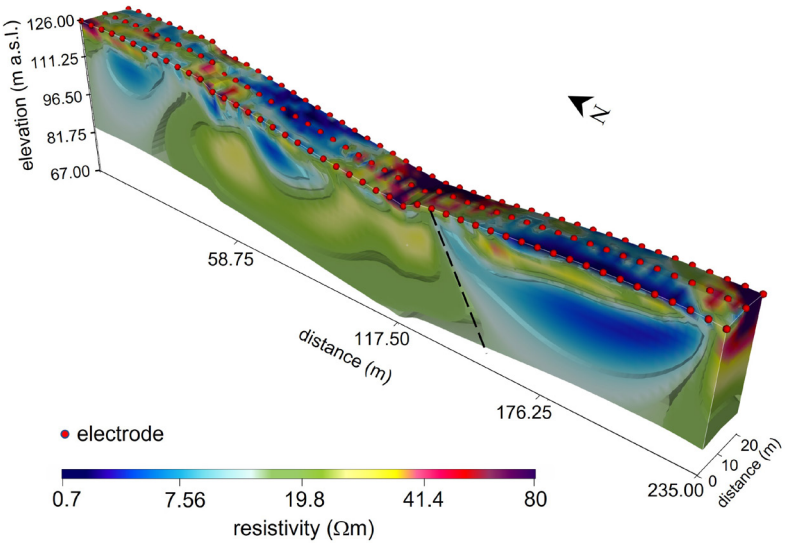


Fig. 2 - 3D resistivity model of the study area. The black dashed line sketches a possible fault plane.

CO_2 flux survey. CO_2 fluxes from the ground were measured in the blue dotted area in Fig. 1c. The data were determined by means of a static accumulation chamber connected to a portable device (Ecoprobe 5) equipped with an Infra-red analyzer and a pump working at variable rates. Measurements were made based on a grid where the position of the measurement stations was denser in correspondence with the ERT profiles. The hourly and daily flux of CO_2 were determined by applying a well-established method. Results in Fig. 3 showed how noticeable higher fluxes (> 39 g m^{-2} d^{-1}) are detected along two main directions which fit well with the hypothesized underlying geological structures. In addition, the measurement made far away

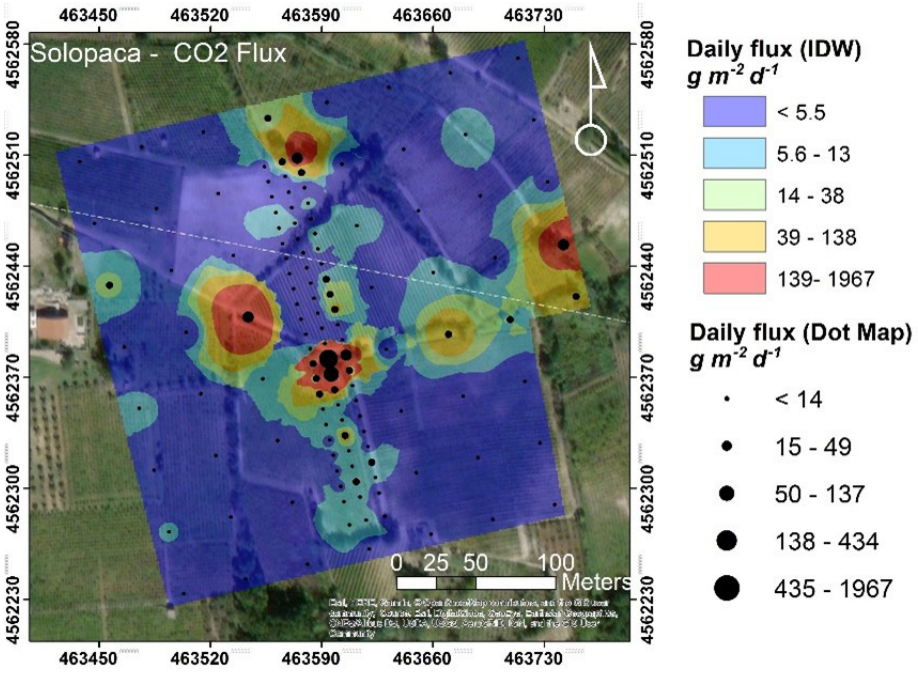


Fig. 3 - CO_2 flux map of the survey area, which is shown in Fig. 1c.

from the higher emissive spots allowed to estimate the average background soil CO_2 emission (<5.5 g m^{-2} d^{-1}) to be used as a reference to discriminate the amount of the gas reaching the surface via the structures.

Conclusions. This multidisciplinary study allows us to characterize the tectonic architecture of the degassing area of the Solopaca spring. The 3D ERT survey well depicts the fault system defined by dominant NW-SE normal faults that act as preferred pathways for the upward migration of CO_2 gases. The CO_2 flux anomalies well-match with the mapped faults, in particular, the main degassing vent is located at the intersection between two major faults. Results indicate that in the Solopaca area, a deep CO_2 source is connected to the surface through NW-SE faults suggesting that a southward prolongation of the SMF system is possible. This feature has important implications for the evaluation of the seismic hazard for the area.

References

Ascione, A., Ciotoli, G., Bigi, S., Buscher, J., Mazzoli, S., Ruggiero, L., Sciarra, A., Tartarello, M.C., Valente, E., 2018: *Assessing mantle versus crustal sources for non-volcanic degassing along fault zones in the actively extending southern Apennines mountain belt (Italy)*. Geol. Soc. Am. Bull. 130 (9e10), 1697e1722. https://doi.org/10.1130/B31869.1.

Byrdina, S., Revil, A., Pant, S.R., Koirala, B.P., Shrestha, P.L., Tiwari, D.R., Gautam, U.P., Shrestha, K., Sapkota, S.N.,.Contraires, S., Perrier, F., 2009: *Dipolar self-potential anomaly associated with carbon dioxide and radon flux at Syabru-Bensi hot springs in central Nepal*. J Geophys Res, 114, B10101.

Boncio, P., Auciello, E., Amato, V., Aucelli, P., Petrosino, P., Tangari, A.c., Jicha, B.R., 2022: *Late Quaternary faulting in the southern Matese (Italy): implications for earthquake potential and slip rate variability in the southern Apennines*. Solid Earth, 13, 553–582, https://doi.org/10.5194/se-13-553-2022.

De Paola, C., Di Maio, R., Piegari, E., 2019: *ERT and SP measurements for the characterization of fault-controlled soil CO_2 degassing*. Proceedings of 25st European Meeting of Environmental and Engineering Geophysics, Near Surface Geoscience 2019, The Hague (The Netherlands), 8-12 September 2019, EarthDoc, Tu_25th_A03, 5 pp., doi: 10.3997/2214-4609.201902390.

Di Maio, R., Salone, R., De Paola, C., Piegari, E., Vitale, S., 2021: *3D numerical simulations of non-volcanic CO_2 degassing in active fault zones based on geophysical surveys*. Surveys in Geophysics, 42, 1443–1478, https://doi.org/10.1007/s10712-021-09666-0.

Morelli, G., LaBrecque, D.J., 1996: *Advances in ERT inverse modelling*. Eur J Environ Eng Geophys, 1(2), 171–186.

Pettinelli, E., Beaubien, S.E., Zaja, A., Menghini, A., Praticelli, N., Mattei, E., Di Matteo, A., Annunziatellis, A., Ciotoli, G., Lombardi, S., 2010: *Characterization of a CO_2 gas vent using various geophysical and geochemical methods*. Geophysics, 75, B137–B146.

Vitale, S., Ciarcia, S., 2018: *Tectono-stratigraphic setting of the Campania region (Southern Italy)*. Journal of Maps 14(2), 9–21.

GPR AND ULTRASONIC TOMOGRAPHY APPLIED TO PRESTRESSED CABLES FOR VERIFYING VIADUCT CONSERVATION STATE

D. Di Massa, P. Luiso, D. Fiore
Socotec Italia srl, Italy

Introduction. The use of prestressed cables has spread in the major infrastructure projects such as bridges and viaducts, in order to improving the resistant behavior of the projects. The phenomenon of the prestressed cables' corrosion is a serious concern; a loss of prestressed system functionality leads to the emergence of criticalities in the structural behavior, favouring of crisis cracking phenomena of the opera.

In the post-strained structures, the cables are located in a sheath filled with cement grout which separates them from the concrete, endorsing better resistance to corrosion. Thus, corrosion problems often arise when grout injection is performed poorly, leading to the local defects' formation; sometimes, the concrete deteriorates, generating small voids, pores or micro-cracks.

The request for information and knowledge on the correct diagnosis of degradation in reinforced concrete and prestressed concrete structures is increasingly frequent. The main difficulty in assessing the degradation level is the inability to access the reinforcement directly, and in a minimally invasive way; thus, indirect investigation techniques are most frequently used (Ferrarella 2021).

For this purpose, ultrasonic tomography (UT) developed in recent years has been used. The UT methodology was developed for the identification of voids and cracks within the concrete, in particular on walls and flooring surfaces (Taffe *et al.*, 2006; Hoegh *et al.*, 2011; White, *et al.*, 2014), for checking the concrete thickness inside tunnels (Gorzelanczyk *et al.*, 2012; Schabowicz 2015) and for the diagnostic study of cultural heritage (Capizzi *et al.*, 2011, Alberghina *et al.*, 2013). Recently, however, the ultrasonic methodology, supported with GPR survey, has been used for locate the prestressed cables and verify of their conservation state. More specifically, the georadar methodology provides a geometric description of the cables even though they are affected by disturbances such as the humidity; the ultrasonic methodology provides information regarding the density variations of the investigated material (Samokrutov *et al.*, 2006; Krause *et al.*, 2009). In this work, we present the potential of the combined methodology carried out above a viaduct in A1; for privacy we are not allowed to name the viaduct.

Methodology of investigation and modelling of geophysical data. The UT methodology is based on the pulse-echo method using the analysis of elastic waves propagation (share waves) to locate areas characterized by structural inhomogeneity, decay, fractures or injuries within the investigated volume. In this work, we used the tomograph Mira A1040 (Fig. 1a) able to create a 3D representation (tomogram) of internal defects in the concrete. MIRA tomograph is based on the pitch-catch method of ultrasound because of the presence of an antenna composed of a matrix of spring-loaded contact transducers (DPC) to conform to an irregular surface, which emit shear waves.

The first transducers' row acts as the transmitter and the remaining transducers' rows of act as the receiver. Thereafter, the next transducers' row is energized and the other rows act as receivers (Fig. 2b). This process is repeated until each of the 11 transducers' rows has acted as a transmitter. It takes less than 3 seconds to complete data acquisition and processing at each location; the measured values of transit times are processed by the computer in order to create a 2D image of the volume below the antenna ("synthetic aperture focusing technique", SAFT). The received signal by a single emitter is affected by structural noise (diffraction due to aggregates, small defects) but the composition of 66 waveforms reduces noise and allows

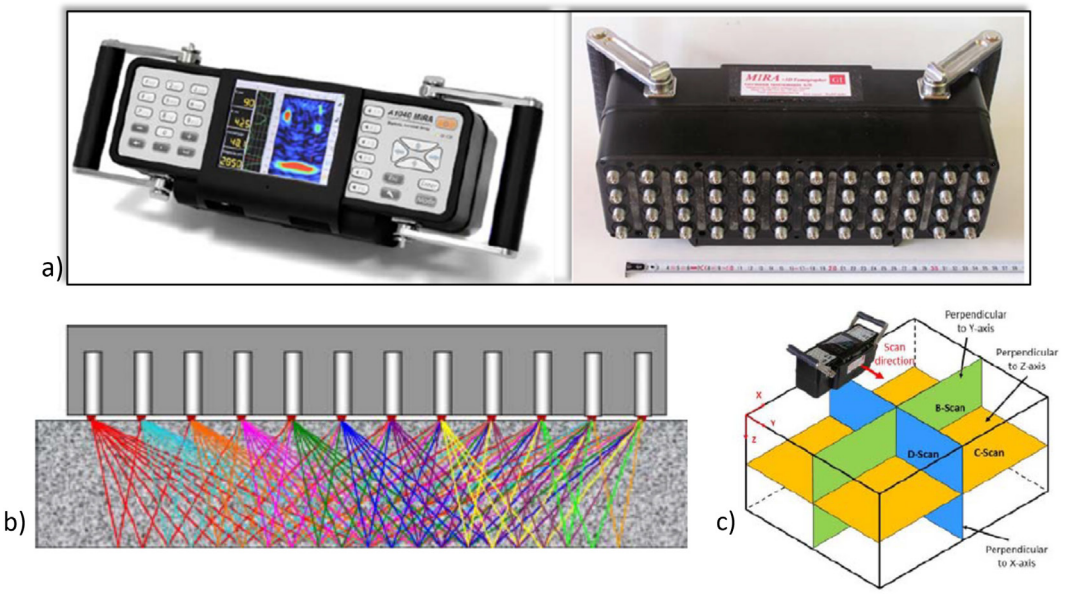


Fig.1 - a) MIRA A1040 tomograph; b) ray paths involved during a measurement; c) Scan sections acquired by the MIRA A1040.

for more precise reflectors' localization. A potential reflector is observed from different angles and with different time delays t and for each point of the image all signals are added to the respective delay times t.

In this work, the SCAN methodology was used; it allows to collect a complete data set using measurements made on a grid of predefined positions on the survey object surface. This mode automatically saves the B-scan data related to each measurement position, having previously allowed the display of the B-scan image that correspond to the sections parallel to the major axis of the instrument (Fig. 1c). The system also stores the settings used and a bitmap image of the MIRA screen display at each point of the grid. Bitmap images are transferred to a folder on a laptop which contains the IDealviewer 3D visualization software that merge the 2D images to create a 3D model of the survey object. The user can manipulate the 3D model by rotating it and looking at different orthogonal planes that cross the model itself. The views on the three orthogonal planes have formal names: the C-scan section appears to be perpendicular to the Z axis; the D-scan section appears to be parallel to the Y axis.

In this work, we investigated some area for each span suggested by the client. For each area, size 0.4 x 1.5 m, the first step is to identify the prestressed cables and define their path using GPR and sign it over the area. More specifically, the GPR survey consisted of transversal line surveys along the whole beams' height (from top to bottom). The GPR strips pitch was 0.25 m in the first and last quarter of the length of the beam and 0.5 m in the remainder. Ultrasound tomography investigations were performed in specific areas characterized by cables' portions performing a variable number of UT scans with a constant pitch of 0.1 m, positioning the instrument transversely investigated cable development. For the ultrasonic tomography survey, a pulse velocity propagation of 2650 m/s was set, obtained following a calibration test performed on the known thickness of the beam. The ultrasonic pulses frequency was chosen following a series of tests at a variable frequency between 20 and 50 KHz; a 35 KHz frequency was chosen, which returned the best result in terms of resolution and noise.

Results and interpretation. The georadar and ultrasound tomography investigations were carried out with the aim of verifying the cables position and locating any injection defects along the viaduct beams.

For the ultrasound tomography sections, the prestressed cables were marked with dashed yellow lines (Fig. 2). A single chromatic scale was chosen for these sections in order to favour a direct comparison between all the data acquired on the entire viaduct and, therefore, to uniquely identify any areas where further investigations are recommended to verify the presence of injection defects. In general, the ultrasonic survey identifies the variations in amplitude once a velocity has been defined (calibration phase): the instrument has to give the position of some elements of known thickness which the real depth is known. All the minimum colour variations in blue and maximum in red, represent variations in the amplitude of the ultrasonic pulse; a variation in amplitude corresponds to a variation in the properties of the medium which can be mainly correlated to density (acoustic impedance). A well-injected prestressed cable incorporated in the concrete presents a low variation in amplitude while the presence of voids, generating a strong amplitude decay (the air does not support the shear stresses), will give result in a high variation; the injected cables are identifiable by anomalies with colour up to yellow, the cables associated with anomalies with shades ranging from orange to red are attributable to possible cables not injected.

More specifically, these anomalies can represent:

- non-injected cables;
- cables with very small voids not identifying with endoscopies;
- cables affected by oxidation and corrosion processes which can lead to the cracks' formation in the surrounding concrete;
- cables injected but embedded in damaged concrete.

After identifying all suspected areas, video endoscopies were set up with the aim of validating (confirming or denying) the results obtained. The video endoscopies, carried out one for each area, confirmed the presence of less injected or corroded cables, or moderately porous concrete for all the areas marked as "to be observed". An example in fig. 2c.

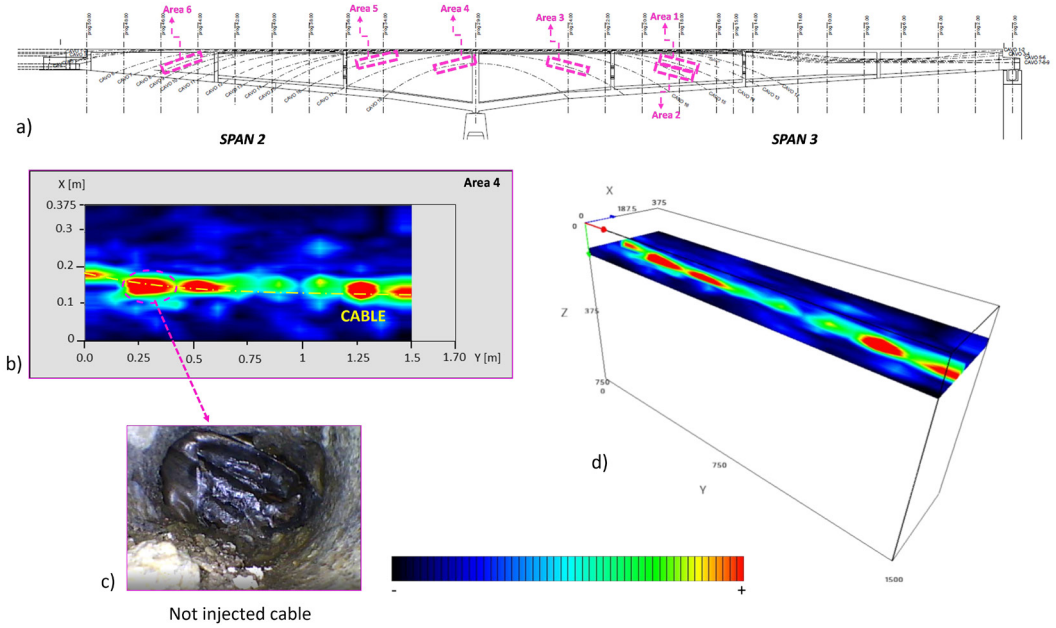


Fig. 2 - a) acquisition scheme; b) B-scan of the cable; c) video endoscopy image; d) 3D UT volume.

Conclusions. The bridges and viaducts monitoring in recent decades has become essential in order to securing the major infrastructures. Thus, a combined analysis is crucial to identify cables and relative difectologies. The combined analysis between GPR and ultrasonic tomography provided good results about it.

The GPR survey allows to correctly locate the cable along the beam length; ultrasonic tomography, carried out along the entire length beam, allows to identify any defects. More specifically, the UT methodologies allows to identify anything that affects the integrity of cables, for example non-injected cables, cables with voids, cables affected by oxidation and corrosion processes and cables injected but embedded in damaged concrete.

References

Alberghina M.F., Capizzi P., Schiavone S.; 2013: *Tecniche non invasive di superficie e di volume per il monitoraggio strutturale delle sculture marmoree.* AIPnD - PnD Congresso 2013, Oct 23-26, Trieste, Italy.

Capizzi P., Cosentino P., Schiavone S.; 2011: *La tomografia ad ultrasuoni per lo studio diagnostico dei beni culturali*. AIPnD - PnD Congresso 2011 Oct 26-28, Florence, Italy.

Ferrarella G.; 2021: *Il degrado e la corrosione negli elementi in c.a. e c.a.p.*. Ed. I (01-2021).

Gorzelanczyk T., Hola J., Schabowicz K.; 2012: *Nondestructive tests aimed at determining the thickness of the concrete shell of a heat pipe carrying tunnel.* 18th World Conference on Nondestructive Testing, 16-20 April 2012, Durban, South Africa.

Krause M., Gräfe B., Mielentz F., Milmann B., Friese M., Wiggenhauser H.; 2009: *Ultrasonic imaging of post-tensioned concrete elements: New techniques for reliable localization of grouting defects*. 2nd International Conference on Concrete Repair, Rehabilitation and Retrofitting, Concrete Repair, Rehabilitation, and Retrofitting II, Cape Town, South Africa, 2009, pp. 215-216.

Hoegh K., Khazanovich L., Yu H.T.; 2011: *Ultrasonic Tomography Technique for Evaluation of Concrete Pavements*. Transportation Research Record: Journal of the Transportation Research Board, No. 2232, pp. 85–94.

Samokrutov A.A., Kozlov V.N., Shevaldykin V.G.; 2006: *Ultrasonic testing of concrete objects using dry acoustic contact. Methods, instruments and possibilities*. The 5th International Conference "Non-Destructive Testing and Technical Diagnostics in Industry". Mashinostroenie, Moscow, Russia, p.152.

Schabowicz K.: *Modern acoustic techniques for testing concrete structures accessible from one side only*. Archives of Civil and Mechanical Engineering, 2015, 15 (4), pp. 1149-1159.

Taffe A., Wiggenhauser H.; 2006: *Validation for thickness measurement in civil engineering with ultrasonic echo*. Proc. of the 9th European Conference on Nondestructive Testing, September, 2006, Berlin, Germany. BB 103-CD, Th. 2.5.3.

White J., Hurlebaus S., Shokouhi P., Wimsatt A.; 2014: *Use of Ultrasonic Tomography to Detect Structural Impairment in Tunnel Linings Validation Study and Field Evaluation.* Transportation Research Record: Journal of the Transportation Research Board. 2407: 20–31.

A GEOELECTRICAL STUDY AT THE SALSE DI NIRANO MUD VOLCANIC FIELD

A. Falconieri[1], D. Patella[1], A. Piombo[2], G. Romano[1], A. Siniscalchi[1], A. Tallarico[1], M. Antonellini

[1] Dipartimento di Scienze della Terra e Geoambientali dell'Università degli Studi di Bari "Aldo Moro", Italy
[2] Dipartimento di Fisica e Astronomia, Alma Mater Studiorum - Università di Bologna , Italy

The Nirano Salse is an active mud volcanos belt located in the northern Apennine foothills near Fiorano Modenese. The belt consists of four cone shaped emission centres, aligned along a N55 direction with basal diameters of about 4-5 m and heights of 2-3 m. Although the area has been widely investigated since the Regional Natural Reserve of Nirano Salse was established in 1982, the subsurface structure is still not well resolved in depth leaving open questions on the feeding related dynamics of the volcanos.

Recent studies (Giambastiani *et al.,* 2021) suggest that gas from a deep reservoir would accumulate in shallow aquifers confined in the first tens of meters of depth and starting point of the conduits forming the mud volcanoes. The features of the fractures system and conduits feeding from the deep source into the shallow aquifers are still unclear.

To this aim, in March 2022 a geophysical field survey was performed and two orthogonal Electrical Resistivity Tomographies (ERT) were acquired crossing the whole caldera-like structure at the bottom of which the mud volcanoes are located.

The shallow (about 60 m of depth) subsurface structure of Nirano main mud volcanic emission centres was already imaged by the geolectrical studies presented in Lupi et al 2016. In the present investigation, the survey was not limited on mud volcanos area but was extended in order to include, as much as possible, the whole caldera-like structure. The use of a large interelectrode spacing and of a data strategy collection based on the application and integration of different geoelectrical arrays (Pole-Dipole, Dipole-Dipole, Wenner and Wenner-Schlumberger) allowed us to gather information on the electrical property distribution from the surface up to ~ 300 m b.g.l.. The integrated interpretation of the ERT results, previously acquired geophysical data, geological and hydrogeological results confirm the main outcome of Lupi *et al.* (2016) in the shallow subsoil portion but also furnish new hints on the subsoil structure at greater dept probably connected with the presence of medium depth source for the Nirano systems. Furthermore, having the survey included also the caldera rims areas, the ERT results help in better define the connections between the surficial hydrogeology of the area and the mud volcanoes activity.

References

Lupi et al., Subsurface fluid distribution and possible seismic precursory signal at the Salse di Nirano mud volcanic field, Italy, *Geophysical Journal International*, 204, 2, 2016, https://doi.org/10.1093/gji/ggv454.

Giambastiani et al., Mud flow dynamics at gas seeps (Nirano Salse, Italy), *Environmental Earth Sciences*, 2021, submitted for publication.

THE SALSE DI NIRANO MUD VOLCANIC FIELD: NEW GEOPHYSICAL RESULTS AND THEIR HYDROGEOLOGICAL IMPLICATIONS

A. Falconieri[1], D. Patella[2], A. Piombo[3], G. Romano[2], A. Siniscalchi[2], A. Tallarico[2]

[1] GEOPROSYS s.r.l., Bari, Italy
[2] Dipartimento di Scienze della Terra e Geoambientali, Università degli Studi di Bari Aldo Moro, Bari, Italy
[3] Dipartimento di Fisica e Astronomia "Augusto Righi", Alma Mater Studiorum - Università di Bologna, Bologna, Italy

The Nirano Salse is an active mud volcanos belt located in the northern Apennine foothills near Fiorano Modenese. The belt consists of four cone shaped emission centres, aligned along a N55 direction with basal diameters of about 4-5 m and heights of 2-3 m. Although the area has been widely investigated since the Regional Natural Reserve of Nirano Salse was established in 1982, the subsurface structure is still not well resolved in depth leaving open questions on the feeding related dynamics of the volcanos.

Recent studies (Giambastiani *et al.,* 2021) suggest that gas from a deep reservoir would accumulate in shallow aquifers confined in the first tens of meters of depth and starting point of the conduits forming the mud volcanoes. The features of the fractures system and conduits feeding from the deep source into the shallow aquifers are still unclear.

To this aim, in March 2022 a geophysical field survey was performed and two orthogonal Electrical Resistivity Tomographies (ERT) were acquired crossing the whole caldera-like structure at the bottom of which the mud volcanoes are located.

The shallow (about 60 m of depth) subsurface structure of Nirano main mud volcanic emission centres was already imaged by the geolectrical studies presented in Lupi et al 2016. In the present investigation, the survey was not limited on mud volcanos area but was extended in order to include, as much as possible, the whole caldera-like structure. The use of a large interelectrode spacing and of a data strategy collection based on the application and integration of different geoelectrical arrays (Pole-Dipole, Dipole-Dipole, Wenner and Wenner-Schlumberger) allowed us to gather information on the electrical property distribution from the surface up to ~ 300 m b.g.l.. The integrated interpretation of the ERT results, previously acquired geophysical data, geological and hydrogeological results confirm the main outcome of Lupi *et al.,* 2016 in the shallow subsoil portion but also furnish new hints on the subsoil structure at greater dept probably connected with the presence of medium depth source for the Nirano systems. Furthermore, having the survey included also the caldera rims areas, the ERT results help in better define the connections between the surficial hydrogeology of the area and the mud volcanoes activity.

Bibliografia

Lupi M., Suski Ricci B., Kenkel J. Ricci T. and Fuchs F.; 2016: *Subsurface fluid distribution and possible seismic precursory signal at the Salse di Nirano mud volcanic field, Italy.* Geophys. J. Int., **204**, 907–917, doi: 10.1093/gji/ggv454

Giambastiani B. M. S., Antonellini M., Nespoli M., Bacchetti M., Calafato A., Conventi M., Dadomo A., Martinelle G., Morena M., Venturoli S. and Piombo A.; 2021: *Mud flow dynamics at gas seeps (Nirano Salse, Italy)* submitted for publication to Environmental Earth Sciences

A MULTI-METHODOLOGICAL SURVEY FOR THE RECONSTRUCTION OF PILES' GEOMETRY: THE CASE OF A VIADUCT IN CALENZANO (FI), CENTRAL ITALY

P. Luiso, M. Taddeo, D. Fiore

Socotec Italia srl, Italy

Introduction. The scheduling of maintenance interventions on major infrastructure projects is based on the principles of safety and operational continuity. Dealing with viaducts and their stability, it is essential to know the foundations' depth and, in particular, the lithologies on which they rest. Thus, it is necessary to distinguish between foundation in loose material (Lombardi *et al*., 1998) or in rock. For a rock, the compressive strength does not take on significant importance so it is often difficult to have structural problems. For loose soils, the problems related to cohesion, friction, viscosity and deformability assume greater importance (Barton *et al.*, 1974). For this reason, it is essential to understand where the foundation is based on, mainly dealing with viaducts whose design schemes are absent.

For this aim, geophysical technology, and in particular a multimethod approach with 3D resistivity tomography surveys (ERT3D) and seismic tomography (SRT2D and SRT3D), allows to obtain not only the physical-mechanical ground characteristics, but also the foundation geometry.

The 3D tomographies are generally used for several purposes such as: investigation of mineral deposits (e.g. Colombero et al., Alile *et al*., 2017), detection of buried fractures on urban areas (e.g. Nappi *et al*., 2021; Chàvez *et al*., 2014), identification of faults extension (Lecocq *et al*., 2017; Petrit *et al*., 2018). Also, the use of both seismic and electrical techniques has commonly been used to detect the cavities geometry increasing confidence in interpretation to limit inaccuracy due to the large amount of heterogeneity in the near surface (Riddle *et al*., 2010; Halihan *et al*., 2006; Van Schoor M., 2002; Cardarelli *et al*., 2010). The 3D resistivity tomography (ERT3D) and seismic tomography (2D-3DSRT) surveys are two techniques that allows both to investigate the subsoil characteristics (Cardenas *et al*., 2022; Chambers *et al*., 2006; 2012) and to reconstruct the pile 3D volumes. In the last ten years, the electrical resistivity and refraction seismic tomographies (with GPR survey support) are used simultaneous with the aim of identifying foundations' depth in order to evaluate their stability. The electrical resistivity tomography technique outlines the interface between substructure and surrounding stratum while the ultra-seismic inspection provides a fine detection of substructure depth (Butchibabu *et al.*, 2017; Cheng *et al*., 2016; Hasan *et al*., 2022; Wang *et al*., 2015, 2017).

In this paper, we present a joined investigation between 3D resistivity and 2D – 3D seismic tomography surveys (SRT) led along specific measurement lines with the aim of identifying the geological characteristics of the area on which the foundations are based on and, more specifically, defining the type of soil / rock that lies beneath the foundation plinths. More specifically, we investigated one of the pile of a viaduct built in 1959 and located in Calenzano (FI) but, for privacy, we are not allowed to name it.

Methodology of investigation and modelling of geophysical data. For this work, we used n°1 2D refraction seismic survey in P and Sh waves (SRT2D), n°1 3D refraction seismic survey in P wave (SRT3D) and n°1 3D electrical tomography (ERT3D); the 3D seismic and electrical tomographies are superimposed because of the limited available space. More specifically:

- 2D refraction seismic consists in the use of 24 acquisition channels (geophones) with an intergeophonic space of 5 m, for a total length of 120 m (Fig.1a). The acquisition time is 1 second and sampling interval is 0.125 μs.
- 3D refraction seismic scheme consists in the use of 72 acquisition channels according to an unconventional geometry; the acquisition was carried out along a rectangular

area perimeter with, in the centre, the foundation to be investigated and using an intergeophonic space is 1 m (yellow rectangle in Fig.1a). Overall, 12 shots along the area perimeter and 4 shots in the internal sector in order were made in order to increase the investigation detail (Fig.1b, c).

- 3D resistivity tomography was carried out using a pole–dipole sequence because it provides better horizontal coverage, reaches a greater depth of investigation (if compared with Wenner, Wenner–Schlumberger and dipole–dipole arrays) and the outcomes are less sensitive to the telluric noise, with respect to the dipole–dipole device. The ERT3D acquisition is superimposed on the SRT3D survey, as shown in figure 1b.

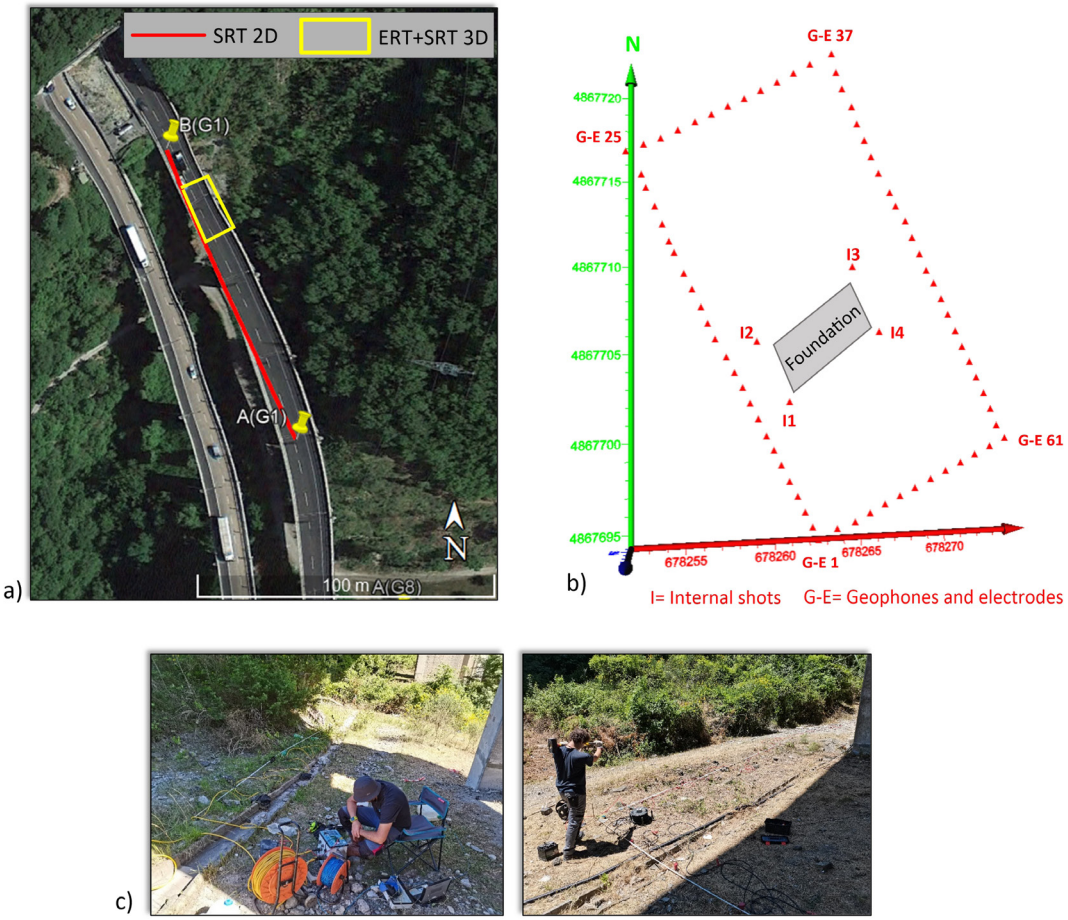


Fig. 1 - Scheme of 3D surveys acquisition; a) 2D refraction seismic acquisition (red line); b) 3D refraction seismic and 3D resistivity tomography scheme acquisition; c) acquisition phases.

The SRT2D dataset processing was carried out using the Rayfract Software (Intelligent Resources Inc., Canada), which allows both the reconstruction of the refractor geometry and the creation of detailed subsurface velocity models, specially in case of deep structures. The SRT3D dataset processing was carried out using the DW TOMO3D (Geogiga Technology Corporation) software designed for the processing of 3D data relating to seismic surveys P waves. More specifically, DW TOMO3D uses a grid ray tracing and the regularized inversion approach to derive the 3D velocity structure directly from first arrival times in 3D seismic

surveys using a non-linear inversion approach (Barryman G. 1990 and reference therein). The ERT3D dataset inversion provided parameterization of resistivity values. The data were merged in a single dataset and implemented in a 3D model that was filtered and processed by software ErtLab_64™ (Geostudi Astier & Multi-Phase Technology) that uses a 3D tetrahedral finite element method. For a 3D visualization of all the inverted dataset, we used software Voxler 4 (3D Well & Volumetric Data Visualization by Golden Software), that is able to generate both planar and vertical views of seismic velocity and resistivity values.

Results and interpretation. The first step was the reconstruction of the geological setting, mainly identifying the presence of the seismic basement (Vs=800, according to the NTC2018). For this reason, 2D seismic tomography was performed, returning the presence of basement at about 15 m of depth. For a more detailed interpretation, the geognostic survey standing 3 meters from the pile, is plotted above the 2D seismic tomography suggesting the presence of fractured marly limestone from about 10 m of depth in the 2DSRT central sector, as shown in figure2.

Then, SRT3D was performed. More specifically, according to recent studies (Ferrari et al., 1991; Di Tommaso et al., 2010 and references therein), the Vp through the concrete ranges from 3000 to over 4600 m/s, depending on the concrete quality; if the concrete is characterized by defects (discontinuity, spaces, earth inclusion, etc.), a longer wave crossing time occurs with a consequent decrease in the propagation velocity. In this study, the 3d seismic tomography, returning Vp maximum value of 7500 m/s, highlights the cylindrical pile shape, suggesting a maximum depth of about 6 m from the ground level, confirming the viaduct design project provided by the client. For a better visualization, the Vp values higher than 5000 m/s, certainly related to the concrete, are saturated with magenta colour (Fig.2, Fig.3).

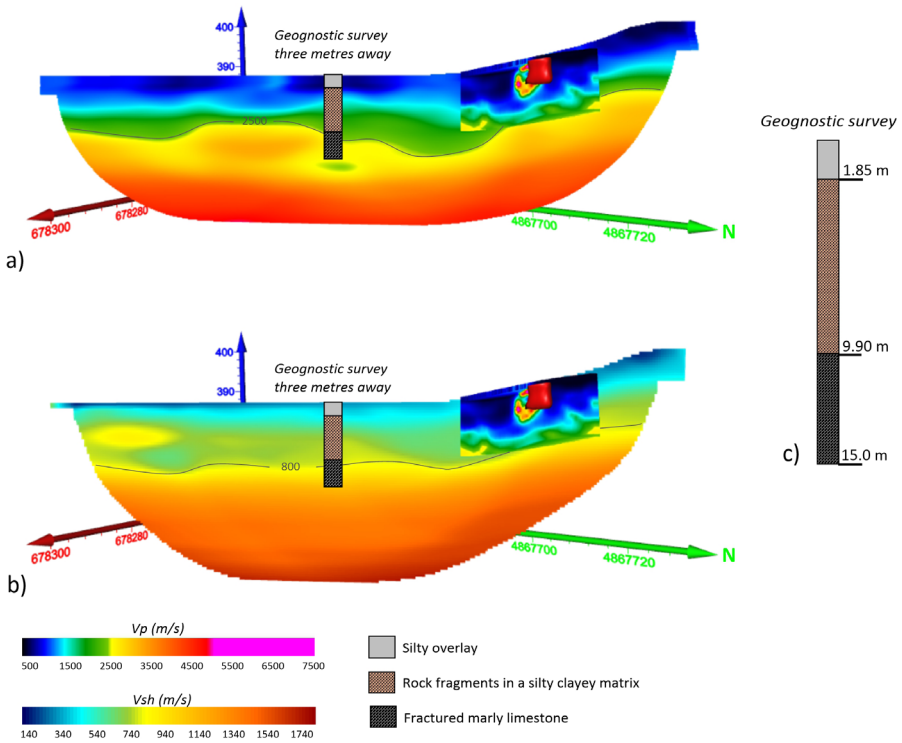


Fig. 2 - SRT2D and geognostic survey in Voxler4 environment; a) SRT3D and ρ volume plotted above SRT2D in P wave; b) SRT3D and ρ volume plotted above SRT2D in Sh wave.

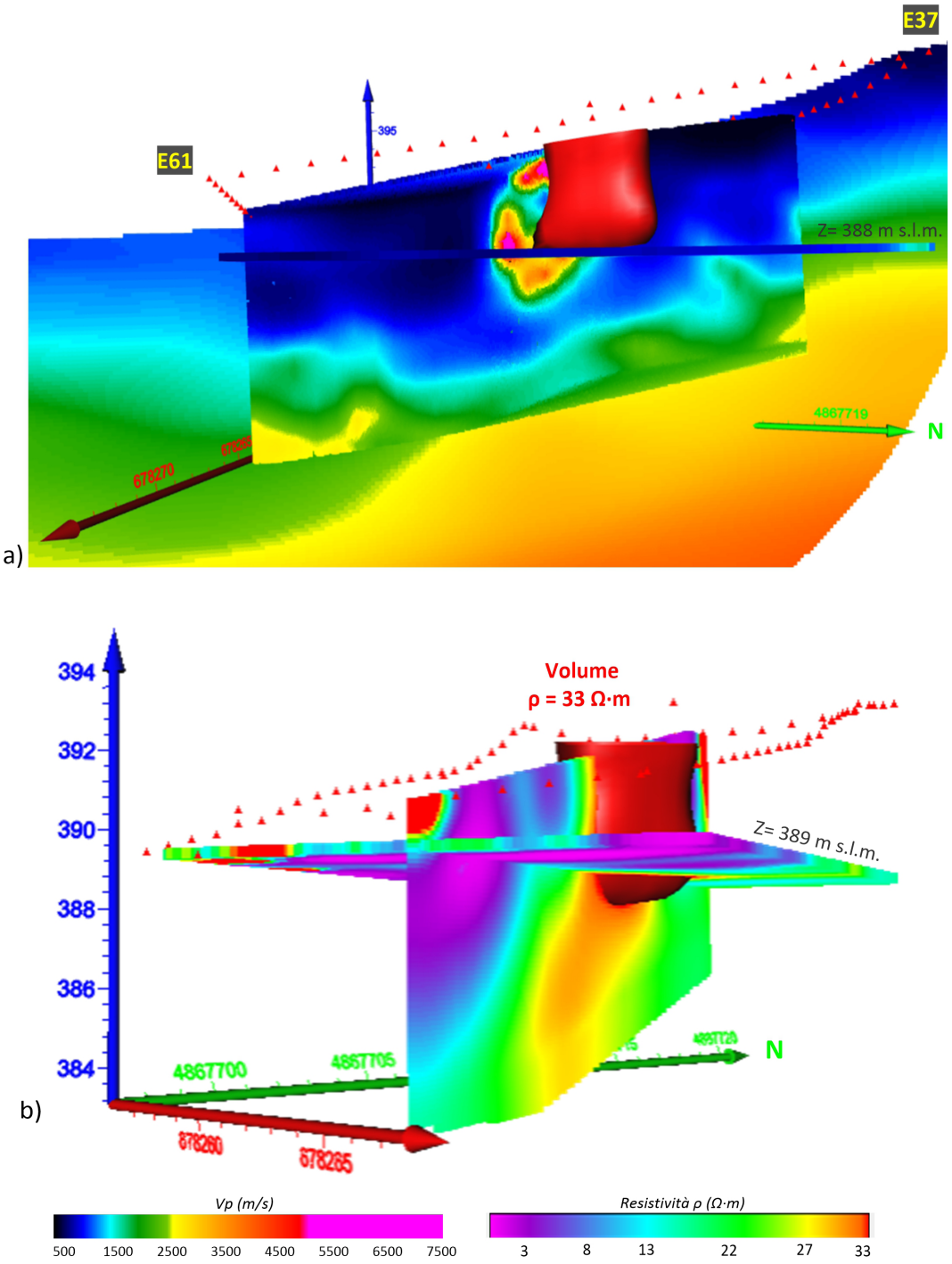


Fig. 3 - Slices of seismic velocity and resistivity values are carried out; a) Vp slices and pile volume plotted above SRT2D in P wave; b) ρ slices intersected with pile volume.

The SRT3D, reconstructing the pile geometry, allows to identify the correct concrete resistivity value to use in order to recreate the same pile geometry with the ERT3D; more specifically, the isosurface representing the average resistivity value, is ρ=33 Ω·m confirming the maximum pile depth. From the ρ isosurface, the pile volume is reconstructed and plotted above both seismic and electrical surveys.

For a better correlation, a series of slices are carried out (Fig.3). In figure 3a, two slices of Vp are plotted above the SRT2D to better highlight the depth difference between the pile and the bedrock, identifying the pile deepest sector at 388 m a.s.l.. The resistivity slices are carried out in order to better characterized the pile shape in a 3D view, highlighting the resistivity value difference with the investigated ground (an example in Fig.3b).

Thus, from the obtained results, the pile is not based on seismic basement; the SRT2D shows the Vs=800 m/s isoline at about 13 – 15 m from g.l. and the SRT3D and ERT3D shows the pile maxim depth at 6 m from g.l.. Thus, the pile is based on different material with lower Vs and low resistivity values; this material seems to be correlated to rock fragments in a silty clayey matrix, as confirmed by the nearby geognostic survey (Fig.2).

Conclusions. The joined geophysical investigations about the viaduct, returning results in good agreement, were carried out with the aim of verifying on which materials the pile is based on. More specifically, 2D seismic tomography allowed to identify the bedrock depth while 3D seismic tomography allowed to reconstruct the pile geometry suggesting the appropriate resistivity value to use in the electrical resistivity tomography 3D. ERT3D tomography is then used to recreate the pile shape and geometry defining the isoline with ρ=33 Ω·m and it is useful when the pile is based on rock characterized by seismic velocity higher than 4000 – 5000 m/s; for this reason, the 3D seismic tomography loses resolution.

The described surveys, carried out individually, would not allow neither to identify the pile geometry nor the pile maximum depth; with the joined analysis of several methodologies it is possible to obtain the geological and engineering information useful for safety and for any maintenance work.

References

Alile O.M., Aigbogun C.O., Enoma N., Abraham E.M., Ighodalo J.E.; 2017: *2D and 3D electrical resistivity tomography (ERT) investigation of mineral deposits in Amahor, Edo State, Nigeria*. Nigerian Research Journal of Engineering and Environmental Science, 2, 1, 215-231.

Barton N., Lien R., Lunde J.; 1974: *Engineering classification of rock masses for the design of tunnel support*. Rock mechanics, 6, 189–236.

Berryman J. G., Kohn R. V.; 1990: *Variational constraints for electrical-impedance tomography.* Physical review letters, 65, 3, 325.

Butchibabu B., Sandeep N., Sivaram Y.V., Jha P.C., Khan P.K.; 2017: *Bridge pier foundation evaluation using cross-hole seismic tomographic imaging*. Journal of Applied Geophysics, 144, 104–114.

Cardarelli G., Di Filippo E., Tuccinardi E.; 2006: *Electrical resistivity tomography to detect buried cavities in Rome: a case study*. Near Surface Geophysics, 4, 387-392.

Cárdenas-Soto M., Gámez-Lindoro J.A., Peña-Gaspar V., Aguirre-Díaz J.P., García-Serrano A.; 2022: *A Pseudo 3D seismic refraction tomography for exploring archaeological structures*. Ingeniería Investigación y Tecnología, 23, 01, 1-9. https://doi.org/10.22201/fi.25940732e.2022.23.1.003.

Chambers .JE., Kuras O., Meldrum P.I., Ogilvy R.D., Hollands J.; 2006: *Electrical resistivity tomography applied to geologic, hydrogeologic, and engineering investigations at a former waste-disposal site*. Geophysics 71, 6, B231–B239.

Chambers J.E., Wilkinson P.B., Wardrop D., Hameed A., Hill I., Jeffrey C., Loke M.H., Meldrum P.I., Kuras O., Cave M., Gunn D.A.; 2012: *Bedrock detection beneath river terrace deposits using three-dimensional electrical resistivity tomography*. Geomorphlogy 177–178, 17–25.

Chávez R.E., Cifuentes-Nava G., Hernández-Quintero E., Vargas D.; 2014: *Special 3D electric resistivity tomography (ERT) array applied to detect buried fractures on urban areas: San Antonio Tecómitl, Milpa Alta, México.* Geofísica Internacional, 53, 4, 425-434.

Cheng J., Xu X., Ren J., Zhang S., Wu X.; 2016: *Probabilistic multi-segment rupture seismic hazard along the Xiaojiang fault zone, southeastern Tibetan Plateau*. Journal of Asian Earth Sciences, 221, 104940. https://doi.org/10.1016/j.jseaes.2021.104940

Colombero C., Papadopoulou M., Kauti T., Skyttä P., Koivisto E., Savolainen M., Socco L.V.; 2021: *Surface-wave tomography for mineral exploration: a successful combination of passive and active data (Siilinjärvi phosphorus mine, Finland)*. EGU 2021. https://doi.org/10.5194/se-2021-121.

Di tommaso R., Mucciarelli M., Vona M., De Bonis M., Masi A.; 2010: *Valutazione delle caratteristiche meccaniche del calcestruzzo mediante misure di velocità di onde acustiche.* Il Giornale delle Prove non Distruttive Monitoraggio Diagnostica 1.

Ferrari G., Contini G.; 1991: *Correlazioni tra la velocità degli impulsi ultrasonici e la resistenza a compressione del calcestruzzo preconfezionato impiegato per strutture in cemento armato precompresso.* Giornate AICAP.

Halihan T., Nyquist J.E.; 2006. *Detection of voids, tunnels and collapse features*. Session 218-T65. Philadelphia Annual Meeting of the Geological Society of America, Philadelphia, PA, October.

Hasan M., Shang Y.; 2022: *Geophysical evaluation of geological model uncertainty for infrastructure design and groundwater assessments*. Engineering Geology, 299, 106560, ISSN 0013-7952, https://doi.org/10.1016/j.enggeo.2022.106560.

Lecocq T., Camelbeeck T.; 2017: *Electrical resistivity tomography data acrossthe Hockai Fault Zone (Ardenne, Belgium).* Data in Brief, 11, 1-4. https://doi.org/10.1016/j.dib.2016.12.028.

Lombardi G., Hegg U.; 1998: *Il progetto delle opere di fondazione di ponti e viadotti*. Politecnico di Milano, corso di aggiornamento.

Nappi R., Paoletti V., D'Antonio D., Soldovieri F., Capozzoli L., Ludeno G., Porfido S., Michetti A.M.; 2021: *Joint Interpretation of Geophysical Results and Geological observations for Detecting Buried Active Faults: The Case of the "Il Lago" Plain (Pettoranello del Molise, Italy).* Remote Sens. 2021, 13, 1555. https://doi.org/10.3390/rs13081555.

Petrit K., Klamthim P., Duerrast H.; 2018: *3D resistivity survey for shallow subsurface fault investigations.* E3S Web of Conferences, 34, 01007. International Conference on Civil & Environmental Engineering.

Riddle G. I., Riddle C. J., Schmitt D. R.; 2010: *ERT and Seismic Tomography in Identifying Subsurface Cavities.* Geo Can Work Earth, 1, 1-4.

Van Schoor M.; 2002: *Detection of sinkholes using 2D electrical resistivity imaging*. Journal of Applied Geophysics, 50, 4, 393-399.

Wang H., Hu C.H., Wang C.Y.; 2015: *NDT-Based Identification on an Unknown Bridge Foundation*. Cultural heritage, 7, P6, P5.

Wang H., Hsleh S.H.; 2017: *Near-Surface Geophysical Inspection on Bridge Foundations.* 15th Asia Pacific Conference for Non-Destructive Testing (APCNDT2017), Singapore.

Sessione 3.3

Metodi e Tecnologia Innovative

Convenor: A. Tognarelli, N. Bienati e G. Gola

INDAGINE MAGNETOMETRICA DA DRONE PER LA MAPPATURA DI UN DICCO INCASSATO IN ROCCE CARBONATICHE

F. Accomando[1], A. Bonfante[2], M. Buonanno[2], G. Florio[1], J. Natale[1], S. Vitale[1,3]

[1] Dipartimento di Scienze della Terra, dell'Ambiente e delle Risorse – Università di Napoli "Federico II", Italy
[2] ISAFOM, Consiglio Nazionale Delle Ricerche (CNR), Portici (NA), Ercolano, Italy
[3] Istituto Nazionale di Geofisica e Vulcanologia - Osservatorio Vesuviano, Italy

Nell'ultimo decennio l'introduzione delle piattaforme UAV (Unmanned Aerial Vehicles), comunemente note come droni, e lo sviluppo di sensori miniaturizzati e leggeri hanno aperto nuove strade per l'acquisizione di dati magnetometrici. La magnetometria da UAV sta diventando un'alternativa o un approccio complementare alle misure al suolo poiché permette di raccogliere dati caratterizzati da una copertura uniforme e da una buona risoluzione, rappresentando una soluzione intermedia tra le classiche prospezioni a terra e quelle aeree ad alta quota. L'uso degli UAV permette inoltre di ridurre costi, tempi e rischi dei rilievi in luoghi di difficile accesso. Ad esempio, in presenza di fitta vegetazione, aree coltivate, paludi, ghiacciai, laghi, aree di battigia o lungo pendii molto ripidi risulta essere la tecnica più adatta.

In questo studio è stata effettuata un'indagine magnetica da drone nell'area di cava in località Taverna San Felice (Presenzano, CE), alla base del versante S-W del Monte Cesima, con l'obiettivo di mappare un dicco magmatico del Pleistocene incassato nei calcari mesozoici. Il dicco è prevalentemente orientato NE-SW, lungo alcune zone di faglia che interessano i calcari. Sul versante affiorano dei depositi stromboliani dovuti ad un sistema di vent monogenetici alimentati dal dicco stesso (Natale *et al.*, 2020). L'elevazione del fronte di cava varia tra 240 e 450 m s.l.m., con una complessa geometria del terreno conformato a gradoni alti 5-7 m.

Considerando la complessa topografia dell'area di studio, si è optato per l'uso di un sistema magnetometrico su UAV. Per coprire l'intera area, sono stati effettuati cinque voli utilizzando un UAV multirotore e un magnetometro atomico a vapori di cesio miniaturizzato (MFAM, Geometrics). Data l'elevata intensità delle anomalie magnetiche previste per un dicco intruso in rocce sedimentarie e le caratteristiche tecniche dell'MFAM, è stata scelta la soluzione di trasportare il magnetometro fissandolo al carrello di atterraggio dell'UAV (Accomando *et al.,* 2021). Questa soluzione aumenta la sicurezza del volo ed evita il rumore nei dati generati dalle oscillazioni del magnetometro nel caso in cui venga sospeso mediante funi al disotto dell'UAV, tipicamente ad una distanza di circa 3 m. D'altra parte, la piccola distanza tra i sensori e la piattaforma (circa 0.5 m) ha l'effetto di aumentare fortemente il rumore elettromagnetico dovuto ai motori del drone. Tuttavia, questo rumore è concentrato alle alte frequenze (Walter *et al*., 2021) e può essere rimosso piuttosto facilmente, grazie all'altissima frequenza di campionamento del magnetometro MFAM (1000 Hz).

Gli elevati contrasti di magnetizzazione tra le rocce carbonatiche e ignee hanno consentito di rilevare con accuratezza forti anomalie magnetiche. Questi dati, integrati con quelli strutturali e di rilevamento geologico, hanno permesso la mappatura dell'area indagata vincolando la geometria del dicco e dei suoi prodotti che, ad oggi, rappresentano un raro esempio di interazione tra vulcanismo e tettonica nell'Appennino meridionale. Ulteriori rilievi magnetici da drone sono in progetto al fine di fornire una mappatura più completa delle anomalie magnetiche, e quindi dell'attività ignea, nel sito di indagine.

Bibliografia

Accomando, F.; Vitale, A.; Bonfante, A.; Buonanno, M.; Florio, G. ; 2021: *Performance of Two Different Flight Configurations for Drone-Borne Magnetic Data*. Sensors 21, 5736. https://doi.org/10.3390/s21175736.

Natale, J., Vitale S., Giordano, G., Isaia, R., Prinzi, E.P., Tramparulo, F.d.A., Ciarcia, S.; 2022: *Middle-Late Pleistocene volcano-tectonic activity in carbonate mountains (southern Apennines, Italy): evidence of tectonic control on dike emplacement and rift-like monogenetic eruption*. Abstract. Cities on Volcanoes 11, Crete.

Walter, C., Braun, A., and Fotopoulos, G.; 2021: *Characterizing electromagnetic interference signals for unmanned aerial vehicle geophysical surveys*. Geophysics, v. 86, no. 6, pp. B321-V488. DOI: 10.1190/geo2020-0895.1.

A BAYESIAN APPROACH TO FULL-WAVEFORM INVERSION: PRELIMINARY RESULTS

S. Berti[1,2], M. Aleardi[1], E. Stucchi[1]

[1] Earth Sciences Department, University of Pisa, Italy
[2] Earth Sciences Department, University of Florence, Italy

Introduction. An important application of the geophysical inverse theory is seismic full-waveform inversion (FWI), in which seismic data recorded at the surface are used to estimate compressional and shear wave velocities. In FWI, seismic waveforms are exploited to update subsurface model parameters by trying to match the recorded data with the estimated data (Virieux and Operto, 2009).

There are two critical issues often related to the traditional FWI problem. First of all, most optimization-based FWI methods are designed to only find the model that best fits the observations according to a specific error function. Nevertheless, the FWI problem is also ill-posed, observed data can be noisy, modelling methods can be inaccurate and prior knowledge can be insufficient. All of these factors introduce uncertainties into the inversion results. In this context, focusing on the best-fitting model only (i.e. deterministic inversion) impedes a complete assessment of the uncertainty affecting the recovered solution (i.e. probabilistic framework).

Additionally, in traditional local optimization-based FWI methods, an objective function, which measures the misfit between observed and estimated data, is minimized with respect to the model parameters. The commonly used *L2*-norm objective function is non-convex because of the highly nonlinear forward mapping and hence the inversion is prone to get trapped into local minima.

We seek the solution for FWI in a Bayesian inference framework to address those two issues (Mosegaard and Tarantola, 2002). Bayesian inference provides a systematic framework for incorporating and propagating the uncertainties in observed data, prior knowledge and forward operator into the uncertainties affecting the recovered model. The final solution of a Bayesian inversion is the so-called posterior probability density (PPD) function in the model space which fully quantifies the uncertainties in the recovered solution.

To efficiently sample the posterior distribution, we introduce a sampling algorithm in which the proposal distribution is constructed by the local gradient and the Hessian of the negative log posterior.

For non-linear problems the Bayesian inversion is often solved through a Markov Chain Monte Carlo (MCMC) sampling. Monte Carlo is a technique for randomly sampling a probability distribution. Markov chain is a systematic method for generating a sequence of random variables where the current value is probabilistically dependent only on the previous state of the chain. Combining these two methods, allows random sampling of high dimensional probability distributions that honors the probabilistic dependence between samples by constructing a Markov Chain that comprise the Monte Carlo sample.

Our algorithm is called gradient-based Markov chain Monte Carlo (GB-MCMC). The GB-MCMC FWI method can quantify inversion uncertainties with estimated posterior distributions given sufficiently long Markov chains.

MCMC sampling methods provide the global view of the model space, so the inversion avoids the entrapment in a local region. Theoretically speaking, GB-MCMC method can accurately estimate the posterior distribution given sufficiently long Markov chains with arbitrary starting points.

However, expensive forward model operators and high-dimensional parameter spaces make the application of MCMC algorithms computationally unfeasible.

A suitable strategy to reduce the computational complexity of this type of inverse problem is to compress the model space through appropriate reparameterization techniques, in order

to reduce the number of data points and model parameters and hence the dimensions of $\boldsymbol{H}_a$ and $\boldsymbol{g}$.

In this work, we propose a GB-MCMC FWI method combined with the compression of data and model space through a discrete cosine transform (*DCT*) and we apply this strategy to a small portion of the 2D Marmousi V_p model.

Method. Gradient-based deterministic inversions are aimed at minimizing a previously defined misfit function, which is usually a linear combination of data error and a model regularization term. For Gaussian-distributed noise and model parameters, the error function can be written as follows:

$$E(m) = \left\| C_d^{-\frac{1}{2}}(d - G(m)) \right\|_2^2 + \left\| C_m^{-\frac{1}{2}}(m - m_{prior}) \right\|_2^2 \quad (1)$$

where the vectors $\boldsymbol{m}$ and $\boldsymbol{d}$ identify the model parameters and the observed data; $\boldsymbol{C}_d$ and $\boldsymbol{C}_m$ are the data and prior model covariance matrices; $\boldsymbol{m}_{prior}$ is the prior model vector and G is the forward modelling operator which maps the model into the corresponding data.

The minimum of $E(\boldsymbol{m})$ can be iteratively approached through a local quadratic approximation of the error function around the current model $\boldsymbol{m}_k$:

$$E(m) = E(m_k + \Delta m) \approx \tilde{E}(m) = E(m_k) + \Delta m^T \nabla_m E(m_k) + \frac{1}{2} \Delta m^T \nabla_m^2 E(m_k) \Delta m + O\left(\| \Delta m \|^3 \right) \quad (2)$$

where $\Delta\boldsymbol{m}=\boldsymbol{m}-\boldsymbol{m}_k$. In particular, it results that

$$\nabla_m E(m_k) = g = J^T C_d^{-1} \Delta d(m_k) + C_m^{-1}\left(m_k - m_{prior}\right) \quad (3)$$

and

$$\nabla_m^2 E(m_k) = H \approx J^T C_d^{-1} J + C_m^{-1} = H_0 + C_m^{-1} \quad (4)$$

where $\Delta\boldsymbol{d}(\boldsymbol{m}_k)=G(\boldsymbol{m}_k)-\boldsymbol{d}$ is the data misfit vector and J denotes the Jacobian matrix expressing the partial derivative of the data with respect to model parameters.

A Bayesian inversion aims to estimate the full posterior distribution in the model space given by:

$$p(m \mid d) = \frac{p(d \mid m) p(m)}{p(d)} \quad (5)$$

where $p(\boldsymbol{m}|\boldsymbol{d})$ is the posterior probability density (PPD), $p(\boldsymbol{d}|\boldsymbol{m})$ is the so-called data likelihood function that measures the fitting between observed and predicted data, whereas $p(\boldsymbol{m})$ and $p(\boldsymbol{d})$ are the a priori distributions of model and data parameters, respectively. For problems in which the $p(\boldsymbol{m}|\boldsymbol{d})$ cannot be expressed in a closed form, a Markov Chain Monte Carlo (MCMC) algorithm can be used for a numerical assessment of the posterior model (*Fig.1*).

In this context, the probability α to move from the current state of the chain $\boldsymbol{m}_k$ to the next proposed state $\boldsymbol{m}_{k+1}$ is determined according to the Metropolis-Hasting (*M-H*) rule:

$$\alpha = p(m_{k+1} \mid m_k) = \left[1, \frac{p(m_{k+1})}{p(m_k)} \times \frac{p(d \mid m_{k+1})}{p(d \mid m_k)} \times \frac{q(m_k \mid m_{k+1})}{q(m_{k+1} \mid m_k)} \right] \quad (6)$$

where $q(\bullet)$ is the proposal distribution that defines the new state $\boldsymbol{m}_{k+1}$ as a random deviate from a probability distribution $q(\boldsymbol{m}_{k+1}|\boldsymbol{m}_k)$ conditioned only on the current state $\boldsymbol{m}_k$ (Hastings, 1970).

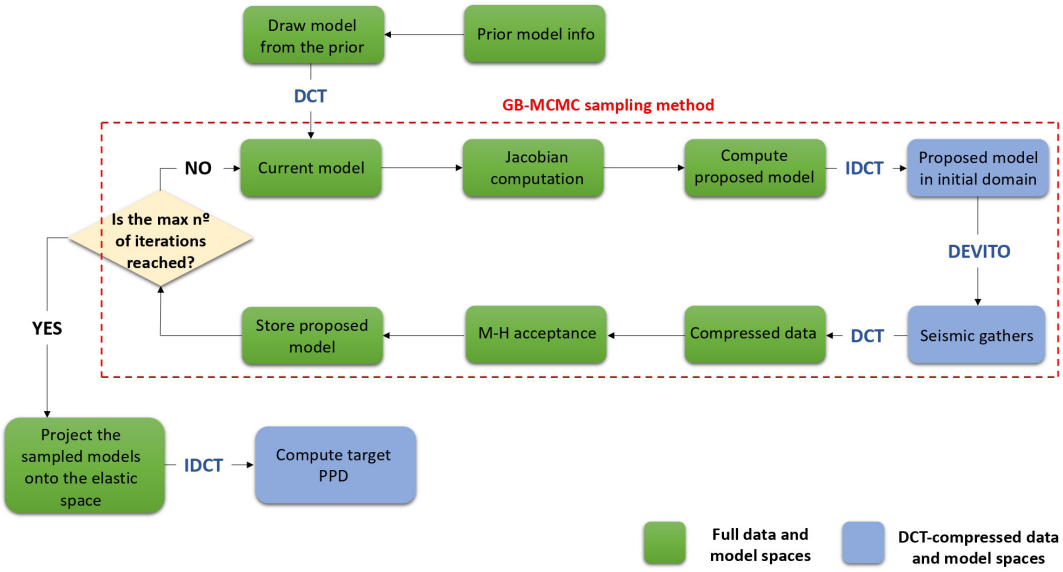


Fig. 1 - Schematic representation of the GB-MCMC inversion procedure. Green and blue rectangles refer to steps performed in the reduced and full spaces.

If $\boldsymbol{m}_{k+1}$ is accepted, $\boldsymbol{m}_k$=$\mathbf{m}_{k+1}$. Otherwise, $\boldsymbol{m}_k$ is repeated in the chain and another state is generated as a random deviate from $\boldsymbol{m}_k$.

Usually, several Markov chains are used, and so multiple random walks are performed starting from different regions of the model space, in order to increase the exploration of the parameters space and to prevent sampling to be trapped in local maxima of the PPD.

The ensemble of sampled states after the *burn-in* period (the first iterations, corresponding to the beginning of the chains where the algorithm moves towards a promising portion of the search space, are discarded from the computation of the PPD) is used to numerically compute the statistical properties (e.g. mean, mode, standard deviations) of the target posterior probability.

We can formulate the Bayesian inversion framework in terms of $E(\boldsymbol{m})$, H and g, under Gaussian assumptions for data, noise and model parameter distributions:

$$p(m) \propto expexp\left(-\frac{1}{2}\left(m-m_{prior}\right)^{T} C_m^{-1}\left(m-m_{prior}\right)\right) \tag{7}$$

$$p(d\,|\,m) \propto expexp\left(-\frac{1}{2}\left(d-G(m)\right)^{T} C_d^{-1}\left(d-G(m)\right)\right) \tag{8}$$

We obtain the approximation of the posterior around $\boldsymbol{m}_k$:

$$p(m\,|\,d) \propto expexp\left(-\frac{1}{2}\left(m-\left(m_k-H_a^{-1}g\right)\right)^{T} H_a\left(m-\left(m_k-H_a^{-1}g\right)\right)\right) \tag{9}$$

After constructing a local Gaussian approximation of the posterior density, we can define a sampling method that uses the following proposal density:

$$q(m) \propto expexp\left(-\frac{1}{2}\left(m-\left(m_k-\alpha H_a^{-1}g\right)\right)^{T} \frac{H_a}{\beta^2}\left(m-\left(m_k-\alpha H_a^{-1}g\right)\right)\right) \tag{10}$$

Each proposed model is accepted according to the Metropolis-Hasting rule explained before. The α and β^2 values are tunable parameters which determine how far to go along the negative gradient direction and how much the model is randomly perturbed.

The major computational requirement of the implemented approach is the computation of the Jacobian matrix associated with each accepted model and, consequently, the manipulation of the Hessian matrix and the gradient vector. Using a finite difference scheme to evaluate the Jacobian, the number of forward evaluations needed for its computation increases linearly with the number of model parameters.

In this work we have used the *DCT* to compress our model and data spaces. The *DCT* of a signal indicates the energy distribution of the signal in the frequency domain spectrum. Usually, most of the energy of the signal is expressed by low-order *DCT* coefficients and consequently, this mathematical transformation can be used for model compression, which is accomplished by setting the coefficients of the base function terms beyond a certain threshold equal to zero.

For the estimation of the optimal number of *DCT* coefficients needed to approximate the model and data spaces, we quantified how the variability of the model and data changes as the number of *DCT* coefficients varies: we have computed the variability as the ratio between the variance of the approximated model and data and the one of the uncompressed model and data (Aleardi, 2021).

Synthetic inversion. we have applied the proposed GB-MCMC FWI method to the 2D Marmousi V_p model.

The grid size for generating the observed data is 251(nx_0) *x* 101(nz_0), with a grid spacing of 0.02 *x* 0.02 *km*, so 25351 parameters form the full model space. A Ricker wavelet with the peak frequency at 5 *Hz* is used as the source. We have simulated 5 shots equally spaced along the horizontal axis and each shot is recorded by 126 receivers with a 0.04 *km* receiver interval. Noncorrelated Gaussian white noise is added to the observed data.

The simulation of the shots has been performed using *Devito*, a new domain-specific language for implementing high performance finite difference partial differential equation solvers. By embedding this kind of language within *Python*, it's possible to develop finite difference simulators quickly using a syntax that strongly resembles mathematics (Louboutin, 2019).

In order to reduce the computational cost of the calculation of the Jacobian matrix using the finite difference approach, we have used the *Multiprocessing Python* package, which allows to parallelize the execution of a function across multiple input values, distributing the input data across processes (data parallelism).

The data and models must be projected onto the *DCT* space, where the MCMC sampling runs. We have observed that less than 20 coefficients along the two *DCT* spatial dimensions explain more than 98% of variability of the original model. This means that the compression allows for a reduction of the 25351-D model space to a 9*x*18 = 162-D domain. A similar analysis has been carried out on our seismic data, and in this case 90*x*100 = 9000 retained coefficients in the data space explain almost the total variability of the uncompressed seismogram. Therefore, the full 751*x*126 = 94626-D data space has been reduced to a 9000-D domain. We can see that all the matrices that we are using in our inversion procedure are a lot more tractable in the compressed domain, for example the 25351*x*25351 Hessian in the full domain has been reduced to a 162*x*162 matrix in the compressed space.

Notice that, although the MCMC inversions run in the reduced *DCT* space, the sampled models must be projected back into the full domain just before the forward modelling phase performed with *Devito,* generates the predicted data needed to compute the likelihood value.

We have used six cores on an Intel® Core™ i7-8700 CPU @ 3.20GHz to run the numerical tests. Each iteration, including computing the Jacobian, the gradient, the Hessian matrix and drawing a sample, takes approximately 45 *s* wall clock time. We have run one single chain with 10.000 iterations, and it finished running within 70 *h*.

The chain starts from a 1D gradient velocity model, using as a prior information the mean of each row of the original velocity model, and we can observe in *Fig*.2 that the mean model

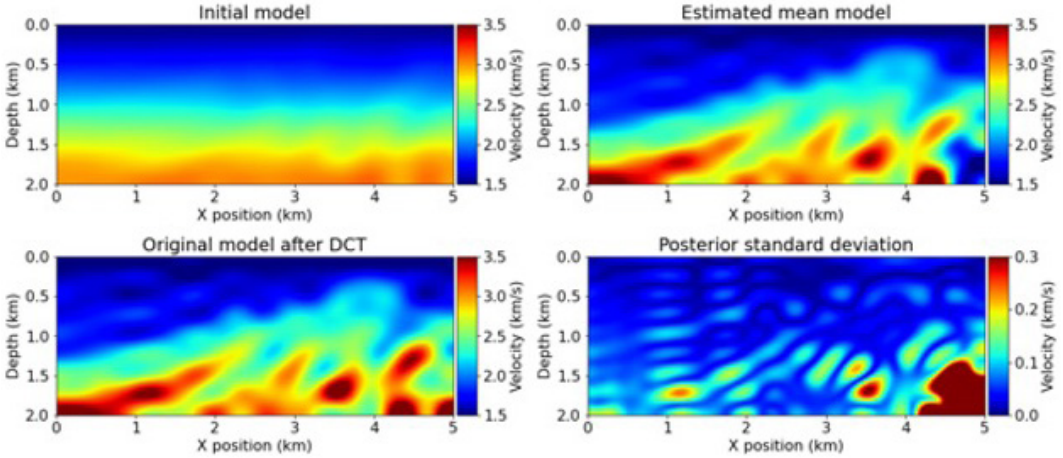


Fig. 2 - Results of the inversion procedure, on the left part the initial model from which the inversion procedure started and the original model; on the right, the estimated mean model and the posterior standard deviation estimated by the GB-MCMC algorithm.

closely reproduces the velocity variations of the true model, even though there is a strong low velocity anomaly in the bottom right part.

Analyzing the evolution of the negative log-likelihood (*Fig.3*) we can observe that after a small number of iterations we have reached the stationary regime, where the likelihood still oscillates but around the same values. We have decided to consider the first 500 iterations as the *burn-in* period and we have discarded the corresponding samples, so only the following 9500 samples for each chain were used to generate the mean and standard deviation models.

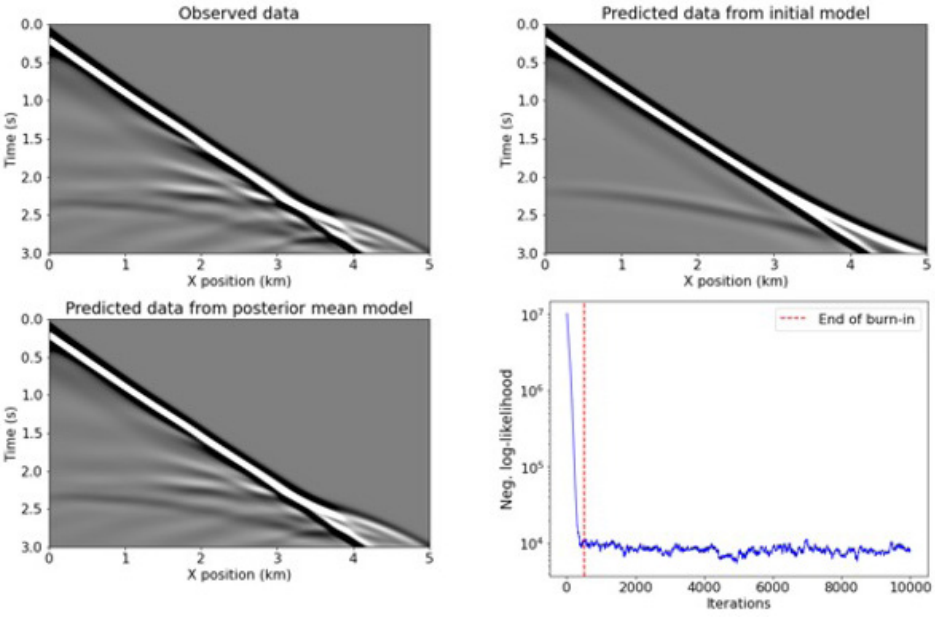


Fig. 3 - On the left part, comparison between the observed data and the predicted data from the estimated mean model; on the right, the predicted data from the initial model from which the inversion procedure started and the evolution of the negative log-likelihood value during the GB-MCMC sampling. The vertical red line indicates the end of the burn-in.

The standard deviation map suggests small deviations in the shallow parts of the model, where we have good data coverage and good illumination. These small deviations indicate that the predicted velocity values are well constrained in these areas and the inversion results have less uncertainties. On the other hand, the deeper parts and the edges of the model have higher variations (0.3 *km*/*s* and above) due to poor data coverage and poor illumination, and so the inverted velocity values are less constrained and have a wider range of values, suggesting larger uncertainties. The highest variations correspond, as expected, to the low velocity anomaly in the bottom right corner of the model (around 1.2 *km*/*s*).

Conclusions. In this work we have presented a GB-MCMC sampling method based on the Bayesian inference framework to solve the ill-posed inverse problem in high dimensions. We have shown that, with the help of the local gradient and Hessian information, a proposal distribution which is a good approximation of the posterior distribution, is easy to construct and samples can be drawn efficiently from the proposal. We have shown the results of the GB-MCMC FWI applied to a synthetic model and, unlike the traditional local optimization-based FWI methods, we have obtained statistical assessments by which the uncertainties related to the inversion can be estimated. The following steps of our research are to use more chains and to mix the information brought from each chain, using the so-called Differential Evolution Markov Chain (DEMC), in order to increase the efficiency and the rate of convergence, and to apply the implemented algorithm to field data.

REFERENCES

Aleardi M.; 2021: *A gradient-based Markov chain Monte Carlo algorithm for elastic pre-stack inversion with data and model space reduction*. Geophysical Prospecting 69(3), doi:10.1111/1365-2478.13081.

Hastings W. K.; 1970: *Monte Carlo sampling methods using Markov chains and their applications*. Biometrika, 57, 97–109.

Louboutin M., Lange M., Luporini F., Kukreja N., Witte, P.A., Herrmann F.J., Velesko P., Gorman G.J.; 2019: *Devito (v3.1.0): an embedded domain specific language for finite differences and geophysical exploration.* Geoscientific Model Development 12, 1165–1187.

Mosegaard K. and Tarantola A.; 2002: *Probabilistic approach to inverse problems*. International Geophysics Series, 81, 237–268.

Virieux J. and Operto S.; 2009: *An overview of full-waveform inversion in exploration geophysics*. Geophysics, 74, no. 6, WCC1–WCC26, doi:10.1190/1.3238367.

GRAVITY AND GRAVITY GRADIENTS JOINT INVERSION IN SALT BASINS THROUGH AN INTEGRATED WORKFLOW

L. Bianco[1], M. Tavakoli[2], A. Vitale[3], M. Fedi[1]

[1] Department of Earth, Environment and Resources Sciences, University of Naples "Federico II", Naples, Italy
[2] Faculty of Mining, Petroleum, and Geophysics, Shahrood University of Technology, Shahrood, Iran
[3] Institute for Electromagnetic Sensing of the Environment, National Research Council, Naples, Italy

In this work, we discuss a new workflow designed to jointly invert gravity and gravity gradients. Our aim is the multi-source modelling with focus on salt basins, still a task of main relevance in exploration. These geological settings include very challenging and relatively deep targets as the base of salt and the mother salt, which produce different wavelength-content anomalies. In this context, the interpretation of gravity and gravity gradients data could be of great significance, as these datasets are characterized by different wavelength-content. The workflow follows the scheme of sequential joint inversion via cross-gradient constraint as proposed by Tavakoli *et al.* (2021). To perform the separate inversions, we modified the focusing algorithm (Portniaguine and Zhdanov 1999, 2002) to incorporate different types of a priori information such as the seismic top of salt and its density, and the inhomogeneous model-weighting function (Vitale and Fedi, 2020) estimated by the MHODE method (Fedi *et al.*, 2015). We applied the method to a model derived from the Seg Advanced Model Phase I model, demonstrating a reliable result for both shallow and deep sources.

References

Fedi M., Florio G. and Paoletti V.; 2010: *MHODE: a local-homogeneity theory for improved source-parameter estimation of potential fields*. Geophysical Journal International, **202**, 887–900, https://doi.org/10.1093/gji/ggv185.

Portniaguine O., and Zhdanov M. S.; 1999: *Focusing geophysical inversion images*. Geophysics, **64**, 874-887, doi: 10.1190/1.1444596.

Portniaguine O., and Zhdanov M. S.; 2002: *3-D magnetic inversion with data compression and image focusing.* Geophyiscs, **67**, 1532-1541, doi: 10.1190/1.1512749.

Tavakoli M., Nejati Kalateh A., Rezaie M., Gross L. and Fedi M.; 2021: *Sequential joint inversion of gravity and magnetic data via the cross-gradient constraint*. Geophysical Prospecting, **69**, 1542-1559, doi: 10.1111/1365-2478.13120.

Vitale A. and Fedi M.; 2020: *Self-constrained inversion of potential fields through a 3D depth weighting*. Geophysics, **85**, G143-G156, doi: 10.1190/geo2019-0812.1.

INVERSIONE CONGIUNTA DEI CAMPI DI GRAVITÀ E MAGNETICO: I PRIMI RISULTATI DEL PROGETTO XORN ED IL CASO STUDIO DEL COMPLESSO DI OKA (CANADA)

M. Capponi[1], D. Sampietro[1], G. Maurizio[2]

[1] Geomatics Research & Development srl, Lomazzo (CO), Italy
[2] Dipartimento di Matematica e Geoscienze, Università degli studi di Trieste, Trieste (TS), Italy

Introduzione. I metodi da potenziale, che si basano su osservazioni del campo di gravità e del campo magnetico terrestre, sono comunemente utilizzati per studiare la struttura della crosta del nostro pianeta. Grazie alle molteplici missioni satellitari dedicate all'osservazione di questi campi, al giorno d'oggi le principali caratteristiche della crosta terrestre sono note a livello globale/continentale con una sufficiente risoluzione per studi su larga scala. A livello regionale e locale invece il dato puramente satellitare non garantisce una risoluzione sufficiente per poter essere impiegato da solo e per tale ragione nel corso degli anni sono stati raccolti dati di gravità e magnetici in molte regioni del mondo con strumenti terrestri o montati su nave e/o aereo. Vista questa ingente mole di dati disponibili, sia a scala globale che locale, una delle più grandi sfide ad oggi consiste nel trovare approcci innovativi per integrarli tra loro in maniera ottimale per sfruttarli al meglio ed estrapolare quante più informazioni possibili sulla struttura della litosfera.

È noto che il campo di gravità ed il campo magnetico sono strettamente influenzati da alcune proprietà della litosfera, rispettivamente dalle densità e dalle suscettività magnetiche dei materiali, e che esistono metodi matematici i quali, con opportune semplificazioni, servono per stimare modelli di distribuzioni di densità e/o suscettività che siano coerenti con i dati osservati. Occorre poi sottolineare che le osservazioni acquisite a quota di satellite o a quota terrestre (con strumenti montati su mezzi come aerei o navi) hanno una diversa sensibilità, o meglio risentono in maniera differente dell'effetto di strutture geologiche che si trovano a profondità che possono essere anche molto diverse; per tale ragione l'utilizzo integrato di dati provenienti da diverse fonti non può far altro che portare beneficio alla conoscenza e caratterizzazione della crosta terrestre. Dal punto di vista matematico sappiamo inoltre che le osservazioni di campi da potenziale se trattate singolarmente, per stimare un modello geologico in un processo di inversione, soffrono della cosiddetta non unicità: questo vuol dire che potrebbero esistere molteplici modelli geologici in grado di generare lo stesso identico segnale osservato. Un modo per ovviare questo problema consiste nell'introdurre nel processo di inversione il maggior numero possibile di informazioni da diversi metodi geofisici, che siano sotto forma di vincoli sulle geometrie delle strutture o sulle proprietà dei materiali. Per tali ragioni anche l'elaborazione congiunta di osservazioni del campo di gravità e del campo magnetico, con vincoli fisici introdotti attraverso profili sismici interpretati o conoscenze di tipo geologico, rappresenta un valido modo per ridurre lo spazio delle soluzioni ammissibili.

In questo lavoro sarà presentato un metodo di inversione 3D, basato su un approccio probabilistico, che consente di processare in maniera congiunta dati di gravità e magnetici. L'algoritmo di inversione congiunta è parte del lavoro da svolgere nell'ambito del progetto XORN (eXperimental jOint inveRsioN), finanziato dall'Agenzia Spaziale Europea a inizio 2022 nel programma EO4Society.

Alla base di questo metodo di inversione congiunta c'è un algoritmo già ampiamente testato e validato di inversione del campo di gravità al quale è stato integrato un nuovo algoritmo per il trattamento di osservazioni del campo magnetico. Il metodo, attualmente in fase di sviluppo, è stato testato su un caso studio costruito sulla base di un'applicazione reale legata al mondo dell'esplorazione delle risorse naturali (in particolare delle cosiddette critical raw materials) nello stato canadese del Quebec, il complesso di Oka. I risultati preliminari di questo test

saranno qui discussi mostrando le principali caratteristiche geologiche dell'area ottenute con inversioni del campo di gravità e magnetico ed evidenziando le potenzialità di un'inversione congiunta.

Metodo. Il metodo di inversione proposto si basa su un approccio probabilistico Bayesiano, esprimibile dal teorema di Bayes, che nella sua formula generica permette di stimare la probabilità di una certa ipotesi date una serie di osservazioni. I fondamenti teorici di questo approccio, a partire dai quali è stato sviluppato un metodo in inversione del campo di gravità, sono stati presentati nel lavoro di Marchetti *et al.,* 2019, ed i molteplici test sia su casi studio sintetici che reali sono descritti nei lavori Sampietro e Capponi 2021 e Sampietro *et al.* 2021. Il primo step per l'applicazione di un metodo di inversione di questo tipo consiste nel raccogliere tutte le informazioni disponibili sull'area di studio in termini di principali strutture/orizzonti geologici, densità medie e ordine di grandezza delle relative accuratezze. Queste informazioni sono poi utilizzate per costruire un primo modello 3D dell'area di interesse e la sua corrispondente probabilità. Questo modello è il punto di partenza dell'inversione che iterativamente modifica geometrie e distribuzioni di densità/suscettività in modo tale da individuare la miglior soluzione che abbia la duplice funzione di massimizzare la probabilità del modello a-priori e contemporaneamente minimizzare i residui rispetto al campo osservato (gravità e/o magnetico). L'algoritmo disponibile per l'inversione del campo di gravità permette di inserire diverse tipologie di vincoli formulati sulla base della conoscenza dell'area.

In termini matematici, partendo dall'inversione del campo di gravità, questo metodo lavora con un volume discretizzato in voxels; ogni voxel *i*, è a sua volta caratterizzato da una coppia di variabili random, ρ_i, variabile continua che rappresenta la densità, e L_i variabile categorica che caratterizza il materiale (e.g. sedimento, crosta, mantello etc.). Per stimare il modello 3D finale, l'algoritmo ricerca attraverso un metodo Monte Carlo con catena di Markov, il set di densità e labels di ogni voxel che massimizza la probabilità a posteriori del modello attraverso questa funzione obiettivo:

$$\phi = \left\{ \frac{1}{2}(\Delta g^o - \mathrm{F}\rho)^T \mathrm{C}_{\Delta g}^{-1}(\Delta g^o - \mathrm{F}\rho) + \frac{1}{2}(\rho - \overline{\rho}_\ell)^T \mathrm{C}_\ell^{-1}(\rho - \overline{\rho}_\ell) + \frac{1}{2}\gamma \sum_{i=1}^{N} s^2(L_i) + \frac{1}{2}\lambda \sum_{i=1}^{N} \sum_{j \in \Delta_i} q^2(L_i, L_j) \right\} \prod_{i=1}^{N} \chi_{[\overline{\rho}_\ell | 3\sigma_\ell^2]}(\rho_i) \quad (1)$$

Dove in questo caso *F* è l'operatore di forward per calcolare l'effetto gravitazionale di ogni voxel, ρ_l, è il vettore che contiene le densità medie associate ad ogni label, C_l è una matrice diagonale contenente le varianze delle densità di una certa label, s^2 e q^2 sono funzioni empiriche che definiscono la "distanza" rispetto al modello geologico iniziale e il grado di "smoothness" della soluzione rispettivamente.

A partire da questo, il progetto XORN ha tra gli obiettivi quello di estendere l'algoritmo di inversione anche al campo magnetico. In particolare, in una prima fase si modificherà la funzione obiettivo sostituendo il primo e secondo termine con due termini analoghi ma relativi al campo magnetico, ovvero si useranno le osservazioni del campo magnetico (H^0) al posto di quelle di gravità (sostituendo il primo termine ed introducendo l'operatore di forward magnetico *G*); ed al posto del termine di densità si introdurrà un termine legato alla suscettività magnetica χ. La nuova funzione obiettivo "magnetica" diventerà quindi:

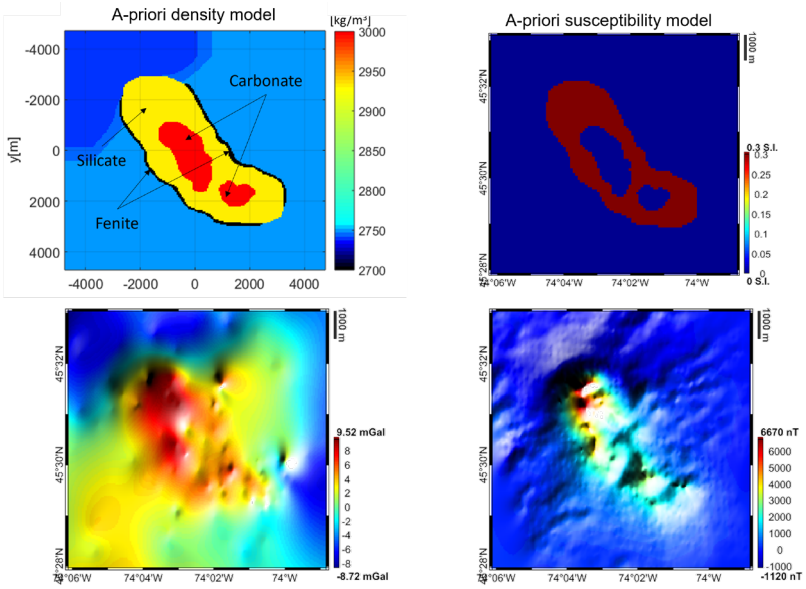
$$\phi = \left\{ \frac{1}{2}(H^o - \mathrm{G}\chi)^T \mathrm{C}_H^{-1}(H^o - \mathrm{G}\chi) + \frac{1}{2}(\chi - \overline{\chi}_\ell)^T \mathrm{C}_{H\ell}^{-1}(\chi - \overline{\chi}_\ell) + \frac{1}{2}\gamma \sum_{i=1}^{N} s^2(L_i) + \frac{1}{2}\lambda \sum_{i=1}^{N} \sum_{j \in \Delta_i} q^2(L_i, L_j) \right\} \prod_{i=1}^{N} \chi_{[\overline{\rho}_\ell | 3\sigma_\ell^2]}(\rho_i) \quad (2)$$

E si otterrà in questo modo un algoritmo in grado di effettuare un'inversione 3D basata solamente sul campo magnetico. Obiettivo finale del progetto XORN sarà poi quello di integrare in un'unica funzione obiettivo sia i termini di gravità che quelli magnetici in modo da poter ottenere un algoritmo per effettuare una completa inversione congiunta.

$$\phi = \left\{ \frac{1}{2}(\Delta g^o - \mathrm{F}\rho)^T \mathrm{C}_{\Delta g}^{-1}(\Delta g^o - \mathrm{F}\rho) + \frac{1}{2}(\rho - \overline{\rho}_\ell)^T \mathrm{C}_\ell^{-1}(\rho - \overline{\rho}_\ell) + \right.$$
$$\frac{1}{2}(H^o - \mathrm{G}\chi)^T \mathrm{C}_H^{-1}(H^o - \mathrm{G}\chi) + \frac{1}{2}(\chi - \overline{\chi}_\ell)^T \mathrm{C}_{H\ell}^{-1}(\chi - \overline{\chi}_\ell) + \frac{1}{2}\gamma \sum_{i=1}^{N} s^2(L_i) + \quad (3)$$
$$\left. + \frac{1}{2}\lambda \sum_{i=1}^{N} \sum_{j \in \Delta_i} q^2(L_i, L_j) \right\} \prod_{i=1}^{N} \chi_{\left[\overline{\rho}_\ell \mid 3\sigma_\ell^2\right]}(\rho_i)$$

Nel presente lavoro i primi studi, e gli sviluppi in termini di algoritmi, condotti per arrivare alla formulazione dell'inversione magnetica e dell'inversione congiunta gravità e magnetico saranno discussi e applicati ad un caso studio.

Risultati. Nell'ambito del progetto XORN, l'algoritmo di inversione 3D di recente sviluppo è stato testato su un caso studio costruito sulla base di un complesso geologico, esempio di applicazione di metodi geofisici nel campo dell'esplorazione delle risorse: il complesso di carbonatiti di Oka in Quebec, Canada. (Treiman and Essene 1985; Gold *et al.,* 1967; Thomas *et al.,* 2016). Questo noto complesso è costituito da una struttura che in vista piana ha una forma ad 8 distorta; è costituito da due corpi centrali (principalmente composti da rocce carbonatiche), circondati da rocce silicatiche alcaline con un'ulteriore aureola esterna di rocce di tipo gneiss. La Figura 1 riproduce il modello semplificato ricostruito per questo test, caratterizzato da tre principali unità geologiche ed un background uniforme. La Figura 1 riporta anche le densità che sono state associate ad ogni label nel modello a-priori. Per quanto riguarda le suscettibilità magnetiche, seguendo le informazioni da letteratura (Chen e Simonetti 2014) si è associato un valore uniforme di 0.3 SI solamente al corpo anulare di silicati. Come osservazioni sono state utilizzate griglie di anomalia di gravità da stazioni a terra (δg) ed il modulo dell'anomalia magnetica totale (TMI) da rilievo aereo con risoluzione nominale spaziale di circa 50 m. Il volume è stato discretizzato in voxel di dimensioni circa 60 m x 60 m in planimetria e spessore variabile tra 50 e 500 m in profondità e per ognuna delle quattro unità geologica sono stati definite le geometrie, le densità e le suscettività con i corrispondenti range di variabilità



Griglia di anomalia di Bouguer da stazioni a terra.

griglia di TMI da rilievo airborne SGL con risoluzione spaziale nominale di 50 m.

Fig. 1 - sezione del modello geologico iniziale con distribuzione delle densità e suscettività magnetiche; in basso le osservazioni di gravità e magnetiche.

ammissibili (da utilizzare per costruire il modello probabilistico a-priori). Sono state effettuate diverse inversioni di cui una in gravità, una magnetica ed una congiunta ed i risultati ottenuti mostrano che il modello a-priori è stato realisticamente modificato in maniera tale da rendere coerente il modello con le osservazioni dei due campi in accordo con le rispettive accuratezze. In Figura 2 si riportano i residui di gravità e magnetici sull'intera area di studio prima e dopo l'inversione ed un dettaglio lungo un profilo diagonale NO – SE dei residui ottenuti nelle diverse inversioni dal quali si evince l'alto grado di coerenza tra osservazioni e segnali generati a partire dal modello finale.

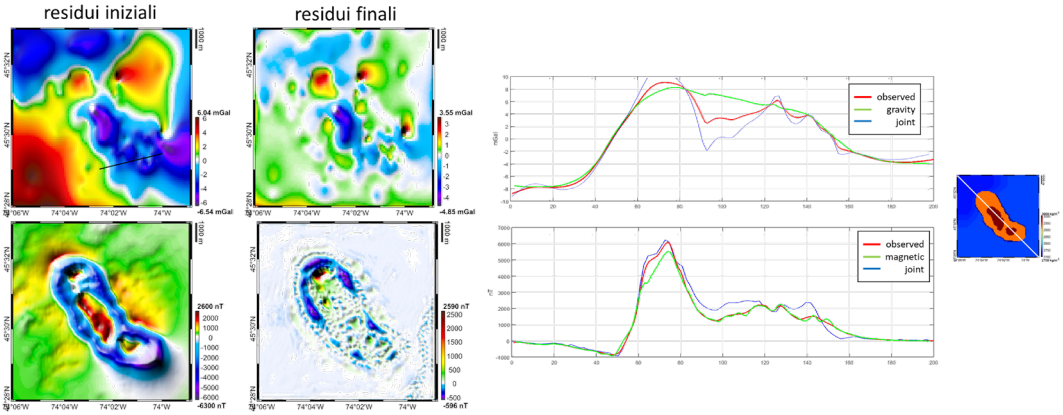


Fig. 2 - Residui iniziali e finali di gravità e magnetici.

Conclusioni. In questo lavoro è stato presentato un metodo di inversione 3D basato su un approccio Bayesiano che consente di effettuare inversioni singole del campo di gravità o magnetico e congiunte dei due campi sviluppato nell'ambito del progetto XORN. I primi risultati di inversione magnetica su un caso studio in Canada sono stati qui presentati e mostrano come l'algoritmo già ampiamente testato con dati di gravità sia in grado di gestire osservazioni del campo magnetico. Il test ha mostrato che l'inversione è stata in grado di adattare il modello geologico in modo tale da renderlo più coerente con le osservazioni di entrambi i campi. Ulteriori test saranno effettuati nell'ambito del progetto XORN con l'obiettivo finale di ottenere un algoritmo di inversione congiunta funzionale per casi studio reali e diverse applicazioni legate all'ambito dell'esplorazione delle risorse naturali.

Bibliografia

Gold D., Valle M. and Charette J.; 1967: *Economic geology and geophysics of the Oka alkaline complex, Quebec*. Canadian Institute of Mining and Metalurgy.

Marchetti P., Sampietro D., Capponi M., Rossi L., Reguzzoni M., Porzio F. and Sansò F.; 2019: *Lithological constrained gravity inversion. A Bayesian approach*. In: 81st EAGE Conference and Exhibition 2019, EAGE Publishing BV, 1–5.

Sampietro D. and Capponi M.; 2021a: *Gravity for Lithosphere Architecture Determination and Analysis: the Central Eastern Mediterranean case study.* Geophysical Prospecting, 70(1), 173–192.

Sampietro D. and Capponi M.; 2021b): *Seismic Constrained Gravity Inversion: A Reliable Tool to Improve Geophysical Models Away from Seismic Information*. Geosciences, 11(11), 467.

Sampietro D., Capponi M., Oikonomopoulos K., Ktenas D., Tartaras E. and Stefatos A.; 2021: *3D model of South Crete offshore area by seismic constrained gravity inversion*. In: Third EAGE Eastern Mediterranean Workshop, European Association of Geoscientists & Engineers, 1–3.

Sampietro D. and Sansò F.; 2012: *Uniqueness theorems for inverse gravimetric problems*. In: VII Hotine-Marussi Symposium on Mathematical Geodesy, Springer, 111–115.

Thomas M., Ford K. and Keating P.; 2016: *Exploration geophysics for intrusion-hosted rare metals.* Geophysical Prospecting, 64(5), 1275–1304.

Treiman A.H. and Essene E.J.; 1985: *The Oka carbonatite complex, Quebec: geology and evidence for silicate-carbonate liquid immiscibility*. American Mineralogist, 70(11-12), 1101–1113.

DETERMINATION OF THE VS PROFILE IN A NOISY INDUSTRIAL SITE: FURTHER EVIDENCES ABOUT THE IMPORTANCE OF LOVE WAVES AND THE OPPORTUNITIES OF THE GROUP VELOCITY ANALYSIS

G. Dal Moro

Institute of Rock Structure and Mechanics - Academy of Sciences of the Czech Republic, Prague, Czech Republic

Introduction. In the last decade, the analysis of surface-wave propagation has become extremely popular especially in the framework of seismic-hazard studies although, as a matter of fact, the determination of the shear-wave velocity (V_S) profile is useful for any geotechnical or geological application that requires the knowledge of the subsurface conditions.

It is well known that the accuracy of the V_S profile depends on the number of observables considered in the inversion process and on the kind of analyses actually put in place. In fact, in spite of the popularity of the approach based on the interpretation of the modal dispersion curves of the vertical component of Rayleigh waves (MASW – Multichannel Analysis of Surface Waves), a wide range of further options are possible and capable of providing better results, free from major ambiguities and pitfalls that characterize the standard MASW approach.

For the present illustrative study, we considered a set of multi-component active and passive data gathered in a NE-Italy heavily-industrialised area home to many industries related to metalworking and therefore characterized by an extremely-high level of microtremors.

Data and analyses. With the goal of defining the best procedures necessary to unambiguously define the subsurface model in a very noisy industrial area in NE Italy, we collected a comprehensive series of active and passive seismic data. Active data were recorded by means of a single 3-component sensor in order to work with the Holistic analysis of Surface waves (HS) (Dal Moro *et al.*, 2019; Dal Moro, 2018; 2020) while passive data were recorded so to define the HVSR (Horizontal-to-Vertical Spectral Ratio), the dispersion curve of the vertical (Z) component of Rayleigh waves via Miniature Array Analysis of Microtremors (MAAM - Cho *et al.*, 2006a; 2006b; 2013; Tada *et al.*, 2007; Dal Moro *et al.*, 2015a; 2018) and the Love-wave dispersion curve via ESAC (Extended Spatial AutoCorrelation - Ohori *et al.*, 2002). MAAM was accomplished considering a triangular geometry with a radius of 1.7 m while data for the ESAC were collected considering various multi-offset linear arrays with total lengths ranging from 44 to 60 m and with different orientations (for a series of clarifications about the performances of the MAAM and ESAC techniques see Dal Moro, 2020).

Since it was systematically observed that Rayleigh-wave phenomenology is extremely complex and therefore prone to significant ambiguities and pitfalls (Safani *et al.*, 2005; Dal Moro *et al.*, 2015b; Dal Moro, 2020), first of all we accomplished the joint inversion of the HVSR together with the effective dispersion curves of the Z and T components (i.e. the vertical component of Rayleigh waves and Love waves) as obtained from MAAM and ESAC, respectively (see data and results shown in Fig. 1).

Since a more common approach is based on the joint analysis of Rayleigh-wave dispersion and HVSR (e.g. Arai and Tokimatsu, 2005), in order to compare the outcomes we also accomplished this kind of simpler approach (in other words, unlike before, now we are not considering the Love-wave dispersion). Fig. 2 shows the obtained results. Although the overall misfits appear quite good and would inevitably represent a very satisfactory result, the comparison with the solution obtained while considering both Rayleigh and Love waves (see Fig. 1 and related text) demonstrates that the use of Rayleigh waves alone can lead to erroneous solution which are necessarily associated to higher V_S values. This is easily and plainly demonstrated if we compute the Love-wave dispersion from the V_S profile shown in Fig. 2c and compare it with the field data (i.e. the velocity spectrum shown in Fig. 1b): the Love-wave phase velocities of the model are significantly higher than the observed ones.

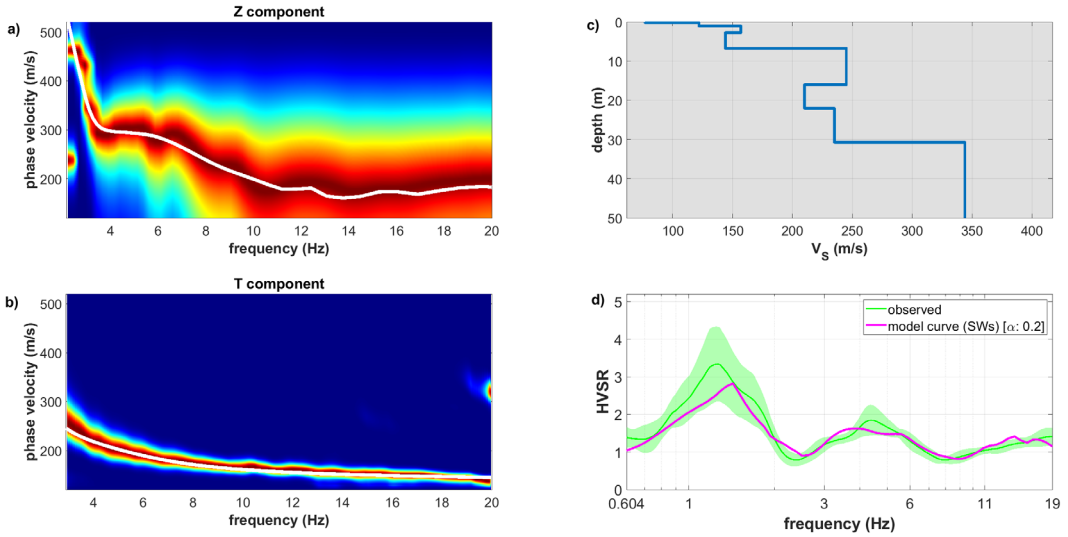


Fig. 1 - Purely passive data: shear-wave velocity profile (*c* plot) obtained through the joint analysis of the phase-velocity effective dispersion curves of the Z (*a* plot) and T (*b* plot) components together with the HVSR curve (*d* plot). In the *a* and *b* plots, the background colours represent the field data while the overlaying white curves are the effective dispersion curves of the identified subsurface model. In the *d* plot, the α value (0.2) in the legend represents the amount of Love waves in the microtremor field (Arai and Tokimatsu, 2004; Dal Moro, 2020).

This is a very common problem (mistake) due to the intrinsic ambiguity of the Rayleigh-wave effective curve which, whether considering active or passive data, can be explained by a large variety of energy distribution and therefore models (Dal Moro, 2020) which cannot be solved by the HVSR (which, in turn, suffers from major non-uniqueness issues). In this case,

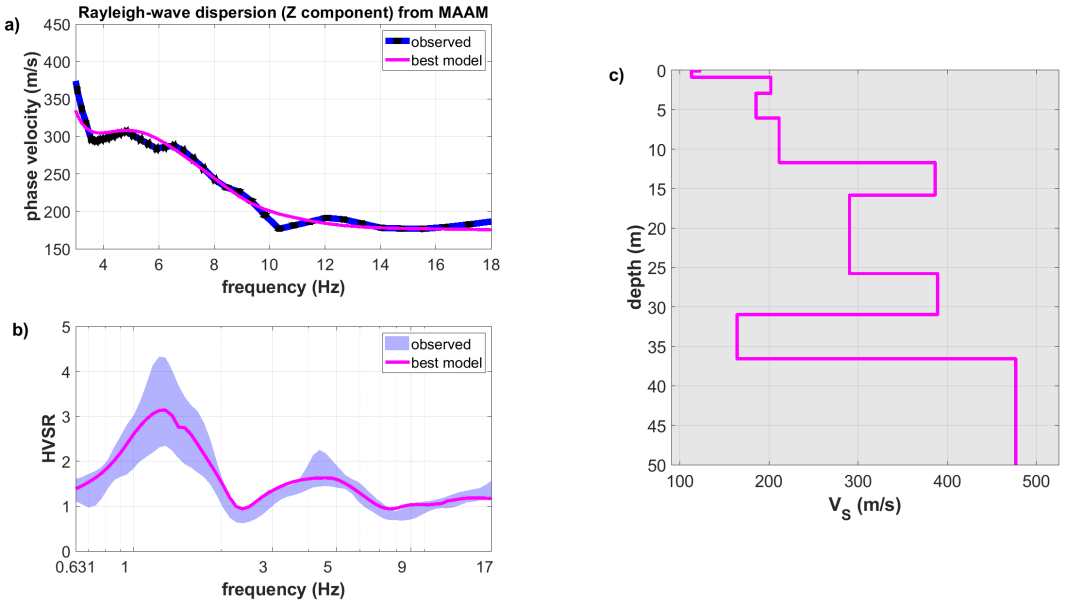


Fig. 2 - Result of the joint analysis of the phase-velocity effective dispersion curve of the Z component (*a* plot) and the HVSR (*b* plot). The ambiguities of the Rayleigh-wave effective dispersion curve (and HVSR) are such that the obtained shear-wave velocities (V_S profile shown in the *c* plot) overestimate the actual values. Compare with the result presented in Fig. 1 and see text for comments.

as in other previously-published (e.g. Dal Moro, 2019; 2020), only the presence of Love waves can properly channel the inversion procedure towards the correct solution.

It should be clearly underlined that in both the accomplished procedures reported in Fig. 1 and 2, the observed dispersion curves were not interpreted in terms of modal curves but modelled according to the mathematics of the effective curve (Tokimatsu *et al.*, 1992; Ikeda *et al.*, 2012).

A different approach to surface-wave analysis is possible through the computation of the group velocities and their holistic analysis jointly with the Rayleigh-wave Particle Motion (RPM) curve (describing the actual particle motion due to the Rayleigh-wave propagation and quite useful in further constraining the subsurface model) and, in case we intend to investigate deeper strata, the HVSR (Dal Moro *et al.*, 2017; 2019; Dal Moro, 2018; 2020). Group velocities are computed via frequency-time analysis (Levshin *et al.*, 1972) and can be obtained both from passive (e.g. Fang *et al.*, 2010) and active data (Ritzwoller and Levshin, 1998; 2002; Dal Moro *et al.*, 2019). Differently than phase velocities, group velocities can be obtained considering a very limited field equipment which is fundamentally based on just one or two 3-component geophones, depending on whether we are considering passive or active data.

Data considered in the present study were recorded by means of a 3-component geophone deployed at a distance of 44 m from the source (a 10-kg sledgehammer). Due to the high noise level, stack was fixed to 25. Fig. 3 shows both the extracted data (group velocity spectra of the Z and R components as well as the RPM curve) and the solution of the holistic analysis of surface waves (HS), i.e. the joint analysis of multi-component group velocities together with the RPM and the HVSR (this latter is useful to extend the investigated profile in depth). It should be underlined that in the HS approach, dispersion data (group-velocity spectra) are not analysed

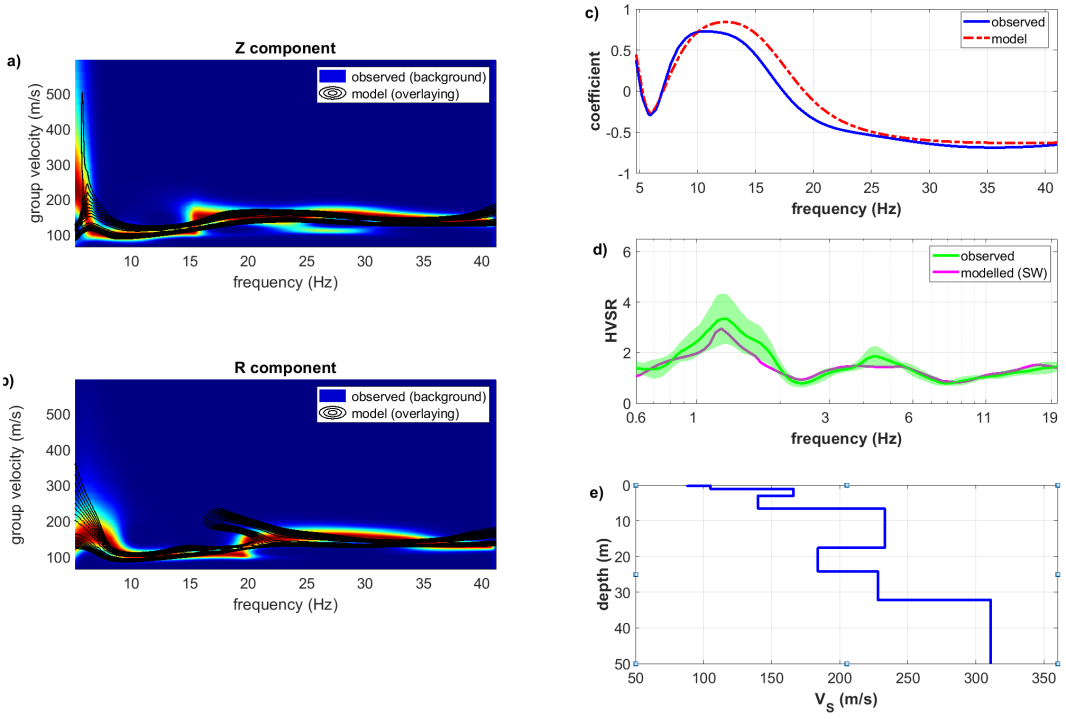


Fig. 3 - Holistic analysis of the group velocities of the vertical (Z) (*a* plot) and radial (R) (*b* plot) components (FVS approach – background colours represent the field data while the overlying black contour lines the obtained model) jointly with the RPM (*c* plot) and HVSR (*d* plot) curves. The obtained V_S profile (*e* plot) is entirely similar to the one obtained while considering the joint analysis of the phase velocities of the Z and T components (see Fig. 1).

through the interpretation of the dispersion curves but through the multi-component Full-Velocity Spectrum (FVS) approach (Dal Moro *et al.*, 2015a; 2015b; 2019; Dal Moro, 2019; 2020).

The result (V_S profile shown in Fig. 3e) is apparently very similar to the one obtained by considering the joint analysis of the phase velocities of the Z and T components together with the HVSR (see Fig. 1).

Conclusions. Accomplished analyses allow to highlight the following evidences:

1) Rayleigh-wave modelling cannot be performed considering an approach based on the modal dispersion curves and the use of the effective curves (for passive data) or the FVS (for active data) is crucial;
2) Because of the intrinsic (i.e. inevitable) ambiguity of the dispersion curve, Rayleigh-wave modelling based on the effective curve does not ensure the correctness of the obtained V_S profile even when performed jointly with the HVSR;
3) Especially when analysing phase velocities, the acquisition and analysis of Love waves reveal decisive to constrain an inversion procedure capable of providing a robust solution free from significant ambiguities;
4) Love-wave dispersion can be effectively obtained from passive data via ESAC even while considering linear arrays (data and analyses are not affected by significant directivity issues);
5) The holistic analysis of multi-component group velocities and RPM curves based on the FVS approach reveal an effective way to obtain robust shear-wave profiles.

Since a solution needs to be of general validity, it is therefore clear that phase velocity analyses based just on Rayleigh waves are not recommended because, due to the complex contribution of different modes, they can lead to overestimated Vs values even if the analyses are accomplished jointly with the HVSR. Due to their simpler phenomenology, Love waves represent an essential tool to properly constrain an inversion procedure.

On the other side, the holistic analysis of multi-component group velocities and RPM data appear an extremely efficient alternative both because it requires a simpler acquisition setting, both because, thanks to the possibility to deal with a large number of observables, it leads to a V_S profile free from major ambiguities.

References

Arai H. and Tokimatsu K.; 2005: *S-wave velocity profiling by joint inversion of microtremor dispersion curve and horizontal-to-vertical (H/V) spectrum*. Bull. Seismol. Soc. Am., **95**, 1766-1778.

Arai H. and Tokimatsu K.; 2004: *S-wave velocity profiling by inversion of microtremor H/V spectrum*. Bull. Seismol. Soc. Am., **94**, 53–63.

Cho I., Tada T. and Shinozaki Y.; 2006a: *New methods of microtremor exploration: the centreless circular array method and two-radius method*. In: Proceedings of the third international symposium on the effects of surface geology on seismic motion, Grenoble (France), 30 Aug-1 Sept, pp 335–344.

Cho I., Tada T. and Shinozaki Y.; 2006b: *Centerless circular array method: inferring phase velocities of Rayleigh waves in broad wavelength ranges using microtremor records*. J. Gophys. Res., **111**, B09315.

Cho I., Senna S. and Fujiwara H.; 2013: *Miniature array analysis of microtremors*. Geophysics, **78**: KS13–KS23.

Dal Moro G.; 2020: *Efficient Joint Analysis of Surface Waves and Introduction to Vibration Analysis: Beyond the Clichés*, Springer, ISBN 978-3-030-46303-8, 273 pages

Dal Moro G., Al-Arifi N. and Moustafa S.R.; 2019: *On the efficient acquisition and holistic analysis of Rayleigh waves: Technical aspects and two comparative case studies*, Soil Dynamics and Earthquake Engineering, **125**, 105742, https://doi.org/10.1016/j.soildyn.2019.105742

Dal Moro G.; 2019: *Surface wave analysis: improving the accuracy of the shear-wave velocity profile through the efficient joint acquisition and Full Velocity Spectrum (FVS) analysis of Rayleigh and Love waves*. Exploration Geophysics, **50**, 408-419, DOI: 10.1080/08123985.2019.1606202

Dal Moro G.; 2018: *Effective Active and Passive Seismics for the Characterization of Urban and Remote Areas: Four Channels for Seven Objective Functions*. Pure and Applied Geophysics**, 176**, 1445–1465, https://doi.org/10.1007/s00024-018-2043-2.

Dal Moro G., Al-Arifi N. and Moustafa S.R.; 2017: *Analysis of Rayleigh-Wave Particle Motion from Active Seismics*. Bull. Seismol. Soc. Am., **107**, 51-62.

Dal Moro G., Ponta R. and Mauro R.; 2015a: *Unconventional Optimized Surface Wave Acquisition and Analysis: Comparative Tests in a Perilagoon Area*. J. Appl. Geophysics, **114**, 158-167

Dal Moro G., Moura R.M. and Moustafa S.; 2015b: *Multi-component Joint Analysis of Surface Waves*. J. Appl. Geophysics, 119, 128-138.

Fang L., Wu J., Ding Z. and Panza G.F.; 2010: *High resolution Rayleigh wave group velocity tomography in North China from ambient seismic noise*. Geophys. J. Int., **181**, 1171–1182.

Ikeda T., Matsuoka T., Tsuji T. and Hayashi K.; 2012: *Multimode inversion with amplitude response of surface waves in the spatial autocorrelation method*. Geophys. J. Int., **190**, 541–552

Levshin A.L., Pisarenko V.F. and Pogrebinsky G.A.; 1972: *On a frequency-time analysis of oscillations*. Ann. Geophys., **28**, 211–218.

Ohori M., Nobata A. and Wakamatsu K.; 2002: *A comparison of ESAC and FK methods of estimating phase velocity using arbitrarily shaped microtremor arrays*. Bull. Seismol. Soc. Am., **92**, 2323–2332.

Safani J., O'Neill A., Matsuoka T. and Sanada Y., 2005. *Applications of Love wave dispersion for improved Shear-wave velocity imaging*. J. Environ. Eng. Geophys., **10**, 135–150.

Ritzwoller M.H. and Levshin A.L.; 2002: *Estimating shallow shear velocities with marine multicomponent seismic data*. Geophysics, **67**, 1991–2004.

Ritzwoller M.H. and Levshin A.L.; 1998: *Eurasian surface wave tomography: group velocities*. J. Geophys. Res., **103**, 4839–4878.

Tada T., Cho I. and Shinozaki Y.; 2007: *Beyond the SPAC method: exploiting the wealth of circular-array methods for microtremor exploration*. Bull. Seismol. Soc. Am., **97**, 2080–2095.

Tokimatsu K., Tamura S. and Kojima H.; 1992: *Effects of multiple modes on Rayleigh wave dispersion characteristics*. J. Geotech. Eng. ASCE 118:1529–1543.

MASW? OLTRE LA SOGGETTIVITÀ NELL'ANALISI DELLE ONDE DI SUPERFICIE: VELOCITÀ DI FASE E GRUPPO NELLA RI-ELABORAZIONE FVS DI UN VECCHIO E COMPLESSO DATASET MULTI-COMPONENTE

G. Dal Moro

Institute of Rock Structure and Mechanics - Academy of Sciences of the Czech Republic, Prague, Czech Republic

Introduzione. Gli sviluppi nel campo dell'acquisizione e analisi delle onde di superficie, hanno di fatto reso privo di un chiaro ed univoco significato il noto acronimo MASW (*Multichannel Analysis of Surface Waves*). Tale acronimo, infatti, non risulta più in grado di definire nulla di puntale: che genere di (combinazione di) geofoni connettiamo ai canali (M)? Che analisi (A) svolgiamo? Quali onde (SW) consideriamo?

Il lavoro presenta i risultati della ri-elaborazione delle onde di Rayleigh di un vecchio dataset multi-componente acquisito con strumentazione dalle caratteristiche che oggigiorno sono da considerarsi obsolete (acquisitore a 16 bit e geofoni con bassa sensibilità – 0.28 V/cm/s) e originariamente analizzato secondo l'approccio congiunto classico a curve modali (interpretate) in Dal Moro (2011). I dati delle due componenti (Z e R) dell'onda di Rayleigh sono qui riconsiderati secondo una tecnica che consente di andare oltre la soggettività delle interpretazioni degli spettri di velocità ed ottenere una soluzione finale (il profilo della velocità delle onde di taglio - V_S) significativamente robusta.

Nel lavoro qui illustrato, gli spettri di velocità sono considerati non tramite interpretazione (soggettiva) delle curve modali ma secondo l'approccio FVS (*Full Velocity Spectrum*) che, in modo analogo a quello considerato da Dou and Ajo-Franklin (2014), consente di riprodurre l'effettiva coerenza degli spettri su tutta la matrice frequenza-velocità (Dal Moro, 2014; 2019). È da sottolineare che, in termini generali, gli spettri di velocità delle componenti verticale (Z) e radiale (R) sono differenti e forniscono dunque informazioni complementari che, grazie all'approccio FVS, risultano utili a meglio definire il profilo V_S. Inoltre, al fine di incrementare la profondità investigata, l'analisi FVS degli spettri di velocità è svolta congiuntamente all'HVSR (*Horizontal-to-Vertical Spectral Ratio*) (Arai and Tokimatsu, 2005).

Il *dataset* considerato è stato raccolto nella media pianura friulana, in un'area in cui complesse alternanze di sedimenti limosi, sabbiosi e ghiaiosi (occasionalmente parzialmente cementati) possono creare importanti inversioni di velocità (strati più rigidi sopra a strati più teneri) e, anche a causa di non irrilevanti variazioni laterali, spettri di velocità particolarmente complessi.

Dati e analisi. Per quanto la definizione delle velocità di fase richieda un numero di canali decisamente inferiore, il *dataset* multi-componente qui considerato fu acquisito considerando 24 canali con spaziatura 2 m e *offset* minimo pari a 4 m. Gli spettri delle velocità di fase delle componenti verticale (Z) e radiale (R) sono mostrati in Fig. 1 unitamente alla curva HVSR e ai risultati dell'inversione congiunta.

È da notare come entrambe le componenti si caratterizzano per il fatto che, tranne una piccola porzione di modo fondamentale attorno ai 25-30 Hz, tutta l'energia si riferisce altrimenti a modi superiori (confronta con Dal Moro, 2011): il segnale che caratterizza gli spettri di velocità per le frequenze inferiori a circa 22 Hz rappresenta di fatto la coalescenza di vari modi superiori e la sua continuità non deve indurre a ritenere sia riferito ad un unico modo (per una panoramica su questi aspetti vedi Dal Moro, 2014).

I sismogrammi sintetici utilizzati per l'analisi FVS sono computati tramite somma modale (Panza, 1985; Hermann, 2013) e l'inversione è svolta sulla base dei criteri del fronte di Pareto (Ramík and Vlach, 2002; Pardalos *et al.*, 2008; Dal Moro *et al.*, 2015).

La correttezza del modello identificato appare evidente dalla sua generale coerenza rispetto tutti i tre osservabili considerati ed è anche confermata dall'analisi delle onde di Love.

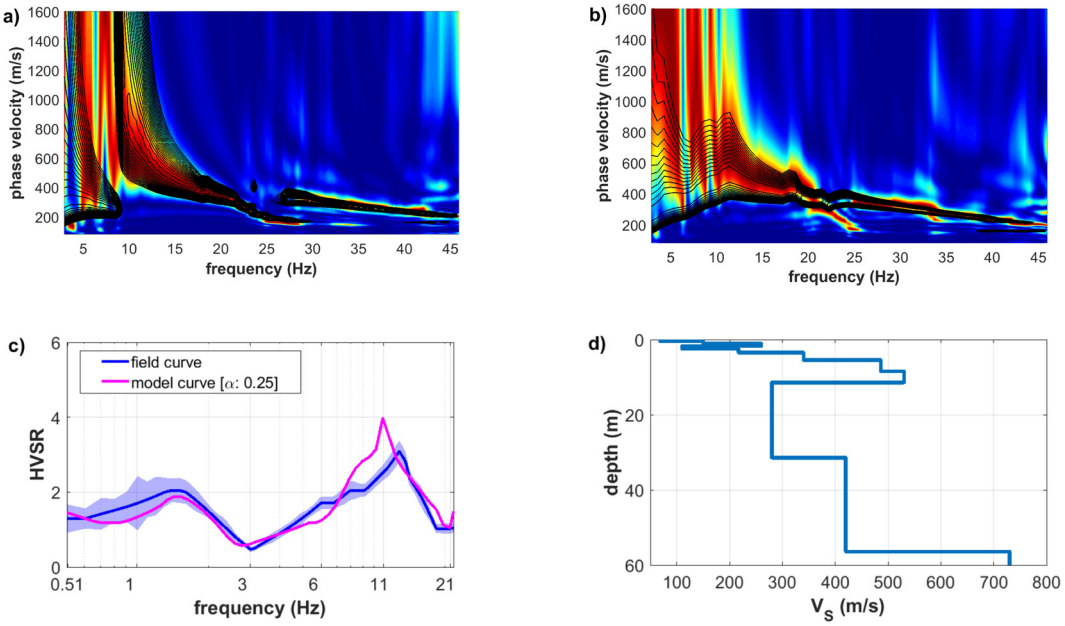


Fig. 1 - Analisi congiunta degli spettri delle velocità di fase delle componenti Z e R (approccio FVS) e della curva HVSR: a) componente Z - velocità di fase dei dati di campagna (colori di sfondo) e del modello identificato (linee di *contour* nere); b) componente R - velocità di fase dei dati di campagna (colori di sfondo) e del modello identificato (linee di *contour* nere); c) HVSR di campagna e del modello (il parametro α indica la quantità di onde di Love utilizzate nella modellazione dell'HVSR - Arai and Tokimatsu, 2004); d) modello V_S identificato dall' inversione congiunta.

Al fine di delineare una procedura efficace per la determinazione non ambigua del modello di sottosuolo è possibile fare un ulteriore passo recuperando ed aggiornando in chiave FVS (Dal Moro, 2018a) il metodo più classico con cui, specie in studi crostali, viene in sismologia analizzata la propagazione delle onde di superficie. Oltre all'analisi delle velocità di fase (la cui definizione richiede l'utilizzo di dati *multi offset*), è infatti possibile analizzare le velocità di gruppo definibili considerando i dati raccolti da un unico sensore (dati *single offset* elaborati secondo l'analisi frequenza-tempo - e.g. Levshin et al., 1972; Ritzwoller and Levshin, 2002).

Nel presente caso, unitamente alla curva HVSR possiamo dunque definire le velocità di gruppo delle due componenti dell'onda di Rayleigh riferendoci alle tracce di un unico *offset*. In Fig. 2 sono riportati i risultati delle analisi eseguite considerando le velocità di gruppo delle componenti Z e R riferite all'*offset* 48 m. Il confronto con i risultati ottenuti considerando le velocità di fase (dati *multi offset* di Fig. 1) mostra l'evidente equivalenza dei due approcci, ponendo dunque in evidenza le potenzialità dell'analisi FVS multi-componente delle velocità di gruppo anche nell'analisi di dati complessi come quelli qui considerati.

In termini generali, sono due gli aspetti che vanno considerati nella valutazione dei risultati di un'inversione svolta secondo le procedure sopra delineate:

1) un'inversione congiunta è sempre ed inevitabilmente un *compromesso* e non è possibile trovare un modello perfetto rispetto tutti gli osservabili considerati; ciononostante il modello determinabile risulta necessariamente più robusto (Dal Moro and Puzzilli, 2017);
2) la presenza di variazioni laterali (che non possono essere prese in considerazione dall'analisi della dispersione) può rendere ulteriormente difficile la ricerca di un buon *match* per tutti gli osservabili considerati (nell'area in esame tali variazioni sono certamente presenti e rivelate dalle differenze nelle curve HVSR determinate in diversi punti dell'area attorno allo stendimento).

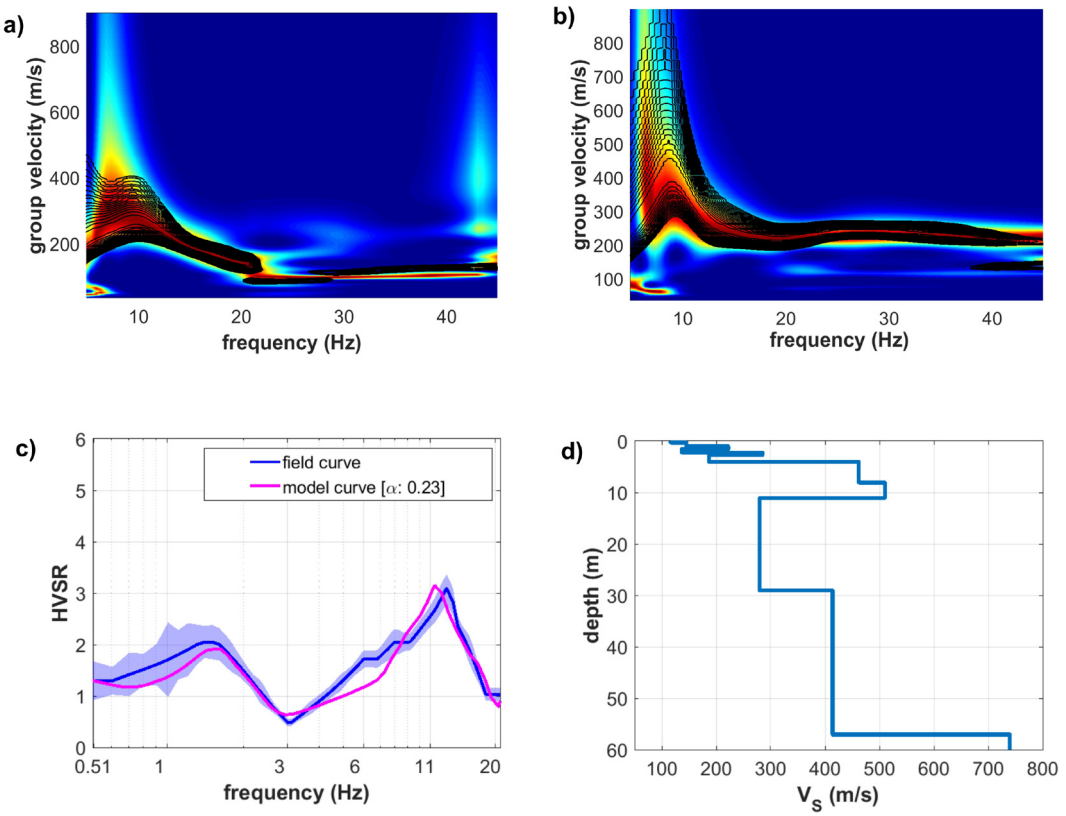


Fig. 2 - Analisi congiunta degli spettri delle velocità di gruppo delle componenti Z e R (analisi FVS) e della curva HVSR. Medesimi dati considerati per le analisi delle velocità di fase riportate in Fig. 1.

Considerazioni conclusive. Riguardo le caratteristiche degli spettri di velocità osservati nel sito in esame, l'evidenza che entrambe le componenti dell'onda di Rayleigh risultino dominate dai modi superiori in modo così deciso può far sorgere la domanda su quale sia il motivo per cui ciò accade. A questo proposito vengono spesso invocate inversioni di velocità presenti nel sottosuolo (strati con V_S inferiori a quelle degli strati superiori) ma, sulla base di una lettura critica di varie modellazioni, tale ipotesi si dimostra mancante di validità generale. Nello specifico dei dati qui esaminati, consideriamo la modellazione illustrata in Fig. 3 in cui sono riportati gli spettri di velocità di fase delle tracce sintetiche computate per le componenti Z, R e T considerando un modello che differisce da quello identificato durante le analisi dei dati di campagna (Fig. 1) unicamente per il fatto che sono state rimosse tutte le inversioni di velocità. Come si nota, l'andamento dell'energia (cioè il fatto che a dominare siano i modi superiori) non cambia in modo significativo.

L'eccitazione dei modi risulta un fenomeno molto comune ma non attribuibile a singoli e specifici aspetti. Oltre alla geometria dello stendimento, i fattori critici risultano il gradiente di velocità nella parte più superficiale, l'azione dell'attenuazione (bassi valori dei fattori di qualità favoriscono l'accentuarsi dei modi superiori - Panza, 1989 e Dal Moro *et al.*, 2015) e alti valori del rapporto di Poisson.

Da un punto di vista prettamente metodologico possiamo rimarcare i seguenti punti:

1) il *dataset* di campagna qui considerato non potrebbe essere risolto correttamente assumendo l'approccio classico basato sull'interpretazione (soggettiva) delle curve modali della sola componente Z in quanto, a frequenze inferiori a circa 22 Hz il segnale,

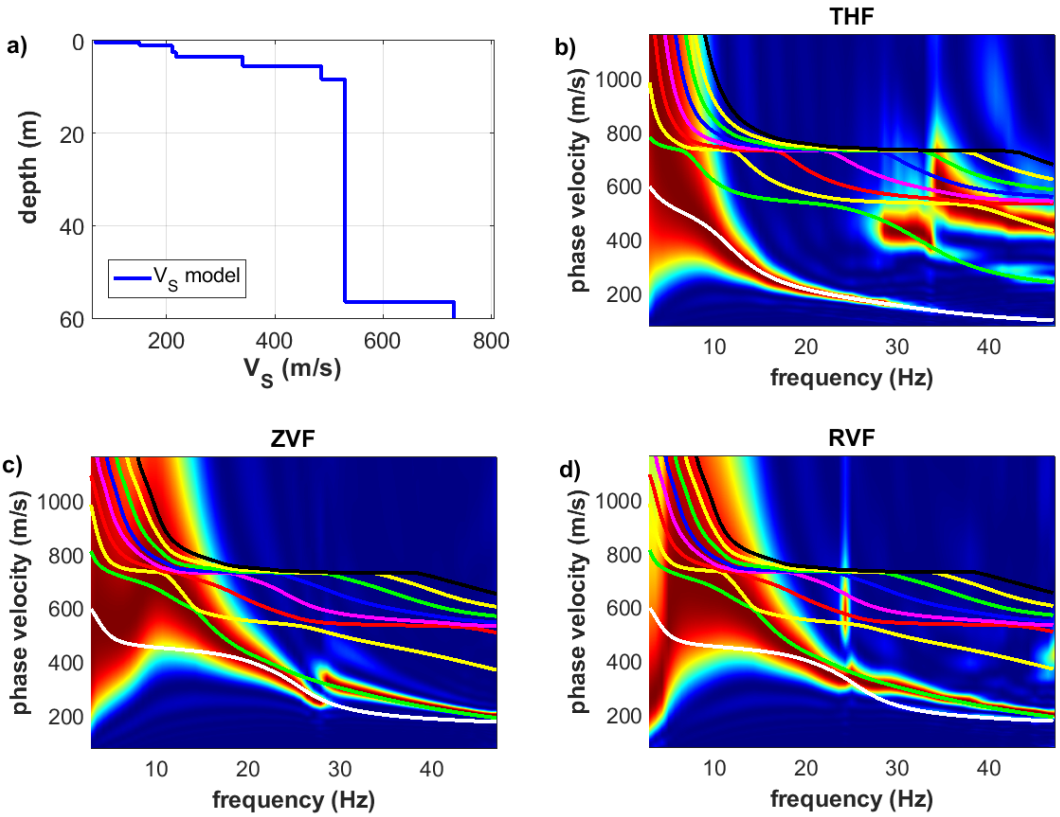


Fig. 3 - Modello (plot *a*) derivato da quello identificato durante l'analisi congiunta delle velocità di fase (Fig. 1d) ma privo di qualsiasi inversione di velocità. Mostrati gli spettri delle velocità di fase delle componenti T (onde di Love – plot *b*), Z (*c*) e R (*d*) con, in sovrapposizione, le curve modali dei primi 9 modi.

pur continuo, è di fatto riferito ad una pluralità di modi (la continuità di un segnale nello spettro di velocità non significa che tale segnale si riferisce ad un singolo modo): interpretare come modo fondamentale la dispersione a frequenze inferiori a 28 Hz porterebbe ad una pesante sovrastima delle V_S;

2) l'utilizzo delle velocità di fase (che richiedono l'acquisizione di dati *multi offset*) o di gruppo (dati a singolo *offset*) risulta necessariamente equivalente;
3) l'elaborazione FVS si rivela utile per l'analisi sia delle velocità di fase che di gruppo;
4) l'analisi FVS della dispersione non richiede alcuna interpretazione degli spettri di velocità e consente dunque di evitare la soggettività dell'approccio standard basato sull'interpretazione delle curve modali;
5) l'elaborazione FVS risulta particolarmente importante durante l'analisi delle velocità di gruppo al fine di risolvere i problemi legati all'analisi frequenza-tempo ("deformazione" degli spettri dovuta all'azione dei filtri Gaussiani utilizzati per la determinazione degli spettri di velocità di gruppo – Dal Moro *et al.*, 2019).

Si può infine considerare che nel processo di inversione è anche possibile aggiungere ulteriori osservabili tra i quali lo spettro di velocità delle onde di Love e la curva RPM (*Rayleigh-wave Particle Motion*) che rappresenta il reale moto della particella al passaggio dell'onda di Rayleigh e, dipendendo dalle condizioni del sottosuolo, risulta utile a vincolare ulteriormente il processo di inversione (Dal Moro *et al.*, 2018a; 2018b; 2019; Dal Moro, 2020).

Tutto questo mostra come l'acronimo MASW abbia perso oramai qualsiasi preciso connotato e i risultati ottenibili dall'approccio standard basato sull'interpretazione (soggettiva) delle curve modali della sola componente verticale siano di fatto superati (per precisione ed oggettività) da quelli ottenibili con diversi tipi di analisi a partire da dati multi-componente raccolti anche ad un unico *offset* dalla sorgente (velocità di gruppo multi-componente). Va da sé che l'utilizzo di un (unico) sensore triassiale consente di definire le velocità di gruppo di tutte le componenti (Z, R e T), della curva RPM e dell'HVSR (e.g. Dal Moro and Puzzilli, 2017; Dal Moro *et al.*, 2018a; 2018b; Dal Moro, 2020).

Riferimenti

Arai H. and Tokimatsu K.; 2005: *S-wave velocity profiling by joint inversion of microtremor dispersion curve and horizontal-to-vertical (H/V) spectrum*. Bull. Seismol. Soc. Am., **95**, 1766-1778.

Arai H. and Tokimatsu K.; 2004: *S-wave velocity profiling by inversion of microtremor H/V spectrum*. Bull. Seismol. Soc. Am., **94**, 53-63.

Dal Moro G.; 2020: *Efficient Joint Analysis of Surface Waves and Introduction to Vibration Analysis: Beyond the Clichés*, Springer, ISBN 978-3-030-46303-8, 273 pages

Dal Moro G.; 2019: *Surface wave analysis: improving the accuracy of the shear-wave velocity profile through the efficient joint acquisition and Full Velocity Spectrum (FVS) analysis of Rayleigh and Love waves.* Exploration Geophysics, **50**, 408-419, DOI: 10.1080/08123985.2019.1606202

Dal Moro G., Al-Arifi N. and Moustafa S.R.; 2019: *On the efficient acquisition and holistic analysis of Rayleigh waves: Technical aspects and two comparative case studies*, Soil Dynamics and Earthquake Engineering, **125**, 105742, https://doi.org/10.1016/j.soildyn.2019.105742

Dal Moro G., Moustafa S.R. and Al-Arifi N., 2018a. *Improved Holistic Analysis of Rayleigh Waves for Single- and Multi-Offset Data: Joint Inversion of Rayleigh-Wave Particle Motion and Vertical- and Radial-Component Velocity Spectra. Pure and Applied Geophysics*, **175**, 67-88

Dal Moro G.; 2018b: *Effective Active and Passive Seismics for the Characterization of Urban and Remote Areas: Four Channels for Seven Objective Functions. Pure and Applied Geophysics*, **176**, 1445–1465, https://doi.org/10.1007/s00024-018-2043-2.

Dal Moro G. and Puzzilli L. M.; 2017: *Single- and Multi-Component Inversion of Rayleigh Waves Acquired by a Single 3-Component Geophone: an Illustrative Case Study*, Acta Geodyn. Geomater., **14**, 431–444, DOI: 10.13168/AGG.2017.0024

Dal Moro G., Moura R.M. and Moustafa S.; 2015: *Multi-component Joint Analysis of Surface Waves*. J. Appl. Geophysics, **119**, 128-138.

Dal Moro G.; 2011: *Some Aspects about Surface Wave and HVSR Analyses: a Short Overview and a Case Study*. BGTA - Bollettino Geofisica Teorica e Applicata, **52**, 241-259 (*invited paper)*

Dal Moro G.; 2014: *Surface wave analysis for near surface applications*. Elsevier, Amsterdam, The Netherlands, 252 pp. ISBN 978-0-12-800770-9

Dou S. and Ajo-Franklin J.B.; 2014: *Full-wavefield inversion of surface waves for mapping embedded low-velocity zones in permafrost*. Geophysics, **79**, EN107–EN124.

Herrmann R.B.; 2013: *Computer programs in seismology: an evolving tool for instruction and research*. Seismol Res Lett, **84**, 1081–1088.

Levshin A.L., Pisarenko V.F. and Pogrebinsky G.A.; 1972: *On a frequency-time analysis of oscillations*. Ann. Geophys., **28**, 211–218.

Panza G.F.; 1985: *Synthetic seismograms: the Rayleigh waves modal summation*. J Geophys, **58**, 125–145.

Panza G.F.; 1989: *Attenuation Measurements by Multimode Synthetic Seismograms*. In: Cassinis, R., Nolet, G., Panza, G.F. (eds) Digital Seismology and Fine Modeling of the Lithosphere. Ettore Majorana International Science Series. Springer, Boston, MA. https://doi.org/10.1007/978-1-4899-6759-6_5

Pardalos P.M., Migdalas A. and Pitsoulis L. (eds); 2008: *Pareto optimality, game theory and equilibria*. Springer, New York. ISBN 978-0-387-77247-9

Ramík J. and Vlach M.; 2002: *Pareto-optimality of compromise decisions*. Fuzzy Sets and Systems, **129**, 119–127.

Ritzwoller M.H. and Levshin A.L.; 2002: *Estimating shallow shear velocities with marine multicomponent seismic data*. Geophysics, **67**, 1991–2004.

UNA TECNICA PER LA SEPARAZIONE DELLE COMPONENTI REGIONALE E LOCALE DEI CAMPI DI POTENZIALE BASATA SULL'USO DI DERIVATE VERTICALI FRAZIONARIE

G. Florio[1], M. Fedi[1], F. Cella[2]

[1] Dipartimento di Scienze della Terra, dell'Ambiente e delle Risorse, Università di Napoli "Federico II", Napoli, Italy
[2] Scuola di Scienze e Tecnologie – Sezione di Geologia, Università di Camerino, Camerino, Italy

Un prerequisito frequente nell'interpretazione di campi magnetici o gravimetrici riguarda la separazione degli effetti di sorgenti profonde dagli effetti di quelle superficiali. Gli approcci comunemente usati cercano di stimare la componente regionale del campo, supposta a grande lunghezza d'onda, analizzando i dati su un'area più ampia di quella di interesse. Le componenti locali vengono quindi trovate sottraendo dai dati osservati il campo regionale stimato. Questo tipo di soluzioni può avere alcune difficoltà di applicazione, poiché il set di dati su una vasta area potrebbe non essere disponibile e altre anomalie locali, presenti in quest'area estesa, potrebbero comunque impedire una stima affidabile del campo regionale nella finestra di interesse. In questo contesto, si presenta un approccio alternativo e semplice al problema della separazione regionale-residuo che non richiede l'analisi su vaste aree e mira a stimare la componente locale del campo, anziché quella regionale. Il metodo che proponiamo si basa sulla naturale amplificazione delle componenti a piccola lunghezza d'onda ottenibile calcolando una derivata verticale di un campo di potenziale. La derivata verticale viene invertita per ottenere una sorgente tipo strato equivalente che viene poi utilizzata per calcolare il campo residuo. L'ordine di differenziazione ottimale può essere ricercato esaminando i risultati ottenuti. Si evidenzia il fatto che l'ordine di differenziazione può assumere anche valori frazionari, per cui il metodo risulta uno strumento molto versatile. L'applicazione del metodo a un caso sintetico complesso e a dati reali dimostra l'utilità di questo approccio. In sintesi, il nostro metodo ha alcune caratteristiche peculiari che lo rendono un'interessante alternativa agli approcci attualmente utilizzati per la separazione delle componenti regionali e locali dei campi di potenziale: a) è un metodo locale, quindi può funzionare bene anche quando si elaborano dataset relativi ad aree di limitata estensione; b) a differenza della maggior parte dei metodi correntemente usati, che mirano a stimare una componente regionale, il nostro metodo produce direttamente una stima del campo dovuto alle sorgenti locali; c) è altamente versatile, in quanto la regolazione del parametro chiave, ovvero l'ordine di differenziazione frazionaria, consente di calibrare la residuazione molto più finemente rispetto ad altre tecniche, fino ad ottenere un campo locale ottimale.

PREDIZIONE DELLA FORMA D'ONDA DELLO SCUOTIMENTO IN PROFONDITÀ, A PARTIRE DA REGISTRAZIONI DI TERREMOTI IN SUPERFICIE: APPLICAZIONE A SITI ED EVENTI GIAPPONESI

M. Hallo, P. Bergamo, D. Fäh

Servizio Sismico Svizzero (SED), Politecnico Federale di Zurigo, Zurigo, Svizzera

Introduzione. Al fine di ridurre i danni e le vittime causati da futuri terremoti, molti paesi hanno introdotto criteri di progettazione antisismica nelle loro normative di costruzione. Esistono più classi di edifici con diversi requisiti di resistenza ai terremoti (ad es. ordinari, istituzionali ed edifici di particolare rilevanza). In tali normative, il livello probabile di scuotimento è richiesto come parametro di input, ed esso dipende dalla posizione geografica poiché la pericolosità sismica è spazialmente variabile. Nel caso di strutture di particolare rilevanza, la pericolosità sismica viene valutata per lunghi periodi di ritorno e deve tenere conto delle condizioni della roccia e del suolo presso la fondazione della costruzione. Tali condizioni specifiche del sito causano amplificazione e attenuazione delle onde sismiche, e possono essere approssimate utilizzando le classi di suolo (CEN 2004, SIA 2021). Tuttavia, le classi del suolo forniscono solo un'approssimazione semplicistica dell'effettiva risposta di sito e non sono applicabili, nella loro forma attuale, per importanti strutture sotterranee. Pertanto, è necessario modellare un possibile movimento del suolo in profondità per strutture sotterranee (es. depositi profondi di scorie nucleari) o per edifici con fondamenta profonde.

Dal punto di vista ingegneristico, lo scuotimento causato dai terremoti può essere caratterizzato attraverso la massima accelerazione registrata al suolo (PGA), la massima velocità al suolo (PGV), i valori di pseudo-accelerazione spettrale a vari periodi (PSA) oppure attraverso forme d'onda (Archuleta *et al.,* 2003, Zhao *et al.,* 2006, Edwards e Fäh 2013). La predizione della forma d'onda viene generalmente effettuata alla superficie del suolo e le previsioni in profondità sono piuttosto rare. Recentemente, Hallo *et al.* (2022) hanno proposto un nuovo metodo per caratterizzare il movimento del suolo ad alta frequenza in profondità, adatto anche per la predizione delle forme d'onda per un range esteso di frequenze. Il metodo fa uso di un nuovo modello stocastico (stochastic model, SM) che mette in relazione il movimento del suolo in profondità e in superficie nel dominio di Fourier. Quindi, è possibile prevedere la forma d'onda in profondità a partire da un'osservazione alla superficie del suolo e da un modello locale di velocità delle onde di taglio.

In questo contributo applichiamo il metodo di Hallo *et al.* (2022) per prevedere il movimento del suolo in profondità da registrazioni in superficie del terremoto di Osaka M_w5.6 del 2018 in Giappone (Kato e Ueda 2019, Hallo *et al.,* 2019). Le previsioni della forma d'onda completa vengono eseguite per siti KiK-net dotati di sensori di superficie e in profondità, che consentono un confronto diretto con dati empirici. Quindi, valutiamo in profondità l'accordo reciproco fra le forme d'onda osservate e previste; il medesimo confronto è effettuato per PGA e PGV. Lo scopo di questo contributo è mostrare la capacità del metodo di prevedere in modo affidabile lo scuotimento ad alta frequenza in profondità, richiesta per la valutazione della pericolosità sismica locale di strutture sotterranee di particolare importanza.

Metodo di modellazione. Assumiamo in input una forma d'onda di accelerazione osservata alla superficie del suolo. La sua trasformata di Fourier produce uno spettro di accelerazione, che può essere correlato allo spettro di accelerazione in profondità attraverso una funzione di trasferimento superficie-profondità. Quindi, la predizione dello spettro di accelerazione in profondità viene semplicemente ottenuta dividendo lo spettro alla superficie del suolo per la funzione di trasferimento predetta superficie-profondità. Infine, la sua trasformata di Fourier inversa fornisce la previsione della forma d'onda dello scuotimento in profondità.

Seguendo Hallo *et al.* (2022), la funzione di trasferimento predittiva superficie-profondità viene valutata utilizzando un modello stocastico (SM). Il SM mette in relazione lo scuotimento del suolo in profondità ed alla superficie utilizzando una coppia di curve spettrali. L'SM è costruito con una procedura in tre fasi: 1) Deriviamo un insieme di mezzi stratificati 1D considerando i possibili effetti di variazione delle proprietà geo-meccaniche sui movimenti del suolo. 2) I mezzi 1D sono usati per il calcolo di un insieme di funzioni di trasferimento dell'onda SH superficie-profondità nel dominio di Fourier. 3) Determiniamo lo spettro medio e le deviazioni standard dall'insieme delle funzioni di trasferimento. L'SM è privo di picchi di risonanza ad alta frequenza non realistici, assomiglia a una risposta empirica del sito osservata ai siti con array di monitoraggio verticale ed è adatto per previsioni di forme d'onda.

Applicazione al terremoto M_w5.6 di Osaka settentrionale del 2018. Il terremoto del nord di Osaka M_w5.6 del 2018 si è verificato il 18 giugno 2018 presso la città di Takatsuki (Osaka, Giappone). Questo terremoto ha causato danni e vittime. È stato causato da movimenti su faglie crostali trascorrenti e inverse (Kato e Ueda 2019, Hallo *et al.,* 2019). A questo terremoto, applichiamo il metodo qui illustrato per prevedere le forme d'onda in profondità a partire da registrazioni dei terremoti osservate sulla superficie del suolo. In particolare, le registrazioni della rete accelerometrica KiK-net (Aoi *et al.,* 2011, NIED 2019). Le forme d'onda previste vengono confrontate con la componente orizzontale trasversale del movimento del suolo

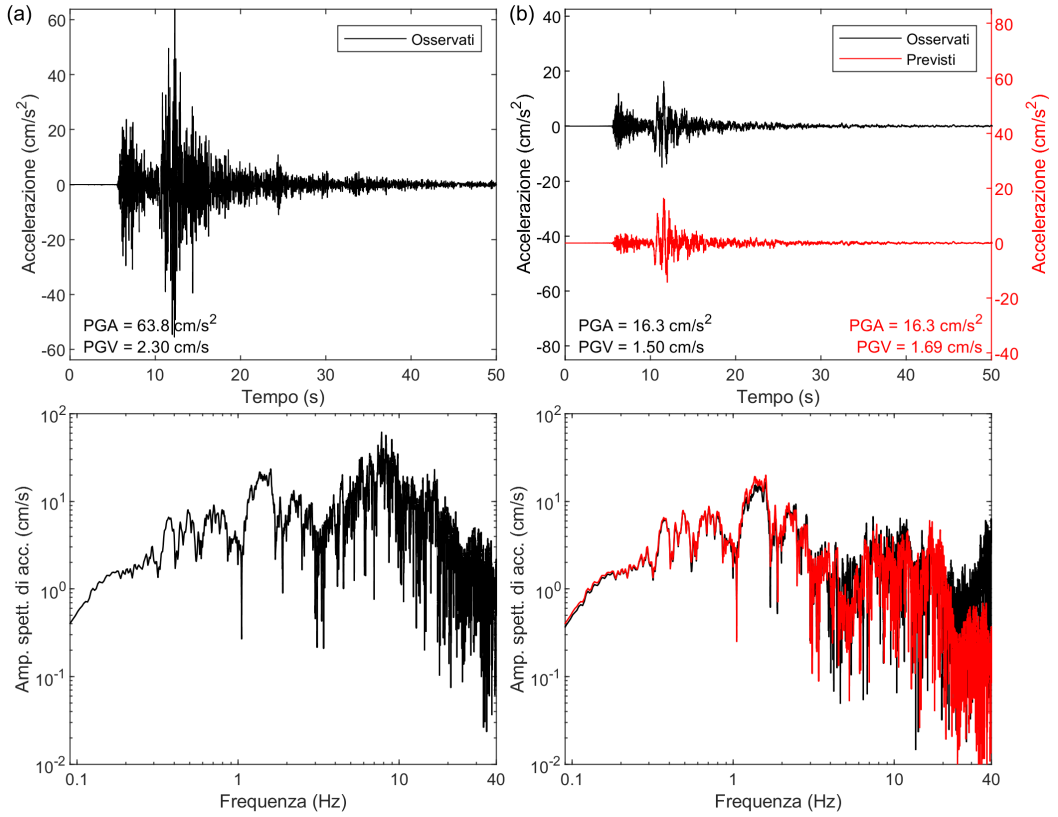


Fig. 1 - Il terremoto di Osaka del 2018: previsione dello scuotimento in profondità nel sito HYGH04. (a) Componente trasversale del moto orizzontale del suolo osservato in superficie. (b) Movimento orizzontale del suolo osservato (nero) e previsto (rosso) nel pozzo a 100 m di profondità.

osservata dagli strumenti in profondità in più siti. Il confronto tra il movimento del suolo previsto e quello osservato in profondità è mostrato nelle Fig. 1 e 2.

Il sito HYGH04 in Fig. 1 si trova a una distanza epicentrale di 40 km; il sensore installato in profondità si trova a 100 m dalla superficie del suolo. In questo caso, la PGA prevista utilizzando la funzione di trasferimento predittiva superficie-profondità è esattamente uguale al valore osservato al sensore di pozzo (16.3 cm/s^2). C'è anche un alto livello di somiglianza fra valori previsti e osservati di PGV in profondità (rispettivamente 1.69 e 1.50 cm/s). Inoltre, si noti che la previsione dell'ampiezza dell'onda P ad alta frequenza è leggermente sottostimata poiché il metodo è inteso per le onde S. Infine, il sito HYGH10 in Fig. 2 si trova a una distanza epicentrale di 75 km. Il valore previsto di PGA in profondità è 7.2 cm/s^2, che è vicino al valore osservato 9.1 cm/s^2. Allo stesso modo, esiste una buona somiglianza fra valori previsti e osservati di PGV in profondità (0.57 e 0.46 cm/s, rispettivamente).

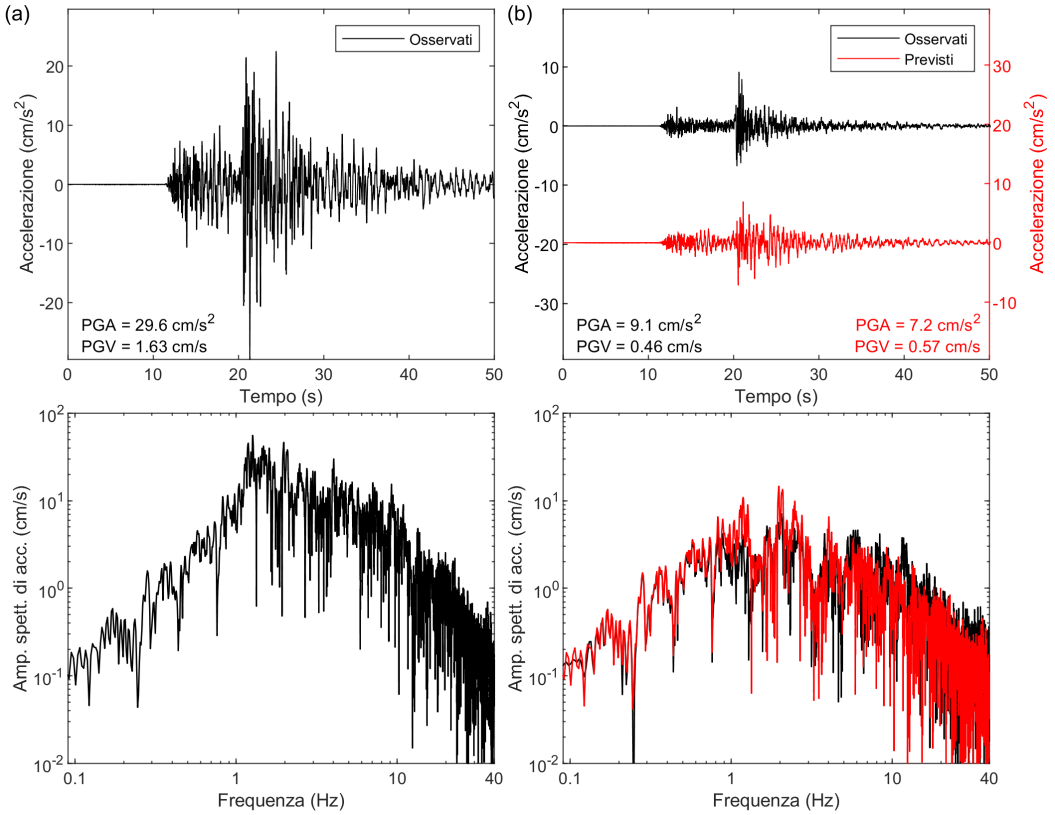


Fig. 2 - Il terremoto di Osaka del 2018: previsione dello scuotimento in profondità nel sito HYGH10. (a) Componente trasversale del moto orizzontale del suolo osservato in superficie. (b) Movimento orizzontale del suolo osservato (nero) e previsto (rosso) nel pozzo a 100 m di profondità.

Conclusioni. In questo contributo, dimostriamo l'affidabilità del metodo proposto nel prevedere lo scuotimento ad alta frequenza in profondità da registrazioni di superficie. Il metodo introdotto da Hallo *et al.* (2022) viene applicato per prevedere le forme d'onda ai sensori di profondità del terremoto di Osaka M_w5.6 del 2018 (Osaka, Giappone). Un confronto tra le forme d'onda di accelerazione previste e osservate nei siti KiK-net mostra un alto livello di somiglianza nell'intervallo di frequenza 0.1–40 Hz. Inoltre, i valori previsti di PGA e PGV sono soddisfacentemente vicini a quelli osservati nella maggior parte dei casi studiati. Per

concludere, il metodo può essere applicato a scopi di progettazione della resistenza sismica, ad esempio la progettazione di depositi in profondità, edifici con fondamenta profonde o per studi di interazione suolo-struttura.

Riconoscimenti. Questa ricerca è supportata da un contratto con l'Ispettorato federale della sicurezza nucleare (ENSI).

Bibliografia

Aoi S., Kunugi T., Nakamura H. and Fujiwara H.; 2011: *Deployment of new strong motion seismographs of K-NET and KiK-net*. In: Akkar S., Gülkan P. and van Eck T. (eds), Earthquake data in engineering seismology geotechnical, geological, and earthquake engineering, vol. 14., Springer, Dordrecht, Netherlands, pp. 167-186.

Archuleta R.J., Liu P., Steidl J.H., Bonilla L.F., Lavallée D. and Heuze F.; 2003: Finite-fault site-specific acceleration time histories that include nonlinear soil response. *Physics of the Earth and Planetary Interiors*, **137**, 153-181.

CEN; 2004: *Eurocode 8: Design of structures for earthquake resistance – Part 1: General rules, seismic actions and rules for buildings*. European Committee for Standardization, EN 1998-1 edition, Brussels, Belgium, 229 pp.

Edwards B. and Fäh D.; 2013: A stochastic ground-motion model for Switzerland. *Bulletin of the Seismological Society of America*, **103**, 78-98.

Hallo M., Opršal I., Asano K. and Gallovič F.; 2019: Seismotectonics of the 2018 northern Osaka M6.1 earthquake and its aftershocks: joint movements on strike-slip and reverse faults in inland Japan. *Earth, Planets and Space*, **71**:34.

Hallo M., Bergamo P. and Fäh D.; 2022: Stochastic model to characterize high-frequency ground motion at depth validated by KiK-net vertical array data. *Bulletin of the Seismological Society of America*, under review.

Kato A. and Ueda T.; 2019: Source fault model of the 2018 M_w 5.6 northern Osaka earthquake, Japan, inferred from the aftershock sequence. *Earth, Planets and Space*, **71**:11.

National Research Institute for Earth Science and Disaster Resilience; 2019: NIED K-NET, KiK-net, National Research Institute for Earth Science and Disaster Resilience. https://doi.org/10.17598/NIED.0004.

SIA; 2021: *SIA 261 Einwirkungen auf Tragwerke*. Société Suisse des ingénieurs et des architectes, Zurich, Switzerland, 136 pp.

Zhao J.X., Zhang J., Asano A., Ohno Y., Oouchi T., Takahashi T., Ogawa H., Irikura K., Thio H.K., Somerville P.G., Fukushima Y. and Fukushima Y.; 2006: Attenuation relations of strong ground motion in Japan using site classification based on predominant period. *Bulletin of the Seismological Society of America*, **96**, 898-913.

INTRODUCTION TO INTERPOLATION UNCERTAINTY OF THE NATURAL NEIGHBORS METHOD (SIBSON)

M. Iurcev[1], M. Majostorovic[2], F. Pettenati[1]

[1] Istituto di Oceanografia e di Geofisica Sperimentale, OGS, Trieste, Italy
[2] Università degli studi di Trieste, Trieste, Italy

Introduction. The Natural Neighbors (Sibson 1980) (NN hereafter) method is a spatial data interpolation method with unique reproducibility (Iurcev *et al.,* 2021). What this method lacks is a qualitative and/or quantitative control of the uncertainty based on the random spatial distribution of the measurements, relative to the true surface of the data. The method is an exact interpolator, in the sense that the original data values are preserved at reference data points. A method such as Kriging, which is considered the BLUE (Best Linear Unbiased Estimator) (Chilès and Delfiner, 1999) inherently provides an assessment of errors, through the minimization of the mean square error. However, Kriging requires several input parameters, a trend analysis for the stationary condition and as main ingredient a semivariogram model in order to estimate the weights which minimize the error variance (for the Universal Kriging version).

One approach to assess the uncertainties in NN is based on cross-validation errors Etherington (2020). This approach involves the computation of the Mean Absolute Error (cross-validation) of the estimate value f^* over data f_i, taking into account the mutual distances between these points. In this note we follow a geostatistical approach that addresses the variance and the spatial structure of the data with respect to the interpolation points.

Method. Let us consider N points in R^2, with coordinates $\mathbf{x}_i$ (i=1…N). We generate a partition of the plane by means of a Voronoi tessellation. The V_i convex polygons have the following property

$$V_i = \{\mathbf{p} \in \mathbb{R}^2 : \forall i \neq j : |\mathbf{p} - \mathbf{x}_i| < |\mathbf{p} - \mathbf{x}_j|\} \quad (1)$$

and the tessellation is uniquely determined (Fig. 1).

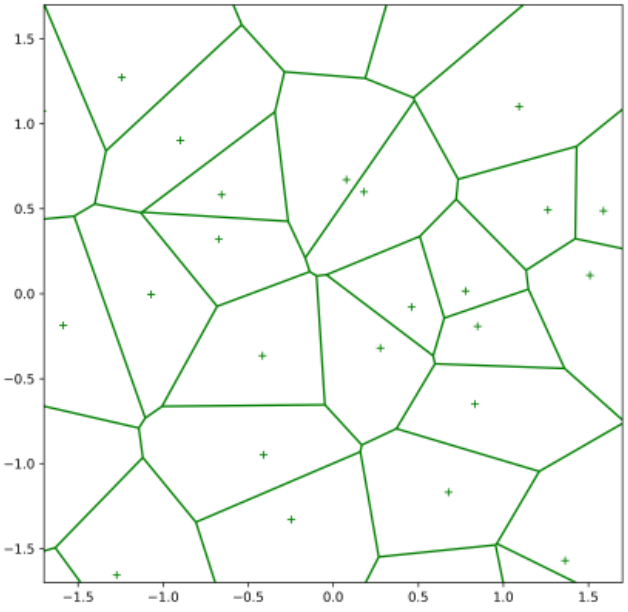


Fig. 1 - Voronoi tessellation of a spatial random distribution of $\mathbf{x}_i$ data.

The NN (Sibson 1980) method considers the interpolation on a point **x*** by means of a convex linear function

$$f_{int} = \sum_{i=1}^{N} w_i f_i \tag{2}$$

where w_i are the weights depending on the relative area of the intersection between *Vi* and the V* generated by **x*** (Fig. 2)

$$w_i = \frac{\mathrm{A}i \cap A*}{A*} \tag{3}$$

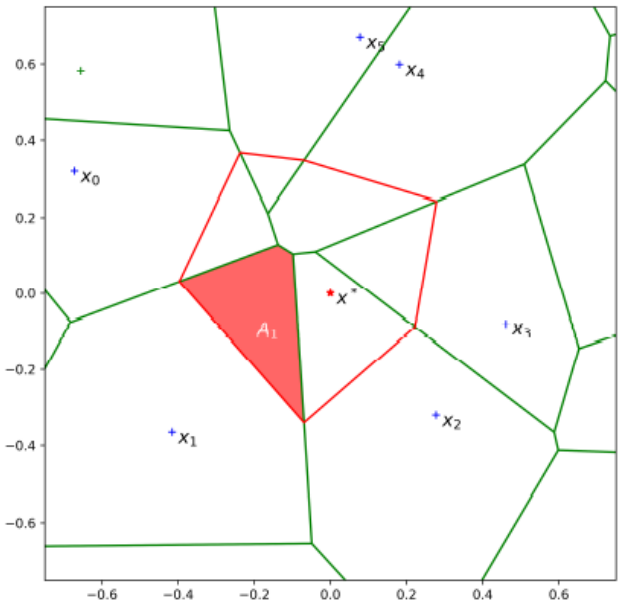


Fig. 2 - Natural Neighbors (NN) pattern, where **x*** is the point of interpolation and the red polygon its relative Voronoi. The red area represents the intersection $A_i \cap A*$.

To estimate the local uncertainties of formula (2), we follow a geostatistical approach by assuming a stationarity condition overall and considering the relationship between the covariance and the theoretical semivariogram γ

$$\gamma(d) = 2\ \mathrm{var}[f(\mathbf{x}) - f(\mathbf{x}+d)] \tag{4}$$

with d being the distances between the points **x**

$$\mathrm{cov}(d) = \mathrm{var}(f) - \gamma(d) \tag{5}$$

Considering a linear semivariogram model γ(d) = ad + b, we achieved the function

$$\mathrm{var}\left(f - f_{int}\right) \leq 2\mathrm{b} + \mathrm{a}\left(2\sum_i w_i d_i - \sum_i \sum_{i \neq j} w_i\, w_j d_{ij}\right) \tag{6}$$

With the V_i configuration of Fig. 1, we show a preliminary result of function (6) in Fig. 3.

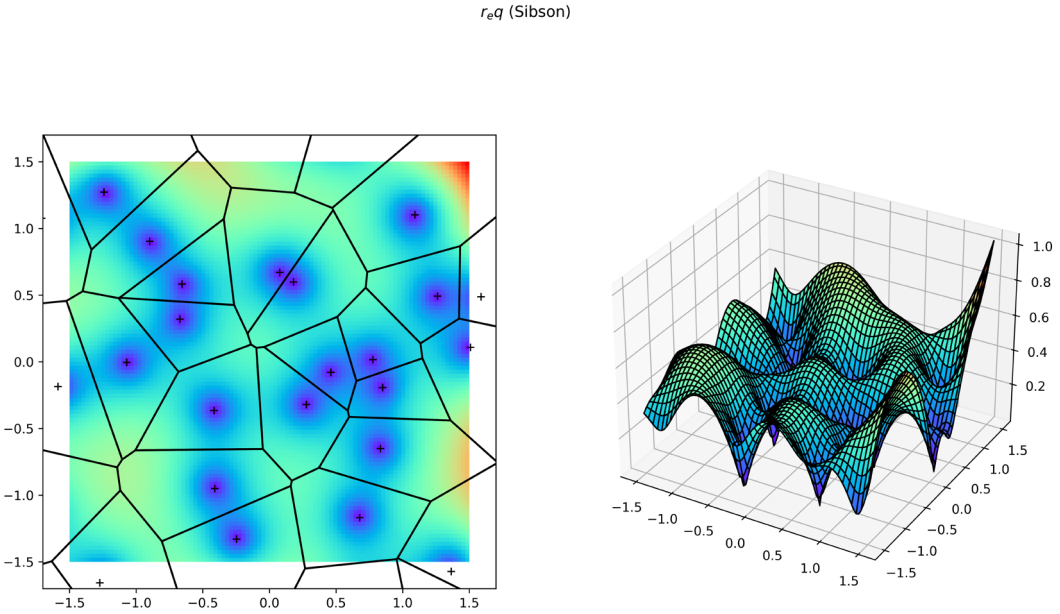


Fig. 3 - the result of function (6) that considers the structure of data in Fig. 1. (the colours start from blue = 0 to red = maximum value).

Discussion. The result in Fig. 3 shows the performance of function (6) which considers the spatial structure between the data (semivariograms), for the NN interpolation scheme. In the case shown, we do not consider the effect of the *nugget* (b in the formulas), which agrees with the property that the original data values are maintained at the reference data points (the colours start from blue = 0 to red = maximum value). As might to be expected, the maximum variance values are found at the edges of V_i polygons, particularly in less information-dense areas. The formula can be applied to other interpolation methods based on convex combination.

Given the promise of the method, we will show further developments, like an exponential semivariogram model and testing on experimental datasets in the future.

References

Chilès J. P. and Delfiner P.; 1999: *Geostatistics*. *Modeling Spatial Uncertainty.* Wiley Series is Probability and Statistics, 695.

Etherington T. R.; 2020. *Discrete natural neighbour interpolation with uncertainty using cross-validation error-distance fields*. PeerJ Comput. Sci. **6**:e282, 1-16, http://doi.org/10.7717/peerj-cs.282

Iurcev M., Pettenati F., Diviacco P.; 2021; *Gridding, boundary definition and interpolation methods for near real-time spatial data.* Bull. Geoph. and Oceanog., **62**, 3, 427-454, September 2021; doi:10.4430/bgta0360.

Sibson R.; 1980. *A vector identity for Dirichlet tessellation*. Math. Proc. Camb. Philos. Soc. **87**, 151–155.

DEEP PRECONDITIONERS FOR SEISMIC INVERSE PROBLEMS WITH APPLICATION TO DEBLENDING

V. Lipari[1], P. Bestagini[1], M. Ravasi[2], S. Tubaro[1]

[1] Dipartimento di elettronica informazione e Biongegneria, Politecnico di Milano, Italy
[2] Earth Science and Engineering, King Abdullah University of Science and Technology, Arabia Saudita

Introduction. Seismic processing and imaging generally involve ill-posed inverse problems which require regularization techniques to drive their solutions with available prior knowledge. Among these techniques we can include sparsity promoting inversion coupled with fixed basis sparsifying transforms. The underlying idea is that in a transformed domain seismic data and seismic images can be represented with few non-zero coefficients. Despite the remarkable results achieved by these techniques, they rely on handcrafted assumptions imposed on the useful signal to be recovered. Therefore, they sometimes fail to adapt to the highly complex features of seismic data. Alternatively, data driven sparse dictionaries can be learned directly from the dataset.

In recent years, sophisticated data-driven based methods based on deep learning techniques have been introduced for seismic processing tasks. However, despite the effectiveness of CNN based methods most of these techniques face generalization issues and need to collect proper training field datasets or to build appropriate synthetic training datasets, which is a hard task.

Deep preconditioners (Ravasi, 2021) represent an alternative approach that combines the advantages of sparsifying inversion with the ability of deep CNNs to learn compact representations of N-dimensional vector spaces. First, a convolutional autoencoder (AE) (Goodfellow *et al.*, 2016). is trained to learn a sparse representation of the desired outcome. Subsequently the trained decoder is used as a non-linear preconditioner for the inverse problem to be solved. The effectiveness of the method is demonstrated through the problem of seismic deblending.

Method. We aim at inverting a geophysical linear problem of the form:

$$\mathbf{y} = \mathbf{A}\mathbf{x}$$

where $\mathbf{x} \in \mathbb{R}^m$ and $\mathbf{y} \in \mathbb{R}^n$ are model and data vector, respectively; and $\mathbf{A} : \mathbb{R}^m \rightarrow \mathbb{R}^n$ is a linear mapping between these two spaces. Unfortunately, most geophysical problems are ill-posed (i.e. several models explain the data) and require some form of prior information, to find a stable and satisfactory solution. A standard way is to find a regularized least square solution of the form:

$$\hat{\mathbf{x}} = \underset{\mathbf{x}}{\operatorname{argmin}} \frac{1}{2} ||\mathbf{y} - \mathbf{A}\mathbf{x}||_2^2 + \lambda \left| \mathbf{R}\mathbf{x} \right|_p,$$

and **R** is a regularization operator.

Alternative to regularization is preconditioning, where the search is carried out in a projected space:

$$\hat{\mathbf{z}} = \underset{\mathbf{z}}{\operatorname{argmin}} \frac{1}{2} ||\mathbf{y} - \mathbf{A}\mathbf{P}\mathbf{z}||_2^2 + \lambda |\mathbf{z}|_p,$$

and the solution is then found as $\hat{\mathbf{x}} = \mathbf{P}\hat{\mathbf{z}}$. The design of regularizers and preconditioners is usually driven by experience.

A popular choice of preconditioner is a transform that projects the model into a space where the model can be explained by a small number of non-zero coefficients leading to sparsity promoting inversion (Candes, 2006). However, fixed coefficient transforms sometimes

fail to accurately describe complex vector spaces such as those spanned by seismic data.

An alternative is to learn the transform directly from the data, which can be performed effectively and efficiently by the non-linear dimensionality reduction obtained through CNNs. This way the inverse problem we wish to solve writes:

$$\hat{\mathbf{z}} = \underset{z}{\operatorname{argmin}} \frac{1}{2} \left| \left| \mathbf{y} - \mathbf{A}\mathrm{D}_{\theta}(\mathbf{z}) \right| \right|_2^2 + \lambda \left| \mathbf{z} \right|.$$

Here $\mathrm{D}_{\theta}(\mathbf{z})$: $\mathbb{R}^k \rightarrow \mathbb{R}^m$ is a non-linear mapping implemented through a trained convolutional decoder. Here, since the functional to be minimized is nonlinear, it is appropriate to use non-linear solvers such as L-BFGS to estimate z. Finally, the solution of the inverse problem is found as $\hat{\mathbf{x}} = \mathrm{D}_{\theta}(\hat{\mathbf{z}})$. The parameters θ of the decoder $\mathrm{D}_{\theta}(\bullet)$ are found alongside those of an encoder $\mathrm{E}_{\theta}(\mathbf{z})$: $\mathbb{R}^m \rightarrow \mathbb{R}^k$ while learning the latent representation by training the convolutional autoencoder $\mathrm{AE}(\bullet) = \mathrm{D}_{\theta}(\mathrm{E}_{\theta}(\bullet))$. This is accomplished by minimizing the following loss function over a training dataset of n_s samples $\{\boldsymbol{u}_1, \boldsymbol{u}_2, \ldots, \boldsymbol{u}_n\}$ that is representative of the data **x** we wish to invert.

$$\hat{\boldsymbol{\theta}} = \underset{z}{\operatorname{argmin}} \sum_{i=1}^{n_s} \left\| \mathbf{u}_i - \mathrm{D}_{\boldsymbol{\theta}}\left(\mathrm{E}_{\boldsymbol{\theta}}(\mathbf{u}_i)\right) \right\|_p,$$

Application to deblending. We demonstrate the effectiveness by applying it to the problem of seismic deblending. In a seismic blended acquisition, multiple sources fire in a short time interval according to a random dithering code: the shots of different sources are then blended. Therefore, in this case the linear operator **A** implements the delays due to the dithering code. The goal of seismic deblending is to recover the unblended seismic data **x** from the blended measurements **y**.

The example is designed by means of a field dataset from Gulf of Suez comprised of 128 shots, 128 receivers and 512time samples with spatial and temporal sampling intervals of 12.5 m and 4 ms, respectively. Blending is performed by applying a random dithering conde where the random delay lies in the time range [0, 0.8s]. Some blended data are shown in Fig.1.

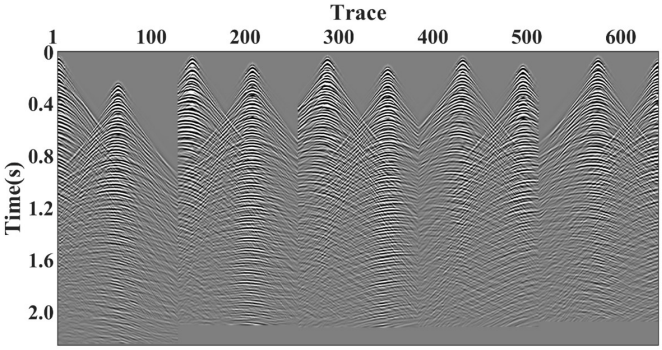


Fig. 1 - Some blended common shot gathers.

An original unblended common shot gather is shown in Fig. 2a and its corresponding pseudo-deblended gather is shown in Fig 2e; notice that the blending noise masks the useful signal especially in the deep area of the first few traces. The deblending result of the proposed method is displayed in Fig. 2d and compared with the results obtained via dictionary learning (Fig 2b) and via end-to-end deep learning (2c). The corresponding residuals are shown in Fig 2f, 2g and 2h. The dictionary learning based deblending method (Fig. 2f) results in strong lending noise residual and signal damage. For the deblending CNN (Fig. 2g), although we can barely

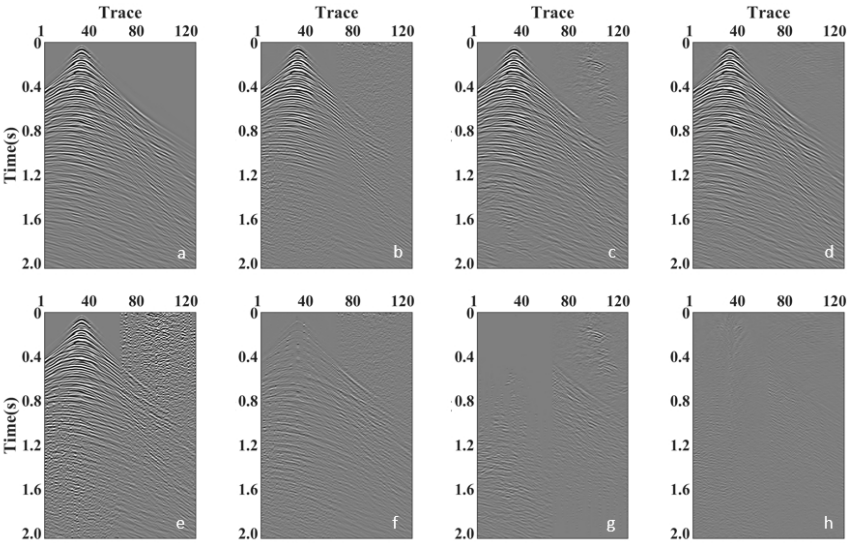


Fig. 2 - An original deblended common shot gather (a) with its corresponding pseudo-deblended gather (e). Result of deblending and corresponding residual with dictionary learning based deblending (b.f), end-to-end CNN deblending (c,g), deep preconditioners based inversion (d,h).

see the blending noise in Fig. 5(b), there is distinct event leakage. Deep preconditioner-based method (Fig. 2h) can effectively remove almost all the blending noise with little useful signal leakage.

A good training dataset is key to train an effective AE. Standard solutions consist in building high-quality synthetic dataset or collecting an appropriate field dataset, but neither is easy to implement. We avoid this by relying on the blended dataset itself to construct the training samples: this means that no extra data is required. Based on reciprocity, unblended common shot gathers (CSGs) are similar to unblended common receiver gathers (CRGs). On the other hand, despite the acquired CSGs are blended, we can still find that the data are coherent and thus they share similar characteristic with the unblended data. On the contrary, blended CRGs are corrupted by random blending noise. Training is performed using the Adam optimizer (Kingma and Ba, 2014) with learning rate lr = 10^-3, weight decay regularization eq = 10^-5, and p = 2.

Discussion and conclusions. Deep preconditioning is a framework that leverages nonlinear based dimensionality reduction to solve of ill-posed inverse problems. We have demonstrated his effectiveness trough an example of seismic deblending. An important feature of this application is that there is no need for any training data beyond the recorded seismic data itself. The choice of the network architecture, the size of the latent representation and the training strategy seem to be the key factors to find a representative sparse representation of our seismic data. Future work will focus on testing the framework on a wide set of seismic processing problems.

References

Candes E. 2006, *Compressive Sampling,* Proceedings of the international congress of mathematicians 3, 1433-1452

Kingma D., J. Ba, 2015 Adam: *A Method for Stochastic Optimization.* International Conference on Learning Representations

Goodfellow I., Y. Bengio, and A. Courville, 2016 *Deep learning.* MIT press.

Ravasi M., 2021, *Seismic wavefield processing with deep preconditioners*, in First International Meeting for Applied Geoscience & Energy, Expanded Abstracts, pp. 2859-2863.

FECS: UN NUOVO METODO PER IL FILTRAGGIO DEI CAMPI DI POTENZIALE

M. Maiolino, M. Fedi, G. Florio

Università degli studi di Napoli "Federico II", Dipartimento di Scienze della Terra dell'Ambiente e delle Risorse, Italy

Il filtraggio dei dati di campi di potenziale è spesso una fase di processing irrinunciabile che precede una loro modellizzazione quantitativa. Lo scopo dei filtraggi può essere vario, dalla rimozione di trend regionali alla rimozione del noise. In questo lavoro si presenta una tecnica di filtraggio dei campi di potenziale denominata "Filtering with Extremely Compact Sources" (FECS). Questa metodologia permette di risolvere le problematiche di interferenza tra anomalie che generalmente complicano l'interpretazione dei dati gravimetrici o magnetici. I fenomeni di interferenza possono consistere nella sovrapposizione di anomalie aventi simili lunghezze d'onda (p.es., generati da sorgenti vicine e a simile profondità) o nella sovrapposizione di campi regionali (prodotti da sorgenti profonde o lontane) alle anomalie di interesse, generate da sorgenti sepolte a più piccola profondità nell'area in studio. La tecnica FECS consiste nella stima di un modello di sorgenti equivalenti estremamente compatte e tra loro ben separate nello spazio. Il campo può quindi essere filtrato tramite un semplice processo di "muting" nel dominio delle sorgenti. Casi sia sintetici che reali mostrano la validità della metodologia per problematiche come la separazione di anomalie interferenti, la rimozione di campi regionali e la riduzione del noise.

DEEP ATTRIBUTES: EXTRACTION OF GPR STATISTICAL FEATURES WITH DEEP LEARNING

G. Roncoroni, E. Forte, M. Pipan

Università di Trieste, Dipartimento di Matematica e Geoscienze, Italy

Introduction. We propose a new way of using Hidden Layer (HL) predictions for the extraction of features from Ground Penetrating Radar (GPR) data, using Long Short Term Memory (LSTM) neurons. The main idea is based on the inference process of a LSTM-based Neural Network: in hidden layers the Neural Network (NN) extracts information related to attributes of input data such as amplitude, phase and frequency and uses them to get the required inference. Deep Learning applications typically ignore the information from the intermediate steps because the main interest lies in the final results. In this work we study the possible exploitation of intermediate prediction steps to characterize features and signatures embedded in GPR data. Following the most popular definitions of seismic attributes (see e.g. Chopra and Marfurt, 2005) and Anstey *et al.*, 2007) we define the new extracted features as "*Deep attributes*" testing their effectiveness on GPR datasets. We find that deep attributes are helpful to get improved and more constrained data interpretation, highlighting zones with the same signature which are not apparent on usual reflection amplitude profiles. Furthermore, deep attributes can be used to classify and correlate features within even large and complex datasets.

Methods. In this paper we focus on LSTM-based NN, but the proposed approach can be applied in principle to any NN geometry. The choice of LSTM is motivated by the causal nature of the Recurrent Neural Network (RNN) which can provide a more reliable representation of the different signal components embedded in the GPR data.

The simplest RNN is made up of a single neuron that receives input, produces an output, and sends that output to itself and to the output vector. At each time step t (often called *frame*), the recurrent neuron receives the inputs x(t) as well as its own output from the previous time step, y(t-1). Each recurrent neuron has two sets of weights: one for the inputs x(t) and the other for the outputs of the previous time step y(t-1). If we consider the whole recurrent layer, instead of just one recurrent neuron, we can place all the weight vectors in two weight matrices Wx and Wy, while Ø is an activation function. Therefore:

$$y(t) = \varnothing\left(W_x^T x(t) + W_y^T y(t-1) + b\right)$$

One of the problems RNNs have is to handle long-term dependencies: to solve this problem some special neurons have been introduced: one of the most used is the Long Short-Term memory (LSTM), introduced by Hochreiter and Schmidhuber (1997). LSTMs are in fact explicitly designed to avoid the long-term dependency problem: they have a chain-like structure, as RNN, but the repeating module has a different structure (see Fig. 1), which is able to keep on information even from *t<t-1*. The ability to spot long time dependencies in a signal is the reason for the choice of this type of layers for the proposed extraction method.

The final aim of the procedure is to automatically extract (i.e. interpret, Roncoroni *et al.*, 2021) horizons, and we train the NN to perform this task (Fig. 2).

The proposed workflow for this application is:

I. Create a LSTM-based NN that fits a specific problem
II. Train the NN, for a specific task, on a synthetic dataset (see e.g. Roncoroni et al., 2021).
III. Apply the trained NN on real data
IV. Use the HL predictions as a set of additional information (i.e. deep attributes) for improved GPR interpretation.

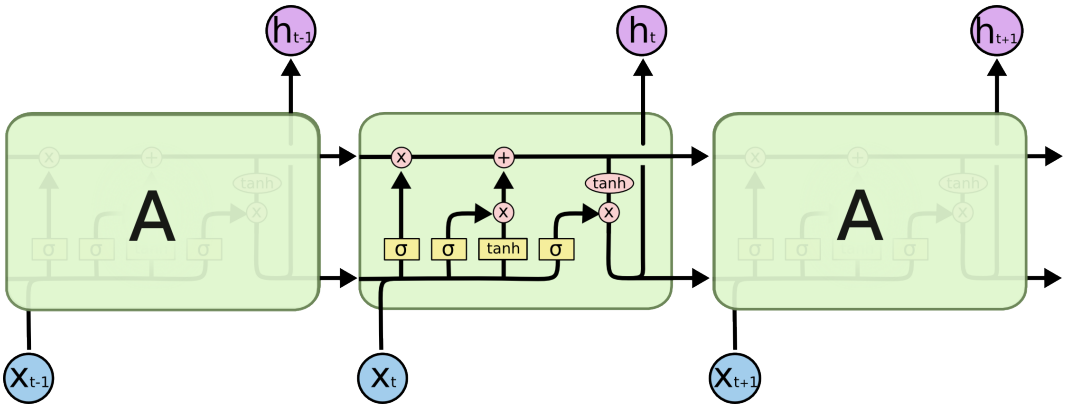


Fig. 1 - The repeating module in an LSTM contains four interacting layers, modified from https://colah.github.io/posts/2015-08-Understanding-LSTMs/.

Once we have a trained NN we can start working on the prediction of each single neuron from each HL. In Fig. 2 we show all the deep attributes produced by the trained NN during the horizons extraction task.

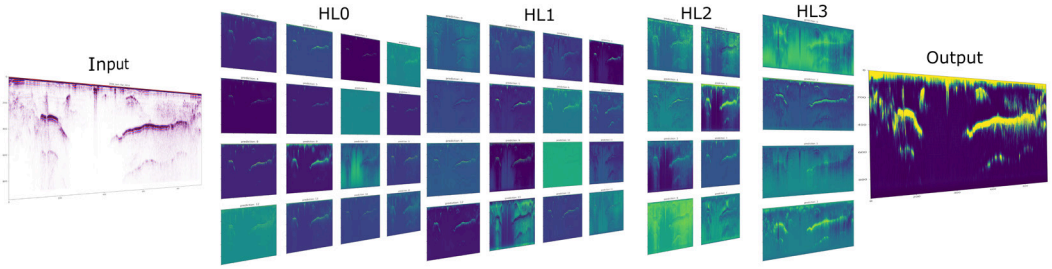


Fig. 2 - Example of the results of Deep Attribute extraction from a real GPR data profile acquired on a perennially frozen lake containing brines, in Antarctica (further details can be found in Forte *et al.*, 2016). From left to right we can see the input GPR amplitude data, the Hidden Layer predictions and the final horizons extraction.

Results. Starting from the HL shown in Fig. 2, we selected some interesting Deep Attributes for evaluation purposes: in Fig. 3 we can see the real data (Fig 3.A), Fig. 3.B is the first deep attribute (Deep Attribute B, from now on), and so on. A discussion on results and possible interpretation follows.

- Deep Attribute B: in this attribute we can focus mainly on noisy areas, we can see the brines identified with green color, while we marked with number 1 a coherent dark blue area. The overall structure of attribute B can be considered a summary of the main features evident in the input data that can also be exploited for automatic extraction. In fact both the main reflectors and homogeneous zones are apparent.
- Deep Attribute C: here we find some areas with higher values - marked with number 2, just above the main horizon. We can link them to low noise zones: they are divided by the intermediate brine area (labeled 5 in (E) below), where we have very high signal attenuation due to the high electrical conductivity of brines.
- Deep Attribute D: this attribute is more linked to a phase attribute, and we can spot the closing of a dipping horizon - marked with number 3 - and some low amplitude but laterally continuous layering - marked with number 4-.

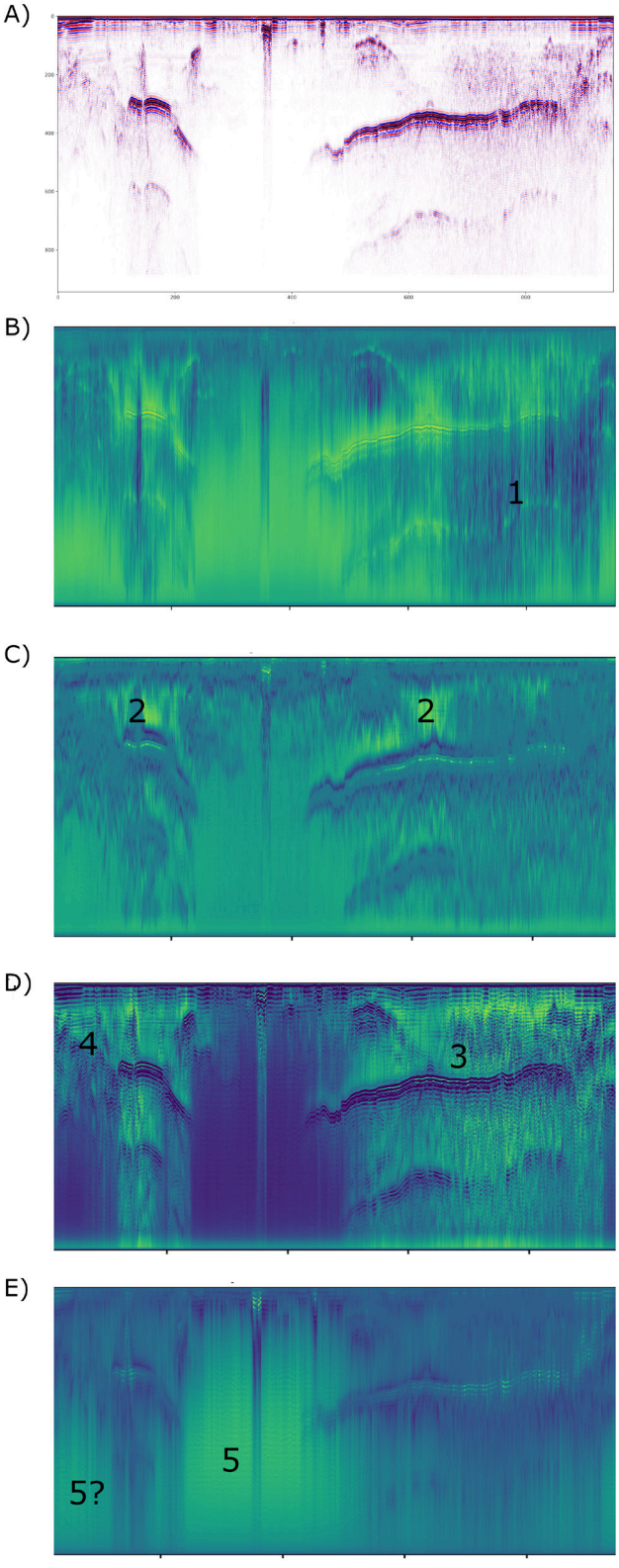


Fig. 3 - Main features resulting from Deep Attributes of interest for the GPR exemplary data used in this study: A is the input data and B-E are some related Deep Attributes. Numbers identify some features of interest, see text for details.

- Deep Attribute E: this attribute highlights very clearly the area where Forte *et al.* (2016) interpreted the salt brine overflow. An interesting feature is the area marked with "5?", which seems to have a signature quite similar to the "5" one, which is the area with brines from the cited literature.

From attribute E, we can check for other confirmations in previously descripted Deep Attributes, and we can see that the area marked with "5?" Is actually very coherent in all the other attributes.

Conclusion. In this work we propose a new approach to GPR attribute estimation. The methodology is fully data-driven and fast. This method can provide further support in data classification / analysis by exploiting features that cannot be extracted from classical approaches and that represent a new class of geophysical attributes. The new attributes lend themselves to extensive use in the interpretation of 2-D profiles or 3-D data cubes not limited to the GPR case. In fact, the proposed procedure is totally suitable for application to any type of reflection seismic data.

The way forward for this approach will be:

- Check and guarantee the method stability.
- Unlink the methodology from a specific task, e.g. from horizon extraction: this would produce more general Deep Attributes.
- Try to fully understand the link between a set of attributes and its actual physical meaning.

Acknowledgements. This research was partially supported by PNRA projects IPECA (PNRA18_00186) and CRIOVEG (PNRA18_00288) and by the project "Dipartimento di Eccellenza" of the Department of Mathematics and Geosciences of the University of Trieste. We gratefully acknowledge the support of Halliburton Landmark through the University Grants Program (UGP).

References

Anstey N., Bahorich M.S., Bridges S. R., Farmer S.L., *et al.*, 2007, *Overview of Seismic Attributes,* Geophysical Developments Series: 1-24, https://doi.org/10.1190/1.9781560801900.ch1.

Chopra S., Marfurt K.J., 2005, *Seismic attributes — A historical perspective,* Geophysics, 70, 5, 3SO-28SO, https://doi.org/10.1190/1.2098670.

Forte E.,Dalle Fratte M., Azzaro M., and Guglielmin M., 2016, *Pressurized brines in continental Antarctica as a possible analogue of Mars,* Scientific Reports, vol. 6, no. 1, p. 33158, Sep. 2016, doi: 10.1038/srep33158.

Hochreiter, S., and Schmidhuber, J., 1997, *Long short-term memory,* Neural computation, 9(8), 1735-1780, doi: 10.1162/neco.1997.9.8.1735

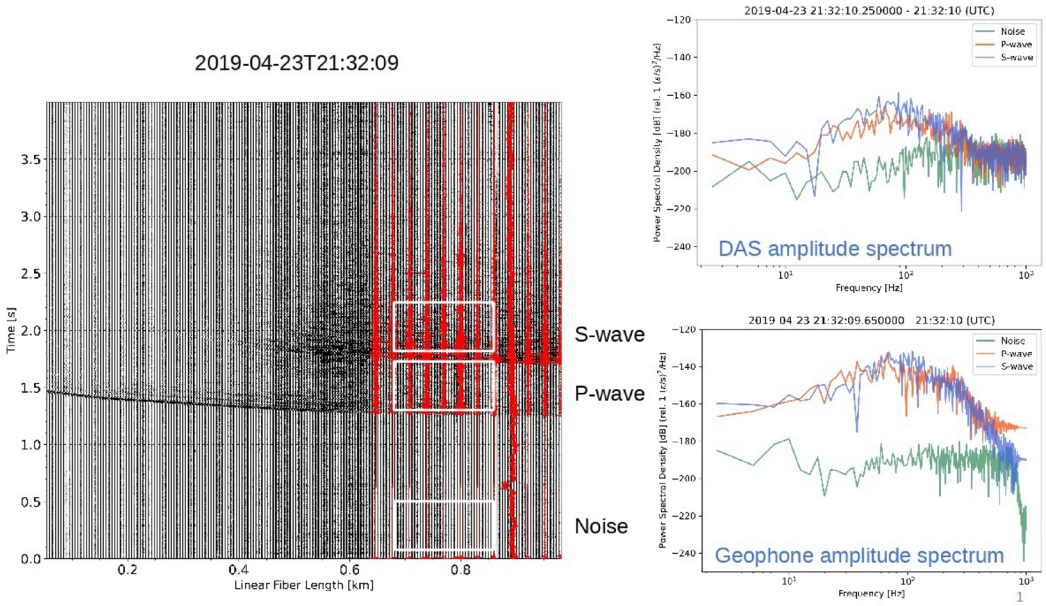
Roncoroni G., Forte E., Bortolussi L., Pipan M., 2021, *Efficient automatic extraction of seismic horizons with deep learning,* proceedings of GNGTS 2021.

A SEMBLANCE BASED MICROSEISMIC EVENT DETECTOR FOR DAS DATA

J. Porras[1], F. Grigoli[1], E. Stucchi[1], K. Tuinstra[2], A. Tognarelli[1], F. Lanza[2], M. Aleardi[1], A. Mazzotti[1], S. Wiemer[2]

[1] Department of Earth Sciences, University of Pisa, Italy
[2] Swiss Seismological Service, ETH-Zurich, Switzerlan

Distributed Acoustic Sensing (DAS) is becoming increasingly popular in microseismic monitoring operations. Fiber-optic cables such as conventional telecommunication or built-for-purpose cables can be turned into a dense array of geophones that samples seismic wavefields continuously for several kilometers. DAS is particularly interesting for microseismic monitoring of geothermal systems since it does not have the same temperature limitations as standard electronic equipment. The sensing fiber can therefore be installed at high-temperature reservoir conditions and in the same well that is being stimulated. Because of these advantages, the distance between the detecting sensor and the induced seismicity can be minimized, maximizing the detection capability. Typical DAS acquisition samples the wavefield at about 1 m spacing and sampling frequencies of 1 kHz or higher. Unfortunately, standard seismological techniques are not capable of exploiting this high spatial density of sensors, hence they are ineffective in processing this kind of data. Here we propose a semblance-based seismic event detection method that fully exploits the characteristics of the DAS data. The detection identifies seismic events by looking at waveform coherence along hyperbolas while changing the curvature and position of the vertex. The method returns a time series of coherence values and, if these values are higher than a determined threshold, it catches a seismic event. First, we test the detector with synthetic data resembling a realistic setup. Finally, we validate the detector by applying it to real DAS data from the Utah FORGE site in the US. This work is supported by the EU-Geothermica DEEP project.



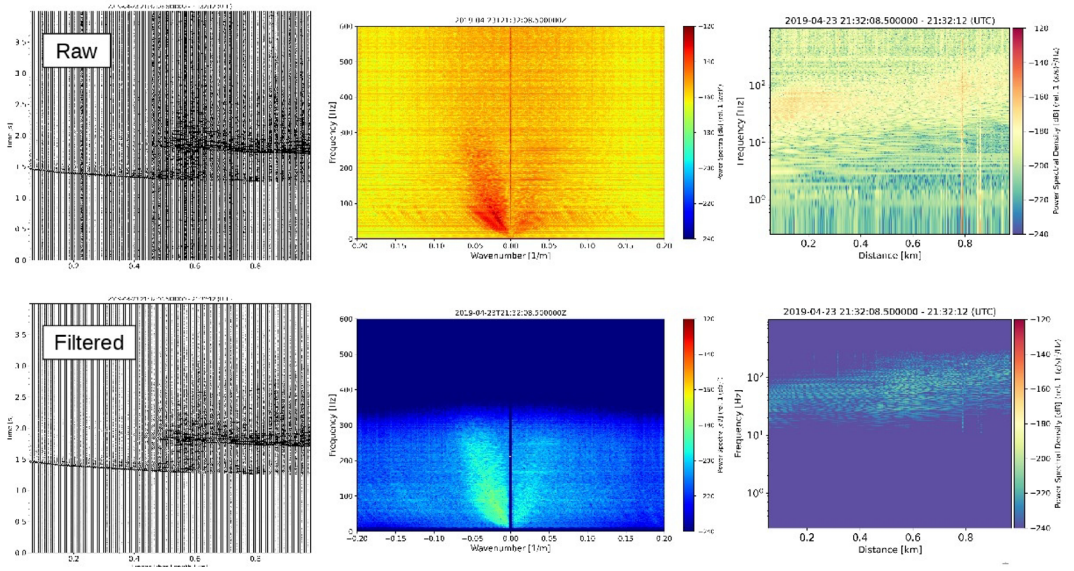


Fig. 2 - On top it is shown the raw (not filtered) dataset with its corresponding Frequency-Wavenumber (FK) spectrum and the spatial variation of the Power Spectral Density (PSD). On bottom, the same data window after a filtering work-flow which removes both the incoherent and coherent noise and its corresponding FK spectrum and PSD.

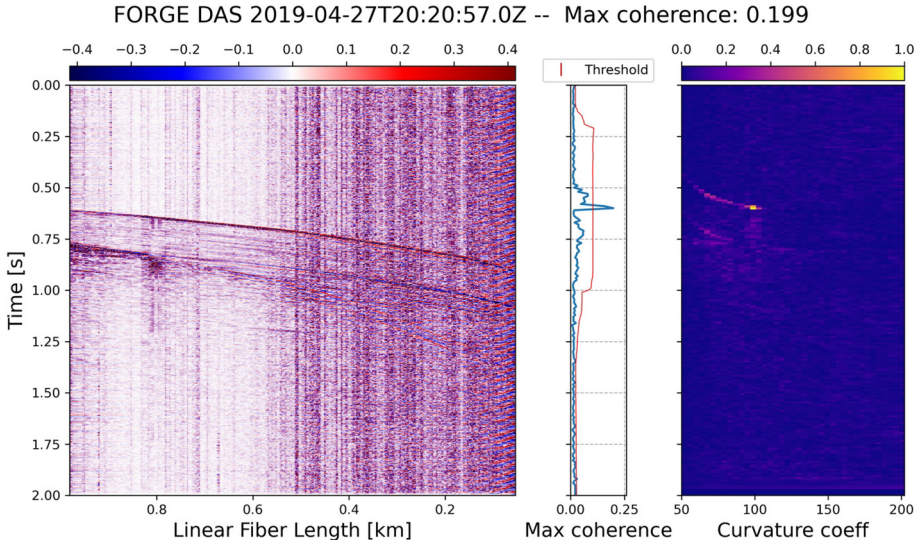


Fig. 3 - Performance of the semblance based event detector for a time window where a microseismic event was recorded. The peak in the time series coherency values that exceeds the dynamic threshold indicates the detection of the seismic event.

BAYESIAN APPROACH TO THE INVERSION OF MAGNETIC DATA FOR NEAR-SURFACE STUDIES. APPLICATION TO THE ARCHAEOLOGICAL SITE OF SAN PIETRO INFINE (SOUTHERN ITALY)

R. Salone[1], S. Tarantino[2,3], L. Spagnuolo[2], A. Frisetti[4], M. La Manna[1], A. Emolo[2], R. Di Maio[1]

[1] Dipartimento di Scienze della Terra, dell'Ambiente e delle Risorse, Università degli Studi di Napoli Federico II, Napoli, Italy
[2] Dipartimento di Fisica "Ettore Pancini", Università degli Studi di Napoli Federico II, Napoli, Italy
[3] Istituto Nazionale Di Geofisica E Vulcanologia, Aquila, Italy
[4] Dipartimento di Scienze Umanistiche, Università degli Studi Suor Orsola Benincasa, Napoli, Italy

Introduction. As it is well known, the geophysical prospecting is a key tool for addressing the archaeological research, due to its capability to identify buried archaeological features, thus allowing to plan a proper excavation work (e.g., Di Maio *et al.*, 2016; 2018). To this purpose, the inversion process of the geophysical data has a fundamental role in the accurate modelling of possible anomalies resulting from any geophysical survey. In this note, we propose a new algorithm for the 2D inversion of magnetic data, which is based on a Bayesian probabilistic approach. The effectiveness of the proposed algorithm is tested on synthetic and field magnetic data for retrieving the parameters of the anomaly causative sources. In particular, the field data come from a high-resolution magnetic survey performed in the archaeological area of San Pietro Infine (Caserta, Southern Italy) (Fig. 1a), which is considered by the archaeologists as relevant for the reconstruction of the ancient Roman settlement. In fact, this site is known since pre-classical times, as it represents the junction of a road axis controlled by the fortified walls of the neighboring areas (Zambardi, 2009). During the Roman colonization, in the 3rd century BC, the pre-existing road axis was crossed by the *Via Latina* (Zambardi, 2007), as shown by the paving stones found near Santa Maria del Piano (Fig. 1a). The church of Santa Maria probably is identifiable with the medieval building of San Pietro *in Flea* (name derived from the roman toponym "*Ad Flexum*"), mentioned by written sources as a property of Montecassino (Fabiani, 1981).

A new algorithm for 2D inversion of magnetic data. The proposed algorithm has been developed in a Bayesian probabilistic framework and validated on synthetic and real magnetic data. The basic concept is the assumption that a volume of magnetic material can be considered as a set of magnetic dipoles (Telford *et al.*, 1990), each of which generates its own anomaly. If these dipoles are aligned with each other, for example, because of induction due to an external magnetizing field, then the body may exhibit residual magnetism. The volume under consideration can therefore be considered as a continuous distribution of dipoles resulting in a dipole moment vector per unit of volume, $\vec{M}$, of intensity M, also called Magnetization Intensity. The inversion algorithm is, in fact, based on the *superposition principle*: the overall anomaly associated with the volume of magnetic material is due to the sum of the anomalies of the various dipoles present in that volume. For the computation of the forward problem, firstly the investigated volume has been discretized into cells to each of which a susceptibility contrast, $\Delta\chi$, has been associated, which represents the parameter to be explored in the inversion procedure. Since the magnetic measurements in the archaeological test area were acquired in gradiometric mode, the gradient associated with each explored section along profiles extracted by the observed 2D magnetic map was calculated and subsequently compared with the acquired data along the selected profiles.

For each possible 2D map of susceptibility, $\Delta\chi_{x_P,z_P}$, the probability density function is as below:

$$pdf\left(\Delta\chi_{x_P,z_P}\right) \propto expexp\left(-\left[G_{x_R,z_R}\left(\Delta\chi_{x_P,z_P}\right) - d_{x_R,z_R}\right]^2\right),$$

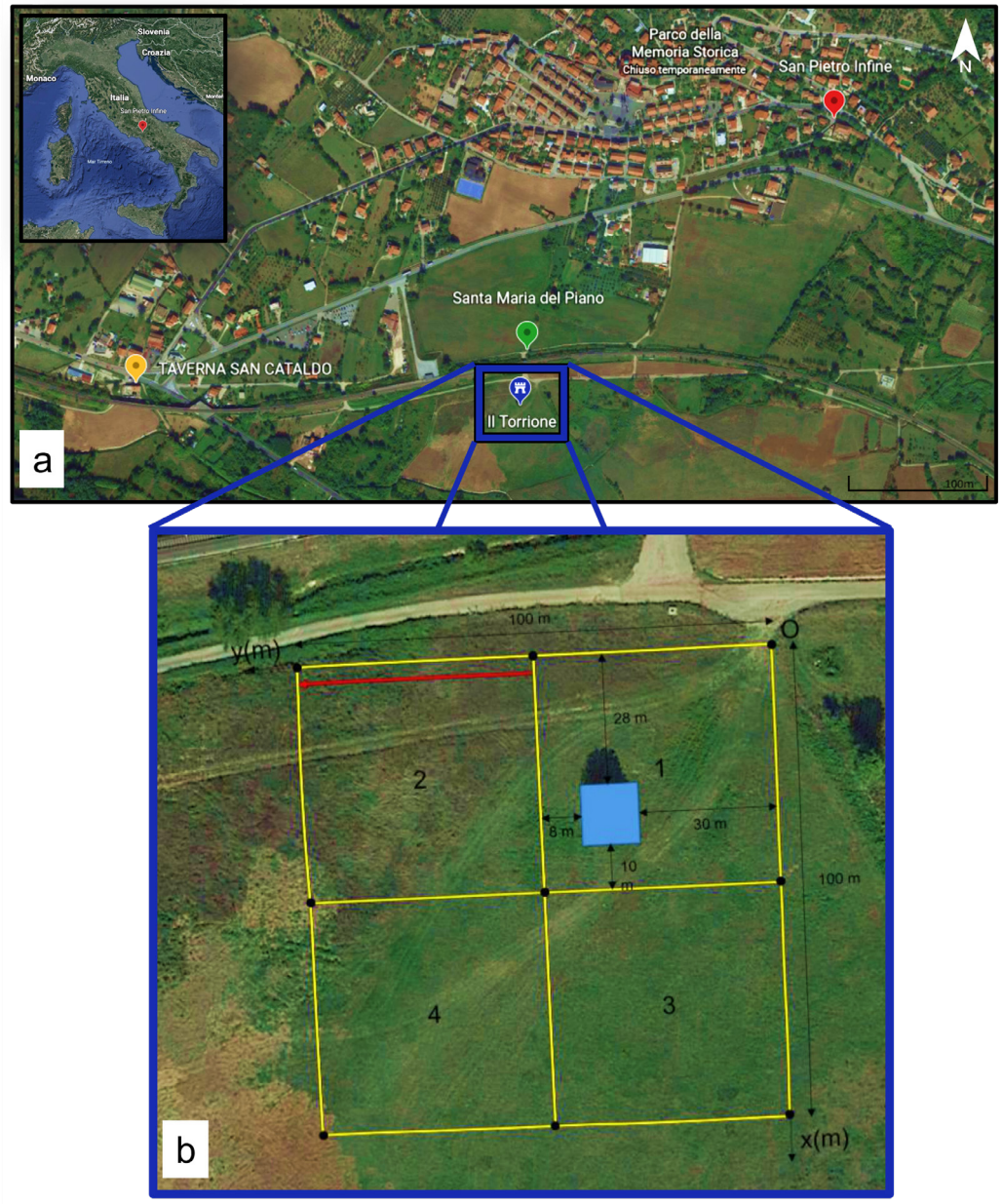


Fig. 1 - a) Google Earth geographical map of the San Pietro Infine archaeological site; b) geophysical surveys area. The yellow lines limit the four meshes where MAG, FDEM, and GPR measurements were performed. The blue square indicates the location of the ancient apse defined as *Il Torrione*.

where d_{x_R,z_R} are the data acquired on the ground surface in the positions x_R,z_R and $G_{x_R,z_R}(\Delta\chi_{x_P,z_P})$ is the theoretical gradient obtained in the positions x_R,z_R by considering the map of susceptibility $\Delta\chi_{x_P,z_P}$ for the investigated section.

The normalized probability values, associated with each magnetic susceptibility 2D map, are sorted in descending order from most likely to less likely. In a second step, the algorithm selects the most likely maps to be furtherly discretized. In particular, the algorithm identifies

the areas corresponding to the highest absolute values of $\Delta\chi$, which correspond to the areas where the dominant anomalies are found. These areas are further sampled in smaller cells and a new inversion is performed. The final map selected is the most likely map (MAP model). It is worth noting that the chosen Bayesian approach easily will allow us to extend the developed algorithm for a jointly inversion of data coming from different geophysical methods in an integrated framework.

The MAG code has been used to invert the data collected during the magnetic survey in San Pietro Infine (Southern Italy), and the obtained results are compared with the information coming from the multi-methodological geophysical prospection performed in the survey area.

Multi-methodological geophysical survey in the archeological site of San Pietro Infine (Southern Italy). Magnetic (MAG), frequency-domain electromagnetic (FDEM) and ground-penetrating radar (GPR) geophysical surveys were carried out in an area of 100×100 m^2 surrounding an outcropping building (*Il Torrione* in Fig. 1), which represents an apse belonging to a layered religious complex, identifiable with the medieval building of San Pietro *in Flea* that was founded on a roman building (probably a *statio* transformed in a *mansio*, which was a post office) (Zambardi, 2007). The geophysical prospecting was aimed at identifying anomalies in the distribution of the observed physical parameters related to the presence of remains likely attributable to both the *Sancti Petri in Flea* church and the surrounding anthropic settlement. In particular, the study area was partitioned into four meshes (Fig. 1b), each 50m×50m in size, in which the data were collected along parallel profiles east-west oriented. Data acquisition parameters were chosen according to the size of the archaeological targets to be detected (i.e., streets, fortification walls, *stationes*, etc.), whose dimensions are expected to be in the range of a few meters. In particular, as it concerns the MAG survey, a distance of 0.5 m between the profiles was selected. The magnetic data were collected by using the GSM19 Overhauser total field magnetometer (GEM System) in gradiometric configuration with two omnidirectional sensors positioned at 50 cm and 70 cm, respectively, from the surface level. Fig. 2 shows the

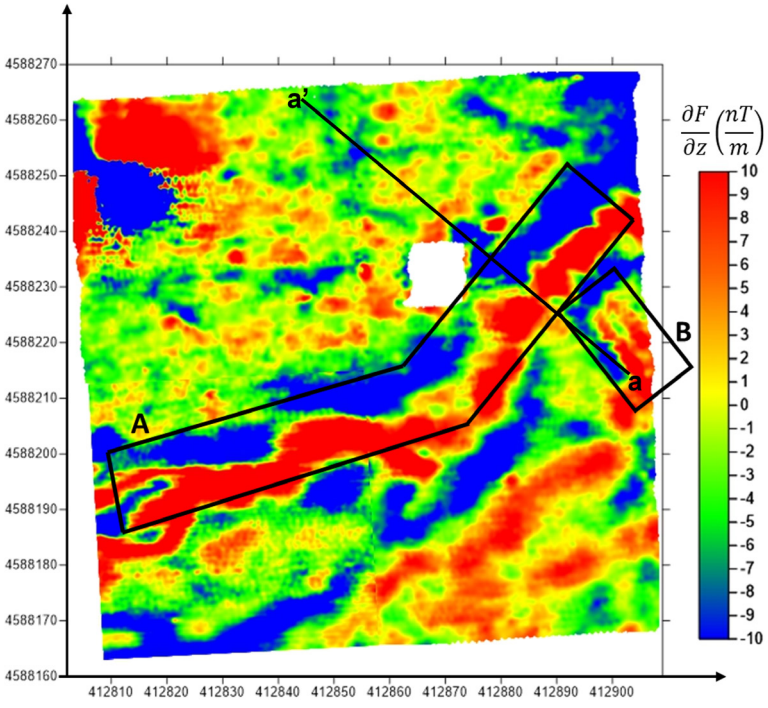


Fig. 2 - Anomaly map of the vertical magnetic gradient observed in the test area (see Fig. 1b). The black aa' line represents the inverted MAG profile.

map of the vertical magnetic gradient after the data processing. The most remarkable features emerging from the map are a long-wavelength dipolar anomaly in the central part of the investigated area (A in Fig. 2), which is elongated in the NE-SW direction and is compatible with the presence of the ancient buried Roman *Ad Flexum* road (Zambardi, 2009), and a shorter wavelength dipolar anomaly with a well-defined geometric shape probably related to the presence of a wall structure (B in Fig. 2). The relatively high number of dipolar magnetic anomalies in the northern side of a much smaller wavelength than those observed in the southern side seems to divide the investigated area into two sub-sectors: one to the north, bordering the modern road giving access to the test site, probably related to buildings (e.g., *stationes*) of an ancient urban settlement (Zambardi, 2009), and one to the south, likely used for agricultural and productive purposes given its morphological structure and proximity to the water-course.

In order to support our interpretative hypotheses, the developed inversion code has been applied to magnetic data extracted along profiles crossing the most important anomalies observed on the magnetic map of Fig. 2. As an example, Fig. 3a shows the results obtained along the aa' profile in Fig. 2, where the blue line indicates the field data, and the red line refers to the theoretical magnetic gradient obtained from the inversion and associated with the MAP model in Fig. 3b. The latter shows the presence of a structure large approximately

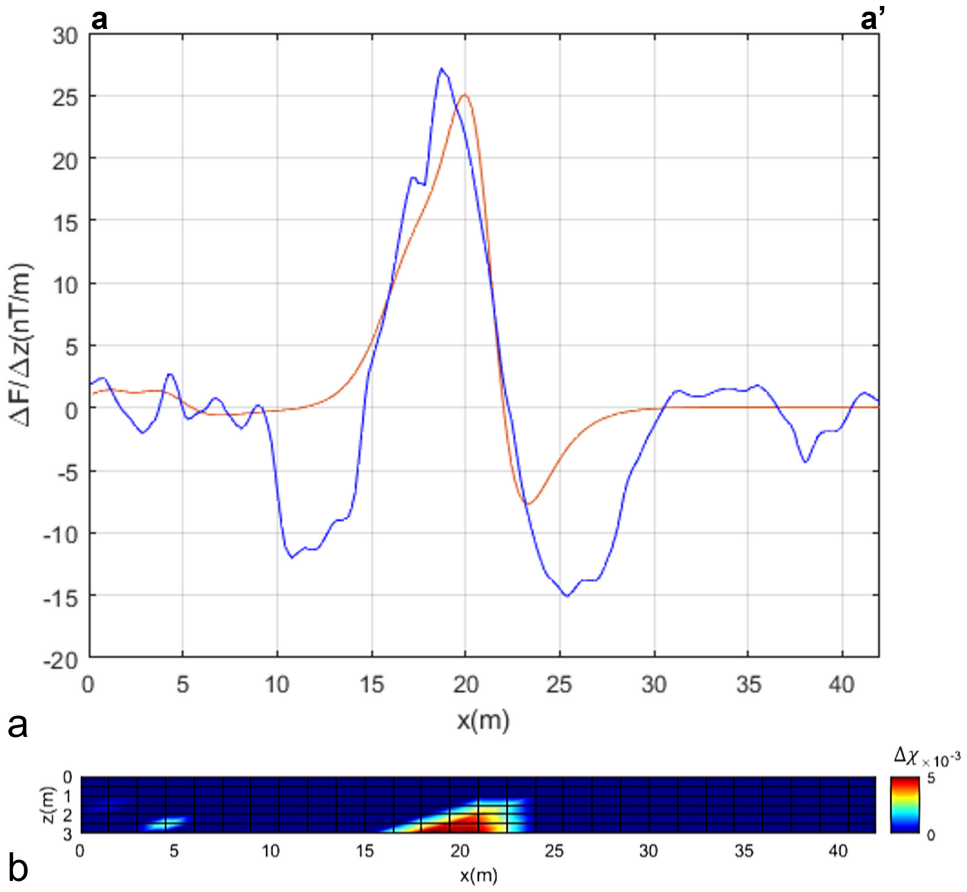


Fig. 3 - a) Comparison between the observed MAG data (blue line) and the calculated gradient (red line) associated with the final MAP model. b) Vertical section of the magnetic susceptibility contrast associated with the final MAP model.

2 m, whose top is at a depth of about 1.5 m. The magnetic susceptibility contrast, $\Delta\chi$, of the structure with respect to the hosting material is about -0.004. Size and depth of such a structure are consistent with those of a road, whose position seems to correspond with the *Ad Flexum* junction. At the same depth, it also appears a second structure characterized by size and susceptibility contrast ($\Delta\chi \approx$ -0.002) lower than that corresponding to the first structure. These findings well agree with the results of the in-phase component map coming from the FDEM survey, which shows an anomaly whose shape and orientation are compatible with the first structure derived from the magnetic data inversion. Conversely, the results from the GPR prospecting well support the characteristics of the second structure provided by the magnetic MAP model.

Conclusions. The proposed algorithm to invert magnetic data has provided reliable results in modeling magnetic anomalies of archaeological interest. In particular, its application to magnetic data acquired in the ancient roman site of San Pietro Infine has highlighted the possible presence of buried structures ascribable to ancient roads of pre-classical and/or medieval age cited in ancient sources. Our findings provide the first hints for the historical reconstruction of this archaeological area whose knowledge is still limited and not yet sufficiently explored.

References

Di Maio, R., La Manna, M., Piegari, E., 2016: *3D reconstruction of buried structures from magnetic, electromagnetic and ERT data: Example from the archaeological site of Phaistos (Crete, Greece).* Archaeological Prospection, 23, 287-299.

Di Maio, R., La Manna, M., Piegari, E., Zara, A., Bonetto, J., 2018: *Reconstruction of a Mediterranean coast archaeological site by integration of geophysical and archaeological data: the Nora town (Cagliari, Italy).* Journal of Archaeological Science: Reports 20, 230-238.

Fabiani, L., 1981: *La terra di S. Benedetto*. *Studio storico-giuridico sull'Abbazia di Montecassino dall'VIII al XIII secolo*. Vol I-II, Ed. Badia di Montecassino.

Telford, W.M., Geldart, L.P., Sheriff, R.E. 1990: *Applied Geophysics*. Cambridge University Press, pp. 770.

Zambardi, M., 2007: *La via Latina nel territorio di ad Flexum, Spigolature Aquinati, Studi storico-archeologici su Aquino e il suo territorio*. Atti della giornata di Studio-Aquino, 19 maggio 2007.

Zambardi, M., 2009: *San Pietro Infine: il sito di Ad Flexum*. Bollettino trimestrale di studi storici del Lazio meridionale 9.2.

DIX INVERSION THROUGH MACHINE LEARNING

M. Tavoletti[1,2], F. Bleibinhaus[2], F. Grigoli[1], E. Stucchi[1]

[1] University of Pisa, Earth Sciences Department, Pisa, Italy
[2] Montanuniversität Leoben, Department of Applied Geosciences and Geophysics, Leoben, Austria

Introduction. Over the past years, machine learning algorithms have been increasingly popular in geophysics (Yu and Ma, 2021) as an alternative to standard approaches.

Along this path, this work investigates the applicability of fully connected artificial neural networks (FC-ANNs; LeCun *et al.*, 2015) to solve the Dix inversion (Dix, 1955) which is known to be an ill-conditioned inverse problem. The Dix inversion is linear when considering the square of the interval velocity to be the unknown, however regularized inversion techniques are needed to tackle the ill-conditioning of this inverse problem (Koren and Ravve, 2006).

In this work we propose the use of FC-ANNs to retrieve interval velocity profiles from the root-mean-square (rms) ones while tackling the ill conditioning of the Dix Inversion.

Solving an inverse problem with machine learning corresponds to approximating the mapping done by the inverse operator given the so-called training dataset, which consists of a set of observed data (input) and the set of the correspondent model parameters (output). In the Dix inversion perspective, the input data is represented by rms velocity profiles while the correspondent blocky interval velocity profiles are the output data. One of the issues in the practical application of ANNs to approximate inverse operators, is the availability of large enough training dataset (real data). In this study we train FC-ANNs with synthetic data and then test it with a real marine seismic dataset (Line 12 of the Viking-Graben 2D marine dataset).

The method. We started generating a synthetic labelled dataset composed by 10,000 regularly sampled blocky interval velocity profiles and the corresponding rms velocity profiles. Each velocity profile was represented in the time-domain and was composed by 1,001 samples with a sampling rate of 0.001 s.

We then split the synthetic dataset in subsets of 9,000, 750, and 250 examples for the training, validation, and test datasets, respectively.

In this study, we used the 3 FC-ANNs represented in Fig. 1.

The training dataset was exploited to update the internal parameters of the FC-ANNs minimizing the L2-norm loss function for a fixed number of epochs equal to 5,000.

The validation dataset was used only to evaluate the evolution of the training phase and not to update the internal parameters of the networks. After the training phase, we used the test dataset to evaluate if the updated network parameters approximated a proper mapping between a rms velocity profile and the correspondent interval velocity profile.

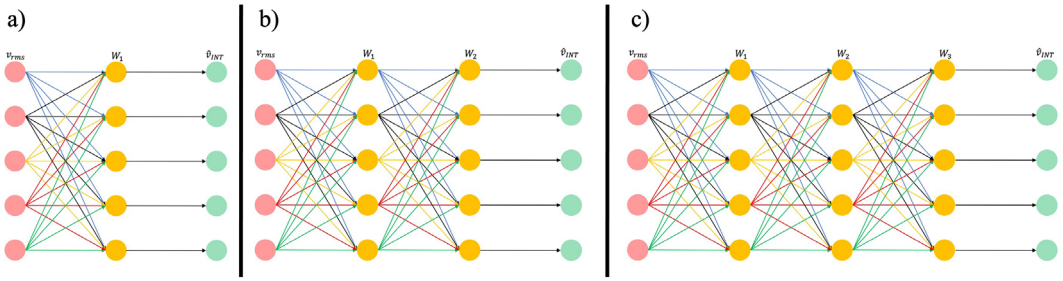


Fig. 1 - Simplified sketch of the 3 fully connected artificial neural networks (FC-ANNs) used in this work. In red the input layer, in yellow the hidden layer(s), and in green the output layer; each layer is composed by 1001 units. For simplicity, the bias terms are omitted. The FC-ANN with 1 hidden layer (a) exploits the tanh activation function. The FC-ANN with 2 hidden layers (b) exploits the ReLU and the tanh for the 1st and 2nd layer, respectively. The FC-ANN with 3 hidden layers (c) exploits the ReLU for the 1st and 2nd layer and the tanh for the 3rd layer.

Synthetic inversion tests. Initially, we trained and tested the above-mentioned architectures (Fig. 1) on synthetic noise-free data. The forward Dix operator was used to calculate the rms velocity profile corresponding to the predicted interval velocity profiles (Fig. 2).

Overall, increasing the depth of the FC-ANNs improved the performance on predicting interval velocity profiles. We expressed the accuracy in terms of the *rmse* between desired and predicted interval velocity profiles and between desired and predicted rms velocity profiles.

Despite the good performance, considering noise-free data the (finite precision) analytic Dix inversion resulted in higher accuracy than the FC-ANNs (Fig. 2). However, the application to noisy data allowed us to evaluate the capability of the FC-ANNs to tackle the ill-conditioning of the Dix inversion. In particular, the training, validation, and test rms velocity profiles were contaminated with noise vectors drawn from a gaussian distribution with mean equal to 0 km/s and standard deviation equal to 0.05 km/s.

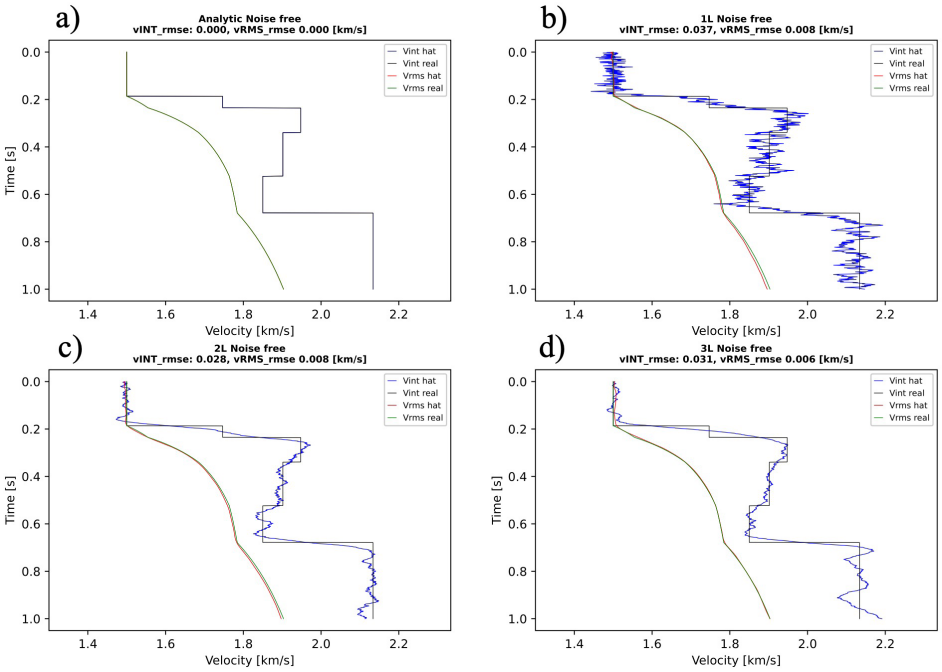


Fig. 2 - Inversion results on synthetic data from different methods: analytic solution (a), 1 hidden layer FC-ANN (b), 2 hidden layers FC-ANN (c), and the 3 hidden layers FC-ANN (d). The predicted and desired interval velocity profiles are the blue and black lines, respectively. The re-calculated and desired rms velocity profiles are the red and green lines, respectively. The *rmse* for the interval and rms velocity profiles are listed in the title of the figures.

The results showed that the deepest architecture performed better than the shallower ones, although the differences in performance were less evident than in the noise free test.

To test the robustness of the FC-ANNs with respect to the statistics governing the noise contaminating the training dataset, we contaminated the test dataset with noise realizations generated under different statistical assumptions (standard deviation equal to 0.1 km/s) and normalized to the energy of the previous noise realizations. The deepest architecture (3 hidden layers) performed better than the shallower ones in predicting the interval velocity profiles. However, the differences in performance were again less evident than in the noise free test.

Contrary to the results obtained on noise free data, FC-ANNs trained on noise contaminated inputs led to better performances than the analytic solution that in turn led to un-physical results.

According to the performance of the different FC-ANNs on both noise-free and noise contaminated synthetic data, we tested the deepest architecture on a real marine seismic dataset.

Real inversion tests. The raw data of the Line 12 of the Viking-Graben 2D marine dataset were acquired in the North Sea by Mobil Corporation and publicly released in 1994 (the dataset can be downloaded at: http://s3.amazonaws.com/open.source.geoscience/open_data/Mobil_Avo_Viking_Graben_Line_12/mobil_avo.html). These data were processed by Berti (2021) through automatic picking techniques (Toldi, 1989) aimed to retrieve the rms velocity profiles for different CMP gathers. Furthermore, Berti (2021) applied shaping regularization (Fomel, 2007) to regularize the Dix inversion and retrieve the interval velocity model for the Viking-Graben dataset.

Since automatic pickers are prone to provide erroneous estimates of the rms velocity profiles, we generated a new noise-contaminated synthetic training dataset considering the range of the Viking-Graben rms velocity model.

Inverting the automatically picked rms velocity profiles with the analytic Dix inversion resulted in an un-physical interval velocity model. It was characterized by strong lateral velocity inversions and NaN values were present on the right side of the model. Interestingly, the interval velocity model predicted by the FC-ANN was less affected by the presence of noise in the rms velocity profiles. Indeed, the strong lateral interval velocity variations were smoothed, and numerical instability did not occur. Differently, the interval velocity model obtained with shaping regularization resulted in a smooth interval velocity model.

Eventually, we compared the interval and rms velocity profiles obtained through shaping regularization and FC-ANN (Fig. 3) to analyse the difference between model-driven (shaping regularization) and data-driven (FC-ANN) techniques in tackling the ill-conditioning of the Dix inversion.

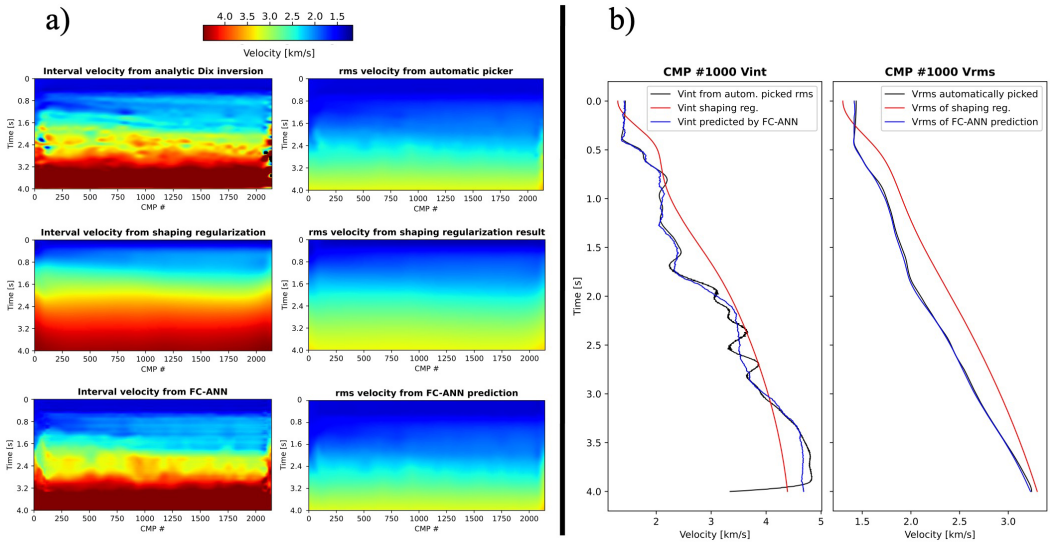


Fig. 3 - Comparison of the inversion results on the Viking-Graben dataset from different techniques. a) Panels on the left column are the interval velocity models estimated from analytic solution (top), shaping regularization (middle), and predicted by the fully connected artificial neural network (bottom); panels on the right are the corresponding rms velocity models. b) Velocity profiles extracted from the various velocity models. The left panel shows the interval velocity profiles obtained with different techniques. In black the profiles obtained with the analytic Dix inversion, in red the outcome of shaping regularization, and in blue the prediction of the FC-ANN. The right panel shows the corresponding rms velocity profiles.

This comparison highlighted that the model-driven technique was mainly driven by the *a priori* assumptions, providing less consistent solutions with the observed data (automatically picked rms velocity). Differently, the predictions obtained by the data-driven technique were governed by the statistics of the training dataset. In particular, the predicted interval velocity profiles were more blocky and less affected by noise than the ones obtained by using the analytic solution. Furthermore, the rms velocity profiles calculated from the FC-ANN predictions were consistent with those obtained with the automatic picker (Fig. 3).

Finally, we migrated the data using the interval velocity model obtained through shaping regularization and the one predicted by the FC-ANN, to fairly compare the quality of the two models. Considering the moderately complex geological setting of the Viking-Graben, we used the pre-stack Kirchhoff depth migration (PSDM) method to generate two migrated seismic sections and extract the common reflection point (CRP) gathers.

Interestingly, the focusing of the seismic sections and the analysis of the flatness of CRP gathers highlighted that the shallower portion was better imaged by the interval velocity model predicted by the FC-ANN. Differently, the deeper portion was more correctly imaged using the model obtained with shaping regularization. This difference could be related to the presence of dipping reflectors in the deeper portion of the Viking-Graben, resulting in the violation of the 1D media assumption of the Dix inversion.

Conclusions. The potentialities of fully connected artificial neural networks (FC-ANNs) in solving non-linear problems are well known and confirmed by their application in this study to solve the Dix inversion.

Considering this very simple inverse problem, a purely data-driven solution could not achieve the same accuracy as the analytic solution in case of noise-free data. Differently, training a FC-ANN on a noise-contaminated labelled dataset allowed to update the internal parameter of the architecture to attenuate the effect of noise in the inference phase. Furthermore, the FC-ANNs were robust with respect to the statistics of noise contaminating the training data.

Eventually, including realistic features and noise within the synthetic training dataset highlighted that machine learning models can be effectively applied to real cases when large amounts of labelled training data are not available.

The results of this study might be integrated with further research focused on combining machine-learning to standard inversion algorithms, exploiting regularizers learned from training datasets. Moreover, methods aimed to explain which aspects drive the predictions of a machine learning model need to be developed.

Acknowledgments. The first author would like to thank Eni S.p.A. for the opportunity to collaborate with the AESI Department. In particular, Doctor Bienati Nicola is gratefully acknowledged for his assistance and supervision during the development of this work. Seismic data migration was performed using the PROMAX® software of Halliburton/Landmark, which is gratefully acknowledged.

References

Berti S.; 2021: *Full wavefield velocity analysis and imaging on a 2D marine dataset.* M.Sc. Thesis in Exploration and Applied Geophysics, University of Pisa (IT).

Dix, C. H.; 1955: *Seismic velocities from surface measurements.* Geophysics, 20(1), 68-86.

Fomel S.; 2007: *Shaping regularization in geophysical-estimation problems.* Geophysics, 72(2), R29-R36.

Koren Z. and Ravve I.; 2006: *Constrained Dix inversion.* Geophysics, 71(6), R113-R130.

LeCun Y., Bengio Y. and Hinton G.; 2015: *Deep Learning.* Nature, 521, 436-444.

Toldi J.A.; 1989: *Velocity analysis without picking.* Geophysics, *54(2)*, 191-199.

Yu S. and Ma J.; 2021: *Deep Learning for Geophysics: Current and Future Trends.* Reviews of Geophysics, 59(3). DOI: 10.1029/2021RG000742.

DEFINING THE BEST PROCESSING PROCEDURE FOR THE EVALUATION OF SEISMO-ELECTROMAGNETIC SIGNALS (SES) MEASURED DURING AN ACTIVE SEISMIC EXPERIMENT

I. Ventola[1], G. Romano[1], A. Siniscalchi[1], M. Balasco[2], S. Tripaldi[1]

[1] Dipartimento di Scienze della Terra e Geoambientali, Università degli Studi di Bari Aldo Moro, Italy
[2] CNR - Istituto di Metodologie per l'Analisi Ambientale, Potenza, Italy

Seismic-electromagnetic signals (SES) consist of transient electromagnetic signals that originate in response to a mechanical perturbation in the subsoil (Gao and Hu, 2010).

Several mechanisms have been proposed in order to explain the phenomenology (e.g. Thompson and Gist, 1993; Pride, 1994; Haarsten and Pride, 1996; Honkura *et al.,* 2004; Gao and Hu, 2010). In all cases it is attributed to the interaction between elastic waves and porous media containing fluids, which play a key-role in the generation of these signals and influence their features. The study of SES could thus be a useful tool for characterizing the subsoil and, in a broader scenario, could provide clues about the role of fluids in the generation of earthquakes (Romano *et al.*, 2018).

In the literature referring to the last two decades, studies reporting the observation of such signals in association with seismic phenomena are increasingly frequent (e.g. Matsushima *et al.*, 2002; Zlotnicki *et al.*, 2006; Johnston *et al.*, 2006, Balasco *et al.*, 2014, Balasco *et al.*, 2015). However, there are no ad-hoc instruments for their detection, and they are generally recorded accidentally during surveys using magnetotelluric (e.g. Balasco *et al.*, 2014), a geophysical method that acquires natural electromagnetic fields to characterize the subsoil in terms of electrical properties.

In this case, the generated transients are added to the signal due to the natural electromagnetic field which varies over time. When this last is particularly intense, it is difficult to recognize these contributions generated by the passage of seismic waves.

In this study we present the results arising out of the analysis of seismic-electromagnetic signals recorded during an active seismic experiment carried out in the Solfatara crater (Campi Flegrei, Southern Italy). We analyzed data collected during the RICEN (Repeated InduCed Earthquakes and Noise) campaign where were performed a two-dimensional active seismic profile with NNE-SSW direction and a three-dimensional active seismic experiment on a dense regular grid of 90 m × 115 m (Serra *et al.*, 2016). The vibroseis truck was the seismic source and the electromagnetic field was acquired by placing three magnetotelluric stations close to the experiments mentioned above.

With the aim of extracting as much information as possible from SES has been necessary to isolate them, minimizing the background variability of the MT signal as well as removing the effects of the seismic source.

First, we applied a frequency deconvolution to remove the instrumental response; then we evaluated the spectra of the natural electromagnetic field comparing the signals of two different stations. In the absence of SES, these spectra were similar, permitting the subtraction in the frequency domain. The correspondent signal in time was then analyzed with typical seismic approaches like vibroseis deconvolution (Brittle *et al.*, 2001).

Finally, for each shot the Green's function was estimated.

References

Balasco, M., Lapenna, V., Romano, G., Siniscalchi, A., Stabile, T., & Telesca, L. (2014). Electric and magnetic field changes observed during a seismic swarm in Pollino area (southern Italy). *Bull. Seismol. Soc. Am., 104*, 1289-1298.

Balasco, M., Lapenna, V., Romano, G., Siniscalchi, A., Stabile, T., & Telesca, L. (2015). The Pollino 429 2011-2012 seismic swarm (southern Italy): first results of the ML=3.6 aftershock recorded by co- 430 located electromagnetic and seismic stations. *Bolletino di Geofisica Teorica e Applicata Vol. 56, n.2*, 203-2010.

Brittle, K.F., Lines, L.R., & Dey, A.K. (2001). Vibroseis deconvolution. *European Association of Geoscientist & Engineers, Geophysical Prospecting*, 49, 675-686.

Gao, Y., & Hu, H. (2010). Seismoelectromagnetic waves radiated by a double couple source in a saturated porous medium. *Geophys. J. Int., 181*, 873–896.

Haarsten, M., & Pride, S. (1997). Electroseismic waves from point sources in layered media. *J.geophys. Res. 102*, 24 745–24 769.

Honkura, Y., Satoh, H., & Ujihara, N. (2004). Seismo dynamo effects associated with the M 7.1 earthquake of 26 May 2003 off Miyagi Prefecture and the M 6.4 earthquake of 26 July 2003 in northern Miyagi Prefecture, NE Japan. *Earth Planets Space 56*, 109-114.

Johnston, M., Sasai, Y., Egbert, G., & Mueller, R. (2006). Seismomagnetic effects from the long- awaited 28 September 2004 M 6.0 Parkfield earthquake. *Bull. Seismol. Soc. Am. 96, no. 4B*, S206–S220.

Matsushima, M., Honkura, Y., Oshiman, N., Baris, S., Tuncer, M., Cerik, C., . . . Isikara, M. (2002). Seimoelectromagnetic effect associated with the Izmit earthquake and its aftershocks. *Bull. 470 Seismol. Soc. Am. 92*, 350-360.

Pride, S. (1994). Governing equations for the coupled electromagnetics and acoustics of porous media. *Phys. Rev. B 50*, 15,678–15,696.

Romano, G., Balasco, M., Siniscalchi, A., Pastoressa, A., & Lapenna, V. (2018). Robust analysis for the characterization of the seismo-electromagnetic signals observed in Southern Italy. *ANNALS OF GEOPHYSICS, 61*, Doi: 10.4401/ag-7811.

Serra, M, Festa, G., Roux, P., Gresse, M., Vandemeulebrouck, J., & Zollo, A. (2016). A strongly heterogeneous hydrothermal area imaged by surface waves: the case of Solfatara, Campi Flegrei, Italy. *Geophysical Journal Internation Advance Access*.

Thompson, A., & Gist, G. (1993). Geophysical applications of electrokinetic conversion. *The Leading Edge 12*, 1169-1173.

Zlotcnicki, J., Le Mouel, J., Kanwar, R., Yvetot, P., Vargemezis, G., Menny, P., & Fauquet, F. (2006). Ground-based electromagnetic studies combined with remote sensing based on Demeter mission: A way to monitor active faults and volcanoes. *Planet Space Sci. 54*, 541-557.

A STOCHASTIC ENSEMBLE BASED APPROACH FOR TIME-LAPSE ERT INVERSION

A. Vinciguerra[1,2], M. Aleardi[2], L. Meldgaard Madsen[3], T.S. Bording[4], A.V. Christiansen[3], E. Stucchi[2]

[1] Università di Firenze, Dipartimento di Scienze della Terra, Firenze, Italy
[2] Università di Pisa, Dipartimento di Scienze della Terra, Pisa, Italy
[3] Hydrogeophysics Group, Department of Geoscience, Aarhus University
[4] Aarhus GeoInstruments

Introduction. The investigation of the subsurface has becoming of increasing interest to mitigate environmental risks. The development of Electrical Resistivity Tomography (ERT) monitoring station systems has triggered the application of Time-Lapse ERT technique to detect the resistivity variations in time. Indeed, the resistivity change can be associated with subsurface processes such as groundwater recharge (Descloitres *et al.*, 2018) and aquifer contamination (Maurya *et al.*, 2017). The ERT data inversion is an ill-posed, non-linear problem that it is usually solved through a deterministic least-square algorithms. Nevertheless, this approach is prone to get stuck in local minima of the error function. A strategy to tackle this issue is to apply stochastic inversion algorithms that consider the model parameters as random variables and the subsurface model as a realisation of a probability density function. However, the main drawback of this approach is the computational burden related to the several forward model evaluations needed to sample the parameter space (Vinciguerra *et al.*, 2022). The Ensemble Based (EB) algorithm is an iterative data assimilation method that assimilates the observed data multiple times with an inflated covariance matrix (Aleardi *et al.*, 2021). The result of this algorithm is an ensemble of realisations from which an approximation of the posterior probability density function (ppd) can be numerically assessed. This algorithm requires less computational time compared to standard Monte Carlo Markov Chain algorithms due to the lower number of forward modelling runs to estimate the ppd. (Aleardi *et al.*, 2021). Nowadays, there exists different Time-Lapse inversion strategies: independent approach in which the data are inverted independently; the cascaded inversion, in which the inversion result of the first dataset is considered as starting model of the second dataset (Miller *et al.*, 2008); or strategies such as the difference inversion that attenuate the effects of the systematic error during the acquisition (Labreque *et al.*, 2001). To perform a Time-Lapse inversion, we rearrange the EB algorithm to obtain the posterior mean model, its variation in time and the uncertainties affecting the solution. In this work, we apply the Time-Lapse EB algorithm to field data acquired by a landfill monitoring station in Pillemark (Samsø, Denmark).

Methods. The aim of the conventional Ensemble Based algorithm is to recover the posterior uncertainties. This algorithm has been validated for the 2.5D ERT tomography case (see Aleardi *et al.*, 2021 for details). In this work, we modify that inversion framework making it suitable for Time-Lapse ERT intent. Let ρ_0 be the subsurface resistivity at the initial time, t_0, ρ_1 the subsurface resistivity at the second time $t_1 = t_0 + \Delta t$ and $\Delta\rho$ the resistivity variation, the problem is formulated as follows:

$$\Delta\rho = \rho_1/\rho_0 = \{(1, \infty) \text{ if } \rho_0 < \rho_1 \text{ resistivity increment } 1 \text{ if } \rho_0 = \rho_1 \text{ no variation } (0, 1) \text{ if } \rho_0 > \rho_1 \text{ resistivity reduction} \quad (1)$$

$$G(m) = G[(\rho_0;\ \rho_0 \cdot \Delta\rho\ )] = [d_0\ \ d_1] \quad (2)$$

Where G represents the forward operator, m is the model vector, d_0 and d_1 are the observed data at t_0 and t_1 respectively; note that the unknowns of the problem are ρ_0 and $\Delta\rho$. Parametrizing the resistivity variation as the ratio between ρ_0 and $\Delta\rho$ implies two different resolutions when the resistivity increases or decreases. It is evident from Equation 1 that when the resistivity increases from t_0 to t_1 the $\Delta\rho$ range is wide (1, ∞), whereas when the resistivity decreases the $\Delta\rho$ values are in the range (0, 1). The definition of $\Delta\rho$ has been chosen

to better solve the increase of resistivity in time. The implemented Time-Lapse EB approach starts with two ensembles of prior realisations of ρ_0 and $\Delta\rho$ which are iteratively updated on the basis of the difference between observed and predicted data. The final output is two ensembles of posterior models from which the standard deviation can be assessed. However, when the means are strongly different from one to another, the standard deviations are not easily comparable. To overcome this issue that could affect the uncertainties interpretation, we calculate the coefficient of variation:

$$cv_i = \frac{\sigma_i}{\mu_i} \times 100 \tag{3}$$

Where the index i is the i-th cell of the model, σ_i is the associated standard deviation, and ρ_i is the mean resistivity value of the i-th cell. The outcomes of the implemented algorithm are benchmarked against the results of a cascaded inversion (Miller *et al.*, 2008), which is a deterministic least-square approach in which the inverted ρ_0 is used as starting model to invert for ρ_1.

Application to field data. The field data that we employ in this work refer to Pillemark landfill monitoring station in Samsø island (Denmark), in which the aim is to supervise the aquifer to assess the pollution risk (Høyer *et al.*, 2019). The geology of the site consists of a layer of fill over a sand stratum of various thicknesses in which an aquifer is flowing, and a second aquifer underlies a thick layer of moraine clay. Due to the vertical resolution and penetration depth limit, we will focus on the shallow aquifer. The data are acquired using the Terrameter LS instrument employing a Gradient and Dipole-Dipole configuration with 22 electrodes and 4 meters spacing. From the database we select two data (d_0 and d_1) acquired after one year, 27th March 2016 and 28th March of 2017 respectively, to attenuate the seasonal effect on resistivity variation (Figure 1a-b). After the processing step the two datasets consist of 336 data points each. The subsurface is discretised with an unstructured mesh employing the pyGIMLI (Rücker *et al.,* 2017) software package and the forward problem is solved by the open-source BERT software (Günther *et al.,* 2006). The Time-Lapse EB algorithm inversion starts with two

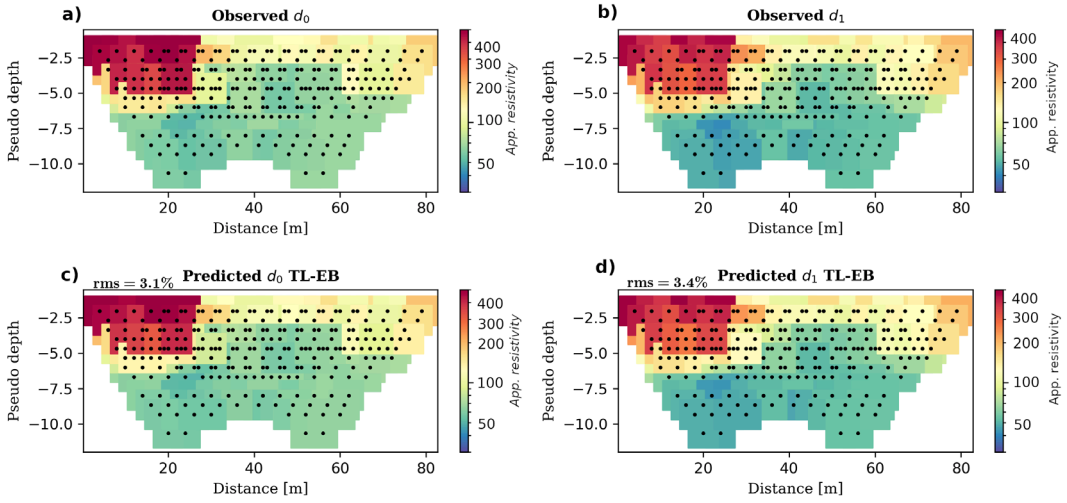


Fig. 1 - a) Observed data on 27th March 2016. b) Observed data on 28th March 2017. c) Predicted data d_0 computed on the posterior mean model ρ_0 and the corresponding rms error. d) Predicted data d_1 computed on the posterior mean model ρ_1 and the corresponding rms error. The black dots represent the points of the pseudosection.

ensembles of 2000 prior realisations drawn from a log-gaussian prior distribution associated with ρ_0 and $\Delta\rho$. The total computational time of 7 iterations is 109 minutes on an Intel Core i7-8700 CPU @ 3.20GHz. The predicted data computed on the posterior mean models are shown in Figure 1c-d. We observe that the observed data d_0 and d_1 are well matched by the predicted pseudo sections, with satisfying rms errors of 3.1% and 3.4% respectively. The mean posterior model ρ_0 (Figure 2a) shows a high resistivity layer with a decreasing thickness moving from left to right. This layer might be interpreted as the shallow layer of dry sand and fill. Underneath this first layer it appears a sub-horizontal low resistivity anomaly which could be associated the sandy aquifer; the resistivity values of about 50 $\Omega \cdot m$ indicates an unsaturated aquifer. Below this zone, the model shows high and low resistivity anomalies that could correspond to the moraine clay. The mean posterior variation, $\Delta\rho$ (Figure 2b), exhibits an evident high ratio value between 16 and 19 meters of elevation that indicates an increase of resistivity from t_0 to t_1. This variation could be explained as a decrease of the saturation of the aquifer in time. At the moraine clay depth, a negative variation seems to indicate a decrease in resistivity. To better understand the features of the subsurface at the time t_1 the resistivity model ρ_1 is calculated using Equation 1 (Figure 2c). To compare the results of our approach, we invert the same datasets using a deterministic least-square Occam's algorithm in which the inverted model at the time t_0 is used as starting model of the inversion of at time t_1 (cascaded inversion, Figure 2d-e-f). The estimated ρ_0 shows the same features of the Time-Lapse EB result with minor differences only in the deeper part of the model where the low data illumination decreases the accuracy of the results . Furthermore, the variation computed by the ratio between ρ_1 and ρ_0 shows the same anomalies previously observed on the posterior mean $\Delta\rho$ model , especially between 19 and 16 meters of elevation. In this field data inversion, the posterior mean models as estimated by the EB inversion and the predictions of the cascaded approach

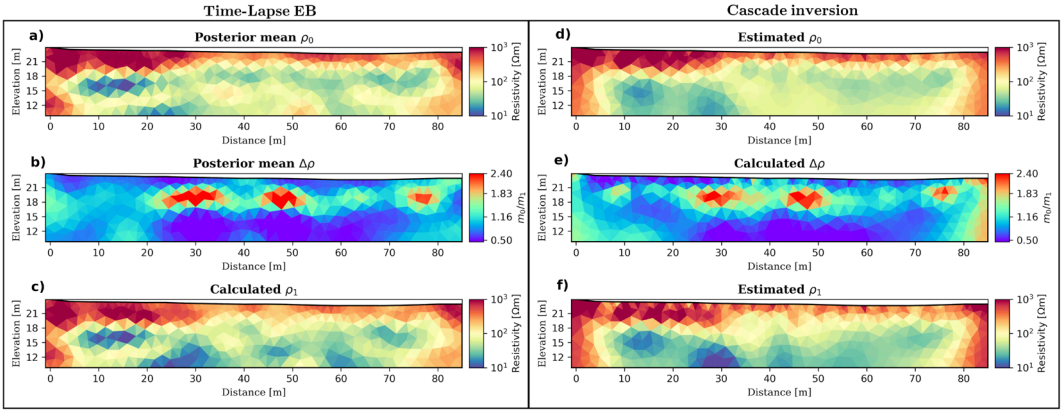


Fig. 2 - a) Posterior mean model ρ_0. b) Posterior mean resistivity variation $\Delta\rho$. c) ρ_1 computed from ρ_0 and $\Delta\rho$. d) Estimated ρ_0 with the deterministic Occam's algorithm. e) Variation obtained from Equation 1. f) Estimated model using the Cascaded Inversion approach.

produce comparable data predictions, with similar rms errors. However, differently from the cascaded inversion, the EB approach also provides information on the uncertainties affecting the solution. As illustrated in Figure 3a-b the coefficient of variations allows to assess the reliability of the recovered subsurface resistivity: we observe high uncertainties at the lateral edge and at the bottom of the study area where the *cv* percentage is almost 50% (Figure 3a) and 25% (Figure 3b). As expected, the largest uncertainties are associated with parameters poorly informed by the observations, thus meaning that in this part of the subsurface model multiple combinations of resistivity values equally reproduce the measured apparent resistivities.

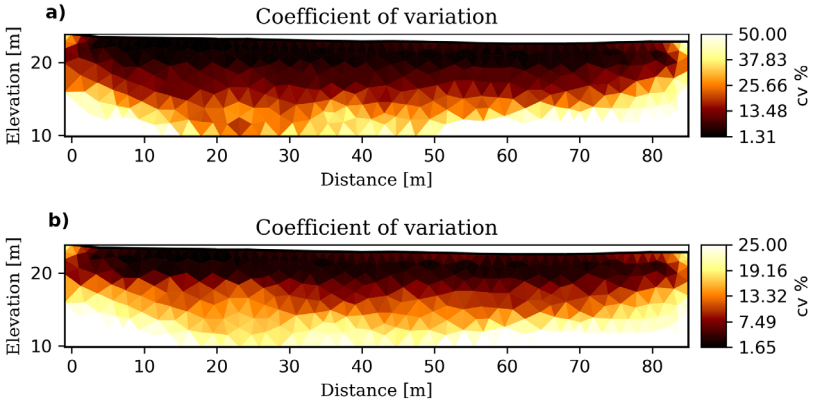


Figure 3. a) Coefficient of variation associated with ρ_0. b) Coefficient of variation associated with $\Delta\rho$.

Conclusion. In this work, we implemented a Time-Lapse EB algorithm to invert TL-ERT data for monitoring purposes. This stochastic approach provides ensemble of posterior realisations pertaining to both the resistivity model at t_0 and the resistivity variation in time. From this ensemble of models, the uncertainties on the retrieved solution can be numerically assessed. Thus, the main advantage of our approach is the assessment of the statistical properties of the inverse problem solution. Due to the broad range of the subsurface resistivity, we evaluate the uncertainties through the coefficient of variation which is independent on the order of magnitude of the mean. The application to Pillemark field data demonstrates the reliability of the Time-Lapse EB in detecting the resistivity variation in time with a satisfying data prediction. The mean posterior variation of resistivity allows to identify the change in aquifer saturation in time. In addition, the retrieved uncertainties provide meaningful information about the low sensitivity side of the model. The comparison with the cascaded inversion confirms the reliability of the estimated posterior mean models. The next step of our research is to apply the algorithm to other monitoring sites and to compare it with other approaches.

References

Aleardi M., Vinciguerra A., and Hojat A.; 2021: *Ensemble-Based Electrical Resistivity Tomography with Data and Model Space Compression.* Pure and Applied Geophysics, **178**, 1781–1803.

Descloitres M., Ruiz L., Sekhar M., Legchenko A., Braun J.J., Mohan Kumar M.S., and Subramanian S.; 2008: *Characterization of seasonal local recharge using electrical resistivity tomography and magnetic resonance sounding.* Hydrological Processes, **22**(3), 384–394.

Günther T., Rücker C., and Spitzer K.; 2006: *Three-dimensional modelling and inversion of dc resistivity data incorporating topography - II. Inversion.* Geophysical Journal International, 166(2), 506-517.

Høyer A.S., Klint K., Fiandaca G., Maurya P., Christiansen A., Balbarini N., Bjerg P., Hansen T., and Møller I.; 2019: *Development of a high-resolution 3D geological model for landfill leachate risk assessment.* Engineering Geology, **249**, 45–59.

Labreque D.J. and Yang X.; *Difference inversion of ERT data: a fast inversion method for 3-D in-situ monitoring.* Environ. Eng. Geophys. 2001, **6**, 83-89.

Maurya P.K., Rønde V.K., Fiandaca G., Balbarini N., Auken E., Bjerg P.L. and Christiansen A.V.; 2017: *Detailed landfill leachate plume mapping using 2D and 3D electrical resistivity tomography - with correlation to ionic strength measured in screens.* Journal of Applied Geophysics, **138**, 1-8.

Miller C.R., Routh P.S., Brosten T.R. and McNamara J.P.; 2008: *Application of time-lapse ERT imaging to watershed characterization.* Geophysics **73**, G7–G17.

Rücker C., Günther T. and Wagner F.M.; 2017: *pyGIMLi: An open-source library for modelling and inversion in geophysics.* Computers and Geosciences, **109**, 106–123.

Vinciguerra A., Aleardi M., Hojat A., Loke M.H. and Stucchi E.; 2022: *Discrete Cosine Transform for Parameter Space Reduction in Bayesian Electrical Resistivity Tomography.* Geophysical Prospecting, **70**, 193-209.

UTILIZZO DI TECNICHE DI INTERFEROMETRIA TERRESTRE PER IL COLLAUDO DEL PONTE SAN GIORGIO DI GENOVA

S. Candela, C. Case, M. Cardamone, D. Fiore, F. Mittiga

[1] SOCOTEC Italia S.r.l., Lainate (Milano), Italy

Introduzione. Sul nuovo ponte autostradale di scavalcamento del fiume Polcevera, presso Genova, sono state condotte una serie di prove di carico statico per il collaudo finale dell'opera. La suddetta verifica è stata eseguita attraverso l'ausilio della tecnica interferometrica per la lettura degli step intermedi e per la verifica dell'avvenuta stabilizzazione dell'impalcato sotto carico, al fine di accelerare l'inizio delle letture ottiche. La tecnica utilizzata permette di valutare lo spostamento della deformata della struttura sotto sforzo in tempo reale

Come esempio viene riportata la prova

- *MOMENTO POSITIVO PR2-PR3*, la prova di carico statico si è svolta procedendo al caricamento della struttura con automezzi pesanti a 4 SPMT, secondo la seguente configurazione:
  - Primo-step di carico 2 SPMT del peso di 131 tonnellate circa.
  - Secondo-step di carico 4 SPMT del peso di 131 tonnellate circa.
- *TEST DINAMICA P6/7* eseguito utilizzando il passaggio dei camion diretti sulla P10 per la prova di momento negativo.

Metodo. L'Interferometria Radar Terrestre (TInRAR) è una tecnica di telerilevamento attraverso la quale è possibile misurare simultaneamente gli spostamenti di numerosi punti di edifici, strutture o altri elementi antropici e naturali, con elevate frequenze di campionamento del dato, consentendo di eseguire contestualmente sia analisi statiche che dinamiche (misura delle vibrazioni). Tale misura viene eseguita completamente in remoto, ovvero senza l'installazione di altri sensori o riflettori a contatto con la struttura, sfruttando pertanto la naturale riflettività alle microonde degli elementi presenti nello scenario irradiato. In particolare, il sensore TInRAR è costituito da un radar interferometrico ad apertura reale "coerente" (in grado quindi di emettere impulsi radar a lunghezza d'onda nota), dotato di una o più antenne emittenti e riceventi. La tecnica interferometrica consente il calcolo degli spostamenti lungo la linea di vista strumento-scenario (LOS), attraverso il confronto delle informazioni di fase dell'onda elettromagnetica emessa e riflessa a differenti intervalli temporali. Lo spostamento è quindi calcolato, simultaneamente, su un elevato numero di punti della struttura, attraverso la relazione fondamentale:

$$d = -\frac{\lambda}{4\pi} \bullet \Delta\varphi$$

Tramite analisi interferometrica differenziale, il sistema fornisce, nella stessa sessione di acquisizione, misure dello spostamento di una struttura sotto l'azione di carichi sia statici che dinamici senza che sia necessario interromperne l'esercizio. Operando a distanza, tale sistema è l'unico in grado di monitorare in tempo reale situazioni di emergenza e di potenziale pericolo, senza necessità di installazione fisica di sensori sulla struttura, il terreno o il sito. Nell'interferometria terrestre l'apertura sintetica (Curlander and McDonough, 1991) viene riprodotta attraverso un sensore radar che emette e riceve un segnale, con frequenza nel campo delle microonde, attraverso apposite antenne. La misurazione dello spostamento (d) dell'oggetto in esame è derivata dalla variazione di fase (Δϕ) misurata dal sensore radar nei vari momenti di acquisizione. Lo spostamento e la variazione di fase sono legate dalla seguente relazione:

$$d \propto \varphi_2 - \varphi_1$$

L'area investita dal fascio d'onda radar viene discretizzata in celle di risoluzione "monodimensionali" nella direzione di range (ovvero lungo la linea di vista strumentale), quindi per ogni cella di risoluzione è possibile ricavare due parametri fondamentali:

1. Ampiezza: fornisce informazioni in merito alla capacità dei target naturalmente presenti nello scenario investigato di riflettere le onde radar;
2. Fase: consente di eseguire misure di spostamento attraverso il confronto tra acquisizioni eseguite a diversi intervalli temporali.

Oggetti ricadenti all'interno della medesima cella di risoluzione non sono pertanto discriminabili e contribuiscono ad un unico contributo di riflessione.

Strumentazione utilizzata. Il sistema IBIS utilizza interferometria per misurare gli spostamenti della struttura che viene illuminata dal fascio elettromagnetico emesso dalle antenne: la testa radar emette una serie di onde elettromagnetiche per tutta la durata della misurazione e ad intervalli regolari ed elaborando le informazioni di fase, è in grado di registrare ogni spostamento che avviene tra una trasmissione e la successiva. Il sistema IBIS–FS è composto da un modulo sensore (un sensore elettromagnetico che si basa sulla tecnica di funzionamento Stepped Frequency – Continuous Wave), deputato alla generazione, trasmissione e ricezione del segnale elettromagnetico, il quale è installato su un treppiede dedicato, provvisto di una testa di movimentazione che consente di orientare il sensore nella direzione voluta. Tale modulo presenta una interfaccia USB per il collegamento a un PC di controllo. Tramite il PC di controllo è possibile configurare i parametri della acquisizione, gestire la misura e visualizzare i primi risultati in real-time. Questa tecnica permette al sistema IBIS-FS di ottenere un'immagine unidimensionale dello scenario di interesse con elevata risoluzione, grazie alla trasmissione di una serie di onde elettromagnetiche (Continuous Wave) di lunga durata a diverse frequenze (Stepped Frequency). Usando questa tecnica, il sistema IBIS-FS può raggiungere una risoluzione in distanza di 50 cm indipendentemente dalla distanza massima misurabile: la risoluzione dell'immagine nella direzione della struttura investigata (risoluzione in distanza a terra) dipende successivamente dall'angolo di vista del sensore rispetto alla struttura.

Nella configurazione IBIS-FS, la tecnica SF-CW permette al sistema di ottenere un un'immagine tridimensionale dello scenario di illuminazione, come mostrato in Fig.4. La dimensione della risposta della gamma bin-ennesima consiste nella risposta dell'intero parte della sfera inclusa nel cono (fascio d'antenna) ed è limitata dalla distanza

$n \bullet \Delta r$ e $(n + 1) \bullet \Delta r$

La risposta ottenuta dal IBIS sistema FS per ogni intervallo bin contiene due tipi di informazioni:

- Ampiezza del segnale di eco, legata alla riflettività dello scenario nell'intervallo bin;
- Fase del segnale di eco, legata alla distanza tra il sensore e la gamma bin.

Se è presente in un bersaglio con una riflettività molto superiore rispetto ad altri, è possibile affermare che le informazioni dei range bin (ampiezza e fase) riguardano il bersaglio con la più alta riflettività.

È importante sottolineare che il sistema IBIS può misurare spostamenti nella direzione di vista del sistema (direzione radiale), cioè lo spostamento nella direzione che unisce il sistema IBIS e il RANGE BIN nella quale l'immagine radar è stata risolta.

Come mostrato in Fig.1, il sistema IBIS-FS misura lo spostamento (dr) (spostamento radiale), da cui lo spostamento reale del punto, d, si può trovare facendo alcune considerazioni geometriche:

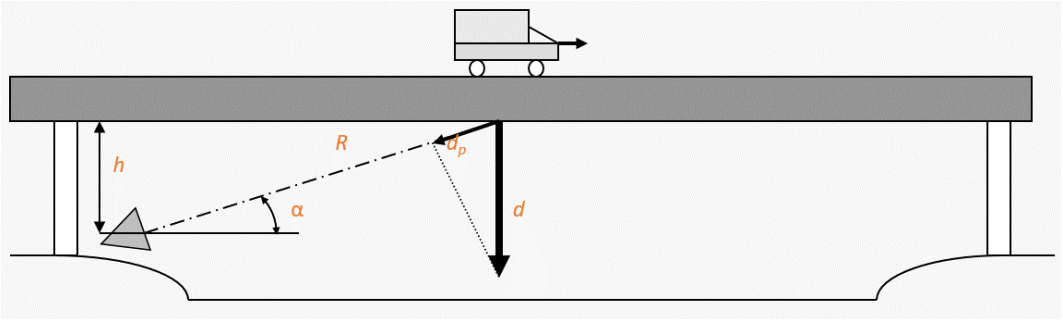


Fig. 1 - Spostamento radiale e spostamento reale.

dr = *d* • *sin* (*α*), tuttavia, poiché h = *R* • *sin* (*α*) si ottiene:

$$d = d_r \frac{R}{h}$$

Il sistema IBIS-FS misura contemporaneamente lo spostamento radiale di tutti i pixel o del range bin della zona illuminata dal fascio dell'antenna. I valori di spostamento misurati con la tecnica interferometrica (ossia il confronto delle fasi di due immagini distinte) ha una precisione che dipende dall'intensità del eco radar registrato per ogni singolo intervallo di bin determinato (in un caso dimensionale) o pixel (caso bidimensionale), o meglio, la precisione dipende dal rapporto segnale-rumore del punto considerato.

La precisione teorica dello strumento può essere sottile come un millesimo di millimetro.

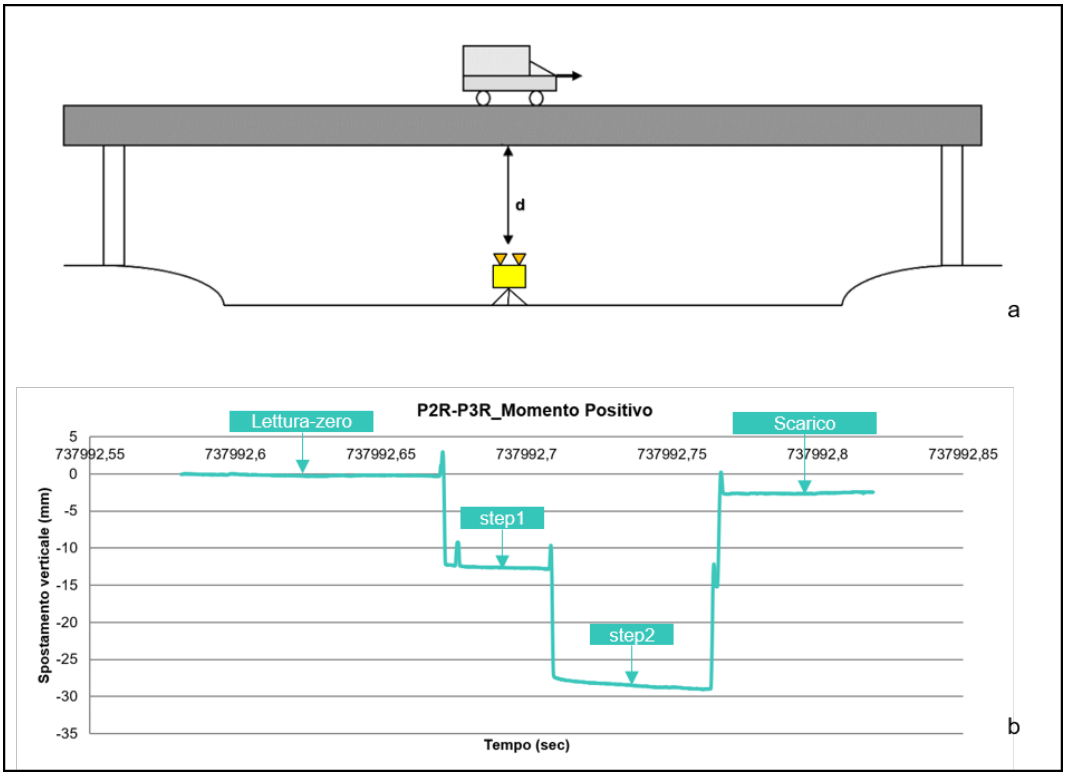


Fig. 2 - Geometria di acquisizione (a); grafico della lettura degli spostamenti (b).

Per ovvie ragioni pratiche, questa precisione non è mai effettivamente possibile durante campagne di misura, ma in ogni caso una precisione di 0.1 millimetri è facilmente raggiungibile. La distanza massima osservabile è 1 km sia in modalità statica che dinamica di monitoraggio. In teoria, non ci sono limiti alla distanza massima osservabile. Tutto dipende dalla modalità di propagazione delle onde elettromagnetiche, che riducono la densità di potenza con il quadrato della distanza percorsa. Ciò significa che più ci avviciniamo al sensore e minore è il rapporto segnale-rumore dei segnali ricevuti. Di conseguenza, la precisione di misurazione si riduce fino ad arrivare a pochi millimetri. Da un punto di vista operativo, questo significa che la distanza massima osservabile dipende dalla riflettività dello scenario. In realtà, la risposta della struttura può essere migliorata installando riflettori artificiali (corner) punti specifici da monitorare. Ciò migliora il rapporto segnale rumore dovuto alla migliore riflettività del bersaglio.

Metodologia di indagine e analisi dei dati. *Momento positivo.* Le indagini sono state condotte con 1 sistema IBIS-FS posizionato a 90° al centro della luce della campata investigata (Fig.2a) (campata 2_ PR2-PR3) in modo tale da investigare la mezzeria della campata.

La strumentazione utilizzata registra in continuo gli spostamenti nell'arco di tempo considerato necessario alla stabilizzazione dei carichi e dello scarico della struttura. In particolare al fine di garantire l'affidabilità delle misure è stato scelto un intervallo di campionamento di 5 secondi.

L'elaborazione fornisce una panoramica degli spostamenti del viadotto relativi alle fasi principali di carico e scarico. Per quanto concerne le tre configurazioni di carico (Fig.2b), sono state eseguite applicando alla struttura un sovraccarico costituito da automezzi pesanti a quattro assi, secondo lo schema riportato di seguito:

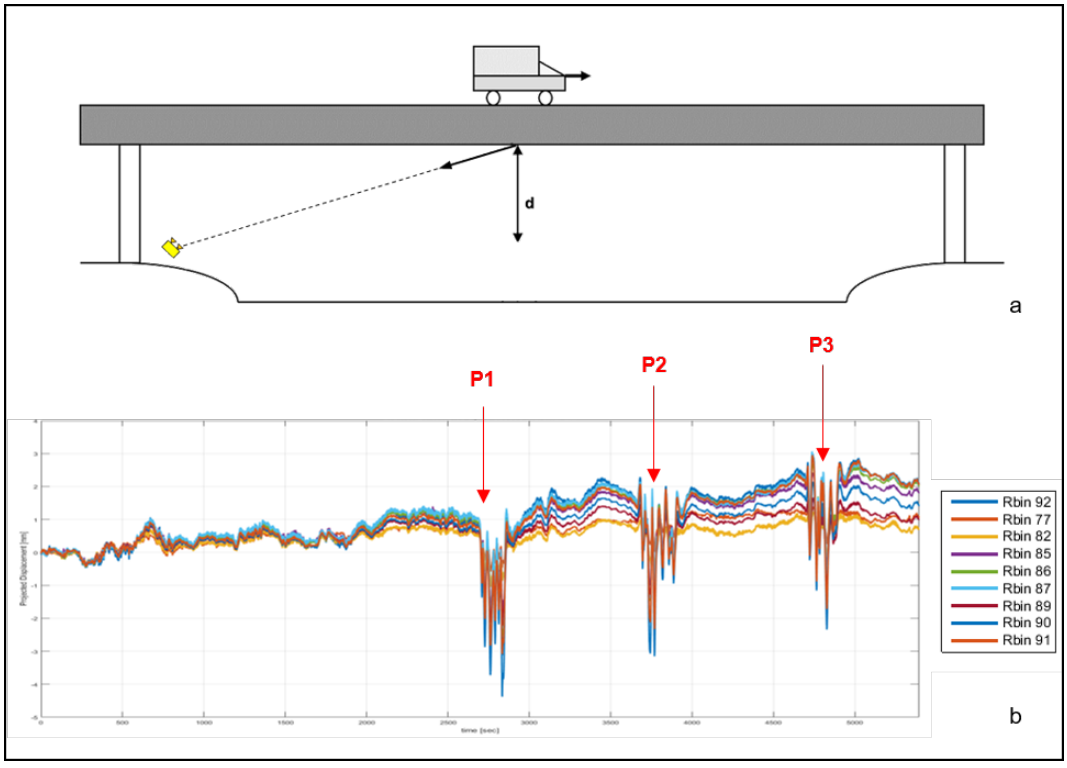


Fig. 3 - Geometria di acquisizione (a); grafico della lettura degli spostamenti (b).

LETTURA DI ZERO – ponte scarico;
1° step: LETTURA CON 2 SPMT AUTOCARRI;
2° step: LETTURA CON 4 SPMT AUTOCARRI;
LETTURA DI SCARICO – successiva alla rimozione completa degli SPMT.

Test dinamica P6/7. La strumentazione utilizzata registra in continuo gli spostamenti nell'arco di tempo considerato necessario alla stabilizzazione della struttura in termini di carico e scarico. Al fine di garantire l'affidabilità delle misure per il test è stata scelta una frequenza di campionamento pari a 100 Hz. L'elaborazione fornisce una panoramica degli spostamenti relativi del viadotto durante le fasi di transito degli automezzi pesanti a 4 assi. Va specificato che essendo un test sono stati utilizzati i camion transitanti sul viadotto per la prova di carico, quindi non si ha un reale controllo sulla velocità e sulle possibili manovre e frenature eseguite durante il passaggio, per questo motivo gli spostamenti e frequenze registrate non sono da considerarsi indicative della struttura. L' indagine è stata eseguita con 1 sistema IBIS-FS posizionato con un angolo di circa 47° in modo tale da investigare la luce della campata 6 (Fig.3a). In questo modo è stato possibile rilevare lo spostamento di nove punti lungo la direzione di vista dello strumento.

Bibliografia

Curlander J.C. and McDonough R.N.; 1991: *Synthetic aperture radar*. Wiley, 11.